CYSENI

The 15th International Conference of Young Scientists on Energy Issues

(CYSENI 2018)

23-25 May 2018

Kaunas, Lithuania

Organized by

LITHUANIAN
ENERGY
INSTITUTE

Chair of the Scientific Committee dr. Sigitas Rimkevičius

Chair of the Organizing Committee Vytautas Akstinas

Sponsors:

AB KAUNO ENERGIJA

CHARLOT

GVT

EUROfusion

REO Investment

A Member of The Linde Group | AGA

In cooperation with:

C-Energy2020

H I A

BEA

KAUNAS

INTERNATIONAL SCIENTIFIC COMMITTEE

Aleksandrs Ļvovs	Latvia	Mantas Marčiukaitis	Lithuania
Andres Siirde	Estonia	Namejs Zeltins	Latvia
Andris Kreslins	Latvia	Pierre-Etienne Labeau	Belgium
Anton Brin	Belarus	Panos M. Pardalos	USA
Alessandro Petruzzi	Italy	Ralf Ebinghaus	Germany
Bernhard Peters	Luxemburg	Sten Bergstrom	Sweden
Bjørn C. Hauback	Norway	Sigitas Rimkevičius	Lithuania
Darius Milčius	Lithuania	Sergej Zhdanok	Belarus
Enn Mellikov	Estonia	Svetlana Danilova-Tretiak	Belarus
Eugenijus Ušpuras	Lithuania	Victor A. Zhovyansky	Ukraine
Finn Ravndal	Norway	Vaclovas Miškinis	Lithuania
Florentin Paladi	Moldova	Virginijus Radziukynas	Lithuania
Luis E. Herranz	Spain	Vytautas Martinaitis	Lithuania
Myriam Lazard	France		

The Board of Reviewers was formed from the experts in the field of the Conference topics.

Board of Reviewers

Aleksandras Iljinas	Lithuania
Alessandro Petruzzi	Italy
Algirdas Gulbinas	Lithuania
Algirdas Jasinskas	Lithuania
Algirdas Maknickas	Lithuania
Alvyra Šlepetienė	Lithuania
Andres Siirde	Estonia
Andrius Jonaitis	Lithuania
Andrius Tamošiūnas	Lithuania
Andris Kreslins	Latvia
Anupras Šlančiauskas	Lithuania
Artur Rogoža	Lithuania
Antanas Kavolynas	Lithuania
Antanas Markevičius	Lithuania
Anton Brin	Belarus
Arturas Klementavičius	Lithuania
Artūras Šmaižys	Lithuania
Artjoms Obushevs	Switzerland
Arvaidas Galdikas	Lithuania
Arvydas Adomavičius	Lithuania
Arvydas Galinis	Lithuania
Asta Malakauskaitė	Lithuania
Asta Narkūnienė	Lithuania
Audrius Dėdelė	Lithuania
Audrius Jonaitis	Lithuania
Aurimas Lisauskas	Lithuania
Aurimas Tonkūnas	Lithuania
Aušra Pažėraitė	Lithuania
Benediktas Čėsna	Lithuania
Bernhard Peters	Luxemburg
Bjørn C. Hauback	Norway
Brigita Abakevičienė	Lithuania
Dainius Martuzevičius	Lithuania
Dainius Vaičiulis	Lithuania
Dalia Grigaliūnienė	Lithuania
Dalia Jankūnaitė	Lithuania
Dalia Štreimikienė	Lithuania
Dalius Tarvydas	Lithuania
Danas Ridikas	Lithuania
Danutė Vaičiukynienė	Lithuania
Kristina Ukvalbergienė	Lithuania
Lina Ragelienė	Lithuania
Linas Miknius	Lithuania
Linas Paukštaitis	Lithuania
Liudvikas Pranevičius	Lithuania
Liutauras Marcinauskas	Lithuania
Luis E. Herranz	Spain
Mantas Marčiukaitis	Lithuania
Marija Eidukevičiūtė	Lithuania
Marijus Šeporaitis	Lithuania
Martynas Lelis	Lithuania
Mindaugas Jakubčionis	Lithuania
Mindaugas Krakauskas	Lithuania
Mindaugas Milieška	Lithuania
Mindaugas Vaišnoras	Lithuania
Mindaugas Valinčius	Lithuania
Myriam Lazard	France
Namejs Zeltins	Latvia
Narimantas Listopadskis	Lithuania
Nerijus Pedišius	Lithuania
Nerijus Striūgas	Lithuania
Panos M. Pardalos	USA
Pierre-Etienne Labeau	Belgium
Povilas Krasauskas	Lithuania
Pranas Kuzas	Lithuania
Pranas Mierauskas	Lithuania
Raimondas Bliūdžius	Lithuania
Raimondas Pabarčius	Lithuania
Ralf Ebinghaus	Germany
Raminta Skvorčinskienė	Lithuania
Ramūnas Gatautis	Lithuania
Rasa Paleckienė	Lithuania
Reda Čerapaitė-Trušinskienė	Lithuania
Regina Kalpokaitė-Dičkuvienė	Lithuania
Renaldas Raišutis	Lithuania
Ričardas Krikštolaitis	Lithuania
Rimantas Pranas Deksnys	Lithuania
Rimantas Levinskas	Lithuania
Rita Plukienė	Lithuania
Robertas Alzbutas	Lithuania

Darius Albrektas	Lithuania
Darius Biekša	Lithuania
Darius Milčius	Lithuania
Darius Virbukas	Lithuania
Diana Adlienė	Lithuania
Diana Meilutytė-Lukauskienė	Lithuania
Diana Šarauskienė	Lithuania
Egidijus Norvaiša	Lithuania
Egidijus Saulius Juodis	Lithuania
Egidijus Urbonavičius	Lithuania
Eglė Biekšienė	Lithuania
Eglė Jaraminienė	Lithuania
Enn Mellikov	Estonia
Ernestas Narkūnas	Lithuania
Eugenija Farida Dzenajavičienė	Lithuania
Eugenijus Perednis	Lithuania
Eugenijus Ušpuras	Lithuania
Farida Dzenajavičienė	Lithuania
Feliksas Zinevičius	Lithuania
Finn Ravndal	Norway
Florentin Paladi	Moldova
Gediminas Stankūnas	Lithuania
Gediminas Vasiliauskas	Lithuania
Gediminas Vilkevičius	Lithuania
Giedrė Streckienė	Lithuania
Giedrius Laukaitis	Lithuania
Giedrius Šiupšinskas	Lithuania
Gintautas Dundulis	Lithuania
Gintautas Miliauskas	Lithuania
Gvidonas Labeckas	Lithuania
Grigorijus Duškesas	Lithuania
Inga Konstantinavičiūtė	Lithuania
Inga Radžiūnienė	Lithuania
Inga Stasiulaitienė	Lithuania
Inga Valuntienė	Lithuania
Irina Kliopova	Lithuania
Iveta Varnagirytė-Kabašinskienė	Lithuania
Jolanta Dvarionienė	Lithuania
Jonas Baltrušaitis	USA
Juozas Gudzinskas	Lithuania
Jūratė Karbauskaitė	Lithuania
Jūratė Kriaučiūnienė	Lithuania
Robertas Navakas	Lithuania
Robertas Poškas	Lithuania
Rolandas Jonynas	Lithuania
Rolandas Paulauskas	Lithuania
Rolandas Urbonas	Lithuania
Romualdas Kėželis	Lithuania
Romualdas Škėma	Lithuania
Saulė Milčiuvienė	Lithuania
Sergej Zhdanok	Belarus
Sigitas Kadiša	Lithuania
Sigitas Masaitis	Lithuania
Sigitas Rimkevičius	Lithuania
Simona Tučkutė	Lithuania
Stanislovas Vrubliauskas	Lithuania
Stasys Šinkūnas	Lithuania
Sten Bergstrom	Sweden
Svetlana Danilova Tretiak	Belarus
Šarūnas Varnagiris	Lithuania
Tadas Kaliatka	Lithuania
Tomas Deveikis	Lithuania
Tomas Sabonis	Lithuania
Vaclovas Kveselis	Lithuania
Vaclovas Miškinis	Lithuania
Vaidas Matuzas	Lithuania
Valdas Girdauskas	Lithuania
Valdas Ragaišis	Lithuania
Valentinas Klevas	Lithuania
Victor A. Zhovyansky	Ukraine
Vidas Lekavičius	Lithuania
Viktorija Bobinaitė	Lithuania
Viktorija Grigaitienė	Lithuania
Viktorija Mimaitė	Lithuania
Vilma Čipinytė	Lithuania
Violeta Makarevičienė	Lithuania
Violeta Pukelienė	Lithuania
Violeta Vaitkevičienė	Lithuania
Virginijus Radziukynas	Lithuania
Virginijus Vileiniškis	Lithuania
Vitas Valinčius	Lithuania
Vykintas Šuksteris	Lithuania
Vytautas Abromaitis	Lithuania
Vytautas Liesionis	Lithuania

Jurij Tonkonogij	Lithuania	Vytautas Grigas	Lithuania
Justas Kažys	Lithuania	Vytautas Martinaitis	Lithuania
Karolina Čepurnienė	Lithuania	Vytautas Stankus	Lithuania
Karolis Gedvilas	Lithuania	Vytis Kopustinskas	Lithuania
Kęstutis Buinevičius	Lithuania	Vladislovas Algirdas Katinas	Lithuania
Kęstutis Čiuprinskas	Lithuania	Žaneta Simanavičienė	Lithuania
Kęstutis Navickas	Lithuania	Žaneta Stasiškienė	Lithuania
Kęstutis Valančius	Lithuania	Žilvinas Nakutis	Lithuania
Kęstutis Venslauskas	Lithuania	Živilė Rutkūnienė	Lithuania
Kristina Brinkienė	Lithuania	Žydrė Kadžiulienė	Lithuania
Kristina Bočkutė	Lithuania		

Dear Colleagues,

We are delighted to see you here in the 15th anniversary CYSENI 2018 conference. Series of this annual conference are focused on energy issues and its wide interpretation. Providing good solutions to our energy sector and sustainable usage of natural resources require interdisciplinary approach, hence this criterion is well fulfilled in this conference. The conference once again has brought together young researchers and scientists to discuss recent trends in energy sector worldwide.

Findings of cost-effective and acceptable methods to improve energy sector in Europe and worldwide are key future targets. Generally, energy covers a wide spectrum of scientific directions with their certain problems and unsolved issues. This calls for high-quality researches and deeper knowledge.

CYSENI 2018 will present recent scientific progress from many areas related to energy issues. In total over 70 research papers were submitted from 17 countries, most of them came not just from Lithuania, but also from many foreign countries – Austria, Belarus, China, Estonia, Finland, Hungary, Italy, Kazakhstan, Latvia, Poland, Russia, Spain, Sweden, Taiwan, Turkey and Ukraine. These contributions have been set to over fifteen scientific sessions covering the conference main theme on energy issues.

We thank all the contributors who made this conference possible. This includes all persons from scientific and organising committees. We also thank all the authors who submitted their research papers. Moreover, special thanks go to four keynote speakers – Tony Donne, Francesco Comiti, Justus Oldenburg and Michael LaBelle. The funding from all the sponsors is well acknowledged and appreciated, therefore once more we would like to thank our main sponsors: Kauno energija, Soil Remediation Technologies, EUROfusion, CHARLOT, REO investment, AGA and cooperation partner Kaunas City Municipality.

Sigitas Rimkevičius
Chair of the scientific committee
Lithuanian Energy Institute

Vytautas Akstinas
Chair of the organizing committee
Lithuanian Energy Institute

CONTENT

KEYNOTE SESSION (4)

I. RENEWABLE ENERGY SOURCES (25)

II ENERGY EFFICIENCY AND RELIABILITY (3)

III SMART ENERGY NETWORKS (1)

IV ENERGY ECONOMICS AND POLICY (6)

V HYDROGEN ENERGY AND FUEL CELL TECHNOLOGIES (1)

VI FUSION ENERGY (3)

VII NUCLEAR FISSION AND RADIATION PROTECTION (5)

VIII COMBUSTION AND PLASMA PROCESSES (9)

IX THERMAL PHYSICS, FLUID MECHANICS AND METROLOGY (6)

X MATERIALS SCIENCES AND TECHNOLOGY (14)

XI GLOBAL CHANGE AND ECOSYSTEMS (3)

THE EUROPEAN ROADMAP TOWARDS FUSION ELECTRICITY

Tony Donné
EUROfusion
Boltzmannstrasse 2, 85748 Garching – Germany
Email: tony.donne@euro-fusion.org

ABSTRACT

The European Roadmap to the realisation of fusion energy breaks the quest for fusion energy into eight missions. For each mission, it reviews the current status of research, identifies open issues, proposes a research and development programme and estimates the required resources. It points out the needs to intensify industrial involvement and to seek all opportunities for collaboration outside Europe.

A long-term perspective on fusion is mandatory since Europe has a leading position in this field and major expectations have grown in other ITER parties on fusion as a sustainable and secure energy source. The roadmap covers three periods: The short term which is roughly until 2030, the medium term until 2040 and the long term.

ITER is the key facility of the roadmap as it is expected to achieve most of the important milestones on the path to fusion power. Thus, the vast majority of resources proposed in the short term are dedicated to ITER and its accompanying experiments. The medium term is focussed on taking ITER into operation and bringing it to full power, as well as on preparing the construction of a demonstration power plant DEMO, which will for the first time supply fusion electricity to the grid. Building and operating DEMO is the subject of the last roadmap phase: the long term. It might be clear that the Fusion Roadmap is tightly connected to the ITER schedule. A number of key milestones are the first operation of ITER (presently foreseen in 2025), the start of the DT operation foreseen in 2035 and reaching the full performance at which the thermal fusion power is 10 times the power put in to the plasma.

DEMO will provide first electricity to the grid. The Engineering Design Activity will start a few years after the first ITER plasma, while the start of the construction phase will be a few years after ITER reaches full performance. In this way ITER can give viable input to the design and development of DEMO. Because the neutron fluence in DEMO will be much higher than in ITER (atoms in the plasma facing components of DEMO will undergo 50-100 displacements during the full operation life time, compared to only 1 displacement in ITER), it is important to develop and validate materials that can handle these very high neutron loads. For the testing of the materials a dedicated 14 MeV neutron source is needed. This DEMO Oriented Neutron Source (DONES) is therefore an important facility to support the fusion roadmap

The presentation will focus on the strategy behind the fusion roadmap and will describe the major challenges that need to be tackled on the road towards fusion electricity. Encouraging recent results will be given to demonstrate the outcome of the focused approach in European fusion research.

Keywords: Nuclear Fusion, ITER, DEMO

CYSENI 2018, May 23-25, Kaunas, Lithuania
ISSN 1822-7554, www.cyseni.com

HYDROPOWER IMPACTS ON RIVER SYSTEMS: THE HYDROMORPHOLOGICAL APPROACH

Francesco Comiti
Free University of Bozen-Bolzano
Piazza Università 5, 39100 Bolzano – Italy
Email: Francesco.Comiti@unibz.it

Barbara Belletti
Polytechnic University of Milan
Via Ponzio 34/5, 20133 Milan – Italy

Martina Bussettini
Italian Institute for Environmental Protection and Research
Via Vitaliano Brancati 48, 00144 Roma – Italy

Massimo Rinaldi
University of Florence
Via Gino Capponi 3r, 50121 Florence – Italy

Paolo Vezza
Polytechnic University of Turin
Corso Duca degli Abruzzi 24, 10129 Turin – Italy

ABSTRACT

Hydropower represents a very relevant source of renewable energy in many countries worldwide but it brings about important negative consequences for river ecosystems, and thus it must be carefully planned and managed to avoid severe environmental consequences. Beside determining obstacles for aquatic fauna (dams and weirs), hydropower exploitation may cause dramatic changes in the hydromorphological conditions of rivers, i.e. water and sediment fluxes, morphological and vegetation characteristics, habitat types and abundance.

The assessment of stream hydromorphological conditions is required for the classification and monitoring of water bodies by the Water Framework Directive 2000/60, and is useful for establishing links between physical and biological conditions. The spatial scale of geomorphic units and related smaller units (hydraulic, river elements) are the most appropriate for defining these links, since geomorphic units represent the template for physical habitats. Geomorphic units (e.g. riffles, pools, islands, etc.) constitute distinct habitats for aquatic fauna and flora, and geomorphic and hydraulic units are generally associated with the mesohabitat or biotope scale. To clarify concepts and linkages between disciplines, a Geomorphic Units survey and classification System (GUS) was developed in the framework of the EU REFORM project. GUS is suited to integrate mesohabitat simulation models (e.g. MesoHABSIM) providing the basis for the assessment of spatio-temporal alterations of habitats, very often associated to hydropower production. Mesoscale habitat models integrated with GUS permit to formulate scientifically-based, sound assessment of environmental water flows to be released by hydropower structures, as well as contribute to identify the best strategies in terms of sediment management in rivers impacted by dams and weirs.

Keywords: hydropower, rivers, environmental impacts, Water Framework Directive

CYSENI 2018, May 23-25, Kaunas, Lithuania
ISSN 1822-7554, www.cyseni.com

NEW REACTORS: INTERNATIONAL DEVELOPMENTS AND SAFETY FEATURES

Justus Oldenburg
Gesellschaft für Anlagen- und Reaktorsicherheit (GRS) gGmbH
Boltzmannstraße 14, 85748 Garching near Munich – Germany
Email: Justus.Oldenburg@grs.de

ABSTRACT

In the years after 2000, many in the international nuclear community predicted a worldwide nuclear renaissance that would lead to a new generation of nuclear power plants (NPPs) in countries that already employ NPPs and in so-called newcomer countries. The anticipated new wave of reactors was designated as generation 3 or 3+, since early reactors and operating reactors were labelled 1 and 2 respectively. Although the global nuclear renaissance has not materialised, new NPPs remain an important strategy in various countries.

In Europe, new nuclear reactors are expected to be designed in such a way that large or early releases of radioactivity are practically eliminated. The reactor designs EPR (Areva) and AP1000 (Westinghouse) offer two very different safety approaches. While the EPR makes use of proven active systems, strong redundant features and a core melt stabilisation system outside the reactor vessel, the AP1000 design approach is heavily based on passive systems, simplification and a core melt stabilisation system that aims at retaining core melt inside the reactor vessel. In order to respond to increasingly standardised new reactor designs, regulators have modified their licensing approach to ensure a more efficient process. As an example, ONR (United Kingdom) and the NRC (USA) are now offering design reviews that take place prior to a site-specific licensing process.

While many large power NPP construction projects have been cancelled, a new type of proposed NPPs has gained momentum: small modular reactors (SMRs). Designers of SMRs try to overcome the huge capital costs and inflexible use associated with large NPPs by small reactor modules that can be manufactured offsite in large numbers and adapted to different power needs by incremental modular extension. The nuclear community has just begun to work on how existing safety requirements (historically developed for large NPPs) can be applied to SMRs.

Keywords: Nuclear renaissance, reactor generations, GEN-3 reactors, requirements for new reactors, EPR, AP1000, passive systems, design review, small modular reactors

CYSENI 2018, May 23-25, Kaunas, Lithuania
ISSN 1822-7554, www.cyseni.com

TRADE-OFFS BETWEEN ENERGY INNOVATION AND PRICE: STATE RESPONSIBILITIES AND ENERGY JUSTICE

Michael LaBelle
Central European University
Nador st. 9, 1051 Budapest – Hungary
Email: labellem@ceu.edu

ABSTRACT

Does the innovation of new energy technologies provide a social good? This paper focuses on the responsibility of state institutions to continuously innovate and improve the efficiency and ecological impact of the energy system while delivering universal access to energy services at affordable prices. The concepts of energy justice and innovation will be addressed. The purpose is to demonstrate the responsibility of the state to ensure innovation and the adoption of newer energy technologies. Deployment of energy technologies and solutions is required to provide adequate and climate friendly energy services. Three questions will be asked that will guide the content of this paper: 1) Do state institutions prioritize short-term affordability over technological renewal? 2) How well do state institutions usher in and out technologies from the energy system (e.g. through systematic or erratic policies and incentives)? 3) How developed is the financial landscape and how diverse are (dis)incentives for new technologies?

Merging the delivery of energy justice with the innovation activities of the state moves beyond a neoliberal 'regulatory state' where equitable energy systems are overseen by energy regulators. Rather, the responsibility of the state has grown to encompass the protection and rejuvenation of energy technologies. As economic activities grow and the energy inputs to economic growth excel, state action must also focus on innovation of new energy technologies to reduce the environmental impact (environmental justice) while increasing access to sustainable sources of affordable energy services (energy justice). Renewable energy technologies and carbon reducing technologies, for the benefit of humanity and the environment, are now an integral part of current and future energy systems.

Keywords: energy justice, innovation, regulation, energy transitions

CYSENI 2018, May 23-25, Kaunas, Lithuania
ISSN 1822-7554, www.cyseni.com

STUDY OF THE CATALYTIC ACTIVITY OF NATURAL MINERALS AND COMPOSITES BASED ON THEM IN PROCESS OF PYROLYTIC TAR DECOMPOSITION

S. V. Vasilevich, A. N. Asadchyi, M. V. Malko, D. V. Degterov
The Institute of Power Engineering
National Academy of Sciences of Belarus
Akademicheskaya str. 15/2, 220072 Minsk – Belarus
Email: asadchyi@tut.by

ABSTRACT

The paper discusses results of experimental studies of the catalytic activity of various natural minerals and composites based on them. The catalytic activity of the natural Belarusian dolomite and composites of this dolomite with $Na_2K_2(SiO_2)n$ as well as with Cambrian blue clay was studied. Samples of natural and medical magnesite, as well as composites of natural and medical magnesite with Cambrian blue clay, were also studied. In addition the catalytic activity of pure Cambrian blue clay as well as lime was investigated at a temperature of 600 ^oC. It has been established that the homogeneous as well as catalytic decomposition of the pyrolysis tar proceeds at a measurable rate only at temperatures above 450 °C. It was found also that natural magnesite has the highest activity in process of pyrolytic tar decomposition at temperatures about 600 ^oC and lower. At temperatures of about 700 °C and higher, the catalytic activity of natural magnesite is comparable to the catalytic activity of natural dolomites, as well as composites based on natural dolomites and Na_2K_2 $(SiO_2)n$. It has been found that the most promising option for creation of the decomposition catalyst for heavy hydrocarbons formed by thermochemical conversion of biomass is a mixture of dolomite (1.5 microns) + Na_2K_2 $(SiO_2)n$ (with a concentration of 30% by weight) with the possible addition of a small amount of charcoal. The possibility of creating dolomitic composites having the same catalytic activity with respect to the process of decomposition of pyrolytic tar formed during pyrolysis of biomass as pure natural dolomites and at the same time having a decrease in abrasion by about 2 orders of magnitude has been experimentally proved.

Keywords: hydrocarbons, catalyst, composite, dolomite, abrasion

1. INTRODUCTION

The possibility of obtaining useful liquid and gas products as a result of thermochemical conversion of biomass attracts close attention of specialists from different countries of the world. As is known [1], pyrolysis of biomass at a temperature of the order of 500 ^oC allows to obtain liquid products that can be used as motor fuel. Conducting thermochemical conversion of biomass in the temperature range of about 800 ^oC allows to obtain gaseous fuel for cogeneration engines.

This possibility is of considerable practical interest. However, it did not find practical use due to the fact that a number of components with a high dew point (heavy hydrocarbons) are formed during gasification [2, 3]. Such components are deposited on the walls of the gas paths and clog the regulating devices.

Researchers from different countries of the world came to the conclusion that catalytic purification of pyrolysis products of biomass, carried out at temperatures above 500 ^oC, is the most appropriate way to eliminate the problem of heavy hydrocarbon formation [2–4].

Catalysts for the decomposition of heavy hydrocarbons formed during pyrolysis of biomass should have high efficiency, maintain their catalytic activity for a long time and be affordable and cheap.

Over the past decades, different types of thermal decomposition catalysts for thermochemical conversion of biomass, including catalysts based on metals such as Fe, Ni, Ru, Rh, Pt, as well as non-metallic catalysts, such as natural dolomites ($CaMg(CO_3)_2$, olivine $(Mg, Fe)_2SiO_4$, and others have been studied.

The high activity of catalysts based on Ni, Ru, Rh, Pt, as well as dolomites and some other natural minerals has been established [4–6]. The catalytic activity of natural dolomites of Belarus in the process of decomposition of tar formed in the pyrolysis of biomass was also established in [7].

Natural dolomites are of particular interest because of their cheapness and availability. For example, the dolomite reserves in Belarus are several billion tons [8]. This allows their wide use in systems for cleaning biomass gasification products to produce gaseous fuels for cogeneration plants.

As is known, dolomite is a mineral that is a double carbonate salt of calcium and magnesium ($CaMg(CO_3)_2$) with impurities of calcium carbonate (calcite), iron oxides, aluminum, silicon, manganese and some other compounds [9].

This report presents the results of an experimental study of the catalytic activity of natural dolomites, composites based on them, and also some other substances carried out at the Institute of Energy of the National Academy of Sciences of Belarus. One of the main aims of the present study was to find the possibility of eliminating such a known shortage of natural dolomites as low strength and high abrasion after annealing was also studied. In order to find ways to overcome this shortcoming, various samples of catalysts based on dolomite, magnesite with various additives in the form of natural clay, lime, composite material Na_2K_2 $(SiO_2)n$, charcoal, etc., were made and investigated. The task was to preserve the catalytic properties of the material at the level of natural dolomite and to increase mechanical properties of it.

2. EXPERIMENTAL INSTALLATION

Experiments to determine the catalytic activity of materials were carried out on the experimental setup of the Institute of Power Engineering of the National Academy of Sciences of Belarus, the main element of which is a high-temperature reactor equipped with an electric heater and allowing the temperature to be maintained up to 1,000 ^{o}C [7].

Fig. 1. General view of a reactor with a condensation system for liquid pyrolysis products

The reactor has a reaction zone in which pyrolysis takes place and a zone of decomposition of pyrolysis products capable of condensation at temperatures of the order of 100 °C or higher.

3. METHOD OF RESEARCH

The method of investigation is described in details in [7]. During the experiments described in the present report, the temperature in the reactor was 600 °C. The wooden material was supplied to the reactor in the form of cylinders with a diameter of 5 mm and a length of 20 mm. The humidity of wooden particles was 15%, the ash content was 0.15%. In the catalytic zone of reactor there was a catalytic material in the form of lump material (natural carbonates), or tablets with a diameter of 2.5 cm (composite materials). Products of pyrolysis of wood passed through the catalytic material and entered the condensation system of liquid pyrolysis products. The mass of liquid pyrolysis products was measured on an electronic Stohl balance with a relative error of 2%.

The catalytic activity of the following materials was investigated:

- dolomite;
- natural magnesite;
- natural magnesite + Na_2K_2 $(SiO_2)_n$;
- dolomite + cambrian clay;
- dolomite + cambrian clay + charcoal;
- dolomite + cambrian clay + $Na_2K_2(SiO_2)_n$;
- dolomite + $Na_2K_2(SiO_2)_n$;
- dolomite + $Na_2K_2(SiO_2)_n$ + charcoal;
- cambrian clay;
- MgO;
- MgO + cambrian clay;
- MgO + $Na_2K_2(SiO_2)_n$;
- lime.

Fig. 2 shows the steps in creating samples of composite materials based on dolomite and the $Na_2K_2(SiO_2)_n$ compound. At the beginning forms were created, then filled with a mixture of the material under study. All samples had holes foreseen for increasing of surface acceptable for pyrolytic tar. After that, the mold with the material was annealed at a temperature of 800 ^{o}C. The annealing time is 3 hours. During this time the form completely burned out.

33% $Na_2K_2(SiO_2)_n$ 44% $Na_2K_2(SiO_2)_n$ 55% $Na_2K_2(SiO_2)_n$

Fig. 2. General view of the stages of composites preparation

The initial view of samples of various substances that were studied for the purpose of revealing the catalytic activity in the process of pyrolysis tarn decomposition is shown in Fig. 3.

Dolomite | Powder of dolomite | Magnesite | Powder of magnesite

Cambrian clay | Cambrian clay with dolomite | Cambrian clay with magnesite | Dolomite with $Na_2K_2(SiO_2)_n$

Fig. 3. The initial view of the samples studied for their catalytic activity during the decomposition of pyrolysis tar

4. RESULTS OF THE STUDY AND DISCUSSION

The work determined the loss of tar (heavy hydrocarbons) formed during pyrolysis, carried out at a temperature of 600 ^{o}C in the reaction zone of the experimental setup. As a quantitative measure of decomposition of the tar, the decomposition parameter, determined in accordance with the expression, was considered: The degree of decomposition of the pyrolysis tar was determined by the formula:

$$x = \frac{(m_0 - m_t)}{m_0} \tag{1}$$

where m_0 and m_t are masses of tar at the beginning of decomposition and at time t.

The degrees of decomposition of the pyrolysis tar formed during the pyrolysis of birch wood at a temperature of 600 °C are presented for comparison in Table 1 and Fig. 4.

As follows from Table 1, the catalytic activity of natural magnesite is significantly higher than the catalytic activity of natural dolomite in the temperature range below 600 °C. Starting at temperatures of about 600 °C, the catalytic activity of natural dolomite becomes comparable with the catalytic activity of natural magnesite.

Table 1. The degrees of pyrolysis of tar decomposition in homogeneous and heterogeneous processes

t,°C	Homogeneous Decomposition	Decomposition in the presence of dolomite	Decomposition in the presence of magnesite
450	0.000	0.000	0.071
500	0.262	0.220	0.860
550	0.420	0.488	0.867
600	0.559	0.830	0.857
700	0.750	0.873	0.867
750	0.688	0.867	-
800	0.832	0.886	-
830	0.850	0.905	-
870	0.832	0.943	-

This means that decisive factors by choosing a catalyst for operation in the temperature range above 600 °C are availability of the catalyst as in case of natural dolomite and magnesite and abrasion characteristics.

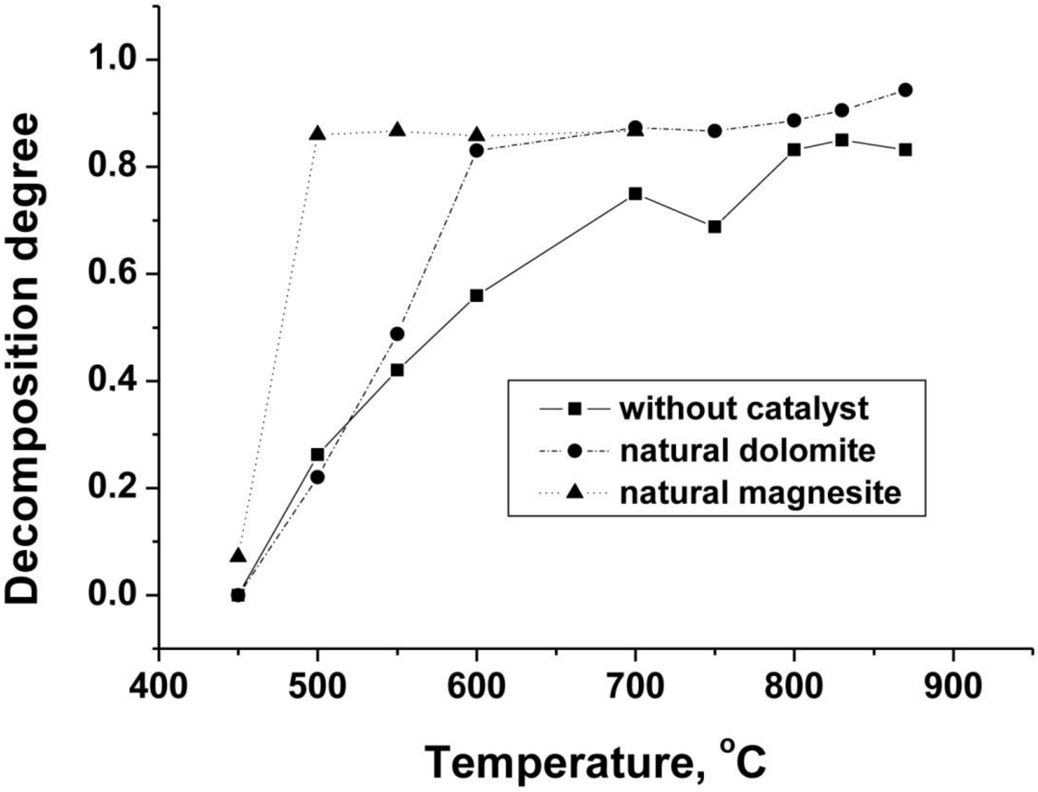

Fig. 4. The dependence of the degree of pyrolysis resin decomposition on temperature in homogeneous and heterogeneous processes

Fig. 5 and 6 shows comparative data on the degrees of decomposition of the tar for various catalytic decomposition conditions at temperatures of 600 and 700 °C.

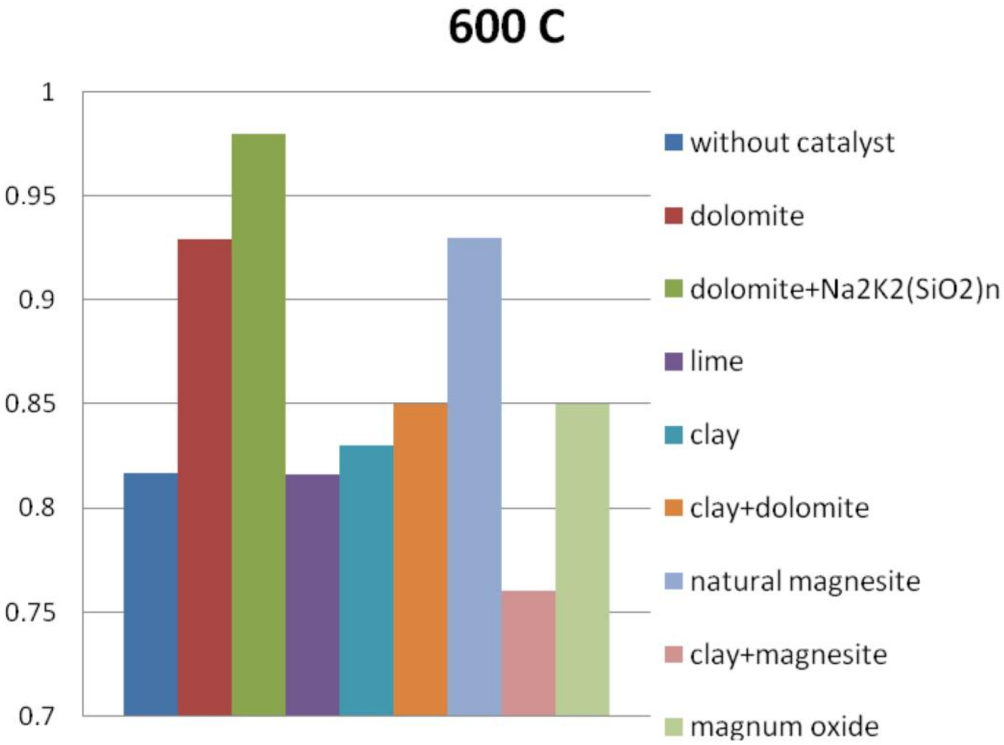

Fig. 5. The decomposition degrees of pyrolysis tar at a temperature of 600 ^{o}C

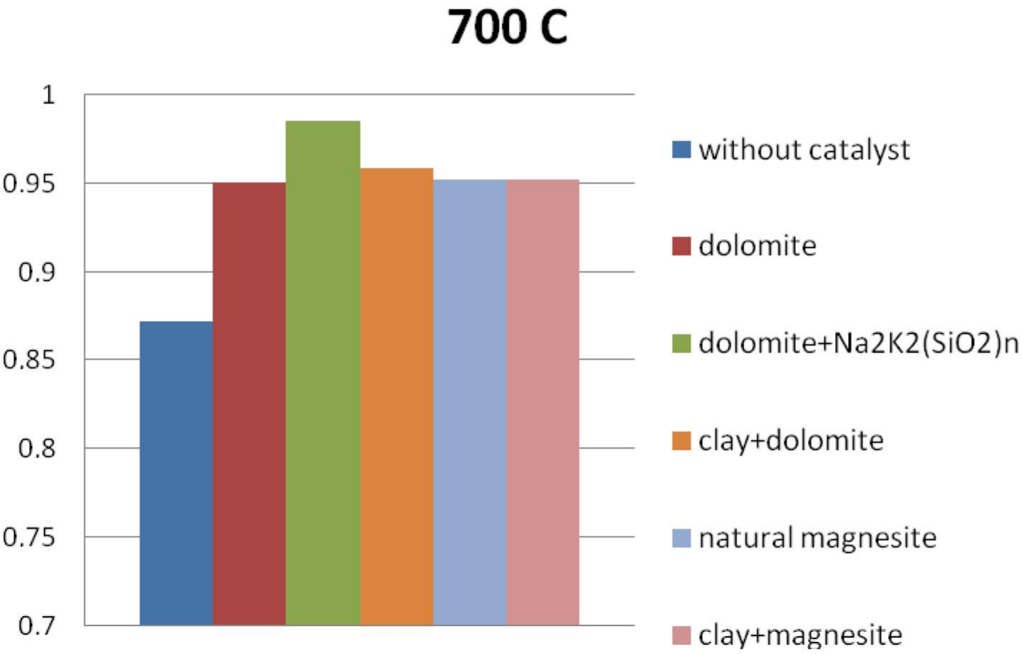

Fig. 6. The decomposition degrees of pyrolysis tar at a temperature of 700 ^{o}C

It follows from Fig. 6 that the highest catalytic activity at 700 °C has a composite material of dolomite + $Na_2K_2(SiO_2)n$.

Fig. 7 shows the catalytic activity of the dolomite + $Na_2K_2(SiO_2)n$ composite from the $Na_2K_2(SiO_2)n$ concentration.

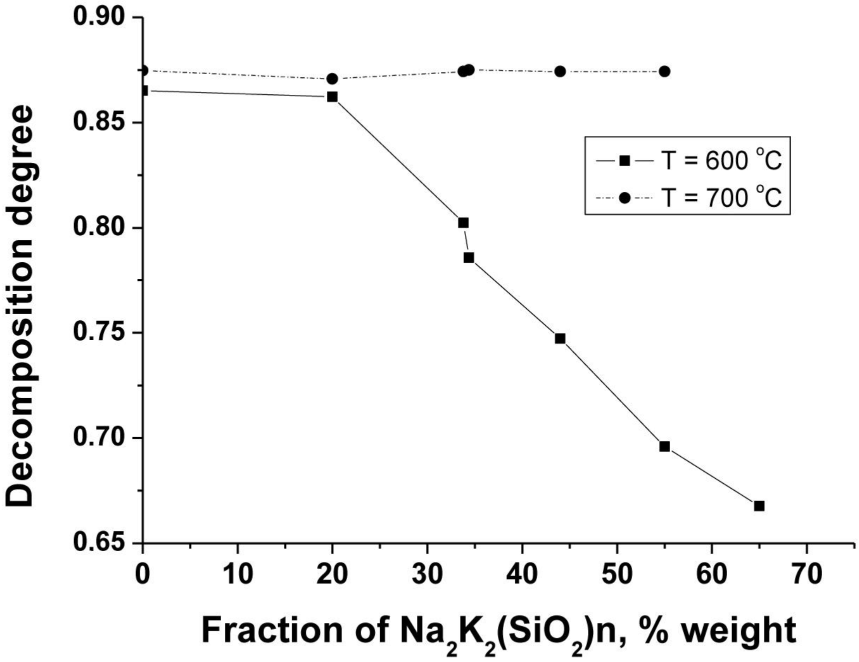

Fig.7. Decomposition degree of pyrolytic tar as a function of the $Na_2K_2(SiO_2)n$ concentration

Data in Fig. 7 show that the catalytic activity of the dolomite + $Na_2K_2(SiO_2)n$ composite at the temperature of 600 °C depends on the mass concentration of $Na_2K_2(SiO_2)n$. It remains constant in the range of $Na_2K_2(SiO_2)n$ concentrations to about 20% by weight and decreases then almost linearly with increasing of concentration of this compound.

At 700 °C the catalytic activity of the dolomite + $Na_2K_2(SiO_2)n$ composite remains constant at least to the concentration of $Na_2K_2(SiO_2)n$ about 60% by weight.

The reasons for such dependence of the catalytic activity of the dolomite + $Na_2K_2(SiO_2)n$ composite in the process of pyrolytic tar decomposition are unclear

It is possible that such a dependence is associated with a rearrangement of the surface structure of the composite or with a change in the pore size of the composite and, consequently, the availability of tar components to the active centers of the composite.

It can be seen from Figs. 5–7 that the catalytic activity of the composite based on natural dolomite and $Na_2K_2(SiO_2)n$ compound exceeds the catalytic activity of natural dolomite available in Belarus. At the same time the strength characteristics of such material as it was established in this work, significantly exceed the strength characteristics of pure samples of natural dolomites of Belarus.

Table 2. Experimental values of the abrasion coefficient and the compressive strength of dolomite composites at 700 °C

Explored property	**Dolomite**	**22.5% dolomite+ 22.5% charcoal+ 55% $Na_2K_2(SiO_2)n$**	**70% dolomite + 30% $Na_2K_2(SiO_2)_n$**	**60% dolomite+ 10% charcoal+ 30% $Na_2K_2(SiO_2)n$**
Abradability coefficient, g/cm^2	5.1	0.038	0.023	0.048
Compressive strength, MPa	≈ 0	1,8	1,9	-

This is indicated by data on the estimation of abrasion of dolomite composites established in the course of this study by using the EF-2 device, as well as the compressive strength of the samples (The device for determining the abrasion of samples EF-2 from ELECTROLAB). The results of these studies are presented in Table 2.

In accordance with data of Table 2 the abradability coefficient of the dolomite composite (70% dolomite + 30% $Na_2K_2(SiO_2)n$ is approximately two orders in magnitude lower than the abradability coefficient of pure natural dolomite.

The comparison of the strength samples of the investigated substances shows that the use of a composite based on natural dolomites and the $Na_2K_2(SiO_2)n$ compound allows a practical solution of such a complex problem as catalyst abrasion, which is the main obstacle to the use of natural dolomites as effective and cheap catalysts for development of the effective technology of purification of products of thermochemical conversion of biomass.

5. CONCLUSIONS

It has been established that natural dolomite of Belarus, natural magnesite and a composite based on natural dolomite and $Na_2K_2(SiO_2)n$ compound possess catalytic activity with respect to the process of decomposition of heavy hydrocarbons (pyrolysis tar) formed in the process of the thermochemical conversion of biomass.

The results of the study show that the catalytic activity of the composite dolomite+ $Na_2K_2(SiO_2)n$ is comparable to the catalytic activity of pure natural dolomite by concentration of the $Na_2K_2(SiO_2)n$ compound content in the composite about 20% by weight at the temperature about 600 ^oC and to the fraction of $Na_2K_2(SiO_2)n$ up to 60% at the temperature 700 ^oC.

The strength of such a composite with respect to abrasion is approximately 2 orders of magnitude higher than the strength of natural dolomite.

Using of dolomite composites based on the $Na_2K_2(SiO_2)n$ compound makes it possible to create a cheap catalyst for purification of products of the thermochemical conversion of biomass.

REFERENCES

1. BRIDGEWATER A.V. Renewable fuels and chemicals by thermal processing of biomass. *Chem. Eng. J.*, 2003. Vol. 91. pp. 87–102.
2. EVANS R.J., MILNE T.A. Molecular characterization of the pyrolysis of biomass. *Energy Fuels*. 1987, V. 1(2), pp. 123–137.
3. GARCIA-PEREZ M., METCALF J. The formation of Polyaromatic Hydrocarbons and Dioxins During Pyrolysis: A Review of the Literature with Descriptions of Biomass Composition, Fast Pyrolysis Technologies and Thermochemical Reactions. Technical Report/ Wachington State University Edition – June 2008, 63 p.
4. DAYTON D. A Review of the Literature on Catalytic Biomass Tar Destruction. Milestone Completion Report. NREL/TP-510-32815, (2002), pp. 3–7.
5. EL-RUB Z.A., BRAMER E.A., BREM G. Review of Catalysts for Tar Elimination in Biomass Gasification. *Ind. Eng. Chem. Res*. (2004), V. 43, pp. 6911–6919.
6. XU C., DONALD J., BYAMBAEW E., OTSUKA Y. Recent advances in catalysts for hot-gas removal of tar and NH3 from biomass gasification. *Fuel.* 2010; 89, pp. 1784–95.
7. MALKO M.V., ASADCHYi A.N., VASILEVICH. S.V., DEGTEROV D.V., Investigation of the kinetics of thermal decomposition of pyrolysis tar. *The Proceedings of the National Academy of Sciences of Belarus. Phys.-Techn. Ser.* 2016. No 4. pp. 84–90 (in Russian).
8. Useful Minerals of Belarus: To the 75th anniversary of BelNIGRI / Edited by KHOMICH P.Z. and others. *Mn .: Adukaciya and Vykhavanne*, 2002. pp. 395-398 (in Russian).
9. Mountain encyclopedia. T.1 / Editor KOZLOVSKY E.A. *Moscow: Soviet Encyclopedia*, 1984. p. 172 (in Russian).

CYSENI 2018, May 23-25, Kaunas, Lithuania
ISSN 1822-7554, www.cyseni.com

RESEARCH AND ANALYSIS OF THE IMPACT OF CHAR OUTLET VELOCITY ON THE PARAMETERS OF BIOMASS GASIFICATION IN A FIXED BED GRAVITY REACTOR

M. Ochnio
Gdańsk University of Technology
Narutowicza 11/12, 80-001 Gdańsk – Poland
Email: ochnio.mateusz93@gmail.com

P. Kazimierski, J. Kluska, D. Kardaś
Institute of Fluid-Flow Machinery Polish Academy of Science
Fiszera 14, 80-231 Gdańsk – Poland

ABSTRACT

Biomass is very important renewable energy resource and fuel for the future. The common usage of biomass is burning in small boilers or furnaces for household. It is the simplest and the cheapest way to heat production, but generates significant air pollution. Therefore, in order to reduce them, exhaust gases should be cleaned, or biomass could be gasified and the syngas cleared, thus reducing the amount of pollutants. Priority for the present is the heat and electricity generation from gasification process. Small scale gasifier can be coupled with boiler, diesel engine or gas turbine for local heat and electricity production.

This work presents the results of hardwood pellet gasification with different speed of char outlet velocity from the bottom of the reactor. The effects of bed movement on the temperature profile, gas composition (using gas chromatograph), carbon conversion efficiency and fuel consumption were taken into account. In order to perform the tests, a small scale reactor was created. The reactor was used for gasification experiments carried out for different outlet char velocity. Slow movement of the bed promotes high reduction zones, while fast bed movement leads to high combustion zones and higher caloric values of syngas. Char outlet velocity influences on temperature profile in entire reactor. In pyrolysis zone convection heat transfer is opposite to conduction one. In effect higher char outlet velocity causes pyrolysis zone to shorten and higher temperature gradient in this part of reactor.

Keywords: gasification, updraft gasifier, hardwood, carbon conversion, bed movement

1. INTRODUCTION

Gasification in fixed bed reactors is a complex thermochemical process to convert biomass or another carbonaceous solid fuel, such as coal or waste, for instance, to gaseous fuel. This process takes place at high temperatures (700–1500 °C) and in the presence of air or oxygen as a gasifying agent [1, 2]. Gas produced in the gasification process can be used for power generation in a gas engine or directly combusted in a boiler, which could minimize the emission of gaseous pollutants and coal contained in dust [3]. These advantages have generated considerable interest in gasification of biomass. However, the problem of tar formation significantly slows down the development of the gasification technology. The main technical aspects are plugging and fouling problems caused by condensed organic compounds. Tars can be defined as complex mixture of organic compounds and are generally assumed to be aromatic [4–6]. Composition of that mixture depends on the feedstock, type of gasifier and operating conditions such as temperature, pressure and gasification agent [1, 4–8], as well as on the applied sampling procedure and analysis of tars [5, 6, 9, 10].

Recent research has focused on obtaining high quality biochar and high purity producer gas by, for example, reducing tar content [11]. Ismail and El-Sala [12] carried out numerical simulations and experimental studies of the influence of temperature in the gasifier and ER (equivalence ratio) on syngas composition and tar yields during updraft gasification of gray pellets. A higher ER ratio corresponds to a larger amount of oxygen in the combustion zone, what promotes oxidization reactions. That leads to more heat generation, higher temperatures in the gasifier and lower heating value of producer gas. These aspects were also presented by Ayyadurai et al. [13], who studied large (1 m in length and 0.06 m in diameter) woody biomass gasification in a 60 kWth updraft gasifier. Obtained results shows that the gasification process with ER = 0.6 allows to reach a temperature of 955 °C in the oxidation zone and receive producer gas which attained a heating value of 4.5 MJ/Nm^3.

Another interesting issue related to updraft biomass gasification has been presented by Huang et al. [14] . Authors studied the characteristics of residual carbon in biomass, including structure and gasification activity. These aspects were investigated using Raman spectroscopy. Residual carbon in the ash is the result of char particles spending only a short amount of time in the gasifier.

Based on current literature, there are no available works that provide detailed information about the influence of time that the fuel spends in the gasifier or rate of bed movement on the gasification temperature and syngas characteristics. The primary objective of this work was to investigate an alternative way to stimulate the updraft gasification process by different char outlet velocity. The main parameters presented in this work include the temperature profile along the gasifier (e.g., the characteristics of the temperature zones), gas composition and caloric value, carbon conversion rate and energy balance. The experiments were carried out in the lab scale gasifier in the Institute of Fluid Flow Machinery, Polish Academy of Sciences.

2. METHODOLOGY

2.1. Proximate and ultimate analysis of fuel

The beech wood samples were first dried using a MAC moisture analyser (RADWAG) to determine the moisture content. The elementary composition was analysed using a CHNS-O Flash 2000 analyser (Thermo Scientific), while the calorific value was measured using a KL-11 calorimeter. The results of the proximate and ultimate analyses are given in Table 1.

Table 1. Proximate and ultimate analyses of beech wood samples

HHV (MJ/kg)[b]	19.6
Moisture (wt.%)[a]	6.1
Proximate (wt.%)[b]	
Volatiles	76.3
Fixed Carbon	21.4
Ash	2.3
Ultimate (wt.%)[c]	
C	48.5
H	5.3
O[d]	45.8
N	0.4

[a] as delivered
[b] db = water free
[c] dry-ash free basis
[d] by difference

2.2. Experimental setup

The updraft gasification stand is shown in Fig. 1. The total height of the gasifier is 135 cm and the internal radius is 22 cm. The air inlet nozzles were installed 52 cm above the reactor bottom level, while the producer gas outlet was 121 cm above this level. The gasifier and the outlet tube were insulated with mineral wool of 5 cm in thickness.

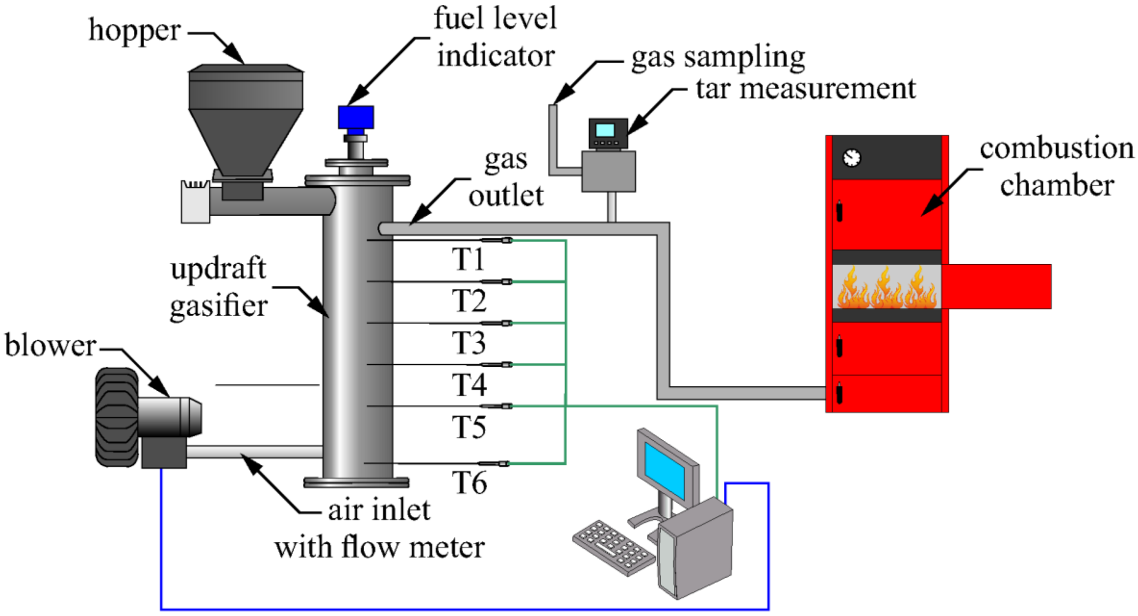

Fig. 1. Schematic diagram of the experimental setup

During the experiment, hardwood pellets were loaded by a screw feeder to the reactor, to the level of 10 cm above the syngas outlet. The thermocouples (type N and S) were installed along the gasifier height at the distance of 30, 55, 72, 88, 90 and 119 cm from the bottom of the reactor. The air was supplied to the gasifier by an and controlled using the inverter and a thermal mass flow meter. The producer gas left the reactor and passed through the outlet tube to the combustion chamber. In the outlet tube, part of the gas was separated and directed to the sampling system for tar and gas analysis.

2.3. Experimental procedure

Prior to starting gasification, a batch of 3 kg feedstock was loaded into the gasifier in each experiment. The initial level of the feedstock was maintained at the level of the air inlet nozzles until a high bed temperature was obtained. After a high bed temperature was obtained, the gasifier was filled to the level of the indicator. In each experiment, the height of the fuel bed was kept at the same level using a rotary fuel level indicator (i.e., 112 cm from the bottom). The amount of supplied air was set at 12, 17, 20 and 23 Nm^3/h, and the duration of each experiment was 120 minutes from the point when the gasification process reached a steady-state condition (i.e., a constant temperature in each zone and a steady amount of received char). The gasification process was performed at atmospheric pressure in the range of 900–1100 °C. The solid residue (char and ash) was gathered from the bottom of the reactor using an inverter coupled with a cyclical screw at a frequency of 5 sec/5min (Case 1) and 10 sec/2.5 min (Case 2), which stimulated slow and fast bed movement in the reactor.

2.4. Gas composition measurement

The producer gas samples were taken using tedlar bags. Before sampling the gas was first directed to the tar sampling stand (Fig. 1) and cleaned. The analysis of the syngas composition were performed using a SRI Instruments 310 gas chromatograph with thermal conductivity detector (TCD). The gas analyser was pre-calibrated using a standard mixture of gas to determine CO, CO_2, CH_4 and H_2. Argon was used here as a carrying medium.

Based on the literature, the amount of the produced gas was calculated using the nitrogen tracer method [2]. It means that knowing the amount of nitrogen in the supplied air, the amount of the producer gas is calculated from the percentage of nitrogen in it. The results, expressed in cubic meters per hour (m^3/h) refer to normal conditions (p = 1013.25 hPa, T = 273.15 K).

3. RESULTS AND DISCUSSIONS

3.1. Temperature profile in the gasifier

Our experimental investigations of hardwood pellet updraft gasification revealed a temperature profile trend in the gasifier, which is consistent with the literature [2, 15]. The results indicated a significant impact of bed movement in the gasifier on the height of the individual process zones (Fig. 2 and Fig. 3). Based on the literature, the boundary of the combustion and (reduction) zone was established at 1000 °C and 750 °C [2, 16, 17]. Our results show that for the Case 1 (slow bed movement in the reactor) the combustion zone attained a height of about 33 cm from the air nozzles.

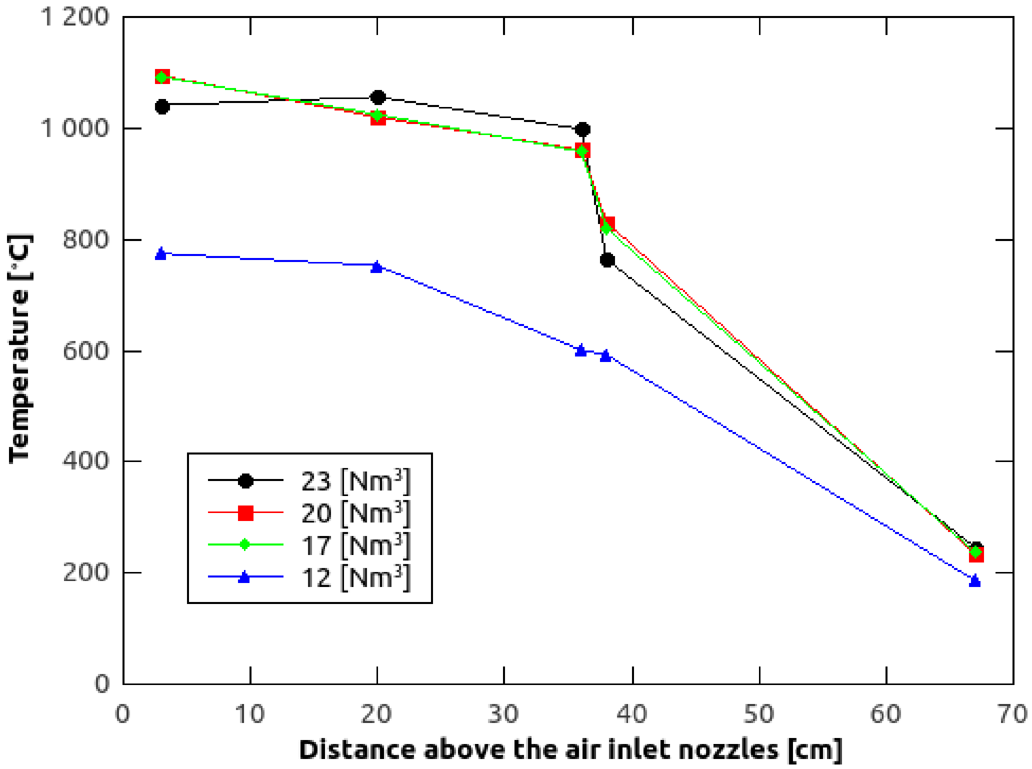

Fig. 2. Characteristic temperature profile in gasifier for Case 1

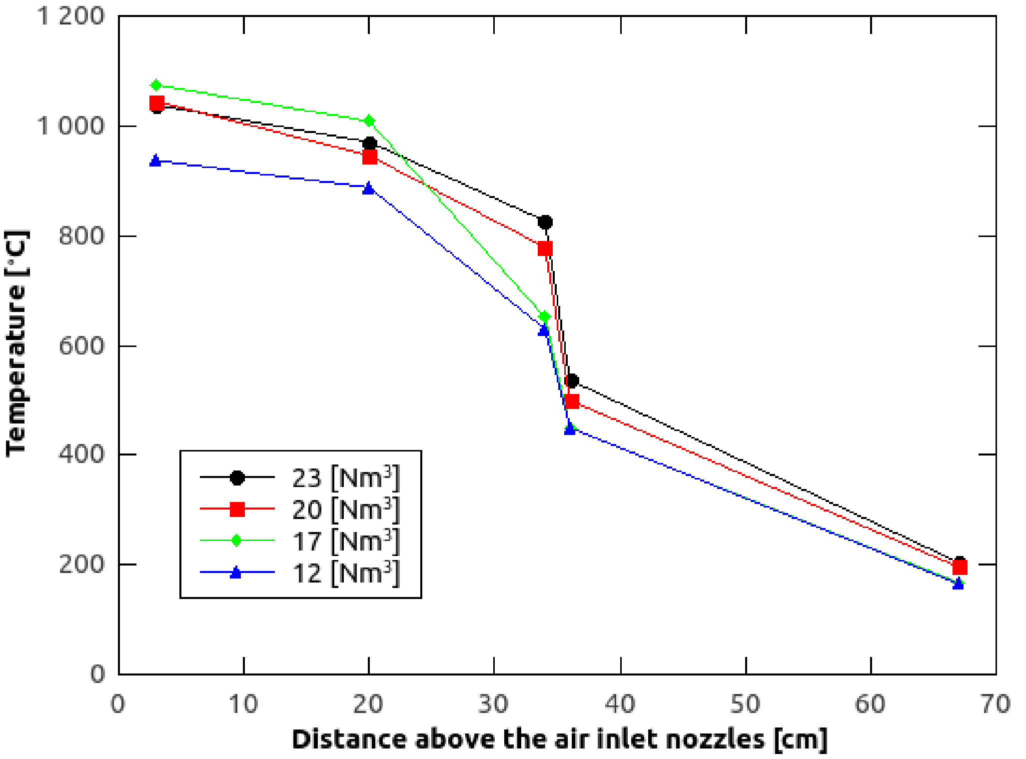

Fig. 3. Characteristic temperature profile and gasifier zones for Case 2

Because the level of the fuel in the gasifier was set at 50 cm from the air nozzles, the pyrolysis zone attained a height of 11 cm. For the Case 2 (fast bed movement in the reactor), the height of the combustion zone attained a maximum of about 20 cm. Case 2 promoted the pyrolysis process with a zone height of 18 cm. Lower temperatures in pyrolysis zone for Case 2 are associated with the intensification of supplied of fresh fuel and consumed heat, supplied by oxidation of biomass at the lower part of the reactor, in endothermic pyrolysis reactions. A significant temperature drop of about 36 cm indicates a high pyrolysis intensity in this area.

The results of the hardwood updraft gasification also indicated that the gradient of the bed temperature was about 6 °C/cm for 12 Nm^3/h of supplied air and 11°C/cm for all other amounts of air for Case 1. For Case 2, the corresponding values were 11–14 °C/cm. Faster bed movement in the reactor resulted in a slightly steeper temperature gradient.

3.2. Performance of the gasification process

Experimental investigation showed importance of comparing the amount of air supplied, fuel consumption and temperature. The result shows the similar temperature and fuel consumption trends as a function of the amount of air for both Cases (Fig. 4 and Fig. 5). Fuel consumption increases with the amount of air supplied, in the case of slow movement of bed is a nearly linear dependence (Fig. 4). Temperature curve has different kind of trend increasing at first but after reaching a maximum (20 Nm^3/h for Case 1 and 17 Nm^3/h for Case 2) decreases for higher amount of supplied air. For the slow movement of the bed in the gasifier it may be caused by imbalance between pyrolysis and combustion/reduction process in the gasifier. The increase of the supplied air amount caused an increase in the intensity of the combustion process, but the amount of generated heat was not sufficient to raise the temperature in the reduction and pyrolysis zone. For the fast movement of the bed (Case 2) a high fuel flow through the reactor (reached 33 kg/h) may cause that fresh part of the biomass or incompletely degassed biomass goes into the reduction and combustion zone.

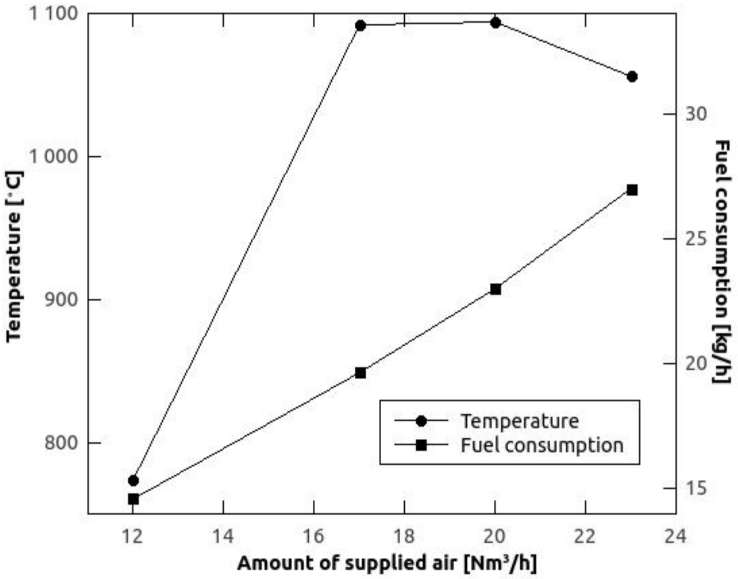

Fig. 4. Relation of amount of supplied air, fuel consumption and temperature in the combustion zone for Case 1

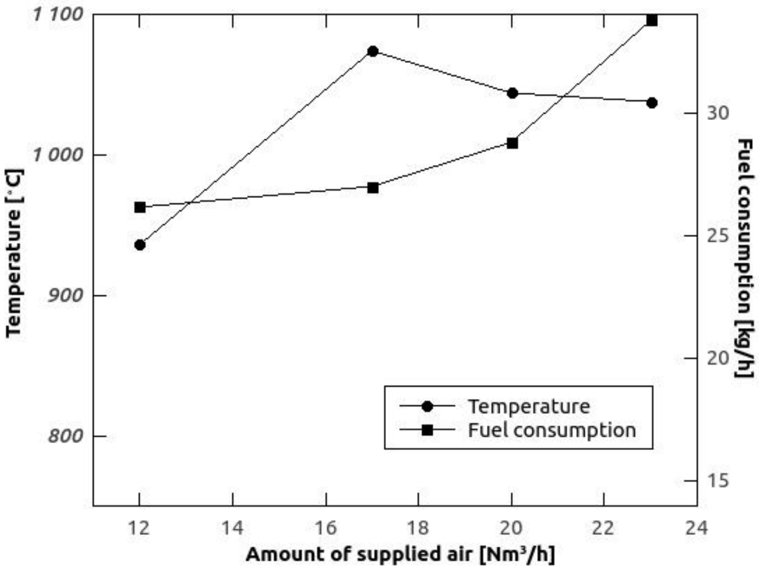

Fig. 5. Relation of amount of supplied air, fuel consumption and temperature in the combustion zone for Case 2

3.3. Char characteristic

Experimental investigations of hardwood pellet gasification revealed the impact of stimulated bed movement in the reactor on fuel consumption (Table 2). As the amount of supplied air increased from 12 to 23 Nm^3/h, the fuel consumption increased from 14.6 kg/h to 26.2 kg/h for Case 1 and from 27.1 kg/h to 33.7 kg/h for Case 2. This relation was also presented by Pedroso et al. [18]. An increase in the amount of air from 21 to 28 Nm^3/h caused an increase in fuel consumption from 10 to 14 kg/h during updraft gasification of woodchips. Furthermore, a larger amount of oxygen supplied to the gasifier intensified the oxidization reaction, which led to an increase in the carbon conversion rate. For Case 1, an increase in the amount of supplied air from 12 to 23 Nm^3/h resulted in increased carbon conversion from 70 to 94%. For Case 2, the corresponding data were 78 and 83%, respectively. A larger amount of oxygen supplied to the gasifier promoted oxidization reactions and led to increased CO_2 generation. These aspects were presented by Kalström et al. [19]. These authors found that an increase in carbon dioxide concentration from 13 to 60% significantly affected the char conversion rate during CO_2 gasification of char particles from torrefied fuels like pine shell, olive stones and straw.

Table 2. Performance data of the gasification process

Amount of supplied air		**Case 1**				**Case 2**			
	[Nm^3/h]	**12**	**17**	**20**	**23**	**12**	**17**	**20**	**23**
Fuel consumption	[kg/h]	14.6	19.6	23.0	27.0	26.2	27.1	28.8	33.7
ER		0.19	0.21	0.21	0.21	0.11	0.15	0.17	0.17
Carbon in the fuel	[kg/h]	7.08	9.52	11.15	13.08	12.68	13.09	13.97	16.37
Char received	[kg/h]	2.57	1.02	0.84	0.76	3.39	3.15	3.54	2.95
Carbon content in the char	[%]	84.0	87.4	97.5	97.8	82.3	87.3	92.8	96.8
Carbon conversion	[%]	70	91	93	94	78	79	76	83
Mass of carbon in the gas	[kg/h]	3.53	6.24	8.01	9.59	6.14	7.18	9.10	10.38
Theoretical char	[kg/h]	4.23	3.75	3.22	3.57	7.95	6.77	5.25	6.19

To analyze the optimum conditions of frequency of removing char from the gasifier, we compared the amount of char receiving during gasification and the calculated amount of the remaining char (Fig. 6 and Fig. 7). The carbon conversion was calculated as the ratio of the carbon difference in biomass and char after gasification compared with the amount of carbon in the biomass. The theoretical amount of char was based on the difference in the mass of carbon in the fuel and the resulting gas taking into account carbon content in the received char. These calculations did not take into account the tars. Our experimental results revealed that optimum conditions were achieved for fast movement of fixed bed in the gasifier (Case 2) for which the smallest difference between the received and calculated amount of produced char was obtained.

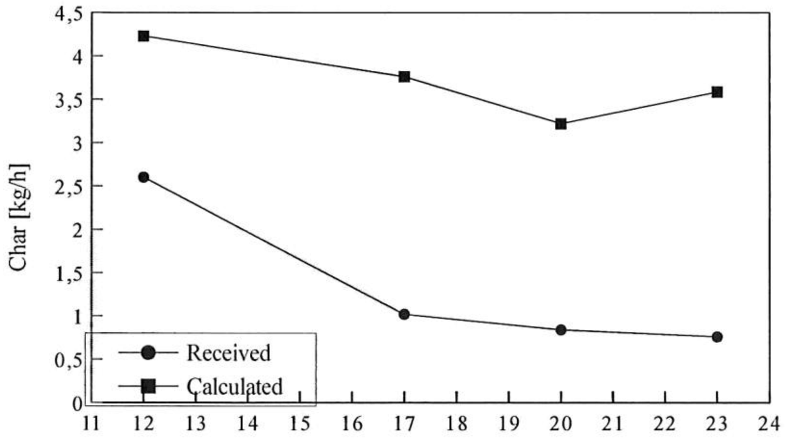

Fig. 6. Received and calculated amounts of char from updraft gasification for Case 1

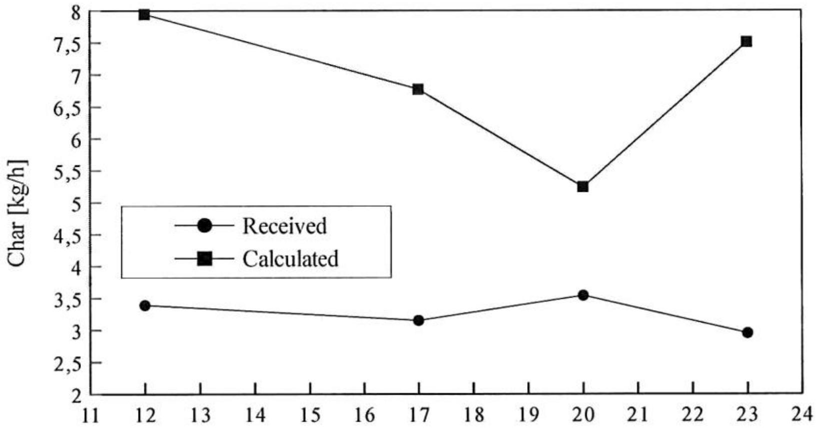

Fig. 7. Received and calculated amounts of char from updraft gasification for Case 2

3.4. The gas caloric value

In an updraft gasifier, carbon dioxide is generated via the oxidation of wood pellets in the lower part of the reactor, and carbon monoxide is produced by a char reduction reaction (Boudouard reaction) in the reduction zone between the bottom and the middle parts of the reactor. Pyrolytic gas is produced in the pyrolytic zone at the lower-middle part of the gasifier [1].

The results of updraft gasification of hardwood pellets for different rates of bed movement revealed the significant influence of generated zone heights in the reactor on syngas composition. Fast bed movement in the gasifier (Case 2) promoted pyrolysis process increasing the height of the zone, which led to a slightly reduced production of pyrolytic gas and higher caloric value of the syngas (Table 3). For Case 1, slow movement of fixed bed resulted in the formation of a high zone of oxidation and reduction that influenced the lower content of carbon dioxide as well as well as hydrogen and methane and a lower caloric value of the syngas.

Table 3. Syngas composition

Case	**Amount of supplied air [Nm^3/h]**	**Syngas components [%]**				**LHV of gas [MJ/Nm^3]**	**Gas yield [Nm^3/kg$_{biomass}$]**	**ER**
		CO	**CO_2**	**H_2**	**CH_4**			
Case 1	12	25.3	5.6	6.9	2.4	4.8	1.4	0.19
	17	33.8	4.8	8.2	1.8	5.8	1.5	0.21
	20	32.2	5.7	8.4	1.3	5.5	1.6	0.21
	23	35.5	4.4	8.5	2.1	6.2	1.6	0.21
Case 2	12	34.6	9.6	14.4	3.9	7.3	1.0	0.11
	17	33.4	7.1	12.1	3.1	6.7	1.2	0.15
	20	33.3	8.3	11.3	2.7	6.4	1.4	0.17
	23	36.8	7.5	11.5	2.6	6.8	1.3	0.17

Based on the literature, the amount of produced gas was calculated using the nitrogen tracer method [2, 20], which relies on knowing the amount of nitrogen in the supplied air. The amount of the syngas can be calculated from the percentage of nitrogen in the producer gas. The results revealed that the slow bed movement in the gasifier led to a larger gas yield per kg of biomass the peak value was 1.6 Nm^3/kg$_{biomass}$ for 23 Nm^3/h of supplied air. The fast bed movement in the gasifier, the corresponding value was 1.3 Nm^3/kg$_{biomass}$. Furthermore, an increase in the amount of air supplied to the gasifier resulted in an increase in the amount of gas yield from per kg of biomass for both cases, which is consistent with the literature [2, 12].

4. CONCLUSIONS

Updraft gasification of hardwood pellets with different bed movement in the reactor and for 12, 17, 20 and 23 Nm^3/h of supplied air has been developed and evaluated. We draw the following conclusions:

1. The results indicated a significant effect of bed movement in the reactor and suggesting that the gasifier could be considered as a flow reactor.
2. Slow bed movement promotes a higher combustion and reduction zone, which leads to lower CO_2 content in the syngas and maximum calorific value about 6 MJ/Nm^3, while fast movement of the bed promotes a higher pyrolysis zone and generates more calorific gas (6–7 MJ/Nm^3).
3. With the increase of ER from 0.19 to 0.21 and from 0.11 to 0.17 the gas yield increased respectively from 1.4 to 1.6 Nm^3/kg$_{\text{biomass}}$ for Case 1 and from 1.0 to 1.3 Nm^3/kg$_{\text{biomass}}$ for Case 2. These results also indicate that slow bed movement generated a higher amount of syngas per kg of fuel.
4. Based on the carbon conversion efficiency, we found that slow movement of the bed and an increase in the amount of supplied air led to a maximum conversion rate (increasing from 70% to 94%).
5. Faster bad movement promotes higher pyrolysis zone, which affects significantly for producer gas composition – especially content of hydrogen.
6. In the case of a need for high fuel consumption (e.g. waste treatment), Case 2 seems to be better. However, if it is more important to get more syngas from fuel, both Cases can be a good solution if the reactor will be heavily loaded due to the large amount of air supplied.

REFERENCES

[1] McKendry P, Energy production from biomass (part 3): gasification technologies. Bioresource Technol 2002; 83: 55–63. https://doi.org/10.1016/S0960-8524(01)00120-1

[2] Chen W, Annamalai K,, Ansley RJ, Mirik M. Updraft fixed bed gasification of mesquite and juniper wood samples. Energy 2012; 41: 454–461. http://dx.doi.org/101016/j.energy.2012.02.052 .

[3] Ma Z, Zhang Y, Zhang Q, Qu Y, Zhou J, Qin H. Design and experimental investigation of a 190 kWe biomass fixed bed gasification and polygeneration pilot plant using a double air stage downdraft approach. Energy 2012; 46: 140–147. http://dx.doi.org/10.1016/j.energy.2012.09.008 .

[4] Yu H, Zhang Z, Li Z, Chen D. Characteristics of tar formation during cellulose, hemicellulose and lignin gasification. Fuel 2014; 118: 250–256. http://dx.doi.org/10.1016/j.fuel.2013.10.080 .

[5] Hernández JJ, Ballesteros R, Aranda G. Characterisation of tars from biomass gasification: Effect of the operating conditions. Energy 2013; 50: 333–342. http://dx.doi.org/10.1016/j.energy.2012.12.005 .

[6] Li C, Suzuki K. Tar property, analysis, reforming mechanism and model for biomass gasification - an overview. Renew Sust Energ Rev 2009; 13: 594–604. https://doi.org/10.1016/j.rser.2008.01.009 .

[7] Devi L, Ptasinski KJ, Janssen FJJG. A review of the primary measures for tar elimination in biomass gasification processes. Biomass Bioenerg 2003; 24: 125–140. https://doi.org/10.1016/S0961-9534(02)00102-2 .

[8] Kihedu JH, Yoshiie R, Naruse I. Performance indicators for air and air–steam auto-thermal updraft gasification of biomass in packed bed reactor. Fuel Process Technol 2016; 141: 93–98. http://dx.doi.org/10,1016/j.fuproc.2015.07.015 .

[9] Nakamura S, Siriwat U, Yoshikawa K, Kitano S. Development of Tar Removal Technologies for Biomass Gasification using the By-products. Energy Procedia 2015; 75: 208–213. https://doi.org/10.1016/j.egypro.2015.07.305 .

[10] Edinger P, Schneebeli J, Struis RPWJ, Biollaz SMA, Ludwig C. On-line liquid quench *sampling and UV–Vis spectroscopy for tar measurements in wood gasification process gases.* Fuel 2016; 59–68. http://dx.doi.org/10.1016/j.fuel.2016.06.127 .

[11] Taupe N.C., Lynch D., Wnetrzak R., Kwapinska M., Kwapinski W., Leahy J.J. 2016: Updraft gasification of poultry litter at farm-scale – A case study. Waste Manage, 50: 324–333. https://doi.org/10.1016/j.wasman.2016.02.036 .

[12] Ismail T.M., El-Sala M.A. 2017: Parametric studies on biomass gasification process on updraft gasifier high temperature air gasification. Appl Therm Eng, 112: 1460–1473. https://doi.org/10.1016/j.applthermaleng.2016.10.026 .

[13] Ayyadurai S., Schoenmakers L., Hernández J.J. 2017: Mass and energy analysis of a 60 kW_{th} updraft gasifier using large size biomass. Fuel, 187: 356–366. DOI: 10.1016/j.fuel.2007.03.028.

[14] Huang S., Wu S., Wu Y., Gao J. 2017: Structure characteristics and gasification activity of residual carbon from updraft fixed-bed biomass gasification ash. Energ Convers Manage, 36: 108–118. https://doi.org/10.1016/j.enconman.2016.12.091 .

[15] Joseph H., Kihedu J.H., Yoshiie R., Naruse I. 2016: Performance indicators for air and air–steam auto-thermal updraft gasification of biomass in packed bed reactor. Fuel Process Technol, 141: 93–98. DOI: 10.1016/j.fuproc.2015.07.015.

[16] Sircar I., Sane A., Wang W., Gore J.P. 2014: Experimental and modeling study of pinewood char gasification with CO_2. Fuel, 119: 38–46. https://doi.org/10.1016/j.fuel.2013.11.026 .

[17] Mani T., Mahinpey N., Murugan M. 2011: Reaction kinetics and mass transfer studies of biomass char gasification with CO_2. Chem Eng Sci, 66: 36–41. https://doi.org/10.1016/j.ces.2010.09.033 .

[18] Pedroso D.T., Machín E.B., Silveira J.S., Nemoto Y. 2013: Experimental study of bottom feed updraft gasifier. Renew Energ, 57: 311–316. https://doi.org/10.1016/j.renene.2013.01.056 .

[19] Karlström O., Costa M., Brink B., Hupa M. 2015: CO_2 gasification rates of char particles from torrefied pine shell. Fuel, 2015; 158: 753–763. https://doi.org/10.1016/j.fuel.2015.06.011 .

[20] Thanapal S.S., Gasification of Low Ash Partially Composted Dairy Biomass with Enriched Air Mixture. Master's thesis, Texas A&M University, 2010.

CYSENI 2018, May 23-25, Kaunas, Lithuania
ISSN 1822-7554, www.cyseni.com

INVESTIGATION OF CHEMICAL COMPOSITION OF PARTICULATE MATTER EMITTED FROM SMALL AND MEDIUM SCALE BIOMASS BOILERS

V. Zaleskas, M. Kulokas, N. Pedišius
Lithuanian Energy Institute
Breslaujos 3, LT-44403 – Lithuania
Email: vladas.zaleskas@lei.lt

ABSTRACT

Chemical composition, size and form of particles determine physical and chemical characteristics of particulate matter (PM). Those in turn greatly influence the efficiency of precipitation methods. The main findings of a literature review was that fine particles usually consist mainly of compounds of volatile alkali metals (K, Na) and less volatile alkali earth metals (Ca, Mg). In contrast, coarse particles mainly consist of non-volatilized minerals such as Ca, Mg, Mn, P, Si and smaller concentrations of the same volatile metals, like K and Na. However, exact composition varies greatly when different types of fuel and different types of wood are used. Therefore, emission dependence on different local biofuel needs further investigation. For that purpose installation for experimental investigations of a small scale water boiler emission dependence from fuel and other parameters was designed and prepared. 25 kW water boiler with pellet burner and a precipitator was used for the experiments. Different emission parameters were measured during the experiment and samples of bottom ash and fly ash were taken for elemental analysis using inductively coupled plasma mass spectrometry. Elemental analysis results show very little concentrations of Na and Mg, indicating that local biofuel has little of these elements. K and Ca mass concentration ratio was 1:5 in bottom ash and 3:1 in fly ash. For comparison purposes samples of PM from district heating unit burning wood chips were taken for elemental analysis. Concentration of Ca and K oxides and sulfates comprised 47% to 57% of PM, but in contrast to the small scale boiler fly ash composition, here K and Ca ratio was 1:5 in particles from multicyclone and 2:3 in PM from electrostatic precipitator (ESP).

Keywords: particulate matter, emission, biomass combustion, chemical PM composition.

1. INTRODUCTION

PM10 directly emitted from residential wood combustion was about 1.2% of the total PM from all sources, but locally could account for as much as 20–90% of the wintertime fine particle emissions as estimated by the United States Environmental Protection Agency [1]. It demonstrates that impact of biofuel industrial and domestic use for heat and energy to atmospheric PM levels is significant and shows the need for investigation of PM emission trends.

Extensive measuring programs of 303 individual measurements of emission from industrial and other plants in Germany were performed to improve the knowledge of fine dust emissions [2]. Authors explained that ultrafine particles are formed in thermal processes, due to sublimation or condensation. On the contrary, mechanical processes usually generate particles larger than 1 μm. Therefore, fraction of PM1.0 was low, 0–30%, in natural stone and sand processing, poultry farming plant, drying, cooling, processing, recycling of waste, asphalt mixing plant PM emissions. In medium to large scale combustion plant emission PM1.0 portion lies between 30% and 60% as presented in Table 1. Both wood and coal small scale combustion units has even higher percentage of PM1.0 emissions ranging from 60% to more than 90% of total dust. Of course, exact size distribution is influenced by a number of factors: the firing and flue gas cleaning technologies, the fuel type, operating conditions and other.

Table 1. Part of PM10/PM2.5/PM1.0 in all emissions from solid fuel combustion plants [2]

Combustion plant	**PM 10***	**PM2.5***	**PM1.0***
Coal	88–96	67–77	34–52
Coal, small	92–95	79–85	64–75
Wood	83–98	53–74	34–61
Wood, small	95–99	80–95	67–92

* 25% to 75% of measured values.

Other investigations report similar findings. Tissari et al. (2009) [3] compared small Finnish batch appliances burning birch logs and determined that emissions from modern masonry heaters (MMH) are similar in mass (51 to 81 mg/MJ) with conventional masonry heaters (CMH), but particles are smaller in size with mass median diameter (MMD) at 179 μm, while MMD of PM emitted from CMH was 277 nm. Therefore, MMH emission number concentration was twice that of CMH: $5.9 \cdot 10^{14}$ #/kg compared to $3.1 \cdot 10^{14}$ #/kg. Sauna stove (SS) represented inefficient batch combustion producing large emissions of PM (257 mg/MJ), carbon monoxide (CO) and organic gaseous carbon (OGC). Largest part of PM was PM2.5 covering from 0.1 to 2 μm range with MMD at 415 μm. On the other hand, pellet boiler represented efficient combustion [4]. Modern boiler with lambda sensor and air intake control burning pine pellets produced only 20 mg/MJ, at 137 μm MMD. Another study of a fully automated 25 kW pellet boiler reported even lower concentrations of PM1.0 at $3.5 \cdot 10^{13}$ #/MJ and 16.2 mg/MJ [5]. Considering that number size distribution being unimode with geometric mean diameter (GMD) of 60 nm PM1.0 for all practical purposes represents all of PM.

Emission from wood pellet and cereal fuels' (cereal seeds of oat and rape, rape bark pellets) differences were investigated using 20 kW cereal and/or pellet burner and fitted boiler [6]. Particle number emissions were stable, 8 to $13 \cdot 10^{14}$ #/kg, except when burning oat, partial load: $27 \cdot 10^{14}$ #/kg. All number distributions were unimodal, geometric mean diameter (GMD) measured with fast mobility particle sizer (FMPS) ranged from 44 nm for rape seed to 68 nm for oat-peat and wood at exact average: 51 nm. Over 95% of PM mass emissions were PM1.0 except when burning oat-kaolin which was only case of two modes: 0.1–0.2 μm and 3–9 μm. As expected, emissions were lowest for wood at 0.21 g/kg, close second being rape seed at 0.27 g/kg. Other were higher, but only 1.7–3.5 fold even though ash content of other cereal fuels was 8–22 fold higher. MMD were similar, 164 to 177 nm except for oat-peat at 249 nm and oat-kaolin – second mode bringing MMD to 385 nm.

Barley straw and reed canary grass (RCG) as a possible fuel for co-combustion were compared to wood chips in 40 kW combustion reactor [7]. Wood chips was spruce (70%) and deciduous tree species (30%) mix while wood/RCG wt% ratio was 78/22 and 78/22 or 67/33 for wood/straw. Adding RCG increased fine particle number emissions thus decreasing GMD from 102 nm for wood to 72 nm, but mass concentration increased only 1.4 fold. Addition of straw on the contrary, increased GMD to 423 nm, decreased number emissions, but because of 4 times larger particles on average PM1.0 mass was 15 fold higher.

A range of different fuels consisting of softwood stem, bark, peat and various mixtures of these materials were studied burning them in 500 kW pellet boiler working at 314–411 kW actual power [8]. PM emissions varied from 14 to 36 mg/MJ and in all cases had two modes: 0.1 to 0.2 μm fine particle mode and 1 to 10 μm coarse particle mode with a peak concentration at 5.1 μm. In all cases majority of PM mass was from PM1.0 (57% to 93%), whole wood and peat having most significant coarse particle mode (40% and 43% respectively). This could be because refractory inorganic compounds Ca, Mg, Fe and Si usually found in coarse particles were more abundant in peat than in woody biomass fuels. Nevertheless, GMDs of number size distribution were 59 to 96 nm measured with ELPI and 53 to 71 nm measuring with FMPS.

Emissions from 2 MW wood briquette district heating boiler were investigated by Johansson [9]. Particle number emissions were dominated by submicron particles with the maxima of the number size distributions between 80 and 300 nm. Unfortunately authors did not present MMD or even PM1.0 mass portion, but from number size distribution micron-sized particle mass portion could be assumed to be larger than that of submicron particle. In addition, from emission measurement at different loads and air feeding shift towards larger particle sizes at low excess air and also at low load was observed.

Medium and large scale combustion units emit fly ash with two distinct modes [10]. As before, fine particle mode is 0.03 to 1 μm with a peak at 0.1 to 0.3 μm and coarse spans from 1 to 100 μm with a peak at 5 to 15 μm [11, 12]. However, PM1.0 amounts to only from 16% (10 MW plant burning sawdust and bark) to 44% (15 MW plant burning wood chips) of total PM mass, measured after multicyclone, before secondary precipitator [10]. Interesting to note that wet scrubber removed coarse particles with 79% and fine particles 44% efficiency enriching PM1.0 from 26% up to 70%. In contrast ESP efficiency was slightly higher for fine particle mode (94% to 95%) than coarse particles (93%).

Tissari [6] analyzed only PM1.0, but in all but one case over 95% of PM was PM1.0, thus it's equivalent of analyzing all of PM. 51% to 83% of PM was ash materials: potassium sulfates, carbonates, chlorides, phosphates. Other materials were mainly particle organic matter (5% to 17%) and elemental carbon (up to 11%). Wood PM was comprised mainly of K and SO_4 and some Cl: 48%, 34% and 16% respectively. Rape fuels emissions stood out as most homogenous, ash materials making 80% and over 86% of those were potassium and sulfate with 8% of phosphates in the follow and no KCl identified at all. Oppositely, oat fuel PM varied the most. Bulk was K (40% to 60%) but SO_4 (up to 23%) was less than PO_4 (up to 40%) also some Cl (5% to 10%) and CO_3 (7% in one case). Interesting to note is that 17% of fuel K was released to PM for wood when only 3% released for oat and as little as 1.3% to 1.8% for rape. This could be explained by high S/Cl, S/K and K/Cl ratios (22, 5.53 and 4.2 fold respectively of those in wood) which caused sulfation of K.

Compatible composition of emissions burning wood pellets in domestic 22 kW burner was reported by Johansson [9]. K_2SO_4 was dominating with 69%, KCl – as second highest concentration compound at 24% and other compounds (K_2CO_3, NaCl, Na_2SO_4) bellow 2% each. In some cases, though, varying composition is presented. For example, Kaivosoja reported PM1.0 composition from 25 kW pellet boiler to have high concentration of Na (17%) beside commonly observed K (37%), Cl (10%) and SO_4 (15%) [5].

Composition of PM1.0 from 40 kW wood chips combustion reactor was in essence equivalent to small scale pellet burner: 40% K, 30% SO_4 and 11% Cl with noteworthy 2% of Zn [7]. Changing air staging setting didn't change ratio of these compounds, but changed amount of EC and OC. In extreme case, reducing total lambda from 2.2 to 1.6 increased PM1.0 15 fold from EC and OC particulate matter alone. Addition of agricultural fuels reduced SO_4 and increased Cl concentrations. In case of reed canary grass – wood mix SO4 reduced to 15% and Cl increased to 21% and even more drastically in case of straw-wood co-combustion: 5% SO_4 and 35% of Cl.

PM1.0 from composition 500 kW pellet boiler burning whole wood was relatively standard: 26% K, 22% SO_4, 13% Cl, significantly lower concentration of Na at 2%, which was even surpassed by Zn at 3% [8]. PM of stem fuels contained larger Cl concentrations of up to 35% Cl, and only 4% of SO_4 in extreme case. PM of stem and peat fuels on the other hand contained higher Na concentrations of up to 15% even exceeding K concentration in peat and peat-stem mix. In contrast, when samples were taken from cyclone of 550 kW biomass combustion plant burning wood chips and forest residue composition of precipitated particles were dominated by Ca (26%), K in the follow with 9%, SO_4 with 8%, Si with 6%, PO_4 with 3.5%, Mg with 2% [13].

In case of 5 to 35 MW district heating boilers [10–12] separate analysis of both fine and coarse particle mode in necessary. The fine particle mode is mainly composed of volatilized ash species that nucleate/condense in the furnace or later during cooling of the flue gas. It primarily consists of K_2SO_4 which in most cases from over 75% of PM1.0 mass with Na, Cl and CO_3 in lesser concentrations [10,11]. Coarse mode typically contains high concentrations of alkali earth metals (Ca, Mg), Si, P, Mn, sulfate, and alkali metals as well. Ca is leading element making up 16% to 17% alone and in the form of $CaCO_3$ making up to 43% of PM. Potassium constitutes substantial part of 8% in coarse particle mode as well, and combined with fine mode K makes up to 15% of total PM.

PM electric resistivity is very important characteristic when considering ESP efficiency. It is believed that ESP is operation is optimal, if PM resistivity is 10^7–$5\cdot10^{10}$ Ω·cm [14] although different authors acclaim wider range of acceptable PM resistivity [15]. If resistivity is too low then precipitated particle transfers the charge to electrode and might tear off back to the flow [16]. If resistivity is too high, then particles keeping electric charge would create opposite electric field and eventually cause back Corona [15]. Not surprisingly, electric resistivity depends on chemical particle composition [17]. For example, silica, aluminum oxides and organic carbon in the fly ash increase the resistivity while sodium and potassium compounds – decrease it [17, 14]. Therefore unsurprisingly PM of coal firing has 2 to 4 orders higher resistivity (10^7 to 10^8 Ω·m) than biofuel firing (10^4 to 10^6 Ω·m).

According to Lanzerstorfer density of the fly ashes varies between about 2200 and 2750 kg/m^3 [18]. The lower values were found for the density of fly ash from wood chips combustion, which is 2620 ± 80 kg/m^3. Fly ashes from straw combustion have lower density, 2260 ± 80 kg/m^3 very likely because of its high content of potassium chloride, which has a relatively low density of 1.988 kg/m^3 [19]. The bulk density of fly ashes from wood chips combustion varied from only 100 to 660 kg/m^3 in one case. Variable bulk density could be explained by different size distribution, namely coarse and bread PM distributions could be a reason for high bulk density. Bulk density of fly ash from straw combustion was much more stable at about 300 kg/m^3. Loo and Koppejan report similar findings as well [20].

Unsurprisingly PM characteristics such as electric resistance and density depend on chemical composition and as well as particle size also other parameters are imperative in choosing precipitation method for the exact application. Literature review shows that PM from biofuel combustion can have one or two modes. Small scale combustion unit usually emit solely fine particle mode, but changing operation parameters or mixing in different kind of fuels could cause particle size distribution shifting to larger diameters or emergence of coarse particle mode. On the other hand, emissions from medium scale plants contain larger portions of coarse mode. Fine particles generally are composed of potassium sulfates and chlorides and less often contain sodium, phosphates and carbonates. Oftentimes Zn is found to be enriched in fine particle mode too. Coarse particle mode has larger concentrations of less volatile elements such as Ca, Mg, Fe, Al, Si. Nevertheless, exact composition could vary greatly depending on the fuel and other combustion parameters therefore emission dependence on different local biofuel needs further investigation.

2. METHODOLOGY

For the investigation of emissions from small scale boilers an experimental installation was designed and constructed. It consists of 25 kW pellet burner with compatible boiler, particle precipitator and PM emission measuring equipment using gravimetric method. It was designed for the purpose of determining PM emissions from different local biofuels to help developing emission reduction apparatus, but to date only initial experiments were performed without changing the fuel type and using only wood pellets. Pellets were 6 mm diameter and 5 to 30 mm length, 11% humidity, 0.39 % ash content. During the measurements, boiler was working at 20 kW capacity. For elemental analysis samples of PM from the precipitator and bottom ash from the boiler were taken.

For comparison purposes, PM samples from bunkers of multicyclones and electrostatic precipitator in district heating burning wood chips. The plant had two 7 MW boilers which had ESP following multicyclones for each boiler. Samples were collected from boilers working at standard condition during nominal power mode. Since samples were taken from the bunkers of ESP and multicyclone it was difficult to determine at what exact time PM were precipitated and retrace the exact characteristics of a fuel used at the time.

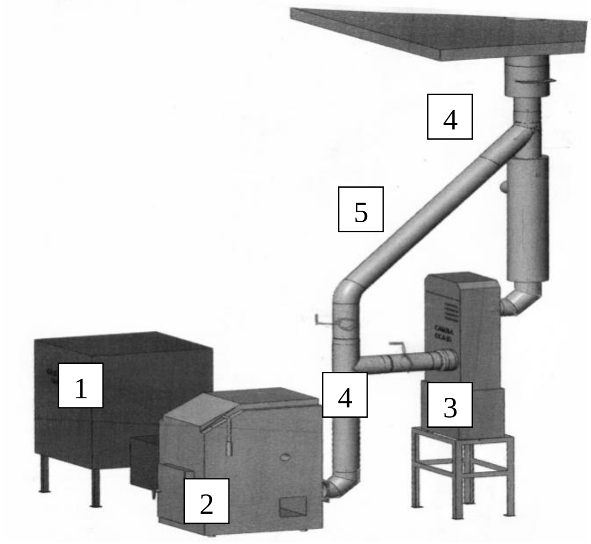

Fig. 1. Experimental setup for measuring emissions from biofuel boiler: 1 – 25 kW pellet burner, 2 – compatible boiler, 3 – particle precipitator, 4 – outlets for emission measuring and 5 – bypass for precipitator

Emission measurements were performed according to standard EN 13284-1:2001 Stationary source emissions – Determination of low range mass concentration of dust – Part 1: Manual gravimetric method. The elemental analyses were performed by inductively coupled plasma mass spectrometry (ICP-MS) and CHNS analysis. Oxygen content in oxides of determined elements was estimated according to standard ISO 16967:2015 Solid biofuels – Determination of major elements – Al, Ca, Fe, Mg, P, K, Si, Na and Ti.

3. RESULTS AND DISCUSSION

3.1. Small scale wood pellet boiler

Ash content of only 51.1% in bottom ash and 31.4% in PM was determined in samples from 25 kW pellet boiler. The fact that large part of both bottom and especially fly ash constitutes organic and elemental carbon indicates incompleteness of combustion process. Nevertheless, element portion in the ash content was calculated, so it could be compared as presented in Fig. 2, a. This way however C and O mass percentage in ash content could not be calculated because these elements also comprises the combustible materials which were discounted.

As expected, potassium was dominating element between alkali and alkaline earth metals with 23% in fly ash, but it’s concentration in bottom ash was low (5%). Alkaline earth metals Ca and Mg, which are less volatile, were found mostly in bottom ash at 24% and 7% respectively. However, they were also present in fly ash with 8% and 2% respectively, which indicates the significant concentration of larger particles. Concentrations of heavy metals were lower than 0.1% in fly ash and even lower in bottom ash with the exception of Zn, which was sparse in bottom ash at 0.2%, but heavily enriched in fly ash at 12%. Relatively high Ca, Mg content in fly ash and surprisingly high concentration of Zn which is known to be enriched in fine particles, but not to such degree calls for further investigation of PM size distribution, chemical composition and their dependence on boiler operation conditions.

3.2. Medium scale district heating unit

Samples from electrostatic precipitator, which was installed after multicyclone in medium scale plant, were taken for chemical composition analysis. Ca, K, Mg and Si oxides and sulfates comprised 50% of PM samples from multicyclone (Fig. 2, b). A concentration of calcium ranges from 23% to 25%, oxygen 15%, potassium 4.3%, carbon 5.4% to 5.7%, silicon 2.8%, magnesium 2.6%, phosphorus 1.2% and sulfur 0.7%. High Ca, O and K but low S and insignificant Cl concentrations would suggest that calcium and potassium oxides are dominating instead of sulfates and chlorides.

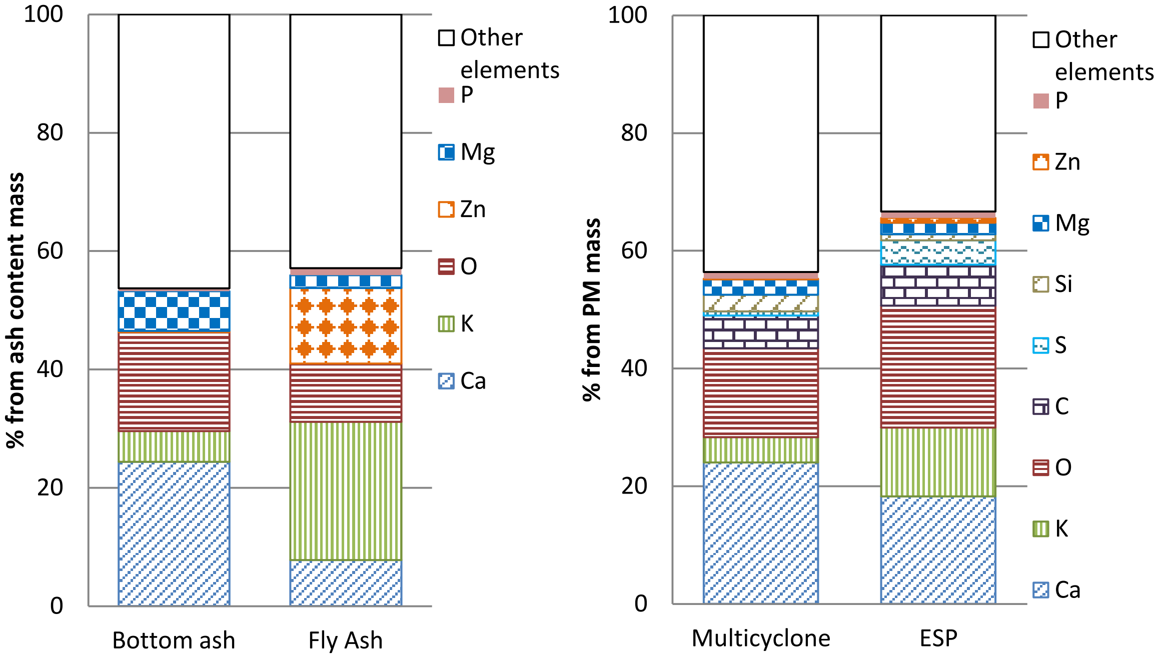

a b

Fig. 2. Elemental composition of a) PM from 25 kW pellet boiler and b) district heating plant

Ca, K, Mg and Si oxides and sulfates comprised majority (58%) of PM in samples from ESP, but they contained considerably lower concentration of Ca at 18.0% to 18.5%, Mg at 2.0%, Si at 1.0%, similar concentration of C (7%), P (1.1%), and higher concentrations of O (21%), K (12%) and especially S (4%). Even accumulation of some low concentration elements could be observed: Zn increased from 0.1% to 0.8%, Na – from 0.2% to 0.3%. All these elements that were enriched after multicyclone are commonly found in fine particle mode, which is plausible, because efficiency of multicyclone decreases rapidly with decreasing particle diameter under 5 µm. Therefore, it is consistent that chemical composition of PM changed this way because of precipitation of coarse particles in multicyclone and subsequently increased fine particle to coarse particle mass ratio. Relatively low carbon content in PM indicates complete combustion process in opposition of 25 kW burner test results.

4. CONCLUSIONS

Results from a number of studies show that PM1.0 constitutes 30% to 60% of PM in industrial biomass combustion emissions and can surpass 95% in small scale combustion emissions. Fine particles generally are composed of potassium sulfates and chlorides, which can sum up to 60–95% of PM1.0 mass and less often sodium, phosphates and carbonates can be found. Oftentimes Zn is found to be enriched in fine particle mode too making up 2–3% of PM1.0. Coarse particle mode has larger concentrations of less volatile elements such as Ca, Mg, Fe, Al, Si. Nevertheless, exact composition could vary greatly depending on the fuel and other combustion parameters.

Determined chemical composition of PM from small scale boiler was similar to one reported in literature in the sense, that potassium is dominating element between alkali and alkaline earth metals with 23%. But it revealed difference as well in that Ca and Mg were also present in the fly ash which indicates the significant concentration of larger particles. Further and more detailed investigation is called for to determine the cause of this mismatch.

Mainly Ca, K and to lesser extent Mg, Si oxides and sulfates comprised 50% to 58% of PM samples from the medium scale boiler. Samples taken after multicyclone contained lower concentration of calcium, magnesium and silicon, similar concentration of carbon and phosphorus but increased concentrations of potassium, oxygen, sulfur and zinc. K, S and Zn are commonly found in fine particle mode, whereas Ca, Mg, Si are found in coarse particle mode, therefore such composition change simply affirms the fact that multicyclone precipitated coarse particles at significantly higher efficiency than fine particles.

REFERENCES

1. US EPA. National Air Pollutants Emission Trends Report, 1900–1998 (2000). EPA-454/R-00-002.
2. Ehrlich C., Noll G., Kalkoff W.-D. Baumbach G., Dreiseidler A. PM_{10}, $PM_{2.5}$ and $PM_{1.0}$–Emissions from industrial plants—Results from measurement programmes in Germany. Atmospheric Environment 41 (2007) 6236–6254
3. Tissari J, Hytönen K., Sippula O., Jokiniemi J. The effects of operating conditions on emissions from masonry heaters and sauna stoves. Biomass and Bioenergy, Volume 33, Issue 3, 2009, 513–520.
4. H. Lamberg, K. Nuutinen, J. Tissari, J. Ruusunen, P. Yli-Pirilä, O. Sippula, M. Tapanainen, P. Jalava, U. Makkonen, K. Teinilä, K. Saarnio, R. Hillamo, M.R. Hirvonen, J. Jokiniemi. Physicochemical characterization of fine particles from small-scale wood combustion. Atmos. Environ., 45 (2011), pp. 7635–7643.
5. T. Kaivosoja, P.I. Jalava, H. Lamberg, A. Virén, J. Jokiniemi. Comparison of emissions and toxicological properties of fine particles from wood and oil boilers in small (20–25 kW) and medium (5–10 MW) scale. Atmospheric Environment, Volume 77, October 2013, Pages 193–201.
6. Tissari T., Sippula O., Kouki J., Vuorio K., Jokiniemi J. Fine Particle and Gas Emissions from the Combustion of Agricultural Fuels Fired in a 20 kW Burner. Energy & Fuels 2008, 22, 2033–2042.
7. M. Kortelainen, J. Jokiniemi, I. Nuutinen, T. Torvela, H. Lamberg, T. Karhunen. Ash behaviour and emission formation in a small-scale reciprocating-grate combustion reactor operated with wood chips, reed canary grass and barley straw. Fuel, 143 (2015), pp. 80–88.
8. Sippula O., Lamberg H., Leskinen J., Tissari J., Jokiniemi J. Emissions and ash behavior in a 500 kW pellet boiler operated with various blends of woody biomass and peat. Fuel Volume 202, 15 August 2017, Pages 144–153.
9. L.S. Johansson, C. Tullin, B. Leckner, P. Sjövall. Particle emissions from biomass combustion in small combustors. Biomass and Bioenergy, Volume 25, Issue 4, October 2003, Pages 435–446.
10. Sippula O., Hokkinen J., Puustinen H., Yli-Pirila P., Jokiniemi J. Particle Emissions from Small Wood-fired District Heating Units. Energy & Fuels 2009, 23, 2974–2982.
11. T. Valmari, E.I. Kauppinen, J. Kurkela, J.K. Jokiniemi, G. Sfiris, H. Revitzer. Fly ash formation and deposition during fluidized bed combustion of willow. J Aerosol Sci, 29 (1998), pp. 445–459.
12. T. Lind, T. Vaimari, E. Kauppinen, K. Nilsson, G. Sfiris, W. Maenhaut. Ash formation mechanisms during combustion of wood in circulating fluidized beds. Proc Combust Inst, 28 (2000), pp. 2287–2295.

13. Lanzerstorfer Ch. Cyclone fly ash from a grate-fired biomass combustion plant: Dependence of the concentration of various components on the particle size. Fuel Processing Technology 131 (2015) 382–388.
14. Zhuang Ye, Kim Y.J., Lee T.G., Biswas P. Experimental and theoretical studies of ultrafine particle behavior in ESPs. Journal of electrostatics 48 (2000) 245–260.
15. Barranco R., Gong M., Thompson A., Cloke M., Hanson S., Gibb W., Lester E. The impact of fly ash resistivity and carbon content on electrostatic precipitator performance. Fuel 86 (2007) 2521–2527.
16. Vassilev S.V., Baxter D., Andersen L.K., Vassileva Ch.G. An overview of the chemical composition of biomass. Fuel 89 (2010) 913–933.
17. Jędrusik M., Świerczok A. *Design Efficiency of ESP*. 2012. ISBN: 978-953-51-0381-3, InTech.
18. Lanzerstorfer Ch. Chemical composition and physical properties of filter fly ashes from eight grate-fired biomass combustion plants. Journal of Environmental Sciences, 30, 2015, 191–197.
19. D.R. Lide. CRC Handbook of Chemistry and Physics. (83rd ed.), CRC Press, Boca Raton (2002).
20. S. van Loo, J. Koppejan. The Handbook of Biomass Combustion and Co-firing. Earthscan, London (2008).

CYSENI 2018, May 23-25, Kaunas, Lithuania
ISSN 1822-7554, www.cyseni.com

EFFICIENT BIOMASS VALUE CHAINS FOR HEAT PRODUCTION FROM ENERGY CROPS IN UKRAINE

O. V. Tryboi
Institute of Engineering Thermophysics
Zheliabova str., 2a, 03680 Kyiv – Ukraine
Email: mrs.tryboi@gmail.com

ABSTRACT

The purpose of the paper is to identify the most efficient willow and Miscanthus value chains for heat production in terms of energy efficiency, environmental sustainability in Ukraine.

The methodology of Life Cycle Assessment (LCA) was used, according to which, the scope of the product system includes the raw material cycle of energy crops cultivation and harvest, and the subsystem of biomass conversion to heat in a 500 kW biomass boiler.

Cumulative energy demand and energy yield coefficient were chosen as energy efficiency indicators. The product system was compared with the similar one using natural gas. Non-renewable energy yield coefficient (EYC_{NR}) was used to define the ratio between energy output and non-renewable energy input. An acceptable value for renewable energy installations and systems is to receive twice as much energy output as was spent of non-renewable energy, however the recommended value assumed in the paper is to receive a 5 times more energy output compared to non-renewable energy input.

As an environmental sustainability indicator, a reduction of GHG emissions was used. The acceptable level of GHG emissions reduction was chosen at a level of 60% for the whole life cycle from cultivation-to-heat, compared to traditional heat production in gas boilers.

Data on technological operations and machinery used in the feedstock cycle are based on consultations with operating producers of energy crops. The input to the system at such stages as growing, harvest with shredding, transporting and storage, and disposal of products of combustion contain consumption of diesel, pesticides and fertilizers.

Analysed papers that assess energy conversion pathways use specific LCA tools usually with a variety of impact categories and receive results as normalized values that show the calculated impact as a proportion of the emissions of an average European citizen. Such approach is not applicable for Ukrainian conditions, as there is lack of required local input data available (for example, emissions of an average Ukrainian citizen). For this reason LCA based on GHG and energy balance was applied in research of forest and agro biomass for heat energy pathways conducted for Ukrainian conditions. The results of LCA for value chains of wood chips and straw bales combustion in 350 kW boiler show the energy efficiency of these pathways for transport distance of up to 150 km for wood chips and up to 200 km for straw bales ($EYC_{NR} > 5$).

Results of the present research show that feedstock cycle for willow chips to heat value chain is similar to feedstock cycle of forest wood chips in terms of non-renewable energy consumption. Miscanthus chips to heat value chain shows even better energy efficiency, than straw-to-heat value chain ($EYC_{NR} > 5$ for 300 km for Miscanthus compared to 200 km for straw) that can be explained by higher net calorific value of Miscanthus compared to straw. GHG emissions reduction of energy crops to heat pathways is less compared to wood and straw pathways due to application of fertilizers and pesticides that have high emission factors, but still performs a 60% GHG emission reduction at transportation distances of 600 km for willow and 900 km for Miscanthus.

Keywords: energy crops, Miscanthus, willow, LCA, energy efficiency, GHG, Cumulative Energy Demand, Energy Yield Coefficient, bioenergy heat

CYSENI 2018, May 23-25, Kaunas, Lithuania
ISSN 1822-7554, www.cyseni.com

DETERMINATION OF KINETIC PARAMETERS OF ORIGINAL AND TORREFIED BIOMASS SAMPLES

A. Çalışkan, H. Haykırı-Açma, S. Yaman
Istanbul Technical University
Maslak, 34469 – Turkey
Email: yamans@itu.edu.tr

ABSTRACT

Rapid escalation in global greenhouse gas emissions (GHG) that is mainly produced by fossil fuel consumption has propelled the world to focus on renewable energy sources and developing new technologies that cause nearly zero emission. Due to the unique feature of 'carbon neutral' nature of biomass, it seems as the most attractive renewable fuel for energy generation worldwide. Agricultural potential of Turkey that can be used as renewable energy source is substantial and has to be benefited due to its numerous advantages. In this study, rhododendron, hybrid poplar and ash-tree were used as biomass sources which are the first primary biomass species in the understory of the forests located in the Black Sea Region of Turkey and the latter are also two of the most rapid growing woody biomass species. In order to increase the heating value of biomass sources and enhance bulk densities, biomass samples were torrefied at 200 °C in a horizontal tube furnace under nitrogen atmosphere. Then, kinetic study of both original and torrefied biomass samples were carried out by using Borchardt & Daniels (B&D) kinetic analysis method for a deep understanding of the thermal behavior of the combustion process. Kinetic parameters such as reaction order, heat of reaction, activation energy, and pre-exponential factor were calculated from the data obtained during a single linear heating rate scan and results were discussed.

Keywords: kinetic study, torrefaction, combustion.

1. INTRODUCTION

Due to the decreasing fossil fuel resources and increasing concerns about global warming, biofuel production has gained considerable importance in recent years [1, 2]. Among the all-renewable energy sources that are solar, wind, hydroelectric, biomass and geothermal power, biomass is the largest and versatile energy source [3]. Its dominance is expected to continue in the future as well since bioenergy contributes to climate change mitigations, provide energy security and generate new jobs. In 2013, the share of renewables in the final energy consumption of the world was 18% in which the contribution of bioenergy was 14% while hydroelectric and other types of renewable energy sources accounted for 4% in total. The amount of sustainable biomass supply is estimated to increase up to three times in the near future. Furthermore, biomass is the only renewable energy source that can substitute fossil fuels in many different industrial sectors thanks to production of solid, liquid and gas fuels [4].

The rate of global biomass production is estimated 146 billion metric tons per year involving mostly wild plant growth [5]. USA and Brazil, which are responsible for approximately 80% of world's biomass production, act as the leader countries in production and consumption of liquid biofuels for transport. Currently, biomass accounts for only 5% of primary energy consumption in industrialized countries contrary to developing countries where this percentage rises to 35% due to the dependence on biomass as an energy source [6]. Furthermore, woody biomass presents nearly 90% of the global primary energy annually produced from all types of biomass sources.

Thanks to the geographic location, Turkey is rich by most of the renewable energy sources. Due to the dependence on foreign energy, particularly oil, gas and high rank coal, utilization of biomass such as wood, hazelnut shell, agricultural waste residues, waste paper and wheat straw, tea waste and olive husk for energy production has become prominent in the country's energy strategy [7]. Turkey's biomass potential is approximately 8,6 million tonnes of equivalent petrol (MTEP) and the amount of biogas that can be produced from the available biomass sources is estimated in the range of 1,5–2 MTEP [8]. As an agricultural country, greatest amount of biomass energy is generated from agricultural wastes in Turkey. Besides, forestry and animal wastes are also important biomass energy sources [9]. Wood is the most significant biomass energy source in Turkey since it accounts for almost 20% of the total biomass production. Moreover, conversion of wood to useful energy is relatively easy when compared to other biomass types [10]. It is estimated that electricity production in biomass based power plants where wood is used primarily, will rise to about 50 GW in 2030 while it was 10 GW in 2009. Related to this capacity increase, 6.4 billion USD in personal and corporate income along with the 250,000 job opportunities is expected as the economic welfares [11].

Unlike fossil fuels, only atmospheric CO_2 that is absorbed by plants recently during photosynthesis is released when biomass burns and it is recycled into the plants achieving net zero emission of CO_2. The unique feature of 'carbon neutral' nature of biomass makes it the most attractive renewable fuel for energy generation worldwide [12]. Due to the almost depleted fossil fuel sources, biomass based power generation is of growing importance to get rid of environmental concerns and the anxieties related to the security of energy supply.

The general classification of biomass materials as fuel resources can be divided into five groups according to their biological diversity, similarity and origin. These groups are named as agricultural, forestry, municipal, energy crops and biological biomass materials [13]. A considerable portion of biomass energy is produced from wood and wood wastes with 64%. Municipal solid waste, agricultural waste and landfill gases follow it by 24%, 5% and 5% shares, respectively [14, 15]. Even though all types of biomass sources can either be used for energy generation by combustion or to derive fuel from it through conversion processes, better quality of fuels are produced by some species in a cost effective manner. Thus, several types of biomass have been grown specific to energy production. Studies on energy crops that encompasses woody crops and grasses/herbaceous plants, starch and sugar crops and oilseeds have been carried out in this context.

Conversion of biomass into solid, liquid and gaseous products via thermochemical methods is performed to improve biomass characteristics and produce biofuel. The primary thermochemical methods for conversion of biomass are combustion, carbonization, torrefaction, pyrolysis, gasification and liquefaction. Torrefaction, which is focused on in this study, is a thermochemical process that is carried out under inert or limited oxygen atmosphere and operated slowly within a specified low temperature range to upgrade ligno-cellulosic biomass to a higher quality and more attractive biofuel. Torrefaction process is operated at low temperature range of 200–300 °C [16]. The removal of oxygen with a final solid product is the main principle of torrefaction process [17]. In other words, O/C ratio is lower in torrefied biomass compared to the raw biomass. Torrefaction of biomass causes a mass loss due to devolatilization, but increases the calorific value. Typically, 70% of the mass is retained in solid products that contain 90% of the initial energy content [18]. Thus, energy density of biomass increases by torrefaction in comparison with original biomass that facilitates transportation to large distances [19]. In order to maximize the solid yield of the process, it is operated at slow heating rate that is one the main important characteristics of torrefaction. Normally, heating rate of torrefaction is less than 50 °C/min. Higher heating rate causes the formation of more amount of liquid products, which is aimed in pyrolysis [13].

Hybrid poplar is a fast growing tree and can be harvested throughout the year [20]. In comparison with similar biomass species, growing rate of hybrid poplar trees is six to ten times faster and their lifespan is more than forty years [21]. Thanks to the desired features of hybrid poplar in terms sustainable biomass energy generation, bio-fuel production is one of the important beneficial uses of hybrid poplar. Rhododendron is the primary biomass species with about 40 metric ton ha^{-1} in the understory of the forests of the Black Sea Region that damages the other species by restricting tree growth, preventing regeneration of target tree species and decreasing the diversity of species. Thus, use of Rhododendron as biomass resource for bio-fuel production helps to control their invasion as well as increase renewable energy generation [22]. Ash tree is one of the fastest growing native biomass after poplar and alder; therefore, it is considered as valuable biomass resource to be utilized in energy generation in Turkey besides in forest products industry [23]. Thus, these biomass materials were used in this study and their differential scanning calorimetry based kinetic study was performed.

2. EXPERIMENTAL

Rhododendron (RD), hybrid poplar (HP) and ash-tree (AT) were selected as biomass materials in this study due to their large amount and important characteristics that are desired for utilization in energy generation. Biomass samples were dried in two steps of which the first in laboratory medium and the second in oven at 105 °C. Then, the samples were grounded and sieved to a particle size of < 250 µm using Retsch AS 200 sieves. Torrefaction of biomass samples was carried out in the horizontal tube furnace which is made of stainless steel. Since torrefaction process is operated at low temperature range of 200 °C–300 °C the final temperature of torrefaction process was determined as 200 °C and the samples were heated from the ambient tempereature to the final temperature at a heating rate of 10 °C/min under a nitrogen atmosphere with a flow rate of 100 mL/min. The reason of performing torrefaction process with only one final temperature is to compare the original and torrefied biomass samples in a well manner. In order for the further decline in the volatile matter content, the samples were kept at the final temperature for 30 minutes. At the end of the thermal treatment, torrefied samples were left to cool down in its own atmosphere in the furnace. Proximate and ultimate analyses of the original and torrefied biomass materials were conducted according to ASTM standards by using TA Instruments SDT Q600 model thermal analyzer with a cylindrical alumina crucible and elemental analyzer Leco TruSpec CHN, and S modules. In addition, gross calorific value measurements were performed by IKA C2000 Basic Calorimeter with a stainless steel calorimeter bomb. Kinetic study of both original and torrefied biomass samples was carried out by using Specialty Library of TA Universal Analysis program that rely on the Borchardt&Daniels (B&D) kinetic analysis method.

2.1. Borchardt and Daniels Kinetics Approach

Borchardt and Daniels (B/D) approach is one of the three common methods applied for differential scanning calorimetry (DSC) kinetic studies and it allows the calculation of activation energy (Ea), pre-exponential factor (Z), heat of reaction (ΔH), reaction order (n), and rate constant (k) from a sole DSC scan [24]. This approach based on the idea of the reaction follows nth order kinetics, comply with general rate equation and Arrhenius principle.

$$\frac{d\alpha}{dt} = k(T) * [1-\alpha]^n \tag{1}$$

where $\frac{d\alpha}{dt}$ – reaction rate (s^{-1}); α – fractional conversion; k(T) – specific rate constant at temperature T; n – reaction order.

$$k(T) = Z.e^{-Ea/RT} \tag{2}$$

where E_a – activation energy (J/mol); Z – pre-exponential factor (s^{-1}); R – universal gas constant = 8.314 (J/molK).

Substituting equation (2) into equation (1) and rearranging gives:

$$\frac{d\alpha}{dt} = Z.e^{-Ea/RT}(1-\alpha)^n \tag{3}$$

$$Ln\left(\frac{d\alpha}{dt}\right) = Ln(Z) - \frac{Ea}{RT} + n\ln(1-\alpha) \tag{4}$$

Multiple linear regression can be used to solve Equation (4) where $d\alpha/dt$ and α are determined from DSC exotherm. Activation energy (E_a) and pre-exponential factor (Z) are obtained from the slope and intercept of plot of $\ln[k(T)]$ versus $1/T$.

3. RESULTS AND DISCUSSION

Proximate analysis results of original and torrefied biomass samples derived from the thermogravimetric analysis (TGA) profiles and higher heating values determined from the bomb calorimeter experiments are given in Table 1. Besides, ultimate analyses results were presented in Table 2.

Table 1. Proximate analyses and calorific value determination results of original and torrefied biomass samples

Sample	**Moisture (%)**	**Volatile matter (%)**	**Fixed carbon (%)**	**Ash (%)**	**HHV (cal/g)**
RD	5.2	79.0	13.7	2.10	4318
RD200	5.7	80.3	12.9	1.00	4449
HP	9.3	79.0	10.9	0.80	4176
HP200	7.2	80.7	11.2	1.00	4201
AT	7.6	80.3	11.1	1.10	4143
AT200	2.6	84.0	13.5	0.04	4370

When moisture contents of the original biomass samples used in the experimental studies are examined, it is seen that RD has the lowest moisture content while HP has the highest. Torrefied biomass samples do not differentiate from their original forms significantly in terms of moisture content. As it can be easily noticed from Table 1, torrefaction caused a slight increase in the moisture content of RD sample in contrast to other biomass species. The reason of this differentiation is due to the absorbed moisture of air by the porous structure of RD that was formed as a result of torrefaction and revealed by the SEM images of both original and torrefied biomass materials in our previous studies. When the SEM images were analyzed, it was seen that RD gained hydrophilic property after torrefaction process due to its newly formed porous structure. Torrefied biomass samples were cooled down to ambient temperature from the torrefaction temperature under nitrogen atmosphere in the horizontal tube furnace. During the cooling stage, treated samples could absorb the moisture in the air because of their porous structure. On the other hand, the sharpest decrease in moisture content of torrefied HP sample can be explained by the low porous structure. Once the biomass materials were torrefied at 200 °C, volatile matter content of each biomass sample increased to a degree since porous structure of torrefied biomass absorbed the gases present in the medium. The highest increase in the volatile matter content of biomass samples after torrefaction process was observed in AT species that was compatible with the results of SEM images. Concerning the change in the calorific value of the biomass samples, it was observed that there was no significant increase in the calorific values of the torrefied biomass samples and relatedly fixed carbon contents. RD is the leading species in all biomass samples in terms of the highest calorific value, while AT is the lowest one in spite of the close value to HP.

Table 2. Ultimate analyses results of original and torrefied biomass samples

Sample	**C (%)**	**H (%)**	**N (%)**	**S (%)**	**O (%)**
RD	48.50	6.48	0.00	0.34	42.44
RD200	49.64	6.56	0.00	0.34	42.36
HP	47.18	6.67	0.00	0.37	44.88
HP200	47.94	6.56	0.00	0.37	44.06
AT	46.64	6.63	0.00	0.35	45.20
AT200	49.29	6.46	0.00	0.34	43.90

According to Table 2, biomass species do not differ from each other significantly in terms of elemental carbon, hydrogen, nitrogen, sulfur and oxygen contents. Elemental carbon contents of biomass species were determined as RD > HP > AT which is consistent with their higher heating values. Torrefaction of biomass samples at 200 °C was resulted in minor increase in the elemental carbon content of each species that changes between 1.61–5.68%. The biggest rise was detected in torrefied AT species whereas; HP was recorded as the least affected biomass sample from torrefaction process that was deduced from its 1.61% increase in the elemental carbon content.

DSC profiles of the original and torrefied biomass samples which were obtained through thermal analysis experiments in our previous studies were used to determine the kinetic parameters including heat of reaction, activation energy and the order of reaction based on Arrhenius Equation. Results of the kinetic analysis of the biomass samples were summarized in Table 3.

Table 3. Kinetic parameters of original and torrefied biomass samples

Sample	**Reaction order**	**Activation energy (kJ/mol)**	**Heat of reaction (J/g)**
RD	3.13	148.3	7221.4
RD200	2.27	115.5	5577
HP	1.54	92.9	7264.5
HP200	2.03	124.3	5961.3
AT	2.08	96.3	8195.5
AT200	2.98	171.1	4741.9

As it is seen from the Table 3, RD has the highest reaction order and activation energy, but least heat of reaction among the original biomass samples. Torrefaction of biomass samples at 200 °C resulted in the 27% decrease in RD, 32% increase in HP, 43% increase in AT sample in terms of reaction order. Since activation energy of a sample indicates the ability of molecules to overcome the barrier for the achievement of burning reactions, lower values are related to the higher reactivity of the investigated sample and easiness of the reaction. Thus, it is likely to say that HP is the most reactive biomass specie whereas RD is the least reactive one.

4. CONCLUSION

This study showed that biomass species investigated in this work are highly different fuels with respect to the kinetic parameters. So that, although torrefaction of HP and AT caused an increase in the reaction order and activation energy, kinetic behaviour of RD was not in compliance with them since the opposite case was observed in RD. Moreover, it was understood that original

HP has the highest reactivity while original RD has the lowest. However, torrefaction of RD sample gave rise to an increase in the reactivity even it became the most reactive biomass species among the torrefied samples.

REFERENCES

1. VASSILEV, S. V., VASSILEVA, C. G., and VASSILEV, V. S. Advantages and disadvantages of composition and properties of biomass in comparison with coal: An overview. *Fuel*, 2015, Vol. 158, p. 330–350.
2. SAMI, M., ANNAMALAI, K., and WOOLDRIDGE, M. Co-firing of coal and biomass fuel blends. *Progress in Energy and Combustion Science*, 2001, Vol. 27, p. 171–214.
3. METZ, B., DAVIDSON, O.R., BOSH, P.R., DAVE, R., MEYER, L.A. (eds.). Climate change 2007: Mitigation of climate change. *Intergovernmental Panel on Climate Change*, 2007, Cambridge, UK: Cambridge University.
4. World Energy Council. *World Energy Resources: Bioenergy 2016*, 2016, London: World Energy Council.
5. World Energy Council. *2010 Survey of Energy Resources*, 2010, London: World Energy Council.
6. EDENHOFER, O., PICHS-MADRUGA, R., SOKONA, Y. (eds.). Special report on renewable energy sources and climate change mitigation. *Intergovernmental Panel on Climate Change*, 2011, Abu Dhabi, United Arab Emirates.
7. KAYGUSUZ, K. and KELES, S. Sustainable bioenergy policies in Turkey. *Journal of Engineering Research and Applied Science*, 2012, Vol. 1, p. 34–43.
8. *Republic of Turkey Ministry of Energy and Natural Resources*. Bio-Fuels. [referred on the 13th of November in 2017 y.]. Link to the internet <http://www.enerji.gov.tr/en-US/Pages/Bio-Fuels>.
9. ACAROGLU, M. and AYDOGAN, H. Biofuels energy sources and future of biofuels energy in Turkey. *Biomass and Bioenergy*, 2012, Vol. 36, p. 69–76.
10. TOKLU, E. Biomass energy potential and utilization in Turkey. *Renewable Energy*, 2017, Vol. 107, p. 235–244.
11. TOKLU, E. and KAYGUSUZ, K. Present situation and future prospect of energy utilization in Turkey. *Journal of Engineering Research and Applied Science*, 2012, Vol. 1, p. 73–86.
12. ABBASI, T. and ABBASI, S.A. Biomass energy and the environmental impacts associated with its production and utilization. *Renewable and Sustainable Energy Reviews*, 2010, Vol. 14, p. 919–937.
13. BASU, P. *Biomass, Gasification, Pyrolysis and Torrefaction: Practical Design and Theory*. London: Academic Press, 2013.
14. DEMIRBAS, A. Combustion systems for biomass fuel. *Energy Sources*, 2007, Vol. 29, p. 303–312.
15. DEMIRBAS, A. Modernization of biomass energy conversion facilities. *Energy Sources*, 2007, Vol. 2, p. 227–235.
16. DEMIRBAS, A. Biorefineries: Current activities and future developments. *Energy Conversion Management*, 2009, Vol. 50, p. 2782–2801.
17. PRINS, M. J., PTANSKI, K. J., and JANSSEN, F. J. J. G. More efficient biomass gasification via torrefaction, *Energy*, 2006, Vol. 31, p. 3458-3470.
18. BERGMAN, P. C. A, BOERSMA, A. R., ZWART, R. W. R., KIEL, J, H, A. Torrefaction for biomass co-firing in existing coal-fired power stations: Biocoal, 2005, (Report ECN-C-05-013). Petten, The Netherlands: ECN.

19. VAN DER STELT, M. J. C., GERHAUSER, H., KIEL, J. H. A., and PTANSKI, K. J. Biomass upgrading by torrefaction for the production of biofuels: A review. *Biomass and Bioenergy*, 2011, Vol. 35, p. 3748–3762.
20. GROOMS, L. A poplar solution, *Farm Industry News*, 2009, Vol. 42, p. 34–34.
21. OZYURTKAN, M. H., OZCIMEN, D. and MERICBOYU A. E. Investigation of the carbonization behavior of hybrid poplar. *Fuel Processing Technology*, 2008, Vol. 89, p. 858–863.
22. AKGUL, M. and CAMLIBEL, O. Manufacture of medium density fiberboard (MDF) panels from rhododendron (R. ponticum L.) biomass. *Building and Environment*, 2008, Vol. 43, p. 438–443.
23. *Republic of Turkey General Directorate of Forestry*. Forest Atlas. [referred on the 15th of November in 2017 y.] Link to the internet <https://www.ogm.gov.tr/ekutuphane/Yayinlar/Orman%20Atlasi.pdf>.
24. BORCHARDT, H.J. and DANIELS, F.J. The Application of differential thermal analysis to the study of reaction kinetics. *Journal of the American Chemical Society*, 1957, Vol. 79, p. 41–46.

CYSENI 2018, May 23-25, Kaunas, Lithuania
ISSN 1822-7554, www.cyseni.com

INVESTIGATION OF THE EFFECT OF KAOLIN ADDITIVE AND DIFFERENT ASHING TEMPERATURE OF AGROMASS

D. Čepauskienė, N. Pedišius
Lithuanian Energy Institute
Breslaujos st. 3, LT-44403 Kaunas – Lithuania
Email: Deimante.Cepauskiene@lei.lt, Nerijus.Pedišius@lei.lt

ABSTRACT

A growing interest has been observed for the use of agricultural residues and herbaceous plants of short rotation in energy sector. However, agrofuel made of agromass has the following negative properties: higher ash content, lower ash softening and melting temperatures, higher content of sulphur, chlorine, alkali and alkaline earth metals. One of the solutions to improve the properties of agrofuels is the use of additives.

Melting behaviour of ashes (reed canary grass, wheat straw, canola straw) produced at 550 °C were investigated using different concentrations (1%, 2%, 3%, 4%, 5%) of kaolin additive. Ash melting behaviour of selected agromass samples were determined using a high temperature furnace with a video camera. The results show that different amount of kaolin additive must be selected for each agromass individually. 1% of kaolin is enough to raise canola straw ash shrinkage starting temperature (SST) from 762 °C to 1304 °C. However the same amount of kaolin added in wheat straw ashes raises the SST temperature 86 °C and reed canary grass ash melting temperature increases of just 37 °C.

The study of different ashing temperature (550 °C, 600 °C, 650 °C, 700 °C and 750 °C) with same agromass samples was conducted monitoring changes in ash content. The results shows that ash content decreases when temperature is increasing. This may be as a result of agromass ash volatilization. However, more reasearch is needed to ascertain the causes and impacts of ash depletion.

Keywords: Agromass, Ash, Melting Temperature, Ashing Temperature

1. INTRODUCTION

Nowadays various kinds of biofuel are being introduced on the market because there is a need for alternatives for fossil fuels. The biomass from which biofuels are produced is the biodegradable fraction of products, waste and residues (including vegetal and animal substances) from biological origin from agriculture, forestry and related industries, including fisheries and aquaculture, as well as the biodegradable fraction of industrial and municipal waste [1]. Generally, biofuel is made from woody biomass but recently more and more attention is drawn to the herbaceous plants of short rotation, agricultural waste such as straw. The fuel produced from such products is usually called agrofuel. However, agrofuel has several negative properties related to high alkali and alkaline earth metals, chlorine and sulphur. Therefore, despite well–known advantages of agromass usage such as carbon dioxide neutrality and high energy generation potentiality of such fuels still rise the technical problems. The main issues with using agrofuel are fouling and slagging, agglomeration and corrosion.

These problems related to potassium and its reactions with other ash forming elements as chlorine, sulfur, phosphorus. Potassium salts are mostly formed during combustion of agrofuel (KCl, K_2SO_4, K_2CO_3). Potassium phosphates are determined in agrofuel which is rich in phosphorus. Moreover, potassium also reacts with silicon and that leads to formation of potassium silicates. Approximately all potassium salts, phosphates and silicate have low melting temperature (~600 °C) [2].

There are several solutions to mitigate adverse effects including leaching, co-firing and the use of additives. Leaching eliminates potassium directly from the source while co-firing as well as additives changes ash composition and diminish the existence of volatile alkali species [3].

Depending on chemical composition of additives, they can be divided into four main groups: aluminium silicates based additives, sulfur based additives, calcium based additives and phosphorus based additives. A high quality additive must have these following characteristics: large surface area, high melting point, high reactivity and temperature stability. Also, the cost of the additive should not severely increase fuel cost. The usage of additive should not cause a negative effect on the combustion process or increase environmental problems. It is also preferably that the required amount of additive should be as small as possible [4]. In order to introduce additive into a combustion system, it can be mixed with raw materials before or during the pellets manufacturing process. Moreover, the introduction of the additive can improve the properties of the pellets. For instance, blending wood waste with a certain amount of sewage or marble sludge improved durability of pellets [5].

Ashing temperature is very important in the investigation of ash melting, because it can have a significant impact on the results. For example, there are no standard for biomass ash analysis in China, so the standard for coal are usually used which is basically inappropriate [6]. In other cases, ashing is carried out at a temperature of up to 600 °C, where 580–600 °C is the temperature range selected. The International Energy Agency has recommended an incineration temperature of 550 °C for straw [7]. The European Committee for Standardization prepared a standard for determination of ash content in solid biofuels which indicating the recommended ashing temperature of 550 °C. However, more reasearch is needed to ascertain the causes and impacts of ash depletion.

The aim of the present work is to investigate the effect of kaolin on melting behaviour of ashes from agricultural waste and herbaceous plants. Ashing test purpose is to produce ash with the least variation in their elements and compounds so as to minimize the impact on ash melting behavior.

2. MATERIALS AND METHODS

The samples selected for the experiments are two types of agricultural waste (wheat and canola straws) and one herbaceous plant (reed canary grass). Wheat and canola straws are commonly available agromass materials in Lithuania. Unlike cereal crops, reed canary grass is only cultivated for experimental purpose trying to assess the suitability of this plant for combustion technologies. All samples were dried in low temperature laboratory furnace under temperature of 105 °C and pulverized in a grinding mill (below 2 mm).

The ash content of samples were determined using a muffle furnace (Nabertherm) at all temperatures (550, 600, 650, 700 and 750 °C) according to ISO 18122:2016. The ashing ration is obtained by weight the mass of raw materials and the corresponding ash. Ash melting behaviour was conducted in a muffle furnaces with the monochromatic video camera CAF DIGITAL 380-415 V with reference to CEN/TS 15370-1. Ashes were grinded with a pestle to obtain particles with a size of less than 0.075 mm. Using a mould with a defined pressure, a moistened (with ethanol) ash powder was used to form cylindrical ash samples with a size of 5 × 5 mm. Samples were heated in ash fusion furnace under reducing atmosphere. A furnace temperature was raised up to 550 °C. Then temperature was gradually raised 5 °C min^{-1} and photos were automatically made every interval of 2 °C till temperature has reached 1500 °C. The temperature at which the phase of the sample changed was recorded.

The calorific value of the samples was determined according to EN 14918:2010 using calorimeter IKA C 5000. Determination of total carbon, hydrogen, nitrogen and sulfur was conducted using a Flash 2000 elemental analyser. The chlorine concentration was obtained with a Dionex ICS-5000 ion chromatography system according to ISO 16994:2015.

3. RESULTS AND DISCUSSION

Chemical composition and energy contents of reed canary grass, wheat straw and canola straw are listed in Table 1. Herbaceous plants and agricultural wastes have higher ash content compared to woody biomass The average ash content of herbaceous plants reaches 4.3%, for agricultural wastes it is about 7.8% while wood and woody biomass is approximately 2.7%. For wood without bark the ash content is even lower and varies within 0.1–2.0% [8]. This can be influence by many reasons, for example, in order to obtain higher grain yield, crops are fertilized with fertilizers of potassium, nitrogen, phosphorus and other elements which are necessary for plant growth. Herbaceous plants which are specially cultivated for energy purpose are as well fertilized in order to increase the amount of agromass. Ash content is also affected by other factors such as genetic plant properties, environmental factors, physiological and morphological characteristics. It has been determined that ash content also depends on plant parts used for production of biofuel [9].

Table 1. Characteristics of the selected agromass types

	Reed canary grass	**Wheat straw**	**Canola straw**
Carbon (%)	47.33	46.02	47.30
Hydrogen (%)	1.25	5.40	5.44
Nitrogen (%)	5.66	0.90	0.92
Sulfur (%)	0.03	0.07	0.24
Oxygen (%)	40.24	39.87	39.57
Chlorine (%)	0.40	0.04	0.19
Heating value (MJ/kg)	17.41	17.45	17.41
Ash (%)	5.49	7.74	6.52

The melting behavior of the ashes without kaolin addition varies significantly between agromass types, but at 950 °C most of the ashes starts to soften and the first stage of ash melting process begins, as it is shown in Fig. 1. As the temperature reaches 1200 °C, all of the ash samples were completely melted. The results from ash melting behavior test with additive showed that kaolin usage positively affects the ash melting temperature. In all cases, the addition of kaolin in the ashes led to melting point increase. However, the equal amount of kaolin does not have the same effect on the ash melting temperature when evaluating the different agromass ashes. 1% of kaolin is enough to raise canola straw ash shrinkage starting temperature (SST) from 762 °C to 1304 °C. However the same amount of kaolin added in wheat straw ashes raises the SST temperature 86 °C and reed canary grass ash melting temperature increases of just 37 °C. It was also observed that in the case of canola straw 1% of kaolin raised SST temperature up to 1304 °C and the further addition of larger amounts of additive does not have significant effect on the ash melting temperature. This tendency is not observed in the case of reed canary grass and wheat straw. Such significant increase in the canola straw SST may be attributed to the fact that most of potassium compounds in the ashes are involved in the reaction with kaolin and in this case 1% of additive is enough to transform the majority of problematic potassium compounds into high melting temperature materials. For this reason, further increase in the amount of the kaolin does not have major impact on the ash melting temperature. The use of kaolin additive modifies the chemical composition and transformation mechanisms of the ashes. Kaolin is basically composed of kaolinite which can react with gaseous potassium compounds to form potassium aluminium silicates which are characterized by high melting temperatures [4].

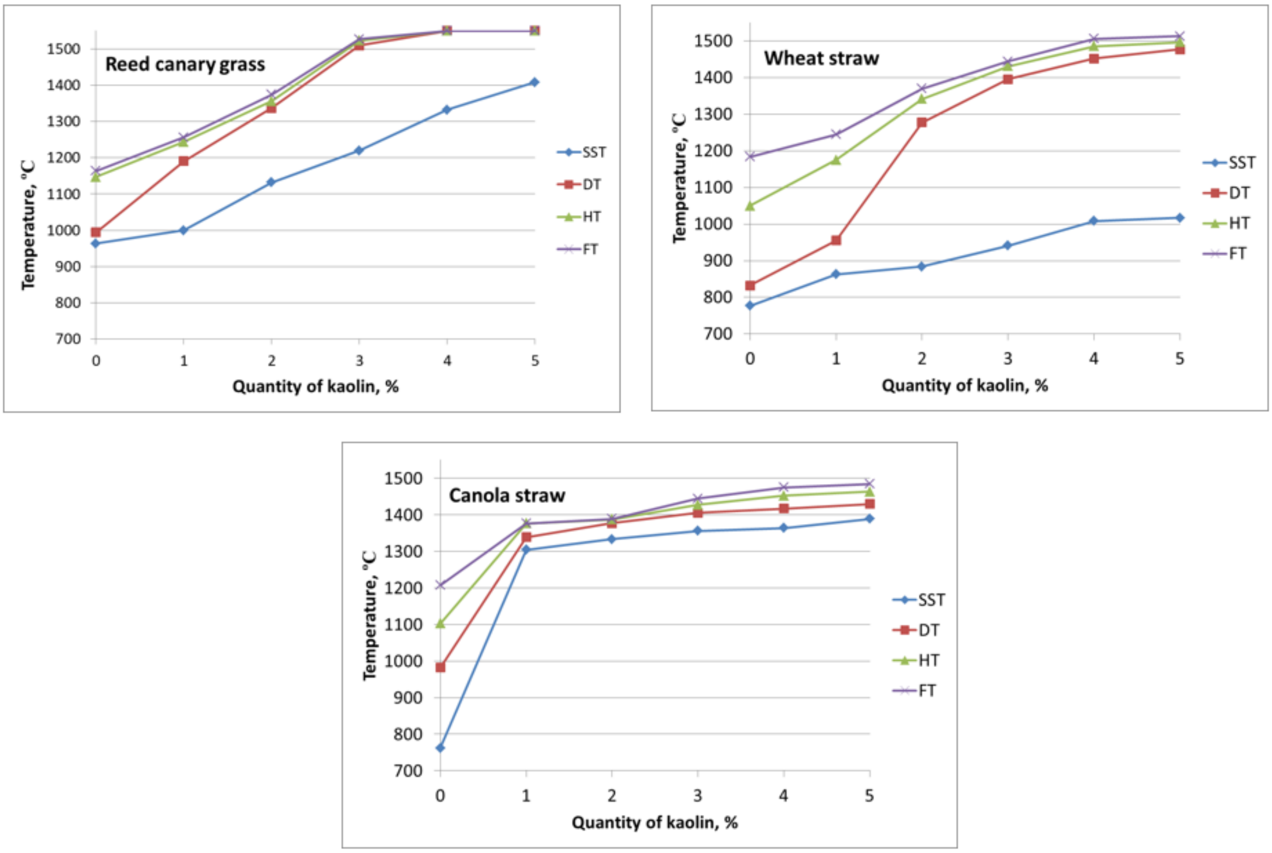

Fig. 1. Melting temperatures of reed canary grass, wheat straw and canola straw ashes with and without kaolin additive

The ash content of agromass at different temperatures (550 °C, 600 °C, 650 °C, 700 °C and 750 °C) are listed in Table 2. As is apparent from the results, increasing ashing temperature leads in declining content of ashes.

Table 2. Ash content of agromass at different temperatures (±SD)

T (ºC)	**Ash (%)**		
	Reed canary grass	**Wheat straw**	**Canola straw**
550	5.80 ±0.05	7.74 ±0.07	7.09 ±0.06
600	5.74 ±0.03	7.53 ±0.01	7.05 ±0.23
650	5.49 ±0.02	7.54 ±0.01	6.23 ±0.04
700	5.32 ±0.01	7.56 ±0.19	6.18 ±0.03
750	5.07 ±0.08	7.08 ±0.21	6.08 ±0.02

This is due to volatile inorganic elements in organic compounds. However, more reasearch is needed to ascertain the causes and impacts of ash depletion. These ash samples will be used in further studies to assess the changes in chemical composition and structure. A similar study was conducted with three kind of biomass including rice straw, pine sawdust and Chinese Parasol Tree leaf burned at three different temperatures. The study has shown that optimal ashing temperature was 600 °C [6].

4. CONCLUSION

The use of kaolin additive helps to form new chemical compounds by converting problematic ash elements into high temperature stable materials. However, the equal amount of kaolin does not have the same effect on the ash melting temperature when evaluating the different agromass ashes: 1% of kaolin added in canola straw ashes raises the SST temperature 542 °C, in case of wheat straw ashes the temperature increase is lower and reaches about 86 °C and reed canary grass ash melting temperature increases of just 37 °C. Therefore, more detailed studies are needed for further understanding interactions between additive and agromass ash. Ashing temperature can also have a significant impact on ash melting behavior due to volatile substances, because increasing ashing temperature leads in declining content of volatile substances and at the same time chemical composition and structure changes.

REFERENCES

1. Parliament of the Republic of Lithuania (2011). *Republic of Lithuania Law on Energy from Renewable Sources* (2011 May 12 No XI-1375) (https://e-seimas.lrs.lt/portal/legalAct/lt/TAD/648259603c3b11e68f278e2f1841c088?jfwid=rivwzvpvg).
2. WANG, L., SKEIBERG, O., BECIDAN, M., LI, H. Investigation of rye straw ash sintering characteristics and the effect of additives. *Applied Energy*, 2016, Vol. 163, p. 1195–1204.
3. NIU, Y., TAN, H., HUI, S. Ash-related issues during biomass combustion: Alkali-induced slagging, silicate melt-induced slagging (ash fusion), agglomeration, corrosion, ash utilization, and related countermeasures. *Progress in Energy and Combustion Science*, 2012, Vol. 52, p. 1–61.
4. WANG, L., HUSTAD, J. E., SKREIBERG, O., SKJEVRAK, G., GRONLI, M. A critical review on additives to reduce ash related operation problems in biomass combustion applications. *Energy Procedia*, 2012, Vol. 20, p. 20–29.
5. WANG, L., SKJEVRAK, G., HUSTAD, E., GRONLI, M. G. Effects of Sewage Sludge and Marble Sludge Addition on Slag Characteristics during Wood Waste Pellets Combustion. *Energy and Fuels*, 2011, Vol. 25, p. 5775–5785.
6. XIAO, R., CHEN, X., WANG, F., YU, G. The physicochemical properties of different biomass ashes at different ashing temperature. *Renewable Energy*, 2011, Vol. 36, p. 244–249.
7. FERNANDEZ LLORENTE, M. J., CARRASCI GARCIA, J. E. Concentration of elements in woody and herbaceous biomass as a function of the dry ashing temperature. *Fuel*, 2006, Vol. 85, p. 1273–1279.
8. VASSILEV, S. V., BAXTER, D., ANDERSEN, L. K., VASSILEVA, C. G. An overview of the chemical composition of biomass. *Fuel*, 2010, Vol. 89, p. 913–933.
9. MONTI, A., DI VIRGILIO, N., VENTURI, G. Mineral composition and ash content of six major energy crops. *Biomass and bioenergy*, 2008, Vol. 32, p. 216–223.

CYSENI 2018, May 23-25, Kaunas, Lithuania
ISSN 1822-7554, www.cyseni.com

DEVELOPMENT AND OPTIMIZATION OF FAST ABLATIVE PYROLYSIS TECHNOLOGY IN UKRAINE

V. I. Zubenko, A. V. Epik, V. O. Antonenko
Institute of Engineering Thermophysics of National Academy of Sciences,
Scientific Engineering Centre "Biomass",
Zhelyabova 2a street, 03067 Kyiv – Ukraine
E-mail: zubenko@biomass.kiev.ua

ABSTRACT

The article contains the description of the development and optimization of laboratory installation for ablative fast pyrolysis performance with productivity 4 kg/hour on input product. The experimental data on the series of experiments (more than 60) with analysis of the influence of certain range of input parameters on the bio-oil yield and qualitative parameters is presented. The optimization of installation regimes and input parameters for bio-oil yield maximization for different biomass types is performed. During the series of experiments the average bio-oil yield was on the level of 44% (by mass related to input products) with the maximum of 51% corresponding to the outside reactor temperature 600 ^{0}C, input product consumption 1.2 kg/hour and velocity of biomass particles 1.2 m/s. On the basis of aggregation of data from all experiments, the determination of the critical process parameters have been carried out, such as temperature (650 ^{0}C) and time of biomass particle existence in reactor (0.75 s). By exceeding any of these parameters a risk of fluctuating from pyrolysis process to other type of process arises. For instance, if the temperature of the reactor is exceeding 650 ^{0}C, the rapid increasing of pyrogas yield is observed (up to 60% by mass of output product) – the process is transforming from pyrolysis towards gasification. In case of exceeding of particle existence time in the reactor for more than 0.75 s, the rapid increasing of biochar yield is observed (up to 50–60% by mass of output product) – the process is tending more to torrefication. The performed laboratory analysis of qualitative parameters of output products and further comparison with the data of foreign authors shows that obtained bio-oil has net calorific value on the level of 13–14 MJ/t (20–30% lower in comparison with the foreign data) and moisture content of the level of 40–50% (20–30% higher in comparison with the foreign data). At the same time the performed elementary analysis and calorific value analysis of pyrolysis by-products – pyrogas and biochar – demonstrated the net calorific value of 12.7 MJ/kg and 28.2 MJ/kg respectively, which are quite high indicators taking into account the quantity of 50–60% of these products according to mass balance. To reveal the process regime with respect to highest energy efficiency of installation, the energy balance of installation has been developed. It demonstrates that the average energy efficiency of the installation is on the level of 65% (with maximum 97%). Calculation and preliminary technical estimations showed that it could be increased to 75% (average level) through additional modifications of installation, such as returning of heat losses from vertical tube between feeding zone and reactor zone to the setting chamber between reactor zone and condensation zone. The additional possibility of reactor heating through utilization of own-produced pyrogas has been considered showing that 40–100% of heat needed for reactor could be covered by energy contained in pyrogas (and 60% in average for 60 experiments). On the basis of obtained laboratory data the scaling of the installation has been performed with development of commercial prototype with productivity of 50 kg/hour serving as a basis for economic indicators determination for commercial-scale installation. The economic indicators calculation shows that the operation of commercial scale pyrolysis installation could be profitable in case of both bio-oil and biochar realization (having cost of energy EUR/MJ on 50–100% lower than for fossil fuels for Ukrainian conditions), but not in case of only one product realization. The respective simple payback period is 3.5 years, IRR – 39%, NPV – 0.25 million EUR with the total capital cost of all project of 1.2 million EUR.

Keywords: fast ablative pyrolysis, cone screw, bio-oil, biochar, pyrogas, energy efficiency, mass balance

CYSENI 2018, May 23-25, Kaunas, Lithuania
ISSN 1822-7554, www.cyseni.com

STUDY OF THE YIELD OF CARBON SORBENTS FROM GRAIN HUSKS TREATED WITH SODIUM CHLORIDE

A. N. Karnitski
The Institute of Power Engineering
National Academy of Sciences of Belarus
Akademicheskaya Str. 15/2, 220072 Minsk – Belarus
Email: AliaksandrKarnitski@gmail.com

ABSTRACT

The research paper gives preliminary results of the experimental study of the yield of carbon sorbents obtained in the process of pyrolysis of grain husks pretreated with a solution of sodium chloride. There were established in experimental studies performed by using a muffle furnace of the Institute of Power Engineering of the National Academy of Sciences of Belarus at temperatures in the range from 250 to 400 °C. The not pre-treated samples of grain husks had following parameters: a bulk density of 200 kg/m^3, moisture of 10.8%, ash content of 2.5%. The concentration of salt in the solution varied from 0% to 20%. Also data on the mass yield of sorbent as a function of salt concentration in the solution are presented in this research. Such data were established mostly at the temperature 400 °C. Dependence of the mass yield of sorbents from concentration of NaCl in the water solution is determined by a parabolic function with existence of evident minimum at this temperature. Parameters of this function were estimated by using a least square method. In course of approximation a standard deviation as well as the Student's coefficient were assessed.

Keywords: carbon sorbents, pyrolysis, grain husks, sodium chloride

1. INTRODUCTION

Carbon sorbents have been used in various industrial processes, such as purification of liquid wastes and gas emissions as well as in medicine, chromatography, etc. [1]. Coal, lignite, peat, various types of biomass, such as wastes of vegetable production, coconut shells, rice husk etc. have been used for their production [2–5].

It is well known that sorbents produced by pyrolysis of biomass and other substances having organic origin require their activation. There are two different possibilities for activation; physical and chemical activation [5].

Physical activation is done by carbonization of carbon precursors in an inert atmosphere to remove non-carbon elements, followed by activation in the presence of oxidizing gasifying agents at a higher temperature [6]. Chemical activation is generally conducted by impregnating with chemical agents such as alkali (KOH, K_2CO_3), alkali earth metal salts ($AlCl_3$, $ZnCl_2$, and $FeCl_3$), or certain acids (H_3PO_4, H_2SO_4), where the porosity is developed by dehydration reactions of the activating reagent [7]. Compared to physical activation, chemical activation provides higher yields under a lower activating temperature and results in less surface damage during the activation of fiber [8].

The chemical activation can be applied very effectively in case of grain husks used for production of high effective sorbents because using of grain husks allows very simply treating of them with different chemical solution. The present report describes preliminary results of experimental investigation of the possibility of obtaining of sorbents on the basis of grain husk pre-treated with solution of NaCl. The positive influence of NaCl can be expected on the basis of results established with such substances as $AlCl_3$, $ZnCl_2$, and $FeCl_3$ [5, 7]. The interest to NaCl is evident because this substance has no negative impact on living organisms and because there are very high resources of it in Belarus.

2. RESEARCH METHODOLOGY

This work was performed using a muffle furnace (SNOL 7,2/1300, 3.5 kW, Lithuania) of the Institute of Power Engineering of the National Academy of Sciences of Belarus.

Proximate analyses and thermal kinetics were examined in course of the present report.

As a pyrolyzable raw material, a grain husk was used with the following parameters established experimentally: a bulk density of 200 kg/m^3, a moisture content of 10.8%, an ash content of 2.5%.

In order to determine the effect of the salt concentration in the solution and the temperature of the process on the mass yield of the sorbent, experiments were conducted in which samples of grain husks weighing 7 grams were placed in crucibles and soaked for three days in an aqueous NaCl solution (0%, 0.5 %, 5%, 10%), the solution completely covered the samples. The weight of the solution for all samples was 40 grams.

After soaking the excess of solution was not merge. Eight identical containers were used for the experiment (two containers were used for each salt concentration value). Each crucible was covered with a fiberglass, fixed with wire. Above, the crucibles were covered with ceramic tiles (Fig. 1).

Fig. 1. Samples in container and their covers

Then the samples were placed in a muffle furnace, where they were held for 4 hours at a temperature of 150 °C to remove moisture, and then for an additional five hours at the appropriate temperature (250, 300, 350, 400 °C). This process was performed at the pressure 1 atm in air.

The masses of the samples were determined by laboratory scales OHAUS. The division of the weights d = 0.0001 g, the error is e = 0.001g.

The mass yield of the product without taking into account the salt of η was calculated by the formula:

$$\eta = \frac{m_s''}{m_s} \cdot 100\% \tag{1}$$

where m_s is the mass of dry matter at the beginning of the experiment, g;
m_s'' – mass of the sample at the end of the experiment minus salt, g.

During the experiments, the values were recorded within a thousandth of a gram, in calculations rounded to the nearest one hundredths.

Regression of experimental data was performed using the ORIGIN 7.0 program.

3. RESULTS AND DISCUSSION

Experimental values of m'_s (mass of substance after process), m''_s and η are given in Tables 1–4 and in Figs. 2–5.

Table 1. Results of the experiment at a temperature of 250 °C

Concentration of salt in solution		**0%**		**0.50%**		**5%**		**10%**	
Mass of substance after process	m'_s, g	3.47	3.52	2.96	3.02	4.55	4.58	6.72	6.41
Mass of substance after the process without salt	m''_s, g	3.47	3.52	2.76	2.82	2.55	2.58	2.72	2.41
Mass yield without salt	η, %	49.6	50.3	39.4	40.3	36.5	36.88	38.9	34.4
Average mass yield	$<\eta>$, %	**50.0**		**39.8**		**36.7**		**36.6**	

Table 2. Results of the experiment at a temperature of 300 °C

Concentration of salt in solution		**0%**		**0.50%**		**5%**		**10%**	
Mass of substance after process	m'_s, g	2.44	2.44	2.31	2.15	3.50	3.58	5.87	5.71
Mass of substance after the process without salt	m''_s, g	2.44	2.44	2.11	1.95	1.50	1.58	1.87	1.71
Mass yield without salt	η, %	34.8	34.8	30.1	27.8	21.4	22.5	26.7	24.4
Average mass yield	$<\eta>$, %	**34.8**		**29.0**		**22.0**		**25.6**	

Table 3. Results of the experiment at a temperature of 350 °C

Concentration of salt in solution		**0%**		**0.50%**		**5%**		**10%**	
Mass of substance after process	m'_s, g	1.83	2.06	1.83	1.71	3.18	3.43	5.36	5.01
Mass of substance after the process without salt	m''_s, g	1.83	2.06	1.63	1.51	1.18	1.43	1.36	1.01
Mass yield without salt	η, %	26.2	29.5	23.3	21.6	16.8	20.4	19.5	14.4
Average mass yield	$<\eta>$, %	**27.8**		**22.4**		**18.6**		**16.9**	

Table 4. Results of the experiment at a temperature of 400 °C

Concentration of salt in solution		**0%**		**0.50%**		**5%**		**10%**	
Mass of substance after process	m'_s, g	1.45	1.79	1.49	1.35	2.88	3.15	5.07	5.20
Mass of substance after the process without salt	m''_s, g	1.45	1.79	1.29	1.15	0.88	1.15	1.07	1.20
Mass yield without salt	η, %	20.6	25.6	18.4	16.4	12.5	16.5	15.3	17.2
Average mass yield	$<\eta>$, %	**23.1**		**17.4**		**14.5**		**16.3**	

The graphs of the dependence of the mass yield on the salt concentration at different temperatures are shown in Figs. 2–5.

The data presented in Tables 1–4 and in Figs. 2–5 show the dependence of the mass yield of the sorbent on the salt concentration in the solution at various temperatures of the process. The increase in temperature leads to a decrease in the mass yield of the sorbent.

The mass yield η in this experiment was calculated using data on the mass of the dry sample prior to the start of the experiment and the product obtained, minus the mass of the salt.

Since the salt in the solution covering the samples was not removed before the start of the process, the mass of the salt in the solution and in the pyrolysis product did not change. The temperature of the thermal decomposition of sodium chloride is on the order of 800 °C, therefore, the salt in the solution does not change its structure.

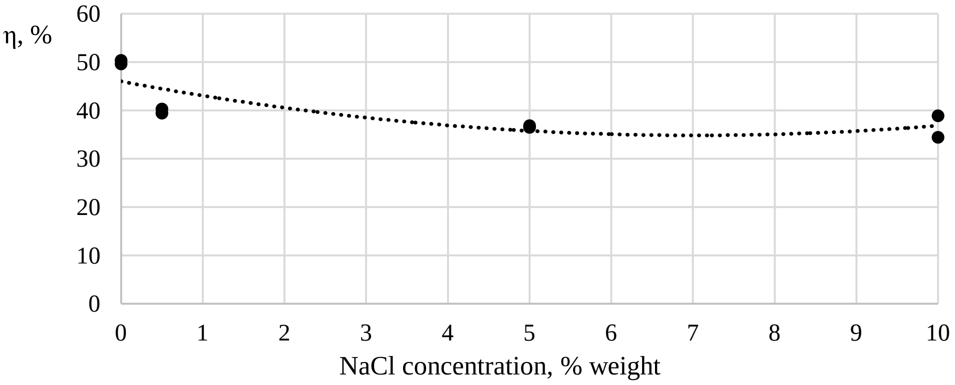

Fig. 2. The dependence of mass yield of sorbent on salt concentration in the solution at 250°C

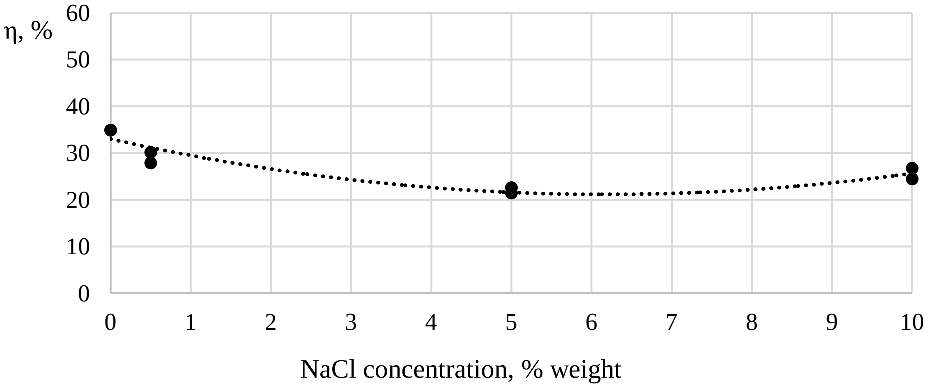

Fig. 3. The dependence of mass yield of sorbent on salt concentration in the solution at 300 °C

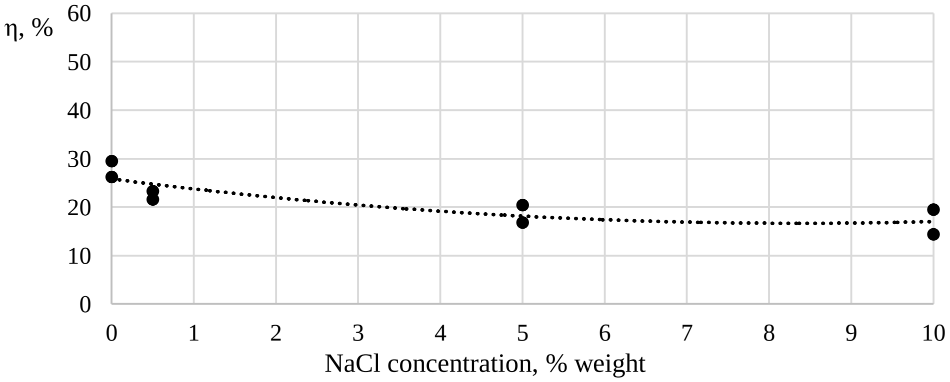

Fig. 4. The dependence of mass yield of sorbent on salt concentration in the solution at 350 ^{o}C

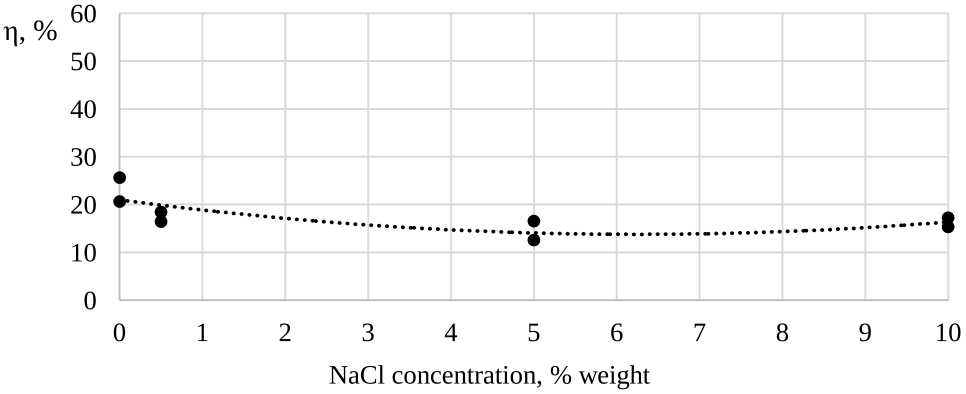

Fig. 5. The dependence of mass yield of sorbent on salt concentration in the solution at 400 ^{o}C

With an increase of the salt concentration in the solution, the mass yield tends to decrease, and then increases. Thus, it can be assumed that there is a minimum on the graph of the dependence of the mass yield of the sorbent on the salt concentration in the solution at a given temperature. The graphs of the dependence of the mass yield on the salt concentration in the solution have a similar form for all four temperatures studied.

Additionally, experiments were performed at 400 °C at varying concentrations of salt in an aqueous solution equal to 0%, 0.5%, 5%, 10%, 15% and 20%. The obtained values of the mass yield of the sorbent are presented in the Table 5.

Table 5. Sorbent yield as a function of the NaCl concentration

NaCl concentration, % weight	**Sorbent yield, % weight**						**Average mass yield output, %**
0	20.64	25.59	20.83	18.51	19.51	17.51	20.43
0.5	18.43	16.44	24.24	24.16	22.54	24.57	21.73
5	16.49	19.33	14.00	12.54	20.39	15.43	16.36
10	15.34	17.19	15.13	14.06	16.99	10.97	14.95
15	11.64	16.27	20.90	16.33	19.93	19.10	17.36
20	20.49	17.40	18.00	17.63	12.99	18.86	17.56

The graph of the dependence of the mass yield of sorbents on the concentration of salt in solution at the experimental temperature of 400 °C is presented in Fig. 6.

The average values of the mass yield of the sorbent, determined as the arithmetic average of six values for each salt concentration in the aqueous solution, presented in Table 5, were used to plot the graph.

Results of regression are presented below:

- the equation $Y = A + BX + CX^2$;
- the coefficient of determination $R^2 = 0.83$;
- the standard deviation SD =1.364;
- $p < 0,071$.

Protocol of regression is shown in Table 6.

Table 6. Protocol of regression

	A	**B**	**C**
Parameters	21.00872	-0.95564	0.04078
SE	±0.97379	±0.27285	±0.01378

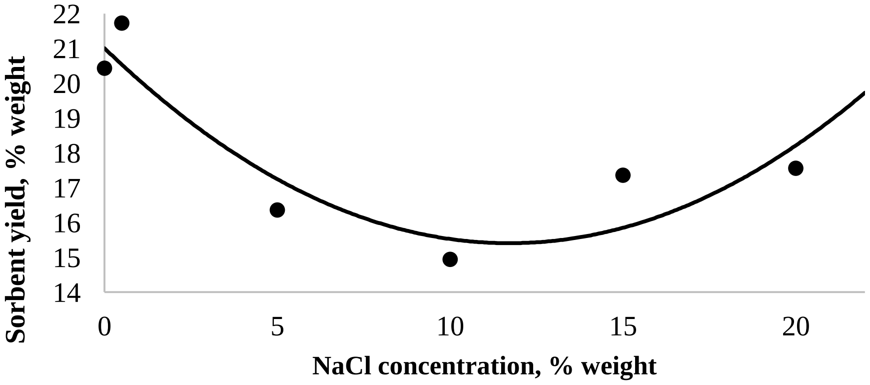

Fig. 6. Sorbent yield as a function of NaCl concentration in solution

Analysis of data given in Table 6 shows that Students coefficients of regression parameters are statistical significant ($p < 0{,}05$): $t_1 = 21.57$, $t_2 = 3.50$, $t_3 = 2.96$.

This indicates correctness of performed regression.

As can be seen from Fig. 6 the minimal value of mass yield is reached at the concentration of NaCl about 12% by weight.

Figs. 7–9 show enlarged images of sorbent particles obtained with different concentrations of salt by means of a microscope.

Analysis of data shown in Figs. 7–9 show an existence of porous structure in samples pretreated in NaCl solutions. It is to see that this structure depends of the concentration of NaCl in solution.

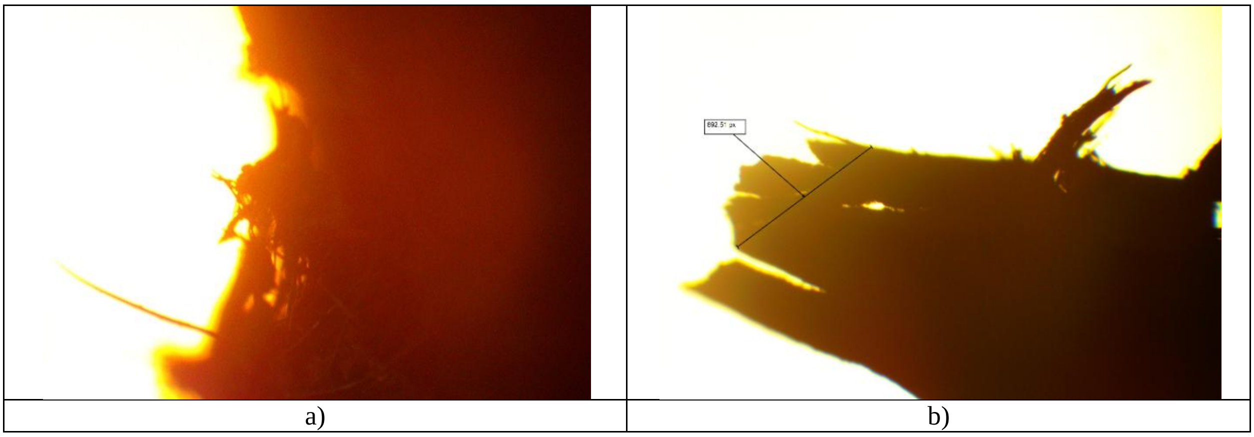

a) b)

Fig. 7. Microphotography of samples pretreated with NaCl solution: a) 0% of NaCl; b) 0.5% of NaCl

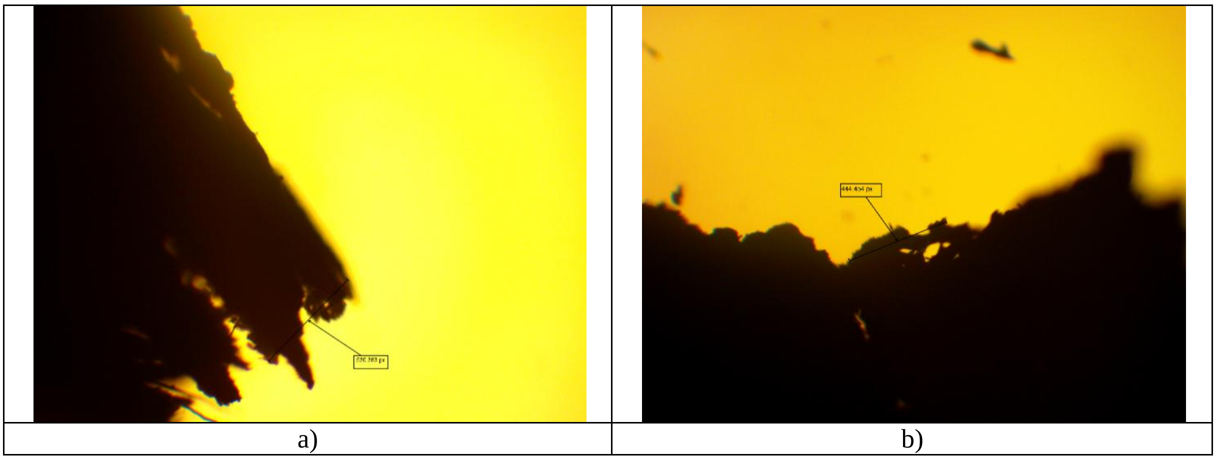

a) b)

Fig. 8. Microphotography of samples pretreated with NaCl solution: a) 5% of NaCl; b) 10% of NaCl

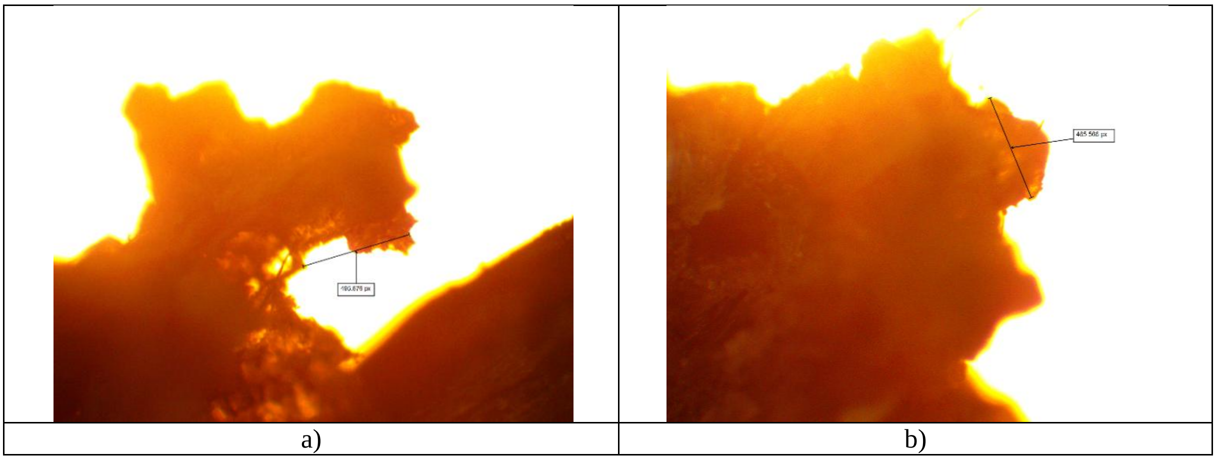

a) b)

Fig. 9. Microphotography of samples pretreated with NaCl solution: a) 15% of NaCl; b) 20% of NaCl

As can be seen in Fig. 7, at a salt concentration of 0%, the pores in the central part of the image are not open, and at 0.5% salt content, separate openings in the sorbent particle are observed in the aqueous solution.

The clearest manifestation of the porous structure is observed in the concentration range from 10 to 15% by weight of NaCl or in the range of minimal yield of sorbent.

This means that NaCl contained in the aqueous solution used in the soaking of the samples influences the formation of pores in the sorbent particles. As follows from established data the pore formation increases with increasing of salt concentration up to the NaCl concentration of about 12% by weight. A further increase in the salt concentration leads to a decrease in porosity.

However the yield of the sorbent by increasing of concentration of NaCl in solution decreases and then increases.

The existence of some opposite processes in the formation of pores requires further studies of pyrolysis of biomass preliminarily treated in an aqueous solution of NaCl.

4. CONCLUSIONS

The mass yield of the sorbent formed in the process of pyrolysis of grain husks pretreated in the water solution of NaCl depends both on the temperature of the process and on the concentration of NaCl in the solution.

The increase of temperature causes practically monotonic decrease of mass yield of the sorbent. The influence of NaCl concentration in the water solution causes a non monotonic change of the yield as well as the porosity of formed sorbents. Detailed studies of this effect was conducted in the present work at the temperature 400 ^{o}C. It was found that at a pyrolysis temperature of 400 °C, the maximum porosity is reached in the range of NaCl concentrations from 10 to 15% by weight and the minimum of sorbent yield is at the concentration of NaCl equal 12% by weight.

REFERENCES

1. BELYAEV, E. Preparation and use of wood-based activated carbons for environmental purposes. *Khimiya rastitel'nogo syr'ya* (*in Russian*), 2000, No. 2, p. 5–15.
2. KUMAR, M., GUPTA, R. C. Industrial uses of wood char. *Energy Sources*, 1998, Vol. 20, No. 7, p. 575–589.
3. OLONTSEV, V., BORISOVA, I., SAZONOVA, E. Pyrolysis of coconut shells for the manufacture of carbon sorbents. *Khimiya Tverdogo Topliva* (*in Russian*), 2011, No. 1, p. 47–52.
4. AHIDUZZAMAN, MD and A. K. M. SADRUL ISLAM. Preparation of porous bio-char and activated carbon from rice husk by leaching ash and chemical activation. *SpringerPlus*, 2016. [referred on the 12th of September in 2017 y.]. Link to the internet https://www.ncbi.nlm.nih.gov/pmc/articles/PMC4972807 .
5. LIU, Z., HUANG, Y., ZHAO, G. Preparation and characterization of activated carbon fibers from liquefied wood by ZnCl2 activation. *BioRes*, 2016, 11(2), p. 3178–3190.
6. WANG, J., and KASKEL, S. KOH activation of carbon-based materials for energy storage. J. Mater. Chem. 22, 2012, 23710–23725.
7. LI, J., NG, D. H. L., SONG, P., KONG, C., SONG, Y., and YANG, P. Preparation and characterization of high-surface-area activated carbon fibers from silkworm cocoon waste for Congo red adsorption. *Biomass Bioenerg.* 75, 2015 p. 189–200.
8. MOHANTY, K., JHA, M., MEIKAP, B. C., and BISWAS, M. N. Removal of chromium (VI) from dilute aqueous solutions by activated carbon developed from Terminalia arjuna nuts activated with zinc chloride. *Chemical Engineering Science 60(11)*, 2005, p. 3049–3059.

CYSENI 2018, May 23-25, Kaunas, Lithuania
ISSN 1822-7554, www.cyseni.com

HEMP ABILITY ACCUMULATE HEAVY METALS FROM HIGH LEVEL FERTILIZED SOIL OF SEWGE SLUDGE AND SEWAGE SLUDGE CHAR

M. Praspaliauskas
Lithuanian Energy Institute
Breslaujos str. 3, LT-44403 Kaunas – Lithuania
Email: Marius.Praspaliauskas@lei.lt

J. Žaltauskaitė
Vytautas Magnus University
Vileikos str.8-223, LT-44404 Kaunas – Lithuania
Email: jurate.zaltauskaite@vdu.lt

ABSTRACT

In Lithuania the cultivation of hemp (*Cannabis sativa L.)* was validated by government only in 2014. According to the law, hemp can be cultivated in the country with the content of tetrahydrocannabinol (THC) not exceeding 0.2 %. Most scientific researches of sewage sludge (SS) or sewage sludge char (Ch) describe it at relatively low levels, for productive crops. Such lack of information requires a wide range of practices for fertilizing hemp with high level of sewage sludge char doses. At this moment there are no guidelines for sewage sludge char fertilization of energetic plants, depending on soil type. The experimental design consisted of five treatments: 1 – control (clay loam); 2 – 25 Mg ha^{-1} DM; 3 – 50 Mg ha^{-1} DM; 4 – 100 Mg ha^{-1} DM; and 5 – 200 Mg ha^{-1} DM of sewage sludge char and municipal sewage sludge per 1 ha. The sown density was 65 seeds per 1 m^2. Hemp seedlings during the experiment were watered 2–3 times per week and after a period of four months hemps were harvested. After harvesting, all hemp parts were separated (roots, stems, leaves) and dried. After drying, heavy metal concentrations in different hemp parts were investigated. It was determined that hemp ability to accumulate heavy metals decreased in all parts, while increasing the fertilisation intensity of sewage sludge and sewage sludge char. Heavy metal distribution of hemp is selective, therefore their contents are decreasing in the following order: roots > stems > leaves.

Keywords: sewage sludge, sewage sludge char, hemp, accumulation factor, heavy metals

1. INTRODUCTION

As fossil fuel reserves are becoming more scarse, the energy crops have been repeatedly reported to have high potential to increase the share of renewable energy. Many crop species are multi-purpose, they can be used to produce more than one type of bioenergy, for example oil and solid biofuel [1]. Industrial hemp (*Cannabis sativa L.)* can potentially fulfil these requirements and has emerged as a potential energy crop along with several key advantages: high land use efficiency and biomass content. Other factors such as low feed-stock cost, good weed suppression, higher dry matter (DM) yield, low nutrients requirement, no/zero pesticide demand and improvement of soil health also justify the use of hemp as an energy crop [2]. Hemp can be effectively grown in diverse climates and can be used in organic crop rotation [3].

It has been reported that the European Union produces about 29% of total world hemp production [4]. Tuck et al. [1] studied hemp cultivation in Europe using different prediction models which estimated that hemp cultivation would disappear from Southern Europe and shift to Northern Europe by the 2050 s and 2080 s. In Lithuania the cultivation of hemp (*Cannabis sativa L.)* was validated by government only in 2014. According to the law, industrial hemp can be cultivated in the country with a content of tetrahydrocannabinol (THC) not more than 0.2%.

Char is the most appropriate pyrolysis end product, which is also preferable from the point view of energy balance [5]. Suitable pyrolysis temperature deserves investigation because biochars obtained at different temperatures have different nutrient properties [6]; in addition microstructures based on their pores and specific areas, heavy metal content and leaching potential, all of which would affect their application as biochar [7]. However there is no reliable information on differences in heavy metal bioaccumulation when biochar was produced at different temperatures [8].

For the testing plant, in addition to its yield, accumulation of heavy metals is another important issue that correlates with biochar application. After enriching agricultural soilwith raw sewage sludge or its biochar, itwas determined that the leaching of Cu, Ni and Zn was lower in the soil treated with biochar than in the soil treated directly with SS, and plant availability of Ni, Zn, Cd and Pb has also been reduced in the biochar-enriched soil when compared to the SS-enriched soil.

In some studies, sewage sludge [9] or sewage sludge char [10] have been applied or described at relatively low levels following recommendations for productive arable crops. This lack of information has led to a wide range of practices for fertilizing hemp with high level of sewage sludge char doses. At this moment no guidelines for sewage sludge char fertilization of energetic plants exist, which could give recommendations depending on soil type.

2. ANALYSIS METHODOLOGY

2.1. Conditions of the experiment

The experiment was carried out in laboratory conditions in climatic chamber with two treatments: sewage sludge and sewage sludge char applications with three repetitions. The temperature of experiment was 21 °C ± 2 °C, relative humidity 60%. The light qualities were 256 $\mu mol \cdot m^{-2} \cdot s^{-1}$ with a duration of 10 h to 14 h. Soil sample was taken in November. The soil on which the experiment was set up was classified as clay loam. According to WRB classification the soil used in this experiment was *Calcari Endohypogleyic Luvisol*. The soil for this experiment was used from the top of the soil in the range of 0–20 cm.

Sewage sludge was obtained from a wastewater treatment plant located in Šilutė (Lithuania). Char was prepared from this sludge. Sewage sludge was pyrolysed at 850 °C ± 10 °C in a laboratory fixed bed reactor under oxygen free (with nitrogen gas) atmosphere approximately for 90 min. A dose of municipal sewage sludge was the first experimental factor and a dose of municipal sewage sludge char was the second experimental factor. The experimental design consisted of four treatments: 1 – 25 Mg DM; 2 – 50 Mg DM; 3 – 100 Mg DM; and 4 – 200 Mg DM of municipal sewage sludge and sewage sludge char per 1 ha and control (without treatment).

Dutch, Italian and English researchers investigated and concluded that sowing 30–90 hemp seeds per 1 m^2 maintains the same plant number at the end of vegetation period. When planting 180–270 hemp seeds per 1 m^2, the plants smooth each other and a lot less plants remain till the end of vegetation – 110–180 units/m^2 [11]. In this experiment hemp seeds were seeded into plant pots. The seed density was 65 seeds per 1 m^2. According to our test conditions 2 seeds were seeded in one plant pot. Hemp seedlings during experiment were watered 2–3 times per week and after four month period, hemps were harvested. After harvesting all hemp parts was separated (root, stem, leaf) and dried at 105 °C for 16 hours.

2.2. Heavy metal determination

The ICP-OES Optima 800, atomic emission spectrometer from Perkin Elmer Company was used for the determination of heavy metal composition in plants and soil materials. Determinations of each of the samples were done in three reps. For the data acquisition of the samples, a quantitative analysis mode was used. The scanning of each single sample was repeated three times to gather reasonably accurate results. During measurements, care was taken to avoid memory effect and therefore a wash-out time of 1 min was used.

Hemp samples were mechanically chopped into 3–4 mm chips. The soil and sewage sludge mixture samples were quantitatively grounded to the size of a 0.5 mm sieve. During the first mineralisation step the samples (approximately 0.2–0.4 g) were flooded with 3 ml of concentrated nitric acid, 3 ml of fluoric acid and 1 ml of hydrochloric acid. The samples were placed in a mineraliser and mineralised for 1 hour and 10 minutes (at 800 W power, pLim: 60 bar, pRate: 0.5 bar s^{-1}), with 10 minutes allocated for heating, 45 minutes for mineralisation (in accordance with established parameters) and 15 minutes for cooling. After the second mineralisation, the samples were flooded with 18 ml boric acid (H_3BO_3 to avoid and eliminate fluoride toxicity) and again placed into a mineraliser for 1 hour and 10 minutes (at 800 W power, pLim: 60 bar, pRate: 0,3 bar s^{-1}). After the mineralisation, the solution was poured into a 50 ml flask and diluted to 50 ml using deionised water. The analysis of the solutions (Cd, Co, Cr, Cu, Ni, Pb, Ti, Zn) was performed according to standards LST EN ISO 16967:2015 and LST EN ISO 16968:2015.

2.3. Calculations

The bioaccumulation factor, (BF) can be used to evaluate the plant’s phytoextraction efficiency. It can be calculated according to equation (1) Metal pollution occurs only in the active rooting zone, that is, top soil layer (0–20 cm) [12].

$$BF = \frac{Me_{Plant\ part}}{Me_{soil}} \tag{1}$$

where BF – bioaccumulation factor (bidimensional number), $Me_{\text{plant part}}$ – heavy metal concentration in hemp part: root, stem or leaf (mg kg^{-1}), Me_{soil} – heavy metal concentration in soil (mg kg^{-1}).

3. RESULTS AND DISCUSSION

3.1. Chemical characteristics of soil

The concentrations of elements collected from the top of fertilized soil, depend on the amount of sewage sludge or sewage sludge char and are presented in Table 1. After heavy metal analysis of soil it is visible, that the increasing doses of municipal sewage sludge or sewage sludge char led to the increased concentrations of Co, Cr, Cu, Ni, Ti and Zn in soil.

Table. 1. Elemental composition of soil without treatment and after treatment of sewage sludge and sewage sludge char (mg kg^{-1} DM) in mean ± SD

Elements	**Soil without treatment**	**Sewage sludge dose (Mg ha^{-1} DM)**				**Sewage sludge char dose (Mg ha^{-1} DM)**			
		25	**50**	**100**	**200**	**25**	**50**	**100**	**200**
Heavy metals									
Co	1.03 ± 0.01	1.55 ± 0.44	3.05 ± 0.47	3.33 ± 0.22	4.08 ± 0.57	2.44 ± 0.12	3.60 ± 0.31	3.81 ± 0.34	4.86 ± 0.14
Cr	89.77 ± 0.14	111.2 ± 12.7	118.03 ± 15.2	113.09 ± 12.41	124.50 ± 10.26	98.98 ± 4.28	121.27 ± 3.05	118.57 ± 3.78	123.30 ± 1.24
Cu	0.55 ± 0.42	4,68 ± 0.13	12.21 ± 0.18	17.66 ± 0.50	27.09 ± 0.55	11.70 ± 0.40	20.94 ± 1.81	25.75 ± 1.77	29.88 ± 2.81
Ni	25.57 ± 2.10	25.76 ± 4.31	30.88 ± 2.01	29.60 ± 1.17	35.81 ± 0.33	31.41 ± 1.84	36.30 ± 3.55	35.19 ± 3.17	38.50 ± 1.16
Ti	1446 ± 55.6	1466 ± 132	1504.67 ± 60.27	1604 ± 72.1	1693.67 ± 23.1	1525.67 ± 57.73	1519.33 ± 68.6	1676.33 ± 78.5	1801.67 ± 50.3
Zn	26.37 ± 1.11	48.76 ± 1.80	108.17 ± 6.11	164.30 ± 14.4	254.97 ± 30.5	88.12 ± 9.40	164.27 ± 15.3	233.27 ± 10.4	387.53 ± 15.6

Sludge and char applications enhanced the total metal concentration in both soils but char treatments showed higher heavy metal concentrations in soil. While comparing the total metal concentration in sludge enriched soils and char enriched soils, Ti was found to be the most abundant metal in both the soils. In sludge or char enriched soil, abundance was as follows Ti >Zn > Cr > Ni > Cu > Co (Table 1).

3.2. Biomass yield

Low plant densities may result in a reduced yield and lower quality of biomass. Industrial hemp yield depends on environmental conditions and cultivation pattern. Optimal planting density has not been researched for growing hemp as a dual-purpose crop [11]. Thus, both of the factors compensate their impacts and resultantly harvesting time becomes insignificant for net energy yield. It is recommended that early harvesting (March-April) should be the preferred option to obtain hemp biomass as a solid fuel, with an average of biomass yield of 10.91 Mg ha^{-1}, and energy yield of 246 GJ ha^{-1} [13].

Mean yields of biomass dry matter, obtained in the experimental time, depending on the treatments, varied within the following range: 4820–64 kg ha^{-1} (Table 2). The research showed that industrial hemp had the highest increase in yield under the influence of 25 Mg ha^{-1} of sewage sludge. The lowest yield of plants was with the 200 Mg ha^{-1} treatment in which sewage sludge char was applied. In the case of industrial hemp, it was found that doses more than 50 Mg ha^{-1} of sewage sludge or sewage sludge char caused a drastical decrease in yield, respectively, over 4 and 20% as compared with the control measurement.

With the treatment of 200 Mg ha^{-1} of sewage sludge, industrial hemp doesn't survive and the mass yield was negative.

Table. 2. The effect of fertilization doses of sewage sludge and sewage sludge char on the biomass yields and plant biometrics (mean ± SD)

	Heigh, cm	**Root length, cm**	**Stem yield (DM), kg ha^{-1}**	**Leaf yield (DM), kg ha^{-1}**	**Biomass yield (DM), kg ha^{-1}**	**Root yield (DM), kg ha^{-1}**
Control	98 ± 15	36 ± 4	860 ± 50	620 ± 21	1480 ± 70	250 ± 13
25SS	113 ± 2	33 ± 2	1800 ± 29	3020 ± 37	4820 ± 32	380 ± 10
50SS	47 ± 13	23 ± 6	260 ± 26	550 ± 49	810± 75	30 ± 9
100SS	31 ± 6	25 ± 8	110 ± 11	190 ± 24	290 ± 35	30 ± 3
25Ch	67 ± 7	19 ± 3	520 ±76	340 ± 33	860 ± 91	120 ± 17
50Ch	46 ± 3	18 ± 4	500 ± 63	400 ±32	900 ± 93	90 ± 10
100Ch	29 ± 2	15±5	100 ± 15	190 ±19	290 ± 34	20 ± 3
200Ch	20 ± 2	10±2	23 ± 2	64 ± 5	64 ± 5	4 ± 0.4

The size of obtained yields of energy crops was directly related to the level of fertilisation with municipal sewage sludge. The studies provided evidence that the best effects on the growth and development of plants are exerted by nitrogen, phosphorus, and potassium [14], [15]. However, sewage sludge contains too little potassium to meet the needs of energy crops, therefore it should be applied in mineral form after a prior evaluation of the soil components.

3.3. Heavy metal uptake by hemp parts

Heavy metal uptake by hemp parts, is presented in Fig. 1 as a set of the entire research period (four months). The concentration of heavy metals varies greatly in different parts of hemp. Metal concentrations were mostly significantly higher in roots rather than in stems and leaves. Variation of all analyzed metals in different parts of hemp may also be due to compartmentalization and translocation in the vascular system.

The dose of municipal sewage sludge or sewage sludge char significantly affected the concentration of heavy metals (Co, Cr, Cu, Ni, Ti, Zn) in the tissue. Generally, increasing doses of sludge and char caused an increase in their content in the aerial parts of hemp. However the concentrations of Zn in hemp stem and leaves showed no differences, which may have been the result of a worse sludge composition. Generally, highest heavy metal concentrations in hemp parts were found in plots fertilised with sewage sludge. The increasing doses of sewage sludge significantly increased the content and uptake of Cu. Significantly greater concentrations of heavy metals were noted in hemp biomass harvested from plots with the different doses of sewage sludge, suggesting hemp ability to accumulate selective heavy metals.

In the case of hemp stem biomass, the highest increase in heavy metal content (at the highest dose of sewage sludge or char) reached 233% for Co (char), 800% for Cu, and 950% for Zn in relation to the control measurement. The research shows that the total content of Cu increased the most in both fertilizations, followed by Co, Cr, Ni, Ti and Zn. In total the lowest increases in the content were recorded in the case of Zn and Ti compared with the control measurement.

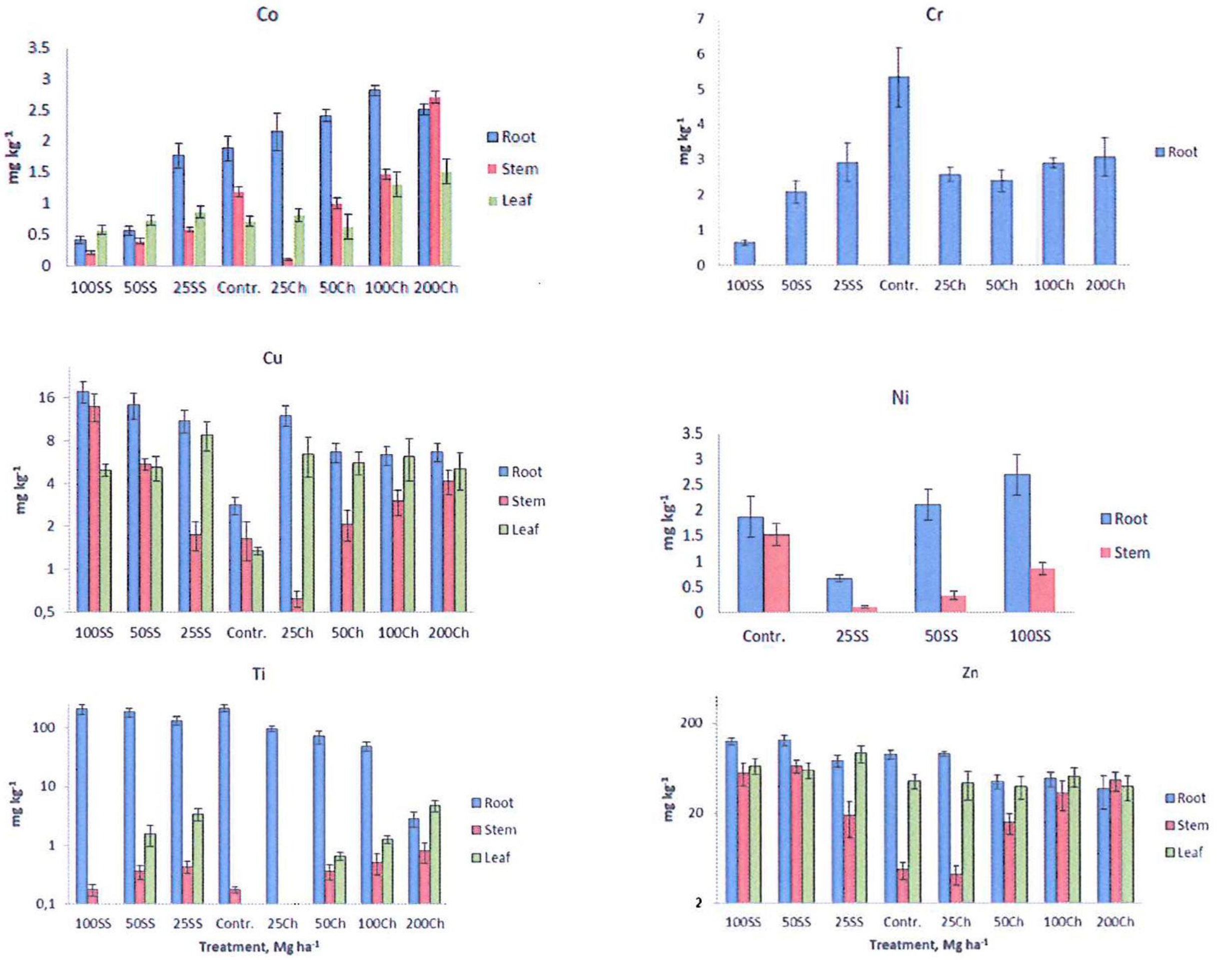

Fig. 1. Accumulated amounts of heawy metals in differnet parts of hemp after treatment of SS an SSCh

The heavy metal uptake of the hemp root yield was highest in plots fertilised with sewage sludge. After the application of sewage sludge char, the uptake of Co and Cr by hemp roots was, respectively higher in comparison to the control measurement where plants without the additional sewage sludge char were cultivated. Generaly the research shows that the content of Cu increased the most, followed by Co, Cr, Ni, Ti and Zn; the lowest increases in the content were those of Cr and Ni. Therefore, the author’s own research shows that the increasing doses of sewage sludge diversify the content of heavy metals in plants.

3.4. Bioaccumulation factor

Bioaccumulation factor (BF) is known as the soil to plant uptake factor. There were large differences between root,stem and leaf concentrations of all studied metals, which indicates an important restriction of the internal transportation of metals from root to steam and leaves. Such metal immobilization in root cells is emphasized by the root/stems, leaf > 1. Thus, BF indicates that heavy metals can accumulate in plant parts in very high amounts over time and accumulation is always greater in leaves rather than stems.

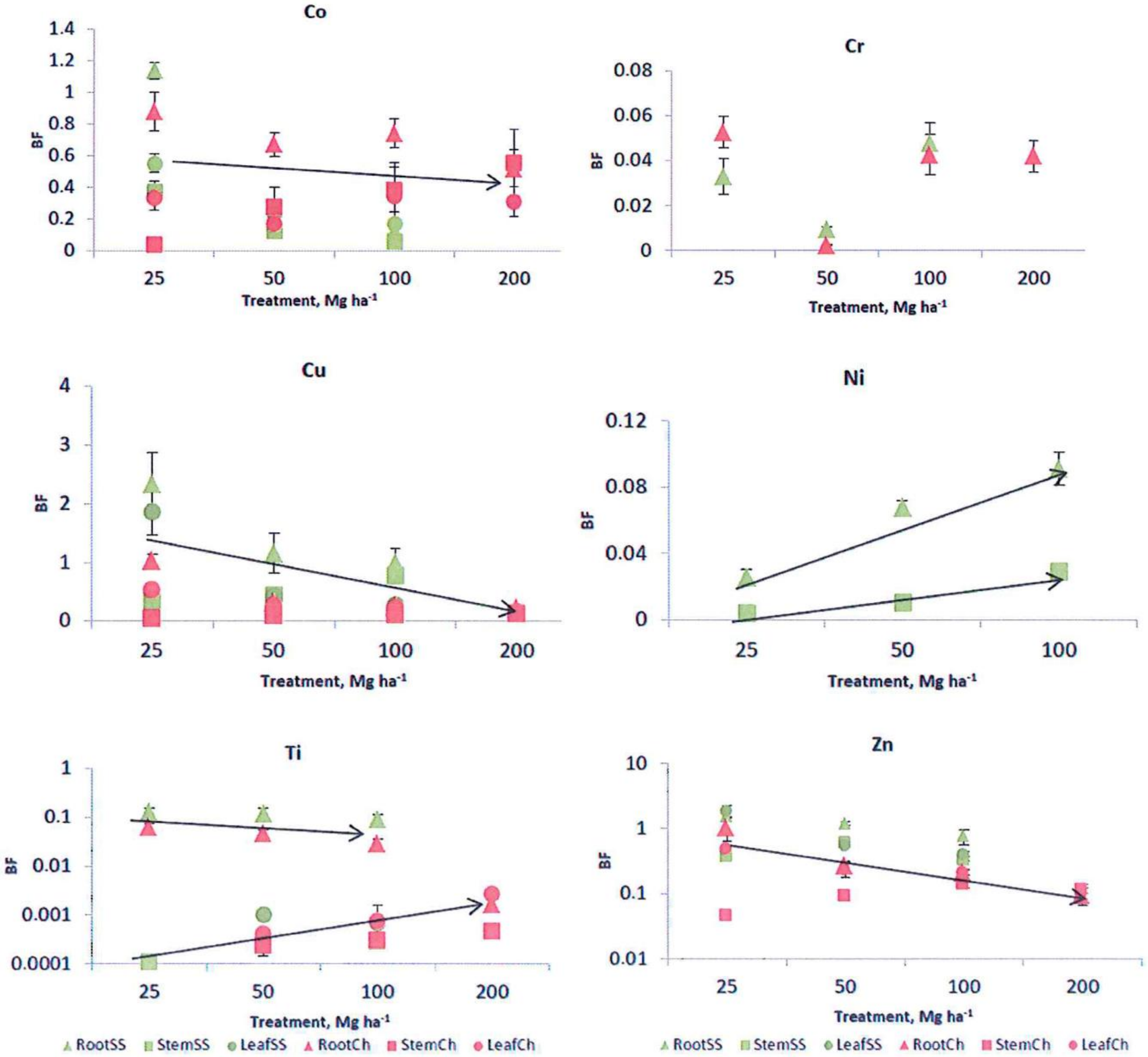

Fig. 2. The influence of added dose of sewage sludge and sewage sludge char to heavy metal accumulation factor in different parts of hemp

Hemp ability to accumulate heavy metals Co, Cu and Zn, depending on fertilisation intensity, decreased in all parts with sewage sludge or sewage sludge char. The bioaccumulation factor in roots and stems increase of Ni in soil fertilized with sewage sludge. Ti accumulation of stems and leaves increased in soil fertilized with sewage sludge and sewage sludge char, but decreased in roots.

4. CONCLUSIONS

Heavy metal concentrations increased in various parts of hemp enriched by sewage sludge or sewage sludge char in soil. The most abundant metal, in total concentrations was Cu and Zn, followed by Co, Cr, Ni, Ti. It was determined that in low amounts of fertilizers the variation of metal concentration was in wide range in contrast to high amounts of fertilizers.

The study has highlighted the potential use of sewage sludge as a source of organic matter for improvement of clay loam soil and a production of bioenergy crops like hemp without the use of inorganic fertilizers. It was found that doses of more than 50 Mg ha^{-1} of sewage sludge and sewage sludge char caused a drastic decrease in biomass yield.

REFERENCES

[1] G. Tuck, M. J. Glendining, P. Smith, J. I. House, and M. Wattenbach, “The potential distribution of bioenergy crops in Europe under present and future climate,” *Biomass and Bioenergy*, vol. 30, no. 3, pp. 183–197, 2006.

[2] T. Prade, S. E. Svensson, A. Andersson, and J. E. Mattsson, “Biomass and energy yield of industrial hemp grown for biogas and solid fuel,” *Biomass and Bioenergy*, vol. 35, no. 7, pp. 3040–3049, 2011.

[3] E. Kreuger, B. Sipos, G. Zacchi, S. E. Svensson, and L. Björnsson, “Bioconversion of industrial hemp to ethanol and methane: The benefits of steam pretreatment and co-production,” *Bioresour. Technol.*, vol. 102, no. 3, pp. 3457–3465, 2011.

[4] L. Barberá, M. A. Pélach, I. Pérez, J. Puig, and P. Mutjé, “Upgrading of hemp core for papermaking purposes by means of organosolv process,” *Ind. Crops Prod.*, vol. 34, no. 1, pp. 865–872, 2011.

[5] L. Y. Yu, L. W. Wang, and P. S. Li, “Study on prediction models of biomass ash softening temperature based on ash composition,” *J. Energy Inst.*, vol. 87, no. 3, pp. 215–219, 2014.

[6] M. K. Hossain, V. Strezov Vladimir, K. Y. Chan, A. Ziolkowski, and P. F. Nelson, “Influence of pyrolysis temperature on production and nutrient properties of wastewater sludge biochar,” *J. Environ. Manage.*, vol. 92, no. 1, pp. 223–228, 2011.

[7] J. Lehmann, M. C. Rillig, J. Thies, C. A. Masiello, W. C. Hockaday, and D. Crowley, “Biochar effects on soil biota - A review,” *Soil Biol. Biochem.*, vol. 43, no. 9, pp. 1812–1836, 2011.

[8] X. D. Song, X. Y. Xue, D. Z. Chen, P. J. He, and X. H. Dai, “Application of biochar from sewage sludge to plant cultivation: Influence of pyrolysis temperature and biochar-to-soil ratio on yield and heavy metal accumulation,” *Chemosphere*, vol. 109, pp. 213–220, 2014.

[9] J. A. & B. K. & E. J. Bielińska, “The use of reed canary grass and giant miscanthus in the phytoremediation of municipal sewage sludge.” pp. 9505–9517, 2016.

[10] J. Finnan and B. Burke, “Potassium fertilization of hemp (Cannabis sativa),” *Industrial Crops and Products*, vol. 41, no. 1. pp. 419–422, 2013.

[11] P. C. Struik, S. Amaducci, M. J. Bullard, N. C. Stutterheim, G. Venturi, and H. T. H. Cromack, “Agronomy of fibre hemp (Cannabis sativa L.) in Europe,” *Ind. Crops Prod.*, vol. 11, no. 2–3, pp. 107–118, 2000.

[12] R. W. and F. E. Okieimen, “HeavyMetals in Contaminated Soils: A Review of Sources, Chemistry,Risks and Best Available Strategies for Remediation,” 2011.

[13] T. Prade, *Industrial hemp (Cannabis sativa L.)–a high-yielding energy crop*. 2011.

[14] H. Borkowska and R. Molas, “Yield comparison of four lignocellulosic perennial energy crop species,” *Biomass and Bioenergy*, vol. 51, pp. 145–153, 2013.

[15] B. Kołodziej, J. Antonkiewicz, M. Stachyra, E. J. Bielińska, J. Wiśniewski, K. Luchowska, and C. Kwiatkowski, “Use of sewage sludge in bioenergy production—A case study on the effects on sorghum biomass production,” *Eur. J. Agron.*, vol. 69, pp. 63–74, 2015.

CYSENI 2018, May 23-25, Kaunas, Lithuania
ISSN 1822-7554, www.cyseni.com

DEMAND-ORIENTED ENERGY SUPPLY BY THE ANAEROBIC DIGESTION OF ORGANIC WASTE

M. Wehner, **W. Müller**, **A. Bockreis**
University of Innsbruck, Unit of Environmental Engineering
Technikerstrasse 13, 6020 Innsbruck – Austria
Email: marco.wehner@uibk.ac.at

ABSTARCT

The share of renewable energy is steadily increasing globally. Nevertheless, power generation from renewable energy sources, such as solar and wind energy, is highly dependent on suitable weather conditions and, therefore, highly fluctuating. Thus, alternatives to compensate fluctuations in the energy production are necessary. Biogas plants have the potential to balance energy generation fluctuations and work independently from unstable weather. Various concepts allow the flexible operation of biogas plants. One is the flexible feeding management for a demand-driven energy supply, which requires the storage of substrates. The aim of this study was to investigate the storage of fresh food waste. This substrate was selected for investigation as tourisms in Tyrol, Austria is of major economic importance and therefore large amounts of food waste are generated in hotels and restaurants.

Fresh food waste was sampled from a canteen and ground with a hand blender by adding tap water to reach 12–13% total solids (TS). The pre-treated food waste was stored in 20-liter plastic containers over 42 days at 20 °C in a climatic chamber. During storage, samples of food waste were taken on days 0, 1, 3, 7, 21 and 42. The samples were analysed for TS, volatile solids (VS), volatile fatty acids (VFA), pH and biomethane potential (BMP). For the analysis of the gas which was built during the storage, gas sampling bags were connected to the plastic containers and the gas was analysed for methane (CH_4), carbon dioxide (CO_2), oxygen (O_2), hydrogen sulphide (H_2S) and hydrogen (H_2) concentration.

During storage, a rapid acidification due to a lactic acid fermentation led to a pH decrease and concomitant organic acids increase, preserving the stored organic waste. This process is usually applied for silage production in agricultural sector to preserve maize or grass. The pH dropped from initially 4.8 to 4 within the first 2 days of storage. It declined until day 10 to 3.6 and stayed at this level until the end of the experiment. Due to a low pH and a high VFA concentration, only minor amounts of gas were produced during storage. CO_2 (mean 60 vol-%) was the main gas component. H_2 and CH_4 were not detected. In addition, no formation of explosive gas mixtures was detected during the storage. Therefore, no safety precautions are necessary to avoid danger from explosion. The BMP test over 21 days showed that the storage of food waste had only marginal impact on its energy content. The main fraction of total biomethane production was generated within the first three days. Thus, pre-condition of organic waste for a flexible feeding and demand-oriented energy supply is technically feasible to balance energy generation fluctuations.

The storage of organic waste is a promising approach to support the demand-oriented energy supply by biogas plants with a flexible feeding management. Future research will focus on feeding strategies to reach a short-term increase in biomethane production to compensate energy generation fluctuations.

Keywords: anaerobic digestion, biogas, demand-oriented energy supply, organic waste

CYSENI 2018, May 23-25, Kaunas, Lithuania
ISSN 1822-7554, www.cyseni.com

DETERMINATION OF THE EFFECTS OF PARTICLE SIZE ON COMBUSTION KINETICS OF CORN WASTE

Ö.H. Çöp, A. Çalışkan, H. Haykiri-Açma, S. Yaman
Istanbul Technical University
34469 Maslak Istanbul – Turkey
Email: ovul_cop@hotmail.com

ABSTRACT

Combustion characteristics of corn waste, which is a renewable and sustainable biomass energy resource, has been investigated in this article by thermal analysis technique. For this, corn cob was milled into several different size fractions of < 0.25 mm, < 1 mm, < 2 mm, and < 4 mm. Thermal treatment which simulates combustion were implemented in thermal analyzer by heating the sample from ambient to 700 °C temperature under dry air flow. Thermogravimetric Analysis (TGA), Derivative Thermogravimetry (DTG), and Differential Scanning Calorimetry (DSC) curves were derived to comment the thermoconversion characteristics and the burning reactivity of these size fractions. It was concluded that particle size plays an important role in the combustion properties of this biomass and the particle size should be taken into account, in order to improve the design of combustion systems and ensure their efficient operation. Effects of the particle size of corn waste to the combustion kinetics were commented based on the Borchardt and Daniels (B&D) kinetic analysis method which uses the thermal analysis data.

Keywords: Biomass, combustion kinetics, corn waste, particle size

1. INTRODUCTION

Biomass that is comprised of woody and herbaceous plants, industrial wastes, forest residue, municipal solid wastes, etc. offers great energy potential. In addition, energy from biomass is renewable, sustainable, and clean energy that does not lead to increase in CO_2 emissions in atmosphere [1–3]. Biomass mainly consists of carbon, oxygen, hydrogen, and nitrogen as well as of relatively small amounts of sulfur and inorganics. Although woody species of biomass produce very little amount of ash, some biomass species such as waste materials may carry considerable amounts of inorganic constituents that lead to high ash yields [4]. Also, unlike fossil energy sources, biomass can be easily found everywhere [5].

Agricultural productivity of Turkey is very suitable for the biomass energy applications where unusable parts of crops is utilized to take advantage of their energy potential [6]. Many different types of agricultural products are grown in Turkey during every season thanks to varying climate and weather conditions throughout the country. For an instance, annual corn production in Turkey is around 6–7 million tones that makes Turkey one of the top countries in corn production and there are national projects to enhance the corn production in the near future. After harvesting the corn cob, very large amount of unusable parts (stalk silage) are left in the cornfield [7]. These wastes are very tall grassy/woody materials, which have energy potential when they are used as fuel source. Alternatively, some biological and thermal conversion methods can be applied to produce gaseous, liquid or solid fuels or products [8].

This study focuses on the combustion behavior of corn waste. Combustion is a thermochemical process that is influenced by a number of parameters including the type of combustor, operational conditions, and the sample related properties. Among these parameters, particle size of the sample is one of the important parameters that affects the burning behavior. The particle size controls the surface area of a material and it is known that the surface area is one of the most significant factors that affect the combustion of the solid fuels. For these reasons, the effects of particle size on the combustion kinetics of corn waste were investigated in this study.

2. MATERIALS AND METHODS

Corn wastes used in this study were provided by local producers in the city of Adana where 16% of the total corn production of Turkey is carried out. These wastes were first dried in an oven at 60 °C for 2 days and then the dried corn wastes were subjected to physical sample preparation operations such as cutting and milling. Since the size of the corn wastes was large, they were cut down first such that their size reduced from 30–60 cm to 1–3 cm and then the samples were exposed to milling process in the vibratory disc mill for about 3 minutes. Standard sieves that have openings of 4 mm, 2 mm, 1 mm, and 0.25 mm were used to separate the different size fractions. The samples passing through each of these sieves were stored as the size fractions which are < 0.25 mm, < 1 mm, < 2 mm, and < 4 mm of corn waste.

Proximate analysis, which involves the heating of the sample under controlled conditions postulated by ASTM standards, was performed to compare the fuel characteristics of each size fraction. In this way, the contents of moisture, volatile matter, ash, and fixed carbon were determined as weight percentages of the initial sample. This procedure is the standard test method to specify the fuel properties of any material.

Combustion of the size fractions was implemented via thermal analysis technique using TA Instruments SDTQ600 model thermal analyzer. For this, 10 mg sample was heated from ambient to 700 ºC by a heating rate of 40 ºC/min under dry air flow of 100 mL/min. Thermogravimetric Analysis (TGA), Derivative Thermogravimetry (DTG), and Differential Scanning Calorimetry (DSC) profiles were derived from the thermal analysis data.

Borchardt and Daniels approach that bases on the DSC profiles was applied to determine the kinetic parameters including the activation energy (E_A), pre-exponential factor (A), heat of reaction (ΔH), reaction order (n), and rate constant (k) [9]. This approach assumes the existence of n^{th} order reaction kinetics, and bases on validity of the general rate equation and Arrhenius principle.

3. RESULTS AND DISCUSSION

Table 1 shows the proximate analysis results of the size fractions. The values of moisture and volatiles are close to each other in every particle sizes. Depending on the size of the fractions some variations exist in the fixed carbon contents and the ash yields that are consistent predictors of a fuel sample to evaluate its quality. The fraction of < 4 mm showed the highest fixed carbon content that is the most reliable indicator of a fuel to consider whether it is a promising fuel that burns steadily. Besides, the ash yield of this fraction is the lowest among the investigated size fractions and this is another desired situation to get rid of the ash related problems encountered in the combustors. From these points of view, the fraction (< 4 mm) can be recommended as the most valuable part of this biomass species. On the contrary, the fraction of < 1 mm has the least fixed carbon content and the highest ash yields that predicts the fact that this fraction has the poorest fuel quality among the investigated size fractions. This can be attributed to the concentrated inorganics in this fraction.

Table 1. Proximate analysis results

Size Fraction	Moisture (%)	Volatiles (%)	Fixed Carbon (%)	Ash (%)
< 0.25 mm	6.15	76.07	12.18	5.60
< 1 mm	6.67	72.94	11.87	8.52
< 2 mm	6.07	72.94	13.72	7.27
< 4 mm	6.35	73.21	17.35	3.09

Burning characteristics of the samples were examined using thermal analysis techniques of TGA (Thermogravimetric analysis), DTG (Derivative Thermogravimetry), and DSC (Differential Scanning Calorimetry). Fig. 1 presents the thermo-conversion profiles comparatively and some significant outcomes can be obtained from these profiles. TGA curves indicated that the weight loss characteristics of the size fractions were more or less similar in each case until temperature reaches around 300 ºC. Beyond that, some differentiations took place in the weights because of the different burning rates. For instance, the size fractions < 0.25 mm and < 2 mm showed serious changes in the sample weights when temperature reached 400 ºC. As temperature further increased, the remaining sample weights tended to level off completely at around 500 ºC since the macromolecular ingredients of cellulose, hemicellulose and lignin already decomposed until 500 ºC. Besides, the rates of the weight losses (burning rates) can be compared using the DTG curves, and the rates of the weight losses reach the maximum values in the temperature interval of 250–350 ºC. Rapid devolatilization of biomass and the ignition of the combustible volatiles resulted in this high rates of the weight losses. Besides, the burning of the fixed carbon took place relatively at higher temperatures and the secondary burning peaks beyond 400 ºC can be assigned to the fixed carbon burning. The highest burning rate was detected in the case of < 1 mm followed by < 2 mm and < 4 mm, respectively. However, < 0.25 mm fraction differed so significantly from the other sizes in terms of the burning rates that it had a maximum value of only 39.5%/min while it was 152.7%/min for < 1 mm fraction.

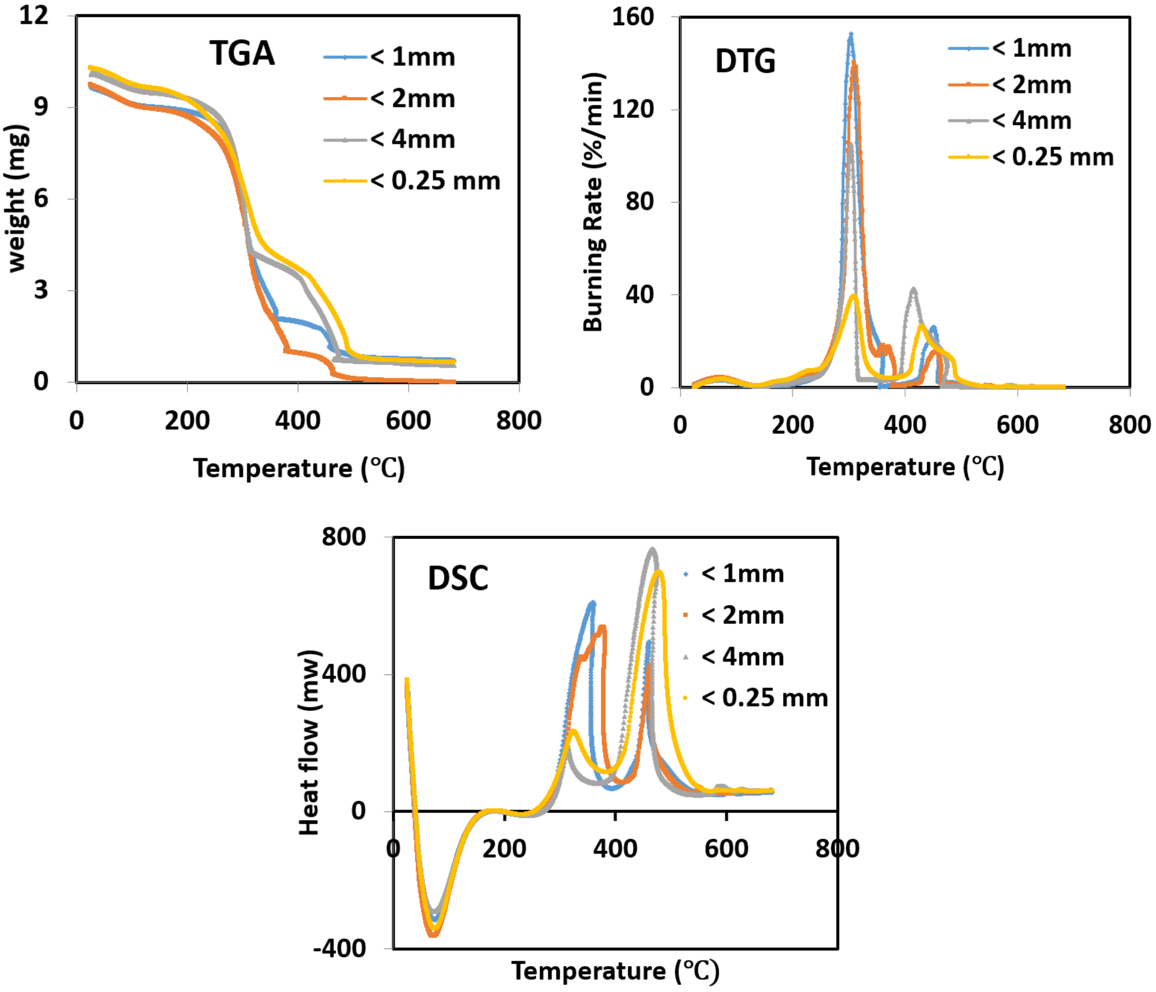

Fig. 1. TGA, DTG, and DSC burning profiles

Meanwhile, the DSC curves show both negative and positive heat flows originating from the endothermic and the exothermic phenomena, respectively. The removal of the moisture content led to endothermic heat flows at around 100 ºC. Then no heat flows were detected in the range of roughly 150–250 ºC and then exothermic regions with two maxima formed. The polysaccharides such as cellulose and hemicellulose are the thermally high reactive ingredients in biomass and accordingly they burn at relatively lower temperatures, while lignin is less reactive and its burning takes place at higher temperatures. Because of this fact, two different maximum points were seen on the DSC curves, indicating burning of the polysaccharides and lignin separately. Actually, polysaccharides lead the formation of volatiles, whereas lignin contributes to the fixed carbon [10]. Accordingly, the fraction < 4 mm that has the highest fixed carbon content, which produces the strongest heat flows in the region where lignin burns.

An illustrative example of Borchardt and Daniels method application that uses the Differential Scanning Calorimetry (DSC) curves from the thermal analysis experiment is explained in Fig. 2. In this analysis, the most critical issue is to correctly choose the lower and the upper temperature limits of the main exotherm where positive heat flows occur because of the burning of sample. Therefore, this method is highly sensitive to the mentioned two temperatures displayed on the DSC curve and the calculations for determination of the kinetic parameters are carried out by the software of TA Instruments.

Table 2 summarizes the results obtained from the kinetic analysis. The order of the reactions changed between 2.08 and 2.83. The activation energies and the pre-exponential factors varied in the ranges of 233.8–523.4 kJ/mole and 17.0–37.8 min^{-1}, respectively, and the highest values of them belonged to the fraction of < 2 mm while the lowest values of these parameters were found for < 4 mm fraction. The heat of reactions changes in very wide range of 1141–5559 kJ/kg. In addition to the useful information taken from the burning profiles, these kinetic parameters also confirm the fact that particle size plays very important roles on the burning behavior and the burning kinetics of such biomass materials.

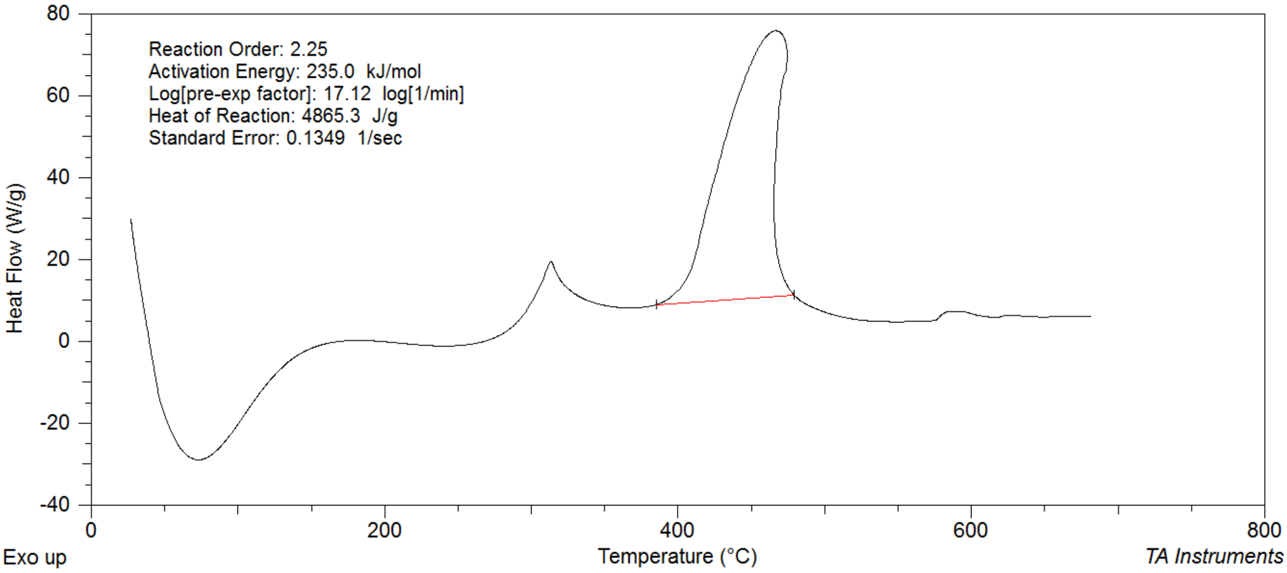

Fig. 2. Illustration of Borchardt and Daniels method to determine kinetic parameters

Table 2. Kinetic analysis results

Sample	Reaction order	Activation energy (kJ/mol)	Pre-exponential factor log(1/min)	Heat of Reaction (kJ/kg)
< 0.25 mm	2.76	249.4	17.8	5559
< 1 mm	2.08	475.3	34.4	1176
< 2 mm	2.83	523.4	37.8	1141
< 4 mm	2.25	233.8	17.0	4941

4. CONCLUSION

Separating corn waste into size fractions of < 0.25 mm, < 1 mm, < 2 mm, and < 4 mm and then performing the proximate analysis and the combustion tests revealed that different size fractions of corn waste have different fuel characteristics and burning behavior. Some size fractions of this biomass have promising fuel characteristics, high fixed carbon contents and low ash yields, compared to others. Besides, the burning related properties such as the burning rates and the heat flows are affected from the size fractions. Moreover, kinetic parameters including the reaction order, activation energy, pre-exponential factor and the heat of reaction also differ significantly depending on the size fractions of the corn waste.

REFERENCES

[1] KLASS, D. L. *Biomass for Renewable Energy, Fuels, and Chemicals.* San Diego: Academic Press, 1998. 29 p. ISBN 978-0-12-410950-6.

[2] ABBASI, T., ABBASI, S.A. Biomass energy and the environmental impacts associated with its production and utilization. *Renewable and Sustainable Energy Reviews*, 2010, Vol. 14, p. 919–937.

[3] YAMAN, S. Pyrolysis of biomass to produce fuels and chemical feedstocks. *Energy Conversion and Management*, 2004, Vol. 45, p. 651–671.

[4] PROSKURINA, S., HEINIMÖ, J., SCHIPFER, F., VAKKILAINEN, E. Biomass for industrial applications: The role of torrefaction. *Renewable Energy*, 2017, Vol. 111, p. 265–274.

[5] TOKLU, E. Biomass energy potential and utilization in Turkey. *Renewable Energy*, 2017, Vol. 107, p. 235–244.

[6] BARUT, Z.B., ERTEKIN, C., KARAAĞAÇ, H.A. Tillage effects on energy use for corn silage in Mediterranean coastal of Turkey. *Energy*, 2011. Vol. 36, p. 5466–5475.

[7] ZHAO, Y., YU, J., LIU, J., YANG, H.Y., GAO, L., YUAN, X.F, CUI, Z., WANG, X. Material and microbial changes during corn stalk silage and their effects on methane fermentation. *Bioresource Technology*, 2016, Vol. 222, p. 89–99.

[8] BASU, P. *Biomass Gasification and Pyrolysis-Practical Design and Theory*. Amsterdam: Elsevier, 2010, 1 p. ISBN 978-0-12-374988-8.

[9] BORCHARDT, H.J., DANIELS, F.J. The Application of differential thermal analysis to the study of reaction kinetics. *Journal of the American Chemical Society*, 1957, Vol. 79, p. 41–46.

[10] CLARK, J., DESWARTE, F. *Introduction to Chemicals from Biomass*. New Delhi: Wiley, 2008, 89 p. ISBN: 978-0-470-05805-3.

CYSENI 2018, May 23-25, Kaunas, Lithuania
ISSN 1822-7554, www.cyseni.com

MECHANICAL PRE-TREATMENT OF MUNICIPAL WASTE FOR BIOGAS PRODUCTION

A. C. P. Lopes, W. Müller, A. Bockreis
Universität Innsbruck
Technikerstraße 13, A-6020 – Austria
Email: alice.lopes@uibk.ac.at

ABSTRACT

Although the waste separation in dwellings is a widespread practice and reinforced by laws in many countries, not all of the waste is source-sorted, leaving mixed waste with relevant amounts of recyclables and organics. The main objective of this paper was to perform a preliminary investigation of a wet mechanical process to separate the organic fraction from municipal solid waste (MSW) for biogas production in a real scale plant. The separation process consists of pulpers followed by hydrocyclones and generates as outputs (1) a light fraction (LF), (2) a heavy fraction (HF), (3) a grit fraction and; (4) a prepared substrate for the anaerobic digestion (AD input). Samples from those outputs were evaluated for impurities content and biogas production potential. Firstly, the wet pre-treatment system significantly reduced the impurities concentration of MSW for biogas production. The preliminary results showed that the LF presented a high share of plastics, while the HF of glass, stones and ceramic. Secondly, the hydrocyclones further removed small particles, mainly between 0.025 and 10 mm. Finally, the combination of pulpers and hydrocyclones provided a pulp from MSW with a low concentration of impurities and with a biogas production potential of 415 Nm^3/t TS.

Keywords: Biogas, Municipal Solid Waste, Wet pre-treatment

1. INTRODUCTION

The increase of energy demand coupled with the increase of waste generation claims for new and sustainable solutions for energy production and waste management. In Tirol, Austria, the co-digestion of source-separated biowaste with sewage sludge is a common practice. In 2016, approximately 25,000 t/a of source-sorted biowaste were utilised as co-substrate in Wastewater Treatment Plants (WWTPs) in Tirol [1]. Due to state regulations, the sewage sludge, even after the anaerobic digestion (AD), is not allowed for land application [2]. Thus, the anaerobically co-digested biowaste loses its capability of substituting mineral fertilizers and has to be incinerated.

In Innsbruck, Austria, residual household waste is sent to a mechanical treatment plant, where the waste is separated into three fractions (high, middle and low calorific fractions) by means of sieving and shredding. The high and middle fractions are mainly composed of plastics, textiles, paper, foam etc., being suitable for incineration. The low calorific fraction (< 40 mm) contains a high concentration of organics fines (about 50% of the weight) [3]. Since the organic matter absorbs water, the fraction < 40 mm has a low calorific value. A potential alternative to better use the energy from the low calorific waste would be the biogas production through the co-digestion with sewage sludge. In this case, the biowaste could be mono-fermented and the digestate used for land application, substituting mineral fertilizers.

Tirol generates 96,600 t/a of household waste (approximately 132 kg per person per year) [4]. Considering that 42% of the household waste is classified as low calorific fraction (< 40 mm) [5] and that its biogas production potential is about 175 Nm^3/t [3], approximately 7.1×10^6 Nm^3/a of biogas could be produced out of the household waste (fraction < 40 mm). Despite this high potential of biogas production from mixed household waste, WWTPs are still sceptic with the use of such material as co-substrate for biogas production, due to impurities content in the substrate.

Mechanical pre-treatment systems are commonly applied for sorting MSW, however impurities are still found in the sorted organics. Remaining impurities in the organics sent to anaerobic digesters might damage pipelines and pumps and increase the expenses of WWTPs. Jank et al. [6] studied the impact of using source-sorted biowaste as co-substrate for biogas production. The composition of the studied biowaste consisted of not only food waste, but also of garden waste, including stones and sand. The authors demonstrated that the costs related to the impurities sent to the digester play a minor role, if the co-substrate is properly pre-treated.

From the best of our knowledge, there is still a lack of research in the area of biogas production using mechanically sorted organic fraction of municipal solid waste (OFMSW), and, in particular, in the real scale application. Literature has reported the potential of biogas production out of MSW at laboratory scale using as substrate food waste, source-sorted OFMSW or hand-sorted OFMSW (e.g. [7]). Thus, this study aimed to perform a preliminary investigation of a mechanical treatment to separate the organic fraction from MSW for biogas production, based on a real scale waste treatment facility.

2. MATERIAL AND METHODS

A newly built mechanical wet pre-treatment system (so-called BTA hydromechanical pre-treatment) at a waste treatment plant in Scotland was chosen to be investigated through laboratory analysis of collected samples. Fig. 1 presents a schema of the BTA hydromechanical pre-treatment. In this process, the incoming waste is sieved in the dry pre-treatment (80 mm sieve) and the coarse fraction is conveyed to different sorting processes. The fraction < 80 mm is sent to the BTA hydromechanical pre-treatment unit (wet-prep), where it is prepared for biogas production. The wet-prep consists of four pulpers of 32 m^3 each (working volume of 27 m^3) and eight grit removal systems (hydrocyclones) split into two individual lines. Each line consists of four hydrocyclones working in series. First, the incoming waste is directed to the pulpers, where process water is added. The pulping process works in batches, taking about 15 min each. Due to centrifugal forces and density difference of the particles, the waste is separated in three fractions: a light fraction (LF), a heavy fraction (HF) and the suspension (Su). The LF is sieved, pressed for water removal and further processed for energy production as refuse derived fuel (RDF). The HF is collected from the bottom of the pulper. The Su is sieved (10 mm) and sent to the hydrocyclone line (grit removal system) for further removal of inert material (grit fraction). The remaining fluid fraction is pressed for water content reduction and it is ready to produce biogas. Fig. 2 presents the appearance of each output fraction.

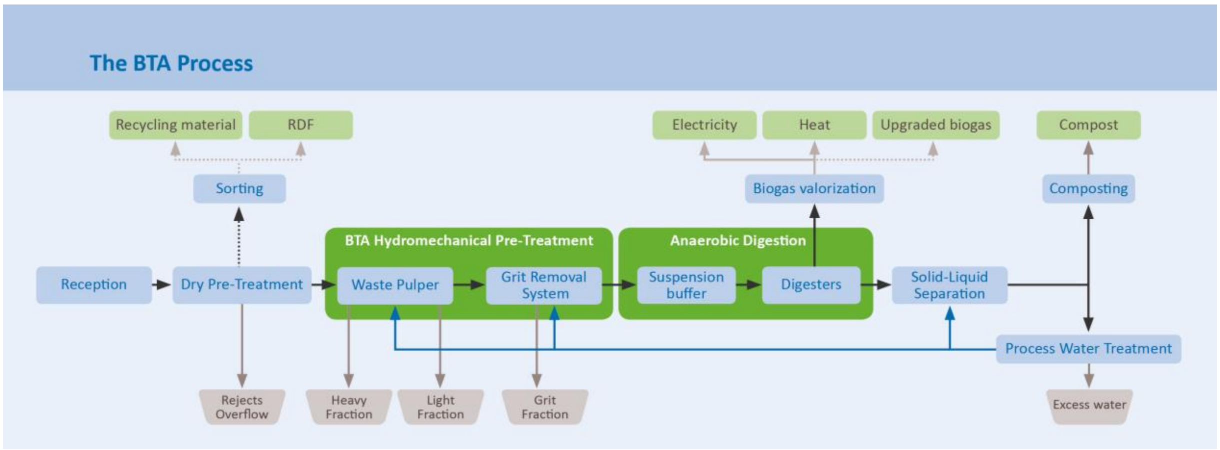

Fig. 1. Wet pre-treatment scheme of BTA process [8]

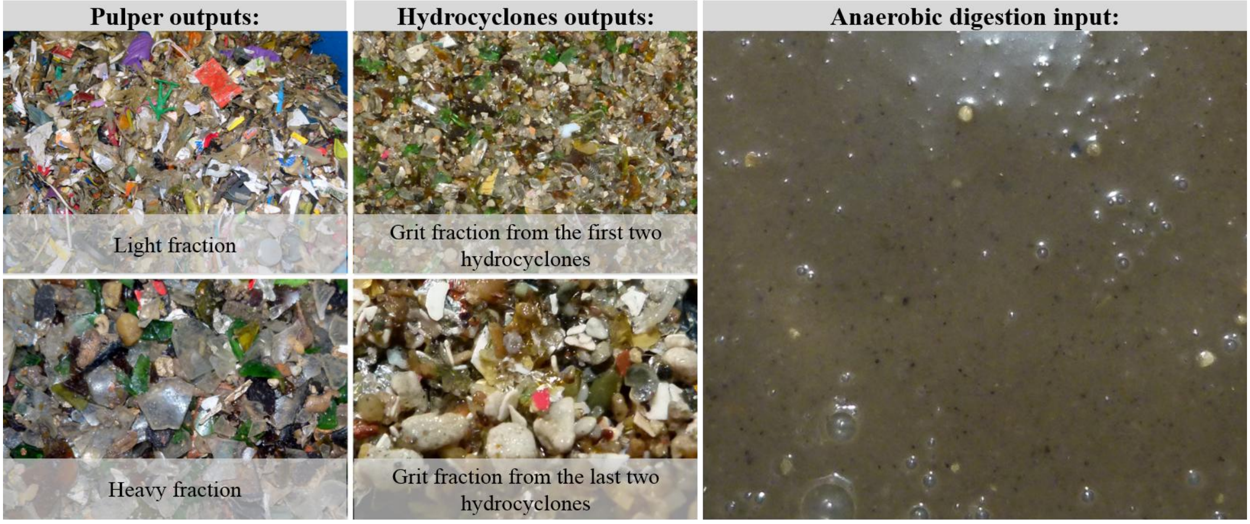

Fig. 2. Output fractions from the pulper (left) and hydrocyclones (middle), and input to the anaerobic digestion (right)

The wet-prep system was evaluated by means of impurities concentration and biogas production potential of each fraction (LF, HF, grit and AD input). The collected samples were dried at the waste treatment plant (WTP) laboratory and shipped to the University of Innsbruck – Unit of Environmental Engineering for determining the impurities content and the biogas production potential tests. Due to differences in the samples consistence, the samples characterization followed different methods.

HF and LF

The HF and LF were hand sorted for (i) minerals (glass, stones and ceramic), (ii) light and hard plastics, (iii) metals (Fe and non-Fe), (iv) textile, (v) eletronics/batteries, and (vi) organics & rest (non-identified materials). The category (i) was further sieved for determination of the particles size distribution (PDS) of the inert material greater than 2 mm. In order to determine the PSD of the inert material smaller than 2 mm, part of the sorted organics & rest was combusted to ash and the ashes were sieved. This method was used, since small stones and gravel were still embeded in the organic material. The remaining part of category (vi) was used as substrate for the biogas production test.

Grit samples

Since the grit samples (grit 1+2 – originated from the first two hydrocyclones, and grit 3+4 – originated from the last two hydrocyclones) were mainly composed of minerals with similar density and characteristics, the hand sorting was not performed. The samples were combusted and afterwards sieved for the PDS determination. Since a high concentration of organics was determined in grit 3+4, the biogas production potential was performed for this sample as well.

AD input

The AD input characterization was performed through three steps. In the first step, 1 L of sample was entirely dried. About 4 g was used for the biogas production test and the remaining mass was combusted for the PSD. In the second step, 2 L samples were wet sieved (2 mm) in order to remove the fine organics, facilitating the sorting of impurities. The last step comprised the sedimentation test: to about 5 L sample, water was added until filling up the bucket and stirred. Then, the stirring was stopped for at least 2 minutes to allow the heavy particles to settle in the bucket. After having a stabilized mixture, about half of the mixture was poured and the bucket was filled again with water. This process was repeated until the mixture turned clear and it was possible to see the sediments on the bottom of the bucket. The sediments were removed by pouring the liquid through a 2 mm sieve. The particles were then dried and combusted to ash and the ashes were sieved.

Biogas production test

The biogas production tests followed VDI 4630 [9]. The tests were performed in batch reactors of 500 mL capacity each, at 37 °C. Each reactor was filled with 300 mL inoculum consisted of digested sludge originated from a wastewater treatment plant in Tirol. The added amount of substrate was calculated in order to guarantee a substrate to inoculum ratio of 0.5 g $VS_{substrate}$/g $VS_{inoculum}$. Due to transportation reasons, it was not possible to perform the biogas tests with the fresh matter, but rather with the dried (105 °C) samples. The initial pH value of all reactors were in the ideal range (7.4–7.9). The tests were performed in triplicates, with exeption of the blanks, which were performed in duplicates. The methane production was monitored through the automatic methane potential test system, from the bioprocess control system [10]. The biogas production potential results were expressed in Nm^3/t TS, considering a methane content in the biogas of 60% (v/v). Fig. 3 presents a summary of the chracterization methods used for each sample.

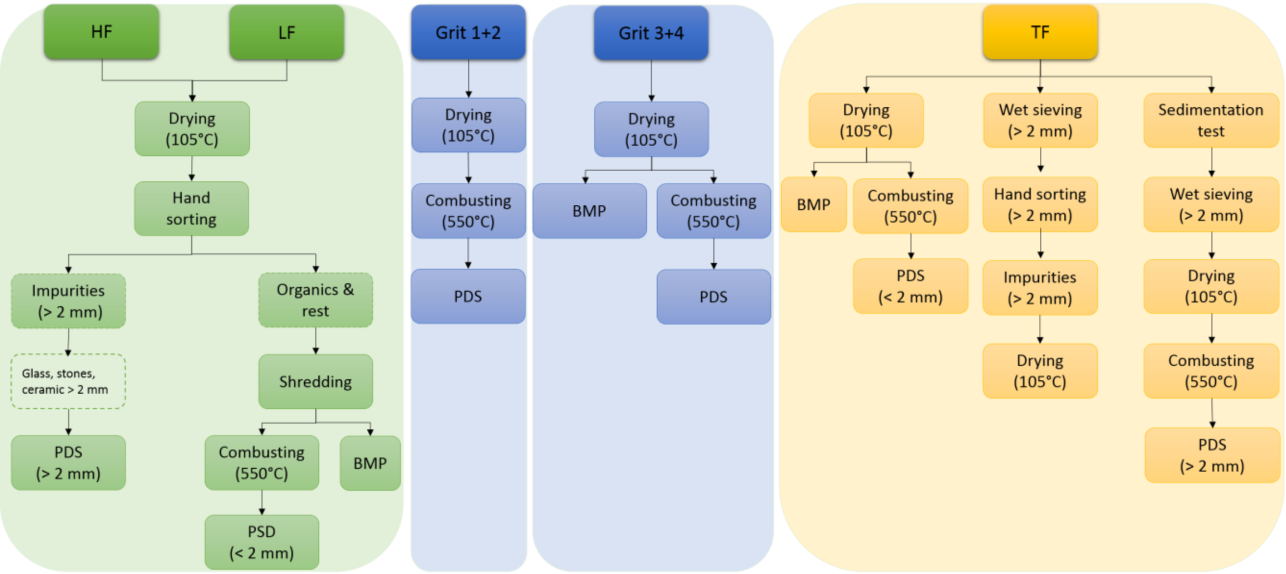

Fig. 3. Sorting methods schema for different waste fractions. BMP: biogas production test. PSD: particles size distribution

3. RESULTS AND DISCUSSION

Fig. 4 and Fig. 5 present the sorted impurities from the light and heavy fractions. Fig. 6 shows the impurities distribution in each analysed fraction. Over 90% of the impurities in the HF were minerals. With regard to the LF, plastics took about 75% of the impurities share. Acording to the hand-sorting results, 40% of the dried sorted matter of the LF was classified as organics & rest, while in the HF, this value was only 2%. These results indicated that the HF was able concentrate glass almost free of organics, presenting the potential to be sent to a glass recycling industry. With regard to the LF, a further processing could be studied for refining the sorting procedure to reduce the organic matter being lost.

Fig. 4. Light fraction (> 2 mm)

Fig. 5. Heavy fraction (> 2 mm)

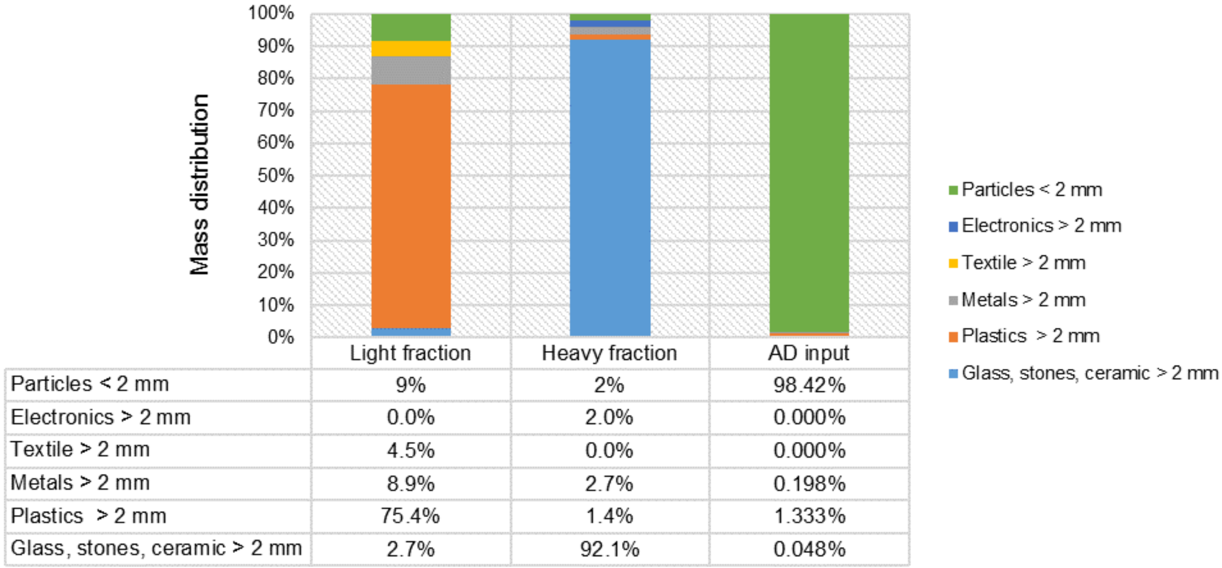

	Light fraction	Heavy fraction	AD input
Particles < 2 mm	9%	2%	98.42%
Electronics > 2 mm	0.0%	2.0%	0.000%
Textile > 2 mm	4.5%	0.0%	0.000%
Metals > 2 mm	8.9%	2.7%	0.198%
Plastics > 2 mm	75.4%	1.4%	1.333%
Glass, stones, ceramic > 2 mm	2.7%	92.1%	0.048%

Fig. 6. Impurities distribution in the light and heavy fractions and in the AD input

The impurities concentration (> 2 mm) in the AD input was very low (smaller than 2% of the impurities share), as Fig. 6 shows. However, among the impurites > 2 mm, plastics presented the highest share, followed by metals (small pieces of aluminium foil). With regard to particles < 2 mm, these were clearly higher for the AD input compared to the LF and HF. In fact, the particles < 2 mm were the combustion product of the organic matter, concentrating not only small stones, but also the ashes originated from the combusted organic matter.

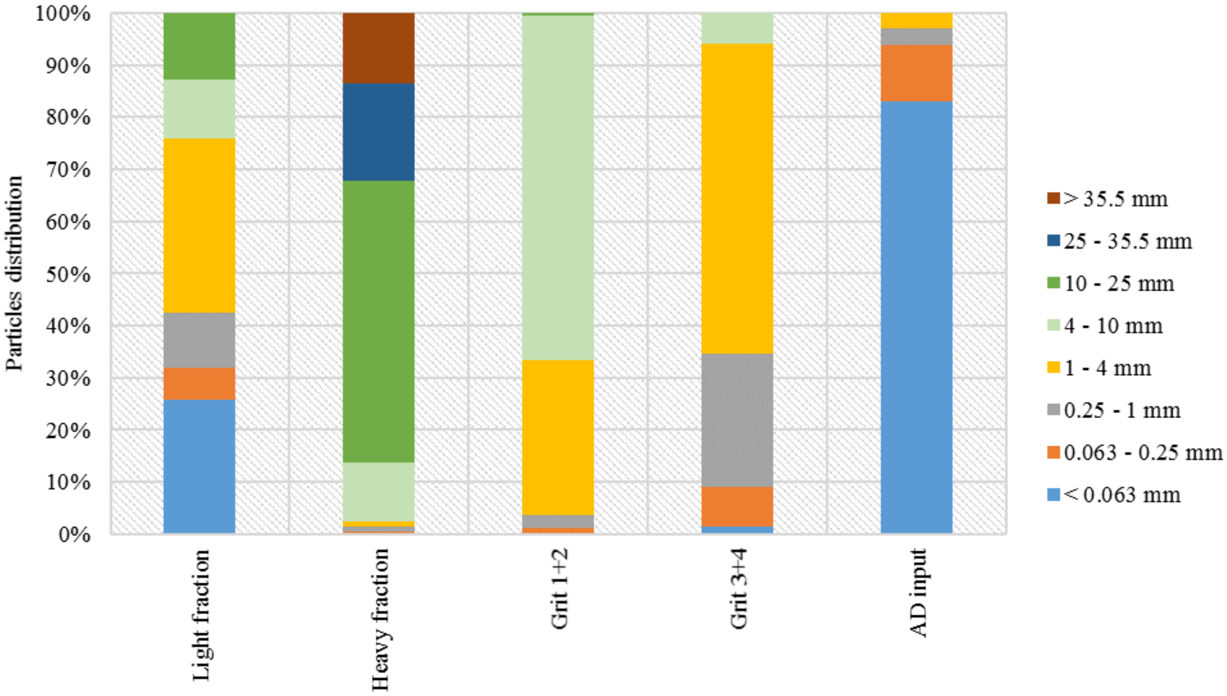

Fig. 7. Particles size distribution in each fraction

Fig. 7 illustrates the particles size distribution of the remaining particles after the combustion. The pulpers were able to efficiently remove particles > 10 mm by the heavy fraction. The hydrocyclones supplemented the pulpers, removing smaller particles: the first two hydrocyclones were able to remove particles between 1 and 10 mm (grit 1+2), while the last two hydrocyclones removed smaller particles, ranging from 0.25–4 mm (grit 3+4). The prepared AD input had a very low concentration of impurities. The high concentration of particles < 0.063 mm in the AD input indicated a high concentration of organics, since these particles are most likely the product of the combustion of the organic matter.

Fig. 8 presents the biogas production potential from the heavy fraction (HF), light fraction (LF), output of the last two hydrocyclones (grit 3+4) and from the pre-treated waste (AD input). The preliminary results indicated that the LF still holds a high potential of biogas production (130 Nm^3 biogas/t TS) compared to the HF and grit 3+4. The MSW after the mechanical pre-treatment, i.e, the AD input, presented a biogas production potential of 415 Nm^3/t TS. Converting this value to methane production potential, considering a concentration of 60% CH_4 (v/v) in the biogas and a 76% VS (in TS basis), it would give a value of 327 NmL CH_4/g VS.

The literature reported a methane yield from OFMSW between 37 mL CH_4/g VS and 570 mL CH_4/g VS, depending on the waste composition, applied pre-treatment and reactor operational conditions [7]. Meirer et al. [3] obtained up to 456 NmL CH_4/g VS after mechnically pre-treating MSW (fraction < 40 mm) through a wet process. Sosnowki et al. [11] achieved a biogas production of 419 mL/g VS from OFMSW under thermophilic conditions.

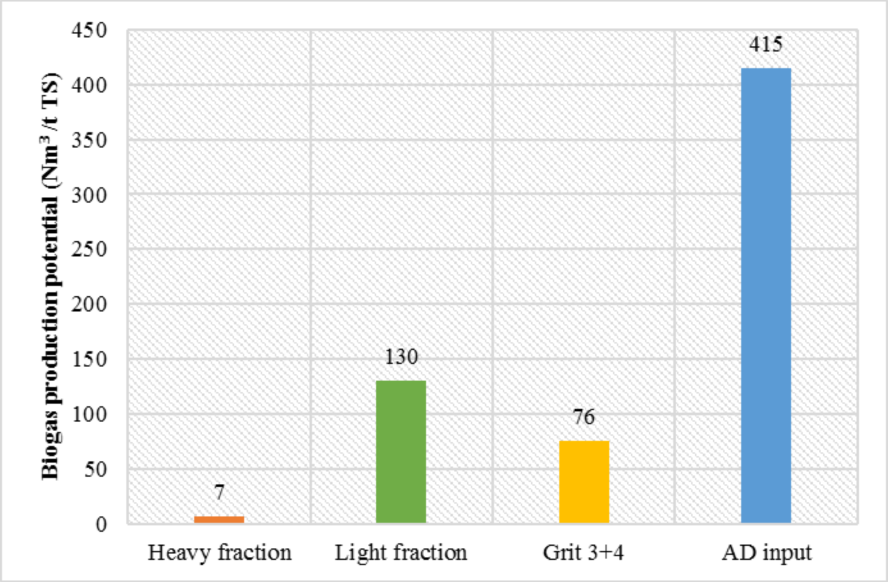

Fig. 8. Biogas production potential of each fraction

Through the mechanical pre-treatment of MSW, it was possible to significantly separate the impurities from the organics. Additional biogas production potential was found in some removed impurities (light fraction). In order to estimate the total amount of biogas that it is really lost in each fraction, it is necessary to perform a mass balance of the entire system. This will be performed as a next step of this project.

4. CONCLUSION

This paper presented the aplicability and the performance of a mechanical pre-treatment process for impuritities removal from MSW for biogas production on real scale. The results of this study indicated that the combination of pulpers and hydrocyclones for impurities removal from MSW showed to be efficient. The wet pre-treatment provided a substrate to the AD with very low concentration of impurities. While the pulpers could mainly remove inert material > 10 mm and plastics, the first two hydrocyclones were able to concentrate particles between 1 and 10 mm. Smaller particles were further removed by the last two hydrocyclones, mainly ranging from 0.25–4 mm. Finally, the pre-treated waste presented a biogas production potential of 415 Nm^3/t TS.

REFERENCES

1. EBNER, C., PÜMPEL, T. Mikrobiologie: Faulturm, 2016 (in German).
2. LGBI (Tirol) Nr. 56/2002: Tiroler Feldschutzgesetz. 2000. Link to the internet: < https://www.ris.bka.gv.at/GeltendeFassung.wxe?Abfrage=LrT&Gesetzesnummer=20000058>. Accessed on 20. Feb. 2018 (in German).
3. MEIRER, M., MÜLLER, W., BOCKREIS, A. Mechanische Abtrennung biogener Reststoffe aus Restabfall für die Co-Vergärung in Faultürmen kommunaler Kläranlagen. *Österr Wasser- und Abfallw*, 2017. DOI 10.1007/s00506-017-0411-2 (in German).
4. Bundesministerium für Nachhaltigkeit und Tourismus. Bundes-Abfallwirtschaftsplan 2017. Teil 1. ISBN: 978-3-903129-32-0 (in German).
5. Recycling Center Ahrental. Link to the internet: <http://www.rz-ahrental.at>. Accessed on 20. Feb. 2018.
6. JANK., A., EBNER, C., MÜLLER, W., FIMML, C., MARKT, R., BOCKREIS, A. Kosten und Erlöse bei der Co-Vergärung von mechanisch aufbereitetem Bioabfall in Faultürmen kommunaler Kläranlagen. *Österr Wasser- und Abfallw*, 2017, Vol. 69, p. 388–396. DOI 10.1007/s00506-017-0409-9 (in German).
7. MATSAKAS, L., GAO, Q., JANSSON, S., ROVA, U., CHRISTAKOPOULOS, P. Green conversion of municipal solid wastes into fuels and chemicals. *Electronic Journal of Biotechnology*, 2017, Vol. 26, p. 69-83. http://dx.doi.org/10.1016/j.ejbt.2017.01.004.
8. BTA International. BTA® Process. Link to the internet: <http://www.btai.de/en/der-bta-prozess/der-bta-prozess0.html>. Accessed on 19. Feb. 2018.
9. VDI 4630. Vergärung organischer Stoffe Substratcharakterisierung, Probenahme, Stoffdatenerhebung, Gärversuche. 2014 (in German).
10. Bioprocess control Sweden. Release History, version 1.3, March 2012.
11. SOSNOWSKI, P., WIECZOREK, A., LEDAKOWICZ, S. Anaerobic co-digestion of sewage sludge and organic fraction of municipal solid wastes. *Advances in Environmental Research*, 2003, Vol. 7, No. 3, p. 609–616.

CYSENI 2018, May 23-25, Kaunas, Lithuania
ISSN 1822-7554, www.cyseni.com

PERFORMANCE CHARACTERISTICS OF SINGLE-STAGE BIOHYTHANE PRODUCTION BY IMMOBILIZED ANAEROBIC BACTERIA

D. T. Ta, C. Y. Lin, C. Y. Chu
Feng Chia University – Green Energy Development Center
No. 100, Wenhua Road, Xitun District, 407 Taichung City – Taiwan
Email: tdthanh.fcu@gmail.com,

T. M. N. Ta
Nha Trang University
No. 02, Nguyen Dinh Chieu Street, 650000 Nhatrang City – Vietnam

ABSTRACT

Due to climate change and dwindling fossil fuel, bioenergy has become a future trend to replace fossil fuel-based economy. H_2 and CH_4 are recently the most widely used gaseous renewable energy carriers, both has its own advantages and downsides. Interestingly, H_2 can be an excellent additive for CH_4 as a mixture called hythane (H_2+CH_4). Biohythane produced via dark fermentation is much greener than the hythane that generated using natural gas. Biohythane production using a single-stage system has potential to increase the economic viability since it requires fewer controls than a two-stage system that having individual hydrogenic and methanogenic reactors. However, production of H_2 and CH_4 have different optimal condition such as pH and HRT. Thus, an essential method to protect hydrogenic and methanogenic bacteria (HB and MB) such as cell immobilization is needed. This technology can provide barrier, fixed-bed and enhance cell density for bacteria's resistance against harsh environment. The present work investigated the performance of a mesophilic single-stage system with a batch mode operation to generate biohythane at different condition of HB/MB ratio, substrate concentration and cultivate pH. HB and MB were entrapped in κ-carrageenan/gelatin beads (2%/2% w/w) using dripping method. The energy yield of 0.41 to 1.48 kJ g^{-1} glucose and the hydrogen content in biohythane ($H_2/(H_2 + CH_4)$) of 0.35 to 0.69 were obtained. These results indicate that different biohythane compositions would be obtained by regulating the HB/MB bacteria concentration ratio. Substrate concentration heavily affected pH value in batch system, which also influences biohythane compositions. A comparison of two-stage and single-stage systems as well as the challenges was also elucidated.

Keywords: anaerobic digestion, biohythane, cell immobilization, κ-carrageenan, gelatin

CYSENI 2018, May 23-25, Kaunas, Lithuania
ISSN 1822-7554, www.cyseni.com

REMOVAL OF INORGANIC CONSTITUENTS FROM CORN STALK BIOMASS

N. Baydar, H. Acma, S. Yaman
Department of Chemical Engineering, Istanbul Technical University
Maslak, Istanbul, 34469 – Turkey
Email: yamans@itu.edu.tr

ABSTRACT

Fossil energy sources provide the most of the global energy need and accordingly inevitable global problems such as the increasing greenhouse gas emissions, climate change, instability in fuel prices, etc. occur. In order to mitigate such problems, the fossil fuels should be replaced by renewable and sustainable energy sources like lignocellulosic biomass that is CO_2-neutral, abundant, and very cheap. Turkey produces large amount of corn, and consequently woody wastes of this crop such as stalks offer great potential to be an energy resource. However, inorganics found in corn stalk impair the combustion behavior of this biomass since some of the inorganics may show either catalytic or inhibitory effects that change the combustion characteristics seriously. Besides, they also cause problematic deposit formations in combustors. In this study, corn stalks were treated by various solutions prepared from chemicals to remove the inorganics and to obtain inorganics-free biomass. Ash contents of the treated biomass were determined according to American Society for Testing Materials (ASTM) standard, and the distribution of the inorganic elements were determined by Inductively Coupled Plasma (ICP) technique. It was found that sodium, potassium, magnesium, calcium and iron elements that have important effects during thermal processing of biomass can be eliminated from the corn stalk. However, the extent of their elimination depends on the type of the solutions and the treatment conditions. It was found out that H_3PO_4 is the most suitable acid to reduce the concentrations of alkali and alkaline-earth elements.

Keywords: corn stalk, biomass, inorganics, ICP

1. INTRODUCTION

Biomass is the general name of all unfossilized biological materials obtained from living creatures [1]. Biomass is a carbon-based material and it also contains hydrogen, oxygen, nitrogen, and other minerals including alkali, alkaline earth, and heavy metals [2]. The ability of biomass to grow easily everywhere, being an inexhaustible source of energy, its renewability and sustainability make biomass as an important energy source [3]. The benefits of using biomass energy can be summarized as follows: to be sustainable, to be easily accessible, can be grown almost anywhere, no harmful effects on the environment, low light intensity and temperature of 5–35 °C is sufficient for growing, it is storable, provides energy security, reduces atmospheric carbon emissions, no greenhouse effect [3–5]. Besides, there are also some negative features such as: threatening protection areas, threatening water resources, low cycle efficiency, creating competition for food production areas and reducing food safety, difficulty in storage areas due to large volume, less calorific value than fossil fuels, unable to reduce fossil fuel use at large scale [3–6].

One of the most important concerns with biomass use arises from the inorganic compounds found in biomass that have harmful effects during the thermochemical conversion processes. In order to avoid this negative aspect, inorganic components should be removed from biomass prior to usage. The reasons for removal of inorganics can be summarized as follows: they cause pollution and corrosion in power generation systems; cause of contamination in the steam boiler; damage heat transfer surfaces in combustion systems and participate in slag formation in grid-fired units; increase corrosion rates in turbines; cause molten deposits and slag formation; over time, they cause equipment malfunctions and difficulties in operating thermochemical energy conversion facilities.

All of these effects lead to increase in facility maintenance costs and decrease in the availability and running time of the equipment, thus reducing the efficiency.

There have been various efforts to demineralize the biomass using various techniques. Deashing of macroalgae biomass by pulsed electric field (PEF) treatment was tested in combination with hydraulic pressing [7]. This study revealed that PEF treatment enhanced the ash extraction from 18.4% to 37.4% of the total ash content. However, such attempts are scarce and can not be applicable easily. In contrast, chemical leaching methods are commonly applied for demineralization of biomass using suitable solvents or chemicals ranging from water to very potent chemicals [8]. The effects of demineralization on the yields of conversion processes such as pyrolysis, gasification, and combustion were elaborated. Tarves et al. [9] studied the effect of hot water extraction pretreatment on pyrolysis of shrub willow, and concluded that the decreased mineral content changed the yields of pyrolytic products. Rodriguez-Machin et al. [10] investigated the effects of citric acid leaching on the demineralization and thermal degradation behavior of sugarcane trash and bagasse, and found that this method removed 38.9–54.1% of ash. Persson et al. [11] attempted to use the acids from pyrolysis of wood (mainly acetic acid) as leaching agent for removal of inorganics. Results of this study indicated that removal of inorganics was in all cases enhanced by higher acidity; time of treatment was only seen to have a positive effect at lower acidity. Similarly, Oudenhoven et al. [12] also washed pine wood by wood-derived pyrolytic acid to remove the alkali minerals, and they reported that this procedure effectively removed the alkali ions initially present in biomass. On the other hand, Jiang et al. [13] applied various chemicals to demineralize the rice straw, and determined that strong acid leaching exhibited higher removal efficiency of minerals, but it affected the biomass structure more severely compared to water and weak acids. They also proposed that different leaching methods give chance to study catalytic effects of intrinsic minerals on thermal behavior of biomass. Demineralization of poplar wood with diverse solvents (HCl, HF, distilled water) led to significant variations in the thermal reactivity and decomposition characteristics [14]. Eom et al. [15] also compared the pyrolytic products from inorganic-rich and demineralized rice straw with hydrofluoric acid (HF). They determined that the total bio-oil yields are higher when rice straw was demineralized. Asadieraghi et al. [16] characterized the thermal degradation of lignocellulosic biomass (palm kernel) and the physiochemical structure when it was demineralized by diverse acid solutions (H_2SO_4, $HClO_4$, HF, HNO_3, HCl). Thermal analysis of the treated biomass showed that the maximum degradation temperatures increased after acid pretreatment due to loss of minerals that have catalytic effects. Yuan et al. [17] prepared demineralized wood dust with dilute nitric acid (HNO_3) and then impregnated it with copper salt to check the effects of copper on pyrolysis.

The versatile nature of the inorganics and the various forms of the mineral phases found in biomass make the demineralization process highly complicated and therefore some chemicals may be inefficient to remove some special inorganics [16]. For these reasons, this study focuses on determination of the effectiveness of several different solvents/chemicals on demineralization characteristics of corn stalk that is a high potential waste biomass material.

2. MATERIALS AND METHODS

2.1. Corn stalk

Corn, as one of the most important crops globally, has been used as human food and animal feed all over the world. In addition, there are also alternative areas of use for this crop such as starch, syrup, beer and production of some industrial products. Not only the corn itself, but also its stems and other leftovers can also be evaluated as an animal feed and renewable biomass energy source. In this context, Turkey is one of the top producers of corn globally, and accordingly large amounts of woody or herbaceous leftovers of corn are formed in the fields and processing of corn in food industry also producers residues that can be used as alternative biomass material. The corn stalks used in this study were collected from Turkish agricultural sector and used after drying at laboratory. The air-dried samples were first milled to reduce the particle size below 250 μm and then dried in oven. Demineralization of corn stalks were performed using the solvents described below.

2.2. Solvents

Reagent-grade (pure) chemicals were mixed/dissolved with distilled water to prepare the following aqueous solutions used in the demineralization experiment:

- Distilled water (H_2O),
- Acetic acid (CH_3COOH , 5 vol.%),
- Hydrochloric acid (HCl , 5 vol.%),
- Sulfuric acid (H_2SO_4 , 5 vol.%),
- Nitric acid (HNO_3 , 5 vol.%),
- Ortho-phosphoric acid (H_3PO_4 , 5 vol.%),
- Sodium hydroxide ($NaOH$, 5 wt.%).

2.3. Removal of inorganics

Air-dried and milled (< 250 μm) corn stalks were further dried in an oven at 105 °C to obtain the completely dried biomass specimen and then representative samples for the experiments were taken according to American Society for Testing Materials (ASTM) standards. 1 gram of milled biomass sample was placed into polypropylene beaker and treated using 100 ml of the solvents/chemicals including either distilled water, acetic acid, hydrochloric acid, sulfuric acid, nitric acid, orthophosphoric acid or sodium hydroxide solutions. Interaction of these solutions with corn stalks was allowed for 120 minutes at ambient temperature. Then the suspensions of the treated biomass and the solvents were filtered through a blue-ribbon filter paper that separates the solid and liquid phases from each other. The extracted solid bulk was dried in an oven at 105 °C and then it was ashed in a muffle furnace by slowly heating to 600 °C. The obtained ashes were dissolved using the reagent of "*Aqua Regia*" that contains the mixture of nitric acid and hydrochloric acid. Solutions obtained from this method was analyzed by Inductively Coupled Plasma (ICP) technique to compare the effectiveness of these solutions on the removal of alkali and alkaline-earth elements such as Na, K, Mg, Ca, Fe. Determination of the effectiveness of these solutions on the removal of inorganics was aimed and therefore the yields of the removals for each element were calculated.

Experiments were repeated several times, and the mean values of the results that don't differ more than 5% were taken.

3. RESULTS AND DISCUSSION

In order to reveal the effects of washing with only distilled water on the inorganics of biomass, the experiments were started with extraction of corn stalk with distilled water for interaction (extraction) times of either 30 min or 120 min. The biomass extracted with water was recovered from the suspension and then it was ashed. The obtained ash were dissolved as explained in the section of materials and methods. ICP technique was applied to analyze the concentrations of main alkali and alkaline earth elements such as Na, K, Mg, Ca, and Fe, and their removal yields. In this way, effects of the interaction time could be determined for the investigated elements as well.

Removal yields of individual elements were calculated considering their concentrations in ashes before and after extraction experiments. Table 1 shows the effects of interaction time on the removal yields of the elements.

Table 1. Effects of extraction time on the removal yields

Time (min)	**Mg (%)**	**K (%)**	**Na (%)**	**Fe (%)**	**Ca (%)**
30	37.8	22.0	18.5	-	6.4
120	31.5	20.8	17.4	-	13.3

The results in Table 1 indicate that Mg, K, Na, and Ca contents of biomass can be reduced by washing with distilled water, and Oudenhoven at al. [12] also reports this fact. Likewise, it is also reported that leaching biomass with water has been demonstrated to be an effective way to lessen alkaline and alkaline-earth minerals (AAEMs) from biomass, and could improve biomass fuel properties for high temperature processes of biomass [13]. Although, pretreatment by hot-water extraction can alter biomass composition [9], we performed this treatment at room temperature to avoid interaction of the organic part of biomass during this treatment. Meanwhile, removal of Fe couldn’t be achieved by treatment with water since Fe is a water-insoluble element and elimination of this element and its compounds require rather acidic conditions [13]. On the other hand, either 30 min or 120 min did not differ seriously with respect to the removal yields of Mg, K, and Na. However, significant improvement took place in the removal of Ca and therefore it can be recommended that treatments with the other chemicals can be also performed for the extraction time of 120 min. In fact, Ca is the most dominant mineral in a number of biomass species [4] and therefore efficient removal of calcium containing minerals is of great importance to mitigate the harmful effects of mineral matter in biomass on the undesirable deposit formations during thermochemical conversion processes. In addition, Ca compounds are also known to lead catalytic effects during combustion and gasification of biomass.

Table 2 gives the yields for removal of alkali and alkaline-earth elements when the other chemicals were applied to biomass. That is, the data given in this table offers the opportunity to compare the effectiveness of the solutions used in this study to remove the inorganics from corn stalk. It is seen from Table 2 that alkali and alkaline-earth elements such as Na, K, Mg, Ca, and Fe are affected more or less depending on the type of the solutions used. While some of these solutions have strong potential to eliminate the most part of definite elements, they may become entirely ineffective on others. Therefore, the most suitable chemical/solvent may be chosen from the list regarding either how many elements can be affected or how deep demineralization is performed on a special element when it is applied.

Table 2. Yields for removal of alkali and alkaline-earth elements

Solution	**Mg (%)**	**K (%)**	**Na (%)**	**Fe (%)**	**Ca (%)**
H_2O	31.5	20.8	17.4	-	13.3
HCl	19.3	-	4.2	5.6	35.0
H_2SO_4	27.8	13.9	43.2	34.6	39.1
H_3PO_4	83.6	65.3	65.0	78.4	62.6
HNO_3	31.0	28.9	-	-	24.1
CH_3COOH	25.0	26.7	-	-	24.4
NaOH	94.0	70.1	-	92.6	78.0

It was determined that the extraction experiments where only distilled water was used provided limited reductions in these elements, whereas no elimination was observed for Fe. In addition, the best demineralization potential was found out for the removal yield of Mg that reached 31.5%. Likewise, extraction of corn stalks using HNO_3 or CH_3COOH did not result in any reductions in Na and Fe contents that predicts that these acids are not recommended to use for demineralization purposes. On the other hand, it was determined that NaOH that is an alkali chemical is able to remove K, Mg, Ca, and Fe in high yields, while the presence of Na is not affected at all. In fact, addition of considerable amount of Na in the solution of NaOH can be attributed to the high concentrations of Na measured in the ash of treated biomass with NaOH. It is also known that NaOH solutions are harmful to the lignin content of biomass. For these reasons, it is almost impossible to find any other comparative studies where NaOH was used for demineralization purpose. Besides, HCl was inefficient to eliminate K from the sample that is another significant inorganics that leads to problematic deposit formations [4]. On the other hand, H_3PO_4 and H_2SO_4 are seen the most effective acids to eliminate all of these elements from corn stalk satisfactorily. In terms of the removal yields of the elements, it is clear that H_2SO_4 did not reach the performance of H_3PO_4. Namely, in case of H_3PO_4 usage, removal yields for Mg, K, Na, Fe, and Ca reached 83.6, 65.3, 65.0, 78.4, and 62.6 %, respectively, which demonstrates that very effective demineralization has been carried out. Thus, H_3PO_4 can be suggested as the most suitable chemical/reagent for removal of the inorganics from corn stalk. Mg that is the most abundant element in such biomass materials could be minimized as much as 83.6% that is followed by 78.4% Fe that couldn't be removed when HNO_3 or CH_3COOH was employed.

Although waste biomass species including agricultural residues contain numerous mineral phases and inorganic compounds, the main inorganic elements found in the ashes of such materials are highly rich in alkali and alkaline-earth elements. Therefore, the applied extraction procedure can be recommended as an efficient way to mitigate the concerns resulting from the content of inorganic in biomass. On the other hand, the concentrations of the solutions used in this study were limited by 5 vol./wt.%, and the higher concentrations would have provided deeper demineralization yields. Besides, handling of large volumes of acidic/alkali solutions in big scale applications is expensive and requires specific installations and safety measures [7]. Therefore, using of only water may be preferred to these chemicals provided that the demineralization yields are tolerable.

4. CONCLUSION

On the basis of the experimental results implemented in this study, it was determined that each of the solvents/chemicals has its own efficiency in demineralization of biomass and removal of the alkali and alkaline-earth elements. This comparative study revealed the fact that the most effective solution for demineralization of corn stalks is ortho-phosphoric acid (H_3PO_4). All of the investigated alkali and alkaline-earth inorganics could be reduced to seriously lower levels when this solution was used. On the other hand, since this study was carried out using only 5 vol./wt% concentrations of the solutions, it can be suggested that the influences of the other concentrations of the solutions as well as different temperature effects may be checked in further investigations.

REFERENCES

1. CLARK, C.; DESWARTE, F. *Introduction to Chemicals from Biomass*. New Delhi: John Wiley & Sons Ltd. 2008. 3 p. ISBN 978-0-470-05805-3.
2. BASU, P. *Biomass Gasification and Pyrolysis-Practical Design and Theory*. Amsterdam: Elsevier. 2010. 27 p. ISBN 978-0-12-374988-8.
3. TOPAL, M., ARSLAN E.I. Biomass Energy and Turkey. UTES 2008. Proceedings of 7th National Clean Energy Symposium. Istanbul: Turkey. 2008 December 17–19 (in Turkish).
4. KLASS, D.L. *Biomass for Renewable Energy, Fuels, and Chemicals*, London: Academic Press, 1998. 30 p. ISBN 978-0-12-410950-6.
5. DEMIRBAS, A. Biomass Resource Facilities and Biomass Conversion Processing for Fuels and Chemicals, *Energy Conversion and Management*, 2001, Vol. 42, No. 11, p. 1357–1378.

6. FIELD, C. B., CAMPBELL, J. E., LOBELL, D. B. Biomass Energy: The Scale of the Potential Resource, *Trends in Ecology & Evolution*, 2008, Vol. 23, No. 2, p. 65–72.
7. ROBIN, A., SACK, M., ISRAEL, A., FREY, W., MÜLLER, G., GOLBERG, A. Deashing Macroalgae Biomass by Pulsed Electric Field Treatment. *Bioresource Technology*, 2018, Vol. 255, p.131–139.
8. LIANG, L, HU, Song, SUN L.S., SU, S., XU, K., HE, L., XIANG, J. Influence of Different Demineralization Treatments on Physicochemical Structure and Thermal Degradation of Biomass. *Bioresource Technology*, 2013, Vol.146, p. 254–260.
9. TARVES, P.C., SERAPIGLIA, M.J., MULLEN, C.A., BOATENG, A.A. Effects of Hot Water Extraction Pretreatment on Pyrolysis of Shub Willow. *Biomass and Bioenergy*, 2017, Vol. 107, p. 299–304.
10. RODRIGUEZ-MACHIN, L., ARTEAGA-PEREZ, L.E., PEREZ-BERMUDEZ, R.A., CASAS-LEDON, Y., PRINS, W., RONSSE, F. Effect of Citric Acid Leaching on the Demineralization and Thermal Degradation Behavior of Sugarcane Trash and Bagasse. *Biomass and Bioenergy*, 2018, Vol. 108, p. 371–380.
11. PERSSON, H., KANTARELIS, E., EVANGELOPOULOS, P., YANG, W. Wood-derived Acid Leaching of Biomass for Enhanced Production of Sugars and Sugar Derivatives during Pyrolysis: Influence of Acidity and Treatment Time. *Journal of Analytical and Applied Pyrolysis*, 2017, Vol. 127, p. 329–334.
12. OUDENHOVEN, S.R.G., WESTERHOF, R.J.M., ALDENKAMP, N., BRILMAN, D.W.F., KERSTEN, S.R.A. Demineralization of Wood Using Wood-derived Acid: Towards a Selective Pyrolysis Process for Fuel and Chemicals Production. *Journal of Analytical and Applied Pyrolysis*, 2013, Vol. 103, p. 112–118.
13. JIANG, L., HU, S., SUN, L., SHENG, S., XU, K., HE, L., XIANG, J. Influence of Different Demineralization Treatments on Physicochemical Structure and Thermal Degradation of Biomass. *Bioresource Technology*, 2013, Vol. 146, p. 254–260.
14. EOM, I., KIM, J., LEE, S., CHO, T., CHOI, I., CHOI, J. STUDY ON THE Thermal Decomposition Features and Kinetics of Demineralized and Inorganic Metal-impregnated Lignocellulosic Biomass. *Journal of Industrial and Engineering Chemistry*, 2012, Vol. 18, p. 2069–2075.
15. EOM, I., KIM, J., LEE, S., CHO, T., HWANMYEONG, Y., CHOI, J. Comparison of Pyrolytic Products Produced from Inorganic-rich and Demineralized Rice Straw (Oryza Sativa L.) by Fluidized Bed Pyrolyzer for Future Biorefinery Approach. *Bioresource Technology*, 2013, Vol. 128, p. 664–672.
16. ASADIERAGHI, M., DAUD, WMAW. Characterization of Lignocellulosic Biomass Thermal Degradation and Physicochemical Structure: Effects of Demineralization by Diverse Acid Solutions. *Energy Conversion and Management*, 2014, Vol. 82, p. 71–82.
17. YUAN, H., XING, S., HUHETAOLI, LU, T., CHEN, Y. Influence of Copper on the Pyrolysis Process of Demineralized Wood Dust through Thermogravimetric and Py-GC/MS Analysis. *Journal of Analytical and Applied Pyrolysis*, 2015, Vol. 112, p. 325–332.

CYSENI 2018, May 23-25, Kaunas, Lithuania
ISSN 1822-7554, www.cyseni.com

TECHNOLOGICAL PROGRESS AND SUBSTITUTION EFFECTS IMPACT ON GREENHOUSE GAS EMISSIONS

G. Liobikienė
Vytautas Magnus University
Vileikos str. 8, LT-44404 Kaunas – Lithuania
Email: g.liobikiene@vdu.lt

ABSTRACT

It is well documented that the reduction of greenhouse gas (GHG) emissions are the core stones of environmental policy. However, there is still open debate on the identification of GHG emission determinants. Thus, the aim of our paper was to estimate the impact of economic growth, energy efficiency (technological progress) and share of renewable energy consumption (substitution effect) on GHG emissions. Applying the robust estimations, it was found that GHG pollution monotonically rises with GDP. Moreover, an increase in efficiency of energy usage by 1% would lead to a direct reduction of GHG pollution by 0.87% and indirect increase of pollution through induced economic growth effect by 0.18%. Meanwhile, if share of renewable energy sources in total final energy consumption would increase by 1%, it would reduce GHG pollution by 0.92% holding other factors fixed. Thus, it could be concluded that an increase of energy efficiency and promotion of renewable energy consumption are one of the main tools to achieve the climate change policy targets at the world level.

Keywords: Climate change policy, energy efficiency, renewable energy, GHG emissions

1. INTRODUCTION

The growth of greenhouse gas emissions (GHG) is the main determinant of climate change. GHG emissions are still growing around the world. Therefore, on 12th of December 2015, almos all world countries published their action plan, where countries intend to reduce their GHG emissions. The Paris Agreement asks to achieve carbon neutrality in the second half of the century. Therefore, the world needs sustainable economic growth. The relationship between GHG emissions and economic growth has been intensively analysed testing the validity of Environmental Kuznets Curve (EKC). The EKC hypothesis postulates that the relationship between economic growth and the environment impact resembles an inverted U-shape curve. That is, environmental impact increase as a country develops, but begin to decrease as rising incomes pass beyond a turning point [1]. The authors analysing the EKC used different methods and analysed different countries. The extensive reviews on the existence of the EKC was done by Kaika and Zervas [2], Azam and Khan [3] and Bilgili et al. [4]. However, while reviewing the literature on GHG emissions we did not find any studies that would encompass diverse countries in the world while evaluating the relationship between economic growth and GHG emissions. Thus this paper fills that gap.

In order to achieve sustainable economic growth it is important that during the growth of economy GHG emissions would increase at slower rate or rather decrease. Considering that the GHG emissions are directly linked with energy consumption, seeking sustainable economic growth, it is very important to increase the energy efficiency. However, energy efficiency (or technological progress) was was rather ignored in the research analysing relationship between GHG emissions and GDP growth. The other authors studies confined only to the analysis of relationship between economic growth, energy consumption and GHG emissions [5–10 and etc.]. When dealing with energy, most studies indicate positive relationship between GHG emissions and energy consumption. However, the decrease of energy consumption with the aim to reduce GHG emissions can have negative effects on economic growth as well [10]. Therefore, the reduction of GHG emissions, boost in technological progress or energy efficiency is required seeking sustainability.

The other very important factor for achieving sustainable economic growth is the renewable energy consumption (or substitution effect). The relationship between economic growth, renewable energy consumption and GHG emissions was analysed by Bölük and Mert [11]. Applying panel data analysis on the EU, they found that renewable energy consumption contributes to GHG emissions around 50% less per unit of energy consumed compared with conventional (fossil) energy source. Marrero [12] found that shifting the energy mix towards renewable sources would yield significant reductions in per capita GHG emissions in the EU. Dogan and Seker [13] by using the dynamic ordinary least squares estimator revealed that renewable energy reduce GHG emissions in the EU as well. Bilgili et al. [4] revealed that in 17 OECD countries renewable energy consumption yields negative impact on GHG emissions. Tiwari [14] stated that was impossible to find a long-run relationship between GHG emissions and renewable energy consumption and renewable energy consumption initially increases emission levels before subsequently reducing them in India. Menyah and Wolde-Rufael [15] analysing the relationship between the USA GHG emissions and renewable energy consumption concluded that the use of renewable energy sources has not helped to reduce GHG emissions. Moreover, Jaforullah and King [16] applying cointegration and Granger causality tests also indicated that GHG emission levels are negatively related to the use of renewable energy in the USA. However, the promotion of renewable energy consumption is required to achieve the sustainable economic growth and decrease the climate change. Thus, the aim of our paper was to estimate the impact of economic growth, energy efficiency (technological progress) and share of renewable energy consumption (substitution effect) on GHG emissions.

2. MODEL AND DATA

2.1. Data specification and descriptive statistics

The main data used in this study was GHG emissions (kt), GDP (PPP, constant 2011 international $). Substitution effect was evaluted using renewable energy consumption as a percent of total final energy consumption, technological progress was used to proxy energy efficiency (GDP per unit of energy use (constant 2011 PPP $ per kg of oil equivalent)). The data used in the analysis was collected from World Bank database.

The changes in GDP, GHG emissions, energy efficiency and share of renewable energy consumption are presented in Fig. 1. As we see, the GDP in the world during the analysed (1990–2011) period increased by two times. Meanwhile, the GHG emissions increased by 56%. Thus the results reveled that in the case of economic growth the GHG emissions in the global level increased as well but at the slower rate.

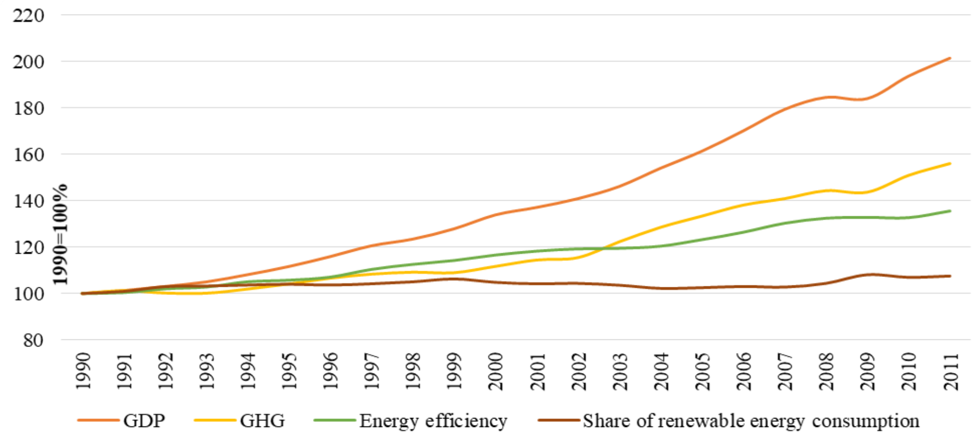

Fig 1. The changes in GDP, GHG, energy efficiency and share of renewable energy consumption in the world

The growth of energy efficiency in the world was observed as well, it increased by 35%. Meanwhile, the changes in the share of renewable energy consumption was rather unaltered and during the analysed period the share of energy consumption increased only by 1.8 percentage points (Fig. 1). Thus this result covers that the promotion of renewable energy consumption in the world is generally lagging in results.

2.2. The model and estimation technique

This subsection presents research methodology suitable to estimate the impact of economic growth on changes in GHG emissions taking into the account the energy efficiency and renewable energy consumption. From the theoretical point of view, if the EKC hypothesis was true, then economic growth would be the key to eventual environmental improvement. The research results support evidence that, in fact, pollution problems mostly addressed to developing economies, disprove classical statement "to poor to be green" [17]. If we assume that there would not be any changes in the technology of the economy, pure economic growth would result in growth in pollution and other environmental problems. However, the changes towards better technology (i.e. approximated by energy efficiency), as well as the increase of energy mix (i.e. approximated by the share of energy used from renewable sources) result in levelling off and gradual decline of environmental degradation. Thus they are both proximate causes of the GHG emissions along with scale of the economy, as well as underlying causes which can also have an effect via the proximate variable – scale of the economy. Formalizing the abovementioned ideas, we modify classic EKC equation by incorporating technological progress (equation (1) and substitution (equation (2) effects:

$$EI_{it} = \alpha + \beta_1 GDPpc_{it} + \beta_2 GDPpc_{it} \cdot EEF_{it} + \beta_3 EEF_{it} + \eta_i + \mu_t + \varepsilon_{it} \tag{1}$$

$$EI_{it} = \alpha + \beta_1 GDPpc_{it} + \beta_2 GDPpc_{it} \cdot REN_{it} + \beta_3 REN_{it} + \eta_i + \mu_t + \varepsilon_{it} \tag{2}$$

where *EI* denotes the environmental indicator (GHG emissions), *GDPpc* denotes per capita income, *EEF* denotes the level of energy efficiency and *REN* denotes the share of renewable energy, α denotes constant, η denotes country-specific effects, μ refers to year specific effects and *i* and *t* refer to country and year, respectively.

Though any actual change at the level of GHG emissions must be a result of change in one of the proximate variables, those variables may be driven by changes in underlying variables that also vary over the course of economic growth. Interactions *GDPpc·EEF* and *GDPpc·REN* show that economic growth through technological progress and substitution effects respectively, could result in decline of GHG emissions but not just through pure economic growth. If we assume that β_1 is positive and statistically significant and β_2 is negative and statistically significant then estimated EKC has a maximum turning point at per capita GDP level. These partial derivatives show that the turning points of income level depend on technological progress and substitution effects, i.e. the higher the energy efficiency or bigger share of energy is used from renewable sources the lower income level is needed to maintain sustainable economy, i.e. enhance decline of GHG emissions. Moreover, both of these effects can occur at the same time and supplement each other in reduction of environmental degradation. Thus taking into account both effects we obtain a modified EKC function:

$$EI_{it} = \alpha + \beta_1 GDPpc_{it} + \beta_2 GDPpc_{it} \cdot REN_{it} + \beta_3 REN_{it} + \beta_4 GDPpc_{it} \cdot EEF_{it} + \beta_5 EEF_{it} + \\ + \eta_i + \mu_t + \varepsilon_{it} \tag{3}$$

The earliest EKCs were simple quadratic functions of the levels of income. However, economic activity inevitably implies the use of resources and, by the laws of thermodynamics, the use of resources inevitably leads to the production of waste. Regressions that allow levels of indicators to become zero or negative are inappropriate except in the case of deforestation where afforestation can occur. A logarithmic dependent variable would impose this restriction. The same could be addressed to the right-hand side (RHS) variables of the equation regarding efficiency of energy usage, share of renewable sources and economic growth, variables that can become zero but just in theory and never negative:

$$\ln(EI_{it}) = \alpha + \eta_i + \mu_t + \beta_1\ln(GDPpc_{it}) + \beta_2\ln(GDPpc_{it}) \cdot \ln(EEF_{it}) + \beta_3\ln(EEF_{it}) + \varepsilon_{it} \tag{1a}$$

$$\ln(EI_{it}) = \alpha + \eta_i + \mu_t + \beta_1\ln(GDPpc_{it}) + \beta_2\ln(GDPpc_{it}) \cdot \ln(REN_{it}) + \beta_3\ln(REN_{it}) + \varepsilon_{it} \tag{2a}$$

$$\ln(EI_{it}) = \alpha + \eta_i + \mu_t+\beta_1\ln(GDPpc_{it}) + \beta_2\ln(GDPpc_{it}) \cdot \ln(REN_{it}) + \beta_3\ln(REN_{it}) + \\ + \beta_4\ln(GDPpc_{it}) \cdot \ln(EEF_{it}) + \beta_5\ln(EEF_{it}) + \varepsilon_{it} \tag{3a}$$

The first three terms on the RHS are intercept parameters which vary across countries *i* and years *t*. The assumption is that, though the level of emissions per capita may differ over countries at any particular GDP, technological progress and substitution level, the income elasticity is the same in all countries at a given income, technological progress and substitution level.

Usually the model is estimated with panel data. Most studies attempt to estimate both the fixed and random effects models. If the country-specific and time-specific variables are correlated with RHS variables, then the random effects model cannot be estimated consistently [18]. Only the fixed effects model can be estimated consistently. However, in any case, simultaneity bias is less serious in dynamic models involving differentiated variables and Generalized Method of Moments (GMM) estimates. As Bond et al. [19] and Hauk and Wacziarg [20] pointed out, the sys-GMM estimators should be used for panel data regressions to estimate more consistent and efficient parameters. Based on the above considerations, the sys-GMM estimator is used to estimate equations (1a)–(3a). To examine the overall validity of the sys-GMM estimation, following Arellano and Bond [21] and Blundell and Bond [22], two tests are to be carried out: (1) the Sargan test which tests the null hypothesis that the instruments are valid; and (2) the AR(2) test which tests null hypothesis that there is no second-order auto-correlation. The sys-GMM estimation results are valid only after passing two tests described above.

3. ESTIMATION RESULTS AND DISCUSSION

Authors suggested that GHG emissions are not a simple function of income alone [10]. That leads to estimate a modified EKC equations (1a–3a) i.e. to analyse the technological progress and substitution effects as both proximate causes of the GHG pollution along with scale of the economy. This section will be finished by discussing estimation results, i.e. impact of economic growth on GHG emissions taking in to the account energy efficiency and renewable energy usage.

Estimation results are presented in Table 1. All estimations are robust and include time-fixed effects. We should point here that depending on data available for efficiency of energy usage and share of renewable sources to proxy technological progress and substitution variables, the number of countries included in analysis varies. Information about countries not included in the estimations along with full set of 180 sampled countries.

Table 1. System GMM estimates of modified EKC. Dependent variable: natural logarithm of GHG

	(1)	(2)	(3)
Y(-1)	0.7740*** (0.0042)	0.7301*** (0.0034)	0.7078*** (0.0056)
Constant	−5.3186*** (0.1205)	−5.4709*** (0.0691)	−5.5865*** (0.1447)
Log of GDP	0.3132*** (0.0063)	0.3385*** (0.0036)	0.3579*** (0.0079)
Log of GDP * Technological progress	0.1813*** (0.0018)		0.1357*** (0.0016)
Technological progress	−0.8730*** (0.0419)		−0.7554*** (0.0373)
Log of GDP * Substitution effect		−0.0116***	−0.0084***

		(0.0008)	(0.0008)
Substitution effect		−0.3469***	−0.2912***
		(0.0204)	(0.0204)
n	2717	3390	2610
Number of countries in the sample	161	174	157
p-value of AR(2) test	0.6824	0.2847	0.8219
p-value of Sargan test	0.9481	0.9390	0.9016

All equations were estimated using 2-step sys-GMM including equations in levels.
* indicates significance at the 10 percent level
** indicates significance at the 5 percent level
*** indicates significance at the 1 percent level
All estimates include time dummies
Asymptotic standard errors are presented in parentheses of estimates

Estimation results in column (1) clearly show that if efficiency of energy usage would remain constant, ecnomic growth by 1% would lead to increase in GHG pollution also by 0.31%, i.e. estimated “pollution elasticity” is about 0.3, holding other factors fixed. We also see here that more efficient use of energy at the same production level reduces GHG pollution. The estimated coefficient of elasticity is about –0.87. What is more interesting here, estimated coefficient on interaction term is positive. It is an evidence of negative effect of technological progress on environment through economic growth. It is not very surprising if we take into account the economic effect of technological progress. The increasing efficiency of energy usage reduces cost of production and that is one of the main factors of supply-side growth affecting further growth of production and that, as we already know, leads to the increase of GHG pollution which reveals the evidence of rebound effect [23, 24]. Thus, energy efficiency indirectly due to rebound effect contributes to the growth of GHG emissions, therefore it is not enough only to increase energy efficiency, it is more important to reduce energy consumption.

If we hold other factors of growth fixed, increase in efficiency of energy usage by 1% would lead to direct reduction of GHG emissions by 0.87% and indirect increase of environmental impact through induced economic growth effect by 0.18%, i.e. total effect of 1% improvement in energy efficiency would lead to reduce in GHG emissions by 0.69%. Therefore, the overall effect of technological progress is in favour of reducing emissions. Thus, we confirmed other authors’ findings that seeking sustainable growth and the occurrence of EKC it is very important to rise the energy efficiency and to promote the technological progress [see: 5, 8, 9, 25–31 and etc.].

Estimation results in column (2) reveals that if share of renewable energy consumption in total final energy would growth by 1% it would decrease GHG emissions by 0.35%. We should note here that estimated effect could look small but just at the first sight because we are dealing here with estimates on changes in per cents and not in percentage points. The mean share of renewables in our sample is about 35.77%. Thus increase by 1% would mean an increase in share by 0.38 percentage points and if share of renewable energy sources would increase by 1 percentage point, it would reduce GHG emissions by 0.92% holding other factors fixed. Thus this result is also in line with other authors’ findings [see 5, 8, 9, 11, 12, 16, 27, 31–34 and etc.) and confirmed that the growth of renewable energy consumption is essential in the climate policy.

Estimated coefficient on the interaction term between economic growth and substitution effect is statistically significant and positive, indicating that transition from polluting to renewable energy sources has indirect effect on GHG emissions through economic growth. It is not very surprising assuming that changes in energy sources mix increase price of the energy. Renewable energy sources costs more compared with energy from traditional sources, despite the fact that price of energy from renewable sources has dropped significantly over last ten years. In such case shift from traditional to environmentally friendly energy sources should increase energy price, production cost, reduce energy consumption and as a constraint of supply-side growth should lead to economic decline and eventually to lower level of environmental impact. Negative and statistically significant coefficient on interaction term provides an evidence supporting these interpretations, thus transition from traditional to renewable energy leads indirectly, as well as directly to the reduction of GHG pollution.

When we put both – technological progress and substitution – effects in one equation (estimation of it is presented in column (3)), signs and significance of estimated coefficients do not differ from what we saw in columns (1) and (2). But we see some changes in magnitude of estimated effects. When we combine both effects, direct effect of energy efficiency on GHG emissions becomes smaller, as well as effect of renewable energy sources if we compare them with separate estimates. That could be because substitution and technological progress are substituting effects at some point while reducing GHG emissions. Ayres and Ayres [35] also declared that these effects substitute each other.

4. CONCLUSION AND POLICY IMPLICATION

This paper analysed the relationship between economic growth and GHG emissions including almost all countries of the world where the data was provided. This was done for several reasons: 1) that world income distribution is highly skewed because of much larger number of people below world mean income than above it, estimations derived from particular country or groups of countries using time series data cannot give a whole picture [2]; 2) including vast majority of world countries we can eliminate the Using time-series analysis the leakage can distort estimation results. In the developed countries GHG pollution can decrease not just because of technological improvements and structural economic changes, but because production along with environmental problems is transferred to developing countries.

Taking into account the economic growth we found that economic influenced the global increase in GHG emissions. Thus, for climate policy at the world level exist huge issues how to reduce the pollution keeping the world within the 2 °C warming boundaries and not restricting economic growth. Therefore all countries should responsibly and promptly tackle the actions to reduce the growth of GHG emissions.

Estimating the impact of growth on GHG emissions in a way to account for technological progress (energy efficiency) and substitution (share of renewable energy consumption) effects which almost are not analysed but are very important in climate policy we revealed that increase in efficiency energy would lead to direct decrease of GHG emissions and indirect increase of emissions through induced economic growth effect. These results showed that it is important to enhance the energy efficiency, but due to rebound effect the contribution to the reduction of GHG emissions could be inconsequential. Therefore, it is more important to increase the reduction of energy consumption.

Considering the share of renewable energy sources we found that the growth of latter variable by 1 percentage point would reduce GHG pollution by 0.92%. Estimated coefficient on interaction term between economic growth and renewable energy consumption is statistically significant and this fact demands a deeper analysis of how renewable energy shapes the impact of growth on GHG emissions through energy mix, higher energy prices and lower demand for energy. These results confirmed that the promotion of renewable energy consumption is essential tool in the climate change policy. However, generally in the world the promotion of renewable energy consumption is lagging in results. Thus, environmental policy should take particular attention to actual use of renewable energy sources.

REFERENCES:

1. Grossman, G.M. and Krueger, A.B. Economic growth and the environment. The Quarterly Journal of Economics, 1995, Vol. 110, No. 2, p. 353–377.
2. Kaika, D. and Zervas, E. The Environmental Kuznets Curve (EKC) theory – Part A: Concept, causes and the CO2 emissions case. Energy policy, 2013, Vol. 62, p. 1392–1402.

3. Azam, M and Khan A.Q. Testing the Environmental Kuznets Curve hypothesis: A comparative empirical study for low, lower middle, upper middle and high income countries. Renewable and Sustainable Energy Reviews, 2016, Vol. 63, p. 556–567.
4. Bilgili, F., Kocak, E., Bulut, U. The dynamic impact of renewable energy consumption on CO2 emissions: A revised Environmental Kuznets Curve approach. Renewable and Sustainable Energy Reviews, 2016, Vol. 54, p. 838–845.
5. Cowan, W.N., Chang, T., Inglesi-Lotz, R., Gupta, R. The nexus of electricity consumption, economic growth and CO2 emissions in the BRICS countries. Energy Policy, 2014, Vol. 66, p. 359–368.
6. Joo, Y.J., Kim, C.S., Yoo, S.H. Energy consumption, CO2 emission, and economic growth: evidence from Chile. Int. J. Green Energy, 2015, Vol. 12, No. 5, p. 543–550.
7. Alshehry, A.S., Belloumi, M. Energy consumption, carbon dioxide emissions and economic growth: the case of Saudi Arabia. Renew. Sust. Energ. Rev. 2015, Vol. 41, p. 237–247.
8. Wang, S., Li, Q., Fang, C., Zhou, C. The relationship between economic growth, energy consumption, and CO2 emissions: Empirical evidence from China. Science of the Total Environment, 2016, Vol. 542, p. 360–371.
9. Wu, L., Liu, S., Liu, D., Fang, Z., Xu, H. Modelling and forecasting CO2 emissions in the BRICS (Brazil, Russia, India, China, and South Africa) countries using a novel multi-variable grey model Energy, 2015, Vol. 79, p. 489–495.
10. Kais, S and Sami, H. An econometric study of the impact of economic growth and energy use on carbon emissions: Panel data evidence from fifty-eight countries. Renewable and Sustainable Energy Reviews, 2016, Vol. 59, p. 1101–1110.
11. Bölük, G. and Mert, M. Fossil & renewable energy consumption, GHGs (greenhouse gases) and economic growth: Evidence from a panel of EU (European Union) countries. Energy, 2014, Vol. 74, p. 439–446.
12. Marrero, G.A. Greenhouse gases emissions, growth and the energy mix in Europe. Energy Economics, 2010, Vol. 32, p. 1356–1363.
13. Dogan, E and Seker, F. Determinants of CO2 emissions in the European Union: The role of renewable and non-renewable energy. Renewable Energy, 2016. Vol. 94, p. 429–439.
14. Tiwari, A.K. A structural VAR analysis of renewable energy consumption, real GDP and CO2 emissions: evidence from India. Econ. Bull. 2011, Vol. 31, p. 1793–1806.
15 Menyah, K, Wolde-Rufael, Y. CO2 emissions, nuclear energy, renewable energy and economic growth in the US. Energy Policy, 2010, Vol. 38, p. 2911–2915.
16. Jaforullah, M and King A. Does the use of renewable energy sources mitigate CO2 emissions? A reassessment of the US evidence. Energy Economics, 2015, Vol. 49, p. 711–717.
17. Dasgupta, S., Laplante, B., Wang, H., Wheeler, D. Confronting the environmental Kuznets curve. Journal of Economic Perspectives, 2002, Vol. 16, p. 147–168.
18. Hsiao, C. Analysis of Panel Data. Cambridge: Cambridge University Press, 1986.
19. Bond, S.; Bowsher, C.; Windmeijer, F. Criterion-based Inference for GMM in Autoregressive Panel Data Models. Economic Letters, 2001, Vol. 73, No. 3, p. 379–388.
20. Hauk, W.; Wacziarg, R. A Monte Carlo study of growth regressions. Journal of Economic Growth, 2009, Vol. 14, No. 2, p. 103–147.
21. Arellano, M.; Bond, S. Some tests of specification for panel data: Monte Carlo evidence and an application to employment equations. The Review of Economic Studies 1991, Vol. 58, No. 2, p. 277–297.
22. Blundell, R.; Bond, S. Initial conditions and moment restrictions in dynamic panel-data models. Journal of Econometrics, 1998, Vol. 87, No. 1, p. 115–143.
23. Madlerner, R. and Alcott, B. Energy rebound and economic growth: A review of the main issues and research needs. Energy, 2011, Vol. 34, No. 3, p. 370-376.
24. Turner, K. and Hanley, N. Energy efficiency, rebound effects and the environmental Kuznets Curve. Energy Ecomomics, 2011, Vol. 33, No. 5, p. 709–720.

25. Pao, H-T. And Tsai, C-M. CO2 emissions, energy consumption and economic growth in BRIC countries. Energy Policy, 2010, Vol. 38, p. 7850–7860.
26. Cansino , M.J., Román. R., Rueda-Cantuche, J.M. Will China comply with its 2020 carbon intensity commitment? Environmental Science & Policy, 2015, Vol. 47, p. 108–117.
27. Yao, C., Feng, K., Hubacek, K. Driving forces of CO2 emissions in the G20 countries: An index decomposition analysis from 1971 to 2010. Ecological Informatics, 2015, Vol. 26, p. 93–100.
28. Rüstemoğlu, H. and Andrés, A.R. Determinants of CO2 emissions in Brazil and Russia between 1992 and 2011: A decomposition analysis. Environmental Science & Policy, 2016, Vol. 58, p. 95–106.
29. Kang, Y-Q., Zhao, T., Yang, Y-Y. Environmental Kuznets curve for CO2emissions in China: A spatial panel data approach. Ecological Indicators, 2016, Vol. 63, p. 231–239.
30. Niu , S, Liu, Y., Ding, Y., Qu, W. China's energy systems transformation and emissions peak. Renewable and Sustainable Energy Reviews, 2016, Vol. 58, p. 782–795.
31. Kumar, S. and Madlener, R. CO2 emission reduction potential assessment using renewable energy in India. Energy, 2016, Vol. 97, p. 273–282.
32. Zhang, W., Yang, J., Sheng, P., Li, X., Wang X. Potential cooperation in renewable energy between China and the United States of America. Energy Policy, 2014, Vol. 75, p. 403–409.
33. Sebri, M and Ben-Salha, O. On the causal dynamics between economic growth, renewable energy consumption, CO2 emissions and trade openness: Fresh evidence from BRICS countries. Renewable and Sustainable Energy Reviews, 2014, Vol. 39, p. 4–23.
34. De Arce, M. P., Sauma, E., Contreras, J. Renewable energy policy performance in reducing CO2 emissions. Energy Economics, 2016, Vol. 54, p. 272–280.
35. Ayres, R.U. and Ayres. L.W. A Handbook of industrial ecology Edward Elgar Cheltenham, UK, Northampton MA, USA, 2002, 680 p.

CYSENI 2018, May 23-25, Kaunas, Lithuania
ISSN 1822-7554, www.cyseni.com

USE OF CELLULAR COMMUNICATION MASTS FOR WIND SHEAR RESEARCH

V. P. Bezrukovs
Institute of Physical Energetics
Krivu 11, LV-1006 Riga – Latvia

V. V. Bezrukovs, S. Upnere, L.Gulbe
Ventspils University College
Inzenieru 101, LV-3601 Ventspils – Latvia
Email: vladislavsb@venta.lv

D. V. Bezrukovs
Riga Technical University
Azenes Srt. 12/1, LV-1048 Riga – Latvia

ABSTRACT

Prior to the start of any Wind Power Park (WPP) construction project, it is necessary to carefully assess available wind potential in the selected area. The costs of such investigative studies is considerable – even with a relatively small 70 m tall mast it reaches several tens of thousands of Euros. In order to reduce costs related to wind speed measurements it is suggested to use existing cellular communication masts that are widely spread in Europe. The study presents a methodological approach and the results of wind speed and wind shear measurements performed with the use of lattice cellular communication masts at the height of up to 100 m. A CFD model of airflow around a cellular communication mast structure was created in order to explore the impact of mast structure on the quality of wind speed measurements. The paper presents the results of the CFD modelling in the form of contour maps depicting the severity of airflow disturbances around the mast.

The experimental measurements were conducted in 2018 in three coastal sites of Latvia located on the shore of the Baltic Sea in the area of Ventspils, Pavilosta and Ainazi. At each site wind speed and direction were measured at the heights of 10, 40, 64 and 84 m along with air temperature and humidity. For the experimental studies, triangular lattice masts of guyed type were chosen, which have a height of about 100 m with side dimensions of 1.2 and 1.4 m, and located in the vicinity of existing ten-meter height masts of meteorological stations. Selected regions are favourable for WPP development. Wind measurements at these sites were started on the following dates: Ventspils – 2017.12.21, Pavilosta – 2018.01.11, Ainazi – 2018.01.21 and scheduled to last at least till the end of 2018. This paper discusses the measurement results obtained until 2018.03.06. Obtained wind speeds were analyzed taking into account corresponding wind flow direction.

The results of the study show that in order to increase the reliability of the results of wind speed measurements, it is sufficient to use two anemometers offset by at least 120° from each other in combination with a wind direction sensor used for filtering out wind speed values measured in the shadow of the mast. Further increase in the number of sensors installed on a mast for the purpose of performing wind speed measurements does not improve the reliability of the flow velocity measurement. The reliability of average wind speed estimation increases after the exclusion of distorted measurements from calculations. As a result of such correction, the speed values at all heights increased by ~1.9 – 3.9 % on average.

The experimentally obtained data in combination with the analysis of modelled CFD results shows the possibility of using cellular communication masts for accurate measurements of wind speed and provides a valid option for significantly reducing the time and material resources required to study the potential of wind energy at the height of up to 100 meters above ground level.

Keywords: wind speed measurements, CFD modelling, lattice mast, wind shear

Acknowledgement: The work is carried out within the project New European Wind Atlas (NEWA), ENER/FP7/618122/NEWA ERA-NET PLUS.

CYSENI 2018, May 23-25, Kaunas, Lithuania
ISSN 1822-7554, www.cyseni.com

THE INVESTIGATION OF FACTORS DETERMINING WIND POWER PREDICTION ACCURACY: CASE STUDY OF WESTERN LITHUANIA

G. Gecevičius, M. Marčiukaitis
Lithuanian Energy Institute
Breslaujos str. 3, LT-44403 Kaunas – Lithuania
Email: Giedrius.Gecevicius@lei.lt

G. Gecevičius
Kauno Kolegija, University of Applied Sciences
Pramones av. 20, LT-50468 Kaunas – Lithuania

ABSTRACT

In order to mitigate climate change, more attention every year is being given to the development of renewable energy sources (RES). In the end of 2016 RES shared 24.5% of global power generation, and it was one of the most developed sectors in the word. Wind energy is the main modern energy source for power generation and acts very important role for the future power generation strategies. However, despite minimal impact of wind turbines for environment and reduced greenhouse gas emissions regarding fossil fuels non-usage, there is negative side as well. Wind speed variations are stochastic process, and it is difficult to predict wind power accurately. Therefore, unpredictable power can disbalance power grid, besides huge power reserves are necessary. Due to this reason wind energy increases power system exploitation expenses.

Wind energy can be forecasted based on statistical, physical or hybrid methods and models. However, all methods and models generate power prediction errors during different time horizons. Statistical methods are more suitable for short term power prediction and physical approach the best appreciate for mid and long-term wind power prediction periods.

Paper presents analysis of wind power prediction errors determining topographical and meteorological conditions based on statistical, physical and hybrid approaches. The methodology of statistical power prediction approach involves non-linear regression with estimated seasonal indicators, new reference models with determined the best suitable parameters for different time horizons and model output statistics function for the analysis of relation between predicted and factual wind power. Moreover, the most suitable parameter for predictable power correction were determined. Physical power prediction methods cover study, detailed surface length and relief variations, research during direct and indirect wind speed conversion process to power.

Investigation of wind power prediction processes revealed, that combination of statistical methods - nonlinear regression, model output statistics, the most suitable power curve and wind speed correction methods, wind power prediction errors reduced up to 4.6%. The highest impact for the improved power prediction process accuracy had integrated model output statistics function with decreased error 1.6% and seasonal autoregression integrated moving average function with decreased error 0.86%. Detailed evaluation of relief variations and surface roughness, wind power accuracy increased by 2% with the highest influence of the evaluation of surface roughness length. Considering to the local conditions in the Western part of Lithuania, it was indicated the best suitable tool for midterm wind power prediction is hybrid model which involves the most accurate physical methods, detailed description of topographical conditions and adaptive statistical tools.

Keywords: wind power forecasting, hybrid model, physical approach, statistical methods

CYSENI 2018, May 23-25, Kaunas, Lithuania
ISSN 1822-7554, www.cyseni.com

COMPARISON OF HYDRODYNAMIC LOADING MODELS ON FIXED MONOPILES IN STEEP REGULAR WAVES

A. Mockutė, E. Marino, C. Borri
University of Florence
Via Santa Marta 3, 50129 – Italy
Email: amockute@dicea.unifi.it

C. Lugni
CNR-INSEAN – Maritime Research Institute - National Research Council
Via di Vallerano, 00128 – Italy

ABSTRACT

Wind is becoming an increasingly important player in the energy field, with cost being its main limitation. The most expensive part of offshore wind turbines is the substructure, therefore more efficient wave load modelling would lead to safer and cheaper future designs. The commonly implemented monopiles are placed in shallow to intermediate waters where wave nonlinearities are high, and may prompt dangerous resonant amplifications of the structural response, known as springing and ringing. The use of linear and weakly nonlinear wave kinematics, i.e. Airy or Stokes theories, with the standard Morison equation have been shown to omit the nonlinear amplifications which are associated with third order. Therefore in this study a selection of hydrodynamic loading models is compared on fully nonlinear wave kinematics to assess how to capture the nonlinear phenomenon in the most computationally efficient way. The loading models compared in the study are: the standard Morison equation consisting of linear inertia and quadratic drag; slender-body theory which suggests additional slender-body terms to correct the linear Morison inertia term to third order; and finally the FNV (Faltinsen-Newman-Vinje) perturbation theory which immediately takes third order loading and wave diffraction into account. Comparison to numerous past experiments on a fixed cylinder in regular waves is shown. Discrepancies are seen between the experimental and numerical results, and none of the models are able to capture the nonlinearities which until recently used to be associated with ringing.

Keywords: offshore wind turbines, numerical wave loading modelling, fully nonlinear wave kinematics, comparison of hydrodynamic loading models

1. INTRODUCTION

To meet the increasing energy demand wind energy converters keep growing in size [1], especially offshore, where visual and noise constraints are a smaller issue. Even though offshore structures are normally designed to have natural frequencies much higher than the predominant wave frequencies, the increase in the turbine size leads to reduced structural frequency, which may then match the third or higher wave frequencies, making them prone to the dangerous resonant amplifications, such as springing and ringing, illustrated in Fig. 1 for a tension leg platform [3]. To illustrate the applicability to monopile-supported offshore wind turbines, a typical structural frequency for a monopile-supported offshore wind turbine is around 0.28 Hz [2] and it is around three times 10 s – a common wave period. Even though both of these phenomena are resonant amplifications, springing is more continuous, was associated with second order wave loading components and was successfully recreated numerically with the methods available back in 1990s [3]. Ringing, on the other hand, is much more unsteady, appearing as a sudden strong amplification with slow deterioration. It was associated with third or higher order loading and was not fully understood or numerically captured at the time, therefore experimental investigations were started and are still ongoing [3].

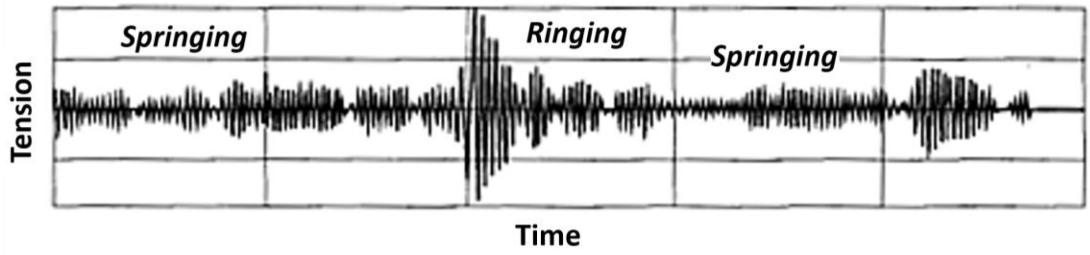

Fig. 1. Illustration of springing and ringing in tension force response. Adapted from [3]

The first experiments on ringing were conducted on fixed vertical cylinders in very steep waves, where strong nonlinearities were observed in the forcing response that were immediately associated with ringing. These nonlinearities appeared as a second peak in loading, around one quarter of the period after the main peak, and were therefore named as the secondary load cycle (*slc*). The physics behind secondary load cycle were long disputed: it was argued whether *slc* is governed by Froude number [4], or wave steepness [5], but neglected flow separation and wave diffraction; there were other claims that viscous environment is predominant ringing [6]; some described *slc* as 'hydraulic jump' without diffraction, and suggested to disassociate it from ringing [7], and others which confirmed the relation between *slc* and ringing but associated ringing with orders higher than third [8–9]. Only recently by a CFD study it has been shown that secondary load cycle is caused by flow separation when two opposing flows – namely the vortex at the back side of the cylinder because of a diffracted wave, and the surrounding flow still ongoing in the wave propagating direction – create a reduction in pressure which is observed as the secondary load cycle [10]. It was also suggested that even though *scl* and ringing are seen to occur in similar wave conditions, the two phenomena are not directly linked, on the grounds that ringing is associated with third order loading components while not even the first seven harmonics managed to recreate the *slc* [10]. The proposition to delink the two occurrences was confirmed by a later experimental study [11], which indicates that even if secondary load cycle is not captured numerically, it does not impose that ringing would be omitted too with the same numerical method.

In the recent literature ringing-like responses have been observed numerically on a monopile-supported offshore wind turbine in severe sea conditions when fully nonlinear wave kinematics were used, but omitted with linear and weakly nonlinear wave kinematics [12–16]. Since the support structure is one of the most expensive parts of an offshore wind turbine, more accurate modelling of wave loading could lead to reduction of the cost of offshore wind energy. Therefore this ongoing study is comparing how three increasingly complex hydrodynamic loading models are recreating the behaviour of slender piles in very steep waves. The three models are: the most widely implemented semi-empirical Morison equation [17], its corrections to third order named 'slender-body theory' [18–19], and FNV perturbation theory [20]; all modelled with fully nonlinear wave kinematics as input and introduced in detail in Section 2.

However, before moving on to the dynamic response of the structure and ringing phenomenon it was necessary to validate the loading models on a fixed cylinder without the interference of the cylinder motion. Moreover, since to the best of the authors' knowledge no successful numerical recreations of secondary load cycle besides the computationally-heavy CFD studies have been seen, it was of interest to see how these three hydrodynamic loading models would behave numerically recreating the experiments on *slc*. Therefore the comparison of the three hydrodynamic loading models on fixed cylinders in steep regular waves the focus of this paper, and comparisons to past experimental data are discussed in Section 3.

Lastly, since this is an ongoing study, Section 4 summarises the conclusions of this phase and introduces the future stages.

2. METHODOLOGY

Fully nonlinear regular wave kinematics for this study were simulated with Higher-Order Boundary Element Method (HOBEM) potential-flow model, introduced in [21–23], which solves the Laplace equation within the domain bounded by quadratic elements for the periodic side and impregnable bottom boundaries, and a free-surface which is stepped in time with fourth order Runge-Kutta method. The solver is initialised and validated by the nonlinear Rienecker-Fenton theory [20], and implements corner continuity [24] and 5-point smoothing [25] to avoid numerical instabilities.

The first hydrodynamic loading model is the most commonly used Morison equation [17], which consists of linear inertia term *M* and quadratic drag *d*, as described in Equation 1. Both terms are integrated from the tank bottom to the instantaneous free surface, as illustrated in Fig. 2. The drag and inertia coefficients C_d and C_m consequently should be determined from past experiments or guidelines, making the model semi-empirical. In this study the drag coefficient was taken from the (C_d,*KC*)-graph in [27], where *KC* is the depth-dependent Keulegan-Carpenter number. The inertia coefficient was chosen to be constant and equal to 2, not only because it is its theoretical potential-flow value, but also for a meaningful comparison with the FNV theory.

$$F_{Mor} = \underbrace{\int_{-h}^{\eta} C_m \rho R^2 \pi \frac{\partial v_x}{\partial t} dz}_{M} + \underbrace{\int_{-h}^{\eta} C_d \rho R \left| v_x \right| v_x dz}_{d} \qquad (1)$$

where: η – instantaneous free surface elevation; R – cylinder radius; ρ – water density; g – gravitational constant; h – water depth; v_x – horizontal water particle velocity.

The second hydrodynamic loading model is slender-body theory by Rainey [18, 19], which separates the Morison inertia term *M* and applies slender-body corrections to it. The corrections, following formulation by [5], are: axial divergence force *A* (Eq. 2), integrated along the length of the pile to the instantaneous free surface; surface intersection force *I* (Eq. 3), point load applied at the intersection with the instantaneous wave elevation, which, together with axial divergence force *A* correct the Morison inertia term *M* to second order; and finally surface distortion force *D*, which corrects the third-order error and is also applied as a point load at the free surface intersection, as illustrated in Fig. 2. The drag component *d* may be applied after the other corrections for comparison, as done in [5], but is not part of the theory.

$$A = \int_{-h}^{\eta} \rho \pi R^2 \frac{\partial v_z}{\partial z} v_x dz \qquad (2)$$

$$I = -\left(\rho \pi R^2 / 2\right) v_x^2 \, \partial \eta / \partial x \qquad (3)$$

$$D = \left(\frac{7 \rho \pi R^2}{2g} \right) v_x^2 \frac{\partial v_x}{\partial t} \qquad (4)$$

where v_z – horizontal water particle velocity.

The third hydrodynamic loading model is a perturbation theory named after its authors Faltinsen, Newman and Vinje – FNV theory. It was originally derived for infinite depth [28], but in this paper the newly generalised finite depth formulation [20] is implemented. As illustrated in Fig. 2, it consists of an integrated term *F'* (Eq. 5) and a point load F^{Ψ} (Eq. 6). The integrated term accounts for the flow nonlinearities on top of the usual inertia values (additional terms on the left hand side of the Equation 5), and also takes diffraction into account (right hand side of Equation 5, where a_{11} is the 2D added mass coefficient). The point load accounts for the additional nonlinear loads due to the piercing of the water surface, and it is applied at the still water lever in accordance with the original FNV theory [28].

$$F' = \int_{-h}^{\eta}\left(\rho\pi R^2\left(\frac{\partial v_x}{\partial t}+v_x\frac{\partial v_x}{\partial x}+v_z\frac{\partial v_x}{\partial z}\right)+a_{11}\left(\frac{\partial v_x}{\partial t}+v_z\frac{\partial v_x}{\partial z}\right)\right)dz \tag{5}$$

$$F^{\psi} = \left(\frac{4\rho\pi R^2}{g}\right)v_x^2\frac{\partial v_x}{\partial t} \tag{6}$$

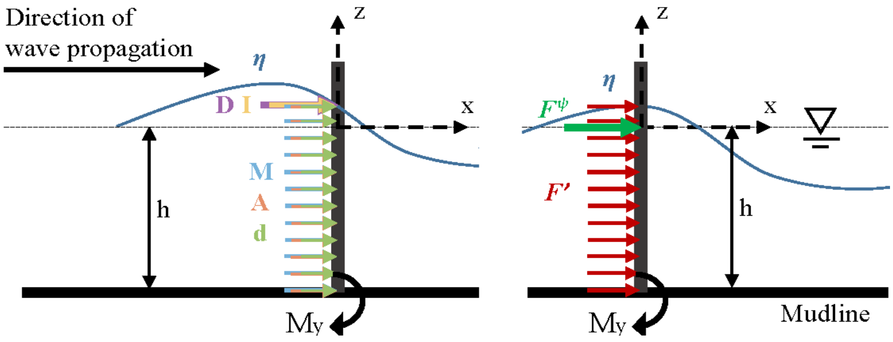

Fig. 2. System coordinates and the forcing components

3. RESULTS

3.1. Comparison with Chaplin et al. (1997)

First of all the experiments by Chaplin et al. (1997) [5] were recreated in order to validate the slender-body theory and to observe the behaviour of the hydrodynamic loading models in case of a clear secondary load cycle.

Fig. 3 shows the base bending moment on a fixed cylinder of 0.1 m diameter in water depth of 0.525 m, subjected to a steep wave of steepness kA = 0.299 over one period of τ = 1.05 s. It must be noted that the experimental values were recorded on a focused wave, which has much harsher kinematics than its equivalent regular wave, therefore the peak of loading should not be matched.

Besides the experimental curve, the original Fig. 6b in Chaplin et al. (1997) [5] shows only *M*, *M*+*A*, *M*+*A*+*I* curves with regular wave kinematics as input, because the *D* term caused a major deviance when the model was used with unsteady wave kinematics, which are more appropriate for the focused wave used in the experiment. Since the three mentioned curves matched their numerical counterparts in [5] well, the slender-body theory is considered validated.

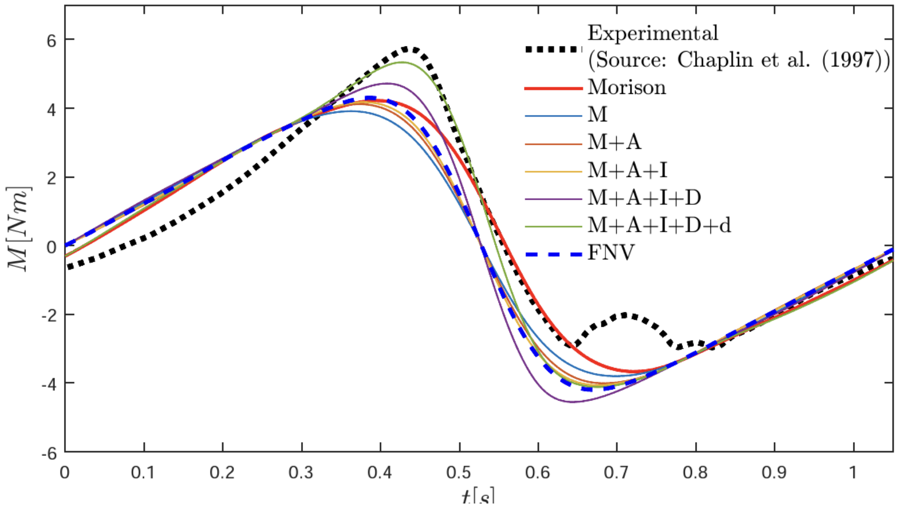

Fig. 3. Comparison of Morison equation [17], slender-body [18-19] and FNV [20] theories with the experimental measurements by Chaplin et al. (1997) on a fixed cylinder in waves with period τ = 1.05 s, steepness kA = 0.299, diameter of 0.1 m, in depth h = 0.525 m

No meaningful discussion of the behaviour of the models in capturing the main trend of loading can be done due to different wave kinematics, but the major discrepancy is seen at time around [0.65–0.85] s, where secondary load cycle is observed experimentally and none of the models manage to capture it numerically. The Morison equation consists of linear inertia and quadratic drag terms, making it of second order, therefore not expected to capture the *slc*. The slender-body theory is valid to third order when all terms are applied, but if the third order term *D* is neglected, as done in [5], because it is derived using the Stokes small amplitude assumption and therefore inappropriate in such high steepness as in this case, then the slender-body theory is also of second order. Nonetheless, since FNV theory is directly taking third order loading components and diffraction into account, it could have been expected to capture the *slc* numerically. Therefore the fact that it does not, implies that secondary load cycle is governed by either three-dimensional effects, which are excluded from this study, or by effects of order higher than third, to which the theory is derived. These findings go in accordance with the literature reviewed in Section 1.

3.2. Comparison with Kristiansen and Faltinsen (2017)

Comparison with the experimental and numerical results of Kristiansen and Faltinsen (2017) [20] allowed for the validation of the finite-depth FNV model and an observation of the change in behaviour as the steepness gradually increases from relatively small ($kA \approx 0.05$), shown in Fig. 4, to intermediate ($kA \approx 0.16$), shown in Fig. 5. Water depth was 0.563 m, while cylinder diameter 0.144 m, period of 2.021 s in all cases.

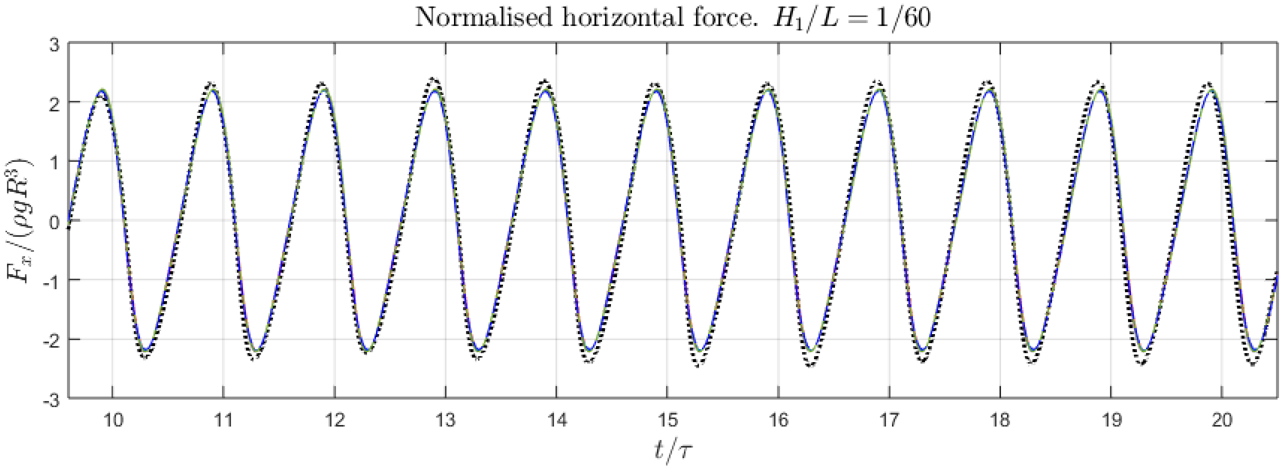

Fig. 4. Comparison of Morison equation [17], slender-body [18-19] and FNV [20] theories with the experimental measurements by Kristiansen and Faltinsen (2017): normalised force on a fixed cylinder of 0.144 m diameter in waves with wavenumber $kR = 0.105$, steepness $H_1/L = 1/60$, in depth $h = 0.563$ m

As it can be seen in Fig. 4, in small wave steepness all models behave nearly identically, recreating the experimental values relatively well, with a slight trend for underprediction. In the higher steepness (Fig. 5), a difference between the models can already be observed at the peaks of the loading with Morison inertia term *M* and the FNV theory being most conservative, while the slender-body corrections (curve *M*+*A*+*I*+*D*) and full Morison equation gave visibly higher predictions. It is difficult to determine a more suitable model since the experimental peaks are unsteady and the lower peaks are matched well by Morison inertia term and FNV theory while the higher peaks – by full Morison equation and slender-body theory. An interesting observation is that the nonlinear terms in the FNV theory corrected it towards reduction of loading, in comparison with the Morison inertia term *M*. The minima of the loading were matched well in general, since the occurrence of secondary load cycle was not observed experimentally; nonetheless, the slender-body corrections caused a weighty deviance in this case.

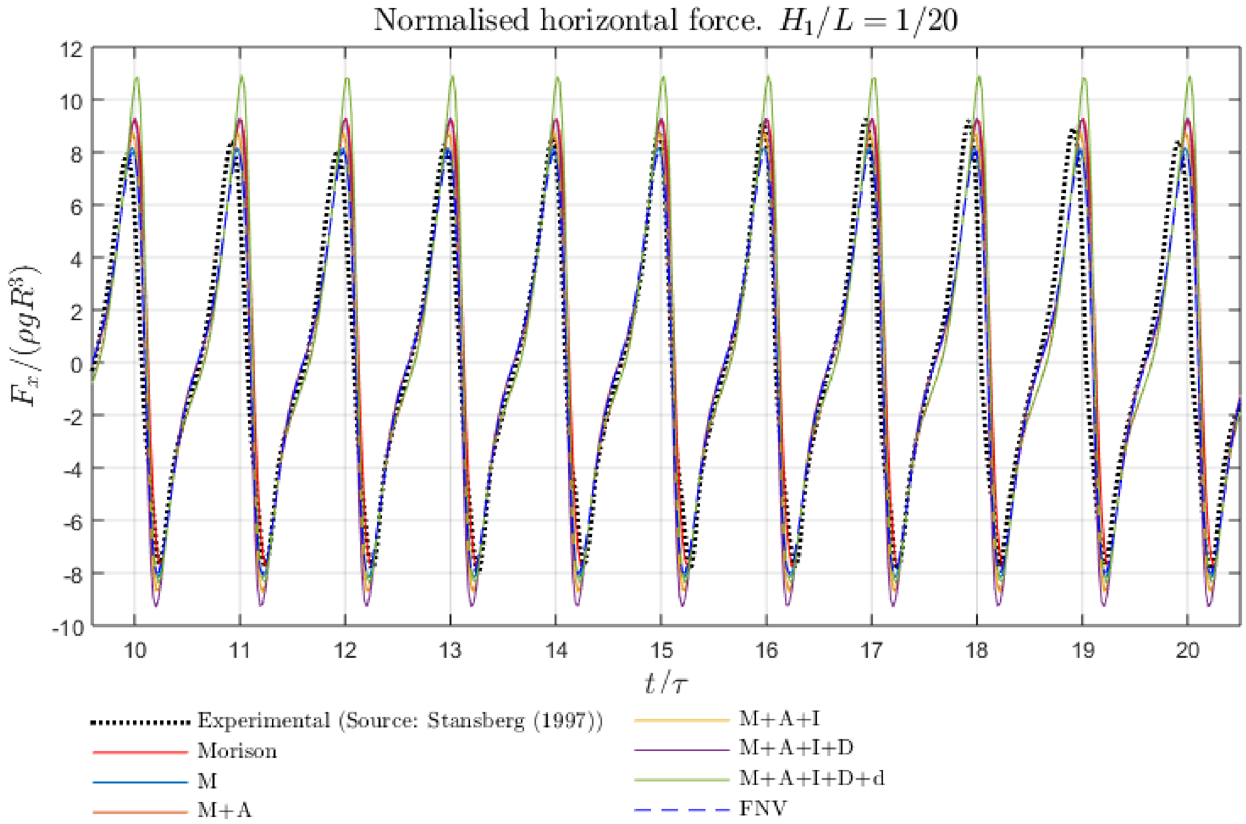

Fig. 5. Comparison of Morison equation [17], slender-body [18-19] and FNV [20] theories with the experimental measurements by Kristiansen and Faltinsen (2017): normalised force on a fixed cylinder of 0.144 m diameter in waves with wavenumber $kR = 0.105$, steepness $H_1/L = 1/20$, in depth $h = 0.563$ m

3.3. Comparison with Stansberg (1997)

Comparison with Stansberg (1997) [29] allows for a clear observation of how the three compared hydrodynamic loading models recreate loading on a fixed cylinder in steep regular waves with the presence of secondary load cycle, as well as the influence of the cylinder size in the same wave conditions. Fig. 6 shows normalised horizontal force on fixed cylinders of 0.1 m radius (top figure) and 0.163 m radius (bottom figure) in wave of steepness $kA = 0.282$, period of 1.52 s, in water depth of 10 m.

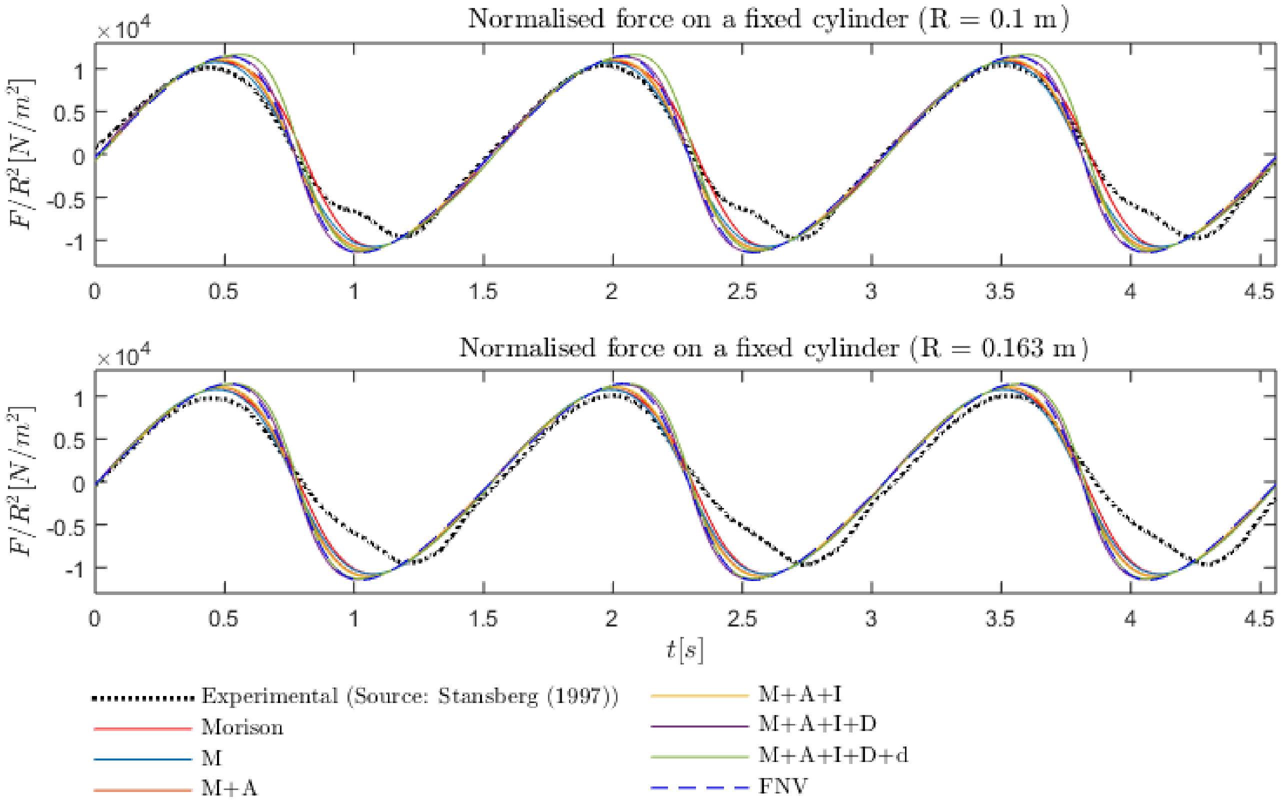

Fig. 6. Comparison of Morison equation [17], slender-body [18-19] and FNV [20] theories with the experimental measurements by Stansberg (1997): normalised force on fixed cylinders of 0.1 m (top) and 0.163 m (bottom) radii in waves with period τ = 1.52 s, steepness kA = 0.282, depth h = 10 m

It can be seen that the main trend of the loading is captured relatively well, with a tendency for overprediction. The instances of secondary load cycle are completely omitted by all models, as already discussed in Subsection 3.1. The influence of the cylinder size is seen from the experimental values as the secondary load cycle in the case of smaller cylinder is more pronounced. A curious reflection from the numerical study is that the tendency for overprediction seems to increase for the larger radius of the cylinder, regardless of the fact that the force series are normalised over the radius squared. Another interesting observation is that in this case the Morison equation is the closest model to the Morison inertia term *M*, while the nonlinear corrections in FNV theory have corrected it towards increase of loading values, making it a close match with the slender-body corrections (*M*+*A*+*I*+*D* purple curve).

3.4. Comparison with Grue and Huseby (2002)

The comparison with experimental values by Grue and Huseby (2002) [8] provides a case with extremely high wave steepness (kA = 0.32). It should be noted that in [8] steepness was defined as $k\eta_{max}$ = 0.34, but for a more meaningful comparison instead of matching the maximum loading the steepness was adjusted to match the mean, which resulted in kA = 0.32. The water depth was 0.6 m, and two periods were analysed of 0.7 s (top figure) and 0.86 s (bottom figure).

In these cases again the secondary load cycle was observed experimentally but omitted numerically, and the experimental peaks were too unsteady to provide a definite comparison but were matched relatively well with a trend of overprediction. The slender-body theory shows the largest values as seen in all previous cases, as well as Morison inertia term giving the lowest values. Nonetheless, FNV theory is much less amplified by the nonlinear corrections than seen in comparison with Stansberg (1997) [29] in Subsection 3.3, and gives values closer to Morison equation. Morison equation again is the closest model to Morison inertia term only, indicating small importance of the drag term. Such inconsistency of the behaviour of the models with increasing steepness indicates that other factors may be of importance, such as the *KC* number, the slenderness to depth ratio of the cylinder and similar.

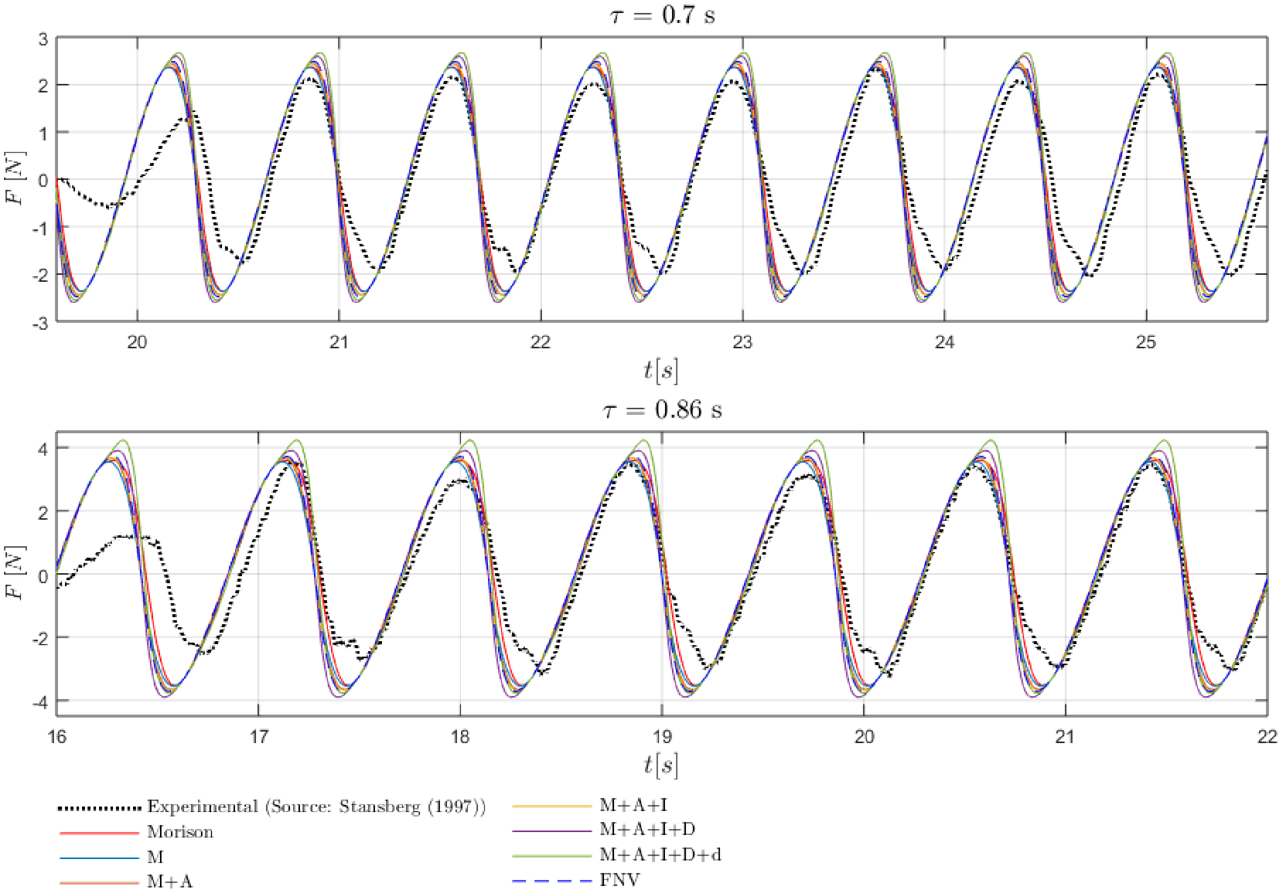

Fig. 7. Comparison of Morison equation [17], slender-body [18-19] and FNV [20] theories with the experimental measurements by Grue and Huseby (2002): horizontal force on a fixed cylinder of 3 cm radius in waves with periods $\tau = 0.7$ s (top) and $\tau = 0.82$ s (bottom), steepness $kA = 0.32$, in depth $h = 0.6$ m

4. CONCLUSIONS

Three hydrodynamic loading models – Morison equation, slender-body theory and FNV theory – were compared against a range of past experimental data on a fixed wave cylinders in a variety of wave conditions. Discrepancies were seen in most cases, and from the current observations it would seem that the slender-body theory was performing worst of the compared models. However, no definite recommendations can be made without further studies. Most pronounced divergences were seen during the presence of secondary load cycle – loading nonlinearities observed experimentally in very steep waves but omitted by all numerical models. Nonetheless, secondary load cycle was recently dissociated from ringing phenomenon, therefore the fact that none of the models managed to capture it does not mean ringing would be omitted too. Therefore the next natural stage of this ongoing research project is to consider the motion of the cylinder, before moving on to irregular waves and full dynamic monopile-supported offshore wind turbine.

REFERENCES

1. GLOBAL WIND ENERGY COUNCIL. *Global wind report: Annual market update 2015*. Brussels: GWEC, 2015. 76 p.
2. JONKMAN, J., BUTTERFIELD, S., MUSIAL, W., SCOTT, G. *Definition of a 5-MW reference wind turbine for offshore system development*, Golden: NREL, 2009.
3. Norwegian Petroleum Directorate, *Annual Report, 1992*. Stavanger: NPD, 1992, pp. 118–119.
4. GRUE J., BJØRSHOL, G., STRAND, Ø. Higher harmonic wave exciting forces on a vertical cylinder. *Institute of Mathematics, University of Oslo Preprint*, No. 2, p. 1–28, 1993.
5. CHAPLIN, J. R. R., RAINEY, R. C. T., YEMM, R. W. Ringing of a vertical cylinder in waves, *J. Fluid Mech.*, 1997, Vol. 350, pp. 119–147.
6. GURLEY, K. R., KAREEM, A. Simulation of ringing in offshore systems under viscous loads. *J. Eng. Mech.*, 1998, p. 582–586.
7. KROKSTAD, J. R., SOLAAS, F. Study of Nonlinear Local Flow. Proceedings of the Tenth International Offshore and Polar Engineering Conference. Seattle: USA. 2000 May 28 – June 2.
8. GRUE J., HUSEBY, M. Higher harmonic wave forces and ringing of vertical cylinders. *Appl. Ocean Res.*, 2002, Vol. 24, No. 4, p. 203–214, 2002.
9. RAINEY, R. C. T. Weak or strong nonlinearity: the vital issue. *Journal of Engineering Mathematics*, 2007, Newman Honorary Volume, p. 1–27.
10. PAULSEN, B. T., BREDMOSE, H., BINGHAM, H. B. An efficient domain decomposition strategy for wave loads on surface piercing circular cylinders. *Coastal Engineering*, 2014, Vol. 86, p. 57–76.
11. SUJA-THAUVIN, L., KROKSTAD, J. R., BACHYNSKI, E. E., DE RIDDER, E.-J. Experimental results of a multimode monopile offshore wind turbine support structure subjected to steep and breaking irregular waves. *Ocean Engineering*, 2017, Vol. 146, pp. 339–351.
12. MARINO, E.; LUGNI, C.; BORRI, C. The role of the nonlinear wave kinematics on the global responses of an OWT in parked and operating conditions. *J. Wind Eng. Ind. Aerodyn.*, 2013, Vol. 123, p. 363–376.
13. MARINO, E.; NGUYEN, H.; LUGNI, C.;; BORRI, C. Irregular Nonlinear Wave Simulation and Associated Loads on Offshore Wind Turbines. *J. Offshore Mech. Arct. Eng.*, 2015, Vol. 137, No. 2, p. 021901.
14. SCHLØER, S., BREDMOSE, H., BINGHAM, H.B. The influence of fully nonlinear wave forces on aero-hydro-elastic calculations of monopile wind turbines. *Marine Structures*, 2016, Vol. 50, pp. 162–188.
15. ROBERTSON, A.; WENDT, F.; JONKMAN, J. et al. OC5 Project Phase Ib: Validation of Hydrodynamic Loading on a Fixed, Flexible Cylinder for Offshore Wind Applications. *Energy Procedia*, 2016, Vol. 94, No. C, p. 82–101.
16. MARINO, E.; GIUSTI, A.; MANUEL, L. Offshore wind turbine fatigue loads: The influence of alternative wave modeling for different turbulent and mean winds. *Renew. Energy*, 2017, Vol. 102, p. 157–169.
17. MORISON, J.R., O’BRIEN, M.P., JOHNSON, J.W., SCHAAF, S.A. The force exerted by surface wave on piles. *Petroleum Transactions*, 1950, Vol. 154, p. 149–189.
18. RAINEY, R.C.T. A new equation for calculating wave loads on offshore structures. *J. Fluid Mech.*, 1989, Vol. 204, p. 295–324.
19. RAINEY, R.C.T. Slender-body expressions for the wave load on offshore structures. *Proceedings: Mathematical and Physical Sciences*, 1995, Vol. 450, No. 1939, p. 391–416.

20. KRISTIANSEN, T., FALTINSEN O. M. Higher harmonic wave loads on a vertical cylinder in finite water depth. *J. Fluid Mech.*, 2017, Vol. 833, p. 773–805.
21. MARINO, E. *An Integrated Nonlinear Wind-Waves Model for Offshore Wind Turbines*, Florence: FUP, Firenze University Press, 2010.
22. MARINO, E.; BORRI, C.; LUGNI, C. Influence of wind-waves energy transfer on the impulsive hydrodynamic loads acting on offshore wind turbines, *J. Wind Eng. Ind. Aerodyn.*, 2011, Vol. 99, p. 767–775.
23. MARINO, E.; BORRI, C.; PEIL, U. A fully nonlinear wave model to account for breaking wave impact loads on offshore wind turbines, *J. Wind Eng. Ind. Aerodyn.*, 2011, Vol. 99, p. 483–490.
24. RIENECKER, M.M., FENTON, J.D. A Fourier approximation method for steady water waves. *Journal of Fluid Mechanics*, 1981, Vol. 104, p. 119–137.
25. GRILLI, S. T., SVENDSEN, I. A. Corner problems and global accuracy in the boundary element solution of nonlinear wave flows. *Engineering Analysis with Boundary Elements*, 1990, Vol. 7, No. 4, p. 178–195.
26. LONGUET-HIGGINS, M. S., COKELET, E. D. The Deformation of Steep Surface Waves on Water. I. A Numerical Method of Computation. *Proceedings of the Royal Society A*, 1976, Vol. 350, p. 1–26.
27. KEULEGAN, G. H., CARPENTER, L. H., Forces on Cylinders and Plates in an Oscillating Fluid. *J. Research of the National Bureau of Standards*, 1958, Vol. 60, No. 5, p. 423–440.
28. FALTINSEN, O.M.; NEWMAN, J.N., and VINJE, T. Nonlinear Wave loads on a slender vertical cylinder. *J. Fluid Mech.*, 1995, Vol. 289, p.179–198.
29. STANSBERG, C. T. Comparing ringing loads from experiments with cylinder of different diameters – an experimental study. *BOSS'97 Behaviour of offshore structures*, 1997, Vol. 2. pp. 95–109.

CYSENI 2018, May 23-25, Kaunas, Lithuania
ISSN 1822-7554, www.cyseni.com

EVALUATION OF THE CALMET MESOSCALE METEOROLOGICAL MODEL AGAINST WIND MEASUREMENTS IN FOUR LANDSCAPE ZONES OF UKRAINE

D. O. Oshurok
Ukrainian Hydrometeorological Institute
37, Nauky Av. Kyiv, 03028 – Ukraine
Email: dimaoshurok@gmail.com

ABSTRACT

Wind is a widely used source of renewable energy. Due to high spatiotemporal variability of wind speed and direction the special methods of wind calculations (interpolation and extrapolation) are necessary for estimation of wind energy capacity of different domains. One of the methods is applying diagnostic meteorological models like CALMET.

This study is devoted to an assessment of the CALMET mesoscale meteorological model, which is a meteorological pre-processor of the CALPUFF dispersion system, in order to define its ability to predict wind field correctly. In the study, four different regions/domains have been considered on the Ukrainian territory. Their spatial scale is approximately 100 km and they differs in relief and landscape type. Calculated wind speed and its U and V components have been compared with measurements obtained at surface and upper air stations during the entire year of 2007. The eight simulations with different values of the main model parameters associated with landscape characteristics and thermal atmospheric stability have been conducted for every domain. The simulations have been assessed on the base of several statistics.

The results of this research have allowed to define sets of the model control parameters that are the most appropriate for each considered Ukrainian region. Overall, wind speed and its components have been predicted more accurately in the domains with relatively flat terrain.

Keywords: wind speed, CALMET model, model evaluation, landscape characteristics

1. INTRODUCTION

Utilization of renewable energy is currently getting more important. According to the worldwide energy policy, the usage of renewable sources (solar, wind, hydropower etc.) is highly preferred in comparison to fossil fuel or nuclear power. Unlike traditional approaches, which lead to atmospheric air pollution, renewable energy is much safer and more environmentally-friendly. Wind power plays an important role among the total production of alternative energy. For instance, 4% of global electricity production (around 16% of renewable energy output) was extracted from wind to the end of 2016 [1].

Wind energy potential is related to wind speed magnitude through the cubic dependence [2]. Therefore, to assess wind energy capacity of different domains more precisely reliable and accurate wind data are necessary. However, wind is extremely variable in time at different scales – from turbulent fluctuations to interannual variability. On the other hand, wind speed and direction also have strong spatial inhomogeneity. The high spatiotemporal wind variability along with rather sparse wind measurement, provided by meteorological/climatological stations, are a big problem in assessment of wind energy capacity of the different domains. To solve it the special methods of wind calculations (interpolation/modelling) are necessary [3–5].

Moreover, wind measurements at surface meteorological stations are usually provided for 10 m height above surface level. However a hub height for a typical wind turbine is larger (up to 100 m) [2, 6]. Data obtained from radiosondes precisely represent wind characteristics in surface or planetary boundary layer just in a small area around radiosonde station site. In order to obtain required information, wind speed is often extrapolated to necessary height using logarithmic or power law equations [2, 4].

Interpolation also should be used in wind resource map development [7]. The other way is wind field calculation by means of numerical weather prediction (NWP) models [8], mass-consistent models [9, 10], microscale wind flow models [3] or coupled mesoscale NWP and diagnostic wind flow models [5, 11–13]. The application of such methods allows to assess wind characteristics more accurately in mountain valleys, on ridges or in coastal areas, but significant computation power is needed in this case. In particular, climatological assessment of wind resources on the territory of Ukraine was conducted by means of some mentioned types of models [14, 15]. Reanalysis datasets like MERRA or ERA-Interim are also used for this purpose [16, 17]. Such data are freely available and cover all parts of the globe. Nevertheless, their spatial resolution both horizontally and vertically is not enough, therefore wind speed extrapolation and interpolation (downscaling) are required. Due to substantial bias between reanalysis data and measurements in areas with complicated orography, some forms of correction would give significant improvement [16].

In this research, CALMET (California Meteorological Model), which is a meteorological preprocessor of the CALPUFF (California Puff) dispersion system [9, 10, 18], is used as a tool for wind calculations. CALMET is mass-consistent non-hydrodynamic mesoscale meteorological model. The preprocessor along with CALPUFF dispersion model have been used in Ukraine to simulate radioactive release after the Chernobyl Nuclear Power Plant accident [19]. However, some matters arise concerning the reliability of obtained estimates of the wind field. It should be noted, that an evaluation of accuracy of wind speed and its direction simulated by CALMET was performed in several studies, for instance in [18]. However, it would be useful to conduct similar research concerning the geographic conditions available in Ukraine.

The purpose of this study is to evaluate the CALMET meteorological model in four landscape zones of Ukraine against wind speed measurements. This verification aims to assess the ability of the model to predict correctly wind speed. Obtained results may provide useful information concerning the selection of optimal model settings at particular landscape conditions.

2. METHODOLOGY

2.1. CALMET model

CALMET is a diagnostic mesoscale meteorological model, which performs spatial interpolation of input meteorological information into a given computational grid. However, orographic impact, surface roughness, type of thermal stability and other factors that cause wind are taken into account in the model. Input information includes geophysical data, required for calculation of roughness parameter, vegetation index and other important surface characteristics, and meteorological data obtained at surface weather and upper air stations. Spatial wind distribution is calculated in three steps [9, 18]:

- *Initial guess wind field.* It is created on the base of extrapolated and interpolated input data. There are several extrapolation options in the model (we used logarithmic equation modified by stability function, which is based on the Monin-Obukhov similarity theory). Interpolation is performed by the inverse distance squared method.
- *Wind field adjustment.* Initial guess field is adjusted for kinematic effects of terrain, slope flows, terrain blocking effects and three dimensional divergence minimization. All effects are described in detail in [9].
- *Objective analysis*. This is the procedure of introducing observational data into the previously calculated wind field.

2.2. Evaluation of the model

2.2.1. Input information

Wind field simulations were carried out at four domains covering territories with different terrain features and land cover peculiarities. These are Kyiv Region (forest landscape and forest steppe), Dnipropetrovsk Region (mainly steppe), Transcarpathian Region (situated mostly in Carpathian Mountains) and Crimean Peninsula (combined landscape conditions of steppe, Crimean Mountains and proximity to the Black Sea and the Sea of Azov). We selected the listed regions in order to compare simulated and observed wind speed in vertical profile, because at least one upper air station must be available. All the following calculations were adjusted to the LCC (Lambert Conformal Conic) geographical map projection.

Terrain elevation was calculated using DEM (Digital Elevation Model) data collected by SRTM30 (Shuttle Radar Topography Mission). Land use/land cover (LULC) data were taken from Global/Eurasia Land Cover Characteristics Data Base. A spatial resolution of both datasets is 1 km [20, 21]. Input meteorological information at surface level included datasets of air temperature, relative humidity, barometric pressure, wind speed and its direction, precipitation and cloud characteristics for the 1-year period with a 3-hour temporal resolution during the entire year of 2007. These datasets were obtained at 73 surface weather stations in Ukraine and were provided by Central Geophysical Observatory. Due to fact that the model time spacing has to be 1 hour, this data was interpolated linearly to achieve 1-hour time resolution. Unfortunately, because of the lack of national radiosonde stations there was no possibility to involve upper air data in simulations. As an alternative approach, ERA-Interim reanalysis datasets of wind components (U, V), air temperature and relative humidity at 16 vertical levels (from 1000 hPa to 500 hPa isobaric level) were used as information required for calculations at upper levels [22]. The analysed reanalysis data have spatial coverage of $0{,}25^{o}\times 0{,}25^{o}$ and temporal resolution of 4 times per day. Modelling domains with surface meteorological and sounding stations are represented in Fig. 1.

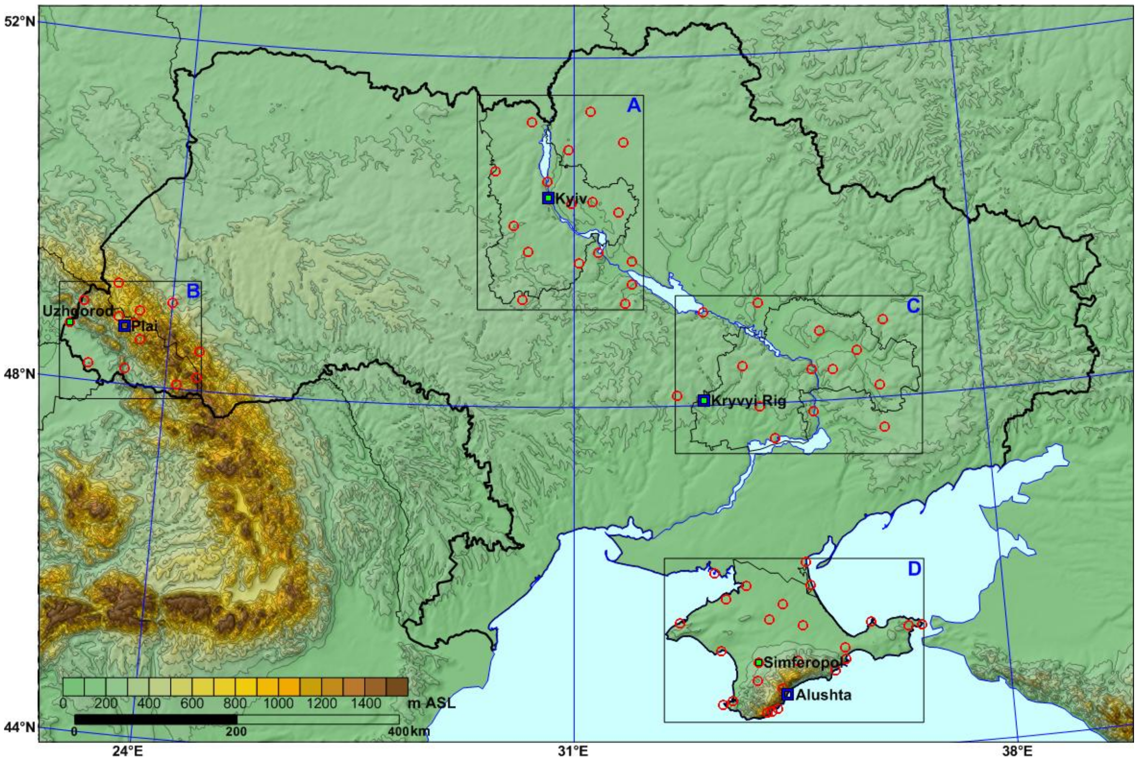

Fig. 1. Modelling domains with the locations of the surface weather stations (○) and the evaluation points – meteorological stations (🟦), upper air stations (🟩): A) Kyiv Region, B) Transcarpathian Region, C) Dnipropetrovsk Region, D) Crimean Peninsula

2.2.2. *Verification process*

Eight simulations (S1-S8) have been performed for the every spatial domain with model grid spacing of 2.5 km for the entire year of 2007. We ran the model with various sets of input parameters (presented in Table 1) in order to evaluate the model behaviour in more detail. Table 2 shows short descriptions of applied CALMET parameters for better understanding what they and their values mean. Mainly, parameter BIAS and orographic effects on the wind flow were specified in a different way.

Table 1. Specification of the CALMET parameters for the simulations S1-S8

Model option		**S1**	**S2**	**S3**	**S4**	**S5**	**S6**	**S7**	**S8**
IKINE		0	0	0	0	0	0	0	0
ISLOPE		1	1	1	1	1	0	0	1
IFRADJ		1	1	1	1	1	1	0	1
IOBR		1	1	1	1	0	0	0	1
IEXTRP		4	4	-4	-4	-4	-4	-4	4
TERRAD		10	10	10	10	10	10	10	10
R1		10	5	10	10	10	10	10	10
R2		10	5	10	10	10	10	10	10
RMAX1		20	30	20	20	20	20	20	20
RMAX2		20	30	20	20	20	20	20	20
BIAS	**Layer 1**	0	0	-1	-1	-1	-1	-1	1
	Layer 2	0	0	-0.9	-0.5	-0.5	-0.5	-0.5	1
	Layer 3	0	0	-0.5	0	0	0	0	1
	Layer 4	0	0	-0.3	0	0	0	0	1
	Layer 5	0	0	0	0	0	0	0	1
	…	…	…	…	…	…	…	…	…

Table 2. Short descriptions of the CALMET control parameters

Parameter	**Description**	**Value**
IKINE	Kinematic effects of terrain	1 – means that initial guess field is modified by the effect. 0 – the effect is not involved into a computational process.
ISLOPE	Slope flows effects	
IFRADJ	Terrain blocking effects	
IOBR	Three dimensional divergence minimization	
IEXTRP	The code of extrapolation scheme used to extrapolate surface wind observations to upper layers	4 – means 'similarity theory is used'. -4 is the same as 4 except layer 1 data at upper air stations are ignored.
TERRAD	Radius of influence of terrain features	In kilometers
R1	Distance from an observational station at which the observation and first guess field are equally weighted in vertical layer 1	
R2	The same as R1 in vertical layers above layer 1	
RMAX1	Maximum radius of influence for meteorological stations in vertical layer 1 over land during construction of final step wind field	
RMAX2	The same as RMAX1 in vertical layers above layer 1	
BIAS	Layer-dependent biases modifying the weights of surface and upper air stations during interpolation process. Defined for every vertical layer	In range from -1 to 1. 0 – means that surface and upper air observations are equally weighted. Negative BIAS reduces the weight of upper air stations, positive BIAS – reduces the weight of surface stations

Computational grid options were set up so that one of the grid points coincided with location of the station, which was chosen for verification. Vertical levels in the model matched to the ones at the considered upper air stations. Based on our targets we used datasets obtained at Kyiv, Plai, Kryvyi Rig and Alushta surface weather stations for the model evaluation at the height of 10 m. Wind speed measurements in four sounding stations in Ukraine served as a basis for the model verification in vertical profile. In particular, this is information obtained at Kyiv, Kryvyi Rig, Uzhgorod and Simferopol for January, April, July and October of 2007. Due to the absence of sounding stations in Ukrainian Carpathian and Crimean Mountains two extra series of simulations were conducted in order to perform an evaluation at the upper layers in Uzhgorod and Simferopol. A verification of wind speed vertical profile was carried out during the four months of 2007 (mentioned above) when upper air data is available for comparison. It should be noted that none of the reference datasets were involved in the computation.

Several statistics were applied for estimating the accuracy of the modelled wind speed and its components separately. Specifically, these are bias (systematic error), mean absolute deviation (MAD), root-mean-square error (RMSE), Pearson correlation coefficient (PCC), factor of 2/5 (FA2/FA5 – the fractional number of cases when the ratio of modelled wind speed to the reference data is between 0.5/0.2 and 2/5) and index of agreement (IA) [18]. The last index is given by:

$$IA = 1 - \frac{\sum_{i=1}^{N} \left(ws_{mi} - ws_{oi} \right)^2}{\sum_{i=1}^{N} \left(\left| ws_{mi} - \overline{ws_o} \right| + \left| ws_{oi} - \overline{ws_o} \right| \right)^2} \tag{1}$$

where ws_{mi} and ws_{oi} are modelled and observed wind speeds, $\overline{ws_o}$ is the mean observed wind speed and N – total number of the reference wind speeds. The IA can vary between 0 and 1, where 1 represents a perfect agreement.

3. RESULTS AND DISCUSSIONS

3.1. Surface layer

On the base of calculated statistics we measured the success of each simulation at the level of 10 m. Besides statistical approach, the obtained time series of simulated U-, V-speeds against observed winds were illustrated. Fig. 2 represents the most accurate ones in July as an example.

Overall we found that the calculated speeds in Plai agreed most closely in simulations S1 and S8. The closest agreement in Kryvyi Rig was obtained within the simulation S2, which is almost the same as S1 and differs by only parameters R1/R2 and RMAX1/RMAX2. In both Kyiv and Alushta modelled wind speeds are best corresponding to the real wind distribution in S5 and S6.

As expected, better results were obtained in relatively flat terrain in comparison to Carpathians and the southern coast of the Crimea. The difference between results on Kyiv and Kryvyi Rig (S5/S6 against S2) might be partially explained by the accuracy of the ERA-Interim reanalysis at different parts of Ukraine or location of the reference station. Wind speed components are strongly underestimated in Plai (as shown in Fig. 2), which is perhaps related to the lack of high-altitude weather stations, because the nearest stations are substantially lower. Obviously, this problem would be resolved better if there were additional points of measurements that represent wind conditions more closely at that region. It was found that the use of ERA-Interim data slightly improved results in Plai. Additional computations applying finer spatial grid (less than 1 km) may give some benefit in accuracy of wind resource modelling, but high-resolution data about landscape characteristics and much more computational power are required in this case. Considerably better results were found in Alushta except PCC, which is worse than in the rest of stations. The noticeable improvement is rather associated with developed surface stations grid in the south of the Crimea. In turn, inclusion of the reanalysis data led to the much worse results. For instance, RMSE varies in range 2.1–2.34 when including just of the surface measurements against 4.23–4.43 in other cases.

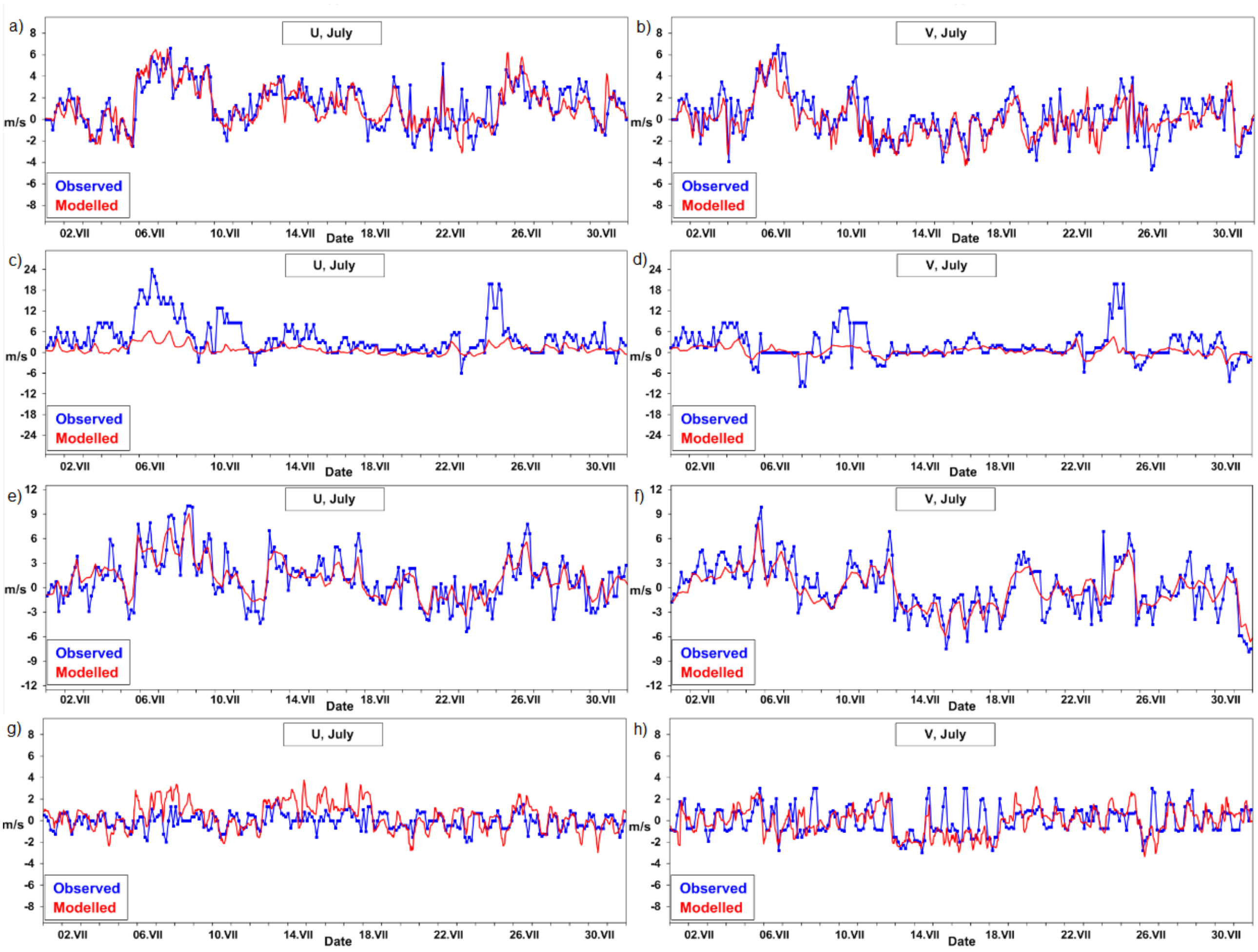

Fig. 2. Time series of the modelled and observed wind speed components (U, V) in July 2007: a, b – in Kyiv (S6); c, d – in Plai (S1); e, f – in Kryvyi Rig (S2); g, h – in Alushta (S6)

Table 3. The evaluation statistics of wind speed at the level of 10 m for the entire of 2007

Station	Error metrics	S1	S2	S3	S4	S5	S6	S7	S8
Kyiv	PCC	0.75	0.76	0.79	0.79	**0.80**	**0.80**	0.79	0.75
	FA2	81	82	81	81	**81**	**81**	81	80
	FA5	93	93	92	92	**92**	**92**	92	93
	RMSE	1.92	1.87	1.46	1.47	**1.46**	**1.46**	1.46	1.97
	IA	0.82	0.83	0.89	0.89	**0.89**	**0.89**	0.89	0.81
Kryvyi Rig	PCC	0.80	**0.80**	0.83	0.83	0.83	0.83	0.83	0.79
	FA2	82	**82**	59	60	62	62	62	82
	FA5	91	**91**	86	86	86	86	86	91
	RMSE	2.26	**2.24**	2.32	2.31	2.29	2.29	2.28	2.28
	IA	0.85	**0.85**	0.80	0.80	0.80	0.80	0.80	0.85
Plai	PCC	**0.60**	0.59	0.46	0.46	0.43	0.43	0.43	**0.59**
	FA2	**28**	28	12	12	18	18	19	**30**
	FA5	**73**	70	39	39	48	49	49	**74**
	RMSE	**6.42**	6.46	7.22	7.22	7.12	7.12	7.12	**6.39**
	IA	**0.49**	0.49	0.46	0.46	0.47	0.47	0.47	**0.49**
Alushta	PCC	0.33	0.33	0.43	0.43	0.45	**0.45**	0.44	0.32
	FA2	32	32	62	62	67	**67**	67	29
	FA5	81	81	93	93	94	**94**	94	80
	RMSE	4.25	4.23	2.34	2.34	2.11	**2.10**	2.17	4.43
	IA	0.34	0.34	0.61	0.61	0.62	**0.63**	0.61	0.32

Overall, the obtained estimates are acceptable at all reference stations except Plai. Index of agreement of the best simulated wind speeds during the entire year is equal to 0.89 in Kyiv, 0.85 in Kryvyi Rig, 0.63 in Alushta and 0.49 in Plai. Root-mean-square error equals to 1.46, 2.24, 2.1 and 6.39 respectively, that also supports our findings. The main statistical parameters are shown in more detail in Table 3.

3.2. Upper layers

The results of the wind speed verification in vertical profile allowed to define the model efficiency at different heights. Because only the lowest layers in atmosphere (up to several hundreds meters) are valuable for the wind energy, we focused on the evaluation of the first three layers. The results of wind speed evaluation in vertical profile are presented in Table 4. According to the obtained IA values we found that simulations S5-S7 were more accurate in comparison to another ones in Kyiv. Similarly, there are S4 in Uzhgorod, S8 in Kryvyi Rig and S1, S2, S8 in Alushta. However, the differences between simulations in all complex of the evaluated error metrics are less noticeable.

Some discrepancies also exist between assessed points. In particular, IA increases steadily in Kyiv and Alushta (from 0.73–0.83 to 0.88–0.91 and from 0.51–0.71 to 0.88–0.9 respectively), while in Kryvyi Rig it rises just at the second level. Another results were given in Uzhgorod, where it is higher only at the third level. RMSE indicates larger deviations on the layers aloft, except Kyiv where it remains almost the same on the two first layers (probably through the small difference in height). Due to the variety of levels at which wind characteristics are measured in considered sounding stations, we had no ability to evaluate model on the common layers. However, we were able to track a general trend of the main statistical parameters with increasing of height. Overall IA and PCC are increasing on the lowest layers, RMSE is also growing. For example, in Kyiv they increase by 0.05–0.18, 0.1–0.12 and 0.48–1.24 respectively. The causes of such trend might be associated with the increase of average wind speed with height. It should be noted that vertical profiles in Kyiv and Simferopol were modelled more precisely in comparison to those obtained in Uzhgorod and Kryvyi Rig, where IA is below at all the considered levels. It might be partially explained by the different quality of the reference data.

Table 4. Index of agreement of the modelled and observed wind speeds on the first three vertical layers (L1-L3) based on four months of 2007

Station	Vertical layer	S1	S2	S3	S4	S5	S6	S7	S8
Kyiv	L1	0.74	0.75	0.83	0.83	**0.83**	**0.83**	**0.83**	0.73
	L2	0.85	0.85	0.86	0.86	**0.86**	**0.86**	**0.86**	0.85
	L3	0.90	0.90	0.88	0.88	**0.90**	**0.90**	**0.90**	0.91
Uzhgorod	L1	0.59	0.58	0.66	**0.66**	0.66	0.67	0.69	0.58
	L2	0.58	0.59	0.57	**0.59**	0.56	0.56	0.57	0.60
	L3	0.70	0.71	0.69	**0.71**	0.70	0.70	0.70	0.72
Kryvyi Rig	L1	0.49	0.49	0.42	0.42	0.43	0.43	0.43	**0.50**
	L2	0.69	0.69	0.66	0.69	0.69	0.69	0.69	**0.70**
	L3	0.68	0.68	0.66	0.68	0.68	0.68	0.68	**0.69**
Simferopol	L1	**0.71**	**0.71**	0.51	0.51	0.55	0.55	0.55	**0.71**
	L2	**0.87**	**0.87**	0.86	0.87	0.87	0.87	0.87	**0.87**
	L3	**0.89**	**0.89**	0.88	0.89	0.90	0.90	0.90	**0.89**

4. CONCLUSIONS

The accuracy of each of the eight simulations was assessed in four domains that are characterized by different landscape conditions. The obtained statistics allowed to reveal the closest simulations with respect to the wind measurements in surface weather stations at the level of 10 m. These results also allowed us to identify the appropriate set of model parameters and weighting of input meteorological data for every domain. It was found that the use of only the surface observations in computation leads to better results in Kyiv and Alushta (S6), while applying both equally weighted surface and upper air data is more justified in Kryvyi Rig (S2) and Plai (S1) or even only ERA-Interim data (Plai, S8). The reasons might be the lack of high-altitude surface stations in Ukrainian Carpathian and significant bias of ERA-Interim wind over the different part of Ukraine, especially in mountains. As a proof, the accuracy of results in the southern coast of Crimea, where surface stations grid is developed, is substantially higher when using only the surface observations. The obtained estimates are acceptable at all reference stations except Plai. Index of agreement and root-mean-square error of the best simulated wind speeds during the entire year equal to 0.89 and 1.46 in Kyiv, 0.85 and 2.24 in Kryvyi Rig, 0.63 and 2.1 in Alushta, 0.49 and 6.39 in Plai.

Wind speed verification in vertical profile is characterized by the small diversity of obtained errors, however, we defined a general trend of the main error measures in vertical direction. Index of agreement and Pearson correlation coefficient are growing on the lowest layers, while root-mean-square error is also increasing with height. It was found that more precise vertical profiles were obtained in Kyiv and Simferopol, where index of agreement is higher on the first three vertical layers.

Overall CALMET demonstrates a good accuracy in regions with relatively flat terrain. However, the model efficiency depends a lot on the density of observation grid, which is crucial in conditions of complicated terrain. Nevertheless, we determined the most suitable sets of the model parameters for wind speed simulations in considered regions of Ukraine. Obtained findings may give some benefits for further research on wind energy assessment in small-scale areas.

ACKNOWLEDGMENTS

The author would like to thank the reviewers for valuable comments and suggestions.

REFERENCES

1. REN21. Renewables 2017 global status report [referred on the 12th of February in 2018 y.]. Link to the internet: <http://www.ren21.net/gsr-2017>.
2. D.J. DE RENZO. *Wind power: recent developments. Front Cover D.J. De Renzo.* William Andrew, Inc., 1979. 347 p.
3. TROEN, I., LUNDTANG PETERSEN, E. *European Wind Atlas.* Roskilde: Risø National Laboratory, 1989. 656 p.
4. HOLT, E., WANG, J. Trends in Wind Speed at Wind Turbine Height of 80 m over the Contiguous United States Using the North American Regional Reanalysis (NARR). *Journal of applied meteorology and climatology*, 2012, Vol. 51, p. 2188–2202.
5. NAWRI, N., PETERSEN, G. N., BJORNSSON, H. etc. The wind energy potential of Iceland. *Renewable Energy*, 2014, Vol. 69, p. 290–299.
6. DRECHSEL, S., MAYR, G.J., MESSNER, J.W., R. STAUFFER. Wind Speeds at Heights Crucial for Wind Energy: Measurements and Verification of Forecasts. *Journal of Applied Meteorology and Climatology*, 2012, Vol. 51, p. 1602–1617.
7. *Атлас енергетичного потенціалу відновлюваних та нетрадиційних джерел енергії України.* К., 2001. 41 с.
8. JAMES, E.P., BENJAMIN, S.G., MARQUIS, M. A unified high-resolution wind and solar dataset from a rapidly updating numerical weather prediction model. *Renewable Energy*, 2017, Vol. 102, p. 390–405.

9. SCIRE, J.S., ROBE F.R., FERNAU M.E., YAMARTINO M. E. *A User`s Guide for the CALMET Meteorological Model (Version 5).* Earth Tech, Inc., 2000.
10. DI BERNARDINO, A., DE SERIO, F., MOSSA, M. Micrometeorological simulations over a coastal area using CALMET model. In book: 2016 IEEE Workshop on Environmental, Energy, and Structural Monitoring Systems Proceedings. 2016. p. 180–185.
11. BEAUCAGE, P., BROWER, M.C., TENSEN, J. Evaluation of four numerical wind flow models for wind resource mapping. *Wind Energy*, 2014, Vol. 17, p. 197–208.
12. Global Wind Atlas [referred on the 12th of February in 2018 y.]. Link to the internet: <https://globalwindatlas.info>.
13. GIOLI, B., GUALTIERI, G., BUSILLO, C. etc. Aircraft wind measurements to assess a coupled WRF-CALMET mesoscale system. *Meteorological Applications*, 2014, Vol. 21, p. 117–128.
14. ЕФИМОВ, В.В., БАРАБАНОВ, В.С., ШОКУРОВ, М.В. та ін. Численное моделирование ветрового энергопотенциала Украины. *Відновлювана енергетика,* 2010, № 1, С. 44–50.
15. ОСАДЧИЙ, В.І., СКРИНИК, О.Я., ОШУРОК, Д.О., СКРИНИК, О.А. Вітрові ресурси Тернопільської області. *Геоінформатика*, 2017, № 4, С. 50–61.
16. STAFFEL, I., PFENNINGER, S. Using bias-corrected reanalysis to simulate current and future wind power output. *Energy*, 2016, Vol. 114, p. 1224–1239.
17. ONEA, F., RUSU, E. Wind energy assessments along the Black Sea basin. *Meteorological Applications*, 2014, Vol. 21, p. 316–329.
18. WANG, W., SHAW, W.J., SEIPLE, T.E. etc. An Evaluation of a Diagnostic Wind Model (CALMET). *Journal of Applied Meteorology and Climatology*, 2008, Vol. 47, p. 1739–1756.
19. GIAIOTTI, D., OSHUROK, D., SKRYNYK, O. The Chernobyl nuclear accident Cs-137 cumulative depositions simulated by means of the CALMET/CALPUFF modelling system. *Atmospheric Pollution Research*, 2018, Vol. 9, p. 502–512.
20. Shuttle Radar Topography Mission (SRTM) [referred on the 5th of September in 2017 y.]. Link to the internet: <http://dds.cr.usgs.gov/srtm/version2_1/SRTM30>.
21. Link to the internet: <http://edc2.usgs.gov/glcc/tablambert_euras_eur.php> [referred on the 1th of September in 2015 y.].
22. ERA Interim, Daily [referred on the 5th of September in 2017 y.]. Link to the internet: <http://apps.ecmwf.int/datasets/data/interim-full-daily/levtype=sfc>.

CYSENI 2018, May 23-25, Kaunas, Lithuania
ISSN 1822-7554, www.cyseni.com

FEASIBILITY ANALYSIS OF AN OFF-GRID PV/WIND/DIESEL GENERATOR HYBRID ENERGY SYSTEM: A CASE STUDY OF BANGLADESH

Tausif Ali, Ma Hongzhong
College of Energy and Electrical Engineering, Hohai University
Nanjing 211100 – China
Email: tausif.ali@hhu.edu.cn

ABSTRACT

In Bangladesh, wind or solar energy based energy systems extensively studied and already under operation in several remote coastal areas of the country. But hybrid renewable energy, especially off-grid PV/Wind/Diesel Generator hybrid energy system has got less attention in the country. This hybrid system is a feasible option for the rural and coastal remote areas where the grid extension is complicated and not economical. In this study, a coastal city of Bangladesh, Patenga has been taken to conduct the case study. The place considered has the community that consists of small and medium houses. The study covered technical and economic analysis of the hybrid energy generation system. To do the design and analysis HOMER (Hybrid Optimization Model for Multiple Energy Resources) has been used. The hybrid system designed with photovoltaics (PV), wind turbine and a diesel generator. After the simulation of the system, the results indicate that the combination of PV/Wind/Diesel Generator is the most feasible option. Results show that for a 15 kWh/day primary load with 1.1 kW peak load the levelized cost of energy (LCOE) for the hybrid system is 0.2 $/kWh and the wasted surplus energy is 18.2%. The study also shows that the diesel generator is an economically competitive option due to the cost of fuel.

Keywords: HOMER; Solar PV; Wind Turbine; Diesel Generator, Load, Off-Grid Hybrid Energy System; Optimization

1. INTRODUCTION

The shortage of fossil fuel in worldwide and also in Bangladesh create the need for the final transition to alternative sources become highly imperative [1]. The calculation shows that 90% of the primary energy consumption will supplly fossil fuel until 2020 and recently, fossil fuel supplies 85.77% of the primary energy consumption of the world and 55% of this amount is used in the transportation sector [2, 3]. At present renewable energy, the share is 17% of the world's energy supply, and this share estimated to increase by 60% within 2070 [4]. In Bangladesh, renewable sources share very little in the total electricity generation. Only 423 MW out of a total 12,261 MW comes from the renewable sources [5]. Except for hydroelectric and solar energy, electricity generation from other renewable sources still negligible [6]. In Bangladesh, the main source of electricity is natural gas. According to the Bangladesh Power Development Board (As on December, 2017) present installed generation capacity including captive power is 13,846 + 2,200 = 16,046 MW, where 62.54% installed capacity based on Natural Gas, 20.87% based on Furnace Oil, 6.36% Diesel, 1.66% Hydro, 1.81% Coal, 4.77% imported power and 0.02% is renewable energy [7]. The observation indicates that Bangladesh power sector still heavily depends on natural gas and negligible amount of renewable energy contributes in total generation system. Therefore, there is no option rather than to increase the electricity generation from renewable sources. Bangladesh Government is giving a strong effort to boost the renewable electrical energy production. Government of Bangladesh has set a target for development of 1211 MW of solar power plants till 2021 with support from development partners and by facilitating private investments. The government has also established Sustainable and Renewable Energy Development Authority (SREDA) to promote renewable energy and energy efficiency. To strengthen international cooperation, Bangladesh became one of the initial members of the International Renewable Energy Agency (IRENA), the only inter-governmental agency working exclusively on renewable energy [8].

Today, near about 18 million people are getting solar electricity, which is around 11% of the total population of Bangladesh [9]. The Infrastructure Development Company Limited (IDCOL) has approved 16 Solar Mini-Grid Projects, among which 7 are operational while the rest are under construction and the company has additional targets to install 50 solar mini-grids by 2018, approved 459 solar irrigation pumps of which 324 are already in operation [10]. According to IDCOL, the mini-grid project has successfully created access to low-emission electricity for almost 5000 rural households in Bangladesh. Bangladesh Power Development Board (BPDB) has installed 900 kW capacity grid connected Wind Plant at Muhuri Dam area of Sonagazi in Feni. Another project of 1000 kW Wind Battery Hybrid Power Plant at Kutubdia Island completed in 2008 which consists of 50 Wind Turbines of 20 kW capacities each. BPDB has plans to set up 7.5 MW off Grid Wind-Solar Hybrid System with HFO/Diesel Based Engine Driven Generator in Hatiya Island, Noakhali. Apart from that, IDCOL has financed 9 biogas based power plants, having a total capacity of 618 kW and two rice-husk based power plants having a total capacity of 650 kW in the country.

Table 1. Installed Sustainable Energy Technologies in Bangladesh

Technology	Off-Grid (MW)	On-Grid (MW)	Total (MW)
Biogas to electricity	5	-	5
Biomass to electricity	1	-	1
Hydro	-	230	230
Solar PV	184	1	185
Wind	1	0.9	1.9
Total	191	232	423

Table 2. Wind turbine installations by the government and non-government organisations

Organization	Location	Type	Installed Capacity (kW)
Grameen Shakti	Grameen offices in the coastal region	3 Hybrid	4.5
	Cyclone shelter in the coastal region	Hybrid	7.5
BRAC	Coastal region	Stand-alone	0.9
		Hybrid	4.32
Bangladesh Army	Chittagong hill tracts	Stand-alone	0.4
IFRD	Teknaf	Stand-alone	1.1
	Meghnaghat		0.6
LGED	Kuakata	Wind-PV hybrid	0.4
Total			19.72

Table 3. Sustainable Energy Target in Bangladesh (MW)

Technology	2015	2016	2017	2018	2019	2020	2021	Total
Solar	222	253	421.75	237	195	203	208	1739.8
Wind	0	20	250	350	350	200	200	1370
Biomass	1	16	6	6	6	6	6	47
Biogas	1	1	1	1	1	1	1	7
Hydro	-	2	2	-	-	-	-	4
Total	224	292	680.75	594	552	410	415	3167.8

From Table 1 [5] and Table 2 [11] it is understood that in term of number and installed capacity of the off-grid hybrid energy system, particularly the combination of wind and solar is significantly low. It is also clearly understood from Table 3 [5] that the renewable energy production target set by the Bangladesh government is bit ambitious and yet not been full filled. The forecasts from International Energy Agency (IEA) showed that about 60% of the additional electricity generation requested to provide universal access to energy, is expected to be generated through off-grid systems. It also indicates that off-grid system essentially required for rural electrification [12]. It is estimated that currently 10% of the rural areas in Bangladesh has electricity connection and some parts of the country may not get the access of electricity from the national grid within the next 30 years [13]. Providing energy to remote areas/islands in a sustainable way is a fundamental requirement nowadays due to depletion of fossil fuel reserve, fuel cost escalation associated with conventional energy generation, population growth, and insufficient waste disposal facilities and that's why off-grid hybrid energy system has become a popular choice for supplying electricity in rural and remote areas in Bangladesh[14]. But few studies have been conducted about the feasibility of off/on-grid hybrid energy system in the country [15–19].

The objective of this paper is to study the feasibility, mainly technical and economical analysis of an off-grid hybrid energy system in a coastal area of Bangladesh. Journal articles, conference proceedings, web materials and government and non-government reports used as data collection sources.

2. METHODOLOGY

An optimal and suitable design of an off-grid renewable hybrid system proposed for Patenga (A coastal area of Chittagong, Bangladesh) which is possible to implement to other coastal and also some remote rural areas of the country. Firstly, solar, wind and diesel based optimized energy system is designed. Then, energy resources of solar and wind are analyzed. The simulation software HOMER [20] used in this study for the optimal planning of sizing of different components of the hybrid system. HOMER performs the energy balance calculations by considering each system configuration. The system cost calculations are analysed, which account costs such as capital, replacement, operation and maintenance, fuel, and interest. This economic analysis is carried out to determine the feasibility of the proposed system.

2.1. Solar and wind resource data

Patenga located at 22 degrees 14.73 minutes North latitude and 91 degrees 47.24 minutes East longitude. In this study secondary data has been used for both wind speed and solar radiation data. HOMER synthesises solar radiation values for each of the 8760 hours of the year. The solar intensity of Patenga varies throughout the year from 4kWh/m^2/d to 5.5kWh/m^2/d with a mean intensity of 4.55 kWh/m^2/d and clearness index 0.455 (Fig. 1). The wind speed data at Patenga recorded at 25 m height. The wind speed varies from 3.25 m/s to 5.8 m/s throughout the year with a mean speed of 3.85 m/s (Fig. 2).

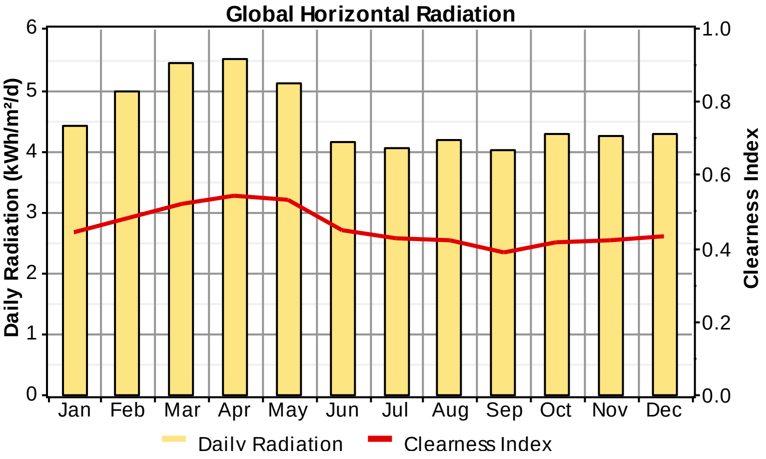

Fig. 1. Solar radiation and clearness index

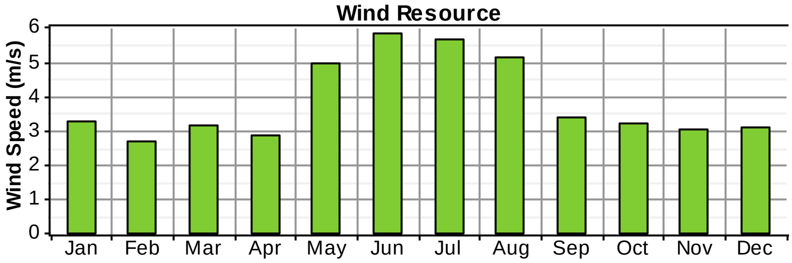

Fig. 2. Monthly average wind speed data

2.2. Hybrid renewable energy system components

The field of engineering concerned with the coupling of PV-Wind systems has just begun recently, and it's a new conception. Solar and wind energy recourses utilised in this study. The hybrid generation system consists of an electrical load, renewable energy sources and other system components such as PV, wind turbines, diesel generator, battery, and converter.

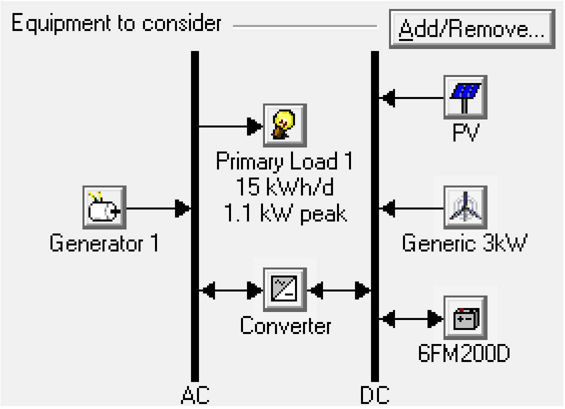

Fig. 3. Proposed hybrid system

2.2.1. *Solar Photovoltaic (PV)*

The PV system considered here is a 2 kW array, and initially it costs around $457 [21]. The replacement cost considered same as the capital cost which has a lifetime of about 20 years and a derating factor of 90%.

2.2.2. *Wind Turbine*

The turbine considered here is a Generic 3 kW turbine. Its lifetime is about 20 years, and the hub height found to be 15 m. The initial capital and replacement cost considered $1500 [22].

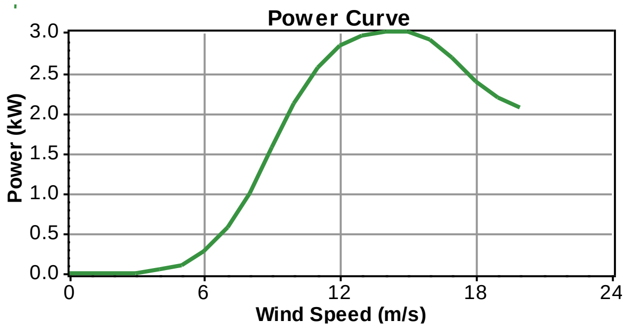

Fig. 4. The power curve of the wind turbine

2.2.3. Diesel Generator

In this study, a 2 kW diesel generator is used. The capital and replacement cost of the diesel generator considered $400 [23] and the fuel price considered $0.78/L [24].

2.2.4. Battery

In the off-grid hybrid energy system battery is required to supply electricity during the night, when there is no sunlight or at times of below sufficient wind speed. The battery considered is 6FM200D. The nominal voltage rating of the battery is 12V and nominal capacity is 2.4 kWh. The round trip efficiency of the battery is 80%.The initial capital cost and replacement cost cosiderd $365 [25] and a lifespan of 4 years.

2.2.5. Converter

A single-phase inverter with a size of 2 kW considered which has a lifetime of 15 years and an efficiency of 85%. It can also operate simultaneously with an AC generator. The initial capital cost and replacement cost considerd around $200 [26].

3. RESULTS

3.1. Technical Analysis

The PV array provided 2,536 kWh/year (35%). The mean output power from the PV was 0.29 kW, and the maximum output was 28.99 kW. The PV penetration was 46% and total hour of operation was 4,380 hr/year. The Levelized Cost of Energy (LCOE) from PV found 0.0342 $/kWh.

The wind turbine provided 1,154 kWh/year (16%). The mean output power from wind turbine was 0.13 kW, and the maximum output power was 2.98 kW. The wind penetration was 21.1% and total hour of operation was 2,921 hr/year. The Levelized Cost of Energy (LCOE) from wind found 0.143 $/kWh.

The generator provided 3,472 kWh/year (48%). The mean output from the generator was 0.567 kW. The maximum and minimum output was 1 kW and 0.3 kW respectively. The mean electrical efficiency of the generator was 27%. The fixed generation cost found 0.06 $/hr and the marginal generation cost found 0.17 $/ kWh. The capacity factor found 40%.

The total AC primary load was 5,475 kWh/year. Excess electricity 1304 kWh/year (18.2%) produced per year.

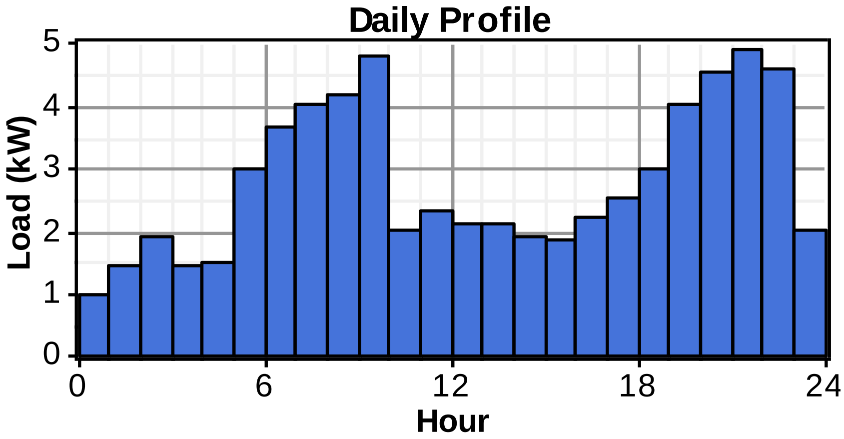

Fig. 5. Load Profile

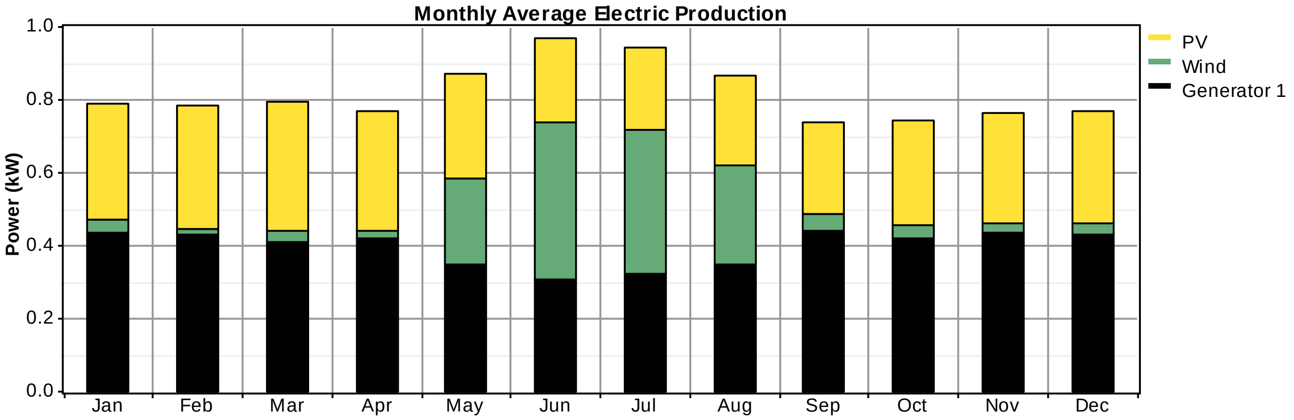

Fig. 6. Monthly average electricity production

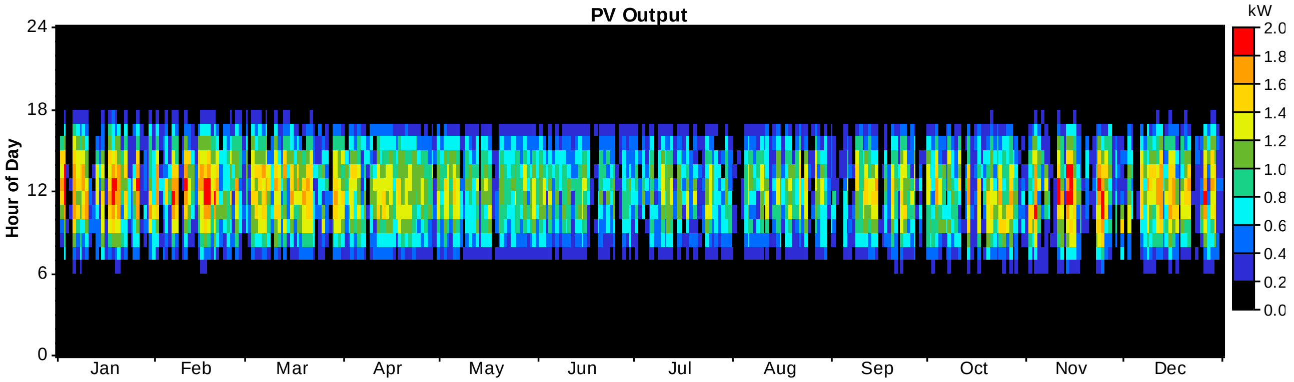

Fig. 7. Power output from PV

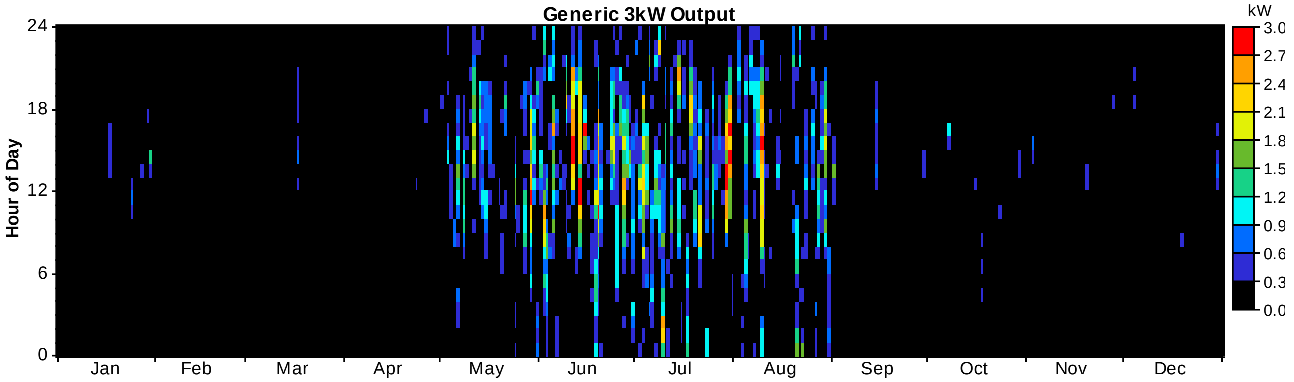

Fig. 8. Power output from the wind turbine (Generic 3 kW)

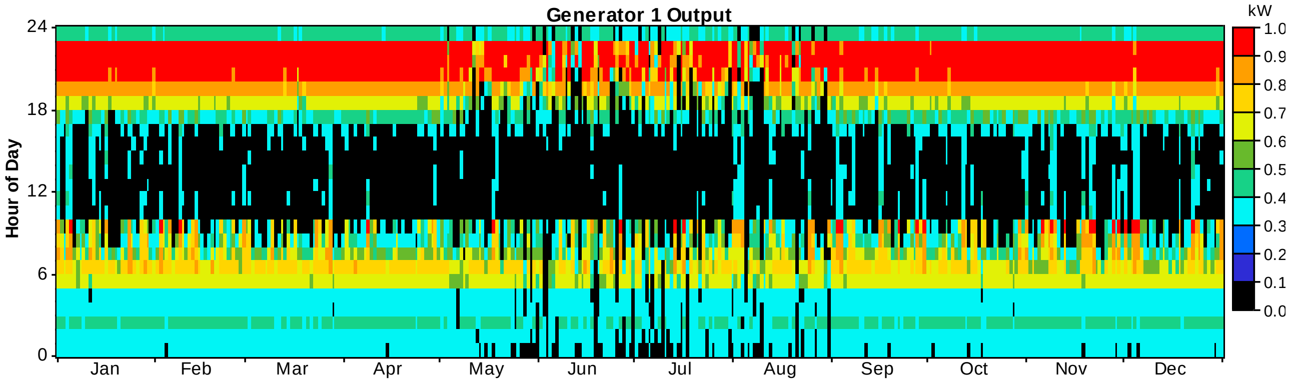

Fig. 9. Power output from the diesel generator

3.2. Economic Analysis

After the simulation, the initial capital cost found $4,266. The operation and maintenance (O & M) cost was $788, replacement cost was $2183, and the fuel cost was $10,699 (Fig. 10). The simulation also showed that wind turbine and the battery had the highest initial capital cost. After that, generator, PV and converter (Fig. 11). From the nominal cash flow diagram, it found that the battery needs to replace 2 times, converter needs to replace 1 time and the wind turbine, and PV array needs to replace 1 time (Fig. 12) over the 30 years. Finally, total NPC found $17,777 and Levelized Cost of Energy (LCOE) found 0.2$/kWh.

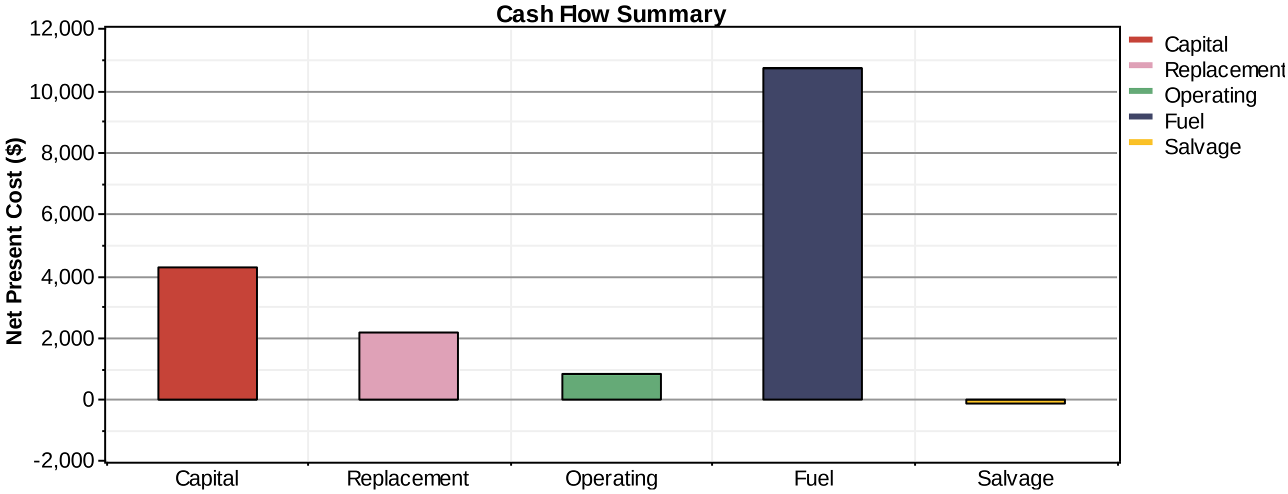

Fig. 10. Cost summary (By cost type)

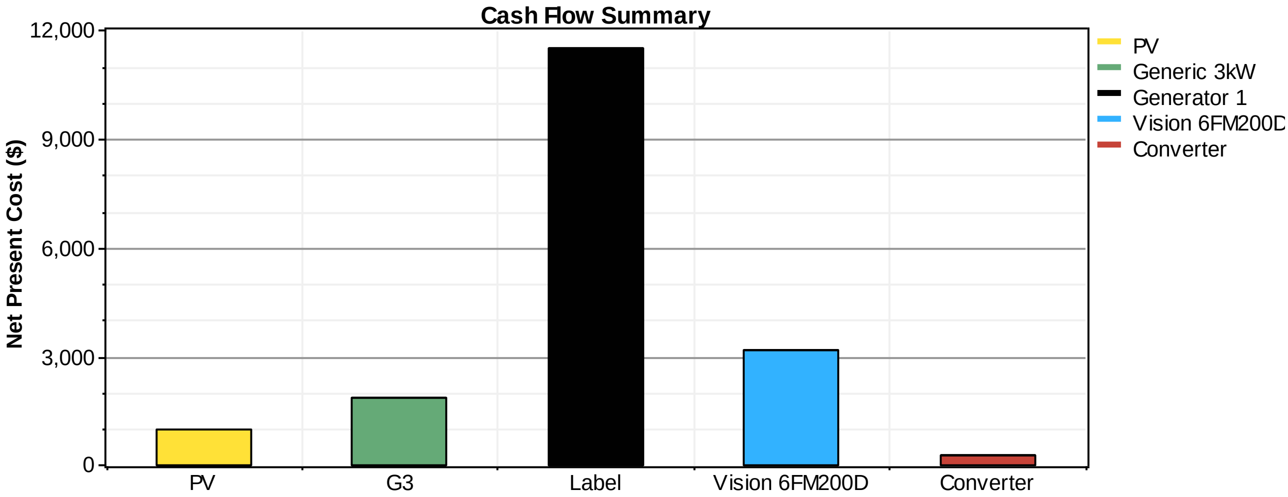

Fig. 11. Cost summary (By components)

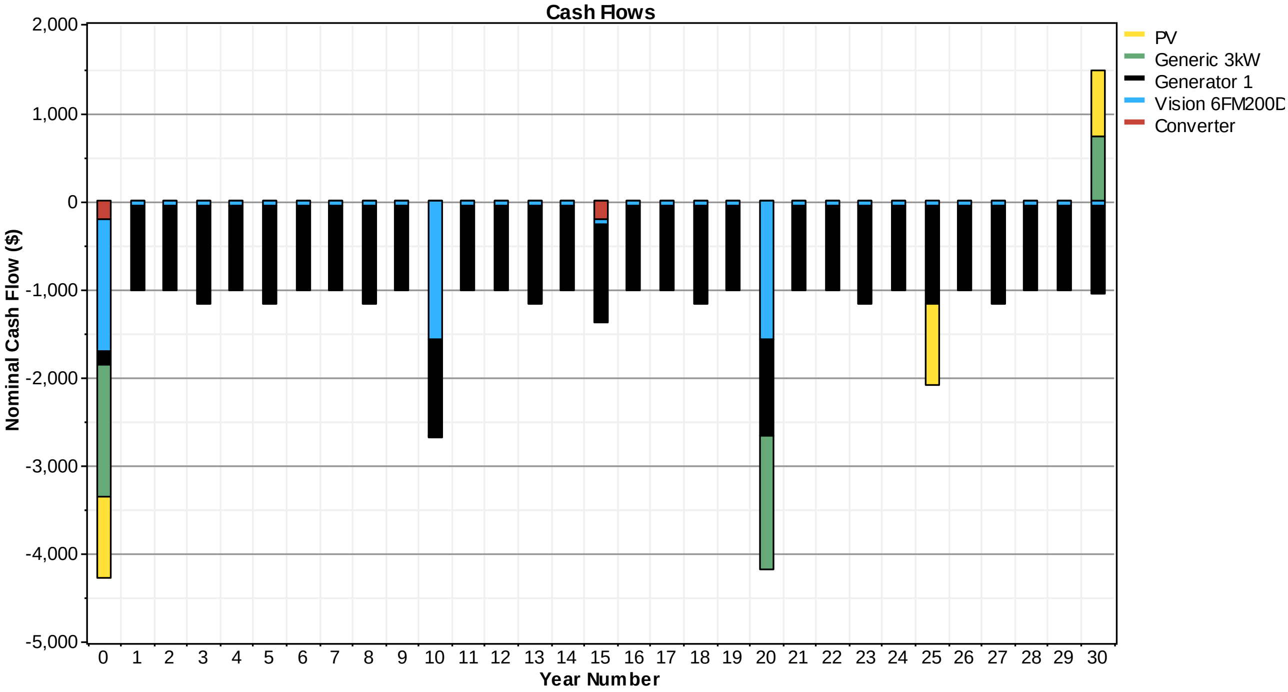

Fig. 12. Nominal Cash Flow with respect to components over a period of 30 years

4. CONCLUSIONS

The price of diesel is increasing rapidly. At the same time, the amount of non-renewable energy sources is depleting. Therefore, it is not feasible to use only diesel as a source of energy generation. Particularly, in the coastal and remote areas where the grid is not connected. Due to the rapid industrialisation and population growth, Patenga needs a constant supply of electricity. Some coastal and remote area do not get proper electricity due to uneconomical and unreliable grid supply. So, the smaller communities in these parts of the city need more economical and reliable sources of energy. An off-grid hybrid energy generation system can be a feasible and optimised solution in this regard. This Wind-PV-Diesel Generator hybrid system discussed in this paper provides an excellent scope for producing electricity that will profoundly reduce the cost of delivering main grid power in the coastal areas.

In summary, the result of HOMER modelling shows that the cost summary, cash flow summary, electrical production and cost of PV-Wind- Diesel Generator hybrid system is feasible. However, the system would become more viable if the wind speed and solar radiation are higher and diesel price is lower. Besides the advantages, the high capital cost stands as an impedance in the development of this hybrid system. Also, one of the significant drawbacks in off-grid energy system is the loss of energy. Regarding the Levelized Cost of Energy (LCOE) it was bit high due to high diesel price. But the little operating and maintenance cost and long lifetime compensate for it. The government, private sectors, and some donor agencies can fund the initial cost or provide a loan at a low-interest rate for setting up the system.

The study in this paper shows only the simulation of a Wind-PV-Diesel Generator hybrid system. The limitation of this study is, only one scenario analysed. Therefore, further research is needed to analyze alternative scenarios. It will be more reliable and suitable to compare the LCOE and other parameters if the different combination of the hybrid system is simulated. A comparative study between HOMER and RETScreen (Clean Energy Management Software) could also be done to analyse the parameters, particularly the LCOE. Besides the optimisation software HOMER, Particle Swarm Optimization (PSO) and Genetic Algorithm (GA) technique could be applied to analyse the data.

ACKNOWLEDGEMENTS

The research supported by National Natural Science Foundation of China (51577050).

REFERENCES

1. HOSSAIN, M. F., S. HOSSAIN, AND M. J. UDDIN. Renewable energy: Prospects and trends in Bangladesh. *Renewable and Sustainable Energy Reviews*, 2017, Vol. 70, P. 44–49.
2. BP (Formerly British Petroleum). BP. Statistical review of world energy 2012. <http://www.bp.com/asstes/bp_inteenet/globalbp/globalbp_uk_english/reports_and_publications/statistical_energy_review_2011/STAGING/local_assets/pdf/statistical_review_of_world_energy_fullreport_2012.pdf>.
3. BP (Formerly British Petroleum). BP. Energy Outlook 2035. <http://www.bp.com/content/dam/bp/pdf/energy-economics/energy-outlook-2015/bp-energy-outlook-2035-booklet. pdf>.
4. HOSSAIN, A. K., AND O. BADR. Prospects of renewable energy utilisation for electricity generation in Bangladesh. *Renewable and Sustainable Energy Reviews*, 2007, Vol. 11, No. 8, p. 1617–1649.
5. Sustainable and Rural Energy Development Authority. <http://www.sreda.gov.bd/>.
6. Energy and Power: Ministry of Finance, Government of Bangladesh. Bangladesh Economic Review 2015. <http://www.mof.gov.bd/en/budget/ 13_14/ber/en/chapter-10_en.pdf>.
7. Bangladesh Power Development Board. <http://www.bpdb.gov.bd/ bpdb/>.
8. ISLAM, SAIFUL, AND MD ZIAUR RAHMAN KHAN. *A review of energy sector of Bangladesh.* Energy Procedia, 2017, Vol. 110, P. 611–618.
9. Infrastructure Development Company Limited (IDCOL). Annual Report 2014-15.
10. Infrastructure Development Company Limited (IDCOL). <http://idcol.org/home/penergy>
11. ISLAM, MAZHARUL. *Renewable Energy Prospects & Trends in Bangladesh.* Bangladesh Power Development Board , 2013.
12. MANDELLI, STEFANO. *Off-grid systems for rural electrification in developing countries: Definitions, classification and a comprehensive literature review.* Renewable and Sustainable Energy Reviews, 2016, Vol. 58, p. 1621–1646.
13. DAS, HIMADRY SHEKHAR. *Proposition of a PV/tidal powered micro-hydro and diesel hybrid system: A southern Bangladesh focus*. Renewable and Sustainable Energy Reviews, 2016, Vol. 53, p. 1137–1148.
14. LIPU, MOLLA SHAHADAT HOSSAIN. *Design Optimization and Sensitivity Analysis of Hybrid Renewable Energy Systems: A case of Saint Martin Island in Bangladesh.* International Journal of Renewable Energy Research, 2017, Vol. 7, No. 2, p. 988–998.
15. SALEHIN S, RAHMAN MM, ISLAM AS. *Techno-economic feasibility study of a solar PVdiesel System for applications in Northern Part of Bangladesh*. International Journal of Renewable Energy Research , 2015, Vol. 5, No. 4, p. 1220–1229.
16. ISLAM AS, RAHMAN MM, MONDAL MAH, ALAM F. *Hybrid energy system for St. Martin Island, Bangladesh: an optimized model.* Procedia Engineering, 2012, Vol. 49, p. 179–188.
17. ZUBAIR A, TANVIR AA, HASAN MM. *Optimal planning of standalone solar-wind-diesel hybrid energy system for a coastal area of Bangladesh*. International Journal of Electrical and Computer Engineering, 2012, Vol. 2, No.6, p.731.
18. MONDAL AH, DENICH M. *Hybrid systems for decentralized power generation in Bangladesh.* Energy for Sustain Devlopment, 2010, Vol. 14, No.1, p. 48–55.
19. ISLAM A, SHIMA FA, KHANAM *A. Analysis of grid connected solar PV system in the msoutheastern part of Bangladesh.* Applied Solar Energy, 2013, Vol. 49, No. 2, p. 116–123.
20. HOMER Energy LLC <https://www.homerenergy.com/>.
21. Bikroy.com. <https://bikroy.com/en/ad/solar-panel-250w-tk-9500-for-sale-dhak>.

22. Alibaba.com. <https://www.alibaba.com/product-detail/off-grid-3kw-wind-turbine-price_60460120817.html?spm=a2700.7724838.2017115.72.376d1f9dZT6BdI>
23. Alibaba.com. <https://www.alibaba.com/product-detail/HF-D2500LE-Diesel-Generator-2kw-diesel_60376783399.html?spm=a2700.7724838.2017115.52.376d1f9dZT6BdI>.
24. Bangladesh Petroleum Corporation. Local Selling Price of Petroleum Products <http://www.bpc.gov.bd/contactus.php?id=39>.
25. OSI Batteries. <https://www.osibatteries.com/p-18390-vision-6fm200d-x-battery-12v-200ah-sealed-rechargeable-deep-cycle.aspx>.
26. Alibaba.com. <https://www.alibaba.com/product-detail/3KW-DC-24V-48V-To-AC_60453581028.html?spm=a2700.7735675.2017127.1.TxUE6Z&s=p>.

CYSENI 2018, May 23-25, Kaunas, Lithuania
ISSN 1822-7554, www.cyseni.com

DEVELOPMENT OF HYBRID THERMOPHOTOENERGY UNIT FOR AUTONOMOUS HEAT SUPPLY

D. S. Prokopenko, R. V. Zaitsev, M. V. Kirichenko
National Technical University "Kharkiv Polytechnic Institute"
Kyrpychova Street 2, Kharkiv, 61002 – Ukraine
Email: prokopenko25ds@gmail.com

ABSTRACT

The main idea of the work is to develop a constructive solution of flexible thin-film solar cells (SC) based on the CdS/CdTe system adapted for the installation of a solar battery from such SC directly to the protective glass of the solar thermal collector, consisting of an autonomous hybrid thermo-photoenergy unit for military and civilian applications based on standard solar thermal collectors with total capacity by heating up to 200 m^2, hot water up to 300 l/day and electric energy at 200 W for autonomous heating, hot water and electricity supply for electronics and battery charging of mobile electronic devices. The main part of the installation is the photoenergy module, which is a standard solar thermal collector on the photoreceiving surface of which is mounted a flexible solar cell based on the CdS/CdTe system.

Keywords: solar collector, thermophotoenergy unit, cadmium telluride, flexible solar cell, solid works flow simulation

1. INTRODUCTION WITH THE WORK EXPEDIENCY EXPLAINED

Most used currently for autonomous heating are installations which based on solar thermal collectors and at the same time requiring an external source of electricity to power up the electronic components and circulation pump up to 100 W, which does not fully consider such autonomous plants. One of the ways to solve this problem is to combine in one installation solar panels and heat collectors. Hybrid solar collectors are capable to generate electricity and heat at the same time and represent a design in which a combined photovoltaic panel and a thermal solar collector are combined [1]. Such hybrid thermo-photovoltaic installations are usually based on solar cells (SC) on the basis of monocrystalline silicon and their electrical characteristics are significantly superior accordingly to their heat characteristics. In addition, the SC based on monocrystalline silicon, due to the properties of the material, has an intense absorption of the near-long-wavelength component of solar radiation with a wavelength more than 1000 nm. Such absorption is photovoltaically ineffective and leads to parasitic heating of the SC and a decrease the efficiency of the thermal part of such hybrid unit. This necessitates the organization of efficient heat removal from the SC to the heat exchanger through intermediate thermo-interfaces, which leads to complication installation design and increase its value. Because of this, as well as the high cost of SC based on monocrystalline silicon, hybrid thermo-photovoltaic modules have a price of 1200 $/module. At the same time, the absorption maximum of flexible thin film SC on the basis of CdS/CdTe concentrated in the range of 400–800 nm, and for near-infrared components they are almost transparent. Therefore, the use of such SC in hybrid photovoltaic units will provide free access to the heat exchanger of the longwave component of solar radiation, and an efficient generation of thermal energy. The currently developed flexible SC based on the CdS/CdTe system is characterized by a record mass-power rating of 2.5 kW/kg and efficiency of 10–11% [2]. The use of hybrid electric units with flexible thin-film SC on the basis of CdS/CdTe produced on polyimide substrate will be able to mount such SC by sticking to the safety glass directly on the photoreceiving surface of standard solar thermal collectors whose price does not exceed 130 $/module. A typical photoenergy unit consists from 4–5 collectors with photoreceiving surface area of 2 m^2 each, providing heating of room with area of 200 m^2 and hot water supply at 300 liters/day and equipping of these collectors solar battery based on a flexible thin film SC will provide the generating up to 200 watts of electric power, which is quite sufficient for the maintenance of the own needs of the thermo-photoenergy unit.

An additional advantage is the ability to reduce the temperature of the SC, due to the cooling of the SC, located on the photoreceiving surface of the collector by coolant used in the thermal part of such device. As is well known, with the increase in the temperature of the SC, the efficiency of electricity generation is reduced, so that additional cooling of the solar cells will increase their efficiency.

2. METHODOLOGY

2.1. The mathematical model of the working the cooling system of the heat-receiving of a prototype sample of a thermo-photoenergy unit based on the SolidWork automation design complex

The SolidWorks package is an application for automated object-oriented design of solid-state models. The SolidWorks software package includes basic configurations and a family of optional SolidWorks Flow Simulation modules for gas/hydrodynamic calculations.

To determine the coefficient of heat transfer at a given temperature of the coolant and the temperature of the flowing surface, it is necessary to determine the temperature gradient on the wall of the heat exchanger. The temperature gradient can be determined from the solution of the energy equation, which, in turn, depends on the distribution of the flow velocity in the studied flow region. In the general form, the solution of the problem of convective heat transfer for fluid flow along the plane is reduced to the solution of the system of differential equations (1). Such a system of equations in general is not an analytical solution, therefore, individual cases are considered.

$$\begin{cases} \frac{1}{\rho}\frac{\partial\rho}{\partial\tau}+\frac{\partial w_x}{\partial x}+\frac{\partial w_y}{\partial y}=0 \\ \frac{\partial w_x}{\partial\tau}+w_x\frac{\partial w_x}{\partial x}+w_y\frac{\partial w_x}{\partial y}=\frac{\mu}{\rho}\left(\frac{\partial^2 w_x}{\partial x^2}+\frac{\partial^2 w_x}{\partial y^2}\right)-\frac{1}{\rho}\frac{\partial p}{\partial x}+g_x \\ \frac{\partial w_y}{\partial\tau}+w_x\frac{\partial w_y}{\partial x}+w_y\frac{\partial w_y}{\partial y}=\frac{\mu}{\rho}\left(\frac{\partial^2 w_y}{\partial x^2}+\frac{\partial^2 w_y}{\partial y^2}\right)-\frac{1}{\rho}\frac{\partial p}{\partial y}+g_y \\ \frac{\partial T}{\partial\tau}+w_x\frac{\partial T}{\partial x}+w_y\frac{\partial T}{\partial y}=\frac{\lambda}{\rho c_p}\left(\frac{\partial T^2}{\partial x^2}+\frac{\partial T^2}{\partial y^2}\right) \\ p=\rho RT \end{cases} \tag{1}$$

In the general form the heat transfer under free motion of the fluid in pipes and channels is described by the following parametric relation:

$$Nu=f\left(Gr,Pr\right),Pr\ >\ 0{,}7\,. \tag{2}$$

A flat collector was chosen for the realization of the thermo-photoenergy unit. Absorber is the main element of a flat collector. Absorber is an ordinary copper plate with a heat-absorbing coating. Copper was chosen because the copper thermal conductivity at a temperature of 20–100 °C is 394 W/(m * K) – higher only in silver. A copper tube is soldered to copper plate with the help of tin, one of the inexpensive methods of brazing copper. To determine the effect of the main parameters of the heat exchanger, such as plate thickness and power consumption on the pump, his computer 3D model was developed in the SolidWorks program, which is shown in Fig. 1, a.

A series of experiments with various parameters, namely the thickness of the plate and the speed of the water flow in the system, were carried out to identify the optimal heat transfer between the plate and the pipe, in addition to Solid Works' Solid Works Flow Simulation. It is necessary to find the optimal balance between these parameters, the uniformity of heat transfer and the price of the system. The thickness of the plate varied in the range from 0.5 mm to 5 mm in increments of 0.5 mm, and at a flow rate of 0.2 m/s to 1 m/s in increments of 0.2 m/s. In Fig. 1, b, a picture is shown on the surface of the 3D model of the heat-receiving device of a thermo-photogenic installation with a speed of 0.1 m/s and a plate thickness of 0.5 mm. The thermal picture shows a poor heat transfer, which passes unevenly across the entire surface of the plate. Figs. 1, c and 1, d show thermal images on the surface of a 3D model with increased speeds up to 0.2 and 0.4 m/s. Heat exchange is more evenly distributed, but the gradient of temperatures of 10 degrees is undesirable for the correct operation of the collector.

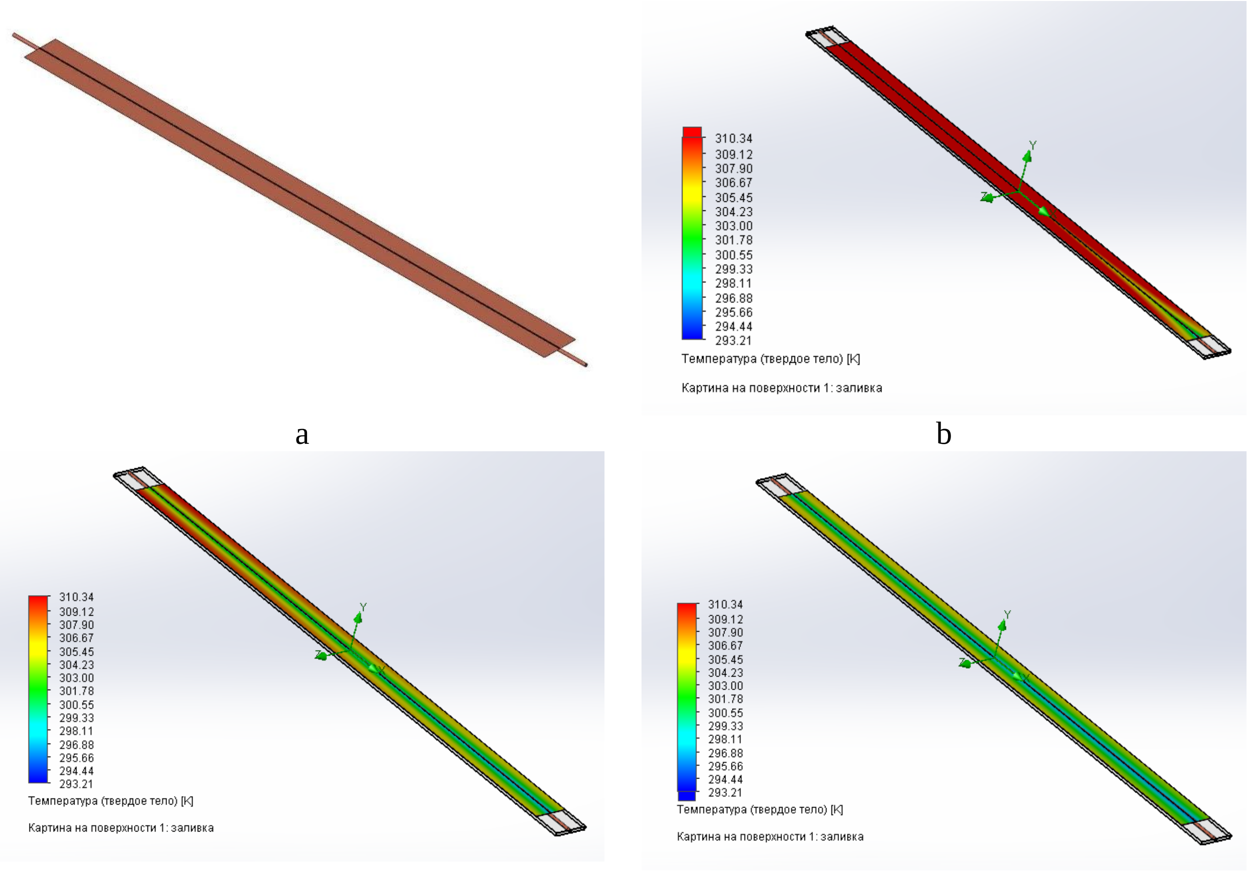

a b

c d

Fig. 1. 3D model of heat-receiver of thermo-photoenergy unit – a, and 3D modeling of the thermal picture on the surface at the flow velocity of the coolant:
b – 0.1 m/s, c – 0.2 m/s, d – 0.4 m/s

From the obtained results, a tendency is observed that with increasing the thickness of the plate and increasing the velocity of the flow the temperature distribution on the surface becomes more even. The problem is that to reach the speed of water more than 0.4 m/s it is necessary to use a very powerful circulation pump, and if the thickness is more than 1 mm thick, the use of such a plate will be inappropriate, because it will have a very large mass and cost.

Proceeding from this, it was decided to improve the solar collector system by organizing the heat exchange between the plate and the system was not through one pipe, but through two. In this way, a more even distribution of heat should be achieved without the use of very high velocities and large thicknesses. The indicated model is shown in Fig. 2, a. In Fig. 2, b, a picture is shown on the surface of the 3D model of the heat-receiver of the thermo-photoenergy unit with a flow rate of the coolant of 0.1 m/s, compared with the model in Fig. 1, b, the heat transfer distribution is much better, the temperature gradient is 10 K, but this is at level the initial version at a speed of 0.2 m/s. Therefore, in Fig. 2, c, a picture is shown on the surface of a 3D model with a flow velocity of a coolant at 0.2 m/s. The temperature gradient has dropped to 7 degrees. This is a valid value, but it is possible to increase the speed to 0.4 m/s, as shown in Fig. 2, d, which will result in a gradient of temperatures of 3 degree.

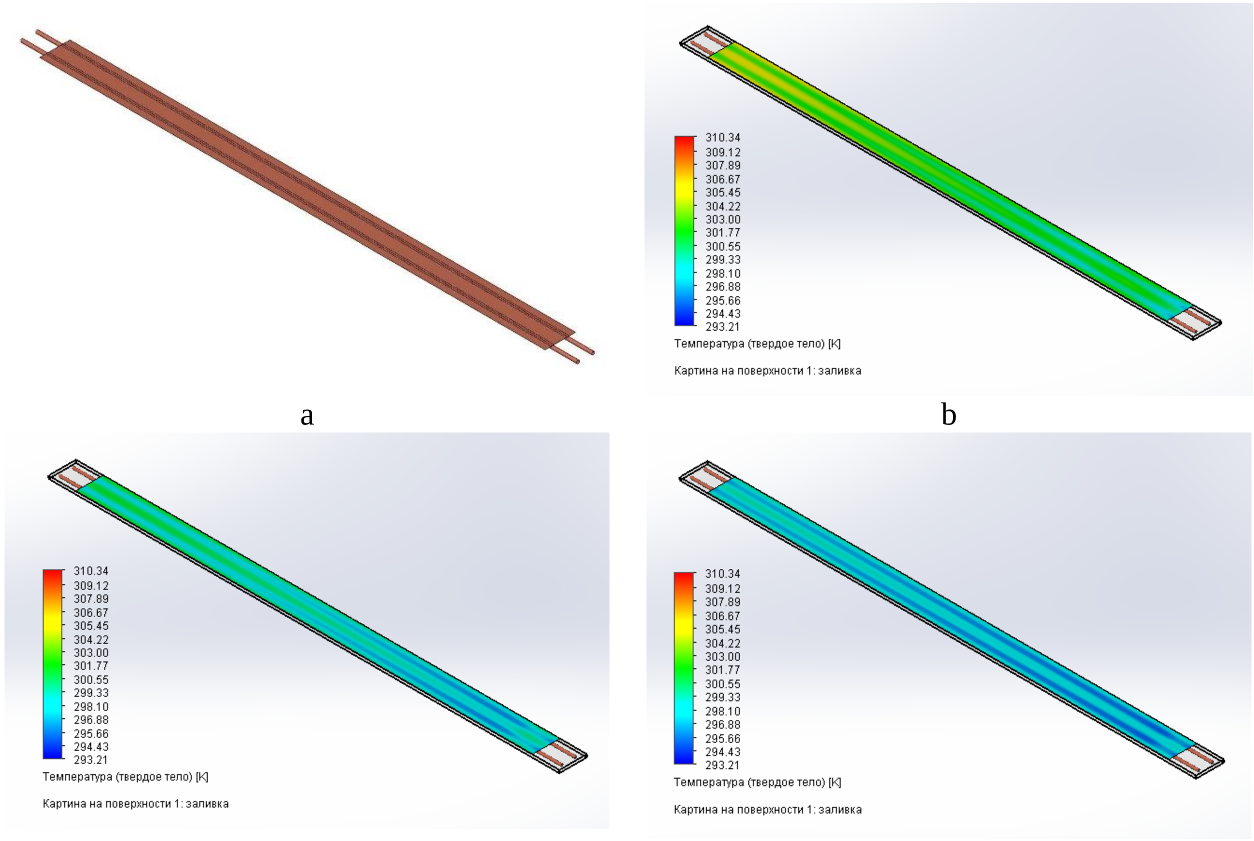

a b

c d

Fig. 2. Enhanced 3D model of heat-receiver for thermo-photoenergy unit – a, and 3D modeling with speeds: b – 0,1 m/s, c – 0,2 m/s, d – 0,4 m/s

From these results, we can see that this design will be much more effective in the work than the previous one. Even with relatively small water flow rates in the system, the pattern of temperature distribution on the plate surface is more even than in the first case. Due to this, the heat from the solar cell will be evenly transmitted from the entire area to the heat-receiver of thermo-photoenergy unit.

Therefore, for further research, it was proposed to simulate the work of the entire heat-receiver of the thermo-photoenergy unit, which consists from ten 3D heat-receiver models, shown in Fig. 2, a. At the moment, two models of plate connections were proposed, as shown in Fig. 3.

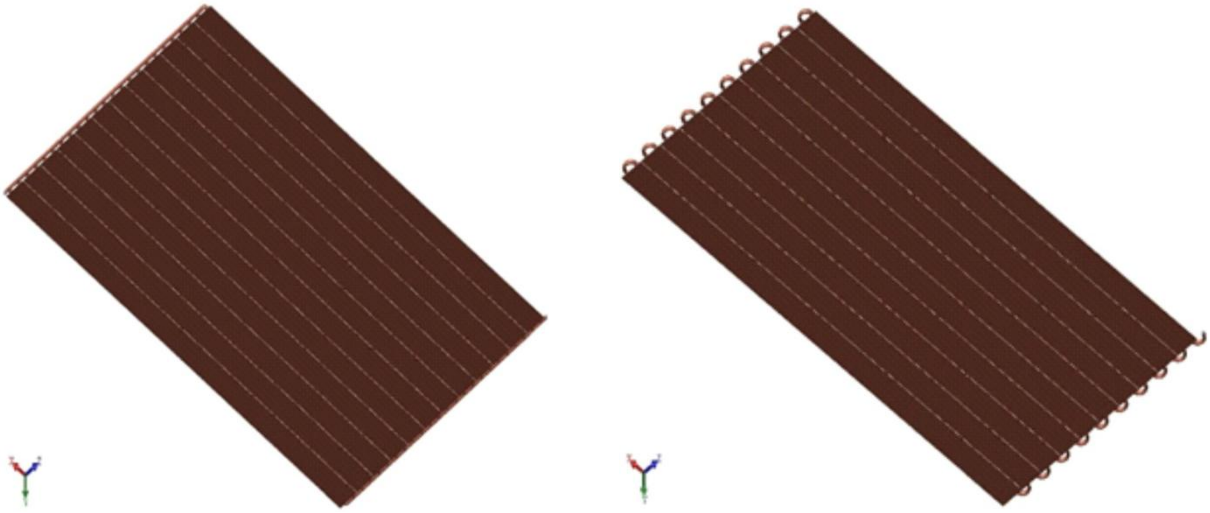

Fig. 3. 3D model of the heat-receiver of the thermo-photoenergy unit , which consists from 10 plates: a – a lyrate shape, b – a z-type form

2.2. A prototype sample of experimental thermo-photoenergy unit and study of its working parameters

Before conducting large-scale experiments it should be shown that the use of a combined system of collector and thin-film solar cells will not greatly reduce the efficiency of the first, and this combination will be advantageous from a practical point of view.

To determine the reference performance of the thermo-photoenergy unit, a prototype sample was made the main components of which was a circulating pump and a heat absorber in the form of an absorber segment from a standard solar collector, interconnected by flexible plastic hoses with a diameter of 10 mm.

The block diagram of the prototype sample of the thermophotoenergy unit is shown in Fig. 4.

The heat receiver in the prototype sample is made on the basis of the absorber from a standard flat solar collector.

The absorber plate is made from copper, which conducts heat well and is less susceptible to corrosion than aluminum. The absorber plate will be treated with a special selective coating that better holds the absorbed sunlight [3] and reduces the reflection of light. This coating consists of a very strong thin layer of an amorphous semiconductor applied to the metal and is characterized by a high absorption capacity in the visible region of the spectrum and a low coefficient of radiation in the long-wavelength infrared region, which provides the absorber plate, usually black.

Conducting experiments from the study of the working parameters of a prototype sample of an experimental thermo-photoenergy unit will consist in measuring the velocity of water flow over a period of time and cooling the heated surface of the heat-receiver.

At irradiation from a light source – a halogen lamp powered by a stabilized voltage source, the heat sink is heated [4]. For its cooling water is used, the circulation of which is provided by the pump.

The results will be compared to simulation in the Solid Works Flow Simulation software environment.

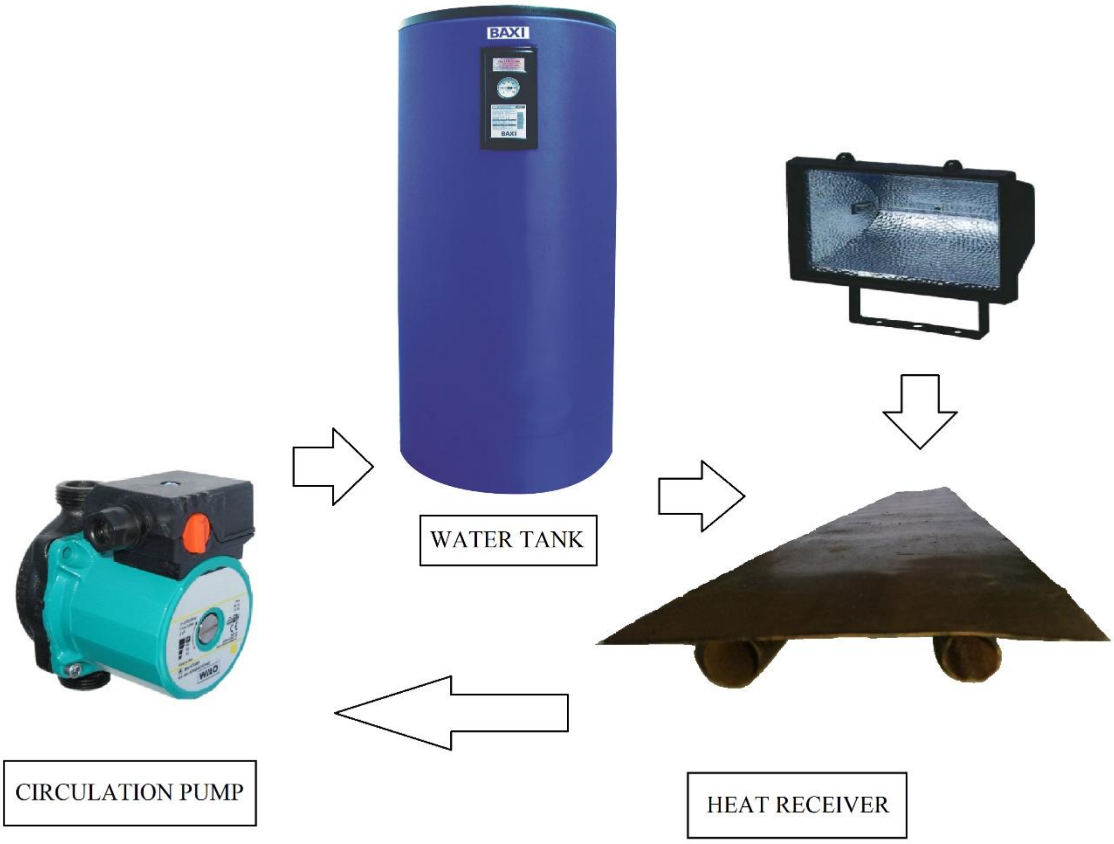

Fig. 4. Block diagram of the prototype sample of the thermo-photoenergy unit

3. CONCLUSIONS

The obtained simulation results in the Solid Works Flow Simulation software environment were confirmed by experiment.

Modeling with Solid Works Flow Simulation software package was performed to optimize the working parameters of the model sample. From the results obtained, one can observe the tendency that, with an increase in the thickness of the plate of the heat-receiving device to 2 mm and an increase in the flow velocity up to 0.6 m/s, the temperature distribution on the surface becomes more even. However, in order to reach the speed of water more than 0.6 m/s it is necessary to use a very powerful circulating pump, and if the thickness of the heat-receiving device increases to 2 mm or more, its mass and price unacceptably increases.

According to the results of additional simulation, it is proposed to equip the heat receiver with two pipes instead of the traditional one. Due to this, a more even distribution of heat across the entire heat receiver's area will be achieved and its efficient transfer without the use of very high circulating coolant velocities and large thicknesses of the heat receiver. For such a system, additional calculations are made.

A prototype sample of a thermo-photoenergy unit was made, and it was carried out by a series of experiments on the study of working parameters of a prototype with a different configuration of the heat-receiving surface: the presence or absence of thin-film solar cells, protective glass and their combination.

According to the results of the conducted research it was established that in the presence of thin-film elements and protective glass on the heat-receiving surface, the heating rate of the coolant remains practically unchanged and does not change the resulting temperature of the heat-receiver. In the presence on the heat-receiving surface only the protective glass without polyimide films, there are also no significant changes in the temperature of the heat-receiver and the heat-carrier heating rate. It is shown that the determining influence on the thermal parameters of the prototype sample is caused by the rate of circulation of the coolant and the amount of coolant in the system.

REFERENCES

1. KAPRALOV, A.I. *Recommendations for the use of liquid solar collectors*. Moscow: VINITI, 1988.
2. KHRYPUNOV, G.S. Film Solar Cells NaCl/ITO/CdTe/Cu/Au. *Physics and chemistry of the solid state*, 2005, Vol. 6, No. 1, P. 153–156.
3. STAROVEROVA, I.G. *Handbook of the designer. Internal Sanitary Equipment.* Ed. 3rd, revised. and additional. Part I. Heating, water supply, sewerage, 1975, 429 p.
4. SHULTSA, S.V. *Handbook of the illuminator*, Hitler: Flint, 2004, 320 p.

CYSENI 2018, May 23-25, Kaunas, Lithuania
ISSN 1822-7554, www.cyseni.com

INVESTIGATION OF HEATING AND COOLING MODES OF A HEAT PUMP PLANT IN THE CLIMATIC CONDITIONS OF THE NORTHERN REGION OF KAZAKHSTAN

A. I. Koshkina, I. V. Koshkin, Y. M. Kandalina
A. Baitursynov Kostanay State University,
47 Baitursynv St., Kostanay, 110000 – Kazakhstan
Email: elektroenergetika@mail.ru

L. A. Azizova
M. Dulatov Kostanay Engineering and Economic University,
59 Chernyshevski St.,Kostanay – Kazakhstan
Email: azizova_leilochka@mail.ru

ABSTRACT

The inevitable issue of an escalating energy deficit and the price growth on most energy carriers demands for the use of effective energy-saving technologies. Thus the research in technologies generating heat and the use of new non-traditional renewable energy sources is a very promising trend. The study considers important issues of optimization and improvement in the field of heat pump technologies within specific climatic features of the Northern region of Kazakhstan. The paper focuses on the state and prospects of using heat pump plants in Kazakhstan. The main characteristics of heat pump systems, their classification characteristics, and the principles of the operation of heat pump plants are described. Based on the traditional and well-known calculation methods, the authors of the article did the calculations of the heat pump system used for the heat supply and cooling of the facility, using data and climatic conditions of the Northern region of the country. The article explains the dependences of the change in the heating capacity of the heating system and the cooling capacity of the air conditioning system, plotted against the outside temperature. The temperature graph of the qualitative regulation of the heating load and conditioning load has been constructed. It is proved that for the climatic conditions inherent in Kostanay region, the heat pumps, which differ from standard heat pumps, should be developed. The heat pumps for the calculated climatic conditions of the Northern region of Kazakhstan should be distinguished by design due to the required high temperatures for heating. The article describes the advantages of using reversible schemes for heat pump systems since the heat energy in the ground is dissipated during the transition of the heat pump to the cold supply mode.

Keywords: Kazakhstan, heat pump, cooling mode, evaporator, compressor, condenser, heat exchanger, electricity

1. INTRODUCTION

To date, one of the priority areas of the energy industry in Kazakhstan is the use of renewable energy sources, as well as secondary energy resources, such as thermal discharges of energy, public utilities and industry, usually having a low temperature potential. It is for this reason that the use of heat pump plants allows, when using them in heat supply systems, to provide not only fuel economy at the heating plant, but also to reduce the cost of heat for the consumer [1].

Modern heat pump systems use low-potential heat not only of natural sources, but also of many technological processes, the heat of condensation of refrigeration units, the heat of ventilation emissions, as well as the cooling systems of recycled water supply and sewage [2].

After that, the recycled water is returned to the technological process with a higher temperature level, simultaneously obtained the thermal energy, exceeding amount of the initial one, taking into account the electricity expended for the work of the heat pump compressor. It is important that when using heat pump plants, it is necessary to take into account not only the saving of primary energy, namely organic fuel, but also other components [3].

For example, when using heat pumps for heating purposes, the costs for transporting fuel and exporting combustion products are eliminated, as there is no need for fuel storage facilities, which in most cases is the decisive factor for their application. In addition, the ecological issue is also important, as it is obvious that when using heat pump systems, the possibility of harmful emissions into the atmosphere is excluded, which makes industrial, residential and public buildings heating environmentally friendly. [4, 5]. Moreover, it should be taken into account that the basic tariffs for the main energy carriers – gas and electricity – are set by the Government of the Republic of Kazakhstan, the prices for coal and fuel oil are determined taking into account the established market prices and are significantly dependent on world oil prices, and location of the region. And tariffs for heat supply are established from the budgets of the subjects of the Republic of Kazakhstan and as a consequence, do not reflect their true value. [6, 7].

This issue is especially topical now, when the problems of energy consumption are solved at the legislative level. According to the Law of the Republic of Kazakhstan "On Energy Saving and Energy Efficiency Improvement" dated January 13, 2013, the technical regulation is implemented in the field of energy saving and energy efficiency, and the energy saving and energy efficiency are promoted, including the use of energy-saving equipment and materials. In this regard, it is important to note that the research on ways to improve the efficiency of heat pump installations is crucial for solving energy saving problems. Currently in Kazakhstan there is a factory "SunDue" located in the city of Ust-Kamenogorsk, which produces heat pumps. Also among domestic enterprises, it is worth noting the enterprise "Astanateplonasos", which has realized many successful projects on installing heat pumps. For instance, two heat pumps were installed in the Komsomolskiy district, located in the city of Astana, with the total heat capacity of 72 kW. Also, in March 2012, in Astana, the heat pump with the heat output of 120 kW was installed in Astana, in a low-rise residential complex in the village of Koshi, Akmola region, the consumed electric power of this heat pump is 26 kW. In addition, in the Akmola region, the village of Borovoe on August 8, 2013, the heat pump with a total thermal capacity of 48 kW was installed and put into operation.

Another company operating on the domestic market of heat pumps is ECO WAY LLP. This company exists in the market of energy-saving technologies since 2009. The main distinguishing feature of this company is the fact that they have specialists trained at the Waterkotte plant located in Germany, these specialists improve their qualification.

2. MATERIALS AND METHODS

For the scientific analysis, the study of existing heat pump installations and thermal mechanical processes has been made. The principles of their functioning have been defined. [2, 8–14]. According to the results of the study of scientific sources, it was concluded that the choice of the low-potential heat sources should be based on the climatic characteristics of the chosen region or region, such as the duration of the heating period, and the depth of soil freezing. The theoretical study revealed the need to develop a methodology and choose a method for calculating heat pump installations within their thermal and technical parameters, to provide for their efficiency in the climate of northern Kazakhstan in the Kostanay region.

The Kostanay region, located in the center of the Eurasian continent, is characterized by a sharply continental climate. Climatic conditions vary widely due to the large extent of the territory, as well as the influence of the Ural Mountains in the west and the Kazakh Upland in the east. The region's climate is characterized by a gradual increase in air temperatures and a decrease in precipitation from north to south. The indicators of the heat supply and moisture supply in this direction range from the following: average annual air temperature from -10 ^{0}C to -6.9 ^{0}C, average July-from +19.3 ^{0}C to +25.1 ^{0}C, average – from -18 ^{0}C to -8.2 ^{0}C. The average duration of the frost-free period is 110–160 days, with a stable snow cover – 160–105 days. The annual amount of precipitation is from 390 mm in the north to 159 mm. Winter is usually cold and snowless, in the cold period the area is under the influence of the Siberian anticyclone, in clear weather the temperature drops to -30–-40 ^{0}C frost, sometimes lower. Summers are hot and dry, despite the relatively high amount of precipitation. A hot period with air temperatures over +20 ^{0}C in the north is short, in the south it lasts three months. The number of extremely dry days with relative humidity less than 30% in the north does not exceed 15–20, and in the south it reaches 60 or more. The autumn period is cloudy, sometimes rainy.

In accordance with the above-mentioned climatic features of the Northern Kazakhstan, it is necessary to compile a methodology for choosing a heat-and-power plant. The methodology should enhance obtaining the most reliable result, taking into account the functioning of the equipment in operating climatic conditions.

To transfer the heat pump operation to the cold supply mode, the four-way compressor valve, as shown in Fig. 1, is switched from the one end position to the other, as a result of which the Freon flow changes the direction. While the compressor and throttle continue to function in the same mode as when heating a building [15, 16].

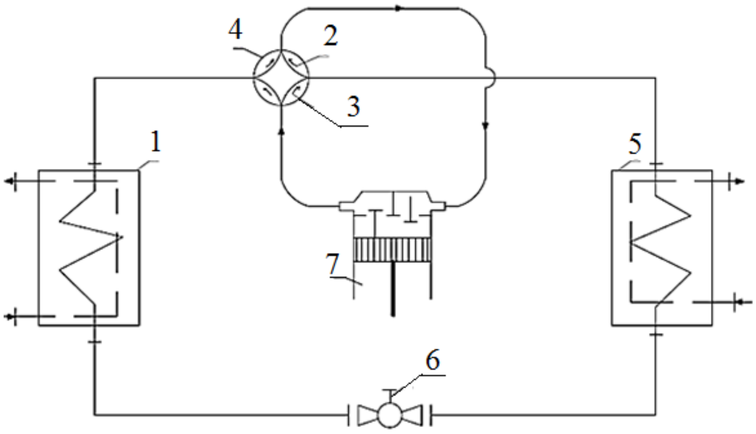

Fig. 1. Schematic diagram of the heat pump transfer to the cooling supply mode: 1 – outer heat exchanger; 2 – direction of coolant movement when cooling the room; 3 – direction of movement of the refrigerant during room heating; 4 – four-way tap; 5 – internal heat exchanger; 6 – control valve; 7 – compressor

After changing the heating\cooling mode, the evaporation process in the evaporator heat exchanger changes to condensation, and the condensation process in the condenser heat exchanger changes to evaporation. As a result, the water that circulates in the cooling circuit is cooled and then this water enters the air conditioning, and the heated freon gives off heat to the ethylene glycol that circulates in the primary circuit. Ethylene glycol gives off heat to the ground, resulting in the dissipation of thermal energy in the ground. [17].

2.1. Method for calculating the heat pump for a heat supply system in the conditions of the Northern region of Kazakhstan

Initial data for the verification calculation:

$Q_P^T = 100\,kW$ – heat output of the heat and cold supply system at the design ambient air temperature;

$t_{source} = 8\ ^oC$ – the temperature of the low potential heat source;

$t_{op}^{direct} = 70\ ^oC$ – the temperature of the “direct” water in the heat network at the at the design ambient air temperature;

$t_{op}^{reverse} = 40\ ^oC$ – the temperature of the “reverse” water in the heat network at the design ambient air temperature;

$t_{d.a.a.t.} = -20\ ^oC$ – the design ambient air temperature;

$t_R = +20\ ^\circ C$ – the temperature in the room.

Table 1 shows the duration of the heating season and the summer conditioning season for the climatic zone inherent in the Kostanay region, depending on the ambient air temperatures:

Table 1. The duration of the heating season and the summer conditioning season

<table>
<tr><th colspan="9">The heating season</th></tr>
<tr><td>T_{a.a.}, °C</td><td>-30…-25</td><td>-24.9…-20</td><td>-19.9…-15</td><td>-14.9…-10</td><td>-9.9…-5</td><td>-4.9…0</td><td>0.1…5</td><td>5.1…10</td></tr>
<tr><td>τ, hours</td><td>270</td><td>437</td><td>348</td><td>469</td><td>726</td><td>600</td><td>1200</td><td>390</td></tr>
<tr><th colspan="9">The summer conditioning season</th></tr>
<tr><td>T_{a.a.}, °C</td><td colspan="4">25–30</td><td colspan="4">30–35</td></tr>
<tr><td>τ, hours</td><td colspan="4">1248</td><td colspan="4">744</td></tr>
</table>

The total duration of the heating season is 4440 hours; duration of the summer conditioning season is 1992 hours.

The heat consumption for heating is related to the ambient air temperature by the dependence (2) [17]:

$$Q^T = Q_p^T \frac{t_R - t_{a.a.}}{t_R - t_{d.a.a.t.}}, \tag{1}$$

where: $Q_p{}^T$ – the design heating capacity of the system, kW; t_R – air temperature in a room, °C; $t_{a.a.}$ – the ambient air temperature °C.

The temperatures of «direct» and «reverse» water are calculated with the equations:[1, 2, 17, 8]:

$$t_\omega^{dir} = t_R + \Delta t' \overline{Q}^{0.8} + \overline{Q}\,\theta'/2\ ; \tag{2}$$

$$t_\omega^{dir} = t_R + \Delta t' \overline{Q}^{0.8} - \overline{Q}\,\theta'/2\ . \tag{3}$$

where

$$\Delta t' = \frac{t_{\omega p}^{dir} + t_{\omega p}^{rev}}{2} - t_R; \tag{4}$$

$$\theta' = t_{\omega p}^{dir} + t_{\omega p}^{rev}; \tag{5}$$

$$\overline{Q} = Q^T / Q_p^T = (t_R - t_{a.a.})/(t_R - t_{d.a.a.}). \tag{6}$$

The formula (6) calculates the ratio of heat consumption at a selected ambient air temperature to the maximum heat consumption at the design ambient air temperature [17].

The mass of water circulating in the heating system is determined by the design heating capacity and the difference in water temperatures in the system at the design ambient air temperature. [1, 2, 17]:

$$G_\omega^c = \frac{Q_p^T}{c_\omega \left(t_{\omega p}^c - t_{\omega p}^{rev}\right)}. \tag{7}$$

The heat output of a heat pump is determined by the formula [18]:

$$Q^{AAT}=G_{\omega}^{c}c_{\omega}\left(t_{\omega}^{k}-t_{w}^{rev}\right), \tag{8}$$

where t_{ω}^{c} – the temperature of the water leaving the heat pump condenser, °C; c_{ω} – water heat capacity.

The temperature of the water leaving the heat pump condenser t_{ω}^{c} is defined with the following formula:

$$t_{\omega}^{c}=t_{c}-\frac{t_{c}-t_{\omega}^{rev}}{e^{m}-1}, \tag{9}$$

where

$$m=k_{c}F_{c}/\left(G_{\varpi}^{c}c_{\omega}\right); \tag{10}$$

$$k_{c}F_{c}=Q^{AAT}/\theta_{c}. \tag{11}$$

According to formula 11, the intensity of the heat transfer in the condenser is determined at the maximum heat output, W/K (assumed unchanged in calculation) [17].

At ambient air temperatures higher than the one at which the heat output of the heat pump is maximum, there is no need to maintain the condensation temperature high. The condensation temperature is determined from the expression [17]:

$$t_{c}=\frac{e^{m}t_{\omega}^{dir}-t_{\omega}^{rev}}{e^{m}-1}. \tag{12}$$

The maximum capacity of the peak heating system is determined by equation:

$$Q^{R}=G_{\omega}^{c}c_{\omega}\left(t_{\omega}^{dir}-t_{\omega}^{c}\right)=Q^{T}-Q^{AAT}. \tag{13}$$

The effective power of compressors N_b is determined by the conditions of the thermodynamic cycle.

The annual energy consumption by compressors of a heat pump working on heat supply is determined by the formula 14, taking into account the unchanged temperature of the outside air by summing the corresponding products [17]:

$$W_{compres} = \Sigma N_{a.a.cpi}\tau_{i} \tag{14}$$

For the initial data, a calculation of the annual energy consumption is:

$W_{compres}$ = 270(8.7 + 9.9)/2 + 437(9.9 + 11.2)/2 + 348(11.2 + 19)/2 + 469(19 + 26.5)/2 +
+ 726(26.5 + 20.8)/2 + 600(20.8 + 11.4)/2 + 1200(11.4 + 6.7/2 + 390(6.7 + 4.4)/2 = 62900 kWh

The power of the circulation pump and the pump to the evaporator is determined by formulas (15) and (16), respectively:

$$N_{circl}= G_{\omega}^{\kappa}H/\eta \tag{15}$$

Obtained: N_{circl} = 0.79·0.49/0.7 = 0.5 kW

$$N_{evap} = G_{\omega}^{u}H/\eta. \tag{16}$$

Obtained: N_{evap}=7.3·0.15/0.7 = 1.6 kW.

The energy consumption by pumps for the heating season is calculated by the formula:

$$W_{pump}=\Sigma N_{pump}\,\tau. \tag{17}$$

As a result of calculation, according to the proposed method, of functioning of the heat pump system in the heating mode W_{pump} = (0.5 + 1.6)4440 = 9324 kWh.

The total amount of heat supplied to the consumer by the heat supply system during the heating season and the share of heat attributable to the heat pump and the peak heating system are determined taking into account their productivity and the duration of the constant external air temperatures by formulas (18)–(20) [17, 18]:

$$Q^{AAT}{}_{year} = Q^{TH}{}_{year} + Q^{R}{}_{year}\,; \tag{18}$$

$$Q^{TH}{}_{year} = \Sigma Q^{AAT}{}_{i}\tau_i\,. \tag{19}$$

Design quantity: $Q^{AAT}{}_{year}$ = 218110 *kWh*=785196 *MJ/s*.

$$Q^{R}{}_{year} = \Sigma Q^{\Pi}{}_{i}\tau_i\,. \tag{20}$$

Design quantity: $Q^{R}{}_{year}$ = 79332 *kWh* = 285595 *MJ/s u* $Q^{T}{}_{year}$ = 297442 *kWh* = 1070791 *MJ/s.*

2.2. Method for calculating the heat pump system for the cold supply system in the Northern region of Kazakhstan

In the summer air-conditioning mode, the heat pump operates as a cooling machine in a conventional regenerative refrigeration cycle [1, 17].

The maximum cooling capacity Q_{or} at the design mode is determined by the formula [17, 18]:

$$\Theta_{0\mathrm{p}} = Q_p^T \frac{t^s_{d.a.a.t.} - t_{r.s.}}{t_{r.w.} - t^s_{d.a.a.t}}. \tag{21}$$

With the proposed conditions, the parameter is equal, kW:

$$\Theta_{0\mathrm{p}} = 100\frac{30-22}{20+20} = 20.$$

$t^s_{d.a.a.t.}$ = 30 °*C* – the design ambient air temperature;

$t_{r.s.}$ = 22 °*C* – the temperature in a room in the period of summer cooling.

Taking into account the heat generation of people, the inflow of heat from solar radiation, with the supply air and from other sources it is accepted that Q_{0r} + 10% = 20 *kW* + 10% = 22 *kW.*

The cooling capacity is determined by the following formula:

$$Q_0 = Q_{0r}\frac{t_{a.a} - t_r}{t_{d.a.a} - t_r}. \tag{22}$$

The difference between the temperatures of the return and the direct water at the design ambient air temperature:

$$t^c_\omega - t^{rev}_\omega = Q_{0r}/\left(G^c_\omega c_\omega\right). \tag{23}$$

The temperatures of the direct and reverse water are determined by the expressions:

$$t^{dir}_\omega = t_0 + \frac{t^{rev}_{\omega p} - t^{dir}_{\omega p}}{e^{m'} - 1}, \tag{24}$$

where $m' = k_u F_u/\left(G^u_\varpi c_\omega\right).$

$$t^{rev}_\omega = t^{dir}_\omega + \left(t^{rev}_{\omega p} - t^{dir}_{\omega p}\right). \tag{25}$$

The annual energy consumption of the heat pump compressors in the summer conditioning mode is determined by the formula:

$$W_{compes} = \Sigma N_{a.a.cpi}\tau_i\,. \tag{26}$$

As a result of calculation according to the proposed procedure $W_{compres}$= 5599.68 *kWh.*

The energy consumption by pumps during the conditioning season is determined by the formula 27:

$$W_{pump} = \Sigma N_{pump}\, \tau, \tag{27}$$

$$W_{pump} = (0.5+1.6)1992 = 4183.2\ kWh.$$

The amount of heat withdrawn from the cooled object during the conditioning season is determined by the expression:

$$Q_{0\ year} = \Sigma Q_{0\ i} \tau_i\ . \tag{28}$$

Design quantity: $Q_{0\ year} = 40621.9\ kWh = 146239\ MJ$.

3. RESULTS AND DISCUSSION

The results of calculating the heat pump system with a nominal power of 100 kW, performed according to the described method, are summarized in Table 2.

Based on the data obtained in Table 2, the graph was constructed to demonstrate the change in the heating capacity of the heating system dependent on the ambient air temperature (Fig. 2).

Based on the data on the duration of the heating season presented in Table 2 and Graph 2, the heating capacity of the heating system was plotted against the seasonal load duration (Fig. 3).

Table 2. Results of heat pump calculation in heating load mode

Quantity	**Ambient air temperature $t_{a.a.}$ °C**								
	-30	**-25**	**-20**	**-15**	**-10**	**-5**	**0**	**5**	**10**
Q^T, kW	125	112	100	87.5	75	62.5	50	37.5	25
Q^{AAT}, kW	63,8	57.3	53.9	52.59	54.74	51.6	50	37.5	25
t_ω^{dir}, °C	80.6	75.33	70	64.6	59.05	53.4	47.6	41.5	35.2
t_ω^{rev}, °C	43.1	41.58	40	38.3	36.55	34.6	32.6	30.3	27.7
t_ω^{c}, °C	62.4	58.9	56.3	34.2	53.1	50.2	47.6	41.5	35.2
G_ω^{c}, kg/c	0.79								
t^c, °C	43	41	40	40	40	37.2	35	33.2	30.4
θ_c, °C		3.2	4	6	7	8	7.5	5.6	3.2
$k_c F_c$, W/mK	7820								
Q^R, kW	61.2	54.7	46.1	34.9	20.26	10.9	0	0	0
G_ω^{i}, kg/c	7.3								
$k_u F_u$, W/mK	9400								
$N_в$, kW	8.7	9.9	11.2	19	26.5	20.8	11.4	6.7	4.4

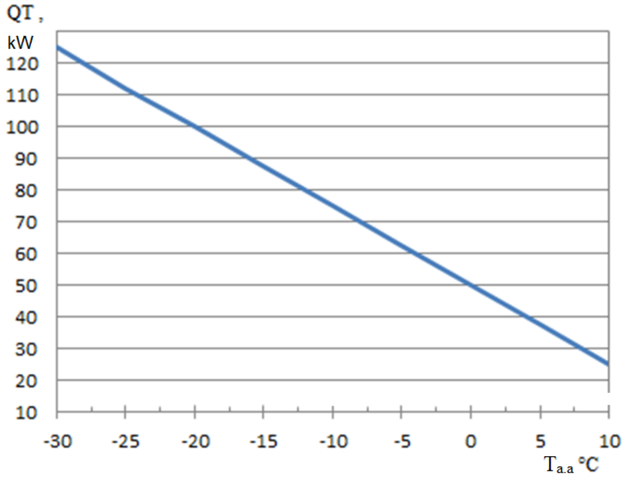

Fig. 2. The graph of the heating capacity rate of the heating system

The calculation of the qualitative regulation system is determined by the temperatures of "direct" and "reverse" water in the heating network, depending on the heat load required in the given conditions. It allows maintaining the necessary internal temperature in the heated rooms. Based on the results of the calculations, for qualitative regulation of the heating load, the temperature graph of the heating network has been constructed, (Fig. 4).

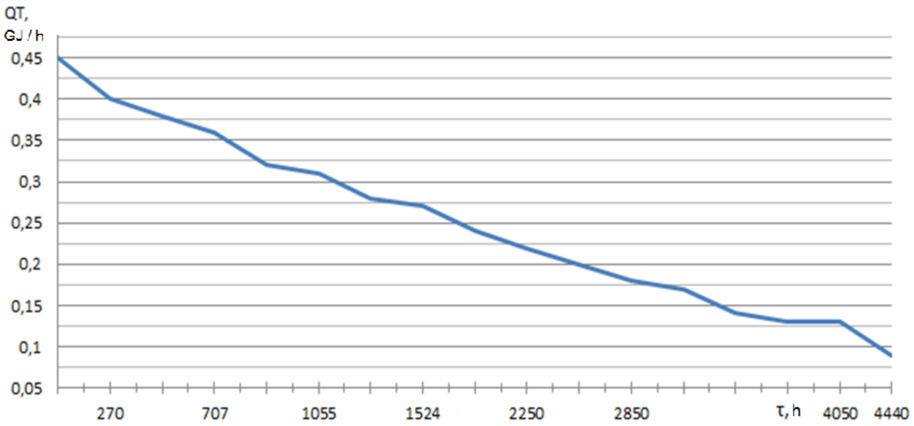

Fig. 3. The range of the heating capacity of the heating system and seasonal load duration

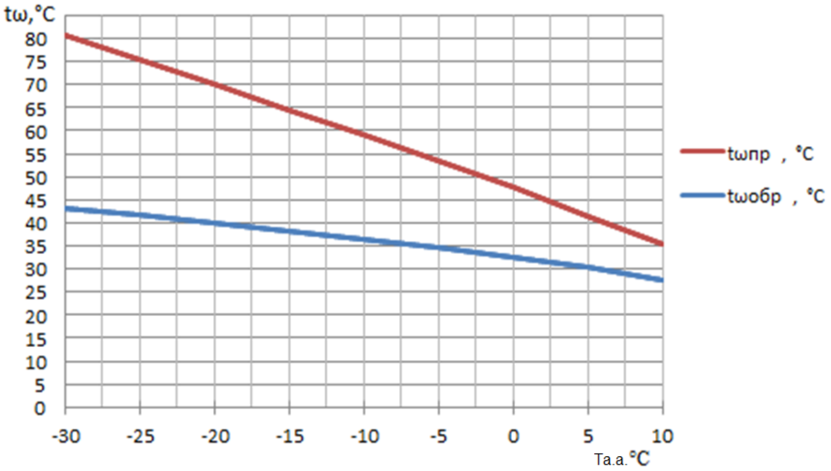

Fig. 4. Temperature graph of the qualitative regulation of the heating load

The results of the verification calculation of the heat pump system functioning in the conditioning mode according to the proposed method are summarized in Table 5.

Table 5. Results of calculation of the heat pump in the mode of summer conditioning

Quantity	**Ambient air temperature $t_{a.a.}$ °C**				
	35	**32.5**	**30**	**27.5**	**25**
Q_0, kW	35.75	28.8	22	15	8.25
$t_\omega^{rev} - t_\omega^{dir}$, °C	10.83	8.72	6.67	4.54	2.5
t_ω^{dir}, °C	1.36	4.79	8.35	12.2	16.03
t_ω^{rev}, °C	12.19	13.5	15.02	16.8	18.5
t_0,°C	0	3.69	7.51	11.67	15.72
$N_в$, kW	5.97	3.8	2.63	2.13	1.4

Fig. 5 shows the graph of the cooling capacity of the cold supply system dependent on the ambient air temperature, which was constructed on the basis of the data obtained in the calculations.

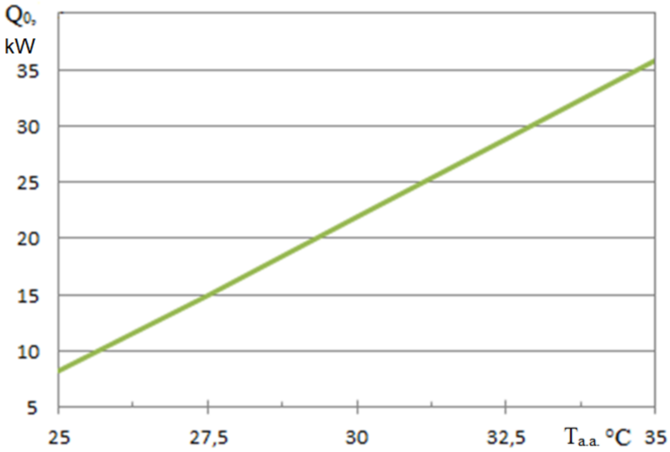

Fig. 5. The graph of changes in cooling capacity of the cold supply system

Based on the data on the duration of the summer conditioning season presented in Table 5 and Graph 5, the line graph was developed for the cooling capacity of the cold supply system versus seasonal load duration, as shown in Fig. 6.

Based on the results of the calculations in Table 5, the temperature graph similar to the schedule for the qualitative regulation of the heating load was constructed to determine the cooling capacity presented in Fig. 7.

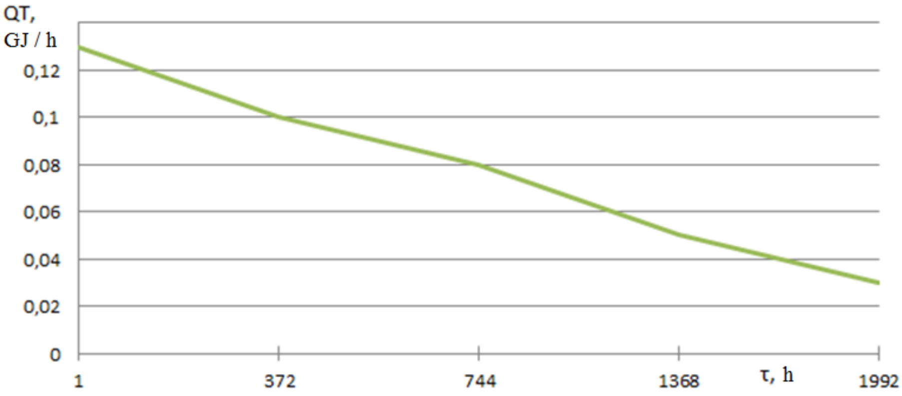

Fig. 6. Cooling capacity of the cold supply system depending on the duration of seasonal load

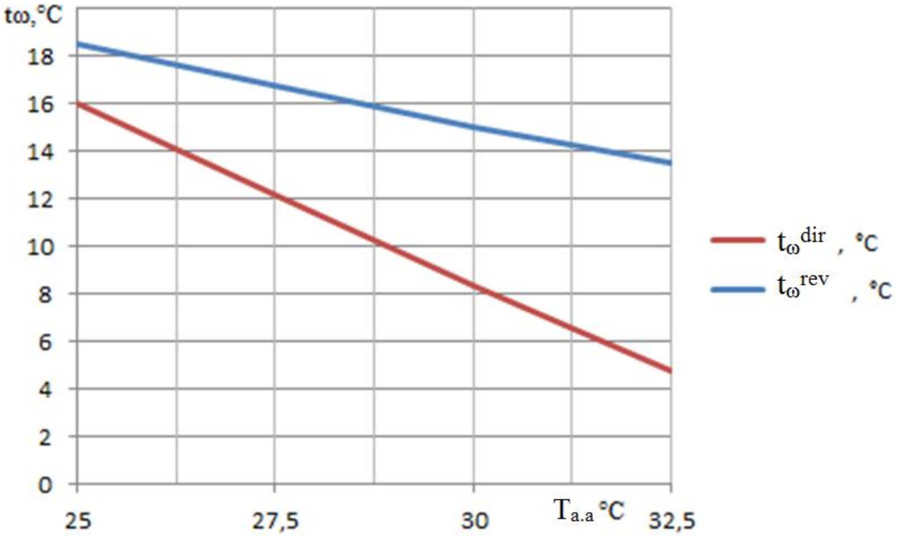

Fig. 7. Schedule of qualitative regulation of cooling capacity

The above graphs assume the determination of the parameters of the heat pump under various operating conditions: the dependence of the performance on the outside air temperature, the dependence of the coolant temperature in the forward and return pipeline on the outside air temperature, and so on. This can help in the design and calculation of the thermodynamic part of the heat pump in the climatic conditions of the northern region of Kazakhstan

4. CONCLUSIONS

The authors of the article have studied the methods of calculation the heat pump system and the parameters of the heating capacity of the system in the heating and cooling capacity of the system in the conditioning mode, depending on the ambient air temperature.

According to the specified algorithm of the method, calculations were made of the heat consumption for heating, the temperature of the direct and reverse water for the heating load, the heat output of the heat pump, the cooling capacity. In the design mode the difference between the forward and reverse water during air conditioning was calculated in the same way.

Calculation of the heating capacity of the heating system was carried out in the temperature range inherent in the Kostanay region during the heating season – from -30 °C to +10 °C. It was revealed that at the lowest possible temperatures, the heat consumption for heating reaches 125 kW, which exceeds the conventional design value taken at 100 kW.

It is proved that in the climatic conditions inherent in Kostanay region, to cover the peak loads of heating, it is required to apply new solutions that involve the use of additional energy sources. The additional potential for increasing the efficiency of heat pumps use in the climatic conditions of the Northern region of Kazakhstan is also found in the possibility of their implementation for heating and hot water supply, and air conditioning, including control and management of indoor air humidity. When the heat pump goes into cold supply mode, the heat energy in the ground is dissipated and its preparation for the heating season. As a consequence, it is more efficient and more expedient to use a heat pump in both heating and air conditioning modes, since during conditioning the soil is saturated with heat.

REFERENCES

1. ERLIKHMAN, V.N. Energy saving in technological processes of the agro-industrial complex using heat pump plants: monograph / V. N. Erlikhman, Yu.A. Fatykhov, A.E. Suslov. Kaliningrad: Publishing house of KSTU, 2007.
2. AMERKHANOV, R.A. Heat pumps. Moscow: - Energoatomizdat. 2005. 160 p.
3. XU, C; WANG, C.L; XU, G; HU, Y; GUO, H; YANG, YP. Thermodynamic and environmental evaluation of an improved heating system using electric-driven heat pumps: A case study for Jing-Jin-Ji region in China. *JOURNAL OF CLEANER PRODUCTION*, 2017, Vol. 165, pp. 36–47.
4. HAN, CJ; ELLETT, KM; NAYLOR, S; YU, X . Influence of local geological data on the performance of horizontal ground-coupled heat pump system integrated with building thermal loads. *RENEWABLE ENERGY*. 2017. Vol. 113. pp. 1046–1055.
5. MAJURI, P. Ground source heat pumps and environmental policy - The Finnish practitioner's point of view. *JOURNAL OF CLEANER PRODUCTION*, 2016, Vol. 139, p. 740–749.
6. AZIZOVA, L.; KOSHKIN, I. Investigation of ways to increase the efficiency of heat pump plants. The multidisciplinary scientific journal *"3I - INTELLECT, IDEA, INNOVATION"*, Kostanay, 2014. Volume 3, pp. 97–100.
7. KOSHKINA A. Efficiency increasing in the heat pump system [Text] / A. Koshkina, M. Melnikov // *RIGA TECHNICAL UNIVERSITY:* the collection of reports of the 57th student scientific and practical conference. Riga. 2016. pp. 17–18.

8. AVERFALK, H.; Ingvarsson, P .; Persson, U .; Gong, M.; Werner, S. Large heat pumps in the Swedish district heating systems. *RENEWABLE & SUSTAINABLE ENERGY REVIEWS*. 2016, Vol. 79, pp. 1275–1284.
9. LI, YC.; LI, WY.; LIU, ZS; LU, J.; ZENG, LY.; YANG, LL; XIE, L. Theoretical and numerical study on the performance of the air-source heat pump system in Tibet. *RENEWABLE ENERGY*. 2017, Vol. 114, pp. 489–501.
10. LIM, H.; KIM, C.; CHO, Y.; KIM, M. Energy saving potentials from the application of heat pipes on geothermal heat pump system. *APPLIED THERMAL ENGINEERING*. 2017, Vol. 126, pp. 1191–1198.
11. ROSELLI, C.; SASSO, M.; TARIELLO, F. Dynamic Simulation of a Solar Electric Driven Heat Pump Integrated with Electric Storage for an Office Building Located in Southern Italy. *INTERNATIONAL JOURNAL OF HEAT AND TECHNOLOGY*. 2016, Vol. 34, pp. 637–646.
12. LUND, R.; ILIC, DD.; TRYGG, L. Socioeconomic potential for introducing large-scale heat pumps in district heating in Denmark. *JOURNAL OF CLEANER PRODUCTION*. 2016, Vol. 139, pp. 219–229.
13. OSTERGAARD, P.; ANDERSEN, A. .Booster heat pumps and central heat pumps in district heating. *APPLIED ENERGY*. 2016, Vol. 184, pp. 1374–1388.
14. Kim, M.H., Pettersen J., Bullard C.W. Fundamental process and system design issues in CO2 vapor compression systems. *Progress in Energy and Combustion Science*, 2004, Vol. 30, pp. 119–174.
15. RAY, D.; MCMICHAEL, D. Heat Pumps: Trans. with English. Moscow: Energoizdat, 1982. 224 p.
16. HEINRICH, G. et al. Heat pump plants for heating and hot water supply: Trans. with him. Ed. B.K. Yavnelya. Moscow: Stroiizdat, 1985. 351 p.
17. VASILIEV, G. Heat and cooling supply of buildings and structures using low-potential thermal energy of surface layers of the earth. M .: "Border", 2006. 173 p.
18. BYKOV, A; KALNIN, I; KRUZE, A. Refrigerating machines and heat pumps. Moscow: VO "Agropromizdat", 1988. 288 p.

CYSENI 2018, May 23-25, Kaunas, Lithuania
ISSN 1822-7554, www.cyseni.com

FEATURES AND RESULTS OF ADVANCED EXERGOECONOMIC EVALUATION OF A HEAT PUMP PROVIDING SPACE HEATING

V. Voloshchuk
National Technical University of Ukraine "Igor Sikorsky Kyiv Polytechnic Institute"
Politehnichna st. 56, 03056 Kyiv – Ukraine
Phone: +380 44 204 8098
Email: Vl.Volodya@gmail.com

A. Nikiforovich
Chernihiv National University of Technology
Shevchenka st. 95, 14027, Cernihiv – Ukraine
Email: Nikiforovich@ukr.net

ABSTRACT

In addition to conventional exergoeconomic evaluation, advanced exergoeconomic analysis provides information about at what rate the inefficiencies and costs can be avoided through technological improvements of the system and components, and in which proportion the inefficiencies and costs are resulted from interactions among components. The objective of the paper is to demonstrate application of the advanced exergetic and exergoeconomic analysis on a heat pump providing space heating in varying operational modes which is typical for built environment and caused by fluctuating in outdoor conditions. For this purpose a simulation model based on quasi-steady state approach was elaborated. The model takes into account thermal performance of a building for the specified time step and appropriate mode of the heat pump system. The analysis included splitting exergy destruction costs and investment costs within each component of the heat pump into unavoidable, avoidable, endogenous and exogenous parts. For this purpose the thermodynamic-cycle-based approach was used. For the analysis cumulative annual (seasonal) values of exergy-based parameters were taken into account. It is shown that in the investigated system the heat pump components due to their total avoidable costs can be sorted in descending order as: evaporator, compressor and condenser. Almost all these costs are endogenous i.e. are associated with the internal operating conditions of the mentioned components. The modified exergoeconomic factor based on avoidable endogenous cost rates shows that the evaporator and condenser are the components to which improvement of the exergy efficiency might be applied. In the other hand the value of the same modified exergoeconomic factor for the compressor illustrates that the cost effectiveness of the heat pump might be improved by reducing the capital investments for this component

Keywords: advanced exergoeconomic analysis; heat pump; space heating

1. INTRODUCTION

Exergoeconomics is exergy-based method providing information about location, magnitude, causes and costs of thermodynamic inefficiencies in an energy-conversion system [1–6]. This methodology identifies the relative cost importance of each component of the system and options for improving the overall cost effectiveness of it.

The conclusions provided from the exergoeconomic assessment can be substantially improved if the investment costs associated with system components and costs of exergy destructions within these components are split into unavoidable/avoidable and endogenous/exogenous parts. The evaluation based on these procedures is called as advanced exergoeconomic analysis which has been proposed and developed at the Institute for Energy Engineering of Technische Universität (TU) Berlin in the past twenty years [1–5, 7].

According to the current knowledge of the author advanced exergoeconomic analysis has been applied mostly to refrigeration machines and industrial heat pump systems where only single modes (design or nominal ones) were investigated [1–6]. A distinguish feature of the heat pump systems providing thermal comfort in buildings is variation of operational regimes.

The scope of the paper is to demonstrate application of the advanced exergoeconomic analysis on a heat pump providing space heating in varying operational modes which is typical for built environment and caused by fluctuating in outdoor conditions.

2. METHODOLOGY

According to the methodology of advanced exergoeconomic analysis the total exergy destruction and total investments costs in each system component can be split into endogenous/exogenous parts ($\dot{E}_{D,k} = \dot{E}^{EN}_{D,k} + \dot{E}^{EX}_{D,k}$ and $\dot{Z}_k = \dot{Z}^{EN}_k + \dot{Z}^{EX}_k$), unavoidable/avoidable parts ($\dot{E}_{D,k} = \dot{E}^{AV}_{D,k} + \dot{E}^{UN}_{D,k}$ and $\dot{Z}_{D,k} = \dot{Z}^{AV}_k + \dot{Z}^{UN}_k$), and combined according to the two approaches of splitting ($\dot{E}_{D,k} = \dot{E}^{UN,EN}_{D,k} + \dot{E}^{UN,EX}_{D,k} + \dot{E}^{AV,EN}_{D,k} + \dot{E}^{AV,EX}_{D,k}$ and $\dot{Z}_{D,k} = \dot{Z}^{UN,EN}_{D,k} + \dot{Z}^{UN,EX}_{D,k} + \dot{Z}^{AV,EN}_{D,k} + \dot{Z}^{AV,EX}_{D,k}$) [1–4, 8–9].

The endogenous part of exergy destruction and investments cost ($\dot{E}^{EN}_{D,k}$, $\dot{Z}^{EN}_k$) are associated only with the k-th component when all other components operate in an ideal way and the component being considered operates with its current efficiency.

The exogenous part of exergy destruction and investments cost ($\dot{E}^{EX}_{D,k}$, $\dot{Z}^{EX}_k$) are caused within the k-th component by remaining components (the irreversibilities that occur in them). The exogenous parts of these variables are calculated as the appropriate difference between total exergy destruction and total investments cost and endogenous parts of these values for a component being considered.

The unavoidable exergy destruction ($\dot{E}^{UN}_{D,k}$) cannot be further reduced due to technological limitations such as availability and cost of materials and manufacturing methods. The unavoidable investments costs ($\dot{Z}^{UN}_k$) will always be exceeded as long as such a component is used in a real system.

During the improvement procedure only the avoidable part of exergy destruction and investments cost ($\dot{E}^{AV}_{D,k}$, $\dot{Z}^{AV}_k$) should be considered as having real potential for system improvement. The differences between total and unavoidable exergy destruction and investments costs for a component respectively are considered as avoidable parts.

To split exergy destructions and investment costs into the above-mentioned parts the thermodynamic-cycle-based approach was used [1, 8, 9]. The product of the heat pump in all analysed cycles remained unchanged.

The sum of cost rates associated with investment costs consists of two contributions: costs due to capital investments ($\dot{Z}^{CI}_k$) and operating and maintanance expenses ($\dot{Z}^{OM}_k$) [1]

$$\dot{Z}_k = \dot{Z}^{CI}_k + \dot{Z}^{OM}_k \, . \tag{1}$$

To figure out these cost rates, the capital recovery factor should be calculated and yearly time of operation for the system, cost of the purchased equipment (PEC) and the factor of the operating and maintenance cost should be stated.

For estimation and sensitivity analyis of the equipment costs the following functions based and adapted from [1] were used

$$PEC_{CM} = \frac{k_{CM} \cdot \dot{m}_{CM}}{\eta^{UN}_{CM} - \eta_{CM}} \left(\frac{p_2}{p_1} \right) ln \left(\frac{p_2}{p_1} \right) \text{ – for compressor} \tag{2}$$

$$PEC_{CD} = k_{CD} \left(A_{CD} \right)^{0.6} \text{ – for condenser} \tag{3}$$

$$PEC_{EV} = k_{EV} \left(A_{EV} \right)^{0.6} \text{ – for evaporator} \tag{4}$$

where k_{CM}, k_{CD}, k_{EV} are constants; $\dot{m}_{CM}$ is mass flow rate of the working fluid through the compressor; p_2/p_1 - pressure ratio in the compressor; η_{CM} and η_{CM}^{UN} are isentropic efficiencies of the compressor in real cycle and corresponding to unavoidable exergy destruction in the compressor respectively (the latter is assumed to be equal to 96%); A_{CD} and A_{EV} are areas of heat-transfer surfaces of the condenser and evaporator respectively. All these values are estimated for the design operating conditions (nominal mode) of the system.

The purchased equipment costs for the throttling valve are neglected in the analysis as being vary small [2, 3].

It should be noted that in every case the cost functions and constants can be different compared to ones proposed in (2)–(4) [1, 11, 12].

The total costs were calculated as sum of costs due to investment and exergy destruction [6], $\dot{Z}_k + c_{F,k} \cdot \dot{E}_{D,k} = \dot{Z}_k + \dot{C}_{D,k}$, where $c_{F,k}$ presents the cost per unit of exergy for fuel of the k-th component and $\dot{C}_{D,k}$ is cost rate associated with the exergy destruction within the k-th component. The values of $c_{F,k}$ were estimated by specific exergy costing method (SPECO-method)) using cost balance and auxiliary equations for the components of the investigated heat pump [5].

The contribution of the investments cost, $\dot{Z}_k$, to the total costs associated with investments and exergy destruction in conventional exergoeconomic assessment is expressed by the exergoeconomic factor [1–3]:

$$f_k = \frac{\dot{Z}_k}{\dot{Z}_k + c_{F,k} \cdot \dot{E}_{D,k}}. \tag{5}$$

Furthermore, to better characterize the process or component being considered the exergoeconomic factor of the conventional exergoeconomic analysis can be adjusted by the help of the modified exergeoconomic factor ($f_k^{AV,EN}$) calculated exclusively on the avoidable endogenous costs as follows [1, 4]:

$$f_k^{AV,EN} = \frac{\dot{Z}_k^{AV,EN}}{\dot{Z}_k^{AV,EN} + c_{F,k} \cdot \dot{E}_{D,k}^{AV,EN}}. \tag{6}$$

The analysis is performed for a typical Ukrainian house. The dwelling has two floors with a gross floor area of 170 m² and a volume of 470 m³. The weighted average insulation value of non-glazed external surfaces is 0.5 W/(m²·K). U-value of windows including frames is 1.67 W/(m²·K). Internal heat gains are defined with a constant value of 5 W/ m². Setpoint for the indoor temperature is 18 °C. The fraction of east and west oriented glazing is 30%, of the south one – 50%, of the north one – 20%. Natural ventilation is used in the dwelling. The design heating capacity of the house is 25 kW. Hydronic system is used for space heating. The heat pump is a basic heater covering 12 kW of heating demand in the design mode and uses water as a low temperature heat source. R134a is chosen as a working fluid in the heat pump.

In the design operating conditions (nominal mode) of the heat pump the following parameter values are set: the low temperature heat source medium (water) is cooled in the evaporator from +6°C to +3°C; the minimal temperature differences in the evaporator and in the condenser are equal to 5 K. The calculated value of the real isentropic efficiency of the compressor in the nominal mode is equal to 82%. For evaluating unavoidable exergy destructions in nominal mode the following parameter values are assumed: the unavoidable temperature differences in the evaporator and the condenser are equal to 1 K. The unavoidable compressor efficiency is equal to 92%. For creating the theoretical cycle of the heat pump the following assumptions are used: the minimal temperature differences in the evaporator and the condenser are equal to 0K; the efficiency of the working fluid compression is equal to 100%; the throttling process is replaced by an ideal expansion process [5].

In order to determine thermodynamic parameters of the refrigeration vapor compresion cycle in different operating modes (off-design modes) during a heating season, which is typical for such kind of heat pumps, the mathematical model was used. The model is based on quasi-steady state approach [12]. A set of nonlinear equations, involving heat, mass balances, heat transfer and equations for calculation of thermodynamic properties of working fluids, was utilized. The equations, solved simultaneously with a gradient numerical method, were established to describe the behaviour of each component and of the system as a whole. During the simulation the temperature the heat source (water) in off-design modes varied in a range from +13 °C to +6 °C.

Daily weather data within a heating season for the city of Rivne located in the western part of Ukraine were used for the analyses. So, 24-hour time step was assumed for quasi-steady state modelling.

For exergetic and exergoeconomic assesment of the heat pump providing space heating it is proposed to take into account annual (seasonal) values (denoted with superscript yr). Within a heating season the investigated parameters are different for different operational modes. And it is not sufficient to analyze only single operational mode (for example, design mode).

In this research the outdoor air exactly follows the fluctuations of ambient conditions, so exergy always cancels out for ambient air.

For different operational modes ambient temperature can be reffered in a different manner to temperatures of working fluids of the heat pump. The reference temperature can be above, below or cross the temperatures of the heat source medium and the refrigerant. In such conditions different formulas should be used for calculating exergy associated with the fuel and product in the components of the system and associated costs per unit of exergy of the fuel and product respectively. Taking into account this features it is proposed to apply the exergoeconomics model for the every 24-hour time step of the assumed quasi-steady state approximation. In calculation of annualized exergoeconomic parameters the averaged over the heating season values of cost per unit of exergy associated with the fuel and product for the kth component were estimated using the formulas

$$c_{F,k}^{yr}=\frac{\sum_{\tau_n=1}^{T} c_{F,k}(\tau_n)\cdot E_{F,k}(\tau_n)}{\sum_{\tau_n=1}^{T} E_{F,k}(\tau_n)}; \tag{7}$$

$$c_{P,k}^{yr}=\frac{\sum_{\tau_n=1}^{T} c_{P,k}(\tau_n)\cdot E_{P,k}(\tau_n)}{\sum_{\tau_n=1}^{T} E_{P,k}(\tau_n)}, \tag{8}$$

where $E_{F,k}(\tau_n)$ and $c_{F,k}(\tau_n)$ are the exergy of fuel and the cost per unit of exergy associated with the fuel of the kth component for the specified time step τ_n; $E_{P,k}(\tau_n)$ and $c_{P,k}(\tau_n)$ are the exergy of product and the cost per unit of exergy associated with the product of the kth component for the specified time step τ_n; T - the total number of time steps within the heating season.

3. RESULTS AND DISCUSSIONS

The results of advanced exergetic analysis of the investigated vapor-compression heat pump are presented in Table 1.

Using results obtained from the conventional (without splitting the exergy destruction) exergetic analysis (see the first column of the Table 1), the following conclusions can be formulated. The most important component from the thermodynamic viewpoint is the throttling valve ($E_{D,TV}^{yr} = 897$ kW·hr/year). The compressor has the second position ($E_{D,CM}^{yr} = 623$ kW·hr/year). The third position is associated with the condenser ($E_{D,CD}^{yr} = 480$ kW·hr/year). And the evaporator is the last important component from the thermodynamic viewpoint ($E_{D,EV}^{yr} = 438$ kW·hr/year). So, the components should be improved in the following order: throttling valve, compressor, condenser and evaporator. These results are misleading to some extent. Among others it can be conluded that in order to reduce the exergy destruction within the throttling valve we should try improve this component. But a throttling process is completely irreversible and there are no ways of improving this process with the help of decreasing irreversibilities in it. Thermodynamic inefficiency in the throttling valve increases when the pressure ratio in it is also increased which can take place due to bigger temperature differences in the condenser and evaporator. So, exergy destruction within the throttling valve can be eliminated with the help of improving condenser and evaporator but not the throttling valve itself. The same conclusion is refferd to the compressor. Also from the conventional analysis we obtain misleading information with respect to the relative importance of the condenser and the evaporator. The matter is that the condenser has the higher exergy destruction without splitting but at the same time compared to the evaporator it can be characterized with the higher exergy destruction which cann‘t be avoided. As a result thermodynamic inefficiency which can be really eliminated in this component can be lower than in the evaporator.

Table 1. Advanced exergetic analysis of the vapor-compression heat pump (splitting the exergy destructions)

Component	**Unit**	$E_{D,k}^{yr}$	$E_{D,k}^{UN,yr}$	$E_{D,k}^{AV,yr}$	$E_{D,k}^{EN,yr}$	$E_{D,k}^{EX,yr}$	$E_{D,k}^{UN,yr}$		$E_{D,k}^{AV,yr}$	
							$E_{D,k}^{UN,EN,yr}$	$E_{D,k}^{UN,EX,yr}$	$E_{D,k}^{AV,EN,yr}$	$E_{D,k}^{AV,EX,yr}$
Compressor	kW·hr/yr	623	209	413	394	228	187	22	207	207
	%	100	34	66	63	37	30	4	33	33
Condenser	kW·hr/yr	480	302	178	474	6	300	2	174	4
	%	100	63	37	99	1	63	0	36	1
Throtling valve	kW·hr/yr	898	704	194	653	245	653	51	0	194
	%	100	78	22	73	27	73	6	0	22
Evaporator	kW·hr/yr	438	202	236	451	-12	208	-6	243	-6
	%	100	46	54	103	-3	47	-1	55	-1

Taking into account the above-mentioned information we need more precise, detailed and additional information about irreversibilities within the system. This can be provided by advanced exergy-based analysis [1–4, 6, 8, 9].

As can be seen from the Table 1 it is possible to decrease 66%, 37%, 22% and 54% of the total exergy destruction in the compressor, condenser, throtling valve and evaporator respectively.

The throtling valve and the condenser have quite close values of exergy destruction which can be really removed ($E_{D,TV}^{AV,yr} = 194$ kW·hr/year and $E_{D,CD}^{AV,yr} = 178$ kW·hr/year). The compressor and the evaporator are characterized with higher values of avoidable exergy destructions ($E_{D,CM}^{AV,yr} = 413$ kW·hr/year and $E_{D,EV}^{AV,yr} = 236$ kW·hr/year).

The results obtained from the advanced exergetic analysis indicate that the endogenous avoidable exergy destruction in the throttling valve is zero. This means that the exergy destruction within this component can be reduced through changes in the remaining components or in the structure of the overall system. Only 207 kW·hr/year of exergy destruction in the compressor can be avoided by improving this component. The endogenous avoidable exergy destructions in the evaporator and condenser are equal 243 kW·hr/year and 174 kW·hr/year respectivetly.

The biggest part of exergy destruction that can be avoided in the compressor is exogenous, i.e. can be eliminated through changes in the remaining components or in the structure of the overall system, and is equal $E_{D,CM}^{AV,EX,yr} = 207$ kW·hr/year. All thermodynamic inefficiency which can be avoided in the throttling valve is due to the remaining components or in the structure of the analyzed heat pump. Very small values of avoided exogenous exergy destruction belong to the condenser and the evaporator.

The results from splitting the investments cost are presented in Table 2. The unavoidable investment costs, $Z_k^{UN,yr}$, of the components are higher than their avoidable ones, $Z_k^{AV,yr}$, and constitute 65%, 83% and 64% for the compressor, condenser and evaporator respectively. Meanwhile, the avoidable investment costs indicate that priority should be given to the compressor. The highest values of the investments cost in the components of the heat pump are endogenous, $Z_k^{EN,yr}$, which shows that component interactions are not of high priority as their internal operation. The results presented in Table 2 show that the largest part of the avoidable endogenous investment cost, $Z_k^{AV,EN,yr}$, is associated with the compressor and is equal to 542 Euro/year. The highest value of the avoidable exogenous investment cost (but with negative value), $Z_k^{AV,EX,yr}$, is also found for the compressor (-151 Euro/year). The latter means that it is possible to decrease to some value the investment costs of the compressor due to decrease exergy destruction within the other components.

Table 2. Splitting the investment costs for components of the vapor-compression heat pump

Component	**Unit**		$Z_k^{UN,yr}$	$Z_k^{AV,yr}$	$Z_k^{EN,yr}$	$Z_k^{EX,yr}$	$Z_k^{UN,yr}+C_{D,k}^{UN,yr}$		$Z_k^{AV,yr}+C_{D,k}^{AV,yr}$	
							$Z_k^{UN,EN,yr}$	$Z_k^{UN,EX,yr}$	$Z_k^{AV,EN,yr}$	$Z_k^{AV,EX,yr}$
Compressor	Euro/yr	1113	722	391	1071	42	529	193	542	-151
	%	100	65	35	96	4	48	17	49	-14
Condenser	Euro/yr	135	113	22	124	11	95	17	28	-6
	%	100	83	17	92	8	71	13	21	-4
Evaporator	Euro/yr	99	64	36	109	-9	76	-12	33	3
	%	100	64	36	109	-9	76	-12	33	3

The results of splitting the total costs, $Z_k^{yr} + c_{F,k} \cdot E_{D,k}^{yr} = Z_k^{yr} + C_{D,k}^{yr}$, for components of the investigated heat pump are presented in Table 3. As seen the compressor presents the highest total costs (1135 Euro/year). The total costs for the condenser, throtling valve and evaporator are characterized with lower values (363, 182 and 790 Euro/year respectively). Table 3 shows that for the system analyzed here, the compressor and the evaporator are the components with the highest potential for reducing the total costs of the overall system. This potential is due to the relatively high avoidable total costs, $Z_k^{AV,yr} + c_{F,k} \cdot E_{D,k}^{AV,yr}$, associated with both components (405 and 408 Euro/year respectively). It is found that for the condenser and the throttling valve the avoidable total costs are lower compared with the compressor or the evaporator and are equal to 107 and 39 Euro/year respectively. Exogenous parts of the total costs, $Z_k^{EX,yr} + c_{F,k} \cdot E_{D,k}^{EX,yr}$ or $Z_k^{AV,EX,yr} + c_{F,k} \cdot E_{D,k}^{AV,EX,yr}$, are not high for the components of the analyzed heat pump. But it is observed that for the compressor, condenser and evaporator exogenous parts of the total costs which can be avoided are negative.

Fig. 1 presents values of the modified exergoeconomic factor, $f_k^{AV,EN}$, based on avoidable endogenous costs. As seen from the Fig. 1, the values of the $f_k^{AV,EN}$ for the evaporator and condenser mean that the cost effectiveness of the heat pump might be improved by improvement of the exergy efficiency of these components (at the expense of increasing investment costs). Moreover, it should be mentioned that inreasing thermodynamic efficiencies within the evaporator and condenser can make the total cost for the compressor lower due to deccrease of the investments cost of this component (negative value of exogenous avoidable part of the investments cost illustrate this in Table 2). Additional information concerning this case can be gained after further splitting the exogenous avoidable total cost for the compressor. The high value of the same modified exergoeconomic factor for the compressor means that reducing the investment cost for this component (at the expense of its efficiency) can substantially decrease the total cost of the investigated heat pump. But this decision is not preferable.

The validity of these conclusions will be verified in further investigations.

Table 3. Splitting the total costs for components of the vapor-compression heat pump

Component	**Unit**	$Z_k^{yr}+$ $+C_{D,k}^{yr}$	$Z_k^{UN,yr}+$ $+C_{D,k}^{UN,yr}$	$Z_k^{AV,yr}+$ $+C_{D,k}^{AV,yr}$	$Z_k^{EN,yr}+$ $+C_{D,k}^{EN,yr}$	$Z_k^{EX,yr}+$ $+C_{D,k}^{EX,yr}$	$Z_k^{UN,yr}+C_{D,k}^{UN,yr}$		$Z_k^{AV,yr}+C_{D,k}^{AV,yr}$	
							$Z_k^{UN,EN,yr}+$ $+C_{D,k}^{UN,EN,yr}$	$Z_k^{UN,EX,yr}+$ $+C_{D,k}^{UN,EX,yr}$	$Z_k^{AV,EN,yr}+$ $+C_{D,k}^{AV,EN,yr}$	$Z_k^{AV,EX,yr}+$ $+C_{D,k}^{AV,EX,yr}$
Compressor	Euro/yr	1135	729	405	1085	50	536	194	549	-144
	%	100	64	36	96	4	47	17	48	-13
Condenser	Euro/yr	363	256	107	349	14	238	18	111	-4
	%	100	71	29	96	4	66	5	31	-1
Throttling valve	Euro/yr	182	143	39	132	50	132	10	0	39
	%	100	78	22	73	27	73	6	0	22
Evaporator	Euro/yr	790	382	408	819	-29	404	-22	415	-7
	%	100	48	52	104	-4	51	-3	53	-1

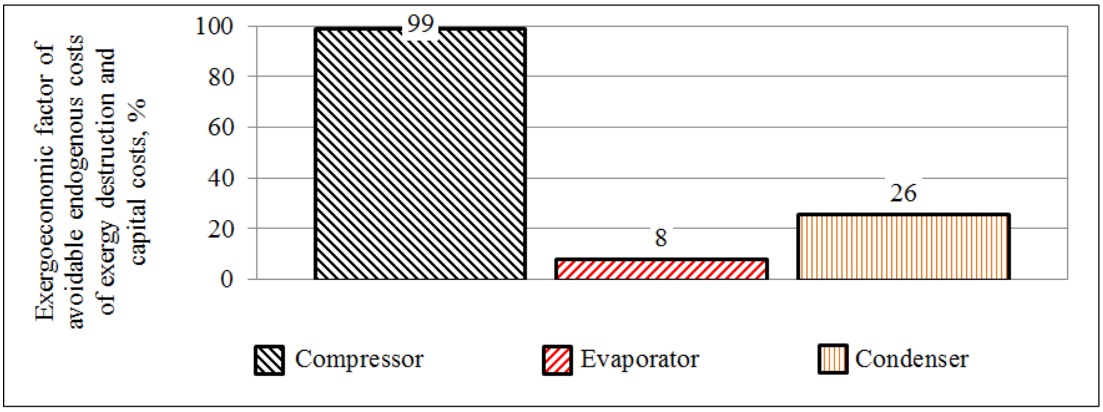

Fig. 1. Values of the modified exergoeconomic factor, $f_k^{AV,EN}$, based on avoidable endogenous costs

4. CONCLUSIONS

1. The advanced exergy-based evaluation enables to distinguish and focus only on avoidable thermodynamic inefficiencies and associated costs. Decisions about changes in the component of a system should be based on the endogenous avoidable and on the exogenous avoidable values of the appropriate variables for the component being considered. This allows to simultaneously evaluate the effectiveness of the component itself and its interactions with the remaining components.
2. The advanced exergy estimation has shown that in the investigated water-source heat pump for space heating the compressor and the evaporator are the components causing the biggest values of exergy destructions (413, and 326 kW·hr/year respectively) which can be removed. The avoidable exergy destructions of the compressor and the throttling valve mostly depend on irreversebilies within other components. On the contrary the avoidable exergy destruction in the condenser and evaporator are caused by thermodynamic efficiency within this component.
3. The biggest part of the heat pump avoidable investment expenditures are due to the compressor (391 Euro/year). This cost can be decreased substantially with the help of increasing thermodynamic inefficiencies within the compressor itself. But, according to the results obtained it is possible to make lower the investment cost of the compressor due to decrease of thermodynamic inefficiencies within the other components (negative value of exogenous investment cost demonstrates this).
4. According to the results received, the compressor and the evaporator are the components with the highest potential for reducing the total costs of the overall system. This potential is due to the relatively high avoidable total costs, $Z_k^{AV,yr} + c_{F,k} \cdot E_{D,k}^{AV,yr}$, associated with both components (405 and 408 Euro/year respectively). Almost all these costs are endogenous e.i. caused by the same components. For the condenser and the throttling valve the avoidable total costs are lower compared with the compressor or the evaporator and are equal to 107 and 39 Euro/year respectively.
5. The values of the modified exergoeconomic factor, $f_k^{AV,EN}$, based on avoidable endogenous costs for the evaporator and condenser indicate that the cost effectiveness of the heat pump might be improved by improvement of the exergy efficiency of these components. The high value of the same modified exergoeconomic factor for the compressor means that reducing the investment cost for this component can decrease the total cost of the investigated heat pump. Meanwhile, further splitting exogenous avoidable total cost for the compressor can provide information concerning how increasing thermodynamic efficiencies within the evaporator and condenser can make the total cost for the compressor lower due to decrease of the investments cost of this component (negative value of exogenous avoidable part of the investment cost illustrate this).

REFERENCES

1. TSATSARONIS, G., MOROSUK T. Advanced exergy-based methods used to understand and improve energy-conversion systems. CPOTE-2016. Proceedings of the 4th International Conference on Contemporary Problems of Thermal Engineering. Gliwice – Katowice: The Silesian University of Technology Institute of Thermal Technology. 2016 September 14–16.
2. TSATSARONIS, G. Exergetic and Economic Performance – Strategies for Optimizing Energy Systems. The LowEx Symposium. Program and Proceedings, Kassel, Germany, October 28–29, 2009. Kassel, Germany, 2009. – P. 18–27.
3. TSATSARONIS, G. Minimization of Costs and Environmental Impact Using Exergy-Based Methods. The Future for Sustainable Built Environments with High Performance Energy Systems. Program and Proceedings, Munich, Germany, October 19–21, 2010. – P. 185–198.

4. TSATSARONIS, G., MOROSUK T. Exergoeconomic evaluation of refrigeration machines based on avoidable endogenous and exogenous costs. The 20th International Conference on Efficiency, Cost, Optimization, Simulation and Environmental Impact of Energy Systems. Program and Proceedings, Vol 3, Padova, Italy, June 25–28, 2007. – P.1459–1467.
5. MOROSUK, T. Elements of exergoeconomics for the analysis of compressor heat pumps. VI Minsk International Seminar “Heat Pipes, Heat Pumps, Refrigerators”. Program and Proceedings, Minsk, Belarus, September 12–15, 2005 – P. 403–409.
6. ERBAY, Z., HEPBASLI, A. Advanced exergoeconomic evaluation of a heat pump food dryer Biosystems engineering. – 2014. – Vol. 124. – P. 29–39.
7. TSATSARONIS G. Strengths and limitations of exergy analysis. Proceedings of the NATO Advanced Study Institute on Thermodynamics and the Optimization of Complex Energy Systems. Neptun, Romania. 1998 July 13-24: Kluwer Academic Publishers. p. 93–100.
8. MOROSUK, T., TSATSARONIS, G. Advanced exergetic evaluation of refrigeration machines using different working fluids. Energy, 2009, Vol. 34, p. 2248–2258.
9. MOROSUK, T., TSATSARONIS, G. New approach to the exergy analysis of absorption refrigeration machines. Energy, 2008, Vol. 33, p. 890–907.
10. WALL, G. Optimization of refrigeration machinery. Int. Journal of Refrigeration. – 1991. – № 7 – P. 336–340.
11. D’ACCADIA, M. D., De Rossi, F. Thermoeconomic Optimization of Refrigeration Plant Int. Journal of Refrigeration. – 1998. – № 21 – P. 42–45.
12. HERBAS, T. B., BERLINCK, E. C., URIU, C. A. T., MARQUES, R. P., PARISE, J. A. R. Steady-state simulation of vapor-compression heat pump. International Journal of Energy Research, 1993, Vol. 17, p. 801–816.

CYSENI 2018, May 23-25, Kaunas, Lithuania
ISSN 1822-7554, www.cyseni.com

INVESTIGATION OF PROCESSES IN A GRATE FURNACE TO INTENSIFY BIOFUEL DRYING

Lina Vorotinskienė, Nerijus Striūgas
Lithuanian Energy Institute
Laboratory of Combustion Processes
Breslaujos str. 3, LT-44403 Kaunas – Lithuania
Email: lina.vorotinskiene@lei.lt

ABSTRACT

Widespread and long-term use of fossil fuel resulted in serious environmental effects, such as global climate warming. Biomass is the most prospective alternative to fossil fuel in thermal energy production therefore, biofuel is also used for district heating especially prevalent in Lithuania. This situation leads to increased demand for biofuel, resulting in biofuel price increase. Price of biofuel depends on its properties, especially the moisture content. The moisture content in biofuel can vary from 30% to 60%. In order to increase efficiency of energy use and to improve the product quality in terms of energy content and to reduce emissions during energy conversion, biofuel must be dried out. The choice of drying process and optimization of drying conditions requires detailed understanding and quantitative estimation of biomass material, requirements for energy transformation and drying process.

The aim of this work is to investigate the possibilities of the biofuel drying intensification process by the experiments performed on the rig, which imitates the processes occurring in the furnace systems.

The work analyses the processes taking place during drying of biofuels in a furnace and their properties. The experiments were performed with three different types of biofuel. The biofuel samples analysed in this work differed from each other not only by their physical and chemical properties, but also by their granulometry.

To investigate the possibilities of biofuel drying intensification, three setups of increasing affection to biofuel drying were implemented, where the biofuel was exposed to: a) heated air, which simulated the furnace primary air inlet, b) heated air and steam, which simulated the flue gas recirculation in the furnace, c) infrared radiation, which simulated the radiation from the hot inside walls of the furnace.. An increase in the inlet air temperature from 50 ^{o}C to 200 ^{o}C resulted in decrease in residual moisture content from 0.87 to 0.72, respectively.

Radiation of the hot surfaces inside the furnace has the largest effect on biofuel drying intensity, whereas injection of recirculating flue gas into the drying zone in the furnace reduces the biofuel drying intensity.

Keywords: biofuel, furnace, moisture content, drying, radiation.

1. INTRODUCTION

Expansion of district heating supply (DHS) systems and efforts to connect not only urban apartment buildings but also most of the individual houses to the DHS networks requires building as large as possible energy market for “clean” and efficient utilisation of local fuel. Implementation of modern technologies, expansion of cheaper biofuel, increasing efficiency of heat production and reduction of heat loss in distribution networks require large financial resources and efforts. Suppliers of district heating in Lithuania chose biofuel as a substitute for gas fuel in order to reduce heat supply costs and to become more competitive. In EU countries, biofuel replaces fossil fuel also due to increasing requirements to produce energy from renewable sources. Grate and fluidised bed furnaces are mainly used for biomass firing. Grate furnaces are most widespread, however, in order to fire biofuel optimally and safely in this type of furnaces, fuel must be of high quality and have a constant moisture content. Ever increasing demand for biofuel results in increasing prices. To remain in the market and to stay competitive, heat producers choose humid biofuel of lower quality, with varying moisture content of up to 60% (by mass) and more. This kind of fuel does not burn on a grate but rather dries out occupying the largest space on the grate [1]. Besides, moisture evaporated from fuel increases CO_2 emissions during combustion and reduces calorific value [2]. In order to combust this type of biofuel smoothly and optimally in grate-based furnaces, it is necessary to measure biofuel moisture content in real time and to correct automatic control instrumentation or to dry fuel out [3].

Moisture content in biofuel is measured either directly (fuel analysis) or indirectly (flue gas analysis). Methods of direct fuel moisture measurement include infrared spectroscopy (NIR), double X-ray analysis, microwave and nuclear magnetic resonance (NMR) analysis [4]. Due to economic considerations and difficulties in adopting direct methods in small biofuel boiler facilities, indirect fuel moisture measurements are applied. There is a number of indirect methods and means for biofuel moisture measurements: Fourier transformed infrared analysis (FT-IR) [5], diode laser spectroscopy [6], relative humidity (RH) sensors [7]. Fourier transformed infrared technology is a sufficiently precise method to determine moisture content in biofuel, but it is an expensive technology requiring great deal of skills. The drawback of the humidity sensor method is the measuring signal delay – time of gas travel from combustion chamber to the measuring position. Niedermayr et al [2] presented an advanced fuel supply system: a smart crane grabber equipped with various sensors, such as ultrasound transducer, humidity sensor and image recognition using a camera. This method might help avoid variations of furnace operation regime due to varying moisture content, as well as reduce CO_2 emissions, but this system has been tried out only in a lab scale (up to 500 kW).

As an alternative to fuel drying, Italian scientists proposed a “smart grabber” system. The storage facility is separated into zones according to properties of stored fuel, and fuel of desired moisture content is supplied to the furnace by means of the smart grabber according to the selected algorithm, thereby ensuring stable operation of the furnace [2]. Additional fuel drying is also used, but such drying requires investments to equipment and increases the price of supplied heat.

This work analyses influence of the processes in the furnace such as primary air supply, recirculation of flue gas and radiation from hot surfaces inside the furnace to biofuel drying on the grate, in order to achieve the optimal fuel combustion in the furnace when supplying moist biofuel without additional investments.

2. MATERIALS AND METHOD

Three different experiments were performed during this analysis: the first experiment was performed in order to investigate the effect of primary air supply, the second one to investigate the effect of recirculation gas and the final one to investigate the effect of radiation to the biofuel layer in the furnace drying zone.

2.1. The methodology for experimental investigation of moisture content variation in biomass layer during drying process

All experiments were performed in order to determine the effect of primary air, recirculation products and radiation of the hot surfaces to biofuel drying process on the grate (Fig. 1). Primary air, as well as the recirculation products, is supplied to the furnace through the grate, get saturated with moisture while permeating the layer of biofuel and thereby desiccates it. In order to investigate the effect of primary air and recirculation products to drying process, an experimental biofuel drying rig was designed and installed in the laboratory (Fig. 2). For the experiments the operation parameters were selected to match those of a real 6 MW furnace. The scheme of the rig is shown in Fig. 2.

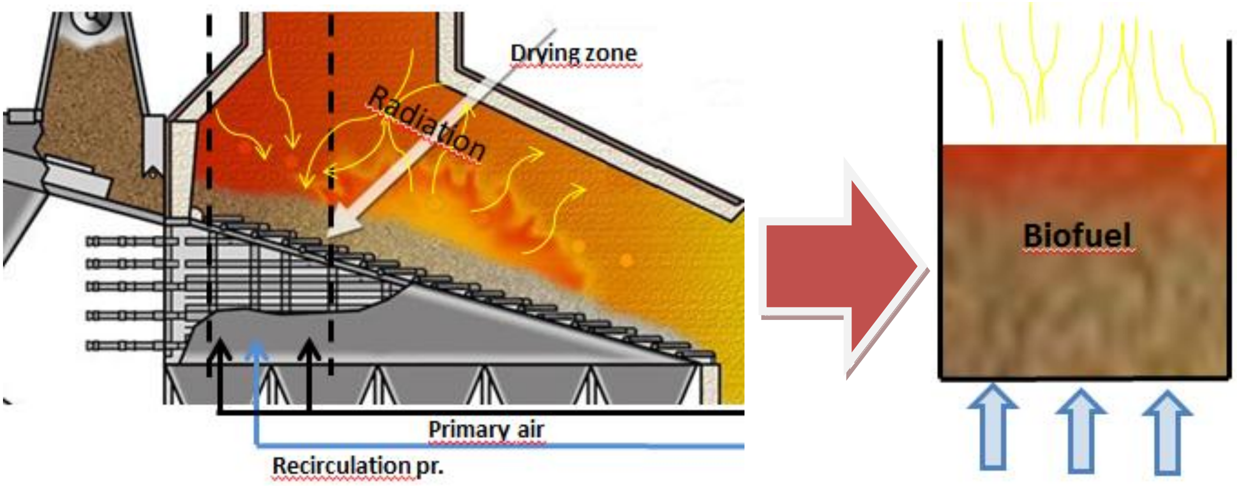

Fig. 1. Effects influencing biofuel drying on the grate

The experimental biofuel drying rig consists of the following main parts: electrical heaters, a steam generator and a drying chamber. Ambient air used for experiments passes through a compressor, a control valve *1* and a rotameter *2* and is preheated as it enters an air duct. According to the installed grate surface area (0.08 m^2), the required air flow rate was calculated to be 17.65 m^3/h. This flow rate is selected to reproduce the real processes in a furnace related to biofuel combustion. For air heating, two heating coils *3* are installed in the air duct with the maximum electrical power of 4000 W. In order to achieve precisely the desired temperature of the air supplied to the grate, the power of the heating coils was reduced by a transformer. The air preheated to the desired temperature is supplied through the duct to the drying chamber *4*. Air enters the drying chamber through a steel mesh *5*. The steel mesh consists of two layers so that small particles of biofuel do not drop into the air duct. The holes of the first mesh, through which preheated air flows, have the diameter of 10 mm, and those of the second one have the diameter of 1 mm. Five k-type thermocouples *6* are installed inside the experimental setup for temperature measurements at various points. In the front wall of the drying chamber, an observation opening *7* was installed, to observe the process and reduce the risk of biofuel ignition. The thermocouples are connected to the data acquisition device *8* PICO TC-08. The data of these temperature sensors gives better understand in what points of the biofuel layer drying is more intense and where it goes on slowly.

For experiments using steam, a steam generator *9* was installed in the setup. Steam flow rate was adjusted by a valve.

To imitate radiation from hot surfaces of the furnace, two infrared lamps (12) were installed above the biofuel layer in the biofuel drying and combustion setup. The maximum power output of the infrared lamps was 4000 W, which corresponds to radiation intensity of 50 kW/m^2 in the furnace.

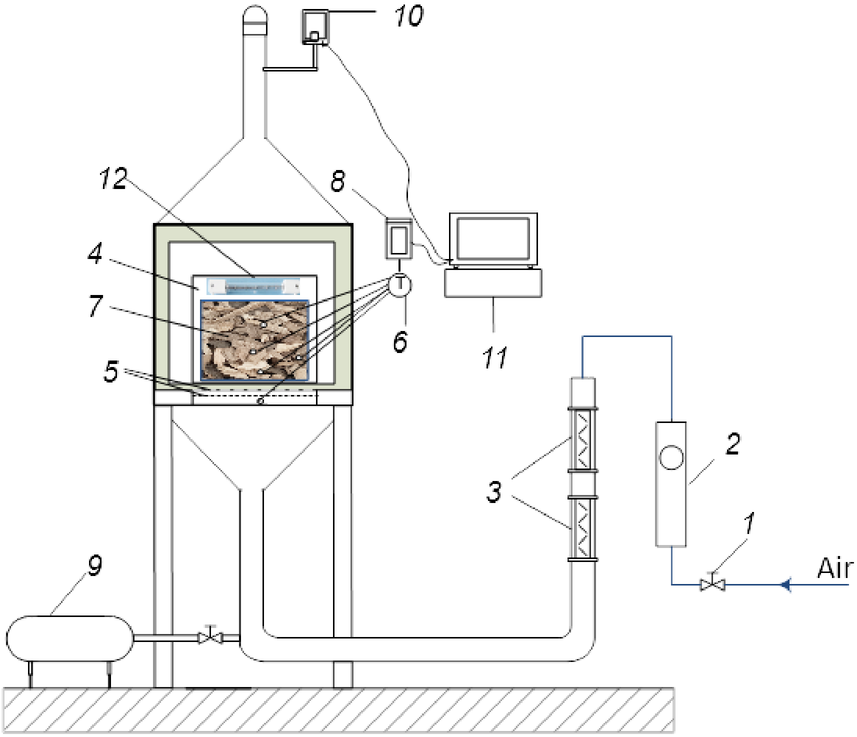

Fig. 2. Biomass drying rig: 1 – control valve; 2 – rotameter; 3 – heating coils; 4 – biomass drying chamber; 5 – steel mesh; 6 – k-type thermocouples; 7 – observation opening; 8 – data acquisition device; 9 – steam generator ; 10 – Testo 454 with a connected RH sensor; 11 – computer data collection and storage; 12 –infrared lamp

In the beginning of a biomass drying experiment, the entire system was preheated. Air heats up to the temperature required for the experiment by flowing around 2 heating coils. During experiments, biofuel was dried with temperatures of 50 ^{o}C, 100 ^{o}C, 150^{o}C, 200 ^{o}C. The temperature of preheated air was measured before flowing through the grate and controlled by the heating coils. After stabilization of the parameters of the unloaded experimental setup, i.e., the selected air flow rate and temperature, the drying chamber (33.5 × 23 × 23,5 cm) was loaded with a 23 cm deep layer of biomass. When using steam in experiments, the supplied steam flow rate was constant in all experiments at 17 g/m^3. The readings of thermocouples were collected and processed using the software of PICO TC-08. The average moisture content of biofuel was estimated by measuring the air humidity at the outflow. Air humidity was measured by a measurement unit Testo 454 with a connected relative humidity (RH) sensor 10 (accuracy, 2%RH of +2 to +98%RH). The humidity analyser and the PICO TC-08 unit processing the readings of the thermocouples were connected to a computer *11* for data collection and analysis.

2.1.1. Used samples

For the second experiment were used biomass was mix of bark chips with chips of different tree branches. The main characteristics of the used sample are presented in Table 1.

Table 1. The characteristics and compositions of used samples

Fuel	**HHV, (kJ/kg)**	**MC wt. %**	**A, wt. %**	**C, %**	**H, %**	**N, %**	**S, %**	**O (diff.), %**
Chips of various species of tree branches with bark	18998	36	3.50	48.6	5.80	0.60	< 0.01	49.99

Before starting the experiments in the biomass drying rig, the samples were soaked until the water content reached up to 60 wt % to correspond to the moisture content of biomass which is supplied to heating plants during cold season. The special stainless steel bucket was filled with the wood chips and the bucket was inserted into the barrel filled with water to soak for 16 hours. After it, the bucket was pulled out and left to dry for 2 hours.

Biofuel particle size parameter is important because many particle systems can be homogenized for a simpler heat and mass transfer considerations. A wood chip particles are non-uniform in their length, and their shapes are similar to hexahedron. During the sieving experiment only the characteristic particle length can be obtained, which actually corresponds to the spherical particle. The characteristic length was determined by sieving through eight meshes of various fractions. The wood chip particles of the average diameter, which was determined from Fig. 3 to be equal to 13 mm, comprise 50% of the total mass [8].

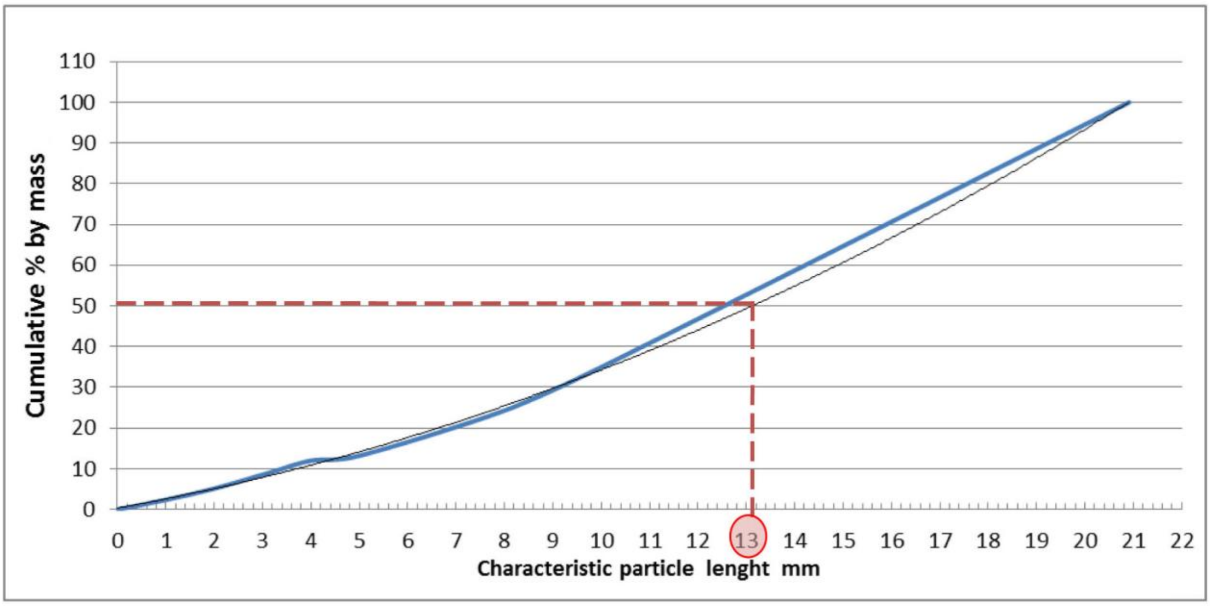

Fig. 3. Distribution of particles of different lengths as cumulative percentages of mass

3. RESULTS AND DISCUSION

3.1. Influence of primary air supply and recirculation products to changes in moisture content in a biofuel layer

Particle size distribution of the tree bark samples used for experiments can be very different and this might influence significantly the shapes of the drying curves, therefore, each experiment was repeated five times. The first experiments were performed using preheated air only. Fig. 4 shows the changes of biofuel moisture content with changing temperature of the supplied air. In the chart, the moisture content is normalized to the maximum value. The results of the experiments show that the drying intensity grows as the supplied air temperature grows. After 30 minutes drying chips of various wood types with bark with 50 °C air the moisture content remaining in the sample decreases by 1%. When drying with air heated to 200 ^{o}C, the moisture content remaining in the wood chips decreases by 13%.

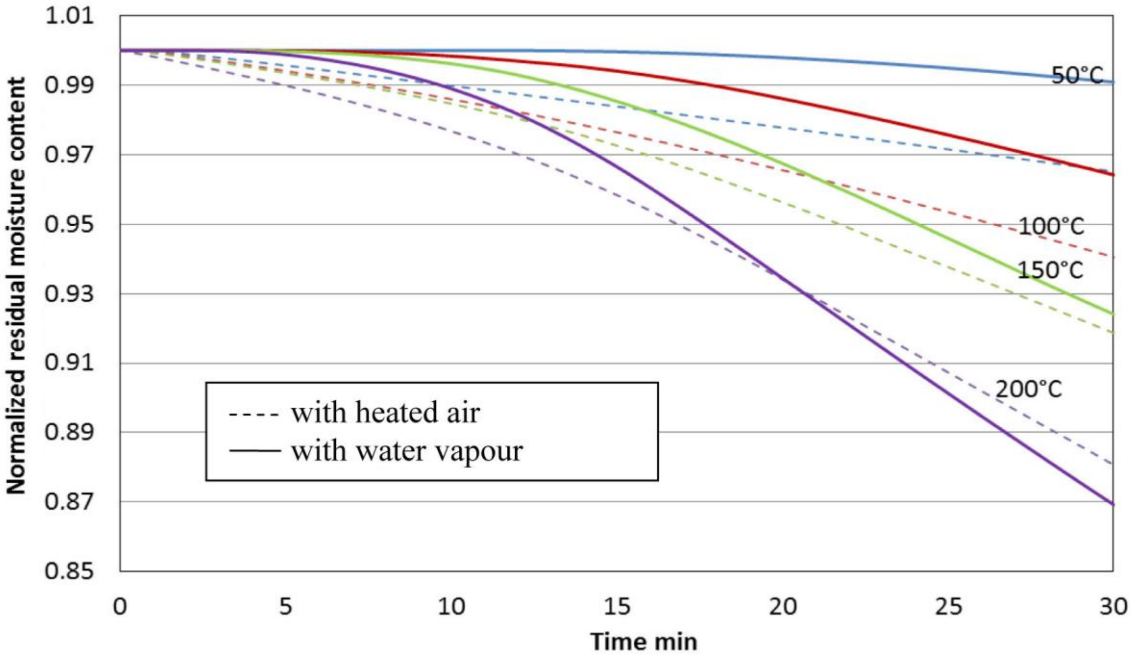

Fig. 4. Changes in biofuel sample moisture content when changing the drying air and water vapour temperatures

Flue gas recirculation is installed in the currently operating biofuel boilers. Recirculation means returning flue gas back into the combustion chamber. The biofuel boilers are designed in a way where the recirculation products are supplied into the combustion chamber through the bottom of the grate. In order to intensify biofuel drying in the drying zone of the grate, it is necessary to research not only the influence of primary air to biofuel drying, but the influence of recirculation products as well. Experiments were performed where biofuel samples were dried using air–water mixture, imitating the influence of recirculation products. The obtained experimental results have shown that drying intensity of biofuel layer depends significantly on the temperature of recirculation products and biofuel properties.

Humidity of flue gas was measured during experiments with air–water mixture. The temperatures of air–water mixture were set equal (50 °C, 100 °C, 150 °C and 200 °C) to those of previous experiments where biofuel was dried with preheated air only. The measurement results are shown in Fig. 4. Supply of low temperature (up to 100 °C) water steam slows down the drying process and the moisture content in biofuel differs by approximately 4% after 30 min compared to the case without steam supply. In this drying situation, moisture evaporation becomes less intense due to condensation process which is unavoidable here due to cold biofuel entering the furnace. The drying agent cools down, gets saturated with moisture as it flows through moist and cold biofuel and condenses on warmer surfaces present in higher layers of biofuel. The more saturated with moisture is the drying agent; the more rapid and intense is this process. Repetitive conversion of water to steam requires energy and time, therefore, recirculation of low temperature flue gas to the drying zone of the furnace extensities drying and combustion of biofuel. When drying chips of branches with bark of various trees by overheated water steam of 150–200°C temperature, we observe initially (for 10–15 min, respectively) the same undesirable slowing down of the drying process, but when drying the sample for 20 min, influence of drying flue gas recirculation products to the drying process decreases, and at the water steam temperature of 200 °C, it doesn’t have influence at all. When drying the sample for 20 min by overheated steam of 200 °C temperature or by air preheated to 200 °C temperature, heating up of biofuel batch and absence of condensation are observed. After the temperatures higher than the dew point are attained in the batch, influence of recirculation products to the drying process is observed. The drying process becomes more intense than in case with preheated water vapour, due to physical properties of steam, whereby steam transfers heat to another medium more rapidly. Preheated steam or hot air heat transfer coefficient depends on many factors such as: temperature, flow rate, thermal conductivity coefficient et al. and may range from 1 to 1000 W/m^{2}K. But when steam becomes saturated steam heat transfer coefficient increases by twenty times [10].

3.2. Influence of primary air supply and radiation of the hot surfaces to changes in moisture content in a biofuel layer

From the experiments imitating injection of recirculation products and primary air from the lower side of the grate, we determined only the influence of drying processes taking place through convection. The biofuel layer on a grate is also influenced by radiation, therefore, we also performed experiments with infrared radiation lamps, imitating radiation from hot surfaces of the furnace.

From the trends shown in Fig. 5 we can state that radiation from hot surfaces of the furnace has large influence to biofuel drying in the furnace. After 30 minutes drying period for chips made from tree branches with bark by air preheated to 200 °C and infrared lamps, moisture content in fuel decreased by 28%, whereas in case of drying by air only, moisture content remaining in sample decreased by only 12%.

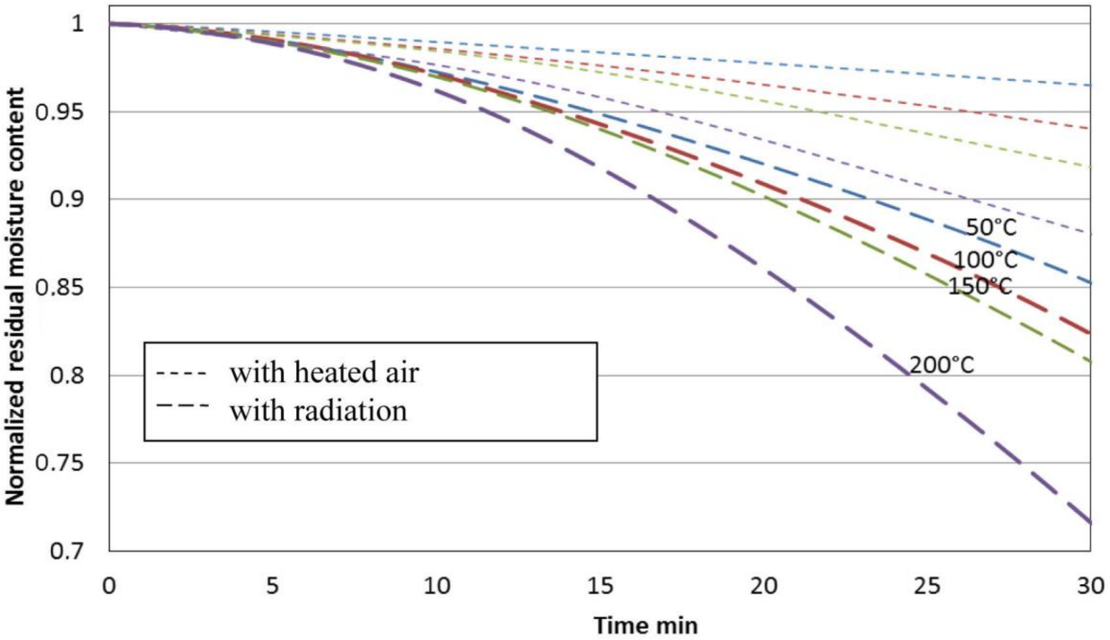

Fig. 5. Changes in biofuel sample moisture content after drying by an infrared lamp and drying air of various temperatures

Fig. 5 shows experimental results of biofuel drying by preheated air and infrared lamps. Changes of moisture content in the sample per time unit is normalized to the maximum moisture content in the sample. The obtained curves show that when drying biofuel with preheated air only, without radiation, the sample dries out during the first minutes in the same way as in the case when the sample is being dried out with both preheated air and radiation. This effect arises because drying air saturates with humidity as it flows through a wet sample and produces a steam canopy above the biofuel layer that is impermeable to radiation. This effect is seen evidently when drying biofuel out by air with the temperature of 200 °C. The same effect was also observed in analysis of biofuel combustion in a furnace reported in Ref. [9].

4. CONCLUSIONS

1. Experiments of drying were carried out with four temperature values of drying air: 50 °C, 100 °C, 150 °C and 200 °C. Analysis of the obtained results imply that increasing the temperature of drying air leads to higher drying rate of biofuel layer on the grate. An increase in the inlet air temperature from 50 ^{o}C to 200 ^{o}C resulted in decrease in residual moisture content from 0.87 to 0.72, respectively. Supply of flue gas recirculation products through the grate extensities the biofuel drying process. Only at high temperatures of recirculation products and only after 20 mins and later, intensification of drying of biofuel layer was observed equivalent to the case of drying with preheated drying air.
2. Radiation from the hot internal surfaces of the furnace was imitated by infrared lamps of 4000 W power output, corresponding to radiation intensity in the furnace of 50 kW/m^2. High temperature of primary air of 200 °C and radiation from hot surfaces of the furnace can reduce the moisture content in biofuel by up to 28% in 30 minutes.

REFERENCES

1. Bauer, R., Gölles, M., Brunner, T., Dourdoumas, N., & Obernberger, I. Modelling of grate combustion in a medium scale biomass furnace for control purposes. Biomass and bioenergy, 2010, 34(4), 417–427.
2. Niedermayr F, Waid S, Auñón DG, Riedl M, Matt D. Design of a scalable and robust woodchip handling control system. SDEWES 2015; 2015-1012:1-9.
3. Pang, S., & Mujumdar, A. S. Drying of woody biomass for bioenergy: Drying technologies and optimization for an integrated bioenergy plant. Drying Technology, 2010, 28(5): 690–701.
4. Nyström, J., & Dahlquist, E. (2004). Methods for determination of moisture content in woodchips for power plants – a review. Fuel, 83(7), 773–779.
5. Bak J, Clausen S. FTIR emission spectroscopy methods and procedures for real time quantitative gas analysis in industrial environments. Meas Sci Technol 2001; 13:150. http://dx.doi.org/10.1088/0957-0233/13/2/302.
6. Bolshov MA, Kuritsyn YA, Romanovskii YV. Tunable diode laser spectroscopy as a technique for combustion diagnostics. Spectrochim Acta – Part B At Spectrosc 2015; 106:45–66.
7. Hermansson S, Lind F, Thunman H. On-line monitoring of fuel moisturecontent in biomass-fired furnaces by measuring relative humidity of the flue gases. Chem Eng Res Des 2011; 89:2470–6.
8. Hartmann, H., Böhm, T., Jensen, P. D., Temmerman, M., Rabier, F., & Golser, M. Methods for size classification of wood chips. Biomass and Bioenergy 2006; 30(11), 944–953.
9. Bauer, R., Gölles, M., Brunner, T., Dourdoumas, N., & Obernberger, I. (2010). Modelling of grate combustion in a medium scale biomass furnace for control purposes biomass and bioenergy, 34(4), 417–427.
10. The steam and condensate loop [interactiv] 2018/ [viawed 2018 01 01], access via: https://cld.bz/R3ycc6i/28/;

CYSENI 2018, May 23-25, Kaunas, Lithuania
ISSN 1822-7554, www.cyseni.com

HEAT EXCHANGE UNIT WITH MICROCHANNELS FOR A THERMOPHOTOENERGY SYSTEM

R. V. Zaitsev
National Technical University "Kharkiv Polytechnic Institute"
2, Kirpicheva str., 61002 – Ukraine
Email: zaitsev.poman@gmail.com

ABSTRACT

Mathematical modeling of the heat exchange unit main parameters for photoenergy system based on general models with forced circulation of heat transfer fluid. To determine the coefficient of heat transfer at a given coolant temperature and surfaces temperature necessary to determine the temperature gradient in the wall of the heat exchanger. Temperature gradients can be determined by solving the equation of energy, which depends on the distribution of the flow rate in the flow. In general, a solution of convective heat transfer fluid to flow along the plane comes to solution of the system of differential equations. In the paper features of the selection of theoretical basis and mathematical modeling of thermal processes in the heat exchange unit for combination photoenergy system are presented. As a result of the simulation conducted we improve and develop high-efficiency heat exchange unit with microchannels. Testing of the proposed unit proved its high efficiency through the implementation of turbulent flow of coolant with heat transfer coefficient at 18 kW/(m^2·K). Analytical testing of the heat exchanger allowed showing that heat exchanger unit provides a stable operating temperature at less than 50 °C with the coolant flow rate is less than 0.3 m/s. Novelty of the proposed heat exchanger is in the optimal design of microchannels to improve the heat transfer coefficient. Practical value. The use of this heat exchanger will improve the quality and uniformity of cooling solar panels and reduce energy costs for circulation of fluid.

Keywords: heat exchanger unit, coolant, solar panels, combined photoenergy system

1. INTRODUCTION

Global energy market trends and the associated increase in the consumption of natural energy resources clearly show the need to find additional sources of energy that could compensate for the lack of available resources, and ideally – completely replace them. As the experience of the USA, Japan, Germany, shows one of the ways to solve this problem associated with the conversion of solar energy into electricity using semiconductor photovoltaic cells (solar cells – SC).

The most common type of SC is devices based on the structure of mono- and polycrystalline silicon thickness of 200 μm. The main problem of their widespread use is the high price of electricity they produce, due to high material and energy intensity of the process of manufacture. To reduce the cost of SC promising is the use of systems operating under concentrated solar radiation. The use of mirrors allows hundreds of times lower cost of SC. However, the use of silicon SC based on traditional designs with concentrated solar radiation reduces the efficiency of the order [1, 2]. At the same time, the use of silicon multijunction SC with vertical diode cells with increasing intensity of solar radiation demonstrates the increased efficiency [3].

Developed earlier [4] photoenergy plant based on silicon multijunction SCs with vertical diode cells or SC based on gallium arsenide, which has a positioning and control system, thus increasing the amount of light energy that comes to the surface power plant has many advantages. Such a photoenergy plant will produce not only electricity but also heat water. But along with this, there were severely difficulties in uniform cooling of installed SC that are needed to specifically address [5–7]. The conventional notation [8, 9] is used in this article.

The goal of the work is mathematical modeling of the main parameters of the heat exchange unit for photoenergy plant based on general models of heat transfer at forced circulation of fluid.

2. METHODOLOGY

In accordance with the general standard requirements for photoenergy plants for industrial equipment, the output voltage of the solar battery (SB) must not exceed U_{NM} = 48 V; load current – I_{NM} = 10.4 A; electric power that SB transits to the load – P_{NM} up to 500 W. Hence, at the $S_{SB} \approx 100$ cm^2 specific electrical power P_{NM} can be calculated, which is given to the load by 1 cm^2 of such SB and which is equal to 5 W/cm^2. However, along with this, at the maximum possible efficiency of SC, for example based on gallium arsenide, at 30%, to provide the necessary parameters, to the SB surface light with power density of at least 16.7 W/cm^2 has come. So the power of 11.7 W/cm^2 is excessive and will come to the SB and the heat exchanger in the form of heat, which will lead to significant and rapid overheating of SB.

The aperture area of the mirror system that concentrates, $S_a \approx 2.4$ m^2. At the solar radiation power P_s = 1000 W/m^2 the energy coming to this area Q_s = 2396 W. By selecting better material for the mirrors, the proportion of energy supplied to the photodetector plate after accounting reflectance of mirrors (r_z = 0.95), and the processes of reflection and absorption system plate – glass, which takes into account absorptive capacity (τ_α) [8] we have $Q_{s1} = r_z Q_s (\tau_\alpha)$ = 1761 W (this corresponds to the effective concentration factor K_{eff} = 386). After conversion of the part of this energy into electrical energy with efficiency η = 30%, giving Q_{s2} = 528 W of electrical energy, into thermal energy $Q_{s3} = Q_{s1}(1-\eta)$ = 1233 W transfer.

To determine the coefficient of heat transfer at given temperature of the coolant and the surface temperature that flowed it is necessary to determine the temperature gradient in the wall of the heat exchanger. Temperature gradient can be determined by solving the equation of energy, which in turn depends on the distribution of the flow velocity in the considered flow region. In general terms, solving the problem of convective heat transfer fluid for fluid flow along the plane comes to solving the following system of differential equations (1) [8]:

$$\begin{cases} \dfrac{1}{\rho}\dfrac{\partial \rho}{\partial \tau} + \dfrac{\partial w_x}{\partial x} + \dfrac{\partial w_y}{\partial y} = 0 \\ \dfrac{\partial w_x}{\partial \tau} + w_x \dfrac{\partial w_y}{\partial x} + w_y \dfrac{\partial w_x}{\partial y} = \dfrac{\mu}{\rho}\left(\dfrac{\partial^2 w_x}{\partial x^2} + \dfrac{\partial^2 w_x}{\partial y^2}\right) - \dfrac{1}{\rho}\dfrac{\partial \rho}{\partial x} + g_x \\ \dfrac{\partial w_y}{\partial \tau} + w_x \dfrac{\partial w_y}{\partial x} + w_y \dfrac{\partial w_y}{\partial y} = \dfrac{\mu}{\rho}\left(\dfrac{\partial^2 w_y}{\partial x^2} + \dfrac{\partial^2 w_y}{\partial y^2}\right) - \dfrac{1}{\rho}\dfrac{\partial \rho}{\partial y} + g_y \\ \dfrac{\partial T}{\partial \tau} + w_x \dfrac{\partial T}{\partial x} + w_y \dfrac{\partial T}{\partial y} = \dfrac{\lambda}{\rho c_p}\left(\dfrac{\partial^2 T}{\partial x^2} + \dfrac{\partial^2 T}{\partial y^2}\right) \\ p = \rho R T \end{cases} \tag{1}$$

Such a system of equations in general defies analytic solution, therefore special cases are considered.

2.1. Heat transfer at the motion of fluid in direct smooth pipes

At moving liquids and gases in pipes and channels there are laminar ($Re_{f,d} \leq 2300$), turbulent ($Re_{f,d} \geq 10^4$) and the transition from laminar to turbulent ($2300 < Re_{f,d} < 10^4$) regimes of fluid flow.

Definitive the parameters for calculating the Reynolds criterion: $T_0 = T_f = 0.5 \cdot (T_{f,in} + T_{f,out})$ – the average temperature of the fluid in the; $R_o = d_{in}$ – internal pipe diameter; $w_0 = G/(\rho \cdot f)$ – average by the pipe section velocity of the fluid movement.

2.1.1. Heat transfer in laminar fluid flow regime in pipes (Re ≤ 2300)

Heat pipes at a stabilized flow and stabilized heat transfer can be calculated at T_w = const and q_w = const by the approximate formula [8]:

$$N_u = 4\varepsilon_t \tag{2}$$

where the amendment εt is calculated by the formula

$$\varepsilon_t = \left(\frac{Pr_{fl}}{Pr_w}\right)^{0.25}. \tag{3}$$

In laminar regime of the movement in the direct smooth pipes and presence of sections of hydrodynamic and thermal stabilization for a more accurate approximation of the experimental data there are two subregimes: laminar viscous and laminar viscousgravitational. Laminar viscous flow regime occurs when Rayleigh numbers $Ra < 8\cdot10^5$ and laminar viscousgravitational mode when $Ra \geq 8\cdot10^5$. Heat transfer at the laminar viscous flow regime in pipes ($Re \leq 2300$; $Ra < 8\cdot10^5$). Average by the internal surface of the pipe of length l heat transfer coefficient is calculated by the formula obtained at $l/(Re\cdot d) \leq 0.05$ and $0.07 \leq \mu_w / \mu_f \leq 1500$ [4]:

$$Nu = 1.55\left(Re\cdot d_{in}/l\right)^{1/3}\cdot\left(\mu_f/\mu_w\right)^{0.14}\cdot\varepsilon_l. \tag{4}$$

The value ε_l of amendment taking into account the impact on heat transfer of hydrodynamic flow stabilization in the initial section of heat:

- at $$\frac{l}{Re\cdot d} < 0.1 - \varepsilon_l = 0.6\left(\frac{l}{Re\cdot d}\right)^{-\frac{1}{7}}\left(1+2.5\frac{l}{(Re\cdot d)}\right); \tag{5}$$

- at $$l/(Re\cdot d) < 0.1 - \varepsilon_l \approx 1. \tag{6}$$

Heat transfer at the laminar viscous-gravitational fluid medium mode in pipes ($Re \leq 2300$; $Ra < 8\cdot10^5$). Average heat transfer coefficient at the laminar viscousgravitational medium mode can be calculated by the M.A. Mikheyev criterion equation [9]:

$$Nu = 0.15\cdot Re_{f,d}^{0.33}\cdot Pr_f^{0.33}\cdot\left(Gr_{f,d}\cdot Pr_f\right)^{0.1}\cdot\varepsilon_t\cdot\varepsilon_l. \tag{7}$$

Correction factor ε_l taking into account the impact on heat transfer of the process of hydrodynamic flow stabilization in the initial section of heat transfer equal to:

- at $l/d < 50$ values of ε_l are founded by experimental data [5]; - at $l/d \geq 50 - \varepsilon_l = 1$.

2.1.2. Heat transfer at the turbulent fluid movement mode in pipes (Re ≥ 10^4)

Average heat transfer coefficient at the turbulent fluid flow in direct smooth pipes is calculated by the M.A. Mikheyev formula [9]:

$$Nu_{f,d} = 0.021\cdot Re_{f,d}^{0.8}\cdot Pr_f^{0.43}\cdot\varepsilon_t\cdot\varepsilon_l. \tag{8}$$

Correction factor ε_l taking into account the impact on heat transfer of the process of hydrodynamic flow stabilization in the initial section of heat transfer equal to:

- at $l/d < 50$-$\varepsilon_l \approx 1+2d/l$; at $l/d \geq 50$-$\varepsilon_l = 1$.

Values of ε_l depending on the Reynolds criterion are presented in [8].

2.1.3. *Heat transfer at the transition fluid flow regime in pipes (2300 < Re < 10^4).*

The transitional flow regime is characterized by mixing laminar and turbulent flows. In this case, the heat transfer coefficient can be calculated by the formula [9]:

$$Nu_{f,d} = K_0 \cdot Pr_f^{0.43} \cdot \varepsilon_t \cdot \varepsilon_l \,. \tag{9}$$

where the complex K_0 depends on the Reynolds number [9], and the amendment ε_l is calculated like at turbulent mode of the fluid flow.

2.2. Heat transfer at the motion of fluid in the channels of arbitrary cross-section

All of the above criterion formula for calculating heat transfer in circular pipe have been used for the calculation of heat transfer during the flow of liquids and gases in channels of other (non-circular) cross-sectional shapes (rectangular, triangular, ring, etc.), the longitudinal washing of pipes beams entered to the channel of arbitrary cross-section, and at the fluid flow that does not fill the entire cross-section of the channel. Here, as the characteristic size equivalent or hydraulic diameter of the channel should be used:

$$R_0 = d_{ekv} = d_r = 4f / P \,, \tag{10}$$

where f is the area of the flow cross-section, m^2; P is the wetted perimeter of the channel, m.

2.3. Heat transfer at the turbulent motion of fluid in the curved pipes

At the movement of liquid in curved pipes (laps, coil) there is its additional turbulence and, consequently, increasing the heat transfer coefficient [10]. To calculate the heat transfer in the curved pipes it is necessary to multiply the Nusselt number the on correction factor:

$$\varepsilon_g = 1 + 1.8 \cdot d_{in} / R_g \,, \tag{11}$$

where *din* is the internal pipe diameter, and R_g is the bend radius.

3. RESULTS AND THEIR DISCUSSION

As shown earlier [5] to reach acceptable temperatures of SB the intensity of the heat transfer should be increased. You can use either increase of the area of heat transfer through the use of radiator, or try to use turbulent flow of coolant to increase the heat transfer coefficient [11].

Based on the proposed theoretical study, two options for designs that are shown schematically in Fig. 1 are considered. The design shown in Fig. 1, a has a large area of the heat exchanger, and the design shown in Fig. 1, b has a large coefficient of heat transfer at the heat exchanger area close to the area of the heat receiving plate.

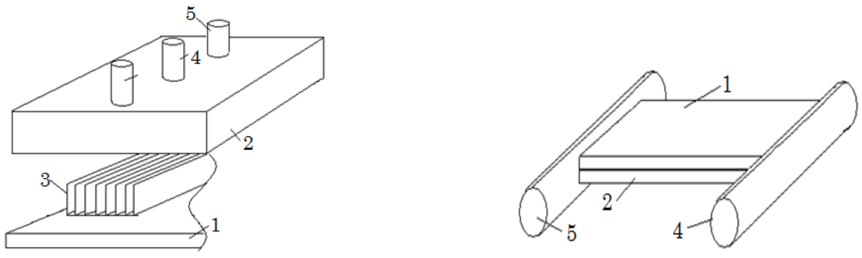

a) b)

Fig. 1. Schematic representation of the designs of the cooling block with plate radiator (a) and ram with a small gap width between the plates (b): 1 – cover of the cooling block, 2 – the cooling block housing, 3 – radiator plates, 4 – tube for feeding coolant, 5 – tube for cooling output

To calculate the heat exchange unit with a radiator with a large area of heat exchange surface (Fig. 1, a), and industrial copper radiator used to cool the elements of computer circuits was chosen as a model. It has the following dimensions: 91×91×25 mm, 56 plates, the distance between them is 1 mm, i.e. there are 55 channels for water leaking of the cross section 1×20 mm (including the thickness of the upper plate of 5 mm), but at the central water supply there are efficiently 110 channels. At coolant (water) consumption in the first closed loop of 10 l/min (0.016 kg/s) the flow velocity (w) in gaps between the plates is 0.0682 m/s. At an average temperature of cooling water ~50 ^{o}C kinematic viscosity of water $\upsilon = 0.556\ 10^{-6}$ m^2/s. Taking into account the effective diameter $d_e = 1{,}9 \cdot 10^{-3}$ we obtain Reynolds number $Re = wd_e/\upsilon = 234$, corresponding to laminar flow. Calculating the Grashof (495) and Rayleigh (1752) numbers we determine that in the selected radiator with indicated coolant consumption the laminar viscous flow regime takes place. Calculation of heat transfer coefficient between the coolant and radiator plates gives $Nu = 1.838$ W/(m^2·K), which is insufficient for effective heat dissipation, and such a heat exchanger cannot be used in the photoenergy unit.

To calculate the heat exchange unit with radiator with a large heat transfer coefficient (Fig. 1, b) it was proposed the following dimensions of the section of the water strait 1×80 mm with length of 60 mm. At such sizes and water consumption as above the flow velocity in gaps between the plates is 1.875 m/s. Taking into account the effective diameter $d_e = 1{,}98 \cdot 10^{-3}$ m we obtain the Reynolds number $Re = wd_e/\upsilon = 6661$, corresponding to the transition mode of the flow leakage. Calculation of heat transfer coefficient between the coolant and the upper plate of the radiator provides $Nu = 13931$ W/(m^2·K). Reducing the distance between the plates to critical, in terms of viscosity, 0.5 mm permits to increase the flow velocity to 2.92 m/s, but with less fluid consumption, since hydrodynamic resistance increases and the pump can provide consumption of 7 l/min that conserves the flow in transient mode. Here $Nu = 18483$ W/(m^2·K).

Based on performed calculations, the basic design of the flat heat exchanger has been improved with the introduction to it of microchannels to increase the coefficient of heat transfer. Block of the heat exchanger is designed as a complete unit. Fig. 2 shows the design of the radiator, which is a skirt design. In this design collecting planes with tubes which feed (outlet) coolant, and ribs that form microchannels for coolant provided are provided. The bottom of the radiator is the basis for fixing SB, thus decreasing the thermal resistance «surface – coolant».

Taking into account the presented design and theoretical investigations the mathematical modeling of such a heat exchanger operation at different fluid velocities was conducted. The main criteria for analysis were uniform cooling surface and its temperature at the supply of the above mentioned amount of heat. The corresponding heat pattern is shown in Fig. 3.

Analysis of the thermal patterns leads to the conclusion that even when the fluid flow velocity of 0.3 m/s for the proposed design of the heat exchanger sufficient cooling surface uniformity is reached (Fig. 3, c). Here, the maximum temperature does not exceed 43.5 ^{o}C, that is enough for SB effective operation without reducing efficiency. At the same time, reduce of the speed of fluid leads to loss of uniformity of cooling and to significant increase in the surface temperature to more than 60 ^{o}C that is unacceptable.

It should also be noted that the required heat exchange parameters are achieved at the speed of 0.3 m/s, which is much less than 2.92 m/s, which were obtained for the classic flat heat exchanger. Here, further increase in the speed of the fluid does not substantially improve uniformity and reduce the temperature, but will require additional energy losses to create flow.

Reducing the effective fluid flow compared with the classic flat heat exchanger indicates higher efficiency of heat transfer. This is possible only during the transition from the transitional regime of fluid flow in a classic flat heat exchanger to the turbulent regime in the proposed design.

To confirm the mode change of fluid flow mathematical modeling of fluid flow in the channels of the heat exchanger was conducted, the pictures are shown in Fig. 4.

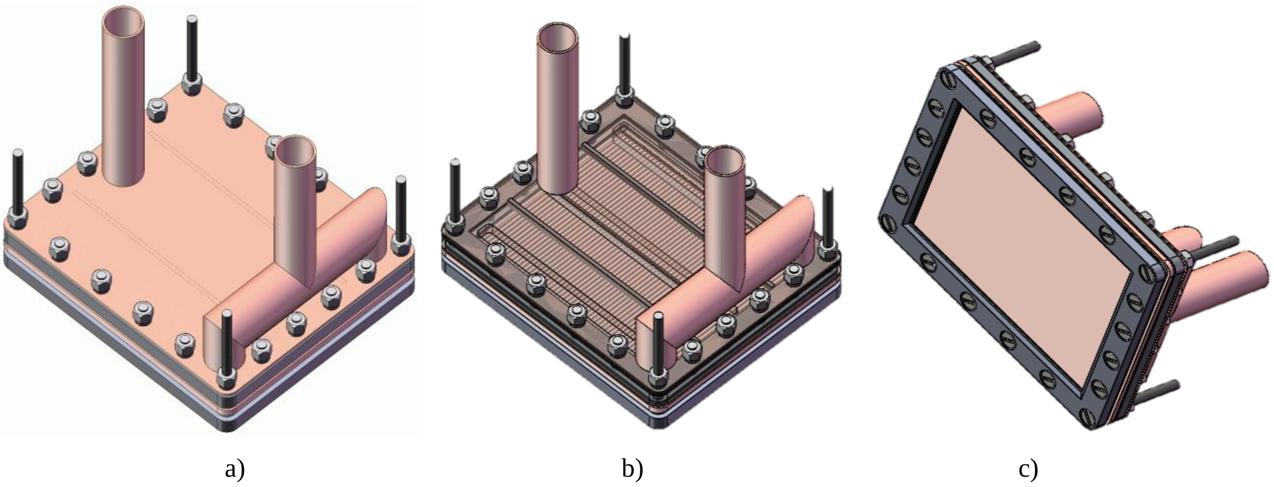

Fig. 2. Schematic representation of the designs of the cooling block with plate radiator (a) and ram with a small gap width between the plates (b): 1 – cover of the cooling block, 2 – the cooling block housing, 3 – radiator plates, 4 – tube for feeding coolant, 5 – tube for cooling output

The analysis of fluid flow confirmed the movement in turbulent regime, which allows maximum heat transfer coefficient and consequently achieves uniformity of cooling and low temperature at minimum energy consumption to create the fluid flow.

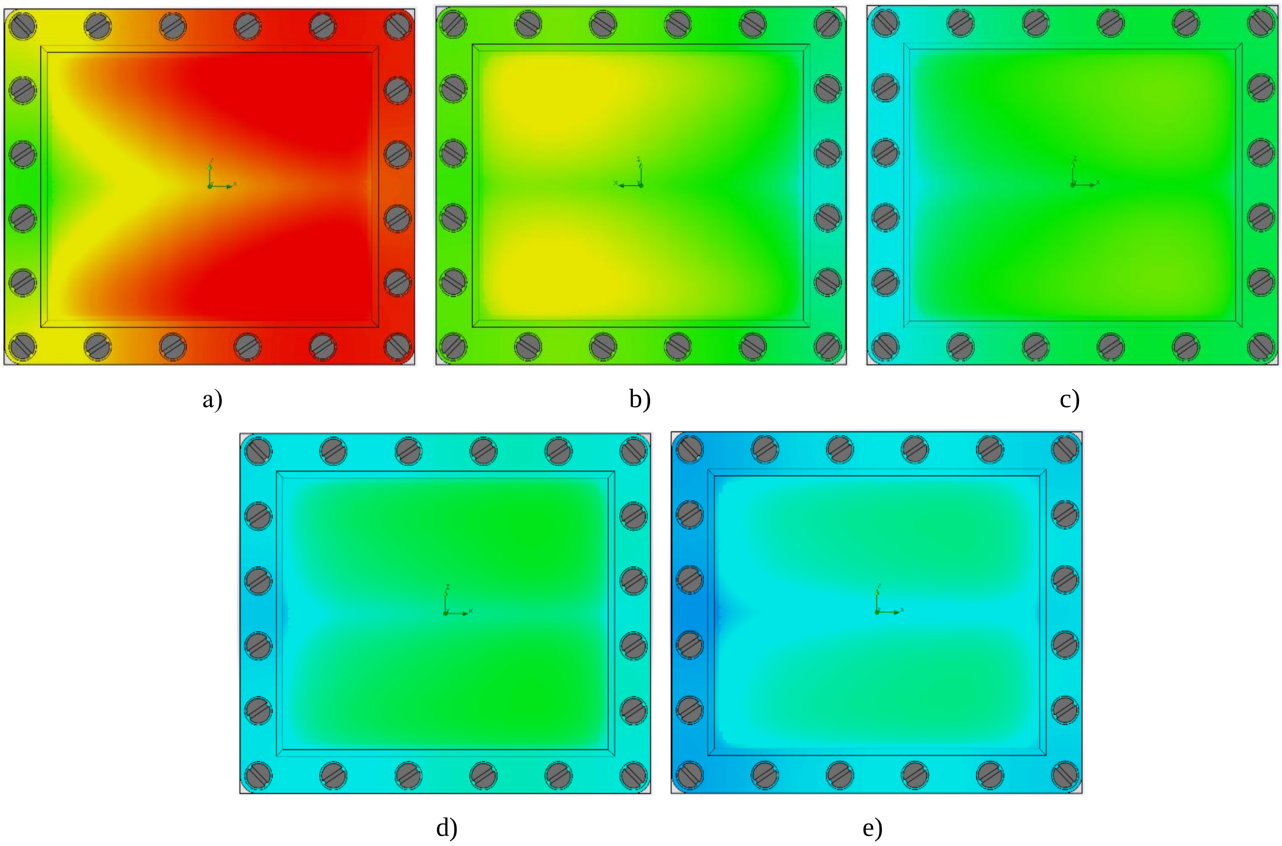

Fig. 3. Thermal patterns of the heat exchanger at following modeling conditions:
a – $w = 0.1$ m/s, maximal surface temperature $T_{max} = 63.25$ ^{o}C; *b* – $w = 0.2$ m/s, $T_{max} = 48.27$ ^{o}C;
c – $w = 0.3$ m/s, $T_{max} = 43.38$ ^{o}C; *d* – $w = 0.5$ m/s, $T_{max} = 39.18$ ^{o}C; *e* – $w = 1.0$ m/s, $T_{max} = 35.72$ ^{o}C

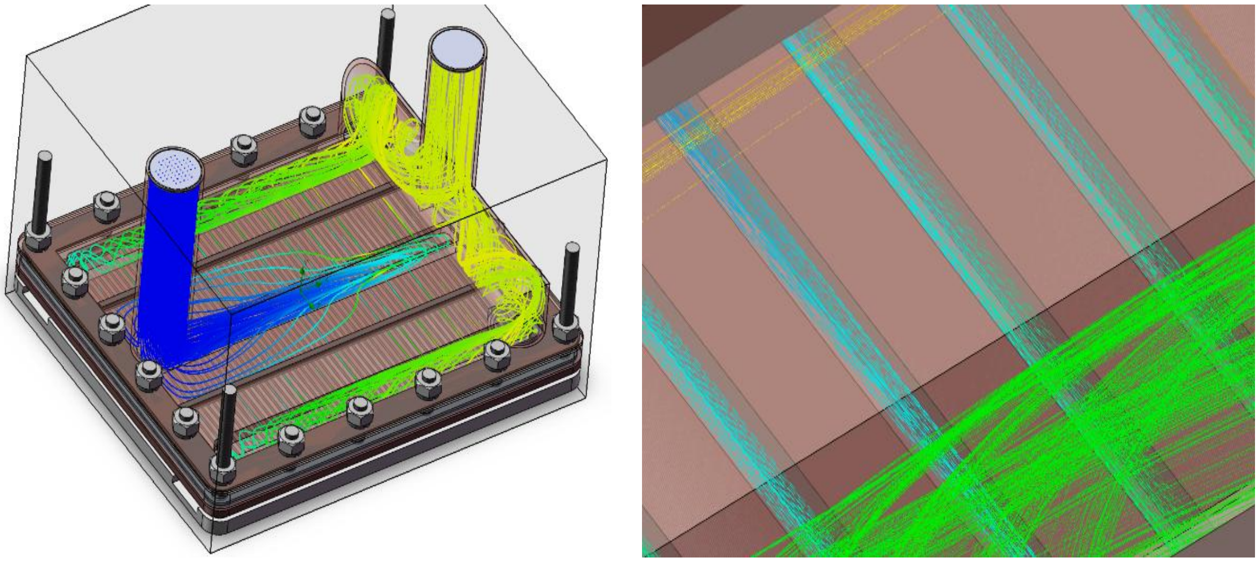
a) b)

Fig. 3. Images of fluid flow modeling pictures in the heat exchanger as a whole (*a*) and in its microchannels (*b*)

4. CONCLUSIONS

1. The theoretical calculations and modeling of heat transfer processes in converting solar energy in the manufactured heat exchange unit of the photoenergy plant are conducted, which showed that the most efficient is a plate heat exchanger equipped with the implementation in it of turbulent fluid flow, which achieves heat transfer coefficient of about 18 kW/(m^2·K).

2. Based on calculations an improved heat exchange unit with microchannels is developed and requirements correction to specifications of the photoenergy plant based on it is carried out.

3. Analytical verification of the heat exchanger permitted to determine that at selected parameters of the photoenergy plant, the heat exchanger unit provides stable operating temperature less 50 ^{o}C with the coolant flow velocity less than 0.3 m/s. The indicated temperature is optimal for solar battery operation at minimum energy consumption to create liquid flow.

REFERENCES

1. JONES, A.D., UNDERWOOD, C.P. A thermal model for photovoltaic systems. *Solar Energy*, 2001, Vol. 70, Issue 4, p. 349–359.
2. TUOMIRANTA, A., MARPU, P., MUNAWWAR, S., GHEDIRA, H. Validation of thermal models for photovoltaic cells under hot desert climates. *Energy Procedia*, 2014, Vol. 57, p. 136–143.
3. STREBKOV, D.S. *Matrix solar cells: Monograph in 3 volumes. Vol. 1*. Moscow: GNU VIESH Publ., 2009. 120 p.
4. SOKOL, E.I., KOPACH, V.R., ZAITSEV, R.V Physical and technical features and practical limits of the photonenergy module of the new generation on the territory of Ukraine. *Renewable energy*, 2011, No. 2(25), p. 18–28.
5. REDDY, K.S., PREMKUMAR, D., VIKRAM, T.S. Heat Transfer Modeling and Analysis of Solar Thermo-chemical Reactor for Hydrogen Production from Water. *Energy Procedia*, 2014, Vol. 57, p. 570–579.
6. STEINFELD, A. Solar thermochemical production of hydrogen - a review. *Solar Energy*, 2005, Vol. 78, Issue 5, p. 603–615.

7. MODI, A., BUHLER, F., ANDREASEN, J.G., HAGLIND, F. A review of solar energy based heat and power generation systems. *Renewable and Sustainable Energy Reviews*, 2017, Vol. 67, p. 1047–1064.
8. ISACHENKO, V.P., OSIPOV, V.A., SUKOMEL, A.S. *Heat transfer*. Moscow: Enegroizdat, 1981. 488 p.
9. MIKHEYEV, M.A. *Fundamentals of heat transfer*. Moscow-Leningrad: Gosenergoizdat, 1960. 208 p.
10. SHOKRI, R., GHAEMI, S., NOBES, D.S., SANDERS, R.S. Investigation of particle-laden turbulent pipe flow at high-Reynolds-number using particle image/tracking velocimetry (PIV/PTV). *International Journal of Multiphase Flow*, 2017, Vol. 89, p. 136–149.
11. SHIRVAN, K.M., ELLAHI, R., MIRZAKHANLARI, S., MAMOURIAN, M. Enhancement of heat transfer and heat exchanger effectiveness in a double pipe heat exchanger filled with porous media: Numerical simulation and sensitivity analysis of turbulent fluid flow. *Applied Thermal Engineering*, 2016, Vol. 109, Part A, p. 761–774.

CYSENI 2018, May 23-25, Kaunas, Lithuania
ISSN 1822-7554, www.cyseni.com

ECONOMIC STUDY OF PITCH SYSTEM IN VERTICAL AXIS WIND ROTOR TYPE STATIONS

T. Komass
Latvia University of Agriculture
2 Liela Street, LV-3001 – Latvia
Email: tf11198@llu.lv

ABSTRACT

For many years now vertical axis wind rotor type stations (VAWRS) have been an integral component of wind energy production. Raising VAWRS efficiency factor is a very important task. Up until now, no manufacturer has produced VAWRS that would be equipped with active blade pitch control system; therefore, it is difficult to precisely determine the costs, income and profits it may generate. Our anticipation is that taking into consideration the simulation data and results therein obtained, it is possible to forecast whether equipping of VAWRS with blade pitch control would be economically beneficial and whether it would bring any return on investment during the service period of the system. Many researches dedicated to VAWRS with pitch system have shown that the system is likely to have good potential. The results shows that in theory the efficiency coefficient grows by using the active pitch control system. The paper provides analysis of the total sum of factors including the potential costs of implementation, service and energy consumption. For the purpose of research accuracy, it is necessary to find proper methods for evaluating and calculating the required size of the pitch system. The electric power of the pitch system directly correlates with the estimated costs of the system. Accuracy of computation of the system electric power volume and correct estimations of annual energy consumption in the process of blade angle control are the key points of economic study. The research results demonstrate potential financial advantages of using the blade pitch system in the VAWRS in certain conditions. Over all research results shows that the blade pitch system has not only economical advantage, but also technical and safety advantages.

Keywords: Servo motor, Active pitch control, Wind energy, Vertical axis wind rotor

1. INTRODUCTION

For many years now, VAWRS have been an integral component of wind energy production. Raising VAWRS efficiency factor is a very important task. Low efficiency is quite often the reason why people prefer not to use VAWRS, because the payback period is too long and the lacks economic justification. Improvement of the efficiency factor using active blade pitch control approach is an effective way to deal with the problem, yet it assumes additional costs. At the same time, it is necessary to compute the costs of equipping VAWRS with the devices, the period of efficient service of the equipment, as well as potential yield for VAWRS owner. Up until now, no manufacturer has produced VAWRS that would be equipped with active blade pitch control system; therefore, it is quite difficult to any accurate estimations about the costs, income and profits it may generate [1].

Statistics shows that household power consumption has increased with the annual figure now exceeding 2000 kWh; such sharp an increase was registered in 2006, when the growth rate was the highest compared to 2001. It can be seen that the number of households with high power consumption remained the same throughout the years from 2010 to 2015 in Latvia. These households could be potentially interested in lowering their electricity bills. According to statistics, approximately 35% to 40% Latvian households consume more than 2000 kWh annually [2].

Tomorrow’s goal and today’s challenge is the ability to produce electric energy right at the consumer’s location or in the immediate vicinity of a consumer. Decentralized energy production brings forth the need for medium-capacity wind stations that could be installed within agglomerations right beside consumers [3]. Modern vertical axis wind turbines are characterised by sufficiently high tip-speed ratios. It means that people, who live at a short distance from the wind stations quite often feel certain discomfort and are concerned about their own safety and security of the surroundings. By using the blade pitch control system it would be possible to secure optimum wind turbine performance also at the lower tip-speed ratios. This is likely to cause friendlier attitude in the neighbourhood towards safer and slower spinning wind turbines.

2. MATHERIALS AND METHODS

An important provision (factor) for correct calculation of the return on investment for blade pitch control system is WTG (Wind turbine generator) capacity and the next most important factor is the capacity of a servo unit (motor). In order to calculate the capacity of servo motor, first it is necessary to calculate the mechanical parameters of WTG and the WTG blade: the moment of inertia of a blade, length of WTG blade, the material of which the WTG blade is made, the diameter of WTG rotor, the tip-speed ratio of WTG performance, centrifugal force on the blade, the resisting torque of active aerodynamic forces of the blade. Through mechanical calculation it becomes possible in a definite way to determine in theory what is the required electric capacity of a servo motor of the blade pitch control system. After the capacity of the servo motor has been defined, it becomes possible to calculate the costs of the required accessory equipment.

2.1. Development of method of calculation of the moment of inertia and mass for NACA0018 blade profile

VAWRS are designed with the help of modern computer design programmes, such as, for example, *Solidworks*, *Solidedge*, *Inventor*, etc. These computer programmes make it possible to design the inner structure of VAWRS blade in such a way as to ensure that the centre of mass coincides with the centre of rotation, which is located on the blade chord at a distance measured approximately as 25% of the blade length. Computer programmes help to obtain the key data: total mass of the blade, location of the centre of mass, value of the moment of inertia [4].

During experimental testing of the possible moments of inertia of NACA0018 blade profile according to selected design, a 1 meter long segment of the blade designed using *Solidedge* programme was examined (Fig. 1).

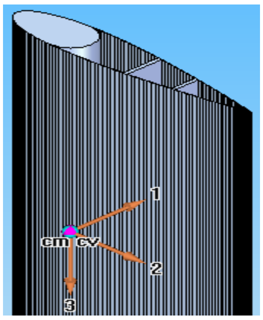

Fig. 1. Designing a NACA0018 profile blade with 1m chord in Solidedge computer programme
1, 2, 3 – arrangement of axes of the programme *Solidedge*

The computer programme *Solidedge* helps to analyse the information about correlation among the moment of inertia of the blade, length the blade chord and the overall blade length (Table 1). For a NACA0018 profile blade the length of the chord is 10% of the overall length of the blade, thus a most efficient aerodynamic airflow in the rotor is achieved [4]. The overall moment of inertia of the blade equals the product of the moment of inertia of a 1 m long blade segment and the required blade length. The moment of inertia of a 1m long blade is 0.233 $kg\cdot m^2$, if the blade is extended by 1 meter the total moment of inertia will proportionally increase.

Table 1. NACA0018 servo system default parameters

Description	NACA0018				
Length of chord c, m	0.20	0.40	0.60	0.80	1.00
Mass of blade segment (1 m), kg	0.76	3.03	6.82	12.13	18.95
Moment of inertia (1 m), kg·m^2	0.001	0.015	0.076	0.239	0.585
VAWRS blade length - l, m	2	4	6	8	10
VAWRS blade mass - m_{sp}, kg	1.52	12.13	40.93	97.02	189.52
Moment of inertia for a blade - J_{sp}, kg·m^2	0.002	0.060	0.456	1.912	5.850

With reference to experimental data, the moment of inertia of a NACA0018 profile blade can be described by the following function: $J_{sp} = 0.0018 \cdot c^{3.5155} \cdot l$. By using this function, it is possible to further calculate the required moment of inertia of the blade J_{sp} depending on the length of the blade chord (Fig. 2).

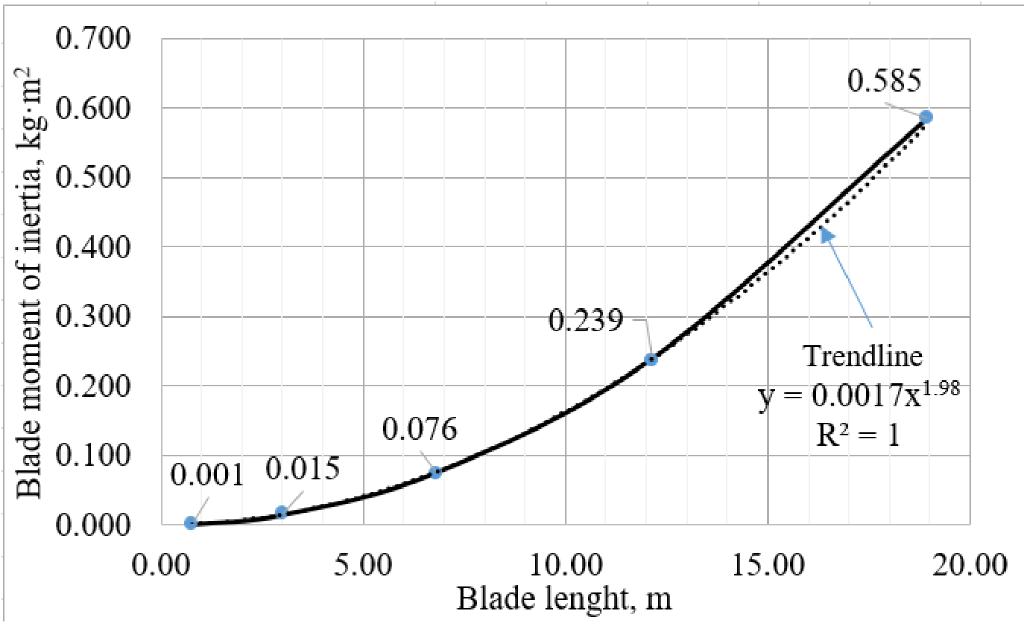

Fig. 2. Moment of inertia of a NACA0018 profile blade as the function of blade length

Experimental data show that the relation between the moment of inertia and mass of the blade is described with the help of the function $J_{sp} = 0.0017 \cdot m_{sp}^{1.98}$, assuming that the centre of mass and of the axis of rotation of the blade coincide in one common point.

2.2. Method of calculating capacity of a servo motor controlling a NACA0018 profile blade

Now that the mechanical parameters of the blade profile have been obtained, it is possible to apply analysis in finding the most optimal capacity of a servo motor [5]. Knowing the nature of the process of dynamic control and using *Drive Size* - the computer programme of the company ABB it is possible to determine the required capacity of servo motor in order to achieve the necessary blade control speed. Based on the experiment the input data were collected for the programme *DriveSize*. [6] Programme output data were processed and summarised in the table depending on the input data (Table 2).

Table 2. Comparison of the moments of inertia of the NACA0018 profile blade

	Indicator	**VAWRS rotor radius, m**				
		1.00	**2.00**	**3.00**	**4.00**	**5.00**
Turbine parameters	Length of chord, m	0.20	0.40	0.60	0.80	1.00
	Blade length, m	2	4	6	8	10
	Blade mass, kg	1.52	12.13	40.93	97.02	189.52
	VAWRS nominal capacity, W	1 500	6 000	12 000	21 000	32 000
	Moment of inertia of a blade, kg·m^2	0.002	0.060	0.456	1.912	5.850
12 ms^{-1}	*Drive Size* torque, Nm	1.428	10.710	36.176	85.234	148.69
	Drive Size capacity, kW	0.067	0.252	0.568	1.004	1.320
	Rotor revolution time, s	0.201	0.403	0.604	0.805	1.006
6 m·s^{-1}	*Drive Size* torque, Nm	0.357	2.677	9.04	21.308	40.54
	Drive Size capacity, kW	0.008	0.032	0.071	0.126	0.188
	Rotor revolution time, s	0.403	0.805	1.208	1.610	2.013
4 m·s^{-1}	*Drive Size* torque, Nm	0.139	1.16	4.02	9.353	17.905
	Drive Size capacity, kW	0.002	0.009	0.021	0.037	0.055
	Rotor revolution time, s	0.604	1.208	1.812	2.415	3.019

By analytically comparing the moments of inertia of the blade and the required capacity values, it is possible to define their interdependency function. With the help of regression method it is possible to define the required capacity of the blade servo motor depending on the moment of inertia using the formula $P_{ss} = 0.7343 \cdot J_{sp}^{0.3813}$ with the coefficient of determination $R^2 = 0.9975$.

2.3. Use of blade pitch control system – feasibility study

Earlier performed experiments point out the possibility to improve the generated power indicators at certain tip-speed ratios by using the blade pitch control system. Based on the results of the research, which purpose was to determine the required electrical capacity of a servo motor to ensure blade pitch control, it is possible to mathematically calculate the payback period and feasibility of the system [7].

The annual amount of electricity generated by VAWRS is calculated on the basis of the average number of days in a year – 365. Based on the wind resources available in Latvia – at a height of 15 meters, the following average wind velocities are selected: 4 m·s^{-1}, 6 m·s^{-1}, 12 m·s^{-1}. Active operation time of a VAWRS is assumed to be 360 days in a year, with allowance for the necessary downtimes.

For VAWRS without the blade pitch control system the amount of generated electric power is calculated in the following way:

$$E_{VES.G.} = E_{VES.D.} \cdot 360/1000; \tag{1}$$

$$E_{VES.D.} = P_{VES} \cdot 24; \tag{2}$$

$$P_{VES} = 0.5 \cdot v^3 \cdot 1.25 \cdot S, \tag{3}$$

where

$E_{VES.G.}$	–VAWRS output in one year, MWh;
$E_{VES.D.}$	–VAWRS output in one day, kWh;
$P_{VES.}$	– VAWRS electrical capacity at a certain wind speed, kW;
S	– VAWRS rotor swept area, m^2;
1.25	– averaged air density, kg·m^3;
v	– wind speed, m·s^{-1}.

For the purpose of control, basing on the above reviewed information about servo system consumption it is possible to calculate the estimated power consumption in annual quantities:

$$E_{SS.P.G} = E_{SS.P.D} \cdot 360/1000; \tag{4}$$

$$E_{SS.P.D} = P_{SS} \cdot 24; \tag{5}$$

$$P_{SS} = f(P_{VES}), \tag{6}$$

where

$E_{SS.P.G}$ – annual consumption of electricity by servo motor for blade pitch control, MWh;
$E_{SS.P.D}$ – daily consumption of electricity by servo motor for blade pitch control, kWh;
P_{SS} – operating capacity of servo motor for blade pitch control, kW.

Motor capacity indicated in the *Drive Size* programme is the maximum required capacity per one blade. In real-life operation, the power consumed by a servo motor in all the time of rotor rotation is not a constant value. In order to secure relevance of the necessary calculation results, the calculations were based on the following assumptions: servo motors are running for 365 days in a year; servo motor load pattern is calculated depending on the average wind speed; servo system operates on a round-the-clock basis (24/7).

Table 3. Electric power consumed by the blade pitch control servo device

		VAWRS rotor radius				
		1 m	**2 m**	**3 m**	**4 m**	**5 m**
Turbine parameters	Chord length, m	0.20	0.40	0.60	0.80	1.00
	Blade length, m	2	4	6	8	10
	Blade mass, kg	1.52	12.13	40.93	97.02	189.52
	Number of blades in a rotor	3	3	3	3	3
	Blade moment of inertia, $kg \cdot m^2$	0.002	0.060	0.456	1.912	5.850
$12\ m \cdot s^{-1}$	Servo system capacity, kW	0.067	0.252	0.568	1.004	1.320
	Daily power consumption, kWh	4.824	18.144	40.896	72.288	95.040
	Annual power consumption, MWh	1.737	6.532	14.723	26.024	34.214
$6\ m \cdot s^{-1}$	Servo system capacity, kW	0.008	0.032	0.071	0.126	0.188
	Daily power consumption, kWh	0.576	2.304	5.112	9.072	13.536
	Annual power consumption, MWh	0.207	0.829	1.840	3.266	4.873
$4\ m \cdot s^{-1}$	Servo system capacity, kW	0.002	0.009	0.021	0.037	0.055
	Daily power consumption, kWh	0.144	0.648	1.512	2.664	3.960
	Annual power consumption, MWh	0.052	0.233	0.544	0.959	1.426

Power consumption savings through using the blade pitch control system can be calculated both in gross and net units by applying the power generation improvement factor that was obtained in the course of previous research - ξ:

$$E_{VES.SS.Bruto} = E_{VES.G.} \cdot \xi; \tag{7}$$

$$E_{VES.SS.Neto} = E_{VES.G.} \cdot \xi - E_{SS.P.G}, \tag{8}$$

where

$E_{VAWRS.SS.Gross}$ – electric power gross annual savings through blade pitch control, MWh;
$E_{VAWRS.SS.Net}$ – electric power gross daily savings through blade pitch control, kWh;
ξ – power savings factor deduced from experiments.

For further review, we selected five VAWRS models available on the market that are suitable for setting up the blade pitch control system. Their capacity range is between 10–50 kW with the efficiency factors varying from 0.18 to 32. The WTG were manufactured by the companies RAPOTEK and Fairwind. These VAWRS have three blades with the profile close to that of

NACA0012 or NACA0018. To make further analyse using equation Nr.4 is important to calculate possible produced energy volume of these VAWRS per year. Calculation is performed using wind speed 4 m·s^{-1} and 6 m·s^{-1}. Calculations shows that difference between energy volume compering these two wind speeds is remarkable (Fig. 3).

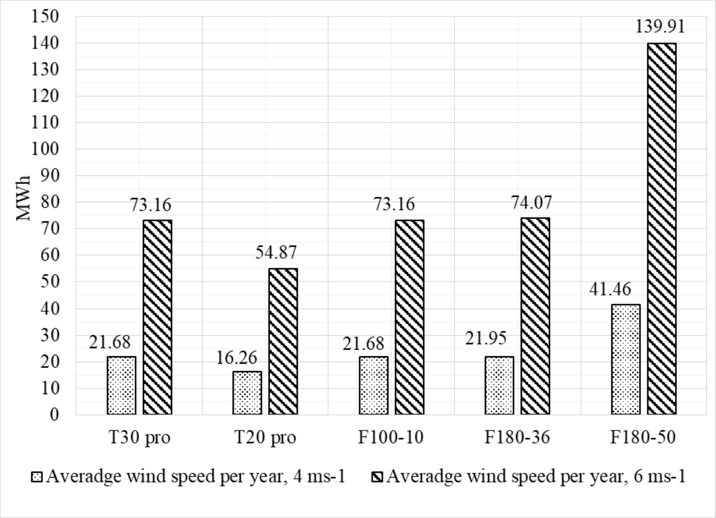

Fig. 3. Calculated energy volume generated by VAWRS per year

Aerodynamic research proved: as the VAWRS rotor tip-speed ratio decreases the savings through blade pitch control system increase. As the results of the research show, at $\lambda = 3.0$ theoretical power saving is $\xi = 14.4\%$, at $\lambda = 2.5$ theoretical power saving is $\xi = 28.4\%$, at $\lambda = 2.0$ theoretical power saving is $\xi = 98.9\%$. By securing higher average wind speed for VAWRS operation, the amount of generated power shows the growth trend, extra amount of power thus obtained is the result of operation of the blade pitch control system (Fig. 4).

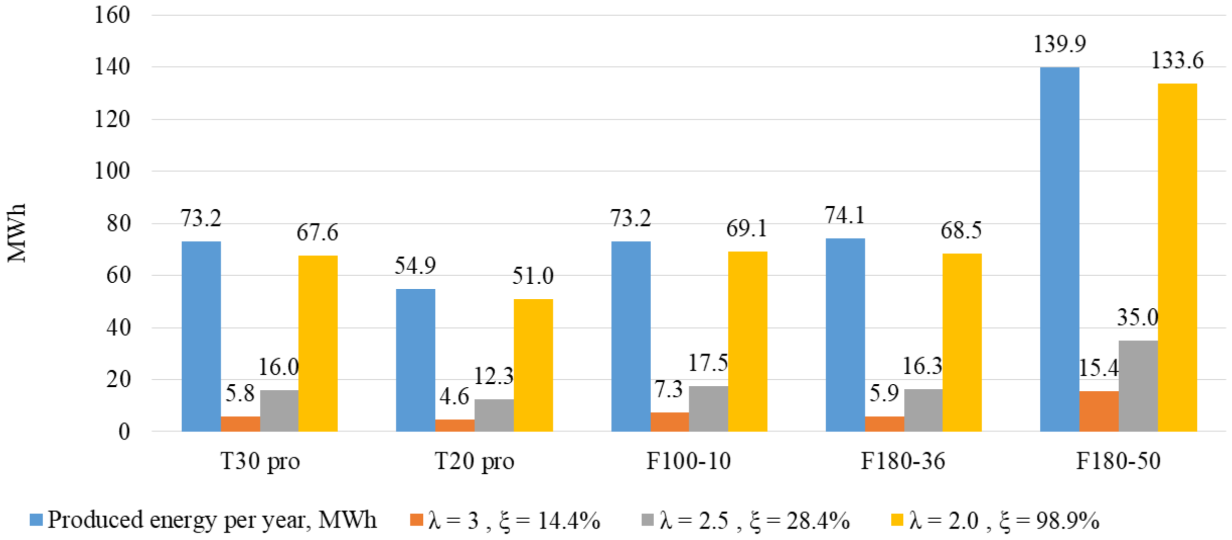

Fig. 4. Electric energy surplus through using blade pitch control system, at the wind speed 6 m·s^{-1}

In order that more low-power VAWRS with the operating capacity ranging from 5 kW to 25 kW could be installed in residential areas, they should be made slower. That can be achieved only by reducing the rotor speed and securing operation at a lower tip-speed ratio. By using the blade pitch control system it is possible to reduce the rotor speed without impacting the required operational efficiency of a VAWRS. This solution would make VAWRS much safer and spark interest of environment-minded younger consumers in buying the wind generators for use at home [8].

Extra costs of installing a servo system on a VAWRS with the capacity of up to 20 kW would be EUR 5260.00, while the costs of installing the device on a VAWRS with the capacity above 20 kW would be twice as large, that is, 9820.00 EUR.

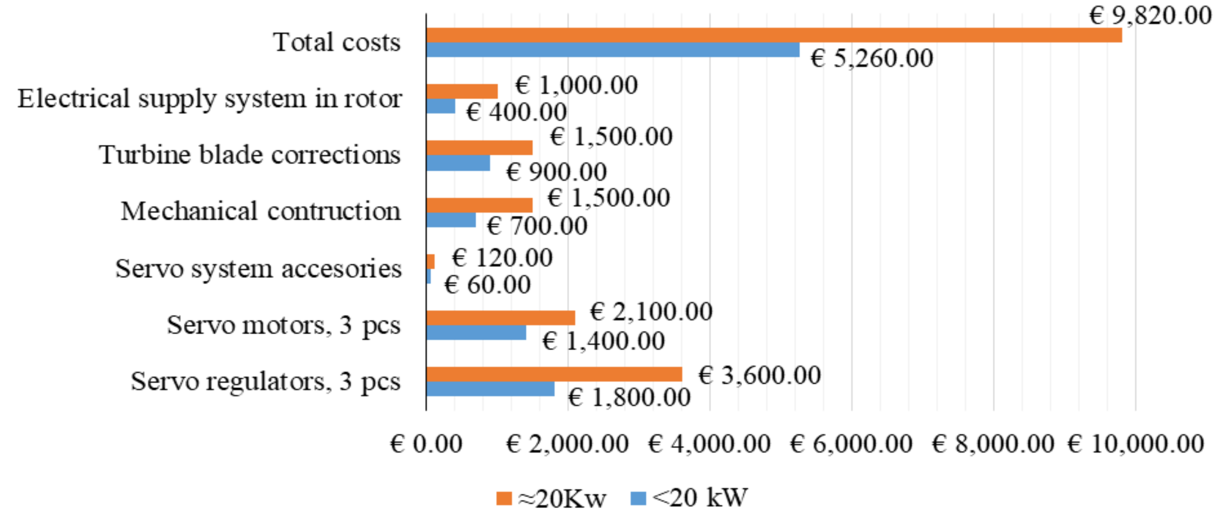

Fig. 5. Costs of installing blade pitch control system on a VAWRS, per one kW

Comparative costs of the blade pitch control system are determined for VAWRS with the capacity of up to 20 kW and above 20 kW. The economic difference between VAWRS that are equipped with blade pitch control system and those without the system lies in the presence of a number of components that create extra costs in order to secure blade control action. The components additionally required for blade pitch control device are as follows: 3 servo motor controllers, 3 servo motors, servo motor connectors, cables, mechanical frame, changes in blade design, rotor power supply.

If a VAWRS system with the capacity under 20 kW is built it may serve for approximately fifteen years. Over that period, it would be necessary to carry out system maintenance during the fifth and the tenth year of operation; the costs of each maintenance would be around EUR 460.00. Total maintenance costs will sum up to EUR 920.00 over a period of fifteen years. Life of a VAWRS with the capacity above 20 kW may be approximately twenty years; there will be three maintenances required during that period. The first two maintenances in the fifth and tenth year of service would cost EUR 620.00, the third maintenance would be required in the fifteenth year of service and its approximate costs would be EUR 840.00. Total maintenance costs would amount to EUR 2080.00 in a period of twenty years.

3. RESULTS AND DISCUSSIONS

Results of the feasibility study of active blade pitch control system demonstrate quite important information. The chart shows the estimated system payback period depending on the average wind speed and tip-speed ratio of a turbine. The chart depicting VAWRS with the capacity below 20 kW shows that the payback period of the active blade pitch control system is 10 years only at the highest average wind speed indicators or at the lower tip-speed ratios. The system payback period is the shortest if the average wind speed in the region is at least 6 $m \cdot s^{-1}$ and the tip-speed ratio of a turbine does not exceed 2.0. The higher is the tip-speed ratio, the longer is the payback period, which may extend from 2 to as long as 8 years (Fig. 6).

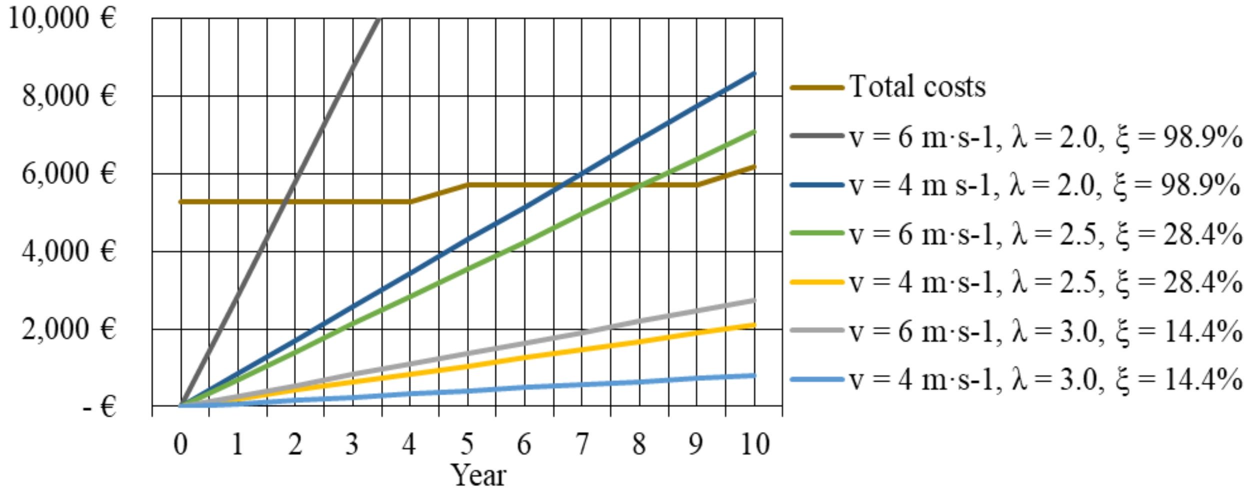

Fig. 6. Feasibility study of blade pitch control system, VAWRS capacity below 20 kW

If one reviews the summarised results for the turbines with the average capacity above 20 kW, it becomes clear, where the payback periods have improved. The payback period of the turbine with the tip-speed ratio 2.5 at the average speed 6.0 m·s^{-1} has improved to become 5.5 years instead of 8 years. This seems to be quite logical and can be proved by the fact that the costs per one kW can be less than that of a lower capacity VAWRS. Higher capacity VAWRS are able to generate more power, thereby leading to proportional increase in energy savings (Fig. 7).

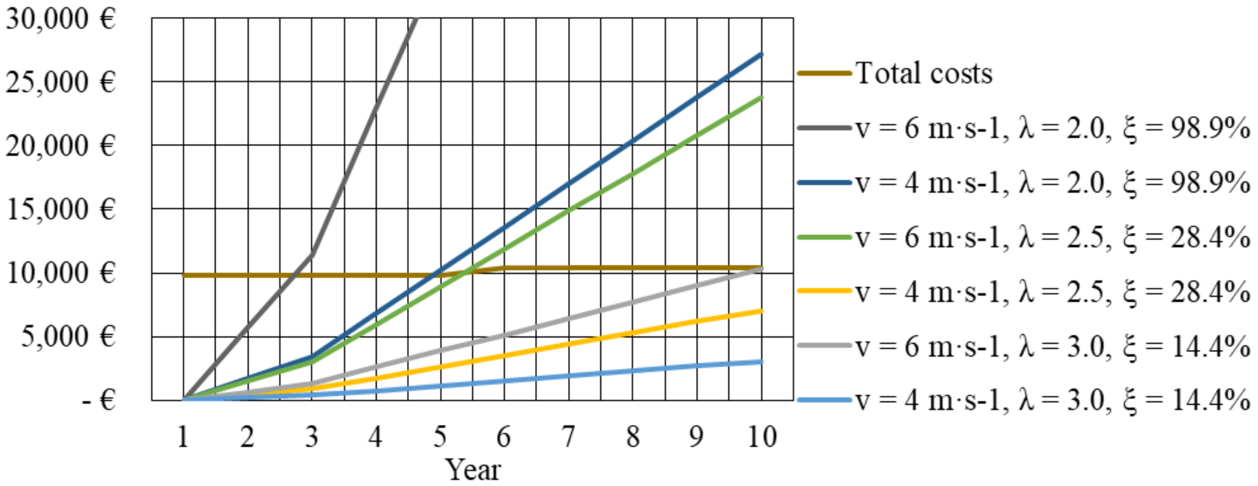

Fig. 7. Feasibility study of blade pitch control system, VAWRS capacity ≈ 20 kW

4. CONCLUSIONS

Finding solutions for raising VAWRS efficiency is an important task and is of great significance for the national economy. It is not sufficient just to find the new technical solutions, it is more important to prove their economic appropriateness. Previous research demonstrated that when the blade pitch control system is applied the operational efficiency noticeably increases. The final survey in the series of researches shows that seemingly unassailable economic solutions can be challenged. After summarising the results of the research, it becomes obvious that the payback period is quite long; besides, the actual costs may increase along with the increase of the price of industrial equipment. Research results demonstrate that the system can provide higher economic benefits only at the lower tip-speed ratios. The payback period is reduced. Surely, when it comes to improvement of VAWRS safety, as was mentioned earlier, it should be remembered that it is possible to operate at lower tip-speed ratios; it is possible to operate at lower wind speeds; it is always possible to install a lower capacity generator on a VAWRS; VAWRS could safely operate at the wind speeds that exceed the nominal capacity of the generator; through the storm, VAWRS would be able to actively rearrange the blades against the wind thus reducing the risk of exposing the turbine to extreme wind load. Use of active blade pitch control system is not just purely economic issue. Quite possible that the above-mentioned extra benefits may prove to be critically important and trigger use of active blade pitch control system in future VAWRS.

REFERENCES

1. KOMASS, T. VAWT blade aerodynamic torque analysis with the help of matlab tools. *American Journal of Energy and Power Engineering*, 2015, Vol. 2, No. 2, p. 20–26.
2. *Ar ES atbalstu izstrādāts jauna vēja ģeneratora prototips*. Delfi (Va.), [referred on the 21st of December in 2017 y.]. Link to the internet http://www.delfi.lv/bizness/uznemumi/ar-es-atbalstu-izstradats-jauna-veja-generatora-prototips.d?id=31673935>.
3. ANDREJ, J.F., STEPHEN, T. Blade offset and pitch effects on a high solidity vertical axis wind turbine. *Wind Engineering*, 2009, Vol. 33, No. 3, p. 237–246.
4. KOMASS, T. Experimental analysis of vertical axis wind turbine active pitch control system with permanent magnet synchronous motor using MATLAB Simulink tools. *Journal ENERGETIKA*, 2016, Vol. 62, No. 1, 2, p. 56–68.
5. *Technical Guide No. 7 Dimensioning of a Drive System*. ABB (Va.), [referred on the 14th of December in 2017 y.]. Link to the internet <https://library.e.abb.com/public/a3ef20fdc69ccc9ac12578800040ca95/ABB_Technical_guide_No_7_REVC.pdf>.
6. *ABB Motion Control Drives*. ABB (Va.), [referred on the 2nd of November in 2017 y.]. Link to the internet <https://library.e.abb.com/public/a56cb4e915dbc494c1257a330050184a/EN_ACSM1_flyer_REVF.pdf>.
7. BENCHERIF, M., BRAHMI, N.B., CHIKHAOUI, A. Optimum selection of wind turbines. *Science Journal of Energy Engineering*, 2014, Vol. 2, Iss. 4. doi: 10.11648/j.sjee.20140204.12.
8. BIEGEL, B., JUELSGAARD, M., KRANING, M., BOYD, S., STOUSTRUP, J. Wind turbine pitch optimization. IEEE International Conference on Control Applications (CCA) Part of 2011 IEEE Multi-Conference on Systems and Control. USA, Denver. 2011 September 28–30.

CYSENI 2018, May 23-25, Kaunas, Lithuania
ISSN 1822-7554, www.cyseni.com

ENHANCING ENERGY EFFICIENCY THROUGH LOW-CARBON TECHNOLOGIES IN BUILDINGS

A. Vitkutė, J. Dvarionienė
Kaunas University of Technology
Gedimino str. 50, LT-44239 Kaunas – Lithuania
Email: ausrine.vitkute@ktu.edu

ABSTRACT

Many of Europe's local/regional actors struggle with developing targeted, implementation oriented policies addressing low carbon challenges. This holds particularly for energy wasting buildings irrespective of their ownership or use. Since buildings are responsible for 40% of energy consumption in the EU this is a highly relevant issue in the European context. The work aim was to analyse the implemented energy efficiency measures for the residential buildings using life cycle approach. The methodology consists of the comprehensive analyses of different technological scenarios used for the residential building renovation and life cycle assessment using the SimaPro software for the life cycle assessment. The results of the research shows, that despite some recent positive changes in energy intensity (EI), the consumption of energy in Lithuania is much higher than the average in the EU or old EU Member States. EI amounted to 311.05 kg of oil equivalent per EUR 1,000 in Lithuania in 2010 (the EU average was 152.08 kg of oil equivalent per EUR 1,000) (Eurostat). Compared to other EU Member States, Lithuania is among the states with the most inefficient energy consumption, especially in building sector. The above data show the magnitude of energy saving potential and call for enforced measures. 66% of the Lithuanian population live in multi apartment buildings (around 60% of these buildings were constructed during the last four decades of the last century). The average thermal energy consumption amounts to 160180kWh/m^2 per year, whereas the standards in newly constructed buildings built after 1993 is around 8090kWh/m^2 per year. The necessity to improve energy efficiency in buildings is illustrated also by the magnitude of public spending on compensations for heating of housing, which increases every year. However the proactive participation of the energy users is essential when ensuring the quality of building works and real energy efficiency increase. The targeted economic energy saving potential is 5.2TWh in residential buildings and their engineering systems and 2.5TWh in public buildings and their engineering systems. However, the situation is positive concerning the amount of the buildings renovated and investment in the building sector, the problem of real energy efficiency remains. Evaluation of the reached energy efficiency is countable not measurable. As there is no real, monitoring system in Lithuania for the evaluation of the energy efficiency reached. The renovation process is oriented to the engagement of the building sector. It means that the primary goal is to renew the buildings based on the principal technologies in order to reach the efficiency described at the technical specification. The building companies are not obliged to guarantee particular level of energy efficiency in the coming years. There is identified the need to implement Life cycle thinking and sustainability approach in order to evaluate the current costs and the quality of technologies and materials implemented in the perspective of the longer period. The awareness of the final consumers, owners of multi-apartment buildings and other stakeholders is closely related to the proactive participation at this process. Successful renovation of residential buildings requires a wider use of technological innovation in this area, namely district-wide renovation, more inventive promotion and management of complex renovation. All new energy efficiency implementations in the residential buildings should be assessed using the life cycle approach. The life cycle impact assessment conducted for the different building renovation scenarios shows that energy use is very closely linked to the environmental burden associated with each of the renovation scenarios.

Keywords: energy efficiency, buildings, low-carbon technologies, life cycle assessment

Acknowledgment: This work is a by-product of research during our work in the “LOCARBO” project financed by the INTERREG EUROPE programme (European Regional Development Fund).

CYSENI 2018, May 23-25, Kaunas, Lithuania
ISSN 1822-7554, www.cyseni.com

INVESTIGATION OF DYNAMIC LINE RATING BASED ON NEURAL NETWORKS

L. Rácz, B. Németh
Budapest University of Technology and Economics
Egry József street 18, 1111 Budapest – Hungary
Email: racz.levente@eszk.org

ABSTRACT

The security of supply with a high level of operational safety and security has a prominent role in the domestic and international electricity networks. Due to the continuous growth of the consumer demand, the integration of renewable energy sources and other related changes in the energy market issues, a number of problems and challenges with the operation and utilization of the existing network have been identified. The need for a higher level of transmission capacity for the transmission network is one of the major challenges in the electricity network.

Dynamic Line Rating (in the following DLR) is a new generation of transfer capacity methods that can provide a cost-effective solution for the security of supply problems without re-planning the existing infrastructure background. The currently used Static Line Rating allows the operators to calculate the transfer capacity determined by the worst-case of the weather conditions on the wires of a particular transmission line. Whereas, practical applicability shifts to security, the result of this calculation method is almost 95% of time less than the real permissible load of the overhead lines. This potential can be exploited with the DLR by always adjusting the maximum current that can be transmitted on the wires. These maximum current values are calculated from the real-time environmental conditions, thus the DLR does not only provide a better security of supply, but also a higher level of availability.

The main issue of the paper is to investigate the calculation of DLR based on the application of non-analytic computational methods different from the current calculations of the international standards (CIGRE, IEEE). The aim of this research is to lay down the basis of a new black-box DLR calculating model and create a neural network capable of recognizing patterns based on the weather data of previous years and the actual current values of the wires.

Via simulations, different neural network structures have been tested for the real-time DLR calculations. According to these simulations, it can be established, that the new black-box DLR model based on the created neural network is applicable for the calculating of DLR with a low rate of error. In this way, it is not only possible to fine-tune, but also accelerate the applied calculation of maximum load capacity.

Keywords: Dynamic Line Rating, transfer capacity, overhead lines, soft computing, neural networks

CYSENI 2018, May 23-25, Kaunas, Lithuania
ISSN 1822-7554, www.cyseni.com

MIXED-INTEGER LINEAR PROGRAMMING BASED LOAD SCHEDULING OPTIMIZATION FOR SMART HOMES IN TURKEY

A. C. Duman, Ö. Güler, Ö. Gönül, K. Deveci
İstanbul Technical University, Energy Institute
Maslak, 34467 – Turkey
Email: dumanan@itu.edu.tr

ABSTRACT

Electrical energy demand varies throughout the day. During on-peak hours, a load stress occurs on the grid. Demand side management (DSM) techniques can achieve load reduction in residential sector by offering customers time-based tariffs. In this paper, a load scheduling optimization as a DSM method is performed for residential households using mixed-integer linear programming (MILP) in MATLAB. The aim of the optimization is to minimize daily total electricity costs of the residents by shifting the loads from the on-peak hours where the cost of electricity is high, to off-peak hours where the cost of electricity is low. At the same time, from the perspective of the power system it is aimed to reduce the stress on the grid by lowering the residential peak demand during on-peak hours. Load scheduling optimization analysis is applied for the shiftable loads such as dishwasher, washing machine and electric vehicle. The proposed method managed to shift the electric loads to off-peak period optimally and reduced daily electricity costs. In addition to single house case, participation of multiple houses in DSM is also investigated and for this case, a centralized scheduling algorithm is proposed to avoid possible excessive peak increases during off-peak hours as a new problem in the grid. The cost-effectiveness of the proposed method in terms of DSM is investigated through current tariff schemes in Turkey.

Keywords: Mixed-integer linear programming, demand side management, smart homes, load scheduling

1. INTRODUCTION

According to International Energy Agency (IEA) [1], worldwide electricity production has increased from 6131 TWh in 1973 to 24255 TWh in 2015. Alongside the significant increase in both energy demand and supply, rapid integration of renewable energy sources to the electricity grid arised new problems and studies are concentrated on the improvement and modernization of the existing grid infrastructure to obtain safe and reliable energy. To deal with such challenges smart grid concept is developed to increase reliability, transparency, security and efficiency of the grid. Within this concept, all players in the aging grid infrastructure are connected to the electric network and interact with each other bi-directionally through the Information and Communication Technologies (ICTs) [2]. To modify residential consumers' pattern of electricity usage according to the grid's advantage Demand-Side Management (DSM) methods are developed as part of Smart Grid. Demand response (DR) which is a DSM technique aims to change consumer behaviour in response to changes in electricity prices and financial incentives. To actively participate in DR programs, Home Energy Management Systems (HEMS) are essential to monitor, control and collect data from smart home appliances and bi-directionally communicate with the grid through smart meters. Moreover, consumers may face with difficulties in managing their increasing number of home appliances and require automation of HEMS. The main requirement of DR is the time-based electricity pricing and thus advanced metering system (AMI) is used to shift loads to cheaper hours within the daily time interval [3].

In this study, a load scheduling optimization is performed to minimize total electricity costs of households by shifting loads from expensive on-peak hours to cheap off-peak hours. Washing machines, dishwashers and electric vehicle chargers were handled as the shiftable loads. The cases of participation of a single house and multiple houses (10 houses) in DSM were examined. For the multiple houses case, a centralized scheduling algorithm is proposed to avoid possible excessive peak increases during off-peak hours as a new problem in the grid. Cost effectiveness of the proposed method is investigated through current tariff schemes in Turkey.

2. SYSTEM DESCRIPTION

2.1. Smart Meter and Home Energy Management System

HEMS and smart meters enables DSM and allows consumers to benefit from DR programs. HEMS users can monitor and manually or remotely control their appliances to manage their energy usage and reduce their energy consumptions. Smart meter bi-directionally communicates with the grid and gets the electric price signal. Receiving the price signal from smart meter, HEMS perform its tasks and schedule appliances under DR program. Components of HEMS in a smart home are shown in Fig. 1.

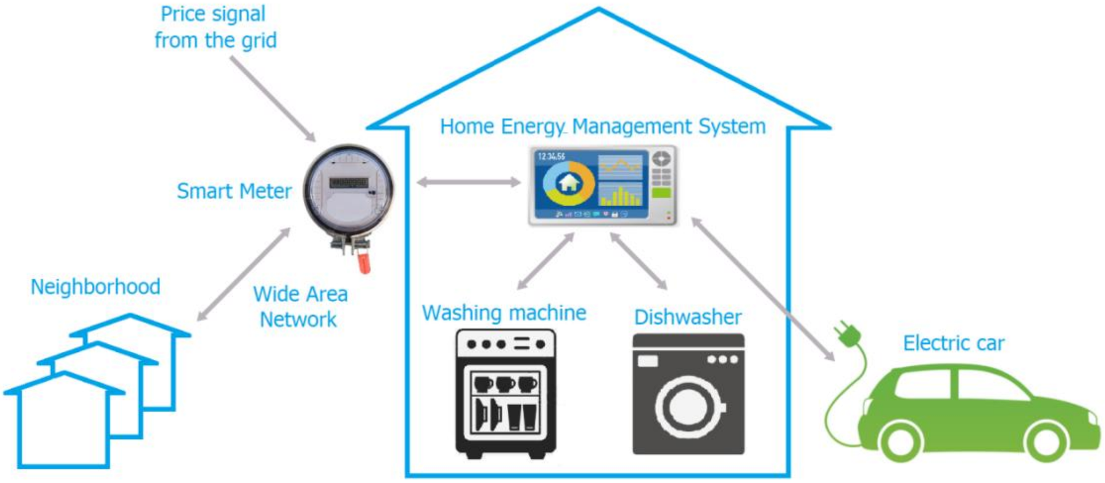

Fig. 1. Components of HEMS in smart grid

2.2. Tariff Schemes in Turkey

To achieve reduction in residential peak demand is one of the main targets of DR programs. In Turkey, residential sector accounts for 22.2% of the total electricity consumption. Residential electricity consumption has increased from 98,296 GWh to 231,204 GWh between 2000 and 2016 in the country [4] and between 2002 and 2010 new appliance purchase rates have increased from 2.8 million to 6.18 million [5]. In Turkey, residential consumers can either use flat rate or time of use (TOU) rate. Electricity prices including taxes are shown in Table 1.

Table 1. Flat rate and TOU rate in Turkey.

	Cost of Electricity (TL/kWh)		
Time of Day	06.00–17.00	(On-peak) 17.00–22.00	(Off-peak) 22.00–06.00
TOU rate	0.3599	0.5408	0.2292
Flat rate	0.3614		

2.3. Load Scheduling Optimization

2.3.1. Decision variables and objective function

In the study, load scheduling optimization problem is solved using MILP. The solver “intlinprog” of MATLAB is used. The objective in the optimization problem is to minimize daily total electricity cost of a household. The solver finds the minimum of a problem specified by

$$f_c = \min \sum C_h \left(\sum_{h \in H} P_{a,h} X_{a,h} \Delta h + \sum_{t \in T} P_{b,h} \Delta h + \sum P_{c,h} \Delta h \right) \tag{1}$$

where P_a represents power consumption of time-shiftable loads with on-off switch, P_b represents power shiftable loads with stand-by power and P_c represents power consumption of constant loads at particular hour $h \in$ H. H = {1, 2, 3..., 24} and Δh is the duration of each time period. X_{ah} is the binary integer vector which represents on/off switch of the appliances. $X_{ah} \in \{0,1\}$. If appliance a is “on” at particular hour h, then X is 1, if the appliance is “off” than X is 0. C_h represents electricity price at hour h. Electric vehicle is chargeable between 19:00 and 08:00 and hour $t \in \mathrm{T} = \{1, 2, \ldots 7\} \cup \{19, 20, \ldots 24\}$. For flat rate, $C_h \in \{0.3614\}$ and for TOU rate $C_h \in \{0.2292, 0.3599, 0.5408\}$. In flat rate scheme, load scheduling does not make sense due to the stable prices. Flat rate is used only to make an economic comparison between TOU rate.

Inspired by the categorizing types in [6] and [7], loads are categorized as time-shiftable, power-shiftable and constant. Appliances which require charging and have some stand-by power are defined as chargeable appliances. These appliances needs to be charged daily and after they are fully charged they still consume some amount of energy in stand-by mode. So, l represents stand-by power and u represents maximum charge power of these appliances. P_{bh} can be constrained as

$$u \geq P_{b,h} \geq l \tag{2}$$

For electric vehicle l standy power is 0.1 kW and u maximum charging power is 1.8 kW due to selected electric vehicle charger’s maximum power output [8]. The route between home and work is assumed to be 17-18 km and a typical electric vehichle approximately consumes 0.21 kWh/km [9]. For the total distance of 35 km, it takes 7.2 kWh energy to fill the battery back up. h_{leave} and h_{arrive} represent hours when residents leave and arrive home. In the study, it is assumed that electric vehicle will not be at home between 08:00 and 19:00 and it is chargeable after it arrives until the next morning. 7.2 kWh daily requirement has to be met during this time.

Dishwasher and washing machine are defined as time-shiftable appliances and they consume 0.9 kWh and 1.5 kWh respectively during their work cycle. Power consumption of these appliances cannot be divided. For instance, 0.9 kWh consumption of dishwasher must occur in one hour and this consumption cannot be divided (e.g. 100 W per hour for 9 hours). So, binary variable X_{ah} works as an on-off condition or a switch.

$$P_{a,h} = [\,0.9\ 0.9\ 0.9\ \ldots\ldots\ 0.9],\quad X_{a,h} \in \{0,1\}^{1\times 24} \tag{3}$$

Also washing machine consumes 1.5 kWh in two hours as 1 kWh in the first hour and 0.5 kWh in the second hour. Work cycle has to be ended in two combined hours and thus, 0.5 kW must be consumed in the next hour of the consumption of 1 kW. All the possibilities for the fixed consumption cycle of the washing machine is given in matrix form as

$$P_{a,h} = \begin{bmatrix} 1\ 0.5 \ldots 0\ 0\ 0 & 0\ 1\ 0.5 \ldots 0\ 0 & 0\ 0\ 1\ 0.5 \ldots 0 & \cdots & 0\ 0\ 0 \ldots 1\ 0.5 \\ 1\ 1\ 1 \ldots 1\ 1 & 0\ 0\ 0 \ldots 0\ 0 & 0\ 0\ 0 \ldots 0\ 0 & \cdots & 0\ 0\ 0 \ldots 0\ 0 \\ 0\ 0\ 0 \ldots 0\ 0 & 1\ 1\ 1 \ldots 1\ 1 & 0\ 0\ 0 \ldots 0\ 0 & \cdots & 0\ 0\ 0 \ldots 0\ 0 \\ 0\ 0\ 0 \ldots 0\ 0 & 0\ 0\ 0 \ldots 0\ 0 & 1\ 1\ 1 \ldots 1\ 1 & \cdots & 0\ 0\ 0 \ldots 0\ 0 \\ \vdots & \vdots & \vdots & \ddots & \vdots \\ 0\ 0\ 0 \ldots 0\ 0 & 0\ 0\ 0 \ldots 0\ 0 & 0\ 0\ 0 \ldots 0\ 0 & \cdots & 1\ 1\ 1 \ldots 1\ 1 \end{bmatrix}_{25\times 576} \tag{4}$$

$$X_{a,h} \in \{0,1\}^{576x1}, \quad P_{a,h}\, X_{a,h} = \begin{bmatrix} 1.5 \\ 2 \\ 2 \\ \vdots \\ 2 \end{bmatrix}_{25\times 1} \tag{5}$$

In (4), first row indicates all the shift possibilities and below rows 2–25 indicates all available cycle sets. From (5), fixed consumption cycle $X_{a,h}$ is obtained in 576×1 vector and the vector was then transformed into 24×1 vector.

Appliances such as ovens, refrigerators, TVs, PCs, lights, water boilers etc. are defined as non-shiftable appliances. Non-shiftalbe loads are steady and cannot be scheduled. They are added into the optimization problem according to user’s own preferences and routines.

2.3.2. Neighborhood participation in DR program

In case of participation of multiple houses in DSM, a new problem can arise in the grid that peak consumption during off-peak hours can reach to an undesirable level. Peak power of off-peak hours can be reduced by performing centralized scheduling in a neighbourhood. Since off-peak hours begin at 22:00 and end at 06:00 (Table 1), it is possible to distribute loads within this 8 hours range. Centralized scheduling algorithms schedules shiftable appliance a_1 of the 1st house to work at 22:00, then shiftable appliance a_2 of the 2nd house works on the next hour at 23:00. The cycle ends after appliance a_8 of the 8th house is scheduled to work at 05:00. After appliances of the first 8 houses are scheduled and all slots within off-peak hours are filled, a new cycle begins and appliance a_9 of the 9th house is scheduled to work at 22:00 again. By applying this method, peak power and PAR value of the neighbourhood during off-peak hours can be reduced without sacrificing from energy cost savings. Centralized scheduling algorithm for multiple houses is given in Fig. 2.

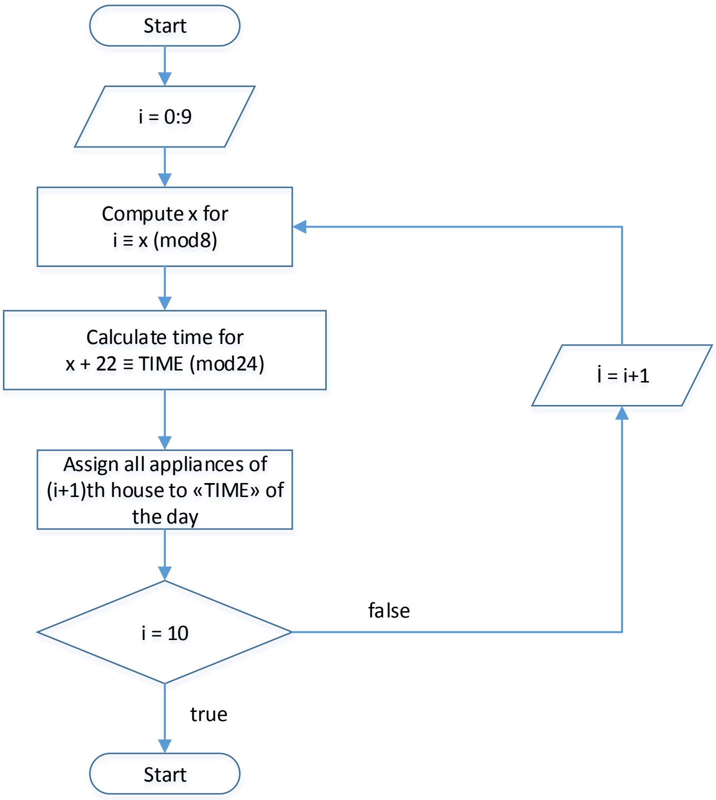

Fig. 2. Centralized scheduling algorithm for multiple houses

3. SIMULATION RESULTS

Simulations are carried out using “intlinprog” MILP solver of MATLAB. At first load patterns are identified as listed in Table 2. Non-shiftable loads are created using electricity energy consumption data of two bedroom house [10].

Table 2. Load patterns of the appliances

Appliance	**Status**	**Load pattern**
Electric vehicle	Power-shiftable	Between 19:00–08:00 with total 7.2 kWh Minimum 0.1 kW stand-by power Maximum 1.8 kW charger output
Washing machine	Time-shiftable	Daily 1 hour with power of 0.9 kW
Dishwasher	Time-shiftable	Daily 2 hours with 1 kW at the 1st hour and 0.5 kW at the 2nd hour.
Fridge, Oven, TV, PC, Water boiler, iron, vacuum cleaner etc.	Non-shiftable	Daily total 18.4 kWh

3.1. Results for Single House

Simulation results in case of using flat rate and TOU rate with and without DSM for single house are given in Table 3. To perform DSM, electricity prices should be time-dependent. Since the electricity prices are the same for every hour in flat rate scheme no matter how the loads are distributed, the electricity bills of the consumers are not affected by load scheduling.

Table 3. Comparison of different tariff schemes with and without DSM for single house

Tariff Scheme	**DSM Status**	**Average Power (kW)**	**Peak Power (kW)**	**PAR**	**Total Electricity Cost (TL)**
Flat Rate	DSM cannot be applied	1.167	3.55	3.043	10.12
TOU Rate	Without DSM				11.35
	With DSM		2.8	2.4	9.48

Average energy consumption at flat rate is found to be 1.167 kW and peak energy power is found to be 3.55 kW with 3.043 PAR. For the flat rate case, the daily total electricity cost of the residents is found as 9.48 TL.

Time-based rates motivate consumers to engage in DSM and make it available to reduce electricity bills. However, in TOU rate without implementing DSM, consumers may face with higher electricity bills due to the higher electricity prices of on-peak hours. In the study, when the residents switched to TOU rate without performing DSM, average energy consumption, peak energy consumption and PAR did not differ from the flat case. However daily total electricity cost increased from 10.12 TL to 11.35 TL, resulting in monthly 36.9 TL loss.

When residents switched from flat rate to TOU rate and applied DSM, peak power of the house reduced from 3.55 kW to 2.8 kW by 21.12% and PAR level reduced from 3.043 to 2.4. It should be noted that, PAR level could also have been increased depending on the load profile. Objective function here is to minimize the total electricity cost which decreased from 10.12 TL to 9.48 TL by 6.32% providing monthly 19.2 TL saving. Daily load profile with and without DSM for single house are given in Fig. 3 and Fig 4.

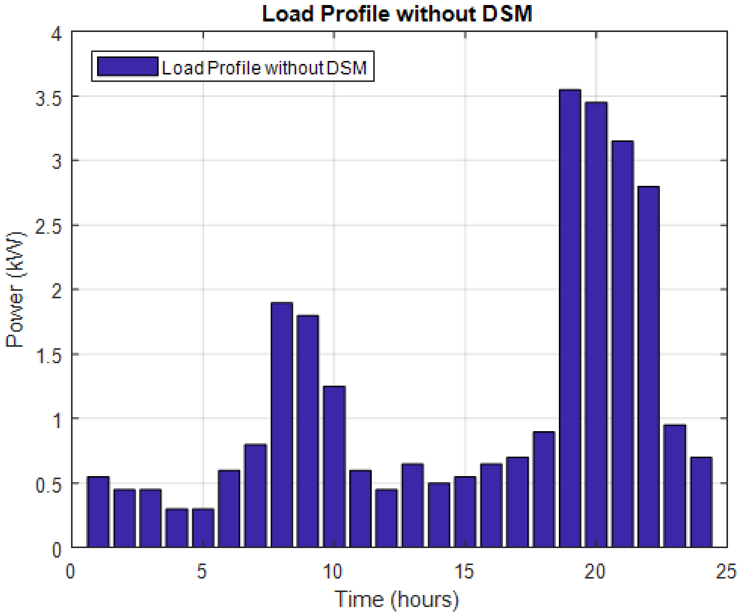

Fig. 3. Daily load profile without DSM for single house

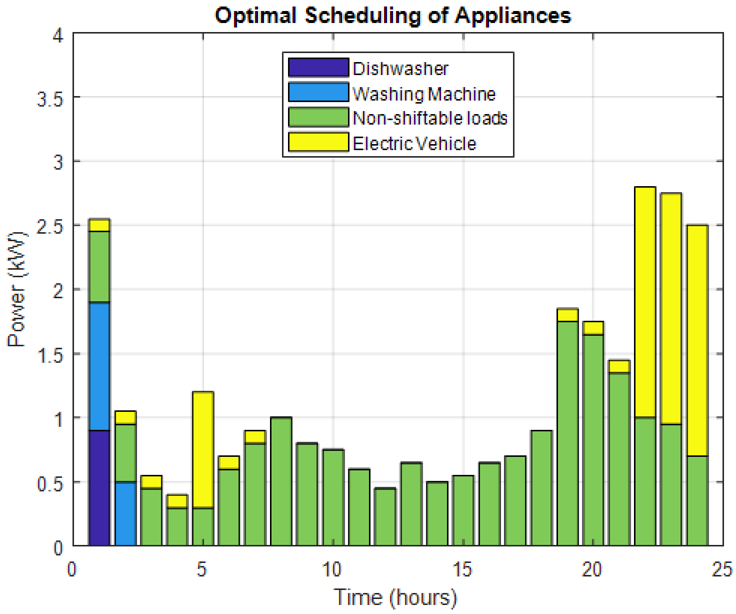

Fig. 4. Daily load profile with DSM for single house

As seen in Fig. 3, the peak power consumption is between 19:00 and 21:00 mostly due to the electric vehicle charging when the residents arrive home and plug in their electric vehicles. When DSM is implemented (Fig. 4), HEMS randomly schedules electric vehicle charging and operation of washing machine and dishwasher on off-peak hours between 22:00 and 06:00 where electricity prices are cheaper.

3.2. Results for Multiple Houses

The simulation results with and without DSM for 10 houses are given in Table 4. The table presents the worst scenario for individual DSM in which 10 individual HEMS shift all the appliances to the same hour of the off-peak period (Fig. 5) and the highest peak demand is obtained.

Table 4. Comparison of different tariff schemes with and without DSM for 10 houses

Tariff Scheme	DSM Status	Average Power (kW)	Peak Power (kW)	PAR	Total Electricity Cost (TL)
Flat Rate	DSM cannot be applied	11.667	35.5	3.043	101.19
TOU Rate	Without DSM				113.53
	With DSM		28	2.4	94.77

The problem can be avoided by developing a centralized scheduling algorithm. In centralized scheduling system, homes can participate in DSM collectively as a neighbourhood through a neighbourhood area network (NAN) while still maintaining their electricity costs reduced. In NAN, homes are in bi-directional communication with both the electricity grid and other houses in the neighbourhood through smart meters. By this way it is possible to schedule all appliances in the neighbourhood as parts of a whole body.

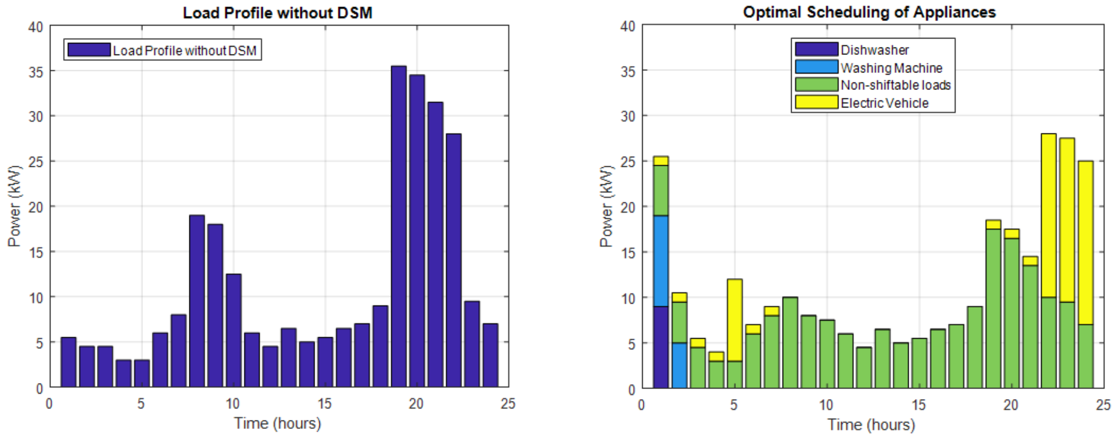

Fig. 5. Daily load profile of 10 houses without centralized scheduling

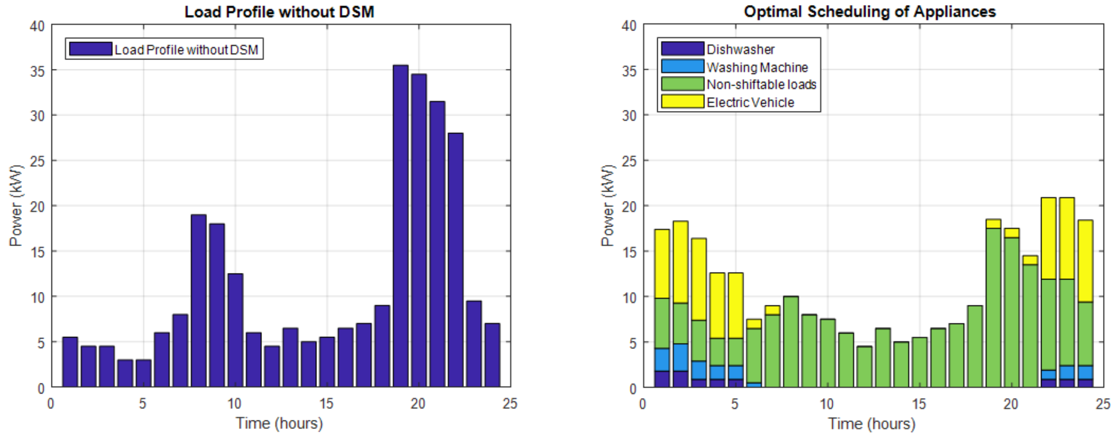

Fig. 6. Daily load profile of 10 houses with centralized scheduling.

Fig. 6 shows daily load profile for the case in which 10 houses participate in DSM with centralized scheduling. In this case, daily total electricity cost of the houses are the same with the decentralized scheduling case (Table 5). However, central scheduling algorithm manages to decrease peak consumption during off-peak hours and peak power redıces from 28 to 20.90 by 25.36% and PAR from 2.4 to 1.79.

Table 5. Comparison of results with and without central scheduling

Tariff Scheme	**Scheduling Type**	**Average Power (kW)**	**Peak Power (kW)**	**PAR**	**Total Electricity Cost (TL)**
TOU Rate	Decentralized	11.667	28	2.4	94.77
	Centralized		20.9	1.79	94.83

4. CONCLUSIONS

In this paper, a MILP based load scheduling optimization is performed to minimize electricity costs of households by participating in DSM. In the study, washing machines, dishwashers and electric vehicle chargers were optimally scheduled under TOU rate. The proposed method managed to reduce total electricity costs of the households by shifting loads from on-peak hours to off-peak hours. In case of participation of multiple houses in DSM, a centralized load scheduling algorithm is proposed to decrease peak increase during off-peak hours. PAR level which was 2.4 in decentralized scheduling is decreased to 1.79 in centralized scheduling. In the simulations, electric vehicle charger output is choosen as 1.8 kW which can be classified under slow chargers. In case of using faster chargers, increase in peak power and PAR level becomes significant even in off-peak hours and centralized load scheduling gains more importance for the grid to operate stably without being jeopardized from high penetration of electric vehicle chargers.

REFERENCES

[1] International Energy Agency. Key World Energy Statistics 2017- [referred on 21th of February in 2018 y.]. Link to the internet <https://www.iea.org/publications/freepublications/publication/Key World2017.pdf>.

[2] PONCE-JARA, MA., RUIZ, E., GIL, R., SANCRISTOBAL, E., PEREZ-MOLINA, C., CASTRO, M. Smart Grid: Assessment of the past and present in developed and developing countries. *Energy Strategy Reviews*, 2017, Vol. 18, p. 38–52.

[3] CLARK, WG. The Smart Grid: Enabling Energy Efficiency and Demand Response. *Lilburn: The Fairmont Press*, 2009. 138 p. ISBN-10: 0-88173-624-4.

[4] Turkish Statistical Institute. Distribution of net electricity consumption by sectors, 2017 – [referred on 18th of January in 2018 y.] Link to the internet <http://www.tuik.gov.tr/PreIstatistikTablo.do?istab_id=1579/>.

[5] SAHIN, M., KOKSAL, M. Standby electricity consumption and saving potentials of Turkish households. *Appl. Energy*, 2014, 114, 531–538.

[6] ZHU, Z., TANG, J., LAMBOTHARAN, S., CHIN, WH., FAN, Z. An integer linear programming based optimization for home demand-side management in smart grid. *2012 IEEE PES Innovative Smart Grid Technologies (ISGT)*, Washington, DC, 2012, pp. 1–5.

[7] MOHSENIAN-RAD, AH., LEON-GARCIA, A. Optimal residential load control with price prediction in real-time electricity pricing environments. *IEEE Trans. Smart Grid*, vol. 1, no. 2, pp. 120–133, Sep. 2010.

[8] Siemens. VersiCharge Electric charge station, - [referred on 15th of January in 2018 y.] Link to the internet <https://www.downloads.siemens.com/download-center/Download.aspx?pos=download&fct=getasset&id1=BTLV_45331>.

[9] US Department of Energy. Charging Plug-In Electric Vehicles at Home, [referred on 26th of April in 2018 y.]
Link to the internet <https://www.afdc.energy.gov/fuels/electricity_charging_home.html>.

[10] GOV.UK – Household Electricity Survey, - [referred on 12th of January in 2018 y.] Link to the internet <https://www.gov.uk/government/collections/household-electricity-survey>.

CYSENI 2018, May 23-25, Kaunas, Lithuania
ISSN 1822-7554, www.cyseni.com

THE COOPERATION OF THE EU WITH THE EASTERN NEIGHBOURS IN SECURING THE GAS SUPPLY AFTER THE NEWLY ADOPTED REGULATION 2017/1938

Mykola Iakovenko
University of Eastern Finland
School of Law
Joensuu Campus, Yliopistokatu str. 2, 80100 – Finland

ABSTRACT

The aim of the article is to explore the prospective of enhancing the EU cooperation with the Eastern Neighbours (in particular Ukraine and Moldova as the Energy Community' Contracting Parties) in securing the natural gas supply using the possibilities of the new EU Regulation 2017/1938. The main focus of the article is the risk assessment and mitigation mechanism in the context of the changes to the EU security of gas supply rules introduced by the Regulation, and the solidarity provision, which sets binding requirements on gas exchange between the geographically connected Member States during the emergency situations. The methodology of the article is based on the analytical law-in-the-context approach, which aims at analysis of the wide context of economic, political and security factors affecting the relevant legal framework and provisions, while the suggestions for the possible options for implementation of the new EU provisions into the Ukrainian and Moldovan legislation are also explored in the prism of the functional approach of legal comparison. The result of the exploration will be a clarification of Ukraine's and Moldova's role in cooperation with the EU in the sphere of security of gas supply (after the new Regulation was adopted) and proposals for improving the legislation of these countries to allow deeper cooperation with the EU. Therefore, the article will provide some new ideas for dealing with the risks of gas supply interruption in the EU during the situations of emergency in cooperation with the Eastern Neighbours.

Keywords: EU, energy law, security of supply, natural gas, Ukraine, Moldova

1. INTRODUCTION

This paper aims at exploration of the new prospective of the EU – Eastern Neighbors cooperation after the adoption of the Regulation No. 2017/1938 concerning the security of natural gas supply and repealing the Regulation (EU) No 994/2010. The analysis focuses particularly on Ukraine and Moldova and their cooperation with the EU in the sphere of natural gas security of supply. These two countries were selected for the analysis due to their participation in the Energy Community – the international organization aiming to create the Pan-European energy market, which shares the regulatory approaches and principles of the EU energy *acquis*. Consequently, all of the Contracting Parties of the Energy Community have the obligation of implementation of the EU energy law to their national legislation (a list of necessary EU energy legislative acts is provided in the Treaty Establishing the Energy Community) [1]. The international legal obligations of Ukraine and Moldova of implementation of the EU legal principles in their national law make the study of these countries' case extremely important for the analysis of the EU cooperation in the security of natural gas supply. The impact of these countries (and especially Ukraine) on the overall security of natural gas supply to the European Union is another issue, which makes the exploration of this topic extremely relevant.

The highlighted relevant issues of the topic lead to the following tasks to be analyzed in the paper in order to achieve its main aim of exploration of the EU – Eastern Neighbors cooperation after the Regulation No. 2017/1938: 1) to analyze the main aspects of the transformation of the EU legislation on the security of natural gas supply; 2) to examine the risk assessment and mitigation mechanisms from the point of view of possible participation of Ukraine and Moldova in this procedures; 3) to identify the possible ways of implementation of the new Regulation's provisions into the national law of Ukraine and Moldova as Contracting Parties of the Energy Community. The paper also focuses on some problematic legal issues, which might occur in the implementation of the mentioned Regulation’s principles in the EU Member States and in Ukraine and Moldova. The conflict of states’ sovereignty and international obligations in implementation of Regulation’s solidarity requirement is analyzed not only from the perspective of the EU, but also from the perspective of the possible limitations in the case of implementation in the non-EU countries. Thus, a broad exploration of the main legal problems and opportunities for their overcoming in is provided in the paper. The methodological approach of the article is based on the analytical law-in-the-context approach, which aims at analysis of the wide context of economic, political and security factors affecting the relevant legal framework and provisions, while the suggestions for the possible options for implementing the new EU law provisions into Ukrainian legislation are also to be analyzed from the perspective of the functional approach of legal comparison.

Therefore, the paper provides one of the first analyses of the possible cooperation of the EU and non-EU countries in the framework of the new Regulation (EU) No. 2017/1938 concerning the security of natural gas supply. The following chapters of the paper analyze the methodology; legal transformations brought by the new Regulation; prospective of non-EU countries participation in risk assessment and mitigation mechanisms and possible problems of implementation the provisions of Regulation into the national law of Ukraine and Moldova. The main paper’s idea suggests that an effective cooperation in the sphere of the security of natural gas supply between the EU and Ukraine and Moldova within a framework of the new Regulation is possible only if some additional measures are adopted. The conclusions of the paper include the main findings of the chapters and suggest the optimal model of this cooperation.

2. METHODOLOGY

The current paper’s main focus – the provision of the security of the natural gas supply in the EU and its Eastern Neighbors - is related to the law-in-the-context research, which focuses on the political, economic and security aspects having an impact on the relevant legal framework. Thus, the political and geopolitical factors are to be analyzed to provide understanding of the main driving forces and attitudes towards the establishment of the natural gas security of suply legislation, since the gas supply issue has always been politicized due to the different relations betweeen the supplier states and the consumer-states. No less important are the market approaches, mainly in the EU, since the development of the EU natural gas market greatly affects the vision of the implementation of particular mechanisms of ensuring the security of natural gas supply. The security aspect (in particular, the aspect of energy security) is another important factor of influence on the natural gas supply legislation, which became especially urgent after the supply crises in the mid-2000s that also led to the risks for economic security and protection of people’s lifes and, in particular, had implications on the extension of possible instruments for ensuring the security of supply in the EU legislation. Therefore, the new legal frameworks for the security of natural gas supply cannot be explored without the analysis of the above-mentioned factors of influence that create a general context and determine the aims of the legislative transformations. This determines our focus on the teleological analysis of the explored legislation through the prism of the initial purposes, factors and attitudes, which affected its enactment.

However, some attention needs to be focused also on the comparative legal methodology in order to identify the possibilities of legal approximation in the sphere of securing the natural gas supply in different legal systems. The functional approach to the legal comparison seems to be the most optimal methodological solution in this paper. Moreover, the functional method has been recognized by many theoretical studies to be one of the most appropriate for the micro-comparative research [2] and, simultaneously, a basic methodological principle of comparative law [3]. Functional legal method can be characterized as a method, which aims at identification of the solution for the same legal problem in different legal systems [4]. Some controversies in application of the functional approach in this case might occur, since this approach is usually provided with an idea of finding the solution of common roots of the legal problems without any regard of countries' and solutions' specificities [5]. Thus, the case of exploration of the legal possibilities of solving the gas security of supply dilemma in the Energy Community and the EU countries seems to be quite an outstanding one. The Energy Community countries have to implement many elements of the EU energy law; on the other hand, they are not integrated into the general EU legal system. Hence, the main issue of this case is related to the adoption of almost the same legal solutions to the common problems, but in different jurisdictions and legal systems. This aspect also makes the situation in Energy Community countries quite complex, since there is no authority of the EU intuitions, which usually participate in implementation of the *acquis* in the Union. Therefore, the functional legal comparative approach in this paper aims at finding the way of implementation of these legal solutions taking into account the specificity of the overall legal systems of the EU, Ukraine and Moldova. It also correlates with one of the main elements of the functional method of legal comparison – focusing not only on the similarities, but also differences between the legal systems [6].

Such methods are used in order to identify the best approach towards the securing of natural gas supply to the EU in cooperation with the Eastern Neighbors states in the conditions of the new reform of the security of natural gas supply legislation in the Union.

3. THE MAIN DISCUSSIONS

The paper focuses on the new opportunities for enhancing the cooperation in securing of the natural gas supply between the EU and Eastern Neighbours after the enactment of the Regulation No. 2017/1938. Some elaborations of the similar topics already exist in the academic researches. In particular, the dilemmas of the security of the natural gas supply had been broadly analyzed in the publications of the Oxford Institute for Energy Studies, which published numerous articles on this issue since the beginning of the supply interuptions to the EU in 2000s [7]. The effect of the security of supply provisions on the evolution of the EU energy law was also analyzed in the general academic literature on the EU energy law and the EU natural gas market development [8]. Finally yet importantly, the security of the natural gas supply issues were broadly presented in the interdisciplinary researches on the energy security, which focused on this problem from the perspective of international relations and domestic policy [9]. Nevertheless, the prospective of the implementation of the Regulaiton No. 2017/1938 in the EU and Energy Community Contracting Parties have not been widely analyzed in the academic literature at the present (at the moment when this paper was written) mainly due to the novelty of this legislation (it was enacted only in October, 2017) and ongoing process of its further implementation. This aspect makes the analyzes of the Regulation No. 2017/1938 an extremely relevant topic, which may begin an important discussion on many complex issues related to its implemenation. Thus, this paper will provide the possible new visions on the prospective of implementation of the legislation and cooperation of the EU and Eastern Neighbors in the mutually important issues of the securing of natural gas supply.

Three main factors can be discussed with a regard to this issue: 1) the transformations brought by this reform of the EU legislation; 2) possibilities of the involvement of Ukraine and Moldova to the risk assessment and mitigation procedures; 3) possibilities of implementation the solidarity provision of the Regulation in the national legislation of these non-EU countries. The discussion of these factors is provided here.

3.1. Current transformations of the EU security of natural gas supply regulations

The security of natural gas supply has been extremely problematic issue for the European Union energy policy since the beginning of the liberalization of the EU natural gas markets in the 1990s. The absence of the sufficient domestic natural gas reserves in the majority of the EU

Member States (approximately 69% of the overall natural gas demand is satisfied with the import) [10] results in a dependency of the Union on foreign suppliers. At the present, the main non-EU supplier countries are the Russian Federation, Norway and the North African countries, where Russia is still one of the dominant suppliers. Ukraine and Moldova are among the main transit countries that provide the transportation of Russian natural gas to the EU territory. Ukrainian gas-transmission system (GTS) is historically connected to the territories of the Western neighbours, having the biggest capacities on the border with Slovakia and Hungary (pipelines Soyuz (Union) and Urengoi – Pomary – Uzhgorod), but also with a separate branch to the South (which connects it with Moldova) [11]. The Moldovan gas-transmission system is directly connected to Ukrainian GTS and transports gas to the Southern European countries in the Balkans [12]. Quite recently, Moldova also began the construction of the Iasi-Ungheni gas pipeline from Romania, which is, however, not fully functioning at the present (the project is supposed to be completed by 2020) [13]. Thus, the connection of these countries gas-transportation systems with the EU markets also results in their significant involvement in securing of the European natural gas supply. Consequently, the evolution of the EU legislation on the security of natural gas supply is related to the developments in this segment of gas transportation and factors, which influence it. The main factors, which currently have an influence on this issue, are: geopolitical confrontation between the EU and Russia (where the Eastern Neighbors share the EU position), vision of the EU natural gas market building (where the prerogative is given to liberalization, free access to infrastructure and hub-pricing) and security task, which aims at avoiding the interruptions of supply crises. Therefore, the legislation seeks to find a balance between all these important goals. The overview of the evolution of the EU security of supply legislation demonstrates these tendencies.

Thus, the early EU legislation on the security of natural gas supply established some important general principles, however, most of the broad requirements did not lead to the strict obligations in the Member States. In particular, the Council Directive 2004/67/EC concerning measures to safeguard security of natural gas supply set some general provisions requiring the Member States to ensure the supply to the households in the event crisis, high demand and extremely low temperatures; monitoring and reporting rules; a list of possible instruments of ensuring the security of gas supply. Besides that, some other important institutions like the Gas Coordination Group (GCG), as well as the first algorithm of actions in emergency (where the Commission had already been granted with a right to require a Member State to assist the other Member State in a situation of emergency) was established by the Directive [14]. However, the first gas supply crisis, which occurred as a result of Russian – Ukrainian political confrontations in 2006 demonstrated that the existing system of the security of natural gas supply is not reliable enough to fully mitigate the risks of undersupplying, thus the consumers in some of the EU Member States reported to have significant problems in receiving the natural gas [15]. The next Russian – Ukrainian transit conflict, which took place in January, 2009 led to even worse outcomes and had a huge implication on the supply to the most of the EU Member States (in some of them it was fully interrupted) [16]. In 2010, the new Regulation No 994/2010 concerning measures to safeguard security of gas supply repealed the previous Directive and set some stricter provisions for the Member States. Thus, the provisions were aimed at the activity of not only Member State's authorities, but also suppliers and transmission-system operators (TSOs). It also enlarged the list of protected consumers (also including the small and medium-size enterprises and heating installations), and set a Member State's obligation to designate the national competent authorities to ensure the implementation of the measures of Regulation [17]. In fact, the national competent authorities also provided the important function of coordination of the activity of national suppliers, TSOs and authorities in the mitigation of risks to the security of natural gas supply. The Regulation also added a notion of the 'infrastructure standard' – an obligation of Member States to keep the ability and technical capacity of gas-transmission systems to satisfy the demand in the event of disruption during a day of exceptionally high gas demand occurring with a statistical probability of once in 20 years (so-called N – 1 formula) [18]. Moreover, the 'supply standard' was also elaborated in the Regulation, requiring the uninterrupted supply to the ‘protected customers’ of the Member State in the event of crisis and obligation of the suppliers to keep the sufficient reserves for that [19]. In addition, the all-Union coordination, as well as the adoption of the national emergency plans were also provided in the Regulation [20]. Thus, the Regulation No 994/2010 had already concerned the extremely sensitive issue of the conflict with the contractual obligations of suppliers and intervention to the commercial activity of operators of natural gas transmission. In particular, the ‘supply standard’ required the suppliers to neglect their contractual obligations with the non-protected consumers in the event of crisis. The ‘infrastructure standard’ had an effect on the activity of transmission system operators, since they were required to keep a certain capacities and invest in the infrastructure, even though the market’s realities might not be in a line with such big investments. However, several factors firmly justified these restrictive obligations: a general need of mitigation the supply risks; clarification of the Union’s role in energy policy (a shared competence in the EU) after the Lisbon Treaty and amendment of the Treaty on Functioning of the European Union with the article 194 on energy, where the security of supply was among the main objectives allowing the Council and Commission to enact decisions in this sphere under the ordinary legislative procedure [21].

Moreover, the fulfillment of the ‘infrastructure standard’, which also might be related to the need of booking the capacity on the trans-border points between two Member States, can, according to M. Glachant, be performed in a less market-restrictive way by concluding the fallback contracts between these TSOs [22]. Some demand-side measures were also prescribed by the Regulation itself [23]. In contrast, G. Block and A. Johnston claim that setting of such a universal standard seems to be inappropriate, since the equilibrium of cost and benefits of such measures might be much different in different Member States [24]. The Regulation also set a requirement of information exchange, which included the obligation to notify the Commission on the infrastructure and supply contracts with the third countries in order to enable it to perform monitoring functions [25]. Finally, yet importantly, the Regulation set possibilities of communication between the GCG and Contracting Parties of the Energy Community in the coordination of emergency measures. Therefore, the Regulation 994/2010 made a significant step forward in the introduction of the common security in natural gas policy, setting, however, some controversial and restrictive practices from the market point of view.

The new revision of the EU security of supply legislation and enactment of the Regulation 2017/1938 took place after the beginning of Russian – Ukrainian conflict, which brought some new threats to the security of supply to the EU. The new Regulation 2017/1938, which repealed the Regulation 994/2010 went even further in setting of the quite restrictive practices. Preserving many elements of the previous Regulation 994/2010 (including the ‘infrastructure’ and ‘supply’ standards, as well as the common risk mitigation procedure), it also established a new provison of solidarity: a Member State (through its competent authority or TSO) has an obligation to deliver a necessary volume of gas to the requesting Member State to ensure the supply to ‘protected customers’ there and cut off the supply to non-protected customers in its own territory, if the necessary amount cannot be delivered otherwise [26]. The Regulation emphasizes that these measures are to be considered as the measures of the last resort, applied only if the situation cannot be solved by the market mechanisms and be compensated afterwards [27]. However, this provision might be considered as controversial to the sanctity of contract obligations and ownership, especially in the case of harmonization of such measures with the Energy Community Contracting Parties, thus the issue seems to be extremely complex (a more detailed discussion on this issue is provided in following sub-chapters). Eventually, the new Regulation also revised the rules of information exchange concerning the notification of the Commission on the new gas supply contracts. Thus, currently the competent authority is required to report to the Commission immediately about the supply contract, where the contracted volume of procured gas exceeds 28 % of the national demand [28]. The Commission or competent authority of the Member State may also request a company to provide an existing contract for monitoring, if there are some motivated concerns on the possible threats to the the supply [29]. The new Regulation also sets obligation of national competent authorities and the Commission to establish the penalties for the national undertakings that infringe the requirement of provision the necessary information of the contracts. Therefore, the new Regulation on the safeguard measures securing the natural gas supply elaborated even harsher measures, which are aimed at mitigation of the potential risks of supply interruption. It is noteworthy that the Regulation sets some particular measures towards monitoring of the long- and mid-term supply contracts (more than 1 year), which might be related to the previous Commissions' attempts to minimize the share of such contracts in the market [30]. Eventually, the solidarity measures might create many difficulties and, at the present are not likely to be even partly implemented in the Contracting Parties of the Energy Community (which is discussed in the following sub-chapters). On the other hand, the Regulation highlights the need of cooperation with the Energy Community countries, which might make some opportunities for enhancing this cooperation in the other aspects of the security of natural gas supply. Following sub-chapters examine these opportunities.

3.2. Possibilities of the involvement of Ukraine and Moldova to the risk assessment and mitigation procedures

The new Regulation 2017/1938 directly prescribes some opportunities for involvement of the Energy Community Contracting Parties in cooperation for ensuring the security of natural gas supply to the EU. In particular, Article 4 provides possibility of participation of the Energy Community countries in the Gas Coordination Group in the coordination of measures of the Union emergency [31], while Article 16 is fully devoted to the issue of cooperation with the Energy Community [32]. The later article also emphasizes that such cooperation is to be aimed at identifying the interaction and correlation of risks and consultations with a view to ensuring consistency of preventive action plans and emergency plans across the border [33]. Therefore, the new Regulation on the security of natural gas supply provides some possibilities for cooperation with the Energy Community Contracting Parties and engagement of these countries to the common security planning.

The current legislation and normative acts of Ukraine and Moldova already set some possibilities for this cooperation. In general, a significant rapprochement of the EU, Ukrainian and Moldovan legislation on the energy, and, particularly, the natural gas supply, took place in 2015 – 2016, when the Parliaments of these countries managed to transpose the main requirements of the Internal Gas Market Directive [34]. The Ukrainian law on natural gas market and Moldovan law on natural gas transposed not only the main elements of the Internal Gas Market Directive, but also some of the EU security of natural gas supply provisions (from Regulation 2017/1938). Thus, the main gas laws of the countries provide the obligation to communicate with the Energy Community Secretariat and EU Gas Coordination Group in preparation of the national action plan in the case of the emergency, as well as monitoring of the security of supply on the natural gas markets. This legislation of Ukraine and Moldova also established the obligation to provide the main principles of infrastructure and supply standards in the national security of gas supply regulation. The Ukrainian Rules on the security of natural gas supply (established by the Ministry's of Energy and Coal Industry Decree) [35] transposed the main elements and formula of infrastructure and supply standards. Another extremely important aspect of the Ukrainian Rules on the security of natural gas is an optional provision of increasing the cross-border capacities and enabling the bilateral gas flow with the gas-transmission systems of the European Union neighboring countries, if the feasibility of technical conditions of infrastructure, level of consumption and financial costs of this action are reasonable [36]. The rules provide an obligation of informing the Energy Community Secretariat in the case, if the option is withdrawn. Noteworthy that Ukrainian rules on the security of natural gas supply also provide an obligation of the risk assessment, which is similar to the EU requirements on the security of natural gas supply [37]. The last simulation of the potential risks for the gas transmission system of Ukraine took place in August, 2017, when the hydraulic modeling of the crisis situation (similarly to what the Regulation provides) was completed in the assistance of the expert group of the European Commission [38]. Finally, the Ukrainian National Action Plan, which was adopted in 2015, provides a guidance for cooperation with the Energy Community and the EU Gas Coordination Group in prevention and combating crises of natural gas supply, including some measures provided by the Regulation in article 9 (definition of protected customers; obligations on natural gas undertakings; information exchange; prohibition of applying non-market measures before the situation of emergency occurred etc.) [39]. The situation with enactment of the similar provisions in Moldova is currently lagging from Ukraine and only in the end of 2017 the Government project of National Action Plan (which, *inter alia*, included the provisions on infrastructure and supply standard) was designed, but still not fully implemented [40]. The lack of the connection of Moldova with the EU Member States' markets makes the issue of adoption of the multilateral security of supply standards extremely difficult in this country; however, the construction of Iasi-Ungheni gas pipeline to Romania might significantly change the situation.

In general, the cooperation between the EU and Ukraine and Moldova in risk assessment and mitigation procedure can be significantly improved by inclusion of these countries to the regional cooperation groups (provided in the Annex I of the Regulation 2017/1938). Moreover, Ukraine is already mentioned among the main gas supply routes for the Eastern regional cooperation group [41]. The Regulation lacks of definitions of the main tasks to be performed by the regional risk groups; however, in the recital 15 it states that the Member States have to agree on the actions and mechanisms within each of these groups [42]. This wide discretion of formulating the groups' agenda can be used to enhance the regional initiatives beyond the EU border and create a common framework for coordination. Thus, some of the already existing practices from the EU Regulation on security of natural gas supply in the legislation of Eastern Energy Community Contracting Parties can be performed without any lagging and within the EU schedule of necessary actions. Further possibilities of implementing the rest of the Regulation's provisions, including the solidarity provision, in Ukraine and Moldova is another important aspect for the analysis.

3.3. The prospective of the implementation of the solidarity provision into the national law of the Contracting Parties of the Energy Community

The exploration of the previous experience of the implementation of the elements of the EU security of supply legislation, as well as the attempts to engage Energy Community Contracting Parties in the common framework of mitigation the supply risks, demonstrates that Ukraine and Moldova have already begun the process of the enactment of some of the important EU security of supply provisions (namely, standards of infrastructure and supply and measures of prevention the energy crises). These attempts took place before the adoption of the new Regulation, although the Energy Community Treaty did not require the Contracting Parties to transpose the Regulation No 994/2010 and, at the present, it also does not set any similar obligations with a regard to the Regulation 2017/1938. However, the new Regulation 2017/1938 has already been discussed in some of the meetings with the Contracting Parties representatives, for instance, in the Energy Community Parliamentary Plenum (took place in Vienna, 19 December 2017), where the delegates considered the possibility of inclusion the Regulation to the Energy Community *acquis communautaire*. [43] Nevertheless, the implementation of some of the Regulation's principles might be quite problematic. The enactment of the Regulation in the EU raised the issues of compliance with the proportionality (in terms of increasing financial and administrative burden to achieve the infrastructure and supply standards) and subsidiarity (in defying the powers of Commission to adopt delegated acts under the Regulation) principles, as well as some controversies on the defining of the regional cooperation – mainly invoked by Bulgaria and Austria within the course of legislative procedure [44]. The main novelty of the Regulation – the solidarity provision –

seems to be the most problematic issues in the case of the Contracting Parties of the Energy Community.

Basically, the possible application of the solidarity provision in the non-EU countries might face a few legal problems: the limitation of the state sovereignty and the lack of harmonization of the relevant rules between the Contracting Parties of the Energy Community. The first issue is mainly determined by the difference in sovereignty approach in the EU and the Energy Community. Thus, the EU is known to be a unique legal system (*sui generis*), where the states deliberately confer the Union with the special competence to attain their common objectives, which is established by the article 5 of the Treaty of European Union [45]. It factually means that the sovereignty of the Member States might be limited in achieving common objectives, however, with the regard to the principles of subsidiarity and proportionality. The requirement of mandatory transfer of the natural gas from the one Member State to the consumers in another Member State, where the emergency situation occurred, can be justified at the EU level, since such measures correspond to the objective of ensuring the security of energy supply provided by article 194 TFEU, which was the legal basis for the Regulation [46]. In contrast, the Energy Community framework does not create such strong relationship between the Contracting Parties and it is still arguable, whether this organization has a sufficient impact on creating the new legal order for the Contracting Parties [47]. A possible voluntary adoption of the solidarity provision in legislation of some of the Contracting Parties (as it was with supply and infrastructure standards) may not be supported by the other Contracting Parties, since the principle of reciprocity is not clarified in the Treaty Establishing Energy Community, which would mean that multilateral measures of solidarity of gas exchange are not likely to be adopted in the Energy Community at present. Nevertheless, the solidarity provision of the Regulation 2017/1938 provides that the Member State shall adopt necessary solidarity measures, including technical, financial and legal arrangements by themselves and to elaborate the most optimal schemes for solidarity supply. This approach towards the fulfillment of solidarity requirement can be useful for the Contracting Parties of the Energy Community, since they may conclude the bilateral agreements on such measures, later this practice can be extended to the agreements with the EU Member States. In this way, the solidarity provision may be partly implemented in the Energy Community, although it would not make the multilateral framework of obligations.

Another problematic issue, which is related to the fulfillment of the solidarity provision, is the possible lack of clarity of the ‘solidarity protected customers’ notion. On the one hand, the Regulation provides the definition of the ‘solidarity protected customers’, which includes the household consumers, heating installation and an essential social service, if it is a protected customer in the relevant Member State, other than educational and public administration services [48]. Nevertheless, the most recent developments in the EU case law demonstrate that such Regulation’s definition can be interpreted in a broader way. In February 2018, the European Court of Justice (ECJ) ruled in the *Eni and Others* case that the previous Regulation 994/2010 did not preclude the national legislations of the Member States to extend the protection under the supply standard to the consumers, who are not listed in a definition of the ‘protected customer’, thus making it broader and allowing Member States to set higher standard of protection than provided in the Regulation [49]. According to the last analyses of this ECJ judgement by Lucila de Almeida and Lavinia Tănase, this approach is very likely to be extended to the new Regulation 2017/1938, which repealed the Regulation 994/2010 [50]. Although the definitions of the ‘protected customers’ and ‘solidarity protected customers’ are different in the new Regulation and refer to different provisions, the fact that ECJ recognized a discretion of the Member States and the fact that these definitions are still provided in quite a similar way to the previous Regulation’s text, may result in the attempts of the Member States to use this notion in order to restrict the application of solidarity provision. In particular, the Regulation provides that Member State shall stop the supply to all the national consumers, except the ‘solidarity protected customers’ in the event of emergency in the other Member State in order to provide the supply to ‘solidarity protected customers’ there. But the possibility of Member States to include a broad range of consumers to the category of 'solidarity protected customers' may provide it with possibility to avoid or significantly decrease its solidarity obligations on the grounds of the need to provide the supply to the national 'solidarity protected customers' first. In the case of implementation of the solidarity provision in the Energy Community Contracting Parties, they may also use such arguments. Moreover, there is a lack of an effective dispute settlement mechanism in the Energy Community (only political measures can be applied to the violators of the *acquis communautaire*), which makes the possibilities to prevent such infringement significantly less effective than in EU.

Therefore, the prospective of the implementation of the Regulation 2017/1938 in the Energy Community Contracting Parties seems to be quite unclear due to its impact on state's sovereignty and some other problematic issues. On the other hand, a wide discretion in defining the category of 'solidarity protected customers' might also result in the decrease of practical implementation of this provision not only in the Energy Community Contracting Parties, but also in the EU. Thus, the only possible option for introduction of this principle in the Energy Community can be a practice of the bilateral agreements between the Contracting Parties on solidarity supply, which, however, is not likely to result in a multilateral practice until the reciprocity provisions of cooperation in the Energy Community are more clarified.

4. CONCLUSIONS

The paper explored the evolution of the security of natural gas supply legislation in the EU and the main provisions of the new Regulation; possibilities to involve Ukraine and Moldova in the common mechanisms and prospective of the implementation of the new Regulation's provisions in the Energy Community Contracting Parties legislation using the law-in-the-context approach and functional approach to the legal comparison. The exploration demonstrated that a significant legal reform took place in the EU in the last decade as a response to the energy threats and possible interruptions of the supply provoked by the geopolitical situation. It also resulted in a stricter approach of the new security of supply legislation towards the fulfillment of the common objectives by the Member States and even possibility of limitation of some of the market liberalization provisions. This legal reform also found a feedback in the Energy Community countries including Ukraine and Moldova, whose legal system is different from the EU, but the threats of the security of supply and aims of their mitigation are quite similar to the Union's. The Energy Community framework did not provide obligation to implement the Regulation 2017/1938 and the previous Regulation 944/2010, but the exploration demonstrated that many important elements were voluntary implemented by Ukraine and are to be implemented by Moldova in the near future. The cooperation with the EU in the security of supply risk mitigation also exists, but the inclusion of Ukraine and Moldova to the mutual activity of the relevant regional groups (Eastern group – Ukraine; South-Eastern – Moldova) could greatly increase the effectiveness of such cooperation. However, a significant difference in the Energy Community's and the EU frameworks, as well as in the legal systems of the EU and non-EU countries obstructs the possibility of implementation of the main new Regulation's provision of the solidarity between the states. The implementation of this provision has numerous difficulties in the EU itself, but the enforcement mechanisms of the EU may solve some of the issues. On contrary, the Energy Community Contracting Parties are likely to implement such provision only by voluntary bilateral agreements, which would deprive these countries of multilateral framework for implementation. The findings of this paper aim at contributing to the increase of cooperation in the security of the natural gas supply in the EU and its Eastern Neighbours. Some progress can be achieved by introduction of some of the mentioned measures: further involvement of the Energy Community countries to the Union and regional cooperation in the risk mitigation procedures; inclusion of the new Regulation to the Energy Community *acquis communautaire* and implementation of its provisions to the national law of

Ukraine and Moldova; using of the mechanisms of bilateral cooperation, since the multilateral framework is not feasible at the present.

REFERENCES

1. Treaty establishing the Energy Community, Art. 10; Annex I.
2. MICHAELS R. ‘The Functional Method of Comparative Law’. in *The Oxford Handbook of Comparative Law*. Eds. Mathias Reimann and Reinhard Zimmermann. Oxford: Oxford University Press, 2006, (information on p. 341) 146 p. ISBN: 9780199535453.
3. SINANI B., SHANTO' K. Methods and Functions of Comparative Law. *Acta Universitatis Danubius. Juridica* Vol 9, No 2 (2013), (information on p. 31) pp. 25–40.
4. MICHAELS R. ‘The Functional Method of Comparative Law’. in *The Oxford Handbook of Comparative Law*. Eds. Mathias Reimann and Reinhard Zimmermann. Oxford: Oxford University Press, 2006, (information on p. 345) 1456 p. ISBN: 9780199535453.
5. HUSA J. *A New Introduction to Comparative Law*. Oxford and Portland, Oregon: Hart Publishing, 2015, (information on p. 129) 298 p. ISBN 1849469512.
6. ZWEIGERT K., KÖTZ H. *An Introduction to Comparative Law*. Oxford: Oxford University Press, 1998, (information on p .11) 744 p. ISBN-10: 0198268599.
7. YAFIMAVA K. *The Transit Dimension of EU Energy Security. Russian Gas Transit Across Ukraine, Belarus, and Moldova.* Oxford Institute for Energy Studies Publication, 2011, 316 p. ISBN: 9780199599226.
8. STERN J., PIRANI S., YAFIMAVA K. *The Russo-Ukrainian gas dispute of January 2009: a comprehensive assessment.* Oxford Institute for Energy Studies Publication, 2009, 66 p., ISBN 978-1-901795-85-1.
9. PIRANI S. *Russian and CIS Gas Markets and Their Impact on Europe.* Oxford Institute for Energy Studies Publication, 2009, 487 p., ISBN-10: 0199554544.
10. PIRANI S., HENDERSON J., YAFIMAVA K. et al. What the Ukrainian crisis means for gas markets. *Paper of Oxford Institute for Energy Studies, March 2014,* pp. 1–21.
11. J.-M. GLACHANT. ‘A vision for the EU gas target mode: MECO-S’ in J.-M. Glachant, M. Hallack, and M. Vazquez (Eds.), *Building competitive gas markets in the EU: Regulation, Supply and Demand,* Cheltenham: Edward Elgar, 2013, p. 282 ISBN-10: 1782540636.
12. JOHNSTON A., BLOCK G. *EU Energy Law,* Oxford: Oxford University Press, 2012, (information on p. 276), 466 p. ISBN: 9780199665242
13. TALUS K. *EU Energy Law and Policy: A Critical Account.* Oxford University Press, 2013, 375 p., ISBN: 9780199686391.
14. ČESNAKAS G. *Energy resources as the tools of foreign policy: the case of Russia*. Lithuanian Foreign Policy Review vol. 35 (2016), 9–40 p., ISSN 1822-9638.
15. HEINRICH A., PLEINES H. (Eds). *Export Pipelines from the CIS Region: Geopolitics, Securitization, and Political Decision-Making*. Columbia University Press, 2014, 300 p., ISBN: 9783838265391.
16. Le COQ C., PALTSEVA E. *Assessing gas transit risks: Russia vs. the EU*. Energy Policy Vol. 42, March 2012, 642 – 650 p. ISSN: 0301-4215.
17. EUROPEAN COMMISSION. *Imports and secure supplies. Diverse, affordable, and reliable energy*. available at: https://ec.europa.eu/energy/en/topics/imports-and-secure-supplies .
18. Annual Report of Naftogaz Company, 2016, available at: http://www.naftogaz.com/files/Zvity/Anual_report_eng_170608.pdf, pp. 134–135.
19. OTILIA NUȚU A., CENUȘĂ D. Interconnecting Moldova’s Gas Market: the Iasi-Ungheni case. *Research paper of Expert-Group Centru Analitic Independent*, February 2016, pp. 1–28.

20. OTILIA NUȚU A., CENUȘĂ D. Interconnecting Moldova’s Gas Market: the Iasi-Ungheni case. *Research paper of Expert-Group Centru Analitic Independent*, February 2016, (information on p.10) pp. 1–28.
21. Council Directive 2004/67/EC of 26 April 2004 concerning measures to safeguard security of natural gas supply. *Official Journal L 127 , 29/04/2004* P. 92–96.
22. STERN J. ‘The new security environment for European gas: worsening geopolitics and increasing global competition for LNG’ in Francois Leveque, Jean-Michael Glachant, Julian Barquin et at (eds.) *Security of energy supply in Europe*. Cheltenham: Edward Elgar, 2010, (information on p. 59) 314 p. ISBN 978 1 84980 032 7.
23. PIRANI S., STERN J., YAFIMAVA K. The Russo-Ukrainian gas dispute of January 2009: a comprehensive assessment, *Paper of Oxford Institute for Energy Studies,* NG 27, February 2009 (information on p.19), pp. 1–66.
24. Regulation (EU) No 994/2010 of the European Parliament and of the Council of 20 October 2010 concerning measures to safeguard security of gas supply and repealing Council Directive 2004/67/EC, *Official Journal L 295, 12.11.2010*, P. 1–22.
25. Regulation (EU) No 994/2010 of the European Parliament and of the Council of 20 October 2010 concerning measures to safeguard security of gas supply and repealing Council Directive 2004/67/EC, *Official Journal L 295, 12.11.2010*, P. 1–22.
26. Regulation (EU) No 994/2010 of the European Parliament and of the Council of 20 October 2010 concerning measures to safeguard security of gas supply and repealing Council Directive 2004/67/EC, *Official Journal L 295, 12.11.2010*, P. 1–22.
27. Regulation (EU) No 994/2010 of the European Parliament and of the Council of 20 October 2010 concerning measures to safeguard security of gas supply and repealing Council Directive 2004/67/EC, *Official Journal L 295, 12.11.2010*, P. 1–22.
28. Treaty on the Functioning of the European Union, *Official Journal C 326, 26.10.2012*, p. 96.
29. GLACHANT J.-M. ‘A vision for the EU gas target mode: MECO-S’ in J.-M. Glachant, M. Hallack, and M. Vazquez (Eds.), *Building competitive gas markets in the EU: Regulation, Supply and Demand*, Cheltenham: Edward Elgar, 2013, (information in p. 160), p. 282 ISBN-10: 1782540636.
30. Regulation (EU) No 994/2010 of the European Parliament and of the Council of 20 October 2010 concerning measures to safeguard security of gas supply and repealing Council Directive 2004/67/EC, *Official Journal L 295, 12.11.2010*, P. 1–22.
31. JOHNSTON A., BLOCK G. *EU Energy Law*, Oxford: Oxford University Press, 2012, (information on p. 276), 466 p. ISBN: 9780199665242.
32. Regulation (EU) No 994/2010 of the European Parliament and of the Council of 20 October 2010 concerning measures to safeguard security of gas supply and repealing Council Directive 2004/67/EC, *Official Journal L 295, 12.11.2010*, P. 1–22.
33. Regulation (EU) 2017/1938 of the European Parliament and of the Council of 25 October 2017 concerning measures to safeguard the security of gas supply and repealing Regulation (EU) No 994/2010, *Official Journal L 280, 28.10.2017, p. 1–56.*
34. Regulation (EU) 2017/1938 of the European Parliament and of the Council of 25 October 2017 concerning measures to safeguard the security of gas supply and repealing Regulation (EU) No 994/2010, *Official Journal L 280, 28.10.2017, p. 1–56.*
35. Regulation (EU) 2017/1938 of the European Parliament and of the Council of 25 October 2017 concerning measures to safeguard the security of gas supply and repealing Regulation (EU) No 994/2010, *Official Journal L 280, 28.10.2017, p. 1–56.*

36. Regulation (EU) 2017/1938 of the European Parliament and of the Council of 25 October 2017 concerning measures to safeguard the security of gas supply and repealing Regulation (EU) No 994/2010, *Official Journal L 280, 28.10.2017, p. 1–56.*
37. TALUS K. Long-term natural gas contracts and antitrust law in the European Union and the United States. *The Journal of World Energy Law & Business*, Vol. 4, Issue 3 (2011), pp. 260–315.
38. Regulation (EU) 2017/1938 of the European Parliament and of the Council of 25 October 2017 concerning measures to safeguard the security of gas supply and repealing Regulation (EU) No 994/2010, *Official Journal L 280, 28.10.2017, p. 1–56.*
39. Regulation (EU) 2017/1938 of the European Parliament and of the Council of 25 October 2017 concerning measures to safeguard the security of gas supply and repealing Regulation (EU) No 994/2010, *Official Journal L 280, 28.10.2017, p. 1–56.*
40. Regulation (EU) 2017/1938 of the European Parliament and of the Council of 25 October 2017 concerning measures to safeguard the security of gas supply and repealing Regulation (EU) No 994/2010, *Official Journal L 280, 28.10.2017, p. 1–56.*
41. Law on natural gas market of Ukraine, *Відомості Верховної Ради (ВВР), 2015, № 27, ст. 234;* Law of Moldova on natural gas *Nr. 108 enacted on 27.05.2016, 08.07.2016 в Monitorul Oficial Nr. 193-203 статья №: 415.*
42. Міністерство енергетики та вугільної промисловості України Наказ 02.11.2015 № 686 *Про затвердження Правил про безпеку постачання природного газу.*
43. Міністерство енергетики та вугільної промисловості України Наказ 02.11.2015 № 686 *Про затвердження Правил про безпеку постачання природного газу.*
44. Міністерство енергетики та вугільної промисловості України Наказ 02.11.2015 № 686 *Про затвердження Правил про безпеку постачання природного газу.*
45. НАФТОГАЗ УКРАЇНИ. *Єврокомісія провела успішне тестування готовності української ГТС до нового опалювального сезону (09.08.2017)*, available at: http://naftogaz.com/www/3/nakweb.nsf/0/78E2A6B1AABD68DCC225817700286C2A?OpenDocument&year=2017&month=08&nt=%D0%9D%D0%BE%D0%B2%D0%B8%D0%BD%D0%B8 .
46. Міністерство енергетики та вугільної промисловості України Нака з m02.11.2015 № 687 *Про затвердження Національного плану дій*
47. Hotărîrea Guvernului. *Planul de acțiuni pentru situații excepționale pe piața gazelor natural,* 2017
48. Regulation (EU) 2017/1938 of the European Parliament and of the Council of 25 October 2017 concerning measures to safeguard the security of gas supply and repealing Regulation (EU) No 994/2010, *Official Journal L 280, 28.10.2017, p. 1–56.*
49. Regulation (EU) 2017/1938 of the European Parliament and of the Council of 25 October 2017 concerning measures to safeguard the security of gas supply and repealing Regulation (EU) No 994/2010, *Official Journal L 280, 28.10.2017, p. 1–56.*
50. Energy Community Parliamentary Plenum. *Joint Report on Security of Energy Supply in the Energy Community Region*, 19 December 2017, Vienna, (information on pp. 7–8). pp. 1–8
51. European Parliament. *Briefing EU Legislation in Progress*, June 2017, (information on p. 6), pp. 1– 8.
52. Treaty of European Union, Article 5.
53. Treaty on the Functioning of the European Union, *Official Journal C 326, 26.10.2012*, p. 96; Regulation (EU) 2017/1938 of the European Parliament and of the Council of 25 October 2017 concerning measures to safeguard the security of gas supply and repealing Regulation (EU) No 994/2010, *Official Journal L 280, 28.10.2017, p. 1–56.*

54. KAROVA R., The Dispute Settlement System of the Energy Community: testing its effectiveness, in D. Buschle and K.Talus, The Energy Community. A New Energy Governance System (Intersentia, 2015), (information in p. 45), 618 p. ISBN 9781780683027
55. Regulation (EU) 2017/1938 of the European Parliament and of the Council of 25 October 2017 concerning measures to safeguard the security of gas supply and repealing Regulation (EU) No 994/2010, *Official Journal L 280, 28.10.2017, p. 1–56.*
56. C-226/16, *Eni and Others* [2017] EU ECJ published in the electronic Reports of Cases, available at: http://curia.europa.eu/juris/liste.jsf?language=en&num=C-226/16 .
57. DE ALMEIDA L., TĂNASE L. Who are ‘protected customers’ for the EU Regulation(s) for security of gas supply? The Eni SpA and Others case (C-226/16) and the margin of discretion of Member States, *European University Institute, published on 29th January 2018*, available at: http://fsr.eui.eu/protected-customers-eu-regulations-security-gas-supply/ .

CYSENI 2018, May 23-25, Kaunas, Lithuania
ISSN 1822-7554, www.cyseni.com

IDENTIFICATION OF BARRIERS AND ACTIONS FOR ELECTRIC VEHICLE ADOPTION AT THE MUNICIPAL LEVEL

P. Mačiulis
Lithuanian Energy Institute
Breslaujos str. 3, LT-44403 Kaunas – Lithuania
Email: povilas.maciulis@gmail.com

ABSTRACT

The transport sector is one of the major polluter of greenhouse gases and other pollutants. Electric vehicles are considered as one of the most effective technologies for decrease greenhouse gas emissions from the transport sector, reduce dependence on oil and improve air quality. Despite potential advantages, significant barriers remain to widespread adoption of electric vehicle technology and currently they represent a small market share of vehicles in service. However, the adoption rate of electric vehicles is relatively slow and varies in different cities. Therefore, in many countries, local authorities have introduced financial and non financial incentives to facilitate the electric vehicle market penetration. Private investors, technology companies and policy makers need to recognise obstacles and factors, which prevent transformation of road transport towards significantly lower carbon emissions. The aim of this article is to identify the main barriers that hamper electric vehicle usage development and define the measures that could help reduce these barriers at the municipal level. Also this paper recommends the framework of solutions, that could help cities to overcome barriers and achieve better results for electric vehicles adoption.

Keywords: renewable energy in transport, electric vehicle, barriers

1. INTRODUCTION

Although electric vehicles can significantly contribute to energy consumption efficiency, reduction of carbon dioxide emissions and independence from petroleum imports, the consistent development of electric vehicle usage is still hampered by different barriers (Kley et al., 2010). According to Rezvani et al. (2015), the differences in technological characteristics determine attribution of electric vehicles to four following groups: hybrid electric vehicles (HEVs), battery electric vehicles (BEVs), extended-range battery electric vehicles (E-REVs) and plug-in hybrid electric vehicles (PHEVs).

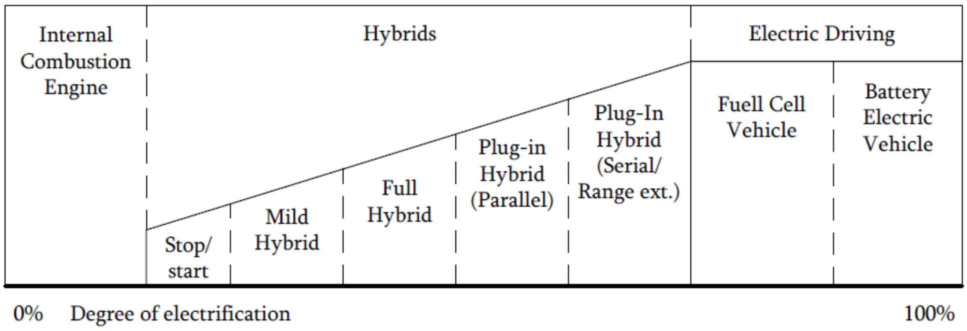

Fig. 1. Degrees of electrification of different vehicle drive-train concepts (Michelin, 2011)

The decision of the author of this article to focus on battery electric vehicles is based on the notion that this technology is considered to be one of the most attractive alternatives to internal combustion engines as it may help reduce dependence from fossil fuels and reach a new level of efficiency in the transport sector. With reference to Brown (2001), environmentally-friendly technologies face the problem of low diffusion rates which is typical of high-priced vehicles.

Nevertheless, despite their higher prices, electric vehicles provide the lower total cost of ownership over the vehicle lifetime in comparison to traditional vehicles with internal combustion engines. This advantage is determined by lower fuel and maintenance costs (Wang et al., 2017). According to Rogers (2013), investment in new technologies is linked to inexperienced benefits. Therefore, a proven and clearly understandable innovation means lower uncertainty for potential consumers, which, in turn, proposes that electric vehicle market penetration largely depends on how potential consumers perceive electric vehicles' benefits, advantages and usage aspects. In other words, rising awareness and experience promote consumption of a product. Despite faster information flows, rapid technological advancement and increasing availability of electric vehicles, the greatest strength of this mean of transportation is its environmental and social value. The review of the main strengths, weaknesses, opportunities and threats of electric electric vehicles, introduced by Quak et al. (2016), who researched the potential of electric vehicles in the truck market, has been presented below.

Table 1. Strenghts, weaknesses, opportunities and threats analysis of electric vehicle (Quak et al., 2016)

Strenghts ○ Low fuel costs ○ Efficiency of operation in case of gvernment support ○ Good environmental performance ○ No noise from vehicle ○ Positive acceptance by public	Weaknesses ○ High procurement costs ○ Limited loading capacity ○ Limited, unreliable and expensive after-sales support ○ No better revenues (limited number of customers paying more) for EV deliveries ○ Grid issues with large fleet ○ Limited availability of vehicles
Opportunities ○ New(er) vehicles have higher range ○ Well-fitting to the specific niches ○ Availability of public charging points ○ Innovative vehicle/battery leasing schemes ○ Decrease in battery price	Threats ○ Unclear regulation regarding certification ○ Better environmental performance of vehicles running on alternative fuels ○ Low oil prices, and increasing energy prices

The studies show that acceptance of any new technologies in the market is hampered by some general barriers: lack of early consumers' awareness, high initial costs and low risk tolerance (Diamond, 2009). The aim of this article is to identify the main barriers that hamper electric vehicle usage development and define the measures that could help reduce these barriers at the municipal level. The research will be conducted on the basis on scientific literature analysis.

The next section discusses the barriers that are divided into three following groups: technical and infrastructure, economic and human barriers.

2. TECHNICAL AND INFRASTRUCTURE BARRIERS

Advanced transport technologies possess the features which require market introduction before becoming an object of consumer consideration. Awareness of the barriers of electric vehicle usage provides the opportunities to identify the market and define the potential of these innovative means of transportation. This section discusses the technical and infrastructural barriers which are linked to the limited electric vehicle potential and lack of appropriate infrastructure.

Limited driving range. Depending on battery capacity, electric cars offer a theoretical driving range, which commonly varies from 200 to 300 km (Larson et al., 2014). The actual driving range, however, largely depends on a driver's actions, such as acceleration or deceleration. An important role is also played by driving conditions, for instance, changing terrain or driving in cities or on highways. The efficient use of a vehicle's regenerative braking and additional energy consumption (for instance, for air conditioning or heating) is no less important (Windisch, 2013). Consumers often have doubts about the actual driving range, which in practice is much shorter than the one declared by manufacturers. In addition, there are concerns that an electric-vehicle battery may quickly wear out, which, in turn, may further reduce a vehicle's driving range (Sierzchula et al., 2014). For instance, *plug-in hybrid electric vehicles*, which exploit battery capacity and a petrol tank to cover a driving range, do not possess this limitation (Windisch, 2013). Similar problems are faced by trucks. In 2013, manufacturers declared that driving range for electric trucks would vary from 100 to 150 km. Although in many cases this range failed to be reached, newer models now are capable of covering longer driving ranges with a single charge. Nevertheless, despite the positive development, this limitation still burdens usage of electric vehicles for logistics operations (Quak et al., 2016).

Battery charge time. Limited driving range is linked to another barrier – battery charge time. It may take up to 5–8 hours to charge an electric car with a fully discharged battery through a domestic power outlet. This duration largely depends on a battery type and capacity. Fast charging points can fully charge a car in 30–60 minutes on average, depending on charging equipment, a battery and its type (Legrand, 2011). Such accelerated charge is usually available in public areas (e.g. streets, shopping centres, etc.). Battery exchange points, where electric vehicles are equipped with fully charged batteries in a few minutes, are also arranged (Windisch, 2013).

Limited access to charging stations. Due to limited battery performance, electric vehicles require frequent charging. For this reason, the successful development of electric vehicle usage calls for sufficient charging infrastructures (Windisch, 2013). The factor analysis helped to identify that strategic support of a state and positioning of charging stations are the main determinants of electric vehicle usage promotion. Arrangement of charging points in residential and work areas is more important in comparison to arrangement of charging points in public areas. What is more, consumers prefer charging their electric vehicles at home in the night time to charging them at work in the day time (Wang et. al, 2017). Public authorities often face a "chicken-and-egg" problem: without well-developed charging and filling station systems, drivers do not want to buy environmentally-friendly vehicles, but it is hard to expect that sufficient infrastructures will be built without any active usage of environmentally-friendly vehicles (Stevens, Schieb, 2013). Perdiguero and Jiménez (2012) are of the opinion that not only development of extensive charging networks, but also constant maintenance of these networks and reversal of past mistakes may contribute to electric vehicle usage promotion.

3. ECONOMIC BARRIERS

The development of new technologies is often difficult due to high market entrance costs. In this section, we will discuss the electric vehicle-price related economic barriers and consumers' uncertainty of the resale value and future savings.

High acquisition costs. One of the main arguments why consumers avoid buying electric vehicles is their price, which is higher than the price of traditional vehicles with internal combustion engines (Windisch, 2013). The main determinants of such high prices are expensive batteries and smaller quantities of electric vehicles manufactured (Quak et al., 2016). In spite of the fact that electric vehicles generate lower exploitation costs, high acquisition costs (which are initially borne by consumers) are an important factor of consumers' decision (Kley et al., 2010). So that an innovation like electric car engines would have a significant impact on environment, it has to be widely-spread (and produce lower emissions in comparison to traditional internal combustion engines). This objective can be achieved on condition the market demand for electric vehicles is high enough for manufacturers to develop these technologies and sell new vehicles. Thus, national governments have to invoke financial incentives to engage consumers in early stages (Sierzchula et al., 2014).

Uncertainty of the resale value. When a consumer is buying an electric car, it is important for him to know for how much he will be able to sell the car in the future, and in this case price difference does not greatly vary from the one estimated when selling traditional vehicles with internal combustion engines. For instance, unlike electric vehicle resale market, diesel and petrol driven vehicle resale market is well-established and clear, which allows to predict the value of these vehicles in *second hand* markets. It is obvious that this factor is closely related to the above-discussed electric vehicle promotion barrier – high acquisition costs (Windisch, 2013).

The situation in the truck market is very similar: as the operators are interested in short-term benefits, price plays a very important role, and absence of second hand markets not only raises consumers' doubts about the reasonableness of their decision to buy, but also discourages credit institutions from provision of leasing or other funding (Quak et al., 2016).

Uncertainty of future savings. In terms of energy and exploitation costs, electric vehicles really offer an opportunity of cost saving in the long run (Windisch, 2013). The growing interest in electric vehicles and their maintenance shows that the regular maintenance costs less and requires less effort. This is because electric vehicles have fewer moving parts than vehicles with internal combustion engines; what is more, electric vehicles do not require regular oil changes, regenerative braking prevents their braking systems from quick wearing, etc. (Quak et al., 2016). Nevertheless, consumers are inclined to attribute a lower value to future savings and are not able to objectively assess the potential benefits (Kley et al., 2010).

4. HUMAN BARRIERS

Electric vehicles are acquired by people, whose decisions are affected by particular preferences, trends and stereotypes. Below in the article, consumer-related barriers that impede the successful development of electric vehicle usage have been discussed.

Consumer preferences. Despite the constant growth in electric vehicle supply, consumers thus far have not been provided with an alternative similar to a vehicle with an internal combustion engine. With a few exeptions, selection of a traditional vehicle can be based on consideration of many options and assemblies, while electric vehicles often occupy only a small share in a particular brand segment (Windisch, 2013). In some cases, manufacturers (e.g. *Tesla*) offer only electric vehicles.

Misunderstanding of a driving range needed. Although electric vehicles provide a limited driving range without an extra battery charge, this not always causes incoveniences. The research, conducted in France in 2011, revealed that more than 90% of the total vehicle daily milage does not exceed 100 km, which indicates that the common daily milage fits into the single-charge capacities of electric vehicles. Nevertheless, electric vehicle buyers, especially those who possess more than one vehicle in a family, want to be sure that the vehicle will meet the need of trips at all possible distances (Windisch, 2013). Consumers' doubts about the capacity of electric vehicles raise the anxiety which forms the image of an electric vehicle as of an inconvenient mean of transportation. This negative image is getting stronger in terms of long-distance trips, for instance, holiday trips (Jin & Slowik, 2017).

Inaccurate knowledge about electric vehicles. In general, consumers in most researched regions are poorly familiar with electric vehicle technologies; they have no knowledge of possible incentives and are hardly informed about the advantages of electric vehicles (Jin & Slowik, 2017). Following prevalent stereotypes, consumers can build the image of an electric vehicle as of a 'small', 'slow', 'cheap-looking' and 'inconvenient' mean of transportation. As previously mentioned, consumers are hardly able to assess the economic benefits of electric vehicles. As a result, greater environmental benefits, delivered by electric vehicles in comparison to traditional vehicles with internal combustion engines, remain a second-plan issue (Windisch, 2013).

5. THE MEASURES INFLUENCING CONSUMERS' AWARENESS

Previous studies reveal that there exists a general lack of the knowledge about electric vehicles, and consumers have various misconceptions about them (Jin & Slowik, 2017). For instance, the results of the research carried out by Singer (2015) disclosed that only less than half of the US consumers can indicate an electric vehicle brand or manufacturer. The survey, conducted in 21 US city, showed that nearly two thirds of the respondents had misconceptions about the basic characteristics of electric cars, and only 5% of the respondents knew about electric car promotion initiatives (Krause, 2013). Jin & Slowik (2017) identified five different elements that are linked to electric vehicle notion in terms of information and promotion measures. These elements include general information, cost comparison, public charger location, incentives and model availability.

Wang et al.'s (2017) study revealed that consumers' perception of electric cars can be a serious barrier to the development of the electric vehicle market. If consumers might obtain precise knowledge of electric vehicles and had an opportunity to regularly try these means of transportation, their attitudes would change, and the wish to acquire electric vehicles would sharpy increase. Different incentives and initiatives are employed to eliminate the above-discussed barriers. The markets, where the spread of electric vehicles is comparatively wide, employ much more comprehensive and sophisticated campaigns. The summary of the promotive activities, reviewed by Jin & Slowik (2017), has been presented below.

Table 2. Exemplary actions from major zero-emissions vehicle markets (Jin & Slowik, 2017)

Category	**Sub-category**	**Example of region**
Info and tools	Technology, cost	U.K.
	Infrastructure, policy	U.S.
	Policy, incentives	California
Public events	Ride and drive	U.S., Québec
	EV showcase	Shanghai
Exposure from fleets	Private fleets	Netherlands, U.K.
	Government fleet	California, Québec
	Carsharing/ Rental cars	Canada, Germany, Netherlands, U.S.
	Company cars	Norway
Exposure in regional planning	Action plan/ Initiative/ Partnership	U.S.
	Demonstration projects	Germany
Consumer awareness campaigns	NA	U.K.
Youth education and Professional development	NA	U.K.
Awards and recognitions	NA	Baveria, Germany
Auto dealer awareness activities	NA	Canada
Consistent signage and labeling	NA	California, Oregon, Québec
Tourism	N/A	Oregon

Previous studies show that potential consumers' notion and understanding are directly linked to the decision to buy an electric vehicle, which is especially felt in the regions that are at the initial stage of the electric vehicle introduction. A wide circle of stakeholders, including different levels of government, non-governmental organisations, academic institutions and local communities, can take an action to raise consumers' understanding and awareness (Jin & Slowik, 2017). Below in the article, the measures that can be employed to promote electric vehicle usage at the municipal level are discussed.

6. ACTIONS AFFECTING OTHER BARRIERS

National authorities can select a specific set of promotion measures with consideration of peculiarities of the current system, universal needs and financial capacities that depend on characteristics of a country, including its geographical position and economic situation (Windisch, 2013). Regardless of the power of national authorities, it should not be overlooked that local authorities are closer to consumers. Therefore, local policies, which promote usage of electric vehicles, can create additional incentives not only for individual consumers, but also for business companies (Kampman et al., 2011). Before national or global implementation of promotive measures, cities can play a leading role in developing and testing innovative policies. In 2015, nearly one-third of global car sales occurred in 14 cities worldwide (Hall et al., 2017). The issue of air quality is the main driving force for cities to stimulate usage of electric vehicles. It is no wonder that the cities which serve as urbanisation centres often occupy larger electric vehicle market shares in comparison to country averages (IEA/OECD, 2017).

Charging infrastructure. Authorities often face the 'chicken-and-egg' phenomenon: without extensive charging and filling station systems, drivers do not want to buy eco-friendly vehicles; on the other hand, it is hard to expect that extensive infrastructures will be built without the active usage of eco-friendly vehicles (Stevens and Schieb, 2013). Perdiguero and Jiménez (2012) and Sunnerstedt (2009) make a conclusion that an extensive charging network and its continuous development are the conditions necessary for promotion of the usage of electric vehicles. What is more, not only network supply development, but also network maintenance and improvement are important determinants of the usage of electric vehicles. Arrangement of the local public recharge infrastructure is an exceptional duty of local authorities. Local public recharge infrastructures can be developed by involving the funds and private investors (Windisch, 2013). For promotion of the usage of electric vehicles, local authorities must focus on the development of recharge infrastructures at homes, works and in public areas (OECD/IEA, 2016). Each of the above-mentioned recharge locations is linked to different types of promotion and policy issues. Most of the experts agree that namely home charging infrastructure is one of the key determinants of electric vehicle sales promotion, especially for those, who start using electric vehicles in the initial stage of development. For instance, London City initially focused on the promotion of home charging stations, and only after that – on work charging stations and public charging stations (Salisbury, 2011). Paris municipality not only granted extra parking benefits and arranged special parking lots for electric cars, but also built electric vehicle charging stations by the Autolib electric car-sharing programme (Hall et al., 2017). In accordance with a car battery type and charging speed preferred, the owners of electric cars may need to upgrade their electrical systems at homes so that their cars could be charged by night and exploited by day. This causes extra costs and information discrepancies, which, in turn, may impede purchase of an electric vehicle. Local authorities may employ the rebates or grants for the purchase or installation of home charging equipment. Rebates can also be employed upon the purchase of equipment or monthly electricity rates can be reduced (Windisch, 2013). For instance, the municipality of Utrecht offers a €500-subsidy for arrangement of a private charging station, and a €1500-subsidy for arrangement of the semi-public charging infrastructure (Hall et al., 2017). The metropolitan area of Amsterdam have made an interesting strategic policy decision for promotion of the development of charging infrastructures: they apply the demand-based approach for zoning actions, i.e. public charging infrastructures are built only after consideration of consumer needs. Electric vehicle buyers may register their needs to have a charging station near their homes, and the municipality builds the stations or looks for private or off-street alternatives (IEA/OECD, 2017). Rushlow et al. (2015) found that potential electric vehicle buyers are 20 times more likely to buy an electric vehicle if they have an access to a charging station in their workplace. Extensive networks composed of workplace and commercial charging stations help the utilities to manage mid-day peaks and match electric vehicle charging to solar energy. Mersky et al. (2016) found that usage of electric vehicles in the municipal level is sensitive to the average household income, while usage of electric vehicles for business purposes much depends on the number of charging stations. What concerns the arrangement of charging stations in public areas, it is important not to underestimate station building costs and to identify who is going to bear these costs. What is more, municipalities and their partners have to decide on electric vehicle charging fees, i.e. they can consider several options from free and unregulated charging when the municipality bears all the costs (which may have a significant impact on eco-friendly car sales) to introduction of the policies when the costs are borne by nearly located business companies taxed a higher utility rates. Charging station users may also pay not for charging itself, but for parking, which drives charging costs down (Salisbury, 2011). In any case, administrative procedures, including arrangement of home charging and public charging stations, have to be simplified (Windisch, 2013). Despite the difficulties to identify a clear need to have charging stations in apartment block yards, the municipal focus on arrangement of charging infrastructures in these yards is logical (Salisbury, 2011), especially minding the fact that it does not require additional public funds. In the municipal level, the additional requirements linked to the development of real estate can be identified. According to Cluzel et al. (2013), the obligation for real estate developers to arrange charging stations in new buildings is the most cost-effective method to raise the attractiveness of electric vehicle usage in workplaces and residential areas. This attitude is supported by Hanley (2011) who notes that such setting of rules hardly generates extra costs for local authorities because all the costs are borne by real estate developers. Later on, these costs are naturally included in the price of the premises on sale. Here are some examples. Vancouver City Council made the decision to amend the Building Code so that each private house could support Level 2 charging infrastructure, and 20% of apartment block parking lots could be adapted for charging of electric vehicles. San Francisco City Council obliged real estate developers to install Level 2 chargers in 10% of newly-built parking premises and prepare the equipment necessary for installation of extra 10% in the future (IEA/OECD, 2017).

Other measures. Regulation instruments, such as fuel economy standards and financial incentives to purchase electric vehicles, can be successfully created at the municipality level, while circulative incentives and the waivers to access restrictions are more commonly employed by national authorities. The advantages of well-adjusted regulatory measures and the need to act at the local level are linked to exploitation of road networks (OECD/IEA, 2016). Local authorities should promote usage of electric vehicles by providing a large and understandable value for consumers with non-financial advantages, such as preferential parking and road access (Cluzel et al., 2013). Parking regulations and zoning actions are the instruments directly linked to urban networks. While making their decisions, local authorities follow the plans of urban network exploitation and development (IEA/OECD, 2017). Such measures as preferential fees (for example, to public parking or congestion charging zones) and preferential access rights are politically acceptable and easily implemented. It is common practice that such measures are accepted in the municipal level as local authorities can best define the scopes of measure implementation with consideration of traffic intensity and lack of parking lots (Windisch, 2013). This attitude is supported by Kampman et al. (2011) who note that such measures as road toll exemptions or parking rebates, which can also be important for promotion of electric vehicles, are commonly employed at the local level. According to Sunnerstedt (2009), drivers like daily benefits granted for usage of eco-friendly vehicles. This means that one-time tax exemption granted for purchase of an electric car is less effective than the offer to use a free parking lot every day. The research, carried by Litman (2016), revealed that charging of parking fees is the second efficient congestion reduction strategy, which is less efficient than employment of peak-period congestion fees, but more efficient than employment of fuel taxes and emission fees. Gradually introduced parking fees, which are politically acceptable and simply administrated, provide more benefits than time-and-location-based road pricing, implementation of which is costly and requires special infrastructures. Permission to drive high-occupancy, bus or transit lanes is another measure that may contribute to promotion of electric vehicle usage. According to Tal and Nicholas (2014), permission to drive *high-occupancy vehicle* lanes is an important non-monetary promotion measure. Hardman (2017) states that in order to prevent jamming of high-occupancy vehicle lanes, the lanes should be made available only to the vehicles with two or more passengers; in addition, lane exploitation time can be fixed. Tal and Nicholas (2014) present the example of California where *high-occupancy vehicle* lanes can be used only with special access permissions: white stickers can be acquired by an unlimited number of low-emission vehicle drivers. With reference to Van der Steen et al. (2015), the research in California revealed that 59% of the respondents treated access to *high-occupancy vehicle* lanes as an extremely important determinant of their decision to purchase an electric vehicle. Bjerkan et al. (2016) note that access to bus lanes is an incentive that does not require governmental expenditure, and therefore can be employed as a marketing tool in small and medium-sized cities till the number of electric vehicles reaches the rate when electric vehicles become a burden to regular public transport flows. Hanley's (2011) matrix of the incentives that can be implemented by local authorities to promote usage of electric vehicles has been presented in Table 3.

Table 3. Matrix of the incentives that can be implemented by local authorities to promote usage of electric vehicles (Hanley, 2011)

Incentive	**Pros**	**Cons**	**Overall effectiveness**	**Local authority appetite**
CO2-based parking policy	Forms a part of a fiscal incentive package for consumers	Potential loss of revenue for local authorities as vehicles become more efficient	High	High for resident permits, can only play an advisory role for workplaces (except council employees)
Free parking for low carbon vehicles	Targets electric vehicles and lowest-emission vehicles	Could contravene the policies to reduce car-based traffic in town centres	Medium	High (the most common measure)
Public charging infrastructure (workplace, retail, park-and-ride)	Contributes to electric and hybrid vehicle market growth	Current consumers may prefer home charging due to the time needed for electric vehicles to reach full charge	Medium	High
Home charging infrastructure	Convenient for low carbon vehicle consumers	In the areas without offstreet, private parking it is difficult to retro-fit points on-street to enable guaranteed overnight charging for all residents	High	Low
Charging points in new developments	Convenient for low carbon vehicle consumers	Points will still need to be communal for city centre residences without garages or driveways	High	High (but the role of local authorities vs. energy suppliers needs clarification)
Reduced business rates for those with low carbon vehicle fleets	Could be effective in Air Quality Management Areas where EU fines for local authorities not meeting monitoring targets can be reduced	Local authorities may lose revenue in the short term	Potentially high	Low
Road pricing and exemptions for low carbon vehicles	Effective at reducing CO2 thrrough both demand reduction and easing traffic flows	Politically unpopular, issues around whether road pricing should be a congestion charge or an	High	Low

	(vehicles can travel at more efficient speeds)	emission-based charge		
Public procurement of low carbon vehicle fleets	Purchasing discounts can be amplified by setting up joint procurement frameworks	Break-even point for most vehicle fleets is still in favour of internal combustion engine vehicles	Medium	High
‘Low carbon vehicles only’ lanes and access to bus lanes	Promotes journey time saving benefits for low carbon vehicle users	Potential road safety impacts on cyclists and motorcyclists	High	Medium
Route/Access restrictions except for low carbon vehicles	Could help to reduce air pollution in inner-city areas	Potential road safety impacts on cyclists and pedestrians	Low	Low
Low Emission Zones (LEZs)	Can reduce emissions over a wide area	Expensive to set up and enforce	High	Medium
Information and marketing	Helps consumers to make an informed choice	Likely to be effective only in combination with incentives and attractiveness of vehicles	Medium	High

In some cities or countries, electric vehicle drivers are exempted from congestion fees charged in the areas with high traffic intensity, for instance, London City in Great Britain. Although daily fees are commonly charged for the entrance to high traffic intensity areas, zero-emission vehicles are exempted from these fees (Lache et al., 2009). Exemptions from road and traffic congestion fees are also applied in China, Germany, Japan, Norway and Sweden (Hardman, 2017). The study, carried out by Windisch (2013), revealed that implementation of such measures at the national level is more an exception than a rule. For example, China implements such measures only in electric vehicle demonstration cities, Portugal – in urban centres, etc. Norway is one of the countries where preferential fees and access rights are implemented at the national level. As it was noted by Kley et al. (2010), congestion charge effects as well as effects of the other municipality-level promotion measures are hard to evaluate because they are strongly influenced by local contexts and consumer patterns. Nevertheless, the pilot projects in London and Stockholm showed that this practice may be particularly interesting in urban conglomeration areas.

7. CONCLUSIONS

The electric vehicle market covers technical and infrastructure barriers, such as limited driving range, battery charge time and limited access to charging stations. The first two barriers cannot be eliminated at the purely municipal level as the decision power belongs to car and technology manufacturers. Nevertheless, municipalities must solve the problems of charging network development as it is the key determinant of the promotion of electric vehicles in cities.

Municipalities may also contribute to elimination of particular economic barriers, including high acquisition costs and consumer uncertainty of the resale value, while uncertainty of future savings can be reduced by providing the accurate and comprehensive information.Consumer preferences, misunderstanding of a driving range needed and inaccurate knowledge about electric vehicles are serious *human* barriers, which can be reduced only by raising consumer awareness. Different types of incentives and initiatives may as well have a significant positive impact on electric vehicle usage promotion. A wide circle of stakeholders, including different levels of government, non-governmental organisations, businesses, academic institutions and local communities, can take an action to raise consumers’ understanding and awareness.

Being closer to consumers, *local authorities* can efficiently communicate with all social groups and co-operate with businesses. The efficient communication and co-operation, in turn, contribute to creation of synergies, development of financial and non-financial promotive measures, initiation of marketing campaigns and provision of the comprehensive information which is necessary in order to raise consumer awareness of the alternative transport. A wide charging network, which can be developed by employing different funds and involving private investors, along with its constant expansion and maintenance are the key determinants of electric vehicle usage promotion. At the municipal level, electric vehicle usage can be promoted by simplification of administrative procedures, establishment of the reqirements for the development of real estate and implementation of financial incentives for the expansion of the charging network, including arrangement of charging points at homes and in public areas.

To promote the usage of electric vehicles, municipalities may possess the right to initiate the reformation of car, public transport and taxi fleets. In addition, they may directly affect the microlevel *focus areas*, which are linked to traffic and transport regulation: *parking policy, traffic management tools and urban access restrictions*. Successful pilot projects, implemented at a city level, cover the variety of promotive measures and may also contribute to reduction of the electric vehicle usage barriers discussed in this article.

REFERENCES

1. Bjerkan, K., Y., Nørbech, T., E., & Nordtømme, M., E. (2016). Incentives for Promoting Battery Electric Vehicle (BEV) Adoption in Norway. Transportation Research Part D: Transport and Environment, 43, 169–180.
2. Brown, M., A. (2001). Market Failures and Barriers as a Basis for Clean Energy Policies, Energy Policy, 29 (14), 1197–1207.
3. Cluzel, C., Lane, B., & Standen, E. (2013). Pathways to High Penetration of Electric Vehicles. Final report for The Committee on Climate Change. Available from internet: https://www.theccc.org.uk/wp-content/uploads/2013/12/CCC-EV-pathways_FINAL-REPORT_17-12-13-Final.pdf .
4. Diamond, D. (2009). The Impact of Government Incentives for Hybrid-Electric Vehicles: Evidence from US States. Energy Policy, 37 (3), 972–983.
5. Hall, D., Moultak, M., & Lutsey, N. (2017). Electric Vehicle Capitals of the World: Demonstrating the Path to Electric Drive. International Council on Clean Transportation. Washington, DC. Available from internet: www.theicct.org/sites/default/files/publications/Global-EV-Capitals_White-Paper_06032017_vF.pdf .
6. Hanley, C. (2011). Going Green: How Local Authorities Can Encourage the Take-Up of Lower-Carbon Vehicles. Royal Automobile Club Foundation. Available from internet: https://www.racfoundation.org/wp-content/uploads/2017/11/61442_racf_lcv-and-la-powers-author-buchanan_aw.2_web.pdf .
7. Hardman, S. (2017). Reoccurring and Indirect Incentives for Plug-In Electric Vehicles – a Review of the Evidence. Plug-in Hybrid and Electric Vehicle Research Center. Institute of Transportation Studies. University of California, Davis;
8. IEA/OECD (2017). Global EV Outlook 2017: Two Million and Counting. International Energy Agency. Available from internet: https://www.iea.org/publications/freepublications/publication/GlobalEVOutlook2017.pdf .
9. Jin, L., & Slowik, P. (2017). Literature Review of Electric Vehicle Consumer Awareness and Outreach Activities, International Council On Clean Transportation, Working paper.
10. Kampman, B., Essen, H., Braat, W., Grünig, M., Kantamaneni, R., & Gabel, E. (2011). Impacts of Electric Vehicles - Deliverable 5. Impact analysis for market uptake scenarios and policy implications. Delft, CE Delft, 11.4058.07.
11. Kley, F., Wietschel, M., & Dallinger, D. (2010). Evaluation of European Electric Vehicle Support Schemes. Working paper sustainability and innovation, S7/2010. Available from internet: http://hdl.handle.net/10419/40019 .

12. Krause, R., M., Carley, S., R., Lane, B.,W., & Graham, J., D. (2013). Perception and Reality: Public Knowledge of Plug-In Electric Vehicles in 21 U.S. Cities, Energy Policy 63, 433–440.
13. Lache, R., Galves, D., Nolan, P., Sanger, K., Kitaura, T., Gehrke, J., Toulemonde, G., Rokossa, T., Rana, S., Chang, S., & Ha, V. (2009). Electric Cars: Plugged In 2. A Mega-Theme Gains Momentum. Global Markets Research. United States. Available from internet: http://www.libralato.co.uk/docs/Electric%20Cars%20Plugged%20In%202%20Deutsche%20Bank%202009.pdf .
14. Larson, P., D., Viáfara, J., Parsons, R,V., & Elias, A. (2014). Consumer Attitudes About Electric Cars: Pricing Analysis and Policy Implications. Transportation Research Part A: Policy Practice, 69, 299–314.
15. Legrand, J.,L . (2011). Livre Vert sur les infrastructures de recharge ouvertes au public pour les véhicules. Available from internet: http://www.louisnegresenateur.fr/wpcontent/uploads/2011/05/livre_vert_vehicules_decarbonnes_net.pdf .
16. Litman, T. (2016). Parking Pricing Implementation Guidelines: How More Efficient Parking Pricing Can Help Solve Parking and Traffic Problems, Increase Revenue, and Achieve Other Planning Objectives. Victoria Transport Policy Institute.
17. Mersky, A.,C., Sprei, F., Samaras, C., & Qian, Z. (2016). Effectiveness of Incentives on Electric Vehicle Adoption in Norway. Transportation Research Part D: Transport and Environment, 46, 56–68.
18. Michelin (2011). Let's drive electric! Electric and hybrid vehicles. Challenge Bibendum Booklet. Available from internet: http://www.michelinchallengebibendum.com/content/download/7018/78148/version/2/file/ .
19. OECD/IEA (2016). Global EV Outlook 2016: Beyond one million electric cars. International Energy Agency.
20. Perdiguero, J., & Jiménez, J., L. (2012). Policy Options for the Promotion of Electric Vehicles: a Review. Working Paper. Research Institute of Applied Economics.
21. Quak, H., Nesterova, N., & van Rooijen, T. (2016). Possibilities and Barriers for Using Electric-Powered Vehicles in City Logistics Practice, Transportation Research Procedia 12, 157–169.
22. Rezvani, Z., Jansson, J., & Bodin, J. (2015). Advances in Consumer Electric Vehicle Adoption Research: a Review and Research Agenda. Transp. Res. Part D Transp. Environ., 34, 122–136.
23. Rogers, E., M. (2003). Diffusion of Innovations, 5th Edition, The Free press, New York, NY.
24. Rushlow, J., Coplon-Newfield, G., LeBel, M., & Norton, E. (2015). Charging Up: The Role of States, Utilities, and the Auto Industry in Dramatically Accelerating Electric Vehicle Adoption in Northeast and Mid-Atlantic States. Conservation Law Foundation. Sierra Club and Acadia Center. Available from internet: https://www.sierraclub.org/sites/www.sierraclub.org/files/uploads-wysiwig/ChargingUp_DIGITAL_ElectricVehicleReport_Oct2015_0.pdf .
25. Salisbury, M. (2011). What Can Cities and Counties Do to Promote the Deployment of Electric Vehicles? Southwest Energy Efficiency Project. Oak Ridge National Laboratory.
26. Sierzchula, W., Bakker, S., Maat, K., & van Wee, B. (2014). The Influence of Financial Incentives and Other Socio-Economic Factors on Electric Vehicle Adoption, Energy Policy, 68, 183–194.
27. Singer, M. (2015). Consumer Views on Plug-In Electricvehicles: National Benchmark Report. Available from internet: http://www.afdc.energy.gov/uploads/publication/consumer_views_pev_benchmark.pdf .

28. Stevens, B., & Schieb, P., A. (2013). Developing Infrastructure for Alternative Transport Fuels and Power-Trains to 2020/2030/2050. A Synthesis Report. OECD.
29. Sunnerstedt, E. (2009). Promoting Clean Cars. Case Study of Stockholm and Sweden. European project BEST - Bioethanol for Sustainable Transport.
30. Tal, G., & Nicholas, M., A. (2014). Exploring the Impact of High Occupancy Vehicle (HOV) Lane Access on Plug-In Vehicle Sales and Usage in California. Research Report – UCD-ITS-RR-14-16.
31. Van der Steen, M., Van Schelven, R., M., Kotter, R., Van Twist M., J., W., & Van Deventer MPA, P. (2015). EV Policy Compared: an International Comparison of Governments' Policy Strategy Towards E-Mobility. E-Mobility in Europe: Trends and Good Practice. Springer International, 1.
32. Wang, F., Yu, J., Yang, P., Miao, L., & Ye, B. (2017). Analysis of the Barriers toWidespread Adoption of Electric Vehicles in Shenzhen China, Sustainability 2017, 9(4), 522.
33. Windisch, E (2013). Driving electric? A Nancial Analysis of Electric Vehicle Policies in France. Statistical Finance [q-n.ST]. Ecole des Ponts ParisTech.

CYSENI 2018, May 23-25, Kaunas, Lithuania
ISSN 1822-7554, www.cyseni.com

COMPARATIVE ANALYSIS OF THE OPTIONS FOR THE SOLID BIOFUEL MARKET DEVELOPMENT IN UKRAINE

A. V. Pastukh
NGO "Renewable energy agency"
Zhelyabova 2a Street, P.O. box 66, Kyiv-67 – Ukraine
Email: pastukh2017@ukr.net

ABSTRACT

In the article, the legal regulation of the solid biofuel market in Ukraine is analysed. The barriers and the opportunities of further reform for the solid biofuels market were identified through the application of comparative analysis, legal analysis and SWOT analysis methods. The most crucial barriers identified are: current unreliability of biofuels supply, instable and unreasonably high prices for biofuels, absence of the mechanisms for biofuels trading and contractors searching. Different options for solving the problems are proposed, namely: improvement of existing principles of commercial wood auctioning, usage of existing state procurement system, creation of new Biofuel Electronic Trading System (BETS). It is concluded that the last market trading mechanism is the most effective instrument to support further development of the biofuel market in Ukraine. It is expected that BETS will ensure performance of mutual obligations between producers, suppliers and consumers of biofuel, price equalization and decreasing due to introduction of competition, reliability and security of biofuel supply, fast and effective search of contractors. For the effective operation of BETS, it is necessary to impose obligation for certain enterprises (state and municipal enterprises that produce or procure biofuel, business entities with granted "green" tariff, business entities with granted stimulating tariff for heat energy from renewable energy sources (RES) to trade via BETS. They also must ensure given quotas on biofuels trading and performance of quality classes requirements. As a result, it is proposed to amend current legislation, in particular, to introduce a new section to the Law of Ukraine "On Alternative Fuels" and appropriate symmetrical changes in connected laws for BETS creation in Ukraine. The respective new legal norms are proposed to National RES Regulator and currently are in process of adoption.

Keywords: solid biofuel, biofuel electronic trading system, legal regulation of solid biofuel market

1. INTRODUCTION

Solid biofuel market is rapidly developing in Ukraine. According to the Statistical data of Energy Balances energy production from biofuels and waste increased by 45% per year [1] (see Fig. 1). The volume of solid biofuel production is about 5 million tons per year, with export about 2 million tons [2]. At the same time, there are a number of barriers that impede the development of the solid biofuel market. They are current unreliability of biofuels supply, instable and unreasonably high prices for biofuels, absence of the mechanisms for biofuels trading and contractors searching. To achieve the national target of 11% of renewable energy sources (RES) in gross final energy consumption in 2020 [3] and for the effective implementation of new bioenergy projects it is necessary to overcome these barriers and to seek ways for further development of the solid biofuel market.

The article is devoted to the comparative analysis of the options for the solid biofuel market development in Ukraine and formation proposals for legislative regulation of solid biofuel market. The essential results of the analyses could be used by national legislative organ during adoption of new legislation for the solid biofuel market regulation.

The legal regulation of the solid biofuel market in Ukraine is not widely researched, although some scientific papers have already been published. Namely, Obolenskaya S. researched the legal regulation of the biofuel production by agricultural producers in Ukraine [4], Kaletnik G. analyzed possible improvement of the legal support for the functioning of the biofuel market in Ukraine [5]. Bioenergy Association of Ukraine had done the deep analyses of the solid biofuel market in Ukraine in the focus for the creation of the competitive biofuel market in Ukraine [1].

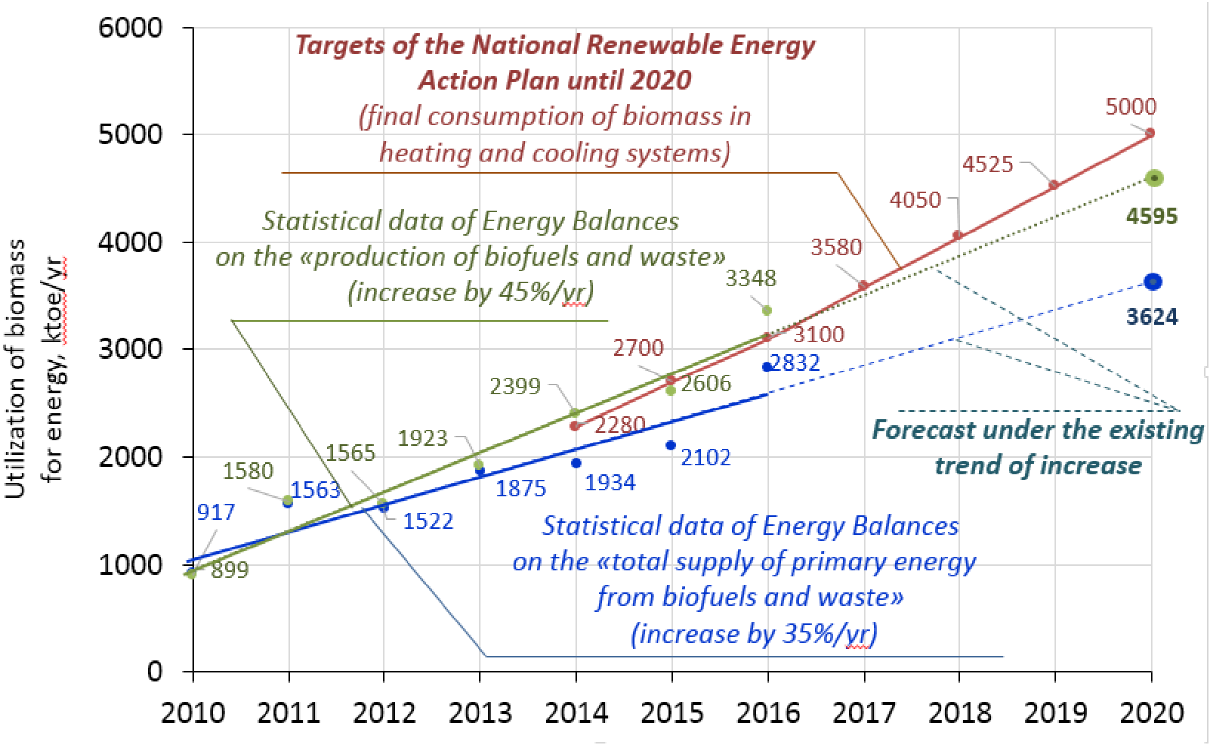

Fig. 1. Trends of bioenergy development in Ukraine

This article aims at analysing the current legal regulation of the solid biofuel market and substantiating the new essential legal provisions for the introduction of the biofuel market trading mechanism.

The tasks to reach the aim of the paper are following:

1) detection of the national legislation that born barriers that impede the development of the solid biofuel market in Ukraine;

2) comparison of the advantages and disadvantages of different possible ways that could be chosen for solid biofuel market renovation;

3) justification of the market mechanism that is the most suitable for further development of the solid biofuel market in Ukraine;

4) finding the necessary steps for the legal implementation of the new biofuel market trading mechanism in Ukraine.

Seeking to implement the aim of the paper, the following methods are used: comparative analysis method, legal analysis and SWOT analysis method.

2. METHODOLOGY

Comparison is a fundamental tool of analyses. Comparative analysis method is a research method that helps to make comparisons across different things. It also sharpens our power of description, plays a central role in concept formation by bringing into focus suggestive similarities and contrasts between cases [6]. Comparative analyses provide the key to understanding, explaining and interpreting diverse processes and their significance for current institutional arrangements. Comparative analysis method used in the article indicated essential causes of barriers occurrence, advantages and disadvantages of different options proposed for solid biofuel market improvement. As the advantages of the creation of new Biofuel Electronic Trading System (BETS) are the most crucial, it is proposed to develop new legislation for BETS introduction in Ukraine.

The legal analysis method is one of the leading methods for legal research. It gives an opportunity to investigate internal structure of legal norms, to analyse the sources (forms) of law, to systematize normative material and to realise the rules of legal technic. The legal analysis method used in the article helped to classify, systematize and transfer the received knowledge about the solid biofuel market in definite regulatory way. Legal analysis method demonstrated ineffective legal provisions that regulates solid biofuel market and helped to formulate the essential points of new legal provisions that are necessary for new trading system implementation. This method has been applied in determining and legalizing the competence of state bodies as well.

A SWOT analysis is an analytical technique used to determine and define several key characteristics: Strengths, Weaknesses, Opportunities, and Threats – SWOT. It is intended to specify the objectives of new “BETS proposals” to the Ukrainian legislation and identify essential factors that are favorable and unfavorable to achieving those objectives.

Strengths and Weakness are frequently internally-related, while Opportunities and Threats commonly focus on environmental placement. SWOT analysis for BETS introduction covers: 1) Strengths – characteristics of the BETS that give it an advantage over other market mechanisms; 2) Weaknesses – characteristics of the BETS that place it at a disadvantage relative to other market mechanisms; 3) Opportunities – elements in the environment that the BETS could exploit to its advantage; 4) Threats – elements in the environment that could cause trouble for the BETS.

3. IDENTIFICATION OF THE BARRIERS FOR THE SOLID BIOFUEL MARKET DEVELOPMENT

Wood biofuel is a dominant biomass type in the total amount of solid biofuels produced in Ukraine. According to estimation of experts of the UABio solid biofuels form about 90% of all biofuels produced in Ukraine [7] (see Table 1):

Table 1. Estimation of the volume and structure of solid biofuels in Ukraine in 2015–2017

Type of biomass/ year	**2015**	**2016**	**2017**
Wood biomass	1.90	1.95	2.12
Straw, stalks	0.05	0.07	0.08
Sunflower husk	0.25	0.26	0.30
Total, Mtoe	**2.20**	**2.28**	**2.50**

As usual, wood biofuel is produced from firewood or felling resides. Most of the forests in Ukraine are state-owned (see Fig. 2). The main subjects of forestry management are the permanent forest users. These are specialized state (municipal) forest enterprises. They manage forests, have the exclusive right to harvest wood and ownership right on harvested wood and income from its sale.

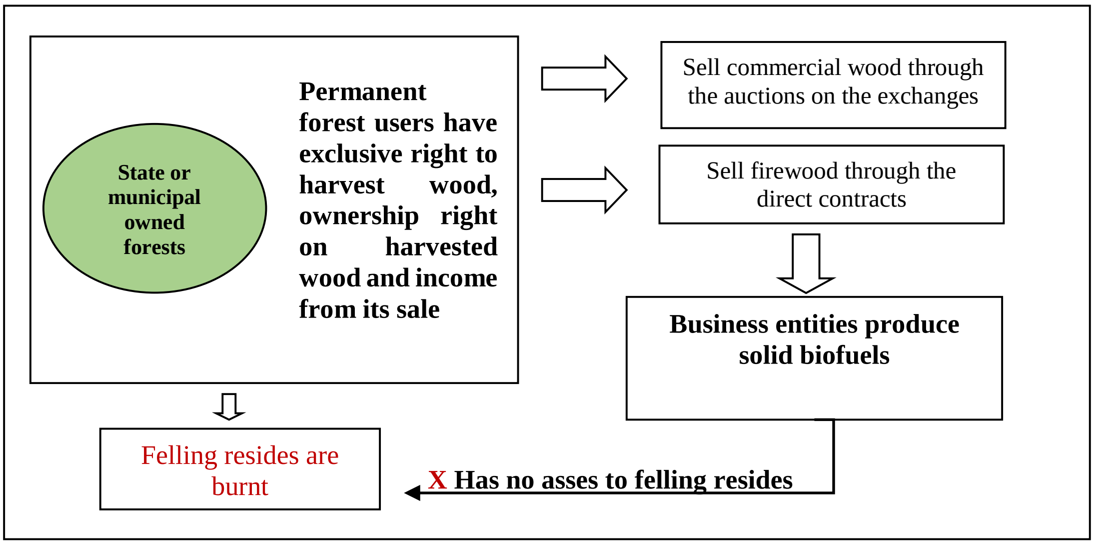

Fig. 2. Existing legal regulation for solid biofuel production

The permanent forest users are obliged to realize unprocessed commercial wood through the auctions on the commodity exchanges. At the same time, they sell firewood through the direct contracts and then, as a rule, other business entities use this firewood to produce solid biofuels.

The permanent forest users simultaneously with cutting operations carry out clearing the felling sites from felling residues. As a rule, the permanent forest users do not use felling residues as raw material for the biofuel production and burn them on felling sites. Ukrainian legislation does not provide private companies an access to felling residues.

Under such legal regulation, combined heat and power plants (CHP) and boiler houses burning solid biofuels for energy production do not receive reliable supply of biofuels. There are situations when solid biofuels-based CHP or boiler houses cannot find sellers of biofuels while biofuel producers from the neighbouring region cannot find buyers for their products.

In order to solve such situation and to increase the amount of raw materials for biofuel production, it is necessary to open an access to felling residues for private companies. It should be done through the obligation of the permanent forest users to take away felling residues to the nearest roads for the purpose of biofuel production for 80% of felling residues by mass, and by introduction a prohibition for general and patch burning of felling residues. For this purpose, it is necessary to amend Forest Code of Ukraine [8] and foresee a new method of clearing felling sites and prohibition for burning of felling residues.

The abovementioned legal regulation and absence of the competition between biofuel producers causes instable and unreasonably high prices for biofuels. They could differs doubly even in the neighbouring regions. According to the latest research of the prices for woody biomass (including VAT, EXW (at the point of production), excluding transport costs) in the 6 regions of Ukraine for the March 2018, the prices for woody biomass in Ukraine are as represented below (see Table 2):

Table 2. Summarized prices for 110 individual producers

Type of biomass	**Price minimum**			**Price maximum**
	EUR/t	**UAH/t**	**EUR/t**	**UAH/t**
Wood logs	16,6	530	39,1	1250
Wood chips	21,0	673	53,1	1700
Wood sawdust	23,4	750	37,5	1200
Wood pellets EN plus A1, A2	87,5	2800	112,5	3600
Wood pellets (industrial EN plus B1, B2)	56,3	1800	87,5	2800
Bulk husk	19,7	630	37,5	1200
Husk pellets	29,7	950	62,5	2000

4. OPPORTUNITIES OF SOLID BIOFUELS MARKET REFORM

There are several different options how to ensure reliable supply of biofuels, to stable prices for biofuel and to improve current legislation.

The first one is to improve the system of auctions for the sale of unprocessed commercial wood. According to “Regulations regarding arranging and holding auctions for the sale of unprocessed wood” [9], all the permanent forest users should sell unprocessed wood through the auctions at an exchange. Unprocessed wood means «wood materials obtained by parting the felled trees and logs into pieces with the purpose of further use and processing». The auction parties are a seller and a purchaser; the organizer is an exchange, with which the seller conclude a contract on holding the auction. The seller is a permanent forest user who legally harvests wood on the territory of Ukraine. The purchaser is an economic entity of any type of ownership, the resident of Ukraine, which wants to purchase unprocessed wood for its own woodworking activity in accordance with the auction terms. The auctions are held once a quarter at commodity exchanges located in regional centers and created according to the legislation of Ukraine.

The sellers of unprocessed wood should tender not later than 15 days before the auction day. Based on the obtained sale proposals, the exchange issues an auction bulletin, which contains information about the amount of unprocessed wood available for sale, the number and size of lots, quality indicators, initial price per one cubic meter, auction step, supply conditions. The exchange organizes and holds the auctions according to the current legislation and rules of exchange trade. In particular, the exchange should:

1) develop the auction procedure;
2) consider unprocessed wood sale proposals and biddings;
3) determine the place, date, time of the auction according to biddings and publish the information in mass media;
4) take and register auction applications;
5) register bidders on the auction day and provide them with numbered auction cards;
6) issue an auction certificate which is basis for concluding a contract between the seller and purchaser;
7) register the concluded sale contracts.

To improve the system of auctions it is necessary to allow the permanent forest users selling firewood on the auctions and recognizing the producers of thermal and/or electric energy as buyers on such auctions. In such case, they would be able to buy biofuel directly from the permanent forest users (see Table 3).

Table 3. Comparison between existing and proposed system of auctions for the sale of unprocessed commercial wood

	Current regulation of auctions for the sale of commercial wood	**Proposed regulation of auctions for the sale of commercial wood**
Organizer of the trading	Commodity exchanges in regions	Commodity exchanges in regions
Sellers	Permanent forest users	Permanent forest users
Buyers	Only woodworking enterprises	Woodworking enterprises and producers of thermal and/or electric energy
Products traded	Only commercial wood (firewood and felling residues are excluded)	Commercial wood, firewood and felling residues

Advantages of the option is that the system of auctions is an existing mechanism and it is under a process of transfer to the electronic form. However, such a mechanism has disadvantages: 1) the system of auctions has no supply guarantees and standards for biofuels; 2) the right to purchase via the system of auctions has a limited circle of sellers (in fact, only permanent forest users); 3) impossibility to trade agrarian biomass that will have a huge percent in the structure of solid biofuel production in Ukraine.

The second option, which could be used for further reform of the solid biofuels market, is based on the usage of the existing state procurement system (ProZorro) (see Fig. 3). ProZorro is a fully online public procurement platform that ensures open access to public procurement (tenders) in Ukraine. Fully implemented in 2016, the hybrid (both centralized public and decentralized private marketplaces) system is one of the most innovative public procurement systems delivering government services in a stakeholder-focused, transparent, effective, fair and low-cost way [10].

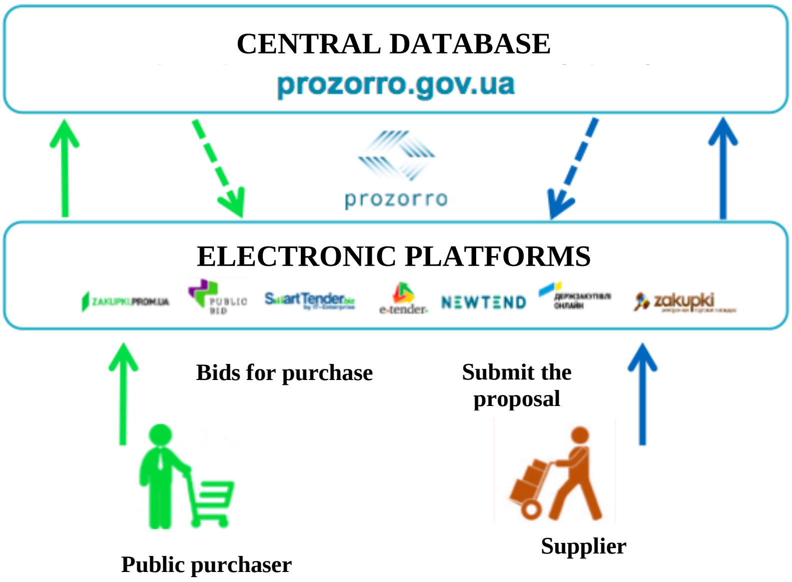

Fig. 3. Existing ProZorro system

Advantages of the usage of the existing ProZorro system are developed and effective legislation, openness and transparency of tenders. However, the ProZorro system has disadvantages: 1) it is applied only for the public procurements (state and municipal enterprises); 2) lack of supply guarantees and standards for biofuels; 3) cannot assure significant competition among the suppliers; 4) and makes weak influence on the changes of solid biofuel price.

Creation of new Biofuel Electronic Trading System (BETS) is the third option for further development of the solid biofuel market (see Fig. 4).

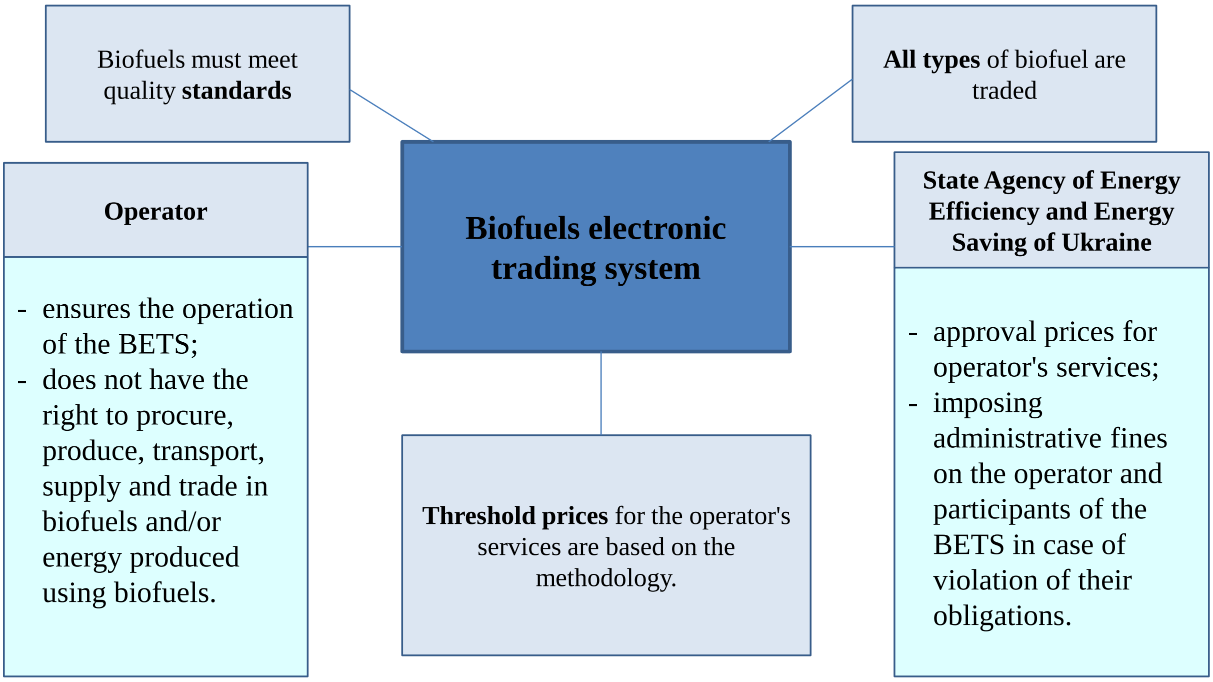
Biofuels must meet quality **standards**

All types of biofuel are traded

Biofuels electronic trading system

Operator

- ensures the operation of the BETS;
- does not have the right to procure, produce, transport, supply and trade in biofuels and/or energy produced using biofuels.

State Agency of Energy Efficiency and Energy Saving of Ukraine

- approval prices for operator's services;
- imposing administrative fines on the operator and participants of the BETS in case of violation of their obligations.

Threshold prices for the operator's services are based on the methodology.

Fig. 4. Specific aspects of the BETS creation in Ukraine

BETS should be created as online platform for trading with all types of biofuels (although, trading only with solid biofuels is expected at the first time of its operation). Biofuels must meet quality standards.

Separate legal entity – operator – should ensure the operation of the BETS. The National Regulator – the State Agency of Energy Efficiency and Energy Saving of Ukraine (SAEE) based on the tender should select the operator. Tender is carried out according to the specified criteria: 1) fitting out with technical means, means of communication, and software necessary for electronic trading; 2) trading experience with biofuels or other energy sources; 3) price of the operator's services and others.

The operator should have the right to establish price for his services, however, no higher than the threshold price. The threshold prices for the operator's services should be calculated based on the methodology. The methodology is approved by SAEE. The operator should not have the right to procure, produce, transport, supply and trade in biofuels and/or energy produced using biofuels.

The National Regulator also should approve prices for the operator's services and impose administrative fines on the operator and the participants of the BETS in case of violation of their obligations.

For supply and demand balancing, it is proposed to impose obligation to trade via the BETS for the following entities:

1) state and municipal enterprises that produce or procure biofuel;
2) business entities with granted “green” tariff;
3) business entities that received a stimulating tariff for heat energy from RES in accordance with the Law of Ukraine "On Heat Supply".

They must ensure given quotas on the biofuels trading. An annual increase of the mandatory percentage (quotas) for trading via BETS is proposed and enterprises should annually report to the National Regulator on compliance with the mandatory percentages. The proposed growth of biofuel share to be traded via BETS with aim to provide gradual transition from current practice to BETS is presents in Fig. 5.

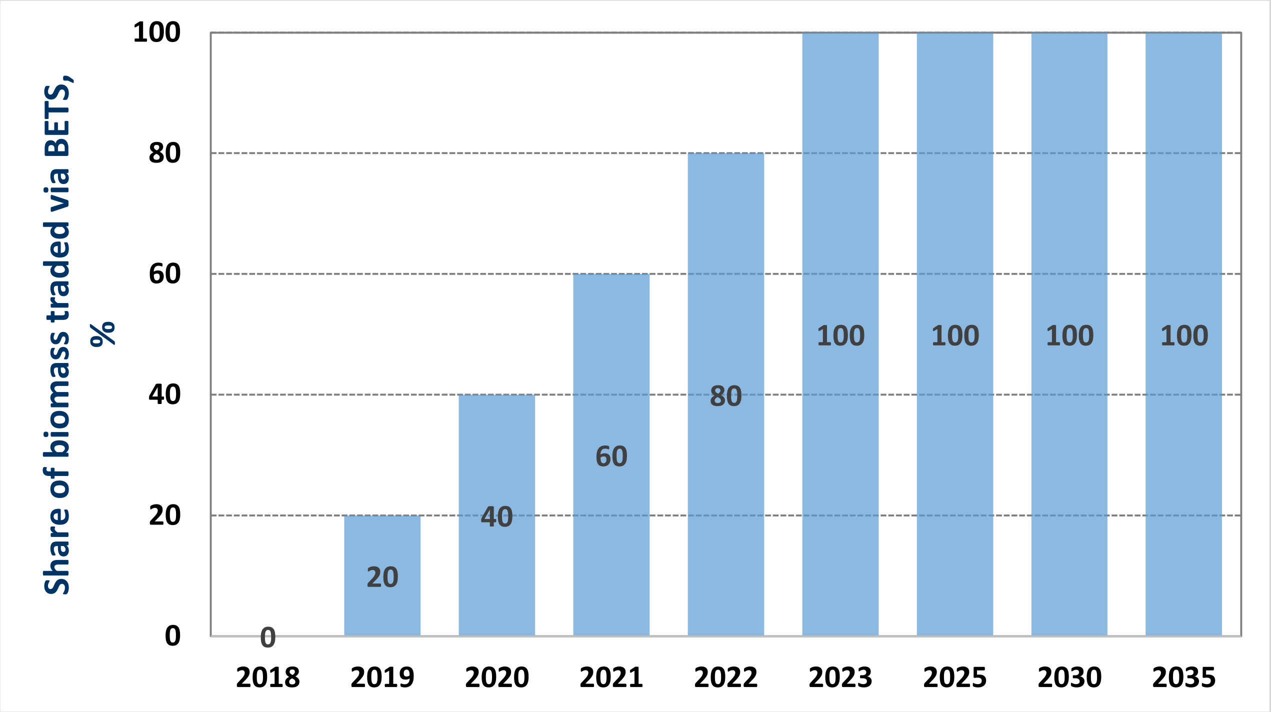

Fig. 5. Increase of the quotas of biomass traded via BETS

Proposition of the introduction of the BETS has Strengths, Weaknesses, Opportunities, and Threats.

Table 4. SWOT analysis for BETS creation in Ukraine

Strengths	**Weaknesses**
✓ Transparency. ✓ Creation of a permanently operating trading site. ✓ Ensured procurement. ✓ Solid biofuel standards introduced on the BETS. ✓ Providing a big number of offers (sellers). ✓ Providing a big amount of biofuels. ✓ Providing competitive trading that leads to justified prices.	✓ It is necessary to oblige state/communal sellers and buyers to realize certain percentage of trading via BETS. ✓ Not sufficient experience in electronic biofuel trading. ✓ Absence of state standards for solid biofuels.
Opportunities	**Threats**
✓ Different types of standardized solid biofuels are available on the BETS. ✓ Biofuel quality is checked. Payment depends on the quality. ✓ It is possible to confirm the binding share of the trading via BETS to the obligation of state/communal buyers on using ProZorro. ✓ State and private companies (including foreign ones) can participate in the BETS trading.	✓ It may be difficult to implement the designed conception of the BETS. ✓ It is necessary to adopt a big package of legislative acts. ✓ Counteraction could be from state forestry enterprises.

It is expected that BETS introduction in Ukraine will have many advantages, namely, transparency of trade, reduction and leveling of prices for biofuels, reliability and security of supply, effective search of contractors, introduction of standards for biofuels sold and purchased via BETS. Therefore, it is the best way for further solid biofuel market development in Ukraine.

Special legislation on Law and following subordinate level of Regulations should be adopted for the introduction of the BETS.

The required improvements in the regulation by Laws is as follows:

1) Introducing a new section to the Law of Ukraine “On Alternative Fuels” [11] and foreseeing main provisions for the BETS operation;
2) Amendments to the Law of Ukraine “On Public Procurement” [12] and imposing the obligation on state and communal enterprises to purchase a certain amount of solid biofuel via the BETS (with information transfer through the ProZorro system);
3) Amendments to the Code of Ukraine on Administrative Offenses and establishing liability for non-compliance with the requirements for the purchase of a certain amount of solid biofuels via the BETS.

The Law Draft has been already developed and submitted to SAEE and currently are in process of consideration and adoption.

The required subordinate level legislation is as follows:

1) The rules for the electronic trading in biofuels, which determine the peculiarities of the electronic trading in different types of biofuel and all the procedural aspects of the trading in biofuels;
2) The methodology for the threshold price setting. It should determine the order of price setting and its application for the operator’s services;

3) The tender procedure for the BETS operator, which determines the procedure for the BETS operator selection;
4) The quality requirements for the biofuels traded in the BETS.

Subordinate legislation will be developed after Law adoption.

5. CONCLUSIONS

The detection of the barriers that impede the development of the solid biofuel market in Ukraine showed that the main problems of it are caused by ineffective forest legislation and absence of market trading mechanism.

Comparison between the advantages and disadvantages of different possible ways that could be chosen for the solid biofuel market renovation has been performed. And it is proved that the most suitable market mechanism for further development of the solid biofuel market in Ukraine is BETS. BETS as specialized mechanism should ensure transparent trade with biofuels. Competition in BETS will make reduction and levelling of prices for biofuels. Using BETS market participants will get effective search of contractors, reliability and security of supply.

The necessary steps for the legal implementation of the new biofuel market trading mechanism in Ukraine should be done in two stages – Law and subordinate legislation adoption.

REFERENCES

1. *Creation of the competitive biofuel market in Ukraine*. Uabio Position Paper №18. Link to the internet <http://uabio.org/img/files/docs/position-paper-uabio-18-en.pdf>.
2. KOLOMIYCHENKO M. Road map on development of the solid biofuel market in Ukraine. // *United Nations Development Program*, 2016. P. 19.
3. National Action Plan for Renewable Energy for the period until 2020. // Link to the internet<http://saee.gov.ua/sites/default/files/documents/Presentation_NAPRES_Norw_OCT_3_Eng%20.pdf>.
4. Legal regulation of biofuel production by agricultural commodity producers in Ukraine [Text]: *author's abstract. dis* ... Candidate lawyer Sciences: 12.00.06 / OBOLENSKAYA S. A.; National lawyer Un-t them. Yaroslav the Wise. - Kharkiv, 2017. - 20 p.
5. KALETNIK G. M. Improvement of legal support for functioning of the biofuel market in Ukraine / G. M. Kaletnik // *Actual. problems of the economy*. - 2008. - No. 12. - P. 48–52.
6. *Political Sience*: The state of the Discipline II. Washington D. C. //ADA W. FINIFTER, ed (1993) Link to the internet<http://polisci.berkeley.edu/sites/default/files/people/u3827/APSA-TheComparativeMethod.pdf>.
7. *Opportunities for wood fuel harvesting in forests of Ukraine*. UABio Position Paper № 19. Link to the internet <http://uabio.org/img/files/docs/position-paper-uabio-19-en.pdf >.
8. Forest Code of Ukraine as of 21.01.1994 № 3852-XII. // Link to the internet <http://zakon2.rada.gov.ua/laws/show/3852-12 >.
9. Resolution by the State Forestry Committee of Ukraine «On improving the procedure for sale of unprocessed wood». // Link to the internet <http://zakon3.rada.gov.ua/laws/show/z0164-07>.
10. Public procurement system ProZorro. // Link to the internet <https://prozorro.gov.ua/en>.
11. Law of Ukraine «On Alternative Fuels» as of 14.01.2000 № 1391-XIV. // Link to the internet <http://zakon2.rada.gov.ua/laws/show/1391-14. >.
12. Law of Ukraine "On Public Procurement" as of 25.12.2015 № 922-VIII. // Link to the internet <http://zakon5.rada.gov.ua/laws/show/922-19>.

CYSENI 2018, May 23-25, Kaunas, Lithuania
ISSN 1822-7554, www.cyseni.com

REPRESENTATION OF STOCHASTIC WIND POWER GENERATION IN ECONOMIC MODELS FOR LONG-TERM ENERGY PLANNING

E. Neniškis, A. Galinis
Lithuanian Energy Institute
Breslaujos str. 3, LT-44403 Kaunas – Lithuania
Email: eimantas.neniskis@lei.lt

ABSTRACT

Economic models for long-term energy planning like TIMES, MESSAGE, BALMOREL are used to evaluate considered energy policy measures and to project how energy sector should develop to meet set national targets with lowest costs. The accuracy of these models depends not only on the accuracy of data and the number of technologies used to represent energy system but also on temporal resolution, especially if power plants, which utilize renewable energy sources, are modelled. When using low temporal resolution wind fluctuations are smoothed and model tends to overestimate installed capacity. High temporal resolution (hourly or higher) is needed to adequately represent variability of wind. However, an increase in temporal resolution results in higher complexity of model and significantly longer optimization time. For large-scale models it might be infeasible to model each hour for all 365 days for each year, because of software or hardware limitations. In order to adequately represent electricity generation from wind fluctuations, without greatly increasing model size, some kind of time aggregation is needed. This can be done by representing only typical demand days (e.g. weekdays and weekends) for each month or season. How many hours wind power plants should produce certain power during these typical days can be calculated from statistical data. But how to determine what power output should be generated at a specific hour? The aim of this article is to describe a methodology on how to create wind curves for each of these typical days.

In described methodology curves for electricity generation in wind power plants are created by using computer code. Code was developed in VBA, but the same principles can be applied in any other programming language. After calculating how many hours wind power plants produce certain power during a typical day, power values are entered into an array. Each element in this array represents a single hour (or other time interval, depending on temporal resolution). Curves for electricity generation from wind are generated by randomly rearranging the elements of this array. Since wind speed changes gradually, in code there is a rule, which prevents placing elements next to each other, whose values differ too much. Difference must not exceed set value, called tolerance.

Methodology was tested by running a simple MESSAGE model of isolated electricity and heat sector of Lithuania. In this model hourly temporal resolution was used. Several scenarios were run. In first scenario each day in a year was modelled (reference scenario). In second a year was represented by 4 seasons and each season by typical workdays and weekends. In third scenario a year was represented by 12 months and each month also by typical workdays and weekends. Wind power plants electricity generation in scenarios with time aggregation were compared to generation in reference scenario. Also, optimization time of each scenario was measured. In “4 seasons” scenario generation differed from -0.25% to 16.43%, depending on a modelled year, but it was optimized in just 2 s. In “12 months” scenario generation differed from 0.01% to 8.56%. and it was optimized in 13 s. Reference scenario was optimized in 4934 s.

There is a trade-off between time aggregation level and accuracy. However, it is possible to choose aggregation level, at which model would not be too big and would have sufficient accuracy.

Keywords: wind, stochastic, power system, development, economic model

CYSENI 2018, May 23-25, Kaunas, Lithuania
ISSN 1822-7554, www.cyseni.com

THE BASE FOR A EUROPEAN ENGAGEMENT MODEL – AN OPEN SOURCE ELECTRICITY MODEL OF SEVEN COUNTRIES AROUND THE BALTIC SEA

H. T. J. Henke, M. Howells, A. Shivakumar
KTH Royal Institute of Technology,
Brinellvägen 68, 100 44 Stockholm – Sweden
Email: haukeh@kth.se

ABSTRACT

This paper presents a long-term open source energy planning model for Denmark, Estonia, Finland, Latvia, Lithuania, Poland, and Sweden, as part of the preparation of a Pan-European model within the Horizon 2020 REEEM project. The model is built using the Open Source Energy Modelling System (OSeMOSYS) and is conceived as a stakeholder engagement model, comprehensive but accessible. It aims to lower the threshold to join and contribute to a model-based discussion about the optimal decarbonisation pathways for the energy supply of the region.

The lowest net present value for the modelled system and period (2015-2050) is calculated by using linear optimization. Existing and planned trans-border transmission capacity between the included countries is considered in the model. New projects are also allowed as far as economically optimal. The electricity exchange to countries not covered by the model are not modelled as of yet. Ten fuels are used by the technologies defined in the model, namely biomass, coal, geothermal, heavy fuel oil, hydro, natural gas, nuclear, wind and waste. In addition to technology parameters like investment cost, fuel cost, and fixed and variable operation and maintenance cost, an increasing emission penalty for carbon dioxide is defined, which represents the cost related to the emission of greenhouse gases (similar to the European emission trading system).

The model provides insights on how the cross-border electricity exchange might develop in the modelled period while decarbonizing the energy sector and considering the unequal distribution of (renewable) resources. But most importantly, the model builds the base for the first fully open source energy model for Europe, including the used data. It shall be conceived as a comprehensive modular tool for engagement in the field of European energy planning, especially for learning in academia, but also by the integration into an open engagement game for decision makers and stakeholders.

Keywords: open-source, long-term, energy planning, trans-border electricity transmission, OSeMOSYS

1. INTRODUCTION

The European energy system is complex. Low cost energy improves economic competitiveness. However, established and long used options - such as coal and oil – are subject to geo-political and environmental concerns. Their price may be volatile and (low cost) suppliers are limited. Other energy forms such as renewables, nuclear and transmission systems, that are needed to support them, are subject to variable levels of social acceptance and can require complex configurations [1].

To analyse possible options and to foster public understanding there is a need for models which could provide transparent and open insight. These are needed to evaluate pathways and help communicate difficult compromises, as for example the choice of energy carriers or the route of transmission lines. Preferably these modelling tools should allow for flexible design to account for new solutions, e.g. new market designs, market integration, new technologies, the appearance of prosumers, and they should be inexpensive to allow easy access to larger groups of analysts.

Yet there are no freely available optimizing energy models of the whole energy system available for all European countries. Models that focus on electricity sector only exist, but they do not include other energy sectors [2]. Models for all energy carriers exist for all countries, but they are not free [3].

We are presenting an effort to change the current situation regarding modelling tools. Using the Open Source energy Modelling System (OSeMOSYS) [4] model generator we generate an electricity system model of seven EU member countries. Using a clear and simple structure, the model is scalable and flexible. Scalable so that other countries could be added in a modular manner using the same generic structure. Flexible as while we focus on a limited set of fuels, more could be added, depending on the scope of the conducted analysis. We call the model, OSeMBE, which is short for the Open Source energy Model Base for the European Union.

2. METHODOLOGY

The work presented in this paper is the outcome of Master‘s thesis of the main author of this paper [5]. The co-authors contributed to the paper by supervising the thesis, reviewing the paper and providing the introduction to the paper. In the following sub-sections of this chapter the methodology used to develop OSeMBE, a model of the European electricity system is described. It describes the modelling system used, the model structure and the key assumptions made. The work done is open source and model source code, data and software used are freely accessible to ensure repeatability and access (www.osemosys.org).

2.1. OSeMOSYS

To develop the OSeMBE model described in this paper, the OSeMOSYS modelling system was applied [6]. OSeMOSYS is a dynamic, bottom-up, multi-year energy system model generator. The optimal investment strategy, production patterns of technologies, and fuels required to satisfy exogenously defined demand(s) are determined by linear optimization [7]. To use exogenously defined demand(s) implies that the model does not consider demand side management or energy efficiency measures. However, changes in demand and their effect on the development of the energy system can be pictured by creating scenarios with different demand assumptions. The analysis of how the system reacts to the changes in the demand is one aspect out of the field of technical, economic and environmental implications that can be analysed in the results. In OSeMBE the analytical focus lies on the system behaviour with increasing shares of (variable) renewable energies.

2.2. Model structure

The current stage of development of OSeMBE includes electricity only and covers the following countries: Denmark, Estonia, Finland, Latvia, Lithuania, Poland, and Sweden. The total electricity demand is specified per country. Demand projections were retrieved from the [8]. An energy chain to satisfy the electricity demand can consist of up to four technologies in the current version of OSeMBE, compare Fig. 1. The final electricity demand, shown on the right hand side of the Reference Energy System (RES) in Fig. 1, can be satisfied either directly by distributed technologies like solar PV or by electricity from the distribution grid (technology “Distribution network”). The distribution grid can receive electricity either from medium sized power plants like small wind parks, or from the transmission network. The transmission network is fed with electricity from centralised power plants, which in turn receive their required fuels from import or extraction technologies, if necessary.

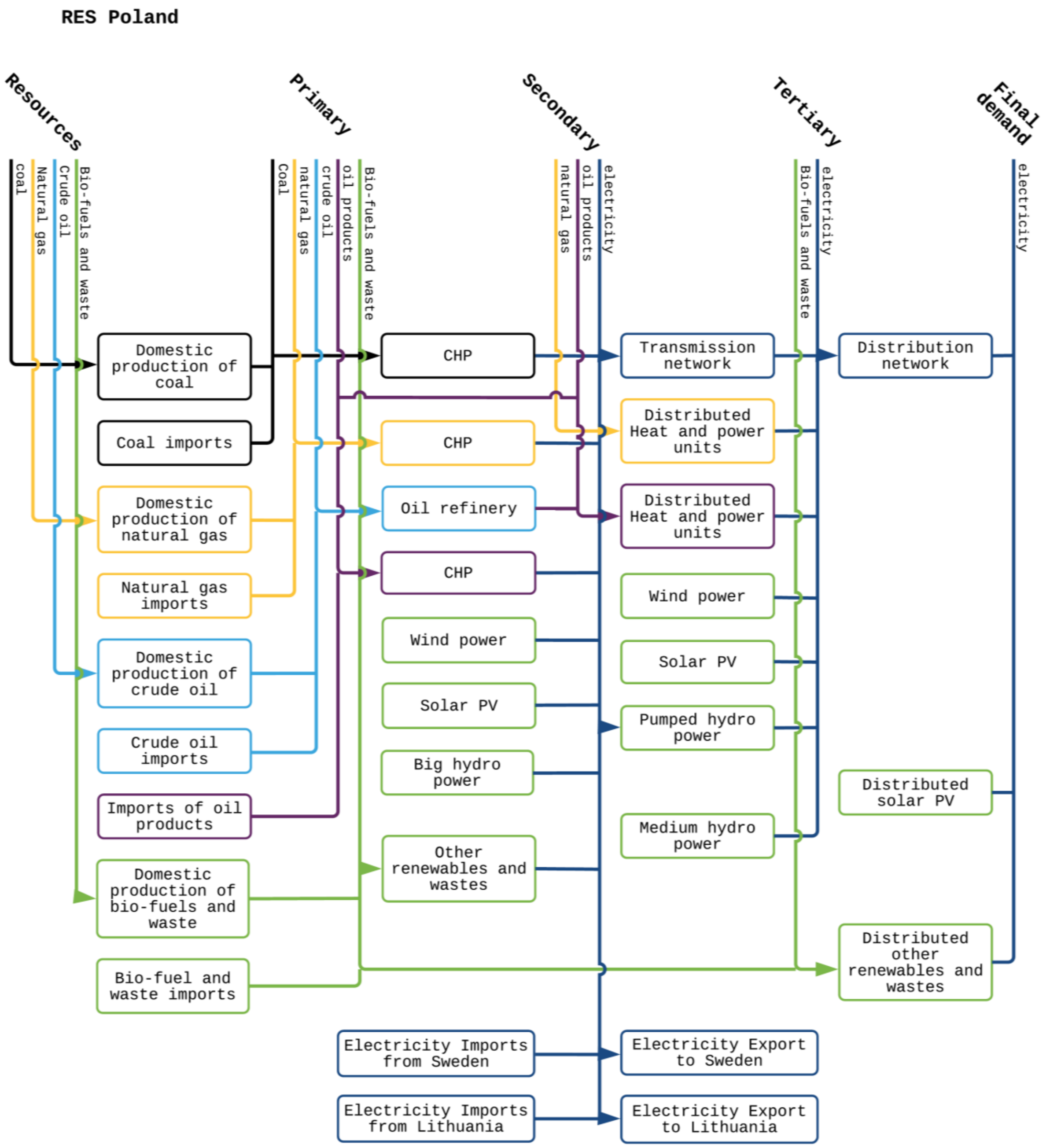

Sources: http://www.iea.org/statistics/statisticssearch/report/?country=POLAND&product=renewablesandwaste&year=2015

Fig. 1. Reference energy system of Poland

2.2.1. *Fuels and generation technologies*

In total there are eight fuels (biomass, coal, heavy fuel oil, natural gas, crude oil, uranium, and waste) and thirteen technologies available (combined cycle power plants (PPs), combined heat and power plants, distributed and utility solar PV, hydropower dams, fuel cells, gas cycle PPs, internal combustion engines with heat recovery, offshore and onshore wind power, steam cycle PPs, and wave power plants). The main source for the techno-economic data of the power plants is [9]. Gaps in [9] where compensated by using [10]–[12]. Some of these power plant types are available in different versions, differentiated by the fuel they require, e.g. steam cycle PP for biomass and steam cycle plants consuming coal. Additional to the domestic transmission and distribution of electricity OSeMBE considers trans-border transmission capacities to neighbouring countries. Due to their line specific techno-economic characteristics transmission technologies are modelled in a simplified way. For the domestic transmission and distribution does this mean that there are no costs related to it, but only a loss of five percent of electricity [13]. The transborder transmission considers existing and upcoming capacities, but the model cannot implement additional new capacities as it can for generation capacities. Anyhow, by creating scenarios with changed transborder transmission lines, congestions and the effect of enhanced trade options could be analysed. Especially in context of the different wind and sun resource quality and availability, this aspect is of high interest for the European power system with currently increasing capacities of wind and solar power [14], [15].

2.2.2. Time definition

OSeMOSYS is designed for long-term energy planning [6], therefore OSeMBE has a time horizon of 46 years, from 2015 to 2060. However, in the results analysis only the time period 2015 to 2050 is considered to avoid the effects of the end of the modelling period on the selection of technologies. The end of the modelling period might affect the results in the way that technologies with a short lifetime are preferred over technologies with a long lifetime since the later might not payback [5]. The year 2015 serves as the base year in OSeMBE and statistical information used was, when possible, taken for this year. Since OSeMBE is still under development the model was calibrated only to a limited extend, e.g. adjustment of the emission penalty and the price for biomass.

In the version of OSeMBE presented here, each of the modelled years is splitted into twelve seasons or rather the twelve months of the year. Each month is considered by one typical day. These typical days are then divided into day, peak, and night, adjusted to the average demand curve of the season. This results in 36 time slices per year.

2.2.3. Resource availability

To be able to capture the variable availability of wind and sun OSeMOSYS provides two ways of indicating the availability of a technology. Firstly there is the “AvailabilityFactor”, by using the AvailabilityFactor it can be indicated for how much time of the year a technology is available. The second option to indicate the availability is the “CapacityFactor”. The CapacityFactor is defined per TimeSlice, i.e. the change in availability per time slice can be considered, for example for solar PV the capacity factor during the night time is 0 and during the day e.g. 0.2 [16]. In this first version of OSeMBE the capacity factors for wind and solar power are national average values calculated based on data from renewables.ninja (renewables.ninja). The data from renewables.ninja is based on “NASA’s Modern-Era Retrospective Analysis for Research and Applications” (MERRA) and was corrected using measured data sets [14], [15].

2.2.4. Reserve Margin

The reserve margin (RM) in OSeMOSYS is defined as the minimum margin of a tagged commodity that a set of tagged technologies needs to be able to provide additional to the peak demand of the tagged commodity. Will say if the RM is set to 1.2 the technologies that are tagged as reserve margin tag technologies need to have enough capacity to generate 20% more than the annual peak demand of the commodity [17]. With the current version of OSeMBE a sensitivity analysis was conducted on how the results vary with a changing RM, the conducted analysis is described in more detail in subsection 2.4 Scenarios and section 3. Results and discussion.

2.3. Key assumptions

There are a certain number of fundamental assumptions made in OSeMBE that are not changed between the scenarios. These key assumptions are summarised in the bullet points below:

- The real discount rate applied is 5%
- The monetary unit is 2015 US$
- The reporting horizon of this study spans from 2015 to 2050. Simulations are undertaken for every year of the entire modelling period.
- As mentioned above, the year is represented by 36 characteristic time slices (12 seasons with day, peak, and night distinction) per year.
- OSeMOSYS assumes a perfect market with perfect competition and foresight [6]

2.4. Scenarios

Due to the development status of OSeMBE the scenarios analysed in this work serve the purpose of validating the results of the model. With the three scenarios created for this paper the change of behaviour of the model with different RM (of 1.15, 1.2, and 1.25) for the final electricity demand was analysed.

3. RESULTS AND DISCUSSION

This section provides some insights into the results OSeMBE is producing. However, it is important to consider that the model presented here is not yet fully fledged. Therefore, some of the results presented here are explicitly not realistic, e.g. trade patterns. In the first three subsections results for the scenario with a RM of 1.2 are presented and discussed.

3.1. Generation capacity

Below in Fig. 2 the development of the installed capacities in Finland and Sweden are shown. In the base year 2015 the installed capacities consist of statistical data on the installed capacities. Considering the expected lifetimes, the residual capacity is reduced year by year and new capacities need to be installed by the model. It is well visible in the two graphs how the availability of resources (mainly referring to hydro and wind) is affecting the capacity mix. The availability of both resources mentioned is lower in Finland in comparison to Sweden. Especially the linear development of installed wind power capacity in Finland indicates that the implemented limit is reached whereas the limit in Sweden is not reached. The different development of the installed capacity of nuclear can be seen in context of the different resource availability as well. While Sweden is almost phasing out of nuclear, Finland increases its capacity. The start is done by the nuclear power plants currently under construction, which are considered in this work due to their high importance for the Finnish electricity system.

In Fig. 2 in the lower sections of the graphs it can be seen that the model phases out power plants using biomass. This is an issue that needs to be addressed in the future work on the model since it is unlikely that power plants running on biomass are going to disappear from the power generation mix in the Nordic countries. It is rather likely that the assumptions made when calculating average prices of biomass were misleading.

The results for the capacity development in the other five modelled countries can be found in Appendix A. Capacity mix results.

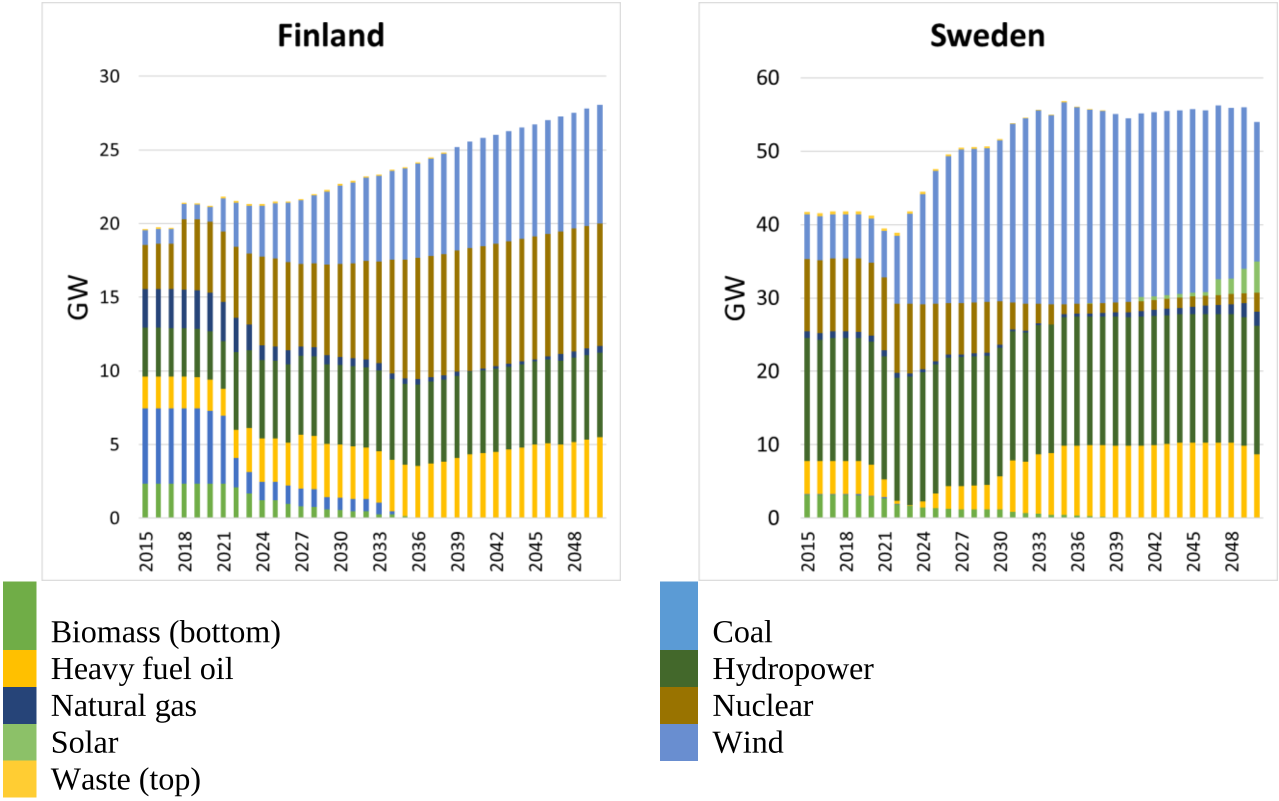

Fig. 2. Installed capacities in Finland and Sweden with RM 1.2

3.2. Electricity generation mix

Fig. 3 below, shows the annual production of Finland and Sweden throughout the modelling period. A red line in the upper half of the graphs indicates the actual electricity demand. Since imports and exports are not shown in the graphs, it can be seen in the graphs if the country is a net importer or a net exporter depending on if the upper edge of the production is below or above the demand curve. Is the upper edge below the demand curve the country is importing, is the edge above the demand curve the country is exporting. Considering this, the results indicate that Finland turns from a net importer to a net exporter. In 2019 a sudden peak in production is shown for Finland, it is caused by the newly added nuclear capacities. The phase out of nuclear in Sweden is compensated by wind power generation. Towards the end of the modelling period a small share of solar appears in the Swedish power mix. Due to its more northerly location this is not happening in Finland.

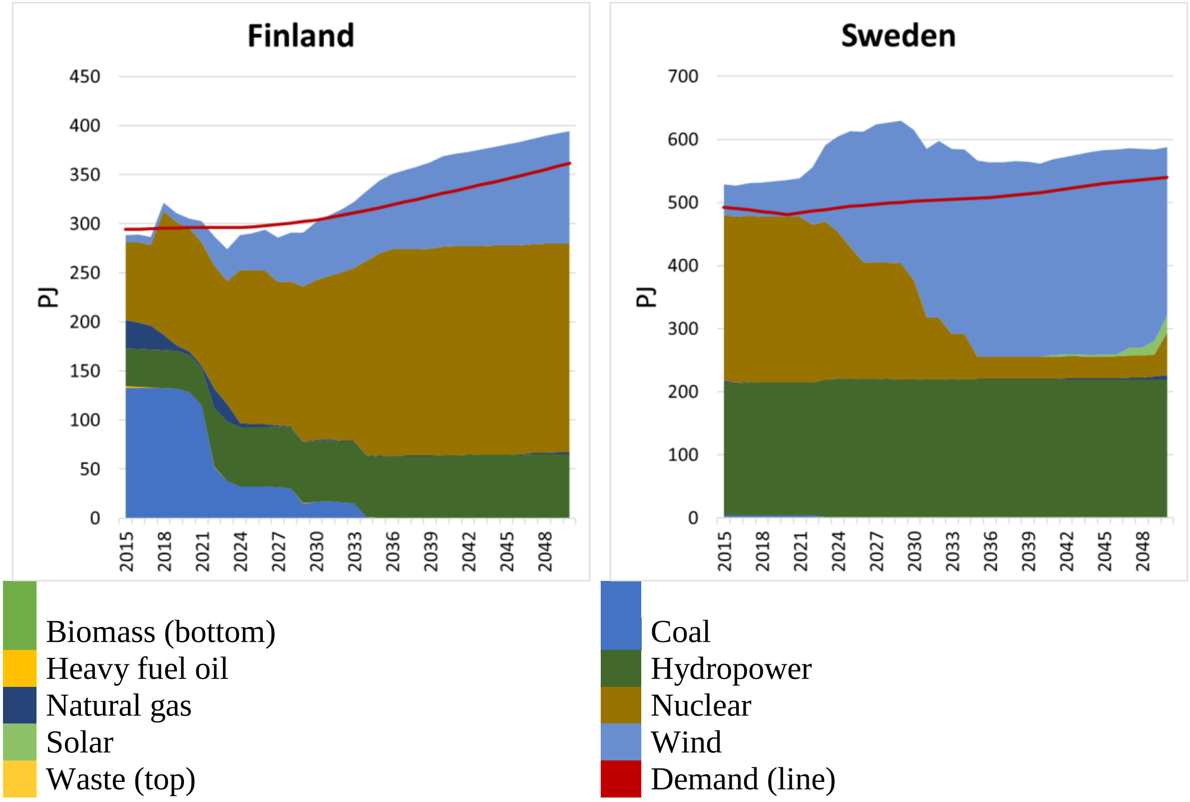

Fig. 3. Annual Production for Finland and Sweden with RM 1.2

The annual production pattern of the other five modelled countries can be found in Appendix B. Generation mix results

3.3. Cross-border electricity trade

Considering that OSeMBE is still under development, two aspects are interesting to contemplate in context of the transborder electricity trade. On the one hand there is the comparison between the modelled 2015 transborder flows and the real 2015 electricity exchange. On the other hand the development of the transborder transmission can be analysed.

Fig. 4, below, shows in the upper graphic the actual transborder electricity flows in the seven modelled countries. The figure at the bottom shows the transborder flows in the presented version of OSeMBE. Fundamental relationships like the export from Sweden to Finland or from Finland to Estonia are captured. However, the in reality almost balanced exchange between Denmark and Sweden shifted to only Denmark exporting in the model. Overall it is important to consider that the exchange with the not modelled/to be modelled countries is not considered so far, this explains e.g. the change in the relationship Poland-Sweden. It needs to be seen how the results will change when the model is extended and the exchange with 3rd countries, for example Russia, is considered.

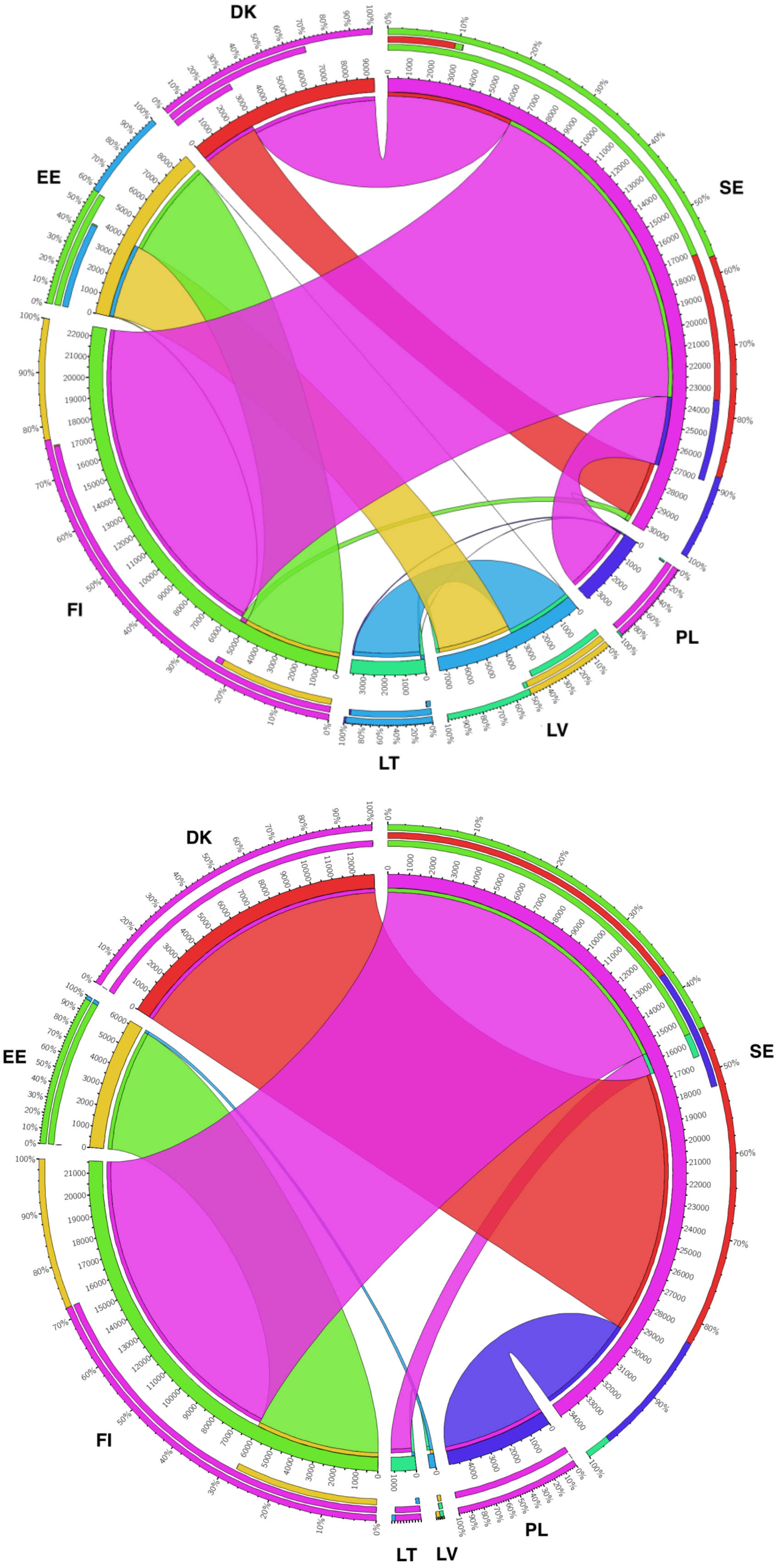

Fig. 4. Comparison of the 2015 real trans-border flows (top) and the trans-border flows in the base case (bottom) in GWh

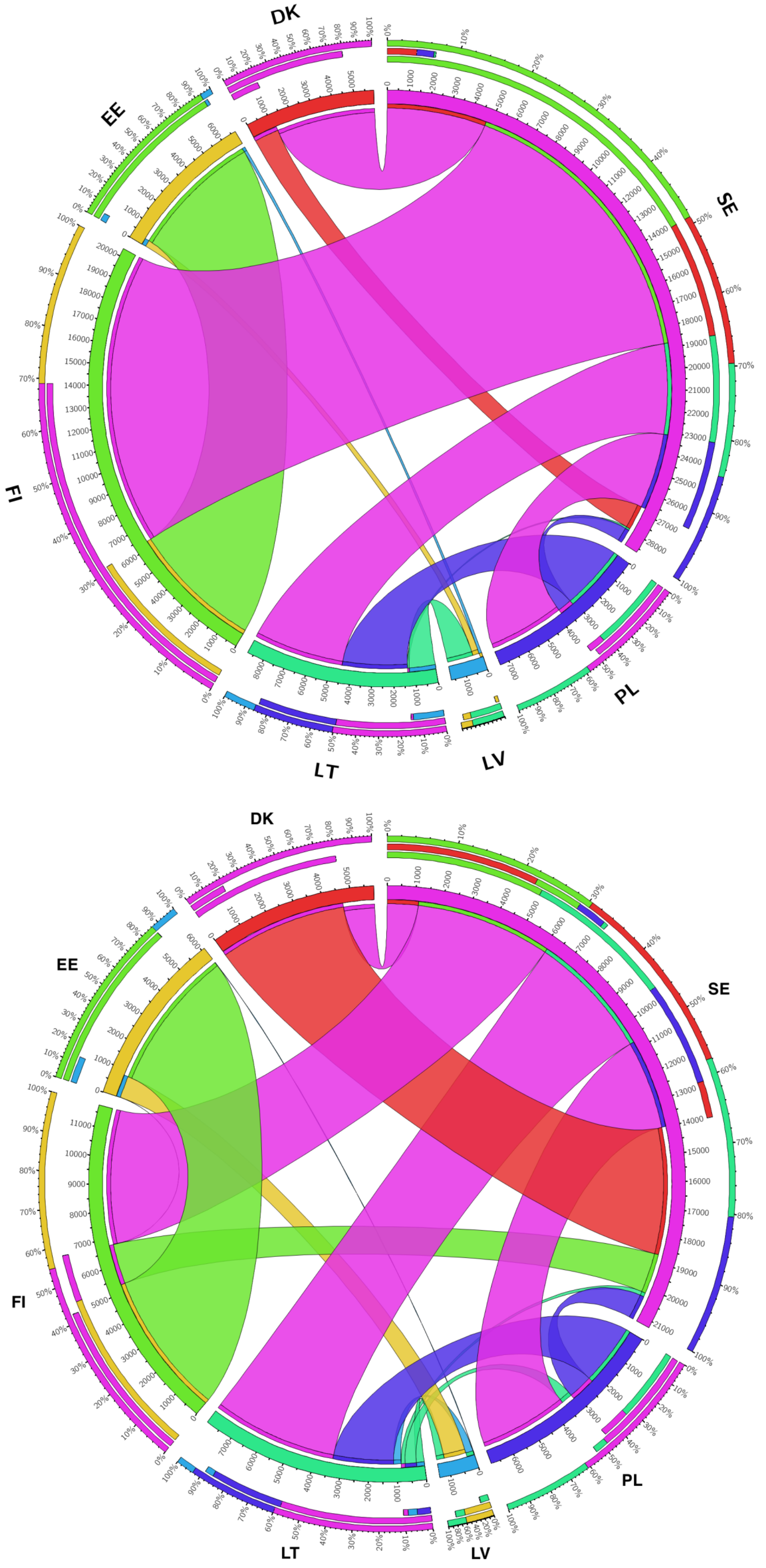

Fig. 5. Transborder flows in the base case scenario in 2030 (top) and 2050 (bottom) in GWh

When analysing the transborder flows in 2030 and 2050, shown in Fig. 5, two aspects can be highlighted: Firstly it is notable that the electricity trade seems to become more bidirectional over the modelling period than shown in Fig. 4 in 2015, where the flow between two countries was either in one or the other direction. The second aspect that can be seen is a decrease in the overall trade volume. The model indicates a trade volume of approximately 34 000 GWh in 2015 for Sweden which decreases to approximately 21 000 GWh in 2050. The change of one directional trade patterns to bidirectional be related to increased shares of variable renewables in the electricity production and their varying availability from country to country. The decrease in the trade volume might happen in cases of currently strong trade dependencies. However, it could also indicate that the chosen time resolution is coarse. This aspect will need to be further investigated in further research.

4. CONCLUSION

This first version of OSeMBE provides the base of an engagement model and tool, which is currently further developed in the REEEM project, funded by the Horizon 2020 EU framework programme. OSeMBE is structured in a simple but comprehensive manner which eases the use in academia and other learning environments like workshops on the energy nexus. Since the open source modelling systems OSeMOSYS was used to create the model and all data used is publicly available it shall also provide the possibility for further in-depth work by other users.

The above and in the appendices shown results indicate that fundamental dynamics of the modelled energy system are pictured, but also that the consideration of neighbouring countries is (modelled or not) and the definition of time slices will be crucial for the generating reasonable results with the enhanced and extended version of the model.

4.1. Future work

The next step in the development of OSeMBE, which is currently conducted, is the extension of the model to the entire European Union. This will allow analysis of electricity flows throughout the Union with the background of increasing shares of variable renewables and their varying availability in the region. As indicated earlier in the section on the generation mix a differentiation of biomass and biofuels will be done to better capture especially power plants using biomass as a fuel.

In the midterm there are five larger aspects that are possibly going to be addressed. These are namely: the integration of storage options like pumped hydro power and batteries, the implementation of heating demands, as already indicated in the RES, a better resource representation of solar and wind, and potentially the integration of the transport sector.

REFERENCES

[1] D. Scholten and R. Bosman, “The geopolitics of renewables; exploring the political implications of renewable energy systems,” *Technol. Forecast. Soc. Change*, vol. 103, pp. 273–283, Feb. 2016.

[2] RLI - Reiner Lemoine Institut, “oemof,” *open energy modeling framework*. [Online]. Available: https://oemof.org/. [Accessed: 23-Feb-2018].

[3] B. Fais, M. Blesl, U. Fahl, and A. Voß, “Analysing the interaction between emission trading and renewable electricity support in TIMES,” *Clim. Policy*, vol. 15, no. 3, pp. 355–373, May 2015.

[4] KTH - dESA, “OSeMOSYS,” *Open Source Energy Modelling System*. [Online]. Available: http://www.osemosys.org/. [Accessed: 23-Feb-2018].

[5] H. Henke, “The Open Source Energy Model Base for the European Union (OSEMBE),” KTH Roayl Institute of Technology, Stockholm, Sweden, Master thesis, 2017.

[6] M. Howells *et al.*, “OSeMOSYS: The Open Source Energy Modeling System,” *Energy Policy*, vol. 39, no. 10, pp. 5850–5870, Oct. 2011.

[7] C. Taliotis *et al.*, “An indicative analysis of investment opportunities in the African electricity supply sector — Using TEMBA (The Electricity Model Base for Africa),” *Energy Sustain. Dev.*, vol. 31, pp. 50–66, Apr. 2016.

[8] EC, *EU energy, transport and GHG emissions: trends to 2050 : reference scenario 2013*. Luxembourg: European Commission (EC), 2014.

[9] EC, *Energy Technology Reference Indicator (ETRI) projections for 2010-2050*. Luxembourg: European Commission (EC), 2014.

[10] IEA, “World Energy Outlook 2014 - Power Generation Investment Assumptions.” International Energy Agency (IEA), 2014.

[11] IEA ETSAP, “IEA ETSAP - Technology Brief E03.” IEA Energy Technology Systems Analysis Programme (ETSAP), Apr-2010.

[12] K. Darrow, R. Tidball, J. Wang, and A. Hampson, “Catalog of CHP Technologies.” U.S. Environmental Protection Agency Combined Heat and Power Partnership, Mar-2015.

[13] EIA, “How much electricity is lost in transmission and distribution in the United States? - FAQ - U.S. Energy Information Administration (EIA),” *U.S. Energy Information Administration*, 29-Jan-2018. [Online]. Available: https://www.eia.gov/tools/faqs/faq.php?id=105&t=3. [Accessed: 13-Apr-2018].

[14] I. Staffell and S. Pfenninger, “Using bias-corrected reanalysis to simulate current and future wind power output,” *Energy*, vol. 114, pp. 1224–1239, Nov. 2016.

[15] S. Pfenninger and I. Staffell, “Long-term patterns of European PV output using 30 years of validated hourly reanalysis and satellite data,” *Energy*, vol. 114, pp. 1251–1265, Nov. 2016.

[16] N. Mosknes *et al.*, “2015 OSeMOSYS User Manual.” KTH Royal Institute of Technology, Nov-2015.

[17] KTH - dESA, “OSeMOSYS documentation.” [Online]. Available: http://osemosys.readthedocs.io/en/latest/. [Accessed: 19-Feb-2018].

APPENDIX A. CAPACITY MIX RESULTS

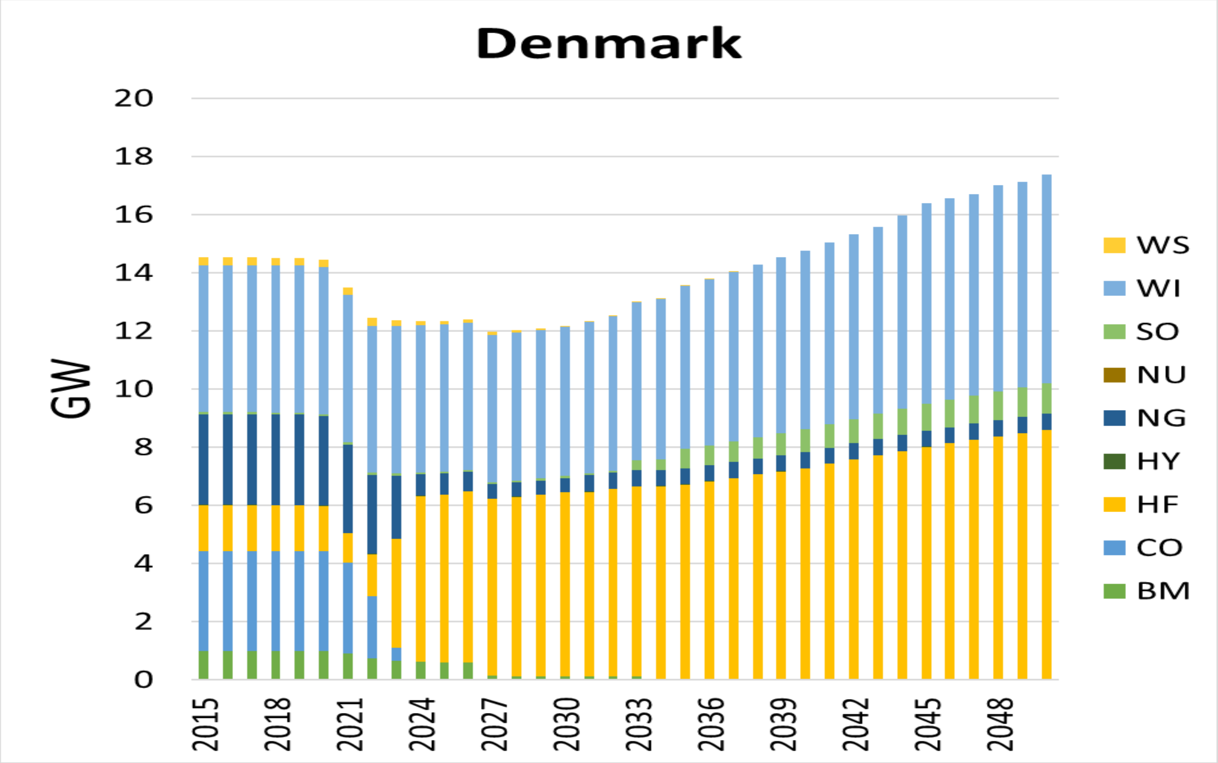

Fig. 6. Installed capacities in Denmark with RM 1.2

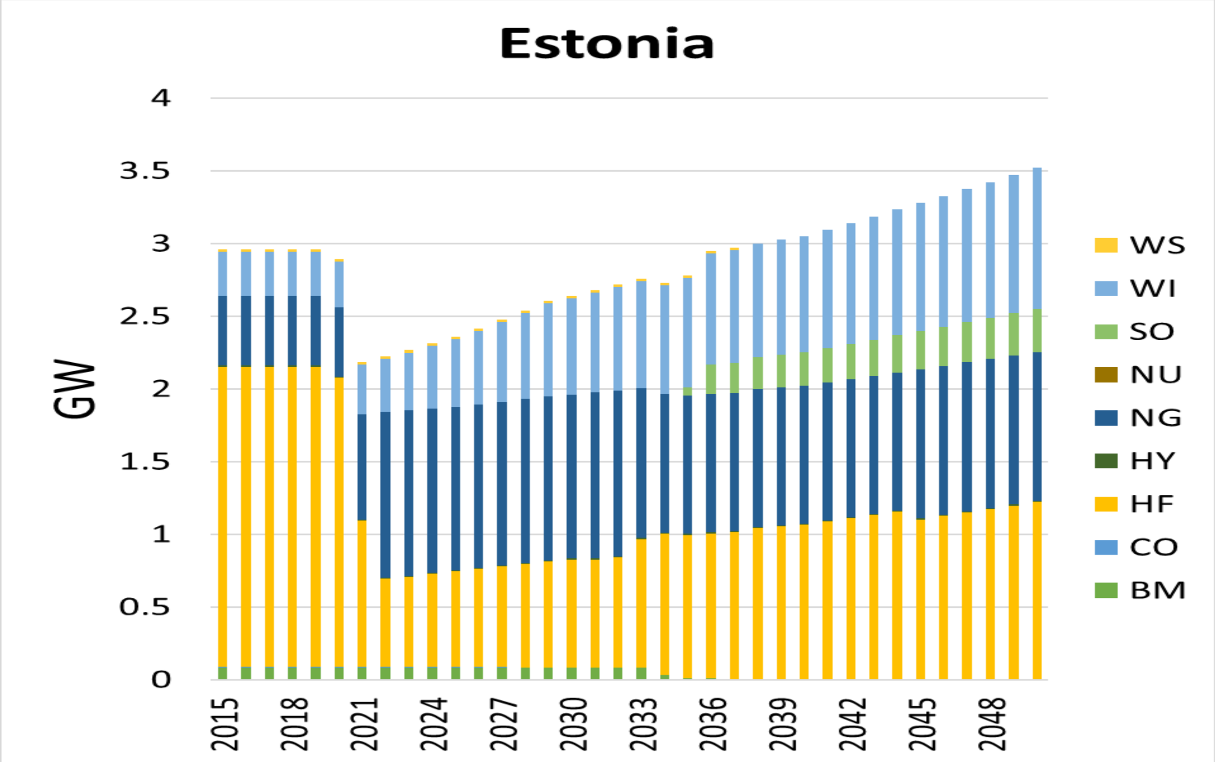

Fig. 7. Installed capacities in Estonia with RM 1.2

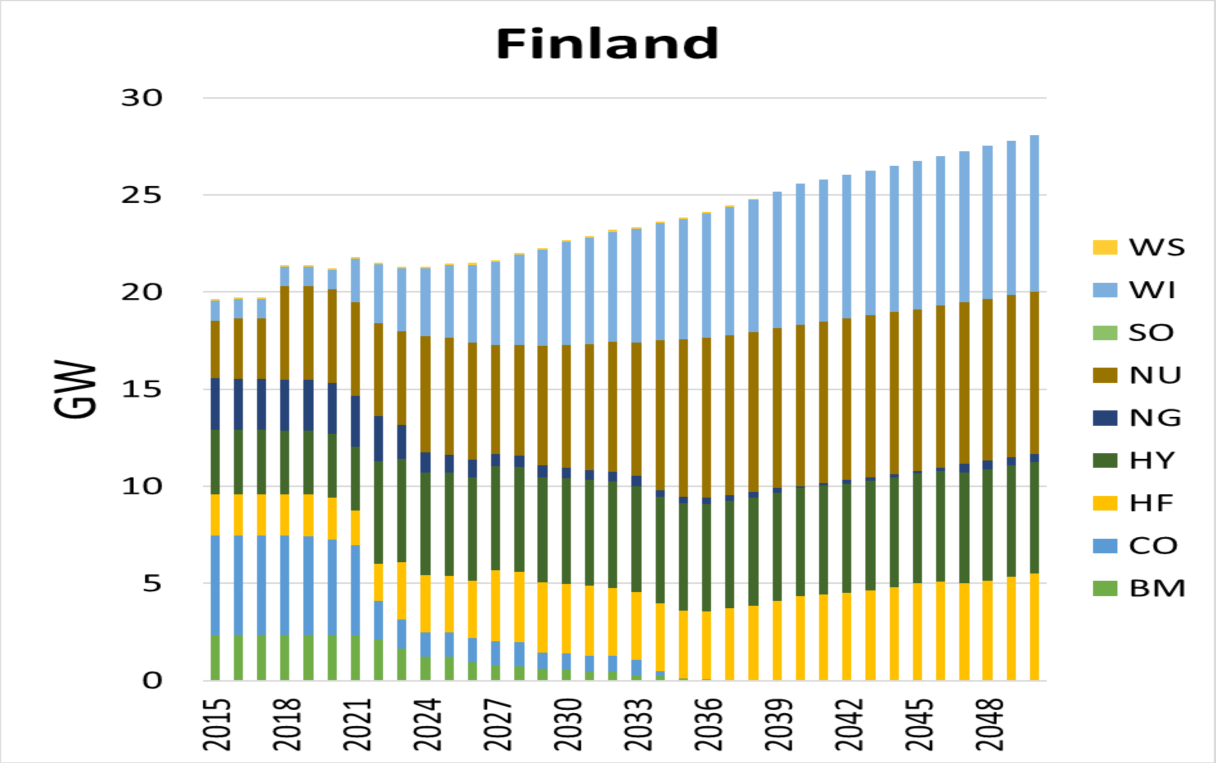

Fig. 8. Installed capacities in Finland with RM 1.2

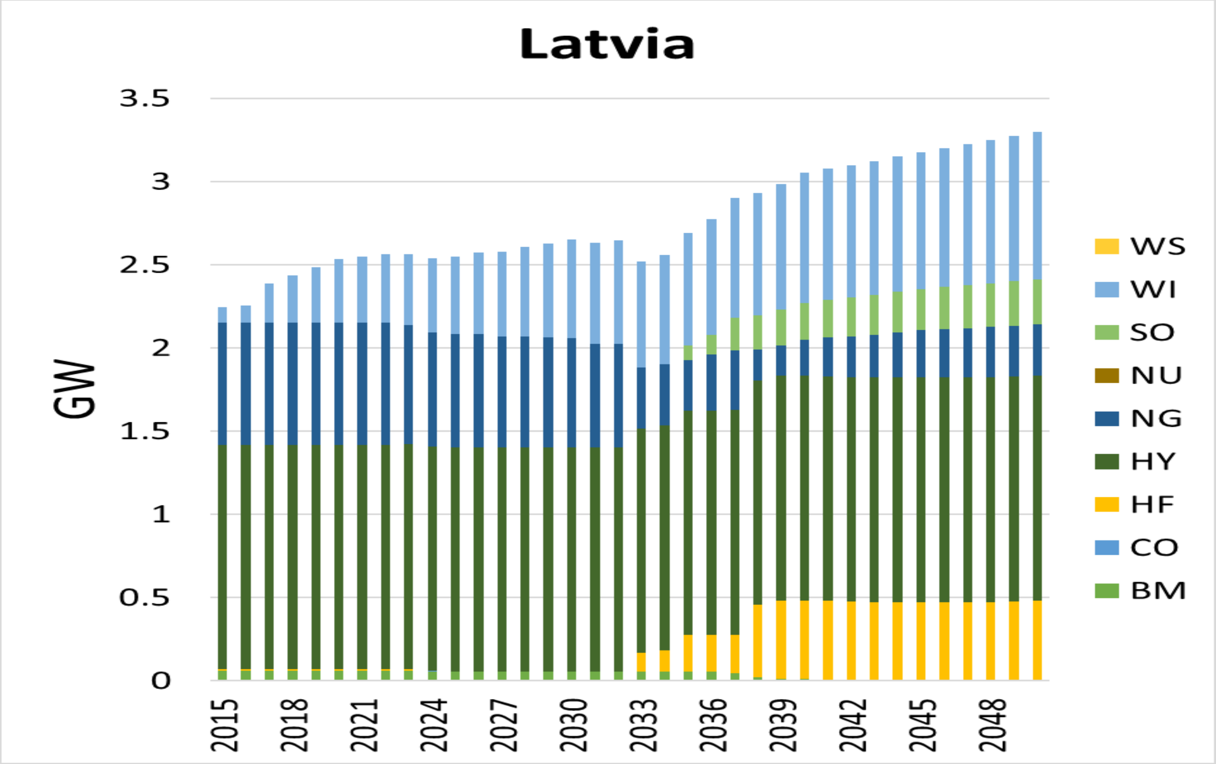

Fig. 9. Installed capacities in Latvia with RM 1.2

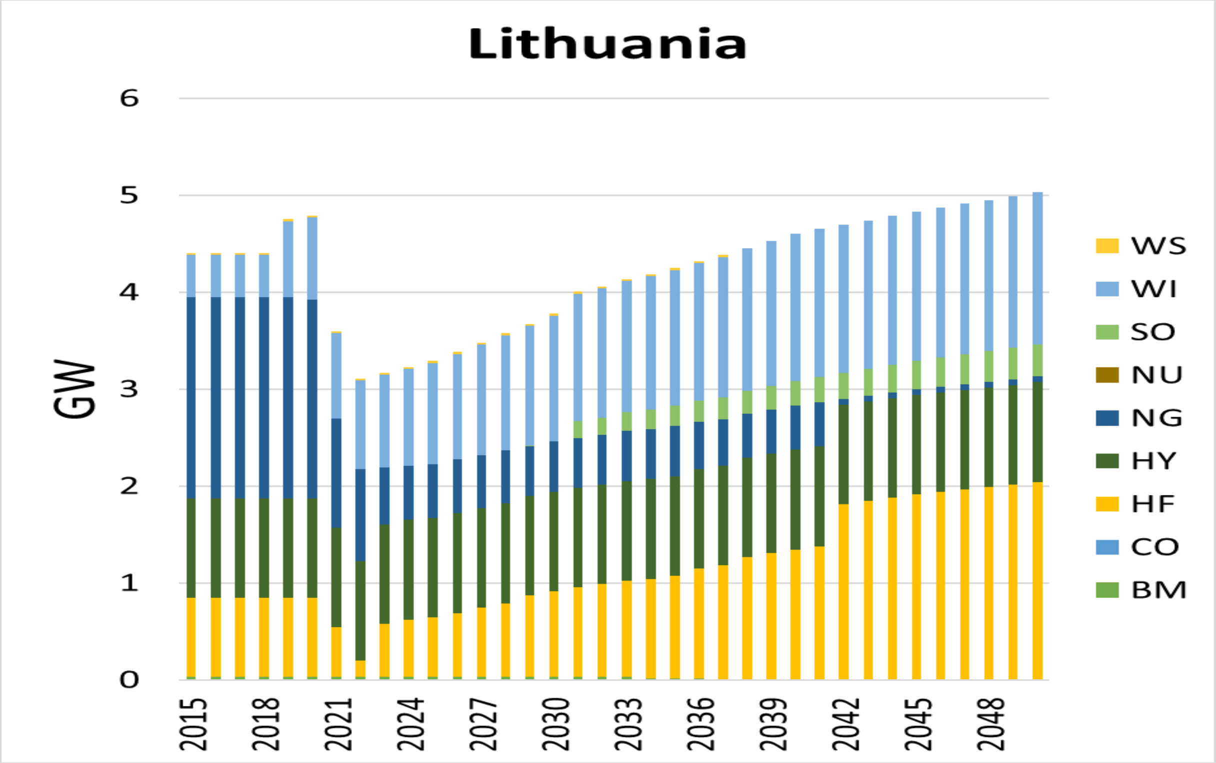

Fig. 10. Installed capacities in Lithuania with RM 1.2

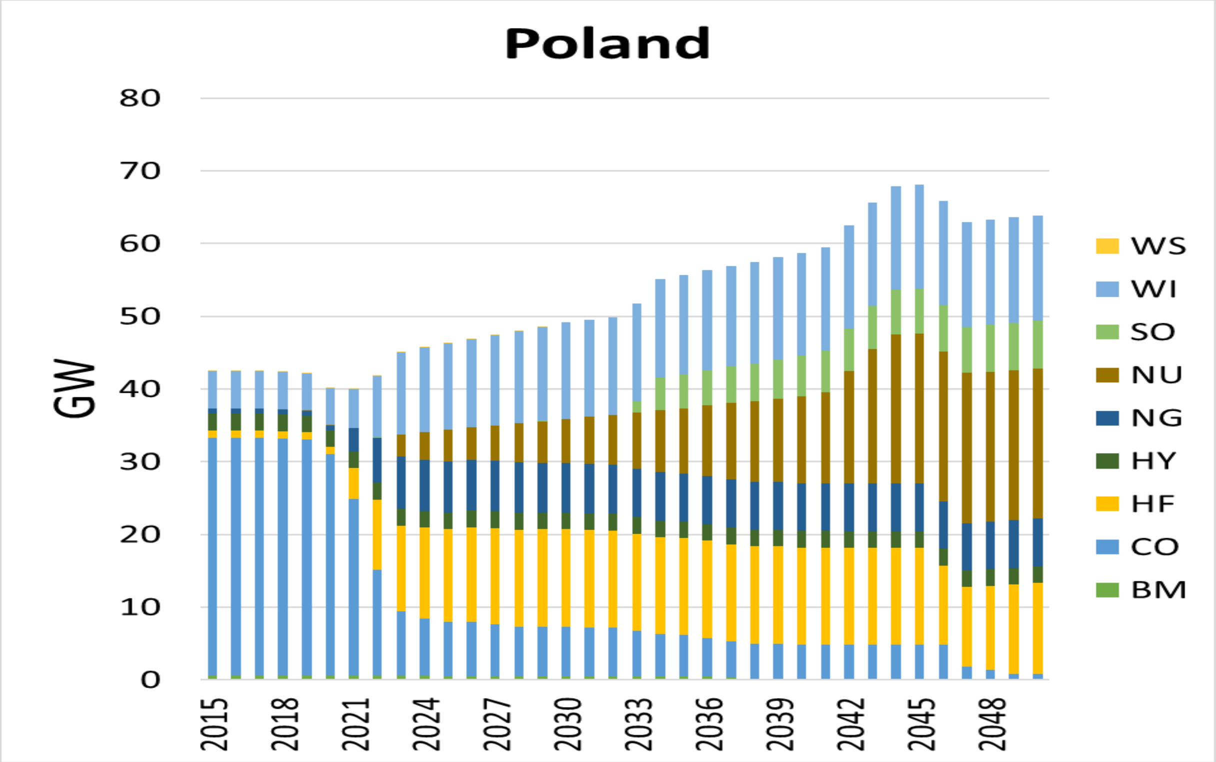

Fig. 11. Installed capacities in Poland with RM 1.2

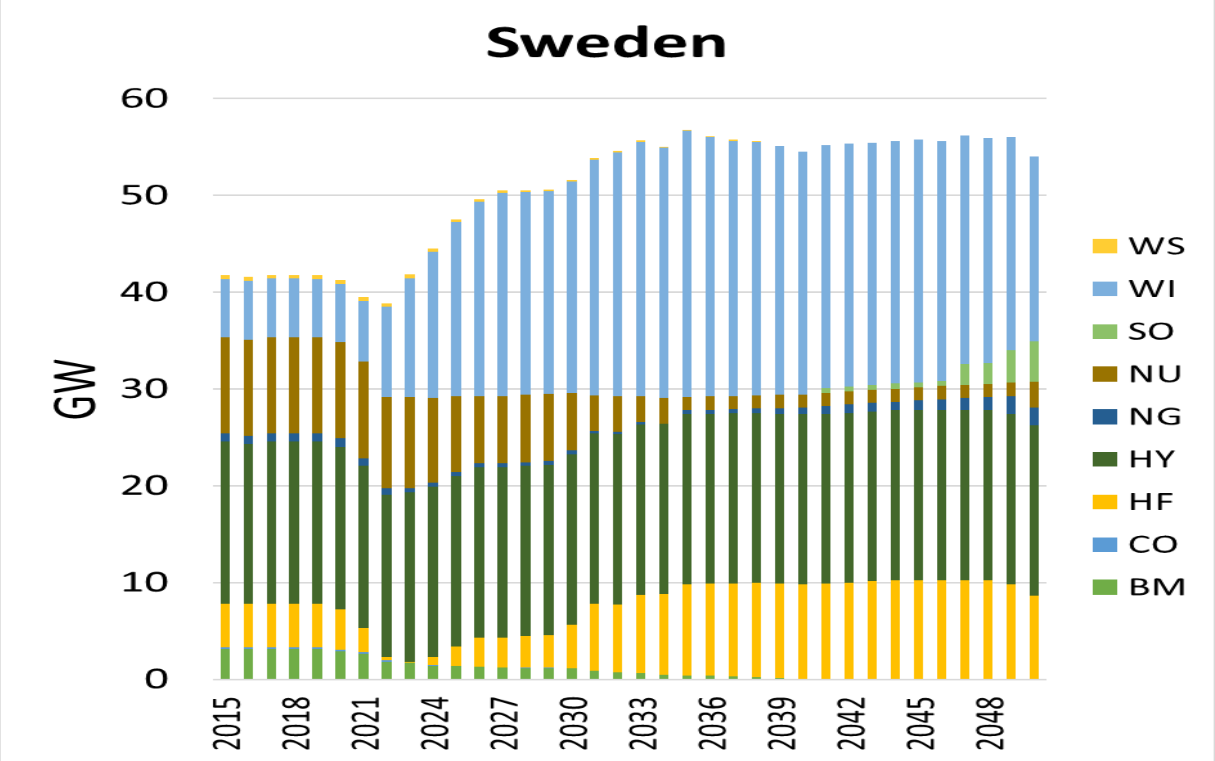

Fig. 12. Installed capacities in Sweden with RM 1.2

APPENDIX B. GENERATION MIX RESULTS

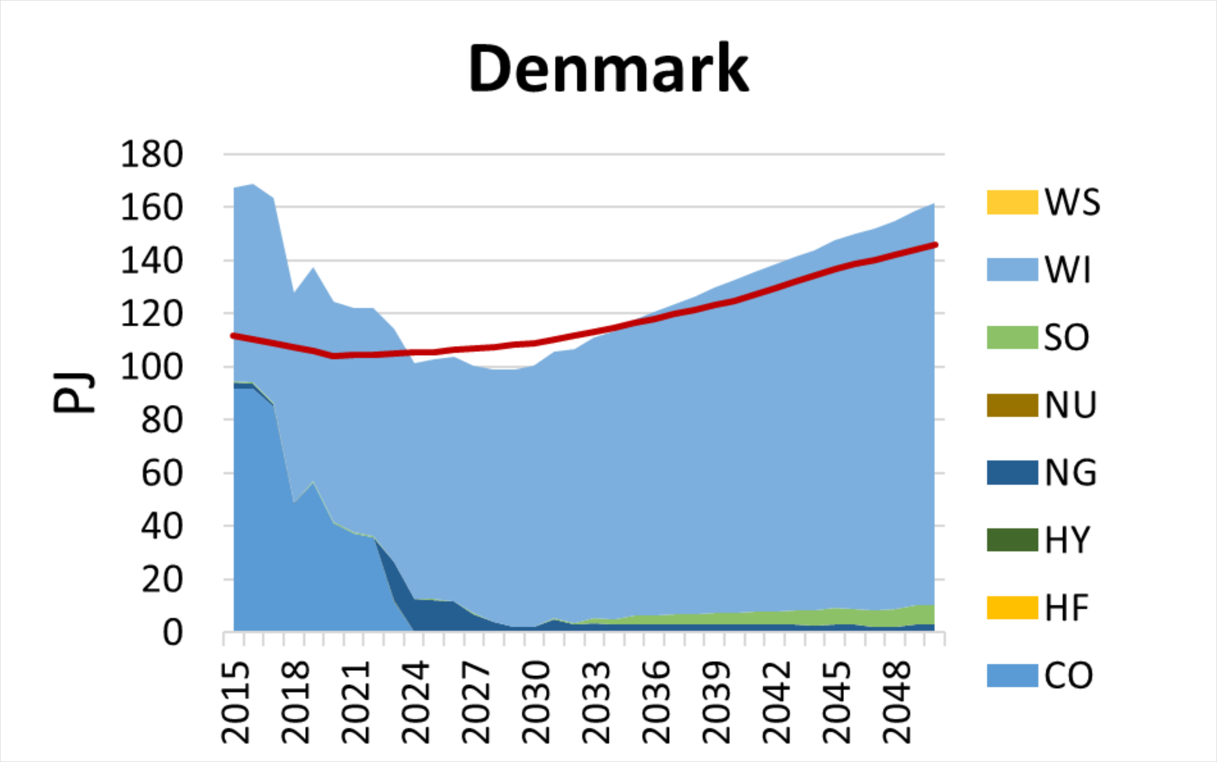

Fig. 13. Annual Production for Denmark with RM 1.2

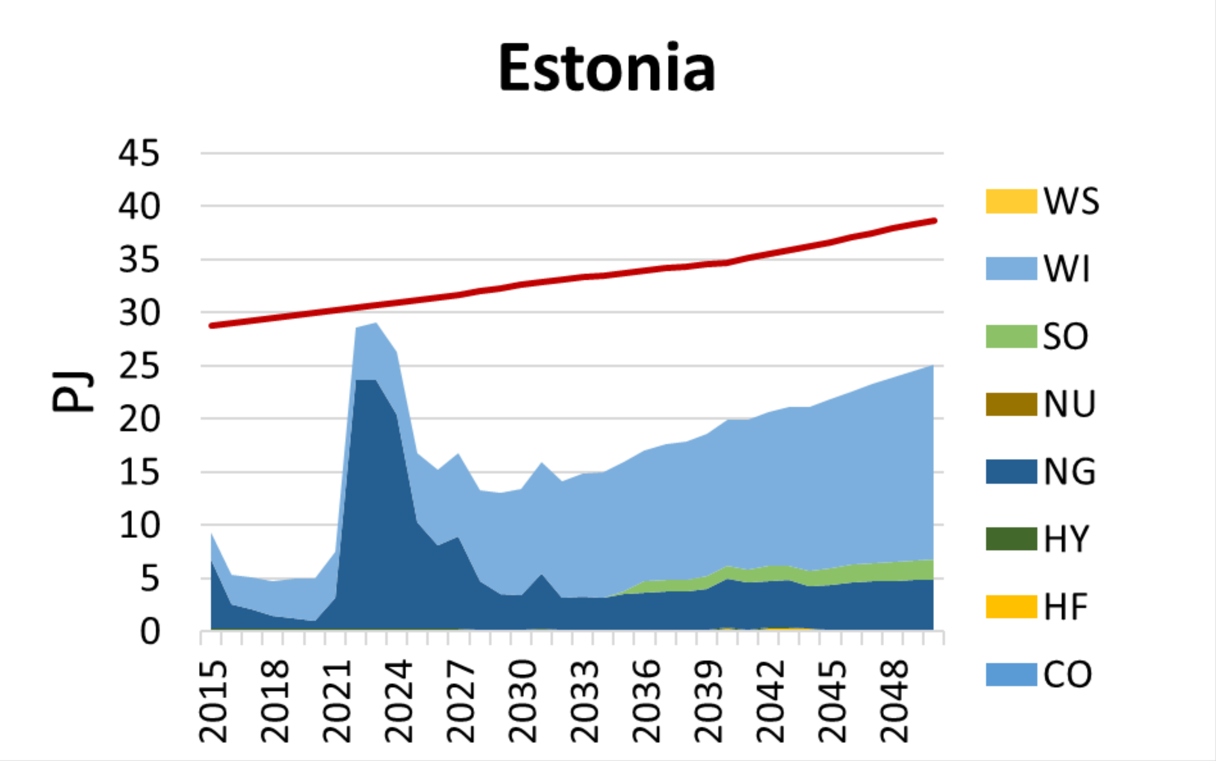

Fig. 14. Annual Production for Estonia with RM 1.2

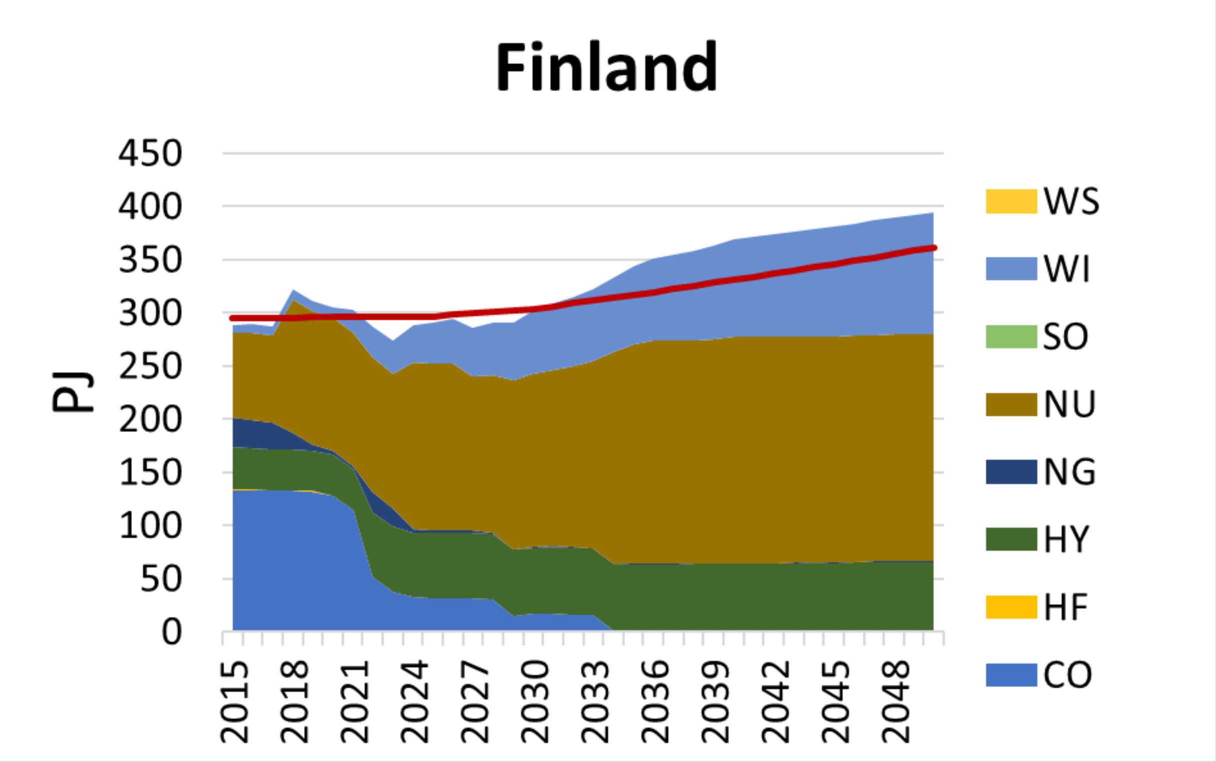

Fig. 15. Annual Production for Estonia with RM 1.2

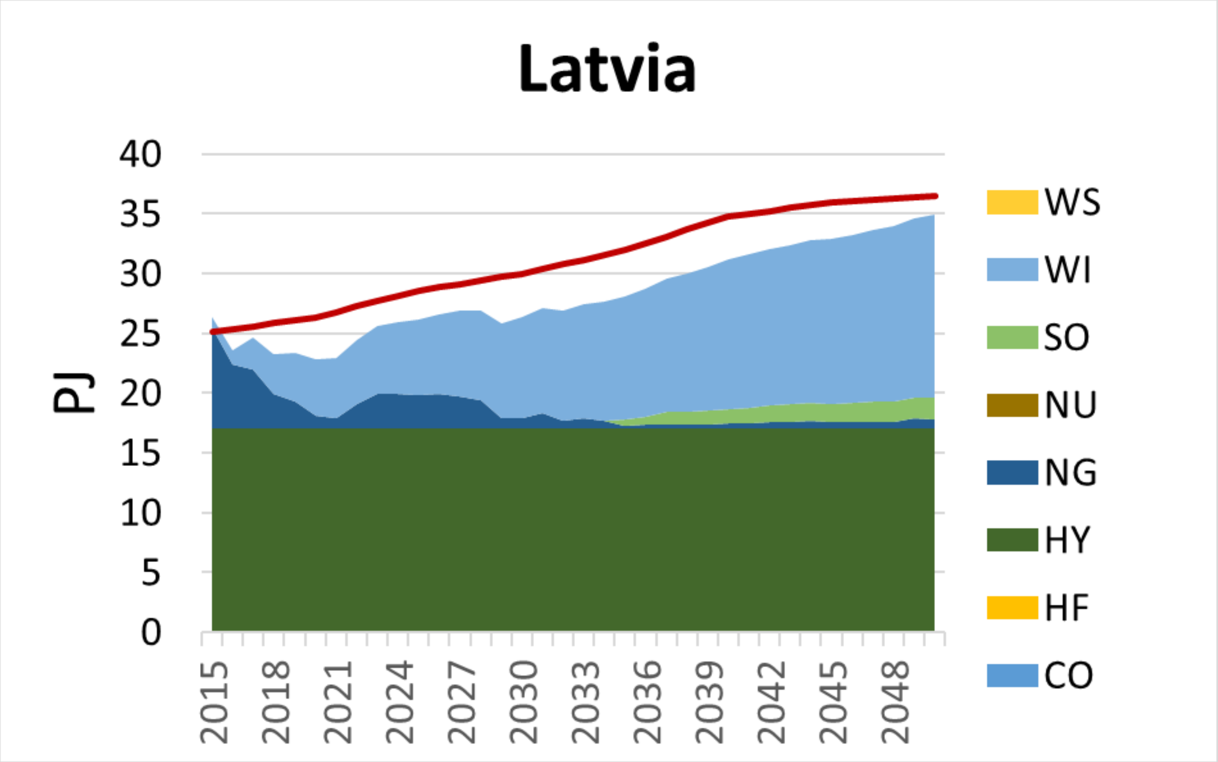

Fig. 16. Annual Production for Latvia with RM 1.2

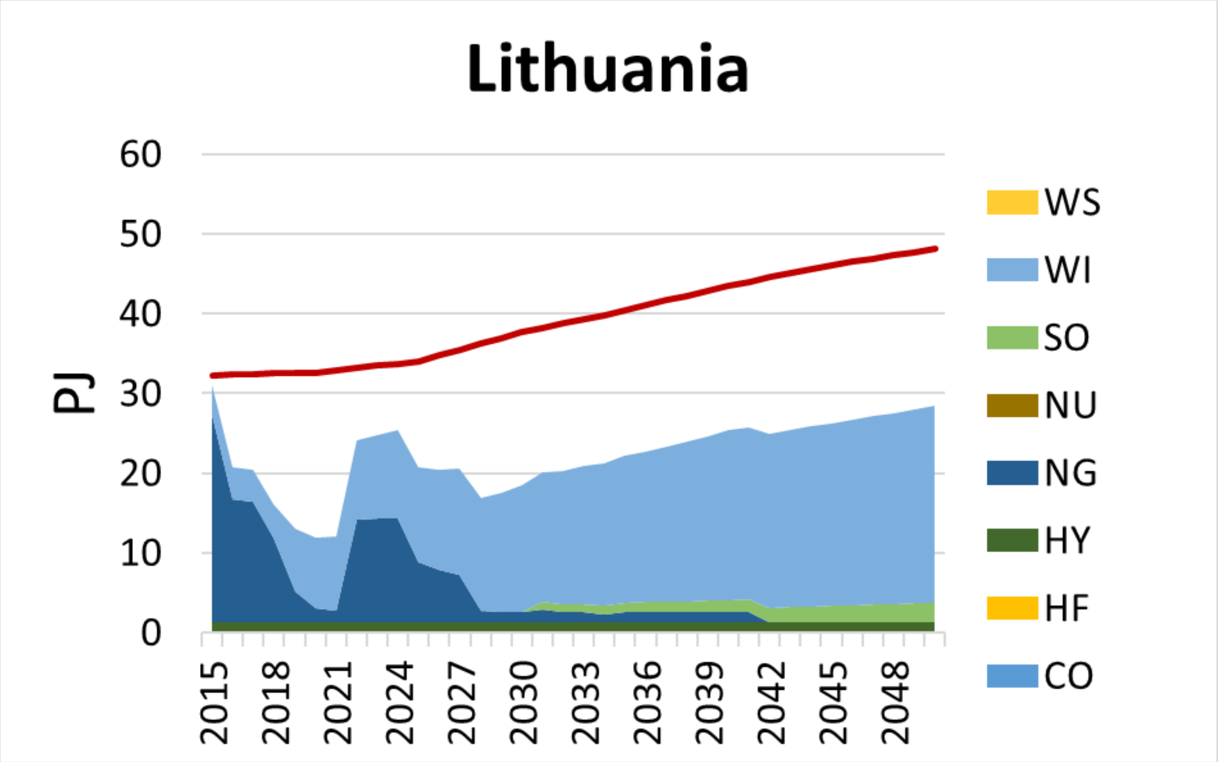

Fig. 17. Annual Production for Lithuania with RM 1.2

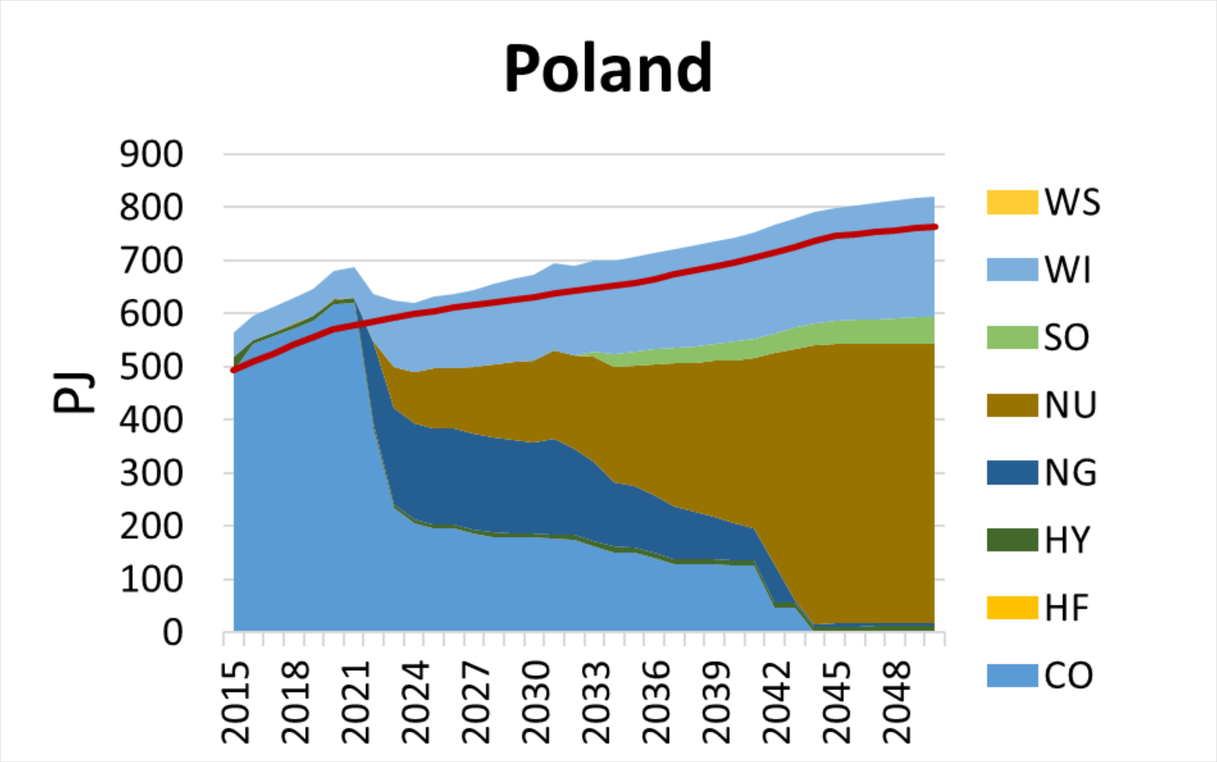

Fig. 18. Annual Production for Poland with RM 1.2

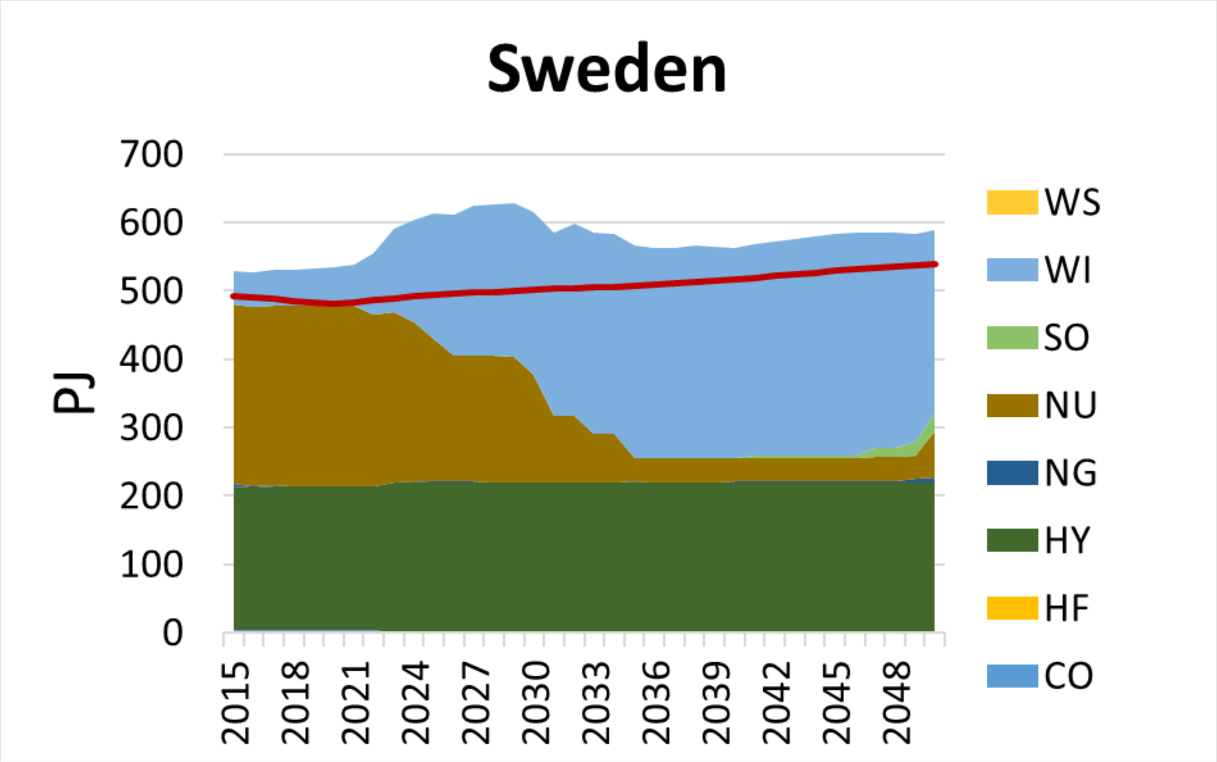

Fig. 19. Annual Production for Sweden with RM 1.2

APPENDIX C. CROSS-BORDER ELECTRICITY TRADE

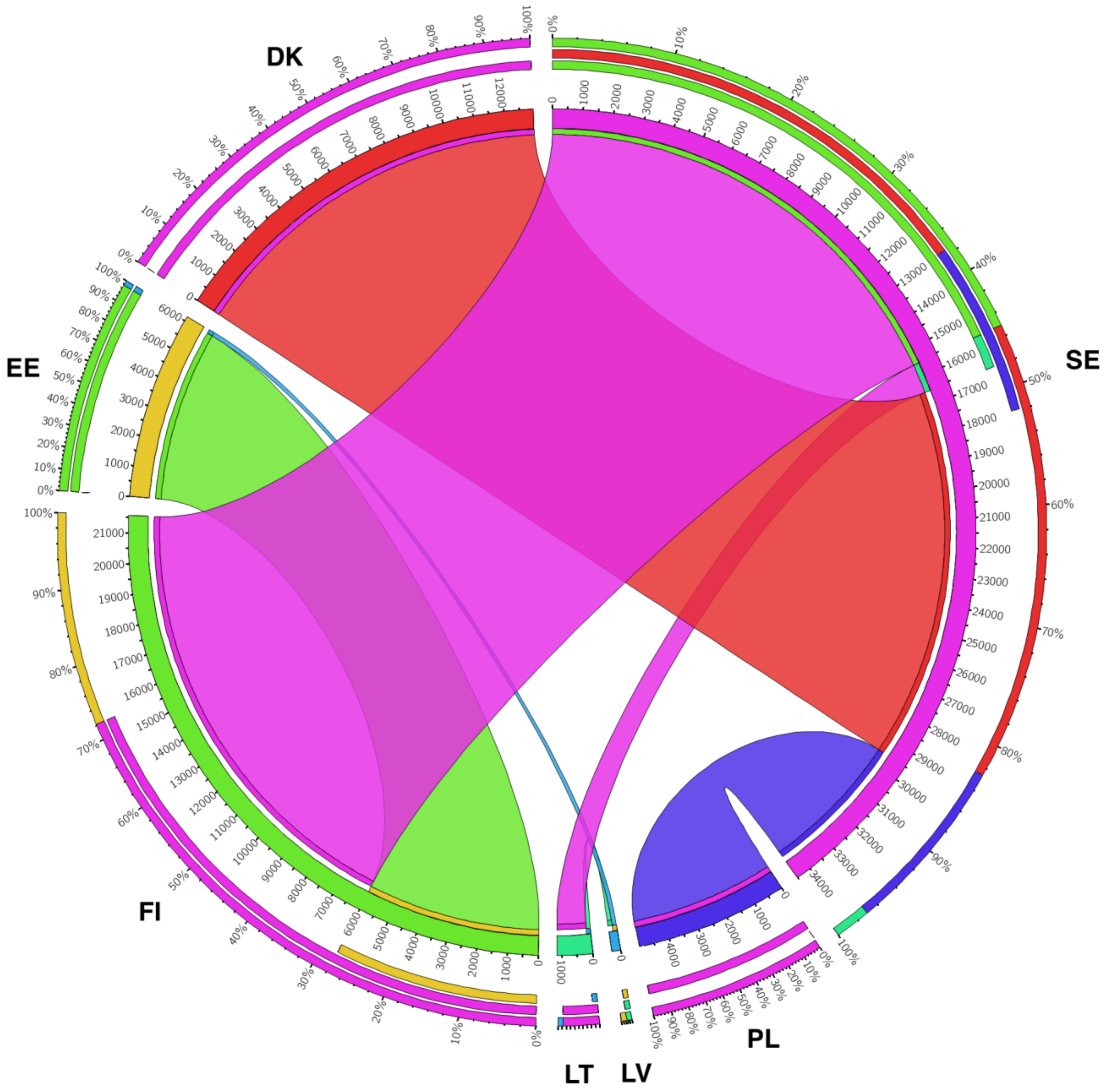

Fig. 20. Transborder electricity flows in the base case scenario in 2015 in GWh

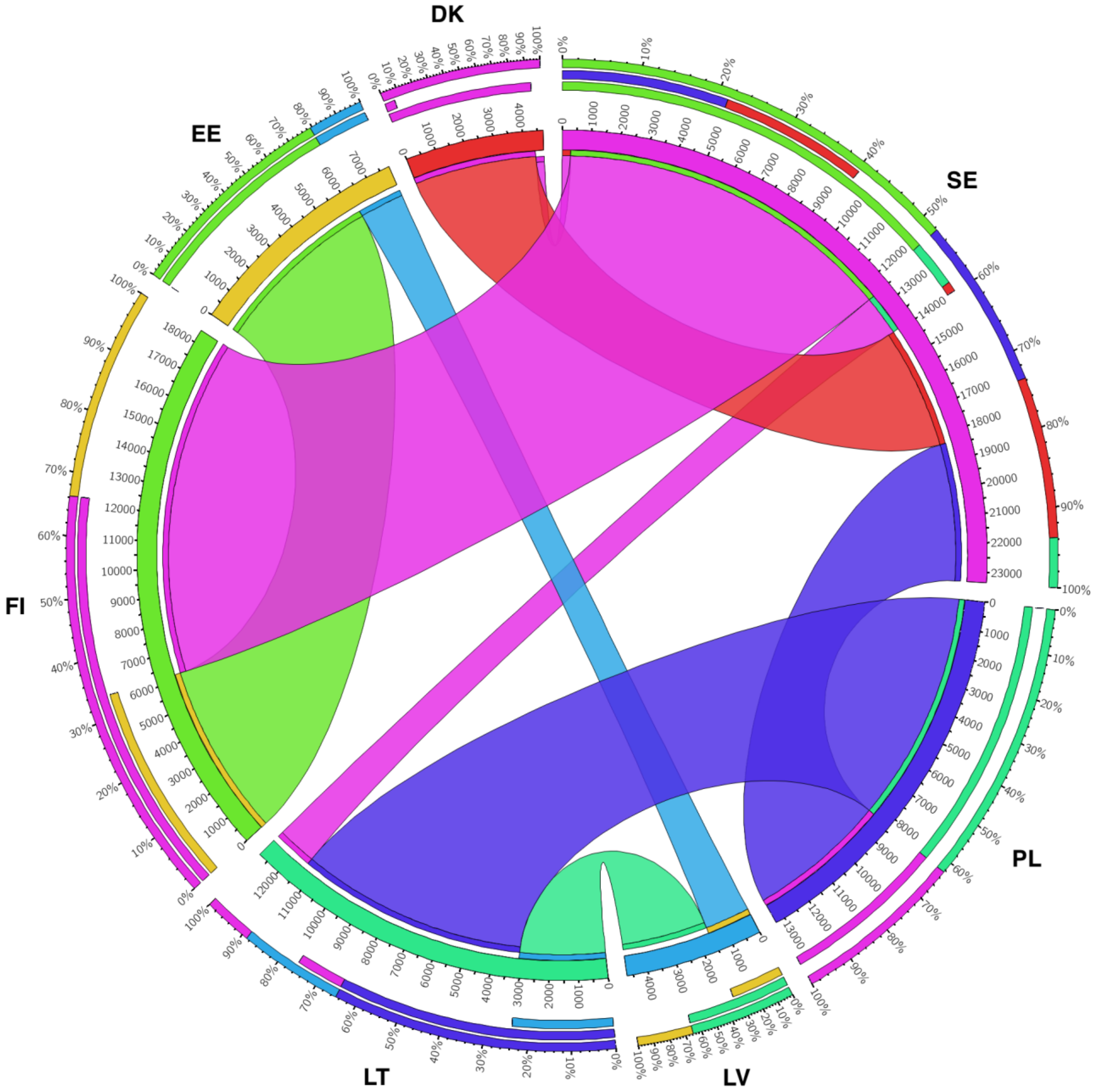

Fig. 21. Transborder electricity flows in the base case scenario in 2020 in GWh

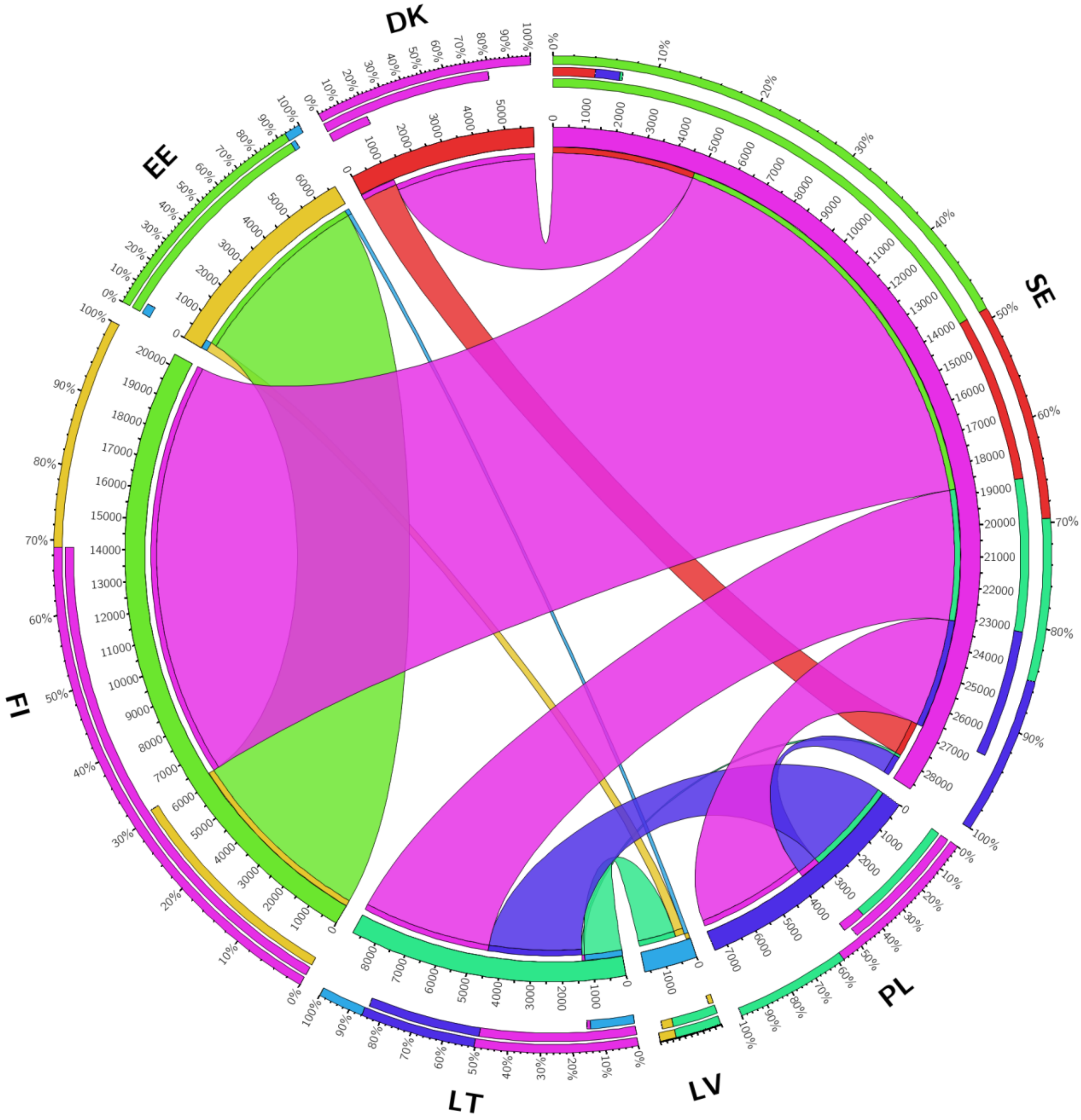

Fig. 22. Transborder electricity flows in the base case scenario in 2030 in GWh

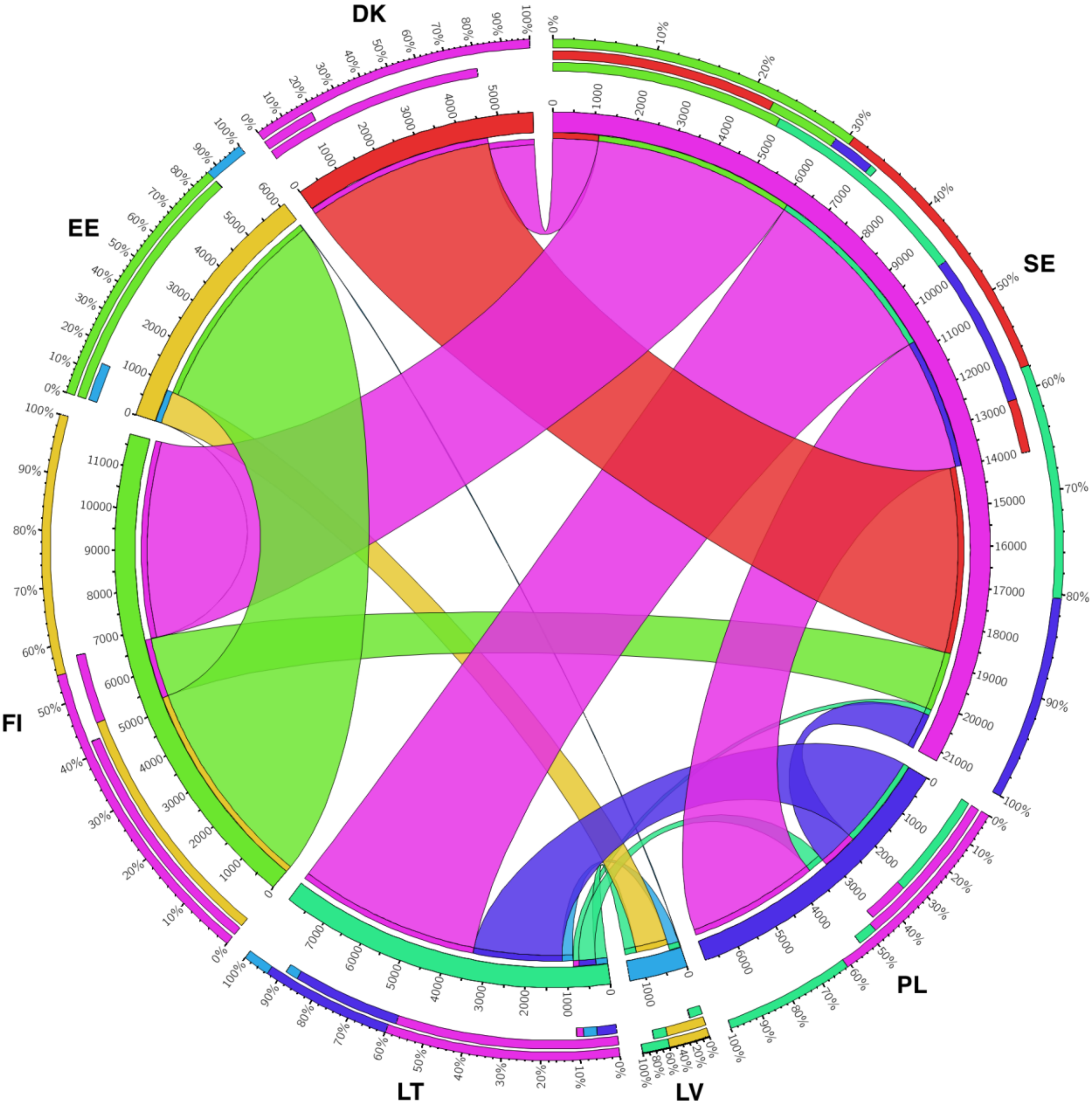

Fig. 23. Transborder electricity flows in the base case scenario in 2050 in GWh

CYSENI 2018, May 23-25, Kaunas, Lithuania
ISSN 1822-7554, www.cyseni.com

BARRIERS OF INDUSTRIAL ENERGY EFFICIENCY

A. Zuoza
Lithuanian Energy Institute
Breslaujos st. 3, LT-44403 Kaunas, Lithuania
Email: andrius.zuoza@lei.lt

V. Pilinkienė
Kaunas University of Technology
Gedimino g. 50 - 334, LT-44029 Kaunas, Lithuania
Email: vaida.pilinkiene@ktu.lt

ABSTRACT

This paper presents the literature review of barriers to industrial energy efficiency investments. It is claimed that primary origin of energy efficiency gap is market failures and barriers. Understanding of market barriers nature will lead to obtain an entire image of a complex problem and suggest better investment decisions for industries or to formulate government policies to diminish the impact of the barriers. As pointed in the literature market barriers are very heterogeneous and also influence all market players. Various market barriers, concerning enterprise, can be divided into external and internal barriers. In more details all external and internal barriers can be categorized into 11 categories: market (1), government or politics (2), technology and service suppliers (3), designers and manufacturers (4), energy suppliers (5), capital suppliers (6), economic (7), behavioural (8), organizational (9), competence (10) and awareness (11) barriers. After a comprehensive literature review, we offer several suggestions for future economic research.

Keywords: energy efficiency gap, market barrier, internal barriers, external barrier, economic barriers, behavioural barriers, organizational barriers

1. INTRODUCTION

Lattes efforts of European commission on boosting industry energy efficiency in European Union is focused on deployment of energy efficiency measures. Based on most recent studies [1–5] it is crucial to understand which barriers are most important. Understanding of barriers nature will lead to obtain an entire image of a complex problem and suggest better investment decisions for companies or to formulate government policies to diminish the impact of the barriers.

In the general case, energy efficiency is defined as the ratio of useful outputs to energy consumption for a system [6]. However, the energy efficiency measurement will depend on what is described as “useful” and how inputs and outputs are measured [7]. There are three possible measures:

1. Thermodynamic measures – output is defined as a heat content or as a capacity of useful work;
2. Physical measures – output is defined as in physical terms, i.e. units of transportation measurement, tonnes of produced productions, etc.
3. Economic measures – output is defined in economic terms, i.e. GDP, value-added.

In this paper, energy efficiency is treated as “a ratio of the output of performance, service, goods or energy, to the input of energy” [8].

From the industry perspective improved energy efficiency leads to direct economic benefit, increased competitiveness[9], productivity [10] and also energy security [11]. The positive effect of the higher energy efficiency from countries perspective includes environmental benefits, increased security of supply and even industrial competitiveness [9].

There is some discrepancy between the potential benefit of energy efficiency and observed amount in practice. This discrepancy is referred as "energy efficiency gap" or sometimes also as "energy paradox" ([12–13], [9], [14–23]). It is claimed that primary origin of energy efficiency gap is market failures and barriers.

Sorrell et al. have defined energy efficiency barrier as "a postulated mechanism that inhibits a decision or behaviour that appears to be both energy efficient and economically efficient" [20].

We have reviewed a total 56 academic paper and "grey" studies. Academic papers were selected from Web of science and Emerald inside databases and "grey" studies from the European Council for an Energy Efficient Economy, the Organization for Economic Cooperation and Development, the International Energy Agency and the United Nation Industrial Development Organization. This sample of the studies is representative but is not expected to be comprehensive.

The aim of the article is to classify energy efficiency barriers, by grouping them according to integrated approach and possibilities to overcome.

This paper is structured as follows: in Section 2 of this paper critical view of the scientific literature is presented. In Section 2.1 internal energy efficiency drivers are reviewed and summarized, in Section 2.2. external energy efficiency drivers are presented. Discussion and proposed classification of energy efficiency barriers are presented in Section 3. Concluding remarks and further research possibilities are reported in Section 4.

2. ENERGY EFFICIENCY BARRIERS

In the scientific papers, there are some different ways to classify energy efficiency barriers. Most studies classifying barriers from an economic point of view, others – use social psychology perspective [24] or organizational theory [25]. Foxon [26] is also using a macro-level perspective for barriers classification. In this paper, an economic concept was used to classify barriers to industrial energy efficiency.

Sorrell at al. identify and characterize 15 barriers [27] and also categorized them into three groups – economic, behavioural, organizational. This research and further modification of this work [20] is the primary reference in the scientific literature on energy efficiency barriers.

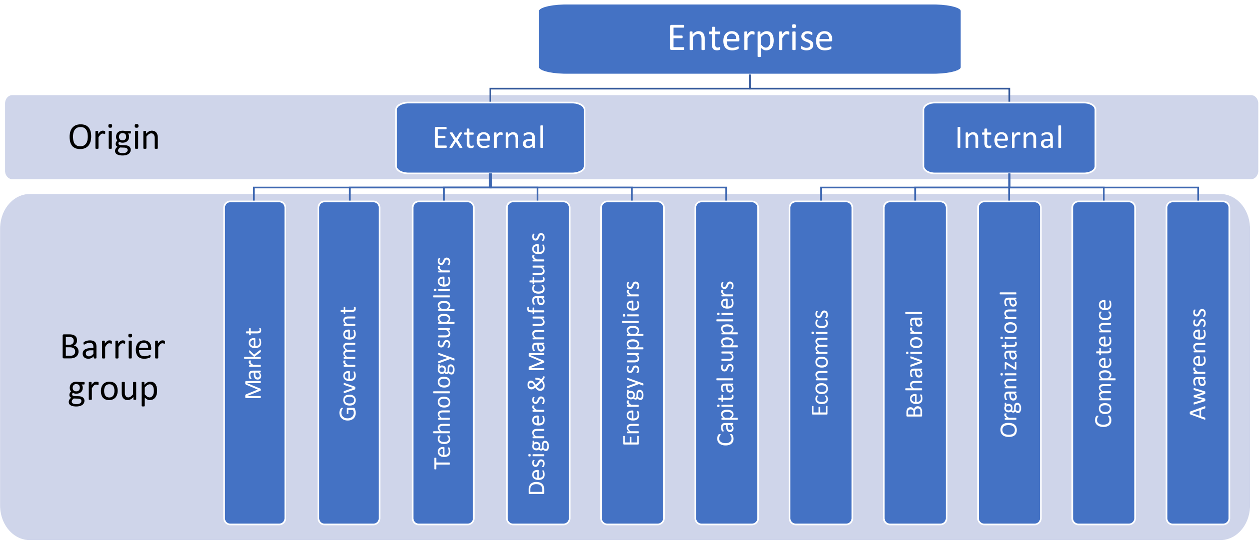

Fig. 1. Taxonomy of energy efficiency barriers [28]

Thollander not only described 15 barriers and categorized them into three categories, but also he named five barriers which are not entirely explaining energy efficiency gap. These five barriers may be grouped as structural and institutional barriers. Cagno et al. observed, that Sorrell et al. has not included several barriers. Cagno et al. [28] supplemented methodology suggested by Sorrell and determined entirely 37 barriers to industrial energy efficiency. He also grouped all barriers, with respect to the enterprise, into external and internal barriers and by the actor affected by the barriers. Cagno at al. also modified some barriers and from the perspective of empirical research grouped them into seven groups – economic, organizational, behavioural, technological, competences, informative and awareness [28].

Followed by Sorrell et al. [6] and Cagno et al. [28] typology of energy efficiency barriers is shown in Fig. 1.

All identified barriers are presented in the section below. Also, it is to be noted that often real-world problems can be explained only be combination of several barriers instead of one specific barrier [17].

2.1. Internal energy efficiency barriers

Various energy efficiency barriers come from enterprise itself. These barriers may be categorized into five groups (economic barriers, behavioural barriers, organizational barriers, barriers related to the competence, awareness) and are presented below.

2.1.1. Economic barriers

In this section, some barriers related to the economic analysis of the investments in energy efficiency are presented.

Hidden cost often is used to explain an energy efficiency gap [29]. As noted by Ostertag hidden cost might vary a lot expected in the investment analysis [30]. These costs are associated with seeking of information, negotiating with suppliers, contracts preparation, lawyer services, etc. If these costs are higher enough, than all investment analysis may be incorrect. Hein and Blok reported that the hidden costs in the sizeable energy-intensive enterprise were between 3% and 8% of the total investment cost [31]. In smaller enterprises, such cost should be even higher [32].

Hidden cost can also be divided to cost, which occurs before the decision to invest in energy efficiency technologies (pre-intervention hidden costs), during the investment and after (post-intervention hidden costs) [28]. Cost such as expenditures for energy efficiency audits [16], research of energy inefficiency or other similar research [33] is typical pre-intervention hidden costs. During the installation of new technology, some cost may also occur, e.g., interruption of normal production operations [27]. Usual post-intervention hidden costs are a cost for personal training, development or adaptation of new procedures for maintenance, etc. [34].

As shown by empirical evidence [28] some companies are rejecting energy efficiency investments because there are *not sufficiently profitable*. The rate of return of such investment is lower than from the required rate of return.

Limited access to capital: investment to energy efficiency technologies is often more expensive than alternative technologies. As shown in several studies companies do not own enough own capital to invest in new energy efficiency technologies [34–35], [3].

Another economic barrier for energy efficiency and a possible explanation for the energy efficiency gap is a *risk*. Typically, as the risk of any investment project counts uncertainty about discount rates for future costs [36–37]. Also, as pointed out by Hirst and Brown managers are unsure whether new equipment will increase total company productivity or not [9]. Stern and Aronson [38] and Hirst and Brown [9] also pointed out, that uncertainty about future energy prices and availability of energy resources can have considerable influence to the estimation of the net costs of investment to energy efficiency.

2.1.2. Behavioural barriers

In this section, some barriers linked to the behaviour of decision-makers is presented below.

Lack of interest in energy efficiency. If companies energy cost is relatively small in comparison to production cost, then decision-makers can underestimate the importance of the energy efficiency [39]. Also if managers are convinced, that energy efficiency level of the company is high enough, then they are also not paying enough attention to the energy efficiency [40]. In a most recent paper on energy efficiency barriers and driving forces, Johansson and Thollander showed that employees with real ambition to increase energy efficiency are crucial and most significant driving force [41].

Inertia. As pointed out by Thollander [32] individuals and organizations is trying to reduce uncertainty, and they resist changes in their environment. Sorrell et at. noted, that the more radical the change, the higher the resistance will be [27].

Lack of sharing objectives. This barrier represents discrepancy between personal behavioural of companies employs and companies energy management goals [15], [42].

Other priorities. This barrier is observed by the companies, where manager are mainly focused on core business activities and are not paying enough attention to energy efficiency systems, which are not critical to the company [34–35], [43].

Imperfect evaluation criteria. Managers, which has a power to make energy-related decisions may lack of knowledge or standards to evaluate the investment. As observed by Sanstad and Howarth sometimes managers decide by the rule of thumb rather than based on complete information [44].

2.1.3. Organizational barriers

There are also barriers which come from organizational theory [27]. These barriers appear from lack of synergy within different organization departments.

Power. As shown by Sorrell et al. [20] questions of energy management and efficiency have low priority among top decision-makers or managers responsible for energy efficiency do not have enough power implement changes.

Split initiatives. This barrier is explained by the fact that decision-makers may not benefit by improved energy efficiency [16].

Lack of time. As noted in the empirical study [45] decision-makers do not have enough time to look into possibilities provided by the energy efficiency investments.

Lack of control. This barrier related to the internal control system of the company. If the existing control system in the company is not efficient, then the company staff may not implement energy efficiency technologies [27].

Long decision-making chain. Decision-making process in industry companies involves multiple managers, with the different responsibility levels. As stated by Benhaddadi and Olivier [45] if information flow between different responsibility levels is not smooth, then management can make the wrong decision.

2.1.4. Competence

The staff of the company should have a set of specific knowledge to implement new energy efficiency technologies. As considered by Trianni et al. mainly employees of the small and medium companies might be trained to operate complex machinery, but they do not have enough experience to identify inefficiencies and possible opportunities [43]. Also, Hochman and Timilsina showed that lack of knowledge awareness is two most important energy-efficiency barriers [46].

There are three possible barriers related to the competence – *identifying the inefficiencies, identifying the opportunities, implementing the interventions [5]*.

2.1.5. Awareness

If lack of awareness is characteristic of the manager of the company, then they can ignore the possible gain related to energy efficiency investments [47]. This barrier is also closely associated with behaviour barriers [5]. By the empirical study in Ukraine it was shown, that awareness is significant barriers to investments to energy-efficient technologies [46].

2.2. External energy efficiency barriers

2.2.1. Market

Barriers, which comes from the market are, for example, distortion of prices for energy, low diffusion of technologies and information, market risk, difficulty in gathering external skills [28].

Energy prices distortion. Variation of energy prices during the day or week or season are not necessary motivating to invest into new technologies [9].

Low diffusion of technologies. Due to the innovating character of the new energy efficiency technologies, they are with the little occurrence, and spread of new technologies are typically slow [16], [48].

Low diffusion of information. As proposed by Jaffe and Stavins this barrier describes, that some time is needed to spread good practice and knowledge about energy-efficiency technologies [49].

Market risk. This barrier covers uncertainty about future market prices [9].

Difficulty in gathering external skills. From the empirical study of Trianni [43] and Cagno [4], availability of external experts and their price may be a barrier to the supply of existing or creating new energy efficiency technologies.

2.2.2. Government/Politics

Government policies, programs, and practices affect business decisions regarding investments and operation of energy-using technologies [32]. Hirst also pointed out, that US government tends to stimulate energy use rather than energy efficiency [9]. On the other hand, European commission promotes energy efficiency ([8], [50]), but some EU members states are not always diligent in adopting EU regulation to national law. However, as shown by Hochman and Timilsina in empirical research existing political barriers do not have significant influence on the adaptation of new technologies [46].

Lack of proper regulation. The absence of the governmental or industrial standards for energy efficiency might be a barrier to choose optimal new energy-efficiency technology [51].

Distortion in fiscal policies. As shown by IPCC [52] this barrier includes subsidies, taxes or other government political programs, that influence costs or the prices of energy resources. Hirst and Brown describe this barrier as “all issues related to distorted fiscal policy” [9].

2.2.3. Technology/service suppliers

Barriers, which comes from technology and service suppliers are, for example, lack of suppliers interest in energy efficiency, suppliers may be not up to dated and scare communication skills of suppliers [28].

Lack of interest in energy efficiency. As shown by Reddy suppliers and especially service suppliers are not always interested in sharing best experience related to energy efficiency with their customers. Suppliers may get higher incomes if their clients use out-of-date energy efficiency technologies [53].

Technology/service suppliers not up to date. If technology and service suppliers are not paying enough attention to the education of their staff, then they also will not share best practice with customers [24].

Scarce communication skills. If technology and service suppliers are communicating with their customer proper about new technologies, then these technologies might be ignored by end users [9].

2.2.4. Designers and manufactures

Barriers, which comes from designer and producers of energy-related technologies are, for example, high initial costs and not adequate technical characteristics [28].

High initial cost reflects high research and development cost of new energy efficiency technologies. As stated by Howarth and Andersson [54] and Reddy and Shrestha [53] is a significant barrier to industrial energy efficiency.

Technical characteristics not adequate. In some cases, energy-efficiency technologies are hard to adopt, or adoption costs are inadequate [47].

2.2.5. Energy suppliers

Barriers, which comes from energy suppliers are, for example, lack of suppliers interest in energy efficiency, scare communication skills of suppliers and distortion of price for energy resources [28].

Lack of interest in energy efficiency. This barrier is similar to technology and services suppliers absence of interest in energy efficiency. In most cases, energy cost reduction causes lower incomes for energy suppliers. Consequently, energy suppliers are not always interested in offering best practices regarding energy efficiency to their clients [55], [53].

Scarce communication skills. This barrier is similar to the corresponding barrier from technology and services suppliers. This barrier is observed in contracts between supplier and buyer of energy resources. Different opinions and economic power of the supplier results in unattractive conditions for the receiver [27].

Distortion of prices for energy. Costs for energy might be an insufficient stimulus for the installation the new technologies, as the higher energy use, the lower rate for the energy per unit [4], furthermore the cost of the energy varies during the day [9], [39].

2.2.6. Capital suppliers

Capital suppliers can encounter with two types of barriers - *cost for investing capital availability* and *difficulty in identifying the quality of the investments*. As underlined by some researchers ([56], [33], [52]) high investigation cost for many of small projects might be a reason to reject this projects. Capital suppliers might have not enough competence to evaluate the investments in innovating energy efficiency technologies [52] and instead prefer to invest in well-known solutions.

3. DISCUSSIONS

In this section, we discuss results observed in the scientific papers and based on these results we propose a slightly different classification of energy efficiency barriers.

Our analysis showed, that 11 groups of the barriers can be identified – market (1), government or politics (2), technology and service suppliers (3), designers and manufacturers (4), energy suppliers (5), capital suppliers (6), economic (7), behavioural (8), organizational (9), competence (10) and awareness (11) barriers. All these 11 barrier groups can be associated in two subgroups – barriers, which derivates from internal of the company (internal barriers) and which derivates from outside of the company (external barriers).

As essential internal barriers can be defined – a group of competence/behavioural/awareness barriers and hidden cost of investment, meantime essential external barriers can be defined – government policy and activity of suppliers.

Some recent empirical studies ([46], [41]) showed that most significant barriers are competence, behavioural and awareness, however previously researchers ([6], [32], [40]) was more concentrated on technological, economic and political barriers.

Cagno et al. also showed [28], that behavioural, competence and organisational barriers have a strong causal relationship; the similar strong causal relationship also has technological, economic and informational barriers. We have not found more research on barriers causal relationship.

Most of the studies are focusing on companies' working in OECD (Organization for Economic Cooperation and Development) countries ([4–6], [11], [28], [32], [41]), and only small part of the researchers are concentrating on developing economies [46].

Based on the results of scientific literature review we can suggest to reorder barriers within groups and classify them considering the possibilities to overcome (Fig. 2). This classification and especially possibility to overcome the barriers is part of authors own personal view should be tested in future research.

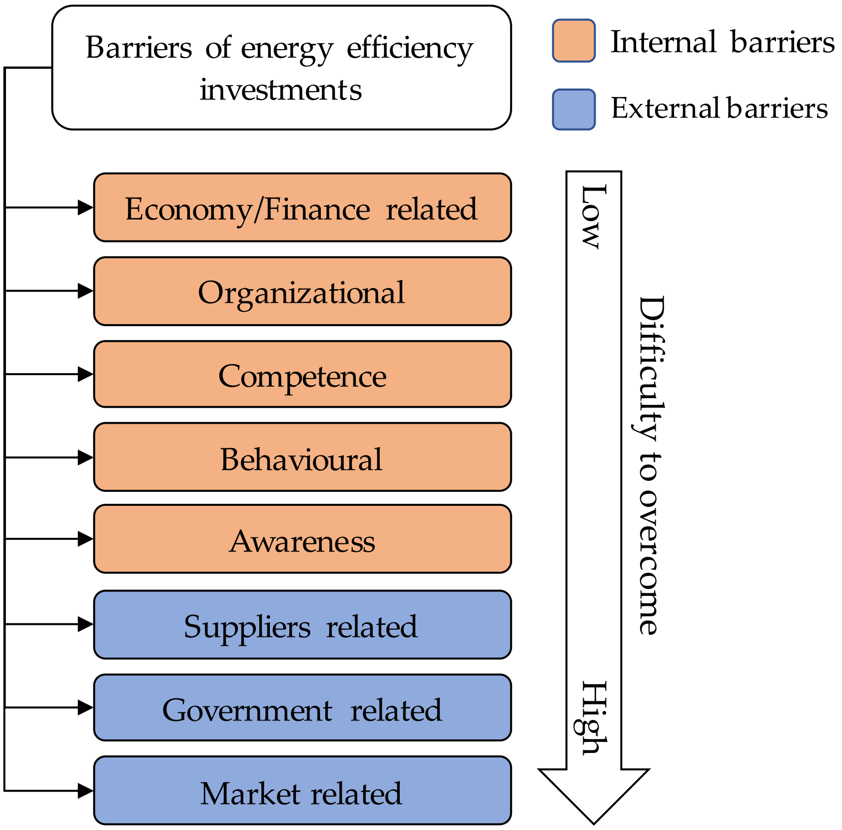

Fig. 2. Proposed classification of energy efficiency barriers

Economy and finance related group include these barriers – limited access to capital, hidden cost, risk, low investment profitability.

Organizational barriers group includes – long decision-making process, lack of control, time and power, split initiatives.

Competence barriers group consist – internal difficulties by implementing of investments, identifying of opportunities and inefficiencies, lack of interest in energy efficiency.

Behavioural barriers group includes – inertia, lack of shared objectives, imperfect evaluation criteria, other priorities.

Lack of awareness – make a separate barriers group.

Suppliers related barriers group includes – barriers related to technology, service, energy and capital suppliers. Also, to this group counts barriers which come from designer and producers of energy-related technologies and low diffusion of technologies and information.

Government related barriers group consist of lack of proper regulation and distortions in fiscal policies.

Market-related barriers are energy price distortion and difficulties in hiring external experts and their price.

4. CONCLUSIONS AND FURTHER RESEARCH

Good knowledge of barriers and sources of them are essential as well for companies as for politicians. In this paper, we reviewed a total 56 academic paper and “grey” studies related to energy efficiency barriers. As a primary result, we presented a new classification of the barriers, regrouped them and ordered by the possibility to overcome them. We suggest to group barriers into eight groups - Economy and finance related (1), Organizational (2), Competence (3), Behavioural (4), Awareness (5), Suppliers related (6), Government related (7), Market-related (8).

However real-world problems can be explained only be the combination of several barriers, instead of one specific barrier or barrier group.

Further empiric research could be carried out for the specific geographical region, for example, we did not find any research on companies working in Baltic states and also on the driving forces that enable to overcome barriers to industrial energy efficiency or barriers causal relationship.

REFERENCES

[1] J. Catarino, J. Henriques, and F. Egreja, “Portuguese SME toward energy efficiency improvement,” *Energy Effic.*, vol. 8, no. 5, pp. 995–1013, 2015.

[2] A. Trianni, E. Cagno, P. Thollander, and S. Backlund, “Barriers to industrial energy efficiency in foundries: a European comparison,” *J. Clean. Prod.*, vol. 40, pp. 161–176, 2013.

[3] E. Sardianou, “Barriers to industrial energy efficiency investments in Greece,” *J. Clean. Prod.*, vol. 16, no. 13, pp. 1416–1423, 2008.

[4] E. Cagno, A. Trianni, C. Abeelen, E. Worrell, and F. Miggiano, “Barriers and drivers for energy efficiency: Different perspectives from an exploratory study in the Netherlands,” *Energy Convers. Manag.*, vol. 102, pp. 26–38, Sep. 2015.

[5] E. Cagno, A. Trianni, G. Spallina, and F. Marchesani, “Drivers for energy efficiency and their effect on barriers: empirical evidence from Italian manufacturing enterprises,” *Energy Effic.*, 2017.

[6] S. Sorrell, A. Mallett, and S. Nye, “Barriers to industrial energy efficiency: A literature review,” 2011.

[7] M. G. Patterson, “What is energy efficiency? Concepts, indicators and methodological issues,” *Energy Policy*, vol. 24, no. 5, pp. 377–390, 1996.

[8] E. Council, “Directive 2012/27/EU on energy efficiency, amending Directives 2009/125/EC and 2010/30/EU and repealing Directives 2004/8/EC and 2006/32/EC,” 2012.

[9] E. Hirst and M. Brown, “Closing the efficiency gap: barriers to the efficient use of energy,” *Resour. Conserv. Recycl.*, vol. 3, no. 4, pp. 267–281, Jun. 1990.

[10] E. Worrell, J. A. Laitner, M. Ruth, and H. Finman, “Productivity benefits of industrial energy efficiency measures,” *Energy*, vol. 28, no. 11, pp. 1081–1098, 2003.

[11] G. Spalina and F. Marchsani, “Drivers for industrial energy efficiency: an innovative framework,” 2012.

[12] C. M. York, “Bibliography on institutional barriers to energy conservation,” 1978.
[13] C. Blumstein, B. Krieg, L. Schipper, and C. York, “Overcoming social and institutional barriers to energy conservation,” *Energy*, vol. 5, no. 4, pp. 355–371, 1980.
[14] P. C. Stern, “What psychology knows about energy conservation.,” *Am. Psychol.*, vol. 47, no. 10, p. 1224, 1992.
[15] S. J. DeCanio, “Barriers within firms to energy-efficient investments,” *Energy Policy*, vol. 21, no. 9, pp. 906–914, 1993.
[16] A. B. Jaffe and R. N. Stavins, “The energy-efficiency gap What does it mean?,” *Energy Policy*, vol. 22, no. 10, pp. 804–810, 1994.
[17] L. Weber, “Some reflections on barriers to the efficient use of energy,” *Energy Policy*, vol. 25, no. 10, pp. 833–835, 1997.
[18] H. L. F. De Groot, E. T. Verhoef, and P. Nijkamp, “Energy saving by firms: decision-making, barriers and policies,” *Energy Econ.*, vol. 23, no. 6, pp. 717–740, 2001.
[19] J. Schleich, “Do energy audits help reduce barriers to energy efficiency? An empirical analysis for Germany,” *Int. J. Energy Technol. Policy*, vol. 2, no. 3, pp. 226–239, 2004.
[20] S. Sorrell, *The economics of energy efficiency : barriers to cost-effective investment*. Edward Elgar, 2004.
[21] J. Schleich and E. Gruber, “Beyond case studies: Barriers to energy efficiency in commerce and the services sector,” *Energy Econ.*, vol. 30, no. 2, pp. 449–464, 2008.
[22] H. Allcott and M. Greenstone, “Is There an Energy Efficiency Gap?,” in *Energy Efficiency*, 2013, pp. 133–161.
[23] K. Bhardwaj and E. Gupta, “Analyzing the ‘energy-efficiency gap,’” *Indian Growth Dev. Rev.*, vol. 10, no. 2, pp. 66–88, Nov. 2017.
[24] J. Palm, “Placing barriers to industrial energy efficiency in a social context: a discussion of lifestyle categorisation,” *Energy Effic.*, vol. 2, no. 3, pp. 263–270, Aug. 2009.
[25] C. Montalvo, “General wisdom concerning the factors affecting the adoption of cleaner technologies: a survey 1990–2007,” *J. Clean. Prod.*, vol. 16, no. 1, pp. S7–S13, Jan. 2008.
[26] T. J. Foxon and Carbon Trust., *Inducing innovation for a low-carbon future : drivers, barriers and policies*. The carbon Trust, 2003.
[27] S. Sorrell *et al.*, “Reducing barriers to energy efficiency in public and private organizations,” *Sci. Policy Technol. Res. (SPRU), Univ. Sussex, Sussex, UK*, 2000.
[28] E. Cagno, E. Worrell, A. Trianni, and G. Pugliese, “A novel approach for barriers to industrial energy efficiency,” *Renew. Sustain. Energy Rev.*, vol. 19, pp. 290–308, Mar. 2013.
[29] S. J. DeCanio, “The efficiency paradox: bureaucratic and organizational barriers to profitable energy-saving investments,” *Energy Policy*, vol. 26, no. 5, pp. 441–454, 1998.
[30] K. Ostertag, “Transaction costs of raising energy efficiency,” in *IEA International Workshop on Technologies to Reduce Greenhouse Gas Emissions: Engineering-Economic Analyses of Conserved Energy and Carbon. Washington, DC*, 1999.
[31] L. G. Hein and K. Blok, “Transaction costs of energy efficiency improvement,” in *The energy efficiency challenge for Europe. ECEEE summer study*, 1995.
[32] P. Thollander, “Towards Increased Energy Efficiency in Swedish Industry : Barriers, Driving Forces & Policies,” Linköping University Electronic Press, 2008.
[33] J. Schleich, “Barriers to energy efficiency: A comparison across the German commercial and services sector,” *Ecol. Econ.*, vol. 68, no. 7, pp. 2150–2159, 2009.
[34] P. Rohdin and P. Thollander, “Barriers to and driving forces for energy efficiency in the non-energy intensive manufacturing industry in Sweden,” *ENERGY*, vol. 31, no. 12, pp. 1836–1844, Sep. 2006.
[35] P. Rohdin, P. Thollander, and P. Solding, “Barriers to and drivers for energy efficiency in the Swedish foundry industry,” *Energy Policy*, vol. 35, no. 1, pp. 672–677, Jan. 2007.
[36] M. Ross, “Capital budgeting practices of twelve large manufacturers,” *Financ. Manag.*, pp. 15–22, 1986.

[37] A. H. Sanstad, C. Blumstein, and S. E. Stoft, “How high are option values in energy-efficiency investments?,” *Energy Policy*, vol. 23, no. 9, pp. 739–743, 1995.
[38] E. Aronson and P. C. Stern, “Energy use: The human dimension,” 1984.
[39] M. A. Brown, “Market failures and barriers as a basis for clean energy policies,” *Energy Policy*, vol. 29, no. 14, pp. 1197–1207, 2001.
[40] E. Worrell and L. Price, “Policy scenarios for energy efficiency improvement in industry,” *Energy Policy*, vol. 29, no. 14, SI, pp. 1223–1241, Nov. 2001.
[41] M. T. Johansson and P. Thollander, “A review of barriers to and driving forces for improved energy efficiency in Swedish industry – Recommendations for successful in-house energy management,” *Renew. Sustain. Energy Rev.*, vol. 82, pp. 618–628, Feb. 2018.
[42] P. Thollander and M. Ottosson, “Energy management practices in Swedish energy-intensive industries,” *J. Clean. Prod.*, vol. 18, no. 12, pp. 1125–1133, 2010.
[43] A. Trianni and E. Cagno, “Dealing with barriers to energy efficiency and SMEs: some empirical evidences,” *Energy*, vol. 37, no. 1, pp. 494–504, 2012.
[44] A. H. Sanstad and R. B. Howarth, “‘Normal’markets, market imperfections and energy efficiency,” *Energy Policy*, vol. 22, no. 10, pp. 811–818, 1994.
[45] N. Nagesha, “Ranking of barriers to energy efficiency in small industry clusters using analytic hierarchy process: an empirical study of three Indian clusters,” *South Asian J. Manag.*, vol. 12, no. 2, p. 75, 2005.
[46] G. Hochman and G. R. Timilsina, “Energy efficiency barriers in commercial and industrial firms in Ukraine: An empirical analysis,” *Energy Econ.*, vol. 63, pp. 22–30, Mar. 2017.
[47] A. T. de Almeida, P. Fonseca, and P. Bertoldi, “Energy-efficient motor systems in the industrial and in the services sectors in the European Union: characterisation, potentials, barriers and policies,” *Energy*, vol. 28, no. 7, pp. 673–690, 2003.
[48] W. H. Golove and J. H. Eto, “Market barriers to energy efficiency: a critical reappraisal of the rationale for public policies to promote energy efficiency,” Lawrence Berkeley Lab., CA (United States), 1996.
[49] A. B. Jaffe and R. N. Stavins, “Energy-efficiency investments and public policy,” *Energy J.*, pp. 43–65, 1994.
[50] E. Council, “Directive 2004/8/EC of the European Parliament and of the Council of 11 February 2004 on the promotion of cogeneration based on a useful heat demand in the internal energy market and amending Directive 92/42/EEC,” *Off. J. Eur. Union*, pp. 50–60, 2004.
[51] S. Wiel and J. E. McMahon, “Governments should implement energy-efficiency standards and labels—cautiously,” *Energy Policy*, vol. 31, no. 13, pp. 1403–1415, 2003.
[52] J. Sathaye *et al.*, “Barriers, opportunities, and market potential of technologies and practices,” *Clim. Chang.*, pp. 345–398, 2001.
[53] B. S. Reddy and R. M. Shrestha, “Barriers to the adoption of efficient electricity technologies: a case study of India,” *Int. J. Energy Res.*, vol. 22, no. 3, pp. 257–270, 1998.
[54] R. B. Howarth and B. Andersson, “Market barriers to energy efficiency,” *Energy Econ.*, vol. 15, no. 4, pp. 262–272, 1993.
[55] A. K. N. Reddy, “Barriers to improvements in energy efficiency,” *Energy Policy*, vol. 19, no. 10, pp. 953–961, 1991.
[56] D. Berry, “You’ve got to pay to play: Photovoltaics and transaction costs,” *Electr. J.*, vol. 8, no. 2, pp. 42–49, 1995.

STUDY OF GLYCINE NITRATE PRECURSOR METHOD FOR THE COMBUSTION SYNTHESIS OF SAMARIUM-DOPED CERIA

A. Stankevičiūtė, F. Kalyk, G. Budrytė, B. Abakevičienė
Kaunas University of Technology
Studentų str. 50, LT-51368 Kaunas – Lithuania
Email: atigla@gmail.com

ABSTRACT

In recent years, a pale white-yellow colour powder or CeO_2 attracted a lot of attention, regarding its applications as a catalyst and for a non-inert support for catalysts. Samarium is one of the most favourable dopant as a result of high conductivity of formed chemical compound which is subsequently $6.1 \cdot 10^{-2}$ S/cm. Samarium-doped ceria (SDC) can be applied as an electrolyte in various types of solid oxide fuel cells (SOFCs), in fossil fuel technology, as well as in gas sensing applications and in the exhaust systems of vehicles. Among the variety of synthesis methods, the combustion synthesis is one of the most frequently used technique for the formation of SDC powders, especially with glycine as a fuel; in addition, it appears to be more useful due to its simplicity and low cost. The glycine nitrate precursor (GNP) method is a very fast process to prepare homogeneous, fine structure nanomaterials based on the combustion of solid oxide fuels in the form of nitrates. In this study, high purity cerium and samarium nitrate hexahydrates were used to form samarium-doped ceria powders through the glycine-nitrate precursor method. To obtain a better insight into the reaction at the GNP process, Fourier-transform infrared spectroscopy (FT-IR) was performed for metal oxides as well as for SDC structures calcined at various temperatures. The Kubelka-Munk function was applied for analysing chemical bonds in SDC structures. It was found that increase of the calcination temperatures is causing of the decrease of O-H stretching bond peak's intensity. This process appears to be due to intense evaporation of water.

Keywords: Samarium-doped ceria, glycine nitrate precursor process, combustion synthesis, FT-IR, DRIFT, solid oxide fuel cells

1. INTRODUCTION

Nowadays, CeO_2 becomes vital for creating three-way catalysts (TWC's) [1]. Mg^{2+}, Co^{2+}, V^{3+}, Cu^{2+}, Sm^{3+}, Gd^{3+}, Zn^{2+}, Nb^{5+}, Ba^{2+}, La^{3+}, Yb^{3+}, Bi^{2+} [2] and Dy^{3+} [3] can be inserted as metal cations (M) or dopants in fluorite type $Ce_{1-x}M_xO_{2-\delta}$. Despite the fact, that there are a lot of dopants which can be inserted in cerium dioxide, notwithstanding, Sm^{3+}, Gd^{3+} and Dy^{3+} are most widely used due to the increase of ionic conductivity [3]. Samarium became a dominant dopant in the cerium based oxides for the sake of diminution of enthalpy which appears between metal cations inserted in ceria and oxygen vacancies [4].

Samarium doped ceria (SDC) has widely used in various solid oxide fuel cells (SOFCs) [5] as an electrolyte and other various applications, including fossil fuel technology [6], gas sensing devices [7] and vehicle exhaust systems [8].

Solid oxide fuel cells (SOFCs) are one of the most promising devices for energy production. In defiance of different branches of fuel cells, SOFCs appear to have no electrolyte loss. They avoid possessing corrosion on the electrode, produce high electrical efficiency and have low activation loss. SOFCs attract many attentions due to the small amount of released pollution, high quality and low cost [3].

Powders of SDC can be synthesised by various methods, including sol-gel [9], Pechini method [10], co-precipitation [11], ion-impregnation technique [12], polyol process [13], micro-emulsion [14], mechanochemical synthesis [15] and various combustion methods [16]. From a variety of different methods, it is known that sol-gel method is a very complex technique because there are a lot of chemical and physical processes which occur in it, for example, hydrolysis, polymerization, gelation, condensation, drying and densification [17], not to mention high cost [18]. Another very popular synthesis method is Pechini. However, this technique can be called as difficult because it is a citrate gel process [19]. Other methods are not suitable to prepare SDC by virtue of not suitability of making high pure compounds with stoichiometry [17], as well as some of them are no longer usable (for example ion-impregnation) [20]. Among other methods, combustion attracted a lot of attention because of its simplicity [21]. There are a lot of types of combustion techniques for SDC, including glycine nitrate which is a very cheap method, powders are often homogeneous and fine [22]. Nevertheless, SDC powders can be produced by using citric acid, alanine [23] and urea [24] as fuel.

The main aim of this research was to prepare samarium-doped ceria powders by using glycine nitrate precursor combustion method and to characterise the chemical functional groups via Fourier transform infrared spectroscopy (FT-IR), using the Kubelka-Munk function.

2. EXPERIMENTAL PROCEDURE

2.1. SDC powder preparation

Samarium-doped ceria (SDC) powders were prepared by using glycine nitrate precursor (GNP) combustion method. In this experiment, metal cations were samarium (III) and cerium (III) in a form of nitrate hexahydrates ($CeN_3O_9\cdot 6H_2O$, 99.0 %, “Fluka”) and ($SmN_3O_9\cdot 6H_2O$, 99.9 %, “Sigma Aldrich”). Glycine nitrate (NH_2CH_2COOH, ≥ 99.0 %, “Sigma Aldrich”) was used as a fuel. To get a precursor, we mixed both nitrates with 40 ml of distilled water in quartz beaker and at the end, we added glycine nitrate to the mixture. According to Singh [25], chemical reactions of nitrate combustion where glycine was used as a fuel, are:

$$18Ce(NO_3)_3 + 30NH_2CH_2COOH \rightarrow 18CeO_{2\ (solid)} + 60CO_{2\ (gas)} + 42N_{2\ (gas)} + 66H_2O + 9H_{2\ (gas)} \tag{1}$$

$$18Sm(NO_3)_3 + 30NH_2CH_2COOH \rightarrow 18Sm_2O_{3\ (solid)} + 60CO_{2\ (gas)} + 42N_{2\ (gas)} + 75H_2O \tag{2}$$

To get a stoichiometry for the final product of $Sm_xCe_{1-x}O_{2-\delta/2}$ with molar content of samarium doped into the complex ceria, x = 0.2 (20 SDC), 0.3 (30 SDC) were used in the experiment. According to chemical reactions given above, the following stoichiometric fuel (glycine) to metal cations (Ce^{3+} and Sm^{3+}) ratios were chosen 1.56 and 1.67, respectively [26]. Due to the complexity of formed SDC powders, synthesised and calcined metal oxides of CeO_2 and Sm_2O_3 were investigated in our experiment to understand their conversion to the final solution.

The combustion process began when the mixture was placed on the magnetic stirrer. The temperature range to form gel was from 90 °C to 150 °C and all process lasted about 1 hour. Then, formed gel was heated up from 200 °C to 350 °C temperature for 15 minutes until combustion started. After the process, yellow powders were calcined in a muffle furnace for 5 hours for all temperatures 200 °C, 600 °C, 800 °C, 1100 °C and 1200 °C.

2.2. Powder Characterisation

Fourier transform infrared (FT-IR) a Vertex 70 spectrometer (Bruker Optik GmbH), equipped with an EasiDiff high quality diffuse reflectance accessory (PIKE Technologies), was used to identify the functional groups of ceria, samaria, and samarium-doped ceria powders. The Kubelka-Munk transformation was applied for the analysis of Diffusive Reflectance Infrared Fourier Transform (DRIFT) spectra of powders. The spectral recording area was from 400 to 4000 cm^{-1} with a resolution of 1 cm^{-1}.

3. RESULTS AND DISCUSSION

The infrared spectroscopy enables to detect the evolution of molecular bonds‘ rotational and vibrational modes, therefore it allows to identify the functional groups of the SDC structure. Furthermore, Diffusive Reflectance Infrared Fourier Spectroscopy (DRIFTs) enhances our abilities to measure the broader variety of samples, including powders.

In this work, four different DRIFT spectra of CeO_2, Sm_2O_3, and 20 SDC, 30 SDC powders at different calcination temperatures were investigated.

Figures 1 and 2 represent the spectra of CeO_2 and Sm_2O_3 powders calcined at 800 °C, respectively. In the DRIFT spectra of CeO_2 and Sm_2O_3 powders, the broad peaks in the 2500–3800 cm^{-1} region can be attributed to O-H stretching mode of H_2O or from surface (Ce or Sm)-OH groups [27, 28]. The peaks in the frequency range from 1200 to 1700 cm^{-1} are related to carbonate species formed by arranged CO_2 molecules onto the coordinative unsaturated CeO_2 and Sm_2O_3 surfaces [29, 30]. The minor peaks in Fig. 1 and 2 are visible near 1050 cm^{-1} and 1060 cm^{-1}, respectively, may also be related to the carbonate group compounds. The 1600, 1540, and 1310 cm^{-1} peaks (Fig. 1) and the 1610, 1500, and 1380 cm^{-1} peaks (Fig. 2) are assigned to the bicarbonate-like and monodentate carbonate species with O-C-O stretching frequencies [29]. The peaks at 770 cm^{-1} can be seen below due to stretching modes of Ce-O (Fig. 1) and Sm-O (Fig. 2).

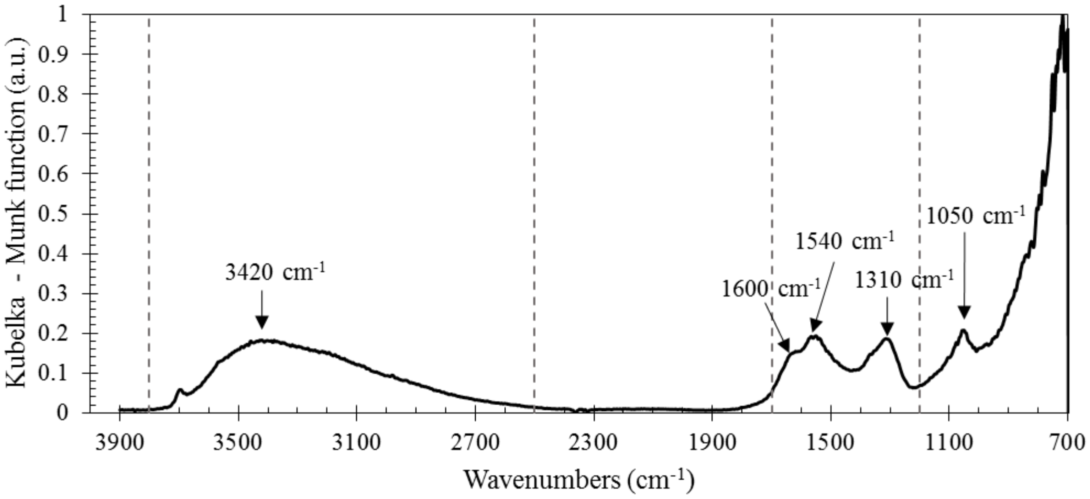

Fig. 1. DRIFT spectrum of CeO_2 powders calcined at 800 °C

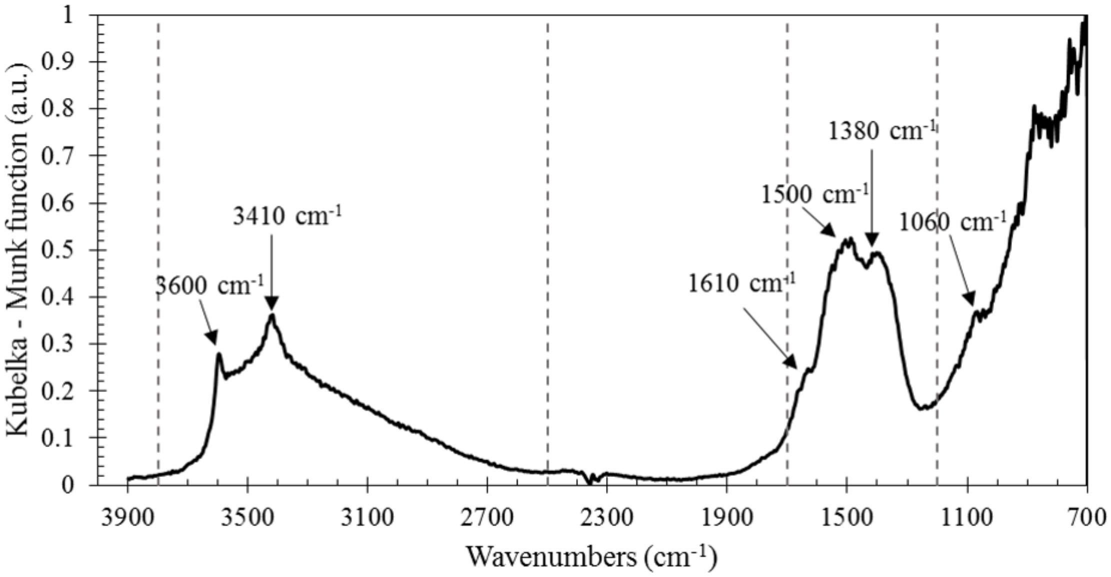

Fig. 2. DRIFT spectrum of Sm_2O_3 powders calcined at 800 °C

DRIFT spectra of 20 SDC and 30 SDC calcined powders at various temperatures are shown in Fig. 3 and Fig. 4. The broad peaks in the 2500-3800 cm^{-1} range can be attributed to O-H stretching mode. The minor band located between the 2300-2400 cm^{-1} region is due to linearly coordinated CO_2 which is adsorbed at the surface [27]. The C=O and C-O vibrations or carbonate species (in the region 1000–1700 cm^{-1}) are indicating that the nitrates and other organic compounds did not yet decompose below 800 °C calcination temperature [10]. However, small amounts of carbonate traces in the region 1000–1700 cm^{-1} are visible at 1100 and 1200 °C calcination temperatures. Even in investigation done by Mokkelbost et al. [27] the carbonate remnants were left after the calcination at 1000 °C for 12 h. The peak at 1060 cm^{-1} was a consequence of the Ce-O-C stretching and Sm-O-C vibrational modes. The intensities of the region 1000–1700 cm^{-1} are decreasing with increasing calcination temperature due to carbonate-like species. It shows that the purity of powder is increasing.

The DRIFT spectra of the 20 SDC and 30 SDC powders calcined at different temperatures exhibit a strong peak below 770 cm^{-1} (mostly in the range of 400-770 cm^{-1}) [10, 27, 31]. This broad peak could be attributed to the metal-oxygen bond, which indicates the formation of the samarium-doped ceria (SDC).

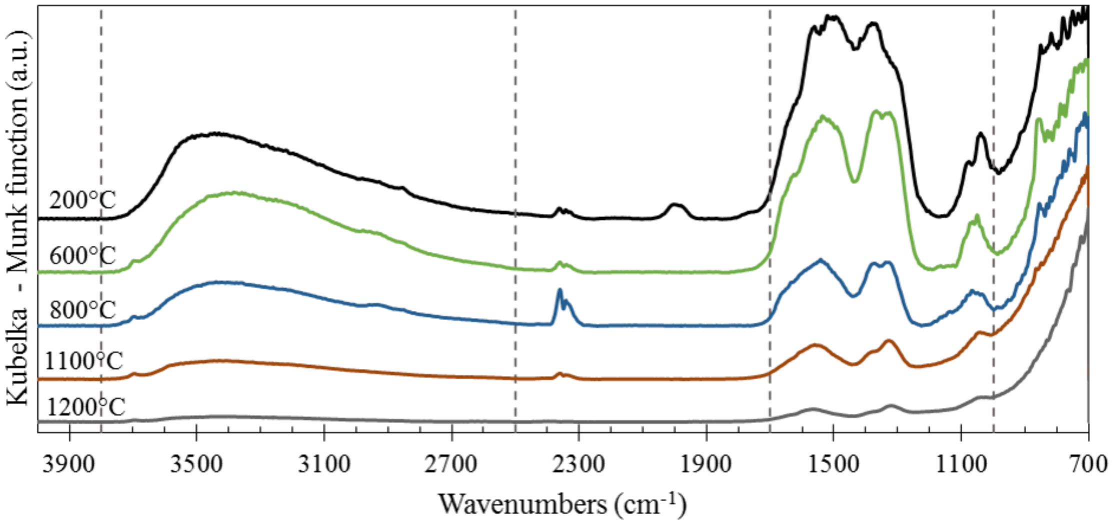

Fig. 3. DRIFT spectra of 20 SDC powders calcined at various temperatures

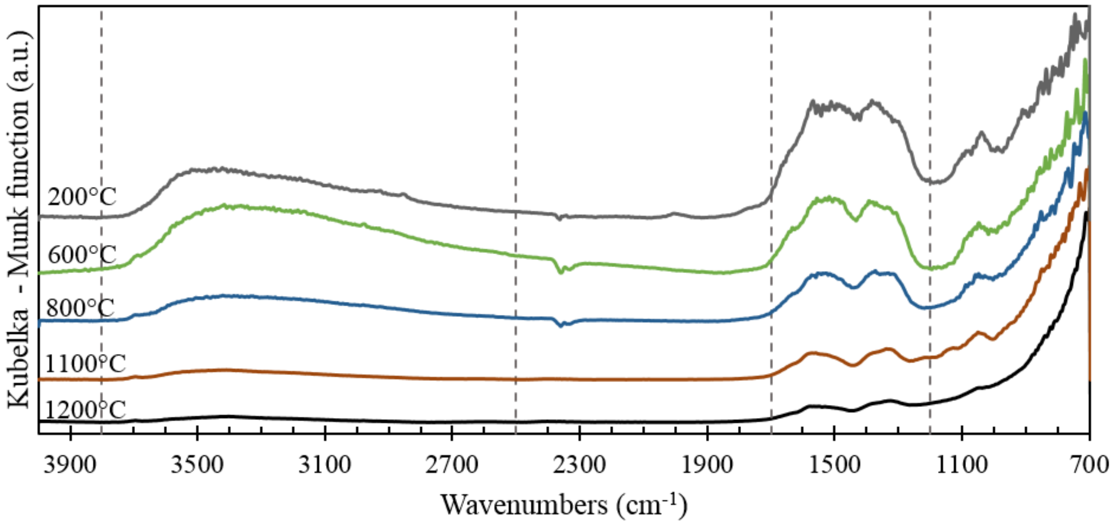

Fig. 4. DRIFT spectra of 30 SDC powders calcined at various temperatures

4. CONCLUSION

To summarise research, glycine nitrate precursor combustion method is one of the most frequently used synthesis‘ techniques which allows forming pure, homogeneous SDC structures. We obtained that DRIFT is a very powerful analytical tool to investigate complex oxide electrolytes in a form of powders. By using Kubelka-Munk transformation, we observed spectra of both metal cation oxides, 20 SDC and 30 SDC powders calcined at different temperatures. Experimental results showed the progress of SDC powder formation in the calcination above the 800 °C temperature. This phenomenon is strongly dependent on thermal effects, as a result, we observed that the peaks‘ intensities are directly proportional to annealing temperature. Temperature plays the most important role in water evaporation process, causing the decrement of O-H bond peaks intensities.

REFERENCES

1. MONTINI, Tiziano, MELCHIONNA, Michele, MONAI, Matteo and FORNASIERIO, Paolo. Fundamentals and Catalytic Applications of CeO_2-Based Materials. *Chemical Reviews,* 2016, Vol. 116, No. 10, p. 5987–6041.
2. VANPOUCKE, Danny E. P., BULTINCK, Patrick, COTTENIER, Stefaan, VAN SPEYBROECK, Veronique and VAN DRIESSCHE, Isabel. Aliovalent doping of CeO_2: DFT study of oxidation state and vacancy effects. *Journal of Materials Chemistry A,* 2014, Vol. 2, No. 33, p. 13723–13737.
3. ARABACI, A. Synthesis and Characterization of Samarium-Doped CeO_2 Powders as a Solid Electrolyte by Using Pechini Method. *ACTA PHYSICA POLONICA A*, 2015, Vol. 127, No. 4, p. 888–890.
4. YANG, Rung-Je, LEE, Maw-Chwain, CHANG, Jen-Chen, LIN, Tai-Nan, CHANG, Yang-Chuang, KAO, Wei-Xin, LEE, Lin-Song and CHENG, Shih-Wei. Fabrication and characterization of a $Sm_{0.2}Ce_{0.8}O_{1.9}$ electrolyte film by the spin-coating method for a low-temperature anode-supported solid oxide fuel cells. *Journal of Power Sources*, 2012, Vol. 206, p. 111–118.
5. PEI, Kai, LI, Hongdong, ZOU, Guangtian, YU, Richeng, ZHAO, Haofei, SHEN, Xi, WANG, Liying, SONG, Yanpeng and QIU, Dongchao. Detonation nanodiamond introduced into samarium doped ceria electrolyte improving performance of solid oxide fuel cell. *Journal of Power Sources,* 2017, Vol. 342, p. 515–520.
6. MA, Ying, WANG, Xiaodi, LI, Shanghua, TOPRAK, Muhammet S., ZHU, Bin and MUHAMMED, Mamoun. Samarium-Doped Ceria Nanowires: Novel Synthesis and Application in Low-Temperature Solid Oxide Fuel Cells. *Advanced Materials*, 2010, Vol. 22, No. 14, p. 1640–1644.
7. PIJOLAT, C., TOURNIER, G. and VIRICELLE, J. P. Detection of CO in H_2-rich gases with a samarium doped ceria (SDC) sensor for fuel cell applications. *Sensors and Actuators B: Chemical,* 2009, Vol. 141, No. 1, p. 7–12.
8. ŽIVKOVIĆ, Lj. S., LAIR, V., LUPAN, O., CASSIR, M. and RINGUEDÉ, A. Samarium-Doped Ceria Nanostructured Thin Films Grown on FTO Glass by Electrodeposition. *ACTA PHYSICA POLONICA A,* 2011, Vol. 120, No. 2, p. 298–302.
9. JAOUDE, M. Abi, POLYCHRONOPOULOU, K., HINDER, S. J., KATSIOTIS, M. S., BAKER, M. A., GREISH, Y. E. and ALHASSAN, S. M. Synthesis and properties of 1D Sm-doped CeO_2 composite nanofibers fabricated using a coupled electrospinning and sol-gel methodology. *Ceramics International,* 2016, Vol. 42, No. 9, p. 10734–10744.
10. ARABACI, A, SERIN, Ö. Characteristics of Samaria-Doped Ceria Prepared by Pechini Method. *ACTA PHYSICA POLONICA A,* 2015, Vol. 128, No. 2-B, p. 118–121.

11. IRSHAD, Muneeb, SIRAJ, Khurram, RAZA, Rizwan, JAVED, Fayyazm AHSAN, Muhammad, SHAKIR, Imran and RAFIQUE, Muhammad Shahid. High performance of SDC and GDC core shell type composite electrolytes using methane as a fuel for low temperature SOFC. *AIP Advances*, 2016, Vol. 6, p. 025202.
12. XU, X., JIANG, Z. FAN, X. and XIA, C. LSM-SDC electrodes fabricated with an ion-impregnating process for SOFCs with doped ceria electrolytes. *Solid State Ionics*, 2006, Vol. 177, No. 19–25, p. 2113–2117.
13. KARACA, Tuba, ALTINÇEKIÇ, Tuba Gürkaynak and ÖKSÜZÖMER, M. Faruk. Synthesis of nanocrystalline samarium-doped CeO_2 (SDC) powders as a solid electrolyte by using a simple solvothermal route. *Ceramics International*, 2010, Vol. 36, No. 3, p. 1101–1107.
14. BABU, S., THANNEERU, R., INERBAEV, T., DAY, R., MASUNOV, A., SCHULTE, A. and SEAL, S. Dopant-mediated oxygen vacancy tuning in ceria nanoparticles. *Nanotechnology*, 2009, Vol. 20, No. 8, p. 085713.
15. HOS, J. P., MCCORMICK, Paul. Mechanochemical Synthesis and Characterisation of Nanoparticulate Samarium-doped Cerium Oxide. *Scripta Materialia*, 2003, Vol. 48, No. 1, p. 85–90.
16. SUN, Haibin, ZHANG, Yujun, GONG, Hongyu, LI, Qisong, BU, Yunfei and LI, Teng. Anode-supported SOFCs based on $Sm_{0.2}Ce_{0.8}O_{2-\delta}$ electrolyte thin-films fabricated by co-pressing using microwave combustion synthesized powders. *Ceramics International*, 2016, Vol. 42, No. 3, p. 4285–4289.
17. BRINKER, C. Jeffrey; SCHERER, George W. *The Physics and Chemistry of Sol-Gel Processing*. London: Academic Press, Inc., 1990, 2 p. ISBN 9780121349707.
18. RADEV, Lachezar, SAMUNEVA, Bisserka, MIHAILOVA, Irena, PAVLOVA, Liliana and KASHCHIEVA, Elena. Sol-gel synthesis and structure of cordierite/tialite glass-ceramics. *Processing and Applications of Ceramics*, 2009, Vol. 3, No. 3, p. 125-130.
19. HUÍZAR-FÉLIX, A. M., HERNÁNDEZ, T., DE LA PARRA, S., IBARRA, J. and KHARISOV, B. Sol-gel based Pechini method synthesis and characterization of $Sm_{1-x}Ca_xFeO_3$ perovskite $0.1 \leq x \leq 0.5$. *Powder Technology*, 2012, Vol. 229, p. 290–293.
20. ZU, Wei, DING, Dong and XIA, Changrong. Enhancement in Three-Phase Boundary of SOFC Electrodes by an Ion Impregnation Method: A Modeling Comparison. *Electrochemical and Solid-State Letters*, 2008, Vol. 11, No. 6, p. B83–B86.
21. KULKARNI, Shrikant, DUTTAGUPTA, Siddhartha and PHATAK, Girish. Study of glycine nitrate precursor method for the synthesis of gadolinium doped ceria ($Ce_{0.8}Gd_{0.2}O_{1.90}$) as an electrolyte for intermediate temperature solid oxide fuel cells. *RSC Advances*, 2014, Vol. 4, No. 87, p. 46602–46612.
22. LIU, Zhangbo, DING, Dong, LIU, Mingfei, LI, Xiaxi, SUN, Wenping, XIA, Changrong and LIU, Meilin. Highly active $Sm_{0.2}Ce_{0.8}O_{1.9}$ powders of very low apparent density derived from mixed cerium sources. *Journal of Power Sources*, 2013, Vol. 229, p. 277.
23. CHUNG, Dong Yong, LEE, Eil Hee. Microwave-induced combustion synthesis of $Ce_{1-x}Sm_xO_{2-x/2}$ powder and its characterization. *Journal of Alloys and Compounds*, 2004, Vol. 374, No. 1–2, p. 69-73.
24. CHEN, Min, KIM, Bok Hee, XU, Qing, AHN, Byeong Kuk, KANG, Woo Jin and HUANG, Duan Ping. Synthesis and electrical properties of $Ce_{0.8}Sm_{0.2}O_{1.9}$ ceramics for IT-SOFC electrolytes by urea-combustion technique. *Ceramics International*, 2009, Vol. 35, No. 4, p. 1335–1343.
25. SINGH, K., ACHARYA, S.A. and BHOGA, S.S. Low temperature processing of dense samarium-doped CeO_2 ceramics: sintering and intermediate temperature ionic conductivity.

Paper presented at the Third International Conference on Ionic Devices, 2007, Vol. 13, p. 429–434.

26. PENG, Ranran and others. Sintering and electrical properties of $(CeO_2)_{0.8}(Sm_2O_3)_{0.1}$ powders prepared by glycine–nitrate process. *Materials Letters*, 2002, Vol. 56, p. 1043–1047.
27. MOKKELBOST, Tommy, KAUS, Ingeborg, GRANDE, Tor and EINARSRUD, Mari-Ann. Combustion Synthesis and Characterization of Nanocrystalline CeO_2-Based Powders. *Chemistry of Materials*, 2004, Vol. 16, p. 5489–5494.
28. ACCARDO, Grazia, FERONE, Claudio, CIOFFI, Raffaele, FRATTINI, Domenico, SPIRIDIGLIOZZI, Luca and DELL'AGLI, Gianfranco. Electrical and microstructural characterization of ceramic gadolinium-doped ceria electrolytes for ITSOFCs by sol-gel route. *Journal of Applied Biomaterials & Functional Materials*, 2016, Vol. 14, No. 1, p. e35–e41.
29. BOLIS, Vera, CERRATO, Giuseppina, MAGNACCA, Giulianna, MORTERRA, Claudio. Surface acidity of metal oxides. Combined microcalorimetric and IR-spectroscopic studies of variously dehydrated systems. *Thermocimica Acta*, 2001, Vol. 379, No. 1–2, p. 63–77.
30. PALNEEDI, Haribalu, MANGAM, Venu, DAS Siddhartha, DAS, Karabi. Effect of fuel-to-nitrate ration on the powder characteristics of nanosized CeO_2 synthesized by mixed fuel combustion method. *Journal of Alloys and Compounds*, 2011, Vol. 509, p. 9912–9918.
31. ARABACI, A, SERIN, Ö. Characterization of Sm-doped ceria ceramics synthesized by two different methods. *Journal of materials Engineering and Performance*, 2015, Vol. 24, No. 7, p. 2730–2737.

LIQUID METAL SOLUTIONS FOR HEAT EXHAUSTION IN FUSION REACTORS

Imants Kaldre
University of Latvia
Miera str. 32, LV-2169 Salaspils – Latvia
Email: Imants.kaldre@gmail.com

ABSTRACT

Liquid metals have high volumetric heat capacity and their upper limit temperature is very high, thus they are considered as solution for high power density cooling for long time. Liquid sodium loops have been used for fission reactor cooling. Currently many countries working on ITER (International thermonuclear reactor) project together. How to extract heat from divertor plates is a technical challenge where liquid metal solution is investigated. Fast liquid metal jets as plasma facing components were present already in the very first proposals when liquid metals were considered as useful for divertor protection and, in the same time, for the extraction of the power. A high-power load capability should be considered as the most distinctive and attractive feature of these proposals, especially, if materials like Ga or Sn are accepted. Estimates show that loads of the order of 50 MW/m^2 and even higher could be expected. Another solution is to use liquid metal capillary porous system (CPS) to protect the surface under high heat loads. CPS approach will be discussed in this paper and calculation of relevant forces on liquid metal will be carried out. So far numerical simulations demonstrate that in these conditions thermoelectric and electromagnetic forces are dominant. Role of capillary forces depends on CPS geometry and size. It is shown that thin CPS layer cooled from bottom by liquid metal convection is the most promising solution.

Keywords: Divertor, Fusion, Liquid metal

1. THEORETICAL BACKGROUND

1.1. Motivation

In nuclear industry liquid metals are considered and used as coolant and liquid target for particle and radiation flows. Liquid metals have numerous benefits like high volumetric heat capacity and high working temperature [1]. Liquid metals are electrically conductive thus can be pumped contactlessly by electromagnetic pumping [2]. University of Latvia is one of the partners in EuroFusion consortium aimed to investigate the aspects of fusion energetics. Institute of Physics University of Latvia (IPUL) is one of the oldest and largest centres in magnetohydrodynamics, dealing with the research of the conductive media in magnetic field. IPUL has been involved in the research of liquid metal-based solution for heat extraction from fusion reaction chamber. Several experimental facilities have been made in IPUL and successfully tested [3]. Research on liquid metal jets in high magnetic field has been done and it is shown that high magnetic field dramatically influences the stability of the jets [4]. Capillary porous system (CPS) can work under high time-varying magnetic field and heat flow. Specially designed CPS can ensure liquid metal surface stability and convective and conducive heat transfer from the hot zone. Recent research activities on CPS-based [5] solution for high heat flow extraction and surface protection has been summarized in this work. Special attention has been paid to the influence of thermoelectromagnetic forces in CPS, which is one of the effects with profound importance in this case because of high magnetic field and thermal gradient present at the wall of the plasma chamber.

1.2. ITER project

International Thermonuclear Reactor (ITER) [6] is large international project which involves more than 70 countries. Idea of the project is to create conditions for the fusion reactions to take place in controlled conditions on the earth. Currently experiment facility is under construction in Cadarache France.

$$^{2}\mathrm{H} + {}^{3}\mathrm{H} \Rightarrow {}^{4}\mathrm{He} + \mathrm{n} + 17.6\ \mathrm{MeV}$$

This reaction takes place on the sun and stars, it requires high temperature and pressure to ensure that tritium and deuterium particles collide with enough force to overcome repulsion and the fusion reaction can take place. In ITER reactor hot plasma is confined in toroidal chamber and contained by strong magnetic field to limit the wall contact. Protection of plasma facing components is one of the crucial problems of this technology because no material can sustain such a high temperature and time variable plasma splashes. One of the perspective solutions of this problem is to use liquid metal to create self-healing and renewable surfaces for plasma facing components.

1.3. Divertor

This work is focused on the design and assessment of performance of divertor plate, which is an essential part of the ITER experimental facility. In nuclear fusion reactor part of the heat is extracted from the plasma chamber through the walls, but significant part is deposited on the divertor plates, which are placed at the top and at the bottom of the toroidal chamber [7]. Role of divertor is to ensure heat extraction from plasma chamber, thus this is the element subjected to the largest heat flux. Particle flow is stirred to divertor by magnetic field. Heat and particle flow hitting divertor can reach up to 50 MW/m^2. No solid material can be exposed to such an extreme heat flow, thus surface should be continuously covered with liquid metal. Liquid metal surface or capillary porous liquid metal system is one of the most perspective way to ensure long term operation of the divertor. This work is devoted to estimate and characterize the forces acting on liquid metal to find the best CPS type for divertor plate. Schematics of the plasma chamber and divertor are shown on Fig.1. Divertor placing in reactor chamber and most essential parts of the chamber are shown on Fig.1(a). Closed look at the divertor is Fig. 1 (b). Technical solution for divertor surface is one of the main aspects to ensure the operability of all facility.

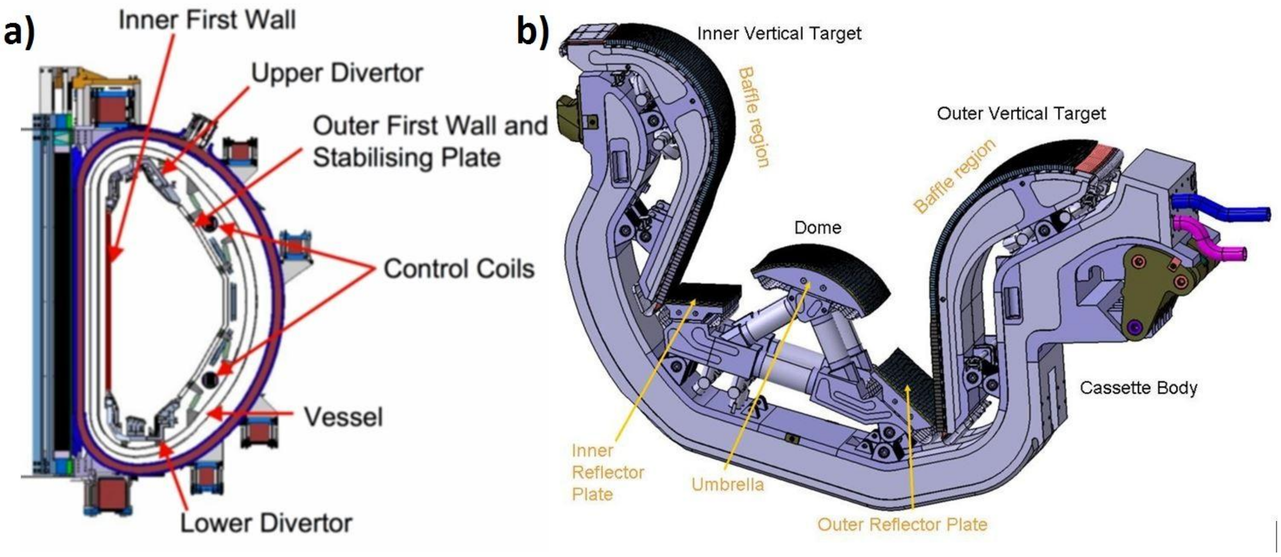

Fig. 1. a) Schematic cross section of the plasma chamber; b) divertor [6]

2. ANALYTHICAL DESCRIPTION

2.1. Simplified divertor model

Divertor surface which is subjected to the highest particle and radiation loads is formed of CPS consisting of solid metal structure surrounded by liquid metal. Such combination is chosen as a balance to ensure conduction and convection heat exhaustion from the hot zone, while splashing and evaporation of liquid metal is limited. Different material combinations and designs has been considered for this task, stainles steel and gallium or lithium are considered [8]. But recently there has been a consensus to search for solution with liquid tin and tungsten CPS structure, which have several advantages due to sfety reasons.

For first assesment of the characteristic forces and summary of physical effects relatively simple geometry has been chosen. CPS is modelled as array of parralel tubes filled with liquid metal. Liquid metal is supplied from the bottom of the CPS layer by small overpressure to ensure that plasma facing divertor surface is covered by liquid metal film at all time. Sizes in this model is chosen based on previous designs, each tube diameter is 0.5 mm and CPS layer thickness is 2 mm. Schamatics of the divertor CPS surface is depicted on Fig. 2.

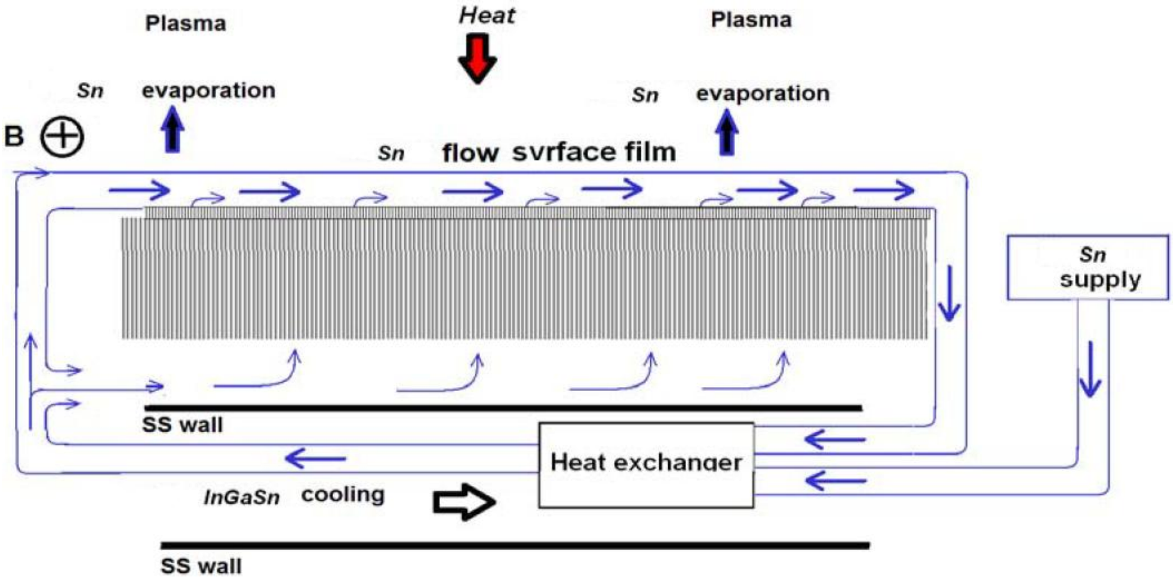

Fig. 2. Liquid metal flow in divertor. CPS here is depicted as array of the vertical tungsten capillaries surrounded and filled by liquid tin

2.2. Forces in liquid metal

Electromagnetic forces can be among the most important forces in such system because of good electrical conductivity of the materials, extremely high magnetic field and heat flow. Due to the small diameter of the capillaries, metal is kept into CPS by capillary force, but small diameter also limits the velocity which supplies metal to the surface. If liquid conductor is moving perpendicular to external magnetic field then electromagnetic force is induced and acting opposite to the motion direction. To predict metal behavior in the system and the performance of divertor, all relevant forces have to be considered and estimated. Divertor is located into the strong magnetic field and is subjected to large heat flow, which may be time varying. Temperature gradient is mostly perpendicular to plasma/CPS interface but it may have also a component parallel to the surface. Temperature gradient can significantly vary over time because heat flow from plasma is non-stationary. Thermoelectromagnetic convection (TEMC) recently is of a particular interest in the field of crystal growth and solidification of metallic alloys under electromagnetic fields [8]. This type of convection emerges as a result of thermoelectric current and applied magnetic field interaction, and may play significant role in solute and mass transport near solidification interface and in the nucleation zone. A high thermoelectric (TE) current density is created by a high differential thermoelectric power, good electrical conductivity and high temperature gradient. Electric potential and current distribution in continuous media is governed by Ohm's law eq(1). In some circumstances thermoelectric term can be dominant source of electric current in the material.

$$\vec{\nabla} V = -S(T)\vec{\nabla} T - \vec{j}/\sigma \tag{1}$$

Physical properties used in force density calculations and numerical models are summarized in Table 1. Characteristic forces in liquid metal CPS in divertor are estimated and summarized in Table 2. Magnetic field in plasma chamber can reach several tesla. In this calculation it is assumed that magnetic field of 1 T perpendicular to the surface is present. Capillary diameter D = 0.5 mm, capillary length L = 2 mm, temperature gradient θ = 100 K/mm, characteristic liquid metal velocity u = 1 mm/s. Capillary force density in wetted d = 0.5 mm diameter and L = 2 mm tube can be calculated as Laplaces force along the perimeter divided by the length of the capillary $F_c = 4\gamma/dL$. Viscous force is calculated from the consideration that liquid metal flow in the tube is laminar Poiselle flow. Thermoelectric and MHD force order of magnitudes are estimated, because precise calculation of these forces would require precise clculation of electric current distribution. This estimation indicates that at low velocities of few mm/s MHD force is insignificant, while TE force may be one of the dominant forces.

Table 1. Material properties

Property		**Liquid Sn**	**Tungsten (600 K)**	**Unit**
Thermal conductivity	λ	66	173	W/m·K
Heat capacity	c_p	540	325	J/kg·K
Electrical conductivity	σ	$3.6\cdot10^6$	$1.8\cdot10^7$	Sim/m
Absolute thermoelectric power	S	1	10	µV/K
Density	ρ	7000	18800	kg/m^3
Surface tension	γ	0.48		N/m
Viscosity	μ	0.002		Pa·s

Table 2. Force density estimation acting on liquid metal in CPS

Force	**Equation**	**Force density**
Capillary force	$F_c = 4\frac{\gamma}{dL}$	2 MN/m^3
Gravity force	$F_g = \rho g$	70 kN/m^3
Viscosity	$F_v = \frac{32\mu u}{d^2}$	250 N/m^3
MHD force	$F_e = \sigma u B^2$	4 kN/m^3
TEM force	$F_{TE}=\sigma\Delta S\theta B/5$	500 kN/m^3

The computing technique developed for metallurgical applications is applied to a quite different field, to fusion technologies in this work. In liquid tin/tungsten CPS system thermoelectric current may create force which may drive a liquid convection or alter pressure distribution in the liquid. Tungsten has high absolute thermoelectric power [10]. Idea to use thermoelectric pumping effect to remove heat from a divertor has been explored by Ruzic [11]. It has been shown that in such a way an intense enough free surface flow can be generated in a system of parallel grooves made of solid material, surrounded by liquid metal. No outer power source is needed, and flow is driven conditionally by the heat flux itself. It is investigated here if TE forces may help to drive convection in favourable direction to improve the performance of the setup and to predict the TE force effect during non-stationary and inhomogeneous heat flux from plasma.

3. RESULTS AND DISCUSSION

3.1. Numerical model

Numerical models have been developed to calculate TE current density and TEM force density if constant and inhomogeneous heat flux is applied perpendicular to the plasma/CPS surface. If homogeneous heat flux is applied to divertor plate depicted in Fig. 3 (a), then TE current flows in one direction through the liquid metal and in opposite through solid metal wall. Direction of the current is defined by the direction of temperature gradient and sign of differential thermoelectric power between solid and liquid phases.

3.2. Results

Calculated TE current density in the case when a constant heat flux is applied and temperature gradient is perpendicular to plasma/CPS surface is shown in Fig. 3. In this case if heat flow is inhomogeneous, then situation is more complicated and current density and force distribution is difficult to predict. If Gaussian shape heat pulse is applied to plasma/CPS surface is numerically analyzed and results are shown and compared to homogeneous case in Fig. 3. Temperature and current distribution are calculated Fig. 3 (b, c). Fig. 3 (d) and Fig. 3 (e) compares TE force densities acting on CPS. Homogeneous heat flow creates almost uniform thermoelectric force perpendicular to plasma/CPS surface. While force density caused by inhomogeneous heat flow also creates force density distribution with component parallel to CPS/plasma surface. Thus in this case thermoelectromagnetic force may cause liquid metal surface deformation and push liquid metal out of the solid mesh in some places. This may lead to the stituation where solid parts are revealed for plasma and may lead to the failure of the device. Thus it is important to estimate and compare electromagnetic and capillary, and other forces acting on liquid metal.

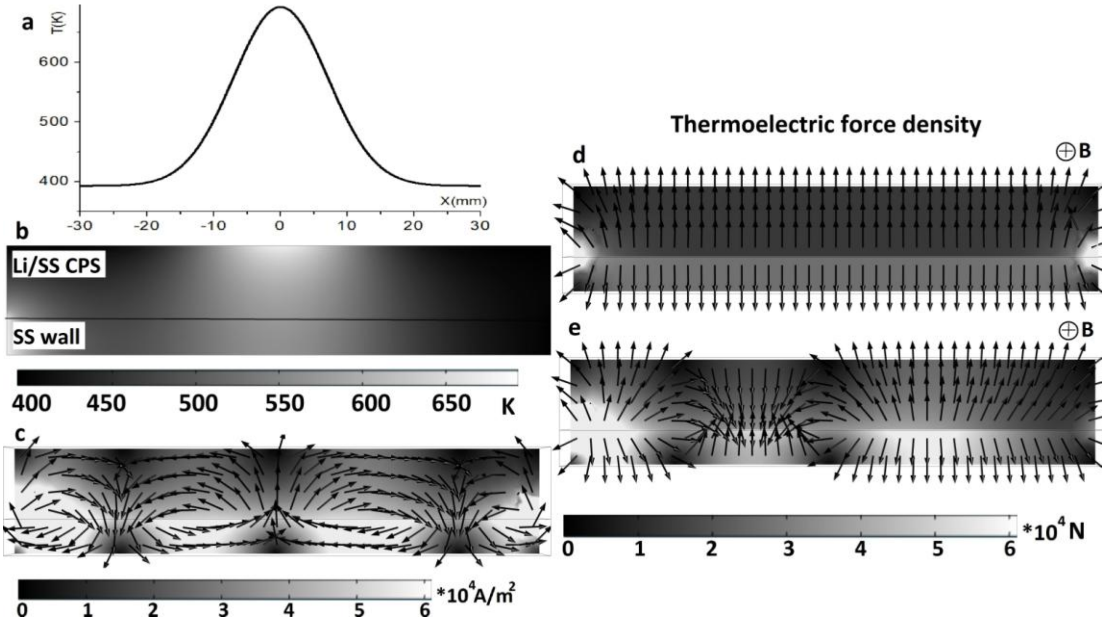

Fig. 3. Thermoelectric current density if nonhomogeneous heat flux is applied. a – temperature profile along plasma/CPS surface, b-temperature distribution in divertor plate, c – calculated thermoelectric current density. Thermoelectric force distribution in case of: d – homogeneous, e – inhomogeneous heat flow. Only CPS and SS wall are shown in this picture

Numerical simulations of this work shows that in proposed CPS design thermoelectromagnetic force may be one of the dominant forces on liquid metal under certain conditions. Order of magnitude estimation of thermoelectromagnetic force gives value larger than calculated by numerical simulation which may be explained by TE current circulation path. In analysed CPS setup effects of thermoelectromagnetic force is negative and TEMC force pushes liquid metal away from the hotter surface region, which is in agreement by observation described in [11]. This effect should be taken into account during design and construction of the experimental facility. In order to predict the magnitude of this effect, heat pulse duration and space distribution parameters should be known. For safety reasons CPS parameters should be sufficient to withstand the highest possible heat pulses. Thus this may be one of the factors limiting the CPS size, because main force maintaining the liquid metal in CPS is capillary.

4. CONCLUSIONS

It is demonstrated that thermoelectric current may create force which has significant effect on the liquid Sn flow within CPS. It is found that liquid metal surface can be deformed, and liquid metal can be pushed away from the hot zone by TEM forces. This force must be considered during design of the system. If nonhomogeneous heat flow is applied, then temperature gradient in the CPS has all three components and TEM force is present in CPS regardless of magnetic field orientation. In case of Gaussian shape heat impulse from plasma zone and constant magnetic field along the surface, liquid metal is pushed away from hot zone as demonstrated by numerical models. Force density estimations indicate that TEM force can be one of the dominant force under certain conditions, thus the influence of thermoelectric phenomena must be carefully analyzed and considered during design of divertor for fusion reactors. This phenomenon needs to be deeper evaluated and understood for better usage of it and to avoid negative effects.

REFERENCES

1. GORSE-POMONTI, D.; RUSSIER, V. Liquid metals for nuclear applications, Journal of Non-Crystalline Solids, Volume 353, Issues 32–40, 2007, Pages 3600–3614.
2. BUCENIEKS, I.; KRAVALIS, K. Efficiency of EM induction pumps with permanent magnets, Vol. 47, No. 1, 89–96, 2011.
3. REMEIRDES, H.; et.al. Towards an Assessment of Alternative Divertor Solutions for DEMO. 42nd European Physical Society Conference on Plasma Physics, Lisbon, Portugal, 22–26 June 2015.
4. LIELAUSIS, O,; KLYUKIN, A.; PLATACIS, E.; PEINBERGS, J. MHD experiments on liquid metal jet-like flows guided by curved substrates, Vol.51, No. 4, 685–694, 2015.
5. KOLESNICHENKO, A.F. Research and development liquid metal system for a tokamak reactor. Fusion Eng.& Design, 1989, No. 8, pp. 283–288.
6. https://www.iter.org/ .
7. HIRAI, T. et.al. Use of tungsten material for the ITER divertor, Nuclear Materials and Energy, Volume 9, 2016, Pages 616–622.
8. EVTIKHIN, V.A.; et.al. Research of lithium capillary-pore systems for fusion reactor plasma facing components, Journal of Nuclear Materials, Volumes 307–311, Part 2, 2002, Pages 1664–1669.
9. KALDRE, I.; FAUTRELLE, Y.; ETAY, J.; BOJAREVICS, A.; BULIGINS, L. Influence on the macrosegregation of binary metallic alloys by thermoelectromagnetic convection and electromagnetic stirring combination, Journal of Crystal Growth, Volume 402, 2014, Pages 230–233.
10. SHERCLIFF, J. (1979). Thermoelectric magnetohydrodynamics. Journal of fluid mechanics, Vol. 91, part 2, pp. 231–251.
11. RUZIC, D.N. (2010). *Lithium Walls: The Ultimate Technology.* Illinois: Center for Plasma-Material Interactions. 3rd international symposium on lithium applications for fusion devices. (2013).

CYSENI 2018, May 23-25, Kaunas, Lithuania
ISSN 1822-7554, www.cyseni.com

IONIZING RADIATION EFFECTS ON THE THERMAL STABILITY OF DEUTERIUM TRAPPING IN SIC

P. Muñoz, A. Moroño, F. J. Sánchez, I. García-Cortés
Laboratorio Nacional de Fusión, CIEMAT,
Avda, Complutense, 40, 28040 Madrid – Spain
Email: patricia.munoz@ciemat.es

A. Maira
Centro de Micro-Análisis de Materiales - Universidad Autónoma de Madrid
Cantoblanco, 28049 Madrid – Spain

ABSTRACT

SiC materials are prime candidates for flow channel inserts in the dual coolant lithium lead blanket concept. Flow channel inserts made of SiC will be exposed to tritium from the Li transmutation, as well as to neutron and gamma radiation. Hence a critical issue for future fusion devices is to clarify hydrogen isotope behaviour in SiC under such conditions. The objective of the work presented here is to study the effect of ionizing radiation on the deuterium trapping in SiC in similar conditions as reactor materials. This effect is evaluated by studying the influence of ionizing radiation on deuterium trapping (for both implanted and loaded SiC samples). Moreover, it is investigated how deuterium trapping may be modified by displacement damage. The ionizing radiation effect on absorption has also been evaluated for samples pre-damaged by self-ion irradiation. The irradiation and implantation experiment have been carried out at the CMAM-UAM accelerator, and the Danfysik implanter and 2 MeV Van de Graaff electron accelerator at CIEMAT. Samples are analysed by thermal desorption spectroscopy and secondary ion mass spectrometry (SIMS) to clarify the mechanisms involved in the trapping processes, depending on the different experimental conditions. The results for the deuterium loaded samples indicate that absorption is increased by ionizing radiation. When samples are pre-damaged by C^{+4} ions, deuterium absorption is increased in the form of Si-D according to SIMS results. Furthermore, the effect of ionizing radiation after deuterium implantation is an enhancement of the deuterium released from SiC. The deuterium release observed in this case is forming hydrocarbons during irradiations.

Keywords: flow channel inserts , fusion reactors, deuterium absorption, displacement damage, deuterium implantation, ionization irradiation, desorption, trapping

1. INTRODUCTION

Silicon carbide materials have many advantages for the usage as flow channel inserts in blankets in fusion devices like high thermal shock resistance, low activation and good resistance to neutron irradiation excellent thermo-mechanical and corrosion properties at high temperatures. [1]. In future fusion reactors a significant radiation field will be present and these components of a fusion reactor will be exposed in an extremely harsh environment and to a high flux of hydrogen isotopes. [2,3]. It is a critical issue for the tritium balance to evaluate the trapping and diffusion of hydrogen isotopes for the assessment of utilization of these materials for flow channel inserts.

This is crucial since, during fusion reactor operation, tritium trapped in the FCIs will be affected by heat and incident particle fluxes as a consequence of the nuclear fusion reactions produced in the plasma. In particular, neutron bombardment will generate ionization and displacement damage that could give rise to direct knock-on collisions that could induce or enlarge tritium traps.

When reviewing the literature, it is seen, in the first instance, that several authors have studied hydrogen isotope retention in SiC [4, 5 and references therein]. Moreover, it is found that ionizing radiation plays an important role in the microstructural evolution of irradiated ceramics [6] and that ionization-induced atomic desorption can also occur in many ceramic materials [7]. Furthermore, other works show that deuterium retention depends on both displacement damage and ionizing radiation [8, 9]. Indeed, it is found that displacement damage, as well as SiC temperature, are critical parameters for thermal desorption [10, 11], i.e., a low temperature (RT-200 ºC) and large displacement damage (1–7) dpa give rise to increased hydrogen isotope trapping in this material. In contrast it has to be noted that the possible source of hydrogen isotopes in FCI materials is twofold: the first is via nuclear transmutation (due to the interaction of a fusion neutron with the material) and the second is via absorption into the material from the Pb-Li liquid that transports the tritium (the tritium being a product of Li + neutrons during fusion reactions). Therefore, it is necessary to expand the fundamental understanding of irradiation effects in SiC related with displacement damage, taking into account the two different insertion paths for deuterium into SiC, implantation or loading, and to study their effect on the deuterium absorption and desorption in this material.

This paper presents the results from a series of experiments that evaluate the influence of fusion relevant levels of ionizing radiation on deuterium trapping in samples of SiC (either implanted or loaded). Moreover, since deuterium trapping may be modified by displacement damage, the effect of ionizing radiation on absorption has also been evaluated for samples pre-damaged by self-ion irradiation.

2. EXPERIMENTAL PROCEDURE

The objective of this work is to investigate the influence of ionizing radiation on deuterium trapping in SiC. This is evaluated here by studying the influence of electron irradiation on the stability of deuterium that had been introduced into the SiC samples in different ways, i.e., implanted or loaded, without or during electron irradiation, and for SiC with different levels of self-ion induced irradiation damage.

Several irradiation facilities have been used in order to simulate the behaviour of FCI materials when exposed to a continuous flux of hydrogen isotopes under concurrent neutron bombardment, which will induce severe damage, and ionizing radiation. The irradiation of the SiC materials with ionizing radiation was carried out using a 1.8 MeV electron accelerator, located in CIEMAT [12]. Next, for displacement damage by ions, the samples were irradiated using C^{+4} ions, accelerated to 25 MeV, at the Centre for Micro-Analysis of Materials (CMAM) [13]. Finally, simulation of the two D sources into these materials is performed by a) implantation of D^+ ions accelerated to 7 keV, at a current density of about 1 mA/cm^2, using a beam line of a Danfysik 60 kV ion implanter [14] and by b) (absorption of D) deuterium loaded experiments performed in a gas cell provided with an oven incorporated onto the electron accelerator line at CIEMAT.

All samples were obtained from a single 15 mm diameter bar of a commercial reaction bonded RB-SiC to ensure uniformity in composition and microstructure. Information about the sample composition and level of impurities can be found in previous works [10, 15].

A set of separate experiments has been designed and carried out. Table 1 summarizes the main experimental conditions for each sample.

Two techniques were used to analyse deuterium trapping; secondary ion mass spectrometry (SIMS) and thermal desorption spectroscopy (TDS). Before and after the TDS tests, SIMS measurements were performed on the samples using a Hidden Analytical SIMS Workstation with a MAXIM HAL 7 analyser. Primary O_2 ions, with energies up to 5 keV, were used. This technique allows the determination of the amount of deuterium remaining as a function of depth in the sample (a profilemeter is used to measure the final sputter crater depth). The desorption study has been performed using an in-house developed TDS system, in which each sample is placed in a chamber equipped with an oven which permits heating the samples up to 950 ºC at a rate of 10 ºC /min during measurements. The deuterium released is measured using a helium leak detector connected to the chamber and selected mass 4.

Table 1. Sample descriptions and experimental conditions

nº	Deuterium introduced into the SiC	Experimental Conditions			Deuterium release D_2/cm^2 *	Max temp desorption peak (ºC)
1	deuterium loaded	not damaged	no irradiation	deuterium loaded at 450 ºC for 7 hours	$3.75\cdot10^{15}$	700–825
2			during irradiation	deuterium loaded at 450 ºC for 7 hours during 1.8 MeV electron irradiation	$4.82\cdot10^{15}$	680–920
3		damaged	no irradiation	25 MeV C-ion implantation + deuterium loaded at 450 ºC for 7 hours	$2.10\cdot10^{15}$	700–820
4			during irradiation	25 MeV C-ion implantation + deuterium loaded at 450 ºC for 7 hours during 1.8 MeV electron irradiation	$2.61\cdot10^{15}$	700–890
5	deuterium implanted	not irradiated after		7 keV - deuterium ion implantation at 450 ºC	$7.44\cdot10^{15}$	685
6		irradiated after		7 keV - deuterium ion implantation at 450 ºC + 1.8 MeV electron irradiation (5400 kGy)	$8.67\cdot10^{15}$	675
7				7 keV - deuterium ion~~s~~ implantation at 450 ºC + 1.8 MeV electron irradiation (40500 kGy)	$4.11\cdot10^{15}$	785
8	deuterium loaded	without irradiation		deuterium loaded at 450 ºC for 7 hours	For measuring the release species either under and without irradiation with a quadrupole mass analyser	
9	deuterium implanted	not irradiated after		7 keV - deuterium ion implantation at 450 ºC		

*Deuterium release is measured up to 950 ºC. However TDS spectra for samples #3 and #4 are not complete at 950 ºC and the deuterium release could be higher.

3. RESULTS

In this section the results obtained for the different sample are detailed. The TDS spectra of samples #1, #2, #3 and #4 are represented in Fig. 1. Comparing the deuterium-loaded SiC #1 and #2 samples, it is found that deuterium release is about 23% lower for the non-irradiated sample ($3.75\cdot10^{15}$ D_2/cm^2) than for the sample loaded during irradiation ($4.82\cdot10^{15}$ D_2/cm^2). The latter shows a double peak structure (maxima at 680 ºC and 920 ºC) that clearly extends to higher temperatures beyond the second peak. When comparing these results with the TDS results from samples #3 and #4, which were pre-damaged with C^{4+} ions, it is found that deuterium release is lower for the pre-damaged case as compared with the undamaged samples. However, the desorption peak is broader although maximum desorption occurs at the same temperature. For the pre-damaged sample, the same occurs as for undamaged samples, i.e., the amount of deuterium released is higher for samples charged during irradiation (sample #3: $2.1\cdot10^{15}$ D_2/cm^2, sample #4: $2.61\cdot10^{15}$ D_2/cm^2).

The SIMS analysis of D and Si-D (D bound to Si) profiles is shown in Fig. 2 for samples #1 and #2. In this case, the quantity of deuterium measured as D and as Si-D is also lower for sample #1 than for the sample loaded during irradiation, either before or after the heating of the sample for TDS analysis. On the other hand, the SIMS results for samples #3 and #4 indicate that the amount of deuterium measured as D and Si-D is higher for those samples pre-damaged before being loaded with deuterium (samples #3 and #4) as compared with the undamaged samples (samples #1 and #2). It is significant the high amount of Si-D observed from pre-damaged samples. When comparing pre-damaged samples only (samples #3 and #4), as in the previous case, more deuterium is measured (as D and Si-D) for the sample loaded during irradiation than for the sample loaded without irradiation.

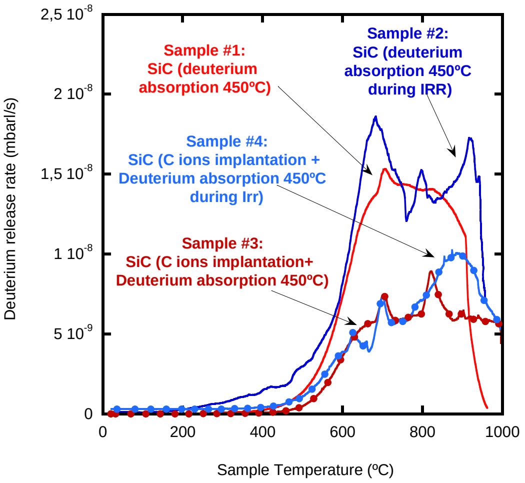

Fig.1. TDS spectra for sample #1 (red, deuterium loaded at 450 ºC), sample #2 (blue, deuterium loaded at 450 ºC during irradiation), sample #3 (claret, predamaged with C^{+4} ions and deuterium loaded at 450 ºC), sample #4 (cyan, predamaged with C^{+4} ions and deuterium loaded at 450 ºC during irradiation

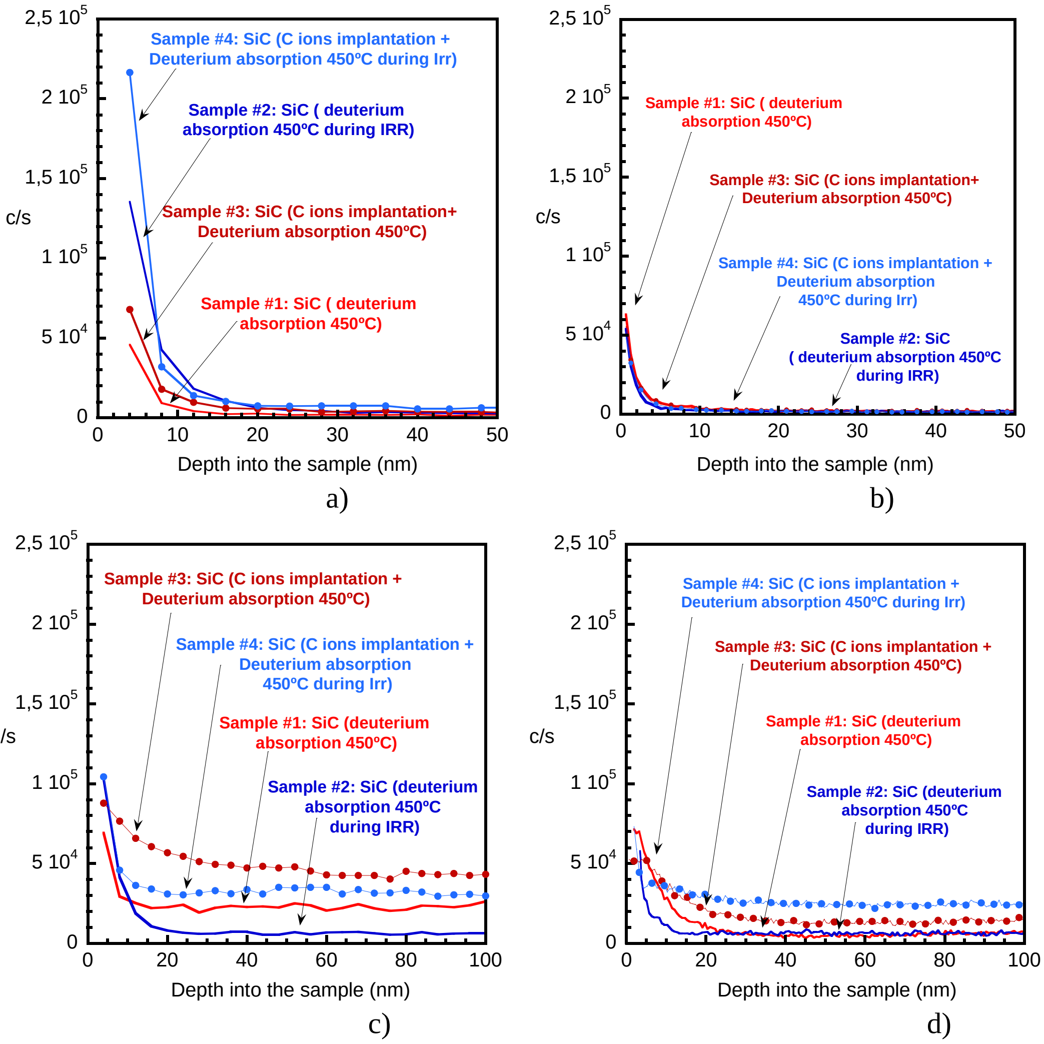

a) b)

c) d)

Fig. 2. SIMS D profiles for sample #1 (red, deuterium loaded at 450 ºC), sample #2 (blue, deuterium loaded at 450 ºC during irradiation), sample #3 (claret, pre-damaged with C^{+4} ions and deuterium loaded at 450 ºC), sample #4 (cyan, pre-damaged with C^{+4} ions and deuterium loaded at 450 ºC during irradiation) for a) before and b) after being heated to 950ºC. Also shown, are SIMS Si-D profiles for the same samples c) before and d) after being heated to 950 ºC

Fig. 3 shows TDS spectra for sample #5 (deuterium implanted at 450 ºC), sample #6 (deuterium implanted at 450 ºC and electron irradiated at 200 ºC to 5400 kGy) and sample #7 (deuterium implanted at 450 ºC and electron irradiated at 200 ºC to 40500 kGy). In the curves, a band is observed at 680 ºC for samples #5 and #6. In addition, the spectra are quite similar. However, for the sample irradiated after implantation at the higher dose (#7), the band shifts up in temperature to 785 ºC and the deuterium released is lower. Finally, the deuterium released reduces from $7.44 \cdot 10^{15}$ D_2/cm^2 (for #5) to $4.11 \cdot 10^{15}$ D_2/cm^2 (for #7).

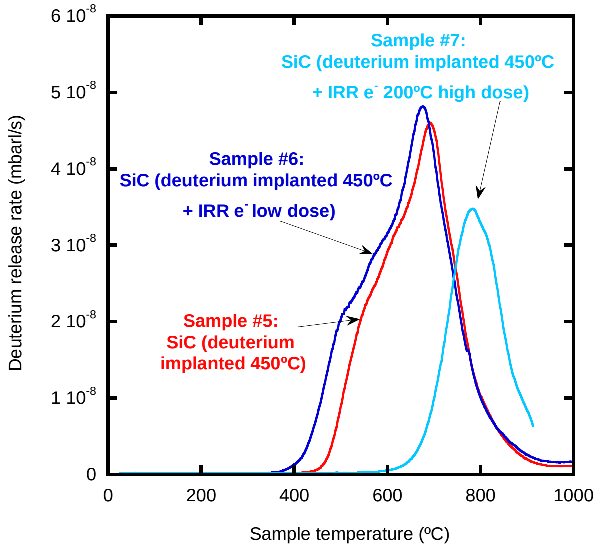

Fig. 3. TDS spectra for sample #5 (red, deuterium implanted at 450 ºC), sample #6 (blue, deuterium implanted at 450 ºC and electron irradiated to 5.4 MGy), and sample #7 (cyan, deuterium implanted at 450 ºC and electron irradiated to 40.5 MGy

In Fig. 4 SIMS D and Si-D profiles are presented for samples #5, #6 and #7 for before and after being heated to 950 ºC during TDS experiments, as explained above. A clear reduction is observed after heating to 950 ºC for the sample irradiated with electrons to a low dose after the deuterium implantation (sample #6) and for the sample not irradiated (sample #5). The behaviour, in terms of deuterium retention for RB-SiC, is completely different when this material is irradiated with electrons to a high dose after implantation. It is found that the retention of D and Si-D was significantly decreased in this case. Moreover, after heating, no change is observed for the Si-D profile, while in the case of the D profile a slight decrease is observed. However, for the other samples (non irradiated deuterium implanted and low-dose electron irradiation after deuterium implantation), a clear decrease in the D and Si-D profiles is observed after heating. Consequently, in these cases the stability of trapped deuterium is reduced when compared to the case of electron irradiation at high dose.

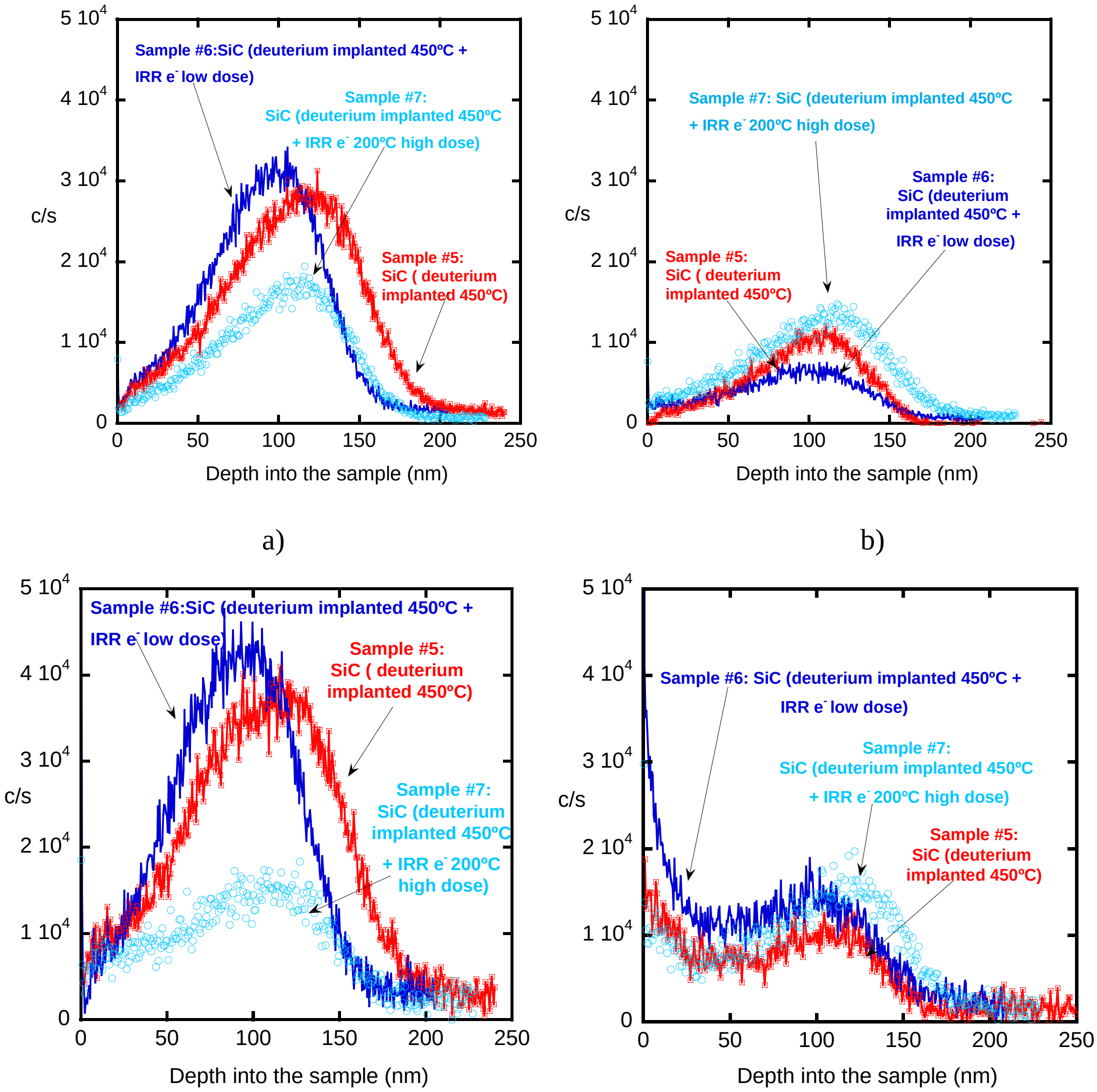

a) b)

c) d)

Fig.4 SIMS D profiles obtained for sample #5 (red, deuterium implanted at 450 ºC), sample #6 (blue, deuterium implanted at 450 ºC and electron irradiated to a low dose), and sample #7 (cian, deuterium implanted at 450 ºC and electron irradiated at a high dose) for a) before and b) after being heated to 950 ºC. Below are shown SIMS Si-D profiles for the same samples for c) before and d) after being heated to 950 ºC

4. DISCUSSION

The aim of this work is to identify the fundamental interactions of deuterium with SiC that can lead to deuterium trapping when undamaged, and self-ion pre-damaged, SiC is subjected to electron irradiation. As mentioned before, in order to address displacement damage effects on radiation induced deuterium absorption, some samples were pre-damaged before absorption. When considering the effect of damage on deuterium trapping, desorption spectra show that deuterium release is lower for pre-damaged samples. However, SIMS results show deuterium (in the form D or Si-D) is higher in pre-damaged samples both before and after heating to 950 ºC. These results point to deuterium being trapped in deep defects, generated by the C^{+4} ion implantation, from which the energy needed for release is sufficiently high that its thermal release is difficult. It is especially significant from SIMS results, in which absorbed deuterium, in its Si-D form, increases in damaged samples. Ion implantation produces direct knock-on displacements and also sputtering that changes the material. In reference [16], it is explained as being due to selective sputtering of C during ion bombardment, i.e., the concentration of C decreases compared to that of Si which results in increased formation of Si–D bonds.

Concerning the influence of electron irradiation on both undamaged and pre-damaged samples, it is seen that the same effect occurs in both cases: deuterium absorption increases during electron irradiation and desorption peaks appear at high temperatures. This effect was reported previously for electron irradiation at lower temperatures [9]. In addition, it is seen here that the TDS profile changes and desorption peaks appear at higher temperatures. This suggests that, when under ionizing irradiation, trapping probabilities for deuterium are modified. It is notable that, in the case of pre C-ion implanted samples, when a sample is electron irradiated during deuterium loading a clear increase is seen by SIMS in deuterium trapped as D when compared with that trapped as Si-D, see Fig 2. These results could indicate that, although deuterium is trapped at silicon dangling bonds produced by the former C^{+4} implantation, electron irradiation breaks the bonds between the deuterium and the silicon.

If it is studied the effect of irradiation with electrons after deuterium implantation a clear evolution from low to high electron irradiation dose was observed: First, for the low dose case a displacement towards the sample surface is seen by SIMS for both D and Si-D profiles. This is in agreement with the slight shift towards a lower release temperature observed in the TDS spectra (this temperature shift would be a result of a lower diffusion time for deuterium to reach the sample surface). This signifies that electron irradiation promotes diffusion of some of the deuterium towards the sample surface. For the high dose case, SIMS observes that part of the deuterium is not released by the electron beam and furthermore that the temperature for release of the remaining deuterium is significantly higher, hence the implanted deuterium is stabilized as a consequence of the electron irradiation. The deuterium release is lower for samples irradiated at high dose and the temperature required is higher. SIMS results show that the ionizing irradiation produces thermally stable traps for this hydrogen isotope. The ionizing component of radiation is very important in the enhanced diffusion processes [17, 18]. Ionizing radiation can induce the recombination of point defects and small interstitial clusters in SiC can become mobile under irradiation [19]. Thus deuterium may be released from D traps as these are modified by ionizing radiation, hence radiation enhanced deuterium desorption could occur for high-dose irradiation.

It is considered that deuterium is released in other forms. Carbon vacancy production during electron irradiation was previously studied [20] showing differences between the deuterium absorbed and implanted samples (for deuterium implanted SiC the electron irradiation induces a higher desorption). This means that trapping behaviour is influenced by the presence of damaged structures produced during the deuterium ion implantation.

It is observed in all samples subjected to a radiation field that part of the deuterium was thermally released at higher temperatures. The radiation-enhanced diffusion of defects can lead to the creation of stable traps for hydrogen isotopes from which release becomes more difficult. Hence, depending on the final operation temperature for FCIs, it is found that as the desorption temperature becomes higher, the ionizing radiation effect must be taken into account for deuterium retention in SiC.

5. CONCLUSIONS

In this work, the effect of ionizing radiation on deuterium trapping in SiC has been investigated. It is observed when samples are deuterium loaded under irradiation that enhanced deuterium absorption occurs. This ionizing radiation effect has also been evaluated for samples pre-damaged by C+4 ion implantation. In such damaged samples direct knock-on displacements result in an increment in the formation of Si-D bonds. Furthermore, it is observed that this displacement damage leads to released deuterium being combined with carbon. Studying the influence of electron irradiation on deuterium stability, after the latter has been implanted into the SiC samples, the behaviour in terms of deuterium desorption for RB-SiC is modified when it is subjected to ionizing radiation Basically ionizing radiation induces two effects that depend on how the deuterium is trapped within the SiC material: firstly, part of the deuterium is subjected to enhanced release from SiC and secondly, the ionizing radiation produces more thermally stable traps for the remaining deuterium.

ACKNOWLEDGEMENT

The authors are indebted to J. Valle, F. Jiménez and Ms. Martín Laso for their help with the experiments. P. Muñoz also acknowledges a pre-PhD contract from the Spanish MEIC. This work has been partially supported by the regional government of Madrid through its research program TECHNOFUSION(II)-CM (S2013/MAE-2745). This work has been also partially supported by Spanish 'Ministry of Economy and Competitiveness' and the 'European Regional Development Fund' under the grant number ENE2016-76755-R (MINECO/FEDER, EU).

REFERENCES

1. L. V. BOCCACCINI et al. Objectives and status of EUROfusion DEMO blanket studies, *Fusion Eng. Design*, 2016, Vol. 109–111, p. 1199–1206.
2. S. SMOLENTSEV, N. B. MORLEY, M. A. ABDOU, AND S. MALANG. Dual-coolant lead–lithium (DCLL) blanket status and R&D needs, *Fusion Eng. Design* , 2015, Vol. 100, p. 44–54.
3. C. SOTO, J. M. MARTÍNEZ-ESNAOLA, C. GARCÍA-ROSALES, Thermomechanical analysis of a Flow Channel Insert based on a SiC-sandwich material concept, *Nucl. Mat. Energy*, 2016, Vol. 7, p. 5–11.
4. Y. OYA, Y. HATANO, M. HARA, M. MATSUYAMA, AND K. OKUNO, Retention and desorption behaviour of tritium in Si related ceramics, *J. Nucl. Mat.* , 2013, Vol. 438, p. 22–25.
5. M. MAYER, M. BALDEN, AND R. BEHRISCH, Deuterium retention in carbides and doped graphites, *J. Nucl. Mat*., 1998, Vol. 252, p. 55–62.
6. A.M. STONEHAM, Radiation effects in insulators, *Nucl. Instrum. Methods: B* , 1994, Vol. 19, p. 1–11.
7. S. J. ZINKLE, V. A. SKURATOV, AND D. T. HOELZER, On the conflicting roles of ionizing radiation in ceramics, *Nucl. Instrum. Methods: B*, 2002, Vol. 191, p. 758–766.
8. A. MOROÑO, E. R. HODGSON, AND M. MALO, Displacement damage effect on the radiation induced deuterium absorption for different types of SiC, *Fusion Eng. Design*, 2015, Vol. 98–99, p. 2042–2045.
9. T. HERNÁNDEZ, A. MOROÑO, E. R. HODGSON, M. MALO, M. VERDÚ, AND F. J. SÁNCHEZ, Radiation induced deuterium absorption for RB-SiC, HP-SiC, silicon and graphite loaded during electron irradiation, *Fusion Eng. Design*, 2014, Vol. 86, p. 2550–2553.
10. P. MUÑOZ, I. GARCÍA-CORTÉS, F. J. SÁNCHEZ, A. MOROÑO, M .MALO, AND E. R. HODGSON. Displacement damage dose and implantation temperature effects on the trapping and release of deuterium implanted into SiC, *J. Nucl. Mater*., 2017, Vol. 493, p. 96–101.
11. F. J. SÁNCHEZ, A. MOROÑO, M. MALO, AND E. R. HODGSON. Trapping and thermal diffusion for energetic deuterium implanted into SiC, *Nucl. Mater. Energy* , 2016, Vol. 9, p. 383–387.
12. E. R. HODGSON, M. MALO, J. MANZANO, A. MOROÑO, AND T. HERNANDEZ, Radiation induced modification of electrical conductivity for three types of SiC, *J. Nucl. Mater*. 2011, Vol. 417, p. 421–424.
13. Laboratorio Nacional de Fusión, CIEMAT, 2017. Electron accelerator. Link to the internet <http://www.fusion.ciemat.es/competitive-access-to-facilities/electron-accelerator/> .

14. A. CLIMENT-FONT, F. PASZTI, G. GARCÍA, M. FERNÁNDEZ-JIMÉNEZ, AND F. AGULLÓ, Nucl. Instrum. *Methods Phys. Res.*, *Sect. B*, 2004, Vol. 400, p. 219–220.
15. Laboratorio Nacional de Fusión, CIEMAT, 2017, Ion implanter. Link to the internet <http://www.fusion.ciemat.es/competitive-access-to-facilities/ion-implanter/>
16. Y. OYA, Y. ONISHI, K. OKUNO, AND S. TANAKA, Trapping and detrapping mechanisms of deuterium in SiC studied by XPS and TDS techniques, *Mater. Trans.*, 2005, Vol. 46, p. 552–556.
17. M. WEISS, M. LU, P. VAN DER HEIDE, S.M. LEE, E. ADA, H. S. LEE, AND J. W. RABALAIS, Radiation enhanced diffusion of Ti in Al2O3, *J. Chem. Phys*., 2000, Vol. 113, p. 50–58.
18. R. GONZÁLEZ, E. R. HODGSON, C. BALLESTEROS, AND Y. CHEN, Effect of environment on radiation-induced out diffusion of deuterons and protons from crystalline LiNbO3 at low temperatures, *Phys. Rev. Lett*., 1991, Vol. 67, p. 2057–2059.
19. H. JIANG, L. HE, D. MORGAN, P. M. VOYLES, AND I. SZLUFARSKA. Radiation induced mobility of small defect clusters in covalent materials, *Phys. Rev. B*, 2016, Vol. 94, 024107.
20. N. T. SON, P. N. HAI, AND E. JANZE, Carbon vacancy-related defect in 4H and 6H SiC, *Phys. Rev. B*, 2001, Vol. 63, 201201(R).

CYSENI 2018, May 23-25, Kaunas, Lithuania
ISSN 1822-7554, www.cyseni.com

APPLICATION OF SENSITIVITY ANALYSIS IN EVALUATION OF AGGREGATE CROSS-SECTIONS FOR IRRADIATED EUROFER AND CUCRZR ALLOYS

A. Tidikas
Lithuanian Energy Institute
Breslaujos str. 3, LT 44403 Kaunas – Lithuania
Email: andrius.tidikas@lei.lt

ABSTRACT

Nuclear data libraries play an integral part in any neutron transport or activation calculation. The key differences between most commonly used nuclear data libraries lay in processing and amount of experimental data. Other practices include subsidiary calculations in order to account for missing or insufficient data. Depending on application, selection of data library might result in significantly different outcome.

In this work, two materials (EUROFER and CuCrZr) with possible application in future nuclear fusion reactors were examined. In addition to that water without any impurities was also investigated. Simulation of DEMO-like irradiation scenario was performed and material activities after shutdown and after 1 month of cooling were obtained. Numerical experiment was carried out with MCNP particle transport code and FISPACT activation calculation code. Handful of different nuclear data libraries were used in calculation including: EAF 2010, ENDF B 7.1, JEFF 3.2, JENDL 4.0, TENDL 2015. Software for Uncertainty and Sensitivity Analyses (SUSA) was used in order to obtain sensitivity values corresponding to particular neutron group in irradiation spectra. These values represent aggregate cross-section peaks of materials as well as show which neutron groups are more impactful for activation characteristics. Sensitivity analysis showed that neutron spectra changes were more impactful with regards to period 4th and 6th metals for EUROFER and period 4th metals for CuCzZr. Comparison of nuclear data libraries resulted in highest differences in activation of water including isotopic makeup. Application of precedent methods might be useful for recognition of materials suited for activation systems or for development of specific reduced activation materials.

Keywords: nuclear fusion, FISPACT, neutron activation

CYSENI 2018, May 23-25, Kaunas, Lithuania
ISSN 1822-7554, www.cyseni.com

ADVANCED SIMULATION TOOL OF NUCLEAR FUEL CYCLE

B. Chmielarz, W. Gudowski, Y. Hrabar, Congjin Ding, Jiali Zou
Royal Institute of Technology – KTH
Roslagstullsbacken 21, 114 21 Stockholm – Sweden
Email: yuliia@kth.se

B. Chmielarz
USNC Europe
2 Route de la Noue, 91190 Gif-sur-Yvette – France

Congjin Ding, Jiali Zou
Tsinghua University
30 Shuangqing Rd, 100084 Beijing – China

Alexander Bidakowski
Uppsala University
Dag Hammarskjölds väg 7, 75105 Uppsala – Sweden

ABSTRACT

This work describes development and benchmarking of a nuclear fuel cycle simulator code – Fuel Advanced Nuclear Cycle Simulation (FANCSEE). The code can lead to better understanding of energy management through comprehension of nuclear fuel cycle.

The idea behind FANCSEE is to create a user-friendly, graphically controlled software which allows to quickly implement, change and simulate complex scenarios. It has the ability to track up to 1307 nuclides over thousands of years. Results of mass, radioactivity and radiotoxicity of sets of isotopes, selected by the user, can be directly exported to MATLAB and used to assist choosing an optimal energy strategy. The target users would include researchers, policymakers and students.

The core physics of the code – solution of the burnup matrix exponential – is calculated using the state-of-the-art Chebyshev Rational Approximation Method. Libraries are separate for each fuel batch, fuel type and reactor type. They are calculated with Monte Carlo particle transport code Serpent 2.

The code is controlled through pre-defined objects which represent facilities in a nuclear fuel cycle – reactors, mines, fuel factories, waste repositories, enrichment and reprocessing plants. Every object has a list of corresponding parameters – for example, reactor power, fuel or reactor type, enrichment, processing capacity. Currently available libraries are for Boiling Water Reactor ABB-III, Pressurized Water Reactor (PWR) Vodo-Vodyanoi Energetichesky Reaktor 440-213, PWR Mixed Oxide and Uranium Oxide fueled reference Nuclear Energy Agency assemblies.

Current development is focused on implementation of new reactor types with focus on Generation IV – Accelerator Driven System Myrrha-like (lead-bismuth cooled), Lead Fast Reactor BREST, Sodium Fast Reactor Phenix and a High Temperature Gas-cooled Reactor design. Next step of development will focus on implementation of new functionalities to the interface, benchmarking and implementation of an economics module calculating costs of the entire nuclear fuel cycle with its back-end stage.

Keywords: nuclear energy, FANCSEE, fuel cycle, reprocessing; breeder

ANALYSIS OF THE CROSS SECTION FUNCTION OF Cd-113 IN THE COLD NEUTRONE ENERGY RANGE

Zs.Tóth
Budapest University of Technology and Economics
Budapest 1111 – Hungary
Email: toth.zsofia@eszk.org

ABSTRACT

The energy dependent cross section gives the probability of the occurrence of nuclear reactions. In the thermal and cold neutron zone it is inversely proportional to the velocity of the neutron for most of the nuclei. These nuclei are called 1/v nuclei for this reason. For some heavy nuclei differences can occur from this 1/v shape because of the resonances that modify the cross section function largely. Neglecting this fact can cause great errors in the calculations so these functions need to be clarified.

In the literature the partial cross section concerning Cd-113 was specified in measurements in water which is a problem because the hydrogen nuclei of water thermalize the neutrons and this effect influences the results of the measurement.

The thermal radiation cross section of cadmium-113 is especially important concerning neutronics calculations of nuclear power plants. In the Hungarian Academy of Sciences Centre of Energy Research the cross section data of cadmium-113 was defined with a supposition of a 1/v shape so they need to be modified to get more precise data.

The main goal of this research work is to precise the radiation cross section data of cadmium-113 in the cold and thermal neutron zone. In this study measurements in the Budapest Research Reactor and Monte-Carlo simulations were performed for the calculations.

In this research, the measurements based on prompt gamma activation analysis and comparator method to define the reaction rates of the examined isotopes were designed. The designed measurements were also simulated with the Monte Carlo N-Particle Code with which the reaction rates were calculated as well and after that compared to the measured results. In the simulation for the correct comparison I wanted to use the latest cross section data concerning cadmium-113. In other research work data by Peter Schillebeeckx and his group and the Breit –Wigner formula were used to define the cross section function for cadmium-113 and this data was used in the simulations as well. The comparison gave the result that the cross section function used is appropriate and precisely writes down the behaviour of the isotope.

Keywords: cadmium-113, radiation cross section, cross section function, cold neutron, comparator method

NUMERICAL INVESTIGATION OF THE THERMAL HYDRAULIC PHENOMENA IN A RECTANGULAR ENCLOSURE

A. Graževičius
Lithuanian Energy Institute
Breslaujos st. 3, LT-44403 Kaunas – Lithuania
Email: audrius.grazevicius@lei.lt

ABSTRACT

In the present study, the natural convection and thermal stratification phenomena in a rectangular enclosure with a horizontal heat source were numerically investigated. The results of numerical simulations shows, that a large natural convection flow occurs above the heated rod and thermal stratifications occurs below the heated rod. These results and improved methodology are compared with the results published at CYSENI 2016 conference. The full-scale computational domain of experimental facility (instead of many simplifications presented at CYSENI 2016) was created. The improved methodology and obtained results provide guidelines for numerical investigations of thermal-hydraulic processes in the spent nuclear fuel pools considering the concreate walls of the pool and main room above the pool.

Keywords: heat transfer, natural convection flow, computational fluid dynamics (CFD), ANSYS Fluent

1. INTRODUCTION

The spent nuclear fuel pools are designed to remove the decay heat from the spent fuel assemblies and to ensure biological shielding. After Fukushima accident on March 11 of 2011, interest of the nuclear safety of the spent nuclear fuel pools has been increased.

Literature review shows, that numerical investigations of thermal-hydraulic processes in the spent nuclear fuel pools are performed taking into account simplifications such as [1–5]:

1. Fluid flow are incompressible flow.
2. The Boussinesq approximation is applied for fluid density.
3. Time solver is steady-state.
4. The solid structures are not considered in numerical simulations.

In order to model realistic thermal-hydraulic processes in the spent nuclear fuel pools, the computational domain must be as close as possible to the real pool. Furthermore, in order to achieve this aim the reliable methodology must be created and tested using experimental data. The primary methodology and test results were presented on CYSENI 2017. In this study, the improved methodology is presented and compared with the primary methodology using the same experimental data [6].

2. DESCRIPTION OF THE EXPERIMENTAL FACILITY

The experimental facility consists of a rectangular enclosure with heated rod (see Fig. 1) [6, 7]. The back wall of the pool is made from 15 mm thick polycarbonate, front and right walls are made from 3 mm thick pyrex glass, 20 mm thick stainless steel is used for bottom and left walls, respectively. The length of the rectangular enclosure is 300 mm, width – 60 mm and height 650 mm. A diameter of the heated rod is 19.05 mm. Total length of heated rod is 160 mm. Five thermocouples were instaled (TF-01…TF-05) to monitor and record the thermal changes during the experiment. These thermocouples were placed in the center of the pool, except the TF-02 thermocouple, which was placed 2 mm away from the heated rod surface.

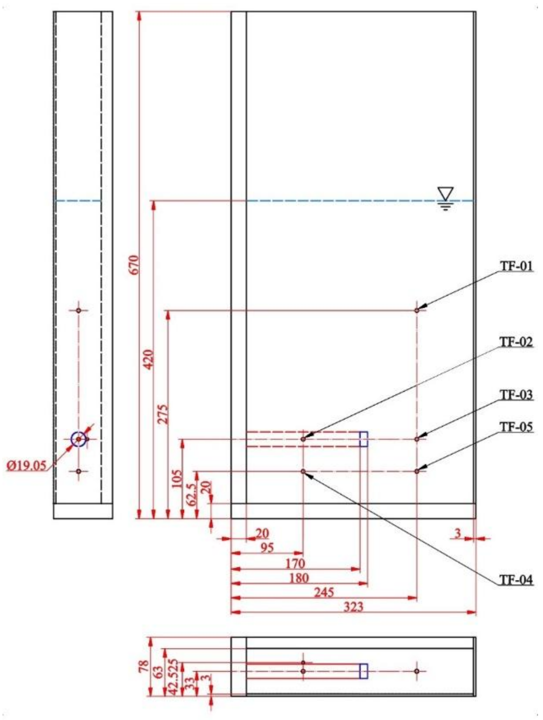

Fig. 1. Experimental facility

3. DESCRIPTION OF THE METHODOLOGY

The natural convection and thermal stratification phenomena were investigated numerically using ANSYS Fluent 17.2 academic research version and high performance computing cluster SGI Altix ICE 4800.

At the publication of CYSENI 2017, the results of numerical simulations of natural convection and thermal stratification phenomena and primary methodology were presented. In this publication, improved methodology is presented for the same experiment and the same thermal-hydraulic proccesses. In both cases, the geometry and mesh of the rectangular enclosure were created using ICEM CFD and taking into account OECD/NEA Best Practice Guidelines recommendations [8]. Comparision of the meshes is presented in Fig. 2, the mesh quality parameters are presented in Table 1, respectively. In the primary methodology, the thermal-hydraulic proccesses were analyzed using one-phase flow in closed domain and not considering solid structures (walls of experimental facility). In the improved methodology, two-phase flow with conjugate heat tranfster (heat transfer through solid structures) were considered. Comparision of the methodologies are presented in Table 2.

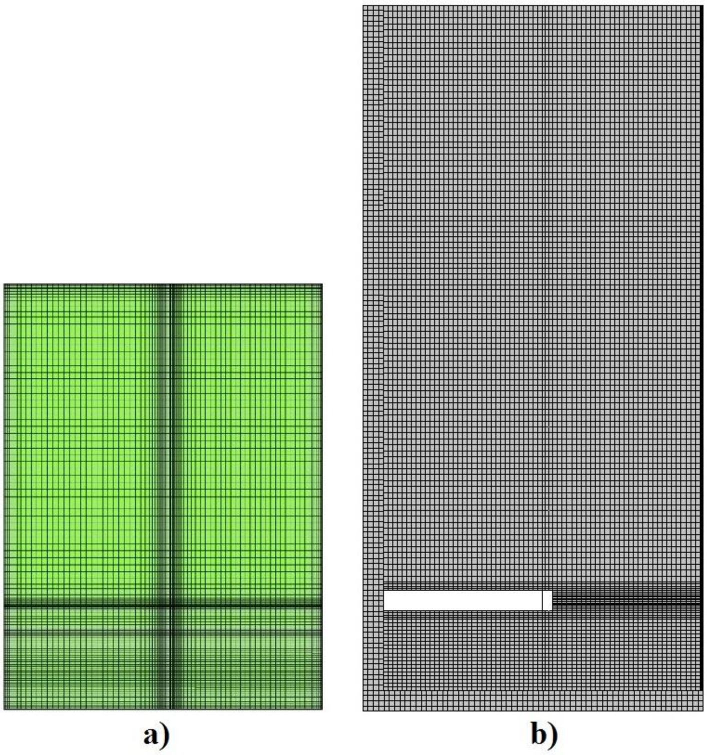

Fig. 2. Mesh of the computational model: a) primary methodology; b) improved methodology

Table 1. Mesh parameters of the computational model

Parameter	The obtained value	The acceptable value
Mesh quality	0.5–1.0	> 0.3
Minimum angle of cell	> 46.6	> 20.0
Aspect ratio	< 11.6	< 100.0
Skewness	< 0.5	< 0.8
Orthonogical quality	> 0.7	> 0.1
Expansion rate	20.0%	< 20.0%

Table 2. Comparision of numerical setup

Parameter	Primary methodology	Improved methodology
Mesh size	433948 cells	218313 cells
Water density	Boussinesq	Variable
Air density	Not considered	Variable
Solid structures	Not considered	Considered
Evaporation/condensation/boiling	Not considered	Evaporation-condensation model
Multiphase flow	One-phase (water) flow	Volume of Fluids model
Volume fraction paramether	-	Explicit
Viscous	k-e realizible with standard wall functions	k-w SST
Solver type	Pressure-Based Solver	
Pressure-Velocity Coupling scheme	PISO	
Gradient interpolation	Least Squares Cell Based	
Pressure interpolation	Body Force Weighted	PRESTO!
Momentum interpolation	First order upwind	Second order upwind
Volume fraction interpolation	-	Geo-Reconstruct

Turbulent kinetic energy interpolation	First order upwind	
Turbulent dissipation rate interpolation	First order upwind	
Energy interpolation	First order upwind	Second order upwind
Time stepping method	Fixed (0.05 sec)	Variable (CFL < 1)

4. EXPERIMENTAL AND BOUNDARY CONDITIONS

The initial water temperature is 32 ℃, and initial walls temperature is approximately 14 °C, respectively. Water level is 400 mm. Thermal power of the heated rod is 600 W. The heated rod heated water till the water temperature reached the saturation temperature. The experiment is divided in two stages. The first stage is water cooling (till 600 sec). The second stage is water heating (from 600 sec till saturation temperature). A heat transfer coefficient applied for surfaces of the computatonal domain is 15.92 W/m·K. Thermal-physical properties of the computational domain walls are presented in Table 3.

Table 3: Thermal-physical properties of the computational domain walls

Properties	**Polycarbonate**	**Pyrex-glass**	**Stainless steel 304**
Density, kg/m^3	1200	2230	8030
Specific heat, j/kg·K	1200	753	500
Thermal conductivity, W/m·K	0.19	1.1	16.2

5. RESULTS AND DISCUSION

The first stage (water cooling) of the experiment was not simulated using primary methodology, while, the first and second stages were simulated using improved methodology.

Fig. 3 shows comparision of velocity fields at the same time. The natural convection phenomenon in both cases is similar, but in simulations using improved methodology, water flow near the free-surface is exposed by opposite direction of air flow. Fig. 4 shows, that thermal stratification is more visible, when simulations were performed using improved methodology. This can be confirmed by Figs. 5–9, were comparision of the TF-01…TF-05 temperatures is presented. Fig. 5 and 7 show a good agreement between numerical simulations (improved methodology) and experimental data. Meanwhile, a large TF-02 temperature difference (see Fig. 6) was noticed. This is because the smaller number of cells is used around the heated rod. Fig 8 and 9 show a comparision of the TF-04 and TF-05 temperatures. The numerical simulations using improved methodology shows better agreement with experimental data than numerical simulations using primary methodology. However, these differences could arise due to the unknown heat losses during the experiment and wrong allocation of the heat losses through the computational domain walls.

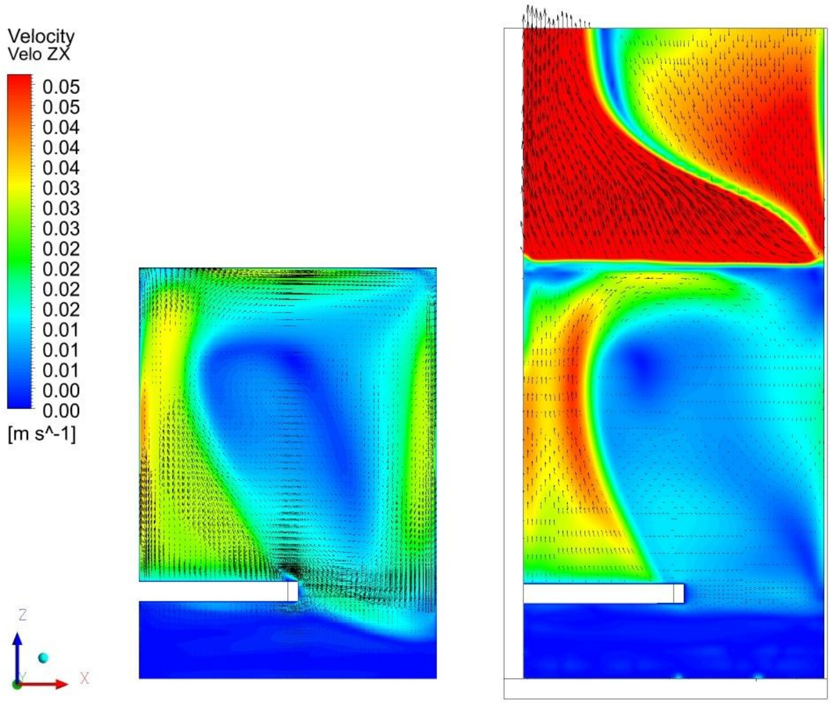

a) b)

Fig. 3. Velocity fields at 3608 sec: a) primary methodology; b) improved methodology

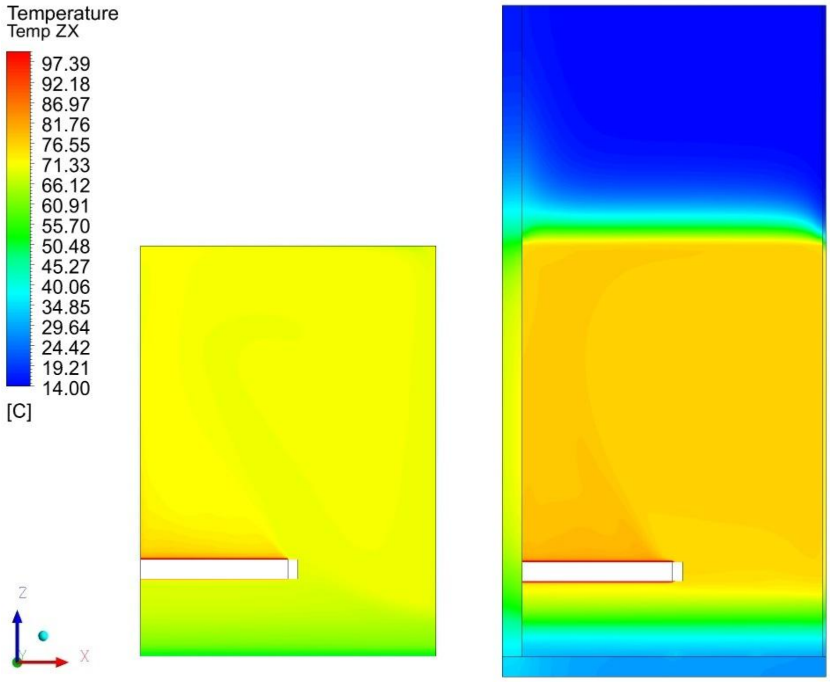

a) b)

Fig. 4. Temperature gradients at 3608 sec: a) primary methodology; b) improved methodology

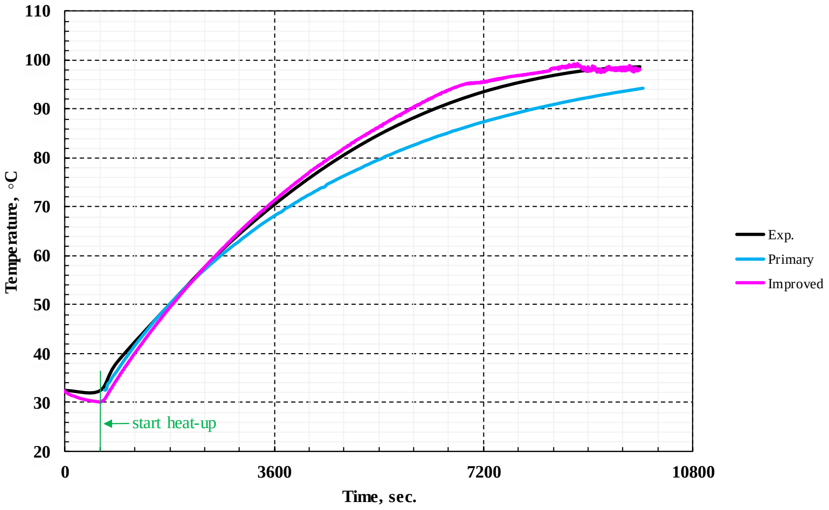

Fig. 5. Comparison of TF-01 temperature

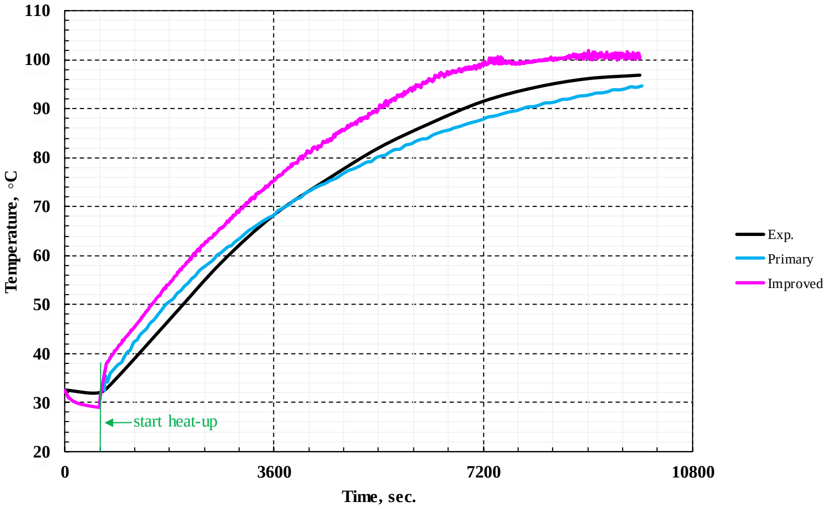

Fig. 6. Comparison of TF-02 temperature

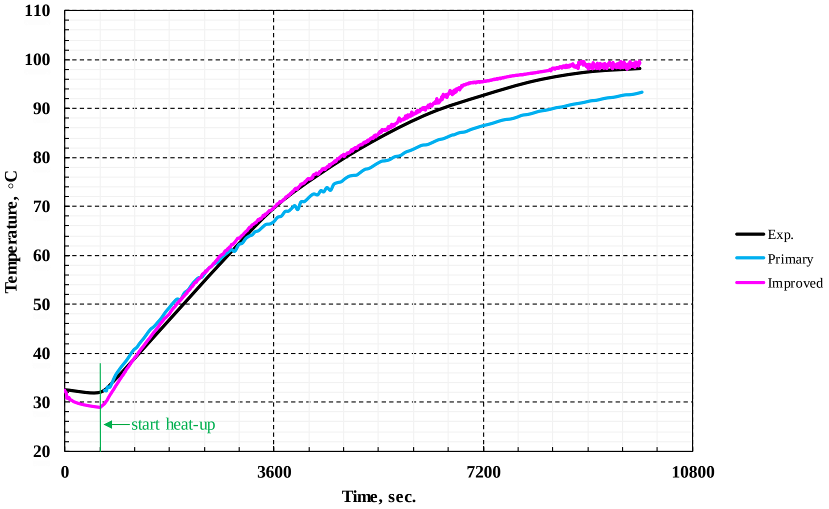

Fig. 7. Comparison of TF-03 temperature

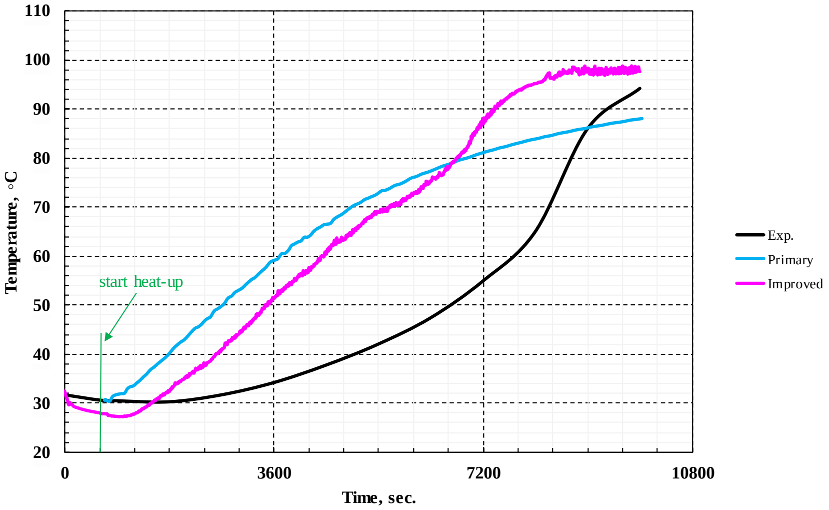

Fig. 8. Comparison of TF-04 temperature

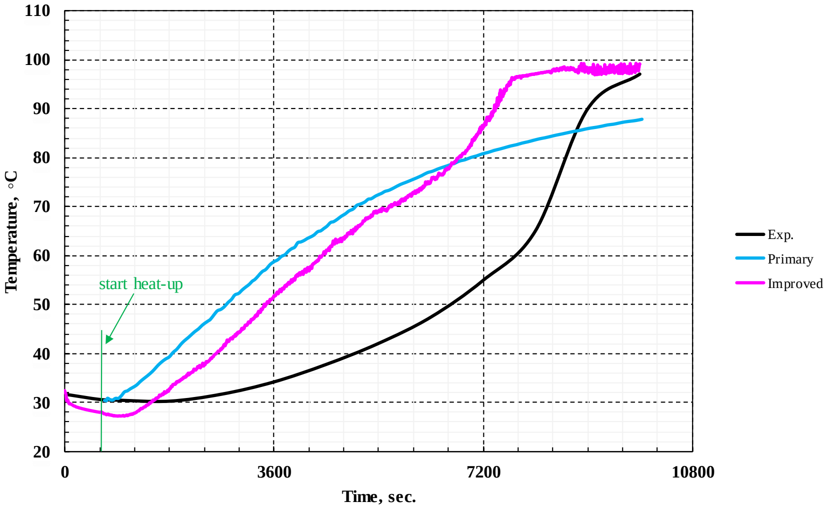

Fig. 9. Comparison of TF-05 temperature

6. CONCLUSION

The natural convection and temperature stratification phenomena in a rectangular enclosure were investigated numerically. Good predictions of measured water temperatures were achieved using improved methodology. The developed methodology provides guidelines for numerical investigations of thermal-hydraulic processes in the spent nuclear fuel pools considering the concreate walls of the pool and main room above the pool. To obtain more reliable results, it is recommended to refine the mesh near the walls according the dimensionless value $Y^+ \approx 1$ and to try smaller thermal power for future numerical simulations of this experiment.

REFERENCES

1. YE, C., ZHENG, M.G., WANG, M.L., ZHANG, R.H., XIONG, Z.Q. The design and simulation of a new spent fuel pool passive cooling systems. Annals of Nuclear Energy, 2013, Vol. 58, p. 124–131.
2. WANG, J.R., LIN, H.T., TSENG, Y.S., SHIH, C.K. Application of TRACE and CFD in the spent fuel pool of Chinshan nuclear power plant. Applied Mechanic and Materials, 2012, Vol. 145, p. 78–82.

3. CHEN, S.R., LIN, W.C., FERNG, Y.M., CHIENG, C.C., PEI, B.S. Development of 3-D CFD methodology to investigate the transient thermal-hydraulic characteristics of coolant in a spent fuel pool. Nuclear Engineering and Design, 2014, Vol. 275, p. 272–280.
4. HUNG, T.C., DHIR, V.K., PEI, B.S, CHEN, Y.S. The development of a three-dimensional transient CFD model for predicting cooling ability of spent fuel pools. Applied Thermal Engineering, 2013, Vol. 50, p. 496–504.
5. TSAO, P.C., HSIEH, K.T., LEE, D.S., KIM, C.N., TSENG, Y.S., HUNG, T.C. Investigation of passive air cooling capacity for spent fuel pool. The 2013 World Congress on Advances in Nano, Biomechanics, Robotics, and Energy Research (ANBRE13), Seoul, Korea, August 25–28, 2013, p. 463–475.
6. KIM, S., KIM, D.E., RYU, S.U., LEE, S.T., EUH, D.J. Experimental investigation on the natural convection flow in pool boiling. Nuclear Engineering and Design, 2014, Vol. 280, p. 349–361.
7. Graževičius, A. Modelling of pool heat-up experiment using ANSYS Fluent. Conference of Young Scientists on Energy Issues 2017, 23 May 2017, ISSN 1822-7554, VII-216–224 p.
8. MAHAFFY, J., et al. Best Practice Guidelines for the use of CFD in Nuclear Reactor Safety Applications – Revision. NEA/CSNI/R(2014)11, February 2015.

CYSENI 2018, May 23-25, Kaunas, Lithuania
ISSN 1822-7554, www.cyseni.com

THERMAL STATE OF WWER-1000 SPENT FUEL ASSEMBLIES AT THE DRY INTERIM STORAGE

D. Lunov, S. Alyokhina
V. N. Karazin Kharkiv National University
Svobody Sq. 4, UA-61022 Kharkiv – Ukraine
Email: d.lunev21@gmail.com

ABSTRACT

Safe thermal conditions of the spent fuel assemblies (SFA) storage are a key issue of the storage facility safety. The numerical estimation of thermal state of SFA was carried out with usage of methodology of the conjugate heat transfer problems solving. Due to slow changes of decay heat of SFA during the storage the modelling of thermal processes inside storage equipment was considered in the quasi-static formulation. The study was conducted for ventilated storage container with hermetic storage cask filled by helium, which is contain 24 WWER-1000 SFA. Detailed structure of storage cask was modelled considering conductive, convective and radiation heat transfer. The temperature field of the concrete container, guided tubes and temperature and velocity fields of the cooling helium inside cask and cooling air outside cask were calculated. The hottest assemblies and the maximum temperatures in each assembly were detected. The calculations were made for normal equipment operation at average summer temperatures of the place, where storage facility is located. The developed computational model was validated by comparison of calculated and measured temperatures of cooling air outside the storage cask. Proposed approach and computational model will be used for the next investigations for the thermal state assessment of SFA under accident conditions and the next safety assessment of the Dry Spent Nuclear Fuel Storage Facility on Zaporizhska NPP (Ukraine).

Keywords: spent nuclear fuel; numerical simulation; conjugate heat transfer; dry storage; WWER-1000; spent fuel assemblies

1. INTRODUCTION

The amount of spent nuclear fuel (SNF) in the world is growing. According to IAEA-TECDOC-1587 [1], the total amount of fuel that is taken from the reactors is 10500 tons per year. It follows that by 2020 the amount of spent fuel generated will be approximately 445000 tons. So, the problem of the SNF handling is very actual.

After 3–4 years of working in reactor, the fuel assembly is removed and placed into spent nuclear fuel pools for 5 years. During this time, the decay heat of each assembly is reduced. Then there are some options: recycling or storage. Dry or wet storage of spent fuel could be one of the storage posibilities. Since 2001, Zaporizhzhya NPP has used dry storage containers for storage of spent nuclear fuel. The storage area is designed for 380 containers, each with 24 assemblies. So, the storage of spent fuel in dry-type containers remains relevant even now.

The safety of SNF storage includes radiation and thermal investigations. Many researchers neglect the thermal state of main storage equipment and stored SNF, giving radiation processes more importance. That approach creates a blind spot in the general understanding of all the processes taking place inside the container. In this paper we will consider only the thermal part.

In many thermal researches, the models of containers are simplified, some physical processes are ignored, or physical properties are generalized. For example, in one of the work on the analysis of the containers temperature state [2–3], the storage cask model was simplified: by summarizing of the temperature properties (thermal conductivity and heat capacity) of the cask and helium, and helium circulation was absent. As a result this approach was not taken detailed information about thermal state of spent fuel assemblies inside storage cask. Another example is the use of a two-dimensional model [4] at numerical simulation. It’s good approach for the resources saving, but this method leaves gaps in understanding of total picture of the SNF thermal state.

The goal of this work is, firstly, a more detailed research of the thermal behavior inside the cask. Secondly, safety assessment and detection of the place with the highest temperature inside each fuel assembly.

2. GEOMETRY OF CASKS

The object of the study is a ventilated container with four inlet channels and with four outlet channels for air (Fig. 1). Inside container is a sealed metal cask with spent nuclear fuel. Cooling the cask occurs by natural convection. The cold air goes through the lower vents, it’s heating due to the contact with the hotter wall of the tight cluster storage cask. Heater air is rising up doe to the density difference and finally going out through the upper vents.

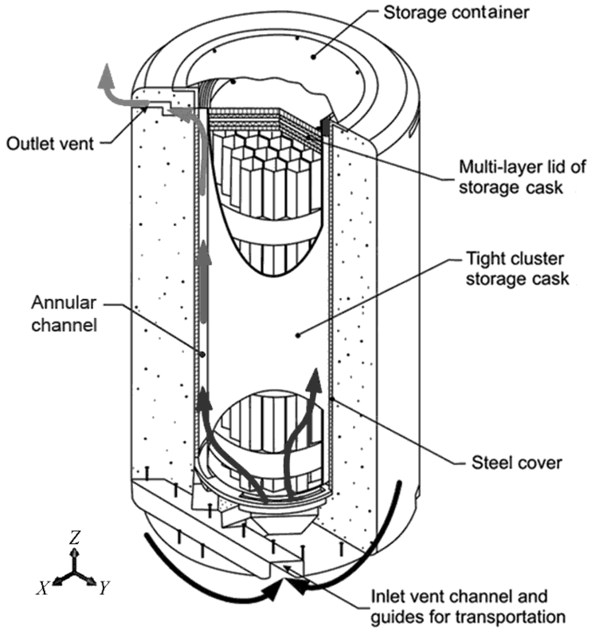

Fig. 1. Structure of storage cask

Inside the cask are 24 assemblies (the heat generation of each fuel assembly should not be more than 1 kW) in individual guide tubes (Fig. 2). The cask is filled by inert gas – helium, which also helps to remove heat from the assemblies. Each SFA consists of 3 parts: head, fuel rods and tail. Heat is released in all assembly, but the highest heat flux is in the middle part of assembly.

Table 1. Geometrical parameters of the container

Parameter	**Value**
Fuel assembly	
Shape	Hexahedron
Number of fuel rods	312
Length	3.837 m
Storage basket	
Number of spent fuel assemblies	24
Height	4.973 m
Diameter	1.715 m
Inner medium	Helium
Container	
Height	5.809 m
Diameter	3.378 m
Width of annular channel	0.07 m

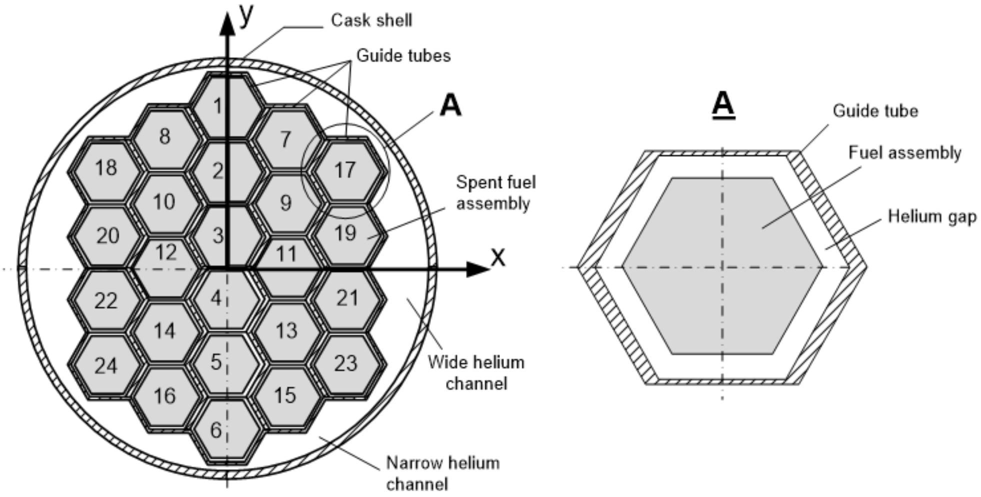

Fig. 2. Structure of storage cask (horizontal section)

All simulations were done for the average summer temperature of the ambient air is 24 degrees Celsius, calm conditions, and the influence of solar irradiation is neglected. The decay heat of each assembly is reduced at time as shown on Fig. 3.

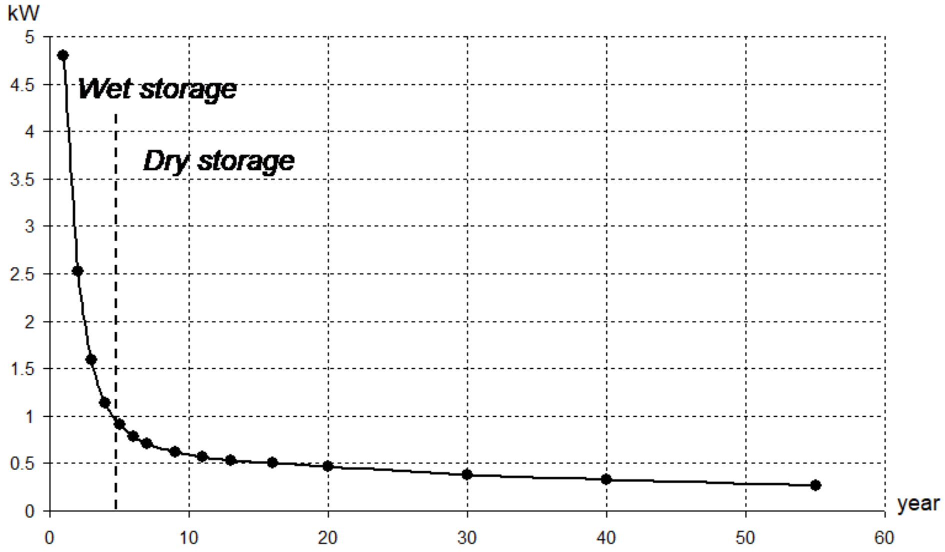

Fig. 3. Decay heat of one fuel assembly

3. METHODOLOGY

Due to dangerous and high level of radioactivity of the investigated object, only numerical simulation was carried out. The effective methodology in this situation is conjugate heat transfer problems, which allow modelling mutual heat transfer in solid and fluid media. Mathematical model includes [5]:

- continuity equation;
- equation of motion of viscous gas;
- energy equation for fluids;
- heat conduction equation for solids;
- equations of k-ε turbulent flow model;
- ideal gas law for calculation of cooling air density;
- equations for calculating thermal properties of helium as a function of temperature;

- equations which describe the radiative heat transfer.

Equations are solved by standard program complexes, which are used methodology based on finite-elements methods.

Two models were used in the simulation. In the first model, the cask was a solid object with equivalent thermal properties. The power of the SFA is uniformly distributed inside cask. With this model, the boundary conditions (the temperature of the ventilation air and the heat transfer coefficient at the cask surface) were obtained. In the second model, a cask with complex geometry inside (assemblies were simplified as a solid body) and with boundary conditions, which were found in the first model.

4. RESULTS AND DISCUSSIONS

Firstly, mathematical model and approach, based on conjugate heat transfer problems, was verified by comparing calculated and measured temperatures of the ventilating air on the exit of container.

Calculation was carried out for container, which operated on storage platform since 2001. Calm conditions of container's operation were chosen for verification. Results are presented on Fig. 4. The difference between calculated and measured temperatures do not exceed 6 ºC for each channel and 3 ºC for average temperature, but it could be caused by local influence of outer factors (for example, wind) at measurements. Verification shows that mathematical model and calculation approach are adequately describe thermal processes in storage container, so they could be used for next investigations.

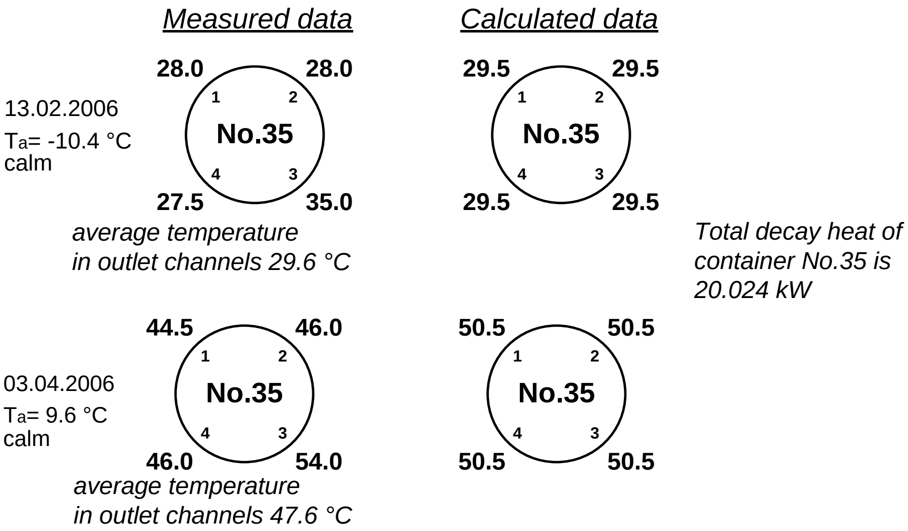

Fig. 4. Measured and calculated temperatures in outlet channels of container

Two types of studies have been done for the cask as a solid body and for cask with the detailed geometry. The second one (Fig. 5) gives more information about thermal state of SFA, so, its usage more preferable at safety assessment of the storage facility.

The study shown that the maximum temperature is reached in the assemblies under the numbers 3 and 4, 339.02 °C (Figs. 5, 6). On Fig. 5 in channel temperature of cooling air is lower than in storage cask and concrete container. Numbers of assemblies can be found in Fig. 2. The point where this temperature is reached is at a height of 2.75 m from the bottom of the cask. Less hot assemblies under numbers 11 and 12, their maximum temperature is 328.27 °C. The coldest are assemblies 1 and 6, their temperature is 107.69 °C. The maximum temperatures in each assembly are presented in Table. 2.

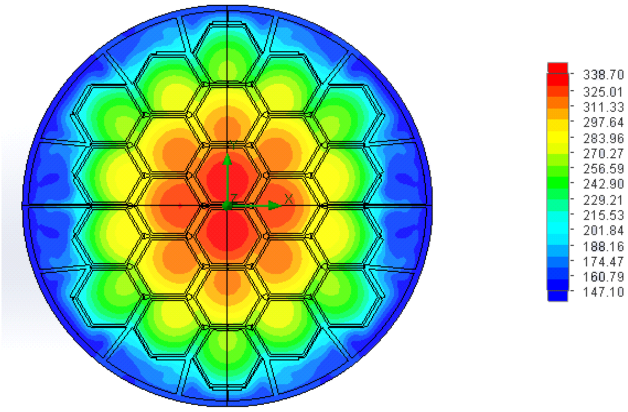

Fig. 5. Cross-section of the cask XY (detailed model)

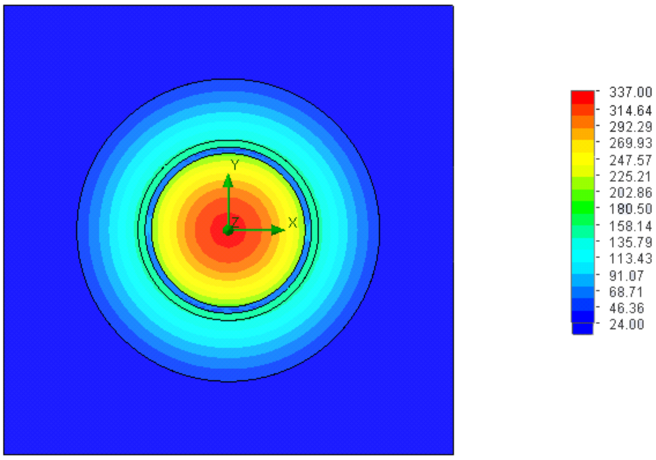

Fig. 6. Cross-section of the cask XY (simplified model)

Table 2. Maximum temperatures in fuel assemblies

SFANo.	**1**	**2**	**3**	**8**	**10**	**12**	**18**	**20**
Temp., °C	261.4	313.41	339.02	277.89	316.95	329.27	262.09	285.75

In the case, when the cask is represented by a homogeneous solid body. The maximum temperature is at the height of 2.22 m (Figs. 7–12), in detailed case at a height of 2.75 m from the bottom of the storage cask. The point of the maximum temperature become upward due to taking into account the helium moving.

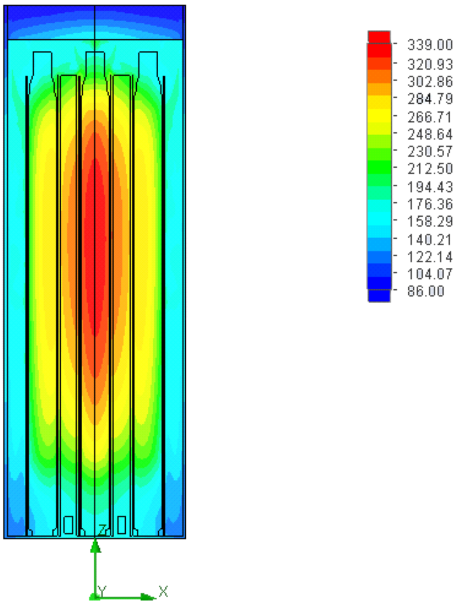

Fig. 7. Cross-section of the cask XZ (detailed model)

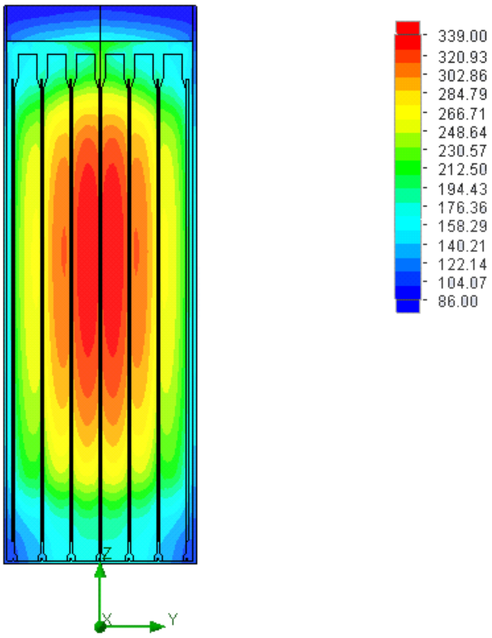

Fig. 8. Cross-section of the cask YZ (detailed model)

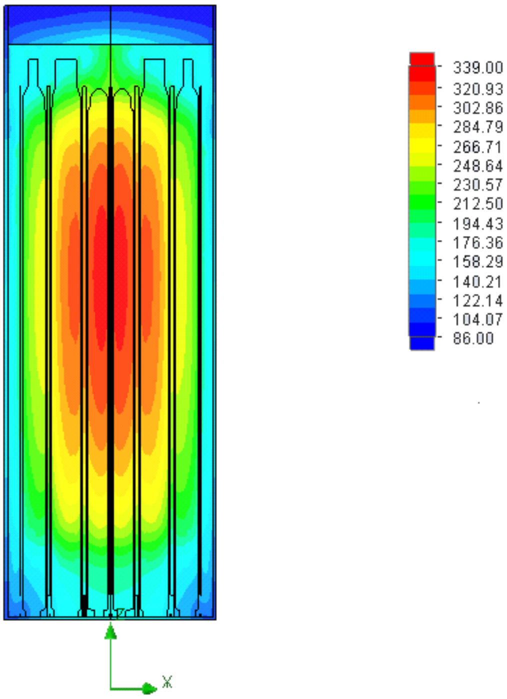

Fig. 9. Cross-section of the cask XZ rotated on 45°
(detailed model)

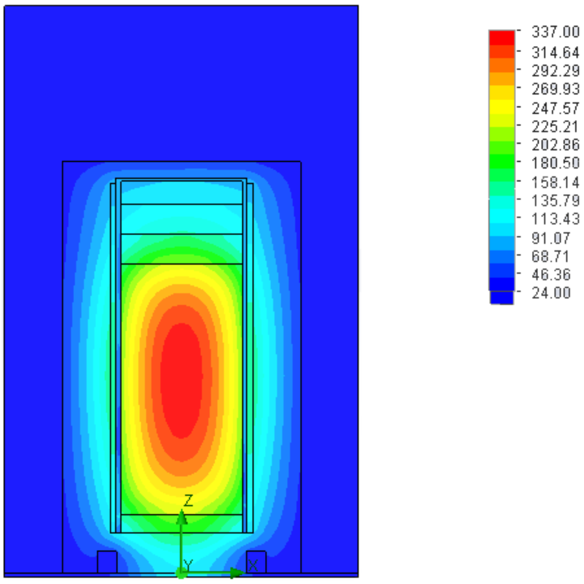

Fig. 10. Cross-section of the cask XZ (simplified model)

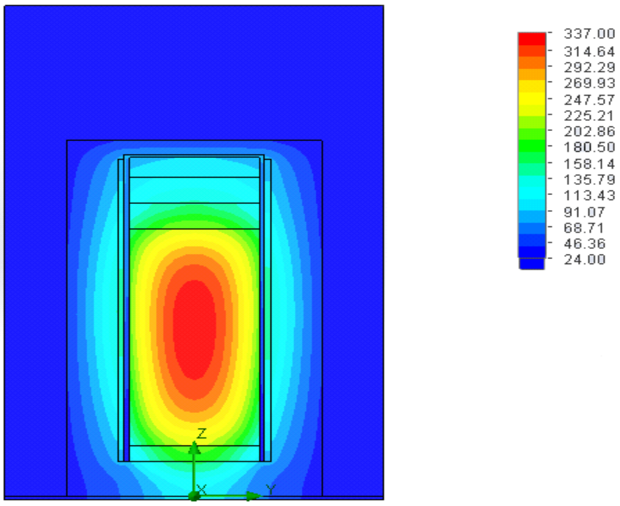

Fig. 11. Cross-section of the cask YZ (simplified model)

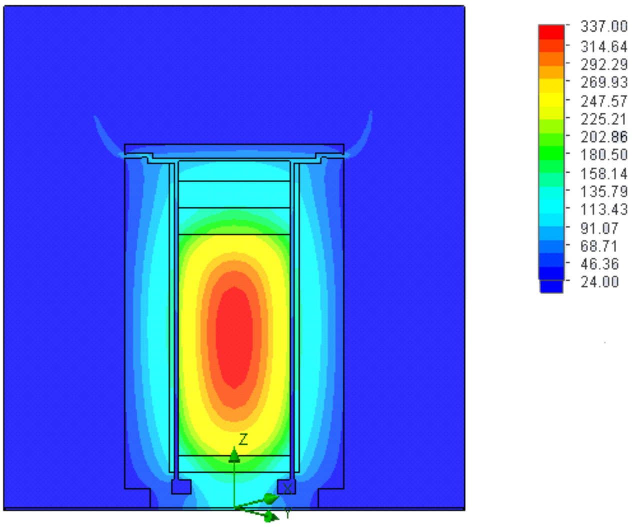

Fig. 12. Cross-section of the cask by vent (simplified model)

Due to unsymmetrical of the inlet vents the 2 variants of the storage cask placement inside container were considered. If the cask is rotated by 90° the maximum temperature does not change much, it will be around 338.2 °C. So, the location of the cask does not greatly affect its thermal state (Figs. 13–14).

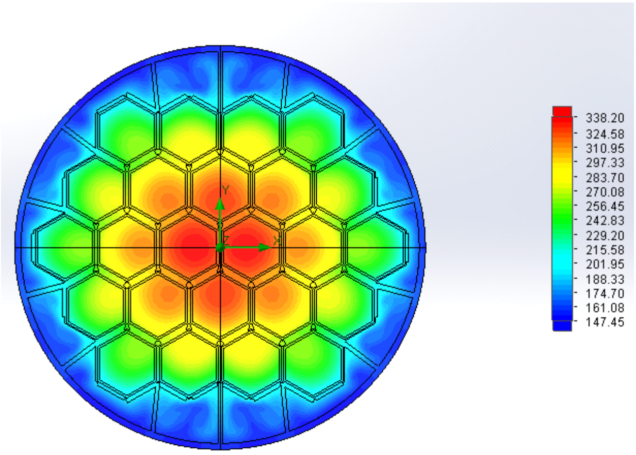

Fig. 13. Cross-section of the rotated cask XY

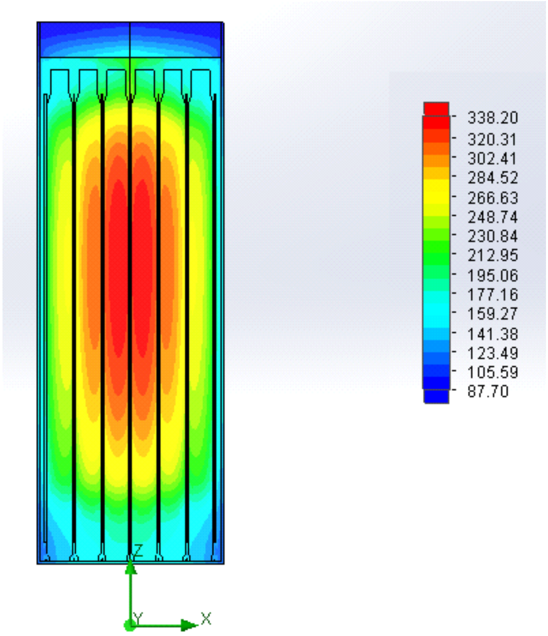

Fig. 14. Cross-section of the rotated cask XZ

For each fuel assembly the changing of the maximum temperatures during the time of storage were calculated (Fig. 15). The rate of maximum temperature decreasing is similar to the rate of the decay heat decreasing of SFA.

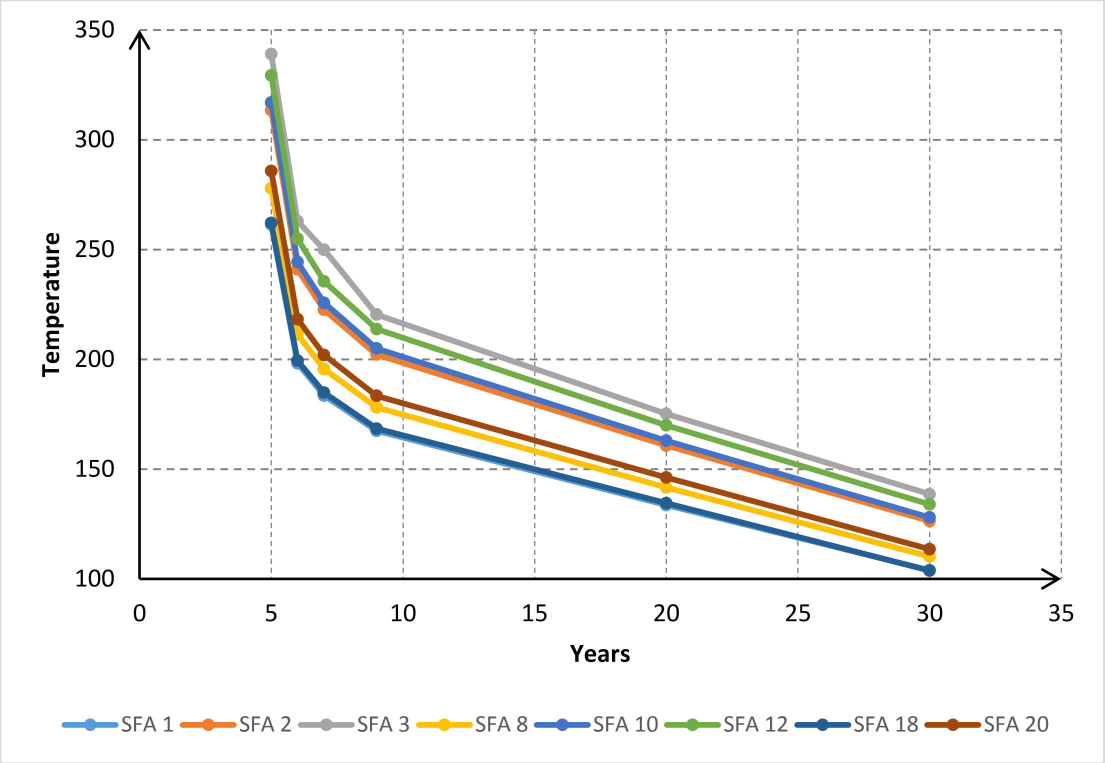

Fig. 15. Maximum temperatures in fuel assemblies during storage time

5. CONCLUSIONS

The results of this study are shown that container operation is safety, because safety criteria limit (350 ºC) wasn’t be achieved. The efficiency of using the iterative methodology in determining the thermal state of the SNF container was demonstrated. The maximum temperatures of each fuel assembly and their dependence on storage time are determined. In the course of thermal modeling, the most effective, from the viewpoint of reducing the temperature level, the location of the SNF cask relative to the input channels is determined.

The results can be used to justify the safety of SNF storage in ventilated storage containers of Zaporizhzhya NPP.

REFERENCES

1. Spent Fuel Reprocessing Options. IAEA-TECDOC-1587. 2008. 144 p.
2. Wataru M., Takeda H., Shirai K., Saegusa T. Thermal hydraulic analysis compared with tests of full-scale concrete casks. *Nuclear Engineering and Design* 2008; 238: 1213–1219, DOI: 10.1016/j.nucengdes.2007.03.036 .
3. Ju-Chan Lee, Kyung-Sik Bang, Ki-Seog Seo, Ho-Dong Kim Thermal analysis of a storage cask for 24 spent PWR fuel assemblies. Packaging, Transport, Storage & Security of Radioactive Material 2005. V.16, I.1. – P. 19–26. DOI: 10.1179/174650905775295611 .
4. H. Yamakawa, M. Wataru, Y. Kouno, T. Saegusa Demonstration test for a shipping cask transport high burn-up spent fuel. Thermal test and analyses.
5. Alyokhina S. Simulation of thermal state of containers with spent nuclear fuel: multistage approach / S. Alyokhina, V. Goloshchapov, A. Kostikov, Yu. Matsevity // International Journal of Energy Research. – 2015. – V. 39, Iss. 14, Nov. – P. 1917–1924, DOI: 10.1002/er.3387 .

CYSENI 2018, May 23-25, Kaunas, Lithuania
ISSN 1822-7554, www.cyseni.com

CALCULATING THE CORRECTION CROSS SECTION FUNCTION OF NON 1/V NUCLEI IN COLD NEUTRON BEAM MEASUREMENTS

Zs. Tóth
Budapest University of Technology and Economics
Budapest 1111 – Hungary
Email: toth.zsofia@eszk.org

ABSTRACT

The cross section function of some nuclei is one of the most important property we have to determine while characterizing nuclear reactions. At thermal or lower neutron energy regions it can be said many times that the reaction cross section of a nucleus is inversely proportional with the velocity of the neutron. These nuclei are the so called one over v (1/v) nuclei. For some medium heavy or heavy nuclei where the density of resonances is high there can be differences considering the cross section values compared to 1/v nuclei. When this difference is not considered there can be a big error in calculations using cross section data as it was a 1/v nuclei. Therefore refining the cross section data of non 1/v nuclei is especially important task.

Determining the radiative neutron capture cross section of 1/v nuclei can be done by measuring the reaction rate with not knowing the shape of neutron flux. In this case we can provide the cross section at any neutron energy value as long as the energy dispersion of the neutron beam is in the 1/v scope. For non 1/v nuclei this method does not give us the correct values so the calculating procedure has to be modified.

The main goal of this research is to elaborate a possibly analytical correction factor with which the cross section data provided with 1/v assumption from the experiments at the Research Reactor of Budapest can be revised for non 1/v nuclei. The obtained corrected cross section values will not be independent from the used differential values measured by others, but it can be applied as an integral benchmark value. The method is especially useful to check the presence and to test the shape of negative resonances, but it is also useful for checking the low energy shape of resonaces close to the neutron binding energy.

While making the calculations for Co-59, Rh-103, Cd-113, Sm-154, Gd-155, Gd-157, Er-167, Lu-175 and Am-241 the correction function was modeled with a polynom that was defined with least squares fitting. In all cases quadratic or linear polynoms were fitted precisely on the points. The correction functions were defined by Taylor series expansion as well. The result of this method gave the same outcome as the fitting so it confirms the results.

Keywords: subthermal neutron cross section, cold neutron beam, integral experiment, comparator method

CYSENI 2018, May 23-25, Kaunas, Lithuania
ISSN 1822-7554, www.cyseni.com

THE USE OF THERMAL PLASMA FOR THE TREATMENT OF SOIL CONTAMINATED BY PETROLEUM HYDROCARBONS

D. Gimžauskaitė, A. Tamošiūnas, M. Aikas, R. Uscila
Lithuanian Energy Institute
Breslaujos str. 3, LT-44403 Kaunas – Lithuania
Email: Dovile.Gimzauskaite@lei.lt

J. Samosionokas
Public Agency "Soil remediation technologies"
Antakalnio str. 42, LT-10304 Vilnius – Lithuania

ABSTRACT

One of the serious environmental problems is soil contamination by petroleum hydrocarbons, which have adverse effect on living organisms. The application of plasma technologies for soil treatment has a great potential because there is no special requirement for the pre-treatment of the raw soil, the remediation process is fast and any additional materials are not needed. Therefore, the aim of this research was to investigate thermal air and water vapor plasmas suitability to remediate soil polluted by petroleum hydrocarbons. Thus, changes of the contaminated soil were investigated before and after interaction with thermal air plasma or thermal water vapor plasma using scanning electron microscopy (SEM), energy dispersive X-ray spectroscopy (EDS). Also, during the interaction between polluted soil and thermal plasmas, measurements were performed using a gas analyser. Results obtained with SEM indicated that interaction of contaminated soil with thermal air plasma or water vapor plasma led to insignificant structural transformations of soil. EDS data showed reduction of carbon content after the soil treatment with thermal plasmas. Furthermore, the measurements of gas phase changes revealed thermal air plasma as well as water vapor plasma suitability to remediate contaminated soil. Moreover, measurements taken with gas analyser specified thermal water vapor plasma appropriateness to generate by-product – synthesis gas (H_2+CO).

Keywords: thermal plasma, petroleum hydrocarbons, soil treatment

1. INTRODUCTION

Environmental pollution associated with petroleum hydrocarbons has been recognized as a globally significant issue. Essentially, petroleum hydrocarbons including crude oil, gasoline, diesel, lubricants can be released to the environment through accidents, managed spills, or as unintended by-products of industrial, commercial or private actions, hereby causing local and diffuse pollution to the environment (e.g. soil, surface water, groundwater), health risks to wildlife and humans [1, 2]. Therefore, the remediation of soil contaminated by petroleum hydrocarbons is crucial. Many alternatives such as thermal, biological, physical, chemical processes are available for the remediation of hydrocarbon contamination in soils [3–5]. Moreover, Advanced Oxidation Processes (AOPs) have been received great emphasis on pollution control because of its ability to oxidize organic contaminants deeply and rapidly. AOPs constitute a family of similar technologies including heterogeneous and homogeneous photocatalysis, Fenton and Fenton-like processes, ozonation, the use of microwaves, electrochemical processes, wet oxidation processes. Furthermore, among the AOPs, the non-thermal plasmas (NTPs) are regarded as highly competitive technologies for the removal of organic pollutants [6–10]. For instance, Redolfi et al. [11] used dielectric barrier discharge (DBD) plasma for the remediation of soil contaminated by kerosene, Mu et al. [12] used DBD plasma to treat soil polluted with pyrene. In both cases, the high degradation efficiency of the pollutants were obtained (~90% and ~76%, respectively). Moreover, plasma technologies are based on the production of very reactive radicals, such as ·O, ·OH and ·H. The type of reactive radicals, which are responsible for the initiation and propagation of plasma chemical reactions, are closely correlated to the type of plasma forming gas [13]. Consequently, the soil remediation performance can be affected by the type of plasma forming gas (e.g. oxygen, air, water vapor). Taking that into acount, the aim of this research was to investigate thermal air and water vapor plasmas suitability to remediate soil polluted by petroleum hydrocarbons.

2. METHODOLOGY

A schematic view of the plasma-chemical reactor used for the treatment of the soil contaminated by petroleum hydrocarbons is shown in Fig. 1. Before the interaction with air or water vapor plasma, soil samples were dried in air at room temperature. The treatment of the contaminated soil with different type of plasma was performed under atmospheric pressure for approximately 30 minutes. Water vapor was generated using 5 bar of pressure water steam generator GAK-50 [14]. The power of the plasma torch was 56 kW and water vapor flow rate was 3.8 g/s. The operating temperature of proposed plasma system was ~ 2800 K. When air was used as a plasma forming gas, the power of the plasma torch and air flow rate was equal to 52.8 kW and 4.9 g/s, respectively. The operating temperature of air plasma system was ~ 2400 K.

Soil characterization was done before and after interaction with air plasma, or water vapor plasma. A scanning electron microscope (SEM, Hitachi S-3400N) was used to investigate surface morphology of the contaminated and plasma treated soil. Energy dispersive X-ray spectroscopy (EDX, Bruker Quad 0540) was employed to determine and compare soil elemental composition before and after remediation process. Multi-component gas analyser (MRU, SWG 300) was used to measure gas concentrations which were obtained during the reactions between soil contaminated by petroleum hydrocarbons and plasma.

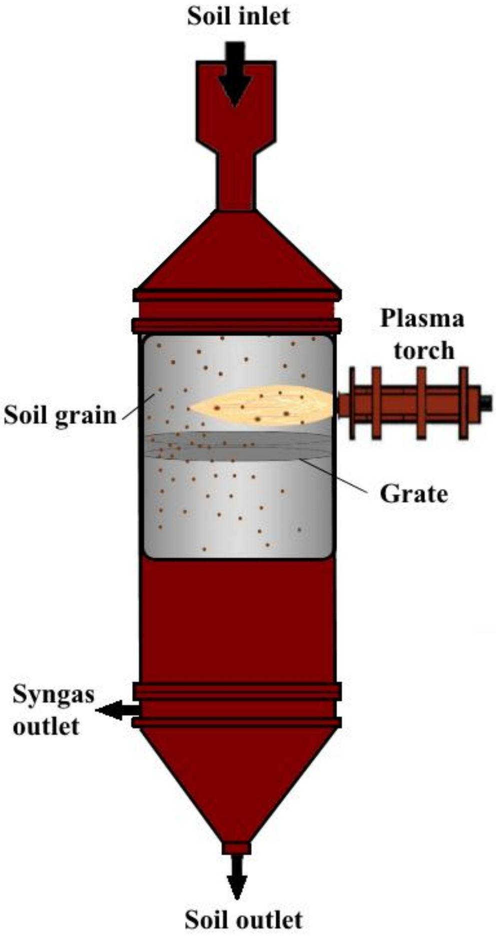

Fig. 1. A simplified scheme of plasma-chemical reactor

3. RESULTS AND DISCUSSION

3.1. SEM analysis of contaminated soil

Surface morphology of untreated and plasma treated soil was investigated by scanning electron microscope (Fig. 2). Soil polluted by petroleum hydrocarbons (Fig. 2 a), b)) has non-uniform, relatively rough surface. Views of soil treated with air plasma (Fig. 2 c), d)) show morphologically insignificant changes, soil consists of similar irregularly-shaped agglomerates with relatively smoother surface. Moreover, after interaction between polluted soil and water vapor plasma, soil surface became slightly altered with better expressed non-uniform agglomerates (Fig. 2 e), f)).

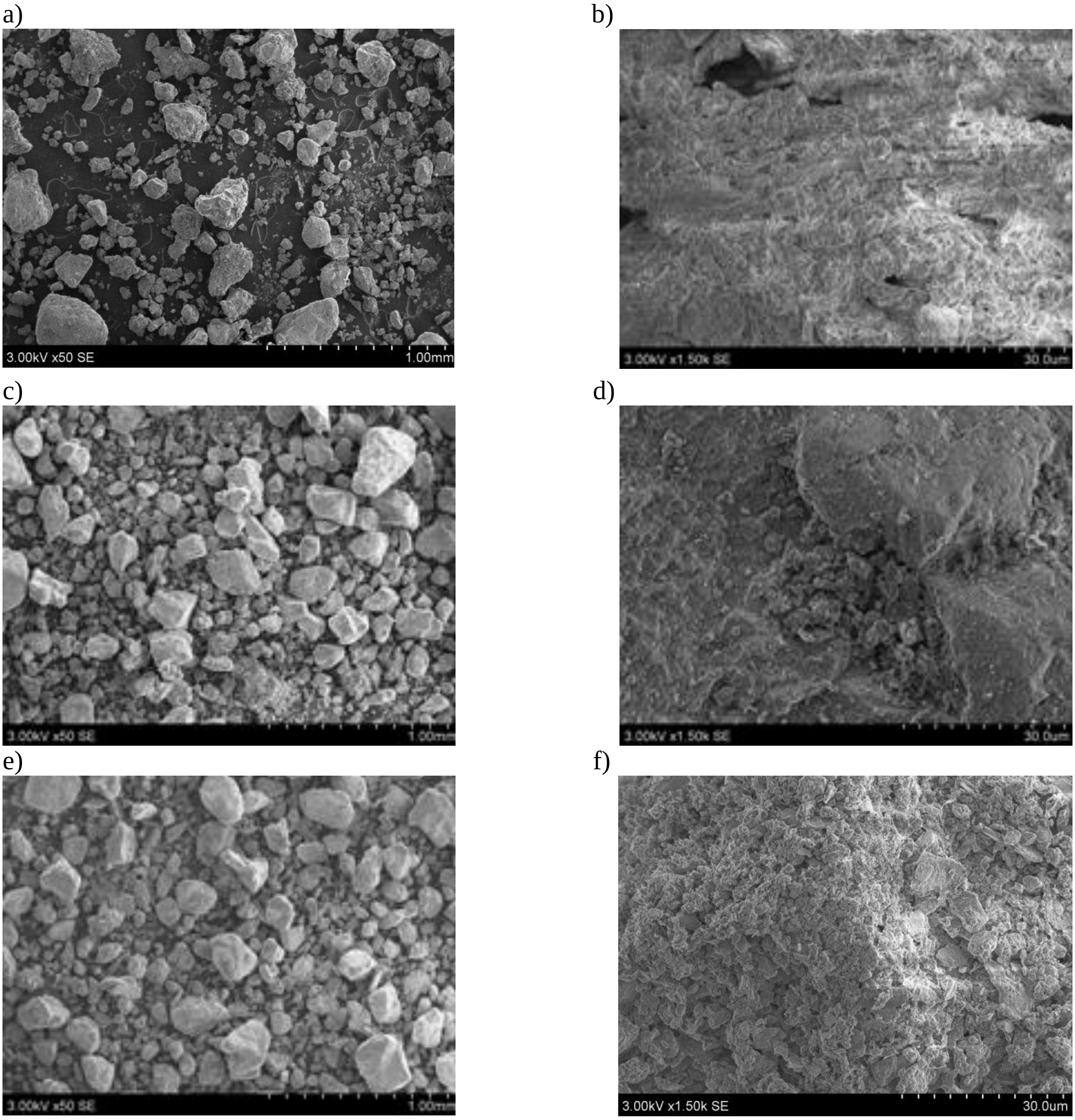

Fig. 2. SEM surface views of soil: a), b) – soil contaminated by petroleum hydrocarbons, c), d) – soil treated with air plasma, e), f) – soil treated with water vapor plasma

3.2. EDS analysis of contaminated soil

Elemental composition of soil before and after interaction with air plasma and water vapor plasma is summerised in Table 1. Untreated soil consisted of 20.82% of carbon, while after treatment with air plasma or water vapor plasma carbon content notably decreased to 3.53% and 7.22%, respectively. Hereby, soil treated with plasma showed significant change in carbon concentrations allowing to assume that during the treatment process conversion of petroleum hydrocarbons took place. Additionaly, it was found that content of soil minerals (K, Ca, Mg, Al, Fe, Na, Ti, S) remained unchanged during the treatment process. Obtained results can be explained by the fact that most of the minerals presented in soil not volatilize, hence remain unaltered [15].

Table 1. Elemental composition of soil

	Untreated soil	**Soil treated with air plasma**	**Soil treated with water vapor plasma**
Element	**Concentration, at %**	**Concentration, at %**	**Concentration, at %**
C	20.82	3.53	7.22
O	58.61	64.78	59.07
Si	10.09	21.87	22.11
K	0.76	1.08	1.34
Ca	4.83	3.81	4.88
Mg	0.59	0.54	0.9
Al	2.94	3.10	3.23
Fe	0.81	0.71	0.79
Na	0.18	0.17	0.26
Ti	0.16	0.21	0.20
S	0.21	0.22	not detected

3.3. Gas analyser results

Changes of gas concentration extracted during interaction between contaminated soil and air plasma is shown in Fig. 3. Apparently, while oxygen content decreased from 20.96% to 4.93%, carbon-based materials (petroleum hydrocarbons from contaminated soil) mainly transformed to gaseous compounds including CO_2, CO and H_2. During the peak of the oxidation process the concentrations of the CO_2, CO and H_2 achieved 12.17%, 0.42% and 0.36%, respectively (Fig. 3 a)). Hence, traces of the syngas (H_2+CO) formation were noticed. Moreover, small amounts of NO (0.21%), NO_2 (0.05%), SO_2 (0.001%) and C_3H_8 (0.002%) were observed (Fig. 3 b)).

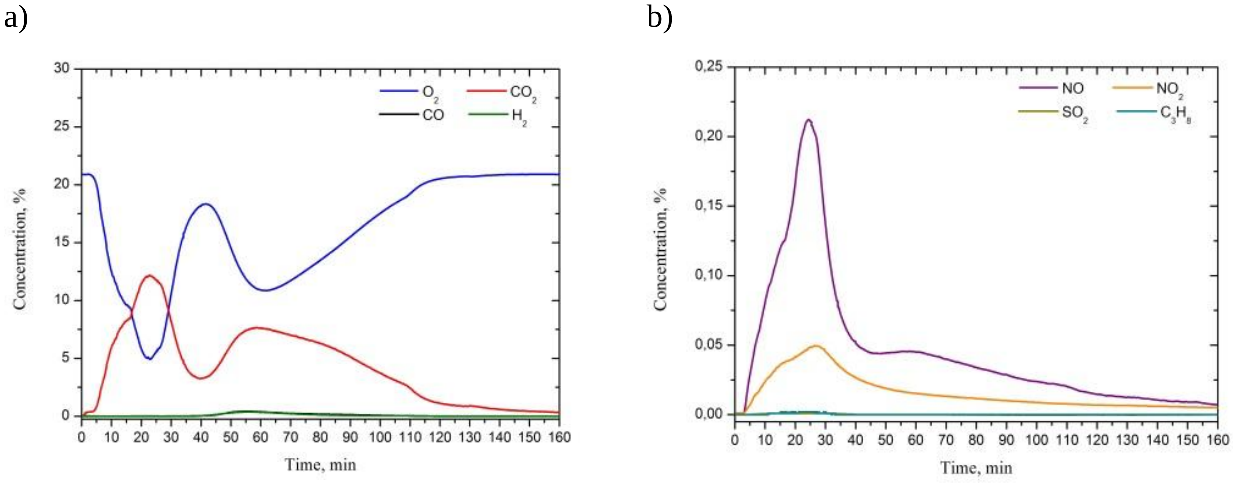

Fig. 3. Gas concentrations extracted during interaction between polluted soil and air plasma

Fig. 4 illustrates gas concentration changes during interaction between contaminated soil and water vapor plasma. Significant decrease in oxygen (from 20.96% to 1.74%) and formation of the syngas (H_2 + CO) were obtained. In this context, up to 37.49% of the hydrogen and 9.17% of the CO were extracted. Moreover, formation of CO_2 (up to 16.52%) and small amounts of NO (0.51%), NO_2 (0.05%,), SO_2 (0.07%) and C_3H_8 (0.27%) were recorded.

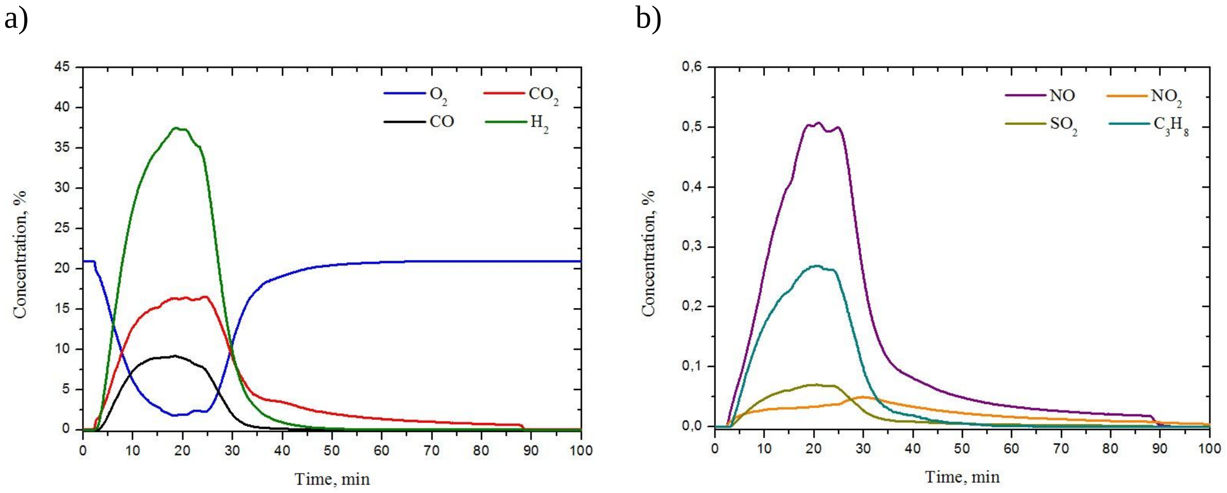

Fig. 4. Gas concentrations extracted during interaction between polluted soil and water vapor plasma

Furthermore, the comparison of soil treatment with air plasma and water vapor plasma reveals that the use of the water vapor plasma is more beneficial due to the formation of the higher amount of the syngas. Such trend is observed due to the fact that during the formation of the water vapor plasma, ·OH and ·H radicals are obtained and these radicals are significantly more reactive than ·O radicals produced during the formation of the air plasma. Thus, generation of ·OH and ·H radicals leads to more intensive decomposition of the petroleum hydrocarbons as well as higher production of the syngas. Consequently, remediation performance of plasma technology can be significantly affected by the type of plasma forming gas.

In addition, produced syngas can be used as fuel in combustion systems, or for generation of electricity, also syngas can be transformed by methanol synthesis or the Fischer Tropsch process into liquid fuels, suitable for transportation [16, 17]. Such possible ways of using syngas, as well as complete treatment of the petroleum hydrocarbons in the soil, makes to consider the possibilities of wider use of plasma technologies for this purpose.

4. CONCLUSIONS

Insignificant soil surface morphology changes were observed by scanning electron microscope (SEM) after treatment with air plasma and water vapor plasma. All soil samples were composed of non-uniform agglomerated particles.

Measurements performed by energy dispersive X-ray spectroscopy (EDS) indicated that carbon content in the soil contaminated by petroleum hydrocarbons was equal to 20.82%. Furthermore, after soil treatment with air plasma and water vapor plasma, carbon content in the soil reduced to 3.53% and 7.22%, respectively. Also, EDS revealed that content of soil minerals (K, Ca, Mg, Al, Fe, Na, Ti, S) remained unchanged during the treatment process.

Measurements performed by gas analyser showed air plasma and water vapor plasma abilities to remediate soil contaminated by petroleum hydrocarbons. Furthermore, the comparison of soil remediation with air plasma and water vapor plasma speficied that the use of the water vapor plasma is more beneficial due to the formation of the higher amount of the syngas. Also, it was revealed that treatment performance of plasma technology depends on the type of plasma forming gas.

ACKNOWLEDGEMENTS

The authors are grateful to Dr. D. Milčius, the Head of Hydrogen Technologies Centre, for the experimental facilities used to perform this work, Dr. S. Tučkutė for the help to perform structural characterization of resultant materials.

REFERENCES

1. PARK, I. S., PARK, J. W. Determination of a risk management primer at petroleum-contaminated sites: Developing new human health risk assessment. *Journal of Hazardous Materials*, 2011, Vol. 185, p. 1374–1380.
2. NG, W., MALONE, B. P., MINASNY, B. Rapid assessment of petroleum-contaminated soils with infrared spectroscopy. *Geoderma*, 2017, Vol. 289, p. 150–160.
3. FERNANDEZ, E. L., MERLO, E. M., MAYOR, L. R., CAMACHO, J. V. Kinetic modelling of a diesel-polluted clayey soil bioremediation process. *Science of the Total Environment*, 2016, Vol. 557–558, p. 276–284.
4. O'BRIEN, P. L., DESUTTER, T. M., CASEY, F. X. M., KHAN, E., WICK, A. F. Thermal remediation alters soil properties e a review. *Journal of Environmental Management*, 2018, Vol. 206, p. 826–835.
5. LIM, M. W., LAU, E. V., POH, P. E. A comprehensive guide of remediation technologies for oil contaminated soil – Present works and future directions. *Marine Pollution Bulletin*, 2016, Vol. 109, p. 14–45.
6. WANG, T., QU, G., SUN, Q., LIANG, D., HU, S. Formation and roles of hydrogen peroxide during soil remediation by direct multi-channel pulsed corona discharge in soil. *Separation and Purification Technology*, 2015, Vol. 147, p. 17–23.
7. GENG, C., WU, C., WANG, H., YI, C. Effect of chemical parameters on pyrene degradation in soil in a pulsed discharge plasma system. *Journal of Electrostatics*, 2015, Vol. 73, p. 38–42.
8. AGGELOPOULOS, C.A., SVARNAS, P., KLAPA, M.I., TSAKIROGLOU, C.D. Dielectric barrier discharge plasma used as a means for the remediation of soils contaminated by non-aqueous phase liquids. *Chemical Engineering Journal*, 2015, Vol. 270, p. 428–436.
9. QU, G. Z., LU, N., LI, J., WU, Y., LI, G. F., LI, D. Simulataneous pentachlorophenol decomposition and granular activated carbon regeneration assisted by dielectric barrier discharge plasma. *Journal of Hazardous Materials*, 2009, Vol. 172, p. 472–478.
10. DEWIL, R., MANTZAVINOS, D., POULIOS, I., RODRIGO, M. A. New perspectives for Advanced Oxidation Processes. *Journal of Environmental Management*, 2017, Vol. 195, p. 93–99.
11. REDOLFI, M., MAKHLOUFI, C., OGNIER, S., CAVADIAS, S. Oxidation of kerosene components in a soil matrix by a dielectric barrier discharge reactor. *Process Safety and Environmental Protection*, 2010, Vol. 88, p. 207–212.
12. MU, R., Liu, Y., Li, R., Xue, G., Ognier, S. Remediation of pyrene-contaminated soil by active species generated from flat-plate dielectric barrier discharge. *Chemical Engineering Journal*, 2016, Vol. 296, p. 356–65.
13. ZHANG, H., MA, D., QUI, R., TANG, Y., DU, C. Non-thermal plasma technology for organic contaminated soil remediation: A review. *Chemical Engineering Journal*, 2017, Vol. 313, p. 157–170.
14. TAMOŠIŪNAS, A., VALATKEVIČIUS, P., GRIGAITIENĖ, V., VALINČIUS, V. Water Vapor Plasma Torch: Design, Characteristics and Applications. *World Academy of Science, Engineering and Technology*, 2012, Vol. 6, p. 10–13.

15. SNELLINGS, R., MERTENS, G., ELSEN, J. Supplementary Cementitious Materials. *Reviews in Mineralogy & Geochemistry*, 2012, Vol. 74, p. 211–278.
16. SANLISOY, A., CARPINLIOGLU, M. O. A review on plasma gasification for solid waste disposal. *International Journal of Hydrogen Energy*, 2017, Vol. 42, p. 1361–1365.
17. YUS, M., SOLER, J., HERGUIDO, J., MENENDEZ, M. Glycerol steam reforming with low steam/glycerol ratio in a two-zone fluidized bed reactor. *Catalysis Today*, 2018, Vol. 299, p. 317–327.

CYSENI 2018, May 23-25, Kaunas, Lithuania
ISSN 1822-7554, www.cyseni.com

NUMERICAL MODELLING OF PLASMA REACTOR FOR GASIFICATION OF WASTES WITH PREDOMINANT ORGANIC PART

A. Liavonchyk, D. Morozov, V. Sauchyn, H. Dalholenka
A. V. Luikov Heat and Mass Transfer Institute
P. Brovka str. 15, 220072 Minsk – Belarus
Email: ita1661@gmail.com

ABSTRACT

Plasma gasification is a perspective method of waste treatment. Combined thermolysis-plasma facility was designed in the A. V. Luikov Heat and Mass Transfer Institute to treat wastes with the predominant organic part. The aim of this work was to develop a numerical model of the plasma reactor which can help to find optimum parameters of the treatment process for different regimes. For this purpose 3D CFD-model of the plasma reactor was developed. Stationary Navier-Stokes equations averaged over Reynolds closed with the help of the turbulence model k-ω SST, the continuity and the energy equations were solved. The problem was conjugate, taking into account the heat transfer through the internal steel walls. Radiation model was P1, physical properties were set depended on pressure and temperature. ANSYS Fluent 18.2 was used to solve the problem.

Warm-up mode and model mixture (23.4 CO_2 + 2 C_6N_6 + 3 C_4H_6) conversion mode of the reactor were considered to determine the effect of a number of parameters (radiation influence, soot fornation, its interaction with radiation, heat losses). Experimental studies of plasma gasification of wastes were carried out. Tire scrap was considered as a model material. It was previously decomposed in a thermolysis reactor in an evaporated volatile hydrocarbon fraction and solid carbon residue. Only the evaporated fraction was subjected to plasma gasification.

Comparison of calculated and experimental data showed that the model correctly describes the qualitative distribution of the temperature field over the volume of the reactor. Influence of radiation heat transfer on the temperature distribution and effect of heat loss through the side walls of the reactor on the temperature distribution and gas concentrations were shown. It was found out that soot formation and its interaction with radiation must be taken into account because of changes in distribution of temperature and CO_2 concentration. Model of soot formation during partial oxidizing of considered hydrocarbons should be improved.

The model qualitatively predicts behaviour of the reactor depending on the regime, but for quantitative prediction it should be improved.

Keywords: plasma gasification, waste treatment, syn-gas, CFD modelling

1. INTRODUCTION

Nowadays the problem of environmental pollution with antropogenic wastes becomes more and more sufficient. A significant part of wastes contains a predominant organic part. Municipal solid wastes (MSW), agricultural, industrial, wooden wastes can be included in this list. Incineration, gasification and pyrolysis are widely used for their utilization. High-temperature processing, in particular plasma gasification [1–5], is a promising environmentally safe alternative to traditional methods of producing syn-gas as the final product. In this paper, we studied the plasma part of a combined thermolysis-plasma facility for processing of wastes with a predominant organic part. The main advantages of using thermal plasma are precise control of the process, possibility of using various gases as a plasma-forming medium, smaller amount of exhaust gas and reduction of the amount of the ballast gases (such as nitrogen) in the product, complete destruction of complex molecules, for example dioxins, relatively small size of the facility and gas cleaning system. In addition, use of thermal plasma provides utilizing such types of waste that can not be treated by other methods, for example, Tetrapack.

Plasma technologies are also used to process hazardous waste. Some of these technologies allow to obtain a commercial by-product, some of them are intended for the complete destruction of the material. The most interesting and significant ones were considered in [6], and the economic justification for the processing of MSW by means of plasma technologies is described in [7].

Plasma reactor of a combined thermolysis-plasma plant was studied in this paper. Firstly the material to be processed is supplied in the thermolysis reactor [8, 9], where it is deconposed by means of temperature of 750–850 K into a volatile hydrocarbon component (hereinafter – evaporated fraction) and a solid residue with a high carbon content. Then, the solid and gaseous parts are processed separately, which greatly simplifies the control of the process, allows to work with materials of different fractions and obtain useful by-products with small changes in technology. The evaporated fraction is processed in the plasma reactor. However, its conversion in a plasma reactor is very difficult to observe directly. Large temperature gradients (the difference in temperature of the plasma jet and the flux of the evaporated fraction is 3500–4000 K), rapid chemical reactions, high temperatures and fluxes speed – all this creates enormous difficulties for direct observation. That is why it is convenient to use numerical simulation to study the peculiarities of the processes in such cases.

In general, numerical modeling of plasma reactors has been described in the literature. For example, modeling the propagation of a plasma jet in a reactor and mixing it with various gases was described in [3]. Simulation of the gasification of a solid particle in a PLASGAS plasma reactor was described in detail in [10, 11]. The reactor model for MSW gasification was considered in [12].

The aim of this work was to study the problem of converting a mixture of gaseous hydrocarbons into a synthesis gas under conditions of high temperatures and the presence of a large amount of CO_2 in cylindrical coaxial reactor. The results will be used in further work on such type of reactors where on the basis of the numerical modeling results optimum parameters of the process may be found.

2. REACTOR DESCRIPTION

A scheme and photo of the plasma reactor are presented in Fig. 1. The reactor is a system of three coaxial tubes made of refractory steel. In the upper part there is an input unit where initial mixing of air from the plasma torch and the processing evaporated fraction takes place. Input unit is lined inside with heat insulation. The plasma torch is attached from above in the center, evaporated fraction is supplied tangentially. The height of the reactor without the input unit is 900 mm, the diameter of the inner tube is 30 mm, of the middle one is 158 mm, of the outer one is 204 mm. The gas mixture comes from the input unit into the inner tube, runs downward along it, unfolds, rises up between the inner and middle tubes, again unfolds and descends downward between the middle and outer tubes. In the lower part, it is collected and discharged through the exhaust tube. The gas velocity in individual areas of the reactor, depending on the operation mode and power of the plasma torch, reaches 100 m/s in the area of connection of the plasma torch, then decreases to 20–40 m/s in the inner tube where the main reactions take place. In the rest of the reactor it is about 2–3 m/s.

Temperature in the reactor was measured by 6 thermocouples: 3 in the middle contour, 3 in the outer contour. The seventh thermocouple was installed near the reactor outlet and this area is not included in the model. Thermocouples were installed in the middle of the gaps between the tubes. Gas sampling was carried out at the reactor outlet. The gas passed through the filters and the cooler and thus was cleaned of soot and water. Gas concentrations were measured by gas chromatograph Agilent 7890A GC.

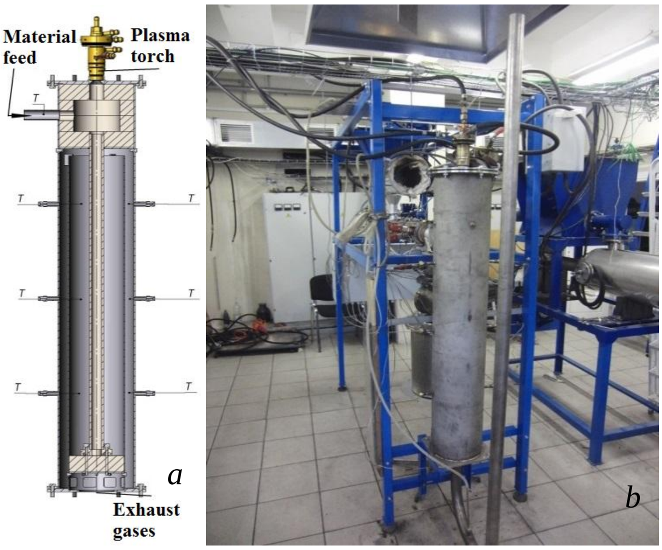

Fig. 1. Plasma reactor scheme (a) and appearance (b)

To study the reactor its 3D model of the internal volume was created. The distribution of the operating parameters (temperature, pressure, velocity field) in the plasma reactor was determined, the numerical simulation results were compared with the experimental data for further possible optimization of the reactor design. The first stage was study the reactor heating to check whether radiation is to be taken into account. Then we studied the case of model mixture conversion. Here we determined effect of soot formation, its interaction with radiation and heat losses. And finally we validated the model on the example of two compositions of the evaporated fraction.

3. NUMERICAL MODELING OF THE PLASMA REACTOR IN THE HEATING MODE

At the first stage of the modeling, it was decided to consider the process of mixing two gas streams in the reactor. For this purpose air was used as the supplied gas mixture. In addition, an important issue was to determine if radiation heat transfer should be taken into account.

In the wall-to-air system, the radiation heat transfer between air and the wall shows strong influence only in the area of the plasma torch attachment, where the gas temperature is up to 5000 K. Heat exchange between the air and the wall in the remaining volume of the reactor is predominantly convective. It must be taken into account that when the evaporated fraction is supplied into the reactor, the radiation heat transfer between the gas mixture and the wall can have a significant impact.

Simultaneously, radiation heat exchange between the walls of the reactor must not be neglected. Let us estimate the flux density radiated by the wall, according to formula

$$Q = \varepsilon\sigma T^4 \tag{1}$$

where Q is the heat flux density, ε is the blackness of the wall, σ is the Boltzmann constant, and T is the wall temperature. At $T = 1400$K and $\varepsilon = 0.7$ it is obtained $Q \sim 1.5 \cdot 10^5$ W/m^2.

Heat transfer from the wall to the gas can be estimated by finding the Nusselt number Nu by the formula for the turbulent flow (considering the twist of the gas). Taking into account flow velocities and tubes sizes, the Reynolds number Re was estimated as $1.7 \cdot 10^5$ in the inner tube, $3.3 \cdot 10^4$ in the middle tube and $1.4 \cdot 10^4$ in the outer tube. Thus, to estimate the Nusselt number, we can use the formula:

$$Nu = 0.018 \cdot Re^{0.8} \tag{2}$$

As a result of calculation we obtain $Nu \sim 3 \cdot 10^2$ for inner tube, $Nu \sim 7 \cdot 10^1$ for middle tube and $Nu \sim 4 \cdot 10^1$ for outer tube. Assuming that the air heat conductivity $\lambda \sim 10^{-2}$ W/(m·K) at 1200 K, the heat transfer coefficient $\alpha \sim 10^1–10^2$ W/(m^2·K). Thus, with a temperature difference between the wall and the air of even 10^3 K, the density of the heat flux will be of the order of $10^4–10^5$ W/m^2.

Obviously, in this case the rediation heat transfer should not be neglected. Nevertheless, numerical modeling of the temperature distribution in the reactor without taking radiation into account and taking radiation into account was carried out.

The formulation of the problem for this case was described as follows. Stationary Navier-Stokes equations averaged over the Reynolds, closed with the help of the k-ω SST turbulence model [13–15], the continuity equation, the energy equation were solved. The turbulence model was chosen on the basis of the general geometry of the system and the character of the flow (Re ~ 10^3–10^4, depending on the specific area of the reactor), since both near-wall flows and free flows away from the walls influence the solution of the problem.The thermophysical characteristics of air were set depending on temperature and pressure [16]. P1 model was used for radiation heat transfer. The task is conjugate, taking into account the heat transfer through the internal steel walls. The mesh size was $2.2 \cdot 10^6$ cells. The mesh image is shown in Fig. 2. The calculation was carried out in ANSYS Fluent 18.2.

The features of the mesh are shown in the Fig. 2. In the input unit area the cell size was set to 3 mm, in the inner tube – 3 mm, in the lower part of the middle tube – 1 mm. The boundary layer was along the inner surface of the inner tube was taken into account. The size of the cells in the remaining area was 5–10 mm. The increase in the number of cells to 12.7 million did not show any significant differences in the results of numerical simulation (the difference in temperatures was not more than 2%), but it took much more time.

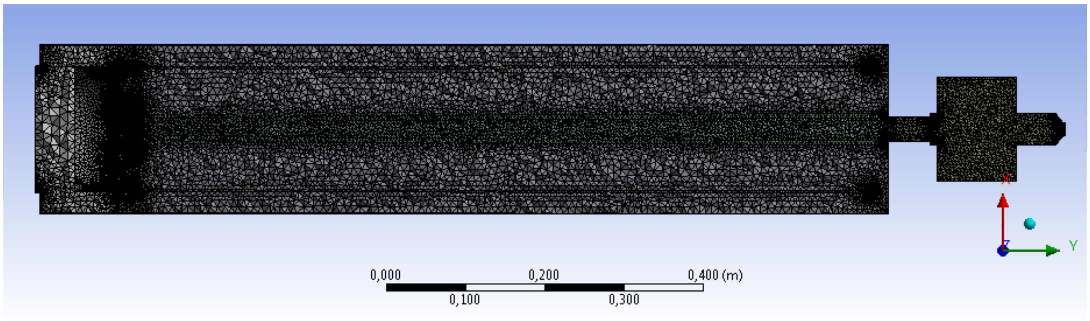

Fig. 2. Mesh used for numerical modelling

The following boundary conditions were set for this case. Air was supplied at the input of the plasma torch at a rate of 1 g/s with pressure of 150 kPa and temperature of 4100 K. The flow was twisted, the ratio of the axial component to the tangential component was 10:1. Air was also supplied to the material inlet. Its flow rate was 4.8 g/s, pressure was 101 kPa and temperature was 470 K. The feed was perpendicular to the input plane. The pressure at the reactor outlet was 100.9 kPa, the temperature was 300 K. The heat losses were simulated by setting the heat flow through the side wall of the reactor with a density of 3 kW/m^2.

Modeling results for cases with radiation and without radiation and the experimental data are shown in Fig. 3. As it can be seen taking into account radiation heat transfer leads to redistribution of the temperature inside the reactor, the inner part remaining more heated than the middle and outer ones. The differences in the experiment and numerical simulation can be explained by the errors in estimating the grayness coefficient for the walls at high temperatures and by setting the uniform heat flux outward along the entire lateral surface. In addition, the properties of the walls are given independent on temperature.

It should be noted that the temperature difference between the upper and lower part is consistent with the simulation data, i.e. qualitative picture of calculation and experiment converges.

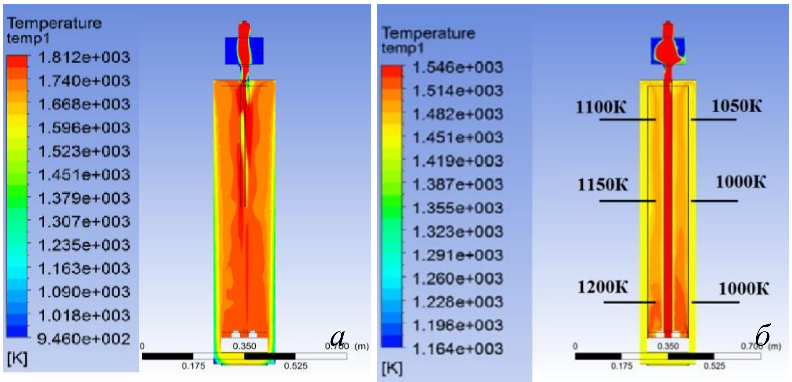

Fig. 3. Temperature distribution without radiation (a) and with radiation heat transfer (b). Numbers perform experimental data

4. NUMERICAL MODELING OF THE CONVERSION OF A MODEL MIXTURE

The next step was modeling the conversion of the model mixture in the reactor. As a first approximation, a mixture of 23.4 CO_2 + 2 C_6H_6 + 3 C_4H_6 was used. Composition was selected on the basis of elemental ratio of the evaporated phase C : H = 4 : 5. Real composition contained more than 200 substances of different types (benzenes, unsaturated hydrocarbons, etc) and it was too difficult to include all of them into the model. CO_2 was used as a transport gas and additional oxidizer.

Effect of the following factors on the results of numerical modeling was evaluated: soot formation, its interaction with radiation, heat loss through the side wall of the reactor.

The following boundary conditions were set. Air was supplied at the input of the plasma torch at a rate of 1 g/s with pressure of 150 kPa and temperature of 4100 K. The flow was twisted, the ratio of the axial component to the tangential component was 10:1. A model mixture of the composition 23.4 CO_2 + 2 C_6H_6 + 3 C_4H_6 was supplied normal to the boundary through the material input. Its flow rate was 1.5 g/s at a pressure of 101 kPa and a temperature of 720 K.

The density of heat flow through the side wall of the reactor was set of 5 kW/m^2, which corresponds to the experimentally obtained estimations. Non-premixed combustion model was used to describe the conversion.

Effect of soot formation and its interaction with radiation was evaluated. To show the effects modeling was carried out for three cases: without soot formation, with soot formation and with its interaction with radiation and with soot formation without its interaction with radiation. Moss-Brookes model [17] was chosen for soot formation model since it most fully describes the process of soot formation in the combustion of hydrocarbons. But it should be noted that all available models were developed and tested for complete combustion of hydrocarbons, and in this paper partial oxidation is considered. This can introduce some error in the model.

The modeling results for all three cases are shown in Figs. 4–7.

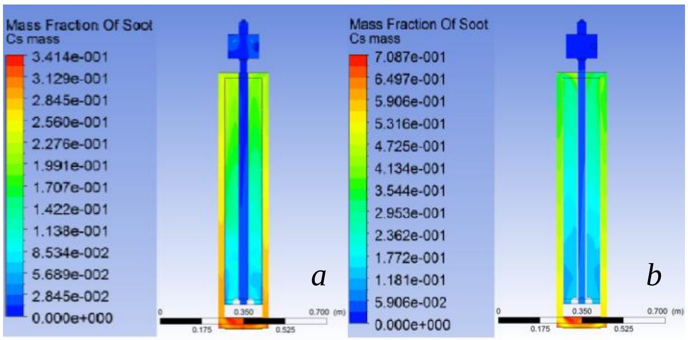

Fig. 4. Mass fraction of soot in case of soot interaction with radiation (a) and without its interaction with radiation (b)

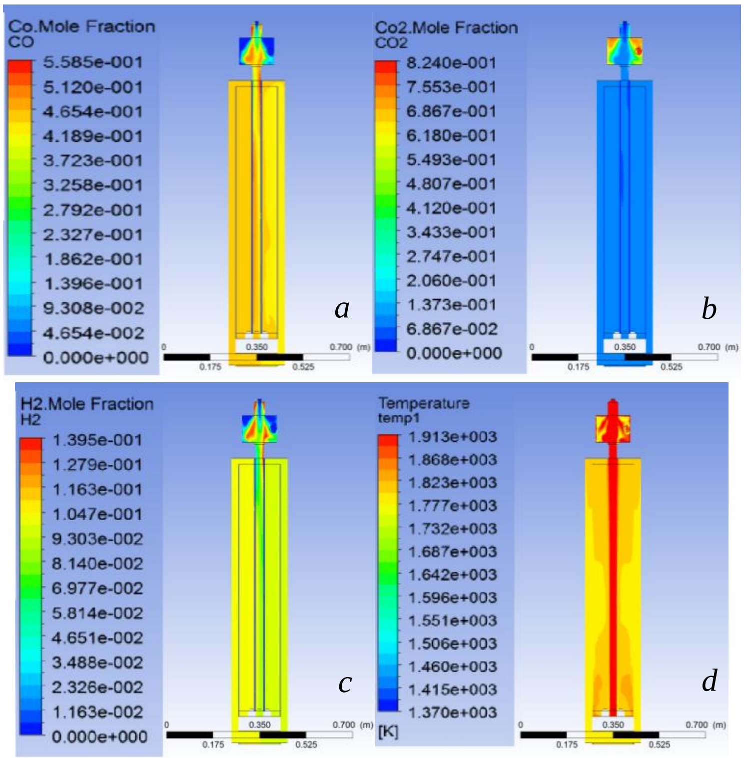

Fig. 5. Concentrations of CO (a), CO_2 (b), H_2 (c) and temperature distribution without soot formation (d)

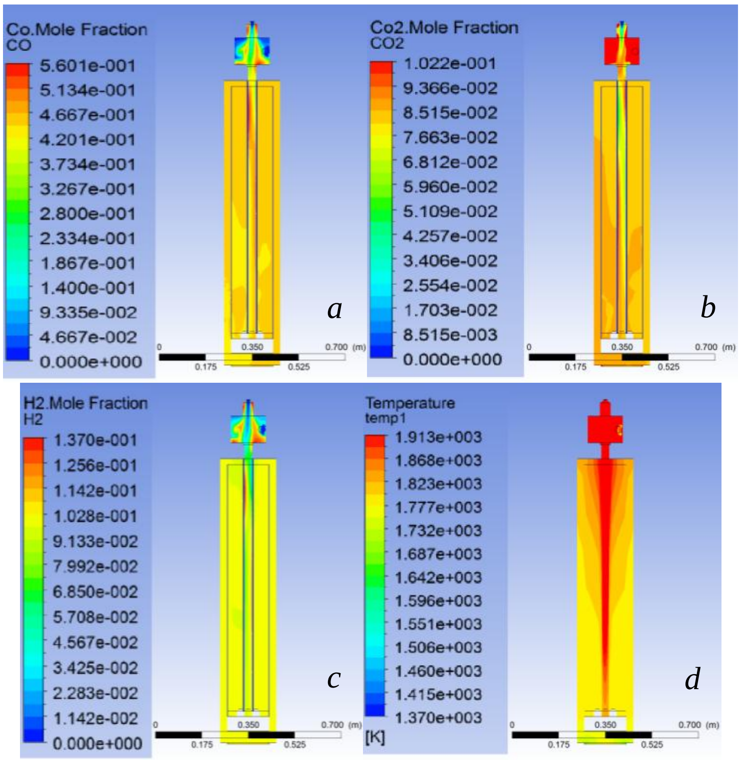

Fig. 6. Concentrations of CO (a), CO_2 (b), H_2 (c) and temperature distribution with soot formation and its interaction with radiation (d)

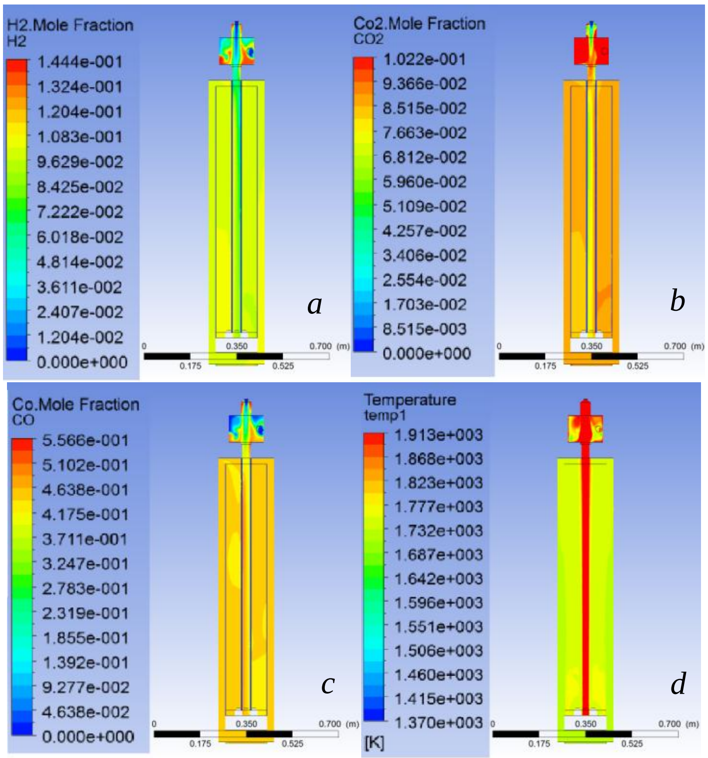

Fig. 7. Concentrations of CO (a), CO_2 (b), H_2 (c) and temperature distribution with soot formation without its interaction with radiation (d)

If we compare the results, it is seen that taking into account soot formation with its interaction with radiation significantly changes the temperature distribution in the reactor. Soot formation changes CO_2 concentration and its interaction with radiation changes temperature distribution in the upper part of the reactor. When the interaction of soot with radiation is considered, its mass fraction significantly changes. It is worth paying attention that in the upper part soot is heated due to radiation and it results in change of the temperature distribution.

Based on the results of numerical modeling interaction of radiation with soot should not be neglected. It was proven in the experiments that the picture of the temperature distribution in the reactor qualitatively corresponds to the case with soot formation and its interaction with radiation.

The effect of heat losses through the side wall on the temperature distribution and the mass fraction of soot in the reactor was estimated. The results of the simulation are shown in Fig. 8.

It can be seen from the figures obtained that when the interaction of soot with radiation is taken into account, its amount varies insignificantly, and the temperature becomes higher in the upper part of the middle and outer contours as the heat flow increases outside.

To test the model, experiments were carried out for the conversion of the evaporated fraction in the reactor. Two cases were tested: the conversion of the gas mixture with CO_2 and the conversion of the mixture with CO_2 and H_2O. In the experiment, the mixture was fed with the same elemental composition as in the model. Mass and heat fluxes and temperatures were as specified in the modeling.

The results of measuring the temperature and comparing the obtained gas concentrations with the calculated ones are presented in Fig. 9 and Fig. 10. The numbers in the figures show experimentally obtained temperatures.

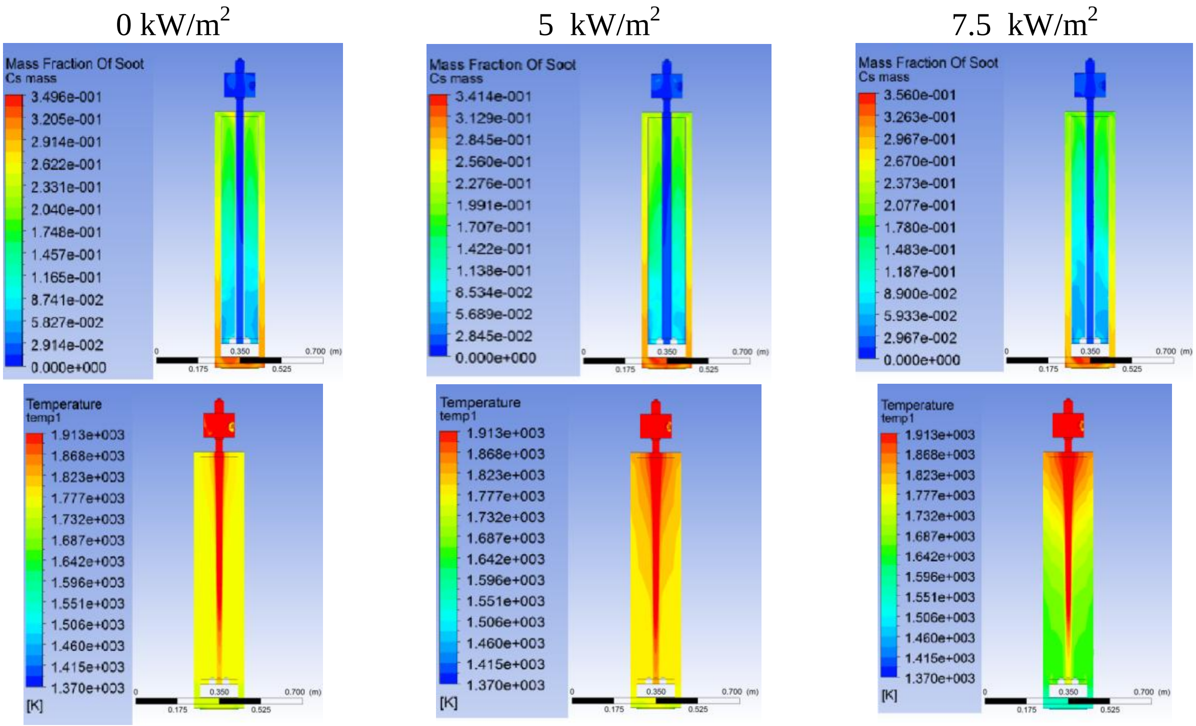

Fig. 8. Mass fraction of soot and temperature distribution for different heat losses

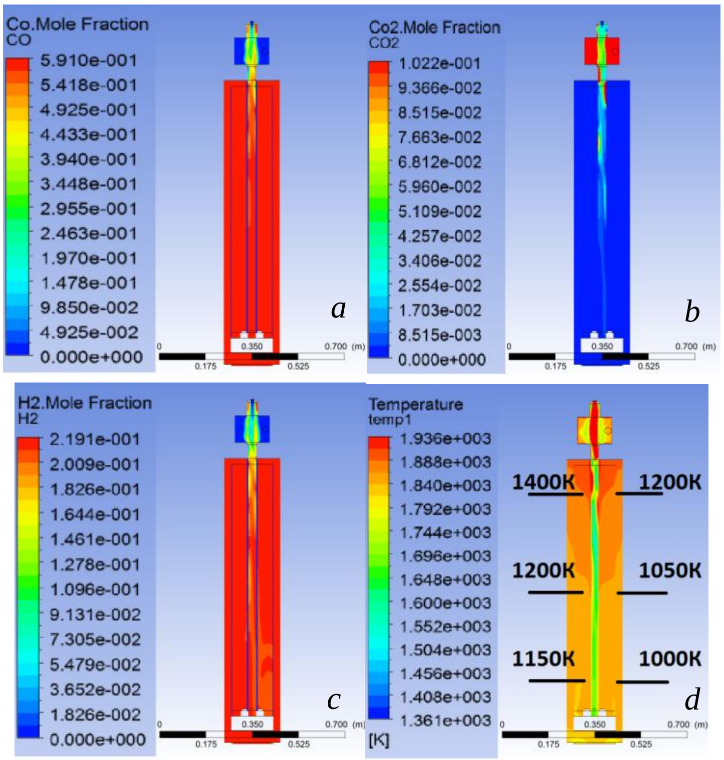

Fig. 9. Concentrations of CO (a), CO_2 (b), H_2 (c) and temperature distribution with CO_2 addition (d)

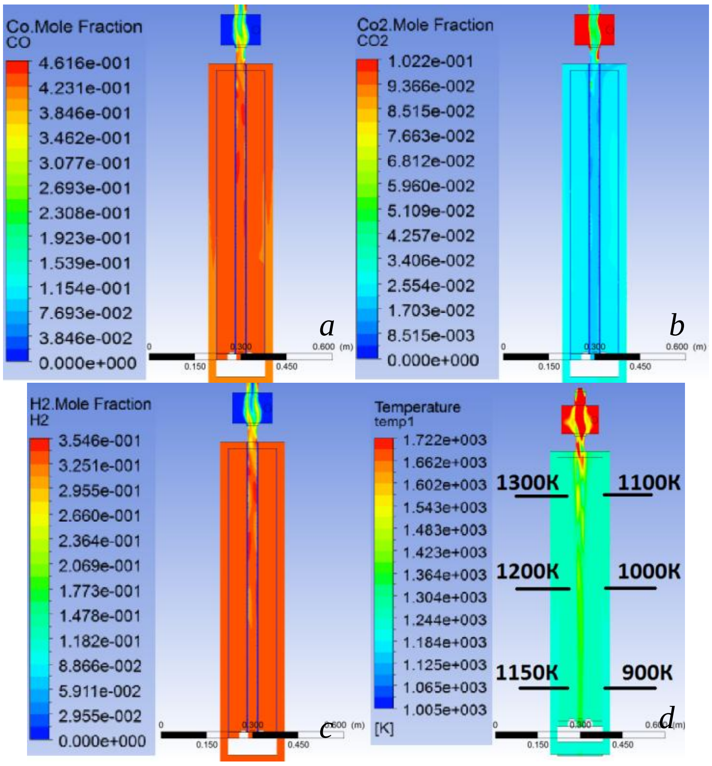

Fig. 10. Concentrations of CO (a), CO_2 (b), H_2 (c) and temperature distribution with CO_2 and H_2O addition (d)

Table 1 shows the results of analyzes of the resulting gas mixture.

Table 1. Gas concentrations

Gas	**CO_2**		**CO_2+H_2O**	
	Exp., % vol	**Calc., % vol**	**Exp., % vol**	**Calc., % vol**
H_2	13.4	21.0	23.0	33.5
C_6H_{14}	0.6	0.0	0.7	0.0
CH_4	5.1	0.4	5.8	1.0
C_2H_6	0.1	0.0	0.1	0.0
C_2H_4	2.2	0.0	2.4	0.0
CO_2	29.0	11.0	18.7	7.5
C_3H_6	0.2	0.0	0.1	0.0
N_2	26.1	23.4	27.4	21.5
C_3H_4	0.3	0.0	0.3	0.0
CO	21.7	44.2	20.2	36.5
Other gases	1.2	0.0	1.1	0.0
Total	100.0	100.0	100.0	100.0
Lower heating value, MJ/m^3	12.7	18.2	13.5	16.8

Comparing the experimental results with the calculated ones, a significant discrepancy can be noticed. In particular, a much larger amount of CO_2 was produced in the experiment. Estimating the concentration of other gases, especially hydrogen, it can be assumed that the main reason for this is the deposition of soot in the reactor with simultaneous CO combustion. It can be explained by much more complicated composition of the gas mixture supplied than the modeled one. In addition, the proposed soot production models work well for complete combustion of hydrocarbons, but there are no data to verify them for particular oxidation case. At the same time, the model adequately reflects the qualitative picture of the temperature distribution over the reactor, allows us to predict the main trends in the change in the final composition of the product when the composition of the initial mixture varies. It also can be used to prevent overheating of critical areas.

5. CONCLUSIONS

Numerical modeling of the plasma reactor is carried out. The temperature field in the reactor in the warm-up mode is calculated. Analysis of the obtained data showed that radiation heat transfer must be taken into account. Comparison of calculated and experimental data showed a numerical discrepancy, but a qualitative similarity. The differences in the experiment and numerical modeling can be explained by the errors in estimating the grayness coefficient for the walls at high temperatures, by setting the uniform heat flux outward along the entire lateral surface and setting properties of the walls independent on temperature.

The importance soot formation for numerical modeling of hydrocarbons partial oxidizing is shown. Interaction of radiation with soot significantly changes temperature distribution in the reactor. Temperature field in this case is qualitatively similar to the temperature field, when the formation of soot is not taken into account at all. It is also shown that heat losses do not significantly influence soot mass fraction, but it has great impact on temperature distribution in the middle and upper part of the reactor.

Comparison of the results of numerical modeling with experiment revealed a significant discrepancy between the calculated equilibrium gas composition and the experimentally obtained one, as well as the discrepancy in the numerical values of the temperature field in the reactor. In the experiment a large amount of hydrocarbons formed in the outer contour as a result of a lower temperature and it is supposed to be the reason for the discrepancy. At the same time, the model reflects the qualitative dependencies of the final product on the feed mixture.

To sum up, numerical model of the reactor with soot formation and its interaction with radiation shows an adequate qualitative picture of the distribution of temperatures and concentrations over the volume of the reactor. Nevertheless, the Moss-Brooks model gives a picture of the soot distribution along the reactor similar to the experimental one. This allows us to assume that its use in other similar tasks will be justified after completion. In addition, this model can be used in determining the optimal parameters and regimes for the conversion of various materials in the reactor.

REFERENCES

1. *Typical plasma facility*. Alter NRG [referred on the 12th of January in 2017 y.]. Link to the internet <http://www.alternrg.com/waste_to_energy/typical_plasma_facility/>.
2. DUCHARME, C. *Technical and economic analysis of Plasma-assisted Waste-to-Energy processes. M.S. Degree in Earth Resources Engineering Theses.* Columbia University, 2010. 79 p.
3. SHAUKAT, S. *Progress in Biomass and Bioenergy Production.* InTech, 2011. 456 p. ISBN 978-953-307-491-7.
4. LIAVONCHYK, A., SAUCHYN, V., DALHOLENKA, H., SKAMAROKHAU, D., KHVEDCHYN, I., SABIRAU, N., Two-stage technology for treatment of waste with high content of organic. CYSENI 2017. Proceedings of annual conference of young scientists on energy issues. [CD]. Kaunas: Lithuanian Energy Institute. 2017 May 25–26.

5. LIAVONCHYK, A. SAUCHYN, V., KHVEDCHYN, I. Wooden waste processing with thermal plasma. VIII International conference Plasma physics and plasma technology (PPPT-8). Minsk, Belarus, 2015 September 14–18.
6. HEBERLEIN, J., MURPHY, A., Thermal plasma waste treatment. *Journal of Physics D: Applied Physics,* 2008, No. 41, p. 1–20.
7. YOUNG, G. *Municipal Solid Waste to Energy Conversion Processes. Economic, technical and renewable comparisons*. Hoboken, New Jersey: John Wiley & Sons, 2010. 384 p. ISBN 978-0-470-53967-5.
8. LOZHECHNIK, A., SAUCHYN, V. Pyrolysis of rubber in a screw reactor. *Journal of Engineering Physics and Thermophysics*, 2016, Vol. 89, Issue 6, p. 1482–1486.
9. LOZHECHNIK, A., NIKANCHUK, A., SAUCHYN, V., DALHOLENKA, H. Technology of rubber waste processing (in Russian). *Proceedings of the National Academy of Sciences of Belarus. Series of physical-technical sciences*, 2014, No. 2, p. 74–78.
10. HRABOVSKY, M., KONRAD, M., KOPECKY, V., HLINA, M., KAVKA, T., CHUMAK, O., VAN OOST, G., BEECKMAN, E., DEFOORT, B. Pyrolysis of wood in arc plasma for syngas production. *High Temperature Material Processes*, 2006, Vol. 10, No.4, p. 557–570.
11. JANSSENS S. *Modeling of heat and mass transfer in a reactor for plasma gasification using a hybrid gas-water torch: B.S. in physics Theses*, Universiteit Gent, 2007, 99 p.
12. ZHANG, Q., DOR L., KUMAR BISWAS, A., YANG, W., BLASIAK W. Modeling of steam plasma gasification for municipal solid waste. *Fuel Processing Technology*, 2013, Vol. 106, p. 546–554.
13. MENTER, F.R. Two-equation eddy-viscosity turbulence models for engineering applications. *AIAA Journal*, 1994, Vol. 32, No. 8, p. 1598–1604.
14. WILCOX, D. C. *Turbulence modeling for CFD*. DCW Industries, Inc. La Canada, California, 1994, 477 p. ISBN 0-9636051-0-0.
15. PLATONOV, D., MINSKOV, A., DEKTEREV, A., SENTJABOV, A. Numerical modelling of flows with flow swirling (in Russian). *Computer investigations and modelling*, 2013, Vol. 5, No. 4, p. 635–648.
16. VARGAFTIK, N. *Reference book of thermophysical properties of gases and liquids*. Moscow, Science, 1972, 721 p.
17. BROOKES, S. J., MOSS, J. B. Prediction of Soot and Thermal Radiation in Confined Turbulent Jet Diffusion Flames. *Combustion and Flame,* 1999, Vol. 116, Issue 4, p. 486–503.

CYSENI 2018, May 23-25, Kaunas, Lithuania
ISSN 1822-7554, www.cyseni.com

THE REVIEW OF PLASMA SPRAY PARAMETERS EFFECT ON THE STRUCTURE OF THE COATINGS

A. Šuopys, V. Grigaitienė
Lithuanian Energy Institute, Laboratory of Plasma Processing
Breslaujos str. 3, LT-44403 Kaunas, Lithuania
Email: airingas.suopys@lei.lt

ABSTRACT

Plasma spray is a very popular technique in depositing a huge variety of coatings on various surfaces and components to provide protection and improve their quality. Plasma spray was first used in 1970s, and since then constantly is being improved. Because of its extremely high temperature (10000–20000 K in the electric arc zone), metal alloys, carbides, ceramics and other refractory materials can be used as coating materials, usually in the form of wire or powder. There are quite a few technological factors that influence the interaction of plasma flow and the feedstock powder and selecting different combinations of operational parameters it is possible to control the spray process and produce the coatings with desired properties and composition. By increasing the temperature of plasma, the coatings become harder and less porous. The properties of the coatings can also be regulated by using the feedstock powder of different shape and size. The selection of optimal plasma spraying parameters is extremely important producing quality coatings avoiding unwanted results or coating defects.

Keywords: plasma spray, coating properties, phase composition, plasma torch

1. INTRODUCTION

The demand for functional materials is always increasing, various systems and their indivudual parts has to be durable and ressistant to different factors i.e. temperature, wear, corrosion, etc. This need drives the technology further, to find new and cost effective solutions, to prolong the lifespan of certain tools and their parts. One of the best way to do so is to apply thin protective layers of another selected material with special properties, to protect the surfaces from oxidation, high temperatures, chemical corrosion, etc. This allows a small ammount of material to be used for huge surface areas with a reasonable cost. Plasma spray is well known coating technology, today widely used in laboratories and industry. and the formed coatings fulfil the needs (hardness, porosity, thermal conductivity, etc.). During the plasma coating spray process the quality of the coatings can be widely controlled by selecting proper spraying conditions. The aim of this paper is to review the plaspa spray parameters effect on the quality and properties of the sprayed coatings.

2. PLASMA GENERATION AND PLASMA SOURCES

Plasma is called the 4th state of matter and was first identified by British chemist Sir William Crookes in 1879 but the term was first described by chemist Irving Langmuir in the early 1900s as the state of matter in the positive column of glow discharge tube [1–2]. The term “plasma” is used in physics to designate the high temperature ionized gaseous state with charge neutrality and collective interaction between the charged particles and waves. Plasma can occur at different temperatures and densities, there should be sufficient energy in the medium to form plasma from the gas. Also, the energy medium should be continuous to sustain the plasma. Important examples of plasma are stars, stellar atmospheres, interstellar gas, lightning, fluorescent tubes, neon signs, plasma displays, tokamaks, corona discharges, electric arcs, laboratory and industrial plasma devices for spraying, welding, cutting, medical treatment, water cleaning, fuel conversion and etc. [2]. A plasma can be defined as a partially or fully ionized gas that satisfies the following criteria:

- Quasi-neutrality. Plasma must maintain charge balance (the number of electrons and ions are very similar):

$$-q_e N_e = q_i n_i \pm \Delta \tag{1}$$

where Δ is extremely small.

- Interactions between individual charged particles are insignificant compared to collective effects.
- The electron-neutral collision cross-section is much smaller that the electron-ion cross section $\sigma_{en} << \sigma_{ei}$ [3].

Plasmas are described by many characteristics, such as temperature, degree of ionization, density, thermodynamic equilibrium, etc. In general, plasmas can be classified as high temperature or low temperature plasma depending on the temperature of the species: the electron temperature (T_e), ion temperature (T_i) and temperature of neutral particles (T_n). On the basis of the temperature of electrons, ions and neutral particles plasma are also classified as thermal equilibrium, local thermal equilibrium, or nonthermal equilibrium.

In thermal equilibrium plasma electrons, ions and neutral particles have the the same temperature. This occurs in high temperature (thermal) and high density plasma, for example, the stars, tokamaks, laser induced plasma [4–5]. In non-equilibrium plasma the electron temperature (Te) is considerably higher than in ions (T_i) and neutrals (T_n), that is, $T_e >> T_i$, T_n. Non-equilibrium plasmas are generated by corona discharge, glow discharge, arc discharge, capacitively coupled discharge, inductively coupled discharge, wave heated plasma, and so on.

Plasma can be artificially generated only by heating or applying electric field to a neutral gas. Any volume of a neutral gas always contains a few electrons and ions that are formed and these free charge carriers are accelerated by the electric field and new charged particles may be created when these charge carriers collide with atoms and molecules in the gas or with the surfaces of the electrodes. This leads to an avalanche of charged particles that is eventually balanced by charge carrier losses, so that a steady-state plasma develops [6].

Plasma generators according to the driving frequency of power supply where plasma is formed are classified as:

- direct current (DC),
- alternating current (AC),
- radio frequency (RF).
- microwave (MW) plasma generators.

The DC and AC-generated plasmas are electrode-discharged plasmas, while RF- or MW-generated plasmas are referred to as inductively-coupled or electrodeless discharged plasmas. Nowadays, plasma is used for many purposes, which include gasification, neutralization and reforming, cleaning and sterilization, surface treatment, synthesis of new materials and coatings, etc. [7].

3. THERMAL SPRAY PROCESS AND APPLICATIONS

Thermal spraying is a cost-effective and widely adopted across many industries as a preferred method which improves or restores the solid surfaces. The process can be applied to a wide range of materials and components producing coatings to provide resistance to wear, heat, erosion, corrosion, friction, etc. or produce coatings with a special catalytic, tribological, hydrofobic, insulation and many other desirable surface properties.

3.1. Thermal spray technologies

Thermal spray involves a group of techniques and coating spray processes that improve the performance of a component by adding functionality to surfaces [8]. Thermal spray is a very versatile technology that can be used in many types of applications and virtually almost on any component, it has grown to become a large worldwide market [9]. Thermal spray is an industrial process that is used for the synthesis of coatings with special properties and consists of a heat source and a coating material in a powder or wire form, which is literally melted into tiny droplets and sprayed onto surfaces at high velocity (Fig. 1.)

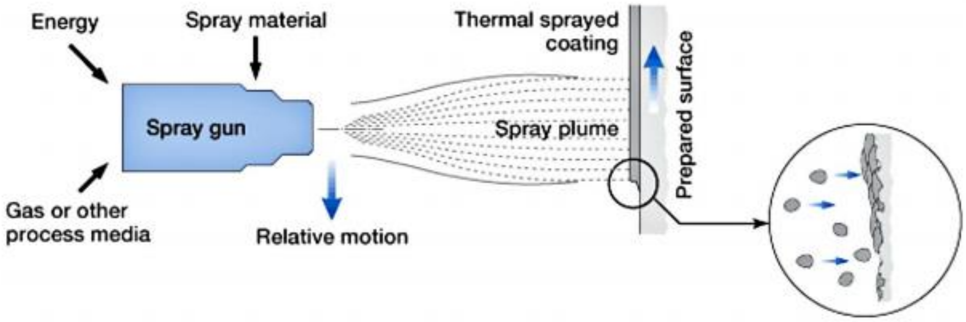

Fig 1. Thermal spray process [10]

Thermal spray technologies according supplied raw material, process duration, temperature and velocity of particles flow, conditions of plasma spray and principles of plasma generator are divided into: flame spray, wire-arc spraying, cold spray, direct current plasma spraying, controlled atmosphere or soft vacuum plasma spraying, RF induction plasmas, detonation gun, high-velocity oxy-fuel spray (HVOF) and etc. Plasma spraying is probably the most versatile of all thermal spray processes because there are few limitations on the material size and shape of the substrate, the coating quality is in the general higher that obtained using flame spraying method. While most of the plasma spray processes exhaust the plasma jet into the open-air environment, the coating qualities such as density, uniformity and reproducibility can be enhanced by spraying in a controlled environment, i.e. a controlled atmosphere chamber or in a low-pressure environment, making the process significantly more expensive. In wire arc spraying, an arc between two wires is melting the wire tips and a high-velocity gas stream is propelling the droplets towards the substrate [11]. This process is more economic, because the use of wires instead of powders (which require special pretreatment), but the choice of materials is limited, since the wires need to be electrically conducting and ductile. Such coatings usually have higher porosity than those of other plasma-based processes. Plasma transferred arc (PTA) process differs from other thermal spray techniques because the substrate serves as one electrode, of the arc that heats the process gases. This allows an excellent bonding between substrate and the coating, with high density.

3.2. Plasma spray technology

Atmospheric plasma spray is an industrially well-accepted and versatile thermal spray technique which enables deposition of variety of materials suitable for plasma spraying including zinc, aluminium, nickel, chromium, copper alloys, tin, molybdenum, some steels, numerous ceramic materials and etc. The size of the powder particles employed in thermal spray process varies from 20 to 150 μm, thus resulting in desirable structured coatings [12]. The advantage of using plasma spray compared to flame spray processes is that the materials with very high melting points can be sprayed, but it requires extra cost and increases the process complexity. In some cases, it could be advantageous to perform plasma spray under controlled environment. The plasma generated for plasma spray usually incorporates on or a mixture of air, argon, helium, nitrogen and hydrogen.

Another advantage of plasma coating spray is that it supplies large amounts of energy through dissociation of molecular gases to atomic gases and ionization. A schematic of a plasma spray process is shown in Fig. 2.

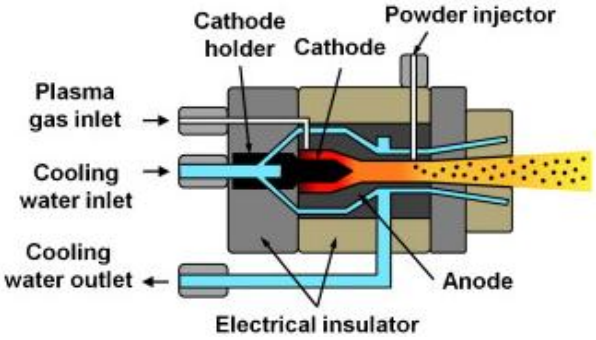

Fig. 2. Schematic of a plasma spray process [9]

The plasma generator generally consists of a copper anode and a cathode that is usually made of lanthanated tungsten, hafniumor zirconium because of its high melting point and good thermionic emission properties [13, 26]. A typical plasma spray system has a degree of ionization within the range of $0.5–4.0 \times 10^{-3}$ [14], which corresponds to a plasma efficiency of less than 10% to over 70% [15]. The degree of ionization depends on the temperature and pressure of the system [16] while the efficiency of a plasma jet is influenced by the plasma jet design, size of mixing chambers and nozzles, input power, secondary gas flow rate, and operating conditions.

A typical plasma coating spray process can be described in the following steps:

- Plasma forming gas mixture flow is injected between water-cooled electrodes: anode and cathode.
- A high intensity DC electric arc passes between cathode and anode and the gas flow is ionized creating plasma to reach high temperatures of the process.
- The coating material in the form of a fine powder conveyed by carrier gas is injected into the plasma jet and is heated to the molten state.
- The molten particles are carried by plasma flow towards the substrate with the particle velocities ranging from 150 to 800 m/s [13].

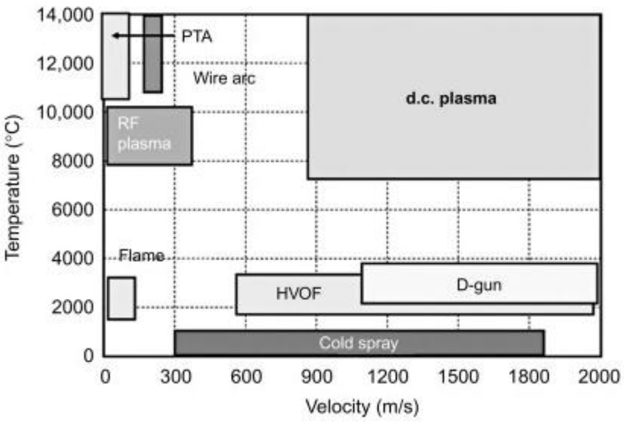

Fig. 3. Temperature and velocity of the gas flow for different thermal coating spray processes [16]

The properties of the coatings are determined by the coating material and the form in which it is provided, also by many process parameters. Besides the parameters characterizing the substrate condition, there are the parameters that define the particle temperature and velocity impact on the coating characteristics. These particles characteristics primarily depend on the temperatures and velocities of the gas flow. Fig. 3 shows the range of temperature and velocity values which can be expected for the gases heated by the different thermal spray processes. One must keep in mind that different materials require different deposit conditions, specific coating properties may require specific particle velocity and temperature, the heat fluxes to the substrate vary for the different coating methods and for some substrates the heat flux must be minimized. Substrate preheating and temperature control during the spraying strongly influence the properties of coatings, residual stresses, and frequently a trade-off exists between coating quality and process economics [11].

4. SPRAY PARAMETERS EFFECT ON THE STRUCTURE OF COATINGS

One of the main parameter that can be controlled during plasma spray process is the power of the plasma torch. C. Wang et al. established the influence of the power of the plasma torch on the structure of alumina coating deposited on Si_3N_4 surface. In this experiment the authors used 15–45 µm of size and 99% of purity α-Al_2O_3 powder. As the carried gas a mixture of hydrogen and argon was selected. The temperature and velocity of plasma flow using different power is shown in Fig. 4. Increasing the power of plasma torch, much higher plasma temperature and velocity can be obtained, and the feedstock powders at higher temperatures are molten more quickly. Higher velocity allows for the same particles to reach higher speeds and hit the surface with higher power [18].

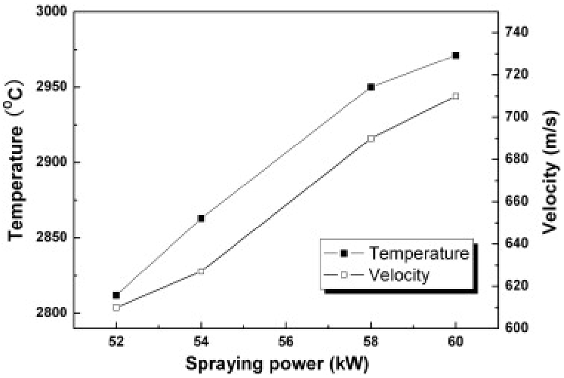

Fig 4. The average temperature and velocity of Al_2O_3 particle at different spraying power [18]

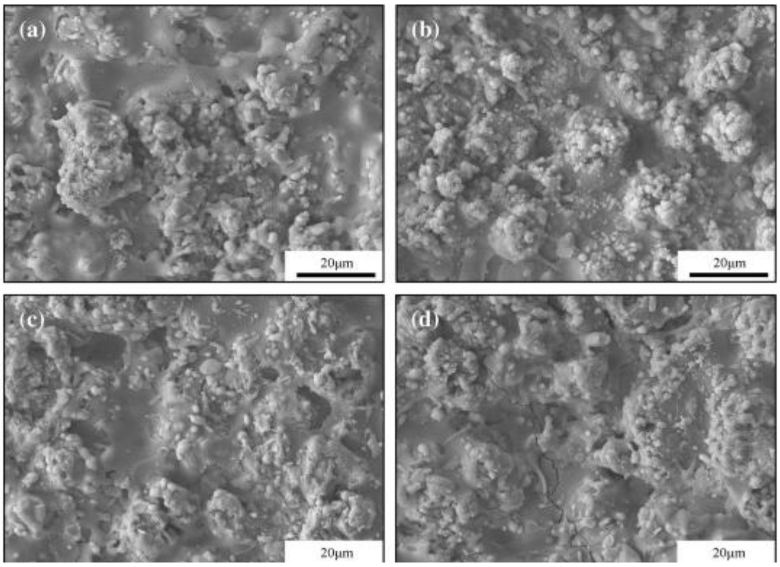

Fig. 5. The surface micrographs of supersonic plasma sprayed alumina coatings:
a) 52 kW; b)54 kW; c) 58 kW; d) 60 kW [18]

Fig. 5 shows the surface morphologies of plasma sprayed Al_2O_3 coatings at the different powers of the plasma torch. A rough surface with lots of large unmelted particles and pores were observed in Fig. 5 a. It is an evident surface feature of coating prepared at low temperature (i.e., low spraying power). As the spraying power increased, the unmelted particles became relatively small (Fig. 5 b.), compared with Fig. 5 a. When the spraying power was 58 kW, a compact pancake shapes surface with splashing structure was observed, and the surface was relatively dense though some pores still existed in the surface (Fig. 5 c). When the spraying power was 60 kW, the obvious large cracks occurred on the surface of coating though the surface of coating was very dense (Fig. 5 d). The reason was attributed to the relatively high residual stress generated by contraction of a single splat with big temperature difference during the cooling.

As the power of the plasma toch was increased from 52 to 58 kW the density of coatings increased gradually from 1.50 g/cm^3 to 1.62 g/cm^3, but the further increasement of the power to 60 kW density starts to drop to 1.59 g/cm^3, because defects were formed within the coating, as can it be seen in Fig. 5 d. Opposite tendencies can be observed in coatings porosity, the increase of power decreases the porosity from 53.0% to 50.6%, and similar appears to density, when power of 60 kW is used the porosity increases to 51.2% due to the same defects formed within the coating. D. Thirumalaikumarasamy et al. noticed that the input power is the most sensitive parameter of the porosity of the coating. The input power has an inversely proportional relationship with the porosity. The spraying power is an important parameter that affects the quality of the coating, since it can influence the temperature and velocity of the powder particles at the moment of striking the substrate. Full particle melting usually results in lower porosity content. At low spraying powers, the powder particles are poorly melted. When they hit the substrate or the already formed coating, they are not able to spread out completely to form splats and therefore, can not conform to the surface [23].

Since the input power of the plasma torch (as shown above) and the flow rate of plasma forming gas are the main parameters to control the nature of formed coatings. Researchers combined these 2 parameters and introduced the critical plasma spray parameter (CPSP) [20]. It is defined using the formula:

$$CPSP = \frac{\text{Input power}}{\text{Gas flowrate}} \tag{2}$$

It is well known that when the power of plasma torch is increased, the particle temperature increases due to increase the temperature of a plasma jet because it is very sensitive to CPSP. The decrease of plasma flow rate, which leads to an increase in the powder in-flight time, has a similar effect on the particle temperature as the increase in the plasma output power, so CPSP can alter the microstructure and properties of the coatings [19].

S. Yugeswaran et al. used 3 different composition coatings and 3 different CPSP parameters. As shown in Fig. 6, 3% and 13% titania + alumina coatings microhardness increased gradually, and the maximum hardness was obtained using the highest CPSP value. It can also be seen that the microhardness tends to decrease with the addition of titania. At the same time, very low hardness is observed for alumina-40% coating, at 1166 CPSP value. This is due to the fact that the increase of power in alumina-40% coatings is increasing its porosity, while the increase of CPSP lowers the porosity of alumina-3% and alumina-13% coatings.

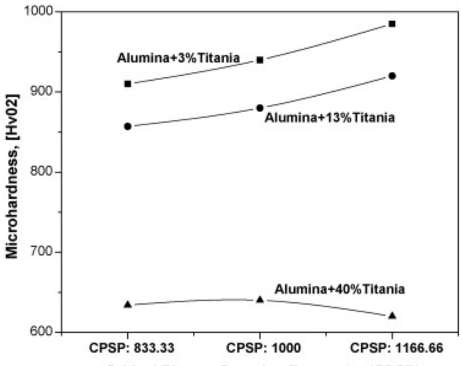

Fig. 6. The effect of CPSP on the microhardness of the plasma sprayed alumina coatings [19]

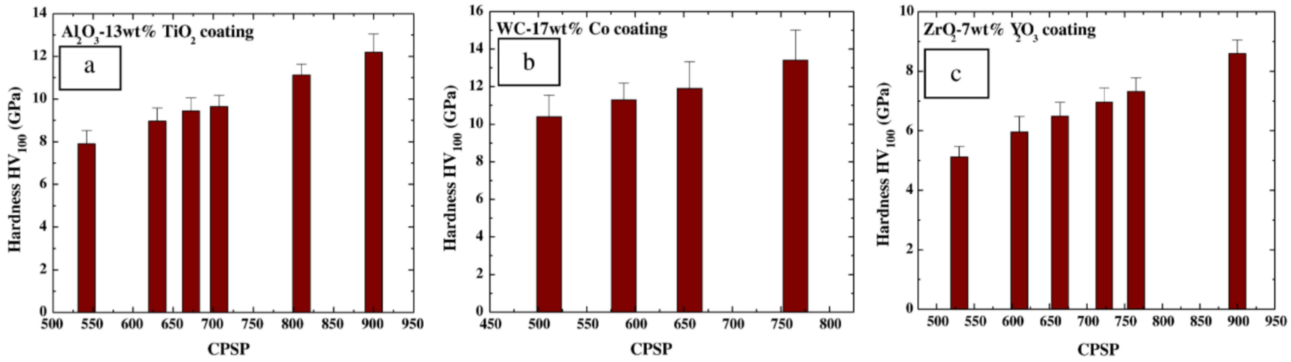

Fig. 7. Microhardness of nanostructured a) alumina-13%wt titania; b) tungsten carbide-17%wt cobalt; c)7%wt YSZ coatings as a function of CPSP [21]

The dependency of CPSP on porosity and thermal conductivity of plasma sprayed coatings was investigated by S. Sivakumar et al. In this paper it was observed that the decrease of CPSP is increasing the porosity of lanthanum zirconate coatings. It was also observed that the increase of porosity from 16% to 18% decreases thermal conductivity from 0.8 Wm^{-1} to 0.6 Wm^{-1} [22].

It is also possible to manipulate the properties of plasma sprayed coating by using different feedstock powders, as was done in Y. Yang's et al. research. Three different kinds of alumina-titania composite powders, with different microstructure were used. The preparation methods of raw powders were different, 1st powders were commercial Mecto 130, manufactured through the laser cladding process, the 2nd were nanocomposite powders, fabricated by spray drying and heat treating and the 3rd werenanocomposite powders, obtained by spray drying, heat treating and jet processing. The microhardness and crack growth resistance of the coatings prepared from the nanocomposite powders were improved comparing it with the conventional micro-composite coating, especially the nanocomposite coating manufactured from the nanocomposite powder with three-dimensional network structure. The lower microhardness and crack growth resistance of the conventional micro-composite coating was observed due to the inhomogeneous distribution of its phase composition evolved from the nonuniform mixing of Al$_2$O$_3$ and TiO$_2$ in the micro-composite powder comparing to the nanocomposite coatings. The sliding wear resistance of the nanocomposite coatings was significantly better comparing it to the conventional micro-composite coating. The nanocomposite coating prepared from the nanocomposite powder with three-dimensional network structure had the highest sliding wear resistance [25].

Table 1. Properties of formed coatings

Coatings	**1st**	**2nd**	**3rd**
Microhardness (HV$_{0\ 3}$)	849 ± 87	908 ± 63	939 ± 57
Crack growth resistance (1/μm)×10^{-3}	3.31 ± 0.64	3.58 ± 0.49	4.44 ± 0.51
Wear rate (×10^{-4} mm^3/N m)	1.42 ± 0.22	0.94 ± 0.17	0.49 ± 0.09

Wear tests from L. Shaw et al. paper suggest that the coatings produced from nano-powder feedstock could have better wear resistance than the coatings produced using commercial coarse-grained powders. It was found that the phase transformation of nanosized Al$_2$O$_3$ and TiO$_2$ during heat treatment, sintering and thermal spraying is, in general, identical to that of micrometer-sized counterparts. Furthermore, the particle temperature during the thermal spray could be divided into three regimes, i.e. low, intermediate and high temperature regimes, according to the characteristics of the coating produced from the nanopowder. The hardness and density of the coating increase with the spray temperature. The phase content and grains size of the coating also exhibit a strong dependency on the spray temperature. The coating sprayed using nanopowder feed displays a better wear resistance than the counterpart sprayed using commercial coarse-grained powder feed [25].

5. SUMMARY

Thermal spray methods are very promising in depositing a huge variety of coatings on various solid surfaces and components to prolong the lifespan, provide protection and improve their quality. Plasma spray technology is one of the thermal spray methods with the advantages of using the materials for spraying with very high melting points, no limitations on the shape of the substrate, quite easy operation of the process and control of the thickness of the produced coatings. This research describes the relationship between the plasma spray processing and obtained microstructure surfaces in order to provide the basis for process control. Applying plasma spraying process the materials with very high melting points of can be sprayed. It is easy to manipulate the properties of plasma sprayed coating by using different feedstock powders and the preparation methods of raw powders. The process is optimal and resulting in desirable structured coatings when the size of powder particles vary from 20 to 150 µm. Some papers showed that the coatings produced from nano-powder feedstock have better wear resistance and higher density than the coatings produced using coarse-grained powders. The power of the plasma torch has a considerable influence to the properties and quality of the produced coatings. It strongly influence the temperature and velocity of the powder particles at the moment of striking the substrate. The hardness and density of the coating increase with the spray temperature. At low spraying powers, the powder particles are poorly melted because of their lower temperatures, but the porosity of produced coatings increases. The selection of optimal plasma spraying parameters has a big influence producing quality coatings with the abilities offering corrosion protection, wear resistance, clearance control – abrasives and abradables, heat and oxidation resistance, electrical resistivity and conductivity and etc.

REFERENCES

1. K. MIYAMOTO, *Plasma Physics for Nuclear Fusion*, Cambridge, 1989.
2. F. CHEN, *Introduction to Plasma Physics and Controlled Fusion*, Plenum Press, 1984.
3. DENDY, *Plasma Physics*, Cambridge University Press, 1995.
4. H. CONRADS, M. SCHMIDT, Plasma generation and plasma sources, *Plasma sources science and technology*, 2000, p. 441–454.
5. SANLISOY, M.O. CARPINLIOGU, A review on plasma gastification for solid waste disposal, *International Journal of hydrogen energy*, 2017.
6. R. WARNECKE, Gasification of biomass: comparison of fixed bed and fluidized bed reactor, *Biomass Bioenergy 18*, 2000, p. 489–497.
7. Z. RAHMAN, H. RAHMAN, MD. A. RAHMAN, Classification and generation of atmospheric pressure plasma and its principle applications, *International journal of mathematics and physical sciences research*, 2014.
8. N. ESPALLARGAS, *Introduction to thermal spray coatings, Future development of thermal spray coatings, types desgins, manufacture and applications*. 2015.
9. J.A. GAN; C.C. BERNDT, Thermal spray forming of titanium and its alloys, titanium powder metallurgy, *science, technology and applications*, 2015, p. 425–446.
10. Sulzer Metco, *An Introduction to Thermal Spray*, Issue 4. 73, 2013.
11. P.L. FRACHAIS, J.V.R. HEBERLEIN, M. BOULOS, *Thermal spray fundamentals from powder to part*, 2014.
12. S. GOEL, S. BJÖRKLUND, N. CURRY, U. WIKLUND, S.V. JOSHI, Axial suspension plasma spraying of Al_2O_3 coatings for superior tribological properties, *Surface and Coatings Technology*, 2017, vol 15, p. 80–87.
13. M. GUPTA, *Desgin of thermal barrier coatings – a modelling appcoroach*, 2015.

14. R. RAMASAMY, V. SELVARAJAN, K. RAMACHANDRAN, Characterization of DC plasma spray torch using energy balance technique and thermo-fluid dynamical consideration, *Plasma Devices Oper., 5 (3)*, 1997, vol 5 p. 161–180.
15. S. SAFAI, H. HERMAN, Plasma sprayed materials, *Materials science & Technology,* vol 20, 1981, p. 183–214.
16. B. GROSS, B. GRYCZ, R.C.G. LECKEY, *Plasma Technology*, Iliffe Books Ltd, London, 1968.
17. P. FAUCHAIS, Current status and future directions of thermal spray coatings and techniques, types desgins, *manufacture and applications*, 2015.
18. WANG C., FAN L., FAN J., ZHANG D., WANG H. Effect of spraying power on microstructure and properties of supersonic plasma sprayed Al_2O_3 coating on porous Si_3N_4 substrate, *Journal of Alloys and Compounds,* 2013, vol 15, p. 152–157.
19. S. YUGESWARAN, V. SELVARAJAN, M. VIJAY, Influence of critical plasma spraying parameter (CPSP) on plasma sprayed Alumina-Titania composite coatings, *Ceramics international,* 2010, vol 36, p. 141–149.
20. E.H. JORDAN, M. GELL, Y.H. SOHN, D. GOBERMAN, L. SHAW, S. JIANG, M. WANG, T.D. XIAO, Y. WANG, P. STRUTT, Fabrication and evaluation of plasma sprayed nanostructured Alumina–Titania coatings with superior properties, *Materials Science and Engineering,* 2001, vol 301, p. 80–89.
21. V. BOLLEDDU, V. RACHERLA, P.P. BANDYOPADHYAY, Microstructure characterization of plasma sprayed conventional and nanostructures coatings with nitrogen as primary plasma gas, *Surface and coatings technology*, 2013, vol 235, p. 424–432.
22. S. SIVAKUMAR, K. PRAVEEN, G. SHANMUGAVELAYUTHAM, S. YUGESWARAN, J. MOSTAGHIMI, Thermo-physical behavior of atmospheric plasma sprayed high porosity lanthanum zirconate coatings, *Surface and Coatings technology*, 2017, vol 326, p. 173–182.
23. D. THIRUMALAIKUMARASAMY, K. SHANMUGAM, V. BALASUBRAMANIAN, Influences of atmospheric plasma spraying parameters on the porosity level of alumina coating on AZ31B magnesium alloy using response surface methodology, *Progress in Natural Science: Materials International*. 2012, vol 22, p. 468–479.
24. Y. YANG, Y. WANG, W. TIAN, D. YAM, J. ZHIANG, L. WANG. Influence of composite powders' microstructure on the microstructure and properties of Al_2O_3–TiO_2 coatings fabricated by plasma spraying. *Materials & Design,* 2015, Vol 65 p 814–822.
25. L. SHAW, D. GOBERMAN, R. REN, M. GELL, S. JIANG, Y. WANG, T. D. XIAO, P. R. STRUTT, The dependency of microstructure and properties of nanostructured coatings on plasma spray conditions, *Surface and Coatings Technology*, 2000, vol 130, p. 1–8.
26. P. L. FAUCHAIS, J. V.R. HEBERLEIN, M. I. BOULOS, "*Thermal Spray Fundamentals: From. Powder to Part* ", Springer, 2014, 1566 p.

CYSENI 2018, May 23-25, Kaunas, Lithuania
ISSN 1822-7554, www.cyseni.com

INVESTIGATION OF COMPRESSION EROSION PLASMA FLOW GENERATED BY A COMPACT ACCELERATOR

P. N. Shoronov
A. V. Luikov Institute Heat and Mass Transfer of the National Academy of Science of Belarus
P. Brovki, 15, 220072 – Belarus
Email: shoronov@hmti.ac.by

ABSTRACT

The paper presents a study of compact end-face erosion accelerator for generating a high-energy compression plasma flow. The discharge device of such system consists of a plexiglas cylinder with opening for electrodes. The central electrode (cathode) is 6 mm in diameter, the outer electrode (anode) is composed of four 3.5 mm diameter rods axisymmetrically arranged along a circle of radius 11 mm. Experiments on the discharge electrical parameters measurement and the study of compression plasma flow formation are described. The main parameters of the electrical discharge were measured with a calibrated Rogowski coil and a compensated RC-voltage divider. The maximum discharge current and voltage of such system is about 20 kA and 800 V respectively; half-cycle duration – 100 μs; the discharge energy is 470 J; the velocity of plasma formation in the flow were measured using a high-speed photorecording camera and made magnitude of the order of $1.8 \cdot 10^3$ m/s. Complex spectroscopic investigation of compression erosion plasma flow are also presented. According to results of qualitative spectral analysis, composition of flow is governed predominantly by the material of an inner electrode of discharge device. The quantitative assessment showed that the concentration of the free electron in plasma flow is about $3.3 \cdot 10^{16}$ cm^{-3}. Temperature of plasma particle – of the order of 1.7 eV.

Keywords: compact end-face accelerator, compression erosion plasma flow, discharge current, discharge voltage, velocity of plasma formation, concentration of free electron, temperature of plasma particle

1. INTRODUCTION

An important problem of plasma physics both from fundamental and practical points of view, is the development of methods for generating and controlling parameters of high-energy supersonic plasma flows, including compression plasma flows (CPF) [1–3]. The activities in this area are becoming of practical importance due to the possibility of using such plasma formation in modification of surface properties of various materials. Most promising in this regard are methods for treatment of surfaces by the compression plasma flows, a working substance for which is a certain gas or gas mixture [4–10]. Along with gas-discharge system, erosion compression plasma accelerators are investigated. Author of [11] was the first to develop compression erosion systems capable of operating both in vacuum and in air at atmospheric pressure; the generated plasma flow features a composition which is mainly governed by a material of a discharge device inner electrode. The discharge device in such systems is typically from 5 to 15 cm in diameter, and the electric energy stored in the capacitor varies from ~37 to ~60 kJ. The compression erosion plasma flows (CEPF) generated by such accelerators possess a number of relatively high parameters, such as velocity of plasma particles directed motion reaching $(20–50) \cdot 10^3$ m/s, the concentration of free electron and temperature of plasma 10^{17}–10^{18} and 1 to 3 eV respectively, and the half-cycle period of 100 μs. The CEPFs with such characteristics offer an opportunity to address a number of research and practical problems. What is more, such systems can be scaled down to produce compact and less energy consuming devices, capable of generating plasma flow with characteristics close to above parameters.

The aim of the paper was to determine the main parameters of compression erosion plasma flows, generated by a miniature accelerator, for their further application in solving various problems of materials science.

2. EXPERIMENTAL SETUP

In the Laboratory of Plasma Accelerators Physics, the A. V. Luikov Institute Heat and Mass Transfer, National Academy of Science of Belarus, a miniature end-face erosion device (mini-EFED) was developed, which is capable of generating compression erosion plasma flows with a high energy content, whose composition is mainly determined by material of the inner electrode.

A mini-EFED discharge device (Fig. 1) includes a plexiglas cylinder base with openings for electrodes. The central electrode is 6 mm in diameter the outer electrode (anode) is composed of four 3.5 mm diameter rods axisymmetrically arranged along a cycle of radius R = 11 mm. The working tips of the electrodes are aligned flush with the surface of dielectric.

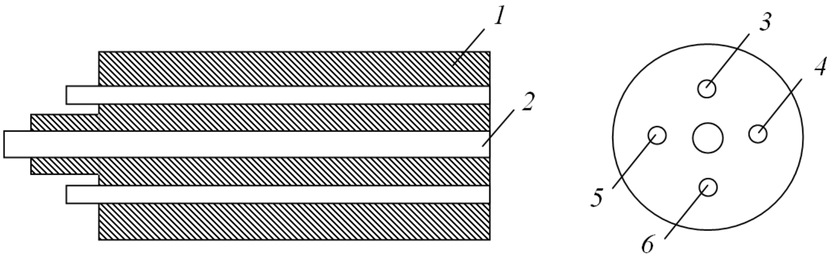

Fig. 1. Discharge device of the mini-EFED: 1 – Plexiglas base; 2 – central electrode (cathode); 3–6 – outer electrode (anode)

The discharge device mounted in the vacuum chamber with dimensions 0.3×0.3×0.7 m which was evacuated to a residual air pressure of ≈ 1.3 Pa. The power source contains a capacitor bank with 400 μF total capacity. Such a configuration of the discharge system results in the formation of current-carrying plasma jets(PJs) at the end of each external rod, whereas the main CEPF originates at the central electrode. Under these conditions, the discharge current in the main CEPF and the sum of the currents is equal of magnitude and opposite in sign. The initial voltage,U_0, at the capacitor bank is varied in the range from 1.0 to 3.0 kV, which corresponds to the energy stored in the battery of 200–1250 J. The discharge device was charged via an IRT-3 ignitron mercury arc rectifier.

3. RESULTS AND DISCUSSIONS

3.1. Discharge parameters in the mini-EFED

The main parameters of the electrical discharge were measured with a calibrated Rogowski coil and a compensated RC-voltage divider. Fig. 2 shows typical oscillograms of discharge current in the miniature end-face accelerator at U_0 = 2.0 kV.

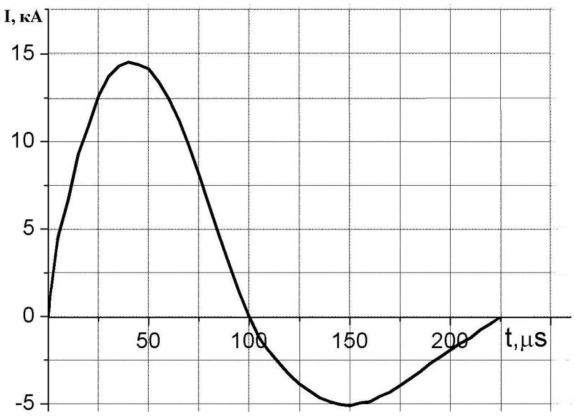

Fig. 2. Oscillogram of the discharge current

It can be seen discharge is oscillatory and strongly damping. The duration of the current half-period is about 100 μs. The current reaches its maximum value of ≈ 15 kA. The energy deposited in the discharge was calculated from the oscillograms of voltage and current by graphical integration method; under the above experimental condition, its value approximately equal to 380 J.

3.2. Formation dynamics of the compression erosion plasma flow

Fig. 3 shows the time-photo of the compression erosion plasma flow generated by a miniature accelerator. The main compression flow running from the tip of the inner electrode measures ≈ 75 mm in length and ≈ 19 mm in admitted diameter. Near the cathode surface, a most intensely emitting area is located. At the tips of anode rods, the developed plasma jets are observed.

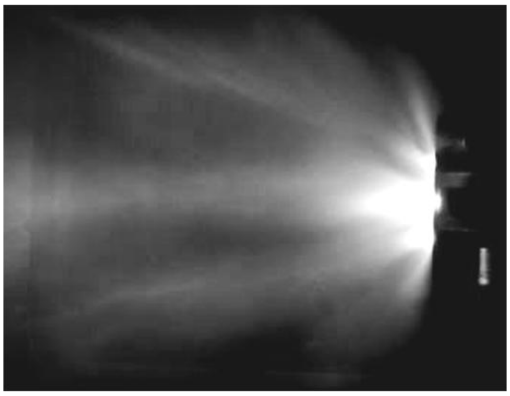

Fig. 3. Integral time photo of the compression erosion plasma flow

Since the current in CEPF and in plasma jets are flowing in opposite directions, electromagnetic force will cause them to repel each other. This prevent to a certain extent the penetration of products eroded from outer electrode rods into the main compression flow, and the CEPF composition will depend primarily on the material of the inner electrode. A relatively long-lasting stability of the main CEPF, its low divergence, and a large flow length-to-diameter ratio indicate the compressive nature of the plasma flow. The formation dynamics of the compression plasma flow was studied using a high-speed photorecording camera, which was operated both in framing and in streaking modes. In the framing mode, the camera was equipped with a two-row relay lens insert. The viewing field of the photorecording device is 150 mm. The rotation speed is 30 000 rpm, which corresponds to the framing rate of 250, 000 fps. Fig. 4 shows a record of the evolution of the compression erosion plasma flow at U_0 = 2.0 kV (only one row of frames from the two recorded is presented, so the time interval between the adjacent photos is 8 μs).

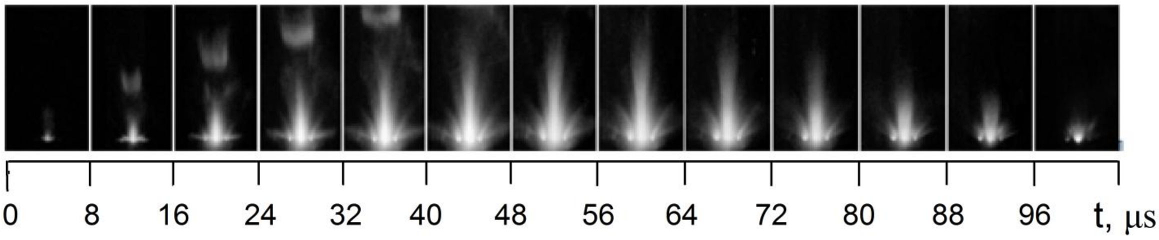

Fig. 4. Time evolution integral photo of the compression erosion plasma flow at U_0 = 2.0 kV (time interval between the adjacent photo is 8 μs)

On the photographs, a leading front is clearly seen, which precedes the developing plasma flow and propagates at a velocity of about 3 km/s. The process of the CEPF formation is completed in 25–30 μs from the beginning of the discharge current, upon which the compression flow retains the stable state for about 50 μs during this period, the CEPF size and emission intensity remains practically unchanged. Starting from the 75th μs after the discharge onset, a process of gradual decay and disintegration of the compression plasma flow begins. Plasma velocity in the compression erosion plasma flow was estimated from results of processing the photographs taken by the camera in the streaking mode. In this mode, camera slit was oriented along the main CEPF axis. The photographic film records a temporal development of the plasma flow in a 50 mm long narrow axial area downstream the end face of the discharge device. The rotational frequency of the camera mirror is 30.000 revolutions per minute. Fig. 5 shows a typical streak photograph of the CEPF emission (first quarter-period of discharge current) taken at U_0 = 2.0 kV.

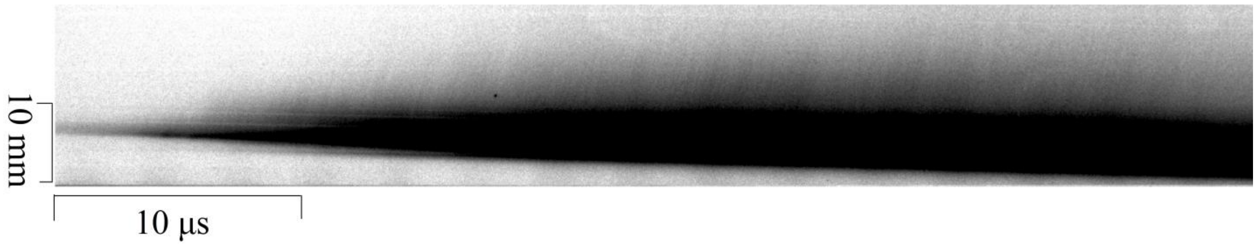

Fig. 5. Typical streak photograph of the compression erosion plasma flow emission

In the photograph, a complex irregular CEPF structure is observed in the form of separate inclined filaments caused by erosion of material of the electrodes and sporadically entering the compression plasma flow [11]. The filaments reflect the propagation dynamics of separate plasma formations.

Their velocity was calculated from the inclination angle of the filaments to horizontal axis and, under the above conditions, reached its maximum value of about $1.8 \cdot 10^4$ m/s by the 30th μs from the discharge beginning. With the increase in the discharge current, the velocity of plasma formation remains almost constant and gradually declines after the current passed its maximum.

3.3. Spectroscopic investigation

3.3.1. Qualitative spectroscopic analysis

As could be expected from general consideration in the previous half of paper, the CEPF composition should be predominantly governed by a material of an internal electrode of the discharge device. This study attempts to qualitative analyze the CEPF composition by of spectroscopic investigation of compression erosion plasma flow.

In this path of the experiments the inner electrode was made of a copper rod, and the outer electrode – four steel rods. Qualitative spectroscopic investigation was conducted with help of an SDH-IV compact automated spectrometer (Solar LS company). The device recorded the total plasma emission from a round (~1 mm in diameter) area on the axis of the accelerator 10 mm above the inner electrode surface. The exposure time of the spectrometer was 10 μs. Spectra in the range of wavelengths from 370 nm to 559 nm were recorded in the maximum of current (50–60 μs after the discharge ignition).

The typical emission spectrum of the compression erosion plasma flow generated by the miniature end-face erosion device is shown in Fig. 6. In the spectral region under study, the strong lines of copper, CuI 406.3 nm and 465.1 nm, are observed. It is worth to note that although sensitivity of the spectrometer considerably falls towards shorter wavelengths, the strongest resonant lines CuI 324.8 nm and 327.4 nm have also been detected. In addition, a number of spectral lines of carbon singly charged ions, with the strongest CII 426.7 nm line, were identified. In our experimental conditions, the C lines are due to the inevitable presence of oil vapors in the vacuum chamber.

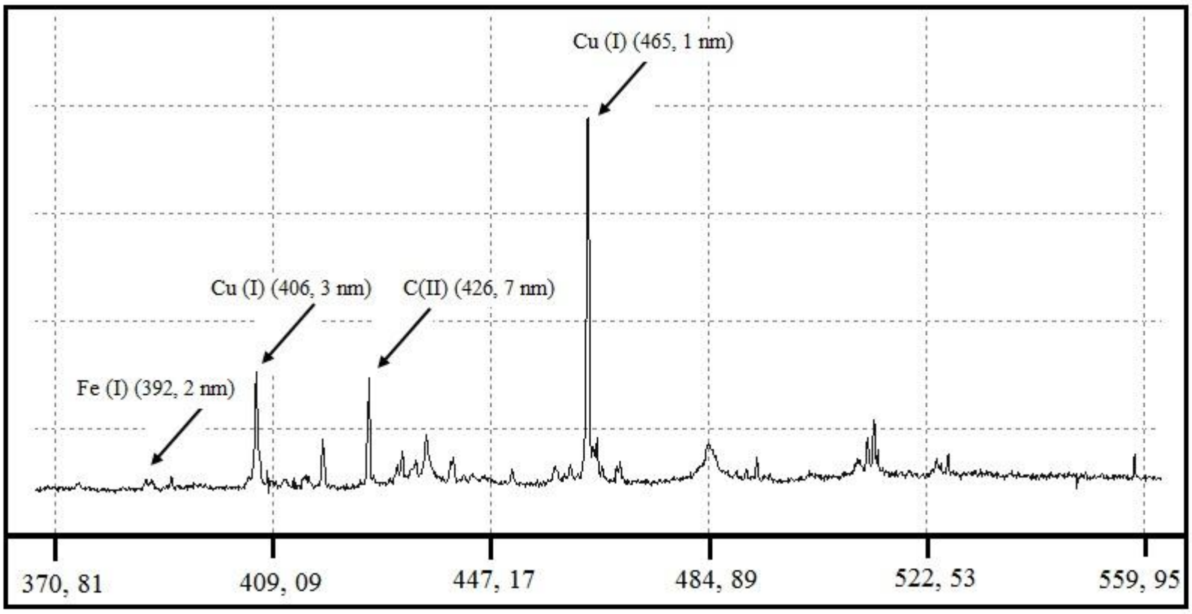

Fig. 6. Emission spectrum of compression erosion plasma flow

The intensities of the strongest lines of iron FeI 390.3 nm and 392.2 nm in the spectral range of interest are close to the detectability limit although their excitation potentials are much lower than those of the copper lines. That means erosion products of the steel outer rods get into the main compression erosion plasma flow in negligible amounts.

3.3.2. Quantitative spectral analysis

Initial quantitative spectral analysis was conducted with help of a monochromator-spectrograph M833 with high spectral resolution. These investigations included measurements of free electron concentration and temperature of plasma particles. Parameters of the experiment were similar ones in previous path of investigation. The concentration of free electron were measured on the Stark broadening of the resonant line of copper with wavelength 324.7 nm and temperature of plasma particle – on the relative intensity of two spectral lines: CuI 453.9.9 nm and CuII 455.5 nm. The typical specter which was used for measurement of plasma particle temperature is presented in Fig. 7.

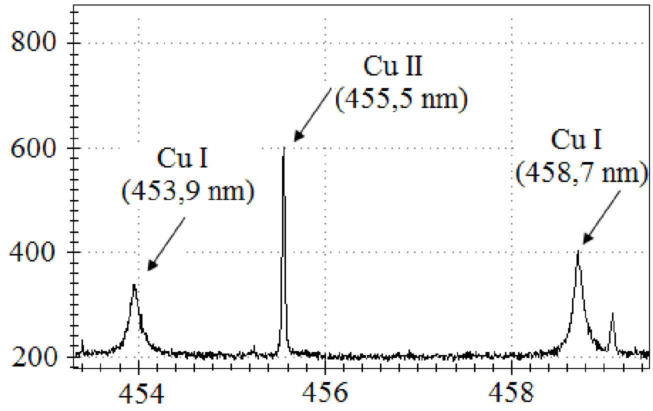

Fig. 7. High resolution emission specter of compression erosion plasma flow

At $U_0 = 3.0$ kV concentration of free electron into the compression plasma flow is equal about $3.3\cdot10^{16}$ cm^{-3} and temperature – 1.7 eV. Such parameters are sufficiently high for effective solution of different material science tasks.

4. CONCLUSION

The results of the studies show that the miniature end-face erosion device (mini-EFED) is capable of generating high-energy compression erosion plasma flows. At the initial voltage of 2.5 kV, the CEPF possesses the following parameters: duration of the discharge half-cycle is ≈ 100 ms, the maximum discharge current is ≈ 18 kA, the discharge energy is ≈ 470 J, the velocity of plasma formations in the flow – of the order of $1.8 \cdot 10^4$ m/s.

Composition of the compression erosion plasma flows generated by the miniature end-face erosion device according to the qualitative spectroscopic analysis is governed by the material of an inner electrode.

Initial quantitative spectroscopic analysis demonstrated that concentration of free electron into the main compression flow is equal $3.3 \cdot 10^{16}$ cm^{-3} and temperature of the plasma particles – 1.7 eV.

REFERENCES

1. MOROZOV, A. Principles of coaxial (quasi-) steady plasma accelerators. *Sov. J. Plasma Phys.*,1990, Vol. 16, P. 69.
2. ASTASHINSKI, V., BAKANOVICH, G., MIN’KO, L. Investigation of the dynamics of plasma formation and the formation of the compression region of a gas electromagnetic plasma accelerator. *Journ. of Appl. Spectr.*, 1980, Vol. 33, No. 4, p. 1061–1064.
3. ASTASHINSKII, V., BAKANOVICH, G., KUZ'MITSKII, A., MIN'KO, L. Choice of operating conditions and plasma parameters of a magnetoplasma compressor. *Journ. of Engineering Physics and Thermophysics*, 1992, Vol. 62, No. 3, p. 281–284.
4. UGLOV, V., ANISHCHIK, V., ASTASHYNSKI, V., CHERENDA, N., GIMRO, I., KOVYAZO, A. Modification of WC hard alloy by compressive plasma flow. *Surf. Coat. Technol.*, 2005, Vol. 200, Iss. 1–4, p. 245–249.
5. UGLOV, V., CHERENDA, N., ANISHCHIK, V., STALMASHONAK, A., KONONOV, A., PETUHOV, YU., ASTASHINSKI, V., KUZMITSKI, A. Surface alloying of metals using a quasi-stationary plasma accelerator. *High Temp. Mat. Proc.*, 2007, Vol. 11, Iss. 3, p. 383–391.
6. PURIC, J., ASTASHYNSKI, V., DOJCINOVIC, I., KURAICA, M. Creation of silicon submicron structures by compression plasma flow action. *Vacuum*, 2004, Vol. 73, Iss. 3–4, p. 561–566.
7. UGLOV, V., KVASOV, N., PETUKHOV, Y., ASTASHINSKII, V., KUZ'MINSKII, A. Phase formation and structural changes in the chromium-silicon system exposed to compressed plasma fluxes, *Journ. of Surface Investigation. X-ray synchrotron and neutron techniques*, 2010, Vol. 4, Iss. 2, p. 338–342.
8. CHERENDA, N., BIBIK, N., UGLOV, V., ASTASHINSKI, V., KUZ’MITSKI, A. Synthesis of surface layers hardened by metal trialuminide compound in Al-Si alloy under compression plasma flows impact. *High Temp. Mat. Proc.*, 2014, Vol. 18, No. 1–2, p. 1–13.
9. CHERENDA, N., KULESHOV, A., SHYMANSKI, V., UGLOV, V., BIBIK, N., RUSALSKI, D., ASTASHINSKI, V., KUZ’MITSKI, A. Formation of Nb-containing alloys in the surface layer of materials by compression plasma flows. *High Temp. Mat. Proc.*, 2015, Vol. 19, No. 2, p. 153–167.
10. ASTASHINSKI, V. Formation of compression erosion plasma flows in dense gases. *Journ. of Appl. Spectr.*, 2000, Vol. 67, No. 2. p. 229 –233.

AUTOIGNITION OF DECANE/AIR MIXTURE IN THE RAPID COMPRESSION MACHINE AT INTERMEDIATE TEMPERATURES

V. V. Leschevich, O. G. Penyazkov, S. Yu. Shimchenko
Heat and Mass Transfer Institute
P. Brovki str. 15, 220072 Minsk – Belarus
Email: sergey.shimchenko@gmail.com

ABSTRACT

Autoignition experiments for homogeneous stoichiometric *n*-decane/air mixture have been performed using a heated rapid compression machine (RCM) under the following conditions at the end of compression stroke: pressures 0.6–1.0 MPa and temperatures 830–1000 K. These conditions provoke interest because ignition delay time of *n*-decane increases as temperature rises - negative temperature coefficient (NTC) phenomenon. Present data are compared with the results for the similar mixture density obtained by shock tube (ST) at high temperatures and available in the literature. Agreement between RCM and ST ignition delay times is found to be satisfactory and they exhibit together a monotonically increasing trend of ignition delay with a decrease in temperature. No evidence of the onset of the NTC-regime for ignition delay for stoichiometric *n*-decane/air mixture is seen for the studied range of conditions. It is shown that autoignition of the tested mixture occurs homogeneously and is insensitive to contaminating burning particles by high-speed video imaging of ignition and combustion processes.
Moreover, it was observed that the addition of aluminum nanoparticles into test chamber did not lead to drastic changes of ignition and combustion processes of *n*-decane/air mixture at the temperature 910 K.

Keywords: *n*-Decane, autoignition, ignition delay, rapid compression machine

1. INTRODUCTION

n-Decane is one of the normal alkanes that are often chosen as the component of surrogate jet and diesel fuels [1]. Studies related to the auto-ignition behaviours of various surrogate neat components are of fundamental and practical importance because it is the underlying phenomenon for the combustor design of most engines and ignition delay data have extensive uses in the development and validation of combustion reaction mechanisms. Experiments on the ignition of *n*-decane have already been carried out and most of them were conducted in the heated shock tube at high temperatures [2–8]. Probably, only in one of these studies ignition delay times of *n*-decane/air mixtures were measured within a wide variation range of temperatures 650–1300 K [2]. Data from this paper show a negative temperature coefficient (NTC) in the Arrhenius plot and afterwards were used as kinetic targets for most kinetic mechanisms of *n*-decane oxidation. Although Zhukov et al. [5] reported ignition delay time data at the temperatures below 1000 K, his measurements are limited in the range of high pressures. The NTC behaviour was found for experimental data at the temperatures of 790–1000 K and pressures about 8 MPa for stoichiometric mixtures and the depth of pothole is even larger in comparison with data of Pfahl et. al [2] at a pressure of 5 MPa. The remaining data of Zhukov et. al. received at 1–1.3 MPa for stoichiometric mixtures and at 8–10 MPa for lean mixtures follow the linear inverse temperature dependence of logarithms of the ignition delay times at the temperatures higher than 1000 K. Using a rapid compression machine (RCM) the ignition of *n*-decane was studied only by Kumar et al. [9]. The ignition delay times for lean and rich mixtures were obtained in the temperature variation range of 635–770 K and pressure range of 0.7–3.0 MPa. Thus, there is a lack of the experimental data for intermediate temperature range, which does not allow to investigate the temperature effects on the ignition delay times of *n*-decane. The objective of this study is to extend the range of available experimental data for auto-ignition of *n*-decane, with special emphasis on temperatures ranging from 800 to 1000 K. Experiments were conducted using a rapid compression machine (RCM) for homogeneous stoichiometric *n*-decane/air mixtures at pressures ranged from 0.6 to 1 MPa in order to connect the new data together with the data obtained by shock tube [7] at the high temperatures. The same study was previously carried out with methane-air mixtures [10]. It was showed the unavoidable presence of contaminating ultrafine particles in the test volume, as well as their capability to be auto-ignited and to provoke earlier ignition of gas mixtures. Therefore, the high-speed imaging system of the auto-ignition and combustion processes was used during each experiment of this study to detect the influence of contaminating particles on time and spatial uniformity of *n*-decane ignition.

2. EXPERIMENTAL PROCEDURES

The RCM is a single-shot, piston-cylinder compression device which compresses a given mass of premixed gaseous mixture to the desired final pressure and temperature in a short interval of time (20–40 ms). The compressed gas temperature at the end of compression or top dead centre (TDC) is achieved by altering the compression ratio by adjusting the stroke length. The pressure at TDC can be independently controlled by varying the initial pressure of the reactants. Details about the RCM design and operational features can be found in Ref. [10]. Since the current experiments are conducted for a relatively low vapor pressure fuel, the combustion chamber walls and its associated feed lines are maintained at an elevated temperature to prevent condensation of the fuel. The preheating temperatures in these experiments, obtained by electrical heating elements, typically about 60 °C. The cylindrical 50 mm in diameter reaction chamber is equipped with a Kistler 6031U18 pressure sensor combined with a Kistler 5015A charge amplifier, a valve providing access to the reactor chamber for feeding reactants and a quartz windows enabling side and end optical access. Through the side wall window (dia. 5 mm) light emission occurring during ignition and combustion was recorded by two photomultiplier tubes (PMT). Interference filter transmitting the wavelength of 430.8 nm was installed in front of the first PMT photocathode for detecting emission of exited CH, while the second PMT with photosensitivity in the wave range of 300–600 nm was used for overall light registration. The quartz window (dia. 50 mm) at the end of the compression cylinder was used for high-speed imaging of the ignition and combustion processes by «LaVision HighSpeedStar X» camera at a frequency of 12,500 frames per second and resolution of 1024 × 1024. A homogeneous stoichiometric mixture of *n*-decane vapor and air (O_2 – 20.73%, N_2 – 77.93%, $C_{10}H_{22}$ – 1.34%) was prepared in a stainless-steel tank of the known volume. The liquid fuel component (about 70 μl) is added under ambient conditions to the vacuumed (< 13 Pa) tank on a gravimetric basis by using burette. Then the volume is filled with the synthetic air (20.9% O_2 and 79.1% N_2) from the other vessel to pressure needed for stoichiometric composition. This pre-mixture is subsequently heated up to a temperature at which the partial pressure of the fuel vapor in the mixture is well below its saturation value. The heating lasts more than 5 h, to enable complete vaporization of the liquid component and mixing with air.

3. RESULTS AND DISCUSSION

Typical experimental pressure and photomultipliers signals records are shown in the Fig. 1. Signals of four experiments are superimposed on consolidated plot by the end of the compression stroke ($t = 0$) that corresponds to the time moment of the maximum pressure rise. All these experiments were conducted under the same initial conditions (13 kPa and 333 K) and adjustments of RCM (compression ratio 21 ± 0.1). The calculation of ideal adiabatic pressure and temperature at the end of compression gives values of 0.706 MPa and 860 K. As it can be seen from the experimental records in Fig. 1, the pressure measured at the TDC varies from test to test and is higher than that of adiabatic value. The TDC temperatures derived from the measured pressures at the start and the end of compression according to “adiabatic core” hypothesis exceed the ideal adiabatic value by 30–70 K. The opposite occurrence is usually observed as a consequence of the heat losses and boundary layer effects. Several reasons may cause this phenomenon. First of all, when piston assembly quickly stops from high velocity (up to 15 m/s) the compression piston makes several longitudinal vibrations near the end position. This causes a short-time increase of the compression ratio and thus the final pressure and temperature. But this occurrence can't fully explain the observed discrepancy because the displacement of about 4 mm has to occur to compensate the entire excess of pressure. On the other hand, this can be attributed to the exothermic reaction occurring in the final stages of compression [11]. Especially it is pronounced for the reactive mixtures that exhibit two-stage ignition. As it was found for *n*-decane ignition [9], the first-stage low-pressure rise is relatively insensitive to temperature variations and is able to quickly initiate even under modest conditions. For example, it took about 1 ms for a lean ($\phi = 0.8$) *n*-decane/air mixture at 14.3 bar and 697 K [9]. This temperature (calculated from pressure traces in the Fig. 1) is achieved at about 3.5 ms before the TDC in experiments 3 and 4. This can explain the more rapid pressure rise as well as shorter ignition delay time in experiment 3 and ignition during compression in experiment 4.

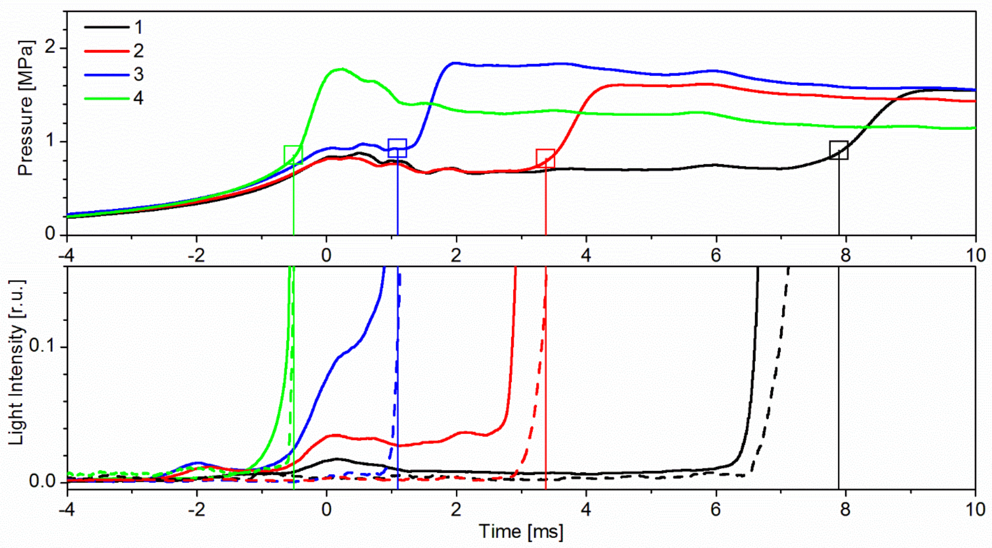

Fig. 1. Top: pressure; bottom: light (solid lines) and CH radical (dashed lines) emission registered in five experiments for stoichiometric *n*-decane/air mixture at the temperature of 860 ± 1 K

Moreover, in experiments 2 and 3, a short-time flash of light was detected by PMT in a low-pressure region at 2 ms before the end of compression while the light emission from excited CH radicals was detected significantly later. A similar light-flash was detected in experiment 1 but it took place a bit after the TDC. In all experiments, the luminescence of CH radicals is in good agreement with the pressure growth caused by the combustion even when the light emitted from the whole volume was collected through the end window by lenses on the photocathode of PMT (experiment 4). The end and side windows light observations are well correlated. This means that the flash in the experiment 4 appears closer to the end of the compression cylinder. No light was registered by a high-speed camera at these time moments perhaps due to the sensitivity limitation of the CCD sensor. Even when the pressure in the test chamber begins to grow for the end of the ignition delay time, the low-intensity images of the reaction zone are still registered (Fig. 2). The time moment of each frame (exposure time is 79 μs) are marked by squares and vertical lines of colour as pressure signals in the Fig. 1. The volumetric ignition was observed simultaneously in several places of the combustion chamber. In addition, at that time, there were no direct observations of burning contaminating particles in the test chamber. They appear later when the combustion zone of *n*-decane extended across the whole cylinder volume.

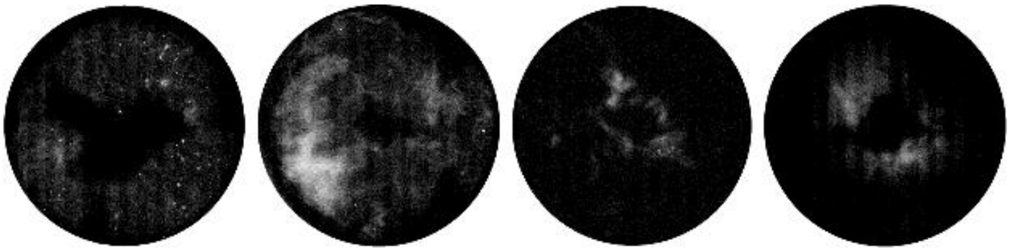

Fig. 2. Images registered at the start of *n*-decane ignition in experiments 1–4 from Fig. 1

The same tendency of *n*-decane ignition behaviour was found at the lower compression ratio (19.63 ± 0.04) that corresponds to the ideal adiabatic pressure of 0.648 MPa and the temperature of 845 K when compression starts from 13 kPa and 333 K. The longest ignition delay is observed when the lowest light-flash appears near the end of compression (experiment 3 in the Fig. 3). The combustion of some contaminants (first frame in the Fig. 4) in the test chamber was found at the time moment corresponding to the high-intensity flash registered by PMT at 1.6 ms after TDC in the experiment 2 as presented in Fig. 3. Probably, it caused more rapid ignition of *n*-decane-air mixture although it has been started in other places of the combustion chamber (frames 2-4 in the Fig. 4).

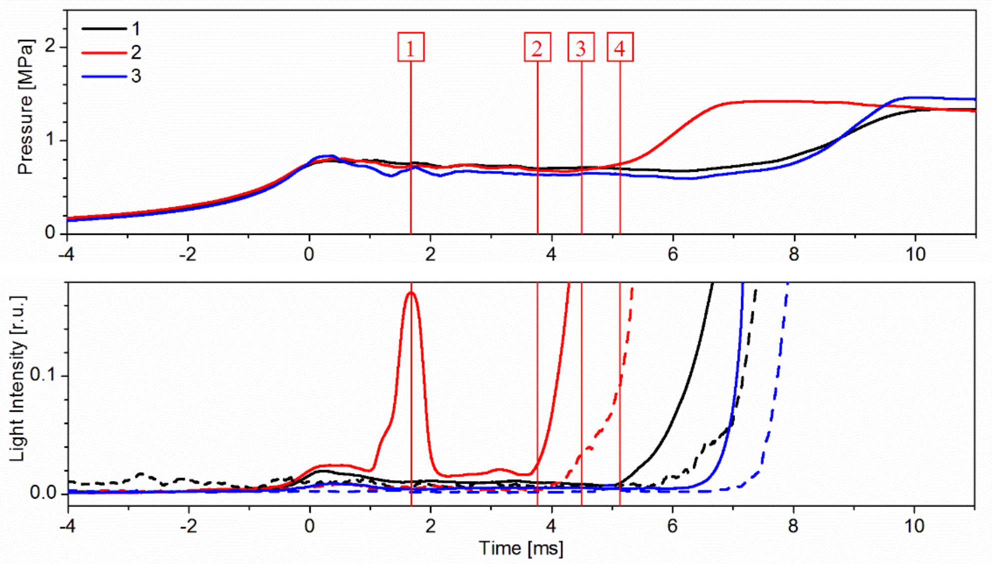

Fig. 3. Top: pressure; bottom: light (solid lines) and CH radical (dashed lines) emission registered in three experiments for stoichiometric *n*-decane/air mixture at the temperature of 845 ± 1 K

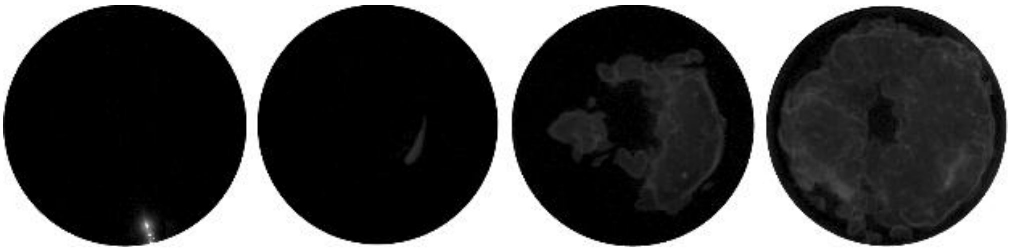

Fig. 4. Frame sequence registered at the *n*-decane ignition in the experiment 2 from Fig. 3

At compression ratio of 18 (adiabatic temperature of 825 K) the ignition of stoichiometric *n*-decane/air mixture was not observed at all. However, PMT registered single flashes of light and high-speed imaging discovered single burning dust particles at these time moments. At the higher compression ratio of 22 (adiabatic temperature of 870 K) the ignition of *n*-decane starts always during the compression process, therefore, the ignition delay times were obtained in a narrow temperature variation range in this study. Moreover, as it was discussed, there is a problem with the definition of temperature at the end of compression. In order to maintain consistency throughout this paper and compare the obtained results with other literature data, the ideal adiabatic value is quoted as the reference temperature. The difference between this value and the temperature derived from the measured pressures at the start and the end of compression is reported as an associated error bar in the Arrhenius plot for the temperature. The ignition delay time was determined by pressure measurements as the time difference between the peak pressure at the end of the compression stroke and the beginning of the pressure rise caused by the ignition of the mixture (5% of the maximum value). The longest time measured during multiple runs under identical conditions is selected as representative data (e.g. experiment 1 in the Fig. 1) and compared with the reported ignition delay data of stoichiometric *n*-decane/air mixtures in a somewhat similar pressure range (0.7–1.4 MPa) in the Fig. 5. Measurements from [9] have been reported for lean and reach mixtures, making it difficult to directly compare these results to the current work, but they are presented on the plot because there are no other data obtained by RCM facility. Similarly, the shock tube data from [5] and [6] measured at the high pressures are shown in Fig. 5 due to the lack of the results at the temperature range of a current study.

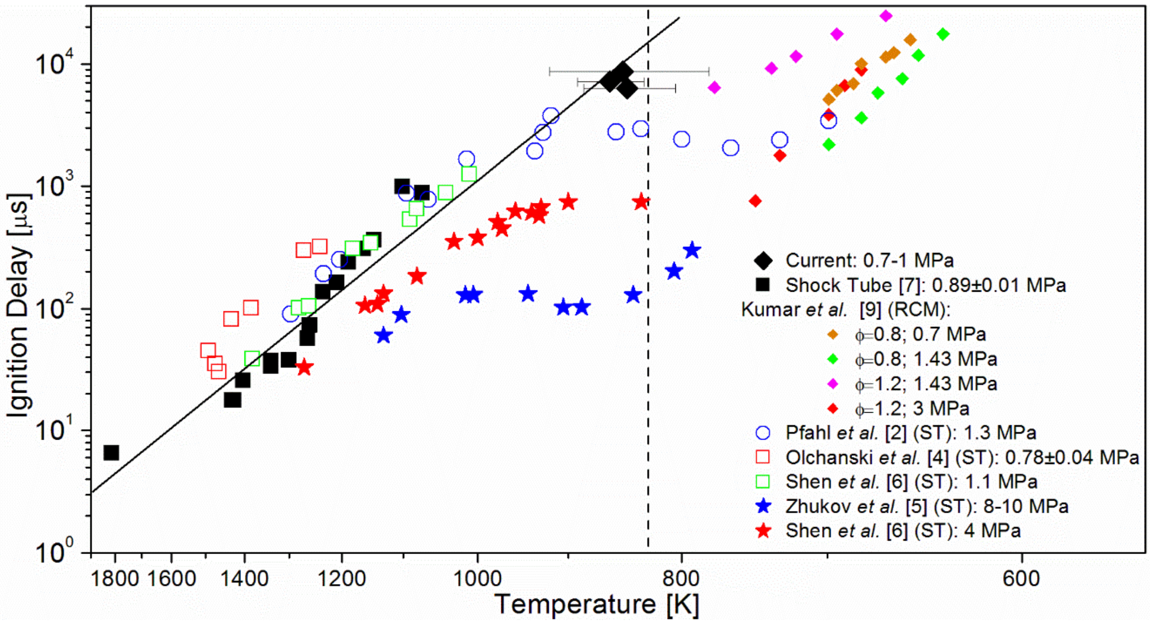

Fig. 5. Comparison of the ignition delay times measured for stoichiometric *n*-decane/air mixture with the literature data

The obtained RCM data complement well as an extension of the high-temperature shock tube data [7] for the same mixture composition and similar density. Measurements of [2] at the post-shock pressure of 1.3 MPa and the same temperatures show shorter ignition delay times and this discrepancy can be even more significant if consider differences in the experimental methods and ignition delay time definitions. Probably, this can be attributed to higher pressures because measurements at 4 MPa from [6] and at 8–10 MPa from [5] show the tendency of drastic reduction of the ignition delay times with increasing pressure. This behavior was also seen in our measurements when a pressure at the end of the compression stroke has been slightly varied. But any relationship has not been established because of the narrow variation range of pressure and discussed the challenge of the temperature interpretation. With regard to RCM data of [9], as an extension of our current RCM and previous shock tube results [7], a better agreement is found for measurements at 1.43 MPa and ϕ = 0.8 in an assumption of a monotonically increasing trend of ignition delay with a decrease in temperature. Moreover, taking into account the absence of ignition at the lower temperature (marked by a vertically dashed line in the Fig. 5) and no evidence of the onset or the inclusion of the NTC-like behavior for the ignition delay for stoichiometric *n*-decane/air mixture with decreasing temperature is seen in the current study.

4. CONCLUSIONS

Ignition of *n*-decane in the air was investigated in RCM at pressures varied from 0.6 to 1 MPa for stoichiometric mixtures within the temperature range of 820–900 K. Volumetric and insensitive to burning contaminating particle ignition was observed simultaneously in several places of the combustion chamber. The significant difference of ignition delay times measured in multiple runs under identical conditions was found. The end and the side wall light emission observation showed that more rapid ignition can be attributed to low-intensity light that can appear in the combustion chamber at different time moments in repeated experiments. Due to sensitivity limitation of CCD sensor of a high-speed camera, this light was not visualized on the images and, therefore, its source was not established. The longest ignition delay times measured from repeated runs were selected as representative data and compared with the reported literature data. Current data match well with that previously obtained at high temperatures in the shock tube for similar mixture density and together exhibit a monotonically increasing trend of ignition delay with the decrease in temperature. No evidence of the onset of the NTC-like behaviour for ignition delay for stoichiometric *n*-decane/air mixture is seen for the studied variation range of pressures.

REFERENCES

1. VIOLI, A., YAN, S., EDDINGS, E. G., SAROFIM, A. F., GRANATA, S., FARAVELLI, T., RANZI, E. Experimental formulation and kinetic model for JP-8 surrogate mixtures. *Combustion Science and Technology*, 2002, Vol. 174, No. 11–12, p. 399–417.
2. PFAHL, U., FIEWEGER, K., ADOMEIT, G. Self-ignition of diesel-relevant hydrocarbon-air mixtures under engine conditions. *In Symposium (International) on Combustion*, 1996, Vol. 26, No. 1, p. 781–789.
3. HORNING, D. C. A study of the high-temperature auto-ignition and thermal decomposition of hydrocarbons. *Report No. TSD-135*, 2001.
4. OLCHANSKI, E., BURCAT, A. Decane oxidation in a shock tube. *International journal of chemical kinetics*, 2006, Vol. 38, No. 12, p. 703–713.
5. ZHUKOV, V. P., SECHENOV, V. A., STARIKOVSKII, A. Y. Autoignition of n-decane at high pressure. *Combustion and Flame*, 2008, Vol. 153, No. 1–2, p. 130–136.
6. SHEN, H. P. S., STEINBERG, J., VANDEROVER, J., OEHLSCHLAEGER, M. A. A shock tube study of the ignition of n-heptane, n-decane, n-dodecane, and n-tetradecane at elevated pressures. *Energy & Fuels*, 2009, Vol. 23, No. 5, p. 2482–2489.
7. DEAN, A. J., PENYAZKOV, O. G., SEVRUK, K. L., VARATHARAJAN, B. Autoignition of surrogate fuels at elevated temperatures and pressures. *Proceedings of the Combustion Institute*, 2007, Vol. 31, No. 2, p. 2481–2488.
8. NIE, X. F., LI, P., ZHANG, C. H., XIE, W., LI, C. S., LI, X. Y. Shock tube study of n-decane ignition at low pressures. *Acta Mechanica Sinica*, 2012, Vol. 28, No. 1, p. 79–82.
9. KUMAR, K., MITTAL, G., SUNG, C. J. Autoignition of n-decane under elevated pressure and low-to-intermediate temperature conditions. *Combustion and Flame*, 2009, Vol. 156, No. 6, p. 1278–1288.
10. LESCHEVICH, V. V., MARTYNENKO, V. V., PENYAZKOV, O. G., SEVROUK, K. L., SHABUNYA, S. I. Auto-ignitions of a methane/air mixture at high and intermediate temperatures. *Shock Waves*, 2016, Vol. 26, No. 5, p. 657–672.
11. GRIFFITHS, J. F., HALFORD-MAW, P. A., ROSE, D. J. Fundamental features of hydrocarbon autoignition in a rapid compression machine. *Combustion and flame*, 1993, Vol. 95, No. 3, p. 291–306.

CYSENI 2018, May 23-25, Kaunas, Lithuania
ISSN 1822-7554, www.cyseni.com

INVESTIGATION OF KINETIC PARAMETERS FOR COMBUSTION OF PET BOTTLE CAPS WITH LIGNITE

S. Mertdinç
Metallurgical and Materials Engineering Department, Istanbul Technical University,
Istanbul, 34469 – Turkey
Email: mertdinc@itu.edu.tr

N. I. Ünal, H. Haykiri-Acma, S. Yaman
Chemical Engineering Department, Istanbul Technical University,
Istanbul, 34469 – Turkey
Email: yamans@itu.edu.tr

ABSTRACT

The huge amount of PET plastic bottles are consumed that leads to serious environmental pollutions and harmful ecological effects. Plastic bottle originated toxic pollutants cause the land, water, air pollutions and damage ecological communities and ecosystem functions. When the plastic bottle caps are used as alternative energy source, the energy and waste management problems and negative environmental effects can be eliminated. The aim of this paper is to evaluate PET bottle caps as renewable energy source in combustion process. In this context, these materials were blended with low quality lignite to improve the thermal properties of the lignite. Thermogravimetric analysis method was employed and the obtained thermal data was evaluated according to Borchardt and Daniels (B&D) kinetic analysis method to determine the kinetic parameters of the combustion of the these PET/lignite blends. The results of this study showed that the burning behavior of PET and lignite differ seriously from each other, and the presence of PET in the blends improved the fuel properties of the lignite.

Keywords: Combustion, fuel, lignite, PET bottle caps, kinetic analysis

1. INTRODUCTION

Across the world, amounts of plastic production increase twenty times within the 50 years and reach the 311 million tones. Amount of the produced plastics for the packaging applications correspond the nearly one fourth of these [1]. PET bottles are widely used plastic packaging materials. According to North Sea Foundation, annual production amount of PET bottles is 530 billion in 2016 around the world and it is expected that these amount increases 4.7 % for every following year [2]. Additionally, one of the world's largest cap manufacturers reported that their bottle cap production amount is 78 billion caps in 2016 [2]. Plastic bottle caps are the third most common found wastes at the beaches after the cigarettes and snack packaging. Because caps are very small to washed up to beaches [2]. Also, huge amount of waste plastics into the ocean ecosystem are hazardous for many species such as not only sea turtles, fishes and birds, but also microscopic planktons [2]. Microplastics or fibers were ingested by the microorganisms into the marine, then this plastic debris participates the marine food chain from microscopic organisms to other animals [3].

Besides, PET bottle caps are produced non-PET materials such as polypropylene (PP), high density polyethylene (HDPE) etc. [4]. Recycling of polymeric materials can be classified into four classes. First, polymeric wastes are cleaned and reshaped [5] Second, polymeric wastes are cleaned, granulated and reformed by using the mechanical size reduction processes [5]. Third, chemical recycling methods are used for PE, HDPE wastes. For example, pyrolysis, gasification, liquid–gas hydrogenation, viscosity breaking, steam and catalytic cracking are the main chemical recycling methods [6, 7]. Waste plastic materials are divided into small molecules, liquids or gases via chemical recycling methods, then these reduced parts of the wastes are used as feedstock for new polymer production [6]. Among these methods, sorting and separation of the plastic wastes are not easy and economical, therefore these wastes can be used for energy recovery applications different from the other three techniques [5]. Organic substances inside the polymeric wastes lead to high calorific values, so ignition of the wastes have high energy potential [8]. Besides, due to increments of the fuel costs, there has been increasing attention on the usage of polymer wastes as source of fuel. Amongst them, PET bottle cap wastes were regarded for energy recovery in this study.

On the other hand, Turkey has abundant lignite reserves, of which Afşin-Elbistan region accounts for the most significant lignite reserves in Turkey [9]. Although, lignite reserves are rich in Turkey, the quality of the lignite is poor due to its low calorific value, high moisture, high sulphur and high ash contents [10, 11]. Nevertheless, these lignites are burned in power plants since oil and natural gas reserves of Turkey are very low, and far from providing the energy need. Although there have been national regulations to protect the air quality, these poor properties of the lignitic coals may lead to several environmental problems when they are used as fuel. Besides, mining and production of the lignite are not easy because of the storage, transportation and purification conditions [10]. Therefore, lignites are unfavorable for consumption. However, the abundant lignite reserves in Turkey must be evaluated in the efficient, economic and environment-friendly ways [9].

In this study, PET bottle caps were blended with the low quality lignite coals to improve the heating properties of the lignite. According to the thermal analysis, kinetic parameters for the blends were determined.

2. MATERIALS AND METHODS

Two different types of samples that are consisted of PET bottle caps and lignite have been used as mentioned at previous study [12]. This study was started with the collection of the PET bottle caps that belong to different commercial brands of PET water bottles sold in Turkey. Collected bottle caps were granulated by using a domestic metallic grate. Granulation was implemented to get samples with sizes in millimeter scale. Aside from the caps samples, Afsin-Elbistan lignite that is the other raw material for this study was prepared. Firstly, Afsin-Elbistan lignite was dried in open container at nearly 25–30 °C conditions for several days. Because, measured moisture content of the lignites was 6.97% [12]. After this drying step, excessive moisture of the lignite samples was reduced. Representative samples were taken according to ASTM D2234-02 and ASTM D7430-17 standards. After that, lignite samples were milled with hammer mill and coal grinder, respectively. Then, milled samples were sieved to get powders with a particle size of under 0.250 mm [12]. Prepared lignite and PET bottle cap samples were mixed with various amounts for this study. 5, 10 and 15% wt. PET bottle caps including lignite samples were blended. Hereafter, blends were mentioned as Lignite – (5, 10 or 15) PET caps.

Thermal analysis of both PET bottle caps/lignite blends were conducted via TA Instruments SDTQ600 model thermal analyzer. This thermal analyzer has temperature range up to 1500 °C with 0.001 °C sensitivity and alumina was used as reference material. Also, it has 0.1 μg balance sensitivity that is important for thermogravimetric analysis. For the thermogravimetric analysis, 10 mg of both samples were placed into alumina crucible and heated up to 900 °C with a 40 °C/min heating rate under dry air atmosphere with 100 ml/min flow rate. Obtained thermal data was evaluated according to Borchardt and Daniels (B&D) kinetic analysis method to determine the kinetic parameters of the combustion of the PET bottle caps/lignite samples.

B&D kinetic analysis firstly bases on the reaction degree as “n” and general rate equation. Accordingly, kinetic parameters are calculated via Equation 1.

$$\frac{da}{dt} = k(T)\,[1-a]^{n} \tag{1}$$

where: da/dt – reaction rate (s^{-1}); a – conversion; k(T) – temperature dependent rate constant; n – reaction degree.

Second assumption for the B&D calculations, k(T) term can be determined with Arrhenius Equation as given at Equation 2.

$$k(T) = Z\, e^{(-Ea/RT)} \tag{2}$$

where: Ea – activation energy ($J.mol^{-1}$); Z – pre-exp factor (s^{-1}); R – gas constant (8,314 $J.mol^{-1}{\cdot}K^{-1}$).

Combination of the both Equation 1 and Equation 2 were simplified at Equation 3.

$$\frac{da}{dt} = Ze^{[-Ea/RT]}[1-a]^{n} \tag{3}$$

Taking the logarithm of the Equation 3 and then linear regressions helps to determination of the kinetic parameters.

3. RESULTS AND DISCUSSION

Kinetic parameters that consist of reaction degree, activation energy ($kJ.mol^{-1}$), heat of reaction ($J.g^{-1}$) and pre-exponential factor ($log.min^{-1}$) were determined according to Borchardt and Daniels (B&D) kinetic analysis and given at Table 1. It is well-known that the combustion of coal is a highly complex process and covers burning of the combustible volatiles in the gaseous phase (homogeneous combustion) and the burning of the fixed carbon through surface oxidation (heterogeneous combustion). The governing mechanisms of these burning stages are quite dissimilar in each case and many burning characteristics including the reactivity and the combustion kinetics change considerably. That is why these very different two combustion regimes can not be modelled properly using a unique simple kinetic model at the same time. Thus, burning of the volatile matter or fixed carbon is generally investigated individually by considering given temperature intervals. Rapid burning of the volatiles take place relatively at lower temperature region, while slow burning of the fixed carbon necessitates higher temperatures. For this reason, Table 1 presents the results of the kinetic parameters obtained for these two regimes separately as well as the whole (total) process. As it can be noticed from the activation energies for lignite, burning of the fixed carbon needs relatively higher activation energy and it is the rate controlling stage. This is also consistent with the fact that fixed carbon burning occurs at higher temperatures compared to that for the volatiles. Accordingly, the highest pre-exponential factor was also determined for the fixed carbon burning. In addition, the reaction degrees also differ from each other seriously.

Fig. 1 also presents the effects of the presence of the PET bottle caps as an additive material in lignite blends. That is, the activation energies for both burning regimes reduced because of improving effect of PET materials on combustibility. Actually, such waste biomass materials are highly rich in volatile matter content at the expense of the fixed carbon content and the addition of them to lignite usually increases the volatile matter content of the blend fuel, leading obvious increases in the thermal reactivity. Therefore, the activation energies especially for the volatile matter burning stage showed definite reductions compared to the case where only lignite was burned. On the other hand, another positive contribution of the PET bottle caps to the combustion characteristics of lignite can also be observed in the improvements of the heat of reaction values. Namely, burning of both volatile matter and fixed carbon contents produced relatively higher heat of reaction values when PET material was added to lignite. This is very evident for the blending ratios of 5 and 10 wt.% additions. Besides, any regular trend could not be found about the effects of the presence of PET bottle caps on the reaction degrees. 5 and 10 wt.% additions of PET reduced the total activation energies compared to that of lignite as expected. This indicates that additive rule is valid for these blending ratios. However, it is impossible to explain the increase in the total activation energy when the blending ratio increased to 15 wt%, and the synergistic behavior should be considered.

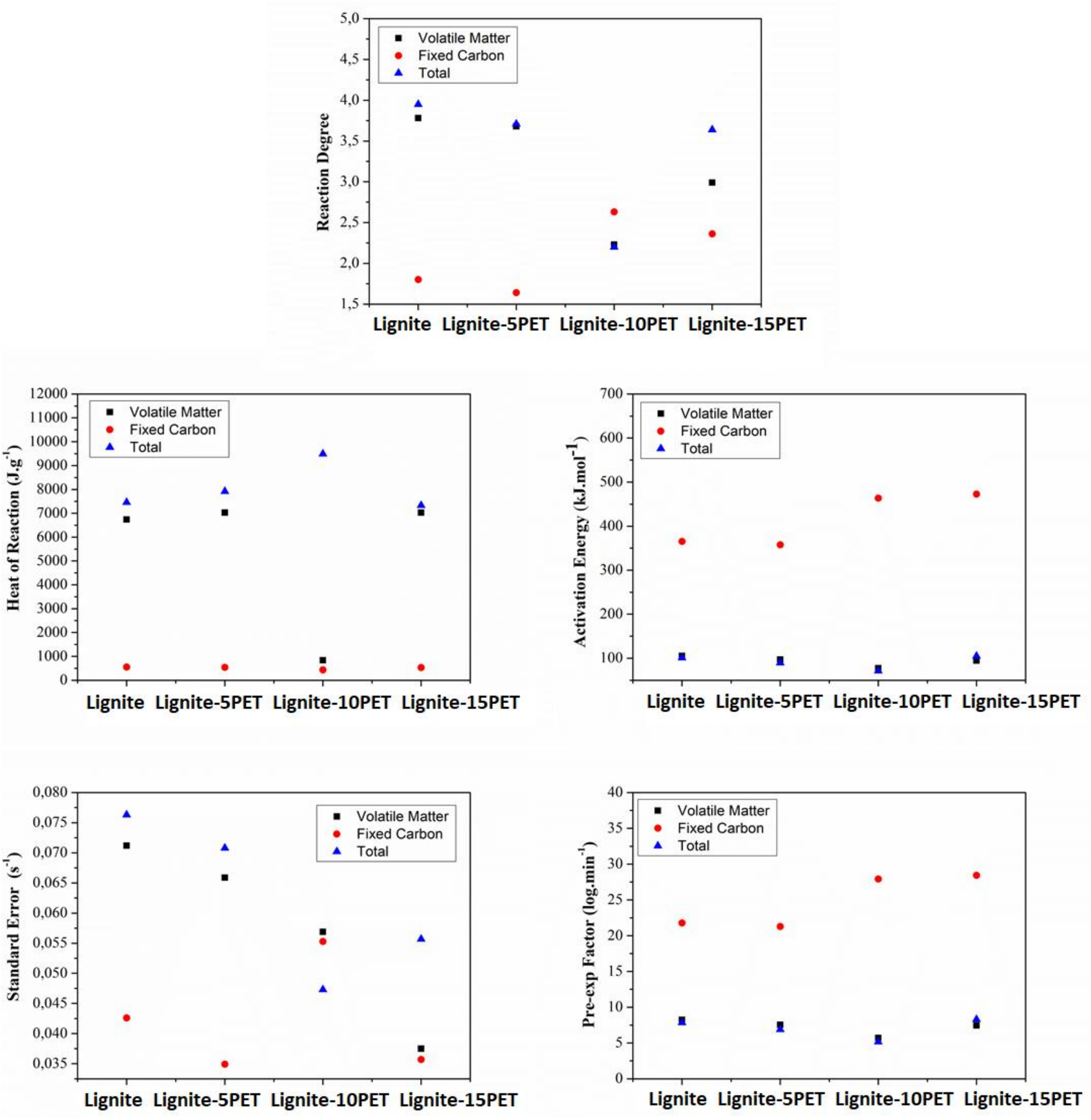

Fig. 1. Kinetic parameters for lignite and lignite/PET bottle caps blends

Table 1. Kinetic parameters

Lignite					
	Reaction Degree	**Activation Energy (kJ.mol^{-1})**	**Heat of Reaction (J.g^{-1})**	**Pre-exp Factor (log.min^{-1})**	**Standard Error (s^{-1})**
Volatile Matter	3.78	105.3	6739.2	8.22	0.0712
Fixed Carbon	1.80	365.1	554.6	21.78	0.0426
Total	3.95	101.3	7461.7	7.84	0.0763

Lignite-5PETcaps					
	Reaction Degree	**Activation Energy ($kJ.mol^{-1}$)**	**Heat of Reaction ($J.g^{-1}$)**	**Pre-exp Factor ($log.min^{-1}$)**	**Standard Error (s^{-1})**
Volatile Matter	3.68	97.1	7029.5	7.55	0.0659
Fixed Carbon	1.64	357.6	540.9	21.28	0.0349
Total	3.71	89.8	7917.4	6.88	0.0708
Lignite-10PETcaps					
	Reaction Degree	**Activation Energy ($kJ.mol^{-1}$)**	**Heat of Reaction ($J.g^{-1}$)**	**Pre-exp Factor ($log.min^{-1}$)**	**Standard Error (s^{-1})**
Volatile Matter	2.23	77.5	841.3	5.70	0.0569
Fixed Carbon	2.63	463.6	430.1	27.91	0.0553
Total	2.20	71.4	9494.4	5.17	0.0473
Lignite-15PETcaps					
	Reaction Degree	**Activation Energy ($kJ.mol^{-1}$)**	**Heat of Reaction ($J.g^{-1}$)**	**Pre-exp Factor ($log.min^{-1}$)**	**Standard Error (s^{-1})**
Volatile Matter	2.99	94.5	7031.4	7.45	0.0375
Fixed Carbon	2.36	472.8	527.5	28.44	0.0357
Total	3.64	104.9	7332.2	8.30	0.0557

Some parameters relevant to the burning characteristics of lignite such as the burning time (t_C), the maximum burning rate (R_{max}), the temperature of the maximum burning rate (T_{Rmax}), and the ignition temperature (T_{ign}) were determined from the DTG (Derivative Thermogravimetry) and DSC (Differential Scanning Calorimetry) profiles upon burning in the thermal analyzer. Table 2 gives the results of these parameters to interpret the effects of PET bottle caps on combustion reactivity of lignite that is may be the most significant factor in the design and operation of a solid fuel burning system. The time for complete combustion of lignite was not affected at all when the blending ratio of PET bottle caps was only 5 wt.%. This may be attributed to the fact that low ratio of PET was added to the fuel blends, and it was incapable of changing the complete combustion time of the blend. However, addition of 10 or 15 wt.% ratios shortened the time from 20 min to 19 min that is almost ignorable. On the other hand, maximum burning rate of lignite was affected from the biomass addition and accordingly R_{max} values increased as the ratio of the biomass increases in the blends. Besides, the temperatures at which the maximum burning rates are observed firstly reduced and than increased. Complex interactions of the constituents found in the individual fuels of the blends may lead such variations. For instance, inorganics in the mineral matter of lignite may show interactions with some organic compounds found in PET through catalytic or inhibiting effects, shifting the temperatures to higher values. Another parameter, ignition temperature, showed a regular trend with PET additions. That is, the highest ignition temperature (255 ºC) belongs to the sample *Lignite-15PETCaps* that is the sample containing the maximum amount of PET bottle caps.

Table 2. Comparison of some combustion parameters

Sample	**t_C (min)**	**R_{max} (%/min)**	**T_{Rmax} (°C)**	**T_{ign} (°C)**
Lignite	20	8.12	776	245
Lignite-5PETCaps	20	8.03	338	247
Lignite-10PETCaps	19	10.95	416	253
Lignite-15PETCaps	19	11.06	760	255

t_C – burning time; R_{max} – max. burning rate; T_{Rmax} – Temperature at max. burning rate; T_{ign} – Ignition temp.

4. CONCLUSIONS

This study showed that the PET bottle caps can be regarded as an alternative waste biomass fuel since it is combustible and also has improving effects on the fuel characteristics of poor quality fuels like low rank coals. On the other hand, this study revealed the differences in the combustion properties of PET bottle caps and a Turkish lignite from Afşin-Elbistan region. Combustion kinetics based on the burning of both volatile matter and fixed carbon stages showed the significant effects of the presence of PET materials in the lignite blends. Also, some parameters relevant to the combustion such as the ignition point and the maximum burning rate also confirmed the fact that addition of PET bottle caps is able to improve the combustion characteristics of the lignite.

REFERENCES

1. Ellen MacArthur Foundation (2016) The New Plastics Economy: Rethinking the future of plastics. Ellen MacArthur Foundation 120 . doi: 10.1103/Physrevb.74.035409 .
2. Foundation NS (2017) The plastic bottle cap report.
3. Thompson RC, Olson Y, Mitchell RP, et al (2004) Lost at Sea: Where Is All the Plastic? Science 304:838 . doi: 10.1126/science.1094559 .
4. Welle F (2011) Twenty years of PET bottle to bottle recycling - An overview. Resources, Conservation and Recycling 55:865–875 . doi: 10.1016/j.resconrec.2011.04.009 .
5. Sinha V, Patel MR, Patel J V. (2010) Pet waste management by chemical recycling: A review. Journal of Polymers and the Environment 18:8–25 . doi: 10.1007/s10924-008-0106-7 .
6. Al-Salem SM, Lettieri P, Baeyens J (2009) Recycling and recovery routes of plastic solid waste (PSW): A review. Waste Management 29:2625–2643 . doi: 10.1016/j.wasman.2009.06.004 .
7. Achilias DS, Andriotis L, Koutsidis I., et al (2012) Recent Advances in the Chemical Recycling of Polymers (PP, PS, LDPE, HDPE, PVC, PC, Nylon, PMMA). Material Recycling - Trends and Perspectives 1–63 . doi: 10.5772/33457 .
8. Yamashita K, Yamamoto N, Mizukoshi A, et al (2009) Compositions of volatile organic compounds emitted from melted virgin and waste plastic pellets. Journal of the Air and Waste Management Association 59:273–278 . doi: 10.3155/1047-3289.59.3.273 .
9. Ediger VS, Berk I, Kösebalaban A (2014) Lignite resources of Turkey: Geology, reserves, and exploration history. International Journal of Coal Geology 132:13–22. doi: 10.1016/j.coal.2014.06.008 .
10. Gurbuz-Beker U, Kucukbayrak S, Ozer A (1998) Briquetting of Afsin-Elbistan lignite. Fuel Processing Technology 55:117–127.
11. Magalhães D, Kazanç F, Riaza J, et al (2017) Combustion of Turkish lignites and olive residue: Experiments and kinetic modelling. Fuel 203:868–876. doi: 10.1016/j.fuel.2017.05.050 .
12. Unal, I., Mertdinç, S., Haykırı-Açma, H., Yaman S (2017) ScienceDirect ScienceDirect The of Comparison the fuel properties and the combustion behavior of PET bottle caps with lignite Assessing the feasibility of using the heat demand-outdoor temperature function for a long-term district heat a demand.

CYSENI 2017, May 25-26, Kaunas, Lithuania
ISSN 1822-7554, www.cyseni.com

INVESTIGATION OF FLAME MONITORING AND Na*, K*, Ca* RADICALS EMISSION DURING COMBUSTION OF BIOMASS PARTICLE

M. Sadeckas, N. Striūgas
Lithuanian Energy Institute
Breslaujos str. 3, LT-44403 Kaunas – Lithuania
Email: Marius.Sadeckas@lei.lt, Nerijus.Striugas@lei.lt

ABSTRACT

Increase of the biomass usage, the quality of the feedstock for energy production becomes worse. During thermal degradation of biomass, various chemical transformation occurs and due to change of fuel properties it is hardly to forecast the whole combustion process. The biggest challenges occurring during combustion is related with an ash issues. Flame and combustion monitoring using chemiluminescence method has received a lot of attention for combustion sensing and diagnostic applications in various fields. For example: flame monitoring in furnaces, combustion optimization, monitoring emitted radicals and to find flame stabilization methods. The main radiative species of radicals in typical hydrocarbon-air flames are CH•, OH•, C_2•, CO_2•. Chemiluminescence from these radicals provides information about certain element concentration during combustion process. In various reaction zones emission of radicals are different and can be indicated as important combustion parameters. It is using on purpose to find the ways to improve combustion performance and furnace or combustor lifetime. The aim of this investigation is the chemiluminescence phenomenon of the main radicals during combustion of single biomass particle by means of atomic spectroscopy method and ICCD (intensified charge-coupled device) camera. This study focuses on the measurement of Na*, Ca*, and K* emission during the combustion of single biomass pellets doped with different amounts of Na, Ca, and K using a spectroscopy method. In this work, wood and straw pellets are compared. A biomass washing, and soaking procedure was used to demineralize and to dope the biomass samples with different concentrations (0.5%, 2%, 5%) of Na, Ca, and K. The biomass pellets were suspended in a natural gas flame. Temperature was measured with a thermocouple placed inside the biomass pellet. Optical bandpass filters were mounted in an ICCD camera and the emission intensity in the corresponding wavelengths was recorded with the Andor software. In this work, few solid fuel types mainly wood and straw are comparing during combustion. Using atomic spectroscopy method, flame is monitoring and emitted photons in particular wavelength were recorded by Andor program. The results of experimental investigation are summarized and shown as radiant intensity in particular wavelengths. The dependencies of emission intensities on burning regime were determined. Results shows, that when fuel is changing during combustion it is possible to predict the emissions of radicals of different fuels and adjust appropriate regime of combustion.

Keywords: chemiluminescence, biomass, combustion, radicals, spectroscopy, potassium, calcium, sodium

1. INTRODUCTION

Recently, the use of biomass for heat and power production became very significant. With the growth of the biomass usage, the quality of the feedstock for energy production becomes an issue when the feedstock variety increases. During the thermal degradation of biomass, a number of chemical or physical transformations occur, and it is not easy to forecast the whole combustion process when the change of fuel composition varies. The combustion of agro-biofuels poses a significant challenge due to the typically high amount of ash, specifically alkali chlorides, which may lead to the corrosion of the boiler's surfaces. The characteristics of biofuels influence directly the combustion process and ash slagging problems can occur [1–4]. Besides, the fly ash deposited on the heat transfer surfaces of the boiler furnace reduces the efficiency of the boilers. The moisture content, ash content and particle size are some of the main biomass characteristics that determine the quality of combustion [2]. In particular, the potassium content in the biofuels is an indicator of the formation of deposits in the surface of the boiler [3, 4].

Burning poor performance featuring biofuels leads to ash slagging problems [1]. Fly ash deposited on the heat transfer surfaces of the boiler, furnace masonry walls. These things effect negatively the performance of the boilers.

Also, the combustion of biomass mixtures with straw or other agricultural crops, where is more ash contains, many alkali chloride which causes corrosion of boiler surfaces. Humidity, mineral impurities, biomass particle size – it is one of the main characteristics of biofuels which determines the quality of combustion and combustion equipment work. The potassium content in biofuels is one of the main characteristics that determine the ash and plaque formation. Therefore, chemiluminescence method was used to determine the straw, wood, sludge during combustion emissions of potassium, sodium, calcium elements ion intensities [7].

For example, potassium largest exuding intensity seen at the beginning of combustion, then this quantity proportionally decreasing [5]. Biofuel thermal decomposition occurring regularities lack of data encourages researchers to engage in the global experimental and numerical studies. In this work the solid biofuel combustion process optimization, covering the flame in the radicals of the chemiluminescent radiation pattern tests, depending on the combustion conditions, aerodynamic parameters, flame-shaped, excited radical emission intensity levels for assessing the potential for combustion process control limits. Estimated study was based on spectroscopic analysis of the flame. Using atomic spectroscopy and high-sensitivity CCD (charge-coupled device) camera can explore the main radicals in flame of the chemiluminescent radiation pattern, depending on the combustion conditions and fuel parameters.

K-emission spectroscopy has been used to measure the emission of potassium during the combustion of pine, eucalyptus, wheat straw, rape straw, miscanthus, olive residue, and willow doped with different concentrations of potassium [5, 6]. It was found that the emission of potassium can be directly connected with the combustion stages, namely devolatilization and char combustion [5]. Potassium is not the only challenging inorganic, others include sodium and calcium are important too[2]. The emission of sodium and calcium has not acquired attention in the past and more studies are needed. Under these circumstances, the aim of the present work is to investigate the chemiluminescence phenomenon from Na*, K*, and Ca* during the combustion of single biomass particle.

2. MATERIALS AND METHODS

2.1. Biomass samples

In this work, two types of biomass that are wooda and straw were used to a procedure to remove the ashes and impregnated different quantities (0.5 wt %, 2.0 wt. %, 5.0 wt. %) of Na, K, and Ca. The washing and doping procedure consists of using HNO_3 acid for the washing procedure and adding the required concentration of minerals for doping the samples. Fig. 1 shows the alkali content found in the original samples, and in the samples before and after the washing and the doping procedure.

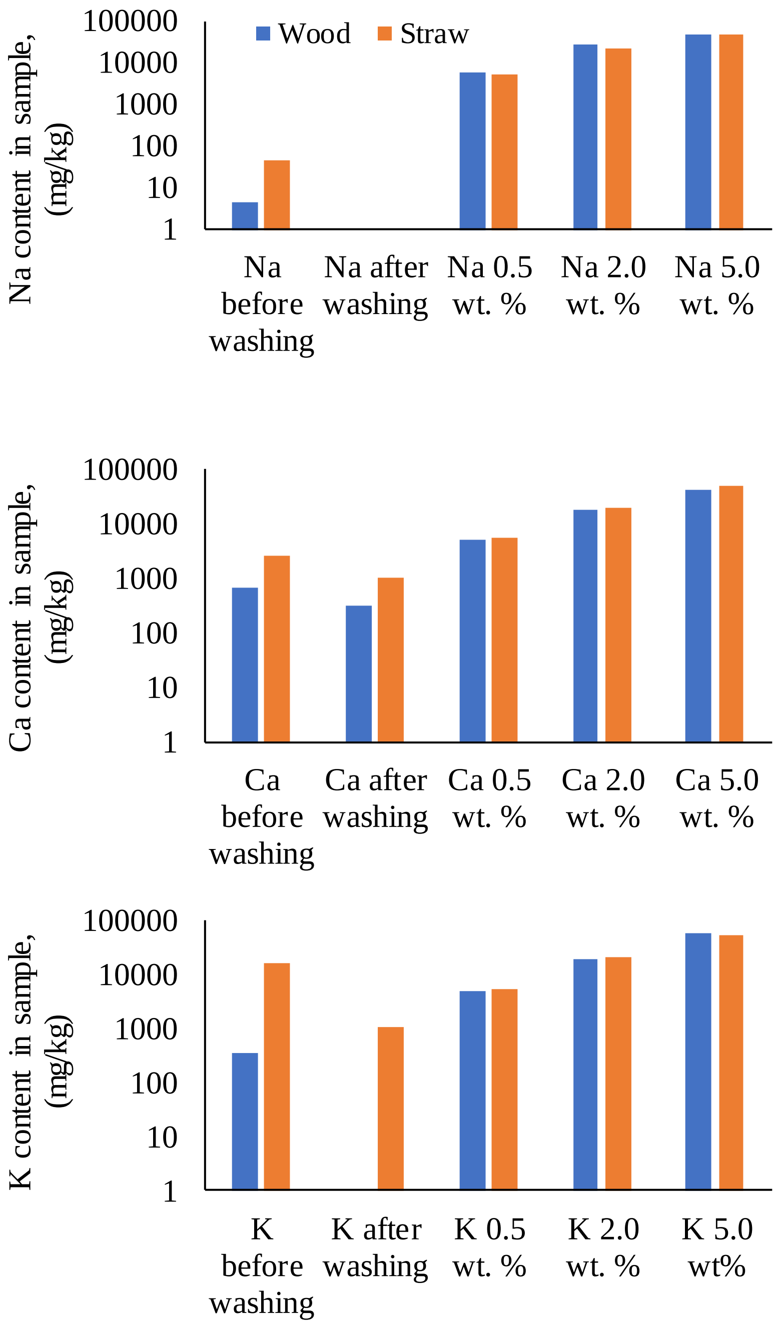

Fig. 1. Alkali content measured in the original samples, and in the samples before and after the washing and the doping procedure

2.2. Laboratory stand and devices

Fig. 2 shows the experimental burner setup. The biomass pellets were placed within a natural gas flame. Temperature of the internal pellets was measured with a thermocouple mounted inside the biomass pellets. Optical bandpass filters were mounted in an ICCD camera and the emission intensity in the corresponding wavelengths were recorded with the Andor software. The optical bandpass filters used in this work were 770 ± 2 nm for K*, 590 ± 2 nm for Na*, and 620 ± 2 nm for Ca*. The principled stand scheme (Fig. 2) consists of gas mixing chamber, ICCD camera, mounted filter's system, natural gas supply, air supply, K type thermocouple for internal pellet's temperature measurement.

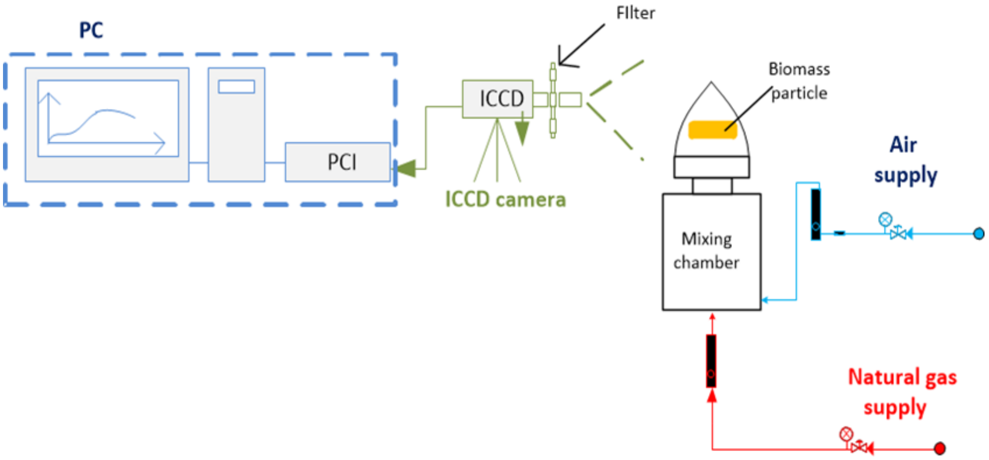

Fig. 2. Experimental setup

2.3. Interference filters

Interference filters are used to record major hydrocarbon radicals and other elements emitted during combustion process as seen at Table 1. These filters are designed to spend only a certain wavelength.

Table 1. Interference filters and their wavelength

	Radicals				
Filter	OH•	CH•	K•	Na•	Ca•
Wavelength, nm	310 ± 2	387 ± 1	770 ± 2	590 ± 2	620 ± 2

3. RESULTS AND DISCUSSION

Fig. 3 shows the internal temperature of the pellets before and after the washing procedure during combustion. In the case of the biomass before washing, it is possible to identify that the combustion process starts around 100 s in the case of the wood and around 75 s in the case of the straw, given the steep increase of temperature. Two stages are identifiable, the first corresponding to the first most intense peak of temperature, and the second corresponding to the second less intense peak of temperature. After washing procedure, the peaks occur early and with a higher magnitude, indicating that the structure of biomass changed, all minerals washed. It is easy to identified devolatilization zone during combustion process.

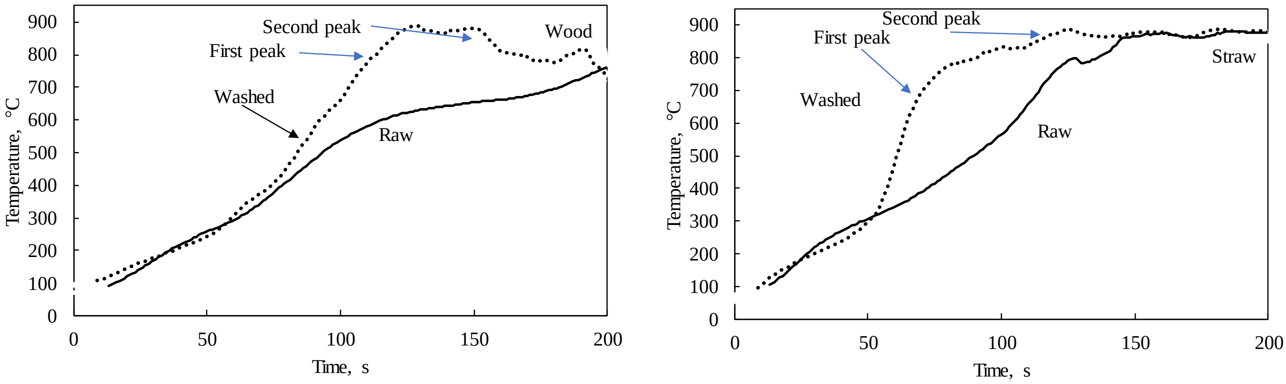

Fig. 3. Internal temperature of the pellets before and after the washing procedure during combustion. Left: wood, Right: straw

Fig. 4 shows the emission of Ca*, K* and Na* of the pellets before and after the washing procedure during combustion. The emission intensity of K* was dramatically reduced after applying the washing procedure to the straw samples, whereas the impact in the emission of Ca* and Na* was marginal. In the case of the wood, the washing procedure yielded marginal differences in the emission of Ca*, K* and Na*.

Fig. 5 shows the emission of Ca*, K* and Na* of the doped with 0.5 wt.%, 2.0 wt.% and 5.0 wt% of Ca, K and Na during combustion. The combustion period can be identified from the temperature profiles of the raw biomass samples and from the Ca*, K* and Na* emission profiles of the doped biomass, occurring roughly between 50 and 150 s, with variations between samples with different treatments. Hence, the Ca*, K* and Na* profiles can be correlated to the combustion period.

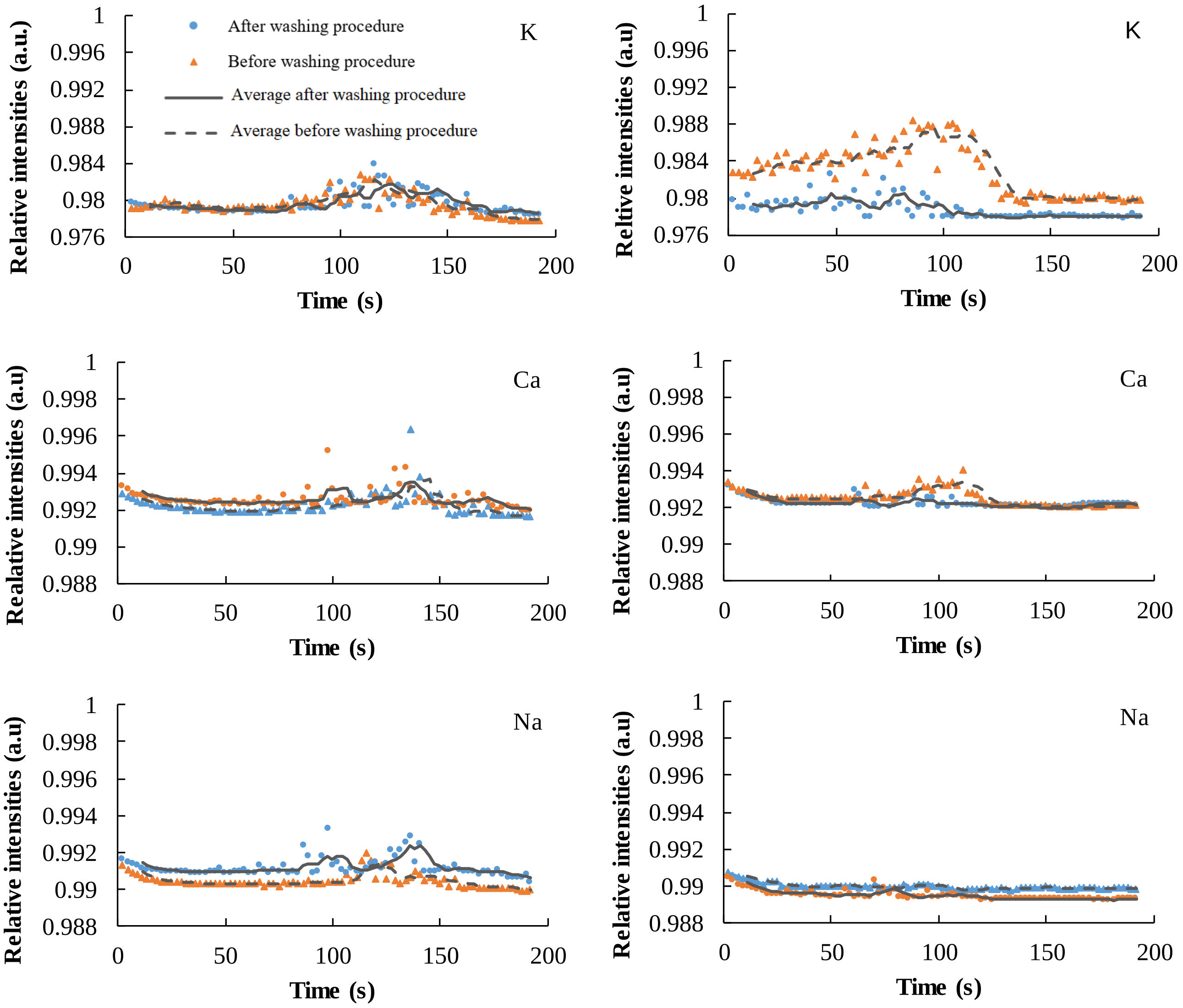

Fig. 4. Ca*, K* and Na* emissions of the pellets before and after the washing procedure during combustion. Left: wood, Right: straw

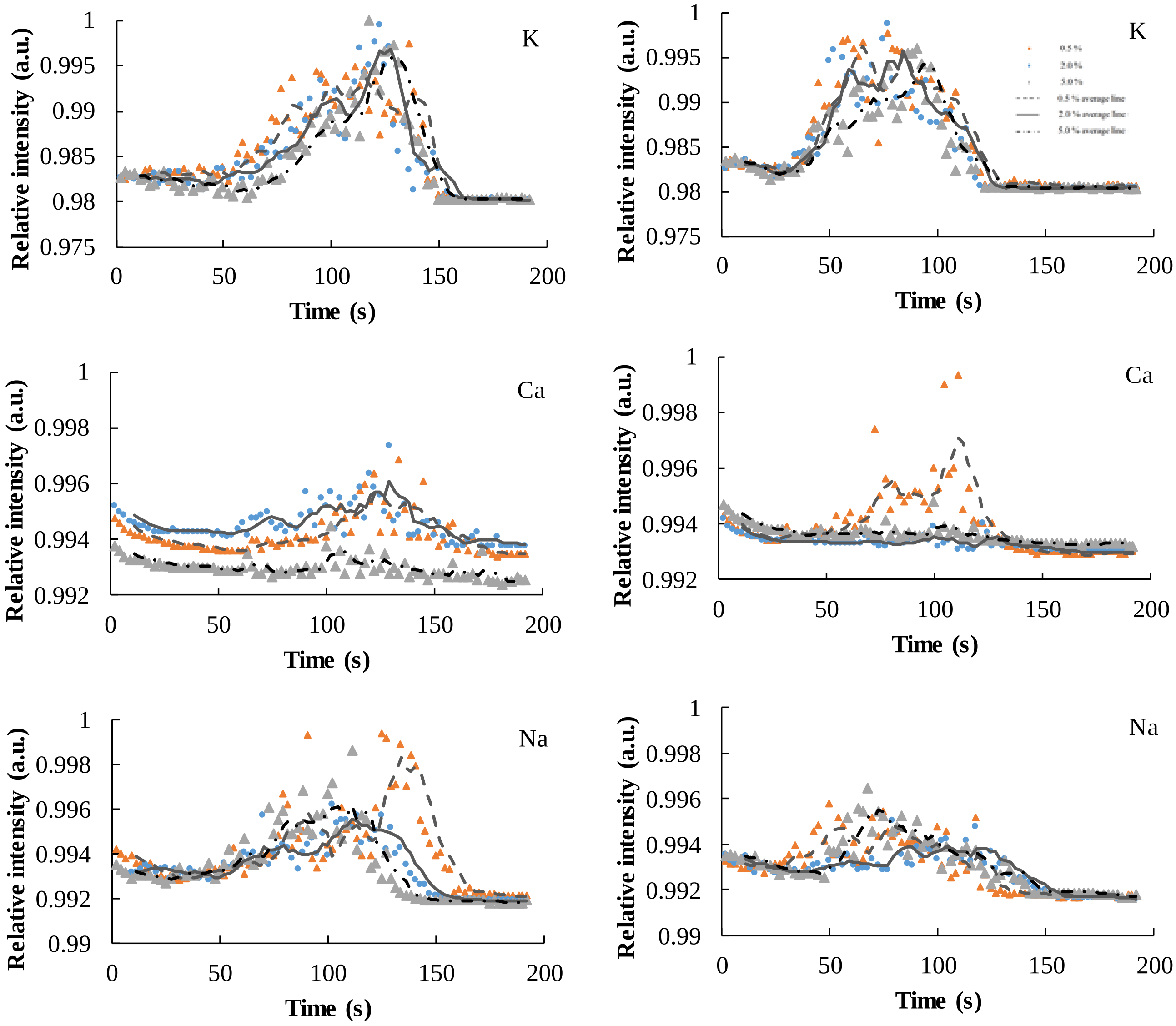

Fig. 5. Ca*, K* and Na* emissions of the pellets doped with 0.5%, 2% and 5% of Ca, K and Na during combustion at 750 ^{o}C. Left: wood, Right: straw

4. CONCLUSIONS AND SUMMARY OF RESULTS

The experimental results show that the emission intensity of K* was dramatically reduced after applying the washing procedure to the straw samples, whereas the impact in the emission of Ca* and Na* was marginal. In the case of the wood, the washing procedure yielded marginal differences in the emission of Ca*, K* and Na*. The combustion period can be identified from the temperature profiles of the raw biomass samples and from the Ca*, K* and Na* emission profiles of the doped biomass, occurring roughly between 50 and 150 s, with variations between samples with different treatments. As such, the Ca*, K* and Na* profiles can be correlated to the combustion period.

REFERENCES

1. S. VRUBLIAUSKAS, E. P. Biomasės ir iškastinio kuro mišinių deginimo ypatumai. Energetika, 2010, 56, 247–253.
2. Dembiras, A. Combustion characteristics of different biomass fuels. Prog. Energy Combust. Sci., 2004, 30: 219–230.
3. KIM, S. S., KANG, Y. S., LEE, H. D., KIM, J. K., & HONG, S. C. Release of potassium and sodium species during combustion of various rank coals, biomass, sludge and peats, J. Ind. Eng. Chem., 2012, 18(6):2199–2203.
4. ZHANG, Z., SONG, Q., ALWAHABI, Z. T., YAO, Q., & NATHAN, G. J. Temporal release of potassium from pinewood particles during combustion. Combust. Flame, 2015, 162(2):496–505.
5. MASON, P. E., DARVELL, L. I., JONES, J. M., & WILLIAMS, A. Observations on the release of gas-phase potassium during the combustion of single particles of biomass. Fuel, 2016, 182, 110–117.
6. MASON, P. E., JONES, J. M., DARVELL, L. I., & WILLIAMS, A. Gas Phase Potassium Release from a Single Particle of Biomass during High Temperature Combustion. Proc. Combust. Inst, 2017, 36(2): 2207–2215.
7. MASON, P. E., DARVELL, L. I., JONES, J. M., POURKASHANIAN, M., & WILLIAMS, A. Single particle flame-combustion studies on solid biomass fuels. Fuel, 2015, 151, 21–30.

CYSENI 2018, May 23-25, Kaunas, Lithuania
ISSN 1822-7554, www.cyseni.com

POSSIBILITY OF FLAME TEMPERATURE MEASUREMENTS BY PHOTOEMISSION METHOD

K. A. Viazava
A. V. Luikov Heat and Mass Transfer Institute
National Academy of Science of Belarus
Minsk, P. Brovki 15, 220072 – Belarus
Email: viazava.kate@gmail.com

ABSTRACT

Photoemission method of temperature measurement is based on dependence of external photoeffect electron's distribution by energy from energy distribution in heated body emission spectrum. In this method, signal from photoelectronic detector in two spectral regions is measured by light flow modulation. It can be done easily at modulation frequency 1 MHz that gives possibility of temperature measurement with 1 μs time resolution. To verify the possibility of using a photoemission pyrometer for temperature measurements of objects with linear spectrum (e.g. flame), temperature measurements for different stoichiometry φ of methane-air mixture were made (φ was calculated for mixture which came from the burner into the environment). At the same time in the same points, flame spectra were measured. By using kinetic schemes of methane burning via CHEMKIN software, thermodynamic temperatures for different stoichiometry ($\varphi = 0.6$, $\varphi = 0.8$, $\varphi = 1.0$, $\varphi = 1.2$) were calculated. Comparison of calculated temperatures with measured temperatures made a good match for $\varphi = 1.2$ in those parts of flame, where flame was visually bright orange and white. In this region, flame had a brightly expressed continuous spectrum which matched a black body spectrum at calculated temperature for $\varphi = 1.2$. This match proves that a photoemission pyrometer can be used for temperature measurements of flame when $\varphi > 1$.

Keywords: temperature measurements, photoemission pyrometer, flame

1. INTRODUCTION

There are many temperature measurement techniques enabling both invasive and noninvasive measurements [1]. Noninvasive methods have advantage over invasive methods because direct contact with the object to be measured is needed. Besides, invasive methods can give a higher measurement error [2]. In high temperature or chemically reactive applications such as flames or plasmas, invasive instrumentation can degrade with time; above the material limits, it can disintegrate completely [1].

Shadow methods [3, 4], methods of absorption and emission spectroscopy [5–7], line reversal method [8], methods based on observation of spontaneous Rayleigh and Raman scattering [9, 10], methods of laser-induced fluorescence [10–12] and methods of optical pyrometry [13] can be used for flames or plasma temperature measurements. However, some of these optical methods are highly expensive, requiring a laser, high quality optics, and specialized data acquisition equipment [1], when pyrometric methods are easy and do not require expensive equipment or difficult software. One of such pyrometric methods is photoemission method.

Photoemission method of temperature measurement is based on dependence of external photoeffect electron's distribution by energy from energy distribution in heated body emission spectrum. There is a correspondence of the displacements of the peaks of the radiation spectrum of a heated body to the short-wave region (Wien's displacement) with an increase in temperature and a Maxwell distribution of photoelectrons over energy levels toward large values [14]. This permits measuring the temperature by the indicated change in the distribution of photoelectrons.

In the present method, the signal from photomultiplier (PM) is measured in two spectral region by modulation not of the luminous but the electronic flux. It can be done easily at modulation frequency 1 MHz that gives possibility of temperature measurement with 1 μs time resolution. Due to this possibility, the photoemission method can be used for measurements of temperature dynamic in the high-temperature fast thermal processes.

The aim of this paper is verifying the possibility of using a photoemission pyrometer for temperature measurements of objects with linear spectrum (e.g. flame).

2. METHODOLOGY AND EXPERIMENTAL SETUP

2.1. Photoemission pyrometer calibration

The photoemission method of optical pyrometry is one of the methods of pyrometry of spectral distribution. The temperature is determined from the identity of the spectral distribution in thermal radiation fluxes of a standard (absolute blackbody (ABB) or temperature lamp) and object in two broad spectral regions. The first, $\lambda_{min} - \lambda_{max}$, is the entire region of spectral sensitivity of the PM, and the second, $\lambda_{min} - \lambda_r$, is the part of this region limited from the longwave side by the value $\lambda_r < \lambda_{max}$, which under conditions of limitation of the photocurrent by a modulating potential becomes the "red limit" of photocathode. The retarding potential U_r in the near-cathode region cuts off the low-energy electrons emitted by longwave radiation of the object. Thus, photocurrents corresponding to two spectral radiation regions are recorded, and therefore the measured "pseudo-temperature" is the color temperature as well as the overall color temperature since the spectral intervals are broad [15].

The retarding field in the cathode chamber is created at the time of the negative half-period during modulation of the electron flux by rectangular pulses of a polarity negative relative to the photocathode. The process of measuring the temperature amounts to recording the two-level oscillogram $U(t)$ of the investigated process (Fig. 1, a), when during one period the voltage across the modulating electrode (modulator) at first is equal to the voltage across the photocathode ($U_r = 0$) and then decreases ($U_r < 0$). From the ratio k of the levels of this signal (or modulation factor), the value of k_i can be calculated in each period with number i. The aggregate of ratios of the level of the modulated signal $k(T)$, which are obtained at different temperatures T with respect to the standard temperature radiator, allows plotting the calibration curve of the instrument $k(T) = (\Sigma k_i)/n$ where n is the number of recorded periods. The dynamics of the temperature $T(t)$ of the given process is determined from the calibration curve $k(T)$ (Fig. 1, b) and function $k(t)$ recorded in the investigated thermal process [16].

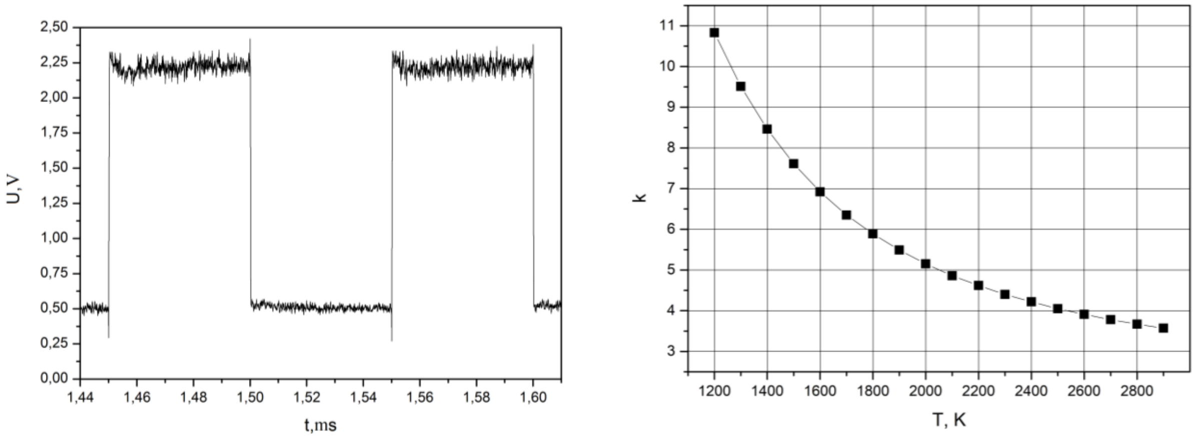

(a) (b)

Fig. 1. Typical oscillogram of the anode signal of PM (a) and typical calibration curve of the photoemission pyrometer (b)

2.2. Experimental setup

Temperature measurements of pre-mixed methane-air flame were made in the folowing way. Methane and air were supplied in the burner chamber where gases were mixed. After pre-mixing, the mixture entered in enviroment and was set on fire. Stoichiometry φ (methane/air relatio) was calculated for mixture which came from the burner into the environment. Temperature of the pre-mixed flame was measured on the central cone axe of flame and on the flame edge on different highs of flame cone. In the same points flame spectra were measured by using spectrometer. By using kinetic schemes of methane burning via CHEMKIN software, thermodynamic temperatures for different stoichiometry (φ = 0.6, φ = 0.8, φ = 1.0, φ = 1.2) were calculated to compare with experimental results.

3. RESULTS AND DISCUSSION

Results for stoichiometry $\varphi \leq 1$ were following. The temperature measured in experiments didn't get any satisfying results after comparison with the calculated temperature (Fig. 2, a-c). It can be explained by the pyirometer calibration. The photoemission pyrometer was calibrated with using satndart temperature lamp, but flames with $\varphi \leq 1$ have linear spectrum. In this way, to measure temperature of such flames proper calibration standart is needed.

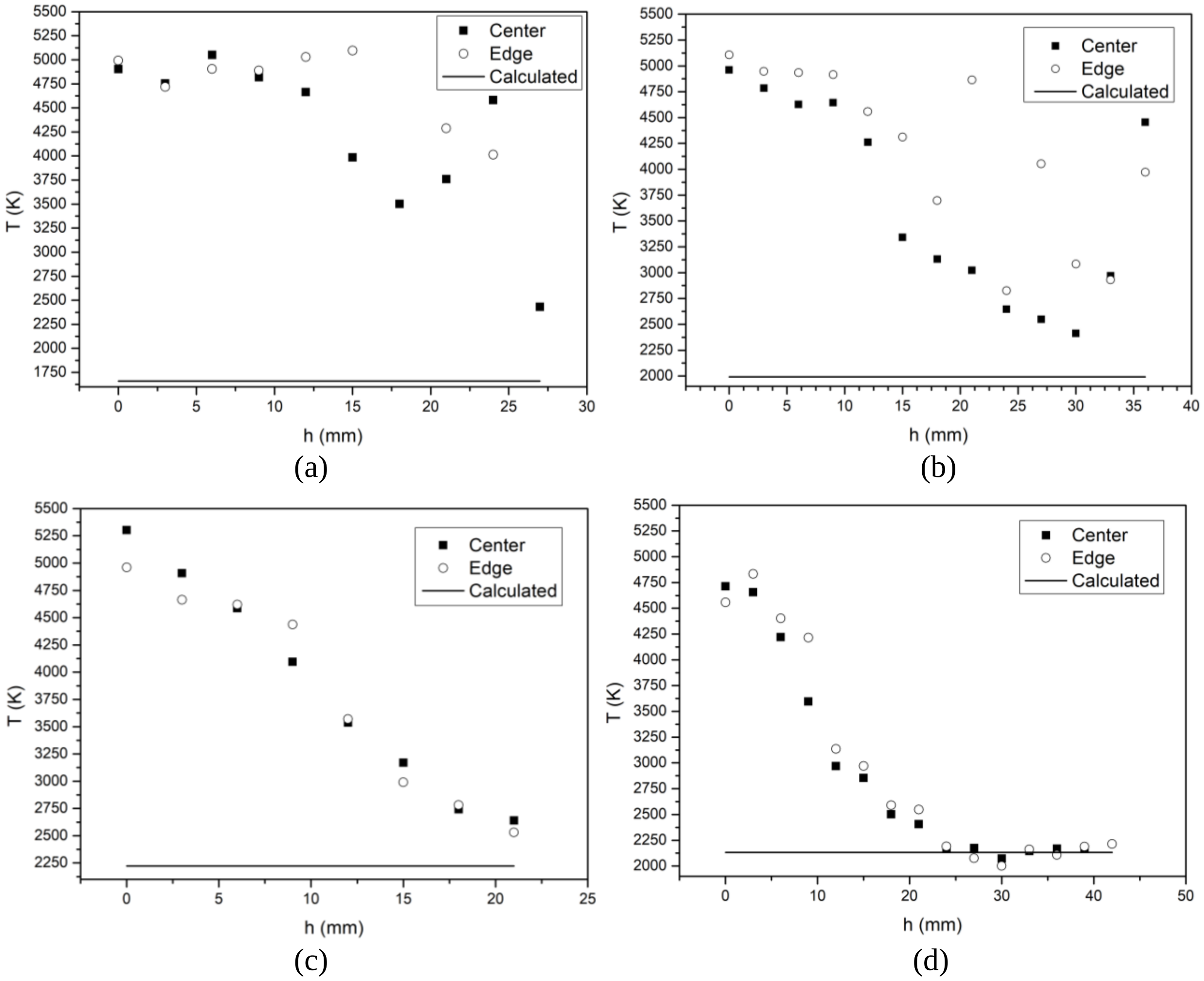

(a)

(b)

(c)

(d)

Fig. 2. The comparison of measured temperature with calculated temperature for pre-mixed methane-air flame with φ = 0.6 (a), φ = 0.8 (b), φ = 1 (c) and φ = 1.2 (d)

Comparison of calculated temperatures with measured temperatures made a good match for $\varphi = 1.2$ (Fig. 2, d) in those parts of flame, where flame was visually bright orange and white (Fig. 3, a), i.e. in region which rich of soot particles. In this region, flame had a brightly expressed continuous spectrum which matched a black body spectrum (Fig. 3, b) at calculated temperature for $\varphi = 1.2$.

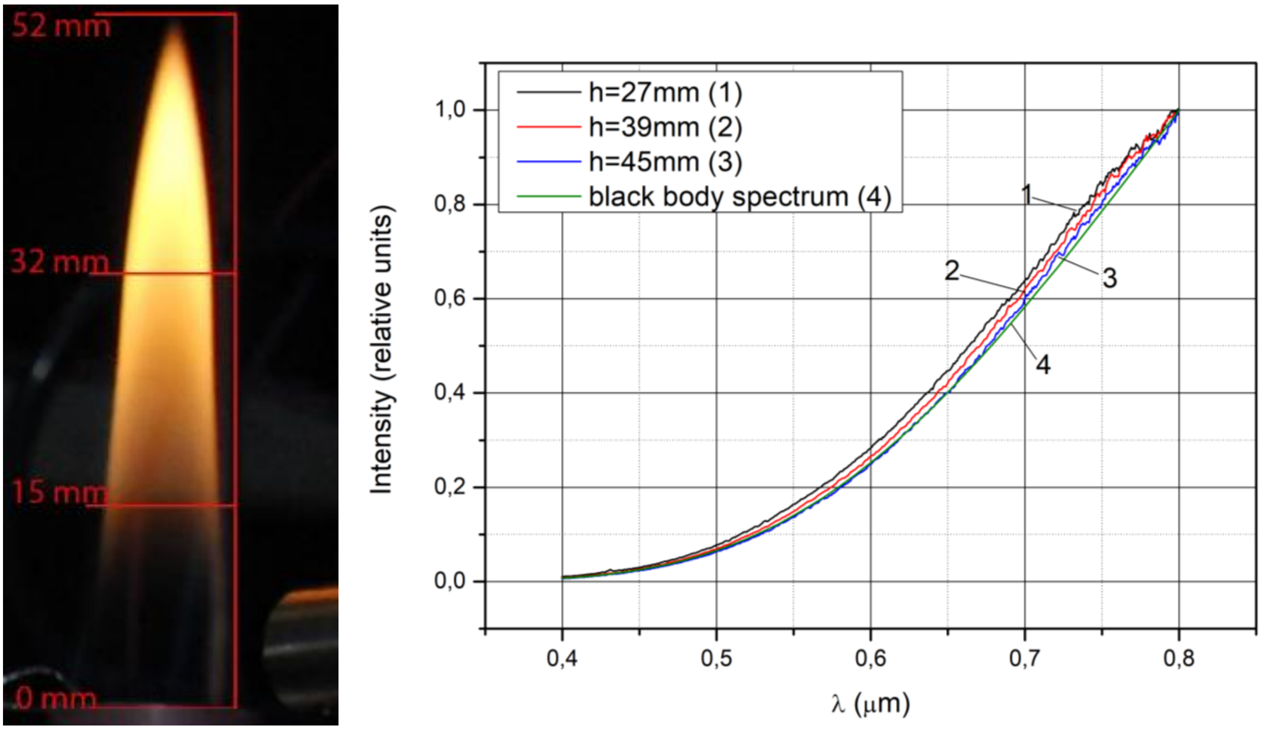

(a) (b)

Fig. 3. Photo of the the pre-mixed methane-air flame with $\varphi = 1.2$ (a) and comparison of the flame spectra on different highs with absolute black body spectrum

4. CONCLUSIONS

Temperature measurements of methane-air premixed flame were made. Comparison of calculated temperatures with measured temperatures made a good match for $\varphi = 1.2$ in those parts of flame, where flame was visually bright orange and white. This match proves that a photoemission pyrometer can be used for temperature measurements of flame when $\varphi > 1$.

REFERENCES

1. CHILDS, P. R. N., GREENWOOD, J. R., LONG C. A. Review of temperature measurement, *Review of scientific instruments*, 2000, Vol.71, No. 8, p. 2959–2978.
2. TERESCHENKO, A.G., KNYAZ’KOV, D.A., SKOVORODKO, P.A. [et al.] Perturbations of the flame structure caused by a thermocouple. I. Experiment, *Fizika goreniya i vzryva*, 2011, Vol. 47, No. 4, p. 34–46 (in Russian).
3. MEIER, G.E.A. Computerized background-oriented schlieren, *Experiments in Fluids*, 2002, Vol. 33, p. 181–187.
4. THAKUR, M., VYAS, A.L., SHAKHER, Ch. Measurement of temperature profile of a gaseous flame with a Lau phase interferometer that has circular gratings, *Applied optics*, 2002, Vol. 41, No. 4, p. 654–657.

5. AIZAWA T. Diode-laser wavelength-modulation absorption spectroscopy for quantitative *in situ* measurements of temperature and OH radical concentration in combustion gases, *Applied optics*, 2001, Vol. 40, No. 27, p. 4894–4903.
6. LIU, X., JEFFRIES, J.B., HANSON, R.K. Measurement of nonuniform temperature distributions using line-of-sight absorption spectroscopy, *AIAA Journal*, Vol. 45, No. 2, p. 411–419.
7. GÜLDER, Ö.L., HYUN, I.J. Soot formation and temperature field structure in co-flow laminar methane-air diffusion flames at pressure from 10 to 60 atm, *Proceedings of the Combustion Institute*, 2009, Vol. 32, p. 769–775.
8. GAYDON, A.G., WOLFHARD, H.G. *Flames. Their structure, radiation and temperature*. New-York: Springer US, 1970. 401 p. ISBN 978-1-5041-2587-1.
9. ROY, S., MEYER, T.R., LUNCH, R.P. [et al.] Temperature and CO_2 concentration measurements in the exhaust stream of a liquid-fueled combustor using dual-pump coherent anti-Stokes Raman scattering (CARS) spectroscopy, *Combustion and Flame*, 2004, Vol. 138, p. 273–284.
10. MEIER, W., BARLOW, R.S., CHEN, Y.-L., CHEN, J.-Y. Raman/Rayleigh/LIF measurements in a turbulent $CH_4/H_2/N_2$ jet diffusion flame: experimental techniques and turbulence-chemistry interaction, *Combustion and flame*, 2000, Vol. 123, p. 326–343.
11. SCHULZ, Ch., SICK, V. Tracer-LIF diagnostic: quantitative measurements of fuel concentration, temperature and fuel/air ration in practical combustion systems, *Progress in energy and combustion science*, 2005, Vol. 31, p. 75–121.
12. LEE, T., BESSLER, W.G., KRONEMAYER, H. [et al.] Quantitative temperature measurements in high-pressure flames with multiline NO-LIF thermometry, *Applied optics*, 2005, Vol. 44, No. 31, p. 6718–6728.
13. MAGUNOV, A.N. Spectral pyrometry, *Pribory i tekhinka eksperimenta*, 2009, No. 4, p. 5–28 (in Russian).
14. KASPAROV, K. N., IVLEV, G. D., BELAZIORAVA, L. I. [et al.] High temperature measurements in fast phenomena by spectrometry of photoelectrons, *High Temperatures – High Pressures*, 2012, Vol. 41, No. 5, p. 325–340.
15. KRASNOV, K. V., OSIPOV G. I., ROSTOVTSEVA V. V. Methods of determining the temperature of by a broadband spectral-ratio optical pyrometer, *Izmeritel'naya Tekhnika*, 1987, No. 3, p. 10–12 (in Russian).
16. VIAZAVA, K.A., KASPAROV, K.N., MIATSELSKAYA, N.S. [et al.] Calibration of photoemission pyrometer without using standard temperature radiators, *Measurement Techniques*, 2017, Vol. 60, No. 6, p. 578–582.

CYSENI 2018, May 23-25, Kaunas, Lithuania
ISSN 1822-7554, www.cyseni.com

RESEARCH OF CH$^+$ CHEMILUMINESCENCE INTENSITY DEPENDENCE ON EXCESS AIR RATIO IN PREMIXED NATURAL AND PRODUCER GAS FLAME

A. Saliamonas, R. Navakas, N. Striūgas, A. Džiugys, K. Zakarauskas
Lithuanian Energy Institute
Breslaujos str. 3, LT-44403 Kaunas – Lithuania
Email: Robertas.Navakas@lei.lt

ABSTRACT

This paper presents flame emission spectroscopy analysis method for registering chemiluminescent radical species of CH* from different angles at same time. The aim of this research is to investigate CH* chemiluminescence intensity distribution along flame from various angles at same time and how this data can be used to determine air equivalence ratio (ER). Also, this is a continuation of experiments in order to investigate how mixing producer gas (PG) (a product of a biomass gasification process) in to the natural gas (NG) flow affects spectral characteristics of flame at specific wavelengths representing formation reactions of CH* radical species. The experiments were carried out when air equivalence ratio ranged from 1 to 1.24. All air, natural gas and producer gas flows were premixed before entering combustion chamber. The producer gas was generated from wood pellets in a lab scale gasification reactor. For flame emission spectroscopy a combination of spectrograph and five optic fibers setup was used to achieve data from 5 different angles and in various heights from burner outlet. After analysing the distribution of chemiluminescent species intensity along the burner vertical axis, it was determined zones in flame, where CH* generation is at maximum and the effect of addition producer gas to natural gas and the CH* chemiluminescence dependence on air equivalence ratio was observed.

Keywords: Chemiluminescence, spectroscopy, producer gas, renewable energy sources, CH*

1. INTRODUCTION

Biomass provides more than 10% of the primary energy resources in the world since 2014. Gasification and other types of procesing of biomass is able to produce high hydrogen content producer gas. Use of this gas is considered environmentally friendly due to the use of fuels coming from natural carbon dioxide consumers, having very low sulfur content and assented as CO_2 neutral.[1]. For price projections which are based on current policies producing biomass-based producer gas directly can be economically competitive with natural gas [2]. However, for future policies associated with major greenhouse gas emission constraints, no direct economic incentive for switching to biomass-based producer gas production is achieved. Despite that producer gas generated from biomass has the potential to partialy or fully replace petroleum and other fossil fuels. To do so the chalenges involving commercial deployment of biomass gasification at large scale such as the presence of deleterious contaminant species [3] must be overcomed. Therefore research and development of better combustion techniques for producer gas combustion optimization is relevant.

Flame chemiluminescence monitoring is one of most promising non intrusive combustion process optimization technique is. According to [4] ratios between various signals corresponding to light collected at different wavelengths (for example, the ratio OH^*/CH^*) are commonly proposed as a reliable parameter to monitor a wide range of practical flames. In a chemiluminescent reaction a released portion of energy turns in to a excited electronic state. The created energy state is short-lived and relaxes through a number of mechanisms, including collisional deactivation which is non-radiative and spontaneous photon emission. In the case of photon emission, species emits a characteristic wavelength, signaling presence of the species [5].

The monotonously increasing trends of OH^*, CH^* and C_2* radical chemiluminescence intensities with the air–fuel equivalence ratio can be seen and, in addition, if light is collected from more than one direction at same time, it is possible to do a computed tomography of chemiluminescence and use it to obtain the instantaneous profile of a flame [6, 7].

This work aims to apply spatial flame chemiluminescence scanning technique to investigate CH^* intensity values along flame when using conventional fuel and with producer gas addition. This article presents comparison of chemiluminescence along flame axis from five different angles registered at same time with optical fiber ant spectrograph system. The experiments cover two fuels: natural gas and mixture of natural gas and producer gas. Experiments where performed for air equivalence ratio ranging from 1 to 1.24.

2. MATERIALS AND METHODS

2.1. Experimental setup and procedure

The experimental setup for all carried experiments consisted of a lab scale gasification reactor system for producer gas supply , an air/gas supply system, a combustion chamber (56 cm height and 6 cm diameter transparent quartz glass pipe.), and a flame optical analysis system(Fig. 1). All supply systems (air, producer gas and natural gas) were connected to combustion chamber. For each measurement of flame chemiluminescence, an initial volumetric gas flow was set with calibrated flow meters. The Combustion chamber was mounted on a gas mixing chamber. Natural gas, producer gas and primary air flows were connected to the mixing chamber via steel pipes. Secondary air was connected direct to combustion chamber, bypassing the mixing chamber. Mixing of fuel/oxidant flows occurred inside the mixing chamber. Secondary air flow was installed to be used for flame stability on low excess air ratios, but in current work it was not used. Air flow was supplied by two separate channels. All gas flows were controlled by flow meters (Operating range 0.5–20 l/min).

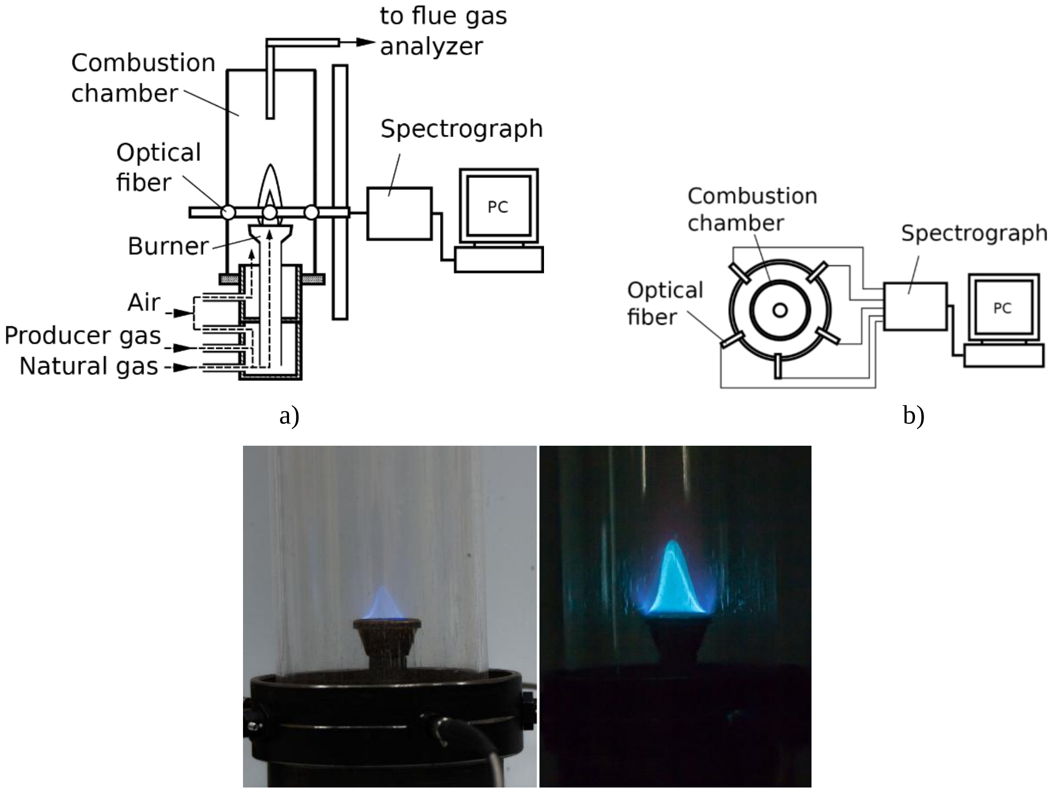

a)

b)

c)

Fig. 1. Experimental setup: a) front view scheme; b) top view scheme; c) actual view

The lab scale gasification reactor for producer gas was described in detail elsewhere [8]. Producer gas was generated by the following procedures: Nitrogen flow (1.8 l/min) for pyrolysis gas transportation was supplied into a container filled with fuel pellets. Pellets made from a mix of pine and spruce wood were used for experiments. The pellet properties are given in Table 1.

Table 1. Properties of wood pellets used in experiment

Ash, wt.%	Moisture content, wt.%	Lower calorific value, MJ/kg	Wood composition, wt.% dry				
			C	H	O	N	S
0.35	5.20	19.00	49.20	6.20	44.46	0.08	0.06

2.2. Optical system

To analyze CH∗ spatial distribution in flame at atmospheric pressure the whole combustion process was observed by an optical system, which produced the output data for further calculation. The system contained ICCD (Intensified Charge Coupled Device) camera for capturing flame images. The sensor was 18 mm size and consisted of 1024 × 1024 pixels sensitive to 200–800 nm wavelength light. The sensor was digitally divided in to 5 equal areas to collect light from each of 5 optical fibers. The ICCD camera was operated with “Solis” software. Single frame exposure was set to 5 s, and 10 frames were accumulated into a single image for each flame condition at 20 measurement planes along flame height. In order to minimize the effect of possible flame instability multiple frames were recorded for each combustion and imaging regime (fuel mixture composition, fuel and air flow rates, selected measurement plane). For registering a combustion process, five optical fibers were used. Fibers where placed in parallel to horizontal plane around the flame. Each fiber was mounted on a metal ring and targeted to flame center. Angle between fibers was 72°. Each fiber has a 10° field of view. Metal ring with fibers was mounted to a vertical ruler for measurements at different height (Fig. 2).

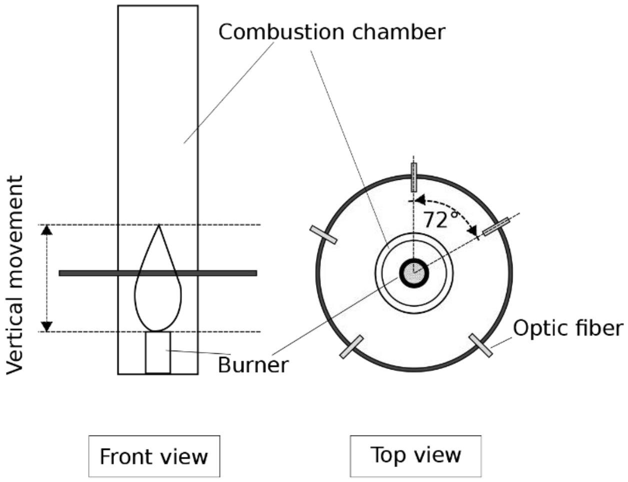

Fig. 2. Optic fiber placement

Optical system working principle is following: light from 5 flame areas was collected with optic fibers at same time. Optic fibers where connected to spectrograph side input. Inside of spectrograph light was dispersed in to spectrum lines. ICCD camera was connected to spectrograph at direct output port. Dispersed light was projected on ICCD camera sensor. Sensor was digitally divided in to 5 areas for each optic fiber signal readout. Five spectrum charts where acquired for further analysis.

2.3. Data processing

Multiple frames were put together resulting in a single image representing the mean values of spatial distribution of emission intensities of respective species in order to reduce flame instability for each flame condition,. To filter out the camera internal noise, a dark frame was taken with a capped camera and the values of this frame where subtracted from the main image. The dark frame was taken with photocathode set to “off” and the camera was covered with a cloth to prevent accidental light leaks during exposure. Collected raw data was saved as Flexible Image Transport System (FITS) files and processed using MATLAB application.

The signal to noise ratio was estimated using the following expression

$$SNR = \frac{D_{qe}P}{\sqrt{\delta_{dark}^2 + \delta_{signal}^2 + \delta_{readout}^2}}$$

where $D_{qe}P$ = 0.25 is the quantum efficiency, P is the number of photons incident upon a camera pixel, δ_{dark} = 0.2 is the dark noise, $\delta_{readout}$ = 2.9 is the readout noise, $\delta_{signal} = \sqrt{D_{qe}P}$ is the signal noise. For a count of 1000 photons per pixel, this gives SNR = 15.55, which is considered a sufficient signal. For most measurements, the photon count per pixel was on the order 2 × 105, resulting in SNR > 200. The uncertainty estimation was based on the best available estimation of the overall equipment precision. The mathematical operations such as mean values calculation were also considered as the other uncertainty source. The experimental equipment was manufacturer calibrated and the traceability of the results was established during that time. The operation parameters and allowed deviations are well described in the standard method and the manufacturer’s manual. The uncertainty of the instrument operation was estimated from a series of repeated observations by calculating the standard deviation as the overall precision of the measurement.

3. RESULTS AND DISCUSSION

3.1. Chemiluminescence intensity distribution in flame

Flame images were collected from five different angles to reconstruct intensity spatial distribution. Each optical fiber signal presented intensity values in 200–800 nm wavelength range. 6 bands of chemiluminescence intensity determination were picked out from all data and compared for different flame conditions.

The chemiluminescence intensity along flame height distributed unevenly, meaning that there was significant zone-dependent amount of chemical reactions that emitted light in UV spectral range in combustion zone. Main chemiluminescent species of interest were CH* radicals at 387.1 nm and 431.4 nm wavelengths coresponding to formation reactions given in Table 2. as they are known to show strongest intensity [9, 10, 11] and tend to have relation to excess air ratio.

Table 2. Wavelengths related to main chemiluminescent radical formation reactions.

Radical	Reaction	Wavelength, nm
CH^*	$C_2H + O_2^- \rightarrow CO_2 + CH^*$	387.1 431.4

Results, gathered from different angles for various flame conditions show that chemiluminescence was strongest at 288 degree angle. In our case this was combined result of non-uniform distribution of chemical reactions in flame, flame instability and possible burner alignment asymmetry (Figs. 5, 6). This result also confirm meaningfulness of using multi-spot flame monitoring, because intensity distribution variations can be significant for accurate local excess ratio and other parameters determination. In CH* chemiluminescence intensity range at 387.1 nm and 431.4 nm it was determined that 431.4 nm wavelength signal is stronger yet showing similar behavior like 387.1 nm. Also addition of producer gas increased overall intensity values, but the relations to excess air ratio remained unchanged (Fig. 5, a and b).

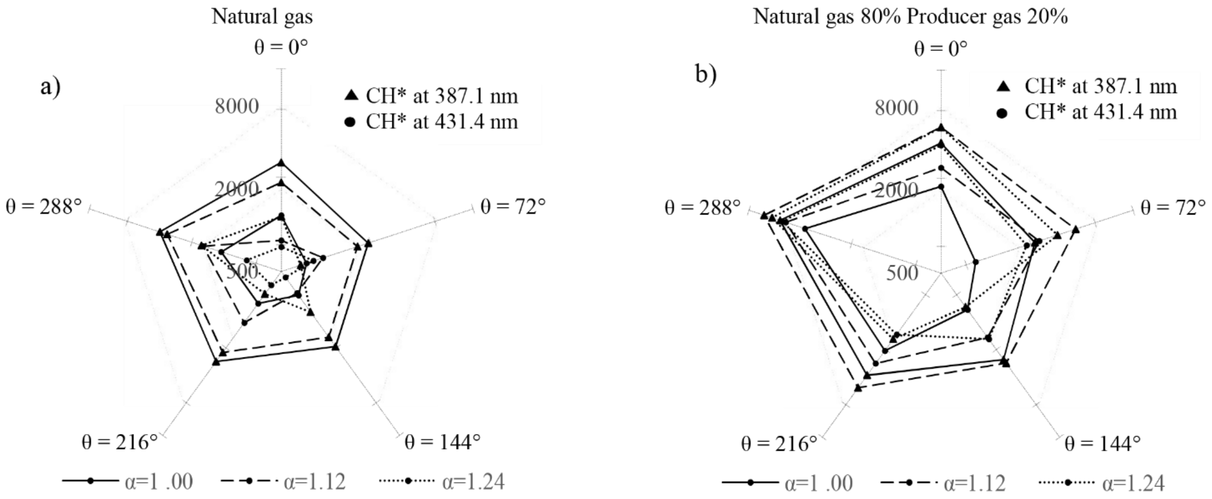

Fig. 5. Mean intensities of CH* chemiluminescence from different angles for a) air + natural gas; b) air + natural gas + producer gas mixture

All registered intensities maximum values were allocated between 0.5 and 1.5 cm distance from burner outlet. According to Hardalupas et al. [12] only the maximum intensity values are important when deciding about chemical reaction at a defined point in space and the areas before and after the peaks are considered as reaction beginning and ending zones. It means that most of chemical reactions related to CH* radical transitions from excited state to ground state [10] occurred near burner outlet Also it can be seen that with addition of producer gas (PG) due to hydrogen presence in the mixture, the reaction zone tends to be even shorter, leaving no recordable signal of chemiluminescence nearly at 4 cm distance from outlet (Figs. 6–8). Hydrogen reacts faster with oxidant than methane and increases temperature in reaction zone so the combustion reactions complete faster and closer to the burner's nozzle. The chemiluminescence intensity shift toward burner's nozzle can be seen in the results [13]. The producer gas composition analysis confirmed hydrogen presence in mixture for combustion.

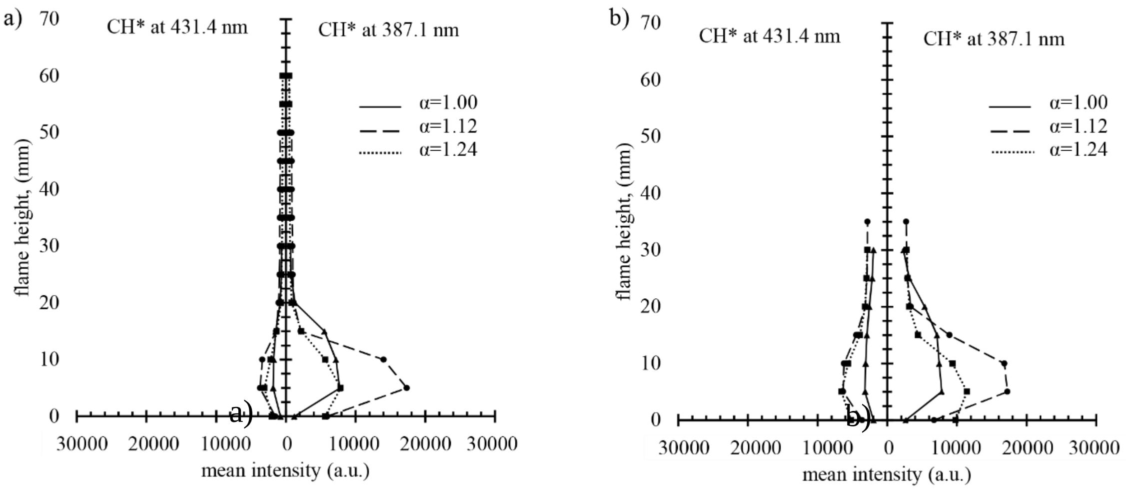

Fig. 6. Mean intensities of CH* chemiluminescence along flame height for a) air + natural gas; b) air + natural gas + producer gas mixture

For comparing chemiluminescence intensity distribution of CH*, all 5 point angular intensity data was merged in to single flame front chemiluminescent intensity curve. The differences between intensities from different angles where taken into account by applying a correction coefficient baed on maximum intensity values. A single curve for every excess air ratio, gas mixture and wavelength was created and representing chemiluminescence intensity distribution along flame height. The tendention of shorter flame can be seen in all images, approving the effect of hydrogen presence in producer gas (Fig. 6).

For evaluating a 3d distribution of flame chemiluminescence intensity all data vas merged in to single image representing one flame condition (Fig. 7.)

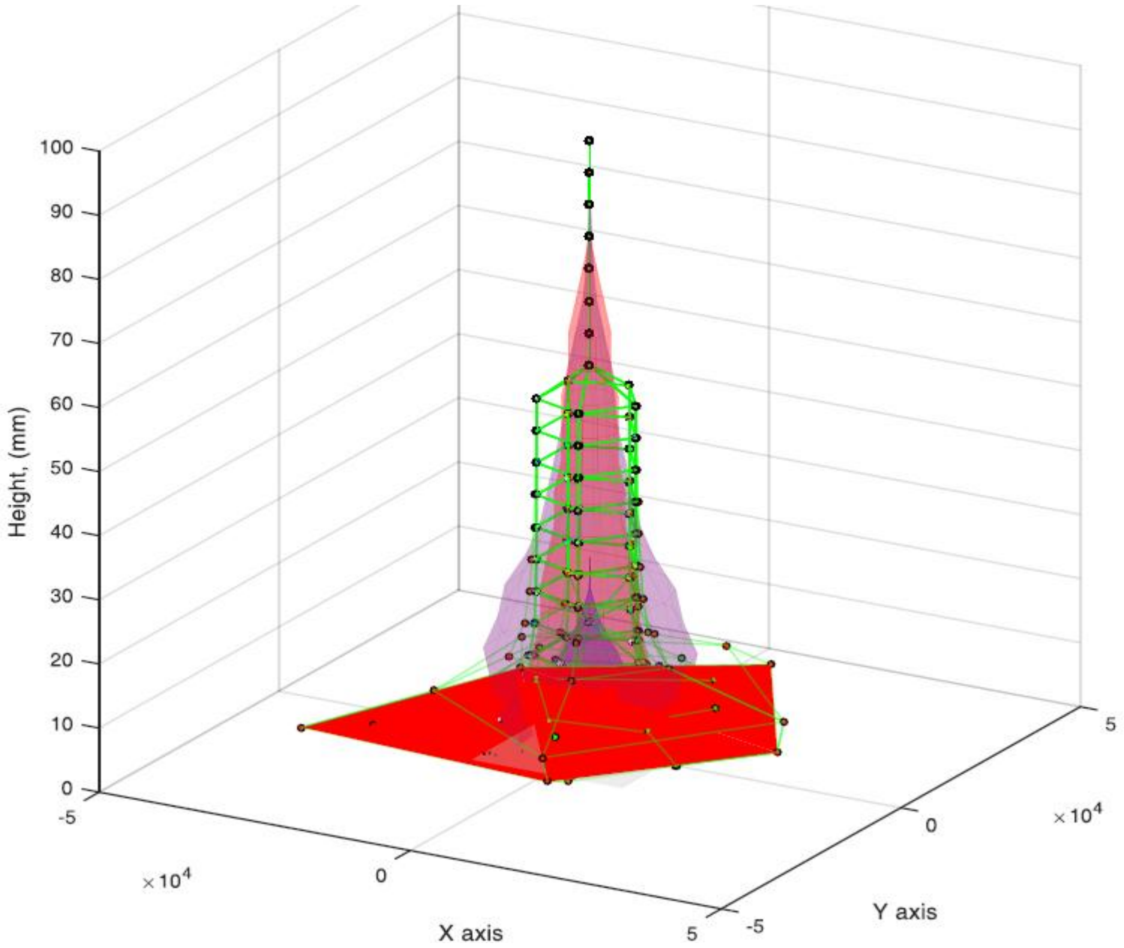

Fig.7. 3D, instantaneous, visible chemiluminescence profiles of a flame chemiluminescence intensity

3.2. Excess air ratio relation with chemiluminescent species

To show excess air ratio relation with chemiluminescent species the experimental points at heights from 0 to 1.5 cm were taken into account. This was the zone, where intensity was registered at maximum values. Results were obtained by interpolating experiment data points with a cubic polynomial. Results show that OH∗/CH* tends to show strongest relation between intensity and excess air ratio all dough more experimental point and a moredetailed model needs to be applied in order to have well defined and numerically expressed correlation. In case when produced gas was used the OH*/CH* vs excess air ratio produced a steeper curve. This result gives suggestion of possible increase of adiabatic temperature [14]. Other radical species chemiluminescence are also related to temperature fields [15] (Fig. 8).

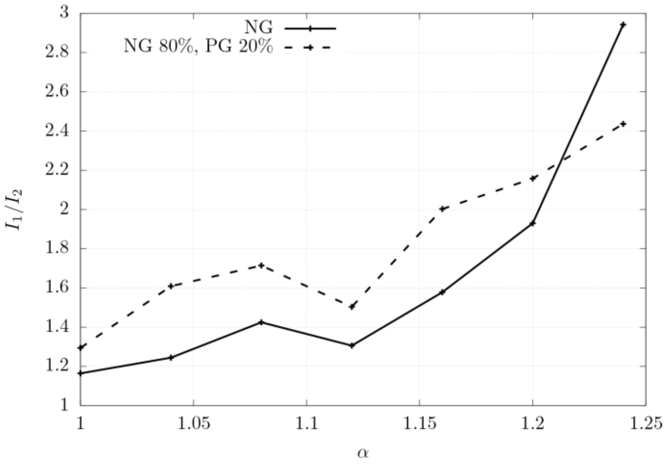

Fig. 8. Excess air ratio dependence on chemiluminescence intensity for OH^*/CH^* in a) air + natural gas; b) air + natural gas + producer gas mixture

4. CONCLUSIONS

The 3D, instantaneous, visible chemiluminescence profiles of a premixed natural gas and natural gas + producer gas flames chemiluminescence intensity were obtained by using multi-point ICCD imaging. Measurements have been performed at excess air ratios between 1 and 1.24, and were processed using Matlab.

Due to different chemical reactions occurring at different flame locations chemiluminescent intensity in flame distributed non uniformly. The locations of known excited state radical species were determined by maximum intensity values at specific wavelengths. In all cases the maximum intensity was between 0 and 1.5 cm from burner outlet. It was assumed that at these locations the reactions from described chemical kinetics mechanism are mostly expected.

It was found that CH* intensity at 431.4 nm has strongest intensity in all experiment result. After determination of highest intensity zones in flame a relation to local excess air ratio and OH*/CH* intensity was found by interpolating experimental points with a cubic polynomial. The addition of producer gas to mixture due to hydrogen presence in mixture makes chemiluminescence intensity values higher and more concentrated at distances near burner outlet. OH*/CH* dependence on excess air ratio in mixture of producer gas and natural gas is more sensitive to changes in air/fuel ratio. This effect might have a relation between OH*/CH* intensity ant flame adiabatic temperature, but to confirm this assumption it is important to expand experiments by adding more excess air ratio values in experiments and to implement a reliable temperature field measurements in combustion chamber. Five different measuring angles gives enough information for further analysis, by using computed flame tomography algorithms.

REFERENCES

[1] Sebastian Caro, Daniel Torres, and Mario Toledo. Syngas production from residual biomass of forestry and cereal plantations using hybrid filtration combustion. *International journal of hydrogen energy*, 40:2568–2577, 2015.

[2] Maria Arvidsson, Matteo Morandin, and Simon Harvey. Biomass gasification-based syngas production for a conventional oxosynthesis plantgreenhouse gas emission balances and economic evaluation. *Journal of Cleaner Production*, 99:192–205, 2015.

[3] Nourredine Abdoulmoumine, Sushil Adhikari, Avanti Kulkarni, and Shyamsundar Chattanathan. A review on biomass gasification syngas cleanup. *Applied Energy*, 155:294–307, 2015.

[4] Tatiana Garcia-Armingol, Yannis Hardalupas, A.M.K.P. Taylor, and Javier Ballester. Effect of local flame properties on chemiluminescence-based stoichiometry measurement. *Experimental Thermal and Fluid Science*, 53:93–103, 2014.

[5] Sunny Karnani and Derek Dunn-Rankin. Visualizing ch* chemiluminescence in sooting flames. *Combustion and Flame*, 160:2275–2278, 2013.

[6] Viktor Jozsa and Attila Kun-Balog. Spectroscopic analysis of crude rapeseed oil flame. *Fuel Processing Technology*, 139:61–66, 2015.

[7] J. Floyd, P. Geipel, and A.M. Kempf. Computed tomography of chemiluminescence (ctc): Instantaneous 3d measurements and phantom studies of a turbulent opposed jet flame. *Combustion and Flame*, 158:376–391, 2011.

[8] N. Striūgas, K. Zakarauskas, G. Stravinskas, and V. Grigaitienė. Comparison of steam reforming and partial oxidation of biomass pyrolysis tars over activated carbon derived from waste tire. *Catalysis today*, 196(1):67–74.

[9] F. Ferro, J. Sanches, and E. C. Fernandes. Spectrum analysis of flames chemiluminescence. *Combustion and Flame*, pages 1–40, 2013.

[10] Trupti Kathrotia. *Reaction Kinetics Modeling of OH*,CH*, and C2* Chemiluminescence*. PhD thesis, 2011.

[11] Venkata Nori and Jerry Seitzman. Evaluation of chemiluminescence as a combustion diagnostic under varying operating conditions. *46th AIAA Aerospace Sciences Meeting and Exhibit*, pages 1–14, 2008.

[12] Y. Hardalupas, M. Orain, C. S. Panoutsos, M. K. Taylor, J. Olofsson, H. Seyfried, M. Richter, J. Hult, M. Aldén, F. Hermann, and J. Klingmann. Chemiluminescence sensor for local equivalence ratio of reacting mixtures of fuel and air (flameseek). *Appl. Therm. Eng*, 24(11):1619–1632, 2004.

[13] B.K. Slim, H. Darmeveil, G.H.J. Van Dijk, D. Last, G. T. Pieters, M. H. Rotink, J. J. Overdiep, and H.B Levinsky. Should we add hydrogen to the natural gas grid to reduce CO2-emissions. consequences for gas utilization equipment. *Proceedings of 23rd World Gas Conference*, 2006.

[14] J.J. HERNANDEZ, J. Barba, and G. Aranda. Combustion characterization of producer gas from biomass gasification. *Global NEST Journal*, 14(2):125–132, 2012.

[15] C. A. Martins, A. P. Pimenta, J. A. Carvalho Jr., M. A. Ferreira, and A. A. Caldeira-Pires. Ch and c2 radicals characterization in natural gas turbulent diffusion flames. *Journal of the Brazilian Society of Mechanical Sciences and Engineering*, 27(2):110–118, 2005.

CYSENI 2018, May 23-25, Kaunas, Lithuania
ISSN 1822-7554, www.cyseni.com

WASTE HEAT RECOVERY FROM FLUE GASES IN FLUE GAS CONDENSERS

V. Kulkovas
Lithuanian Energy Institute
Breslaujos str. 3, LT-44403 Kaunas – Lithuania
Email: Vladislavas.Kulkovas@lei.lt

ABSTRACT

The energy policy of Lithuania focuses on renewable energy sources, efficient energy generation and emission reduction. Considering the national level, the use of biofuel in Lithuanian thermal energy production in the last five years has increased by 1,85 times, and according to the National Energy Independence Strategy, the aim is to increase the production of heat from biofuel by 3,5 times by 2020 compared to 2010. Taking into account the reasons mentioned before, in order to efficiently use renewable energy sources, reduce emissions and produce competitive heat energy, the most direct way is to maximize the potential of biofuel heat recovery facilities. Unlike other types of fuel used in industrial power plants, biofuel is characterized by high moisture content (about 50% moisture). To evaporate moisture, an additional amount of energy is required, which is recovered in flue gas condensers. Although since their inception flue gas condensers have significantly improved, both in corrosion resistance and heat recovery issues, as well as emission reduction issues, condensation processes in flue gas condensers have not yet been thoroughly investigated. Heat recovery from wet flue gases is a complicated process since the moisture amount in the flue gases is not constant, but is changing due to the amount of moisture in the fuel and air, as well as the unstable regulation of the combustion process. Another very important condition influencing the efficiency of a flue gas condenser is the temperature of the cooling water, which is also a variable size. The presentation analyses heat transfer processes in flue gas condensers of biofuel boilers, particle emission problems affecting more efficient heat recovery and their solutions.

Keywords: heat recovery, flue gas condenser, energy efficiency, biofuel boilers

SUBSTANTIATION AND THE RANGE OF APPLICATION OF A NEW METHOD FOR HEAT TRANSFER PREDICTION IN CONDENSING INSIDE PLAIN TUBES

V. G. Rifert, V. V. Gorin, P. A. Barabash, A. S. Solomakha
National Technical University of Ukraine – Igor Sikorsky Kyiv Polytechnic Institute
Politehnichna 6, 03056 Kyiv – Ukraine

V. V. Sereda
National University of Water and Environmental Engineering
Soborna 11, 33028 Rivne – Ukraine
Email: volodya.81.vs@gmail.com

ABSTRACT

Since the publication of Tepe and Mueller's one of the first works and until now, there were published hundreds of studies with the results of heat transfer investigations in vertical and horizontal tubes with vapor condensing of various liquids. There were proposed dozens of methods and formulas based both on the results of the theoretical research, and on the experimental data.

The existing discrepancy in more than 50% between different experimental data and various empirical and theoretical relationships is shown. The accuracy of heat transfer prediction in theoretical solutions depends on the knowledge of shear stress (friction coefficient) for which there are no correct equations up to now. At that, the absence of both substantiation of different methods, and explanations of methods disagreement both between themselves and with different experiments is noted. Also, there are often no remarks concerning boundaries for use of the proposed relationships.

There is proposed simple semi-empirical correlation for the local and average heat transfer prediction in condensing inside the plain tubes at the annular and intermediate flow of the phases. This correlation is based on the nature of film condensation process and on the specific features of the theoretical solutions results. It is shown that the influence of liquid Reynolds numbers on film Nusselt numbers cannot be taken into account when the influence of vapor velocity on heat transfer exists. The slight decrease of film Nusselt numbers along with the growth of takes place only at high vapor velocity. It is determined that the boundary of changes liquid Reynolds numbers from 800 to 20000 are typical for all freons, water, hydrocarbon fluids and carbon dioxide. It is noted that the influence of liquid Froude number (vapor velocity) power on heat transfer also include the influence of friction coefficient. So, there is no need to define friction coefficient while using suggested correlation. The range of application of the complexes, which determine the heat transfer process is also substantiated.

Good convergence of a new method with the experimental data on condensation various fluids inside horizontal and vertical tubes is shown. The data used for the correlation's validation includes: freons R134a, R125, R32, R410A and R236ea; organic fluids R245fa, NOVEC649 and HFE-700; hydrocarbon refrigerants propylene, propane, dimethyl ether and isobutene; carbon dioxide and water. The range of parameters includes tube diameters from 3.5 to 18 mm, inlet mass velocities from 19 to 1700 kg/(m^{2}s), all liquid Reynolds numbers from 800 to 20000, all liquid Prandtl numbers from 0.85 to 8 and all heat fluxes from 5 to 1200 kW/m^2. A total of 332 data points from 6 sources are generalizes with the error less than 25%.

Keywords: film condensation, heat transfer, plain tube

CYSENI 2018, May 23-25, Kaunas, Lithuania
ISSN 1822-7554, www.cyseni.com

PARAMETRIC ANALYSIS OF RECIRCULATING FLOW DYNAMICS IN MICROCAVITY

P. Vilkinis, N. Pedišius
Lithuanian Energy Institute
Breslaujos str. 3, LT-44403 – Lithuania
Email: paulius.vilkinis@lei.lt

ABSTRACT

Fluid flow structure in various shapes of channels plays an important role in most fluid dynamics problems. Flow in various shapes of microcavities has a wide range of applications related to the fluid mixing, heat transfer enhancement, microelectromechanical systems, also cell isolation and sorting. In this study computational fluid dynamics (CFD) software was used to investigate the recirculation zone structure in open, transitional and closed-type microcavities in wide Reynolds number interval. Parametric analysis was performed changing length and depth of microcavity. Recirculation zone length dependence on cavity geometry and Reynolds number was investigated. Recirculation zone structure changed from stationary vortex near backward-facing step to elongated vortex taking up whole cavity and vortex systems consisted of several counter-rotating vortices.

Keywords: CFD, microcavity, open-type cavity, transitional-type cavity, open-type cavity, reattachment point, recirculation zone

1. INTRODUCTION

The flow separation caused by the abrupt channel expansion, backward-facing step or obstacles in channels is well known and highly investigated [1–4]. This phenomenon is investigated not only for deeper understanding of flow dynamics; it is also helpful for engineering devices where flow separation and its control play a major role. Furthermore, in most devices, channel expansion is limited in length and whole geometry is in the shape of cavity. Some examples of conventional size cavities flow are flows over aircraft hulls, weapon bays, wheel wells, while microcavities of various shapes can be found in microelectronic chips, micro heating devices and also in various biomedical analytic devices.

Faure et al. [5] experimentally investigated flow structure in rectangular cavity with aspect ratio from 0.5 to 2 and in Reynolds number range from 1150 to 10670 and visualized dominant vortices. Authors found that flow structure in investigated cavities depends on cavity geometry and has little influence on Reynolds number. Sheryl et al. [6] noticed differences of recirculating flow structure in the shallow cavity of aspect ratio of 4 under conditions of laminar and turbulent upstream boundary layers. Esteve et al. [7] experimentally investigated rectangular cavity of aspect ratio of 10 at low Reynolds number and observed no reattachment of the shear layer to the bottom of cavity. Zhang et al. [8] numerically investigated flow structure in wide range of cavity aspect ratios at supersonic speed and determined critical cavity length-to-depth (L/h_1) ratios. According to authors the transition from open to transitional-type occurs at L/h_1 from 10 to 12, and change from transitional to closed-type occurs at $L/h_1 = 14$. Ritchie et al. [9] used experimental and computational methods to investigate flow structure in open and closed-types cavities in the transonic flow regime. The result comparison revealed lower experimental flow velocities in open-type cavity and higher experimental velocities in closed-type cavity compared with simulated flow fields.

Three major flow types occur in cavity depending on geometrical parameters. The type of cavity is determined by the ratio between length of the cavity L and its depth h_1. According to Charwat [10] and Sarohia [11] open-type cavity is when $L/h_1 < 6$–8. Open-type cavity can also be described as a *deep* cavity. Flow structure in this type of cavity highly depends on its depth and may consist of several vortices [12]. According to Plentovich [13] and Dix et al. [14] closed-type cavity flow is when $L/h_1 > 12–14$. Respectively, this type of cavity can be described as a *shallow*. In this type of cavity flow reattachment to the bottom of cavity is observed. At very large L/h_1 values, when influence of forward-facing step is negligible, flow in closed-type cavity becomes similar to flow over widely investigated backward-facing step. Transitional-type cavity has L/h_1 values that fall between open and closed-types. This type of cavity can be characterized by flow fields observed in both open and closed-types cavities depending on flow regime.

The aim of this study is to numerically investigate flow structure in the cavity with different depth and length values in wide Reynolds numbers interval. The main attention is providing to the dynamics of recirculation zone length. Two cases when channel expansion ratio is constant and a variable at different L/h_1 values are investigated in this study.

2. NUMERICAL SET-UP AND CONDITIONS

The shape of cavity presented in Fig. 1 is investigated in our previous study [14]. The flow structure and dynamics of recirculation zone in this type of cavity is investigated using micro particle image velocimetry and computational fluid dynamics methods. Previous results are used for comparison in present study.

In one case, the length of cavity is changed while the depth is kept a constant (h_1 = 0.4 mm) and the ratio L/h_1 is in the range from 4 to 18. In other case, the length is kept a constant (L = 4 mm) and the depth of cavity is changed from shallow to deep. L/h_1 varies in the range from 3.3 to 40 and the ratio between inflow channel h and expanded channel H is not a constant and changes from 1.25 to 4. As it can be seen, in such manner all three types of cavities are covered. All values and types of cavities for each case are presented in Table 1.

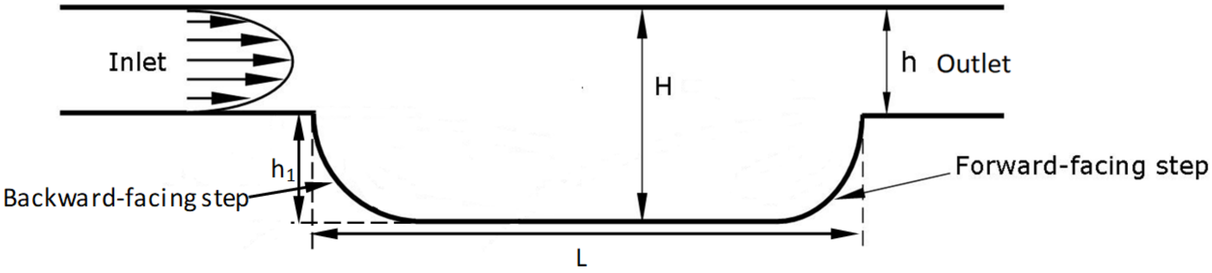

Fig. 1. Shape of investigated cavity

Table 1. Geometrical dimensions of simulated cavities

L, mm	h_1, mm	L/h_1	H/h	Type
4	0.1	40	1.25	Closed
4	0.2	20	1.5	Closed
4	0.4	10	2	Transitional
4	0.6	6.7	2.5	Open
4	0.8	5	3	Open
4	1.2	3.3	4	Open
1.6	0.4	4	2	Open
2.4	0.4	6	2	Open
3.2	0.4	8	2	Transitional
4.8	0.4	12	2	Transitional
5.6	0.4	14	2	Closed
6.4	0.4	16	2	Closed
7.2	0.4	18	2	Closed

Commercially available CFD package *Ansys Fluent* is used in present investigation. Reynolds stress – BSL and k-ω SST turbulent models are chosen for two-dimensional simulations. Reynolds Stress – BSL model is the most physically complete turbulent model and is obvious choice for complex and separated flows. SST k–ω is an improvement over standard k-ω and k-ε models and can better predict flow separation and reattachment with lower computational resources compared to RSM-BSL. SIMPLEC solution algorithm and second order discretization schemes are used in simulations. Convergence criterion is set to 10^{-6} for all variables. Water is set as working fluid in the simulations.

Cavity geometry is created using *DesignModeler*. Mesh consisted of increased number of cells near the boundaries. Fifteen cell layers were used to resolve the boundary layer with a minimum cell height being in the order of 10^{-6} m, in such manner y^+ value is below 1. Minimum cell size is set to $1 \cdot 10^{-7}$ m and maximum cell size is $4 \cdot 10^{-6}$ m. Mesh independence test showed that while decreasing cell size and increasing number of cells the change of flow structure is negligible. Depending on the parameters of the cavity total number of quadrilateral cells varies from 132000 to 594000.

In this investigation Reynolds number is calculated as $Re_{Dh} = v \cdot D_h / \nu$, where v – is averaged velocity in the channel, D_h – hydraulic diameter and ν – kinematic viscosity. Water is used as the working fluid in current investigation. The location of reattachment point to the bottom of cavity is determined according to the lowest value of wall shear stress.

3. RESULTS AND DISCUSSIONS

3.1. Dynamics of recirculation zone length

Examples of flow structure in the different types of cavities at $Re_{Dh} = 1330$ are presented in Fig. 2. At given Re_{Dh} open-type cavity ($L/h_1 = 3.3$) is completely filled with recirculation zone, which center is located near forward-facing step (Fig. 2, a). Recirculation zone height remains constant all over the length of cavity. Small secondary vortex is formed at the center part on the bottom of cavity. In transitional-type cavity ($L/h_1 = 8$) recirculation zone is concentrated near backward-facing step (Fig. 2, b). The recirculation zone is descending across the cavity and is lowest near forward-facing step. In closed-type cavity ($L/h_1 = 16$) recirculation zone reattaches to the bottom of cavity at a certain location x_r.

Fig. 3 presents the dependence of recirculation zone length on Re_{Dh} when the depth of cavity is constant ($H/h = 2$) and the length is changed. Results presented in Fig. 3 are obtained by using RSM-BSL model. At $L/h_1 = 4$ no reattachment on the bottom of cavity is observed in whole investigated Re_{Dh} range. In the case of $L/h_1 = 6$ cavity falls on the border between open and transitional-type of cavity according to Charwat and Plentovich et al. [10, 12]. In this cavity geometry flow reattachment to the bottom is observed only at Re = 80 and recirculation zone length is equal to 2.9 depths of cavity. At higher Reynolds numbers whole cavity is filled with recirculation zone without reattachment to the bottom wall. The absence of flow reattachment at mediocre Reynolds numbers remains until $L/h_1 = 12$.

Cavities which $6 < L/h_1 < 12$ fall in the transitional-type cavity category. These cavities can be characterized by three distinct stages. In the laminar flow regime recirculation zone length increases linearly. At increased Re_{Dh} flow is detached from the bottom wall and no reattachment is observed. In this case whole cavity is filled with stagnant recirculating flow. After transition to turbulent flow regime recirculation zone length is decreasing in linear manner. As it can be seen from Fig. 3 the laminar-transitional and transitional-turbulent flow regime transitions depend on cavity geometry. For shorter cavity this transition is earlier for laminar-transitional and later for transitional-turbulent flow regimes.

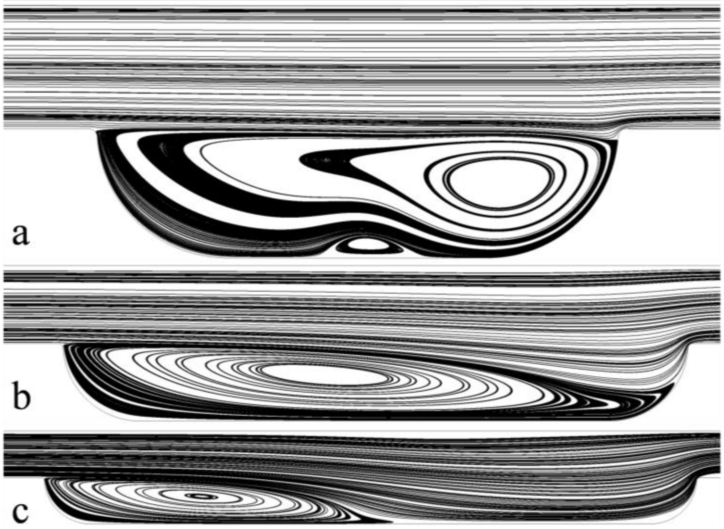

Fig. 2. Flow structure in different types of cavities at Re_{Dh} = 1330: a) open-type, b) transitional-type and c) closed-type cavity. Results obtained using RSM-BSL model

In closed-type cavities ($L/h_1 \leq 14$) flow reattaches to the bottom of cavity in whole Re_{Dh} range. The length of recirculation zone is linearly increasing until reaches its maximum at Re_{Dh} = 530 (Fig. 3). The maximum recirculation zone length value depends on cavity geometry and decreases when L/h_1 increases when H/h is constant. While further increasing Re_{Dh} recirculation zone length is rapidly decreasing. At turbulent flow regime the rate of recirculation zone shortening while increasing Re_{Dh} is very low and obtained x_r/h_1, where x_r is the location of reattachment point to the bottom of cavity, values are similar independently on the cavity geometry.

Compared to experimental results for transitional-type cavity (L/h_1 = 10) obtained in previous study [15], simulation results satisfactory coincides with experimental ones in laminar and transitional flow regimes, but high discrepancies are observed at turbulent flow regime. These discrepancies are already explained by flow three-dimensionality and underestimation of turbulent energy generation by RSM-BSL model.

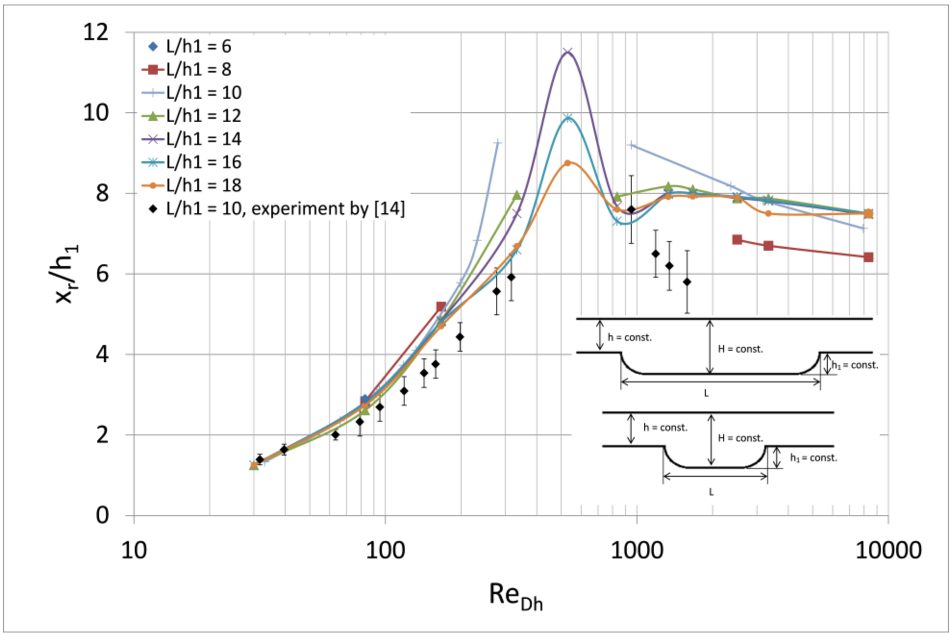

Fig. 3. Dependence of the reattachment length on Re_{Dh} for different cavity geometrical parameters. Results obtained using RSM-BSL model

Fig. 4 presents the dependence of recirculation zone length on Re_{Dh} when the length of cavity is constant and (L = 4 mm) and depth is changed. In this case channel expansion ratio is also changing in the range $1.25 \leq H/h \leq 3$. The trend of recirculation zone length on Re_{Dh} is similar to presented in Fig. 3. In addition, channel aspect ratio influence on length of recirculation zone is observed. For a fixed Re_{Dh}, relative recirculation zone length increases as channel expansion ratio increases. These results for laminar flow regime correlate with simulation data presented by Nag and Datta [16]. This trend is also noticeable in turbulent flow regime, but differences between recirculation zone length values are smaller. Longer recirculation zone at higher expansion ratios can be explained by stronger vortex determined by a higher adverse pressure gradient at the inlet of the cavity.

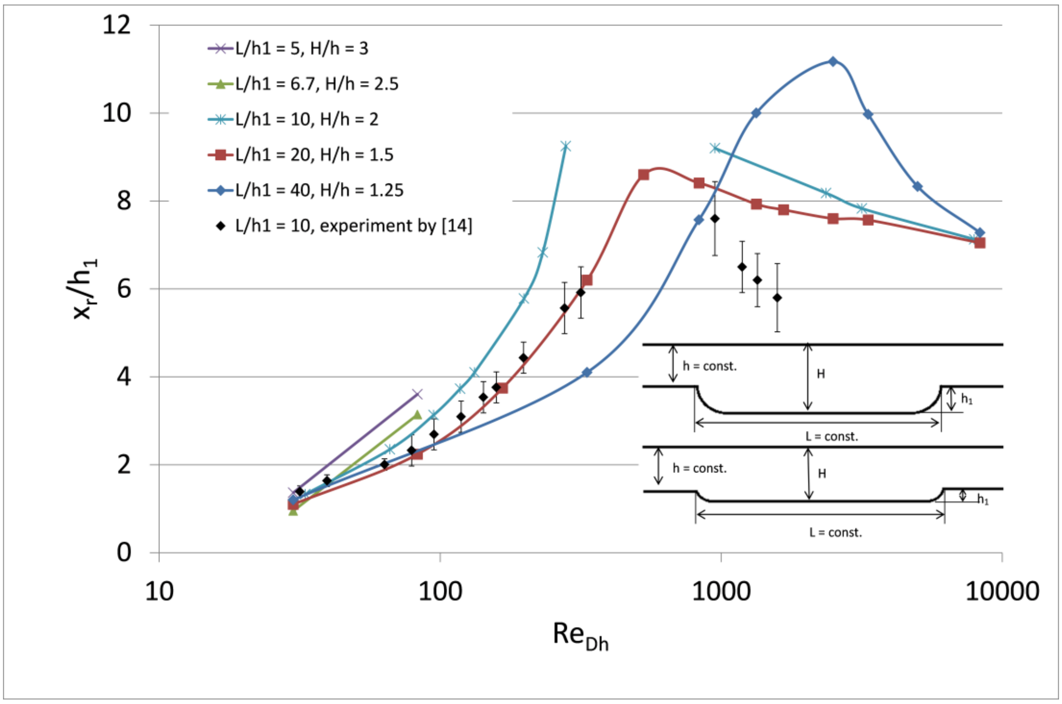

Fig. 4. Dependence of the reattachment length on Re_{Dh} for different cavity geometrical parameters. Results obtained using RSM-BSL model

3.2. Comparison of CFD models

RSM-BSL and k-ω SST results are compared in order to determine which one is more suitable for present investigation. Streamlines obtained by both models at different flow regimes are presented in Fig. 5. As it can be seen there are no significant differences flow topology in laminar flow regime (Fig. 5, a and b). At transitional flow regime, $Re_{Dh} = 830$, in both cases (Fig. 5, c and d) cavity is filled with recirculation zone with no reattachment to the bottom wall. Insignificant topological differences are observed between two models. The center of vortex of flow field obtained by k-ω SST (Fig. 5, c) model is shifted to the middle part of the cavity in respect of flow field obtained by RSM-BSL model (Fig. 5, d). Consequently, the vorticity is stronger near forward-facing step for flow field obtained by k-ω SST model. Flow fields obtained by both models in laminar and transitional flow regimes correlate with experimental results presented in our previous study [14]. More differences between both models are observed in turbulent flow regime (Fig. 5, e and f). Flow structure obtained by RSM-BSL model (Fig. 5, e) follows experimental results and flow is reattached to the bottom wall of the cavity. However, k-ω SST model in turbulent flow regime provides flow field similar to the one obtained at transitional flow regime with no reattachment to the bottom wall of the cavity. Both flow fields feature secondary vortex in the corner behind the backward-facing step.

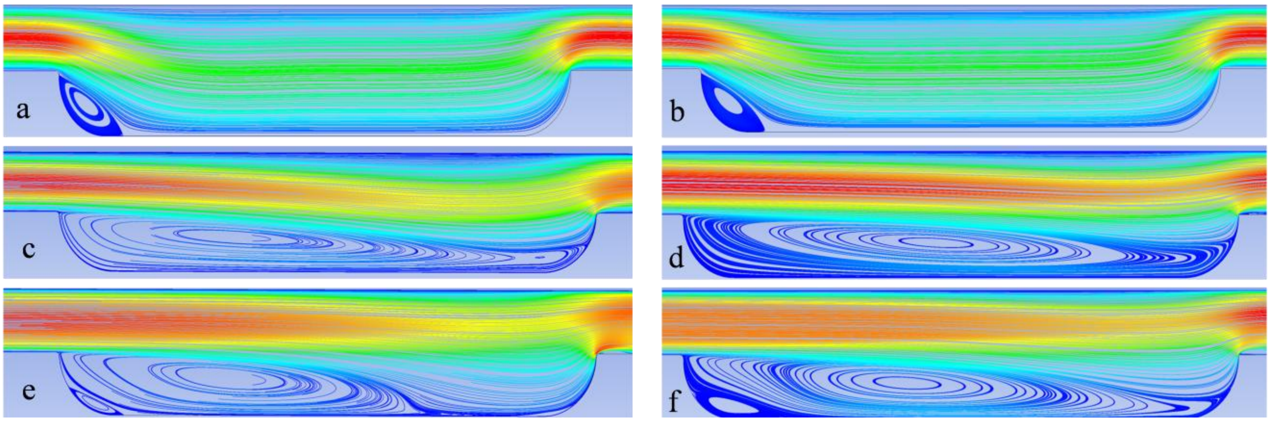

Fig. 5. Comparison of flow structure at different flow regimes obtained by different CFD models: a), c) and e) obtained by RSM-BSL at Re_{Dh} = 30, 330 and 3300 respectively; b), d) and f) obtained by k-ω SST at Re_{Dh} = 30, 330 and 3300 respectively

In Fig. 6 comparison of recirculation zone lengths obtained by both models are presented. In the case of L/h_1 = 40 (Fig. 6, a) the minor differences are observed at turbulent flow regime. k-ω SST provides higher peak of recirculation zone length and decreases more abrupt at turbulent flow regime. In the case of L/h_1 = 16 (Fig. 6, b) more differences are observed in whole Re_{Dh} range. k-ω SST provides lower values of recirculation zone length in laminar flow regime and higher values in turbulent flow regime compared to results obtained by RSM-BSL model.

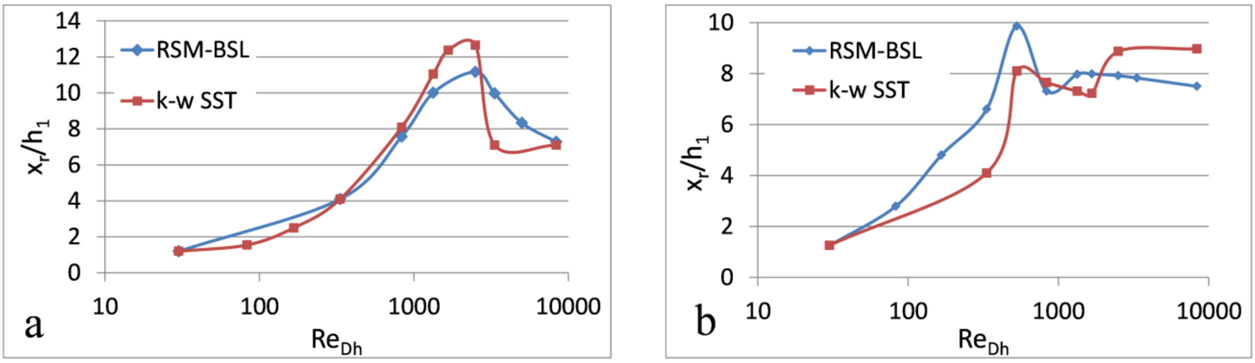

Fig. 6. Comparison of recirculation zone length obtained by different models, when a) L/h_1 = 40 and b) L/h_1 = 16

4. CONCLUSIONS

In this article flow structure in different types of cavities was numerically investigated using different computational fluid dynamics models. Results were compared with experimental results obtained in our previous work.

Cavities with different length-to-depth ratios covering cavities from open-type to closed-type were simulated using RSM-BSL and k-ω SST models. In the case of open-type cavity flow reattachment to the bottom of cavity is not observed in whole Re_{Dh} range. At the boundary of transitional-type cavity (L/h_1 = 6) flow reattachment is observed at laminar and turbulent flow regimes, while at transitional flow regime reattachment to the bottom of cavity is absent. After transition to closed-type cavities flow reattachment is permanent for all flow regimes. The peak value of recirculation zone length depends on the ratio L/h_1 and decreases as ratio increases. Also, recirculation zone length linearly depends on channels expansion ratio. Transition to turbulent flow regime which is indicated by abrupt decrease of peak value of recirculation zone length is later at lower expansion ratio.

RSM-BSL is superior k-ω SST model considering the discrepancies of recirculation zone structure in the transitional-type cavity.

REFERENCES

1. ARMALY B.F., DURST F., PEREIRA C.F., and SCHONUNG B. Experimental and theoretical investigation of backward-facing step flow. *Journal of fluid mechanics*, 1983, Vol. 127, p. 473–496.
2. CANTWELL, C.D., BARKLEY, D., and BLACKBURN, H.M. Transient growth analysis of flow through a sudden expansion in a circular pipe. *Physics of Fluids*, 2010, Vol. 22, No. 3, p. 034101.
3. BACK, L., ROSCHKE, E. Shear-layer flow regimes and wave instabilities and reattachment lengths downstream of an abrupt circular channel expansion. *Journal of Applied Mechanics,* 1972, Vol. 39, No. 3, p. 677–681.
4. GOHARZADEH, A., RODGERS, P. Experimental measurement of laminar axisymmetric flow through confined annular geometries with sudden inward expansion. *Journal of Fluids Engineering*, 2009, Vol. 131, No. 12, p. 124501.
5. FAURE T.M., ADRIANOS P., LUSSEYRAN F., PASTUR L. Visualizations of the flow inside an open cavity at medium range Reynolds numbers. *Experiments in fluids*, 2007, Vol. 42, No. 2, p. 169–184.
6. SHERYL M., GRACE W., GARY DEWAR W., WROBLEWSKI D.E. Experimental investigation of the of the flow characteristics within a shallow wall cavity for both laminar and turbulent upstream boundary layers. *Experiments in fluids*, 2004, Vol. 36, p. 791–804.
7. ESTEVE, M., REULET, P., and MILLAN, P. Flow field characterization within a rectangular cavity. 10th International Symposium Applications of Laser Techniques to Fluid Mechanics 2000, Lisbon, Portugal.
8. ZHANG J., MORISHITA E., OKUNUKI T., and ITOH H. Experimental investigation on the mechanism of flow-type changes in supersonic cavity flows”, *Transactions of the Japan Society for Aeronautical and Space Sciences*, 2002, Vol. 45, No. 149, p. 170–179.
9. RITCHIE S. A., LAWSON N. J., KNOWLES K. A PIV and CFD investigation of cavity flows in the transonic flow regime. 24th international congress of the aeronautical sciences. 2004, Yokohama, Japan, 29 August – 3 September.
10. CHARWAT, A. An investigation of separated flows-Part I: The pressure field. *Journal of the Aerospace Sciences*, 1961, Vol. 28, No. 6, p. 457–470.
11. SAROHIA V. Experimental investigation of oscillations in flow over shallow cavities. *AIAA Journal*, 1977, Vol. 15, No. 7, p. 984–991.
12. CHENG M, HUNG K. C. Vortex structure of steady flow in a rectangular cavity. *Computers and fluids*, 2006, Vol. 35, p. 1046–1062.
13. PLENTOVICH E. B., STALLINGS R. L. Jr., TRACY M. B. *Experimental cavity pressure measurements at subsonic and transonic speeds. Static-pressure results*, 1993, *NASA technical paper 3358*.
14. DIX R., BAUER R. Experimental and predicted acoustic amplitudes in a rectangular cavity. 38th Aerospace sciences meeting and exhibit. 2000, Reno, Nevada, 10–13 January.
15. VILKINIS P., PEDIŠIUS N., VALANTINAVIČIUS M. Investigation of flow dynamics over transitional-type microcavity. *Journal of fluids engineering*, 2018. doi:10.1115/1.4039159.
16. NAG D., DATTA A. Variation of the recirculation length of Newtonian and non-newtonian power-law fluids in laminar flow through a suddenly expanded axisymmetric geometry. *Journal of fluids engineering*, 2006, Vol. 129, No. 2, p. 245–250.

CYSENI 2018, May 23-25, Kaunas, Lithuania
ISSN 1822-7554, www.cyseni.com

INVESTIGATION OF A COMPLEX FLUID-STRUCTURE INTERACTION PROBLEM IN A PATIENT SPECIFIC OPHTHALMIC ARTERY USING FIBER-REINFORCED ARTERY WALL CONSTITUTIVE MODEL

E. Misiulis, A. Džiugys
Lithuanian Energy Institute
Breslaujos str. 3, 44403 – Lithuania
Email: edgaras.misiulis@lei.lt

ABSTRACT

The framework for the study of blood flow-tissue interaction problems is composed of several procedures, of some of which are: the reconstruction of geometry, consideration of solver package, consideration of the artery wall constitutive model, and finally the numerical study of the fluid-structure interaction (FSI) problem. Any of these procedures can be performed with a variety of methods proposed in the scientific community.

To demonstrate the proposed framework applicability the case study of blood flow-arterial wall interaction problem emerging in the noninvasive intracranial pressure measurement method was performed. Geometry reconstruction of the ophthalmic artery was done from the obtained magnetic resonance imaging (MRI) data. The constitutive arterial wall model exhibited the micro-scale parameter - the fiber directions and thus the fibrous-structure was formed, where the relatively stiffer material the collagenous fibers are immersed into the relatively less stiff matrix. Matrix mechanical response is governed by the neo-Hookean constitutive material model, while the H-G-O constitutive model is used to describe the mechanical behavior of the collagenous fibers. Finally the time-dependent FSI study was performed, in which the inner pressure changed according to scientific data available. The properties of fluid was that of a blood in a relatively big arteries, where the Newtonian behavior is still observed. Obtained results showed the feasibility of the proposed framework.

Keywords: fluid-structure interaction, geometry reconstruction, arterial wall mechanics, blood flow, fiber-structure

1. INTRODUCTION

One of the noninvasive Intra-Cranial Pressure (ICP) measurement methods uses a unique Ophthalmic Artery (OA) morphological property [1]; assessed clinical research on human OA shows that in general OA crosses several different segments: Intracranial Ophthalmic Artery (IOA) segment, which is inside the skull, Optic Canal (OC) segment and Extracranial Ophthalmic Artery (EOA) segment, which is in the eye socket [2].

OA is a first major bifurcation of Internal Carotid Artery (ICA) and supplies oxygenated blood to the eye [2]. Blood flow and arterial blood pressure (ABP) are generated by heartbeat pulses, which are further transferred via circulatory system, thus also reaching OA. IOA segment is inherently affected by ICP, which acts on the outside wall of artery (contracts it), while EOA is basically unaffected by any additional outside pressure [3]. So the basic idea is to artificially add external Pressure (Pe) on the EOA segment by a specifically designed head mask so that the comparative evaluation of ICP could be performed.

In order to understand the underlying principles of the noninvasive intracranial pressure measurement numerical simulations must be performed as some *in vivo* experiments are hardly possible, and some are even impossible to perform.

A theoretical model of blood flow in arteries using the finite element method was implemented by [4]. Authors [2] employed an open source software CMGUI (www.cmiss.org/cmgui) to digitize centerline of the ophthalmic artery and a few other major arteries (ICA, Anterior

Cerebral Artery (ACA), Middle Cerebral Artery (MCA)) using key nodes and a one-dimensional cubic Hermite mesh from a Computed Tomography Angiography (CTA) image. In their study a patient-specific case was investigated, although for simplicity artery wall was assumed to be rigid. [5] have proposed a phenomenological constitutive model for arterial wall mechanics in which the strong stiffening effect is incorporated into the model, but no reference to any histological feature is addressed and given arbitrary list of parameter combinations the strain-energy density function can become non-convex. [6] have proposed another phenomenological constitutive model for arterial wall mechanics, were strong stiffening effect is incorporated into the model with an assumption of the histological artery wall feature - a fibrous collagen structure, in which the strain-energy density function is always convex. [7] have proposed a new multiscale approach for the flow-tissue interaction modeling and showed the feasibility of the proposed method. The arterial tissue in the [7] is modeled as a nonlinear multiscale constitutive rationale, and all the parameters used have a clear biomechanical and histological meaning. The blood flow in [7] is solved by coupling the patient-specific spatial domain of the artery with a model that takes into account the influence of downstream vasculature.

The aim of this study was to propose a framework for the blood flow-tissue interaction problem modeling and show the feasibility of the proposed method.

2. METHOD

It is not a trivial task to model the blood flow-tissue interaction due to a multi-field expertise requirements. Problem of blood flow-tissue interaction falls into a more general category of fluid-structure interaction (FSI) problems. FSI problems incorporates both the solid and the fluid domains with the interface boundary in between. FSI problems can be separated into two categories: problems that involves small displacements and small deformations of structures coupled with a potential flow, and problems where the displacements and deformations are large and the full Navier-Stokes equations need to be solved in a moving mesh.

In the consideration of the blood flow-tissue interaction modeling the strong coupling with the use of monolithic approach is recommended [8]. This ensures the numerical stability, as the blood density is close to the artery wall density and in such case the weak coupling can become unstable.

Modelling of patient-specific blood flow-artery wall interaction problems consist of several features, here only some of them are considered:

- Geometry reconstruction from medical imaging.
- Consideration of solver package.
- Constitutive artery wall model consideration.
- Blood flow model considerations.

2.1. The reconstruction of ophthalmic artery

Ophthalmic artery (OA) was reconstructed from the Magnetic Resonance Imaging (MRI) data using the „vmtk 1.3“ computer software. The reconstruction procedure is as follows:

- Reconstruction of a patient-specific lumen volume of OA.
- Determination of a centerline.
- Generation of OA geometry using the parametrization of a centerline.

The colliding fronts initialization was used as the level set method, where source and target seed points were selected for the OA lumen volume extraction [9]. The marching cubes algorithm [10] was used on the obtained image to generate the OA surface. Centerline of an artery was computed using the same vmtk 1.3 software. For the details about the centerline computations please refer to the [11]. The finalized OA geometry is shown in Fig. 1.

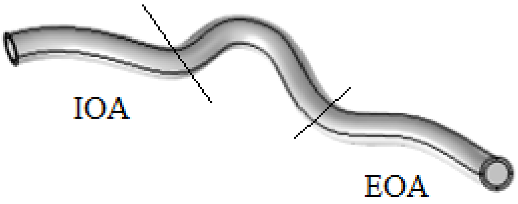

Fig. 1. Reconstructed OA geometry with highlighted IOA and EOA segments

2.2. Solver package considerations

Naturally, the structure is described in the Lagrangian formulation and the fluid flow in the Eulerian formulation, the coupling then can be performed by the use of Arbitrary Lagrangian-Eulerian (ALE) formulation. One description either the Lagrangian or the Eulerian is not optimal for the entire FSI problem domain. The use of Lagrangian formulation for the fluid domain is limited as it can only handle small deformations, while the use of Eulerian formulation for the solid domain is not optimal in terms of the loss in accuracy.

COMSOL Multiphysics software package has a build in ALE formulation and can be readily used to solve the blood flow-tissue interaction problems.

In the ALE method the boundary between the artery wall and blood is treated as a fluid-structure interface. Blood flow dynamics is solved by Navier-Stokes equations, which provides a blood flow velocity field $\mathbf{v}$. The total exerted pressure $\boldsymbol{\sigma}$ by the blood acting on artery wall boundary is estimated as follows:

$$\boldsymbol{\sigma}=\mathbf{n}\cdot\left\{-p\mathbf{I}+\left(\mu(\nabla\mathbf{v}+(\nabla\mathbf{v})^T)-\frac{2}{3}\mu(\nabla\cdot\mathbf{v})\mathbf{I}\right)\right\} \tag{1}$$

where p is the pressure, μ is the dynamic viscosity of blood, $\mathbf{n}$ is the outward normal to the boundary, and $\mathbf{I}$ is the identity matrix. The transformation of the force, due to calculations performed in different configurations, is performed by $\mathbf{F}=\mathbf{f}\cdot dv/dV$, where dv is the scale factor of the mesh element for the spatial reference frame and dV for the material reference frame. For the blood domain, the arterial wall boundary acts as a moving wall through structural velocities calculated by $\partial\mathbf{u}/\partial t$, where $\mathbf{u}$ is the displacement of the artery wall.

2.3. Constitutive artery wall model

Artery wall can be considered as a multi-scale structure. The tiniest scale to be considered is the nano-scale, with the entropic and energetic behavior of the molecules. Interconnected molecules forms fibrils that interconnects to form protein collagen fibers (micro-scale). Eventually the protein collagen fibers, embedded in a relatively less stiff material, is the key component that makes the artery so stiff at high stretch ratios. In order to model the mechanical behavior of artery wall due to a fibrous structure (micro-scale) here we introduce a constitutive artery wall model proposed by [6] where the anisotropic part that encompass the strong stiffening effect at high pressures due to fibrous structure is defined accordingly:

$$\overline{\Psi}_{\text{aniso}}(\bar{I}_4,\bar{I}_6)=\frac{k_1}{2k_2}\sum_{i=4,6}\{\exp[k_2(\bar{I}_i-1)^2]-1\} \tag{2}$$

where $k_1>0$ is a stress-like material parameter and $k_2>0$ is a dimensionless parameter, the isochoric invariants are defined as follows: $\bar{I}_4=\mathbf{M}_1\cdot\overline{\mathbf{C}}\mathbf{M}_1$, $\bar{I}_6=\mathbf{M}_2\cdot\overline{\mathbf{C}}\mathbf{M}_2$, where isochoric part of right Cauchy-Green deformation tensor is as follows: $\overline{\mathbf{C}}=\overline{\mathbf{F}}^{\mathrm{T}}\overline{\mathbf{F}}$, isochoric part of deformation tensor is as follows: $\overline{\mathbf{F}}=\mathbf{F}\cdot J^{-1/3}\mathbf{I}$, deformation tensor is defined by: $\mathbf{F}=\frac{\partial\mathbf{x}}{\partial\mathbf{X}}$, where $\mathbf{X}$ denotes the position vector in the reference configuration and **x** denotes position vector in current configuration, tensors defining fiber directions are as follows: $\mathbf{M}_1(\beta) = \mathbf{m}_{01}(\beta) \otimes \mathbf{m}_{01}(\beta)$, $\mathbf{M}_2(\beta) = \mathbf{m}_{02}(\beta) \otimes \mathbf{m}_{02}(\beta)$, where β defines fiber angle with respect to radial component of cylindrical artery.

2.4. Fiber directions in a curved artery wall

In order to use the constitutive artery wall model, fiber directions must be obtained in the reference configuration prior to the main FSI study. There are several proposed methods [12-15] of whom we implemented the method that uses the principle stresses to define the fiber directions. The idea is to perform the linear elastic study before the main study to obtain the principal stresses, which was shown to point in three local cylindrical directions and can be used as a local basis for the fiber direction definition. Fiber directions in a local cylindrical coordinate system is defined as follows:

$$\mathbf{m}_{01}(\beta) = \begin{bmatrix} 0 \\ \cos(\beta) \\ \sin(\beta) \end{bmatrix}, \ \mathbf{m}_{02}(\beta) = \begin{bmatrix} 0 \\ \cos(\beta) \\ -\sin(\beta) \end{bmatrix} \tag{3}$$

Smoothed and direction preserving streamlines representing the obtained fiber structure are shown in Fig. 2.

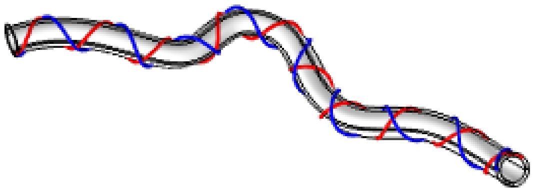

Fig. 2. Streamlines representing a part of the obtained fiber structure. Fiber directions are defined in all Gauss points of OA wall and if all represented would be visually indistinguishable

2.5. Case study: blood flow-artery wall interaction analysis

Following our proposed framework, the case study on the emerging blood flow-tissue interaction problem in the noninvasive intracranial measurement method was performed. The idea was to show the framework feasibility for such problems.

Numerical analysis covered 2 heartbeat pulses. Initial heartbeat pulse period was used to obtain the diastolic state of the system.

ICP = 20 mmHg was applied on the outside surface of the wall of IOA segment. Pe was raised from 0 to 40 mmHg and applied on the outside surface of the wall of EOA segment.

Laminar inflow and outflow pressures were prescribed on the OA inlet and OA outlet, respectively. ABP limits were (80; 120) mmHg. Pressure at the inlet boundary varied according to [16], while outlet pressure was held constant $P_{dist} = 70.15$ mmHg at specific distance $L_{exit} = 25.63$ cm. The end surfaces of OA vessel walls were prescribed to be immovable.

Blood dynamic viscosity μ was 0.003675 kg·m^{-1}·s^{-1}, density ρ_b was 1060 kg·m^{-3}. Parameters used for the artery wall are defined in Table 1 [17].

Table 1. Parameters of OA wall

Parameter	Value	Units
k_1	0.52	kPa
k_2	195.32	1
β	33.78	deg
ρ_a	1000	kg/m^3

3. RESULTS AND DISCUSSION

The obtained blood velocity distribution at discrete times of (1, 1.1, 1.36, 2) *s* is presented in Fig. 3.

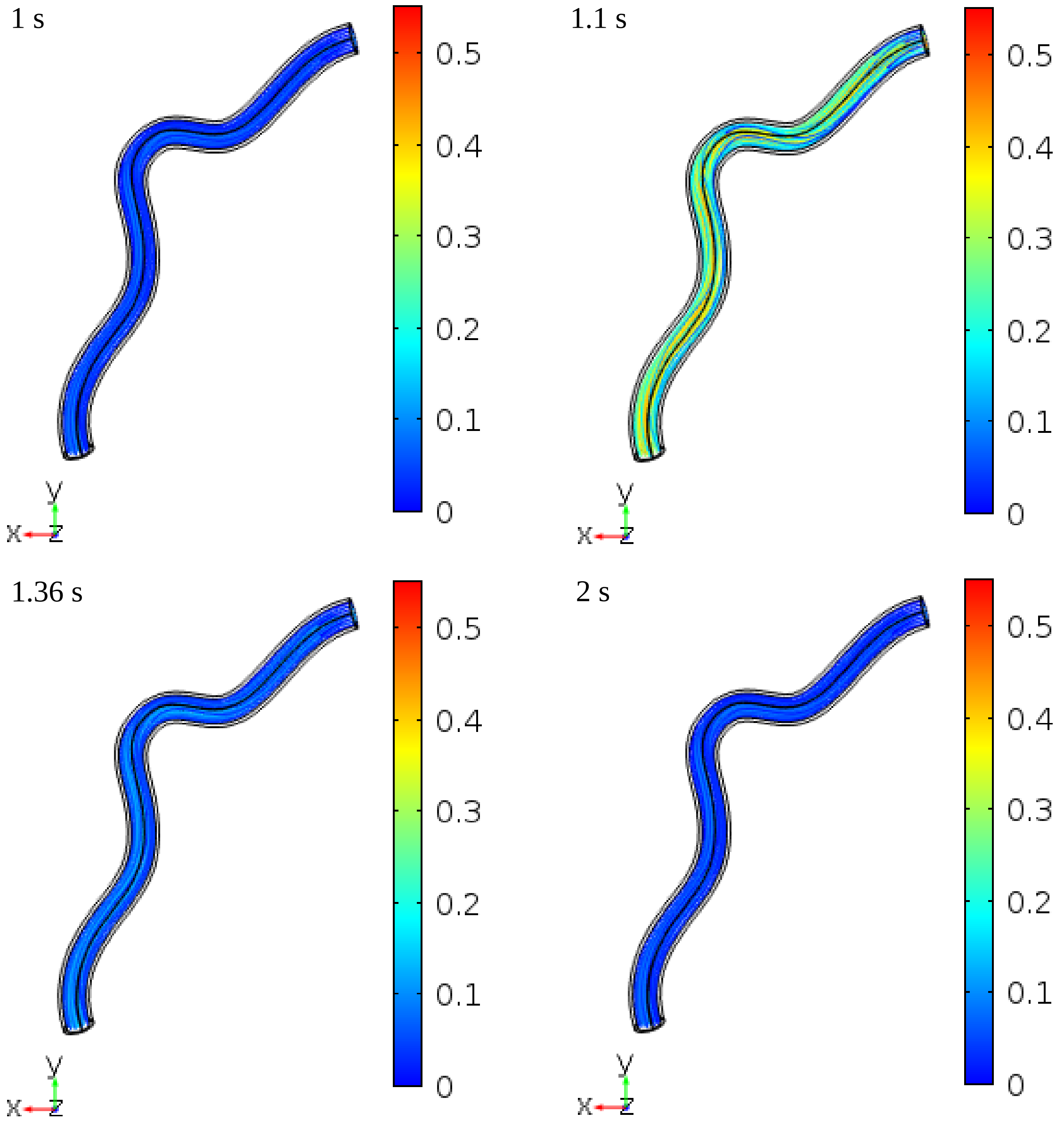

Fig. 3. Streamlines representing the blood flow velocity distribution at discrete time points (1, 1.1, 1.36, 2) s. Legend denotes the velocity in m/s

Highest velocity values are obtained at 1.1 s (at the time of systole). The maximum velocity of 0.545 m/s is in agreement with the measured systolic velocity of 0.5648 m/s [17]. The obtained velocity distributions shows the method feasibility to simulate the Newtonian blood flow in relatively big OA. The static and dynamic pressures due to blood flow generates the traction force which further is used as an external surface force for the structural analysis. This external force generates internal stresses in the OA, which can be measured in various ways. The true stresses are the Cauchy stresses, which has a real physical meaning as an acting force per unit area. However here we analyze a different stress measure – the von Mises stress, which is the uniaxial tensile stress and can be used to predict yielding of materials under complex multiaxial loading conditions using results from simple uniaxial tensile tests. The von Mises stress is a metric with intention of simplifying structural analysis by making a scalar value to give the same deviatronic strain energy as the actual three-dimensional stress tensor. The von Mises stress distribution at discrete times of (1, 1.1, 1.36, 2) is shown in Fig. 4.

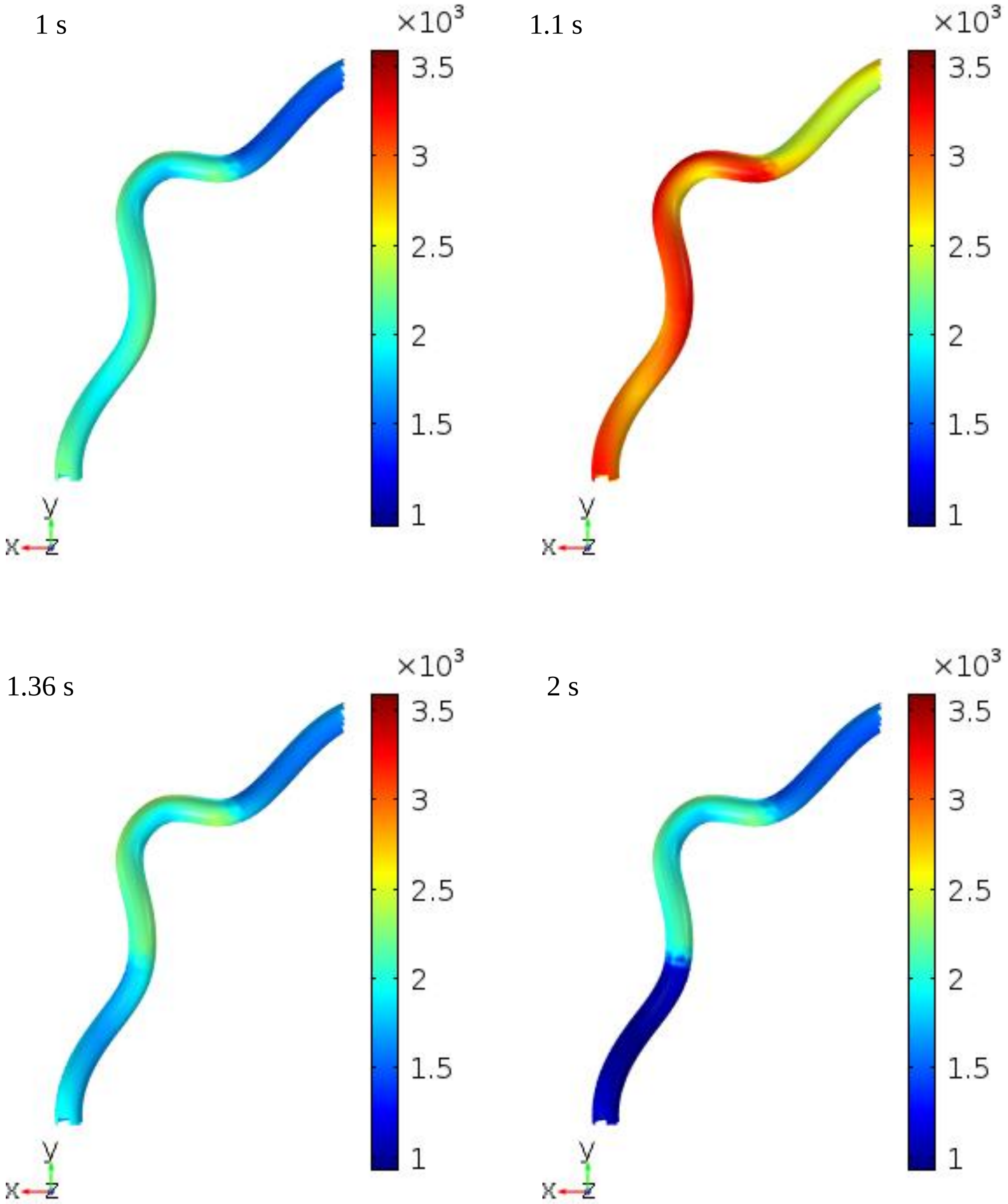

Fig. 4. The von Mises stress distribution at discrete times of (1; 1.1; 1.36; 2) s

Highest stresses are at the time of systole (at 1.1 s). The external pressures acting on the IOA and EOA outer walls relieves some of the internal stresses that was in equilibrium with the traction force applied by the blood flow. The displacements of the vessel wall are too small to have a huge influence on the blood flow velocity.

The study was limited by the lack of scientific data available on the properties of OA wall. Also although we have recommended the use of monolithic solver, here we performed the segregated solve, by which the accuracy of the obtained solutions may be impeded.

4. CONCLUSIONS

The framework for solving the blood flow-tissue interaction problems was proposed in which some of the steps were covered in more detail. The case study of blood flow-tissue interaction problem emerging in the noninvasive intracranial measurement method was performed to show the feasibility of the proposed framework. Eventually the obtained results that may be impeded by the lack of scientific data available on the OA wall mechanical properties and the use of segregated approach, are showing the ability to simulate the blood flow-tissue problem and provide the expected results. Thus we conclude that the proposed method is feasible for a wide variety of well-conditioned problems.

REFERENCES

1. A. RAGAUSKAS, G. DAUBARIS, AND A. DZIUGYS, “Method and apparatus for determining the pressure inside the brain,” 1999.
2. H. HO, C. MCGHEE, AND P. HUNTER, “Numerical analysis for the blood flow in a patient-specific ophthalmic artery,” Med. Eng. Phys., vol. 34, no. 1, pp. 123–127, Jan. 2012.
3. G. RODRÍGUEZ-BOTO, M. RIVERO-GARVÍA, R. GUTIÉRREZ-GONZÁLEZ, AND J. MÁRQUEZ-RIVAS, “Basic concepts about brain pathophysiology and intracranial pressure monitoring,” Neurología, vol. 30, no. 1, pp. 16–22, 2015.
4. T. TEKORIUS, “Simulation and investigation of vessel wall movement by the use of mathematical model of blood vessel,” Biomedicininė inžinerija, pp. 44–47, 1997.
5. Y. C. Fung, K. Fronek, and P. Patitucci, “Pseudoelasticity of arteries and the choice of its mathematical expression,” *Am. J. Physiol. Circ. Physiol.*, vol. 237, no. 5, pp. H620–H631, Nov. 1979.
6. G. A. HOLZAPFEL AND R. W. OGDEN, “Constitutive modelling of arteries,” Proc. R. Soc. A Math. Phys. Eng. Sci., vol. 466, no. 2118, pp. 1551–1597, Jun. 2010.
7. D. Bianchi, E. Monaldo, A. Gizzi, M. Marino, S. Filippi, and G. Vairo, “A FSI computational framework for vascular physiopathology: A novel flow-tissue multiscale strategy,” *Med. Eng. Phys.*, vol. 47, pp. 25–37, Sep. 2017.
8. J. Tu, K. Inthavong, and K. K. L. Wong, *Computational Hemodynamics – Theory, Modelling and Applications*, vol. 58, no. 12. Dordrecht: Springer Netherlands, 2015.
9. N. Forcadel, C. Le Guyader, and C. Gout, “Generalized fast marching method: applications to image segmentation,” *Numer. Algorithms*, vol. 48, no. 1–3, pp. 189–211, Jul. 2008.
10. T. S. Newman and H. Yi, “A survey of the marching cubes algorithm,” *Comput. Graph.*, vol. 30, no. 5, pp. 854–879, Oct. 2006.
11. L. Antiga, “Patient-specific Modeling of Geometry and Blood Flow in Large Arteries,”, *Phd thesis*, 2002.
12. D. E. Kiousis, S. F. Rubinigg, M. Auer, and G. A. Holzapfel, “A Methodology to Analyze Changes in Lipid Core and Calcification Onto Fibrous Cap Vulnerability: The Human Atherosclerotic Carotid Bifurcation as an Illustratory Example,” *J. Biomech. Eng.*, vol. 131, no. 12, p. 121002, Jan. 2009.
13. N. Karajan, W. Ehlers, B. Markert, A. Acartürk, and C. Wieners, “FE Treatment of Inhomogeneities Within the Intervertebral Disc,” *PAMM*, vol. 5, no. 1, pp. 237–238, Dec. 2005.
14. D. Roy, G. A. Holzapfel, C. Kauffmann, and G. Soulez, “Finite element analysis of abdominal aortic aneurysms: Geometrical and structural reconstruction with application of an

anisotropic material model," *IMA J. Appl. Math. (Institute Math. Its Appl.*, vol. 79, no. 5, pp. 1011–1026, 2014.

15. V. Alastrué, A. Garía, E. Peña, J. F. Rodríguez, M. A. Martínez, and M. Doblaré, "Numerical framework for patient-specific computational modelling of vascular tissue," *Int. j. numer. method. biomed. eng.*, vol. 26, no. 1, pp. 35–51, Jan. 2010.
16. D. W. Holdsworth, C. J. D. Norley, R. Frayne, D. A. Steinman, and B. K. Rutt, "Characterization of common carotid artery blood-flow waveforms in normal human subjects," *Physiol. Meas.*, vol. 20, no. 3, pp. 219–240, Aug. 1999.
17. E. Misiulis, A. Džiugys, "An investigation of the balance principle implemented by non-invasive intracranial pressure measurement method by means of computational modeling," // *The 14th International Conference of Young Scientists on energy Issues (CYSENI 2017)*, Kaunas, Lithuania, May 25–26, 2017, ISSN 1822-7554. pp. 298–307, Kaunas: LEI, 2017.

CYSENI 2018, May 23-25, Kaunas, Lithuania
ISSN 1822-7554, www.cyseni.com

ESTIMATION OF THE INFLUENCE OF WOOD-FIRE RETARDANTS ON FIRE BEHAVIOR OF SOME TYPES OF WOOD CONSTRUCTION MATERIALS

D. P. Kasymov, M. V. Agafontsev, V. V. Perminov
Tomsk State University
Lenin Ave. 36, 634050 Tomsk – Russia
Email: denkasymov@gmail.com

ABSTRACT

In this paper the effect of fire front on the surface of wood samples (pine, aspen and larch) was presented to estimate the effect of different wood-fire retardants. Infrared thermography was used as a diagnostic method. Modern methods of IR-diagnostics and the use of thermal imagers eliminate the need for a large number of thermocouples, which perturb the investigated medium during measurements. At the same time, a much better resolution in space and time can be obtained using infrared diagnostics. The surface temperature distribution was obtained for the test wood samples after exposure to a fire front that was modeled using pine needles. The ignition probability was estimated for the chosen experimental parameters for each kind of wood. In the infrared region the sample surface characteristics were recorded using a thermal imager JADE J530SB with a 2.5–2.7 micron optical filter that allowed a temperature to be measured in the range of 500–850 K. In order to record a temperature in the range of 293–550 K, the recording was conducted without a filter. The fire hazard characteristics of wood after fire retardant treatment showed a significant reduction in the surface temperature and the resistance to fire for the chosen parameters of the experiment compared to the same untreated samples.

Keywords: wildfires, infrared diagnostics, fire behaviour, wood-fire retardants, construction materials

1. INTRODUCTION

The problem concerning wildland fires becomes more urgent. All countries of the world, especially Brazil, Australia, China, Greece, Portugal, the United States and Russia are faced with this problem.

Wildland fires are known to be a powerful, natural and anthropogenic factor that significantly changes the condition of forests. Tens of thousands of hectares of forests and lands burn out. Often fires occur and develop near settlements and cities. In Russia, where forests occupy a large territory, forest fires are a national problem, and damage to the real economy is estimated at tens and hundreds of millions of dollars per year.

In the literature there are a lot of experimental studies concerning the fire hazard of wood, which demonstrate the influence of various factors on the fire hazard indices (species of wood, conditions and duration of operation, humidity, fire intensity, etc.) [1–7]. In these works the pyrolysis and thermal oxidative degradation of wood are studied, thermal and physical characteristics are determined, and the values of carbonization rates are obtained for various temperature modes. These data can be used to evaluate the fire resistance of wooden structures, but most of the methods applied to assess the fire hazard of wood are referred to contact methods (micro thermocouple techniques, molecular-beam mass spectrometry, thermal analysis methods, etc.). Contact methods are often used for recording temperature fields, heat fluxes, carbonization rates, ignition delays, etc. to model combustion processes under laboratory conditions; however, a large number of thermocouples are required to record temperature fields under field and semi-field conditions, which causes difficulties for processing the results.

At present, thermal imaging equipment is not often used in the study of wildland fires, since this method application depends on a large number of parameters and requires a detailed study of a radiation coefficient. It should be noted that information on the application of contactless methods in the fire tests of building fragments and structures [8], as well as the application of IR thermography in the study of urban and peat fires [9–10] are still in lack in the literature. Contact methods are the traditional methods for measuring the temperature during fire-engineering tests of building structures.

In this paper, the effect of various flame retardants was evaluated to study the influence of the fire front on the surface of wood building material samples. Preliminary results of the experiments are presented in [11, 12]. IR thermography was used as a diagnostic method. At present, the IR method, along with thermal non-destructive testing methods which do not cause damage to the integrity of controlled objects and do not introduce disturbances into the process, represents innovative research area that combines achievements in the theory of heat transfer, IR technology, and computer processing of experimental data [13].

2. METHODOLOGY OF THE EXPERIMENT

Combustion, simulated by forest fuel (FF), consisted of pine needles (*Pinus Pinaster*) and represented a site with a width that was close to the size of the wood sample. The samples of pine, aspen and larch were used as the samples which imitated the wood used in constructions. The dimensions of the samples in the experiment were (L × W × H): 0.23 × 0.02 × 0.1 m for pine, 0.17 × 0.02 × 0.1 m for aspen, and 0.16 × 0.02 × 0.12 m for larch.

Fig. 1 shows a scheme of the experiment:

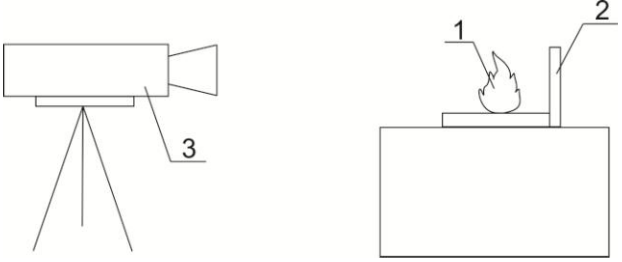

Fig. 1. Experimental setup. 1 – site with FF, 2 – wood sample, 3 – thermal imager JADE J530SB

A wood building material, in addition to the available flat pine, aspen and larch samples [14–15], was used to imitate a pine bar (“Blockhouse”) for evaluating the effect of the geometry of wood samples on ignition, as well as the effect of flame retardants on fire hazard characteristics. The size of the samples in the experiment was (L × W × H): 0.25 × 0.02 × 0.11 m. Fig. 2 shows a photograph of the building material sample used for imitating a bar.

Fig. 2. “Blockhouse” samples

The non-contact method presented in [14–15] was used to determine the temperature fields on the surface of the studied wood samples subjected to the model forest fire. A continuous thermal imaging survey of 50 FPS. The survey was conducted within 5 minutes from the moment of ignition of the forest combustible material.

The following solutions were considered: fire-bio retardant treatment for wood “FUKAM” [16], fire retardant treatment with an antiseptic effect for wood “Pirilax-Classic” [17], a fire retardant “SENEZH OGNEBIO PROF” [18], as well as a fire-retardant composition “MIG-09” [19].

The consumption of fire-retardant compositions, as determined by the manufacturer's technical specifications, guaranteed the II group of fire-retardant efficiency (The second group corresponds to incombustible materials that burn or smolder only if there is a source of fire. After its removal, the combustion stops) in accordance with GOST R53292 [20]. The sample surface subjected to the thermal action of the combustion front was uniformly coated by a flame retardant composition with a brush. The samples were kept for 24 hours and then were placed in a drying oven ShSP-0.5 – 200 at a temperature of 70 °C until the moisture content was W = 2%. Moisture content of the samples is controlled by the moisture analyzer AND MX-50 with an accuracy of 0.01%, the weight of the samples is controlled by the electronic scale AND HL-400 with an accuracy of 0.01 g.

3. RESULTS AND DISCUSSION

The use of the non-contact method allowed us to obtain the distribution of the temperature fields on the surface of the sample subjected to the combustion source.

The analysis of the data obtained for untreated wood shows that the larch samples are resistant to ignition for the selected experimental parameters. The other samples (pine, aspen), irrespective of geometry, are ignited by the combustion source. Figure 3, as an example, shows the thermograms of untreated pine wood (Fig. 3, a) and pine wood treated by a fire-retardant composition “FUKAM” (Fig. 3, b); untreated “blockhouse” sample (Fig. 3, c) and treated one by the antiseptic for wood “Pirilax-Classic” (Fig. 3, d); untreated aspen sample (Fig. 3e) and specimen treated by fire retardant “SENEZH OGNEBIO PROF” (Fig. 3, f); untreated larch sample (Fig. 3, g) and treated one by fire-retardant composition “MIG-09” (Fig. 3, h).

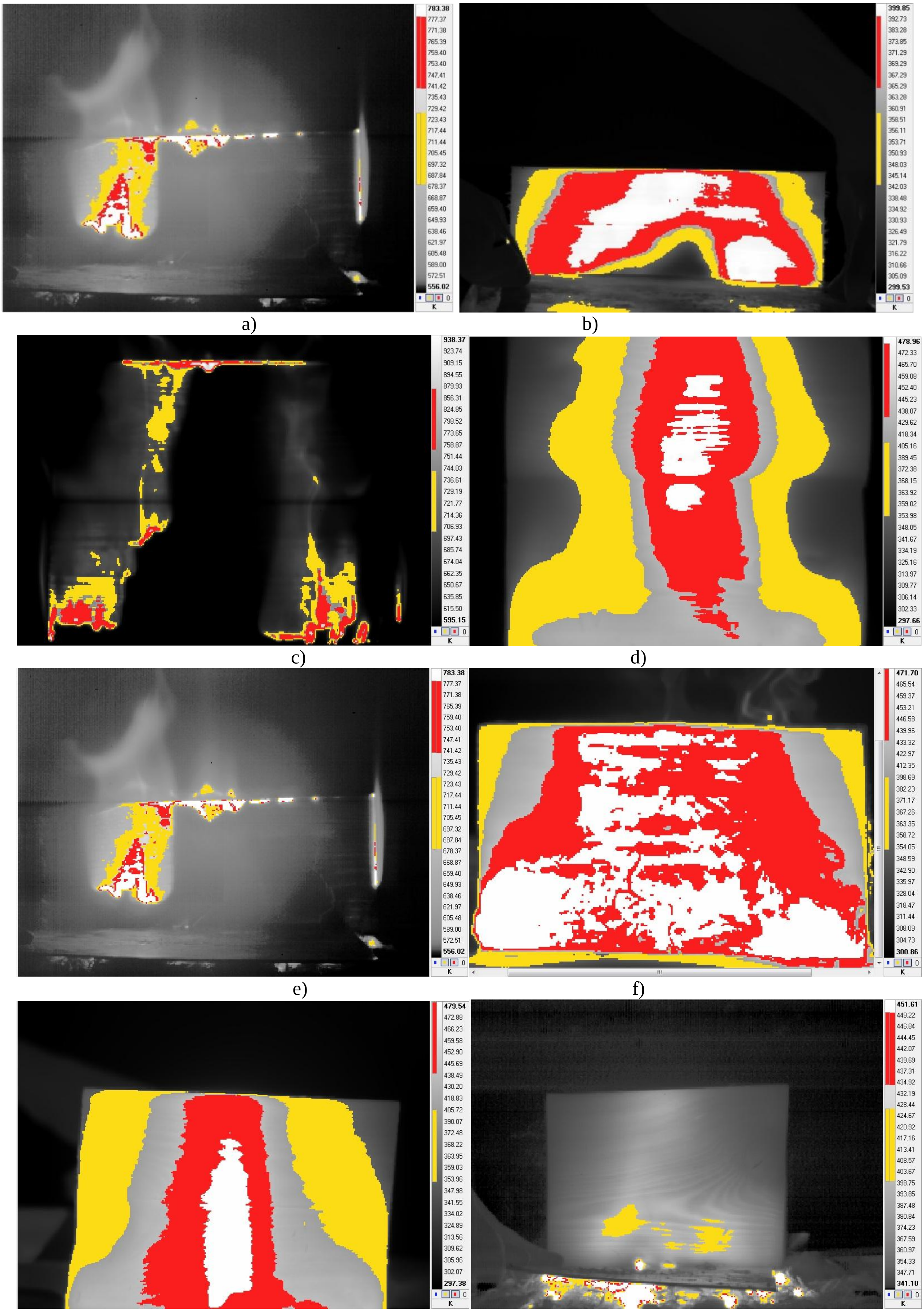

Fig. 3. Thermograms of sample surfaces after fire exposure

4. CONCLUSIONS

The influence of the various fire-retardant compositions (fire-bio retardant treatment for wood “FUKAM”, fire-retardant treatment with an antiseptic effect for wood “Pirilax-Classic”, protective means for wood “SENEZH OGNEBIO PROF”, fire-retardant composition “MIG-09”) was experimentally analyzed to study the fire-hazard characteristics for the wood samples of various geometry (flat pine, aspen and larch samples and wood building material for the imitation of a pine bar (Block House)). Comparative analysis shows that depending on the kind of wood the best fire-retardant characteristics are demonstrated by different compositions such as the fire-bio retardant treatment for wood «FUKAM» for the samples of block house; the fire-retardant treatment with an antiseptic effect for wood “Pirilax-Classic” for the building larch board; the protective means for wood “SENEZH OGNEBIO PROF” for the building pine and aspen board.

This work was carried out with financial support from President of Russian Federation grant MK – 3885.2018.8

REFERENCES

1. BARTLETT, A. I., HADDEN, R. M., BISBY, L. A., LAW, A. Analysis of cross-laminated timber charring rates upon exposure to nonstandard heating conditions. 14th International Conference and Exhibition, Proceedings. *Fire and Materials*, 2015, p. 667–681.
2. RESZKA, P., TORERO, J. L. In-depth temperature measurements in wood exposed to in-tense radiant energy. *Experimental Thermal and Fluid Science*, 2008, Vol. 32, No. 7, p. 1405–1411.
3. FRANGI, A., FONTANA, M., HUGI, E., JÜBSTL, R. Experimental analysis of cross-laminated timber panels in fire. *Fire Safety Journal*, 2009, Vol. 44 No. 8, p. 1078–1087.
4. BABRAUSKAS, V. Charring rate of wood as a tool for fire investigations. *Fire Safety Journal*, 2005, Vol. 40 No. 6, p. 528–554.
5. GRISHIN, A.M., FILKOV, A. I., LOBODA, E. L. et al. A field experiment on grass fire effects on wooden constructions and peat layer ignition. *International Journal of Wildland Fire*, 2014, Vol. 23, No. 3, p. 445–449.
6. KUZNETSOV, V. T., FIL'KOV, A.I. Ignition of various wood species by radiant energy. *Combustion, Explosion and Shock Waves*, 2011, Vol. 47 No. 1, p. 65–69.
7. SIVENKOV, Andrei B.; ASEEVA, Rosa M.; SERKOV, Boris B. *Combustion of wood and its fire hazard properties*. Academy of State Fire Service of the Ministry of Emergency Measures of Russia, 2010, 262 p. ISBN 978-5-9229-0045-4. (in Russian).
8. MEL’NIKOV, V. S., HASANOV I. R., KIRILLOV S. V. et al. Thermography of building elements and building structures during fire tests. *Fire Safety*, 2015, No. 3, p. 83–90. (in Russian).
9. VERMESI, I., DiDOMIZIO J. M., RICHTER F. et al. Pyrolysis and spontaneous ignition of wood under transient irradiation: Experiments and a-priori predictions. *Fire Safety Journal*, 2017, Vol. 91, p. 218–225.
10. PRAT-GUITART, N., BELCHER C. M., HADDEN R. et al. Infrared image analysis as a tool for studying the horizontal smoldering propagation of laboratory peat fires. *Coal and peat fires: A global perspective*. Publisher Elsevier, 2015, p. 121–139. ISBN 978-0-444-52858-2.
11. ZIMA, V. P., KASYMOV, D. P. Investigation of the Effect of the Combustion Site on Wood Specimens with the Use of IR Diagnostics. *Journal of Engineering Physics and Thermophysics*, 2016, Vol. 89, No. 2, p. 466–470.
12. GRISHIN, A. M., ZIMA, A. M., KASYMOV, D. P. Fire hazard system analysis of wood construction elements on exposure to wildfire. North of Russia: strategies and development

pro-spects 2016. Materials of the II All-Russian Scientific and Practical Conference, 2016, p. 260–263. (in Russian).

13. VAVILOV, Vladimir. P. *Thermal/Infrared Nondestructive Testing*. NDT Handbooks series. Spectrum Publisher, 2009, Vol. 5, 450 p. ISBN 978-5-904270-03-2.
14. AGAFONCEV, Michael V., KASYMOV, Denis P. *Actual problems of thermophysics and physical hydrodynamics*. Novosibirsk, 2016, 81–82 p. (in Russian).
15. AGAFONCEV, M. V., KASYMOV, D. P. Investigation of the Fire Hazard Characteristics of Wood Using Infrared Thermography. *Proceedings of the 8th European Combustion Meeting*.. Dubrovnik, Croatia, 2017- [referred on the 29th of September in 2017 y.]. Link to the internet <https://www.researchgate.net/publication/317040588_Investigation_of_the_Fire_Hazard_Characteristics_of_Wood_Using_Infrared_Thermography>.
16. Fire-bio protective composition "Fukam", [referred on the 5th of December in 2017 y.]. Link to the internet < http://www.fukam.ru/English>.
17. Biopyrene (fire retardant antiseptic) "Pirilaks": instructions for use. «NORT». [referred on the 5th of December in 2017 y.]. Link to the internet < https://www.nort-udm.ru/en/ >.
18. Means protective for wood, instruction on application. [referred on the 12th of December in 2017 y.]. Link to the internet <http://www.strsezon.ru/ognebio_prof.pdf>. (in Russian).
19. Biopyrene (flame retardant antiseptic) "Mig-09": instructions for use "NORT". [re-ferred on the 12th of December in 2017 y.]. Link to the internet < https://www.nort-udm.ru/en/>.
20. *GOST R 53292-2009. Fire-retardant compounds and substances for wood and materials based on it. General requirements. Test methods.* Moscow FRUP "Standartinform", 2009- [re-ferred on the 12th of December in 2017 y.]. Link to the internet <http://bpl32.ru/bank/normativnye-dokumenty/gost-r-53292.pdf>. (in Russian).

CYSENI 2018, May 23-25, Kaunas, Lithuania
ISSN 1822-7554, www.cyseni.com

NUMERICAL MODELING OF WOOD CHIPS PACKED BED DRYING

G. Skarbalius, E. Misiulis, A. Džiugys, L. Vorotinskienė
Lithuanian Energy Institute
Breslaujos str. 3, 44403 Kaunas – Lithuania
Email: gediminas.skarbalius@ktu.edu

ABSTRACT

Over the years biomass incineration plants were adapted to perform well with a high quality and a relatively dry biomass. However, recently most of the biomass comes with a high moisture content. The process of biomass drying has become one of the essential technological processes used in biomass incineration furnaces, due to a large energy savings available, while also the extensive use of a biomass poses a hazard to the environment and therefore drying process improvements are very promising. In order to investigate the drying process of biomass, a mathematical model for a porous media was developed and used to numerically investigate the drying of a porous packed bed of wood chips. Drying properties, such as convective heat and mass transport coefficients as well as all other required parameters were taken from literature related with wood drying processes while value of specific area in porous bed was obtained by tuning model results with data acquired from experiment, which was carried out by heating wood chip packed bed with a 100 ºC temperature air flow. Temperature was measured at 3 different points in a packed bed of wood chips to provide valuable information on how temperature varies over time at different bed heights. Then specific area and coefficients required for describing porosity spatial distribution were determined by choosing values which gives best fit with experiment.

Keywords: mathematical model, drying process, convective heat and mass transport, specific area

1. INTRODUCTION

Fossil fuel based conventional energy sources such as oil, coal and natural gas have been effective stimulus for economic growth and progress. However, fossil fuels are finite and non-renewable energy resources as all deposits of fossil fuels are limited either physically or economically [1]. This arises from the fact that millions of years are required for fossil fuels to accumulate while deposits are extracted rather quickly, making it impossible for the rate of production to catch up to the rate of consumption. Today, these sources are vanishing and it is predicted that oil sources might be depleted by year 2050 [2]. Furthermore, continued extraction and combustion of fossil fuels at growing rates are now accepted to be dominant driver of climate change [3]. Usage of renewable energy sources is convenient way to reduce consumption of fossil fuels and biomass is a promising and environmentally-friendly alternative as an energy source [4].

Regardless of prospects of biomass, the great problem that impedes its further efficient usage is the high moisture content [5]. Biomass such as wood chips, sawdust, recycled wood, forestry waste or bark gains popularity in many countries, however, wood biomass frequently comes with moisture content around 50 wt. % on wet basis (wb) and bark biomass exceeds 70 wt. % (wb) and might be even higher depending on the season [6]. For this reason, biomass energy density is low when compared with conventional fossil fuels. Biomass drying before combustion consumes a great amount of energy while moist fuel leads to a high transportation costs and storage difficulties. Furthermore, direct feed of biomass with high moisture content into combustion chamber reduces efficiency of thermochemical conversion processes [7] which leads to a lower plant productivity. Therefore, it is necessary to remove a great amount of water from biomass before conversion and as a result, biomass drying processes play an essential role for efficient and successful energy production from biomass.

Various biomass drying methods have been developed over the years such as conveyor dryers, rotary dryers of single or multiple passes, and the fixed and moving bed dryers. Moving bed and rotary dryers are used most frequently for industrial purpose. Developed mathematical models of these dryers predict that in shorter than 30 minutes time period ideal moisture contents for efficient biomass conversion which is 34–40 wt. % (wb) could be reached [8]. However, building such drying system in power plants requires a huge investment which takes time to pay off. Solution for this problem might be the optimization of biomass drying process. The biomass drying takes place while traveling along the moving grate in the furnace, since the prevailing combustion system in bioenergy plants is grate firing [9]. The optimized biomass drying could lead to great energy and capital savings, since there would be no need to build any additional drying facilities in order to reach suitable biomass quality before conversion and eventually the combustion regime would not be influenced by a varying moisture content of biomass over time. The convenient way to investigate this possibility is numerical modelling of biomass drying processes, since nowadays computer power is ever increasing and experimental way of drying optimization is expensive and time-consuming process, especially when its necessary imitate biomass drying on the moving grate system.

The main goal of this work is to develop a mathematical model for porous media drying process and to determine all unknown parameter values in case of wood chips biomass drying. Therefore, the stationary numerical study was performed in order to simulate the fixed wood chips biomass packed bed drying. Most of the model parameters for wood and air were used from scientific literature proposed by other authors. Other parameters that could not be obtained from literature or measured experimentally, were determined by parameter optimization study according to experiment where dry wood chips packed bed was being heated with a 100 ºC temperature dry air flow.

2. EXPERIMENTAL STUDY

We modelled the environment of a biomass furnace by taking into account the up-flow of heated air, the flat plate as a stationary furnace grate. Wood chips biomass was piled into a box with dimensions $w_x = 0.4\,m$, $h_y = 0.19\,m$ and $d_z = 0.265\,m$ as shown in Fig. 1. Packed bed was heated with 100 °C temperature hot air flow. Mass of dry wood chips $W_{dry} = 5.2289$ kg and volumetric air flow velocity is $Q_{V,a} = 23.76\,\frac{m^3}{h}$. The average porosity $\bar{\epsilon}$ and mean particle size $\bar{D}_p$ was obtained by performing the porosity measurements. Temperature of air in wood chips packed bed were measured with thermocouples in three different points with coordinates in xy plane: $T_1 = (0.2; 0.1)$, $T_2 = (0.06; 0.085)$ and $T_3 = (0.21; 0.025)$.

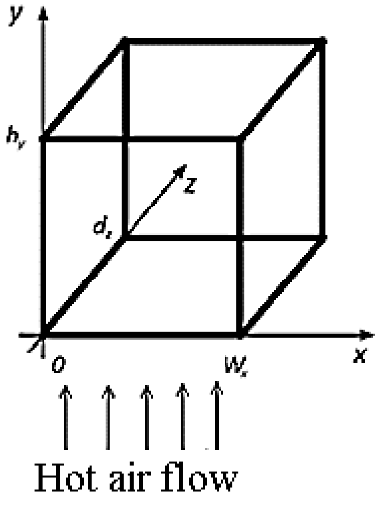

Fig. 1. A packed bed of wood chips

3. NUMERICAL STUDY

The numerical model was created to numerically simulate the experiment. Numerical model incorporated laminar dry air flow, local thermal non-equilibrium heat transfer between wood chips and air flow and a transport of water vapour through a porous packed bed of humid wood chips. The depth of the packed bed is assumed to be long enough to consider a two-dimensional cross-section. Whole study plane xy and gaseous $\Omega_{g,1}, \Omega_{g,2}$and porous Ω_p domains together with boundaries $\varphi_{1..10}$ are depicted in Fig. 2. However, we took into account the porosity distribution ϵ due to near wall effects in an orthogonal plane (xz) to evaluate the air flow rate in the plane of numerical study xy at $z_m = d_z/2$, as shown in Fig. 3.

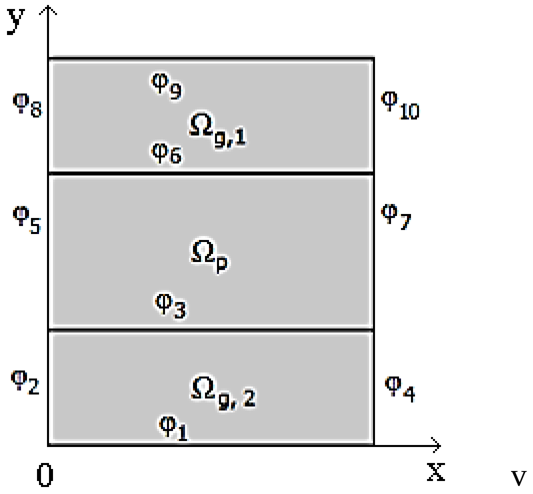

Fig. 2. Plane of numerical study with denoted gaseous and porous domains

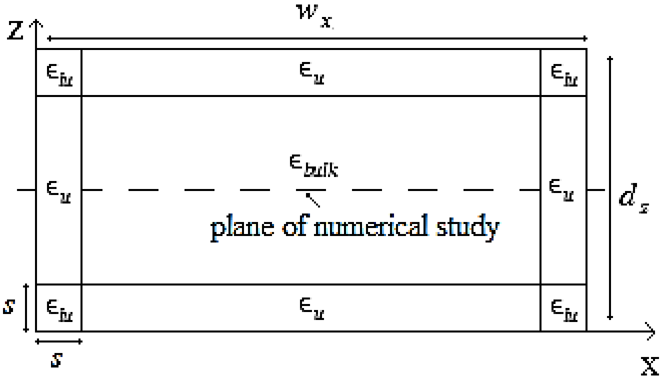

Fig. 3. xz plane of porous domain with denoted all porosity regions and plane of numerical study

3.1. Laminar air flow

Air flow momentum is conserved by incompressible Navier-Stokes equation formulation for laminar flow in a porous media:

$$\frac{1}{\epsilon}\rho_{av}\left(\frac{\partial \mathrm{u}_{\mathrm{av}}}{\partial t}+(\mathrm{u}_{\mathrm{av}}\cdot\nabla)\mathrm{u}_{\mathrm{av}}\frac{1}{\epsilon}\right)=-\nabla p\mathrm{I}+\nabla\left(\mu_{av}(\nabla\mathrm{u}_{\mathrm{av}}+(\nabla\mathrm{u}_{\mathrm{av}})^{\mathrm{T}})\right)-\mu_{av}\kappa^{-1}\mathrm{u}_{\mathrm{av}}+F \qquad (1)$$

where κ is permeability of porous packed bed, ρ_{av} and μ_{va} is density and dynamic viscosity of the moist air. The first term on the left-hand side of the Eq. (1) represents the transient momentum response and the second term represents the advection and diffusion of momentum. The first term on the right-hand side represents the force due pressure gradient and the second term accounts for viscous forces. The third term accounts for the Darcian force and the last term represents the force due to gravity.

Air mass flow is conserved by continuity equation:

$$\mathrm{\rho}_{av}\nabla \cdot (\mathrm{u}_{\mathrm{av}}) = 0. \tag{2}$$

The dependent variables are moist air velocity vector field u_{av} and a static gauge pressure field p for whom Eq. (1) and Eq. (2) are solved.

3.2. Heat transfer in moist air

Heat transfer in moist air is described by equation:

$$d_z(\mathrm{\rho}_{av}C_{p,av})_{\mathrm{av}}\frac{\partial T_{av}}{\partial t} + d_z(\mathrm{\rho}_{av}C_{p,av})_{\mathrm{av}}\mathrm{u}_{\mathrm{av}} \cdot \nabla T_{av} + \nabla \cdot \mathrm{q}_{\mathrm{av}} = d_z Q_{e/c} \tag{3}$$

and conductive heat flux of moist air q_{av} is as follows:

$$\mathrm{q}_{\mathrm{av}} = -d_z k_{av}\nabla T_{av} \tag{4}$$

In Eq. (3) $C_{p,av}$ is heat capacity of moist air, d_z is depth of wood chips packed bed. In Eq. (4) k_{av} is thermal conductivity of moist air. The first term on the left-hand side of Eq. (3) corresponds to the transient thermal response, second term corresponds to the adjective energy transfer due to buoyancy driven flow and the third term represents the conductive energy transfer. The term on the right-hand side represents the heat energy source term due to evaporation or condensation.

Dependent variable is a temperature field of a moist air T_{av} for which Eq. (3) is solved.

3.3. Heat transfer in wood chips

Heat transfer in wood chips is described by equation

$$d_z(\mathrm{\rho}_{wc}C_{p,wc})_{\mathrm{wc}}\frac{\partial T_{wc}}{\partial t} + \nabla \cdot \mathrm{q}_{\mathrm{wc}} = 0 \tag{5}$$

and conductive heat flux of wood chips packed bed q_{wc} is as follows:

$$\mathrm{q}_{\mathrm{wc}} = -d_z k_{wc}\nabla T_{wc} \tag{6}$$

In Eq. (5) and Eq. (6) $\mathrm{\rho}_{wc}$, $C_{p,wc}$ and k_{wc} is density, heat capacity and thermal conductivity of wood chips packed bed respectively. The first term of Eq. (5) represents the transient thermal response and the second term accounts for the conductive heat transfer.

Dependent variable is a temperature field of wood chips T_{wc} for which Eq. (5) is solved.

3.4. Local thermal non-equilibrium between moist air and a porous packed bed of wood chips

Local thermal non-equilibrium between air and porous packed bed are described by following equations:

$$Q_p = \frac{q_{sf}}{1-\epsilon}(T_{av} - T_{wc}) \tag{7}$$

and

$$Q_{av} = \frac{q_{sf}}{\epsilon}(T_{wc} - T_{av}) \tag{8}$$

where q_{sf} is a volumetric heat transfer parameter which is equal to a product of specific area of wood chips a_{sf} packed bed and heat transfer coefficient between air and wood chips h_{wc}. Value of $h_{wc} = 15\ \frac{W}{m^2K}$ was chosen as proposed by other authors who modelled wood drying with hot air flow [10] while value of a_{sf} were determined by comparing model results with experimental data, where dry wood chips packed bed was heated with 100 °C temperature air.

3.5. Diluted species: liquid water and water vapour

Liquid water is treated as immovable and its concentration does not affect the overall porosity. Water concentration can only change in time due to evaporation or condensation, which in a governing form is:

$$\frac{\partial c_w}{\partial t} = R_w \tag{9}$$

where R_w is volumetric evaporation ratio.

Water vapour can be transported due to diffusion and advection, which is the second and third terms in the Eq. (10), respectively. The first and the last terms are the reaction terms, whom are used to account for the concentration change in time due to evaporation or condensation of water vapour:

$$\frac{\partial c_v}{\partial t} + \nabla \cdot (-D_v \nabla c_v + \mathrm{u_v} c_v) = R_v \tag{10}$$

where R_v is evaporation ratio as well and $R_v = -R_w$.

Dependent variables are water concentration c_w and water vapor concentration in air c_v for whom Eq. (9) and Eq. (10) are solved.

4. RESULTS AND DISCUSSION

4.1. Moist air parameters

The molecular weight of water vapour is $M_v = 0.018\frac{\mathrm{kg}}{\mathrm{mol}}$, molecular weight of air is $M_a = 0.02897\frac{\mathrm{kg}}{\mathrm{mol}}$. Then the molecular weight of moist air $M_{av}$is calculated as follows:

$$M_{av} = M_v X_v + M_a X_a \tag{11}$$

where X_v and X_a are water vapor and air molar fractions in vapor-air mixture.

The absolute pressure $p_A$is calculated by equation:

$$p_A = p + p_{atm} \tag{12}$$

Moist air density ρ_{av} is calculated according to the ideal gas law:

$$\rho_{av} = \frac{p_A M_{av}}{RT} \tag{13}$$

Air dynamic viscosity is also dependent on the temperature, however in the temperature range of study interest it can be approximated as a constant value of $\mu_a = 1.81 \cdot 10^{-5} \frac{\mathrm{kg}}{\mathrm{m \cdot s}}$. Also, the same can be done with a dynamic viscosity of water vapour $\mu_v = 1.8 \cdot 10^{-5} \frac{\mathrm{kg}}{\mathrm{m \cdot s}}$.

The coefficients for moist air viscosity and conductivity $\phi_{aa}, \phi_{vv}, \phi_{av}, \phi_{va}$ are calculated as follows:

$$\phi_{aa} = 1 \tag{14}$$

$$\phi_{vv} = 1 \tag{15}$$

$$\phi_{av} = \frac{\left(1 + \left(\frac{\mu_a}{\mu_v}\right)^{\frac{1}{2}} \left(\frac{M_v}{M_a}\right)^{\frac{1}{4}}\right)^2}{\left(8\left(1 + \frac{M_a}{M_v}\right)\right)^{\frac{1}{2}}} \tag{16}$$

$$\phi_{va} = \frac{\left(1 + \left(\frac{\mu_v}{\mu_a}\right)^{\frac{1}{2}} \left(\frac{M_a}{M_v}\right)^{\frac{1}{4}}\right)^2}{\left(8\left(1 + \frac{M_v}{M_a}\right)\right)^{\frac{1}{2}}} \tag{17}$$

These coefficients were used to calculate viscosity of moist air μ_{av} as follows:

$$\mu_{av} = \frac{\mu_a X_a}{X_v \phi_{av} + X_a \phi_{aa}} + \frac{\mu_v X_v}{X_v \phi_{vv} + X_a \phi_{va}} \tag{18}$$

4.2. Heat transfer in moist air

Heat capacity of air is dependent on temperature, however in the temperature range of study interest it can be approximated as a constant value of $C_{p,a} = 1.006 \frac{\mathrm{kJ}}{\mathrm{kg \cdot K}}$. Also, the same can be done with heat capacity of water vapour $C_{p,v} = 2.062 \frac{\mathrm{kJ}}{\mathrm{kg \cdot K}}$.

Heat capacity and thermal conductivity of moist air $C_{p,av}$ can be calculated with following equations:

$$C_{p,av} = \frac{M_v X_v C_{p,v} + M_a X_a C_{p,a}}{M_{av}} \tag{19}$$

and

$$k_{av} = \frac{k_a X_a}{X_v \phi_{av} + X_a \phi_{aa}} + \frac{k_v X_v}{X_v \phi_{vv} + X_a \phi_{va}} \tag{20}$$

The latent heat of water evaporation or condensation is $H_{e/c} = 2454 \frac{\mathrm{kJ}}{\mathrm{kg}}$. The heat source due to evaporation or condensation $Q_{e/c}$at porous domain $\Omega_p$is calculated as follows:

$$Q_{e/c} = -H_{e/c} M_w \dot{c}_{e/c} \tag{21}$$

4.3. Heat transfer in wood chips

Thermal conductivity of non-porous packed bed of wood chips is taken $k_{wc} = 0.17 \frac{\mathrm{W}}{\mathrm{m \cdot K}}$.

Moisture content on dry basis of porous packed bed of wood chips $X_{m,p}$ is calculated as follows:

$$X_{m,p} = \frac{c_v M_w}{\rho_{wc} + c_v M_w} \tag{22}$$

Heat capacity of porous packed bed of humid wood chips $C_{p,hp}$is assumed to be equal to the bulk heat capacity of wood and is provided by:

$$C_{p,hp} = 4190 \left(\frac{26.6 + 0.116(T - 273.15) + 100\left(X_{m,p}\right)}{100 + 100\left(X_{m,p}\right)} \right) \tag{23}$$

4.4. Spatial porosity distribution

In experimental study, an uneven temperature rise in near wall and bulk area was observed. Therefore, a spatial distribution of porosity of packed bed $\epsilon(x)$ was introduced to account for the experimental results of temperature at certain points obtained using thermocouples. It was assumed that value of porosity decreases linearly when distance from the wall increases up to certain length. When distance is greater than this certain length, value of porosity becomes constant and independent from spatial coordinates. In that case, our spatial porosity distribution function in our study plane of interest xy has form of:

$$\epsilon = \epsilon(x) = \begin{cases} -\dfrac{\epsilon_{wall} - \epsilon_{bulk}}{s} x + \epsilon_{wall}\ , when\ 0 < x \leq s \\ \epsilon_{bulk\ ,when\ s<x\leq w_x - s} \\ \dfrac{\epsilon_{wall} - \epsilon_{bulk}}{s} \mathrm{x} + \epsilon_{bulk}\ , when\ w_x - s < x \leq w_x \end{cases} \tag{24}$$

In Eq. (24) ϵ_{wall} and ϵ_{bulk} are coefficients that describes porosity at near wall and bulk regions respectively and s is a minimal length in which wall of the box has influence on porosity. The regions near walls are denoted as ϵ_u as shown in Fig. 3. Corner regions where porosity is affected by both corner walls are denoted as ϵ_{lu}. Region where distance from wall is greater than minimal length s and porosity is constant, is denoted as ϵ_{bulk}.

4.5. Parameter optimization study

Most of parameters for moist air and wood were calculated from experiment or chosen from literature related with modelling of wood chips packed bed drying processes. However, some parameter values were difficult to obtain or they can highly deviate from ones which were obtained experimentally. In our case unknown parameters were specific area of wood chips packed bed a_{sf} and porosity distribution coefficients ϵ_{bulk}, ϵ_{wall} and s. These values were obtained by parameter optimization study in which model results were compared to experiment, where dry wood chips packed bed was heated with 100 °C temperature dry air from below. The case of dry wood chips heating was chosen in order to avoid condensation or evaporation during the experiment. Therefore, no additional heat sources in the domain were generated and all changes in air and wood temperature were due to heat transfer between wood and air.

Parameter optimization was carried out by parametric sweep study where value limits of each parameter and value step were determined. Then calculations were performed with all possible parameter value combinations between these limits. In each parameter combination, a mean quadratic deviation between model output and experimental data was calculated. The values giving best fit, i.e. ones giving the least mean quadratic deviation between model results and experiment are considered to be correct parameter values.

Wood chips packed bed temperatures at three different points are shown in Fig. 4. One can notice that model results deviates significantly from experiment in first 20 minutes of calculation. This deviation occurs because experiment chamber, as well as all thermocouples were heated with 100 °C temperature hot air before a room temperature packed bed was inserted into the chamber. Therefore, temperature of thermocouples at the beginning decreases rapidly to a certain value before starting to increase while in numerical study, initial air and biomass temperature was set to room temperature T = 15 °C and started to increase with time. Because of this reason, a deviation between results was calculated after 20 min. mark. From Table 1 we can see that obtained value for specific area a_{sf} = 560 $\frac{m^2}{m^3}$. Since convective heat transfer coefficient for wood drying is known, we can show that authors [6] obtained value of specific area ranges from 40 to 167 $\frac{m^2}{m^3}$ depending on wood particle size in biomass and type of wood. In our case, determined value is in same order, however, deviation from [6] could be explained by different wood particle sizes and mixture composition of our biomass, since the exact composition is not precisely know.

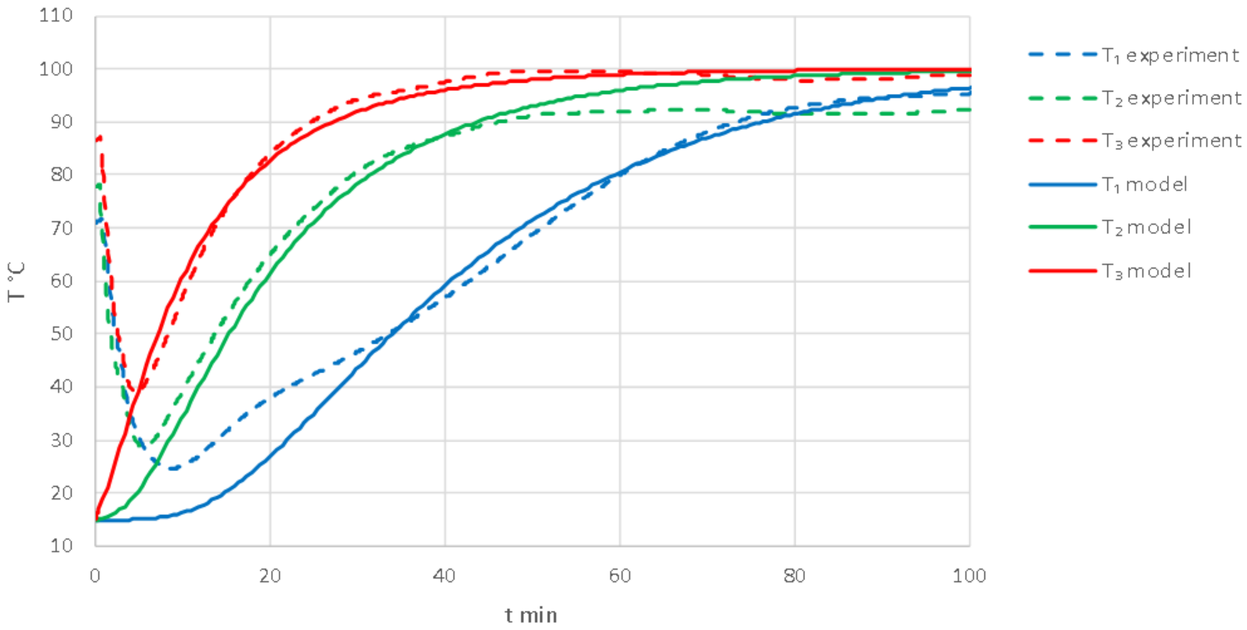

Fig. 4. Wood chips packed bed temperatures at three different points. Dotted lines represent experimental data while solid lines correspond to model results

Table 1. Model parameter values which gives best fit to experiment. ϵ_{bulk} and ϵ_{wall} are dimensionless quantities

$a_{sf}, \frac{m^2}{m^3}$	ϵ_{bulk}	ϵ_{wall}	s, m
560	0.4656	0.7600	0.074

5. CONCLUSIONS AND FUTURE WORK

A mathematical model of porous media drying was developed which was applied for numerical investigation of wood chips packed bed drying process. This model accounts convective heat transfer and water vapor mass transfer between wood particles and flowing air. Model parameters for air and wood were taken from literature concerning wood drying with air. Unknown parameter values were determined by parameter optimization study, where model results were compared to experimental data. We obtained that specific area a_{sf} = 560 $\frac{m^2}{m^3}$ and porosity spatial distribution coefficients are ϵ_{bulk} = 0.4656, ϵ_{wall} = 0,7600 and s = 0.074 m. Model results shows good match with experiment when best fitting parameters is used.

In future, we plan to investigate a various parameter influences in the drying of a packed bed of high moisture content wood chips by using our created numerical model. To validate full model with drying included, firstly model results will be compared with experiment. After model validation, it will be used to simulate biomass drying on a moving grate system where we will investigate drying rate dependencies on primary air temperature, thermal radiation intensity from combustion chamber and biomass mixing.

REFERENCES

[1] Höök M, Tang X. Depletion of fossil fuels and anthropogenic climate change-A review. Energy Policy 2013;52:797–809. doi:10.1016/j.enpol.2012.10.046.

[2] Goyal HB, Seal D, Saxena RC. Bio-fuels from thermochemical conversion of renewable resources: A review. Renew Sustain Energy Rev 2008; 12:504–17. doi:10.1016/j.rser.2006.07.014.

[3] Nel WP, Cooper CJ. Implications of fossil fuel constraints on economic growth and global warming. Energy Policy 2009; 37:166–80. doi:10.1016/j.enpol.2008.08.013.

[4] Stigka EK, Paravantis JA, Mihalakakou GK. Social acceptance of renewable energy sources: A review of contingent valuation applications. Renew Sustain Energy Rev 2014;32:100–6. doi:10.1016/j.rser.2013.12.026.

[5] Liu Y, Aziz M, Kansha Y, Bhattacharya S, Tsutsumi A. Application of the self-heat recuperation technology for energy saving in biomass drying system. Fuel Process Technol 2014;117:66–74. doi:10.1016/j.fuproc.2013.02.007.

[6] Huttunen M, Holmberg A, Stenström S. Modeling fixed-bed drying of bark. Dry Technol 2017;35:97–107. doi:10.1080/07373937.2016.1161645.

[7] Liu Y, Peng J, Kansha Y, Ishizuka M, Tsutsumi A, Jia D, et al. Novel fluidized bed dryer for biomass drying. Fuel Process Technol 2014; 122:170–5. doi:10.1016/j.fuproc.2014.01.036.

[8] Pang S, Mujumdar AS. Drying of woody biomass for bioenergy: Drying technologies and optimization for an integrated bioenergy plant. Dry Technol 2010; 28:690–701. doi:10.1080/07373931003799236.

[9] Li H, Chen Q, Zhang X, Finney KN, Sharifi VN, Swithenbank J. Evaluation of a biomass drying process using waste heat from process industries: A case study. Appl Therm Eng 2012; 35:71–80. doi:10.1016/j.applthermaleng.2011.10.009.

[10] Tremblay C, Cloutier A, Fortin Y. Experimental determination of the convective heat and mass transfer coefficients for wood drying. Wood Sci Technol 2000; 34:253–76. doi:10.1007/s002260000045.

PRELIMINARY STUDIES OF SELECTED CALCIUM FLY ASHES AS THE SUBSTRATES OF GEOPOLYMER MATERIAL

M. Kubeł, N. Czuma, P. Baran, K. Zarębska, B. Samojeden
AGH University of Science and Technology, Faculty of Energy and Fuels
Al. Mickiewicza 30, 30-059 Cracow – Poland
Email: maciejkubel@gmail.com

ABSTRACT

The parameters of the synthesis reaction were investigated to establish how modification of fly ash composition should affect the properties of fabricated geopolymers. Calcium fly ash used in the study was formed because of brown coal burning. To obtain the modified product, fly ash was subjected to magnetic separation and unburned carbon was removed. Thus, prepared fly ashes were activated with an alkaline solution composed of mixture of sodium silicate and highly concentrated NaOH solution. Thus, obtained products were analysed to establish their properties, particularly the compressive strength. Experiments revealed that removal of ferromagnetic components significantly improves the strength parameters. The sample, which had the highest strength, was that in which the proportion of NaOH during the synthesis was the largest.

1. INTRODUCTION

Fly ash is a solid residue formed because of fuel burning. The main source of fly ash is power generation in heat-power plants. Looking from a global perspective not all fly ash is directed to further use and some of it goes to landfills, which is regarded as an environment-unfriendly solution (occupation of land, deterioration of the environment and ecosystems) and not wholly cost-effective. As regards chemical composition, fly ash is mainly composed of SiO_2, Al_2O_3, CaO and Fe_2O_3, which exists in the form of amorphous and crystalline oxides or various minerals. The composition of fly ash makes it suitable for use in mine backfilling, soil stabilization, road building, and concrete production or in more advanced technologies such as metal recovery, adsorbents or zeolite production [1].

A potential of fly ash utilization is its transformation into geopolymers. The term “geopolymer” and the material itself were introduced in the 1970s by Joseph Davidovits to denote chains or networks of mineral molecules linked with co-valent bonds. Geopolymerization is actually a process of geosynthesis yielding inorganic polymeric materials. Geopolymers are presently developed and applied in 10 main classes of materials [2]:

- Waterglass-based geopolymer, Si : Al = 1 : 0;
- Kaolinite / Hydrosodalite-based geopolymer, Si : Al = 1 : 1;
- Metakaolin MK-750-based geopolymer, Si : Al = 2 : 1;
- Calcium-based geopolymer, Si : Al = 1, 2, 3;
- Rock-based geopolymer, 1 < Si : Al < 5;
- Silica-based geopolymer, Si : Al > 5;
- Fly ash-based geopolymer;
- Ferro-sialate-based geopolymer;
- Phosphate-based geopolymer, $AlPO^{4-}$based geopolymer;
- Organic-mineral geopolymer.

Generally, these materials have very good physico-chemical and mechanical properties, which includes low density, micro-porosity or nano-porosity. Additionally, they exhibit negligible shrinkage, high strength, thermal stability, high surface hardness as well as fire and chemical resistance [3]. Geopolymers also have a good ability to immobilize toxic metals [4].

Unlike Portland cement production (properties of geopolymer –based cement is very similar to those of Portland cement), it was shown that CO_2 emissions can be significantly reduced by replacing the conventional cement (containing limestone that is calcined and decomposed at high temperatures) with geopolymer-based cement [5].

The use of fly ash as a product for geopolymer production is an attractive solution as it allows for both efficient recycling of power engineering waste and production of material with good mechanical properties suitable for applications in the construction, transportation, road building, aerospace, and mining and metallurgy sectors [3].

Despite extensive research work investigating the process of geopolymerization [3, 6, 7], the mechanism of geopolymer fabrication is not well recognized yet [8]. Additionally, variations in fly ashes composition affect the properties of thus formed geopolymers. Therefore, the influence of fly ash variations and modification on the final product of geopolymerization still merits a rigorous study.

2. EXPERTIMENTAL

2.1. Characteristic of fly ash

Fly ash used in the experiments came from one of the brown coal-fired power-plants in Poland. As a result, fly ash contains high amounts of calcium oxide and unburned carbon. To determine the exact amounts of unburned carbon, the loss on ignition (LOI) was analyzed by keeping 1 g of fly ash in a furnace at temperature of 800 ^{o}C for 6 hours. The actual composition of fly ash was determined by XRF method. Results are summarized in Table 1.

Table 1. Composition of fly ash used for geopolymer production

Component	**SiO_2**	**CaO**	**SO_3**	**Al_2O_3**	**Fe_2O_3**	**MgO**	**TiO_2**	**K_2O**	**P_2O_5**	**MnO**	**Na_2O**	**LOI**	**Free CaO**
Amount [%]	45.25	19.50	2.00	19.67	4.60	1.34	1.54	0.15	0.12	0.04	0.01	3.70	2.80

When fabricating geopolymers from fly ash, of major importance are the properties of used raw materials, such as: morphology of fly ash particles, content of CaO, the number of crystalline phases, phase defects, contents of unburned carbon particles (mostly sulfur and iron compounds) as well as their forms of occurrence. Too high content of the latter compound is undesired in the case of geopolymer production. High content of unburned carbon leads to an increased demand of water, while iron compounds (hematite and magnetite) adversely affect fly ash solubility, as they tend to accumulate on the grain surfaces and inhibit liquid phase access to the glassy phase. The main role of the raw material is that the appropriate amount of silicon oxide and aluminum has to be admitted into the activating solution, moreover, it is their r mutual ratio not only the amount that are of importance [9, 10].

The raw fly ash composition underwent certain modifications. The aim of the first modification was the removal of ferromagnetic compounds, using the separator shown *in Fig. 1*. Raw ash was inserted between the separator covers from the top and ferromagnetic particles were retained on one of the covers.

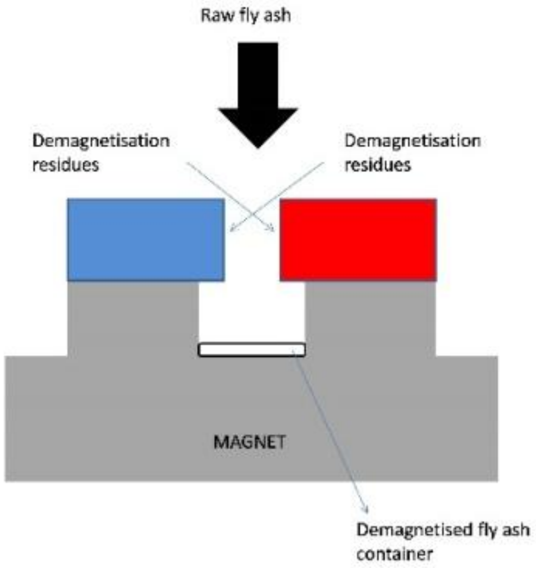

Fig. 1. Separator for ferromagnetic elements removal

The second modification was performed to remove unburned carbon from fly ash. Raw fly ash samples as well as those obtained after magnetic separation were kept in a furnace at the temperature of 800 ^{o}C for 6 hours.

Geopolymers sample was synthesized using sodium hydroxide of concentration 8 mol/dm^3 and sodium silicate (water glass) of concentration 40%.

2.2. Experimental methodology

6 geopolymer samples were fabricated in the laboratory conditions in two stages. In the first stage, 3 samples of geopolymers were obtained. The synthesis the raw fly ash used sodium hydroxide and water glass according to their volume ratios summarised in Table 2.

Table 2. Ratios of components used

Sample	Sodium silicate, V/V	Fly ash, V/V	8 mol/dm^3, NaOH V/V
GEOa	1	4	1.6
GEOb	1.6	4	1
GEOc	1.3	4	1.3

In the second stage, the synthesis reaction was conducted from components in the same proportions as used for sample GEOb, yet with addition of modified fly ash:

- Demagnetized, without removing unburned carbon, designated as GEOb1;
- Demagnetized, with removed unburned carbon, designated as GEOb2;
- Not demagnetized, with removed unburned carbon, designated as GEOb3;

Geopolymer samples were prepared by mixing the ingredients in the appropriate proportions. The ingredients were stirred until a homogenous, dense and plastic mass was obtained which was then transferred to a normalized metal mold to determine the strength of cement beams 160 × 40 × 40 mm (PN-EN 196-1). Samples remained there for approximately 20 min and then were transferred to a dryer. Beams were seasoned at 60 ^{o}C for 12 hours under the atmospheric pressure. After 30 days, the samples were subjected to compressive strength tests.

Compressive strength tests were performed at The Strata Mechanics Research Institute of the Polish Academy of Science using the Instron 8500 device. Changes in sample dimensions were recorded using extensometers. Fig. 2 shows a geopolymer beam with extensometers installed.

Fig. 2. Geopolymer sample with extensometers installed

Extensometers are configured as a flexible beam, covered with tensometers for the measurement of tension. Identical converters are installed opposite to each other with respect to the sample axis, which allows for elimination of bending moments. An extensometer incorporates a flexible beam equipped with tensometers on both sides, installed with the use of an overlay and three pads to the main body. Tensometers with the base 5 mm and resistance 350 Ω are connected to a half-bridge system. Half-bridges of two extensometers operated at same time may be integrated in the bridge system, which allows for obtaining averaged signals from both converters. Measurement data are transmitted to the computer for registration and analysis [11].

The morphology of geopolymers was determined by the SEM (Scanning Electron Microscope) FEI Quanta 250 FEG.

3. RESULTS AND DISCUSSION

The strength test results for the first series of geopolymers samples are summarised in Fig. 3. A relatively slow force increase in elastic range is observed in all samples. In addition, for all samples, the critical zone in which cracks tend to occur resulting in a slow force decrease, is observed at the same time moment of the test (after approximately 50 minutes).

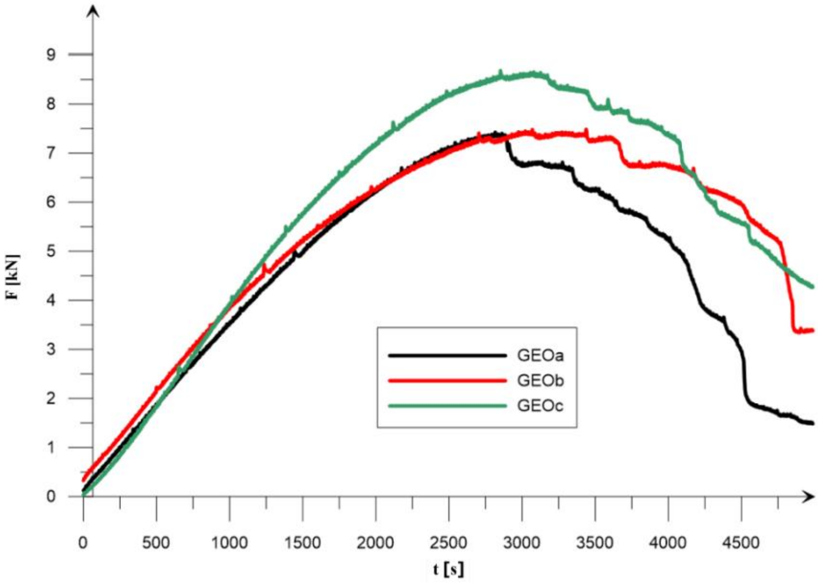

Fig. 3. Compressive strength tests for the first series of examined samples

Slightly different results were obtained for samples in which fly ash was modified prior to the synthesis (Fig. 4).

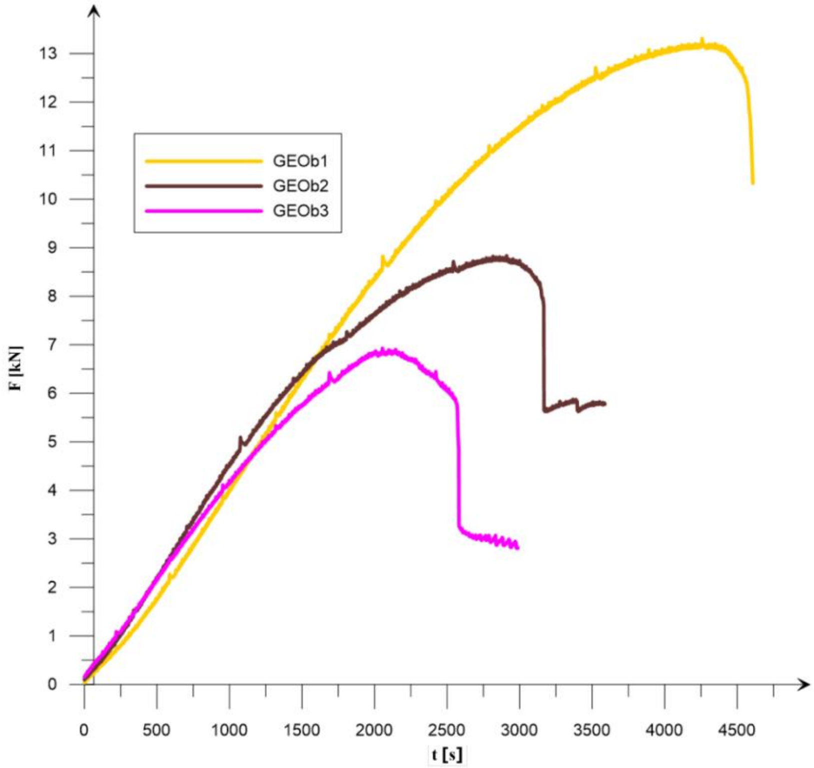

Fig. 4. Compressive strength tests for the second series of examined samples

In the first stage, there is a slightly faster force increase in the elastic range (greater slope), however the critical area is observed at a different time moment. In addition, the maximums of curves are distinct from those registered in the first series.

Axial stress and axial strain until failure were determined by experiments with the use of a press. Results are compiled in Fig. 5.

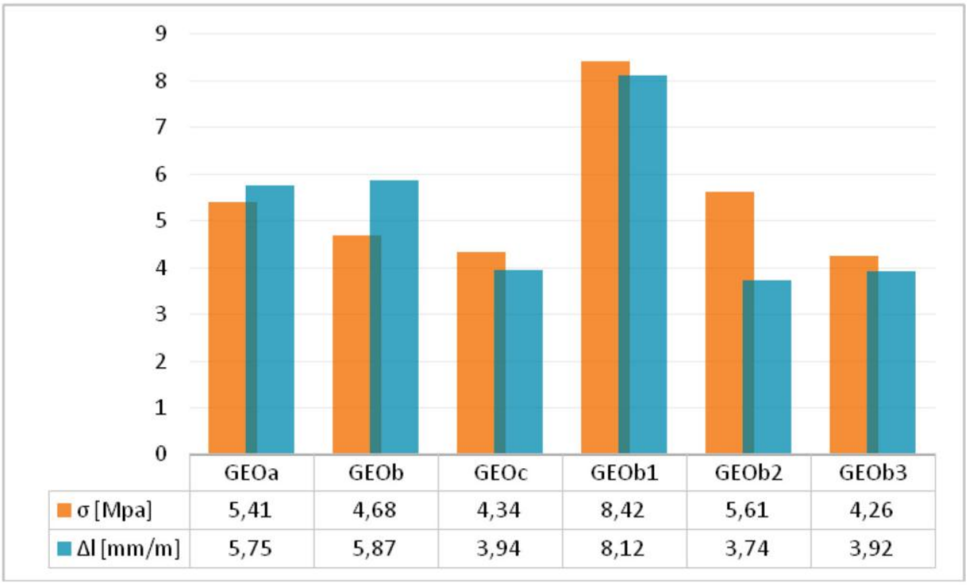

	GEOa	GEOb	GEOc	GEOb1	GEOb2	GEOb3
🟧 σ [Mpa]	5,41	4,68	4,34	8,42	5,61	4,26
🟦 Δl [mm/m]	5,75	5,87	3,94	8,12	3,74	3,92

Fig. 5. Axial stress and axial strain until the point of destruction analysis results

As regards the samples obtained in the first stage, their strength parameters were found to be similar for all tested samples. The sample with the highest compressive strength at this stage was GEOa synthesized with the use of significant amounts of NaOH whilst the polymer made of equal volume of water glass and NaOH solution (sample GEOc) had the lowest compressive strength. This result, however, may be considered not wholly reliable because the sample was broken and damaged during the test (the sample, due to incorrect placement in the press during the measurement, was destroyed, making it impossible to determine the maximum compressive strength). The section of the stress and strain plot suggests that the geopolymer could have a higher compressive strength than GEOb but lower than GEOa. The actual compressive strength values are not high when compared to commercially available concrete. They still agree well with results presented in another study [12], investigating the properties of geopolymers made from calcium fly ashes.

Differences in mechanical properties are attributable to variations in the number of components used for synthesis. Analyzing the volume ratios used in the synthesis of samples, it is reasonable to conclude that a higher amount of NaOH in relation to water glass gives more resistant geopolymers. The NaOH concentration in the aqueous phase of the geopolymeric system acts on the dissolution process, as well as on the bonding of solid particles in the final structure [3]. This is probably because the concentrated base solution is responsible for dissolution of the aluminosilicate source. Insufficient amount of NaOH decreases the dissolution rate of fly ash, as a result, there are less aluminum and silicon ions which are needed to form a stable network. The water glass solution is a source of sodium ions necessary to stabilize the geopolymer network and of silicon ions that form polymer chains with aluminum. It is therefore an essential ingredient for the creation of good geopolymers, but in the case of investigated samples, increasing the amount of water glass did not improve the mechanical properties of the material obtained. It is therefore necessary to use a large amount of NaOH to enhance the dissolution of fly ash. The use of a higher concentration base often results in an increase in strength parameters. In the work of Somna et al. [13] increase in NaOH concentration from 4.5 to 14.0 mol/dm^3 increased the strength of geopolymer samples. Microstructure studies indicated that NaOH concentrations of 12.0–14.0 M created new crystalline products of sodium aluminosilicate. In contrast, a large increase in NaOH concentration did not cause such a significant increase in compressive strength. Therefore, from an economic and environmental point of view, the use of NaOH with very high concentration is debatable. Results obtained in the second stage of the experiment were recalled to establish how fly ash modifications affect the strength parameters of fabricated inorganic polymers. The highest without the removal of unburned coal (about 8.5 MPa).

The lowest compressive strength is registered for the GEOb3 sample, made from ash non-demagnetized, fly ash with unburned coal removed (about 4.26 MPa). It is worthwhile to mention that removal of ferromagnetic elements from fly ash nearly doubles the geopolymer's compressive strength and increases its deformability. On the other hand, the removal of unburned coal from fly ash does not significantly change the strength parameters, regardless of the actual contents of ferromagnetic elements; moreover, it reduces the sample’s deformation capacity.

SEM data in Fig. 6 reveal that microstructure of the samples is very compact; however, the sample structure in all microphotographs is not uniform. Undissolved solid particles of fly ash are visible, among the amorphous geopolymeric frame of aluminosilicate compounds. Insoluble fly ash particle/amorphous geopolymeric frame boundaries in SEM microphotographs give space for micro cracks, which may be responsible for lower mechanical strength tests results. This may be partly confirmed by the fact that in the sample GEOb1 (Fig. 6, d) which has the highest strength, the number of micro cracks observed visually is the smallest among other samples.

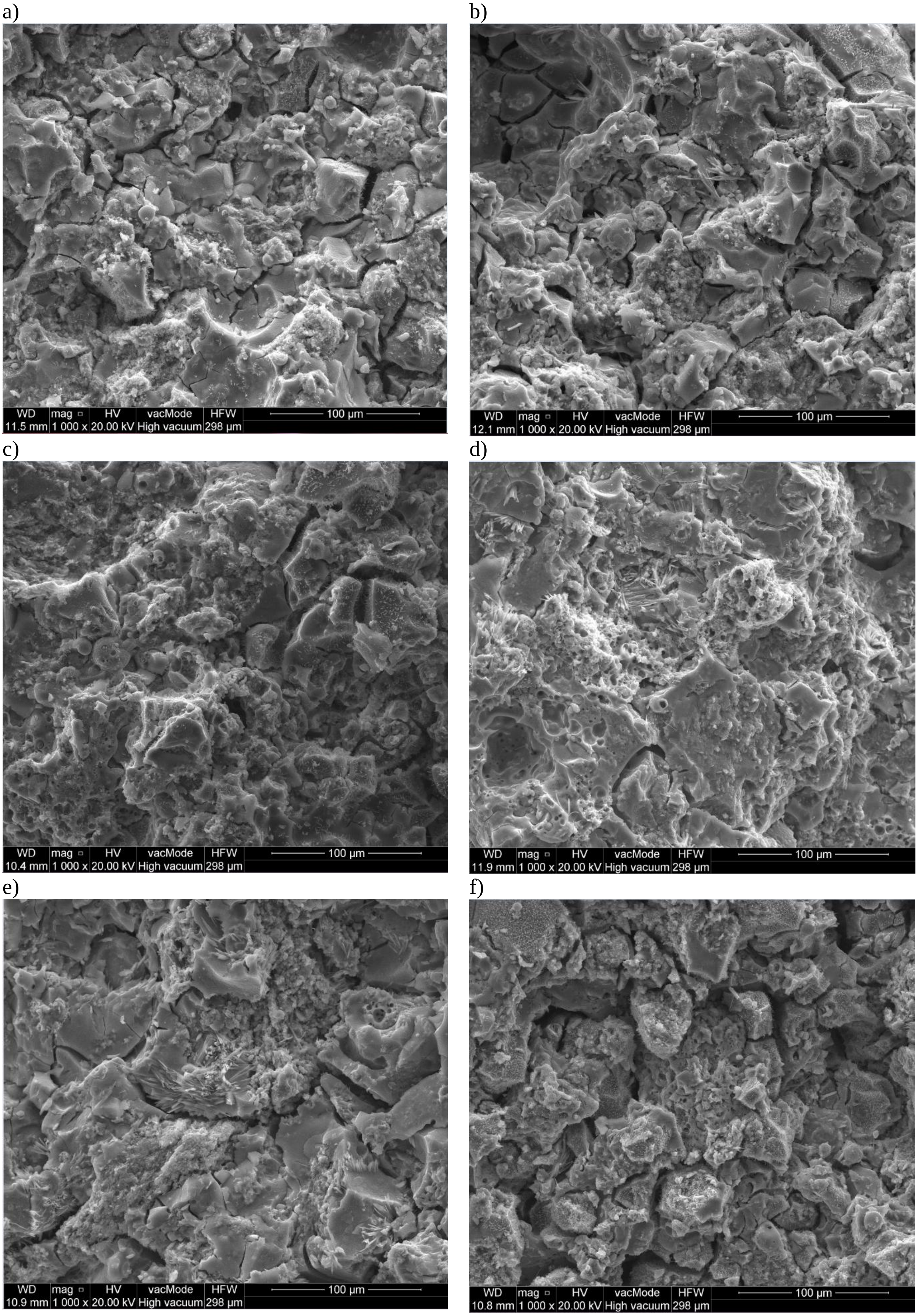

Fig. 6. SEM analysis of samples: a) GEOa; b) GEOb; c) GEOc; d) GEOb1; e) GEOb1; f) GEOb1; magnification 1000×

4. CONCLUSIONS

Geopolymers investigated in this study had a low strength compared to geopolymers made from silicate fly ashes. The high CaO content increases the binding rate, which may inhibit dissolution of compounds in the geopolymer mass. Experiments conducted using the varied volume NaOH solution to water glass ratio allowed for investigating the impact of synthesis parameters on compressive strength of geopolymers. The results lead us to the following conclusions:

1. Volume ratios used in the synthesis do not differentiate the samples in terms of mechanical properties. The obtained compressive strength values are similar and the strength test patterns in the elastic range are the same.

2. Increasing the ratio of NaOH solution to water glass improves the properties of the fabricated geopolymers. This is so because there is a sufficient amount of concentrated base for dissolution of fly ash and release of ions into the mixture. Reducing the solution ratio prevents sufficient fly ash dissolution and the resulting products will have a lower strength.

As regards samples synthesized from fly ash subjected to not complicated modifications, removal of compounds of ferromagnetic character from fly ash is found to be necessary. This uncomplicated process resulted in a nearly double increase in bending strength and improved strain susceptibility. Removal of ferromagnetic particles may serve positively in case of enhancing dissolution of material. The presence of non-reacted elements on the fly ash surface may lead to presence of areas vulnerable to break. As this is a preliminary study, authors regard it as valuable to perform test on usage of differentiated synthesis procedures in order to increase the strength of the samples, based on demagnetized fly ash.

ACKNOWLEDGMENTS

This work was financed by AGH University Grant No. 11.11.210.374

REFERENCES

[1] Heidrich, C., Feuerborn, H., Weir, A. (2013): Coal Combustion Products: a Global Perspective, in World of Coal Ash, 22-25.04.2013 p. 17.

[2] What is a geopolymer? Introduction https://www.geopolymer.org accesed 07.07.2017.

[3] Panias, D., Giannopoulou, I. P., Perraki, T. (2007): Effect of synthesis parameters on the mechanical properties of fly ash-based geopolymers - *Colloids and Surfaces A: Physicochem. Eng. Aspects* 301: 246–254.

[4] Mozgawa, W., Deja, J. (2009) Spectroscopic studies of alkaline activated slag geopolymers - *Journal of Molecular Structure* **924–926:** 434–441.

[5] Turner, L. K., Collins, F. G. (2013): Carbon Dioxide Equivalent (CO2-e) Emissions: A Comparison Between Geopolymer and OPC Cement Concrete - *Construction and Building Materials* **43:** 125–130.

[6] Fernandez-Jimenez, A., Palomo, A. (2005): Composition and microstructure of alkali activated fly ash binder: Effect of the activator - *Cem. Concr. Res.* **35:** 1984–1992.

[7] Bakharev, T. (2005): Geopolymeric materials prepared using Class F fly ash and elevated temperature curing - *Cem. Concr. Res.* **35:** 1224–1232.

[8] Komnitsas, K., Zaharaki, D. (2007): A review and prospects for the minerals industry - *Minerals Engineering* **20:** 1261–1277.

[9] Mikuła, J. (2014): Rozwiązania proekologiczne w zakresie produkcji : praca zbiorowa. T. 1, Nowoczesne materiały kompozytowe przyjazne środowisku; Wydawnictwo Politechniki Krakowskiej, (in Polish).

[10] Derdacka-Grzymek, A., Stok, A. (1980): *Aktywacja syntetycznych żużli alkaliami* - *Cem. Wapno Bet.* **8–9:** 217-220 (in Polish).

[11] Kanciruk, A. (2009): Urządzenia do pomiarów wielkości mechanicznych i temperatury przy użyciu przetworników rezystancyjnych i przykłady ich zastosowania; Instytut Mechaniki Górotworu PAN (in Polish).

[12] Rajczyk, K., Giergiczny, E., Szota, M. (2015): Mikrostruktura i właściwości stwardniałych spoiw geopolimerowych z popiołu lotnego - *Pr. Inst. Ceram. i Mater. Bud.* **8**: 79–89 (in Polish).

[13] Kiatsuda Somna, Chai Jaturapitakkul, Puangrat Kajitvichyanukul, Prinya Chindaprasirt, NaOH-activated ground fly ash geopolymer cured at ambient temperature, Fuel, Volume 90, Issue 6, 2011, Pages 2118–2124, https://doi.org/10.1016/j.fuel.2011.01.018.

CYSENI 2018, May 23-25, Kaunas, Lithuania
ISSN 1822-7554, www.cyseni.com

INVESTIGATION OF THE BEHAVIOUR OF FIBROUS MATERIALS' ADHESIVE BONDS

G. Mikalauskaitė, G. Vadeikė, V. Daukantienė
Kaunas University of Technology
Studentų str. 56, LT-51424 Kaunas – Lithuania
Email: gerda.mikalauskaite@ktu.edu

ABSTRACT

Adhesive bonding is applied mostly in the sportswear and leisure clothing industry. It is suitable for the assembling of synthetic materials which are made from polyester, polyamide and other usual fibres or microfibers. Bond properties are influenced by textile structure, raw material content, finishing, bonding technological parameters as well as by many other factors. The researches published previously are more focused on the bond strength testing but they do not analyse the comfort properties of textiles after their assembling into a garment applying bonding technology. Thus, the aim of this research was to investigate the peeling strength of bonds and the bond influence on the air permeability of polyester knitted fabric containing different amount of elastane fibre. Overlapped bonds were laminated using thermoplastic polyurethane adhesive film of 0.175 mm thickness at 5.6 kPa pressure applying 140 °C temperature for 40 s. Peeling strength in N/mm of bonds was examined at ambient temperature and humidity using the computerized tension machine H10 KT (Tinius Olsen) at 50 mm peeling velocity. Fabric air permeability was estimated according to the standard LST EN ISO 9237 at 100 Pa air pressure difference. The research results revealed that peeling strength was dependent on the amount of elastane in the knitted fabric, and it varied from (1.638 ± 0.077) N/mm up to (5.461 ± 0.477) N/mm. Test results have shown that the air permeability of textiles is dependent on their structure and raw polymeric material content and it varied from (235.6 ± 8.4) mm/s up to (444.2 ± 25.1) mm/s. Adhesive bonds influenced considerable decrease in the fabrics' air permeability. The changes in the air permeability parameter varied from 19.9 % up to 60.0%. Consequently, it should be noted that the changes in the air permeability may impair the clothing comfort properties.

Keywords: polyester, elastane, knitted fabric, bond, strength, extensibility, air permeability

1. INTRODUCTION

Bonding is considered as a joining of two textile layers with the application of thermoplastic polyurethane adhesive film which is reactivated by applying high temperature and pressure for certain duration. Nowadays, adhesive bonding technology is not widely applied in clothing manufacture, but it is considered as a good alternative for replacing the sewing. P. Jana analyzed the distinguished characteristics and developments in assembling technologies such as sewing, welding and bonding and noticed that there is a distinct shift towards the use of bonding in functional clothing because of reduced bulk and weight, cleaner appearance, etc. [1]. The main requirement for sport, functional and leisure clothing assortment seams are low stiffness, air permeability and strength. N. Seram and T. Nandasiri made the comparison between the bonding and sewing of textile used for sport wear and determined that the strength of sewn seams was lower than the one of bonded seams [2]. Bond properties are influenced by many factors. Ž. Jakubčionienė and V. Masteikaitė analyzed the influence of bonding parameters on the bond strength and determined that the strength of bonds is dependent on both bonding temperature and textile structure [3]. Here also was proven that bond strength increases when the bonding temperature increases as well. But the increased bonding duration decreases bond strength [3]. G. Mikalauskaitė and V. Daukantienė investigated the peculiarities of textile bond exploitation and determined that their strength is dependent on the adhesive film thickness, textile structure and bond delamination velocity [4]. Ž. Jakubčionienė *et al.* investigated the strength of bonded seams applying both different seam construction and type of their fixing in a tension machine. They determined that bond strength depends on the bond area created between two textile layers with the application of adhesive film [5]. The previous researches [6] also proved that bond strength is dependent on both film surface density and thickness as well as on the influence of external moisture which may decrease bond strength.

Bonded clothing quality is dependent not only on their strength characteristics but also on their comfort properties like an elasticity which ensures the ease of wearers' movements. Knitted fabrics containing elastane fiber demonstrate higher elasticity than traditional ones. Also, it should be mentioned that the hygienic properties are very important during clothing quality evaluation. They are mainly dependent on the textile capability to dissipate the sweat moisture through the garment layers to the atmosphere. S. H. Eryuruk and F. Kalaoglu determined a significant relationship between elastane amount and air permeability. [7]. There were also determined by the previous researches [8–11] that the air permeability highly depends on fabric porosity. Such factors, as course count and yarn number [8], knit type [12], thickness [9], raw material content [10] and others also influence the textile air permeability.

The literature review revealed that the air permeability of textiles has been investigated quite deeply, while little attention has been addressed to the impact of seams.Thus, the aim of this research was to investigate the bond peeling strength and the influence of bonded seams on the air permeability of polyester knitted fabric containing different amount of elastane fiber.

2. METHODOLOGY

2.1. Investigated materials

Commercially available polyester knitted fabrics suitable for leisure and sportswear manufacture due to their specific properties were selected for the current research. The characteristics of textiles were determined experimentally according to the standard methods and are presented in Table 1. Knit type of the five knitted fabrics (K2, K3, K7, K6 and K8) was plain jersey, and the one of K1 fabric – interlock. The investigated knitted fabrics contained different amount of elastane (EL) fibre which varied from 4 % (K1) up to 20 % (K7).

The specimens prepared for the textile structure analysis, uniaxial tension, peeling strength and air permeability tests were conditioned according to the standard LST EN ISO 139 [13].

Table 1. Characteristics of investigated knitted fabrics

Characteristics / Code		**K1**	**K2**	**K3**	**K6**	**K7**	**K8**
Fibre content		96 % PES, 4 % EL	84 % PES, 16 % EL	90 % PES, 10 % EL	81 % PES, 19 % EL	80 % PES, 20 % EL	82 % PES, 18 % EL
Knit type		Interlock	plain jersey	plain jersey	plain jersey	plain jersey	plain jersey
Density[1]	Course count, cm^{-1}	18.0±0.5	21.0±0.5	14.0±0.5	19.0±0.5	20.0±0.5	20.0±0.5
	Wale count, cm^{-1}	22.0±0.5	33.0±0.5	28.0±0.5	20.0±0.5	23.0±0.5	26.0±0.5
Surface density[2], g/m^2		251.6±2.0	218.8±2.0	235.5±1.8	207.1±4.9	262.3±2.5	195.0±5.0
Thickness[3], mm		0.90±0.02	0.69±0.02	0.59±0.01	0.93±0.01	0.70±0.02	0.60±0.01
Tension strength[4], N	Wale	819.5±61.6	232.1±46.1	469.2±36.4	368.7±31.4	375.3±12.8	391.5±36.1
	Course	403.9±20.0	352.0±35.6	425.8±22.5	301.3±22.4	374.4±33.9	397.5±11.8
Extensibility[4], %	Wale	136.1±7.8	324.1±12.9	285.4±9.6	286.6±8.5	318.2±8.9	341.7±14.0
	Course	266.2±7.7	309.0±13.5	261.4±8.7	276.5±21.3	339.8±22.9	320.2±7.2

Notes: PES – polyester; EL – elastane; [1]determined according to the standard EN ISO 14971 [14]; [2]determined according to the standard LST EN 12127 [15]; [3]determined according to the standard EN ISO 5084 [16]; [4]determined according to the standard LST ISO 13934-1 [13].

Textile bonds were laminated with the thermoplastic polyurethane (PU) film of 8 mm width and 0.175 mm thickness delivered from the manufacturer FAIT PLAST S.P.A. being attached to silicon paper.

2.2. Bond peeling strength and elasticity tests

The pairs of 20 × 80 mm^2 lengthwise knitted fabric specimens were bonded with PU film strips of 50 mm length applying the pressing device DEA 25R (GTK) at 5.6 kPa pressure. The adhesive film was reactivated by heat in two technological steps. In the first step the film through the silicon paper was transferred onto the right side of lower fabric strip at 110 °C for 5 s. In 5 min the silicon paper was peeled off. In the second step the left side of upper fabric strip was laid on thermoplastic film and bonded at 140 °C temperature for 40 s.

Bond peeling strength testing was carried out at ambient temperature [13] using computerized CRE type tension machine H10 KT (Tinius Olsen) at 50 mm/min velocity. Extensibility testing (Fig. 1, a) was carried out at the same ambient temperature using the tension machine H10 KT at 100 mm/min velocity. Five or six specimens in a group for both peeling strength test and extensibility test were tested for each sample set (every fabric sample group) ensuring the variation coefficient not higher than 10 %.

2.3. Air permeability testing

Air permeability of the knitted fabrics and their bonds (Fig. 1, b) was evaluated according to the standard LST EN ISO 9237 [18] using the air permeability tester L 14 DC. According to the standard the permeability is considered as the ability of textiles to pass the air through their structure in 20 cm^2 area of tested specimen at 100 Pa difference-pressure.

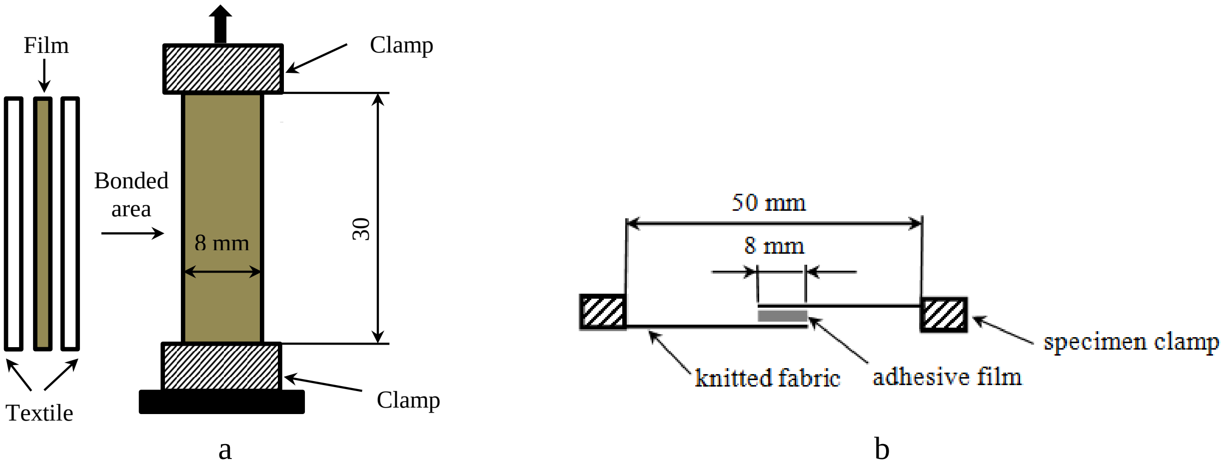

Fig. 1. The schemes of the bond testing for air permeability (a) and for extensibility

3. RESULTS AND DISCUSSION

The results summary representing the influence of elastane amount on the peeling strength *F* is presented in Fig. 2. Here it could be seen that the peeling strength of fabric bond decreases in 70% after decrease in the amount of elastane fibre from 5.461 N up to 1.638 N. The highest value of the peeling strength (5.461 N) was determined for K1 fabric with the lowest amount of elastane (4%). The weakest bond (1.638 N) was for K7 fabric with the highest (20%) elastane per cent in its structure. The most significant decrease in peeling strength (in 54.4%) during comparing two fabrics between themselves was when the elastane amount changed from 4% up to 10%. The differences in the peeling strength in the group of knitted fabrics: K2 (16%), K8 (18%), and K7 (20%) were not significant as they varied within limits of the measurement errors.

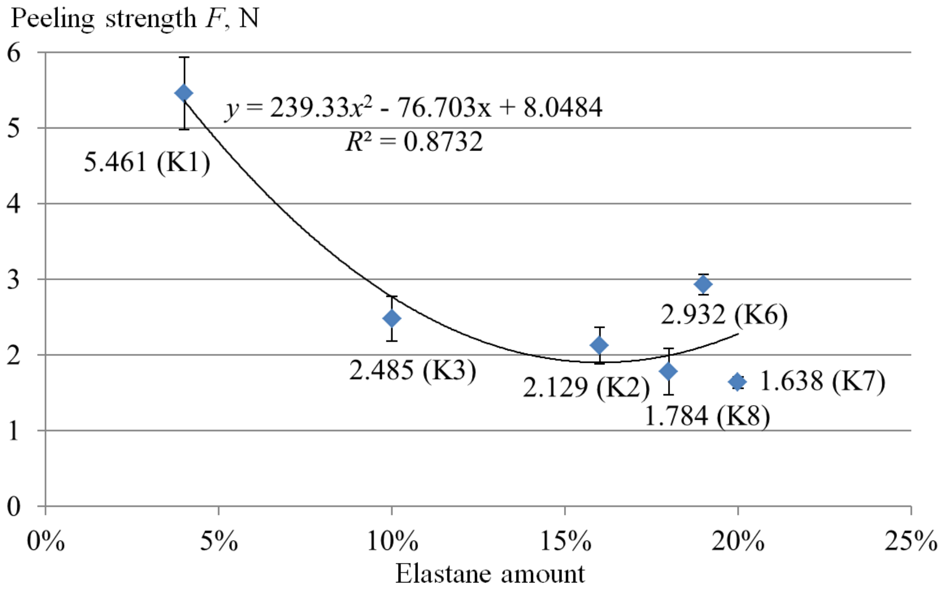

Fig. 2. The dependency between the peeling strength and elastane amount

The dependencies between the extensibility and amount of elastane in both wale wise and course wise specimens are presented in Fig. 3.

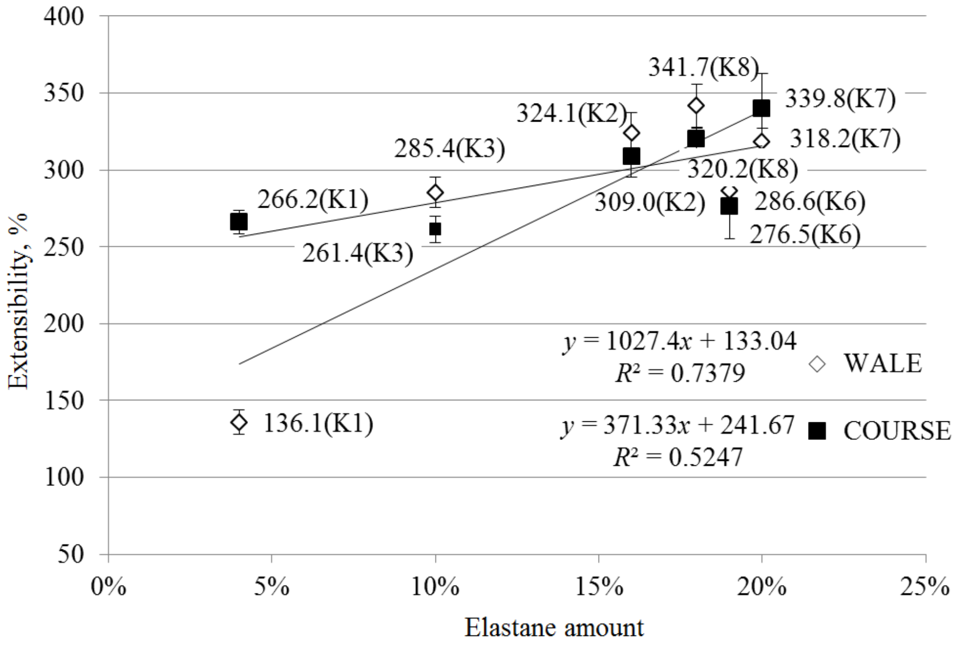

Fig. 3. The dependency between the fabric extensibility and elastane amount

More significant dependency between the extensibility and elastane amount was found for the wale wise specimens compared with the course wise specimens. The highest extensibility difference (48.9%) between wale and course fabric directions was determined for K1 fabric. The reason for this may be interlock knit type as it was different than one of other investigated fabrics. For that case it was plain jersey. Interlock pattern is knitted in weft-knitted structure similarly to plain jersey. But it uses the two-bed knitting machine which determines the double knitted structure of K1 fabric. Thus, it may be seen that extensibility of investigated fabrics is dependent on knit type. This statement was also concluded by the previous researches. It is known, that the extensibility of rib pattern in course direction is approximately from 3 up to 4 times higher than in wale direction. And in purl knit pattern the extensibility in both wale and course directions is roughly the same

[19]. Also, considering from the view point of this research focus, it may be stated that the increase in elastane amount influences the increment tendency of fabric extensibility .

Three of the investigated fabrics were tested for bond extensibility aiming to compare their results (Fig. 4) between both specimens without seams and specimens with bonds. It can be seen from Fig. 4 that the bond extensibility increased for both K1 fabric (17.2%) and K3 fabric (23.0%). The extensibility of K2 fabric with highest elastane amount (16%) in their structure was almost unchanged.

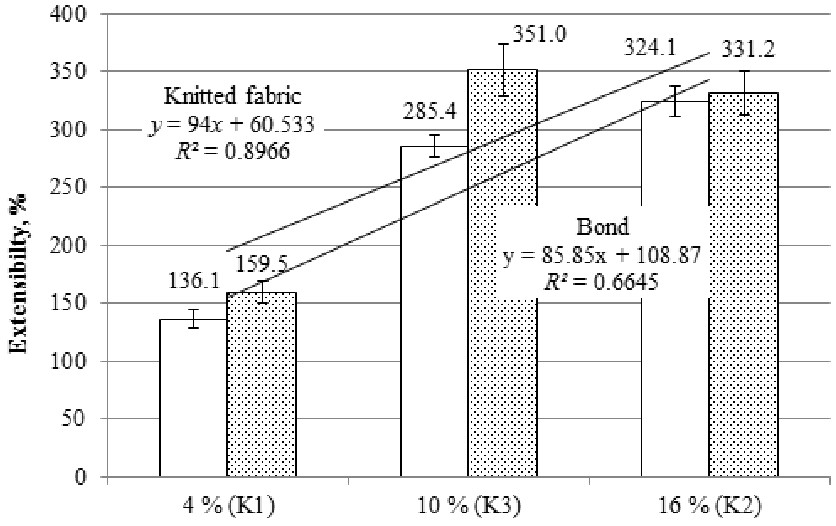

Fig. 4. The extensibility of knitted fabrics without seams (white columns) and with bonds (dotted columns)

The summary of air permeability results presented in Fig. 5 shows that the air permeability is independent on the amount of elastane fiber for both knitted fabrics and their bonds.

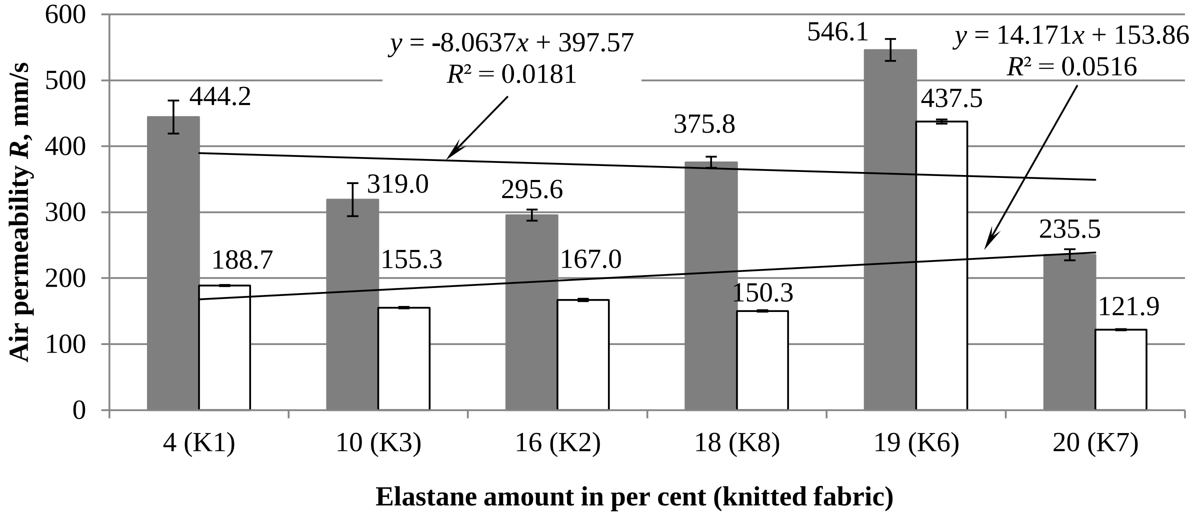

Fig. 5. The dependency between the air permeability and elastane amount in knitted fabrics for both specimens without seams (grey columns) and ones with bonds (white columns)

It can be seen that the air permeability of knitted fabrics without seams is lower than the one of the specimens with bonded seams. The air permeability of bonded seams decreased from 19.9% (K6) up to 60.0% (K8) compared with the one of knitted fabrics. Consequently, based on the determined results, it may be stated that the changes in textile air permeability may impair clothing comfort properties.

4. CONCLUSION

- The investigation of the influence of elastane amount in knitted fabrics on bond peeling strength has shown that peeling strength depends on elastane amount. Bond strength was highest for K1fabric with lowest elastane per cent (4%), and lowest one – for K7 fabric with highest elastane amount (20%).
- The analysis of the dependency between the extensibility and elastane amount in knitted fabrics has shown that their extensibility is dependent on the elastane yarn amount.
- The extensibility of bonded seams is higher than one of textile without the seams.
- The air permeability of the knitted fabric samples with bonds is lower than the one of specimens without the bonds. It decreases from 19.9% up to 60.0% dependently on knitted fabric structure.

REFERENCES

1. JANA, P. Assembling technologies for functional garments: An overview. *Indian Journal of Fibre and Textile Research*, 2011, Vol. 36, No. 4. p. 380–387.
2. SERAM, N. and NANDASIRI, T. A Comparison between bonding and sewing: Application in sports performance wear. *Journal of Academia and Industrial Research* (JAIR), 2015, Vol. 3, No. 8. p. 343–345.
3. JAKUBČIONIENĖ, Ž., MASTEIKAITĖ, V. Investigation of textile bonded seams. *Materials Science* (*Medžiagotyra*), 2010, Vol. 16, No. 1. p. 76–79.
4. MIKALAUSKAITE, G., DAUKANTIENE, V. Influence of the delamination loading velocity on textile bonds and sewn seams strength, *International journal of clothing science and technology*, 2017, Vol. 29, No. 6, p.768–775.
5. JAKUBČIONIENĖ, Ž., MASTEIKAITĖ, V., KLEVECKAS, T., JAKUNČIONIS, m., Kelesova, U. Investigation of the strength of textile bonded seams. *Materials science* (*Medžiagotyra*), 2012, Vol. 18, No. 2. p. 172–176.
6. PODERSKIS, S., GULBINIENĖ, A. Technologinių parametrų įtaka tekstilinių laminatų klijuotinių siūlių išsluoksniavimo stipriui. Konferencijos pranešimų medžiaga. Gaminių technologijos ir dizainas. Kaunas: KTU. 2011.
7. ERYURUK, S. H., KALAOGLU, F. Analysis of the performance properties of knitted fabrics containing elastane, *International journal of clothing science and technology*, 2016, Vol. 28, No. 4, p. 463–479.
8. BHATTACHARYA, S.S., AJMERI, J.R., Factors affecting air permeability of viscose & excel single jersey fabric, *International journal of engineering research and development*, 2013, Vol. 5, No. 7, p. 48–54.
9. TOU N, A. An Investigation of arcing in two structure weft knit fabrics, MSc Thesis, North Carolina State University, Textile & Apparel Technology & Management, 2005, 127 p.
10. JORDEVA, S., ĆORTOŠEVA, S., MOJSOV, K., ŽEŽOVA, S., RISTESKI, S., KUZMANOSKA, V. D. The influence of the structural characteristics of cotton and polyester knitted fabrics on the thermos-physiological comfort, *Advanced technologies*, 2017, Vol. 6, No. 1, p. 88–92.
11. HAVLOVÁ, M., ŠPÁNKOVÁ, J. Porosity of knitted fabrics in the aspect of air permeability – Discussion of selected assumptions, *Fibres & textiles in Eastern Europe* 2017, Vol. 25, No. 3, p. 86–91.
12. DEHKORDI, S. S. H., GHANE, M., ABDELLAHI, S. B., SOULTANZADEH, M. B. Numerical modelling of the air permeability of knitted fabric using computational fluid dynamics (CFD) method, *Fibers and polymers*, 2017, Vol. 18, No. 9, p. 1804–1809.

13. LST EN ISO 139 Textiles. Standard atmospheres for conditioning and testing, 2006.
14. LST EN 14971 Textiles. Knitted fabrics. Determination of number of stitches per unit length and unit area, 2006.
15. LST EN 12127 Textiles. Fabrics. Determination of mass per unit area using small samples, 1999.
16. LST EN ISO 5084 Textiles. Determination of thickness of textiles and textile products, 2000.
17. LST ISO 13934-1 Textiles. Tensile properties of fabrics. Part 1: Determination of maximum force and elongation at maximum force using strip method, 2013.
18. LST EN ISO 9237. Textiles. Determination of permeability of fabrics to air.
19. TREIGIENĖ, R., MIKUČIONIENĖ, D. Mezginių mechanika ir projektavimas. Kaunas: Technologija, 2012. 88 p. ISBN 978-609-02-0720-8.

CYSENI 2018, May 23-25, Kaunas, Lithuania
ISSN 1822-7554, www.cyseni.com

INFLUENCE OF HYBRID LOADING ON THERMAL BEHAVIOR AND THERMOPHYSICAL PROPERTIES OF POLYAMIDE

K. V. Nikolaeva
A. V. Luikov Heat- and Mass Transfer Institute
P. Brovka Str., 15, 220072 – Belarus
Email: nikolajewa@hmti.ac.by

ABSTRACT

The peculiarities of hybrid loading influence on thermal behavior and thermophysical properties of composites based on polyamide are presented in the paper. As a fillers the carbon nanomaterial, carbon fibers, SiO_2, Al, SiC have been chosen. Thermal conductivity increases exponentially with loading independently on the type of filler. Most significant rise (almost 9 times) of thermal conductivity was registered at 60 wt.% of hybrid loading that is explained by percolation chains formation in the composite. No clear synergistic effect of fillers was observed in polyamide composites.

Keywords: thermophysical properties, thermal behavior, composite, polyamide, hybrid loading.

1. INTRODUCTION

Loading of the polymer with hybrid fillers leads to an improvement in thermophysical, electrophysical and mechanical properties. Since there are many problems in which heat transfer from thermally loaded elements is most important, then this work emphasises on thermophysical properties and thermal behavior of polymer composites.

Polyamides are plastics based on linear synthetic high-molecular compounds containing amide groups in the main chain. Polyamide has a high melting point of 220 ^{o}C, high strength, and, therefore, it is widely used in aircraft and machine building, in the space industry and in other areas.

To improve the properties, fibrous fillers and carbon materials are introduced into the polyamide. The introduction of carbon nanomaterials (CNM) reduces the dielectric characteristics of the polymer, and at the certain concentration of CNM the material becomes electrically conductive [1–3]. The authors of [4, 5] showed that carbon nanotubes increase the degree of crystallinity of polyamide due to the creation of additional centers of crystallization on the surface of carbon nanotubes. It was shown in [6, 7] that thermal conductivity of a polymer can be increased by introduction of high-conductive fillers. For this purpose next fillers can be used: carbon nanotubes (thermal conductivity coefficient from 3000 W/m·K [8]), carbon fibers (110–375 W/m·K [9]), aluminum (230 W/m·K [10]). At the same time, nanoscale silicon dioxide SiO_2 is of interest as a filler for polymers due to its active and developed surface despite the very low value of thermal conductivity. Silicon dioxide makes the polymer more viscous, leads to increasing the density, and hence the strength and thermal conductivity of the material. Silicon dioxide increases resistance to delamination and sticking and impairs the fluidity of polymer compositions [11].

The introduction of hybrid fillers can lead to the realization of a synergistic effect of improving the properties of thermoplastics [12, 13]. Therefore, the aim of this work is to study the influence of different types of nanofillers and their combination on the thermal properties of polyamide and to identify a synergistic effect for this type of polymer.

2. MATERIALS

The influence of the type and concentration of the filler on the melting and crystallization temperature, as well as the thermal conductivity, heat capacity, and thermal diffusivity of the composites were investigated in the work. As a polymeric matrix for composite samples the polyamide 6 (PA) was used. As a fillers the next materials were chosen: silicon carbide (SiC) and carbon nanomaterial (CNM) (obtained in the laboratory of disperse systems of A. V. Luikov Heat&Mass Transfer Institute of NAS of Belarus) as well as Tarcosil T80 (SiO_2) nanopowder and aluminum nanopowder (Al) (Khristianovich Institute of Theoretical and Applied Mechanics SB RAS).

The composition and density of the test samples are presented in Table 1.

Table 1. Composition of experimental samples based on PA

Sample №	Type of sample	Density, kg/m^3
1	PA	1100
2	PA + 5% CNM	1119
3	PA + 3% CNM + 2% SiO_2	1120
4	PA + 2% CNM + 8% CF	1159
5	PA + 10% CF	1126
6	PA + 10% Al	1202
7	PA + 20% CNM	1196
8	PA + 20% CNM + 10% Al	1221
9	PA + 50% CNM	1300
10	PA + 4% CNM + 56% SiC	1860
11	PA + 20% CNM + 10% SiO_2	1336

Samples of composite materials were prepared by solution method in the Grodno branch of A. V. Luikov Heat&Mass Transfer Institute of NAS of Belarus. For thermophysical properties measurements the samples were made in the form of cylinders with a diameter of 12.8 mm and a height of ~ 1.5 mm.

3. METHODOLOGY

Thermogravimetry and differential scanning calorimetry measurements were performed by STA449F3 Jupiter (NETZSCH) to analyze the thermal behavior of polymer composites under interest. The mass of the test samples was 30-80 mg. The study of thermal behavior was carried out under a nitrogen atmosphere in the temperature range from room temperature to 300 °C. Heating/cooling rate was 5 K/min. The temperature research program includes five segments: heating - holding - cooling - holding - heating. The first segment is to remove thermal prehistory of the samples and for possible removal of moisture. Holding segments allow stabilizing the furnace temperature.

Thermophysical properties were evaluated by laser flash method by LFA457 Microflash (NETZSCH) instrument. In the experiments the thermal diffusivity and specific heat were determined, and then the thermal conductivity was calculated according to equation:

$$\lambda = aC\rho \tag{1}$$

where λ is the coefficient of thermal conductivity, a is the thermal diffusivity, C is the specific heat, and ρ is the density. Determination of sample density was carried out by hydrostatic weighing.

The measurement error on the STA449F3 Jupiter (NETZSCH) is 3%, on the LFA457 Microflash (NETZSCH) for measuring the thermal diffusivity the error is 3%, the thermal conductivity is 8%. Since the thin surface layer of the sample is heated to a temperature more than 10 times higher than the maximum temperature of the back surface of the sample during the action of the laser pulse, the measurements were carried out in the temperature range from room temperature to 155 °C in order to exclude the temperature range of softening of the polymer.

4. RESULTS AND DISCUSSION

4.1. Thermal analysis

The crystallization curves of pure PA and PA based composites are presented in Fig. 1. For pure PA only one crystallization peak is observed at a temperature of 176 °C (see Table 2). For all investigated composites the crystallization peak shifts to higher temperatures which indicates that the fillers act as nucleating agents, and the growth of crystallites in polymer composites begins earlier than in the pure polymer. Thus, at low concentrations of CNM, the temperature of the crystallization peak increases by an average of 19 °C and the maximum temperature shift is observed for a composite containing 50 wt.% of CNM and it is almost of 40 °C. It is interesting that introduction of a large amount of SiC does not increase the crystallization temperature, which may be due to the peculiarities of the surface of the SiC particles and their interaction with the polymer.

It should be noted that for some composites containing CNM two peaks of crystallization are observed and the position of the second peak shifts to even higher temperatures. The peak of double crystallization in nanocomposites can be interpreted by the formation of crystallites of different morphologies, degree of defectiveness or size. [4, 14]. A sample with 50 wt.% of CNM can not crystallize in the same way because of the limited mobility of chains of PA macromolecules at such high concentration of carbon nanofiller in the polymer matrix. In addition an increase in the width of the crystallization peak at high concentrations of 20 wt.% and 50 wt.% indicates, apparently, a significant dispersion of crystallite sizes [4].

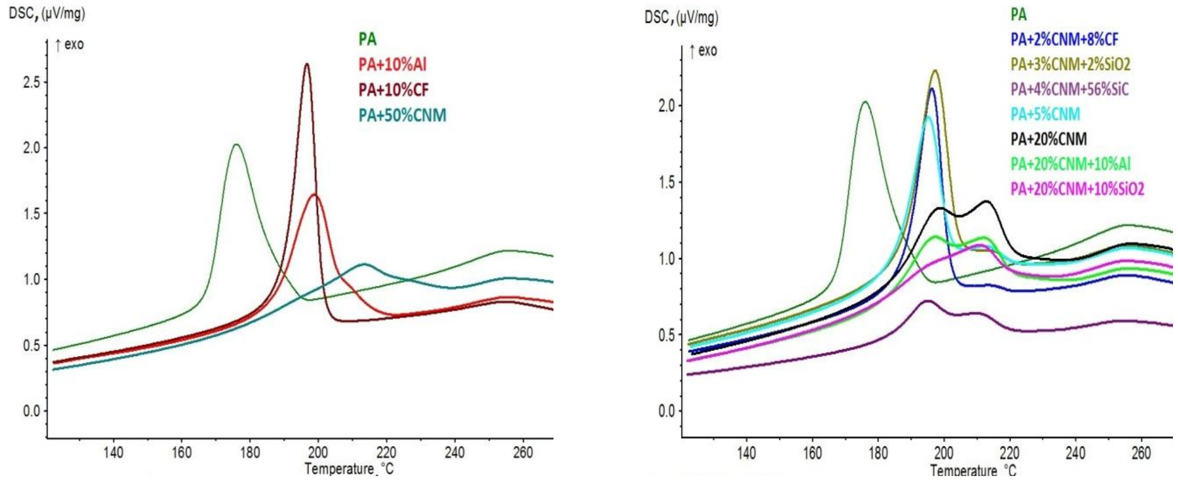

a) b)

Fig. 1. Crystallization curves of pure PA and PA based composites

The melting curves of pure PA and PA based composites are presented in Fig. 2. For pure PA the melting peak corresponds to a temperature of 228.3 °C. For loaded polymers a slight shift in the melting peaks toward low temperatures is observed (see Table 2), which indicates a decrease in the thermal stability of the samples. At low filler concentrations (Fig. 2, a), the main parameters characterizing the thermal behavior of the composite remain practically unchanged compared to the initial polymer matrix. While concentration of CNM increases up to 20 wt.% the temperature of melting peak decreases by 3 °C in comparison with pure PA (Fig. 2, b). The loading by 10 wt.% of SiO_2 reduces the temperature of the melting peak by almost 7 °C. It should be noted that increasing of filler concentration leads to decrease of the melting peak area. This indicates the destabilization of the composite. As the filler concentration increases the energy required to break the bonds between the filler and the matrix decreases. This effect is also observed with the addition of

10 wt.% Al or 10 wt.% SiO_2 to the composite consisting of PA + 20 wt.% CNM. A different intensity of the effect is associated with the features of the surface of the added particles and their interaction with the polymer matrix.

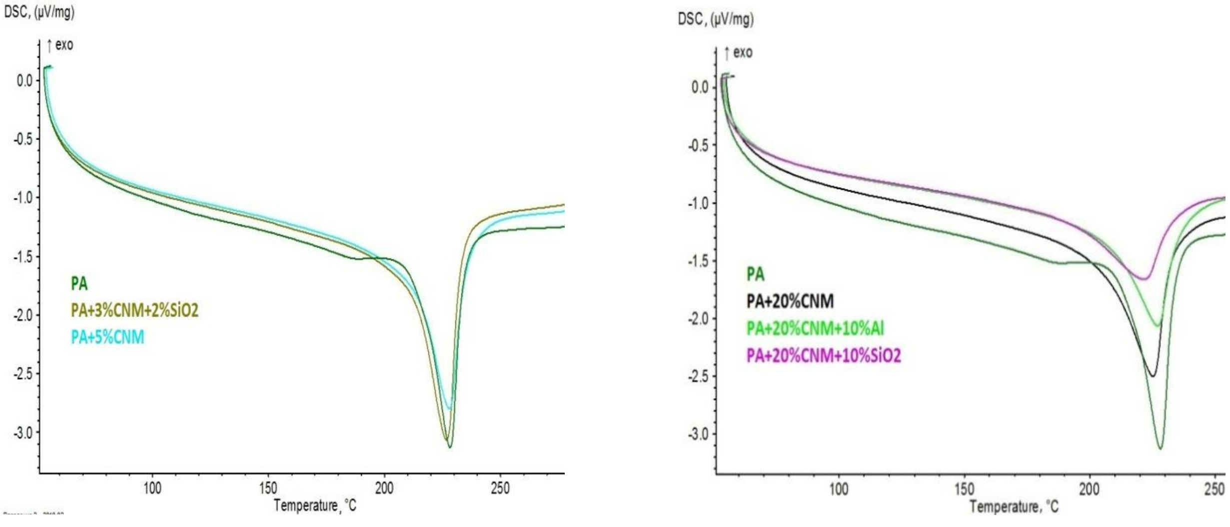

a) b)

Fig. 2. Melting curves of pure PA and PA based composites

Table 2. Results of thermal analysis of pure PA and PA based composites

№ sample	Type of sample	Melting	Crystallization	
		T_m, °C	$T_{c.1}$, °C	$T_{c.2}$, °C
1	PA	228.3	176.0	-
2	PA + 5% CNM	228.0	195.2	212.5
3	PA + 3% CNM + 2% SiO_2	226.8	197.2	212.6
4	PA + 2% CNM + 8% CF	226.0	196.3	213.4
5	PA + 10% CF	225.8	196.7	-
6	PA + 10% Al	228.1	198.8	-
7	PA + 20% CNM	225.2	198.8	212.8
8	PA + 20% CNM + 10% Al	227.1	197.3	211.9
9	PA + 50% CNM	223.7	213.4	-
10	PA + 4% CNM + 56% SiC	226.6	195.0	209.5
11	PA + 20% CNM + 10%	221.7	208.0	211.0

4.2. Thermophysical properties

The experimental data of thermophysical properties of the materials under interest are presented in Fig. 3. At low concentrations of hybrid filler up to 10 wt.% the thermal conductivity and thermal diffusivity of the composites increase by a factor of 1.5–2 (at room temperature). In the samples with 20 wt.% CNM and 10 wt.% of different fillers Al or SiO_2 the coefficients of thermal conductivity and thermal diffusivity increase approximately 3 times. That means the fillers Al and SiO_2 have the same effect on the thermophysical properties of materials while the thermal conductivity of the fillers themselves differ by orders of magnitude. It can be assumed that such effect is due to nanoscale and a well-developed surface of SiO_2, and its addition contributes to an additional compaction and leveling of the carbon filler in the PA matrix that is confirmed by atomic force microscopy (AFM) images (Fig. 4). As a result we observe an increase in thermal conductivity. Solid particles of Al influence in the same manner limiting the mobility of the macromolecules of the polymer and thereby compacting its structure.

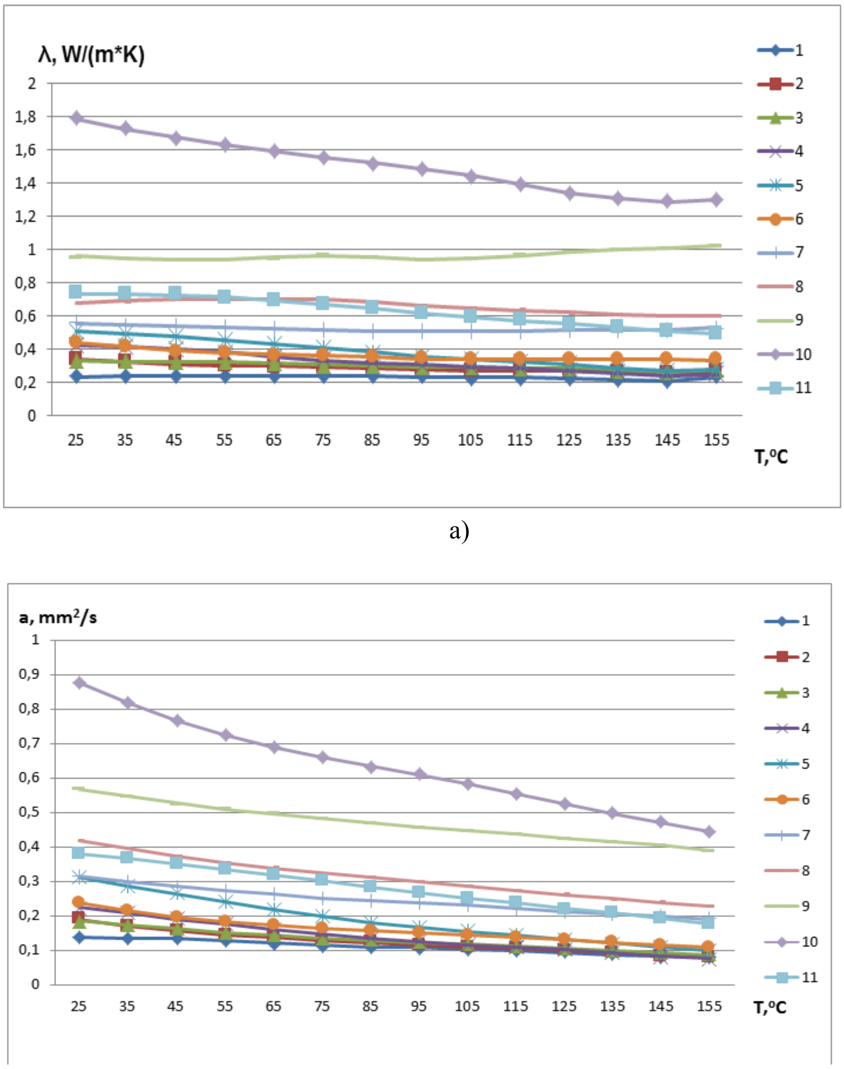

a)

b)

Fig. 3. Temperature dependence of thermophysical properties of the samples under study (numbering of the samples is according to Table 1): a – thermal conductivity; b – thermal diffusivity

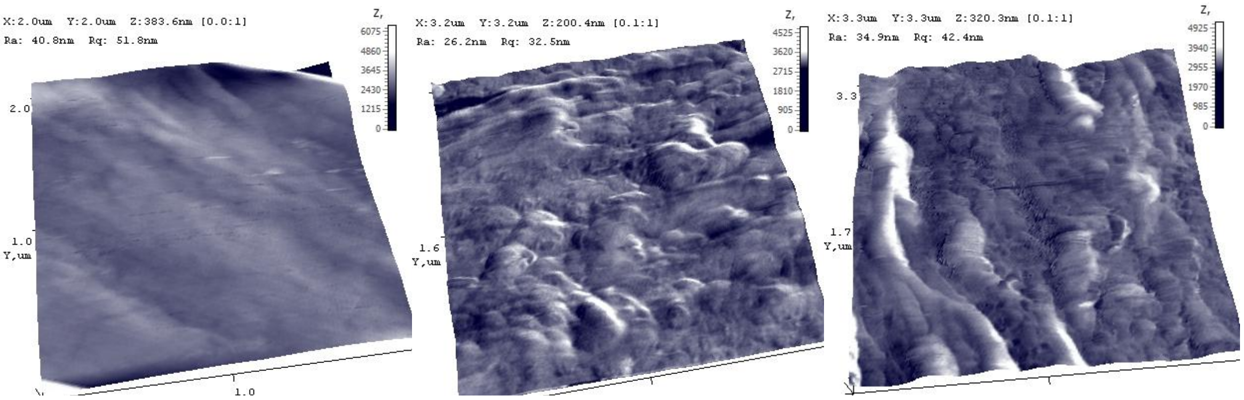

a) b) c)

Fig. 4. AFM images of polymer composites: a) pure PA; b) PA + 20 wt.% CNM; c) PA + 20 wt.% CNM + 10 wt.% SiO_2

Thermal conductivity and thermal diffusivity of nanocomposite with 50 wt.% of CNM rise more than four times in comparison with pure PA and in the case of a hybrid filling of 60 wt.% the parameters increase up to 8 times.

Temperature dependence of specific heat of the investigated nanocomposites on temperature is shown in Fig. 5. Specific heat decreases with increase of nanofiller concentration that is due to mobility restriction of the polymer macromolecules. Due to specific shape of particles, the CNM filler limits the mobility of polymer macromolecules in a greater extent than SiO_2 or Al. On the other hand, if samples 4 and 5 are compared then replacing 2% of carbon fibers to 2% of CNM leads to increase in the specific heat that indicates that carbon fibers limit the mobility of polymer molecules in a greater extent due to their strong structurization and longitudinal shape.

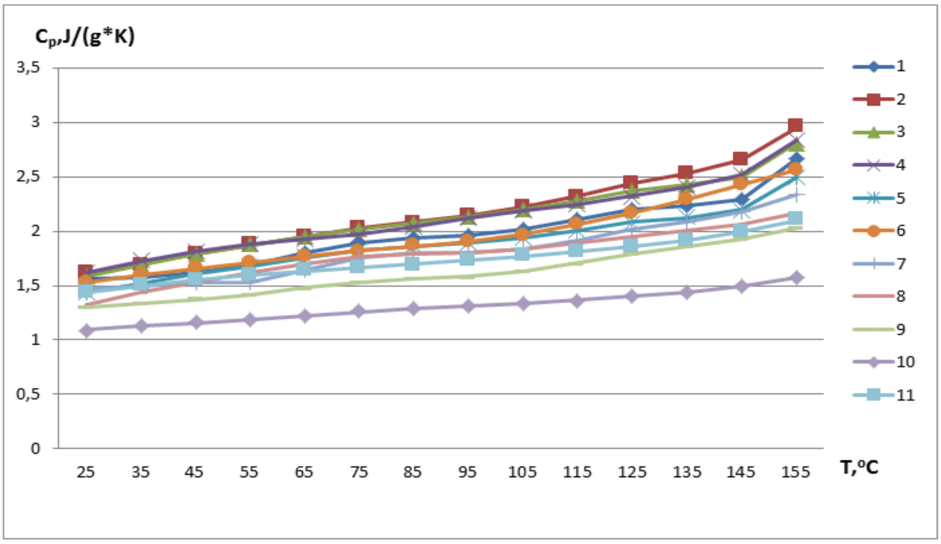

Fig. 5. Temperature dependence of specific heat of test samples
(numbering of samples is according to Table 1)

For PA based composites an exponential dependence of thermal conductivity on the filler concentration is observed independently on its type (Fig. 6).

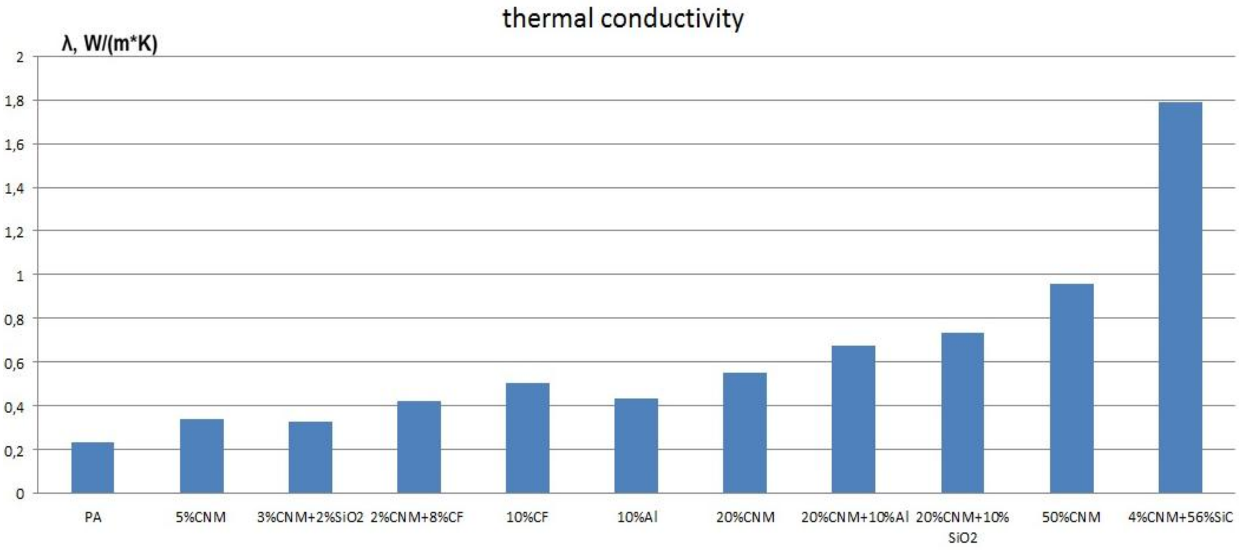

Fig. 6. Thermal conductivity of PA based composites at 25 °C

It should be noted that the filler Al has almost the same effect on thermal conductivity as fillers like CNM and CF, although the efficiency of combined use of fillers is lower (samples 4–6). This result can be explained by increase in the boundaries amount and the creation of additional barriers for heat transfer within the composite which, as it is known, is realized in polymers by the phonon mechanism.

Loading of PA by 10 wt.% of CF leads to thermal conductivity enhancement twice. Chemical peculiarities of interaction between matrix and filler, we are suggested in our discussions, are proved by comparison of this result with the case of epoxy loading by 5–7 wt.% carbon fibers [15]. In dependence of dispersion state of fillers thermal conductivity of epoxy-CF composite rises not more than 20% of epoxy alone.

The greatest increase of thermal conductivity is observed in a sample with a maximum concentration of a hybrid filler where 56 wt.% is SiC. It is assumed to be due to alignment of percolation chains of the filler in the polymer matrix similarly as we observed in epoxy or PET matrices (Fig. 7).

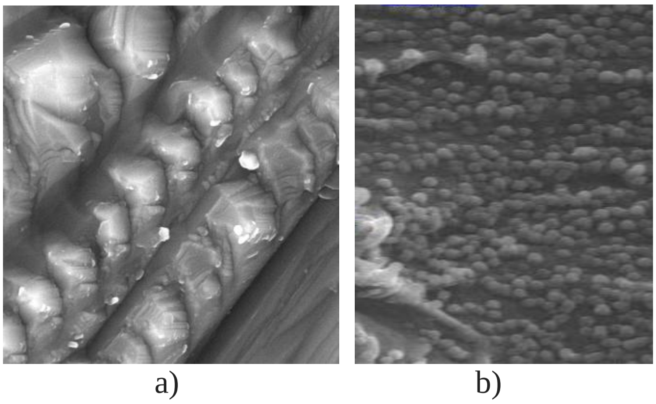

a) b)

Fig. 7. SEM images of polymer composites
on the basis of epoxy (a) and PET (b) loaded by 60 wt.% of SiC

Similar effect of hybrid loading of polymer by SiC with carbon material (multi-wall carbon nanotubes) was observed by Zhou et all. [16]. They analysed thermal conductivity of epoxy with hybrid filler and compared it with the case of separate SiC and carbon material loading. It was found that thermal conductivity is 24.3 times that of the epoxy when 5 wt.% multi-wall carbon nanotubes + 55 wt.% micro-SiC are added, while 6 wt.% of SiC results in 2.9 times and 71.7 wt.% of carbon nanotubes leads to 20.7 times thermal conductivity rising in comparison with epoxy alone.

At the same time the combined use of CNM and Al does not lead to any anomalous increase in thermal conductivity. It should be noted that CNM we used has not so strict structure as carbon nanotubes and concentration of Al particles is not enough to create the percolation chains, so we couldn`t expect the significant rise of thermal conductivity as in the case mentioned above and sinergetic effect is expressed not so clearly.

Analysis of thermal conductivity values of samples № 6, 7 and 8 shows that its growth is only due to an increase in filler concentration. Similarly samples № 2 and 3 contain filler in the same concentration and are characterized by similar thermal conductivity values despite the presence of SiO_2 particles in one of them. It should be noted that SiO_2 exhibits more obvious synergistic effect in the case of a polyethylene matrix [1]. This may be due to peculiarities of interaction of fillers with different types of polymer matrices.

5. CONCLUSIONS

Investigation of thermal behavior of PA based composites showed that the introduction of CNM give an impulse to change in the melting and crystallization peaks temperature. In addition the presence of CNM is a reason of double peak of crystallization that can be explained by formation of crystallites of different morphologies, degree of defectiveness or size according to statements of other researchers [4, 14].

The energy required for bonds break between the filler and the matrix decreases with increasing of filler concentration. This effect has different intensity depending on filler type - Al or SiO_2, that is assumed to be due to the features of the surface of added particles and their interaction with the polymer matrix.

Thermal conductivity of polymeric composites increases exponentially with increasing of filler content regardless of its type. The maximum increase is observed in the case of hybrid filling by 60 wt.% that is mainly due to alignment of percolation chains. Introduction of high-thermal conductivity fillers does not always have an obvious effect in terms of thermal conductivity increasing. Low-thermal conductivity SiO_2 has the same influence on thermophysical properties of the composite as does the high-thermal conductivity Al filler. This is maybe due to the surface features of the filler particles and their interaction with the polymer. Specific heat capacity of loaded composites decreases with increasing of filler concentration that can be explained by mobility restriction of polymer macromolecules with filler particles.

The results obtained do not allow one to conclude unambiguously that hybrid loading has a synergistic effect in improving of thermophysical properties of polymer composites.

ACKNOLEDGEMENT

I would like to express my very great appreciation to specialists from Nanoprocesses and Technologies Lab. of A. V. Luikov Heat- and Mass Transfer Institute for AFM analysis of some samples.

REFERENCES

1. KRAVTSEVICH, A. Influence of hybrid micro- and nanofiller on mechanical, electrical and thermal properties of polyethylene based composite. *Heat and mass transfer - 2015*. Minsk: HMTI, 2016. p. 261–268. *(available in Russian).*
2. KROTOV, Y., Lee, D., Louie, S. *Phys.Rev.Lett*., 1997, Vol. 78, p. 4245.
3. WHITE, C., ROBERTSON, D., MINTMIRE, J. *Phys.Rev.B*, 1993, Vol. 47, p. 5485.
4. LOGAKIS, E., PANDIS, C., PEOGLOS, V. [et al.] Structure–property relationships in polyamide 6/multi-walled carbon nanotubes nanocomposites. *J. Polymer Science B*, 2009, Vol. 47, Iss. 8, p. 764–774.
5. BOSE, S., KHARE, R. A., MOLDENAERS, P. Assessing the strengths and weaknesses of various types of pre-treatments of carbon nanotubes on the properties of polymer/carbon nanotubes composites: A critical review. *Polymer*, 2010, Vol. 51, p. 975–993.
6. DANILOVA-TRETIAK, S., EVSEEVA, L. Experimental investigation of thermophysical properties of polyamide based composites with hybrid loading. *Heat and mass transfer - 2016*. Minsk: HMTI, 2017. p. 205–209. *(available in Russian).*
7. MAHMOOD, N., ISLAM, M., HAMEED, A., SAEED S. Polyamide 6/Multiwalled Carbon Nanotubes Nanocomposites with Modified Morphology and Thermal Properties. *Polymers*, 2013, Vol. 5, p. 1380–1391.
8. RAKOV, E. Nanotubes and fullerenes. Moscow: University book, 2006. 376 p. *(available in Russian).*
9. MOLCHANOV, B.I., CHUKALOVSKIY, P.A., VARSHAVSKIY, V. Ya. Carbonplastic. Moscow: Chemistry, 1985. 208 p. *(available in Russian).*
10. Thermophysical properties of substances. Reference book. Moscow: State energy publishing house, 1956.
11. KATZ, G., MILEVSKI, D. *Fillers for polymer composites*. Moscow: Chemistry, 1981.

12. CHO, J. W., PAUL, D. R. Nylon 6 nanocomposites by melt compounding. *Polymer,* 2001, Vol. 42, Iss. 3. p. 1083–1094.
13. PACK S. et all. Segregation of carbon nanotubes/organoclays rendering polymer blends self-extinguishing. *Macromolecules*, 2009, Vol. 42, Iss. 17. p. 6698–6709.
14. YUAN, P., ZHONG, J., LIU, X. Nylon 66/nano $CaCO_3$ composites. Characterization and Application of Nanomaterials, 2018, Vol. 1, No. 1. P. 19–29.
15. SONG, Y.S, YOUN, J.R., Influence of dispersion states of carbon nanotubes on physical properties of epoxy nanocomposites. Carbon, 2005. No. 43. P. 1378–1385.
16. ZHOU, T., WANG, X., LIU, X., XIONG, D. Improved thermal conductivity of epoxy composites using a hybrid multi-walled carbon nanotube/micro-SiC filler. Carbon, 2010. No. 48. P. 1171–1176.

CYSENI 2018, May 23-25, Kaunas, Lithuania
ISSN 1822-7554, www.cyseni.com

NUMERICAL PREDICTION OF MECHANICAL PROPERTIES OF ZIRCONIUM ALLOY WITH HYDRIDES USING FINITE ELEMENT METHOD

R. Janulionis, R. Kriūkienė
Lithuanian Energy Institute
Breslaujos str. 3, LT-44403 Kaunas – Lithuania
Email: remigijus.janulionis@lei.lt

ABSTRACT

During Nuclear Power Plant (NPP) operation degradation effects like ageing, corrosion, fatigue, and others may significantly impact component integrity. Various nuclear power plant components have direct contact with water where corrosion may occur. High heat and pressure and radiations have big effect on ageing of components. One of the degradation mechanisms is hydrogen absorption. This is very important for the fuel claddings and fuel channels which are made of Zr alloys. Until now there are known 4 hydrogen absorption mechanisms: absorption due to corrosion process in high temperature water solutions; direct reaction between Zr surface and gas state of hydrogen; hydrogen diffusion through metallic bond with other metal where hydrogen is in more active form; cathodic polarization of Zr in the electrolyte. All these mechanisms are met in in NPP reactors. When hydrogen concentration in zirconium alloy exceeds solubility limit the formation of Zr hydrides under certain conditions starts. Hydride is a brittle form of Zr and hydrogen compound. Hydrides have a shape of platelets and are distributed all around the Zr alloy. The sufficient amount of hydrides does have an influence to material properties of Zr alloy. Therefore, determination of material properties under different levels of hydrogen concentration in zirconium alloy is important. Usually material properties are determined by conducting an experiment. However, it is not always possible. To conduct an experiment the sample of test material must by present in certain amount that is required to machine a specimen, the material might be contaminated by radioactive nuclides and etc. Therefore, there is a need for prediction of material properties of Zr alloy with hydrides by alternative methods. This article presents the numerical prediction of material properties of zirconium alloy with hydrides.

In this work the Finite Element (FE) model was created which evaluates hydride influence on Zr alloy. The size and volume part of hydrides in zirconium alloy at different hydrogen concentrations were determined by experimental measurements of real specimens. In finite element model the size of zirconium alloy surrounding hydride platelet was selected in such a way that hydride volume part in the model would match experimental measurements. By knowing mechanical properties of hydride and Zr alloy our presented finite element model allows to predict mechanical properties of Zr alloy with different levels of hydrogen.

For numerical calculations and model creation finite element code ABAQUS was selected. The numerical prediction of mechanical properties of Zr alloy with hydrides at three different hydrogen concentrations was done. The prognosis results were compared with the experimental found in literature and good agreement with experimental data was obtained (see Fig. 1).

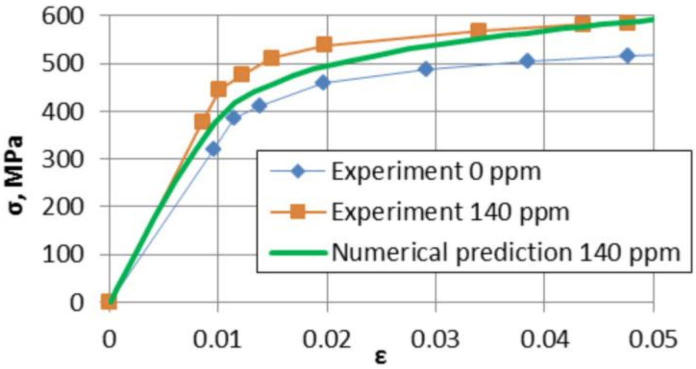

Fig. 1. The experimental and modeled stress strain curve of zirconium alloy with hydrogen concentration of 140 ppm

Keywords: finite element method, hydride, hydrogen, zirconium alloy, mechanical properties

CYSENI 2018, May 23-25, Kaunas, Lithuania
ISSN 1822-7554, www.cyseni.com

DEFROSTING CHARACTERISTICS OF INDIUM TIN OXIDE FILM COATED WINDSHIELDS

P. Dolmantas, R. Ramanauskas, V. Marudinas, A. Iljinas
Kaunas University of Technology
Studentų str. 50, LT-51368 Kaunas – Lithuania
E-mail: Paulius.dolmantas@ktu.edu

ABSTRACT

Indium tin oxide is doped n-type semiconductor with high visible spectrum transmittance (around 80%) and electrical conductivity (~10^5 S/cm). Currently, it finds many applications in research and industry such as detectors, solar cells, liquid crystals, transparent electrodes, smart windows and more. In this study we investigated ITO film ability to defrost a glass surface when a voltage is applied (voltage range used – 12–27 V). The films were formed using reactive plasma assisted thermal evaporation method under 4 Pa oxygen pressure at 350 ^{o}C substrate temperature with different indium and tin mass ratios. Measurements were done using film which had shown best optical and electrical properties. Furthermore, experiment was done to determine voltamperic characteristic of the film – in a range from 0 to 27 V the film obeys Ohm's law. Defrosting under different voltages was investigated using Peltier element. It was obtained that when sample is at -10 ^{o}C a voltage of 24 V was enough to melt ice in 10 seconds. The main heat transfer parameters were calculated.

Keywords: indium tin oxide, thin films, plasma assisted thermal evaporation, defrosting

1. INTRODUCTION

Driving in regions where during cold seasons average temperature drops below 0 ^{o}C is difficult: not only light day time greatly shortens which increases risk of accidents and vehicle requires different equipment but there is additional discomfort of windshields being perpetually frozen when left on longer periods of time. Conventional ways of dealing with this problem are mechanical frost removal or waiting for vehicles internal heating to melt it. Both are relatively time consuming and ineffective. Moreover, residual frost can permanently ruin windshields wiper rubber. Sometimes usage of frozen rubber causes annoying sounds which distract driver. There are additional problems with windshield wiper blades: if the wind is strong, wiper blades tend to leave a small spacing between windshield reducing wiping effectiveness.

One possible solution to this problem is using transparent conductive oxides (TCO's) as heating elements in a form of thin films on vehicles windshield [1]. To make such films applicable for windshield coating, they must satisfy certain requirements. Firstly, according to Lithuanian technical motorized means of transport requirements, vehicles windshields transparency must be no less than 75%. [2]. Secondly, films should have low and stable resistance, at least up to certain voltage, required to defrost a windshield. Finally, TCO and used electrodes should have ohmic contact, that is, contact should not limit electric current. To qualitatively assess the quality of a film, which satisfies first and second requirement, one can use one of many figures of merit [3].

Indium – tin oxide (ITO) films are good fit for vehicle windshield coating as it is transparent (transmittance around 80%) conductive (conductivity ~10^5 S/cm) n-type semiconductor. It is already used for transparent conducting layers in various optoelectronic devices such as detectors [4], solar cells [5], liquid crystals [6], transparent electrodes [7] and smart windows [8], [9] and more. There are also plenty of film deposition methods such as spray pyrolysis [10], electron beam evaporation [11], ion beam evaporation [12], DC and RF magnetron sputtering [13], [14], chemical vapor deposition [15], pulsed laser deposition [16], cathodic arc deposition [17].

The main objective of this work was to form thin ITO films using reactive plasma assisted thermal evaporation and evaluate its practical application as a glass defrosting layer by investigating indium to tin ratio effects on its optical, electrical and thermal properties.

2. METHODOLOGY

Thin indium-tin oxide films were deposited on soda lime glass substrate using resistive thermal evaporation system UVM shown in Fig. 1. The highest vacuum possible to achieve with this system is about $5 \cdot 10^{-3}$ Pa. Using this system it is possible to adjust oxygen flux in the range from 0–500 cm^3/min. Plasma is created in the region between substrate and holder using high voltage power source. Evaporation is achieved by putting pieces of metals (indium and tin in this case) into molybdenium boat. Different film elemental composition is acquired by putting correspondingly different masses of these metals. The scheme of used system is shown in Fig. 1. Films were formed at 4 Pa oxygen pressure. Initial residual pressure was $5 \cdot 10^{-3}$ Pa. Substrate temperature was 350 ^{o}C. The distance from tray to substrate was 10 cm. Plasma voltage of 400 V was used. Discharge current and vaporizer current was 0.625 A and 75 A respectively. The required indium and tin mass was measured using analytic A&D GR 202 model scales. Error of the scales – 0.01 mg. The thickness of films was measured using profilometer. In total 6 indium-tin oxide films were deposited with different indium – tin masss ratios.

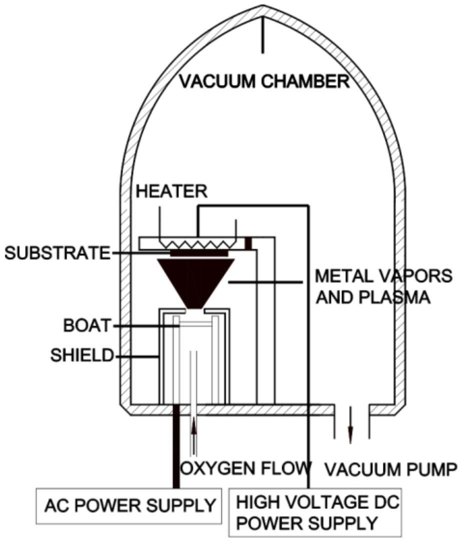

Fig. 1. Scheme of a system UVM

XRD analysis was performed using standard database PDF-2 file (JCPDS: 71-2194).

Sheet resistance of obtained films was measured using four-probe method. When films thickness is much smaller than its width and length the sheet resistance of such film can be calculated by:

$$R_s = \frac{\pi}{\ln 2} \cdot \frac{U}{I} \tag{1}$$

where R_s is sheet resistance, U – voltage drop across a specimen, I – current, $\frac{\pi}{\ln 2}$ is geometrical correction factor (CF) [18]. Resistivity is given by the following formula:

$$\rho = R_s \cdot d \tag{2}$$

where ρ is electrical resistivity, d – film thickness.

Defrosting characteristics, current-time dependence, voltamperic relation, were investigated using AIM-TTI INSTRUMENTS, PL303QMD DC power supply (voltage range 0–30 V), ampermeter Agilent 34410A, multimeter Mastech MS 8229 with thermocouple probe. Measurements at lower temperatures (up to -10 °C) were performed using Peltier element. Optical transmitttance was measured using optic fiber spectrometer “Ocean Optics” USB4000. This device allows to vary light wavelenght from 250 nm to 850 nm. Absorption coefficient was obtained using following equation:

$$\alpha = \frac{1}{d} \cdot \ln\left(\frac{1}{T}\right) \tag{3}$$

where d is thickness of a film and T is transmittance. Using gathered data Tauc method was applied to determine band gap of the material by extrapolating linear part of a graph $(\alpha h\nu)^2 = f(h\nu)$. To decide which deposited film had best combination of optical transmittance and electrical conductivity the following formula was used [3]:

$$\Phi_{T,C} = \frac{T^{10}}{R_s} \tag{4}$$

where T is transmittance at λ = 555 nm.

3. RESULTS AND DISCUSSION

Sample No. 5 XRD analysis show that deposited ITO film had polycrystalline structure, having all main cubic system Ia3 space group orientation peaks: (211), (222), (400), (440), (622), as well as some minor peaks. Peaks fit well with standard database PDF-2 file (JCPDS: 71-2194) peak position.

3.1. Optical measurements

As seen in Fig. 2, films optical transmittance increases as the wavelenght increases. Optical transmittance measurements allowed to determine correlation between films transparency and indium to tin mass ratios (Fig. 3). As seen in Fig. 3, transmittance is a linear function of metal mass ratio.

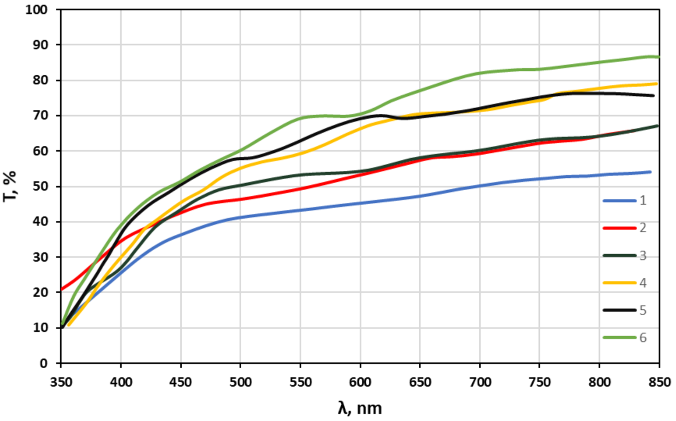

Fig. 2. Optical transmittance of all deposited films

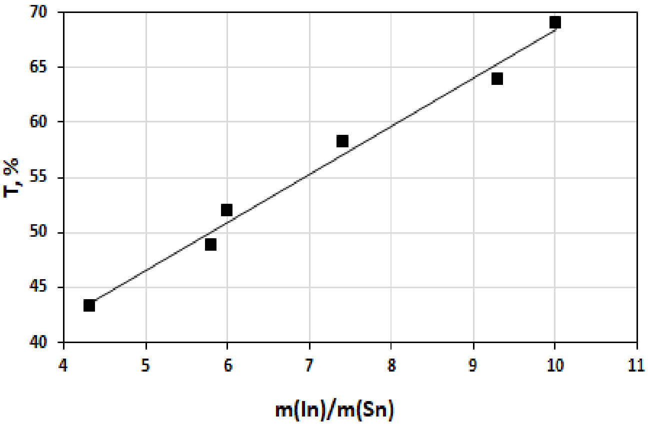

Fig. 3. Coating transparency at 555 nm dependence from indium - tin mass ratio

Using Tauc method it was obtained that synthesized film optical band gap is 3.35 eV (Fig. 4). It depends on films deposition method and substrate, but is similar to other authors results [19], [20] which were 3.6 eV and 3.99 eV respectively. This quantity determines energy threshold for photons to be absorbed [21].

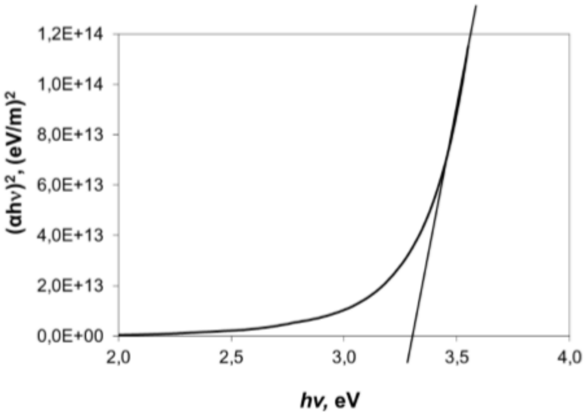

Fig. 4. Tauc plot

3.2. Electrical stability measurements

Results obtained from profilometer, four – probe and optical spectrometer are shown in Table 1. As seen from the Table 1, as the quantity of tin in film decreases, sheet resistance increases from 92 Ω/sq to 560 Ω/sq and absorption coefficient decreases from $11 \cdot 10^3$ cm^{-1} to $5 \cdot 10^3$ cm^{-1}.

Table 1. Electrical and optical characteristics of indium - tin oxide films

Nr.	***d, nm***	***R, Ω/sq***	***ρ, Ω·cm***	***α, cm^{-1} (555 nm)***	***m(In)/m(Sn)***	***$\Phi_{T,C}$, Ω^{-1}***
1	800	92	$7.36 \cdot 10^{-3}$	$11 \cdot 10^3$	4.3	$2.3 \cdot 10^{-6}$
2	755	117	$8.83 \cdot 10^{-3}$	$10 \cdot 10^3$	5.8	$6.8 \cdot 10^{-6}$
3	803	151	$12.1 \cdot 10^{-3}$	$7 \cdot 10^3$	6.0	$9.6 \cdot 10^{-6}$
4	796	173	$13.8 \cdot 10^{-3}$	$6.5 \cdot 10^3$	7.4	$2.5 \cdot 10^{-5}$
5	802	211	$16.9 \cdot 10^{-3}$	$6 \cdot 10^3$	9.3	$5.5 \cdot 10^{-5}$
6	780	560	$43.7 \cdot 10^{-3}$	$5 \cdot 10^3$	10.0	$4.4 \cdot 10^{-5}$

Film number 5 was chosen for further investigations as it has shown best optical and electrical properties: resistivity – $16.9 \cdot 10^{-3}$ Ω·cm, optical transmittance at 555 nm and 507 nm of 64% and 58% respectively. Also, as seen from Table 1, figure of merit $\Phi_{T,C}$ was highest for this film. The main reason for comparing films transmittance at these specific wawelenghts is that as Gross, Herbert and others [22] established maximum spectral sensitivity of the average healthy human eye under daylight conditions is at 555 nm and 507 nm during night time.

It was obtained that electric current dependence on applied voltage is linear and therefore it obeys Ohm's law and contact is ohmic (Fig. 5). This behaviour is desireble as it assures most stable electrical characteristics. Current measurement over time has shown that films resistance is relatively stable over a course of two minutes (Fig. 6).

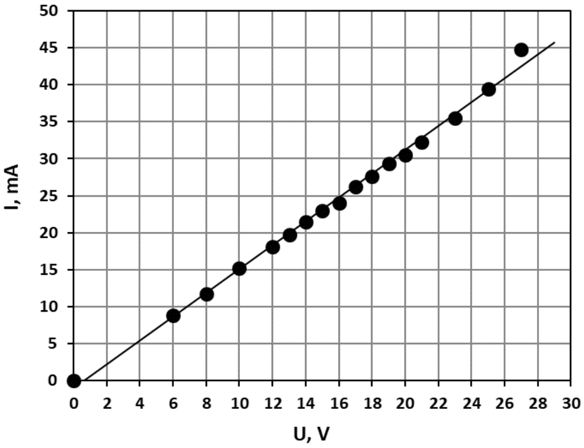

Fig. 5. Sample No. 5 voltamperic characteristic

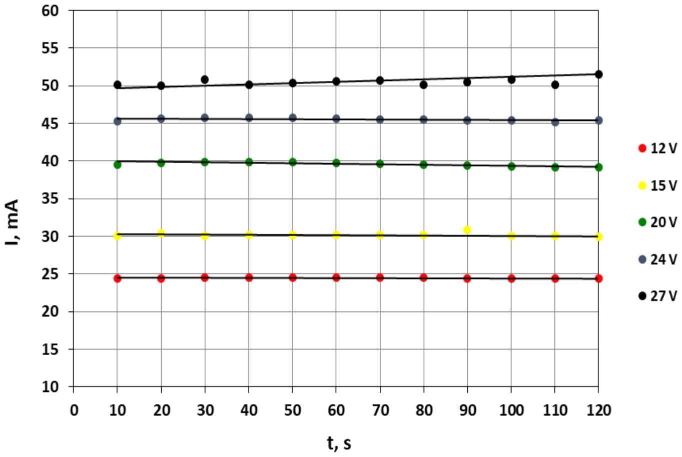

Fig. 6. Current dependency on time

3.3. Defrosting measurements

Films defrosting properties was investigated using Peltier element. During the measurements two opposite processes were competing: heat generation caused by electric current flowing through a resistor (film) and cooling of Peltier element. Initial temperature of film was -10 ^{o}C (Fig. 7). It was found that voltage of 12 V and 15 V was not enough to defrost the surface of a film. In two minutes corresponding films temperatures were -5 ^{o}C and -3 ^{o}C. However, when a voltage of 20 V was applied it was obeserved that films temperature had risen to 0 ^{o}C but a layer of frost remained. Finally it was found that voltage of 24 V was enough to defrost the film. Time constant of defrosting process under 24 V was determined to be $\tau = 5.84$ s. It shows the time required to lower the temperature difference by $e \approx 2.71828$.

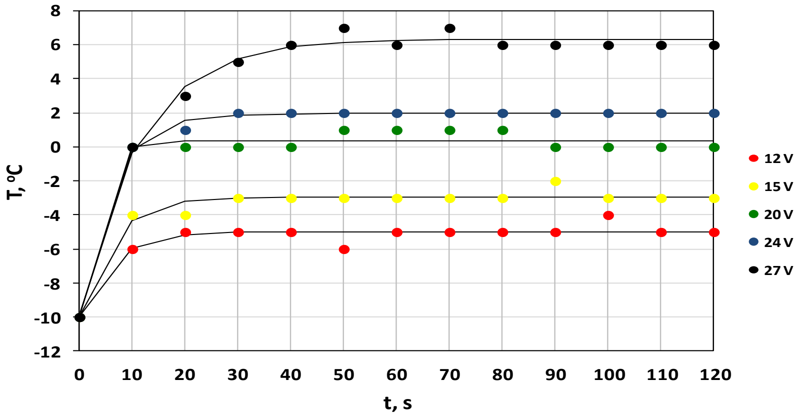

Fig. 7. Sample No. 5 defrosting characteristics under different heating voltages

4. CONCLUSIONS

It is known that ITO films electrical conductivity depends on carrier density. One might expect that for each tin atom added, one electron would be introduced, therefore increasing carrier density. However this is only true up to a certain tin concentration. After reaching peak, carrier concentration decreases because of structural changes in the lattice (low conduction precipitates such as $In_4Sn_3O_{12}$ can form) [23]. Higher transparency over visible spectrum can be reached using annealing [24]. By combining In:Sn ratio and annealing films, even higher figure of merit can be obtained. Of all six indium tin oxide films deposited using plasma assisted thermal evaporation method sample No. 5 showed most fitting combination of electrical and optical properties for defrosting. Its deposition indium to tin mass ratio is 9.3, sheet resistance – 211 Ω/sq . Film shows ohmic contact – resistance is stable and equal to 670 Ω, band gap – 3.35 eV, absorption coefficient $6 \cdot 10^{3}$ cm^{-1} and transmittace 64% at 555 nm wavelenght. It was shown that a relatively small voltage of 24 V is enough to melt frost layer on a glass in 30 s. Under this condition time constant $\tau = 5.84$ s.

REFERENCES

1. Kiju Im, Kyoungah Cho, Jonghyun Kim, Sangsig Kim, Transparent heaters based on solution-processed indium tin oxide nanoparticles, Thin Solid Films, Volume 518, Issue 14, 2010, Pages 3960–3963, ISSN 0040-6090.
2. Valstybinė kelių transporto inspekcija prie Susisiekimo ministerijos. TECHNINIAI MOTORINIŲ TRANSPORTO PRIEMONIŲ IR JŲ PRIEKABŲ REIKALAVIMAI: 2008-07-29. Document no. :2B-290. [intercative] [last time viewed 2018-02-21]. Access: https://e-seimas.lrs.lt/portal/legalAct/lt/TAD/TAIS.325585
3. Mazur, Michal & Domaradzki, Jaroslaw & Kaczmarek, Danuta & Moh, Sara & Placido, Frank. (2010). Sheet resistance and optical properties of ITO thin films deposited by magnetron sputtering with different O2/Ar flow ratio. 10.1109/STYSW.2010.5714168.
4. Yanlei Wang, Congchun Zhang, Juan Li, Guifu Ding, Li Duan, Fabrication and characterization of ITO thin film resistance temperature detector, Vacuum, Volume 140. 2017, Pages 121–125, ISSN 0042-207X.
5. Shui-Yang Lien, Characterization and optimization of ITO thin films for application in heterojunction silicon solar cells, Thin Solid Films, Volume 518, Issue 21, Supplement, 2010, Pages S10–S13, ISSN 0040-6090.
6. Jiun-Haw Lee, Wei-Fu Chang, Cheng-Che Wu, Chi-Feng Lin, Jiunn-Yih Lee, Tien-Lung Chiu, Fabrication of an organic light-emitting diode inside a liquid crystal display, Thin Solid Films, Volume 545, 2013, Pages 471–475, ISSN 0040-6090,
7. Tae Kyoung Kim, Yeo Jin Yoon, Seung Kyu Oh, Yu Lim Lee, Yu-Jung Cha, Joon Seop Kwak, Ohmic contact mechanism for RF superimposed DC sputtered ITO transparent p-electrodes with a variety of Sn2O3 content for GaN-based light-emitting diodes, Applied Surface Science, Volume 432, Part B, 2018, Pages 233–240, ISSN 0169-4332.
8. Kentaro Utsumi, Osamu Matsunaga, Tsutomu Takahata, Low resistivity ITO film prepared using the ultra high density ITO target, Thin Solid Films, Volume 334, Issues 1-2, 1998, Pages 30–34, ISSN 0040-6090.
9. Gi-Seok Heo, Jong-Woon Park, Seok-Eui Choi, Michael H.-C. Jin, Dong-Chan Shin, Modification of optical and electrical properties of ITO using a thin Al capping layer, Thin Solid Films, Volume 518, Issue 4, 2009, Pages 1160–1163, ISSN 0040-6090.
10. Gérard Blandenet, Michel Court, Yves Lagarde, Thin layers deposited by the pyrosol process, Thin Solid Films, Volume 77, Issues 1–3, 1981, Pages 81–90, ISSN 0040-6090.
11. Mika Yamaguchi, Ari Ide-Ektessabi, Hiroshi Nomura, Nobuto Yasui, Characteristics of indium tin oxide thin films prepared using electron beam evaporation, Thin Solid Films, Volumes 447–448, 2004, Pages 115–118, ISSN 0040-6090.
12. H.J. Kim, J.W. Bae, J.S. Kim, K.S. Kim, Y.C. Jang, G.Y. Yeom, N.-E. Lee, Electrical, optical, and structural characteristics of ITO thin films by krypton and oxygen dual ion-beam assisted evaporation at room temperature, Thin Solid Films, Volumes 377–378, 2000, Pages 115–121, ISSN 0040-6090.

13. Leandro Voisin, Makoto Ohtsuka, Svitlana Petrovska, Ruslan Sergiienko, Takashi Nakamura, Structural, optical and electrical properties of DC sputtered indium saving indium-tin oxide (ITO) thin films, Optik - International Journal for Light and Electron Optics, Volume 156, 2018, Pages 728–737, ISSN 0030-4026.
14. Negin Manavizadeh, Farhad Akbari Boroumand, Ebrahim Asl-Soleimani, Farshid Raissi, Sheida Bagherzadeh, Alireza Khodayari, Mohammad Amin Rasouli, Influence of substrates on the structural and morphological properties of RF sputtered ITO thin films for photovoltaic application, Thin Solid Films, Volume 517, Issue 7, 2009, Pages 2324–2327, ISSN 0040-6090.
15. Jeffrey M. Gaskell, David W. Sheel, Deposition of indium tin oxide by atmospheric pressure chemical vapour deposition, Thin Solid Films, Volume 520, Issue 12, 2012, Pages 4110–4113, ISSN 0040-6090.
16. Cristian Viespe, Ionut Nicolae, Cornelia Sima, Constantin Grigoriu, Rares Medianu, ITO thin films deposited by advanced pulsed laser deposition, Thin Solid Films, Volume 515, Issue 24, 2007, Pages 8771–8775, ISSN 0040-6090.
17. B.J. Chen, X.W. Sun, B.K. Tay, Fabrication of ITO thin films by filtered cathodic vacuum arc deposition, Materials Science and Engineering: B, Volume 106, Issue 3, 2004, Pages 300–304, ISSN 0921-5107.
18. Chen, A., et al., A new investigation of oxygen flow influence on ITO thin films by magnetron sputtering. Solar Energy Materials and Solar Cells, 2014. 120, Part A: p. 157–162.
19. Elmas, S., Ş. Korkmaz, and S. Pat, Optical characterization of deposited ITO thin films on glass and PET substrates. Applied Surface Science, 2013. 276: p. 641–645.
20. Amutha Chinnappan, Jeremy Kong Yoong Lee, W.A.D.M. Jayathilaka, Seeram Ramakrishna, Fabrication of MWCNT/Cu nanofibers via electrospinning method and analysis of their electrical conductivity by four-probe method, International Journal of Hydrogen Energy, Volume 43, Issue 2, 2018, Pages 721–729, ISSN 0360-3199.
21. Hilmi Ünlü, A Thermodynamic Model for Determining Pressure and Temperature Effects on the Bandgap Energies and Other Properties of Some Semiconductors, Solid-State Electronics, Volume 35, Issue 9, 1992, Pages 1343–1352, ISSN 0038-1101.
22. Gross, Herbert; Blechinger, Fritz; Achtner, Bertram (2008). Gross, Herbert H., Ed. Handbook of Optical Systems. 4. Weinheim, Germany: Wiley-Vch. P. 40. ISBN 978-3-527-40380-6.
23. Nadaud, N., Lequeux, N., Nanot, M., Jové, J., & Roisnel, T. (1998). Structural Studies of Tin-Doped Indium Oxide (ITO) and In4Sn3O12. Journal of Solid State Chemistry, 135(1), 140–148.
24. N. M. Khusayfan and M. M. El-Nahass, “Study of Structure and Electro-Optical Characteristics of Indium Tin Oxide Thin Films,” Advances in Condensed Matter Physics, Vol. 2013, Article ID 408182, 8 pages, 2013.

CYSENI 2018, May 23-25, Kaunas, Lithuania
ISSN 1822-7554, www.cyseni.com

STUDY ON THE PROPERTIES OF TiO_2 THIN FILMS DEPOSITED BY ULTRASONIC SPRAY PYROLYSIS

Z. J. Chen, I. Oja Acik, I. Dündar, A. Mere
Laboratory of Thin Film Chemical Technologies
Department of Materials and Environmental Technology
Tallinn University of Technology
Ehitajate tee 5, EE-19086 Tallinn – Estonia
Email: zengjunchen001@gmail.com

ABSTRACT

In present work, we have studied the structural, optical and electrical properties of TiO_2 thin films deposited at different substrates temperature for solar cell applications. Ultrasonic spray pyrolysis method was used to fabricate TiO_2 thin films because of its low-cost operation, absence of vacuum system and convenience of use. The films were sprayed from solution containing titanium(IV) isopropoxide, acetylacetone in molar ratio of 1 : 4 in ethanol and deposited onto substrate of microscopy glass and n-type Si (100) wafer at temperatures of 200 to 500 °C. The resulting films were annealed at 500 °C and 700 °C for 1 hour in air. The films were characterized by UV-vis spectroscopy, XRD, Raman, and I-V measurements. Results showed that the total transmittance of TiO_2 thin films decreased after annealing. The annealed film thickness increased from 80 to 510 nm with increasing deposition temperature from 200 to 500 °C. The optical properties showed the band gap for TiO_2 thin films decreased as the deposition temperature increased. As deposited films prepared below 500 °C were amorphous, whereas crystalline anatase films were obtained at 500 °C. Further annealing at 700 °C in air led to anatase crystalline formation when films were deposited below 500 °C whereas the films deposited at 500 °C consist of anatase and rutile phases.

Keywords: TiO_2, Ultrasonic spray pyrolysis, thin films

1. INTRODUCTION

Titanium dioxide (TiO_2) is one of the most important semiconductor oxides with attractive chemical, electrical, optical properties. After the first report by Fujishima and Honda (1972) on the photolysis of water by TiO_2 [1], numerous studies in the properties of nanocrystalline TiO_2 have been generated due to their promising applications in antireflection coatings [2], transparent conductors [3], dielectrics [4] and self-cleaning surfaces [5], and in solar cells, such as dye-sensitized [6], perovskite [7] or organic [8].

TiO_2 belongs to the family of transition metal oxides. It is known that TiO_2 has three crystal structures: anatase, brookite, and rutile. Anatase and rutile have a crystalline structure that corresponds to the tetragonal system while brookite has an orthorhombic crystalline structure. Rutile phase is thermodynamically stable at high temperatures. The anatase phase is metastable and transforms irreversibly to rutile at elevated temperatures [9].The brookite phase is the rarest of the natural TiO_2 polymorphs and is the most difficult phase to prepare in the laboratory. Anatase phase has a band gap of 3.2 eV, while the rutile phase has a smaller band gap of 3.0 eV [10].

In general, anatase phase is preferred in solar cells and photocatalytic applications because anatase phase has a larger band gap, potentially higher conduction band edge energy and lower electron-hole pair recombination rate [11].

Nakaruk *et al.* [12] studied TiO_2 films deposited onto quartz substrates at 400 °C by ultrasonic spray pyrolysis method and annealed at 600 °C, 800 °C, 1000 °C show anatase phase, a mixture phase of anatase and rutile phases, and pure rutile phase, respectively. They showed also that the indirect band gap decreased from 3.54 eV to 3.26 eV and transmission of the films decreased after annealing at 600 °C and 1000 °C, respectively. Oja *et al.* [13] have reported that the phase composition of the TiO_2 films deposited by sol-gel pneumatic spray pyrolysis method is controlled by both deposition and annealing temperature. They reported that as-deposited TiO_2 films grown below 500 °C were amorphous. Only the deposition or annealing at 500 °C results in films with anatase phase and free of contaminants. Annealing at 700 °C leads to crystalline anatase if films are deposited below 400°C whereas the films grown at either 435 °C or 500 °C consist of a mixture of anatase-rutile or rutile, respectively.

Various methods have been used for preparing nanocrystalline titania, such as sol-gel [14], screen-printing [15], dip-coating [16], chemical vapor deposition [17] and ultrasonic spray pyrolysis [12], [18]. Among all these methods, ultrasonic spray pyrolysis method has been drawn considerable attention due to its simplicity, cost-efficiency and convenience for fabricating TiO_2 thin films. In this paper, TiO_2 thin film was deposited on the silicon and microscopy glass substrates by ultrasonic spray pyrolysis method. The aim of this work is to deposit TiO_2 thin films at different substrate temperature and to investigate its structural, optical and electrical properties for solar cell applications.

2. METHODOLOGY

TiO_2 thin films were deposited onto microscopy glass and c-Si substrates at different substrate temperature using ultrasonic spray pyrolysis method. The precursor solution is composed of titanium(IV) isopropoxide (TTIP) as a titanium source, acetylacetone (AcAc) as a stabilizer and ethanol as solvent. 0.2molL^{-1} TTIP concentration and TTIP:AcAc molar ratio of 1:4 were used as starting solution. The solution was atomized by a ultrasonic generator of 1.7MHz frequency, produced aerosol was carried directly to the heated substrates using compressed air as carrier gas in a flow rate of 5 L/min and director gas (1.2 L/min) was used to adjust the spray direction. The deposition temperature (T_s) vary in the range 200 to 500 °C. The number of spray cycles were set to six.

The as-deposited films grown on glass and Si-substrates were annealed for 1 hour at 500 °C in air. The films on silicon substrates where additionally thermally treated at 700°C for 1 hour in a laboratory furnace. The structural property of the samples was investigated by X-ray diffraction (XRD) and Raman spectroscopy methods. XRD patterns were recorded by a Rigaku Ultima IV diffractometer with Cu Kα radiation ($\lambda = 1.5406$ Å, 40 kV at 40 mA) using Si strip detector. The measurements were performed in 2 theta configurations with scan range of 20–60°, with a step of 0.02° and a scanning speed of 2°/min. The mean crystallite size was calculated by the Scherrer method from the FHWM (full width at half maximum) of the (101) peak of TiO_2 anatase phase. Raman spectra were acquired on a micro-Raman spectrometer HORIBA Jobin Yvon Model HR800 in the spectral range of 100–800 cm^{-1} using 532 nm laser line which delivers 5 mW of power at 10 μm laser spot size during measurement.

The total transmittance of TiO_2 thin films are measured by Jasco V-670 spectrophotometer with spectral range between 250 and 1200 nm. The film thickness was calculated by using interference fringes from optical spectrum.

Current-Voltage (I-V) measurement was performed to investigate the electrical properties of TiO_2 thin film on n-Si substrate. The I-V measurement was performed with using graphite contact and Si as a second contact. The Autolab PGSTAT 30 system was used for measuring of I-V curves of the films.

3. RESULTS AND DISCUSSION

3.1. Structural properties

3.1.1. X-ray diffraction

The XRD patterns of TiO_2 thin films on glass substrates deposited at different deposition temperatures from 200 to 500 °C are given in Fig. 1. The diffraction peaks at 25.3°, 37.7°, 48.1°, 53.9° and 55.1° correspond to the (101), (004), (200), (105) and (211) anatase planes [19]. XRD studies showed that the as-deposited films prepared at substrate temperatures below 500 °C were amorphous. The anatase peak (101) becomes apparent for the films deposited at 500 °C. Annealing at 500 °C results in anatase phase for films deposited at or above 300 °C.

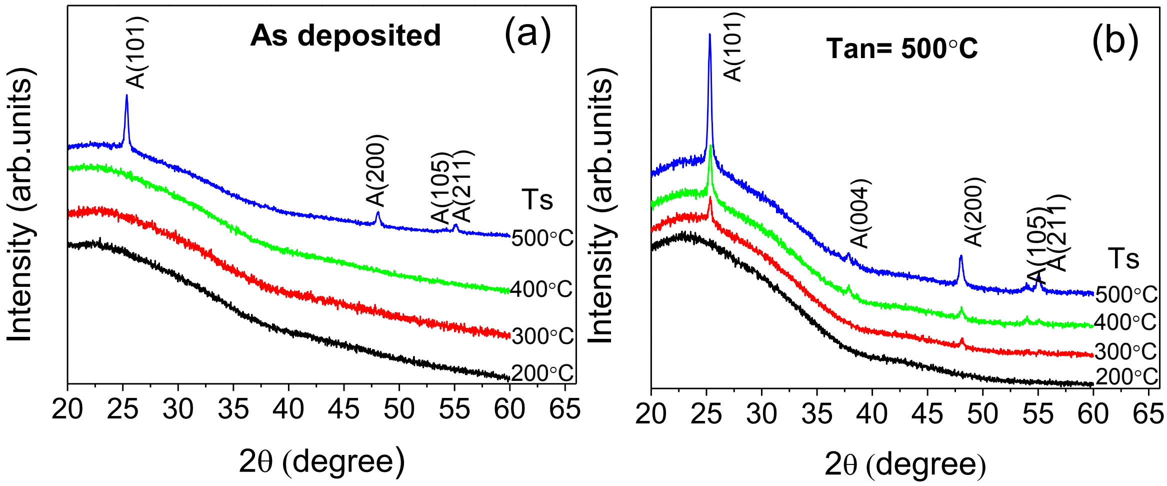

Fig. 1. XRD patterns of TiO_2 thin films with glass substrates deposited at various temperatures from 200 to 500 °C: (a) as-deposited thin films, (b) thin films annealed at 500 °C

Fig. 2 shows XRD patterns of TiO_2 thin films deposited on silicon substrates. XRD result showed the films deposited at or below 300 °C were amorphous, however the films deposited at or above 400°C have anatase structure. Annealing at 500 °C results in formation of anatase phase regardless of the deposition temperature. Further annealing at 700 °C has significantly changed the film structure, the films deposited below or at 400 °C remain anatase, however the films deposited at 500 °C compose of the mixture of anatase and rutile phases.

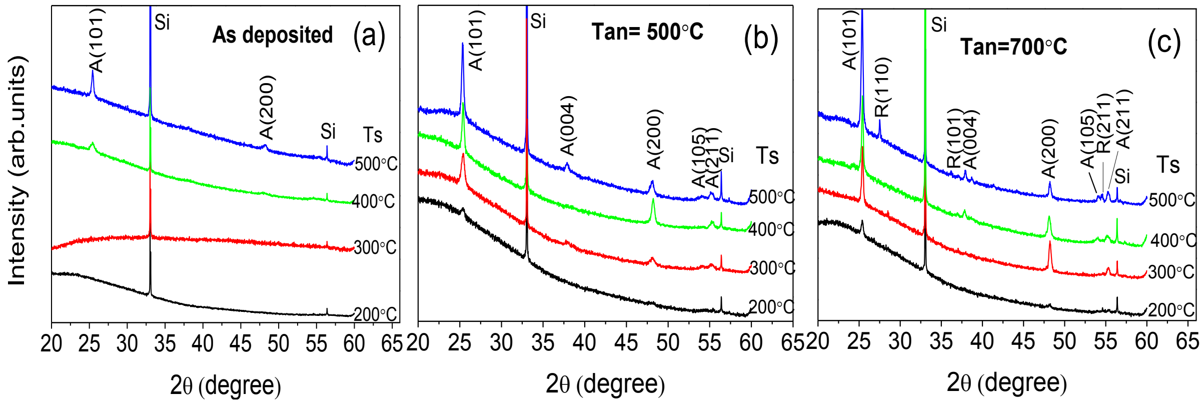

Fig. 2. XRD patterns of TiO_2 thin films on silicon substrates. (a) as-deposited thin films, (b) thin films annealed at 500 °C, (c) thin films annealed at 700 °C

The mean crystallite size of the TiO_2 films deposited onto different substrates and annealed at different temperatures were calculated by applying the Scherrer's formula [13] on the (101) anatase peak and the values obtained are presented in Table 1. The mean crystal size of anatase phase increased with the increasing deposition temperature. Annealing of TiO_2 thin films can improve their crystallinity and also increase the mean crystal size [20].

Table 1. The mean crystallite size of TiO_2 thin films deposited at different deposition temperature (T_s) and annealed at 500 °C and 700 °C

Deposition temperature T_s (°C)	**Mean crystallite size (nm)**				
	Glass substrate		**Silicon substrate**		
	As-deposited	**Annealed at 500 °C**	**As-deposited**	**Annealed at 500 °C**	**Annealed at 700 °C**
200	-	-	-	21	30
300	-	26	-	28	37
400	-	29	17	31	40
500	28	32	31	32	42

3.1.2. Raman spectroscopy

Raman spectrum was used to further confirm the crystal phase of TiO_2 films. Fig. 3 shows Raman spectra of TiO_2 films grown at different substrates and annealed at 500 °C and 700 °C. TiO_2 thin films grown onto glass substrates and annealed at 500 °C (Fig. 3, a) exhibit the bands at around 142 (E_g), 197 (E_g), 398 (B_{1g}), 520 (B_{1g}) and 639 (E_g) cm^{-1} which are assigned to TiO_2 anatase [21]. TiO_2 thin films deposited on silicon substrates and annealed at 500 °C (Fig. 3, b) showed in addition the peaks at 302 and 520 cm^{-1} belonging to the Si substrate. No rutile peaks were detected after annealing at 500 °C. TiO_2 films deposited on Si-substrate and annealed at 700 °C showed anatase phase when grown in the temperature range of 200–400 °C. However, TiO_2 films deposited at 500 °C and annealed at 700 °C showed additional Raman bands at round 232 ($B_{1g)}$ and 440 (E_g) cm^{-1} which belong to rutile phase [22], and thereby confirm a mixture of anatase and rutile phases in these films. The mixture phases after annealing above 700 °C have been also observed in sol-gel spin coating and ultrasonic spray pyrolysis [12, 13].

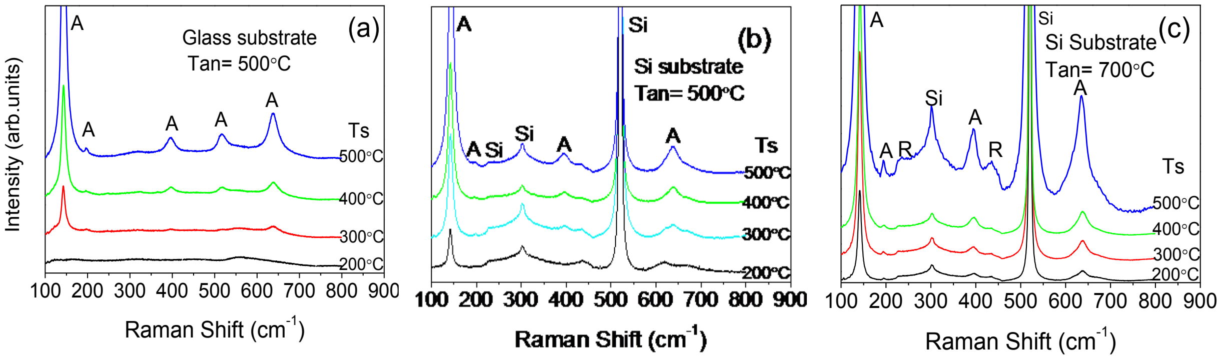

Fig. 3. Raman spectrum of TiO_2 films deposited at various temperatures: (a) as-deposited films on glass substrate, (b) films deposited on Si- substrate and annealed at 500 °C, (c) films deposited on Si-substrate and annealed at 700 °C. Si means Si-substrate, A- anatase, R- rutile

3.1.3. Optical properties

The optical transmittance spectra of TiO_2 thin films deposited onto glass substrates at temperatures from 200 to 500 °C and followed by annealing at 500 °C are presented in Fig. 4. The TiO_2 thin films were highly transparent in the visible region with transmittance above 90% for the as-deposited samples and above 80% for the annealed samples. The total transmittance decreased with increasing the deposition temperature. The interference patterns indicate the homogeneity of the films. The decrease in the optical transmittance after annealing can be related to the increase of the light diffusion with the crystallite size and particle aggregation [23].

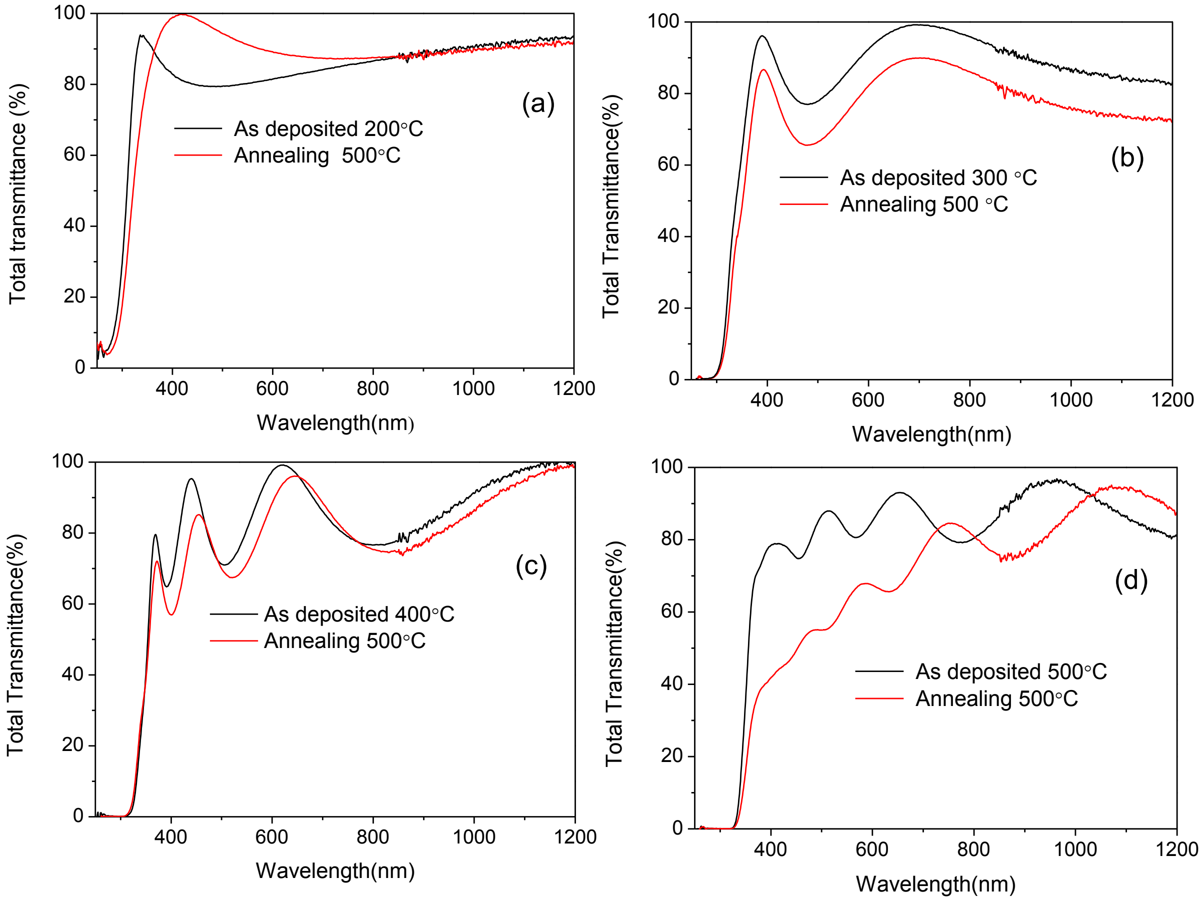

Fig. 4. Total transmittance spectra of TiO_2 thin films on glass substrates: (a) as-deposited at 200 °C and followed by annealing at 500 °C, (b) as-deposited at 300 °C and followed by annealing at 500 °C, (c) as-deposited at 400 °C and followed by annealing at 500 °C, (d) as-deposited at 500 °C and followed by annealing at 500 °C

The optical band gap was determined using the Tauc expression [24],

$$\alpha = \frac{A}{hv}\left(hv - E_g\right)^n \tag{1}$$

where A is a proportionality constant, hv is the photon energy, Eg is the band gap and n = ½ for direct or n = 2 for indirect optical transitions. The optical band gap was obtained by extrapolating the linear part of the plot of $(\alpha hv)^2$ against hv to the photon energy axis by assuming direct band gap is shown in Fig. 5.

The band gaps of the as-deposited films were 3.46, 3.41,3.36, 3.29 eV respectively with increasing deposition temperature from 200 to 500 °C and it decreased slightly after annealing at 500 °C, was 3.45, 3.35, 3.27 and 3.22 eV respectively. The decrease in the optical band gap of the TiO_2 films with annealing temperature might be the result of the increased crystallinity of the annealed films [20].

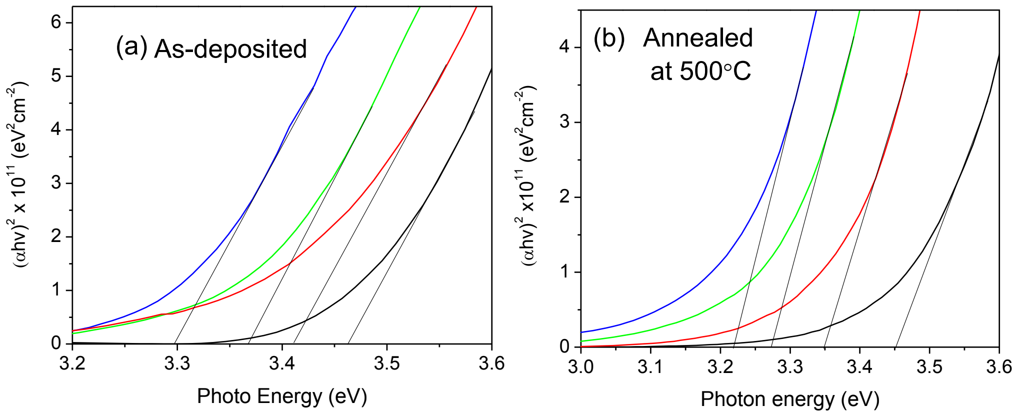

Fig. 5. Band gap of TiO_2 thin films with glass substrates: (a) as-deposited films deposited at substrate temperature from 200 to 500 °C. (b) as-deposited films followed by Annealing at 500 °C

The thickness of films on glass substrates is shown in Table 2. The thickness of as-deposited films increased from 110 to 620 nm with increasing deposition temperature from 200 to 500 °C and decreased after annealing at 500 °C. Since the solution feed rate was consistent, then it is implicit that the film thickness increased with increasing deposition temperature owing to the corresponding increase in the reaction rate. The film thickness decreases after annealing at 500 °C, compared to as-deposited films, is related with the burning out of the organic residues in the film [25].

Table 2. Film thickness of as-deposited and annealed films, deposited onto glass substrates at various substrate temperatures (T_s)

T_s(°C)	**As-deposited**		**Annealed at 500 ° C**	
	Film thickness	**Band gap (eV)**	**Film thickness**	**Band gap (eV)**
200	120	3.46	80	3.45
300	180	3.41	170	3.35
400	370	3.36	320	3.27
500	620	3.29	510	3.22

3.2. Electrical Resistivity

Fig. 6 shows the resistivity of the as-deposited and annealed TiO_2 films on silicon substrates. The resistivity of the films decreases with increasing deposition temperature from 200 to 300 °C, which may be due to the change of crystal structure from amorphous to crystalline anatase phase. The resistivity also decreased when increasing the annealing temperature, this phenomenon is due to increase in the grain size which leads to a decrease in the grain boundaries and hence resistivity [25].

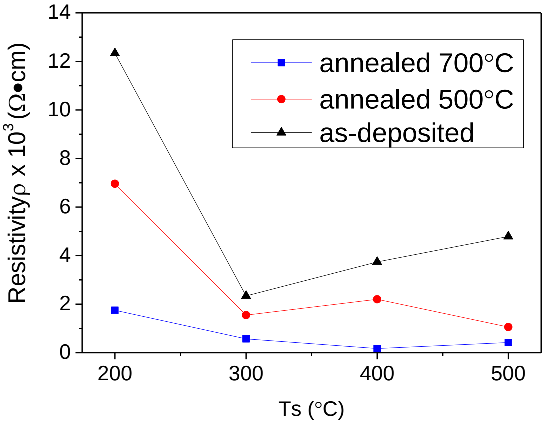

Fig. 6. Resistivity of TiO_2 films deposited on silicon substrates at various substrate temperatures (Ts) and after various annealing temperatures

4. CONCLUSION

Ultrasonic spray pyrolysis method was used to deposit TiO_2 film and the effect of deposition and annealing temperature on the structural, optical, electrical properties was investigated. The XRD data reveals that the as-deposited grown below 400 °C onto glass substrate and below 300 °C onto Si substrate are amorphous. Annealing at 500 °C results in formation of anatase structure, if the films are deposited at temperatures $\geq$ 300 °C onto glass substrates or in the temperature range 200–500 °C onto Si substrates. The mean crystallite size of anatase structure remains in the range of 20–32 nm irrespective of the deposition, annealing temperature and substrate. Further annealing of TiO_2 films on Si substrate at 700 °C led to the formation of the mixture of anatase and rutile phase if deposited at 500 °C and increase in the average crystallite size of the anatase structure to the range of 30–40 nm. As-deposited TiO_2 films show high optical transmittance and band gap values in the range of 3.5–3.3 eV if deposited at 200–500 °C. Film thickness was found to increase with deposition temperature and decrease after annealing at 500 °C. The resistivity of TiO_2 films depends on the deposition temperature and was found to decrease with increasing the annealing temperature. The films deposited above 300 °C and annealed at 500 °C are applicable as window layer in solar cell devices and will be tested in further research.

ACKNOWLEDGEMENT

This study was financially supported by the Estonian Ministry of Education and Research project IUT19-4, and by the European Union through the European Regional Development Fund project TK141 “Advanced materials and high-technology devices for energy recuperation systems”.

REFERENCES

[1]. KOHTANI, S., KAWASHIMA, A., MIYABE, H. Reactivity of Trapped and Accumulated Electrons in Titanium Dioxide Photocatalysis. *Catalysts*, 2017, Vol. 7.

[2]. RODRIGUEZ, DF., PERILLO, PM., BARRERA, MP. High performance TiO_2 nanotubes antireflection coating. *Materials science in semiconductor processing,* 2017, Vol. 71, p. 427–432.

[3]. SINGH, S., SHARMA, V., SACHDEV, K. Investigation of post annealing effects on Nb: TiO_2 transparent conducting thin films. *Advanced science letters,* 2016, Vol. 22, p. 3773–3776.

[4]. ALI, T., AHMED, A., SIDDIQUE, MN., TRIPATHI, P. Enhanced dielectric properties of Fe-substituted TiO_2 nanoparticles *Physica B-condensed matter*, 2017, Vol. 534, p. 1–4.

[5]. CARMONA-QUIROGA, PM., MARTINEZ-RAMIREZ, S., VILES, HA. Efficiency and durability of a self-cleaning coating on concrete and stones under both natural and artificial ageing trials. *Applied surface science*, 2017, Vol. 433, p. 312–320.

[6]. MA, QL., MA, SQ., HUANG, YM. Enhanced photovoltaic performance of dye sensitized solar cell with ZnO nanohoneycombs decorated TiO_2 photoanode. *Materials letters*, 2018, Vol. 218, p. 237–240.

[7]. NOURI, E., MOHAMMADI, MR., XU, ZX., DRACOPOULOS, V., LIANOS, P. Improvement of the photovoltaic parameters of perovskite solar cells using a reduced-graphene-oxide-modified titania layer and soluble copper phthalocyanine as a hole transporter. *Physical chemistry chemical physics,* 2018, Vol. 20, p. 2388–2395.

[8]. LIRA-CANTU, M., CHAFIQ, A., FAISSAT, J., GONZALEZ-VALLS, I., YU, YH. Oxide/polymer interfaces for hybrid and organic solar cells: Anatase vs. Rutile TiO_2. *Solar energy materials and solar cells,* 2011, Vol. 95, p. 1362–1374.

[9]. MAHALINGAM, S., EDIRISINGHE, MJ. Characteristics of electrohydrodynamically prepared titanium dioxide films. *Applied physics a-materials science & processing*, 2007, Vol. 89, p. 987–993.

[10]. PAUL, S., CHOUDHURY, A. Investigation of the optical property and photocatalytic activity of mixed phase nanocrystalline titania. *Applied nanoscience*, 2014, Vol. 4, p.839–847.

[11]. LUTTRELL, T., HALPEGAMAGE, S., TAO, JG., KRAMER, A., SUTTER, E., BATZILL, M. Why is anatase a better photocatalyst than rutile? Model studies on epitaxial TiO_2 films. *Scientific reports*, 2014, Vol. 4, No. 4043.

[12]. NAKARUK, A., RAGAZZON, D., SORRELL, CC. Anatase-rutile transformation through high-temperature annealing of titania films produced by ultrasonic spray pyrolysis. *Thin solid films*, 2010, Vol. 518, p. 3735–3742.

[13]. OJA, I., MERE, A., KRUNKS, M., NISUMAA, R., SOLTERBECK, CH., ES-SOUNI, M. Structural and electrical characterization of TiO_2 films grown by spray pyrolysis. *Thin solid films*, 2006, Vol. 515, p. 674–677.

[14]. YU, JG., ZHAO, XJ., ZHAO, QN. Effect of surface structure on photocatalytic activity of TiO_2 thin films prepared by sol-gel method. *Thin solid films*, 2000, Vol. 379, p. 7–14.

[15]. WATANABE, F., MOTODA, S., MORITA, M. Photo-Potential Property of TiO_2 Electrode Prepared by the Screen Printing Method. *Batteries and energy technology joint general session*, 2017, Vol. 75, p. 93–100.

[16]. NEGISHI, N., TAKEUCHI, K. Preparation of TiO_2 thin film photocatalysts by dip coating using a highly viscous solvent. *Journal of sol-gel science and technology*, 2001, Vol. 22, p. 23–31.

[17]. SUN, HF., WANG, CY., PANG, SH., LI, XP., TAO, Y., TANG, HJ., LIU, M. Photocatalytic TiO_2 films prepared by chemical vapor deposition at atmosphere pressure. *Journal of non-crystalline solids*, 2008, Vol. 354, p. 1440–1443.

[18]. ENNACERI, H., BOUJNAH, M., TALEB, A., KHALDOUN, A., SAEZ-ARAOZ, R., ENNAOUI, A., EL KENZ, A., BENYOUSSEF, A. Thickness effect on the optical properties of TiO_2-anatase thin films prepared by ultrasonic spray pyrolysis: Experimental and ab initio study. *International journal of hydrogen energy*, 2017, Vol. 42, p. 19467–19480.

[19]. FAZLI, FIM., AHMAD, MK., SOON, CF., NAFARIZAL, N., SURIANI, AB., MOHAMED, A., MAMAT, MH., MALEK, MF., SHIMOMURA, M., MURAKAMI, K. Dye-sensitized solar Cell using pure anatase TiO_2 annealed at different temperatures. *OPTIK*, 2017, Vol. 140, p. 1063–1068.

[20]. C.-P, LIN., H. CHEN, A. NAKARUK, P. KOSHY, C.C. SORRELL. Effect of annealing temperature on the photocatalytic activity of TiO_2 thin films. *Energy Procedia*, 2013, Vol. 34, p. 627–636.

[21]. BOUACHIBA, Y., BOUABELLOU, A., HANINI, F., KERMICHE, F., TAABOUCHE, A., BOUKHEDDADEN, K. Structural and optical properties of TiO_2 thin films grown by sol-gel dip coating process. *Materials Science-Poland*, 2014, Vol. 32, p. 1–6.

[22]. JUMA, AO., ACIK, IO., MIKLI, V., MERE, A., KRUNKS, M. Effect of solution composition on anatase to rutile transformation of sprayed TiO_2 thin films. *Thin solid films*, 2015, Vol. 594, p. 287-292.

[23]. BEN KAROUI, M., KADDACHI, Z., GHARBI, R. Optical properties of nanostructured TiO_2 thin films. TUNISIA-JAPAN SYMPOSIUM, 2015, R&D of Energy and Material Sciences for Sustainable Society. [CD]. Gammarth, TUNISIA, 2014 Nov 28–30.

[24]. TAUC, J. Optical properties and electronic structure of amorphous Ge and Si. *Physica status solidi (b)*, 1966, Vol. 15, p. 627–637.

[25]. Oja, I., Mere, A., Krunks, M., Solterbeck, C-H., Es-Souni, M. Properties of TiO_2 Films Prepared by the Spray Pyrolysis Method. *Solid State Phenomena*, 2004, Vol. 99–100, p. 259–264.

[26]. BAKRI, AS. Effect of Annealing Temperature of Titanium Dioxide Thin Films on Structural and Electrical Properties. ICESNANO 2016, International Conference on Engineering, Science and Nanotechnology. [CD]. Solo, Indonesia. 2016 Aug 03–05.

CYSENI 2018, May 23-25, Kaunas, Lithuania
ISSN 1822-7554, www.cyseni.com

THE USE OF MATHEMATICAL MODELS FOR MODELLING OF SULPHUR DIOXIDE SORPTION ON MATERIALS PRODUCED FROM FLY ASHES

N. Czuma, K. Zarębska, P. Baran
AGH University of Science and Technology
Al. Mickiewicza 30, 30-05 Cracow – Poland
Email: nczuma@agh.edu.pl

P. Gauden
Nicolaus Copernicus University in Toruń
Gagarina ul. 7, 87-100 Toruń – Poland

ABSTRACT

Fly ash-derived zeolites may become attractive alternative for natural zeolites as well as for zeolites produced out of pure chemicals. Growing awareness of need to protect environment is an incentive for the use of waste materials as a raw materials for production of microporous, multi application materials - zeolites.

Additionally, environmentally friendly actions undertaken in order to reduce air pollution intensify needs to search for new options for capturing hazardous air pollutants out of flue gases. Zeolites can be used as air pollutants sorbents.

In this work there were presented results of sulphur dioxide, one of flue gases component, sorption experiments. The adsorbent used was zeolite synthesized from fly ash, from selected polish power plant.

For the purpose of investigation there were chosen fly ash zeolite samples synthesised with the use of different methods. Parameters were selected in such a way that one type of zeolite material was received. For the purpose of description of received results the mathematical models were used.

As a result of performed experiments it was found that the synthesized materials may be used as sulphur dioxide sorbents. Analysis of experimental data allows for noticing significant differences in adsorbed amounts of sulphur dioxide in case of different synthesis methods. Despite the fact that the same type of zeolite was received, samples presented differentiated values for capture, due to different conversion factors of fly ash into zeolite materials. All the sorption tests were performed three times on the same sample in order to check how sorption process will look like after regenerating the sample. Additionally it was a preliminary check of regeneration possibilities itself, which allowed to draw conclusions that material will regenerate.

Freudlich and Langmuir models were used to describe the received data. Freudlich adsorption isotherm generally better described the obtained data, despite the first sorption cycle where Langmuir isotherm seemed to provide better results. This fact was attributed to different mechanism of sorption in first cycle – chemisorptions. Freudlich isotherm data confirmed heterogeneity of adsorbents surface.

Keywords: fly ah, zeolite, sorption, modelling

CYSENI 2018, May 23-25, Kaunas, Lithuania
ISSN 1822-7554, www.cyseni.com

THE TRIBOLOGICAL PROPERTIES OF Al_2O_3 BASED COMPOSITE COATINGS DEPOSITED BY PLASMA SPRAYING

J. S. Mathew, L. Marcinauskas, B. Thanigachalam, R. Česnavičius
Kaunas University of Technology, Kaunas – Lithuania
Email: jacob.mathew@ktu.edu

M. Milieška, R. Kėželis
Lithuanian Energy Institute, Kaunas – Lithuania

A. Kupec, M. Kalin
Laboratory for Tribology and Interface Nanotechnology
Bogišićeva 8, 1000 Ljubljana – Slovenia

ABSTRACT

The aim was to determine the tribological properties of Al_2O_3, Al_2O_3-graphite and Al_2O_3-ZrO_2 coatings. Using atmospheric plasma spraying, ceramic coatings were deposited on stainless steel substrates. For the deposition process, Al_2O_3, Al_2O_3-10 wt.% graphite and Al_2O_3-10 wt.% ZrO_2 powders were employed. The flow rates of air and hydrogen were 4.7 g/s and 0.1 g/s, respectively. The employed torch power was ~40 kW. The surface morphology was examined using a scanning electron microscope (SEM) Hitachi S-3400N. The elemental composition of the coatings was determined by energy dispersive X-ray spectroscopy (EDS) Bruker Quad 5040 spectrometer. The surface roughness was measured using a Mitutoyo Surftest-SJ-210-Ver2.00 profilometer. Structural characterization of the coatings was carried out using X-ray diffractometry. The tribological properties of the samples were measured using a CETR-UMT-2 ball-on-disc tribometer. The surface roughness (R_a) of the Al_2O_3 coatings was 4.04 μm and with the addition of graphite, it was 3.41 μm. For Al_2O_3-ZrO_2 coatings, the surface roughness was 3.65 μm. It could be seen from the SEM images that with increase in torch power, the surface disorder had increased and with addition of graphite, sphere-like globules were formed. The XRD measurements indicated that the dominant phases in the Al_2O_3 and Al_2O_3-graphite coatings were α-Al_2O_3 and β-Al_2O_3. And with Al_2O_3-ZrO_2 it was tetragonal-ZrO_2. Friction coefficient of the Al_2O_3 coatings at 1 N load was ~0.72, with graphite it was ~0.59, and with ZrO_2 it was ~0.75. The wear rate for the coatings were similar being in the range of ~10^{-5} mm^3/Nm with an exception for alumina-zirconia coatings wherein a plastic deformation was observed.

Keywords: plasma spraying, alumina, coatings, tribological properties

1. INTRODUCTION

The wear of metallic surfaces is a common feature arising from continuous use of equipment that is a huge demerit. There are varied contact forces acting at the tribological level that cause high friction and abnormal wear rates [1–4]. One of the most commonly used alloy in the material industry is steel but it is found to have low intrinsic hardness. Therefore, to override this demerit, having tribological applications in mind, it would be effective to use plasma spraying to coat the alloy. The merits of using the plasma spraying technique are the high flame temperature, high particle velocity and increased melting-degree rate with good surface characteristics. It is generally most expedient to coat the alloy with ceramic materials considering their high hardness and therefore promisingly reduced wear rates [5–9]. Within ceramic coatings, Al_2O_3 coatings have traditionally had an edge due to high hardness, excellent toughness and strength, and neat tribological wear properties [10–16].

Riedl et al. [17] obtained that the coefficient of friction for Al_2O_3 coatings varied in the range from 0.6–0.8, while wear rates spanned from $(1–3)\cdot10^{-5}$ $mm^3/N\cdot m$. R. Younes et al. [13] demonstrated the importance of having an additive such as zirconia which had a higher toughness in comparison to alumina. Zirconia also exhibits a very high strength but relatively lesser hardness in comparison to alumina [13]. Therefore, to juxtapose both would mean using the merits of alumina (for higher hardness) and zirconia (for higher toughness). It was demonstrated that for a case with reinforcements of 25 wt.% ZrO_2 into the Al_2O_3 coatings, the friction coefficient was 0.45 which was quite meritorious [13]. A facet of its employment can be found be in high temperature applications which require superior durability which is imperative to address [13, 15]. P. Bagde et al. [18] showed the imperativeness of using a dry (self) lubricant such as graphite into alumina coatings where Al_2O_3-13%TiO_2 coatings had an upper-range friction coefficient of ~0.40 and with the addition of graphite and Ni, it dropped down to ~0.35 for the highest load condition. Graphite has been known typically to reduce friction coefficients because of good interfacial compatibility and lubricative properties [18, 19]. In another case, depicting the importance of alumina, for pure NiCrAlY, a wear rate of $5\cdot10^{-4}$ $mm^3/(N\cdot m)$ with the addition of Al_2O_3 (18 wt.%), was found to decrease to $5\cdot10^{-6}$ $mm^3/(N\cdot m)$ albeit an increase in friction coefficient from ~0.5 to ~0.7. The properties of aluminium oxide are therefore quite imperative to research with varied additive materials. Another aspect would be in advanced orthopaedics which employs alumina ceramic coatings on plastic components [22, 23]. Therefore, it is important to study the tribological properties of alumina-based composite coatings to tailor-make according to the specific needs of the industry.

Additionally, the properties of the coatings by plasma spraying also depend on process parameters such as type of additive material, its relative concentration etc. [10–17, 20]. Within process parameters, the commonly used gas mixture is either argon-hydrogen or nitrogen-hydrogen [9, 14, 15, 20], we have herein employed air-hydrogen, air being primary gas, as the procurement, availability, toxicity etc. work out more feasible and we can therefore research the same. The mechanical and tribological definitions of the coatings have a significant effect arising from the employed torch power and the spraying distance [21]. Therefore, the research here aims to study the tribological effects of Al_2O_3-based composite coatings using air-hydrogen plasma with different additive materials at a definite torch power and spraying distance. The coatings are as-sprayed Al_2O_3 *(A)*, Al_2O_3-10 wt.% graphite *(AG)* and Al_2O_3-10 wt.% ZrO_2 *(AZ)* coatings

2. EXPERIMENTAL SETUP

The coatings were sprayed on stainless steel substrates (AISI 304L) at atmospheric pressure using a direct current plasma torch. The plasma torch used in this experiment was constructed at the Lithuanian Energy Institute [24]. The steel substrates (dimensions of 40 × 10 × 1.5 mm) were polished and chemically cleaned before starting the formation process. The steel substrates were placed on a water-cooled sample holder. Air was used as both the primary gas (total flow rate of 4.72 g/s) and the powder-carrier gas (flow rate of 0.60 g/s). Hydrogen (0.1 g/s) was used as the secondary gas to increase the plasma temperature. The experiments were performed using a cylindrically shaped length of 150 mm reactor which was connected to the exit of the anode.

The coatings were obtained using the three following feedstock materials: Al_2O_3 *(A)*, Al_2O_3-10 wt.% graphite *(AG)* and Al_2O_3-10 wt.% ZrO_2 powders *(AZ)*. Sprayed alumina powders were of a non-regular shape with a size range from 63 to 140 μm. Meanwhile, the graphite feedstock powders were non-regular flake-like shaped with a size range 20-63 μm. The zirconia powders were mostly spherical in shape of 106 ± 11 μm in diameter. The feedstock powders were dried for 18 h at ~330 K before starting the spraying process. The powders were injected into the reactor nozzle at a distance of 150 mm from the exit. The duration of the deposition process was 40 s. The plasma torch was moving in the x-axis direction both forward and backward during the deposition. The spraying distance was 70 mm. The coatings were deposited at a torch power of ~40 kW. Each coating-series had a set of three samples to ensure a feasible repeatability factor.

Average plasma temperature in the injection locale of the powders was 3330 ± 50 K. Meanwhile, the mean plasma temperature and velocity at the nozzle outlet was 3445 ± 50 K and 1360 ± 20 m/s, respectively. The mean temperature of the plasma jet at the exhaust of the plasma torch was calculated from the heat balance corresponding to the plasma enthalpy. The methodology of the plasma velocity and temperature calculation is found here [25, 26]. The surface morphology of the as-sprayed coatings was characterized by scanning electron microscopy (SEM) using a Hitachi S-3400N. The elemental composition of the coatings was investigated by energy dispersive X-ray spectroscopy (EDX) (Bruker Quad 5040 spectrometer, AXS Microanalysis GmbH). The measurements were performed for a surface area of 1.05 mm^2 at 5 different points. The surface roughness of the as-sprayed coatings was measured on a portable surface roughness tester Mitutoyo Surftest SJ-210 Series (Version 2.00 with standard ISO 1997). Roughness was measured with standard surface indenter and the length of one measurement was 4 mm. For relevant statistical evaluation, the measurements on each coating were done at least 4 times. The coating structure was analyzed by X-ray diffraction (XRD) (Bruker D8 Discover) with a standard Bragg-Brentano focusing geometry in a 5–80° range using the CuKα (λ = 0.154059 nm) radiation. The tribological tests were performed on a tribometer (UMT-2, Bruker, USA) using a ball-on-disc configuration. The upper specimen was an Al_2O_3 ceramic ball and the lower specimen was stainless-steel coated with Al_2O_3 based coating. The counter-part material (upper specimen) used in the tribological tests was a commercially available ceramic ball (Al_2O_3 – 99.5%) of grade 10 and diameter 10 mm. Tribological tests were conducted using a reciprocating-sliding process that had a stroke length of 5 mm. The sliding velocity was 0.05 m/s and the frequency was 10 Hz. The test duration was 3000 s with the overall sliding distance being 150 m. The tribological testing was performed at 1 N load. All tribological sliding tests were conducted in dry-sliding contact (without additional lubrication) at 21 °C and relative humidity RH = 20 ±5%. The measurement on each coating-type was performed three times to ensure relevant statistical evaluation. Hereby presented values of the friction coefficient show an average value of the steady-state friction coefficient; in case a steady-state friction coefficient had not been reached, the last 10% coefficient of friction COF with the corresponding standard deviations were considered. The amount of material lost in the wear scars left after the tribological tests was analyzed with a 3D white-light optical interferometer (Counter GT- K0, Bruker, USA), with the use of software Vision64. Measurement analysis was performed to get a better view of the affected area. The normalized wear rates of different coatings were calculated as per the standard procedure [27].

3. RESULTS AND DISCUSSIONS

It could be seen from the SEM image (Fig. 1, a) that in the case of Al_2O_3 coatings, there were agglomerates that were rather irregular in shape and its size was ~10 μm at large. The coating contained semi-melted particles and a few microcracks were also observed. The coating was fairly-well adhered to the substrate. With the addition of graphite, (Fig. 1, b) it could be seen that globules were formed that were larger in size. The voids in the interface had increased and there was a mixture of particles, i.e. fully-melted and semi-melted. The size of the particles in this case ranged from 2 to 20 μm. The surface texture of the coatings seemed to be disordered in comparison to the former.

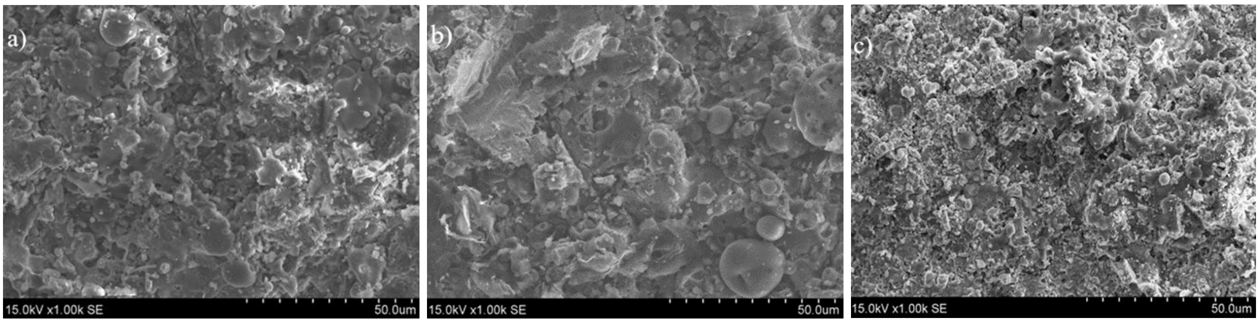

Fig. 1. SEM micrographs of (a) Al_2O_3 coatings-*A*, (b) Al_2O_3-10 wt.% Graphite-*AG*, (c) Al_2O_3-10 wt% ZrO_2-*AZ*

With the addition of ZrO_2 to the Al_2O_3 coating (Fig. 1, c), compactness in the coatings could be noted with a formation of globules and lamellae. There were no predominant microcracks at large. The percentage of melted particles was high. Size-ranges from 5 to 25 µm were observed. The porosity of the coating was perceived to be quite less. The coating seemed to be relatively homogeneous and ordered compared to alumina and alumina-graphite coatings.

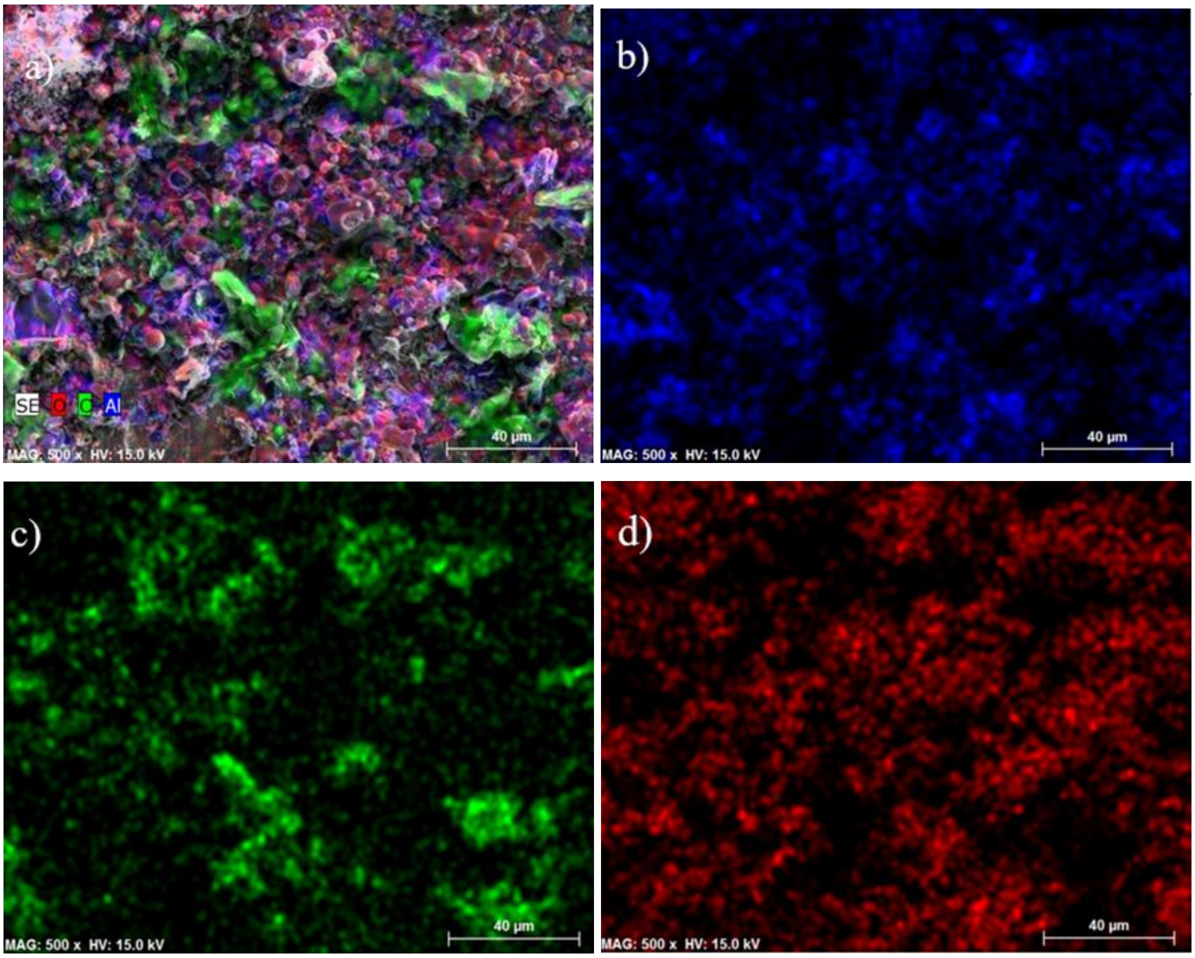

Fig. 2. SEM micrographs and elemental maps of (a) AG, (b) Aluminium, (c) Carbon, (d) Oxygen

The elemental distribution of the Al_2O_3 coating with the addition of graphite is represented in the above Fig. 2. It was observed that there was a clear homogeneity in the elemental distribution of the coating. The graphitic particle-size ranged from 10 to 40 µm. The mass ratio of O/Al for the graphitic coating was recorded to be 1.60 while in the case of pure Al_2O_3 coating it was 0.99. The percentage-by-weight of graphite in the coating was found to be ~27 wt. % and there was also a substantial percentage of silicon to the tune of ~7 wt.%. In the case of Al_2O_3-ZrO_2 coatings (Fig. 3), the O/Al ratio was observed to be 1.32 with ~57 wt.% of zirconium. The size range of zirconia particles was found to be 5–20 µm.

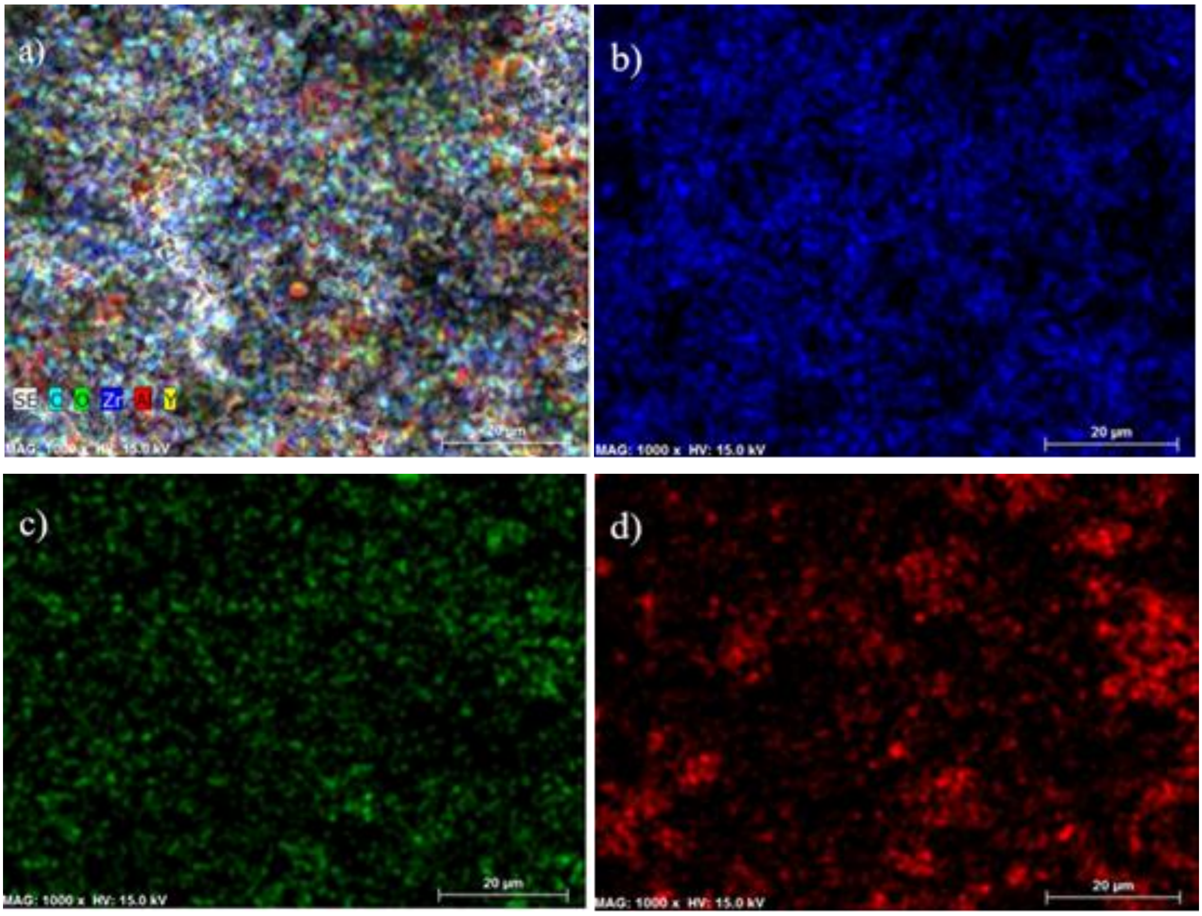

Fig. 3. SEM micrographs and elemental maps of (a) AZ, (b) Zirconium, (c) Oxygen, (d) Aluminium

The surface roughness (R_a) of the Al_2O_3 coatings (Fig. 4) was observed to be 4.04 µm and with the addition of graphite there was an evident drop in the surface roughness to 3.41 µm, reasons are attributed to well-known self-lubricating properties and bonding properties of graphitic particles. With the addition of ZrO_2 to Al_2O_3, the surface roughness had also decreased but not as much as graphite, to a tune of 3.65 µm. In this case, since an isotropic nature in the morphology distribution was observed, this could be a reason for the reduction in friction coefficient.

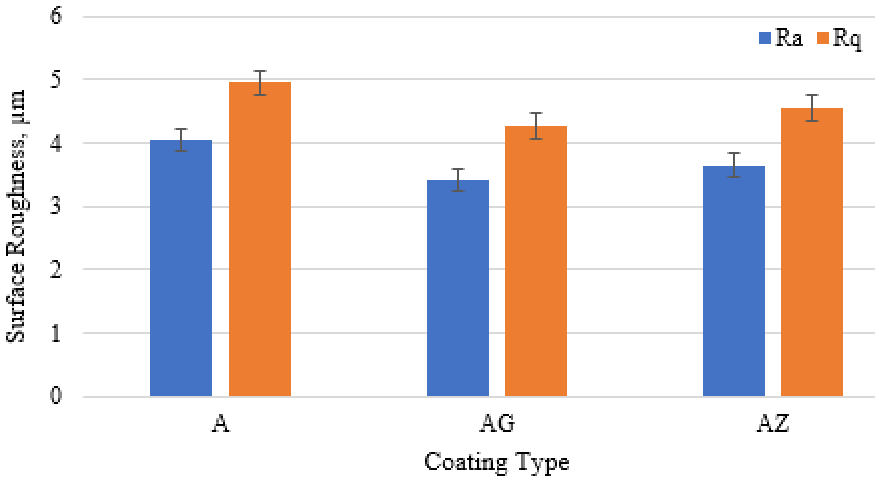

Fig. 4. Surface Roughness of the Al_2O_3 based coatings

Fig. 5 demonstrates the XRD patterns of as-sprayed Al_2O_3 and Al_2O_3-graphite coatings and Al_2O_3-ZrO_2 coatings. Al_2O_3 coatings were composed of rhombohedral α-Al_2O_3, hexagonal β-Al_2O_3

and cubic γ-Al_2O_3 phases. Additionally, it was found that β-Al_2O_3 is the dominant phase of the as-sprayed Al_2O_3 coatings. The high and low intensity peaks at ~7.8°, and ~15.7° are associated with sodium aluminium oxide (card No. 32-1033) with the β-alumina (002), and (004) orientations, respectively. The highest intensity peak obtained at ~43.7° could be attributed to α-Al_2O_3 (113) phase in addition to signals from the steel substrate. α-Al_2O_3 (012) at 25.7°, (104) at 35.2° and (116) 57.6° diffraction peaks were also observed in the coatings. The low intensity peaks at 45.9° and 66.9° could be related to γ-Al_2O_3 phases. With the addition of graphite, significant changes in the XRD patterns of the as-sprayed Al_2O_3-graphite coatings were noted. The additional narrow peak (g) at $2\theta = 26.60°$ is attributed to the formation of graphite (002) plane in the coatings. The intensities of the alumina peaks were diminished with graphite incorporation. In the case of ZrO_2 coatings, the peak intensities were observed at 30.42°, 35.33°, 50.47° and 59.96° for tetragonal-ZrO_2 (t) with orientations (101), (110), (200) and (211) respectively. And less predominant peaks for monoclinic-ZrO_2 (m) at 30.76° and 43.79°. The strength and toughness of the matrix is expressed to be quite dependent on the phase t-ZrO_2 [28].

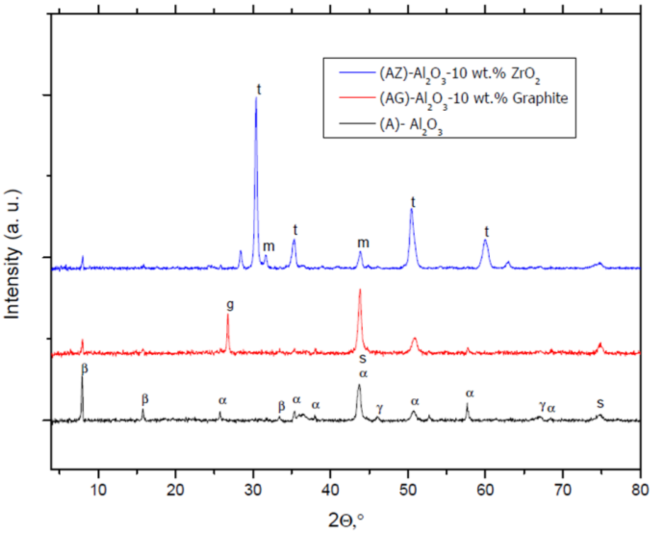

Fig. 5. X-ray diffraction patterns of the Al_2O_3-based coatings

The scheme of dry sliding friction coefficient with sliding distance for sample coatings are described in the Fig. 6. The friction-coefficient curve of the coating was characterized by two distinct regimes, called running-in and steady state. These were associated to the different types of wear mechanisms, typically noticed during dry sliding friction tests of coatings when plasma sprayed [20, 21]. During the running-in stage, due to contact area expansion caused by the decrease in roughness of the counteracting material surfaces, the friction coefficient has an uptrend.

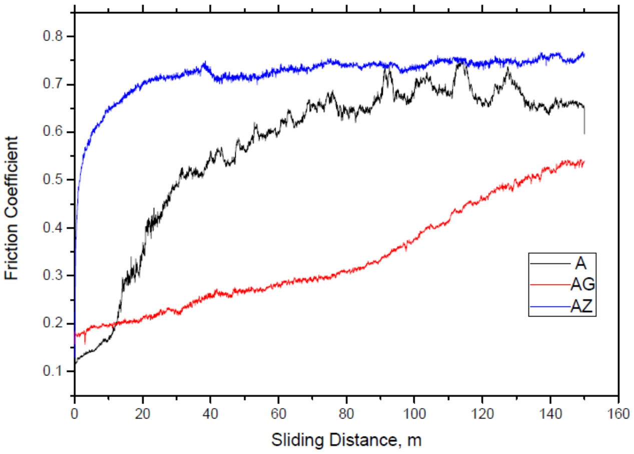

Fig. 6. Friction coefficient evolution as a plot of sliding distance

Consecutively, the coefficient of friction stabilizes due to high asperities under cutting process and thus, represents the wear behavior of the coating and its counterpart Al_2O_3 ball [20]. The friction coefficient of the coatings had increased with sliding distance, as seen from the Fig. 6. For the as-sprayed Al_2O_3 coatings, the friction coefficient had increased from 0.108 to 0.596 and with the addition of graphite it was 0.158 to 0.54. In the case with ZrO_2 coatings which had the highest friction coefficient, the span was from 0.13 to 0.759. The increase in friction coefficient during the wear tests could represent the acceleration of wear or in the worst scenario, a coating failure [29]. The presence of wear-debris that increases with time could possibly result in a higher friction coefficient due a ploughing action in the interface between the coating and the test-ball.

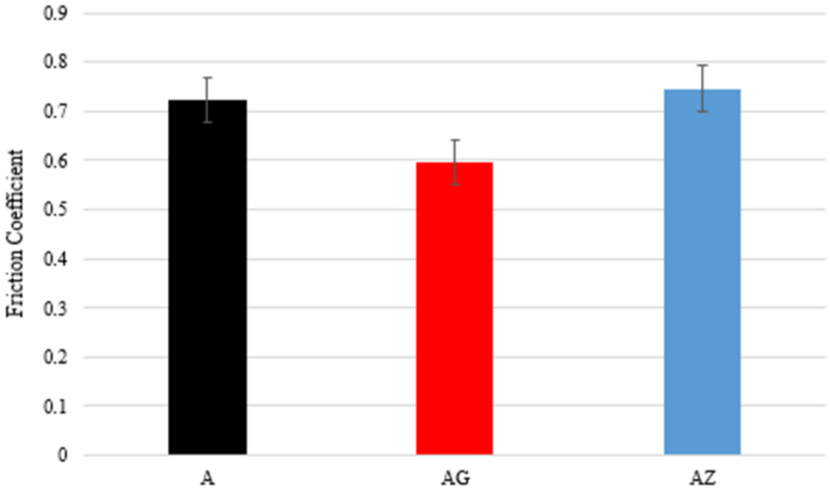

Fig. 7. Friction coefficient of the coatings

The Fig. 7. represents that the average steady state friction coefficient for the Al_2O_3 coatings was 0.72 ± 0.044, and with the addition of graphite, the friction coefficient dropped to 0.59 ± 0.11. In the case with ZrO_2 coatings, the friction coefficient was 0.75 ± 0.029. It can therefore be seen that the addition of 10 wt. % graphite decreases the friction coefficient and 10 wt.% ZrO_2 increases the friction coefficient. It was demonstrated that for a coating that employed graphite which produces a lubricating layer, the friction coefficient had a downtrend. A sacrificial layer being formed between counterfaces that hampers a direct tribological contact. The merit would be significant alleviation of adhesive wear in ceramic coatings. Other advantages are the reduction of shearing stress and the plastic deformation of a surface that is worn. This hereby increases the tribological effectiveness of the ceramic coating [1].

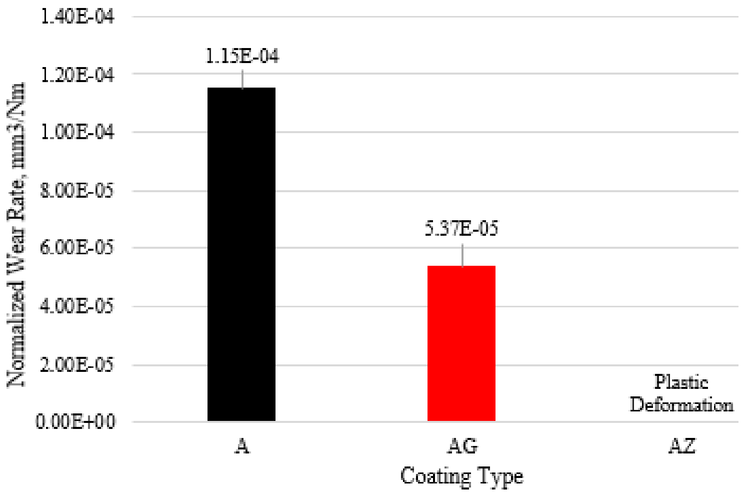

Fig. 8. Normalized wear rate for the Al_2O_3-based coatings

It can be seen from the above Fig. 8 that the normalized wear rate for as-sprayed Al_2O_3 coating was $11.5\cdot10^{-5}$ $mm^3/N\cdot m$ and with the addition of graphite, the wear rate decreases quite sharply which is an indispensable merit. The wear rate decreases more than twice to $5.37\cdot10^{-5}$ $mm^3/N\cdot m$. In the case of ZrO_2 coatings, no significant wear could be detected because of mere material transfer by plastic deformation.

With Al_2O_3 coatings there could be a significant mismatch of thermal heat coefficients that led to humongous heat generation and external stresses. This further could have been potentially impacted in producing a condition of a high friction coefficient and a large wear [29]. It was observed that coatings with high thermal conductivities have a greater wear resistance [15, 29, 30]. This explains a low wear in ZrO_2 coatings.

It was observed that the wear resistance of the coatings had a strong influence on the hardness and its microstructure and the phase composition specifically as in t-ZrO_2 influenced its toughness [28]. With regard to the microstructure, the properties such as grain size, porosity etc. mattered quite substantially [3, 16]. With a high degree of γ-Al_2O_3 in the coatings, there was a reduced abrasive wear-loss [34]. In a study it was shown that with α-Al_2O_3 proliferation, the microhardness and wear resistances improved [35]. In a case for employment of conventional to suspension forms of Al_2O_3 powders, the wear resistance had dropped from $55\cdot10^{-5}$ $mm^3/(Nm)$ to $4\cdot10^{-5}$ $mm^3/(Nm)$. A finer porosity, reduced splat size and proliferated interlamellar bonding had improved the tribological property [20]. Therefore, the size of the powders and its uniformity in deposition influence most evidently the tribological properties of the coatings. Thus, 10 wt.% graphite and 10 wt.% ZrO_2 had lamellar structures defined for a reduced friction-coefficient and a high wear-resistance respectively. Therefore, for high temperature applications (e.g. engine components, cutting tools) that have requirements as in high durability and anti-corrosion properties, alumina-zirconia coatings can be used, the reasons owing to a superior wear resistance [13, 15]. For applications such as in advanced biomedical ceramics [22], wherein Al_2O_3 is primarily used, alumina-graphite coating with a low friction coefficient could be employed. The major utilizations of alumina in general for these are for orthopaedics and articulation devices such as in joints (e.g. hip, shoulder, knee) [22, 23].

4. CONCLUSIONS

Al_2O_3, Al_2O_3-graphite and Al_2O_3-zirconia composite coatings were deposited by atmospheric plasma spraying using air-hydrogen plasma. It was observed that the surface roughness of the as-sprayed alumina coatings (4.04 μm) had decreased with graphite addition (3.41 μm) and zirconia addition (3.65 μm). The oxygen concentration increased with the incorporation of graphite (1.60) and zirconia (1.32) into the as-sprayed coating (0.99) due to the formation of graphite oxide and zirconium dioxide. The friction coefficient dropped from 0.72 to 0.59 with the addition of graphite and escalated from 0.72 to 0.75 with zirconia addition. The normalized wear rate reduced twice less to $5.37\cdot10^{-5}$ $mm^3/N\cdot m$ from $11.5\cdot10^{-5}$ $mm^3/N\cdot m$ with graphite incorporation. Whereas with zirconia incorporation, the result was plastic deformation thereby leading to an insignificant and immeasurable wear. The highlight therefore would be a low friction-coefficient with 10 wt.% graphite and a wear-resistance that is quite high with 10 wt.% zirconia. Therefore for high temperature applications, alumina-zirconia coatings can be used as this would serve a longer life, withstanding wear. Alumina-graphite coatings could be employed in low friction orthopaedic components and articulation devices.

REFERENCES

[1] DENG, W., LI, S., LIU, X., ZHAO, X., AN, Y., ZHOU, H., CHEN, J., A novel approach to fabricate hybrid materials with excellent tribological properties from spray-formed ceramic, *Material Letters*, 2017, Vol. 193, p. 199–202.

[2] TLILI, B., BARKAOUI, A., WALOCK, M., Tribology and wear resistance of the stainless steel. The sol–gel coating impact on the friction and damage, *Tribology International*, 2016, Vol. 102, p. 348–354.

[3] HOLMBERG, K., LAUKKANEN, A,, GHABCHI, A., ROMBOUTS, M., TURUNEN, E., WAUDBY, R., SUHONEN, T., VALTONEN, K., SARLIN, E., Computational modelling based wear resistance analysis of thick composite coatings, *Tribology International*, 2014, Vol. 72, p. 13–30.

[4] HE, L., TAN, Y.-F., TAN, H., ZHOU, C.-H., GAO, L., Tribological properties of nanostructured Al_2O_3–40%TiO_2 multiphase ceramic particles reinforced Ni-based alloy composite coatings, *The Transactions of Nonferrous Metals Society of*, 2013, Vol. 23, p. 2618–2627.

[5] WAN, S., Li D., ZHANG, G., TIEU, A.K., ZHANG, B., Comparison of the scuffing behaviour and wear resistance of candidate engineered coatings for automotive piston rings, *Tribology International* , 2017, Vol. 106, p. 10–22.

[6] GEORGIOU, E.P., VAN DER DONCK, T., PEETERS, M., DREES, D., CELIS, J.-P., Proposed method to examine the effect of cycling temperatures on friction illustrated with intermetallic Ni-Sn coatings sliding against corundum, *Wear*, 2016, Vol. 368–369, p. 453–460.

[7] WANG, K., UNGER, J., TORREY, J.D., FLINN, B.D., BORDIA, R.K., Corrosion resistant polymer derived ceramic composite environmental barrier coatings, *Journal of European Ceramic Society*, 2014, Vol. 34, p. 3597–3606.

[8] MCENTIRE, B.J., BAL, B.S., RAHAMAN, M.N., CHEVALIER, J., PEZZOTTI, G., Ceramics and ceramic coatings in orthopaedics, *Journal of European Ceramic Society*, 2015,Vol. 35, p. 4327–4369.

[9] HEIMANN, R.B., *Plasma Spray Coating Principles and Applications*, Wiley-VCH, 2008.

[10] FAUCHAIS, M.B.P.L., HEBERLEIN, J.V.R., *Thermal Spray Fundamentals. From Powder to Part*, Springer, US, 2014.

[11] KANG, J., XU, B., WANG, H., WANG, C., Influence of contact stress on rolling contact fatigue of composite ceramic coatings plasma sprayed on a steel roller, *Tribology International*, 2014, Vol. 73, p. 47–56.

[12] YANG, Y., WANG, Y., TIAN, W., YAN, D., ZHANG, J., WANG L., Influence of composite powders' microstructure on the microstructure and properties of Al_2O_3-TiO_2 coatings fabricated by plasma spraying, *Materials and Design*, 2015, Vol. 65, p. 814–822.

[13] YOUNES, R., BRADAI, M.A., SADEDDINE, A., MOUADJI, Y., BILEK A., BENABBAS, A., Effect of TiO_2 and ZrO_2 reinforcements on properties of Al_2O_3 coatings fabricated by thermal flame spraying, *The Transactions of Nonferrous Metals Society of*, 2016, Vol. 26, p. 1345–1352.

[14] SONG, E.P., HWANG, B., LEE, S., KIM, N.J., AHN, J., Correlation of microstructure with hardness and wear resistance of stainless steel blend coatings fabricated by atmospheric plasma spraying, *Materials Science and Engineering A*, 2006, Vol. 429, p. 189–195.

[15] LIANG, B., ZHANG, G., LIAO, H., CODDET, C., DING, C., Friction and wear behavior of ZrO_2–Al_2O_3 composite coatings deposited by air plasma spraying: Correlation with physical and mechanical properties, *Surface and Coatings Technology*, 2009, Vol. 203, p. 3235–3242.

[16] MARCINAUSKAS, L., MILIESKA, M., KEZELIS, R., Effect of torch power on the microstructure of plasma sprayed Al_2O_3 coatings, *Surface and Interface Analysis*, 2016, Vol. 48, p. 552–555.

[17] RIEDL, A., SCHALK, N., CZETTL, C., SARTORY, B., MITTERER, C., Tribological properties of Al_2O_3 hard coatings modified by mechanical blasting and polishing post-treatment, *Wear*, 2012, Vol. 289, p. 9–16.

[18] BAGDE, P., SAPATE, S.G., KHATIRKAR R.K., VASHISHTHA N., Friction and abrasive wear behaviour of Al_2O_3-13TiO_2 and Al_2O_3-13TiO_2+Ni Graphite coatings, *Tribology International*, 2018, Vol. 121, p. 353–372.

[19] YANG, J., ZHANG, Y., ZHAO, X., AN, Y., ZHOU, H., CHEN, J., HOU, G., Tribological

behaviors of plasma sprayed CuAl/Ni-graphite composite coating, *Tribology International*, 2015, Vol. 90, p. 96–103.

[20] GOEL, S., BJÖRKLUND, S., CURRY, N., WIKLUND, U., JOSHI, S. V, Axial suspension plasma spraying of Al_2O_3 coatings for superior tribological properties, *Surface and Coatings Technology*, 2017, Vol. 315, p. 80–87.

[21] SAHAB, A.R.M., SAAD, N.H., KASOLANG, S., SAEDON, J., Impact of Plasma Spray Variables Parameters on Mechanical and Wear Behaviour of Plasma Sprayed Al_2O_3 3%wt TiO_2 Coating in Abrasion and Erosion Application, *Procedia Engineering*, 2012, Vol. 41, p. 1689–1695.

[22] MCENTIRE, B.J., BAL, B.S., RAHAMAN, M.N., CHEVALIER, J., PEZZOTTI, G., Ceramics and Ceramic Coatings in Orthopaedics, *Journal of European Ceramic Society*, 2015, Vol. 35, p. 4327–4369.

[23] MARCHIORI, G., LOPOMO, N., BOI, M., BERNI, M., BIANCHI, M., GAMBARDELLA, A., VISANI, A., RUSSO, A., MARACACCI, M., Optimizing thickness of ceramic coatings on plastic components for orthopedic applications: A finite element analysis, *Materials Science and Engineering C*, 2016, Vol. 58, p. 381–388.

[24] BRINKIENĖ K. P.L., KĖŽELIS R., MEČIUS V., Effect of outlet nozzle design on the YSZ particle in-flight characteristics in plasma jet generated by DC plasma torch, in: Advanced Heat Transfer Engineering, Proceedings of 4th Baltic Heat Transfer Conference, 2003, p. 629–636.

[25] VALINČIUS, V., KRUŠINSKAITE, V., VALATKEVIČIUS, P., VALINČIŪTE, V., MARCINAUSKAS, L., Electric and thermal characteristics of the linear, sectional dc plasma generator, *Plasma Sources Science and Technology*, 2004, Vol. 13, p. 199.

[26] MARCINAUSKAS, L., KAVALIAUSKAS, Ž., KĖŽELIS, R., Formation of carbon composite coatings by plasma spraying, *Vacuum*, 2015, Vol. 122, p. 326–331.

[27] KALIN, M., VIZINTIN, J., The Tribological Performace of DLC Coatings under Oil-Lubricated fretting conditions, *Tribology International*, 2006, Vol. 39, p. 1060–1067.

[28] SINGH, A.K., NAKATE, U.T., Microwave Synthesis, Characterization, and Photoluminescence Properties of Nanocrystalline Zirconia, *The Scientific World Journal*, 2014, Vol. 2014, p. 1–7.

[29] RONG, J., YANG, K., ZHAO, H., LIU, C., ZHUANG,Y., Tao S., Tribological performance of plasma sprayed Al_2O_3–Y_2O_3 composite coatings, *Surface and Coatings Technology*, 2016, Vol. 302, p. 487–494.

[30] YANG, K., ZHOU, X., LIU, C., TAO, S., DING, C., Sliding Wear Performance of Plasma-Sprayed Al_2O_3-Cr_2O_3 Composite Coatings Against Graphite under Severe Conditions, *The Journal of Thermal Spray Technology*, 2013, Vol. 22, p. 1154–1162.

[31] ŽIVCOVÁ, Z., GREGOROVÁ, E., PABST, W., SMITH, D.S., MICHOT, A., POULIER, C., Thermal conductivity of porous alumina ceramics prepared using starch as a pore-forming agent, *Journal of European Ceramic Society*, 2009, Vol. 29, p. 4327–4369.

[32] ARIHARAN, S., NISAR, A., BALAJI, N., ARUNA, S.T., BALANI, K., Carbon nanotubes stabilize high temperature phase and toughen Al_2O_3-based thermal barrier coatings, *Composites Part B*, 2017, Vol. 124, p. 76–87.

[33] ZHOU, C., CHEN, D., ZHANG, X.B., CHEN, Z., ZHONG, S.Y., WU, Y., Ji, G., WANG H.W., The roles of geometry and topology structures of graphite fillers on thermal conductivity of the graphite/aluminum composites, *Physics Letters A*, 2015, Vol. 379, p. 452–457.

[34] LI, C.-J., SUN, B., Effects of spray parameters on the microstructure and property of Al_2O_3 coatings sprayed by a low power plasma torch with a novel hollow cathode, *Thin Solid Films*, 2004, Vol. 450, p. 282–289.

[35] DHAKAR, B., CHATTERJEE, S., SABIRUDDIN, K., Influence of process parameters on the formation of phases and mechanical properties of plasma sprayed Al_2O_3–Cr_2O_3 coatings, *Materials Research Innovations*, 2017, Vol. 21, p. 367–376.

CYSENI 2018, May 23-25, Kaunas, Lithuania
ISSN 1822-7554, www.cyseni.com

APPLICATION OF RADIOGRAPHIC METHODS IN PYROLYSIS AND GASIFICATION OF A SINGLE BIOMASS PARTICLE

P. Kazimierski, P. Tiutiurski, D. Kardaś
Institute of Fluid-Flow Machinery, Polish Academy of Science
Fiszera 14, 80-231 Gdańsk – Poland
Email: pkazimierski@imp.gda.pl

M. Ochnio
Gdańsk University of Technology
Narutowicza 11/12, 80-001 Gdańsk – Poland

ABSTRACT

The work describes new methodology of analysis for the pyrolysis process of a single particle of wood. Biomass pyrolysis is the process of thermal decomposition of cellulose, hemicellulose and lignin, performed in the oxygen-free atmosphere. This complex process consists in decomposing chemical compounds to smaller molecules under the action of energy supplied from outside. During experiments thermogravimetry pyrolysis, pyrolysis in high temperature furnace and radiography techniques were used. The thermal decomposition rate presented as a function of time. In laboratory experiments pine cubes of size 18 mm were used. High temperature furnace research was preceded by a thermogravimetric analysis to determine the temperature range in which the process takes place. The samples after the experiments were analysed using radiographic methods to visualize the changes in wood structure as a function of time. Pine cubes were inserted into the furnace for successively 60, 120, 180, 240 and 300 seconds. After the pyrolysis, the samples underwent radiographic inspection, which was assumed to be qualitative by nature. This inspection consisted of irradiating the sample with the aid of the X-ray tube (70 kV) at the exposition time 0.01 s, after which the obtained images were recorded on the computed radiography (CR) image plate. The analysis of the radiographic images allowed to determine volume of wood which was thermally decomposed. The radiography images showed that pyrolysis started from the corners of the sample, however the samples cores remained relatively untouched by pyrolysis.

Keywords: pyrolysis, gasification, radiography, thermal gravimetric analysis

1. INTRODUCTION

Pyrolysis is a process of thermochemical decomposition performed in oxygen-free atmosphere. This complex process consists in decomposing chemical compounds to smaller molecules under the action of energy supplied from outside (Kardaś, [2014]). The majority of reactions taking place during the pyrolysis are endothermic in nature. The pyrolysis process can be symbolically presented in the form of the following reaction.

$$C_nH_mO_p \xrightarrow{\text{heat}} \sum_{(\text{liquid})} C_xH_yO_z + \sum_{\text{gas}} C_aH_bO_c + H_2O + C_{\text{char}}$$

The products created as a result of pyrolysis are composed of three fractions, which are:

- Biochar - coal concentrate with mineral particles coming from the pyrolysis substrate,
- Liquid fraction, consisting of organic part, with very complex chemical composition, and water part, which comprises acetic acid and/or methanol, among other compounds,
- Gas fraction, being the mixture of CO_2, CO, H_2, and hydrocarbons – mainly methane.

The conditions in which the pyrolysis takes place affect considerably its products, Zolezzi [2004], Ronewicz [2016]. In his monograph, Basu [2010] collected such pyrolysis parameters as maximal temperature and process duration, and analysed their effect on the obtained products:

biochar, bio-oil, and pyrolytic gas. This knowledge has both cognitive and practical value, as it refers to the first stage of thermal decomposition of solid fuels during combustion and gasification processes. As already mentioned, the course of pyrolysis depends not only on the temperature and the heating rate, but also on the size of particles and the gas pressure. The research by Wardach-Święcicka [2017] has showed how much the pyrolysis temperature depends on the size of particles, which then translates into the composition of pyrolysis products. In practice, the pyrolysis, being the first phase of the gasification or combustion process, frequently takes place at the atmospheric pressure. A typical size of woodchip particle undergoing gasification ranges from 5 to 50 mm. Examining the course of pyrolysis of a particle with dimensions of an order of 20 mm as a function of temperature in atmospheric pressure conditions extends the knowledge on the subject and can contribute to designing better industrial devices and installations. The paper describes the potential of radiographic methods for examining wood pyrolysis in the above described conditions and compares the obtained results with those recorded using the thermogravimetric method. Here, the radiography gains in importance as a new tool for examining the pyrolysis of particles of tens of millimetres in size, which allows us to get a deeper insight into the fuel structure during different pyrolysis process phases. The use of radiographic methods for examining gasification and pyrolysis processes was initiated by Kazimierski [2016] in the PAS Institute of Fluid-Flow Machinery, who determined the deposit sedimentation rate in gasifying reactors. In the present work the radiographic method is used for another purpose, which is examining the internal structure of the particle during successive phases of its thermal decomposition. In the further perspective, the performed research is expected to contribute to improving the radiographic research methodology as a pyrolysis examination tool. The pyrolysis process radiography will allow the wood samples to be examined on-line, without stopping the process and damaging the sample.

2. REASERCH METODOLOGY

The basic goal of the research was developing and using the radiographic method to determine the course and characteristics of wood pyrolysis. Since the radiographic method provides the information on structural changes in the pyrolysed wood, is was complemented by thermogravimetric examination. As a consequence, the entire research comprised three stages, the first of which was thermogravimetric analysis of wood samples of several milligrams in weight using the Thermal Gravimetric Analyser, TGA, while the next stage comprised pyrolysis of full-scale wood particles (geometric cubes of edge length of 19 mm), performed in a high-temperature furnace. The third stage was radiographic analysis of samples after the pyrolysis. During the first stage, performed with the aid of TGA, the temperature was determined at which the process takes the fastest course, and the temperature was checked at which the wood is totally pyrolysed and all volatile parts are released. This stage was also used for selecting proper temperatures for experiments in the muffle furnace. The next stage comprised pyrolysis experiments in the high-temperature furnace, (Fig. 1), heated to the temperature of 500 °C. After its removal from the high-temperature furnace, each sample underwent radiographic inspection to assess visually the pyrolysis degree inside the biomass sample. The radiographic examination was performed using an X-ray tube as the radiation source, (Fig. 1).

Fig. 1. High-temperature furnace and X-ray tube

The wood samples were inserted into the heated furnace and kept in there for the time of, successively: 60 s, 120 s, 180 s, 240 s, and 300 s. When inserting the samples, the furnace was rinsed with the flow of argon to ensure the non-oxidative atmosphere. Moreover, after their removal from the furnace, the samples were immediately placed into the aluminium container, in which the non-oxidative atmosphere was also ensured. The wood samples were weighted before and after the pyrolysis, when they have cooled down. The percentage loss of mass was used to calculate the sample pyrolysis degree, (Table 1). Then the samples underwent radiographic inspection, which was assumed to be qualitative by nature. The inspection consisted of irradiating the sample with the aid of the X-ray tube, (Fig. 2), with the voltage power of 70 kV and the exposition time of 0.01 s, and recording the obtained image on the CR image plate. The density differences between the non-pyrolysed wood and the biochar were observed as differences in colours on the mapped sample image in the radiographic record: brighter areas corresponded to larger density, i.e. lower pyrolysis degree. Visual observation made the basis for estimating how deep the pyrolysis penetrated into the sample, and recording other changes (cracks, for instance) being the result of high temperature acting on the sample.

3. RESULTS

3.1. Thermogravimetric analysis

3.1.1. Results of thermogravimetric TGA analysis

Thermogravimetric analyses of the biomass sample were performed to study the rate of thermal processes and temperatures at which they take place. This type of analyses allowed us to determine optimal conditions of the process and the dynamics of pyrolysis of different feedstock materials. In this study, presented results of thermal biomass decomposition were obtained using the thermogravimeter SDT Q600. The average mass of the sample was 10 mg. According to the literature, for biomass the pyrolysis interval begins at temperatures of 160–200 °C. The characteristic of thermal decomposition of pine wood sample at the heating rate of 15°C/min has revealed that the beginning of the sample gasification process is at the temperature of 180–190 °C, while the most intensive gasification takes place at 375 °C. The performed analysis has also revealed that at 500°C the sample is totally pyrolysed and has no volatile matter. This temperature was assumed optimal for experiments to be performed in the high-temperature furnace.

3.1.2. Experiments in high-temperature furnace

To compare the effects of pyrolysis in the high-temperature furnace and in the thermogravimeter, an experiment was performed in which the biomass samples were heated successively to: 100, 200, 300, 400 and 500 °C. Each time after heating by 100 degrees, one sample was removed and the furnace was thermally stabilised at this temperature for 10 minutes, after which the temperature was increased again by the next 100 degrees. Thermal stabilisation aimed for reaching the same pyrolysis degree in the entire volume of the sample. The removed samples were weighted and the recorded mass loss as the function of temperature made the basis for creating a diagram which was compared with mass loss changes recorded during thermogravimetric pyrolysis, (Fig. 2).

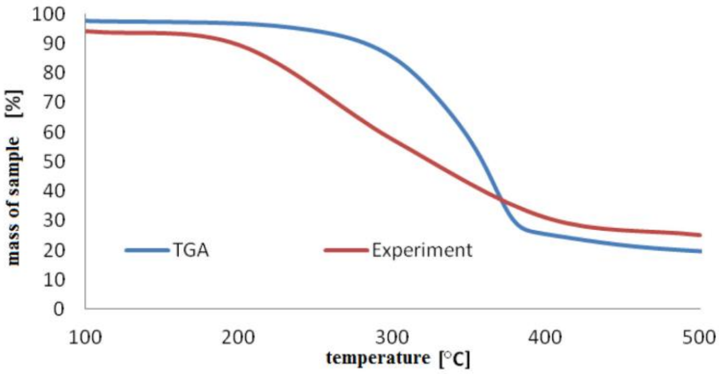

Fig. 2. Mass loss as function of temperature in TGA analysis and experiment in high-temperature furnace

3.2. Pyrolysis in high temperature furnace

Other pyrolysis experiments were performed in which the wood mass loss was determined as the function of time as the sample stayed at the temperature of 500 °C. The results are shown in Fig. 3. The mass loss was recalculated as the ratio of final mass (mk) to initial mass (m0). For full pyrolysis, this ratio was equal to 0.25. Then the pyrolysis degree was determined as the ratio of the current sample mass loss to that measured after full sample pyrolysis. These results are collated in Table 1. The most intensive sample gasification took place between seconds 120 and 180 of the pyrolysis. After 240 seconds, the sample was almost entirely degasified, and the pyrolysis degree was equal to 94%.

Table 1. Sample mass loss and pyrolysis degree for different pyrolysis times

Parameter Time of pyrolysis [s]	mk / m0 [1]	Pyrolysis degree [m/m$_0$]
60	0.81	0.26
120	0.72	0.37
180	0.41	0.78
240	0.29	0.94
300	0.25	1

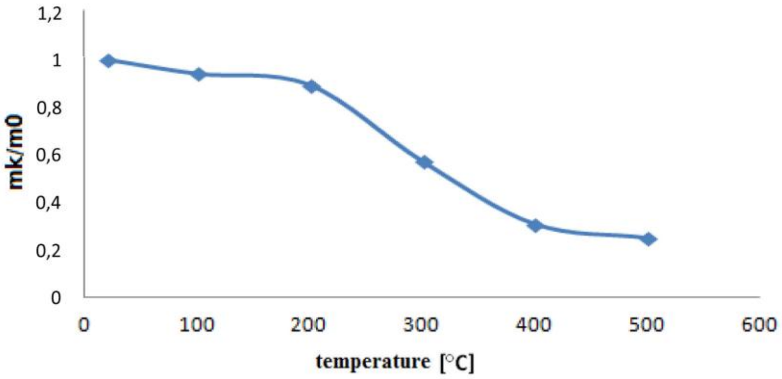

Fig. 3. Wood mass loss as function of temperature of sample staying at temperature of 500 °C

The observed mass loss and carbonisation of the sample was accompanied by its deformation, growing with the progress of pyrolysis. Photos of samples taken at different stages of volatile part gasification are shown in Fig. 4. The image of the sample which stayed in the furnace for 60 seconds clearly shows that the pyrolysis is most intensive at corners, as the effect of large heat transfer surface against small mass of wood in this part of the sample. Faster pyrolysis can also be observed on the side walls, compared to the upper surface of the cube of wood. This effect is caused by different ways of gas flow about these surfaces, and different rates of heat penetration into the walls, resulting from differences in wood filament arrangement: parallel or perpendicular to the heat penetration plane. It was observed that sample deformations are not even in all planes. The cube walls perpendicular to the rings in the wood are least deformed. The walls situated parallel to wood filaments have widened, which is especially noticeable in their middle parts.

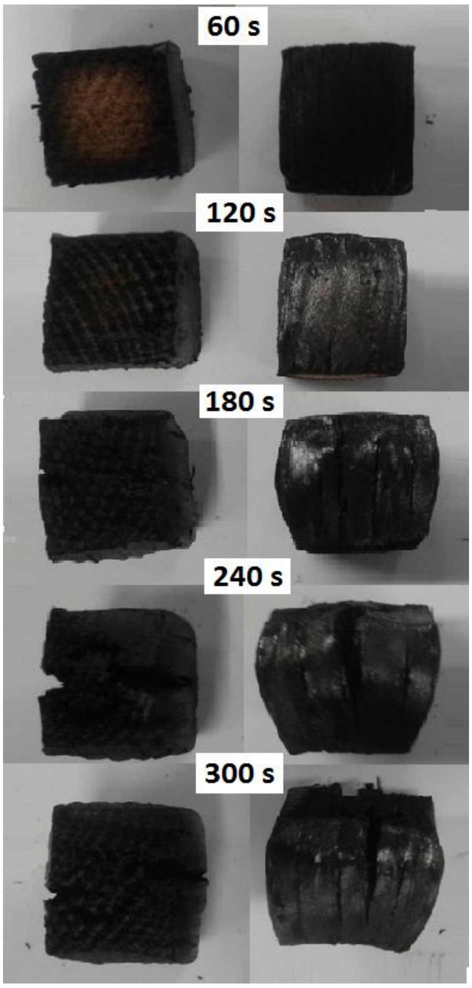

Fig. 4. Wood samples after removal from high-temperature furnace

3.3. Radiography analysis of sample after pyrolysis

After the pyrolysis the samples underwent radiographic examination, which was assumed to be qualitative by nature. It consisted in irradiating the samples using the X-ray tube, at the exposition time of 0,01 s, and further recording of the obtained image on the CR image plate, (Fig. 5.) The analysis of the radiographic photos allowed us to assess where the wood pyrolysis took place and which part of the sample was thermally decomposed.

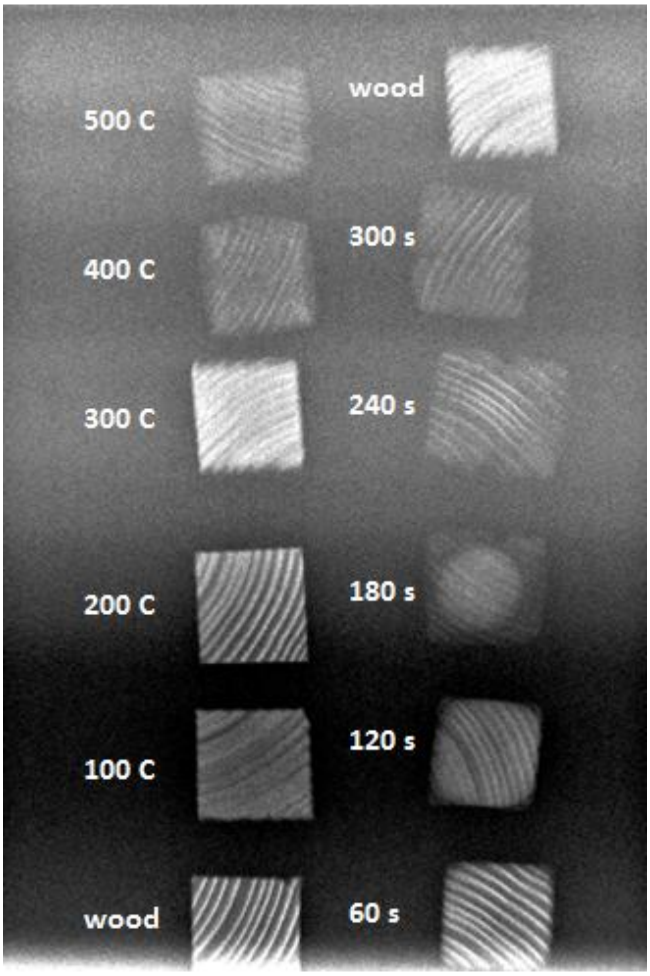

Fig. 5. Radiographic photos of samples

After 60 s, the beginning of pyrolysis is observed at wood sample corners. Darker colour of the corners in the X-ray photo testifies to smaller density in those places, as a result of wood gasification to the biochar. After 120 s, the pyrolysis takes place in the entire outer part of the walls, mainly in the corners. After 180 s, a non-pyrolysed sample core is observed, along with first deep cracks of the wood. After 240 s, the radiographic image of the core has a similar colour as the remaining part of the sample, which testifies to high progress of pyrolysis also in this part of the sample. After 300 s, the cube has undergone full pyrolysis, numerous cracks in the wood structure can be observed.

4. CONCLUSION

Radiographic analysis provides wide opportunities of examining pyrolysis processes. The qualitative information gained with the aid of this technique refers to the depth to which the pyrolysis has penetrated into the particle, and the degree to which the particle is degasified. The assessment of pyrolysis degree based on the density of the sample and its change of mass due to the action of temperature corresponds to averaging the pyrolysis degree over the entire particle. In case of fast pyrolysis, a situation can occur when the outer part of the sample is fully pyrolysed, while its core is not degasified. Estimating the pyrolysis degree from sample density changes is only a global approach, while radiographic methods allow us to assess also local structural changes in the sample. Moreover, radiographic photos allow us to analyse the course of cracks inside the sample without its damage. The wood pyrolysis in the high-temperature furnace differed from that performed using the gravimeter: the former started at lower temperatures and revealed lower total gasification.

REFERENCES

1. AKHTAR J.; AMIN N.S. A review on operating parameters for optimum liquid in biomass pyrolysis. *Renewable and Sustainable Energy Reviews*, 2012. P. 5101–5109.
2. BASU P. *Biomass gasification and pyrolysis practical design and theory*. Oxford; 2010.
3. BLASI C., (2009). Combustion and gasification rates of lignocellulosic chars. *Progress in Energy and Combustion Science*, p. 121–140.
4. BRIDGWATER A.V., MEIER D., RADLEIN D., An overview of fast pyrolysis of biomass. *Organic Geochemistry*, 1999, p. 1479–1493.
5. BRIDGWATER A., ALCALA A., Upgrading fast pyrolysis liquids: Blends of biodiesel and pyrolysis oil, *Fuel*, 2013, p. 417–426.
6. KARDAŚ D., KLUSKA J., KLEIN M., KAZIMIERSKI P., HEDA L., Teoretyczne i eksperymentalne aspekty pirolizy biomasy i odpadów. 2014. Olsztyn.
7. KAZIMIERSKI P., KLUSKA J., KARDAŚ D., Effect of biomass settling in the fixed bed gasification reactor, CYSENI 2016, Proceedings of annual conference of young scientists on energy issues. Kaunas, Lithuania Energy Institute.
8. MOHAN D., PITTMAN C.U., Pyrolysis of wood/biomass for bio-oil: a critical review. *Energy Fuel* 20, 2006. p. 848–889.
9. RONEWICZ K., KARDAŚ D., Experimental and Theoretical Investigation over the Wood Permeability to Air as a Function of Pyrolysis Temperature, *Applied Mechanics and Materials*, 2016. Vol. 831, pp. 295–305.
10. TAUPE, C., LYNCH, D., WNETRZAK, R., KWAPINSKA, M., KWAPINSKI, W., LEAHY J., (2016), Updraft gasification of poultry litter at farm-scale – A case study. *Waste Manage*, 50, p. 324–333.
11. WARDACH-ŚWIĘCICKA I., KARDAŚ D., Modeling of heat and mass transfer during thermal decomposition of a single solid fuel particle, *Archives of Thermodynamics* 2013.
12. WEI L., XU S., ZHANG L., LIU C., ZHU H., LIU S., Characteristics of fast pyrolysis of biomass in a free fall reactor. Fuel Process Technology, 2006. p. 863–871.
13. ZHANG X, YANG W, BLASIAK W., Thermal decomposition mechanism of levoglucosan during cellulose pyrolysis, Journal of Analytical and Applied Pyrolysis, 96, 2012 p. 110–119.
14. ZOLEZZI M., NICOLELLA C., FERRARA S., IACOBUCCI C., ROVATTI M., Conventional and fast pyrolysis of automobile shredder residues (ASR), *Waste Management*, 2004. p. 691–699.

CYSENI 2018, May 23-25, Kaunas, Lithuania
ISSN 1822-7554, www.cyseni.com

INVESTIGATION OF THIN FILM DEPOSITION RATE DEPENDENCY ON MAGNETIC FIELD INDUCTION

D. Stankevičius, A. Iljinas
Kaunas University of Technology
Studentų str. 50, LT-51368 Kaunas – Lithuania
Email: doras.stankevicius@ktu.edu

A. Iljinas
Kauno kolegija, University of Applied Sciences,
Pramonės av. 20, LT-50468 Kaunas – Lithuania

ABSTRACT

Magnetron sputtering deposition is a physical vapor deposition (PVD) method thoroughly used to develop electronics, solar cells, hydrogen fuel cells and batteries, and various coatings. It is effective to deposit most materials not depending on their vaporization point, changing its chamber gas composition can lead to creation of oxides or nitrides, due to magnetic field is able to work in higher vacuum. The examination of magnetic field induction distribution was performed on a “Kurt J. Lesker” magnetron sputtering system composing of three “Torus” magnetrons. We measured the magnetic flux density dependence on the distance to the magnetron center and on the height (ranging from 5 to 30 mm) above the surface of its cathode using Hall-effect probe. The yielded results infer that the magnetrons possess different magnetic inductions with the first one having the biggest value of 268 mT at the lowest height. Further on, we deposited zirconium thin films on silicon substrates. The layers thicknesses were measured with a profilometer. With only the magnetic field induction varying between the depositions we were able to obtain the dependency of thin film deposition rate to magnetic induction of magnetron. The dependence is linear: greater the magnetic field induction greater the deposition rate.

Keywords: magnetron sputtering deposition, magnetic field induction, thin films.

1. INTRODUCTION

Zirconium is a transitional metal first discovered in 1789 by Martin H. Klaproth [1], most often used as a compound in a form of zircon, but it is also being converted into metal. It is well known for its strength, refractory qualities and resistance to corrosion. Zirconium is often added to other metals conferring its resistance to physical stress [2] and resistance to corrosion [3], it is being used as a cladding material for nuclear power rods [4] due to its ability to conduct neutrons and in developing solid proton conducting materials [5]. This metal also finds its application in medicine as a tomography imaging agent [6]. Zirconium composite ZrO_2 is used in all three of its phases in monoclinic as an opacifier [7], in tetragonal phase as a great physical property ceramic [8] and in cubic harnessing its strength and hardness in high speed cutting tools and in jewelry with respect to its familiarity to diamond. Magnetron sputtering is fit to deposit both zirconium dioxide [9] and metal zirconium films.

Magnetron sputtering is a plasma coating technique widely used in research and in industry patented in 1974 by J. S. Chapin [10]. It is advantageous against other physical vapor deposition (PVD) methods due to the fact that it does not depend on the vaporization point of the target material, the cathodes can be shaped to best suit the substrates [11] and can yield a smooth surface [12]. This method allows a variance of many factors such as power, pressure, substrate bias [13], target composition, gas composition, target-sample distance and rotation [14], magnet configuration [15], substrate temperature [16], target temperature [17], making it a very versatile tool in the hands of an expert.

The quality of magnetron sputtering deposition of metal layers is also determined by the rate of deposition, because of the fact that there might be oxygen in the chamber, due to imperfect vacuuming so quicker deposition means less time for metal to oxidize. The aim of this work is to determine magnetron deposition rate dependency on magnetic field induction.

Similar work regarding the deposition rate dependency on the lateral and axial distance from the magnetron sputterer has been conducted [18].

2. METHODOLOGY

The magnetic field induction distribution was measured on three “Kurt J. Lesker” magnetrons. They have a nominal power of 700 W in direct current mode and 300 W in radio frequency mode. It can operate in 0.133–6.66 Pa pressure. The magnetic assembly is constantly cooled with a water current of 0.17 m^3/h, the assembly cannot heat up above 110 ^oC, which would start an irreversible change in magnetic properties, due to its Curie temperature [19].

The magnetron sputtering is a physical vapor deposition (PVD) method that relies on intersecting electric and magnetic fields to create plasma. The magnetic field allows for plasma to be acquired in lower pressures by prolonging the path of electrons causing them to move in trochoids and spirals, which is essential for the effectiveness of gas ionization. The positive ionized gas is accelerated towards the negative electrode (target) and collides with it, sputtering the material. The sputtered vapor usually has a neutral charge, not affected by the electric field it is able to reach the substrate and condense on it.

The magnetic field induction was measure with Hall Effect probe (measurement error ±6%) from 5 mm to 30 mm in height and 87 mm in width. The zirconium was deposited in 1 Pa pressure of argon on polished silicon wafers. A layer was deposited by each magnetron with 0.5 A plasma current and voltage of 240 V, a layer by each with 1 A plasma current and voltage of 360 V in direct current mode. The height of thin films was measured by „Ambios XP-200 Profilerr“ profilometer with minimum vertical resolution of 1Å [20].

3. RESULTS AND DISCUSSION

3.1. Magnetron magnetic field induction distribution

The magnetic flux lines are directed from the north pole of a magnet in the center to the south poles in the edges of the magnetron sputterer, for this reason the highest magnetic flux density is near the center. We measured the vertical component of the magnetic field induction to attain a distribution depending on the distance to the center axis and to the height from the surface of the cathode.

The result showed that the highest value of magnetic field induction which is 268 mT is of the first magnetron at the lowest height. The second and third magnetrons have highest induction values of 148 mT and 128 mT accordingly. As we were measuring the vertical component of the magnetic flux density the magnetrons have three peaks: two near the edges where the south poles are and the biggest one in the center where the one north pole is.

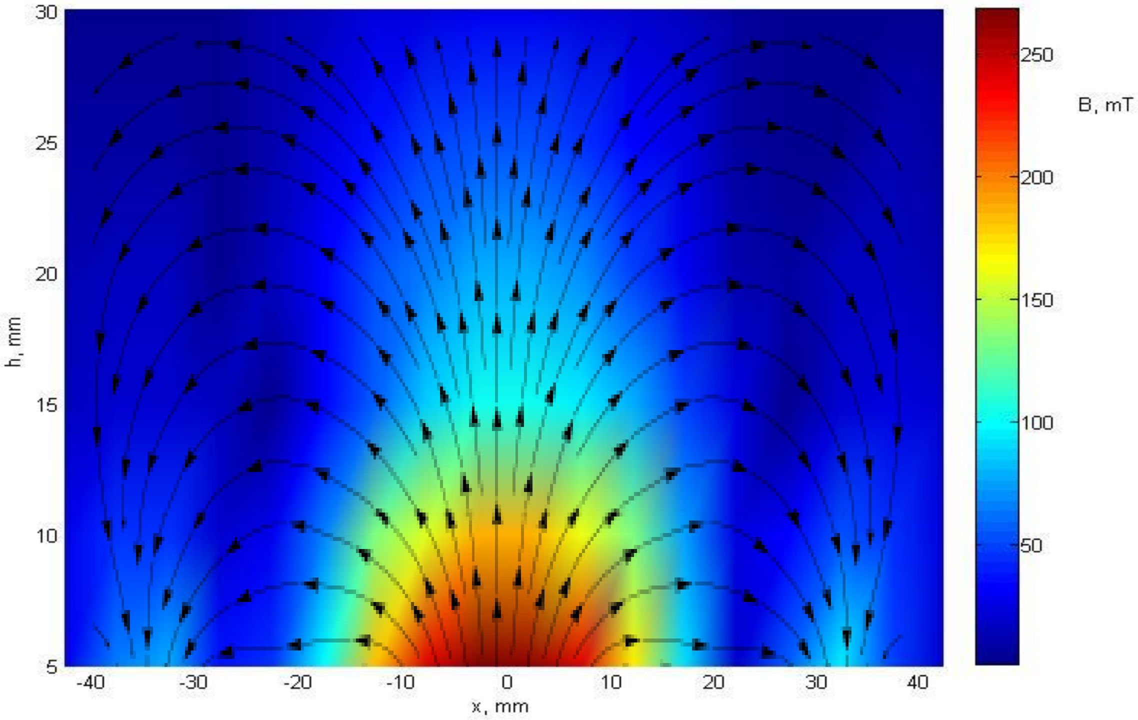

Fig. 1. Magnetic field induction distribution with magnetic lines

All three magnetrons exhibit similar graphs. The characteristic points of all magnetrons are shown in the table (Table 1).

Table 1. The characteristic magnetic field induction points of all magnetrons

Distance from centre, mm / Height, mm	-32			-28			-22			0			22			28			32		
30	77	56	18	37	32	10	43	13	6	268	148	128	30	20	11	58	31	7	96	59	16
25	43	29	10	21	18	5	28	1	9	187	89	83	23	7	12	34	19	2	54	26	9
20	21	13	5	14	9	1	1	3	8	103	48	50	23	8	12	5	4	1	22	10	4
15	16	8	2	2	5	2	14	6	6	79	36	31	10	9	7	5	1	3	14	4	0
10	5	4	0	2	1	2	11	3	6	53	21	22	9	6	7	2	1	4	1	3	1
5	1	2	0	4	0	2	9	4	5	28	15	13	7	5	5	1	1	3	3	1	1

▨ First magnetron magnetic induction, mT
▒ Second magnetron magnetic induction, mT
☐ Third magnetron magnetic induction, mT

3.2. Deposition rate dependency on magnetic field induction

There were two layers deposited by each magnetron. The first layer was being deposited with the glow discharge current of 0.5 A for 1 minute. The discharge voltage was about 240 V varying by 10 V between magnetrons, which is considerably a small difference so will not be taken into account. The difference in magnetic field induction led to different thicknesses of the films, the first was 80 nm, the following where: 17 nm and 5 nm. For the sake of legibility, we performed another deposition with 1 A discharge current for 1 min, with voltage of about 360 V and this time the thicknesses where: 400 nm, 232 nm and 210 nm. Due to the fact that the magnetic field induction is the only variable we were able to distinguish a dependency of deposition rate to the magnetic field induction (Fig. 2).

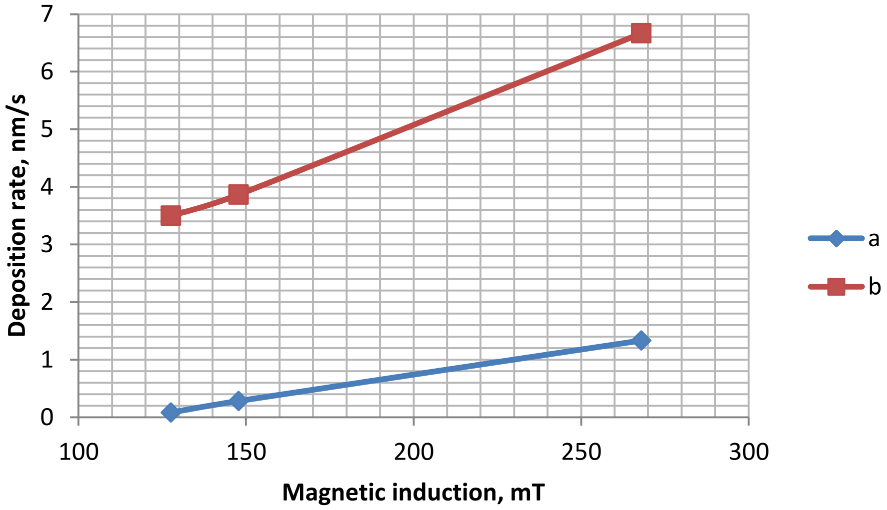

Fig. 2. Deposition rate dependency on magnetic field induction (a) with current of 0.5 A and (b) with current of 1 A

The graph shows that the dependency is linear: higher is the magnetic field induction, higher is the deposition rate. In the case of 0.5 A the deposition rate rises from 0.083 nm/s to 1.33 nm/s according to the rise of magnetic field induction from 128 mT to 268 mT. And in the case of 1 A the deposition rate rises from 3.5 nm/s to 6.67 nm/s and that is almost a double growth in rate.

The reason why the deposition rate increases with the increase in magnetic field induction is the effect of Lorentz force. As electrons ejected from the cathode are accelerated towards the anode they are also forced to twist their path perpendicular to their movement direction and to the direction of magnetic field lines. In the case of magnetron sputtering making them move in spirals. As the magnetic field increases, the spiral loop get more dense increasing electron path length and also increasing the chance of ionizing collisions with neutral gas particles. More ionized particles means more bombardment thus leading to increased sputtering rate.

4. CONCLUSION

Zirconium films were deposited and dependency of deposition rate to magnetic field induction was investigated. The measured magnetic distribution revealed that the highest magnetic induction which is 268 mT is possessed by the first magnetron; other magnetrons have magnetic inductions of 148 mT and 128 mT. According to these differences in magnetic field induction a difference in deposition rate was observed: increasing of magnetic induction leads to an increase in deposition rate. The dependency as expected appears to be linear. At 1 A current about two times stronger magnetic field led to about two times higher deposition rate.

REFERENCES

1. Turner, E. (1830). *Elements of chemistry: including the recent discoveries and doctrines of the science*. 3rd American, from the 2nd London ed., with notes and emendations / Philadelphia: J. Grigg., p. 305.
2. Ting Wang, Yongyun Zhang, Siyuan Jiang, Xiaopeng Li, Binggang Zhang, Jicai Feng, *Stress relief and purification mechanisms for grain boundaries of electron beam welded TZM alloy*

joint with zirconium addition, Journal of Materials Processing Technology, Volume 251, 2018, P. 168–174, ISSN 0924-0136.

3. T.-L. Yau and V.E. Annamalai, *Corrosion of Zirconium and its Alloys*, In Reference Module in Materials Science and Materials Engineering, Elsevier, 2016, ISBN 9780128035818, Pages 2094–2134.
4. Siddharth Suman, Mohd Kaleem Khan, Manabendra Pathak, R.N. Singh, *Effects of hydrogen on thermal creep behaviour of Zircaloy fuel cladding*, Journal of Nuclear Materials, Volume 498, 2018, Pages 20–32, ISSN 0022-3115.
5. Peng Sun, Zhongfang Li, Mingfeng Song, Suwen Wang, Xiaoyan Yin, Yuxin Wang, *Preparation and characterization of zirconium phytate as a novel solid intermediate temperature proton conductor*, Materials Letters, Volume 191, 2017, Pages 161–164, ISSN 0167-577X,
6. Lachlan E. McInnes, Stacey E. Rudd, Paul S. Donnelly, *Copper, gallium and zirconium positron emission tomography imaging agents: The importance of metal ion speciation*, Coordination Chemistry Reviews, Volume 352, 2017, Pages 499–516, ISSN 0010-8545.
7. S. Naher, A.S.M.A. Haseeb, *Production and purification of zircon opacifier from zircon found in the coastal area of Bangladesh*, Journal of Materials Processing Technology, Volume 205, Issues 1–3, 2008, Pages 203–206, ISSN 0924-0136.
8. I. Nettleship, R. Stevens, *Tetragonal zirconia polycrystal (TZP) – A review*, International Journal of High Technology Ceramics, Volume 3, Issue 1, 1987, Pages 1–32, ISSN 0267-3762.
9. R. Yusoh, M. Horprathum, P. Eiamchai, P. Chindaudom, K. Aiempanakit, *Determination of Optical and Physical Properties of ZrO2 Films by Spectroscopic Ellipsometry*, Procedia Engineering, Volume 32, 2012, Pages 745–751, ISSN 1877-7058.
10. John S. Chapin (1974), US Patent No. *US4166018A.*
11. G. Bräuer, B. Szyszka, M. Vergöhl, R. Bandorf, *Magnetron sputtering – Milestones of 30 years*, Vacuum, Volume 84, Issue 12, 2010, Pages 1354–1359, ISSN 0042-207X.
12. G. Schmidl, J. Dellith, N. Teller, A. Bochmann, S. Teichert, O. Stranik, A. Dathe, V. Tympel, F. Schmidl, E. Kessler, T. Wieduwilt, W. Fritzsche, *Confocal sputtering of (111) orientated smooth gold films for surface plasmon resonance approaches*, Vacuum, Volume 138, 2017, Pages 55–63, ISSN 0042-207X.
13. A.A. Solovyev, K.V. Oskomov, A.S. Grenadyorov, P.D. Maloney, *Preparation of nickel-containing conductive amorphous carbon films by magnetron sputtering with negative high-voltage pulsed substrate bias*, Thin Solid Films, 2018, ISSN 0040-6090.
14. R.B. Tokas, S. Jena, J.S. Misal, K.D. Rao, S.R. Polaki, C. Pratap, D.V. Udupa, S. Thakur, Sanjiv Kumar, N.K. Sahoo, *Study of ZrO2 thin films deposited at glancing angle by radio frequency magnetron sputtering under varying substrate rotation*, Thin Solid Films, Volume 645, 2018, Pages 290–299, ISSN 0040-6090.
15. Takeo Nakano, Yudai Saitou, Kei Oya, *Transient evolution of the target erosion profile during magnetron sputtering: Dependence on gas pressure and magnetic configuration*, Surface and Coatings Technology, Volume 326, Part B, 2017, Pages 436-442, ISSN 0257-8972.
16. Stephan Gleich, Rafael Soler, Hanna Fager, Hamid Bolvardi, Jan-Ole Achenbach, Marcus Hans, Daniel Primetzhofer, Jochen M. Schneider, Gerhard Dehm, Christina Scheu, *Modifying the nanostructure and the mechanical properties of Mo2BC hard coatings: Influence of substrate temperature during magnetron sputtering*, Materials & Design, Volume 142, 2018, Pages 203–211, ISSN 0264-1275.
17. Raymond Y. Chau, W-S Ho, J.C. Wolfe, Darian L. Licon, *Effect of target temperature on the reactive d.c.-sputtering of silicon and niobium oxides*, Thin Solid Films, Volume 287, Issues 1–2, 1996, Pages 57–64, ISSN 0040-6090.

18. S. Gopikishan, I. Banerjee and S. K. *Mahapatra*, *Influence of magnetic field on plasma parameters and thin film deposition along axial and radial distances in DC magnetron*.
19. Kurt J. Lesker, *Torus® 3” HV CIRCULAR SPUTTERING SOURCE INSTALLATION & OPERATION MANUAL*, 2015.
20. McGILL Nanotools-Microfab, *Ambios XP200 Profiler Operation manual*.

SOLVENT EFFECT ON EXTRACTION OF PYROLYSIS TYRE OIL

T. M. Henarava, V. V. Sauchyn, V. V. Grushevskiy
A. V. Luikov Heat and Mass Transfer Institute
National Academy of Sciences of Belarus
P. Brovki str. 15, 220072 Minsk – Belarus
Email: tatiana-susliako@mail.ru

S. M. Leschev
Belarussian State University
Leningradskaya str. 14, 220030 Minsk – Belarus

ABSTRACT

Pyrolysis tyre oil is a promising feedstock for chemicals and fuels. An important step in the recovery of chemicals from pyrolysis tyre oil is primary fractionation due to separate it into less complex fractions or mixtures. A potential fractionation method is solvent extraction with pentane, toluene, methanol, diethyl ether, n-hexane, dichloromethane, and water. The pyrolysis process of tyre particles was carried out at temperature of 500 °C. The yield of products obtained from the pyrolysis process was following: liquid product 49%, carbon black 43% and gas 8%. The extraction of liquid pyrolysis product was studied in such extractants as water, «hexane-acetonitrile» system and sulphuric acid using gas chromatography-mass spectrometry (GC-MS). The distribution constants of chemical compounds for additional identification of the chemical composition of analyte were calculated as well.

The distribution coefficient and extraction yield of a compound are determined by its polarity and solubility, and the nature of pyrolysis oil. GC-MS analysis and calculated distribution constants showed that the pyrolysis tyre oil is formed from complex mixture of organic compounds. It was found that the extractive separation in system «hexane-acetonitrile» can be used to analyze pyrolysis tyre oil. The influence of the extractant on the chemical composition of liquid pyrolysis product was established as well.

Keywords: extractant, system hexane-acetonitrile, pyrolysis tyre product, gas chromatography-mass spectrometry, distribution constant

1. INTRODUCTION

Today there is a huge problem of environmental pollution with waste tyres. It is known that pyrolysis is one of the actual methods used for this purpose [1–2]. Pyrolysis of waste tyres is sufficiently promising method due to its processing into valuable chemical compounds [3]. Fast pyrolysis of tyre gives solid char, liquid oil and non-condensable gas. The yield of each product is dependent on tyre feedstock as well as operating conditions. Tyre typically yields 54–56% liquid, 36–38% solid carbon, and 6–9% gas. The gas-phase products are typically C1 – C4 hydrocarbons and hydrogen and can be used on-site as a fuel to provide the energy requirements for the pyrolysis process [4, 5]. Solid carbon can be used as an additive to concrete, as solid carbon is known to improve operational concrete properties [3]. The liquid-phase products are typically a mixture of paraffins, olefins and aromatic compounds [6, 7].

Pyrolysis of waste tyres with the purpose of fuel production for the usage as a fuel in internal combustion engine can be seen as efficient way of disposing them [1]. Pyrolysis oil is regarded as a very suitable feedstock for valuable chemical compounds or as a liquid transportation fuel [8].

One possible approach to make the pyrolytic processing of waste tyres more attractive (from an economical point of view) is the recovery of valuable chemicals. Distillation is not applicable due to thermal and chemical instability of pyrolysis oil. By using such fractionation method until final distillation temperatures in range of 250–300 ºC the pitch undergoes intense polymerisation, becoming hard and decreasing its solubility in organic solvents [9].

It is known that the pyrolysis oil contains many valuable chemicals, such as, dipentene (further limonene), benzene, toluene, xylenes, ethylbenzene, amongst others. Dipentene comprises of the racemic mixture of the two enantiomers d- and l-limonene [10]. Its systematic name is 1-methyl-4-(1-methylethenyl)-cyclohexene, an unsaturated hydrocarbon classified as amonoterpene. It is the dimer of two isoprene units, which originate from the (either natural or synthetic) polyisoprene content of the tyre. The price of limonene currently ranges between 1500 and 2500 US$ per metric tonne, depending mostly on its purity. It is mainly used as an industrial solvent, as a cleaning agent for, e.g., electrical circuit boards, as a dispersing agent for pigments, or as an active ingredient in different pesticide products [11].

The high complexity of the pyrolysis oil limits the possibility of direct analysis using a single technique. HPLC is widely used for prefractionation, however, this technique consumes too large solvent volumes to be useful for a rapid pyrolysis oil analysis. The separation, identification and quantification of specific compounds is difficult enough in pyrolysis oil. GC-MS has been one of the main analytical method in chemical identification due to the high resolution, high sensitivity, good reproducibility, a large number of standard spectra libraries, and the low solvent usage [7, 11, 12].

Commonly, prior to chromatographic analysis of pyrolysis fractions, fractionation procedures are required to dehydrate samples and separate target chemicals from oil [6]. An important step in the recovery of chemicals from pyrolysis oil is primary fractionation where pyrolysis oil is separated into less complex fractions or mixtures. Chemical distribution depends on pyrolysis oil properties, oil nature and extraction process. A potential fractionation method is solvent extraction, which is commonly applied for pyrolysis oil characterisation. Some extractants used in pyrolysis oil analysis are pentane, toluene, methanol, diethyl ether, n-hexane, dichloromethane, water, inorganic salt solutions and other organic solvents [13–17].

The main aim of the study is to research the possibility of using pyrolysis tyre oil obtained from waste automobile tyre after the process of extraction with different solvents.

The achievement of the aim can be fulfilled through the following tasks: analysis of chemical composition of pyrolysis oil, study of separation possibility of chemical compounds by extraction with hexane-acetonitrile system, distribution constants of chemical compounds of pyrolysis oil determination, quantitative analysis of polycyclic aromatic hydrocarbons (PAHs) and extraction of pyrolysis oil components with water, hexane – acetonitrile system, distribution constants determination in «hexane-acetonitrile» system and effect of sulfuric acid to pyrolysis oil extraction were investigated in this work.

2. METHODS

2.1. Materials

Analytical grade solvents: distilled water, n-hexane (99.5%), acetonitrile (99.5%), dichloromethane (99.9%) and sulfuric acid (95.6%) solvents were used.

2.2. Experimental procedure

2.2.1. Extraction

Extraction experiments were conducted in 10 mL glass flasks for 4 h at 20 °C. Extractant -to-oil volume ratio was varied in the range of 0.5–1. The minimum extractant -to-oil ratio was determined based on visual observation of phase separation. Both phases were then separated and analysed by GC-MS. Before GC-MS analysis liquid oil was firstly prepared by following treatments:

1. Solvent deasphalting of pyrolysis oil with n-hexane from 4 to 8 °C and decanting was done.
2. Hexane extract was extracted with distilled water in ratio 1 : 100.
3. Hexane extract was extracted with acetonitrile in ratio 1 : 1.
4. Hexane extract was mixed with sulfuric acid in ratio 1 : 0.5.

2.2.2. Pyrolysis

The pyrolysis of tyre was carried out in the inert environment with nitrogen.

Fig. 1. Scheme of the facility: 1 – dozer; 2 – screw pyrolysis reactor; 3 – solid residue bunker; 4 – condensate reactor

According to the scheme (Fig. 1) the tyre particles are loaded into the dozer (1) and then fed into the screw reactor (2). The material is heated in the reactor at 500 °C in nitrogen gas. Due to the heating, material decomposes and an organic vapour condenses in a condensate reactor (4) where pyrolysis oil is formed. And the solid residue is collected in the bunker (3). The yield of tyre products obtained from the pyrolysis process was following: liquid product 49%, solid carbon 43% and gas 8%.

2.3. Gas chromatography–mass spectrometry conditions

2.3.1. General chemical compound analysis

The analyses were performed in Agilent Technologies 7890A gas chromatograph, equipped with mass-detector and a capillary column “DB-5MS” (30 m × 0.25 mm × 0.25 μm). The initial oven temperature was maintained at 50 °C for 3 min and then ramped at 10 °C/min to 300 °C, which was held for 22 min. The measurement accuracy was determined to be within 4%.

2.3.2. Quantitative analysis of PAHs

Qualitative and quantitative GC–MS analyses of PAHs were carried out with Agilent Technologies 7890A equipped with a “DB-5MS” column (30 m × 0.25 mm × 0.25 μm) and coupled to an Agilent Technologies 5975C mass spectrometer. The spectrometer was operated in the single ion monitoring (SIM) mode using the molecular ion (m/z) of each compound at 1.23 scans/s. The transfer line was held at 295 °C and the source at 230 °C. Electron impact mass spectra were acquired at 70 eV. A 1 μl aliquot of the sample was injected using a splitless injector (60 s of equilibrium time). Helium was used as carrier gas at a constant flow rate of 1 ml/min. The oven program was started and was held at 80 °C for 2 min, then in 10°C/min heated up to 200 °C, and finally in 5 °C/min up to 300°C and held for 20 min.

2.4. Definitions

Extraction capability is denoted as distribution coefficient (D). The distribution coefficient of a particular component (Di) is defined as the ratio of the equilibrium mass fraction of that component in the hexane extract phase (xi,hex) and its equilibrium mass fraction in the acetonitrile phase (xi,acn).

$$Di = xi,hex/xi,acn \tag{1}$$

The standard error does not exceed ± 10%.

3. RESULTS AND DISCUSSION

3.1. Researches carried out in this field

Typically, the pyrolysis oil can be characterized, based on its properties, between a light and medium fuel oil [1, 2]. It consists predominantly of alkylated benzenes, alkylated naphthalenes, alkanes and alkenes [3]. However, the crude pyrolysis oil has a higher viscosity and sulfur content. The sulfur contained in the fuel is oxidized in the engine combustion chamber and is mostly discharged in the exhaust gas as sulfur dioxide. Higher smoke, HC and CO emissions were recorded in the experimentation [1, 8]. Pyrolysis oil is considered to be a perspective product from which valuable chemical compounds can be extracted. Liquid-liquid extraction of pyrolysis oil gives an opportunity to extract this valuable chemical compounds.

Limonene is a main component in the pyrolysis oil obtained from pyrolysis of automobile tyre wastes. Some authors have studied limonene separation from pyrolysis oil [18, 19]. It can be concluded, based on presently available information in the literature, that at least 2.5 wt% of the steel-free tyre can be converted to limonene. The main operating conditions during pyrolysis influence this yield significantly, of which temperature seems to be the most important one. Additionally, some studies have indicated that the above mentioned yields can be further improved. The use of vacuum pyrolysis has been propounded as such a possible improvement [20]. Also, the use of basic additives, e.g., NaOH, seems to improve the final limonene yields. However, more conclusive data (such as calibrated limonene yields for systematic studies of vacuum or NaOH catalyzed pyrolysis) are required [21, 22].

GC methods are used for determination of limonene in pyrolysis oil. The paper of Kyari et al. supplies very insightful results in this respect, as they report for one experiment both the %-area (13.79%) using a GC-MS instrument and the calibrated wt% (3.11%) of limonene [3]. In a typical GC-FID chromatogram of a pyrolysis oil, a large ‘hump’ of unresolved material is often encountered (especially for relatively fast separations) [3, 8]. Although almost all studies report that limonene is the most abundant component present in the pyrolysis oil, should limonene be produced as a value-added chemical from waste tyre pyrolysis, it needs to be separated from the multitude of other components [18, 19].

While a significant number of publications have considered the pyrolysis proper, considerably less work has been performed on the fractionation of pyrolysis oil or on the separation and purification of possible valuable chemicals from pyrolysis oil. Analysis of the distillation curves of various pyrolysis oils show that it has a wide boiling range with up to 50 wt% of the sample distilling before 200 °C. Approximately 10 wt% of the oil has a normal boiling point between 160 and 200 °C, the fraction in which limonene would typically be present [9]. While it is relatively easy to obtain a limonene enriched light naphtha (or similar) fraction, further purification is not so simple. It was also found that separation of limonene from 1,2,3-trimethylbenzene, 1-methyl-3-(1-methylethyl)benzene (m-cymene), and indane is very difficult due to their similar boiling points (all between 175 and 176 °C). In addition to obtaining a fraction concentrated in limonene, it is also important to consider the other components present, in particular the sulfur-containing components. Sulfur-containing components, even in very low concentrations, can result in a foul odor to the oil, thus reducing the quality and economic value thereof. Williams et al. found that the pyrolysis oil contains approximately 1.4 wt% sulfur, which is rather significant in this respect [22].

3.2. Solvent effect on pyrolysis oil extraction

The pyrolytic liquids obtained from pyrolysis of automobile tyre wastes, which are oily organic compounds, appears dark-brown-colour with a strong acrid smell. The pyrolysis oil has many impurities and odour, which causes its use difficult. Further chemical and physical treatment is required to remove this. The colour of pyrolysis oil is not stable, it changes with time as there some sludge remains. To prevent this problem some further steps should be taken.

It was found that the percentage of sulphur content was about 1.5%, and asphaltenes with undissolved compounds were about 5%. Limonene is the major organic compound with concentrations up to 25 wt%. Some authors use a pre-fractionation step before analysis [13–15].

Reactive liquid-liquid extraction is a well-established technology for the recovery of organic components from complex mixtures [12, 13]. Extraction of pyrolysis oil was studied with a purpose to separate chemical compounds of pyrolysis oil and also preconcentrate toxic pyrolysis polycyclic aromatic hydrocarbons as well. We determined the distribution constants of pyrolysis oil in «hexane-acetonitrile» system to clarify the chemical nature of samples and to make additional identification of compounds.

It should be noted that pyrolysis oil extraction with water did not give any result.

Typical chromatograms of acetonitrile extract compared with hexane extract are shown in Fig. 2. Practically all limonene (up to) is concentrated in hexane extract.

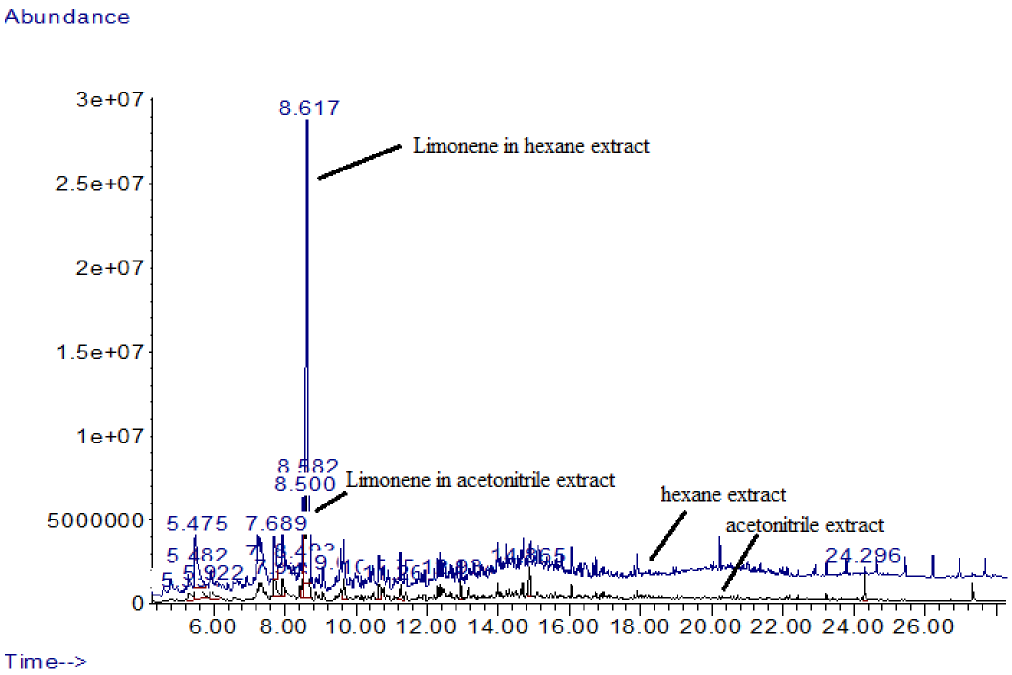

Fig. 2. Typical chromatograms of hexane extract (after extraction with acetonitrile) compared with acetonitrile extract

Results of NIST library (after having chosen the appropriate chemical compounds according to constant distribution of compound in hexane-acetonitrile system) are presented in the Table 1.

Table 1. Major chemical composition of pyrolysis oil and distribution constants of compounds in hexane-acetonitrile system

Chemical compound	**Rt, min**	**Relative content, %**	**D_i**
Ethylbenzene	5.29	7.00	1.4
o,p-Xylene	5.48	14.51	1.42
1,3-Cyclopentadiene, 5-(1-methylethylidene)-	5.93	7.10	0.86
alpha.-Methylstyrene	7.70	6.52	1.41
Benzene, 1,2,4-trimethyl	7.95	5.76	1.56
Benzene, 1-methyl-3-(1-methylethyl)-	8.52	6.17	2.71
Limonene	8.66	25.00	4.01
Benzene, 1-methyl-3-(1-methylethyl)-	9.07	3.45	2.79
Benzene, 1-methyl-4-(1-methylethenyl)-	9.66	3.30	1.83
1H-Indene, 3-methyl	10.65	6.20	1.28

Also it is found that in some cases NIST library has not correctly determined the chemical compound in pyrolysis oil. During the detailed research of the chemical composition of a pyrolysis oil it was found that the NIST library gave a few chemical compounds with the same probability which make the identification of it difficult. Using constant distribution value, it is possible to choose the correct chemical compound from the list presented in NIST library.

In a single extraction step, hexane – acetonitrile extraction efficiencies up to 65 wt% were achieved without significant limonene transfer to the acetonitrile phase. Thus, hexane – acetonitrile system can be used to separate limonene with aliphatic hydrocarbons from pyrolysis oil. However it is not a trivial exercise to obtain a highly concentrated limonene fraction of sufficient quality.

Typical chromatograms of initial hexane extract in comparison with hexane extract after sulfuric acid extraction are presented in Fig. 3.

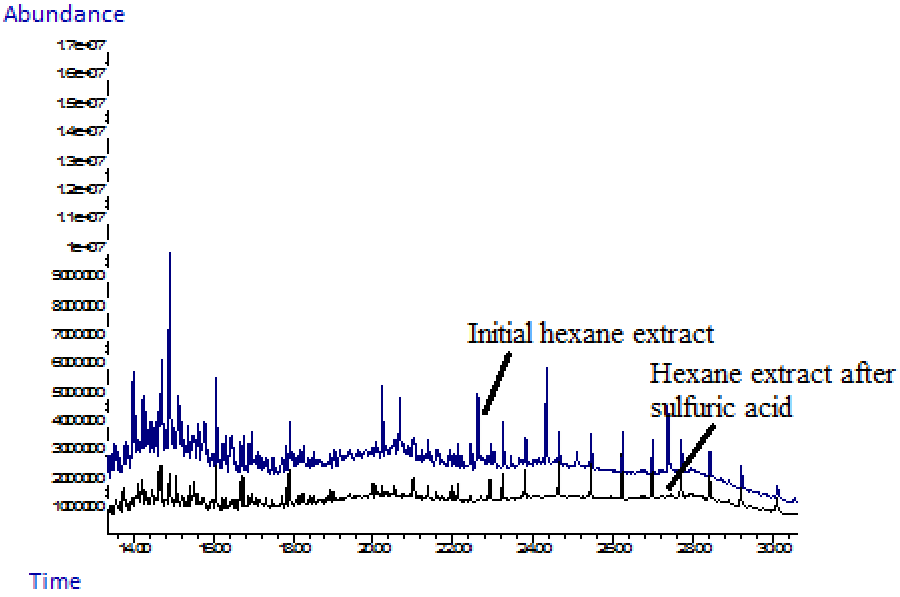

Fig. 3. Typical chromatograms of hexane extract (after deasphthalting) compared with hexane extract (after sulfuric acid extraction)

Extraction of pyrolysis oil with sulfuric acid makes it possible to separate the ultimate hydrocarbons from unsaturated hydrocarbons. Therefore, the hexane extract after treatment with sulfuric acid consists of alkanes, naphthenes and cycloalkanes.

3.3. PAHs analysis results

PAHs content was obtained by EPA TO-13 method (Compendium of Methods for the Determination of Toxic Organic Compounds Using Gas Chromatography/Mass Spectrometry (GC-MS) method). The 16 studied PAHs range from two- to six-ring aromatic compounds [23–25]. The analysis of PAHs was performed by using a selected ion mode (SIM-mode) of mass-detector (in the Table 2 monitored ions are presented). It is shown that PAHs were concentrated in acetonitrile extract according to the values of D_i.

Table 2. Monitoring ion profile, concentration and distribution constants of PAHs in hexane-acetonitrile system

Compound	**Monitored ions**	**Rt, min**	**Concentration, mg/kg**	**D_i**
naphtalene	128–129	7.29	83.24	0.71
acenaphthylene	152–153	11.05	73.46	0.61
acenaphtene	154–153	11.47	51.00	1.02
fluorene	166–165	12.73	25.20	0.67
phenanthrene	178–179	15.08	23.04	0.57
anthracene	178–179	15.22	25.58	0.62
fluoranthene	202–203	18.72	20.28	0.52
pyrene	202–203	19.49	2.24	0.65
benzo[a]anthracene	228–226	24.30	0.27	0.39
chrysene	228–226	24.44	n.d.*	0.43
benzo[b]fluoranthene	252–253	28.71	25.46	0.35
benzo[k]fluoranthene	252–253	28.83	60.52	0.41
benzo[a]pyrene	252–253	29.92	76.04	0.44
indeno[1,2,3,-c,d]pyrene	276–277	33.94	31.83	0.35
dibenz[a,h]anthracene	278–279	34.09	78.82	0.28
benzo[g,h,i]perylene	276–277	34.78	17.45	0.47

*n.d. – not detected

We have found out that limonene can be separated in hexane extract and PAH can be preconcentrated in acetonitrile extract using hexane – acetonitrile system. Thus, we can remove toxic PAHs from analysed mixture. Content of PAHs in pyrolysis oil was about 0.1%. Distribution constants of PAHs were calculated for standard solution. Obtained values are matched with calculated distribution constants of pyrolysis oil. These results can be used for PAH identification in hexane – acetonitrile system.

4. CONCLUSIONS

After having made this study, we demonstrated the major chemical composition of pyrolysis tyre oil derived from automobile tyre wastes. Moreover, the pyrolysis liquids contain olefins, specially limonene and light aromatics, whose have higher market values as chemical feedstock than their use as fuels. Thus, the extraction of pyrolysis oil was studied for the purpose of separating valuable chemical compounds of pyrolysis oil. The distribution constants of pyrolysis oil were determined in «hexane-acetonitrile» system to clarify the chemical nature of samples and to make additional identification of compounds. It was found that the main valuable component of pyrolysis oil is limonene (25%).

It has also been established that hexane-acetonitrile system extraction of pyrolysis oil components allows limonene to separate with aliphatic hydrocarbons from PAHs. Quantitative analysis of PAHs has shown that the amount of these compounds is about 0.1% in the mixture.

In a single extraction step, hexane – acetonitrile extraction allows limonene to separate from pyrolysis oil in hexane extract. However, limonene is not pure and it is in a mixture with saturated and unsaturated hydrocarbons. Research activities on the regeneration of the extract phase to obtain purified limonene are in progress. Especially, the separation of limonene from some other compounds presented in the pyrolysis oil and the removal of the sulfur-containing compounds (1.5%), due to their foul odour, is essential for future research.

REFERENCES

1. CUMALI, I. et al. Fuel production from waste vehicle tires by catalytic pyrolysis and its application in a diesel engine. *Fuel Processing Technology*, 2011, Vol. 92, p. 1129–1135.
2. JALE, Y. et al. Fast pyrolysis of agricultural wastes: Characterization of pyrolysis products. *Fuel Processing Technology*, 2007, Vol. 88, p. 942–947.
3. BARBOOT, I M. M. et al. Optimization of pyrolysis conditions of scrap tyres under inert gas atmosphere. *J. Anal. Appl. Pyrolysis*, 2004, Vol. 72, p. 165–170.
4. KYARI, M. et al. Characterization of oils, gases, and char in relation to the pyrolysis of different brands of scrap automotive tires. *Energy Fuels*, 2005, Vol. 19, p. 1165–1173.
5. LARESGOITI, M. F. et al. Chromatographic analysis of the gases obtained in tyre pyrolysis. *J. Anal. Appl. Pyrolysis*, 2000, Vol. 55, p. 43–54.
6. CUNLIFFE, A. M., WILLIAMS, P. T. Composition of oils derived from the batch pyrolysis of tyres, *J. Anal. Appl. Pyrolysis*, 1998, Vol. 44, p. 131–152.
7. LARESGOIT, I M. F. Characterization of the liquid products obtained in tyre pyrolysis. *J. Anal. Appl. Pyrolysis*, 2004, Vol. 71, p. 917–934.
8. MURUGAN, S. Assessment of pyrolysis oil as an energy source for diesel engines. *Fuel Processing Technology*, 2009, Vol. 90, p. 67–74.
9. LOPEZ, F. A. et al. Distillation of granulated scrap tires in a pilot plant. *J. Hazard. Mater.*, 2011, Vol. 190, p. 285–292.
10. QUEK, A., BALASUBRAMANIAN, R. Liquefaction of waste tires by pyrolysis for oil and chemicals – a review. J. Anal. Appl. Pyrolysis, 2013, Vol. 101, p. 1–16.
11. DANON, B. A review of dipentene (DL-limonene) production from waste tyre pyrolysis. *J. Anal. Appl. Pyrolysis*, 2015, Vol. 112, p. 1–13.
12. RATHSACK, P. et al. Analysis of pyrolysis liquids from scrap tires using comprehensive gas chromatography-mass spectrometry and unsupervised learning. *J. Anal. Appl. Pyrolysis*, 2014, Vol. 109, p. 234–243.
13. RASRENDRA, C. B. et al. Recovery of acetic acid from an aqueous pyrolysis oil phase by reactive extraction using tri-n-octylamine. *Chemical Engineering Journal*, 2011, Vol. 176, p. 244–252.
14. MAHFUD, F. H. Acetic Acid Recovery from Fast Pyrolysis Oil. An Exploratory Study on Liquid-Liquid Reactive Extraction using Aliphatic Tertiary Amines. *Separation Science and Technology*, 2008, Vol. 43, p. 3056–3074.
15. VITASARI, C. R. Water extraction of pyrolysis oil: The first step for the recovery of renewable chemicals. *Bioresource Technology*, 2011, Vol. 102, Issue 14, p. 7204–7210.
16. TAMADA, J.A. Extraction of carboxylic acids with amine extractants. *Ind. Eng. Chem. Res.*, 1990, Vol. 29, p. 1327–1333.

17. HIRTH, J. Isolation of carbohydrate carboxylic acids from aqueous solutions by reactive extraction. *Chem. Eng. Technol.,* 2003, Vol. 26, p. 656–660.
18. PAKDEL, H. et al. Production of dl-limonene by vacuum pyrolysis of used tires. *J. Anal. Appl. Pyrolysis*, 2001, Vol. 57, p. 91–107.
19. ROFIGUL, I. M. et al. Limonene-rich liquids from pyrolysis of heavy automotive tire wastes. *J. Environ. Eng.*, 2007, Vol. 2, p. 681–695.
20. ZHANG, X. T. et al. Vacuum pyrolysis of waste tires with basic additives. *Waste Manage*, 2008, Vol. 28, p. 2301–2310.
21. MASTRAL, A.M. et al. Influence of process variables on oils from tire pyrolysis and hydropyrolysis in a swept fixed bed reactor. *Energy Fuels*, 2000, Vol. 14, p. 739–744.
22. WILLIAMS, P. T. Pyrolysis of waste tyres: a review, *Waste Manage*, 2013, Vol. 33, p. 1714–1728.
23. BUCOA, S Analysis of polycyclic aromatic hydrocarbons in contaminated soil by Curie point pyrolysis coupled to gas chromatography–mass spectrometry, an alternative to conventional methods. *Journal of Chromatography A*, 2004, Vol. 1026, Issues 1, p. 223–229.
24. NAZLY, E. et al. Quantification of polycyclic aromatic hydrocarbons (PAHs) found in gas and particle phases from pyrolytic processes using gas chromatography–mass spectrometry (GC–MS). *Fuel*, 2013, Vol. 107, p. 246–253.
25. PIMENTA, A. S. Characterisation of polycyclic aromatic hydrocarbons in liquid products from pyrolysis of Eucalyptus grandis by supercritical fluid extraction and GC-MS determination. *Fuel*, 1998, Vol. 77, No. 11, p. 1133–1139.

LEAD FERRITE SYNTHESIS BY REACTIVE MAGNETRON SPUTTERING AND ANALYSIS

B. Beklešovas, V. Stankus
Department of Physics, Kaunas University of Technology
Studentu str. 50, LT-51368 – Lithuania
Email: benas.beklesovas@ktu.edu

ABSTRACT

The interest in multiferroics increased in 2000 when methodology, synthesis and analysis technologies have advanced. Multiferroics are materials where at least two ferroic properties coexist These unique properties provide new opportunities in developing electronic components, research and especially creating novel memory elements. In this work lead ferrite ($Pb_2Fe_2O_5$) thin films have been investigated. Recent researches showed coexistence of ferroelectric and magnetic properties in PFO. Five samples were synthesized by reactive magnetron sputtering at temperature range from 450 ºC to 650 ºC. Lead ferrite thin films were formed successfully starting from 500 ºC to 600 ºC. P – E measurements showed the best ferroelectric properties in sample synthesized in 500 ºC – remnant polarization (P_r) ~54 μC/cm^2 and the coercive electric field (E_c) ~68,6 kV/cm. XRD analysis supplements P – E measurements and approves successful formation of lead ferrite structures by direct current reactive magnetron sputtering.

Keywords: multiferroics, lead ferrite, reactive magnetron sputtering, thin films, ferroelectric

1. INTRODUCTION

The interest of multiferroics has increased rapidly in the past decade [1]. Improvement of sophisticated experimental techniques for complex oxide synthesis as well as advanced analysis equipment and theoretical methods made big impact in development of novel memory elements such as MRAMs or FeRAMS [2, 3]. Multiferroics material is characterized by coexistence of two primary ferroic properties such as ferroelectricity, ferromagnetism (antiferromagnetism), ferroelasticity or ferrotoroidicity [4–6]. Materials with these properties are used in wide range of technologies such as novel memory media, sensors, next-generation spintronics devices and other applications [7]. The great atention is paid to multiferroic memory applications, where high efficiency products is produced. FeRAMS is known for its durability, low power consumption and faster read/write process comparing to Flash memory elements [8]. The most studied coexistence is coupling between ferroelectricity and (anti)ferromagnetism otherwise called magnetoelectric effect [9]. As known ferroelectric compound has the electric polarization as the order parameter, ferromagnetic compound – magnetization. Ferroelectricity is caused by empty d shell (so called d^0-ness) and ferromagnetism occurs due to partially filled d or f shell. In this case these effects should cancel each other [9, 10]. Therefore, there are different mechanisms for these properties to coexist, one could be reached by synthesizing two different systems – one responsible for ferroelectricity and another for magnetic properties. In this mechanism usually prevails perovskites where A site cation provides ferroelectric properties, B site – magnetic [7, 10]. Other way to obtain multiferroic properties is complex lattice distortion such as geometric ferroelectricity in hexagonal manganates [11]. Due to these geometric distortions ferroelectric and magnetic properties origin is the same. These multiferroics are called improper and show very strong coupling between ferroelectric and magnetic orders, although polarization and magnetization values are lower than proper multiferroics [4, 10]. Magnetoelectric effect provides possibility to control magnetism with electric field and vice versa. Although, these characteristics are unique, there are not so many multiferroic materials due to the complexity of the magnetoelectric effect mechanisms and low Curie temperature. Today's main challenge is to improve theoretical and synthesis methods to deposit materials which obtain multiferroic properties at room temperature. Although there are many ferroelectric and ferromagnetic materials, only few are multiferroics, even less of them show these properties in room temperature or higher [5, 9, 12].

In this work $Pb_2Fe_2O_5$ (PFO) was investigated. Though there are reports about lead ferrite formation by chemical deposition methods [13, 14], physical deposition was not used yet. The advantages of reactive magnetron sputtering are in situ deposition – materials could be grown directly on substrate without post-annealing, usage of high purity targets and high vacuum [15, 16].

2. METHODOLOGY

The first step to determine synthesis parameters is to investigate its separate components deposition rates. Synthesis of PbO and Fe_2O_3 were performed by layer-by-layer reactive magnetron sputtering using very pure, oval shape, flat cathodes of Fe and Pb (purity 99.999 %). Thin films were deposited in oxygen environment at 1.3 Pa pressure for 1 hour. The thickness of the samples was measured by Linnik interferometer (accuracy ±5 nm). In Fig. 1 is shown PbO and Fe_2O_3 layers thickness dependence from magnetron discharge current.

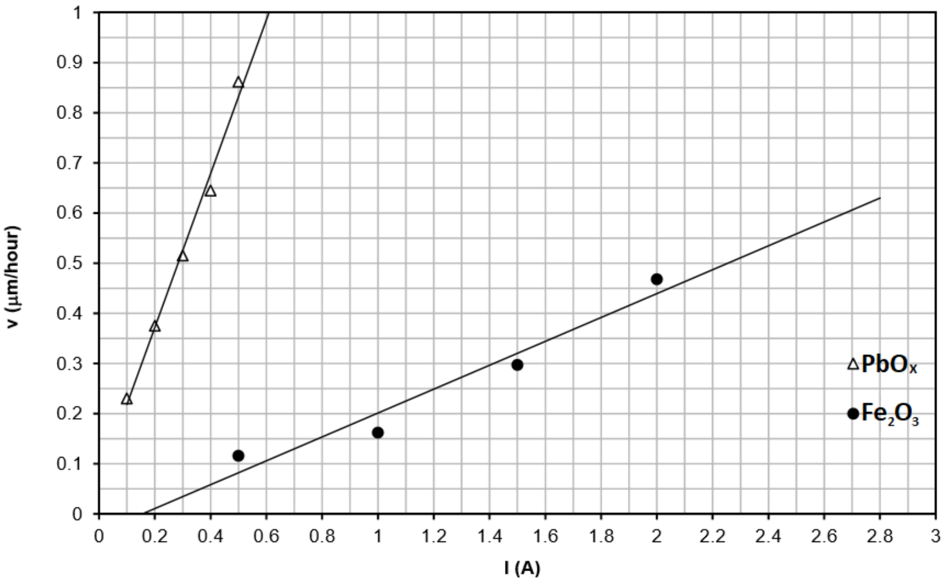

Fig. 1. PbO and Fe_2O_3 layers thickness dependence from magnetron discharge current

Formula for the amount of material:

$$\upsilon = \frac{N}{N_A} \tag{1}$$

where: υ – the amount of material (mol); N – the number of molecules; N_A – Avogadro constant ($6.02 \cdot 10^{23} mol^{-1}$). Using deposition rates showed in Fig. 1 and formula for the amount of material (1), the magnetron deposition parameters for $Pb_2Fe_2O_5$ could be determined when Pb and Fe oxides ratio 1 : 2.

Table 1. The parameters of magnetrons

Cathodes / Cathode par.	Ratio of oxides	
	Fe/Pb 1 : 2	
	Pb	Fe
Discharge current, A	0.38 ± 0.01	2.00 ± 0.01
Discharge voltage, V	293 ± 1.00	275 ± 1.00

After determination of possible magnetron properties five samples (10 × 10 mm) of lead ferrite thin films were synthesized in O_2 gas environment. Magnetron and sample layout is shown in Fig. 2, where: 1 – substrate on which PFO is formed, 2 – heating element, 3 – direction of movement of the substrate during synthesis, 4 – material target from which PFO is formed, 5 – cooling system, 6 – DC power source.

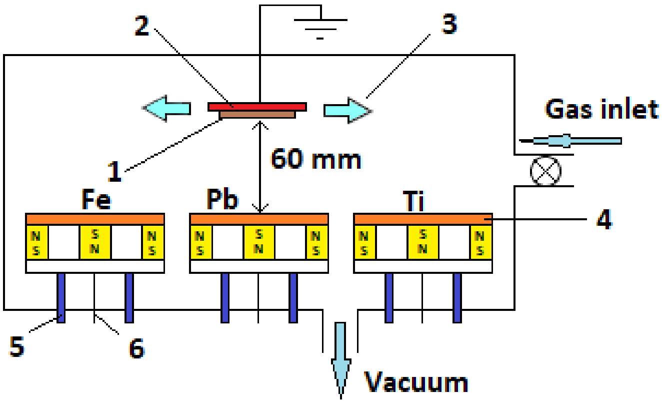

Fig. 2. Diagram of magnetron and sample layout

Temperature range was chosen from 450 °C to 650 °C (50 °C interval). For Lead ferrite identification of the best ferroelectric properties multilayer system of $Al/SiO_2/Si$ with the thickness of Al (50 nm) and SiO_2 (1 μm) was used. Al layer was deposited by thermal evaporation method and SiO_2 by thermal oxidation which was synthesized on Si (1 0 0) substrate.

For XRD measurement PFO thin films another substrate was used – $Pt/Ti/SiO_2/Si$. The thickness of Pt, TiO_2 and SiO_2 layers are 200 nm, 50 nm and 1 μm respectively. As in previous substrates SiO_2 layer was prepared by thermal oxidation method. Titanium and platinum layers were deposited by reactive magnetron sputtering. Before formation of lead ferrite seeding layer was deposited. Titanium was selected as seeding layer which was prepared also by reactive magnetron sputtering method at temperature of 750 °C and argon environment (1.3 Pa). The duration of deposition was 7 s, after that Ti layer of 5 nm thickness has been synthesized (the thickness was investigated earlier). Immediately after titanium synthesis temperature was lowered to the required temperature and argon environment changed to pure oxygen. Temperature range was selected according obtained ferroelectric properties. Lead ferrite thin films were deposited for 1 hour in situ layer-by-layer method using magnetron parameters as determined in Table 1, the distance between magnetrons and substrate was 65 mm. The finishing was done by formation of top electrode by thermal evaporation method where 1.3 mm in diameter Al electrodes were synthesized. The crystallographic structure of sample was investigated by X-ray diffraction (XRD) (Bruker D8 series diffractometer using monochromatic CuKα radiation with Bragg-Brentano geometry) (accuracy ± 0,002º). Measurement of polarization dependence on electric field was performed by using Sawyer and Tower method with oscilloscope Rigol DS1102E (accuracy ± 4%), leakage current measurement was performed with “Agilent 34410A“ (accuracy ± 1%).

3. RESULTS AND DISCUSSION

Five samples of lead ferrite were synthesized on Si substrate with aluminum electrodes for identification in which temperature range the best ferroelectric properties are obtained. Samples synthesized from 500 ºC to 600 ºC P – E hysteresis are shown in Fig. 3. Thin films formed at temperatures of 450 ºC and 650 ºC did not show any ferroelectric properties. In one case the temperature was too low for PFO formation and in the another too high which led to Pb desorption.

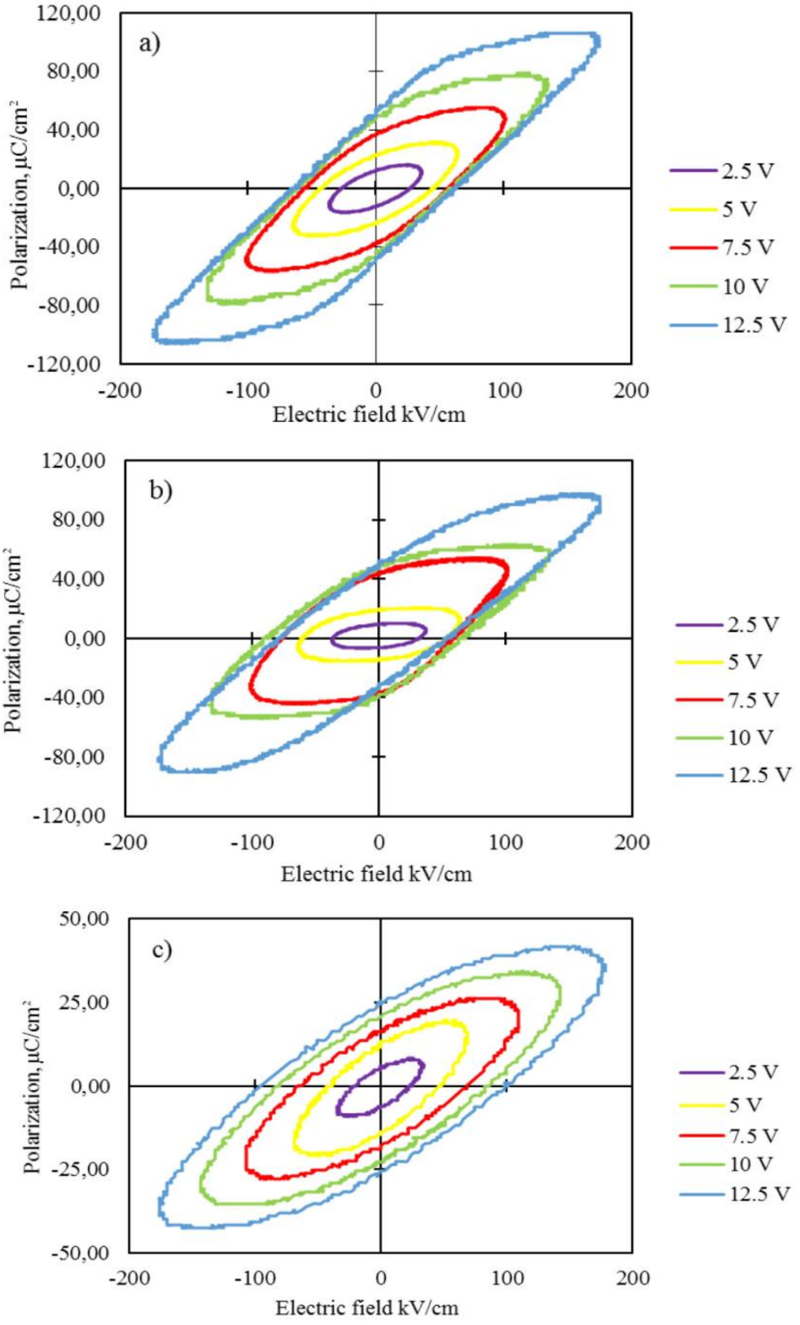

Fig. 3. $Pb_2Fe_2O_5$ thin films hysteresis family measured with external electric field up to 12.5 V at 50 Hz: a) synthesized at 500 ºC; b) synthesized at 550 ºC; c) synthesized at 600 ºC

Lead ferrite synthesized at 500 ºC shows the best ferroelectric properties with remnant polarization of ~54 µC/cm^2 and coercive field ~68.6 kV/cm. These values were obtained by Saywer – Tower measurement circuit with 150 nF reference capacitor. Thin films were able to withstand up to 12.5 V, 50 Hz external electric field voltage. In Fig. 3, a hysteresis loop shows proportional development of remnant polarization and quite good saturation compared with other two samples (Fig. 3, b and c). With increase of temperature the decreasing film saturation is obtained. In sample synthesized at temperature of 550 ºC (Fig. 3, b) ferroelectric properties are similar to the first sample, where P_r ~52 µC/cm^2 and coercive field ~71 kV/cm. Hysteresis oval shape shows incomplete saturation, this could happen due to defects in thin films such as oxygen vacancies, interaction with substrate electrode, which could have been affected higher leakage currents. The last lead ferrite sample was formed at 600 ºC, which performed the worst ferroelectric properties of all specimens. Remnant polarization reached ~25 µC/cm^2 and E_C ~100 kV/cm at maximum external electric field value of 12.5 V. The oval shape of hysteresis loop shows very high leakage current which could occur for the same reason as in previous sample, particularly high desorbtion of lead from the sample and thin film interaction with electrodes.

To acquire accurate measurements of PFO ferroelectric properties the thickness of layers was measured. The dependence of layer thickness from synthesis temperature is shown in Fig. 4. The constant decrease of thickness could be observed. This dependence could supplement hysteresis shape change with temperature increase. Due to increase of temperatures the bigger amount of lead could desorb from sample at same time interaction between thin layer and substrate electrode could occur which possibly explain steady decrease of PFO layer thickness with temperature increase.

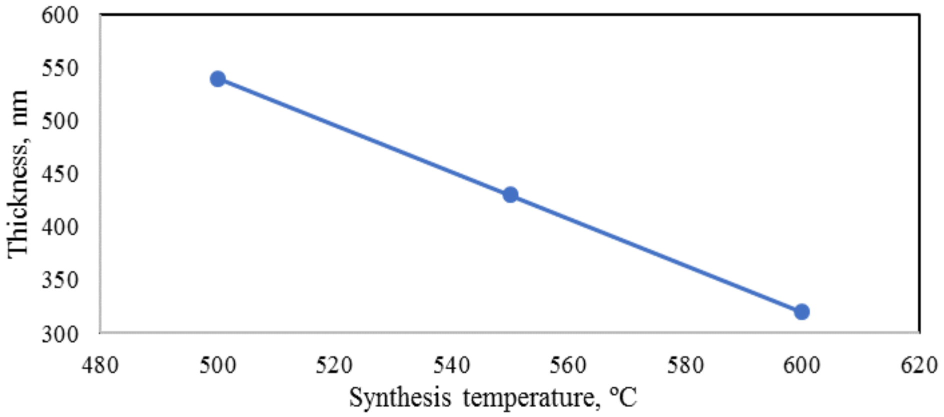

Fig. 4. PFO layer thickness dependence from synthesis temperature

For further investigation synthesis temperature in which PFO showed the best ferroelectric properties were chosen (500 ºC). Lead ferrite sample on platinized silicon were prepared by reactive magnetron sputtering. Later sample was analyzed by XRD (Fig. 5). Diffraction spectrum confirmed hysteresis measurements, highest PFO peaks of (2 2 0), (3 1 2), (3 0 4), (4 0 4) and (4 2 4) at 29.7º, 31.5º, 37º, 53.6º and 56.5º respectively were obtained (PDF# 33-0756) on the sample synthesized at 500 ºC. Artem M. Abakumov et. al conducted a research study of PFO structure, where lead ferrite was identified as monoclinic structure [17]. Although PFO structures were formed, other parasitic oxides were unable to avoid – Fe_2O_3 and PbO. Small peak of iron oxide was obtained only, where lead oxide was the bigger concern. Min Wang et al. in his work investigated PFO structures with different Fe/Pb oxide ratios and reported that the research group were unable to decrease or even eliminate lead oxide structures and suggested that due to crystallographic shear planes PFO corresponds to general formula of $Pb_2Fe_2O_5$–xPbO [13]. One of the reasons could be that all oxides have the same oxidations states and is formed at the same synthesis conditions.

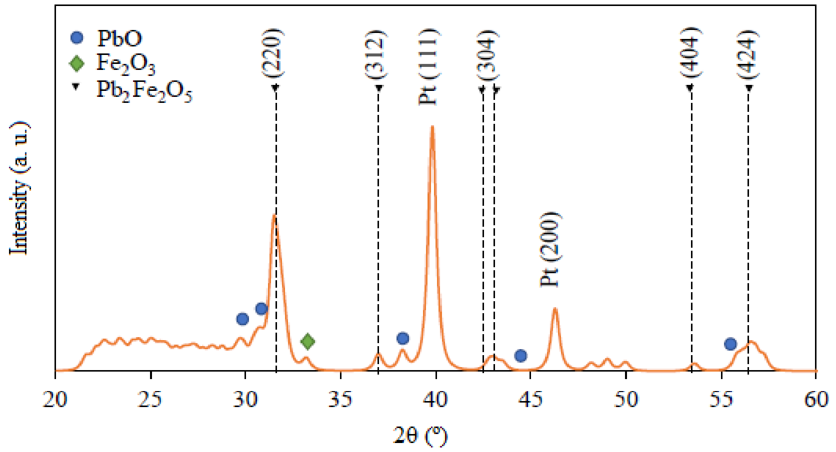

Fig. 5. XRD spectrum of PFO synthesized on platinized silicon at 500 ºC

To all samples which showed ferroelectric properties further investigation were made. In Fig. 3 all hysteresis loops have oval shape. Leakage current may be responsible cause for unsaturated PE hysteresis loops. Fig. 6 shows voltampere characteristic and leakage current densities J in PFO films which were synthesized at 500 ºC, 550 ºC and 600 ºC temperature. After plotting the leakage current density graph, it turned out that in all samples ohmic conduction dominates, an exponential of a ~1,5 (Fig. 6, b). Ohmic conduction occurs when electrons from the cathode are quickly transported via the conduction band.

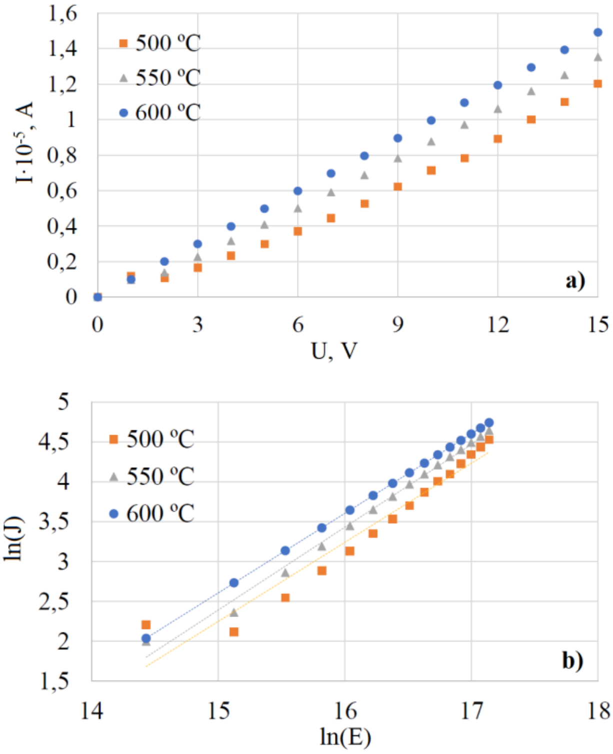

Fig. 6. Leakage current characteristics of PFO thin films synthesized at 500 ºC, 550 ºC and 600 ºC; a) voltampere characteristic; b) leakage current density

4. CONCLUSION

Before formation of $Pb_2Fe_2O_5$, lead oxide and iron oxide thickness dependence from magnetron discharge current were established. Thin films formed at 500 ºC, 550 ºC and 600 ºC showed quite good ferroelectric properties where the best sample synthesized at 500 ºC obtained remnant polarization of ~54 $\mu C/cm^2$ and coercive field ~68.6 kV/cm when external electric field voltage was up to 12.5 V at 50 Hz. Samples showed good ferroelectric values although not fully saturated hysteresis loops were observed. It could be due to oxygen vacancies formed during synthesis and interaction between PFO and substrate electrode. Measured leakage currents across formed PFO capacitors showed quite large leakage currents which could approve the obtained oval shape of P - E hysteresis loops.

Lead ferrite layer thickness dependence from synthesis temperature shows decrease of thickness with temperature increase which could mean structural changes of PFO films due to interaction with electrode and lead desorption. These results supplement hysteresis measurements.

The best ferroelectric properties of PFO were obtained when synthesis temperature was 500 ºC. At this temperature additional sample of PFO was formed on platinized silicon which was analyzed with X-ray diffraction spectrometer. Obtained XRD spectrum showed successful formation of PFO structures, although PbO and Fe_2O_3 peaks were detected.

REFERENCES

[1] Wu, J., et al., *Multiferroic bismuth ferrite-based materials for multifunctional applications: Ceramic bulks, thin films and nanostructures.* Progress in Materials Science, 2016. 84: p. 335–402.

[2] Wang, L., et al., *Comparative investigating the properties of Pb-based multilayer ferroelectric thin films for FeRAM.* Journal of Materials Science: Materials in Electronics, 2006. 17(7): p. 509–514.

[3] Ren, T.-L., et al., *Studies of a PT/PZT/PT sandwich structure for feram applications using sol-gel processing.* Integrated Ferroelectrics, 2001. 39(1–4): p. 215–222.

[4] Achary, S.N., O.D. Jayakumar, and A.K. Tyagi, *4 – Multiferroic Materials*, in *Functional Materials*. 2012, Elsevier: London. p. 155–191.

[5] Ivanov, S., *Chapter 7 – Multiferroic complex metal oxides: Main features of preparation, structure, and properties*, in *Science and Technology of Atomic, Molecular, Condensed Matter & Biological Systems*, B.S. Tara Prasad Das and E. Olle, Editors. 2012, Elsevier. p. 163–238.

[6] Vytautas Stankus, S.T., *Funkcinė keramika*. Vol. 1. 2007: Vitae Litera. 168.

[7] Eerenstein, W., N.D. Mathur, and J.F. Scott, *Multiferroic and magnetoelectric materials.* Nature, 2006. 442(7104): p. 759–765.

[8] Meena, J.S., et al., *Overview of emerging nonvolatile memory technologies.* Nanoscale Research Letters, 2014. 9(1): p. 526–526.

[9] Wang, K.F., J.M. Liu, and Z.F. Ren, *Multiferroicity: the coupling between magnetic and polarization orders.* Advances in Physics, 2009. 58(4): p. 321–448.

[10] Khomskii, D., *Classifying multiferroics: Mechanisms and effects.* Physics. 2(20).

[11] Lilienblum, M., et al., *Ferroelectricity in the multiferroic hexagonal manganites.* Nat Phys, 2015. 11(12): p. 1070–1073.

[12] Khomskii, D.I., *Multiferroics: Different ways to combine magnetism and ferroelectricity.* Journal of Magnetism and Magnetic Materials, 2006. 306(1): p. 1–8.

[13] Wang, M. and G. Tan, *Multiferroic properties of Pb2Fe2O5 ceramics.* Materials Research Bulletin, 2011. 46(3): p. 438–441.

[14] Gil, D.M., et al., *Lead nitroprusside: A new precursor for the synthesis of the multiferroic Pb2Fe2O5, an anion-deficient perovskite.* Materials Chemistry and Physics, 2013. 141(1): p. 355–361.

[15] Musil, J., et al., *Reactive magnetron sputtering of thin films: present status and trends.* Thin Solid Films, 2005. 475(1–2): p. 208–218.

[16] Safi, I., *Recent aspects concerning DC reactive magnetron sputtering of thin films: a review.* Surface and Coatings Technology, 2000. 127(2–3): p. 203–218.

[17] Abakumov, A.M., et al., *Crystallographic Shear Structures as a Route to Anion-Deficient Perovskites.* Angewandte Chemie International Edition, 2006. 45(40): p. 6697–6700.

CYSENI 2018, May 23-25, Kaunas, Lithuania
ISSN 1822-7554, www.cyseni.com

CHARACTERIZATION OF CHEMICAL COMPOSITION AND PARAMAGNETIC CENTRES IN LATVIAN SHEEP BREED WOOL

V. Voikiva, L. Avotina, V. Kinerte, G. Kizane
University of Latvia, Institute of Chemical Physics
Jelgavas street 1, LV-1004, Riga – Latvia
Email: vanda259@inbox.lv

L. Baumane
Latvian Institute of Organic Synthesis,
Aizkraukles street 21, LV-1006, Riga – Latvia

ABSTRACT

The amount of substances in sheep wool depends of the sheep breed, age, gender and climatic zone, so it is important to know how much of each substance is in the wool, if it is planned to produce or excreted some products from sheep's wool. To evaluate the difference of chemical composition and the radiation influence to wool, was used Fourier transformation infrared (FT-IR), electron paramagnetic resonance (ESR) and X-ray fluorescence (XRF) spectrometry. Element composition determination and thermal analysis methods give additional information about Latvian sheep breed wool.

Keywords: Sheep wool, Fourier transformation infrared (FT-IR), electron spin resonance (ESR), X-ray fluorescence (XRF) spectrometry, electron irradiation

1. INTRODUCTION

Sheep wool is natural and easily obtainable material, which is used in different ways. One of the most important sheep products is wool, which is used for insulation, construction materials, manufacture of yarns, blankets, clothes, rugs, packaging materials. Sheep wool contains a lot of different useful substances and items, such as lanolin, that is a valuable raw material for the production of cosmetics, lubricants and rust protectors. In USA wool clips produce 2–4 kg of lanolin per 100 kg [3]. There are patents about lanolin extraction by centrifugation and washing in water [4], centrifugation with additions of NaOH [5], centrifugation at elevated temperatures [6]. In other countries scientists are investigating how to improve lanolin extraction methods by using volatile hydrocarbons [7] supercritical fluid extraction [8], Soxhlet extraction [9], however in these methods cancerogenic solvents such as dichloromethane and toluene are used. Chemical treatment can cause changes in scale structure of wool [10]. Among refining methods of lanoline is mentioned use of polar solvents [1]. Presently in Latvia lanolin is not produced/obtained. There are some investigations about element content in sheep wool in different world regions [11]. In Baltic region there are some researches about sheep breeding in general and handbooks are made [12, 13]. But wool is still very cheap, and overall sheep breeding is not as beneficial as it could be. The main factor that impact Latvian sheep wool price is that sheep in Latvia are breeding mainly for meat and wool is more by-product and it cannot compete with wool from sheep who is breed specially for wool. The use of wool can be increased by modifying it. To rise wool fibre strength and elasticity by making it more durable to mechanical deformations like stretch and tongue. It will prolong the use of wool products such as insulation, construction materials, manufacture of yarns, blankets, clothes, packaging materials or even let us make new products and use wool there where it was not possible before. Modification can be done chemically, physically and with accelerated electron radiation. Investigations and radiation modifications of Latvia sheep wool are important in order to in estimate the lanolin release potential compared to sheep wool in the other climatic zones. So we studied sheep wool chemical composition to understand wool properties and chemical structure to rise the sheep wool price and make the sheep breading more beneficial for farmers. Radiation modification of Latvian sheep wool with accelerated electrons (linear accelerator, ELU-4, absorbed dose up to 500 kGy) is performed to improve its characteristics.

2. EXPERIMENTAL

From different places in Latvia sheep wool from one breed sheep and from mixed breed sheep was collected to evaluate the differences in wool structure. Wool was split up to small parts (about 1 gram) and putted in plastic bags. Examples were taken as similar as possible with the same brightness to objectively evaluate changes. Wool was not cleaned or washed, just taken from the places with the least amount of debris. To compare the samples between the different places was taken wool from sheep with same age, gender and breed, the exposure of the natural radiation did not exceed the norms established by Latvian legislation. Both farms feeds sheep only with natural products without chemical additives. All sheep wool examples are shown in Table 1.

Table 1. Latvian sheep wool examples

Nr.	**Region**	**Example name**	**Breed**	**Age**	**Gender**
1	North region	S1	LT	48 mon	Female
2	Central region	K1	LT	48 mon	Female
3		J205	XX 68.75% VMV 25.00% LT 6.25%	8 mon	Male
4		J201	XX 87.50% LT 12.50%	10 mon	Male
5		J139	VMV 50.00% XX 39.06% LT 10.94%	12 mon	female
6		J121	VMV 75.0% XX 18.75% LT 6.25%	16 mon	female
7		J113	XX 87.50% LT 12.50%	33 mon	female

VMV – German merino sheep; LT – Latvians dark-headed sheep; XX – half-breed

Were performed three parallel measurements by Fourier transformation infrared (FT-IR) attenuated total reflectance (ATR) module, ±2 resolution, 20 background scans, 20 sample scans, 2.95 hPa pressure was used, to analyse and prove functional group being in the wool. Samples were taken in the state they were, without any simulations.

The chemical compositions of the sheep wool were determined using a Bruker S8 Tiger wavelength-dispersive X-ray fluorescence (XRF) spectrometer equipped with Rh anode X-ray tube and 4 kW excitation power was used. Measurements were performed under helium atmosphere at 50 kV and 50 mA. ESR measurements were performed using Bruker Biospin X-band ESR spectrometer: microwave frequency: 9.84 GHz, microwave power: from 0.2 up to 31.7 mW, modulation amplitude: from 1 up to 5 G, field sweep width: 80, 200 and 4000 G, Sweep time: from 15 up to 60 sec, Time const: 5–20 ms, conversion 20 ms, operating at room temperature, to observed the free radicals or disappeared bonds. All samples was prepared in same way, so that data would be as accurate as possible. These methods have been used in wool research, because they are sample preserving and do not require any further processing or specific preparation.

Radiation modification of Latvian sheep wool was performed with accelerated electrons (linear accelerator, ELU-4) up to 500 kGy was performed in room temperature, 90 cm from flank and with current strength 0.1 mA.

3. RESULTS AND DISSCUSSIONS

3.1. The FT-IR spectra of central and north region sheep wool

The FT-IR spectra of central region sheep wool (K1), modified with accelerated electrons, are shown in Fig. 1. To estimate the differences between irradiated and non-irradiated material, an intercomparison between the FT-IR spectra was performed. Intensity changes in modified sheep wool are not smooth, up to 50 kGy intensity decreases then from 100 to 150 kGy its increases, and up to 500 kGy it is sharply decreasing.

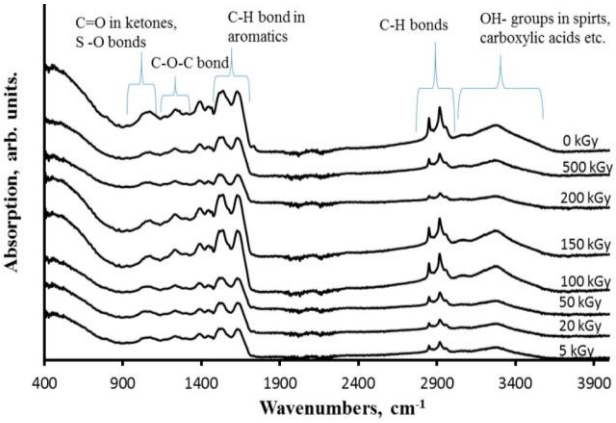

Fig. 1. FT-IR spectra of non-irradiated and radiated central region of Latvia K1 sheep wool

Intensity changes are not smooth all over the spectrum, for example, aliphatic ethers bond signal at 1050 cm^{-1} suddenly increases at absorbed dose 5 kGy, while nearby C=O bond at 1100 cm^{-1} signal intensity in the ketones does not change (Fig. 2).

The similar situation is with C-H bond signal 1550 cm^{-1} in aromatics which will intensify, but the intensity of the adjacent signal decreases steadily. The C-O-C bond signal at 1250 cm^{-1} decreases sharply while the intensity of the adjacent signal decreases steadily, and reaching the amount of absorbed dose of 100–150 kGy, the intensity of the signal increases, but in excess of this absorbed dose, the intensity of the signal is rapidly decreasing again. These changes can be observed in (Fig. 2).

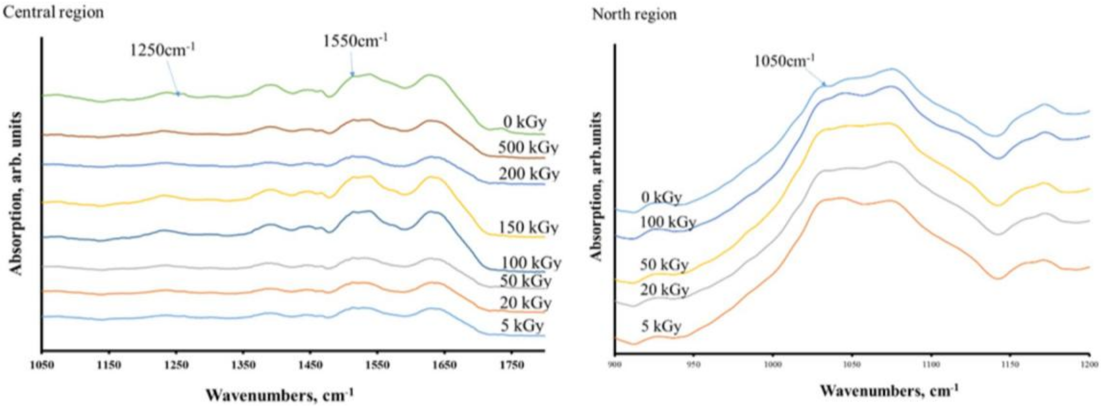

Fig. 2. Non-irradiated and irradiated central and north region of Latvia sheep wool spectra

Sheep wool chemical composition, the amount of elements and substances also depends on the age of the sheep. It is hard to say which factor influences the amount of substances more, but it is clear that in the wool of Latvia's dark-headed sheep, the ether, ester and alkane groups, 1250 cm^{-1}, 1550 cm^{-1} and 1700 cm^{-1} (which are in lanolin), are much less than in mixed with the VMV breed sheep wool. There are more samples needed to determine the impact of each factor, but all sample signal intensity can be observed in Fig. 3.

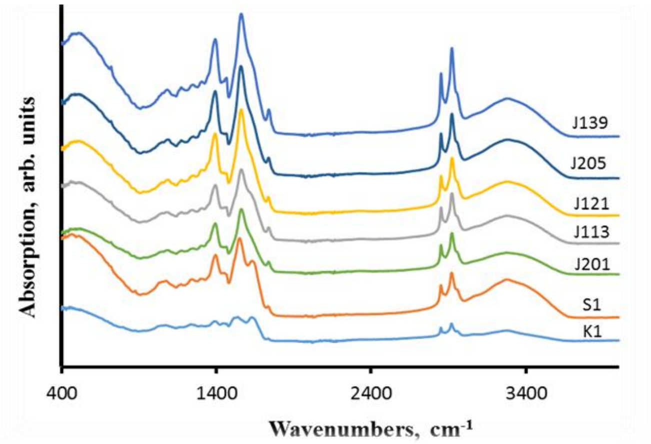

Fig. 3. FT-IR spectra of central and north regions of non-irradiated Latvia sheep wool

3.2. ESR spectra of irradiated central region sheep wool sample K1

Unmatched and wired ESR specimens have been captured at different values of microwave power. At low power (0.2 mW) in the magnetic field in the spread spectrum from 1600 to 5600 G, two signals are seen: one broad at g-value of 2.1 and a second narrow signal at g-value of 2.003. The dose of irradiation increases the register signal intensity. At high dose of irradiation also some other radical appearance is observed. Figs. 4, 5 and 6 show ESR spectra for a central region wool sample K1 irradiated with accelerated electrons from 5 up to 200 kGy.

Fig. 4 shows the signal that is detected in the wool sample in the range of organic free radicals and the magnetic field standard signal at g-value (g) 1.9800. The non-irradiated wool has one weak narrow signal at g = 2.0036–2.0046 with a line width (ΔH) 2.66 G. When irradiated wool with accelerated electrons, the shape and intensity of the signal change. In irradiated samples, a second signal with a g = 2.0051–2.0052 and ΔH = 10.17 G is formed and augmented. Both these signals can be attributed to semihinon-type radicals in melanin or other substances [20, 21].

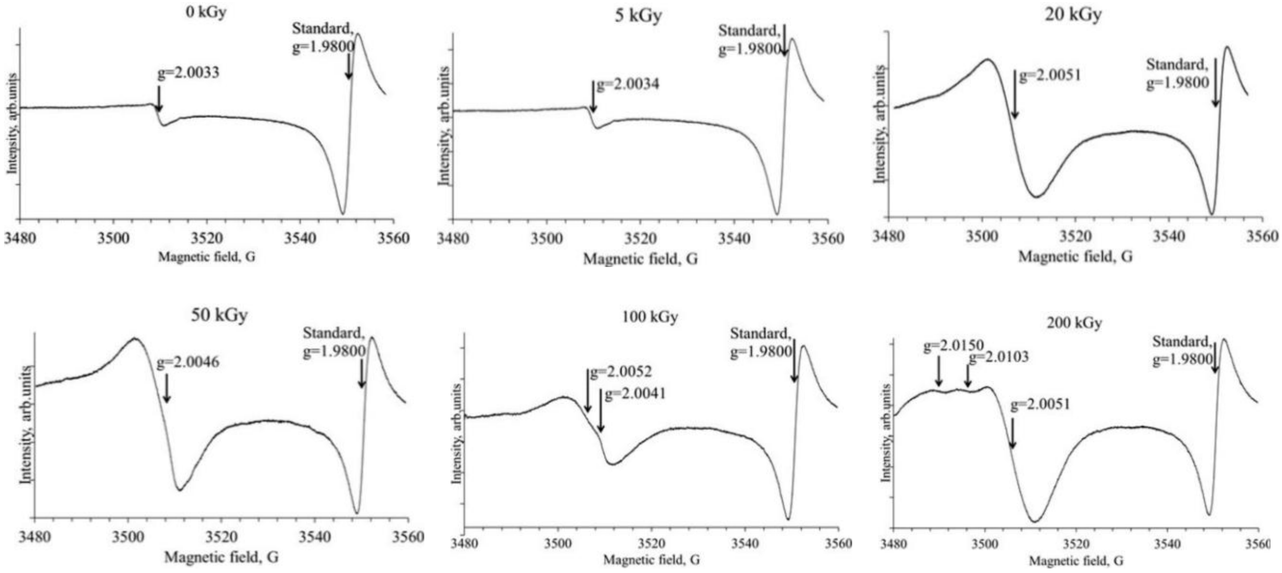

Fig. 4. ESR spectra of organic free radicals for a wool sample K1 at different radiation doses. Standard signal at g = 1.9800. Spectrum recording parameters: frequency 9.84 GHz, power 31.7 mW, sweep width 80 G, mod. ampl 1 G, sweep time 60 sec, time const. 20 ms, conversion 20 ms

From the radiation dose, a third signal appears in the 100 kGy ESR spectrum, which partially overlaps with the previous one and increases in intensity to a radiation dose of 200 kGy (Fig. 5). We have not identified the nature of this radical. In this ESR spectra hyperfine structure is observed, its to width exceeds 100 G, g = 2.026. This may be due to the radiation induced changes of disulphide bonds [16, 18].

Fig. 6 shows ESR spectra for sample K1 with different radiation doses in the magnetic field range from 1500 to 5500 G. In this spectrum, a composite natural signal with a g-factor value from 2.15 to 2.22 is shown. The signal width is between 500 and 1000 G. This may be due to Fe (III) ions in wool composition. It is known that lanolin released from wool is followed by a similar signal [15].

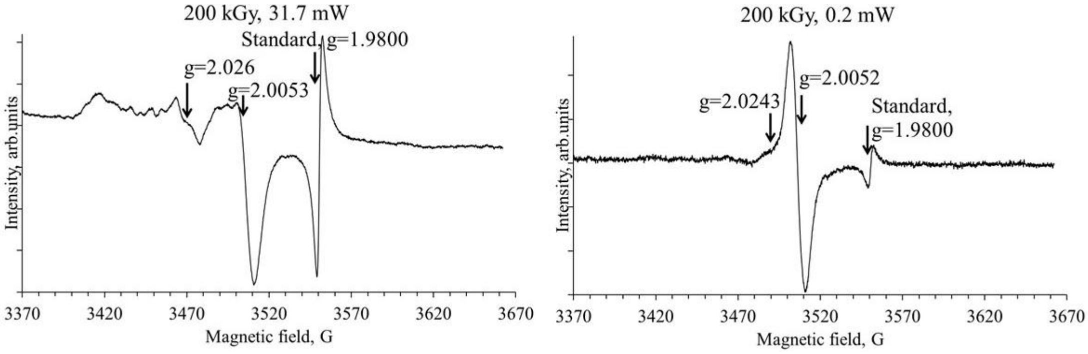

Fig. 5. The ESR spectra of wool sample K1 (left HFS's power 0.2 mW on right 31.7 mW), irradiated with 200 kGy

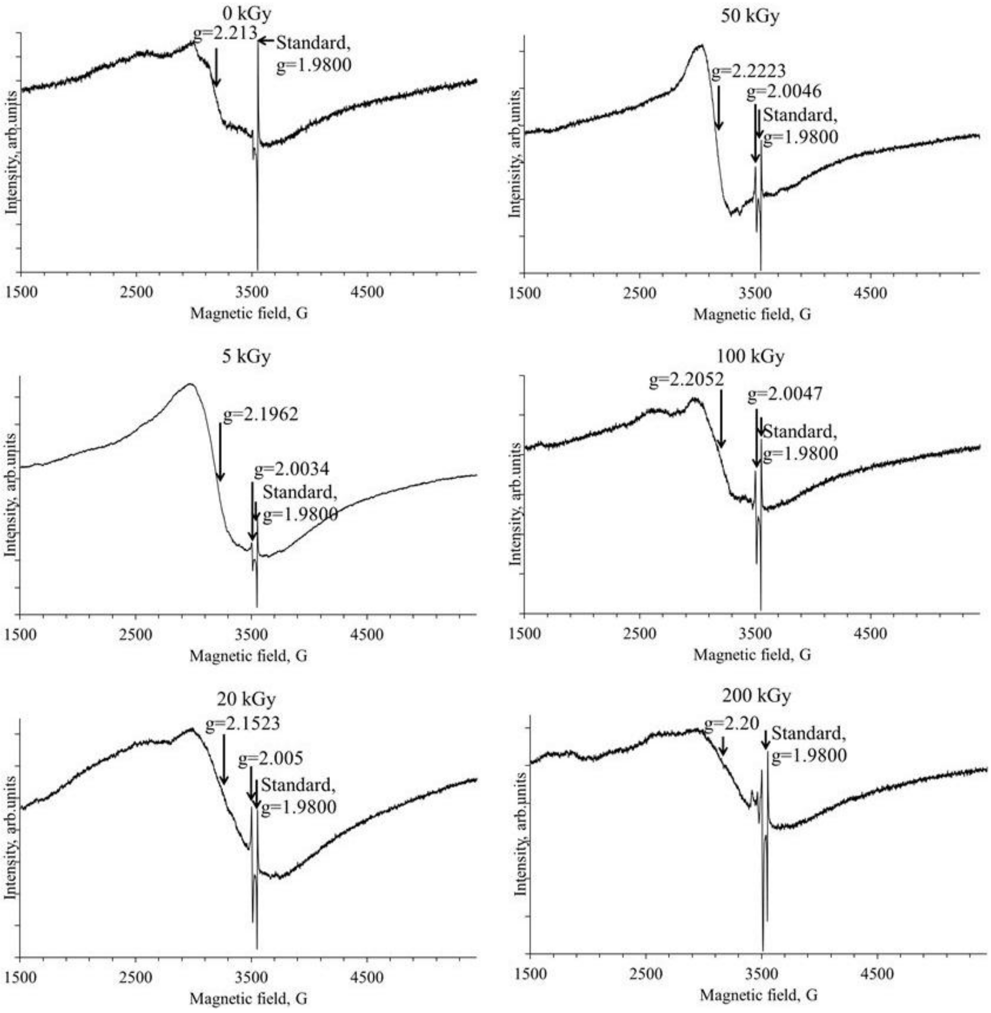

Fig. 6. ESR spectra of probe K1 sheep wool with different absorbed doses in the magnetic field range from 1500 G to 5500 G. Spectrum recording parameters: frequency 9.84 GHz, power 20 mW, sweep width 4000 G, mod. ampl 1 G, sweep time 15 sec, time const. 2.5 ms, conversion time 5 ms

3.3. Element composition

The average quantity of elements in sheep wool for each farm is given in Table 2. Quantity is shown in mg/kg of wool. There is shown the average quantity of three parallel measurements of each sample. As shown in the table, the amount of elements in the sheep wool is quite different, even within the same region. The presence of elements in wool up to a maximum of 100 mg/kg is highly questionable and can be practically equated to their not-existence in wool.

Table 2. The quantity of chosen micro and macro elements in central and north region of Latvia sheep wool

Elements	**K1 (mg/kg)**	**J (all) (mg/kg)**	**S1(mg/kg)**
Potassium (K)	66700 ± 7600	110 000 ± 21000	153200 ± 71500
Sulphur (S)	48300 ± 3200	38 800 ± 45	31700 ± 2500
Chlorine (Cl)	4200 ± 600	47 000 ± 300	4100 ± 1500
Calcium (Ca)	4400 ± 1100	2500 ± 1300	1500 ± 1100
Iron (Fe)	3800 ± 1300	2800 ± 1200	8000 ± 400
Silicon (Si)	3400 ± 800	< 100	< 100
Manganese (Mn)	1800 ± 400	900 ± 700	< 100
Aluminium (Al)	1200 ± 500	< 100	< 100

In Table 3. is summarized the number of elements in sheep wool from different countries of the world [1]. As shown in the table, the amount of iron, manganese, potassium and sulphur in the wool of Latvia is significantly higher than in other countries of the world, but the amount of phosphorus, magnesium and sodium is much smaller. Sulphur amount from south to north increases, but iron amount in sheep wool increases from north to south countries. Iron and sulphur amount in Latvian sheep wool is significantly different, that is larger than in other countries.

Table 3. The quantity of chosen elements in sheep wool from different countries

Element	**Poland [1] (mg/kg)**	**Greece [1] (mg/kg)**	**Syria [1] (mg/kg)**	**Latvia* (mg/kg)**
Calcium (Ca)	1790.0^{a} ± 392.0	2900.0^{b} ± 591.0	1800.0^{a} ± 351.0	**2657.14 ± 1107.6**
Phosphorus (P)	148.0^{a} ± 32.3	206.0^{b} ± 49.2	284.0^{c} ± 59.8	**< 100**
Sodium (Na)	1486.7^{a} ± 234.2	165.0^{b} ± 573.1	1745.5 ± 1 152.6	**< 1 00**
Potassium (K)	718.6 ± 307.7	643.0 ± 312.9	755.0 ± 295.3	**109971.4 ± 26375.8**
Magnesium (Mg)	120.8^{a} ± 17.2	383.5^{b} ± 65.4	590.8^{c} ± 133.5	**< 100**
Sulphur (S)	22038.3^{a} ± 663.9	20758.0^{b} ± 947.5	18733.4^{c} ± 1 212.4	**39166.7 ± 5235.3**
Iron (Fe)	22.03^{a} ± 3.55	76.70^{b} ± 27.37	513.17^{c} ± 201.79	**2695.24 ± 1088**
Aluminium (Al)	53.65^{a} ± 5.46	127.00^{b} ± 24.58	620.83^{c} ±304.51	**< 100**
Manganese (Mn)	3.37^{a} ± 1.65	4.43^{a} ± 1.8	22.93^{b} ± 13.93	**914.3 ± 631.0**

a, b, c $P < 0.05$ *Average value from central and north region of Latvia.

4. CONCLUSIONS

The non-irradiated and irradiated Latvian dark-headed breed and mixed breed sheep wool was studied by XRF, ESR and FT-IR techniques. The results obtained from FT-IR spectra indicate uneven collapse of bonds at in separate spectrum stages. More precisely at 1050 cm^{-1}, 1250 cm^{-1} and 1500 cm^{-1} referring to the functional groups of ketones, aromatics and ethers. The intensity of these three functional groups also varies considerably between different sheep wools, while the intensity of the C-H and O-H bonds is unchanged or slightly different.

In the ESR spectra different signals are observed, the main signals are from presence of hinon type radicals and iron (III) ions. The change in the intensity of the iron (III) ion signal is not directly proportional to the absorbed dose change. There are two hinon type radicals – intensity of one radical signal with $\Delta H = 2.66$ G and $g = 2.0036$ reduced, while the intensity of another radical signal with $\Delta H = 10.17$ G and $g = 2.0051$ increases with increasing the absorbed dose.

From results of XRF spectrometry is clear that there is significant differences in the quantity of elements in sheep wool from different farms. Iron and sulphur amount in Latvian sheep wool is significantly different, that is larger than in other countries. Sulphur amount in Latvian sheep wool is much bigger than in south countries as it should be.

ACKNOWLEDGNET

The work is performed in the frames of the University of Latvia financed project No. Y9-B044-ZF-N-300, “Nano, Quantum Technologies, and Innovative Materials for Economics” with support of researcher Anna Trubaca-Boginska from the University of Latvia, Faculty of Chemistry, Department of Physical Chemistry.

REFERENCES

1. Patkowska-Sokoła, B., Dobrzański, Z., Osman, K., Bodkowski, R., & Zygadlik, K. (2009). The content of chosen chemical elements in wool of sheep of different origins and breeds. *Arch Tierz*, *4*(52), 410–418. Retrieved from http://arch-anim-breed.fbn-dummerstorf.de/pdf/2009/at09p410.pdf.
2. Ahmad, S., Khan, M. S., & Khan, M. F. U. (2010). Factors affecting wool characteristics of Kari sheep in Pakistan. *Turkish Journal of Veterinary and Animal Sciences*, *34*(6), 485–492. https://doi.org/10.3906/vet-0705-21.
3. Stepanek Schiflett J., Sheep industry economic impact analysis, 2008, prepared for the American Sheep Industry Association.
4. Braun O., Lieberreich O., Method of treating wool-oil to produce lanolin, United States Patent Office, Patent No. 271192, January 23, 1883.
5. Broadgate W.C.,Method and process of making lanolin, United States Patent Office, Serial No. 285301, 28 September, 1920.
6. Суюнчалиев Р.С., Серебряков Р.А., Ермолова Л. С., Калиниченко А.Б., способ получения шерстного жира-ланолина и устройство для его осуществления, Заявка: 2004111276/13, No. 108679, 14.04.2004.
7. Жузе Т.П., Юшкевич Г.Н., Геккер И.Е., Способ получения ланолина из сырого шерстяного жира, 15.04.1957, No. 571188.
8. Lopez-Mesas, M., Cristoe J., Carillo F., Crepsi M., Supercritical fluid extraction with cosolvents of wool wax from wool scour wastes, J. of Supercritical Fluids 35 (2005) 235–239.
9. Tucker, P.A., Scale heights of chemically treated wool and hair fibers, Textile Res. J. 68 (3) 229–203 (1998).
10. Арутюнян Н. С., Васиьева Л.Г., Рогачев В.Н., Способ получения шерстного жира, No. РФ2083647, 10.07.1997.

11. *Knowsheep*. Developing a Knowledge-based Sheep Industry on the Baltic Sea Islands, 2013- [referred on the 27th of March in 2018 y.]. Link to the internet <http://projects.centralbaltic.eu/ project/401-knowsheep>.
12. Aitu-rokasgramata. <http://old.llkc.lv/files/biblioteka/201406/20140610-1850>.
13. Porubská, M., Hanzlíková, Z., Braniša, J., Kleinová, A., Hybler, P., Fülöp, M., … Jomová, K. (2014). The effect of electron beam on sheep wool. *Polymer Degradation and Stability*, *111*, 151–158. https://doi.org/10.1016/j.polymdegradstab.2014.11.009.
14. Hanzlikova, Z., Hybler, P., Fülop, M., Ondruska, J., Jomova, K., Porubska, M., & Valko, M. (2015). Irradiated lanoline as a prospective substance for biomedical applications: A spectroscopic and thermal study. *Radiation Physics and Chemistry*, *113*, 41–46.
15. Porubská, M., Hanzlíková, Z., Braniša, J., Kleinová, A., Hybler, P., Fülöp, M., Jomová, K. (2014). The effect of electron beam on sheep wool. *Polymer Degradation and Stability*, *111*, 151–158.
16. Pielesz, A., & Weselucha-Birczynska, A. (2000). The identification of structural changes in the keratin of wool fibre dyed with an azo dye using the Raman and Fourier transform infrared spectroscopy methods. *Journal of Molecular Structure*. Retrieved from isi:000166228200037.
17. Park, M., Kim, B. S., Shin, H. K., Park, S. J., & Kim, H. Y. (2013). Preparation and characterization of keratin-based biocomposite hydrogels prepared by electron beam irradiation. *Materials Science and Engineering C*, *33*(8), 5051–5057.
18. Cardamone, J. M., Nuñez, A., Garcia, R. A., & Aldema-Ramos, M. (2009). Characterizing wool keratin. *Research Letters in Materials Science*, *2009*.
19. Gasimov, O.K., Mamedov, Sh.V., Aslanov, R.B., Nuriyev, S.R., L'vov, K.M. The primary processes by free radicals occurring in the mechanical destruction of collagen(1989) *The VII International Conference of Magnetic Resonance in Biology and Medicine* Cernogolovca, Russia.
20. Mamedov, S. V., Akta, B., Cantürk, M., Aksakal, B., Alekperov, V., Bülbül, F., … Aslanov, R. B. (2002). The ESR signals in silk fibroin and wool keratin under both the effect of UV-irradiation and without any external effects and the formation of free radicals. *Biomaterials*, *23*(16), 3405–3412.

CYSENI 2018, May 23-25, Kaunas, Lithuania
ISSN 1822-7554, www.cyseni.com

FORMATION OF DOPED AMORPHOUS DIAMOND-LIKE CARBON FILMS BY DC MAGNETRON SPUTTERING

V. Dovydaitis, L. Marcinauskas, A. Iljinas
Kaunas University of Technology
Studentų str. 50, LT-51368 Kaunas – Lithuania
Email: vilius.dovydaitis@ktu.edu

ABSTRACT

Direct current magnetron sputtering technology was used to form carbon coatings transparent in the visible region (about 60–78% at 550 nm). Thin film deposition was done by sputtering graphite target in argon environment. The influence of deposition duration on growth rate, structure and properties of carbon film were investigated using various techniques. Fourier-transform infrared spectroscopy showed that there was no presence of CH_x bonds in films which indicates that the films were hydrogen free. Micro-Raman spectroscopy results revealed that all deposited films displayed strong diamond-like features. However, the bonding structure of carbon coatings were dependent on technological deposition parameters. Therefore, different deposition conditions resulted in change of optical properties which were measured by UV-VIS-NIR spectrometry and null-ellipsometry. Optical band gap was calculated using Tauc method. The band gaps of oxygen doped amorphous carbon films reached up to 1.9 eV, while the refractive indexes varied between 1.77 and 2.20. The addition of titanium resulted in increase of band gap up to 2.7 eV. The changes in elemental composition were determined by the energy dispersive X-ray spectroscopy. The influence of deposition parameters on thickness, surface morphology and wettability of carbon films were investigated by high resolution stylus profiler, atomic force microscopy and DropSnake method.

Keywords: amorphous carbon, dc magnetron sputtering, micro-Raman, optical properties, surface wettability

1. INTRODUCTION

Amorphous diamond-like carbon (DLC) films have been a research object for many scientists for several decades because of its unique optical, mechanical and electrical properties. These properties can be tailored by changing the carbon bonding structure. C=C sp^2 bonds are responsible for graphite like features, while C-C sp^3 bonds for diamond-like properties. It is possible to achieve desired properties by selecting the right C=C sp^2 and C-C sp^3 bonds concentration in the film structure [1]. Therefore, amorphous carbon films have a wide variety of applications. They could be used in such fields as medicine (coatings for joint implants), optics (anti-reflective coatings), microelectronics (micro-electromechanical cantilevers, semiconductor devices, solar cells), tribological protection coatings (automotive industry, cutting tools) and etc. [1–4].

There are numerous chemical and physical vapour deposition techniques to produce amorphous hydrogen-free carbon (a-C) and amorphous hydrogenated carbon (a-C:H) (various plasma-enhanced chemical vapor deposition (PE-CVD) methods [5, 6], laser ablation, arc evaporation, ion beam methods, magnetron sputtering and etc. [1, 4, 7–11]). Since DLC properties are very sensitive to technological deposition parameters (such as temperature, power, vacuum, gas type, flow rate and etc.) magnetron sputtering is an attractive technique to form DLC films because it allows to control the deposition process easily, deposition rates are relatively high, and the coatings could be grown on large surfaces [11]. There are many configurations of magnetron sputtering (radio frequency (RF) magnetron sputtering, high power impulse magnetron sputtering and etc. [8, 12–15]) but the simplest is direct current (DC) magnetron sputtering. The structure of films can be modified not only by changing deposition parameters but also by adding dopants to rearrange the sp^3/sp^2 ratio [16, 17]. DC magnetron sputtering allows to dope a-C films with desired materials easily.

It has been reported that the addition of various metallic (Ti, Ni, W and etc.) and non-metallic (N, Si, B, F, O and etc.) elements into amorphous carbon matrix improves DLC properties, adhesion and thermal stability [18–23]. A.S. Chaus et al. [19] reported that adding Si to a-C films results in decreased of both the residual stresses and the surface energy and in increase of C-C sp^3 site concentration. C. Zeng et al. [24] investigated the structure of nitrogen doped amorphous carbon films and their tribological properties and found that the addition of nitrogen results in improved adhesion and tribological properties. P. Safaie et al. [25] revealed that doping DLC films with oxygen (O at.% from 0 to 11%) reduce the water contact angles from 78.4° to 66.0°. In the another paper P. Safaie et al. [26] demonstrated that with increasing the oxygen content in the film's structure, optical band gap increased and refractive index decreased. L. Sun et al. [27] showed that co-doping DLC films with Cu and Cr caused the lowering of residual stress and increased film’s hardness. Authors also indicated that the co-doping caused the wettability transformation from hydrophilic to hydrophobic state due to increased graphitization and oxidation of copper, which resulted in decrease of the total surface energy. Z. Wu et al. [21] claimed to form chromium doped DLC (Cr-DLC) films which exhibited excellent corrosion resistance. H. Wong et al. [28] showed that electrical conductivity of DLC increases by increasing amount of zinc dopant. A. Solovyev et al. [20] also obtained that the doping of carbon with nickel increased electrical conductivity.

One of the most common research objects nowadays is titanium. Titanium and titanium dioxide exhibit antibacterial properties, biocompatibility and also have catalytical properties. In addition to that, it tends to improve the tribological properties of the coatings when used as a dopant [29–32]. Therefore, diamond-like carbon films are no exception and titanium or titanium oxide are commonly used as a dopant. C. Nie et al. [33] investigated the friction of DLC coated steel alloy in environment of engine oil. Authors determined that Ti doped DLC coatings exhibited lower friction coefficients than conventional DLC coatings. C. C. Wachesk et.al. [6] demonstrated that incorporation of TiO_2 nanoparticles into a-C:H coatings increased the concentration of C=C sp^2 bonding sites. Authors also showed that increase of titanium oxide content in coatings caused decrease in water contact angle. Y. Jo et al. [30] determined that the adhesion strength, electrical resistivity, electrochemical activity and reversibility of the DLC films could be greatly improved by Ti doping.

There are plenty of studies about doped a-C:H films, however, there are only few studies about titanium or/and oxygen doped hydrogen-free a-C films. Therefore, the aim of this work is to deposite a-C:Ti:O and a-C:O films using DC magnetron sputering method and to investigate the influence of technological parameters on the properties and structure of films.

2. EXPERIMENTAL METHODS

The oxygen and titanium doped DLC thin films were grown using layer-by-layer DC magnetron deposition method [34] in 2–3 Pa argon environment. The deposition was carried out in the room temperature. Films were grown using two flat magnetrons with 3 inch graphite and titanium targets. To reduce the flux of titanium atoms the titanium magnetron was covered and only the slit of 30 mm wide was left. The substrate holder was fixed on the rod parallel to magnetrons and was moving periodically in arc with a constant 0.3 Hz frequency (see Fig. 1). Si (100) and glass substrates were positioned 65 mm above from the targets. Sputtering currents used for film deposition were 1 A for titanium and 1.5 A for graphite target. The targets were sputter-cleaned for 5 min. before the deposition. When the substrate moves above operating magnetron, layer of carbon or titanium atoms was deposited on the substrate. Three oxygen doped carbon films were deposited for 180 s, 600 s and 1200 s. The duration of titanium doped carbon film deposition was 1200 s.

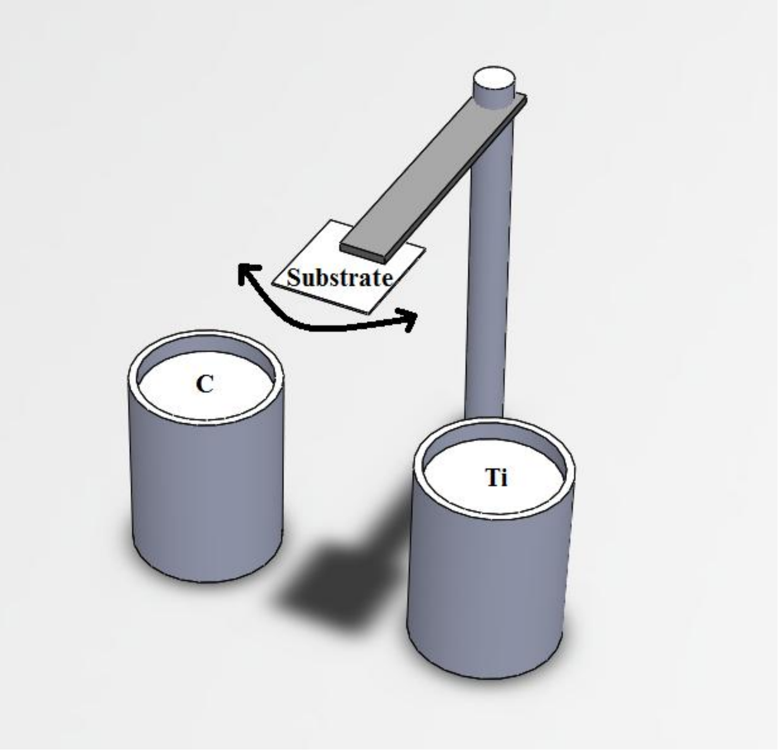

Fig. 1. Experimental setup

Energy dispersive X-ray spectroscopy (EDX) (Bruker Quad 5040 spectrometer, AXS Microanalysis GmbH) was used to determine the elemental composition of coatings. Accelerating voltage of 15 kV was used during the measurements. The data was acquired from 1.25 mm^2 surface area and the results were presented as an average of 3 measurements. The thickness of the coatings was determined using high resolution stylus profiler (Ambios XP-200). The thickness provided in the paper was determined from average of 3 different measurements. The optical properties were measured using null-ellipsometry (Gaertner L117 with a He-Ne laser (632.8 nm)). The transmittance spectra of the coatings were measured at a normal incidence with UV–VIS–NIR spectrophotometer (Ocean Optics USB4000). Optical band gap E_g was calculated using Tauc method. The bonding structure of films was analyzed by µRaman spectroscopy (Renishaw inVia spectrometer, using 2.25 mW excitation at the wavelength of 532 nm, focused to 4 µm spot, the exposure time was 3 s, accumulations quantity – 10) in the spectral range of 100–4000 cm^{-1}. The Raman spectra were fitted by two Gaussian-shape lines in the spectral range of (1000–1800) cm^{-1}. The FTIR spectra of carbon coatings were measured using attenuated total reflectance (ATR) and an internal reflection element made of diamond using ALPHA series Platinum spectrometer. Measurements were done in the 375–4000 cm^{-1} range, spectral resolution 4 cm^{-1}, one spectrum was obtained by taking the average of 24 measurements. Water contact angle was measured from photos using ImageJ program plugin DropSnake.

3. RESULTS AND DISCUSSION

The increase in coating deposition time resulted in relatively smoother surface of the coatings that could be seen in Fig. 1. The average growth rate (0.27 nm/s) of oxygen doped carbon films was determined from the slope value of thickness dependency over the time (Fig. 2, a).

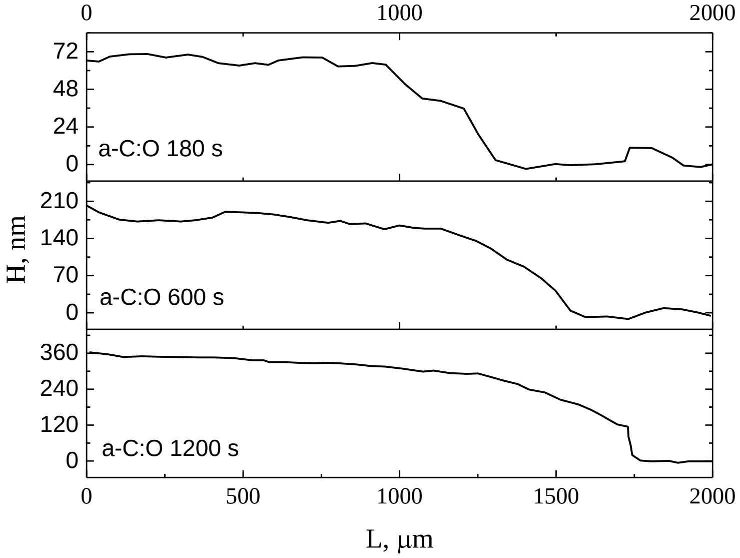

Fig. 1. Profiles of a-C:O coatings deposited for 180 s, 600 s and 1200 s

As was expected, the surface images showed that all a-C:O and a-C:Ti:O films had no particular texture and were smooth and homogenous (Fig. 2, b), since coatings deposited by magnetron sputtering with no additional heating tend to repeat surface morphology of the substrate.

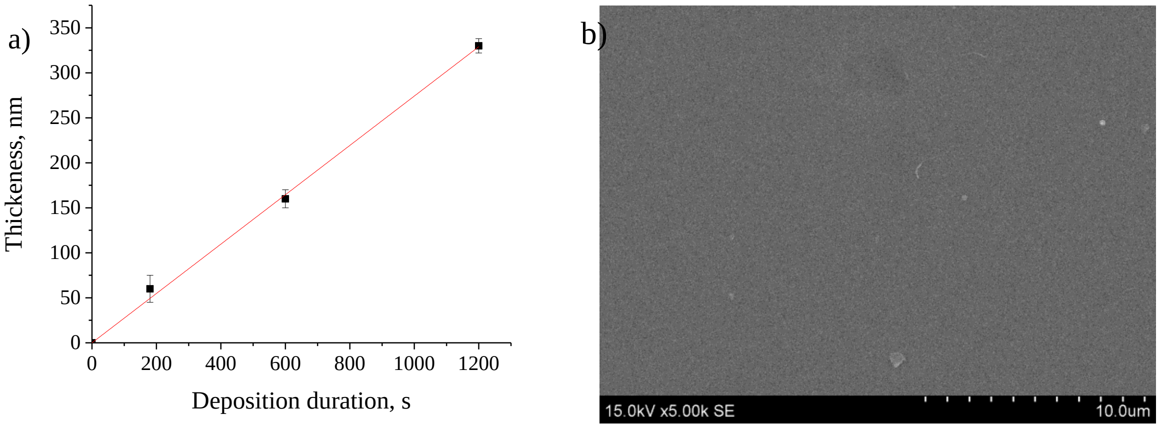

Fig. 2. a) a-C:O film thickness dependency on deposition duration; b) surface image of a-C:O coating deposited for 600 s

The results of the elemental analysis revealed no obvious trend between deposition duration and oxygen concentration in coatings. Despite the variation of deposition duration the oxygen content in the coatings was between 18–21 at.%, also a low amount of bismuth was obtained. However, when coatings are additionally doped with 5.5 at.% titanium the oxygen concentration increased by 7 at.% (up to 28 at.%). This could be explained by the high reactivity of titanium. Titanium has a strong chemical affinity for oxygen and tends to form oxides even at room temperature [35]. Therefore, the titanium dopant could have worked as oxygen gatherer in the coatings, resulting in increase of oxygen content. K. Kidena et al. [31] exposed hydrogenated Ti-DLC films to atomic oxygen irradiation. The XPS analysis indicated that oxygen irradiation changed Ti-C and C-C bonds to Ti-O and C-O resulting in decreased carbon content and increased oxygen and titanium content in the coatings. Similar phenomena might have occurred in our experiments, molecular oxygen left in chamber because of insufficient vacuum could have been slit into atoms because of discharge or plasma reactions and caused formation of Ti-O and C-O bonds in the coatings. Other authors also have deposited titanium doped carbon films with significant content of oxygen [31].

Since EDX technique is not capable to detect hydrogen in coatings, Fourier-transform infrared spectroscopy analysis was performed to investigate coating's bonding structure and to determine indirectly if there was hydrogen present in the coatings. In Fig. 3 FTIR transmittance spectrum of glass substrate and the spectrum of a-C:O were presented. In both spectra there were low intensity absorption peaks ant 2850 cm^{-1} and 2920 cm^{-1} that correspond to CH_2 vibrations [36]. These peaks might have occurred due to organic contamination or residue of acetone cleaning, since no other $C\text{-}H_x$ bands could be found. 1425 cm^{-1} peak was attributed to C-C vibrations, and broad band at 1620 cm^{-1} was a result of aromatic C=C stretching vibrations [36]. The band at ~3400 cm^{-1} occurred due to OH vibrations [36] and could be result of water vapor adsorption.

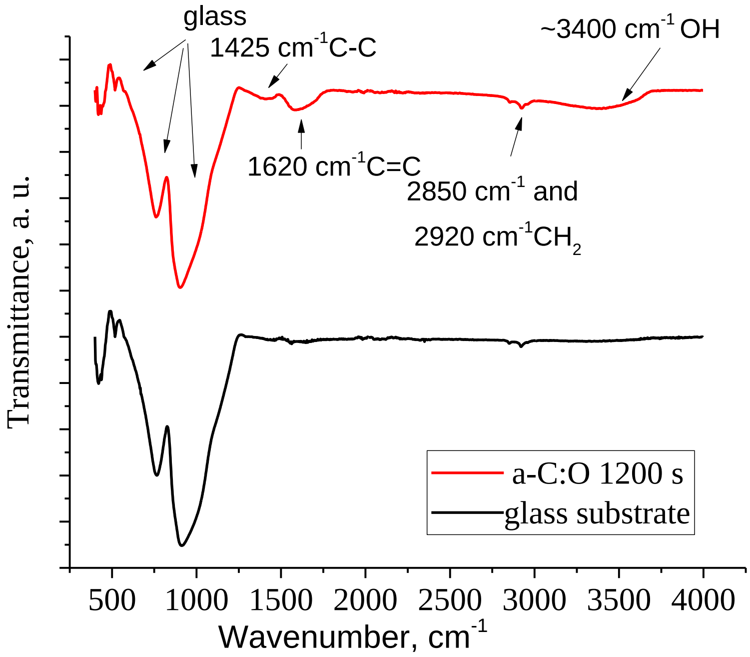

Fig. 3. FTIR transmittance spectra of the glass substrate and a-C:O coating

The Raman spectra of carbon films in the range from 1000 to 1800 cm^{-1} are presented in Fig. 4. All spectra exhibited strong diamond-like features. The broad and overlapping D and G bands were positioned at 1387–1419 cm^{-1} and 1547–1582 cm^{-1}, respectively. D band is responsible only for the breathing vibrations in sp^2 bonded carbon rings, while G peak is related to the stretching vibration of any pair of sp^2 carbon sites [1]. As the deposition time increased, the G peak width (ΔG) got narrower (from 138 cm^{-1} to 125 cm^{-1}), it suggests that disorder in the films decreased and number of graphite-like C=C sp^2 sites increased. During the deposition of coatings, the interaction between plasma and substrate caused heating, therefore, resulting in increased substrate temperature. Since deposition was carried out in vacuum the cooling of the substrate occurred only due the heat exchange between substrate and substrate holder. Therefore, the longer deposition duration was the higher temperature was reached. It is known that the graphite-like carbon formation favors higher temperatures [37]. The addition of titanium dopant narrowed G band even more from 125 cm^{-1} to 93 cm^{-1}. It has been reported in other authors' works that doping amorphous carbon films with titanium caused graphitization [38]. As the deposition time increased form 180 s to 1200 s the G band shifted to higher wavenumber values from 1547 cm^{-1} to 1563 cm^{-1} and with the addition of titanium it shifted even more (to 1582 cm^{-1}). According to J. Robertson's three stage model [1] the increase of the intensity ratio of D and G bands (I_D/I_G) (some authors use the ratio of D and G band areas (A_D/A_G) [37]) and G band shift to higher wavenumbers occurs because of transformation of C-C sp^3 sites into C=C sp^2 sites, in other words - graphitization. With the increase of the deposition time the I_D/I_G ratio increased from 0.47 to 0.55 and A_D/A_G increased from 1.08 to 1.27. Even stronger graphitization occurred in a-C:Ti:O coating, the I_D/I_G and A_D/A_G ratios increased up to 0.81 and 2.96, respectively. Some authors suggests that the oxygen also increase the fraction of C=C sp^2 sites in carbon films [17]. Therefore, a-C:Ti:O coating exhibited the most prominent graphite-like features compared to oxygen doped coatings. Titanium dioxide has several peaks in Raman spectrum positioned in the range of 100–700 cm^{-1} [39]. However, in the Raman spectrum of a-C:Ti:O in the range from 100 cm^{-1} to 800 cm^{-1} there were no distinguished sharp titanium oxide peaks, only few very broad bands of low intensity and sharp peak of Si at 520 cm^{-1}. Since the coatings were deposited at relatively low temperature and there was not enough oxygen, titanium formed various amorphous and non-stoichiometrical oxides.

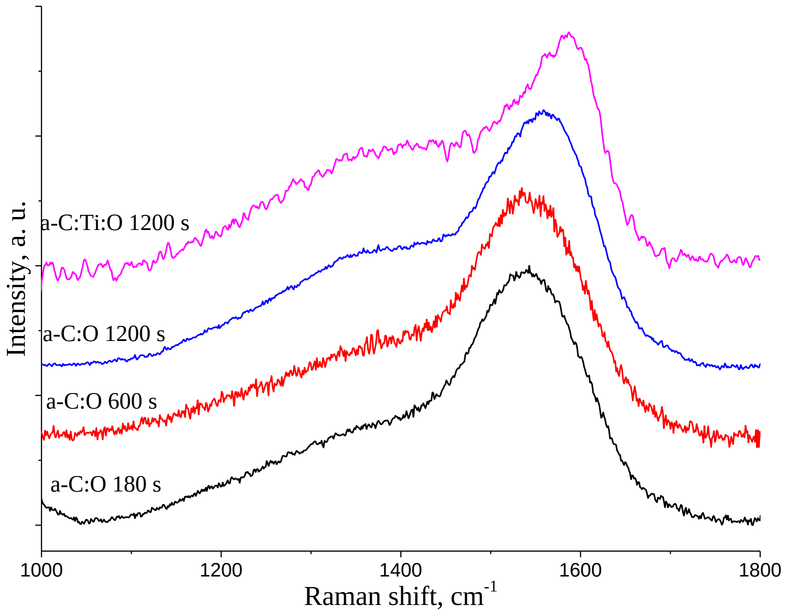

Fig. 4. Raman spectra of carbon coatings

The optical transmission spectra of doped DLC films are provided in Fig. 5. All coatings exhibited a high optical transparency at NIR ~80–90%. The transmission at 550 nm wavelength varied between 60% and 78%. At this wavelength the most transparent was the a-C:O coating deposited for 600 s. Meanwhile, the lowest transparency was obtained for a-C:O coating deposited for 1200 s. The addition of the titanium (5.5 at.%) had no negative influence on transparency of the coating.

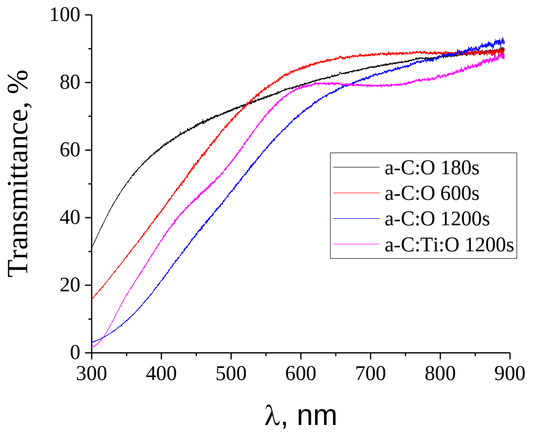

Fig. 5. Transmittance spectra of carbon films

Tauc method was used to determine the optical band gaps of the coatings. The highest value for a-C:O coatings (1.9 eV) was achieved at 180 s deposition time. a-C:O 1200 s coating had a band gap of 1.7 eV. The results corresponded well with the results of Raman spectroscopy. The highest C-C sp^3 sites concentration resulted in highest band gap. It has been reported that C=C sp^2 sites tend to decrease the value of optical band gap. However, the a-C:Ti:O coating that had the strongest graphite-like features had the widest band gap (2,7 eV). This phenomenon could be explained by formation of titanium oxides. The band gap of titanium oxides usually are higher than 3 eV [32].

Similar tendency could be seen in evaluation of refractive index (*n*). H.Y. Dai et al. [40] reported that the DLC coatings with the highest fraction of sp^3 sites has the highest refractive index. The highest refractive index (*n*) of 2.20 was obtained for the coating deposited for 180 s. a-C:O 600 s coating had *n* equal to 1.85 and the a-C:O 1200 s coating had index of 1.77. The values of refractive index decreased with decreasing sp^3 content in the coatings. The addition of titanium dopant resulted in increase of *n* from 1.77 to 1.85. That might have occurred due to the fact that the titanium oxides have a higher refractive index (~2.6 [41]) than carbon films disscussed in this work.

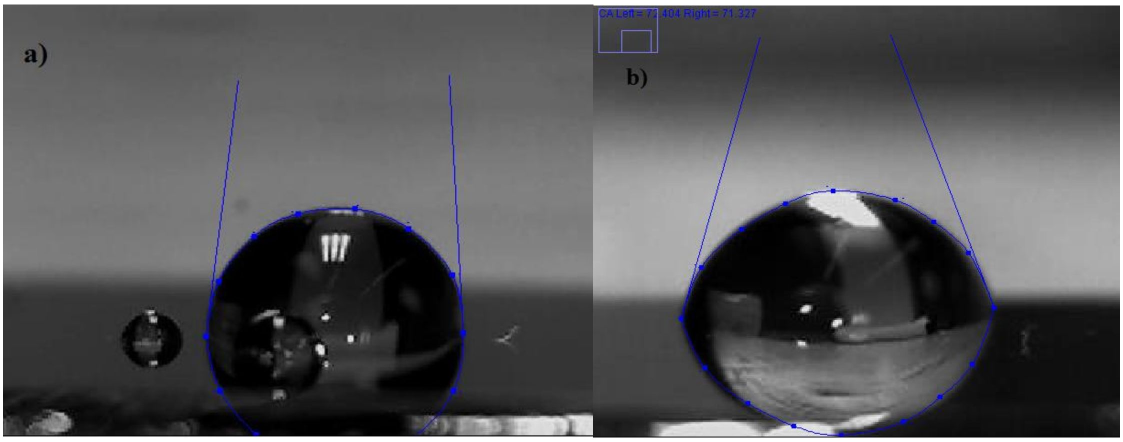

Fig. 6. Water contact angle test on a) a-C:O 600 s and b) a-C:Ti:O 1200 s coatings

Water contact angle tests showed that only the coating that was deposited for 180 s exhibits hydrophobious behavior (Fig. 6, a). The increase of deposition time resulted in decrease of water contact angle. Water contact angles for the coatings deposited for 180 s, 600 s and 1200 s were 92^o, 88^o, 86^o, respectively. The addition of titanium resulted in the further decrease of the water contact angle (Fig. 6, b). The angle decreased down to 71^o. C. C. Wachesk et al. [6] claimed that the incorporation of titanium reduces water contact angle. It is known that sp^2 carbon sites and C-O bonds have higher polarity compared to sp^3 sites and C-C bonds, respectively [25]. Therefore, coatings that were deposited for 600 s or 1200 s had hydrophilic properties, since their Raman scattering analysis showed higher sp^2 content.

4. CONCLUSIONS

Oxygen doped and titanium doped diamond-like carbon films were grown by direct current magnetron technique. It was determined that the growth rate of a-C:O films was ~0.27 nm/s. The variation of the deposition time had a slight influence on the oxygen concentration. Additionally doping carbon films with titanium (5.5%) resulted in increase of the oxygen content up to ~28%. The I_D/I_G and A_D/A_G ratios increased, and the G band narrowed with the increase in growth duration. Such results indicated that the longer the deposition time was the more heat was transferred from the plasma to the substrate and more C-C sp^3 sites transformed into C=C sp^2 sites. The water contact angle of the doped films decreased from 92^o to 86^o with the increase of deposition duration form 180 s to 1200 s. Doping films with titanium resulted in even further decrease of water contact angle values (down to 71^o). The coating that was deposited for 180 s had the highest refractive index of 2.20 due to the high fraction of sp^3 sites. The band gap of the oxygen doped DLC films varied from 1.6 eV to 1.9 eV. The doping of amorphous carbon films with Ti resulted in the highest band gap value (2.7 eV). Oxygen doped and titanium doped carbon films were optically transparent in the visible range (about 60–78% at 550 nm), because of that and high transparency in IR region these coatings might find applications in the field of optics. The most promising coating for optical applications was a-C:O 180 s coating because of good transparency in invisible region and the highest refractive index. Also, a-C:O 180 s and a-C:Ti:O 1200 s coatings might find application in the field of semiconductors, due to relatively high band gap values. However, further research on the other properties of the coatings must be done.

REFERENCES

[1] ROBERTSON, J. Diamond-like amorphous carbon. *Materials Science and Engineering: R: Reports*, 2002, Vol. 37, No. 4–6, p. 129–281.

[2] MORIGUCHI, H., OHARA, H., TSUJIOKA, M. History and Applications of diamond-like carbon manufacturing processes. *SEI Technical Review*, 2016, No. 82, p. 52–58.

[3] HAUERT, R., THORWARTH, K., THORWARTH, G. An overview on diamond-like carbon coatings in medical applications. *Surface and Coatings Technology*, 2013, Vol. 233, p. 119–130.

[4] VETTER, J. 60years of DLC coatings: Historical highlights and technical review of cathodic arc processes to synthesize various DLC types, and their evolution for industrial applications. *Surface and Coatings Technology*, 2014, Vol. 257, p. 213–240.

[5] PSYLLAKI, P.P., JEANDIN, M., PANTELIS, D.I., ALLOUARD, M. Pin-on-disc testing of PE-CVD diamond-like carbon coatings on tool steel substrates. *Surface and Coatings Technology*, 2000, Vol. 130, No. 2–3, p. 297–303.

[6] WACHESK, C.C., TRAVA-AIROLDI, V.J., DA-SILVA, N.S., LOBO, A.O., MARCIANO, F.R. The Influence of Titanium Dioxide on Diamond-Like Carbon Biocompatibility for Dental Applications. *Journal of Nanomaterials*, 2016, Vol. 2016.

[7] TEO, K.B.K. et al. Highest optical gap tetrahedral amorphous carbon. *Diamond and Related Materials*, 2002, Vol. 11, No. 3–6, p. 1086–1090.

[8] BI, F., HOU, K., YI, P., PENG, L., LAI, X. Mechanisms of growth, properties and degradation of amorphous carbon films by closed field unbalanced magnetron sputtering on stainless steel bipolar plates for PEMFCs. *Applied Surface Science*, 2017, Vol. 422, p. 921–931.

[9] ZHANG, S., BUI, X.L., FU, Y. Magnetron sputtered hard a-C coatings of very high toughness. *Surface and Coatings Technology*, 2003, Vol. 167, No. 2–3, p. 137–142.

[10] SOLOMON, I. et al. Diamond & Related Materials Correlation of structural and optical properties of PVD grown amorphous carbon thin films. *Diamond & Related Materials*, 2017, Vol. 75, p. 69–77.

[11] COŞKUN, Ö.D., ZERRIN, T. Optical, structural and bonding properties of diamond-like amorphous carbon films deposited by DC magnetron sputtering. *Diamond and Related Materials*, 2015, Vol. 56, p. 29–35.

[12] WIATROWSKI, A. et al. Deposition of diamond-like carbon thin films by the high power impulse magnetron sputtering method. *Diamond and Related Materials*, 2017, Vol. 72, p. 71–76.

[13] DAI, H.Y., ZHAN, C., DU, J. Studies on the influence of sputtering power on amorphous carbon films deposited by pulsed unbalanced magnetron sputtering. *Optik - International Journal for Light and Electron Optics*, 2016, Vol. 127, No. 5, p. 2512–2515.

[14] LIN, C.R., WEI, D.H., CHANG, C.K., LIAO, W.H. Optical properties of Diamond-like

Carbon films for antireflection coating by RF magnetron sputtering method. *Physics Procedia*, 2011, Vol. 18, p. 46–50.

[15] RUBIO-ROY, M., PASCUAL, E., POLO, M.C., ANDÚJAR, J.L., BERTRAN, E. Structural and optical properties of diamond like thin films deposited by asymmetric bipolar pulsed-DC reactive magnetron sputtering. *Surface and Coatings Technology*, 2008, Vol. 202, No. 11, p. 2354–2357.

[16] UTU, I., MARGINEAN, G. Effect of electron beam remelting on the characteristics of HVOF sprayed Al2O3-TiO2 coatings deposited on titanium substrate. *Colloids and Surfaces A: Physicochemical and Engineering Aspects*, 2017, Vol. 526, p. 70–75.

[17] SAFAIE, P., ESHAGHI, A., BAKHSHI, S.R. Structure and mechanical properties of oxygen doped diamond-like carbon thin films. *Diamond and Related Materials*, 2016, Vol. 70, p. 91–97.

[18] RAY, S.C., PONG, W.F., PAPAKONSTANTINOU, P. Iron, nitrogen and silicon doped diamond like carbon (DLC) thin films: A comparative study. *Thin Solid Films*, 2016, Vol. 610, p. 42–47.

[19] CHAUS, A.S., JIANG, X.H., POKORNÝ, P., PILIPTSOU, D.G., ROGACHEV, A.V. Improving the mechanical property of amorphous carbon films by silicon doping. *Diamond and Related Materials*, 2018, Vol. 82, p. 137–142.

[20] SOLOVYEV, A.A., OSKOMOV, K.V., GRENADYOROV, A.S., MALONEY, P.D. Preparation of nickel-containing conductive amorphous carbon films by magnetron sputtering with negative high-voltage pulsed substrate bias. *Thin Solid Films*, 2018,.

[21] WU, Z. et al. Microstructure and surface properties of chromium-doped diamond-like carbon thin films fabricated by high power pulsed magnetron sputtering. *Applied Surface Science*, 2013, Vol. 276, p. 31–36.

[22] KIDENA, K. et al. Properties of DLC and nitrogen-doped DLC films deposited by DC magnetron sputtering. *Tribology of Diamond-Like Carbon Films: Fundamentals and Applications*, 2015, Vol. 130, No. SUPPL.1, p. 200–204.

[23] SÁNCHEZ-LÓPEZ, J.C., FERNÁNDEZ, A. Doping and alloying effects on DLC coatings. *Tribology of Diamond-Like Carbon Films: Fundamentals and Applications*, 2008, No. Dlc, p. 311–328.

[24] ZENG, C. et al. Enhancement of mechanical, tribological and morphological properties of nitrogenated diamond-like carbon films by gradient nitrogen doping. *Diamond and Related Materials*, 2017, Vol. 76, No. May, p. 132–140.

[25] SAFAIE, P., ESHAGHI, A., BAKHSHI, S.R. Oxygen doping effect on the wettability of diamond-like carbon thin films. *Journal of Non-Crystalline Solids*, 2017, Vol. 471, No. March, p. 410–414.

[26] SAFAIE, P., ESHAGHI, A., BAKHSHI, S.R. Optical properties of oxygen doped diamond-like carbon thin films. *Journal of Alloys and Compounds*, 2016, Vol. 672, p. 426–432.

[27] SUN, L., GUO, P., KE, P., LI, X., WANG, A. Synergistic effect of Cu/Cr co-doping on the wettability and mechanical properties of diamond-like carbon films. *Diamond and Related Materials*, 2016, Vol. 68, p. 1–9.

[28] WONG, H., FOONG, Y.M., CHUA, D.H.C. Improving the conductivity of diamond-like carbon films with zinc doping and its material properties. *Applied Surface Science*, 2011, Vol. 257, No. 22, p. 9616–9620.

[29] ZHAO, F. et al. Ti-DLC films with superior friction performance. *Diamond and Related Materials*, 2010, Vol. 19, No. 4, p. 342–349.

[30] JO, Y.J., ZHANG, T.F., SON, M.J., KIM, K.H. Synthesis and electrochemical properties of Ti-doped DLC films by a hybrid PVD/PECVD process. *Applied Surface Science*, 2018,

Vol. 433, p. 1184–1191.

[31] KIDENA, K. et al. Resistance of Hydrogenated Titanium-Doped Diamond-Like Carbon Film to Hyperthermal Atomic Oxygen. *Metals*, 2015, Vol. 5, No. 4, p. 1957–1970.

[32] LÓPEZ, R., GÓMEZ, R. Band-gap energy estimation from diffuse reflectance measurements on sol-gel and commercial TiO2: A comparative study. *Journal of Sol-Gel Science and Technology*, 2012, Vol. 61, No. 1, p. 1–7.

[33] NIE, C.Y., LIU, X.K., WATANABE, H. The Lubrication Properties of Diamond-Like Carbon Coatings in Engine Oil. *Materials Science Forum*, 2009, Vol. 610–613, p. 652–657.

[34] ILJINAS, A., STANKUS, V., ČYVIENE, J., ABAKEVIČIENĖ, B. Formation of PbTiO3 thin films on seed layers using DC magnetron layer-by-layer deposition. *Vacuum*, 2015, Vol. 122, p. 310–313.

[35] OKABE, T.H., OISHI, T., ONO, K. Preparation and characterization of extra-low-oxygen titanium. *Journal of Alloys and Compounds*, 1992, Vol. 184, No. 1, p. 43–56.

[36] MOYO, P., MUGADZA, T., MEHLANA, G., GUYO, U. Synthesis and characterization of activated carbon–ethylenediamine–cobalt(II) tetracarboxyphthalocyanine conjugate for catalytic oxidation of ascorbic acid. *Research on Chemical Intermediates*, 2016, Vol. 42, No. 8, p. 6511–6529.

[37] CHENG, L. et al. Low temperature synthesis of graphite on Ni films using inductively coupled plasma enhanced CVD. *J. Mater. Chem. C*, 2015, Vol. 3, No. 20, p. 5192–5198.

[38] JIANG, J. et al. Comparative study on structure and properties of titanium/silicon mono- and co-doped amorphous carbon films deposited by mid-frequency magnetron sputtering. *Surface and Interface Analysis*, 2014, Vol. 46, No. 3, p. 139–144.

[39] VERMA, R., GANGWAR, J., SRIVASTAVA, A.K. Multiphase TiO_2 nanostructures: a review of efficient synthesis, growth mechanism, probing capabilities, and applications in bio-safety and health. *RSC Adv.*, 2017, Vol. 7, No. 70, p. 44199–44224.

[40] DAI, H.Y., WANG, Y.Q., CHENG, X.R., ZHAN, C.Y., HUANG, N.K. Characterization and properties of amorphous carbon coatings prepared by middle frequency pulsed unbalanced magnetron sputtering at different substrate bias. *Applied Surface Science*, 2012, Vol. 258, No. 14, p. 5462–5466.

[41] SHIMIZU, W., NAKAMURA, S., SATO, T., MURAKAMI, Y. Creation of high-refractive-index amorphous titanium oxide thin films from low-fractal-dimension polymeric precursors synthesized by a sol-gel technique with a hydrazine monohydrochloride catalyst. *Langmuir*, 2012, Vol. 28, No. 33, p. 12245–12255.

CYSENI 2018, May 23-25, Kaunas, Lithuania
ISSN 1822-7554, www.cyseni.com

VARIABILITY OF PROJECTIONS OF MAXIMUM DISCHARGES IN THE LITHUANIAN RIVERS

V. Akstinas
Lithuanian Energy Institute
Breslaujos str. 3, LT-44403 Kaunas – Lithuania
Email: vytautas.akstinas@lei.lt

ABSTRACT

Climate change affects whole surrounding environment including resources of water bodies. Therefore scientists are interested in changes of river runoff parameters according to different climate change scenarios in the future. Nowadays hydrological studies are focused on evaluation of projection of rivers runoff and especially on hydrological extremes related to climate change. According to hydro-meteorological conditions of Lithuania, the biggest damages and losses during spring floods are caused. Therefore, assessing of past flood as well as projected floods in the future is very important. Maximum discharge is one of the most apprehensible variable, which describes flood peak during the spring season. Historical observations showed numerous floods with hazardous discharges in Lithuanian rivers, meanwhile the future projections of maximum discharges are not sufficient investigated. Consequently, the evaluation of projections of maximum spring discharge according to the newest RCP (Representative Concentration Pathways) scenarios including statistical downscaling (SD) in Lithuanian rivers is the main task of this research. Three rivers (Šventoji, Nevėžis and Minija) were selected for this study. Hydrological models of these rivers were created with HBV software. The future maximum discharges were projected according to three RCP scenarios (RCP2.6, RCP4.5 and RCP8.5), three GCMs (GFDL-CM3, HadGEM2-ES and NorESM1-M) and three SD methods (Bias Correction with variable (BC), Change Factor with variable (CF) and Quantile Mapping (QM)) for near (2016-2035) and far (2081-2100) future. The projected extreme values of near and far future with maximum discharges in reference period (1986-2005) were compared. The hydrological extremes directly impact ecological processes in riverine ecosystems, therefore the results of this research could be used in any kind of impact model related to climate change.

Keywords: runoff projections, climate change, RCP, statistical downscaling, GCM

CYSENI 2018, May 23-25, Kaunas, Lithuania
ISSN 1822-7554, www.cyseni.com

SUSTAINABLE DEVELOPMENT AND INNOVATION AS FACTORS OF COMPETITIVENESS

D. Silakalne–Arāja
Riga Technical University
Kalnciema str. 6, LV-1048 Riga – Latvia
E-mail: danha@inbox.lv

ABSTRACT

The aim of the research is to develop a sustainable economic environment. The key result – investigated innovation as a factor of competitiveness for sustainable development of society.
Latvia has set a quantitative target to increase investment in research and development funding for 1.5% of the Latvian GDP by 2020.
The main objective of the EU Sustainable development strategy is protection of the environment. There is a direct link between economic growth and environmental degradation. The environment prevention and environmental pollution reduction, promoting sustainable consumption and production thus economic growth.
In this research were used the theoretical research methods, such as analysis of scientific literature, documents, legislation, the information which is obtained on the internet and graphic analysis.
The results show, that science, technology, and innovation (STI) are crucial for sustainable long-term economic growth, both in developed and developing countries, even more so in the aftermath of the economic crisis. Action have to be taken by the governments at national and regional levels to help promote innovation, research, and development in both the private and public sectors, including putting in place the necessary “framework conditions” such as openness to international trade and investment.

Keywords: competitiveness, sustainable development, innovation, environment protection, long-term growth strategy, sustainable economy, economic crisis

1. INTRODUCTION

The article characterizes and analyses the concept and process of innovation within the context of competitiveness. As the main problem has to be highlighted the lack of cooperation between scientists and businessmen in organizing complex innovative activity for sustainable public development. Science-technology-innovation (STI) based at global competitiveness level, it is required the transformation of the knowledge-based economy for the countries. The base of innovative activity is scientific development, the introduction of scientifically justified innovations within production can aid companies in maintaining and strengthening market position, fighting with competitors, increasing turnover, thus creating the advantages of long-term development. The main objective of the EU Sustainable development strategy is protection of the environment. There is a direct link between economic growth and environmental degradation.The environment prevention and reduced environmental pollution reduction, promoting sustainable consumption and production thus economic growth.

1.1. Innovation – competitiveness and science – technology

Innovation is the implementation of a new scientific, technical, social, cultural or another kind of ideas, elaborations and technologies within the form of a product or service. Innovation has been explained as a process during which new scientific, technical, social, cultural and another kind of ideas, elaborations and technologies are implemented in the form of competitive and marketable product or service (Latvian long-term development strategy until year 2030).

There are four areas of innovation: product innovation, process innovation, marketing innovation and organisational innovation [9]

A product innovation is the introduction of a good or service that is new or significantly improved with respect to its characteristics or intended uses. This includes significant improvements in technical specifications, components and materials, incorporated software, user friendliness or other functional characteristics.

A process innovation is the implementation of a new or significantly improved production or delivery method. This includes significant changes in techniques, equipment and/or software.

A marketing innovation is the implementation of a new marketing method involving significant changes in product design or packaging, product placement, product promotion or pricing.

An organisational innovation is the implementation of a new organisational method in the firm's business practices, workplace organisational or external relations.

Innovation as a factor of competitiveness has related with sustainable economic growth in both micro economy level and macro economy level. The World Economic Forums (WEF) Global Competitiveness Index (GCI) defines competitiveness as the set of institutions, policies, and factors that determine the level of productivity of a country. Innovations are very important for the competitiveness of the countries. Innovations that increasing productivity are the main sources of the competitiveness of nations with factor endowments of nations, which lead to the national prosperity (see Fig. 1).

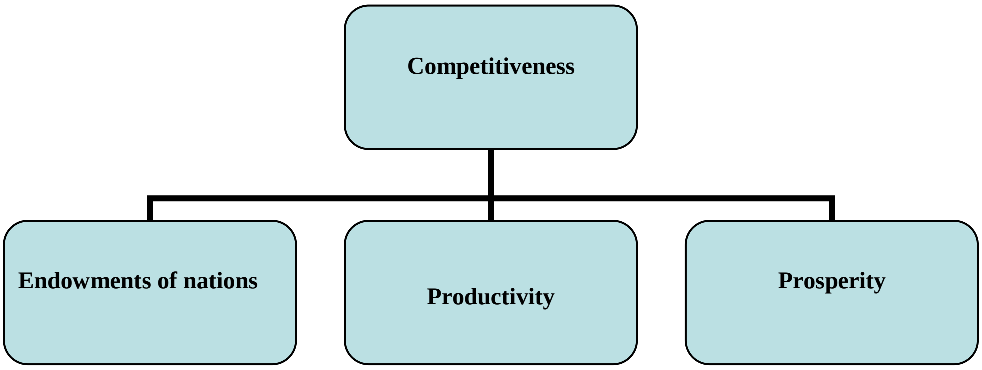

Fig. 1. Defining Competitiveness (World Economic Forums, WEF)

Global structures of research and development, science performance, invention and innovation are in a multidimensional transition process. Altough the (Organisation for Economic Co-operation and Development) OECD and other economies continue to be characterised by persistent diversity, strong trends are nevertheless in evidence and are reshaping global patterns of research, technology and innovation. Among the main elements underpinning developments have been the increasingly knowledge-driven nature of innovation; the quickly changing organisation of research, driven by informatics, collaboration and the sharing of knowledge: improving connectivity and the development of platform technologies and standarts as globalisation and changes in markets, the competition environment and technology. In recent years, the macroeconomic context for research and development, tehnology and innovation activities has been favourable. In OECD countries, there is considerable policy interest in a range of new technologies that promise growth opportunities or solutions to pressing social and economic problems. These include most notably biotechnology and general life sciences, nanotechnology, and environmental sciences and technologies [10].

2. SCIENTIFIC TECHNOLOGICAL INNOVATION

Higher education and science has an important role in the process of innovation realization within the framework of **National innovation systems (**NIS). The objective of higher education is not only to produce highly qualified professionals, but also to carry out research work, generate new ideas that would change into competitive production, service or technology.

Research and development of technologies – systemic creative work to increase the fund of knowledge, including human, social and cultural knowledge, with the aim to use the fund for the development of new ideas. Research and development incorporates the development of fundamental research, applied research and technologies.

Fundamental research is an experimental or theoretical work carried out in order to gain new knowledge about some phenomenon or fact observed. The kind of research is connected with the analysis of characteristics, structures and relationships with the aim to formulate and test the hypothesis, theories and rules. Usually the results of fundamental research are not sold, but published in scientific periodicals and offered to interested colleagues.

Applied research is the investigation of original in order to gain new knowledge. It is aimed at the achievement of previously set *practical* aims.

Development of technologies incorporates systematic work based on the existing knowledge gained form previous studies and practical experience and aimed at the production of new materials, products and equipment, the introduction of new processes, systems and services, or considerable improvement of the existent goods, services and processes.

2.1. Activities of scientists and innovative institutions

Success of innovative process highly depends on the creative capacity of companies. Unfortunately both material and human resources, which can be actually used by Latvian companies for innovative activity, are insufficient. Thus the involvement of highly qualified specialists in the development of new products and their cooperation with business becomes the determinant in the development of innovative economics. The cooperation of universities and scientific institutions with companies has to be aimed at the apprehension increase regarding the innovative capacity of companies and the business activity of academic institutions, the integration of academic society intellectual potential and business qualifications of employers, thus achieving synergy effect and radically increasing the yield of research in Latvian national economy.

However, as it has been indicated by the analysis of situation, only a small part of companies cooperates with researchers, with an overwhelming majority even not being aware of the fact that researchers would be able to take part in creating and improving products. Nevertheless, scientists are far from being active in searching for contacts with companies, in many cases even considering it to be the degradation of science. Overcoming the existing large gap between research and business is the task of national importance in the fulfilment of which each activity is of a great importance:

- development of innovative business principles and methodology by incorporating the model of cooperation (legal, financial, institutional, a. o.) between a the university and the company;
- on national scale there has to be implemented the programme of applied researches and innovation projects with a state defined topic and obligatory additional financing for projects; the above will enable to decrease business expenses for the development of new products, as well as more chances for successful marketing;
- a special kind of national programme for joining additional business financing with applied and innovative projects supported by the EU structural funds;

- Latvia is too small for building competition between scientific institutions regarding research work; hence it is important to create a unified centre of Latvian science for the observation, coordination and consolidation of capacity;
- the support for creation and operation of specialized technological centres/parks, business incubators/parks in prior branches; the accessibility of different foreign services (financial, economic, legal, technological, vehicular, a. o.) is important for the innovative companies integrated in them, by giving them a chance to concentrate on basic activity.

All the above and other activities aimed at increasing of our country's general capacity are also significant in the EU context. Reticulate model of cooperation, which is the basis for cooperation between the EU countries, alongside with a number of advantages unfortunately brings several unpleasant features; one of them is: the network emphasizes and increases the differences between partners, it gives a chance for the big and strong one to become even bigger and stronger in comparison with the smallest and weakest one. With weak economics being influenced by the pressure of the EU competition soon we will reach the state in which the advanced countries are in a more beneficial situation, hence the growth of our own capacity plays a crucial role. By joining the force of information technologies, biotechnology and new material specialists Latvia will become a much stronger competitor.

Yet another important aspect connected with the necessity for certain changes in the mentality of our people. Currently in Latvia there can be observed explicitly insufficient level of initiative, too few people are ready to undertake business risk and become employers. Obviously the fear for being unsuccessful and going bankrupt is still strong, but innovative business is connected with a much higher degree of risk because prior activities and/or the success of prior product does not guarantee the success of the next one. The above factors alongside with disbelief in ones own and national future perspectives, the tendency to highlight failures and constantly bring ones own problems outside the country, does not give us a chance to create the image of a strong and confident partner. That definitely greatly harms our development and is the cause of our country taking numerous low positions in different ratings.

The management of knowledge on national scale is the main condition of national development.

On the whole there are a number of national development scripts for implementing Latvian strategic goals:

- pessimistic script – the current uncoordinated process is continuing; with the increase of base level the rate of development rapidly decreases, simultaneously the public tension becomes stronger; the fulfilment of goals becomes problematic;
- stagnation script – the process fits to the slowest ones; in Latvia during the lifetime of one generation we are not able to achieve ES-25 average quality of life; society loses motivation for long-term investments and activities, as well as for getting education;
- optimistic convergence script – rapid and stable approaching of ES-25 average quality of life level; only this script would agree with the interests of social layers; this can be achieved only by setting priorities and coordinating all activities, which means implementing previously approved strategic solution.

Obviously when judging by the aspect of using our strategic resource only the third script agrees with our national interests. The present scientific resources have to be increased and improved, they have to be used immediately and with maximum possible yield. Spontaneous, uncoordinated, slow activities do not agree with the present development level of the country, they are not compatible with the efforts of reaching future perspectives. Besides that, let us not forget that we live in the dynamic region of the Baltic Sea – not only it grants us with certain advantages, but also delegates certain responsibilities, if we want to be wholesome partners of the Scandinavian countries, not just the suppliers of cheap labour.

From the small review it is possible to make a clear conclusion that in order to implement the convergence script there is necessary coordinated action of all social layers, but to this effect –

socially and politically accepted future vision and long-term complex national development strategy for reaching the vision. Only in that case it will be possible to achieve stable increase of knowledge resources and their effective use by coordinating activities and directing them in unified flow.

The words conception, strategy, programme in the context of political documentation in our country have declined. There have been written numerous documents but each of them is dedicated to a certain subject, thus they are no only uncoordinated, but in many cases also mutually contradictory. Hence the policy of foreign affairs and science is not connected with the economic policy, rural development plans do not consider economic diversification and the change of employment principles, National development plan devoted to the use of the EU structural funds has nothing in common with the national investment plans, as well as the concept of national priorities for activity in the EU.

Certainly pointing out only one of the many economic, political and social aspects of the national development it is not possible to achieve considerable effect. However neither Saeima, nor any of the governments has reviewed and approved joint, integrated vision of future and a strategy for fulfilling it.

Since there is being considered a model of development based on knowledge, in fact this means the implementation of knowledge management principles on national scale. That would mean:

- creating, storing, acquiring, spreading, and using of coordinated and guided knowledge;
- general accessibility of knowledge by reducing the existing asymmetry among people;
- guaranteed access to the required information for the right people at the right time;
- increasing strategic role of leaders and constant work for employees of any level.

Latvia supports the promotion of scientists' mobility by indicating that it is necessary to improve the situation on national scale. Considering the fact that a large part of Latvian scientists work abroad, it is necessary to evaluate the development of scientist return programme, which possibly could be connected with the development of science excellence centres' programme. The proposal of management group is to develop a strategy within the framework of Latvian migration policy that would help in attracting foreign scientists for work and life in Latvia, thus in general promoting scientists' mobility in the country.

As a tool for the attraction of investments in Research and Development (R&D) it is necessary to promote and improve the cooperation between public – private sector. Besides that, to promote technological initiatives based on the public – private sector cooperation at the European scale, it is necessary to take pains to organizing coordinated activity of all the institutions connected with the specific problem both on the national and EU scale.

In order to promote the tieback of public – private sector and active cooperation in research work and development of innovative technologies, in Latvia there has been approved and introduced State support programme ''Support for the development of new products and technologies''. The programme is administered by Latvian investment and development agency and it gets additional financing from the European Regional Development Fund. In order to continue improving the cooperation between the sectors of education, science and industry, that would promote the formation of new competitive products and companies, there is necessary national support in developing the support infrastructures for innovations (competence centres, technological centres, parks). In such kind of centres there would be coordinated educational activities of new specialists, promoted the cooperation between scientists and businessmen, as well as considered the issues connected with development strategies of the branch.

2.2. Cooperation of scientists and science centres with businessmen

The role of innovations in our economics is constantly growing: it promotes the development of certain companies, as well as the growth of national economy and social welfare. The creation and implementation of new ideas is important for all businessmen – whatever the type and amount of their activity is. Innovation process gives profits not only to businesspeople, but also to its participants – scientists, national institutions, educational establishments – and to the society in general. Innovations in business play an important role in the promotion of Latvian businessmen competitiveness, especially after Latvia has joined the European Union.

However, the statistics shows that in Latvia only one fifth of companies introduce innovations. The state financing granted to science and research in Latvia considerably falls behind the level of the advanced EU countries. One of the fundamental barriers for the development of innovative activity in Latvia is insufficient cooperation between businessmen and scientists. Businessmen in Latvia lack information (and wherewith interest) about the possible cooperation with scientists and introduction of innovations. Nevertheless, a large part of scientists work on fundamental research, which certainly is important for their academic career, but still does not promote the emergence of innovative products in the market. In Latvia there have been developed a number of documents and strategies connected with the improvement of innovation policy, however the introduction mechanisms of these documents do not function in practice and thus the situation is improving slowly.

In order to promote the mutual interest of businessmen and scientists regarding the development and introduction of new competitive products, the Employers' Confederation of Latvia (LDDK) has developed suggestions for the cooperation between businessmen and scientists, by defining the role of LDDK in the promotion of cooperation. The model of cooperation has been built on the report about the situation of innovation policy in Latvia, innovation support programmes and structures, for example, the cooperation of businessmen with Latvian and foreign scientists, and the conclusions given by Science and Business Partnership Council. The model of cooperation consists of three parts:

1) summary of cooperation obstacles;
2) strategy of cooperation model;
3) necessary actions to be taken.

Businessmen and scientists have to work together on the development of suggestions for legal mechanisms that would promote the investments in innovations. The wish of businessmen to invest in innovations definitely would be encouraged by so called ''reinvested profit'', when a company grants a part of its profit to the development of innovative products and in return gets, for example, a discount for business tax. Yet another important issue to be considered is faults in the systems of education and science. Businessmen and scientists have to develop offers and represent their own interests in order to turn students' attention to technological branches and stimulate scientists' interest regarding applied research.

3. INNOVATIVENESS OF AMERICAN AND JAPANESE COMPANIES IN SOCIO-CULTURAL CONTEXT

Corporate innovation system is a subsystem of the economic system. The economic system is assumed here as a subsystem of the socio-political context, which ultimately is a subsystem of the overarching cultural context. The most comprehensive environmental factor determining the innovation system of a country is its culture. Most relevant to the influence of innovation: uncertainty avoidance, power distance and individualism [3].

- ✓ **Cultural contextual factors:** uncertainty avoidance, power distance, individualism.
- ✓ **Sociopolitical contextual factors:** overall economic system, educational system, socio - demographic factors.
- ✓ **Economic contextual factors:** corporate environment, importance of industrial sectors, drivers of innovation.
- ✓ **Management related contextual factors:** corporate governance, management strategies, organizational structure.

Uncertainty avoidance – Countries with high uncertainty avoidance cultures tend to avoid risk and ambiguity and prefer incremental innovations, where each step is small and ambiguity is more easily kept under control.

Power distance – Countries with a high level of power distance have tendency to avoid challenging or openly criticizing authority systems. In such cultures incremental innovation adds to existing knowledge, but rarely challenges it. In countries low in power distance paradigm shifts that are based on challenging existing authority such as traditionally held beliefs, institutions or individual power figures occur more frequently and innovations tend to be therefore more transformational.

Individualism – Cultures with high degrees of individualism stress the potential and value of ideas emanating from the single individual whereas collectivistic cultures exhibit more trust in group efforts and outcomes. Transformational innovations are often realized by few individuals and often by outsiders who exhibit strong beliefs in themselves.

Japan displays particularly high levels of incertainty avoidance, a high degree of power distance and a low degree of individualism which makes it culturally predisposed to favor incremental innovations. This contrasts starkly with the US culture which displays low degrees of uncertainty avoidance and power distance, and very high degree of individualism making it a perfect candidate for transformational innovations [3].

Innovate America: educate next – generation innovators; deepen science and engineering skills; explore knowledge intersections; equip workers for change; support collaborative creativity; energize entrepreneurship; reward long – term strategy; build word – class infrastructure; invest in frontier research; attract global talent; create high – wage jobs [4].

4. SUSTAINABLE DEVELOPMENT STRATEGY AND SYSTEM IN LATVIA AND EUROPEAN UNION

The key objective of the scientific and technological policy development in Latvia and European Union is to build science and tehnology as the basis for the long term development of a civil society, economics and culture, ensuring the implementation of the knowledge economy and its sustainable growth. In determining the scientific and technological development policy goals and objectives, the following principles are taken into account [1]:

- science and research are the basis of a competitive higher education and the knowledge society;
- research and technological development is the basis of science-intensive production and technological manufacturing industries;
- scientific and technological development is a key factor for Latvias sustainable economic development, public welfare, environment and natural resource conservation;
- science and research, especially in the humanities, in the basis of self –confidence and the necessary precondition of the development of national culture, national identity;
- Latvian science, research and innovation is a integral and harmonious part of the world of science and the European Research area.

European Unions strategy for smart, sustainable and inclusive growth, "Europe 2020" raised the basic objective of investing 3% of the European Union (Gross Domestic Product) GDP in research and development. Latvia has set quantitative target to increase investment in research and development funding for 1.5% of the Latvian GDP by 2020 [23].

5. ENVIRONMENT PROTECTION EUROPEAN UNION

Over the past decades the European Union has put in place a broad range of environmental legislation. As a result, air, water and soil pollution has significantly been reduced. Chemicals legislation has been modernised and the use of many toxic or hazardous substances has been restricted. Today, EU citizens enjoy some of the best water quality in the world and over 18% of EU's territory has been designated as protected areas for nature.

The 7th Environment Action Programme (EAP) will be guiding European environment policy until 2020. Healthy environment stem from an innovative, circular economy where nothing is wasted and where natural resources are managed sustainably, and biodiversity is protected, valued and restored in ways that enhance our society's resilience. Our low-carbon growth has long been decoupled from resource use, setting the pace for a safe and sustainable global society.

It identifies three key objectives:

- ✓ to protect, conserve and enhance the Union's natural capital;
- ✓ to turn the Union into a resource-efficient**,** green, and competitive low-carbon economy;
- ✓ to safeguard the Union's citizens from environment-related pressures and risks to health and wellbeing.

Four so called "enablers" will help Europe deliver on these goals**:**

- ✓ better implementation of legislation;
- ✓ better information by improving the knowledge base;
- ✓ more and wiser investment for environment and climate policy;
- ✓ full integration of environmental requirements and considerations into other policies.

Two additional horizontal priority objectives complete the programme:

- ✓ to make the Union's cities more sustainable
- ✓ to help the Union address international environmental and climate challenges more effectively [26].

6. INTERNATIONAL COOPERATION FOR DEVELOPMENT AND ECONOMIC GROWTH

Science, technology, and innovation (STI) and innovation are crucial for sustainable long-term economic growth, both in developed and developing countries, even more so in the aftermath of the economic crisis. STI also has a major part to play in addressing the global challenges which are discussed in the following sections, including adaptation to climate change, food, water and energy security and health.

Action needs to be taken by governments at national and regional levels to help promote innovation, research, and development in both the private and public sectors, including putting in place the necessary "framework conditions" such as openness to international trade and investment, a healthy financial system [25].

The OECD is a unique forum where governments work together to address the economic, social and environmental challenges of globalisation. The OECD is also at the forefront of efforts to understand and to help governments respond to new developments and concerns, such as corporate governance, the information economy and the challenges of an ageing population. The Organisation provides a setting where governments can compare policy experiences, seek answers to common poblems, identify good practice and work to coordinate domestic and international policies.

The key engine for development: economic growth and a stronger global economy. They are: macro-economic policy, trade, investment, financial regulation, science, tehnology and innovation. If there were ever any doubt about the importance of economic growth, the interconnectedness of the global economy and the need for concerted collective action, the economic crisis has dispelled it. A crisis which began in the financial sector of developed countries spilled over rapidly into the real economy of those countries, and then into the global economy-with a direct impact on development.

These challenges are inextricably interlinked both with each other and with our development agenda. They are challenges which lie at the very heart of the OECD mission. The first aim set out in its founding Convention is to promote policies designed to achieve the highest sustainable economic growth and employment and a rising standard of living in Member countries, while maintaining financial stability and thus to contribute to the development of the world economy.

The second aim is to contribute to sound economic expansion in member and partner countries in the process of economic development.

The OECD is working on a number of policy areas, including: cross-cutting work on green growth and innovation; economic analysis and forecasting, analysis of trade policy issues and its role in setting export credit rules; monitoring investment policies and setting guidelines for multinational enterprises; developing guidance on financial markets, banking and insurance; assessing how science, tehnology, and innovation policies can contribute to sustainable economic growth and meeting global development objectives; and on social (employment, education, health) and environmental policy issues [8].

7. CONCLUSIONS

- Competitiveness system: Innovation embedded in its socio-cultural context factors: cultural contextual factors (uncertainty avoidance, power distance, individualism); sociopolitical contextual factors (overall economic system, educational system, socio - demographic factors); economic contextual factors (corporate environment, importance of industrial sectors, drivers of innovation); management related contextual factors (corporate governance, management strategies, organizational structure).
- The quality of community development is characterized by the following priorities – smart growth, sustainable growth and inclusive growth.
- In the article there was discussed and analysed the concept of innovation – innovation as creative process and innovation as technological process of introducing innovations, which results in the development of new products, services and industrial technologies. Scientifically technological innovation is connected with eight kinds of activities: research and development of technologies (fundamental research, applied research, development of technologies); acquisition of nonmaterial technologies; acquisition of material technologies; industrial engineering; pre-production activities; marketing of new products; designing work; acquisition of another capital.
- Schematically innovation process can be depicted by linear and nonlinear model. In the linear model innovation process is depicted as one-way flow of information without any feedback. However the processes of nonlinear model are simultaneous and happen through interaction, which means continuous cooperation between scientists and the market.
- For successful implementation of innovative activity in advanced countries systems of national innovation are formed, where innovative companies are in mutual interaction, the system of education – science, the system of government and finance. In the article there have been disclosed optimal activity features of national innovation system. It is important for universities and scientific institutions to produce not only highly qualified specialists, but also to meet the demand for scientific research and output.
- Innovative organization is the kind of organization which carries out any kind of innovations, which carries out technological innovations, which gets the state support for innovative activity – financial stimulus. In the context of the work done by scientists and innovative organizations Latvia has the following scripts of further progress – pessimistic, stagnation and optimistic convergence script. The process of innovations gives profits not

only to businessmen, but also to its participants – scientists, state institutions, educational establishments – and the society in general.
- When considering the mutual cooperation between businessmen and scientists and their interest in creating and introducing new, competitive products, it is important to be aware of the obstacles mentioned by Latvian businessmen and scientists, which have been disclosed in the conclusions part of the article
- Healthy environment stem from an innovative, circular economy where nothing is wasted and where natural resources are managed sustainably, and biodiversity is protected, valued and restored in ways that enhance our society's resilience. Our low-carbon growth has long been decoupled from resource use, setting the pace for a safe and sustainable global society.

REFERENCES

1. Bāliņa, S. (2011) *Development of Science and Technology in Latvia, 2011.* Ministry of Education and Science.
2. Burns, P. (2001) *Entrepreneurship and small business.* Great Britain: Antony Rowe Ltd, Chippenham.
3. Hofstede, G. (2001) *Culture_s consequences. Comparing values,behaviors, institutions and organizations across nations.* (2nd ed.). Sage, London, Thousand Oaks.
4. Innovateamerica (2005) *Innovateamerica.* National innovation initiative summit and Report. Council on Competitiveness.
5. Latvijas ilgtspējīgas attīstības stratēģija līdz 2030.gadam. (2010) Rīga: LR Saeima.
6. Lane Distefano and Maznevski, 1997 The modern business has no place to hide. It has no place to go but everywhere.
7. Martin, R., Kitson, M., Tyler, P. (2006) *Regional Competitiveness.* United Kingdom: Routledge.
8. OECD (2011) *Better policies for Development. Recommendations for Policy Coherence.* OECD and Eurostat.
9. OECD, Eurostat (2005) *Oslo Manual Guidelines For Collecting And Interpreting Innovation Data*. Third edition , A joint publication of OECD and Eurostat.
10. OECD (2008) *Science, Technology and Industry Outlook: Science & Information Technology.* OECD.
11. Pelše, G., Ruperte, J. (2003) *Uzņēmēja rokas grāmata.* Rīga: SIA *J.L.V.*
12. Porter, M. E. (2009) *Moving to a New Global Competitiveness Index in World Economic Forum.* The Global Competitiveness Report 2008–2009. WEF.
13. Pudelko, M., Mendenhall, M. E. (2008) *The contingent nature of best practices in National competitiveness: The case of American and Japanese innovation processes.* Elsevier Ltd.
14. Reģionu attīstība Latvijā 2009. (2010). Rīga: Valsts reģionālās attīstības aģentūra.
15. Sener, S., Saridogan, E. (2011) *The Effects of Science-Technology-Innovation on Competitiveness and Economic Growth.* Published by Elsevier Ltd. Selection and/or peer-review under responsibility of 7th International Strategic Management Conference.
16. Stillman, J.R. (1996) *Public Administration. Concepts and Cases.* Boston, Toronto: Houghton Mifflin Company.
17. The European Charter for Researchers (2006) Brussels: European Commission, Directorate – General for Research.
18. Timmons, Jeffry, A. (1994) *New venture creation: entrepreneurship for the 21st century*. New York, USA: WM. C. Brown Communications, Ins.

19. Vaidere, I., Vanags, E., Vanags, I. u.c. (2006) *Reģionālā politika un pašvaldību attīstība Eiropas Savienībā un Latvijā.* Rīga: Latvijas Universitātes Akadēmiskais apgāds, Latvijas Statistikas institūts.
20. Vanags, E. (2007) *Valsts pārvaldes reformas ārvalstīs un Latvijā.* Rīga: Latvijas Statistikas institūts.
21. Zinātne, pētniecība un inovācija Latvijas izaugsmei. (2007) Rīga: SIA Apgāds *Zinātne*.
22. Ziņojums par Latvijas tautsaimniecības attīstību. (2010) Rīga: LR Ekonomikas ministrija.
23. http://europa.eu/pol/rd/index_lv.htm .
24. http://unesdoc.unesco.org/images/0023/002354/235407e.pdf .
25. http://ec.europa.eu/environment/sustainable-development/index_en.htm .
26. http://ec.europa.eu/environment/action-programme/ .

CYSENI 2018, May 23-25, Kaunas, Lithuania
ISSN 1822-7554, www.cyseni.com

IMPROVEMENT OF THE KTU EXPERIMENTAL DEVICE FOR THE REDUCTION OF NO_X USING CHARCOAL

E. Kaliatkienė
Kaunas University of Technology
K. Donelaičio str. 73, LT-44249 Kaunas – Lithuania
Email: edita.kaliatkiene@ktu.edu

ABSTRACT

Kaunas University of Technology (KTU), Thermal and Nuclear Energy Department has experimental device in which experiments based on the selective catalytic methods are provided. The experimental device consisted of gas fired water heating boiler, temperature control system, flow control devices and gas analyzer of O_2, CO, NO, NO_2 and NO_x. Using this experimental device experiments for the NO_x reduction using charcoal were provided. Preliminary results, provided in the early investigations by other KTU PhD students, showed 65% of NO_x reduction efficiency using charcoal as a catalytic material. Catalysis using charcoal is attractive because of its economic and ecological aspects. It was decided to continue the investigation and experiments in this field. However, to continue the investigations of NO_x reduction using activated carbon it is needed to update and to calibrate existing experimental device. In this article short literature overview of charcoal usage for the NOx reduction are presented as well as updated experimental device and preparation to the experiment.

Keywords: selective catalytic, NOx reduction, carbon.

1. INTRODUCTION

The combustion products that contain a wide range of harmful substances, such as nitrogen oxides (NO_x) and carbon monoxide (CO), are emitted into the environment during the combustion of the fuel. In Lithuania, as well as throughout the European Union, strict environmental requirements are applied. Emission limits for combustion plants are reducing increasingly. Consequently, emission reduction techniques that reduce the emission of harmful substances in the combustion products are very relevant. One of the ways to reduce contamination in combustion products is the selective catalytic method. This NOx reduction method is usually based on the cleaning of combustion products using catalytic materials. However, efficient catalysts are based on rare and expensive metals and are therefore expensive and not widely used [1, 2, 3].

These days more and more catalysts are produced which are based on cheaper materials. The Department of Thermal and Atomic Energy in Kaunas University of Technology (KTU) has tested the NO_x reduction method which is based on the usage of charcoal instead of catalytic materials. This is an attractive way to reduce NOx due to its economic and ecological aspects. The experimental study showed promising results. The NOx reduction efficiency of 65% was achieved [4].

The main idea of this study is to use the charcoal (activated carbon) as environmentally friendly and inexpensive material to maximize NOx reduction in the combustion gases. An analysis of scientific literature has shown that there are several ways to use charcoal for the reduction of NO_X.

2. NO_X REDUCTION USING AN ACTIVATED CARBON

There are a lot of technically tested processes and combustion technology modification measures in order to reduce the formation of nitrogen oxides. Each method has its advantages and disadvantages, and not all methods could be successfully applied in combustion plants. In this work, the method of reducing NO_x by using charcoal is considered.

The reaction of carbon with the three nitrogen oxides – NO_2, NO and N_2O are presented in [5]. At low temperatures a mixture of NO and O_2 will equilibrate to include significant amounts of NO_2 and N_2O_4. Fig. 1 depicts the equilibrium concentrations dependence on temperature of a mixture containing the equivalent of 500 ppm of NO and 10% O_2 in nitrogen. The formation of NO_2 is strongly favoured at temperatures below 500 °C. Below 100 °C the condensation of NO_2 into N_2O_4 becomes prominent. The rate of the $2\ NO_2 \leftrightarrow N_2O_4$ equilibrium is rapid, so that an NO_2 feed at low temperature will contain some N_2O_4.

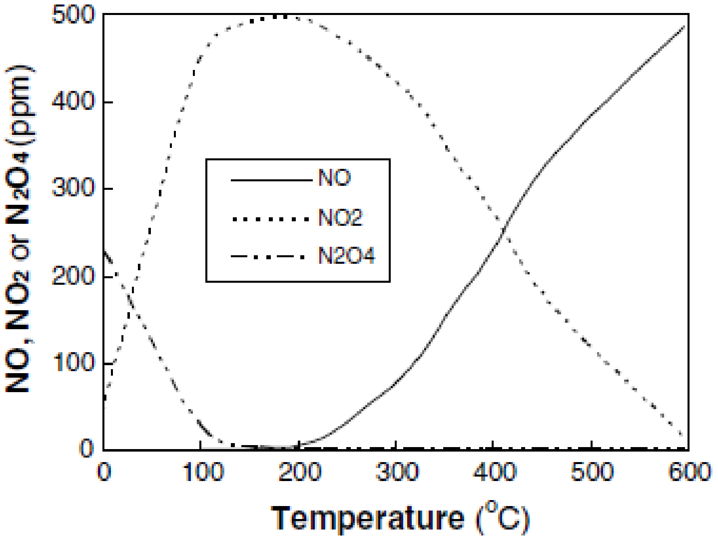

Fig. 1. The equilibrium concentration of the NO and O_2 mixture depending on the temperature [5]

Carbon reaction with the NOx are presented here:

- Carbon reaction with NO_2

$$2\ NO_2 + C = 2\ NO + CO_2 \tag{1}$$

$$NO_2 + C = 1/2\ N_2 + CO_2; \tag{2}$$

- Carbon reaction with NO

$$2\ NO + C = N_2 + CO_2 \tag{3}$$

2.1. NO_x reduction using activated carbon together NH_3 and O_2

The NO reduction process is already starting at 150 °C. This NO reduction method is effective if using activated carbon with vanadium additives, ammonia (NH3) or water vapor. Using this method, NO can be reduced to 90%. The activated carbon with about 3% of vanadium without other additives, can reduce NO to 25% to 45%. In order to have greater NOx reduction, it is necessary include other materials in the process. The comparision results are presented in Fig. 2 [1].

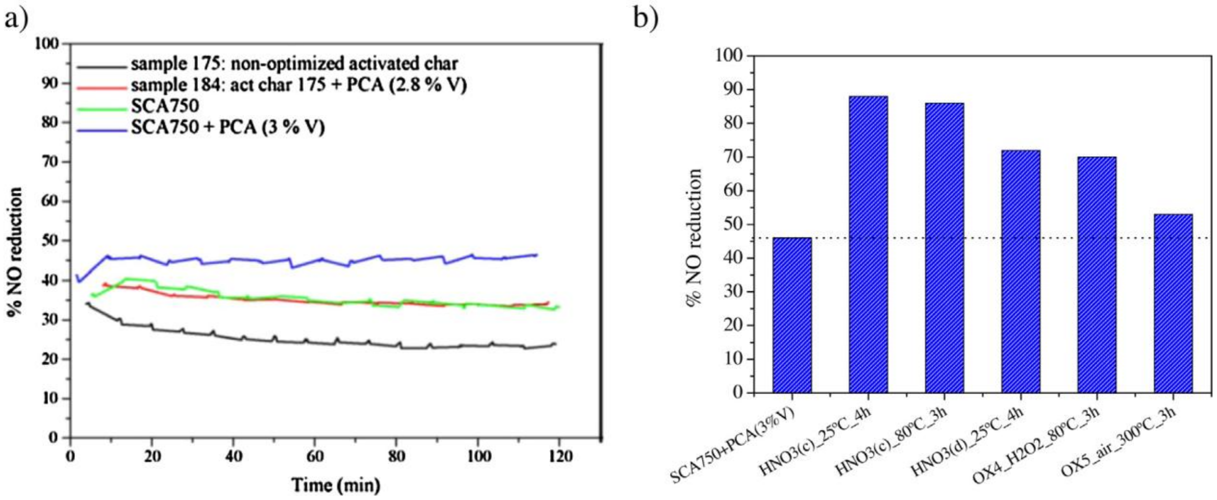

Fig. 2. (a) Vanadium-coated activated carbon; (b) catalysts prepared using pre-oxidized carbon supports [1]

2.2. Activated carbon briquettes

Another way to reduce NO is to use activated carbon briquettes. After treatment carbon briquettes with HNO_3, H_2SO_4, may have a high conversion rate of NO.

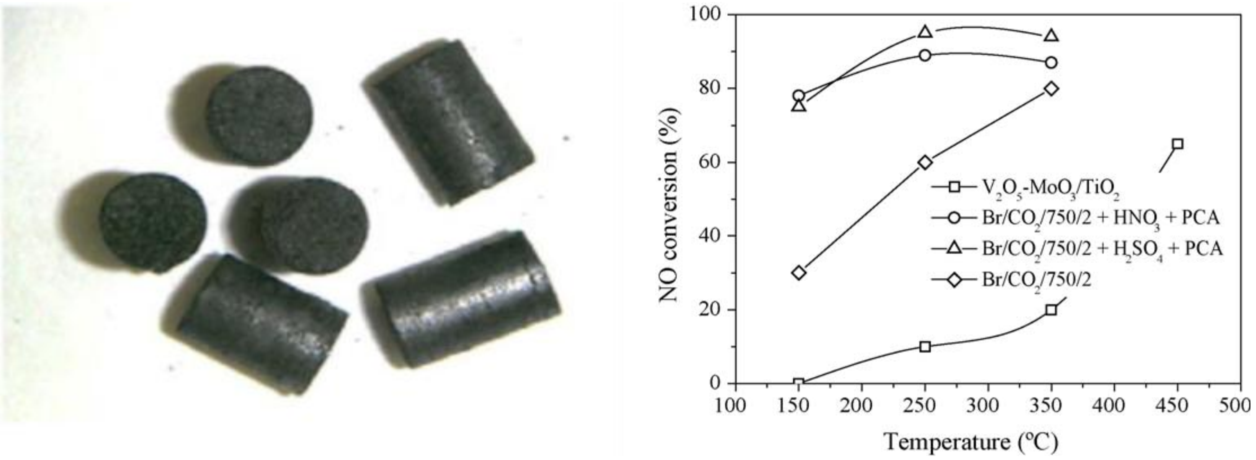

a) b)

Fig. 3. a) image of the carbon briquettes; b) NO conversion as a function of temperature for a commercial V_2O_5–MO_3/TiO_2 catalyst, for the PCA-loaded catalytic briquettes oxidized with HNO_3 and H_2SO_4 and for the non-loaded carbon briquette Br/CO2/750/2

Fig. 3 shows the NO conversion measured for the catalytic briquettes treated with HNO_3 and H_2SO4 at different reaction temperatures, in comparison with the activity determined for a commercial V_2O_5 (1.5%)–MO_3 (6%)/TiO_2 catalyst, under 800 ppm NO, 800 ppm NH_3 and 0.9% O_2, using a total gas flow of 120 mL/min. Non-loaded Br/CO_2/750/2 briquette shows lower activities in the whole temperature range. The increased catalytic activity obtained as a result of adding a metallic active phase is much more noticeable at lower temperatures, i.e. 30% NO conversion measured for the carbon briquette versus 78% obtained for the HNO_3-oxidized catalytic briquette loaded with PCA.

NO conversion increases with increasing temperatures for the catalytic carbon-based briquettes, reaching maximal conversions around 90–95%, slightly higher than the ones measured at 350 ^{o}C. The commercial TiO_2-based catalyst yields very low conversions at lower temperatures.

Conversion increases with increasing reaction temperature, but even at 450 °C this catalyst is able to convert only up to 65% of the NO present in the inlet gas.

2.3. Carbon coated monoliths

Experimental studies shown that the 100% conversion of NO at 207 °C temperature was achieved when initial mixture of 5% vanadium was treated with sulfuric acid (SO_2) or steam (H_2O). Meanwhile, with an initial catalyst mixture containing 5% vanadium, the highest conversion value is reached up to 60% at 247 °C temperature [3].

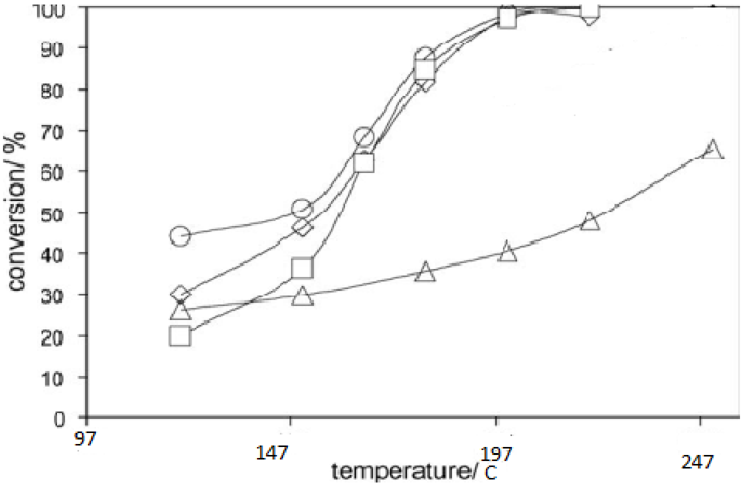

Fig. 4. NO reduction versus temperature. Initial gas mixture for the catalysis: 500 ppm NO, 600 ppm NH3, 3% O_2 and Ar. (△) 5% V/CCM catalyst; (○) 5% V sulphate catalyst; (◊) 5% V sulphate catalyst with additionally suplemented of SO_2 100 ppm; (□) 5% V sulphate catalyst with additionally suplemented of vapor 5% [3]

3. EXPERIMENTAL DEVICE IN KAUNAS UNIVERSITY OF TECHNOLOGY

In the experimental device, located at Kaunas University of Technology, the efficiency of catalysts was investigated using realistic combustion products for water heating boilers [7]. This experimental device was constructed 10 years ago, in 2008. Schematic view of this device is presented in Fig. 5.

The combustion products, using vacuum pump 10, are pumped through an experimental section with catalytic elements. The flow rate of combustion products pumped through catalytic elements could be regulated between 2.75 and 30 l/min. The flow of the combustion products are regulated using valve 11, and set by the gas meter 9. The experimental section through which the combustion products are flowing is heated by electrical heaters. The two electric heaters EC1 and EC2 are in the heating zone of the combustion products, i.e. at the front of the experimental section. In this way, the combustion products are heated to the required temperature prior to the catalytic elements. The part of the experimental section where the catalytic elements are located also heated by separate two electric heaters EK3 and EK4. Their purpose is to compensate heat loss to the environment. The power and load of the heaters are regulated. The heater load is changed by switching on or off the heater. The heater power is regulated changing the voltage supply within the 0–220 V range. In this way, the temperature of the combustion products could be increased, decreased or kept constant during the time. The deviations from the set temperature could be ± 5 °C. The temperature range of the combustion products could wary between 50 to 700 °C. The temperature of the combustion products is measured using K type thermocouples. Thermocouples are connected to devices that could display and regulate the current temperature with the help of electric heaters. Thermocouples are located on the axis of the experimental section.

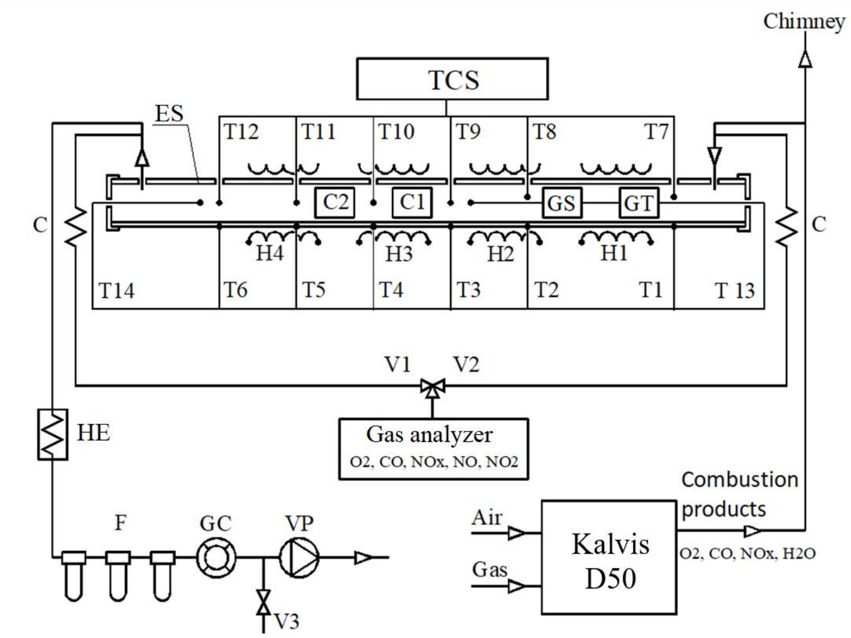

Fig. 5. Scheme of the experimental device. F – filters; C – air cooler in order to measure the combustion products; R – flow meter; ES – experimental section; GT – gas flow turbulizer; GS – gas flow stabilizer; C1 and C2 – catalysts; GC – gas flow counter; VP – vacuum pump; GA – gas analyzer; V – valve; TCS – temperature control system; H – electric heater; T – thermocouple; HE – heat exchanger

Combustion products are generated in the boiler "Kalvis D50". In the boiler generated combustion products mainly flows to the chimney. Part of combustion products using vacuum pump (VP) are taken from the chimney and access the experimental section (ES) through the outlet. The combustion products are flowing through the experimental section, which is heated using the heaters H1 - H4 (temperature controlled by thermocouples). Further, combustion products flows through the outlet to the cooler (HE), which is cooled with water. The combustion products from the cooler get to the filters (F), which filter and observe the water from the combustion products. Later the combustion products pass through a gas meter (GA) and through the vacuum pump (VP) and exhausted to the ventilation.

3.1. Experimental results

Various experimental studies were performed using experimental device which was described in the previous section. The purpose of these experimental studies was to investigate catalytic elements and to find witch catalytic element have biggest NO_x reduction rate. NO_x having combustion products was going through the catalytic elements constructed from the cheap materials comparing to the expensive, in the industry used. Used catalytic elements were composed of Al, Cu, Mg, Co. The experimental results of these catalytic elements were presented in literature [7, 4].

In the one of the experiments, the charcoal was used as a catalytic substance. This experiment differs from the other ones in which the metals were used. The charcoal was shredded to increase the area of the "active" surface. The crushed charcoal is placed in a metal container and covered with a sieve. During this experiment, a very small flow of combustion products (2.8 l/min) was flowing through the experimental section. The temperature in the experimental section was changed from 50 to 600 °C. Also, during the experiment, the oxygen content in combustion products was changed (0.2%, 0.6%, 1.2% of O_2 concentration was used). In this study the NO_x reduction effect was studied. Experimental results showed that NOx reduction depends on the temperature. However, oxygen concentration did not have significant results to the NO_x reduction. Experimental resultas are presented in Fig. 6. As it is shown in the Fig. 6, ~65% of the NO_x reduction could be achieved. The charcoal catalyst is also attractive due to its economic and ecological aspects.

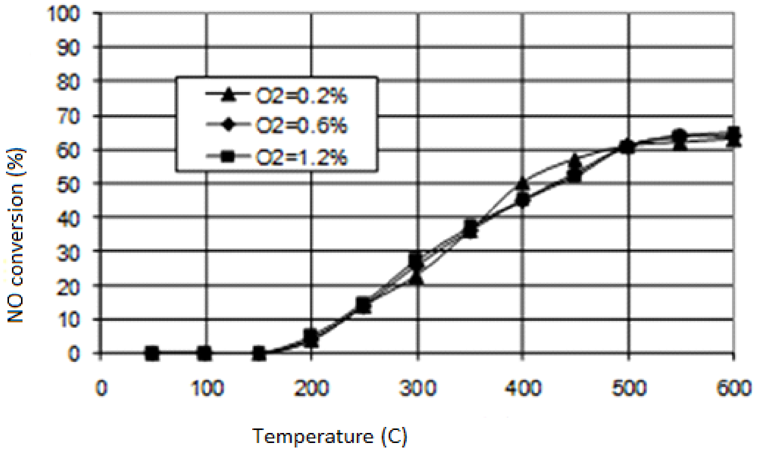

Fig. 6. Nitrogen oxide reduction using charcoal. Composition of combustion products at the entrance was: CO = 4500 ppm; NO_x = 40 ppm; G = 2.8 l/min [6]

4. IMPROVING OF THE EXPERIMENTAL DEVICE

The last experimental test was conducted in 2008. Therefore, inorder to continue exploitate an experimental device it is need to make certain changes.

4.1. Improvements of the experimental section

In the previous version of experimental device the temperature control system (TCS) was used where 14 thermocouples was used. However in the experiments with the charcoal there is no need to use so many thermocouples. For the proper work of the TCS 6 thermocouples are enough, so it was decided to reduce the number of the thermocouples. It was done to optimize the experimental work and do not have redundant information. Scheme of the improved experimental section is presented in the Fig. 7.

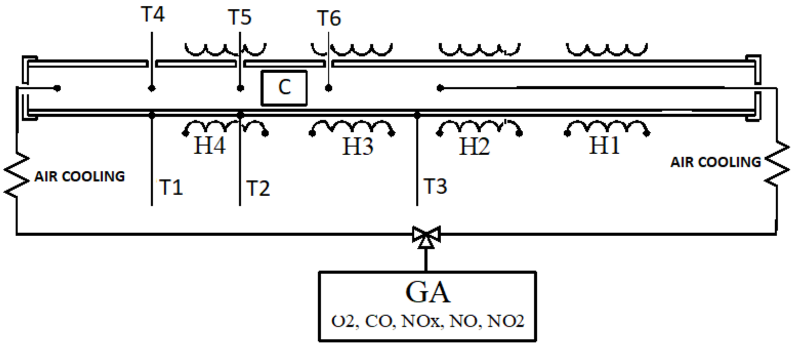

Fig. 7. Scheme of the improved experimental section

Another change in experimental device was related to the pumping of combustion products – old vacuum pump has been replaced with the new one with different characteristics, which are more suitable for the experiments. However, in order to stabilize the flow rate it was needed to add additional volume. The three-way valve has been replaced with two valves. Additional rotameter was mounted to experimental device in order more easily detect and control appropriate flow of the combustion products during the experiment.

In the improved experimental device the measure points of gas composition was changed (Fig. 7). It was decided using Gas Analyzer (GA) to measure combustion gases ~10 cm before the container with charcoal and ~15 cm after container instead of making measurements at the beginning and end of the experimental section. These improvement gives opportunity to reduce influence of the dilution of the combustion gases due to the possible small leakages in the experimental section.

4.2. Improvement of the container with charcoal

In the experimental device the combustion products are going through the experimental section where the container with the charcoal is located. Due to the ongoing NO_x reaction with the carbon, the quantity of charcoal in the container is decreasing and due to gravity slips down. Consequently, the gap between the top wall of container and the charcoal appears. This place has a much lower hydraulic resistance, so combustion products flows through this gap and did not contact with the charcoal (Fig. 8, a). This situation gives inaccurate experimental results. To avoid these consequences, a container with the charcoal was improved. Two metal plates were placed in the container (Fig. 8, b). These plates create resistance and combustion products should flow through the middle of the container. This ensures that during the experiment the combustion products contacts with the carbon from the charcoal and experimental results will be more precise.

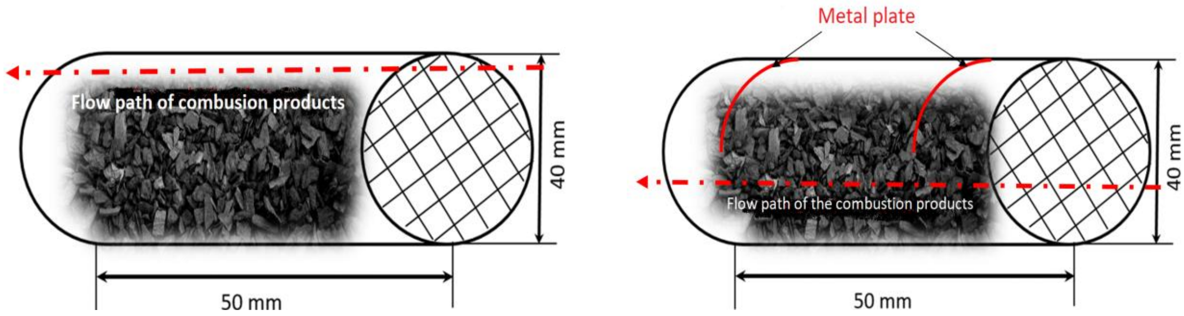

a) b)

Fig. 8. Container with charcoal: a) original version; b) improved version

5. CONCLUSIONS

1. The literature review shows that charcoal is not widely used for NO_x reduction and these experimental studies would be useful.
2. Previous studies carried out at the experimental device in the Kaunas Technical University showed that NO_x could be reduced using the charcoal as catalytic material. ~65% of the NOx reduction could be achieved.
3. The experimental device was improved. Some primary experiments are provided, but do not presented in this article. In the future it is planned to provide various experimental studies: to variate the fraction of the charcoal, temperature of combustion products, different excess of oxygen in the combustion gasses and other parameters.

REFERENCES

1. Marı´a Jesu´s La´zaro, Sonia Ascaso, Sara Pe´rez-Rodrı´guez, Juan Carlos Caldero´n, Marı´a Elena Ga´lvez, Marı´a Jesu´s Nieto, Rafael Moliner, Alicia Boyano, David Sebastia´n, Cinthia Alegre, Laura Calvillo, Veronica Celorrio. Carbon-based catalysts: Synthesis and applications. International Symposium on Air & Water Pollution Abatement Catalysis (AWPAC) – Catalysis for renewable energy. 2015.
2. M.E. Gįlvez, A. Boyano, R. Moliner, M.J. Lįzaro. Low-cost carbon-based briquettes for the reduction of NO emissions: Optimal preparation procedure and influence in operating conditions. Instituto de Carboquķmica (CSIC), Miguel de Luesma Castįn, 4, 50018 Zaragoza, Spain. Journal of Analytical and Applied Pyrolysis 88 (2010) 80–90.
3. E. Garcı´a-Bordeje´, J.L. Pinilla, M.J. La´zaro, R. Moliner. NH3-SCR of NO at low temperatures over sulphated vanadia on carboncoated monoliths: Effect of H_2O and SO_2 traces in the gas feed. Instituto de Carboquı´mica (CSIC), Miguel Luesma Casta´n 4, 50015 Zaragoza, Spain. 12 May 2006.
4. Kestutis Buinevicius, Regimantas Melkunas. Catalytic Reduction of NOx AND CO emissionS from boilers. May 22-23, 2008. 7th International Conference Environmental engineering. Kaunas University of Technology, Department of Thermal and Nuclear Energy, K.Donelaicio 20, Kaunas, Lithuania.
5. B.R. Stanmore, V. Tschamber, J.-F. Brilhac. Oxidation of carbon by NOx, with particular reference to NO2 and N2O. Laboratoire Gestion des Risques et Environnement, Universite´ de Haute Alsace, 25 rue Chemnitz, 68200 Mulhouse, France. 21 May 2007.
6. R. Melkūnas, K. Buinevičius. Oxygen Effect on Catalytic Reduction of Nitrogen Oxides. Conference materials Heat energy and technology 2008, Kaunas University of Technology, January 31-February 1, Kaunas. (in Lithuanian)
7. R. Melkūnas, E. Puida, Experimental facility, Conference Materials Heat Energy and Technologies 2007, Kaunas University of Technology, 1-2 February, Kaunas (in Lithuanian).